



## Raman spectroscopy of ZnS quantum dots



J. Trajić<sup>a,\*</sup>, R. Kostić<sup>a</sup>, N. Romčević<sup>a</sup>, M. Romčević<sup>a</sup>, M. Mitrić<sup>b</sup>, V. Lazović<sup>a</sup>, P. Balaž<sup>c</sup>, D. Stojanović<sup>a</sup>

<sup>a</sup> Institute of Physics, University of Belgrade, 11080 Belgrade, Serbia

<sup>b</sup> Institute Vinča, University of Belgrade, 11000 Belgrade, Serbia

<sup>c</sup> Institute of Geotechnics, Slovak Academy of Sciences, 043 53 Košice, Slovakia

### ARTICLE INFO

#### Article history:

Received 2 February 2015

Received in revised form 2 March 2015

Accepted 3 March 2015

Available online 10 March 2015

#### Keywords:

Nanostructured materials

Scanning electron microscopy

X-ray diffraction

Light absorption and reflection

### ABSTRACT

ZnS nanoparticles were synthesized mechanochemically by high-energy milling. In order to investigate influence of milling time to sample properties, samples were produced in three different milling times (5 min, 10 min and 20 min). The morphology of samples has been investigated by scanning electron microscopy (SEM) and high resolution transmission electron microscopy (HRTEM). X-ray diffraction (XRD) investigation of synthesized nanocrystals identified cubic structure. From XRD, ZnS size of crystallites was estimated as 1.9 nm (after 5 min milling time), 2.3 nm (10 min) and 2.4 nm (20 min), implying that we are in strong confinement regime. The optical properties were studied by Raman spectroscopy, in spectral region 100–500  $\text{cm}^{-1}$ , excitation source was 514.5 nm ( $E_i = 2.41$  eV), which means that we are in off resonant regime. Dominant spectral structures, of comparable intensity, are registered in spectral region 130–180  $\text{cm}^{-1}$ , around 265  $\text{cm}^{-1}$  and around 345  $\text{cm}^{-1}$ . First two are assigned as second-order ZnS modes. A theoretical model of continuum medium was used to calculate frequencies of the confined optical phonons in ZnS. Satisfactory agreement with experimental results was found and mode at 345  $\text{cm}^{-1}$  is assigned as LO type phonon confined in ZnS nanocrystal.

© 2015 Elsevier B.V. All rights reserved.

### 1. Introduction

The preparation and characterization of different chalcogenides have attracted considerable attention due to their important unique physical and chemical properties [1–4]. Research on semiconductor nanoparticles stimulated great interest in recent years because of their unique optical and electrical properties. Among the semiconductor nanoparticles, zinc sulfide (ZnS) as an important II–VI semiconductor has been investigated extensively because of its broad spectrum of potential applications such as in catalysts, cathode-ray tubes (CRT) and field emission display (FED) phosphors for a long time. It can also be used for electroluminescent devices and photodiodes [5–7].

Nanoparticles differ from bulk particles because of the high surface to volume ratio, which induces the structural and electronic changes. These differences depend on particle sizes, shape and surface characteristics. The decrease of particle sizes causes an extremely high surface area to volume ratio. The enhanced surface area increases surface states, which change the activity of electrons and holes, and affects the chemical reaction dynamics. Therefore, much research on ZnS particles and their physicochemical

properties has been carried out and various methods have been used for the preparation of these nanoparticles [8–13].

In resonant Raman spectroscopy energy of the incident laser light is close to energy of electronic transition. Energy of basic interband transition ( $1s_h-1s_e$ ) in the quantum dots increases as the dimension of the dot decreases. Simple model based on effective mass approximation can estimate transition energy of QD [14]. This energy depends on the dimension of the dot, and parameters of the bulk material like energy gap, dielectric permittivity, and electron and hole effective masses. If one uses parameters characteristic for bulk ZnS ( $E_g = 3.66$  eV,  $\epsilon = 8.1$ ,  $m_{\text{eff}} = 0.28$  and  $m_{\text{heff}} = 0.49$ ) [15,16], QD transition energy  $E(1s_h-1s_e)$  for dimension  $\sim 2$  nm is over 4 eV. If energy of the incident laser light is smaller than energy of electronic transition, as in this case, Raman spectroscopy is in off resonance regime.

Exciton Bohr radius of material is the measure of confinement. If a size of QD is smaller than exciton Bohr radius the dot is in a strong confinement regime and energy spectrum is discrete. ZnS exciton Bohr radius, for parameters given in previous paragraph, is  $\sim 2.5$  nm. So we are investigating ZnS QDs in strong confinement regime.

In this paper we report Raman spectroscopy studies of the ZnS nanoparticles which are mechanochemically synthesized using high-energy milling. Samples characterization was performed using X-ray diffraction (XRD), scanning electron microscopy

\* Corresponding author. Tel.: +381 11 3713035; fax: +381 11 3713 052.

E-mail address: [jelena@ipb.ac.rs](mailto:jelena@ipb.ac.rs) (J. Trajić).

(SEM) and high resolution transmission electron microscopy (HRTEM), while optical properties were analyzed using Raman spectra measurements.

## 2. Samples preparation and characterization

Mechanochemical synthesis of ZnS nanoparticles was performed in a Pulverisette 6 planetary mill. The milling condition were: 50 balls of 10 mm diameter; weight charge of total powder mixture in the mill was 14.2 g, ball charge in the mill was 360 g, material of milling chamber and balls was tungsten carbide and rotation speed of the planet carrier was 500 rpm. Milling time was 5, 10 and 20 min using an argon atmosphere as a protective medium in the mill [17].

### 2.1. Scanning electron microscopy (SEM)

The morphology of samples has been investigated by SEM using high resolution electron microscope MIRA3 FEG-SEM, Tescan at accelerating voltage lower than 29 kV. Before that, the surface of samples was coated with an ultrathin gold layer using SC7620 Mini Sputter Coater, Quorum Technologies, with the purpose to prevent the accumulation of static electric fields at the specimen due to the electron irradiation required during imaging.

Micrographs of ZnS nanoparticles observed by SEM are presented in Fig. 1. As it can see powder is composed by well-defined and separated nanoparticles. The clusters and nanoparticles are clearly visible. These nanoparticles are spherical and have about 2 nm of diameter, which is close to the microscope resolution limit. Increase in milling time causes better nanoparticles separation, but their dimension remains almost unchanged.

### 2.2. High resolution transmission electron microscopy (HRTEM)

High resolution TEM (HRTEM-Philips Tecnai 200 operated at 200 kV), is an excellent method to study metal sulfide semiconductor nanostructures, where core-shell or stoichiometric systems can be distinguished [18,19]. HRTEM images determine the size of the nanoparticles [20], the type of structures produced [21], and also the morphologies that are possibly induced [22]. The samples were not covered by any type of conductive material to maintain their original properties. In Fig. 2 two different micrographs are shown. The HRTEM images for all three samples are very similar and we choose to present only one. In Fig. 2(a) an area of  $16 \text{ nm} \times 16 \text{ nm}$  is observed. Several clusters are clearly identified, and particularly three of them having sizes of 2.6, 3.7 and 3.4 nm respectively. The corresponding fast Fourier transform (FFT) denotes the polycrystalline material, which must be composed of nanocrystals. Lattice distance of the samples can be determined by applying a higher

magnification. In the case in Fig. 2(b) a square contrast is found in the center of the micrograph with interplanar distances of 0.27 and 0.28 nm, which implies a region with axis zone near to direction [001] [17].

### 2.3. X-ray diffraction (XRD)

The structural characteristics were obtained by the XRD powder technique. All samples were examined under the same conditions, using a Philips PW 1050 diffractometer equipped with a PW 1730 generator, 40 kV  $\times$  20 mA, using Ni filtered Co K $\alpha$  radiation of 0.1778897 nm at room temperature. Measurements were carried out in the  $2\theta$  range of 10–100° with a scanning step of 0.05° and 10 s scanning time per step.

The X-ray diffraction patterns of the ZnS powders obtained after various milling times are presented in Fig. 3. Diffraction patterns show mainly the reflection of cubic phase, according to card JCPDS 03-0524. The refracting planes denoted with (*hkl*) indices are 111, 220 and 311, respectively. Some divergence from the compared results can be explained by the fact that X-ray powder diffraction analysis gives a statistical result and that samples are with smaller size than as usually.

Using the X-ray Line Profile Fitting Program (XFIT) with a Fundamental Parameters convolution approach to generating line profiles [23] the coherent domain sizes of the synthesized powders were calculated. ZnS crystallite size was estimated to 1.9 nm (after 5 min milling time), 2.3 nm (10 min) and 2.4 nm (20 min). Nanocrystallite sizes estimated from XRD spectra are in agreement with values obtained by applied microscopic methods.

## 3. Results and discussion

The Raman spectra of ZnS powders obtained in a manner described in previous chapter were measured in the spectral range 100–500  $\text{cm}^{-1}$  at room temperature. The micro-Raman spectra were taken in the backscattering configuration and analyzed by Jobin Yvon T64000 spectrometer, equipped with nitrogen cooled charge-coupled-device detector. As an excitation source we used the 514.5 nm (2.41 eV) line of an Ar-iron laser. This excitation energy is in off-resonance regime even in bulk ZnS. It is clear, that in the QD case Raman spectroscopy is very far from the resonant regime. As we expected, registered spectral features were of low intensity. The measurements were performed at different laser power in order to optimize the signal in the whole spectral region 100–500  $\text{cm}^{-1}$ .

The Raman spectra of ZnS powders obtained after various milling times, in the spectral range from 100  $\text{cm}^{-1}$  to 500  $\text{cm}^{-1}$ , are presented in Fig. 4. Experimental Raman scattering spectra are analyzed by the deconvolution to Lorentzian curves [24].

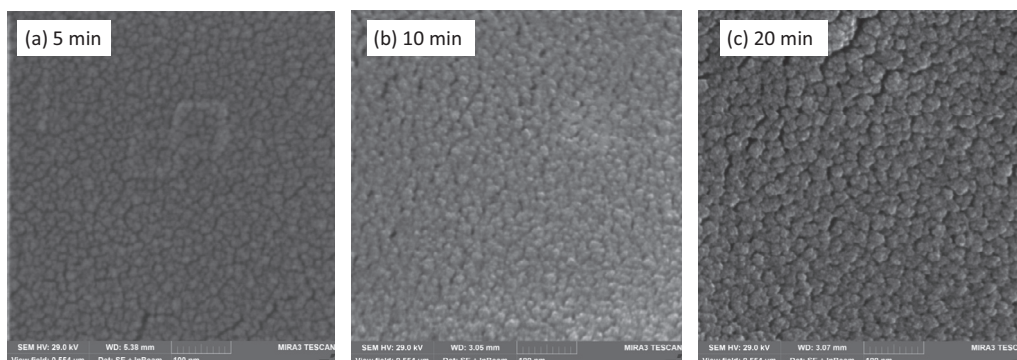
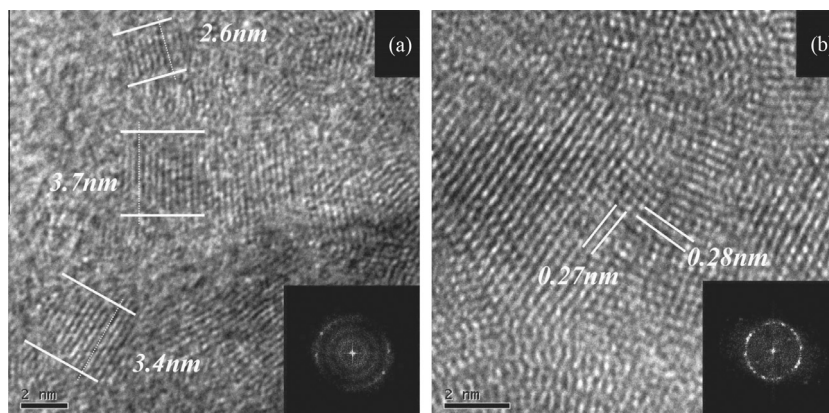
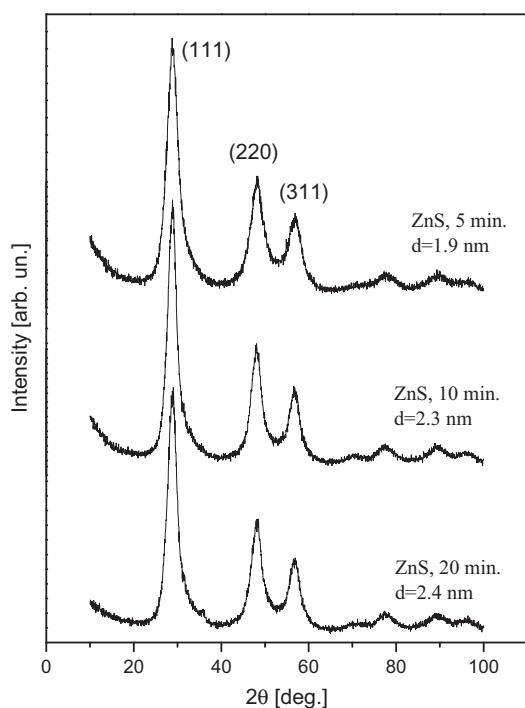


Fig. 1. SEM images of ZnS nanoparticles obtained after milling time of 5 min (a), 10 min (b) and 20 min (c).



**Fig. 2.** HRTEM analysis of mechanochemically synthesized ZnS nanoparticles: (a) identification of nanoparticle with size around 3 nm and (b) determination of structure using the interplanar distance measurement.



**Fig. 3.** XRD spectra of ZnS powders obtained after various milling times.

Black thick line presents resulting spectral curve. Positions of Lorentzians are given above the curves in Fig. 4.

Dominant wide structures in experimental spectra are: wide multimodal feature in region  $130\text{--}180\text{ cm}^{-1}$ , wide structure centered at  $\sim 265\text{ cm}^{-1}$  and wide structure centered at  $\sim 345\text{ cm}^{-1}$ , Fig. 4. These “dominant wide structures” in experimental spectra are practically of small intensities. These dominant structures are analyzed in detail.

In spectral region  $\sim 220\text{ cm}^{-1}$  there is a feature in spectra of 10 min and 20 min milling sample. This mode is hardly visible in 5 min milling sample. Also in a region  $\sim 310\text{ cm}^{-1}$ , there is a small intensity feature. These structures are briefly discussed.

In order to identify properly experimentally registered vibrational modes we will briefly review vibrational properties of cubic structure bulk ZnS.

ZnS crystallizes in cubic (zinc-blende, sphalerite,  $\beta\text{-ZnS}$ ) or hexagonal (wurtzite) structure. Lattice constant of cubic cell is:  $a = 5.4\text{ \AA}$ . The cubic unit cell contains four formula units. The space

group of the cubic unit cell is  $F\bar{4}3m(T_d^2)$ . The primitive unit cell is trigonal and contains only one formula unit i.e. two atoms. That is why the structure has six degrees of freedom, three acoustic and three optical. In the first order Raman effect only phonon wave vectors very near the Brillouin zone center (BZC) can participate. For zinc-blende structure at the BZC (point  $\Gamma$ ), both acoustic and optical modes are triply degenerate, and have symmetry species  $\Gamma_{15}(F_2)$ . In polar crystals, like ZnS, the macroscopic electric field associated with LO vibrations makes the LO mode energy greater than the TO mode energy. This effect removes triply degeneration in the BZC, producing doubly degeneration of TO mode and single degeneration of LO mode. The optical modes which we expect to see in the first-order Raman scattering of bulk sample are double degenerate TO and a nondegenerate LO phonon. Frequencies of these modes in ZnS are well established through calculations [25,26] and experimentally by polarized Raman [26–28] or

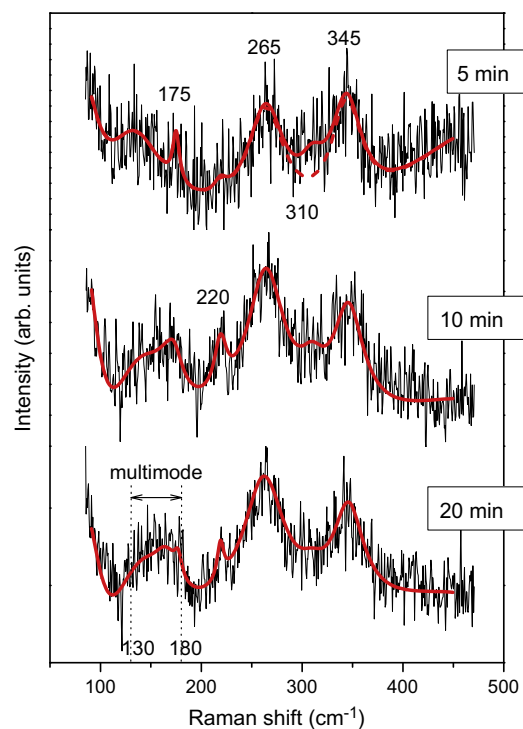


**Fig. 4.** Raman spectra of ZnS powders obtained after various milling times – 5 min:  $d = 1.9\text{ nm}$ , 10 min:  $d = 2.3\text{ nm}$  and 20 min:  $d = 2.4\text{ nm}$ .

neutron scattering [25] studies:  $\omega_{LO} \approx 350 \text{ cm}^{-1}$  and  $\omega_{TO} \approx 275 \text{ cm}^{-1}$ . If we are in resonant regime Raman scattering of LO mode will be dominant and sometimes TO mode is hard to detect especially in nonpolarized spectra. If we are in non-resonant regime all intensities decrease. Intensity of TO mode becomes even smaller and practically only LO mode is registered. Registered LO mode is wither and also of lower intensity than in resonant case. According to [26], ratio of the TO and LO mode integrated Raman intensities for excitation energy  $E_L = 2.41 \text{ eV}$  is about 0.1, as consequence of high value of corresponding electron–phonon deformation potential (DP), obtained after taking into account the antiresonance.

In the second order Raman effect momentum conservation involves two phonons. The second order Raman selection rules must be satisfied. The selection rules of the two phonon states at critical points are derived from the reducible direct product representation of the corresponding one phonon states. Scattering process originates from the BZC ( $\Gamma$ ) or from the BZ boundary points of face centered cubic lattice as: point  $X(D_{2d})$ , point  $L(C_{3v})$ , point  $W(S_4)$ , or critical directions as: direction  $\Sigma(\Gamma \text{ toward } K)$  [110]. Double degeneration of transversal modes in  $\Gamma$  point results in two traversal branches (both optical and acoustical) in direction  $\Sigma$ . Upper branch is often assigned by index  $u$  and the lower branch by index  $l$ . As wave vectors at the BZ boundary are much larger than the wave vector of the excitation used in experiments, two phonons created or destroyed in the second order scattering that satisfy momentum conservation, originate from the same point of the Brillouin zone. The combined states density tends to be large at the critical points or critical directions on the BZ boundary. Detailed investigation of ZnS vibration properties, that include calculation (based on the bond charge model lattice dynamics) of the densities of one- and two-phonon states and polarized Raman scattering measurements, is presented in [26]. Raman spectra of bulk ZnS samples with different isotopic compositions, their dependence on temperature and pressure and enable reliable assignation of observed Raman features. Strong DP for two-phonon process of cubic ZnS (two orders of magnitude higher than in the single-photon process) is responsible for the increase in the two-phonon scattering.

These information about structure are vibrational properties of bulk ZnS are the starting points for analysis that concerns ZnS QDs. In nanocrystals optical modes are confined, bulk selection rules are ruined, high surface to volume ratio increase the role of surface properties, but there is fundamental track of bulk properties. Analysis of the Raman spectra presented in Fig. 4 starts from the optical phonon region i.e. region  $275 \text{ cm}^{-1}$  ( $\omega_{TO}$ ) to  $350 \text{ cm}^{-1}$  ( $\omega_{LO}$ ).

A continuum model of the optical phonon confinement in QD is used. Parameters were transferred from the bulk phonon dispersion curves. It is limited to nanoparticles of regular shape. Although this is not the case in real nano-crystallites, we present results of calculation for ideal spherical ZnS QD. One small spherical ZnS crystal, isotropic and homogeneous inside, is considered. This consideration of confined optical vibrations in nanocrystals is based on macroscopic equation for the relative displacement of the positive and negative ions [29,30].

Parameters of this macroscopic equation are: reduced mass density,  $\omega_{TO}$ : the TO bulk frequency, the transverse charge, the unit cell volume, and  $\beta_T$  and  $\beta_L$  phenomenological bending parameters of TO and LO bulk dispersion curves. This equation is solved in spherical coordinates. The spherically symmetric solutions of equation must belong to the irreducible representations of the three-dimensional rotation-inversion group  $O(3)$  labeled as  $D_0^g$  (even) and  $D_l^u$  (odd upon inversion). The mixed modes belong to  $D_0^g, D_1^u, D_2^g, \dots$ . The dipole operator responsible for FIR absorption belongs to  $D_1^u$  while Raman transition operator for allowed

scattering belongs to  $D_0^g$  and  $D_2^g$  [31]. Frequencies of the spherical ( $l=0$ ) and spheroidal quadrupole modes ( $l=2$ ) can be calculated and in principal observed by resonant Raman scattering.

If we assume, as in [32,33], that at the surface of the sphere all components of displacement are almost zero, the electrostatic potential and the normal component of the electric displacement are continuous. After applying these assumptions one can obtain frequencies of the Raman active ( $l=0$  and  $l=2, n=1, 2, 3, \dots$ ) and FIR-active ( $l=1, n=1, 2, 3, \dots$ ) modes,  $l$  and  $n$  being the spherical quantum numbers.

The most important contribution to one-phonon Raman scattering corresponds to  $l=0$  (the quadrupole modes are active only under resonance conditions and their contribution is much smaller). This mode is excited for parallel polarizations of the incident and scattered light. The corresponding frequencies are:

$$\omega_n^2 = \omega_{LO}^2 - \beta_L^2 \left( \frac{2\mu_n}{d} \right)^2 \quad (1)$$

$\omega_{LO}$  is the LO bulk frequency ( $\omega_{LO} = 350 \text{ cm}^{-1}$  in ZnS),  $d$  is the diameter of the sphere,  $\mu_n$  is the  $n$ -th node of the Bessel spherical function  $j_1$  ( $\mu_1 < \mu_2 < \mu_3 < \dots$ ). Frequency shift (difference between  $\omega_n$  and  $\omega_{LO}$ ) for fixed  $d$  depends on  $\beta_L$ .  $\beta_L = 2.6 \cdot 10^3 \text{ m/s}$  for bulk ZnS.  $\omega_n$  increases as the dimension of the dot ( $d$ ) increases, and in the limit:  $d \rightarrow \infty$  frequencies  $\omega_n$  converge to  $\omega_{LO}$ . Fig. 5 presents dependence of optical vibration modes frequencies ( $l=0, n=1, 2, 3$ ) on the diameter of ZnS QD. The smaller the diameter the lower is the frequency of confined mode. As concerns intensity, this model predict the most intensive peak in QD Raman spectra to be the mode  $\omega_1(n=1)$ . Exact positions, from the deconvolution of experimental spectra, of mode at  $\sim 345 \text{ cm}^{-1}$  for three dimensions: 1.9 nm (5 min milling time), 2.3 nm (10 min) and 2.4 nm (20 min), Fig. 4, are marked with stars in Fig. 5. It is evident that experimental values are in very good agreement with calculated values. In reality there is QD size distribution, QD shape irregularity, inhomogeneity inside, some interaction between nanoparticles, etc.

The more the QD behaves as rigid sphere the vibration modes produce less electric field outside the sphere, there is less interaction associated with this mode between nano-crystals. So, the Raman cross-section of an array of scatters is simply a superposition of their individual contributions, and it is proportional

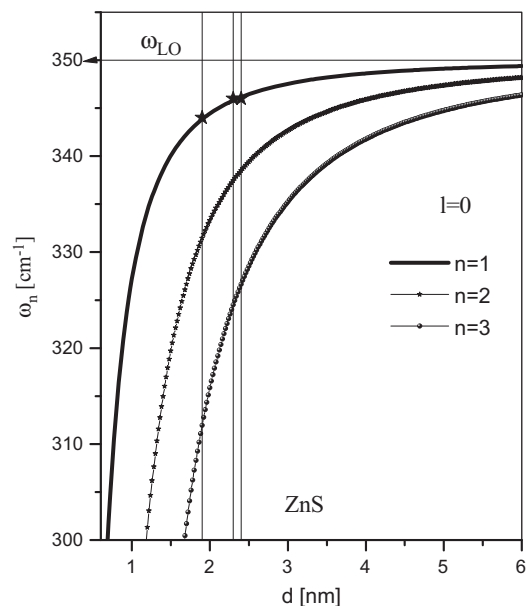


Fig. 5. The radial dependence of  $l=0$  optical modes for ZnS spherical QD.

to the volume fraction of semiconductor. During milling dimension of ZnS QDs slightly increases, agglomerates and clusters become bigger but more separated, Fig. 1. Volume fraction does not change too much. That is why intensity of mode at  $\sim 345\text{ cm}^{-1}$  does not change significantly in all three samples, Fig. 4.

While analyzing Raman spectra of the sample of the smallest diameter QD ( $d = 1.9\text{ nm}$ ) we find out that adding spectral structure in region  $300\text{--}330\text{ cm}^{-1}$  (centered at  $310\text{ cm}^{-1}$ ) reproduces experimental spectra better than without it (dashed line in Fig. 5). Similar procedure was applied for the other two samples. We tried to explain origin of this structure. We focused to the spectra of the sample of the smallest diameter QD ( $d = 1.9\text{ nm}$ ). Calculated optical vibration modes of  $d = 1.9\text{ nm}$  ZnS QD, Fig. 5, are  $\omega_2 = 330\text{ cm}^{-1}$  ( $n = 2$ ) and  $\omega_3 = 340\text{ cm}^{-1}$  ( $n = 3$ ). Predicted Raman intensity of these modes is much smaller than intensity at  $\sim 345\text{ cm}^{-1}$  ( $n = 1$ ) mode. One of possible explanation is that the contribution of these two modes is registered.

If we go back to vibrational properties of bulk ZnS we can find out that the frequencies of second order ZnS Raman peaks measured at  $\sim 304\text{ cm}^{-1}$  and  $\sim 312\text{ cm}^{-1}$  are assigned as  $[\text{LA} + \text{TA}]_W$  and  $[\text{LA} + \text{TA}]_{W,\Sigma}$  [26].

If non polar matrix surrounds QD, there is one surface mode for each  $l$ . In case of ZnS QD without matrix i.e. in vacuum ( $\epsilon_{\text{matrix}} = 1$ ) frequencies of  $l = 1$  and  $l = 2$  surface phonons are  $\sim 330\text{ cm}^{-1}$  and  $\sim 334\text{ cm}^{-1}$ . If assume that dots inside agglomerate are in non polar matrix of dielectric permittivity higher than vacuum, frequencies of surface modes will be lower. Raman scattering spectra of ZnS QD, mean size  $\sim 2.8\text{ nm}$ , are presented in 29]. The Raman spectra of the structures with ZnS QDs contain single line at frequency  $\sim 320\text{ cm}^{-1}$ . Calculated surface mode frequency ( $l = 1$ ,  $\epsilon_{\text{matrix}} = 2.4$  in their case) is  $316\text{ cm}^{-1}$ , and this mode was identified as surface mode [34].

These are possible origins of this wide, low intensity structure in spectral region  $300\text{--}330\text{ cm}^{-1}$ .

We continue analysis of the Raman spectra presented in Fig. 4 in region wide and relatively strong spectral feature centered at  $\sim 265\text{ cm}^{-1}$ .

Spectral structure centered at  $\sim 265\text{ cm}^{-1}$  is of the same order of intensity as the mode at  $\sim 345\text{ cm}^{-1}$ . Frequencies of bulk second order ZnS Raman peaks established by calculations at  $\sim 244\text{ cm}^{-1}$ ,  $\sim 256\text{ cm}^{-1}$  and  $\sim 257\text{ cm}^{-1}$  are assigned as  $[2\text{TA}]_{\Sigma}$ ,  $[\text{LA} + \text{TA}]_W$  and  $[\text{LO} - \text{TA}]_X$  [26]. We believe that this wide structure can be a sum of these contributions. Similar spectral structure in bulk ZnS unpolarized Raman spectra was also registered, and assigned as combination mode in point  $W$  [28]. Raman scattering studies of ZnS nanoclusters of typical sizes  $2.2\text{--}5\text{ nm}$  are presented in [35]. Raman spectra with the visible excitation ( $532\text{ nm}$ ) of nanoclusters of the size ( $d \sim 2.5\text{ nm}$ ) i.e. smaller than exciton Bohr radius, shows a structure centered at  $\sim 256\text{ cm}^{-1}$  comparable in intensity to the structure centered at  $\sim 350\text{ cm}^{-1}$ . For ZnS nanoparticles of  $d = 2.2\text{ nm}$  structure centered at  $\sim 256\text{ cm}^{-1}$  dominates over the structure centered at  $\sim 350\text{ cm}^{-1}$  [35].

There is additional weak spectral feature at  $\sim 220\text{ cm}^{-1}$ , Fig. 4. In case of  $d = 1.9\text{ nm}$  (5 min milling) this feature is almost invisible. But for larger nanocrystals ( $d = 2.3\text{ nm}$  and  $d = 2.4\text{ nm}$ ) it is clearly seen. Frequency of second order ZnS Raman peak calculated and registered at  $\sim 218\text{ cm}^{-1}$  is assigned as  $[\text{TO} - \text{TA}]_X$  [26]. The weak but wide feature at about  $218\text{ cm}^{-1}$  was registered in Raman spectra of ZnS nanoparticles synthesized using Langmuir–Blodgett technique and attributed to second order scattering [36]. We assigned this peak as second order  $[\text{TO} - \text{TA}]_X$  scattering.

There is lack of results in spectral region below  $200\text{ cm}^{-1}$ . It is very difficult to get spectra in this region. Presented spectra were performed at very low laser power. We registered wide feature of irregular shape in region  $130\text{--}180\text{ cm}^{-1}$ . Frequencies of second order ZnS Raman peaks calculated at  $\sim 137\text{ cm}^{-1}$ ,  $\sim 143\text{ cm}^{-1}$ ,

$\sim 167\text{ cm}^{-1}$  and  $\sim 180\text{ cm}^{-1}$  are assigned as:  $2\text{TA}_L$ ,  $[\text{TO}_u - \text{LA}]_{\Sigma}$ ,  $[\text{LO} - \text{LA}]_{\Sigma}$  and  $2\text{TAX}$  [26]. We believe that this wide structure can be a sum of these contributions. Registered integral intensity of this spectral structure, which originate from few second order modes, is comparable to the intensity of confined LO mode. In sample produced after 5 min milling time ( $d = 1.9\text{ nm}$ ) a single weak spectral feature at  $\sim 175\text{ cm}^{-1}$  is more prominent than in the other samples, Fig. 4. Raman activity in low frequency region, below  $200\text{ cm}^{-1}$ , is hard to detect, and there are no results of the other groups about QD Raman spectroscopy to compare with. So, feature of irregular shape in region  $130\text{--}180\text{ cm}^{-1}$  is recognized as group of second order modes.

#### 4. Conclusion

We report Raman spectra of mechanochemically synthesized ZnS nanocrystals. Milling time was varied. Dimension of nanocrystals are of  $\sim 1.9\text{--}2.4\text{ nm}$  depending of the duration of milling. Small dimension of ZnS QD results in the strong confinement regime. Raman spectra were measured in off resonance regime.

A continuum model of the optical phonon confinement in QD is used for investigation in optical phonon region i.e. region  $275\text{ cm}^{-1}$  ( $\omega_{\text{TO}}$ ) to  $350\text{ cm}^{-1}$  ( $\omega_{\text{LO}}$ ). Despite the fact that this model treats an ideal case, measured frequency of mode at  $\sim 345\text{ cm}^{-1}$  is in a very good agreement to predicted values. This mode, few  $\text{cm}^{-1}$  below bulk  $\omega_{\text{LO}}$ , is identified as a confined LO ( $l = 0$ ) mode. As we expect, this mode is of much lower intensity, compared to the bulk ZnS.

Registered intensities of multimodal spectral features in spectral region  $130\text{--}180\text{ cm}^{-1}$  and  $\sim 265\text{ cm}^{-1}$ , are comparable to the intensity of confined LO mode. These multimodal structures are sums of two-phonon Raman scattering from the BZ boundary. ZnS is a system of large deformation potential in the two-phonon processes. That is why there is remarkable Raman activity in spectral region  $130\text{--}180\text{ cm}^{-1}$  and  $\sim 265\text{ cm}^{-1}$  of two-phonon scattering processes in ZnS QD, even in off resonant regime.

#### Acknowledgements

This work in Serbia was supported by Serbian Ministry of Education, Science and Technological Development under Project III45003. This work was also supported by Slovak Grant Agency VEGA (Project 2/0027/14).

#### References

- [1] K.J. Klabunde, *Nanoscale Materials in Chemistry*, Wiley Interscience, New York, 2001.
- [2] M. Fayette, R.D. Robinson, *J. Mater. Chem. A* 2 (2014) 5965.
- [3] X.R. Rui, H.T. Tan, Q.G. Yan, *Nanoscale* 69 (2014) 9889.
- [4] J. Chang, E.R. Waclawik, *RSC Adv.* 4 (2014) 23505.
- [5] H. Wang, X. Lu, Y. Zhao, C. Wang, *Mater. Lett.* 60 (2006) 2480.
- [6] N. Habubi, M. Hashim, A. Al-Yasiri, *Baghdad Sci. J.* 7 (2010) 1421.
- [7] J.S. Jie, W.J. Zhang, I. Bello, Ch.-S. Lee, S.T. Lee, *Nano Today* 5 (2010) 313.
- [8] P. Balaz, M. Balintova, Z. Bastl, J. Briancin, V. Sepelak, *Solid State Ionics* 101 (1997) 45.
- [9] S.A. Chen, W.M. Liu, *Langmuir* 15 (1999) 8100.
- [10] N.A. Dhas, A. Zaban, A. Gedanken, *Chem. Mater.* 11 (1999) 806.
- [11] L.P. Wang, G.Y. Hong, *Mater. Res. Bull.* 35 (2000) 695.
- [12] N.R. Pawaskar, S.D. Sathaye, M. Bhadbhade, K.R. Patil, *Mater. Res. Bull.* 37 (2002) 1539.
- [13] J. Chen, Y. Li, Y. Wang, J. Yun, D. Cao, *Mater. Res. Bull.* 39 (2004) 185.
- [14] L.E. Brus, *J. Chem. Phys.* 79 (11) (1984) 5566.
- [15] M. Sahin, S. Nizamoglu, A.E. Kavruk, H.V. Demir, *J. Appl. Phys.* 106 (2009) 043704.
- [16] E.C. Nicolescu, M. Cristea, A. Spandonide, *Superlattices Microstruct.* 62 (2013) 1.
- [17] E. Dutkova, P. Balaz, P. Pourghahramani, S. Velumani, J.A. Ascencio, N.G. Kostova, *J. Nanosci. Nanotechnol.* 9 (2009) 6600.
- [18] F. Paraguay-Delgado, W. Antunez-Flores, M. Miki-Yoshida, A. Aguilar-Elguezabal, P. Santiago, J.R. Diaz, J.A. Ascencio, *Nanotechnology* 16 (2005) 688.
- [19] O. Šolcová, Ch.D. Uecker, U. Steinike, K. Jiráťová, *Appl. Catal. A* 94 (1994) 153.
- [20] M. José-Yacamán, J.A. Ascencio, H. Liu, *J. Vac. Sci. Technol.* B19 (2001) 1091.

- [21] J.A. Ascencio, C. Gutiérrez-Wing, M.E. Espinosa-Pesqueira, M. Marín, S. Tehuacanero, C. Zorrilla, M. José-Yacamán, *Surf. Sci.* 396 (1998) 349.
- [22] J.S. Ascencio, H.B. Liu, U. Pal, A. Medina, Z.L. Wang, *Microsc. Res. Tech.* 69 (2006) 522.
- [23] R.W. Cheary, A.A. Coelho, *J. Appl. Cryst.* 25 (1992) 109.
- [24] B.H. Henry, J.R. Doring (Eds.), *Raman Spectroscopy: Sixty Years On*, vol. 10, Elsevier, Amsterdam, 1990.
- [25] B.D. Rajput, D.A. Browne, *Phys. Rev. B* 53 (1996) 9052.
- [26] J. Serrano, A. Cantarero, M. Cardona, N. Garro, R. Luck, R.E. Tallman, T.M. Ritter, B.A. Weinstein, *Phys. Rev. B* 69 (2004) 014301.
- [27] W.G. Nilsen, *Phys. Rev.* 182 (3) (1969) 838.
- [28] Y.C. Cheng, C.Q. Jin, F. Gao, X.L. Wu, W. Zhong, S.H. Li, Paul K. Chu, *J. Appl. Phys.* 106 (2009) 123505.
- [29] M.P. Chamberlain, C. Trallero-Giner, M. Cardona, *Phys. Rev. B* 51 (1995) 1680.
- [30] R. Roca, C. Trallero-Giner, M. Cardona, *Phys. Rev. B* 49 (1994) 13074.
- [31] E. Duval, *Phys. Rev. B* 46 (1992) 5795.
- [32] C. Trallero-Giner, A. Debernardi, M. Cardona, E. Menendez-Proupin, A.I. Ekimov, *Phys. Rev. B* 57 (1998) 4664.
- [33] N. Romčević, R. Kostić, M. Romčević, M.I. Comor, J.M. Nedeljković, *J. Phys. D: Appl. Phys.* 38 (2005) 4321.
- [34] G. Milekhin, L.L. Sveshnikova, S.M. Repinskii, A.K. Gutakovskii, M. Friedrich, D.R.T. Zahn, *Phys. Solid State* 44 (10) (2002) 1976.
- [35] S. Dhara, A.K. Arora, Santanu Bera, Jay Ghatak, *J. Raman Spectrosc.* 41 (2010) 1102.
- [36] G. Milekhin, N.A. Yeryukov, L.L. Sveshnikova, T.A. Duda, C. Himcinschi, E.I. Zenkevich, D.R.T. Zahn, *Appl. Phys. A* 107 (2012) 275.



## Full Length Article

# Inducing subwavelength periodic nanostructures on multilayer NiPd thin film by low-fluence femtosecond laser beam



Aleksander G. Kovačević<sup>a,\*</sup>, Suzana Petrović<sup>b</sup>, Vladimir Lazović<sup>a</sup>, Davor Peruško<sup>b</sup>, Dejan Pantelić<sup>a</sup>, Branislav M. Jelenković<sup>a</sup>

<sup>a</sup> Institute of Physics, University of Belgrade, Pregrevica 118, 11080 Belgrade, Serbia

<sup>b</sup> Institute of Nuclear Sciences "Vinča", University of Belgrade, PO Box 522, 11001 Belgrade, Serbia

## ARTICLE INFO

## Article history:

Received 28 October 2016

Received in revised form 10 March 2017

Accepted 15 March 2017

Available online 18 March 2017

## Keywords:

Periodic surface structures

Femtosecond beam

Multilayered thin film

Surface modifications

## ABSTRACT

During femtosecond interaction with surfaces, the processes of liquid and solid-state dewetting could be responsible for the generation and regrouping of nanoparticles and nanoparticle clusters. The occurrence of surface plasmon polariton most probably induces the LIPSS arrangement. We have used low-fluence scanning femtosecond beam to generate sub-wavelength periodic structures on multilayer Ni/Pd thin films on Si. The spatial period of LIPSS increases with the change of scanning directions in respect to the polarization direction due to the phase difference increase between the incoming and induced oscillations.

© 2017 Elsevier B.V. All rights reserved.

## 1. Introduction

One of the inherent phenomena related to the irradiation of solid surfaces by ultrashort-pulse laser is the emergence of periodic grating structures on the surface (laser induced periodic surface structures, LIPSS). Being the topic of research for a long time, the phenomenon has been approached from the points of view of material types, modes of operations, beam parameters, and possible applications [1–12]. LIPSS formation has interest both form the fundamental point on view and also considering the change in properties of the nanostructured surfaces.

Two types of LIPSS are reported, low spatial frequency LIPSS (LSFL) and high spatial frequency LIPSS (HSFL) [13]. Named after their size (magnitude of spatial frequency), their orientation in respect to the polarization direction is not yet fully understood. While for LSFL it is dependent on the dielectric permittivity – it seems that LSFL orientation is perpendicular to polarization for metals and semiconductors and parallel for dielectrics ( $|\epsilon'| < 1$ ) and sometimes perpendicular – for HSFL is not well explained [2,14–16].

The most probable causes of the LIPSS emergence are the surface plasmon polaritons (SPP) generated on the material surface in the irradiation area (leading to spatial periodic distribution of energy

over the surface) or self-organization of the material upon the pulse impact [17,18].

The applications of thin films play an important role in many fields, like semiconductor technology, optics, chemistry, mechanics, magnetics, electricity. Various types of coatings for protection, diffusion barriers, filtering, reflection/antireflection, sensing, waveguiding, decorative and other purposes are just some to mention. Structuring of thin films can enhance their characteristics. The interaction of femtosecond laser beam with thin films can generate LIPSS. Thin films and alloys based on Ni and Pd have specific physico-chemical as well as mechanical characteristics, like high corrosion resistance, durability and high tensile strength and due to its mechanical characteristics and the catalytic activity, the applications range from catalyst and hydrogen storage material to holography [19]. In this work, we have demonstrated the generation of sub-wavelength periodic structures on the multilayer Ni/Pd thin films by the scanning low-fluence femtosecond laser beam. The structures have been identified as HSFL probably caused by the SPP. The influence of the scanning direction to the spatial period of HSFL is seen in the phase difference increase between the incoming and induced oscillations for scanning direction approaching the perpendicular to the polarization direction.

## 2. Experimental setup

The experimental setup is based on a femtosecond laser (Coherent Mira 900). The laser beam was focused by a GF Panachromium

\* Corresponding author.

E-mail address: [Aleksander.Kovacevic@ipb.ac.rs](mailto:Aleksander.Kovacevic@ipb.ac.rs) (A.G. Kovačević).

objective (40x/0.65) on the specimen. The wavelength of the beam was monitored with the fiber coupled spectrometer (Ocean Optics HR2000CG-UV-NIR). Irradiated samples were Ni/Pd bilayers, with five layers of each metal, deposited on the silicon (100) wafer. The depositions were performed by the Balzers Sputron II apparatus using 1.3 keV argon ions and with 99.9% of Ni and Pd targets purity. Each layer (Ni or Pd) was of  $\sim 13$  nm thickness reaching the total thickness of bilayer group of  $\sim 130$  nm. The irradiations of the top (Ni) layer of the Ni/Pd bilayer system were performed in air with focused femtosecond laser beam under normal incidence. The laser beam properties were: wavelength 760–880 nm, pulse duration  $\sim 100$  fs, repetition rate 76 MHz, power of 175–195 mW, linear polarization in the horizontal plane, Gaussian-like profile, spot diameter  $\sim 200$ –1000 nm. Femtosecond laser interactions have been performed in two modes, with laser beam being static or scanning. The results of the interactions have been analyzed by scanning electron microscopy (SEM) – the TESCAN MIRA3 system.

### 3. Results and discussion

In order to examine the response of the material to irradiations in both static and dynamic modes, the beam was moved from point to point over the surface of the sample by computer-controlled pair of galvo-scanning mirrors. When irradiating the samples, two time intervals have been used as experimental parameters: the “dwell time”, or the time the beam is at the same point, and the “flight time” or the time for travelling between two points. The pattern drawn by the scan of the beam is a matrix, consisted of 80 points in the 8 by 10 scheme (Fig. 1).

The beam was positioned in the center of the area – central hole in Fig. 1, where it dwelled for predefined dwell time. It then scanned during flight time to the top left point (top left hole) and waited for dwell time. Point by point, the beam scanned and dwelled, thus engraving the pattern in the predefined area. The distance between two points was  $7.5 \mu\text{m}$  in the direction parallel to the polarization direction and  $8.5 \mu\text{m}$  in the direction perpendicular to the polarization direction.

The sample has been irradiated with femtosecond beams of single-pulse fluences below  $146 \text{ mJ}/\text{cm}^2$  which is single-pulse ablation threshold for  $5x(\text{Ni}/\text{Pd})/\text{Si}$  multilayer system [20]. For single-pulse fluences below the ablation threshold and shorter expositions, the LIPSS are typically formed. For longer expositions, the accumulation of pulses would lead to melting in some materials, but in some materials the LIPSS would remain stable.

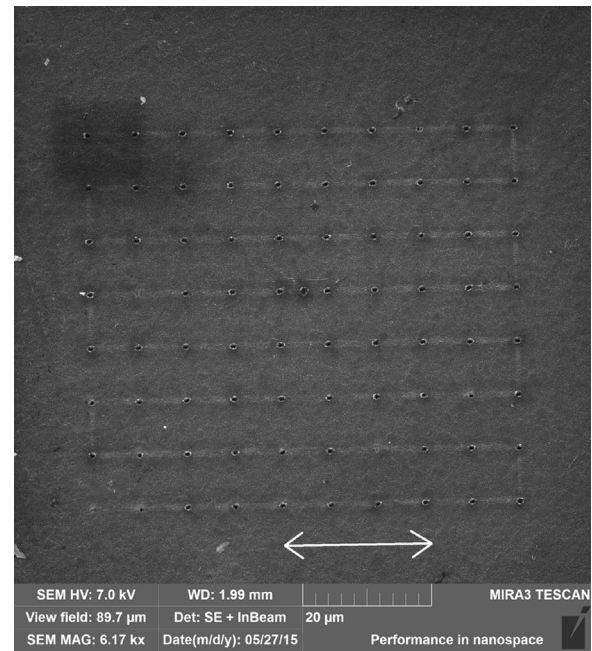


Fig. 1. Upper left part of the pattern (double arrow indicates polarization direction); wavelength 880 nm, power 175 mW, fluence  $135 \text{ mJ}/\text{cm}^2$ , dwell time 20 ms, flight time 20 ms.

The main objective was to investigate the appearance of LIPSS (HSFL) during scanning. During static irradiation, the number of pulses delivered to the irradiated area (the spot) is dependent on the exposition time. During scanning, the number of pulses that irradiate the area of the same size as in static irradiation (the spot) depends on the scanning rate.

For examining the influence of the scanning direction to the spatial frequency of the induced HSFL, the sample was irradiated in similar pattern, with inter-point distances of  $7 \mu\text{m}$  (direction parallel to polarization) and of  $8.3 \mu\text{m}$  (direction perpendicular to polarization). The laser beam parameters were: wavelength 880 nm, power 175 mW, single pulse fluence  $\sim 142 \text{ mJ}/\text{cm}^2$ , dwell time 10 ms, flight time 10 ms. Scanning rate was  $830 \mu\text{m}/\text{s}$  (direction parallel to polarization),  $700 \mu\text{m}/\text{s}$  (direction perpendicular to polarization) and  $4015 \mu\text{m}/\text{s}$  (direction oblique to polarization,  $\sim 38^\circ$ ). Static irradiation led to hole drilling, while scanning modified the material surface.

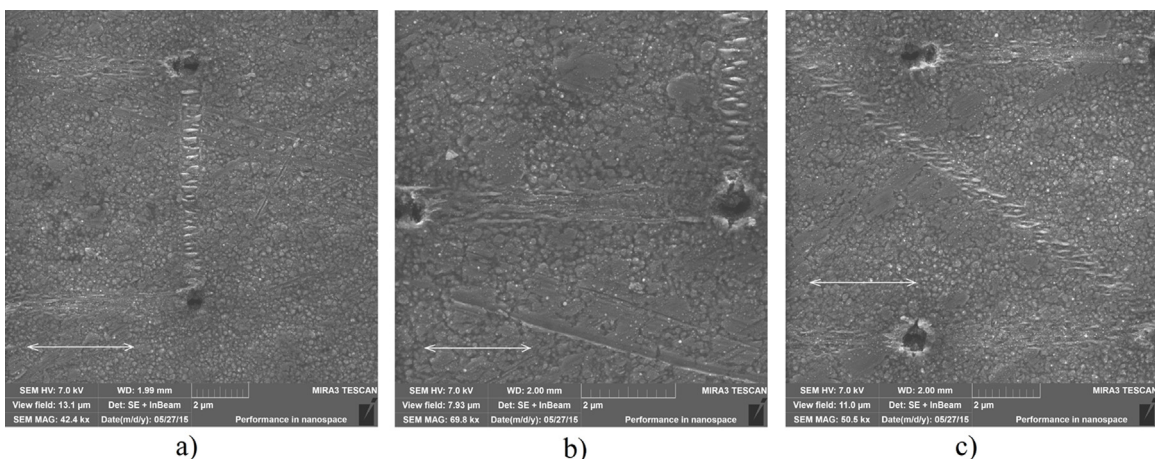
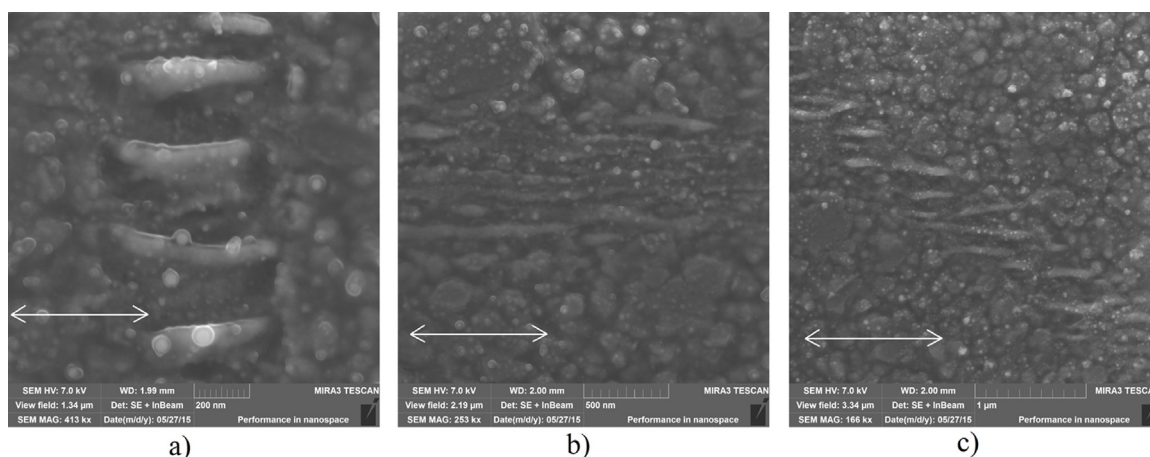


Fig. 2. SEM micrographs of irradiated areas (wavelength 880 nm, power 175 mW, dwell time 10 ms, flight time 10 ms, double arrow shows polarization direction): a) scanning perpendicular to polarization direction; b) scanning parallel to polarization direction; c) scanning oblique to polarization direction.





**Fig. 3.** SEM micrographs (higher magnification) of irradiated areas presented in Fig. 2 (wavelength 880 nm, power 175 mW, dwell time 10 ms, flight time 10 ms, double arrow shows polarization direction): a) corresponding to Fig. 2a; b) corresponding to Fig. 2b; c) corresponding to Fig. 2c.

During dwell time of 10 ms the spot area was irradiated with 760,000 pulses (static). For scanning rate of  $830 \mu\text{m/s}$ , the same area was irradiated with  $\sim 92,700$  pulses, which is  $\sim 8$  times less accumulated energy. For scanning rates of  $700 \mu\text{m/s}$  and  $4015 \mu\text{m/s}$ , the number of pulses was 110,000 and 19,200, respectively.

The image analysis (Gwydion program) from the figures shows that the LIPSS height is 15–35 nm (Fig. 2a), 4–12 nm (Fig. 2b) and 10–15 nm (Fig. 2c) above the average level measured at the unmodified area, while the LIPSS depth is 5–10 nm (Fig. 2a), 2–4 nm (Fig. 2b), and 5–9 nm (Fig. 2c) below it.

Optical penetration depth for Ni depends on the irradiation wavelength and is  $\sim 18$  nm [21,22]. Thermal penetration depth, while being high for high fluences, for low-fluence regime is close to the optical penetration depth [23]. Due to the exponential decrease of the intensity, it is most likely that only the first (top) layer (Ni) is affected in LIPSS formation.

In Fig. 2 is presented that static irradiation not only enabled drilling, but also melting and the molten material dispersion around the crater as well. The HSFL are more prominent for scan direc-

tion perpendicular (Fig. 2a) to the polarization direction than for direction parallel (Fig. 2b) to the polarization direction.

The areas presented in Fig. 2a–c are presented in Fig. 3a–c with higher magnification. The parallel structures (HSFL) are aligned in the irradiated area. The direction of the structures is parallel to the polarization direction and the spatial frequency is  $\sim 300$  nm for scanning direction perpendicular to the polarization direction (Figs. 2a and 3a),  $\sim 135$  nm for scanning direction parallel to the polarization direction (Figs. 2b and 3b) and  $\sim 180$  nm for scanning direction oblique,  $\sim 38^\circ$ , to the polarization direction (Figs. 2c and 3c).

The irradiation on different wavelengths also generated HSFL: for 800 nm, scanning direction oblique to polarization (Fig. 4a) and for 760 nm scanning directions oblique and parallel to polarization (Fig. 4b). In Fig. 4a, only scanning part is presented. Single pulse fluence of  $175 \text{ mJ/cm}^2$  and 570,000 pulses, delivered to the area equivalent to the spot area in static irradiation, generated the HSFL of spatial frequency of  $\sim 250$  nm. In Fig. 4b, different pattern has been used, with  $\sim 2 \mu\text{m}$  of distance between two consecutive points. The single pulse fluence of  $175 \text{ mJ/cm}^2$  and 36500 pulses, delivered to the area equivalent to the spot area in static irradiation,

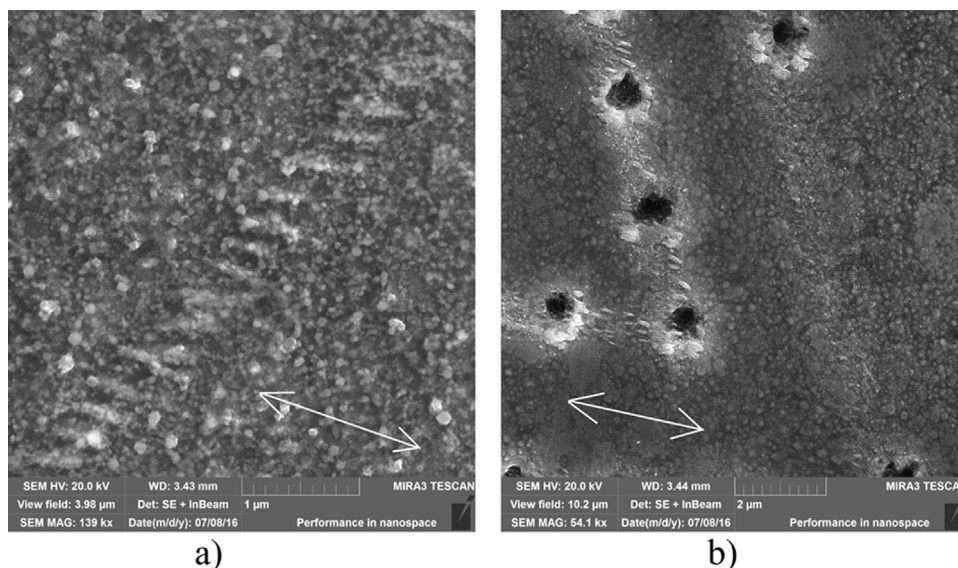


**Fig. 4.** SEM micrographs of the HSFL generated by: a) scanning oblique to polarization, wavelength 800 nm, power 188 mW, dwell time 500 ms, flight time 5 ms and b) scanning oblique and parallel to polarization, wavelength 760 nm, power 180 mW, dwell time 40 ms, flight time 2 ms.

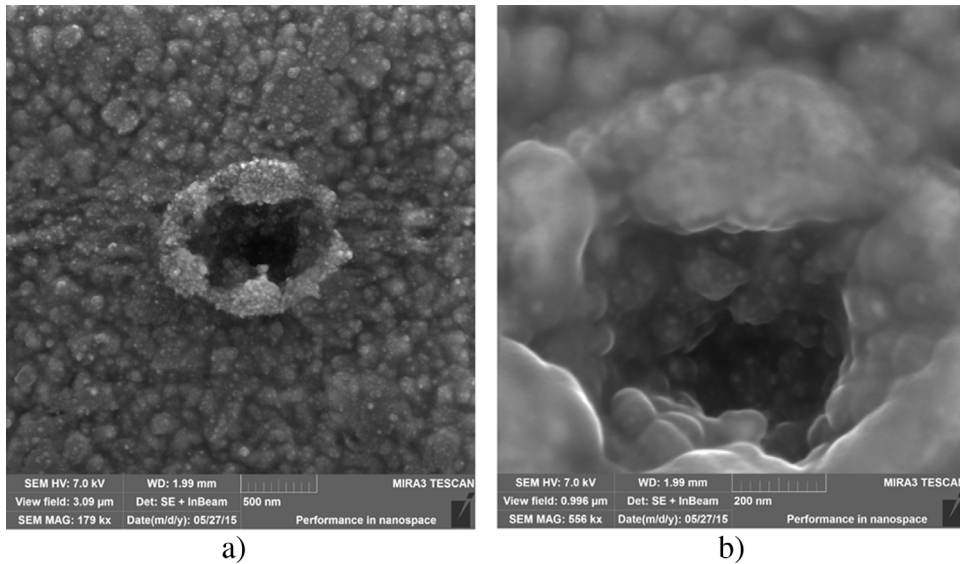


**Fig. 5.** SEM micrograph of hole drilled by the beam of parameters: wavelength 880 nm, power 175 mW, fluence 135 mJ/cm<sup>2</sup>, dwell time 20 ms, flight time 20 ms; a) crater and surroundings, b) magnified central area of the crater.

tion, generated the HSFL of spatial frequency of  $\sim 170$  nm during oblique scanning.

In Fig. 5, the static irradiation which led to hole drilling is presented. The material migrated from the area of highest fluence and was displaced around the crater, with the appearance of smaller grains.

Higher magnification (Fig. 5b) of the hole shows that the newly formed smaller nanoparticles (diameter < 40 nm) have even smaller nanoparticles (diameter < 10 nm) on their surface. For lesser single pulse fluences (16.3 mJ/cm<sup>2</sup>, Fig. 6), the effects of modifications were strongly suppressed. Only during static irradiation the material showed the emergence of the surface modification in the irradiation area. The original grain structure of  $\sim 200$  nm (smooth grains) changed. At the surface of each grain, smaller grains of less than 40 nm, appeared (Fig. 6b and c).

The scanning direction parallel to the polarization direction causes the HSFL to be of higher spatial density ( $\sim 135$  nm, though not so pronounced) compared to oblique ( $\sim 180$  nm), and especially to perpendicular direction ( $\sim 300$  nm spatial period), Figs. 2a–c and 3a–c. The cause might be linked to the causes of the HSFL direction. When the beam scans in various directions over the periodic distribution of energy at the material, the phase difference of the

coupling between incoming and induced waves increases when the scanning direction approaches the perpendicular direction to the polarization direction, in that way increasing the spatial period of the HSFL.

In Fig. 6, the process of greater nanoparticles size reduction could be noticed. The greater nanoparticles (crystal grains) ( $\sim 200$  nm diameter), which existed on the surface before the interaction, experienced some changes upon the beam irradiation. On the particle surface, nanoparticles of smaller diameter (less than 40 nm) appeared. Supposedly, smaller nanoparticles, Figs. 3 and 4, regroup and form elongated particles arranged in the form of parallel periodical structures. Since the signs of melting are not pronounced in the area where HSFL appeared, it could be that some non-resonant processes like dry dewetting and non-thermal melting took part [24–31]. Due to the ablation and high accumulated energy during static irradiation, it is probable that the material was ejected out of the crater, while material mixture occurred inside the crater.

The existence of the craters for static irradiation point to excessive deposited energy, which ablated the material (Fig. 5). On the other hand, scanning reduced the average energy the surface unit received thus prevented overheating and simple thermal melt-

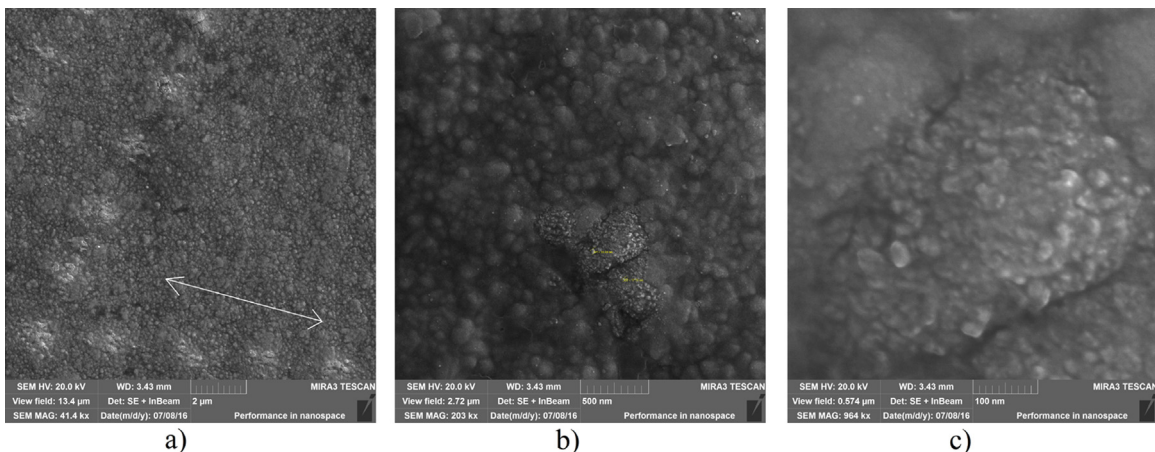


**Fig. 6.** SEM micrograph of areas irradiated by the beam of parameters: wavelength 800 nm, power 195 mW, dwell time 250 ms, flight time 5 ms.

ing. In this case, possibly the processes of non-thermal melting took place. The presence and the characteristics of the underneath layer play an important role in the formation of parallel structures. The evolution of the surface morphology upon the irradiation of a femtosecond laser beam into a LSFL via HSFL and the difference between LIPSS formation on the single layer and on the multi-layer surfaces is explained in [32].

Ni and Pd have similar thermo-physical properties suggesting that the heat would smoothly transfer from one layer to the other. However, slightly lower thermal conductivity of the underneath layer would support the propagation of heat along the interface (laterally) [20]. The differences in electron-phonon coupling lead to different evolution of the reflectivity and absorption coefficients during the irradiation [33]. While quickly transferring the energy to the electrons of the inner layer, excited electrons of the upper layer couple less effectively with the lattice inducing the increase of the lattice temperature of the interface and lateral propagation of heat. A delay in response between the layers is induced with the reflection of light at the internal interface. The interplay between heat localization and transferring the heat away from the interaction zone forms the lattice temperature.

#### 4. Conclusion

We have irradiated the multilayer Ni/Pd thin films by the low-fluence femtosecond laser beam. The beam induced the SPP on the surface, which most probably generated the sub-wavelength periodic structures on the surface, the HSFL. The scanning direction in respect to the polarization direction influences the spatial period of the HSFL: the period increases for the phase difference increase between the incoming and induced oscillations; this increases as the scanning direction approaches the perpendicular direction towards the polarization. The HSFL structures are most probably caused by the SPP, where the mechanisms of dry dewetting and non-thermal melting took place.

#### Acknowledgement

This work has been supported by the by the Ministry of Science of the Republic of Serbia with projects O1171005 and III45016.

#### References

- [1] H.M. van Driel, J.E. Sipe, J.F. Young, Laser-induced periodic surface structure on solids: a universal phenomenon, *Phys. Rev. Lett.* 49 (1982) 1955–1958.
- [2] J.E. Sipe, J.F. Young, J.S. Preston, H.M. van Driel, Laser-induced periodic surface structures. I. Theory, *Phys. Rev. B* 27 (1983) 1141–1154.
- [3] J.F. Young, J.E. Sipe, H.M. van Driel, Laser-induced periodic surface structure. III. Fluence regimes, the role of feedback, and details of the induced topography in germanium, *Phys. Rev. B* 30 (1984) 2001–2015.
- [4] I. Ursu, I.N. Mihailescu, A.M. Prokhorov, V.I. Konov, V.N. Tokarev, On the role of the periodical structures induced by powerful laser irradiation of metallic surfaces in the energy coupling process, *Physica B + C* 132 (1985) 395–402.
- [5] D.W. Bäuerle, *Laser Processing and Chemistry*, Springer, Berlin, 2000.
- [6] J. Wang, C. Guo, Ultrafast dynamics of femtosecond laser-induced periodic surface pattern formation on metals, *Appl. Phys. Lett.* 87 (2005) 251914 (3pp).
- [7] A.Y. Vorobyev, V.S. Makin, C. Guo, Periodic ordering of random surface nanostructures induced by femtosecond laser pulses on metals, *J. Appl. Phys.* 101 (2007) 034903 (4pp).
- [8] A.Y. Vorobyev, C. Guo, Femtosecond laser-induced periodic surface structure formation on tungsten, *J. Appl. Phys.* 104 (2008) 063523 (3pp).
- [9] M.S. Trtica, B.B. Radak, B.M. Gaković, D.S. Milovanović, D. Batani, T. Desai, Surface modifications of Ti6Al4V by a picosecond Nd:YAG laser, *Laser Part. Beams* 27 (2009) 85–90.
- [10] J. Bonse, J. Krüger, Pulse number dependence of laser-induced periodic surface structures for femtosecond laser irradiation of silicon, *J. Appl. Phys.* 108 (2010) 034903 (5pp).
- [11] B. Gaković, C. Radu, M. Zamfirescu, B. Radak, M. Trtica, S. Petrović, et al., Femtosecond laser modification of multilayered TiAlN/TiN coating, *Surf. Coat. Technol.* 206 (2011) 411–416.
- [12] A.Y. Vorobyev, C. Guo, Direct femtosecond laser surface nano/microstructuring and its applications, *Laser Photonics Rev.* 7 (2013) 385–407.
- [13] J. Bonse, J. Krüger, S. Höhm, A. Rosenfeld, Femtosecond laser-induced periodic surface structures, *J. Laser Appl.* 24 (2012) 042006 (7pp).
- [14] Magdalena Forster, Wolfgang Kautek, Nicolas Faure, Eric Audouard, Razvan Stojan, Periodic nanoscale structures on polyimide surfaces generated by temporally tailored femtosecond laser pulses, *Phys. Chem. Chem. Phys.* 13 (2011) 4155–4158.
- [15] Esther Rebollar, Javier R. Vázquez de Aldana, Ignacio Martín-Fabiani, Margarita Hernández, Daniel R. Rueda, Tiberio A. Ezquerro, Concepción Domingo, Pablo Morenob, Marta Castillejo, Assessment of femtosecond laser induced periodic surface structures on polymer films, *Phys. Chem. Chem. Phys.* 15 (2013) 11287–11298.
- [16] D. Dufft, A. Rosenfeld, S.K. Das, R. Grunwald, J. Bonse, Femtosecond laser-induced periodic surface structures revisited: a comparative study on ZnO, *J. Appl. Phys.* 105 (2009) 034908 (9pp).
- [17] A.Y. Vorobyev, V.S. Makin, C. Guo, Periodic ordering of random surface nanostructures induced by femtosecond laser pulses on metals, *J. Appl. Phys.* 101 (2007) 034903 (4pp).
- [18] J. Reif, O. Varlamova, F. Costache, Femtosecond laser induced nanostructure formation: self-organization control parameters, *Appl. Phys. A* 92 (2008) 1019–1024.
- [19] K. Suresh Kumar, P. Haridoss, K.S. Seshadri, Synthesis and characterization of electrodeposited Ni–Pd alloy electrodes for methanol oxidation, *Surf. Coat. Technol.* 202 (2008) 1764–1770.
- [20] S. Petrović, B. Gaković, M. Zamfirescu, C. Radu, D. Peruško, B. Radak, C. Ristoscu, S. Zdravković, C.L. Luculescu, I.N. Mihailescu, Femtosecond laser processing of NiPd single and 5x(Ni/Pd) multilayer thin films, *Appl. Surf. Sci.* 417 (2017) 16–22, <http://dx.doi.org/10.1016/j.apsusc.2016.12.142>.
- [21] J. Hohlfeld, S.-S. Wellershoff, J. Gudde, U. Conrad, V. Jahnke, E. Matthias, Electron and lattice dynamics following optical excitation of metals, *Chem. Phys.* 251 (2000) 237–258.
- [22] T. Saito, O. Matsuda, O.B. Wright, Picosecond acoustic phonon pulse generation in nickel and chromium, *Phys. Rev. B* 67 (2003) 205421 (7pp).
- [23] R. Le Harzic, D. Breiting, M. Weikert, S. Sommer, C. Föhl, S. Valette, C. Donnet, E. Audouard, F. Dausinger, Pulse width and energy influence on laser micromachining of metals in a range of 100 fs to 5 ps, *Appl. Surf. Sci.* 249 (2005) 322–331.
- [24] C.W. Siders, A. Cavalleri, K. Sokolowski-Tinten, C. Toth, T. Guo, M. Kammler, et al., Detection of nonthermal melting by ultrafast X-ray diffraction, *Science* 286 (1999) 1340–1342.
- [25] J.A. van Vechten, R. Tsu, Nothermal pulsed annealing of Si; plasma annealing, *Phys. Lett.* 74A (1979) 422–426.
- [26] J.A. van Vechten, R. Tsu, F.W. Saris, D. Hoonhout, Reasons to believe pulsed laser annealing of Si does not involve simple thermal melting, *Phys. Lett.* 74A (6) (1979) 417–421.
- [27] S. Herminghaus, K. Jacobs, K. Mecke, J. Bischof, A. Fery, M. Ibn-Elhaj, et al., Spinodal dewetting in liquid crystal and liquid metal films, *Science* 282 (1998) 916–919.
- [28] J. Bischof, D. Scherer, S. Herminghaus, P. Leiderer, Dewetting modes of thin metallic films: nucleation of holes and spinodal dewetting, *Phys. Rev. Lett.* 77 (1996) 1536–1539.
- [29] T. Zier, B. Bauerhenne, V. Lipp, D.S. Ivanov, E.S. Zijlstra, M.E. Garcia, Ab initio and classical molecular dynamics simulations of ultrafast structural phenomena in laser excited solids, in: *Book of Abstracts ICPEPA-10*, University of Transilvania, Brasov, 2016 (August 29–September 2, 2016), p. 70.
- [30] D.S. Ivanov, L.V. Zhigilei, Combined atomistic-continuum modeling of short-pulse laser melting and disintegration of metal films, *Phys. Rev. B* 68 (2003) 064114 (22pp).
- [31] K. Sokolowski-Tinten, J. Bialkowski, M. Boing, A. Cavalleri, D. von der Linde, Thermal and nonthermal melting of gallium arsenide after femtosecond laser excitation, *Phys. Rev. B* 58 (1998) R11805–R11808.
- [32] A.G. Kovačević, S. Petrović, B. Bokić, B. Gaković, M.T. Bokorov, B. Vasić, et al., Surface nanopatterning of Al/Ti multilayer thin films and Al single layer by a low-fluence UV femtosecond laser beam, *Appl. Surf. Sci.* 326 (2015) 91–98.
- [33] G.D. Tsibidis, Thermal response of double-layered metal films after ultrashort pulsed laser irradiation: the role of non-thermal electron dynamics, *Appl. Phys. Lett.* 104 (2014) 051603 (5pp).



## Preparation and characterization of bismuth germanium oxide (BGO) polymer composites



Ljiljana M. Brajovic<sup>a,\*</sup>, Dusica B. Stojanovic<sup>b</sup>, Pedja Mihailovic<sup>c</sup>, Smilja B. Markovic<sup>d</sup>, Maja Romcevic<sup>f</sup>, Miodrag Mitric<sup>e</sup>, Vladimir Lazovic<sup>f</sup>, Dragan Dramlic<sup>f</sup>, Slobodan Petricevic<sup>c</sup>, Nebojsa Romcevic<sup>f</sup>

<sup>a</sup> University of Belgrade, Civil Engineering Faculty, Bulevar Kralja Aleksandra 73, 11000 Belgrade, Serbia

<sup>b</sup> University of Belgrade, Faculty of Technology and Metallurgy, Karnegijeva 4, 11120 Belgrade, Serbia

<sup>c</sup> University of Belgrade, Faculty of Electrical Engineering, Bulevar Kralja Aleksandra 73, 11000 Belgrade, Serbia

<sup>d</sup> University of Belgrade, Institute of Technical Sciences of SASA, Knez Mihailova 35/IV, 11000 Belgrade, Serbia

<sup>e</sup> University of Belgrade, Institute of Nuclear Sciences Vinča, P.O. Box 522, 11001 Belgrade, Serbia

<sup>f</sup> University of Belgrade, Institute of Physics, P.O. Box 68, Pregrevica 118, Zemun, 11080 Belgrade, Serbia

### ARTICLE INFO

#### Article history:

Received 31 May 2016

Received in revised form

24 September 2016

Accepted 16 October 2016

Available online 17 October 2016

#### Keywords:

Composite materials

Polymer

Elastic scattering

Optical properties

Optical spectroscopy

### ABSTRACT

Bismuth germanium oxide  $\text{Bi}_{12}\text{GeO}_{20}$  (BGO) has very interesting electrical, optical and magnetic properties. In order to make devices based on this material more flexible, its powder was used for preparing polymer composites. This study reports investigation of the effects of using different solvents and polymers in preparation of BGO composite on the microstructural and optical behaviour of the resulting material. Preparation of such composites by a solution casting method is described. Poly (methyl methacrylate) (PMMA) and polystyrene (PS) were used as matrix materials and acetone and chloroform as solvents. Their microstructure and the quality of BGO dispersion and deaggregation in polymer matrix were analyzed by SEM, Raman, XRD and optical spectroscopy. The influence of particle size distribution, their shapes, and concentration on the optical transmission is calculated based on Mie scattering theory and discussed, too.

© 2016 Elsevier B.V. All rights reserved.

### 1. Introduction

As a member of sillenite single crystals, Bismuth germanium oxide,  $\text{Bi}_{12}\text{GeO}_{20}$  (BGO) has only one non-bismuth metal atom in a formula unit of 33 atoms. Its structure with only one Ge atom for every 12 Bi atoms and only four of 20 oxygen atoms involved in  $\text{GeO}_4$  tetrahedron is foundation for many interesting properties such as photoconductivity, magneto-optical effect, electro-optical effect, piezoelectricity, electrogyratory effect and photorefractivity [1–3]. These properties are applicative in the fields of optical sensors, optical memories, holography, etc. [4–8]. Composites with polymer matrix are materials of great interest because their properties can be adjusted by: controlling the content, morphology and composition of the particle reinforcement, different processing techniques and modification of the polymer matrix [9–11].

Using BGO powder as reinforcement for creating composite

materials would potentially broaden and technologically improve its applications.

BGO large refraction index compared to the matrix polymers leads to high scattering on powder particles and radiation loss. Although high loss can be acceptable for sensing applications it is of interest to find a suitable technological procedure to make samples homogenous in particle size distribution and more transparent.

In this paper preparation and characterization of composites with poly (methyl methacrylate) (PMMA) or polystyrene (PS) matrix and milled BGO powder as reinforcement are described.

The solution casting method is chosen since it gives the better transparency of the samples compared with melt compounding methods [12]. For PMMA based samples two solvents were used acetone and chloroform, and for preparing PS sample chloroform is used as solvent. Particle size distribution of powder itself and of prepared composites based on their SEM images is used to compare homogeneity of samples, as well as, the size and shapes of their particles and aggregates. X-ray diffraction (XRD) and Raman spectra analysis of the samples were done to authenticate

\* Corresponding author. Tel.: + 381 11 3218585.

E-mail address: [brajovic@grf.bg.ac.rs](mailto:brajovic@grf.bg.ac.rs) (L.M. Brajovic).

powdered single crystal BGO in the composite samples and to investigate how different preparing procedure influence the obtained spectra. Besides characterization of the samples the optical spectroscopy was used for comparing the measured and calculated transmission of samples based on Mie scattering theory.

To the best of our knowledge, the selected Bi<sub>12</sub>GeO<sub>20</sub>-PMMA and Bi<sub>12</sub>GeO<sub>20</sub>-PS composite systems has not been previously reported in the literature.

## 2. Experimental

### 2.1. Materials

Bi<sub>12</sub>GeO<sub>20</sub> single crystals were grown by the Czochralski technique using a MSR 2 crystal puller controlled by a Eurotherm. The charge for preparing this yellow crystal was a stoichiometric mixture of Bi<sub>2</sub>O<sub>3</sub> (99.999 wt%) and GeO<sub>2</sub> (99.9999 wt%). Details of the preparation are presented in Ref. [13]. Powdering of synthesized single crystals was done by milling in planetary high energy ball mill (Fritsch Pulverisettes).

The polymer components of the composites were: a) commercially available heat resistant injection grade PMMA pellets, Acryrex<sub>CM-205</sub> (Mw = 90400, Chi Mei Corporation, Taiwan) with no detected solute according to RoHS Directive, b) commercially available Polystyrene (PS) pellets, Empera<sup>®</sup>251 N, Ineos Nova, c) acetone purchased at Beta Hemm and d) chloroform purchased at Fisher Scientific from UK.

### 2.2. Preparation of composite samples

The composite samples were prepared with a solution casting method. Three samples with different polymer or solvent are prepared, but all with the same BGO mass fraction of 1.0 wt%.

The first sample (in following text denoted as no.1) was obtained by dissolving PMMA in acetone for 24 h, and then by adding BGO powder to the solution with continuous magnetic stirring. The mixture was poured in the Petri dish through a 5 µm mesh sieve to prevent bubbling and left inside an oven at constant temperature of 50 °C for another 24 h, and then in a vacuum drying oven for 8 h at 50 °C.

The second sample (no.2) was prepared by dissolving PMMA in chloroform and then adding BGO powder to the solution with continuous bath ultrasound (15 min) and magnetic stirring for 24 h. The mixture was then poured into 50 mm diameter Petri dishes, left inside an oven at constant temperature of 50 °C for another 24 h, and then in a vacuum drying oven for 8 h at 50 °C.

The sample no.3 was obtained by dissolving Polystyrene (PS) in chloroform and then adding BGO powder to the solution with continuous bath ultrasound (15 min) and magnetic stirring for 24 h. The mixture was then poured into 50 mm diameter Petri dishes, and the further procedures were the same as for sample no.2. The thickness of all prepared samples was 0.6 mm.

### 2.3. Characterization methods

The particle size distribution (PSD) of BGO powder was determined by a laser light-scattering particle size analyzer (PSA). The used instrument was Mastersizer 2000 (Malvern Instruments Ltd., UK) particle size analyzer based on laser diffraction, covering the particle size range of 0.02–2000 µm. For the PSA measurements, the powder was dispersed in distilled water, in ultrasonic bath (low-intensity ultrasound, at a frequency of 40 kHz and power of 50 W), for 20 min.

SEM imaging of BGO polymer composites was performed using field emission scanning electron microscope FESEM (TESCAN MIRA

3) in order to investigate differences in dispersion and deaggregation of particles in composite samples. The size distribution of particles in the composites was obtained through manual measurements and analysis of SEM images using program Image Pro Plus 6.0 (Media Cybernetics).

X-ray diffraction (XRD) analyses of powdered single BGO crystals and composite samples were performed on a Philips 1050 X-ray powder diffractometer using a Ni-filtered CuK<sub>α</sub> radiation and Bragg-Brentano focusing geometry. The patterns were taken in the 10° < 2θ < 100° range with the scanning step of 0.05° and exposure time of 5 s per step.

The Raman spectra of polymer composites were obtained by the micro-Raman and were analyzed using Jobin Yvon T64000 spectrometer, equipped with nitrogen cooled charge-coupled device detector. The measurements were performed at 20 mW during 200 s at room temperature. The spectral range of Raman was from 50 to 900 cm<sup>-1</sup>, in back scattering geometry.

Optical transmission spectra of the single crystal, composite samples and pure polymer films as a control were measured in VIS and IR ranges using DU 720 General purpose UV–VIS spectrometer (300–1100 nm).

## 3. Results and discussion

### 3.1. Powder particle size distribution

The particle size distribution, based on number, of the analyzed BGO powder is presented in Fig. 1. The particle size distribution was relatively narrow (*span* = 2.243) where 10% of particles, *d* (0.1), have diameter smaller than 0.125 µm, 50% of particles possess diameter of *d* (0.5) = 0.240 µm, while 90% of particles, *d* (0.9), are smaller than 0.670 µm.

### 3.2. SEM analysis and obtaining the PSD of composite samples

Three SEM of sample no.1 with different magnifications (6.17k, 11.3k and 40.0k) are presented in Fig. 2. The first one shows the broad area of composite and distribution of various powder particle sizes in composite. The second micrograph shows the marked detail of the first one in order to establish shapes and sizes of various kinds of powder particles and aggregates that are formed. The third one shows structure of aggregates for micrograph detail marked in the second one. It is obvious that the aggregates have mostly round shapes and their size is up to 10 µm.

Similar three micrographs of sample no.2 are presented in Fig. 3 whose magnifications were 4.08k, 26.1k and 83.9k respectively. This sample has more homogeneous structure compared to sample no.1, the particle and aggregate sizes are up to 4 µm and their shapes are mostly round.

In Fig. 4, three micrographs of sample no.3 are presented with magnifications of 3.77, 8.64k and 29.1k. The particles and aggregates are pretty uniformly distributed, but their shapes are quite different compared to other two samples. Shapes of aggregates and particles are not spherical in the majority, but more ellipsoidal, sometimes even pyramidal and their size is up to 9 µm.

Additional SEM micrographs of all sample types are presented in the Supplement data.

In order to compare samples, PSD analysis is obtained. Since the shapes of particles are different as well as their visibility, the analysis was done manually using Image ProPlus 6.0. The measured values denoted as *d* were the longest dimensions of the particles.

The histograms presenting size count probabilities for all three samples for the sizes up to 8 µm are presented in Fig. 5.

The number of analyzed particles *N*, minimum and maximum observed size, mean size value, standard deviation, as well as

d (0.5) and d (0.9) values are shown in Table 1.

Comparing the powder PSD from paragraph 3.1 and PSDs of prepared samples, it is obvious, that although all preparing procedures have some kind of particles dispersion in the polymer solution, during evaporation of the solvent and forming the composite, the various aggregates of particles were formed. The values of d (0.5) and d (0.9) have higher values for the prepared samples no.1 and no.3 than in powder PSD which illustrates those statement. The best homogeneity and the smallest aggregates have sample no.2.

### 3.3. XRD characterization of pure crystal and composite samples

XRD characterization was performed to authenticate powdered single crystal BGO in the composite samples. The presented graphs in Fig. 6 show XRD patterns of powdered single BGO crystals and of composite samples. XRD pattern of pure PMMA is recognizable in graphs for the samples no.1 and no.2 by their broad amorphous maximums observed around  $2\theta = 15^\circ$ ,  $30.2^\circ$  and  $42.2^\circ$  as reported in the literature [14]. The specific broad diffraction peaks of pure PS around  $2\theta = 20^\circ$  and  $43^\circ$  observed in XRD pattern of sample no.3 are characteristic for pure PS [15]. From the graphs presented in Fig. 6., the BGO crystal characteristics are very good recognized both for samples no.1 and no.3, but some peaks ( $2\theta = 49.3^\circ, 79^\circ, 80.3^\circ$  and  $81.6^\circ$  are clearly visible only at XRD pattern of the sample no.3. The reasons are most probably that the particles of BGO at the top of the samples no.3 and no.1 are larger than those in sample no.2. and the broad XRD pattern peaks of PS do not coincide with those from pure crystal BGO.

### 3.4. Raman spectra

The Raman spectra of BGO single crystal and composite samples are presented in Fig. 7. In order to differentiate composite samples from polymers, observed modes were also compared with Raman spectra of pure PMMA and PS. Intensity modes at 553, 600, 730, 810, 965–999 (broad peak), 1180, 1237,  $1450\text{ cm}^{-1}$  in the Raman spectra of samples no.1 and no.2 are characteristic for pure PMMA as it is presented in literature [16,17]. In Raman spectra of sample no.3 intensity modes at 366, 405, 621, 796, 1001, 1031,  $1450$  and  $1584\text{ cm}^{-1}$ , belong to pure PS, as it is described in Refs. [18–20].

The frequencies of the peaks observed in Raman spectra of the yellow  $\text{Bi}_{12}\text{GeO}_{20}$  single crystals and the symmetry types of

corresponding vibrations are presented in the first and second column of the Table 2 based on the results presented in previous article [13] and literature [21]. The registered intensity modes for composite samples are presented in Table 2, where notation s indicate that the peak is of low intensity or hardly to differentiate from the broad peak of the pure polymer.

In Raman spectra of the sample no.1 the intensity modes are weakly perceived. Sample no. 2 have two well defined intensity modes and they are  $269$  and  $538\text{ cm}^{-1}$  both of symmetry A which shows "breathing" of Bi and O1 and O2 atoms [13]. In sample no.2 the other intensity modes of symmetry A as well as of other symmetry types are observed. Sample no.3 have best observable intensity maximum at  $620\text{ cm}^{-1}$ , of symmetry E, which shows Bi and O1, O2, O3 vibrations elongating the cluster along either  $\langle 100 \rangle$  or  $\langle 001 \rangle$ ,  $\langle 100 \rangle$  or  $\langle 010 \rangle$ , respectively.

### 3.5. Optical transmission spectra

The described composite samples were prepared with high mass fraction in order to obtain XRD and Raman measurements that clearly distinguish BGO particles from polymer matrix and in this way investigate whether powder particles in such composites keep their crystal characteristics.

Optical transmission spectra were measured for the single crystal BGO plate, pure polymer samples and composite samples.

Single crystal plates of size  $4\text{ mm} \times 4\text{ mm} \times 10\text{ mm}$  were cut from the boule with cutting plane perpendicular to the crystal growth direction and mechanically and chemically polished. The transmission spectrum of such a plate is presented in Fig. 8a). The pure BGO crystal plate is almost not transparent for wavelengths less than  $500\text{ nm}$ . This is in agreement with literature [22], since the energy gap of crystal BGO is about  $3.2\text{ eV}$  and the yellow color of this crystal is due to a broad absorption shoulder in the photon energy range from  $2.3\text{ eV}$  to  $3.2\text{ eV}$  (corresponding to the wavelengths from  $539$  to  $387\text{ nm}$ ). At the same graph in Fig. 8a) the optical spectra of pure PMMA and pure PS polymer  $0.6\text{ mm}$  thick plates are presented, too.

Optical transmission spectra of composite samples are presented in Fig. 8b). All presented spectra are normalized to the air transmission spectra.

The similar shapes of spectra for the samples no.1 and no.2 resemble to pure PMMA measured spectra. Although the samples no.1 and no.2 have the same initial BGO mass fraction  $1\text{ wt}\%$  the real mass fraction of the sample no.1 is most probable smaller than initial because of the filtering during preparation. Particles in sample no.2 have smaller sizes then those in sample no.1, according to the presented SEM analysis (paragraph 3.2.), so the light scattering is more intensive in this sample and since its real mass fraction is higher, its transmission is worse. Sample no.3 has low but almost linear transmission spectra versus wavelength.

The composite samples, thanks to polymer matrix, have wider transmission spectra than the BGO crystal. This allows using this material for double-wavelength techniques, where one of the wavelengths is chosen to be outside BGO transmission spectra. In case of using this material for fiber optic sensors this signal can be used as the normalization signal which compensates the effects of fiber bending and vibration.

### 3.6. The calculations of composite sample transmission

The described composite samples were prepared with high mass fraction, as previously explained and for this reason their measured transmissions were low, as expected. Those measured values were used therefore for comparison with calculated, based

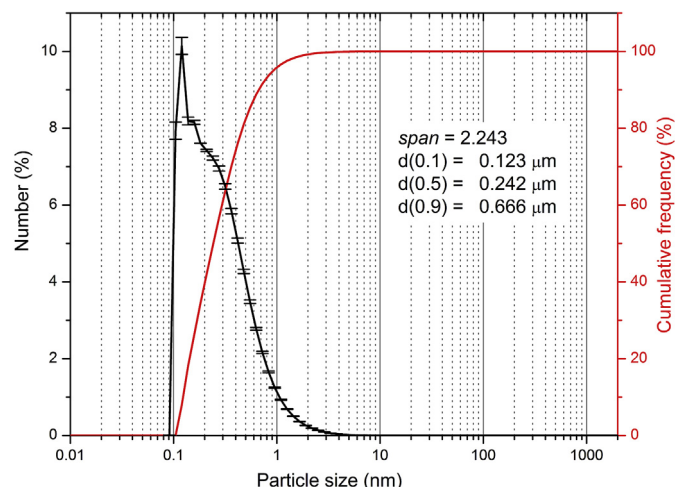


Fig. 1. Particle size distribution of BGO powder.

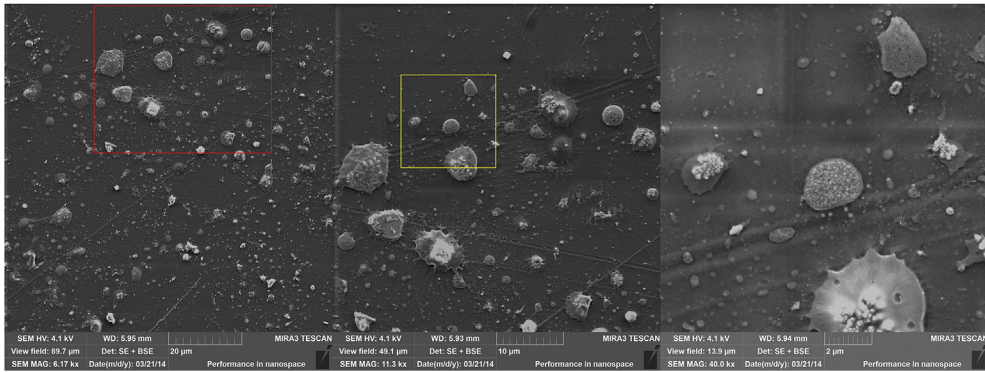


Fig. 2. SEM micrographs of the sample no.1 with different magnifications.

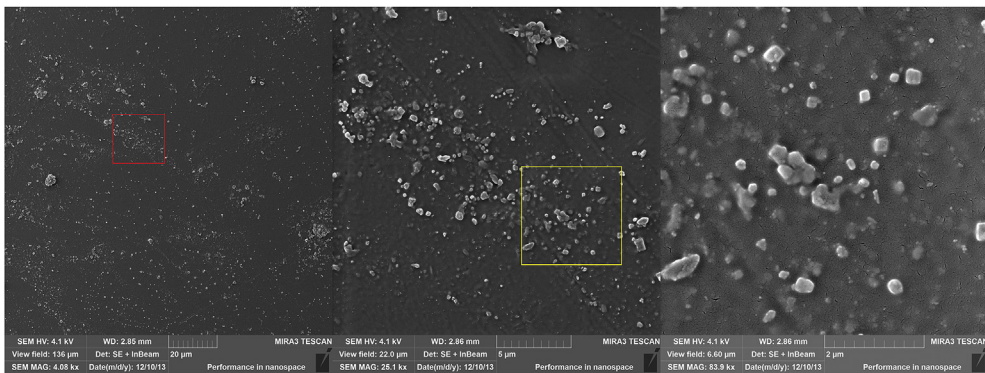


Fig. 3. SEM micrographs of the sample no.2 with different magnifications.

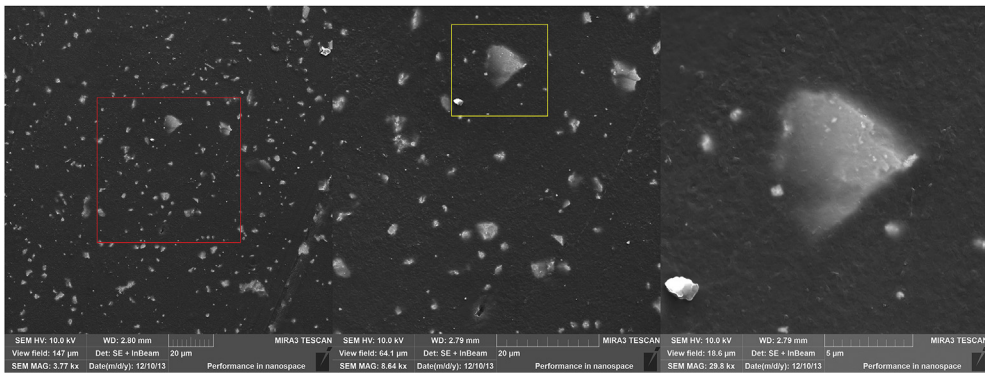


Fig. 4. SEM micrographs of the sample no.3 with different magnifications.

on Mie scattering theory, in order to check at what extent they correlate and if it is possible to predict the initial mass fraction of BGO for preparing the samples with sufficient transmission for the optical applications.

The electromagnetic radiation incident at the particle can be partially scattered and partially absorbed and the transmission of a material with dispersed particles depends on both processes. The amount of scattered and absorbed energy related to the incident is expressed in terms on scattering and absorption cross sections. The total energy loss based of both processes is called extinction and it is presented by extinction cross section as a sum of scattering and absorption cross sections. In the case of non-absorbing medium the scattering and extinction cross section are the same. One way of presenting both propagating and absorbing properties of a material

for some kind of electromagnetic radiation is to introduce complex index of refraction. The existence of imaginary part shows that the material is absorbing for that kind of electromagnetic radiation and its value directly influences the absorption coefficient of the material.

The scattering cross section is ratio of scattered radiation power on the particle and incident intensity of radiation. Mie scattering theory presents the solution for the electromagnetic scattering by a sphere of radius  $R$  embedded in a homogeneous and isotropic medium illuminated by a plane wave. If the index of refraction of a particle material is  $n_p$ , and of medium  $n_m$ , for some electromagnetic radiation of wavelength  $\lambda_0$  in vacuum the scattering cross section depends on: size parameter which compare dimension of a particle and medium wavelength, given as  $\chi = 2 \cdot \pi \cdot R \cdot n_m / \lambda_0$ , for spherical

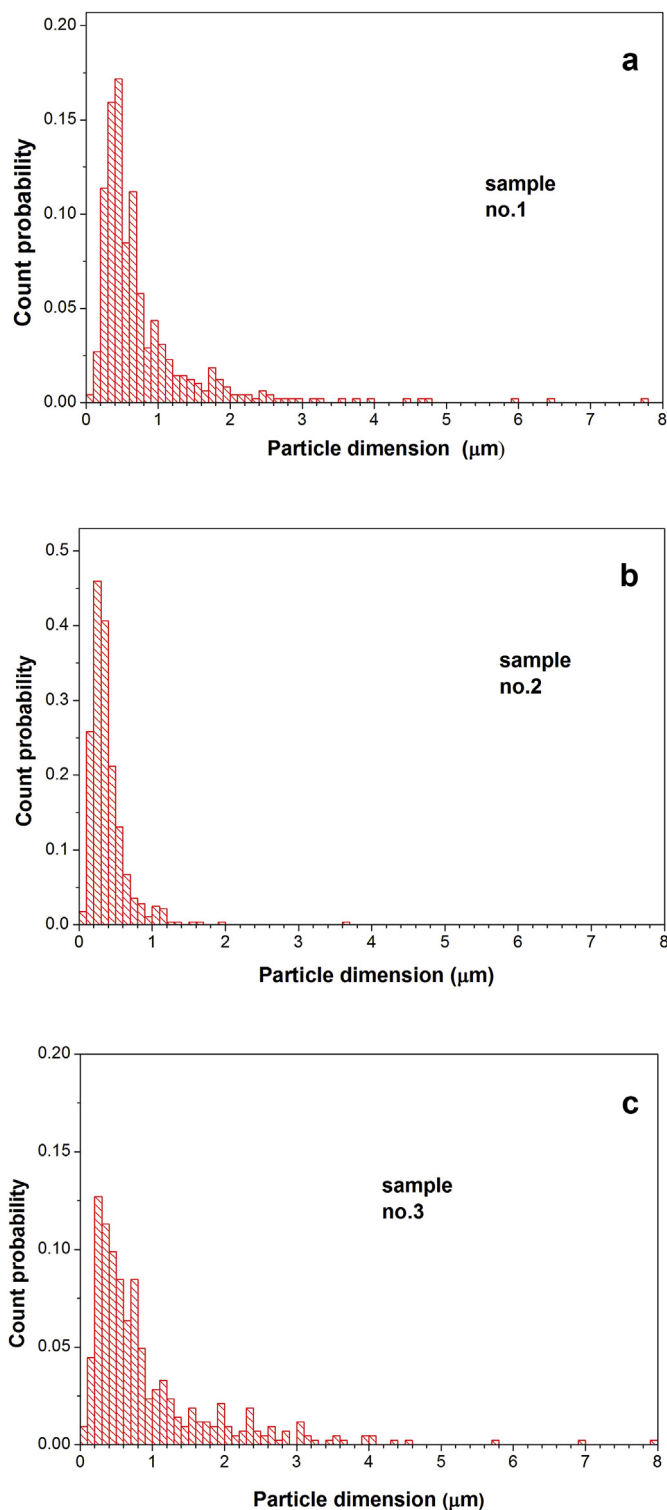


Fig. 5. Particle size distribution based on SEM analysis a) sample no.1, b) sample no.2 and c) sample no.3.

Table 1

Statistics parameters of PSD in composite samples based on SEM analysis.

Sample	<i>N</i>	min <i>d</i> , μm	max <i>d</i> , μm	mean <i>d</i> , μm	st. dev., μm	<i>d</i> (0.5), μm	<i>d</i> (0.9), μm
no.1	484	0.044	9.34	0.802	0.897	0.532	1.65
no.2	483	0.082	3.61	0.389	0.280	0.325	0.659
no.3	425	0.071	7.93	0.960	0.796	0.639	2.25

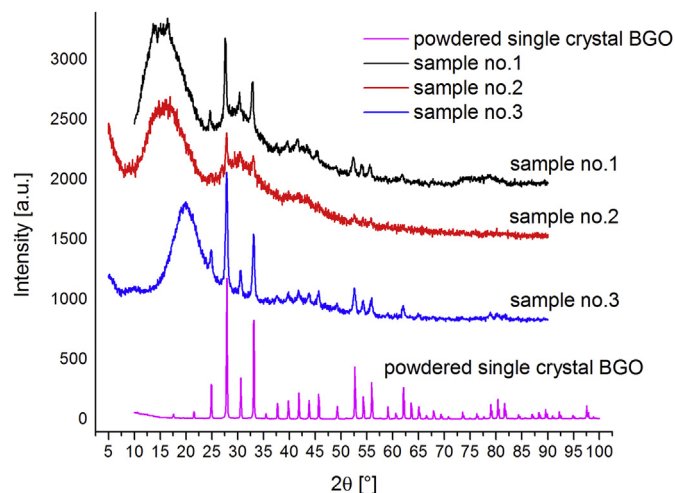


Fig. 6. XRD patterns of powdered BGO single crystal and composite samples.

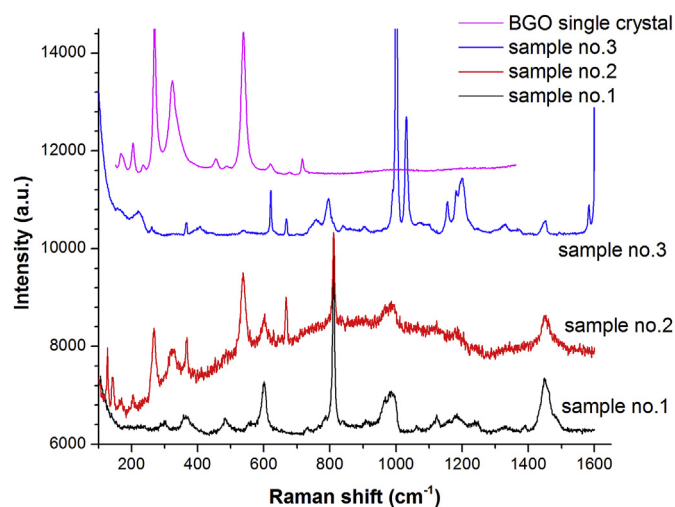


Fig. 7. Raman spectra of BGO single crystal and composite samples.

particle, and from the ratio of indices of refraction of particle and medium given as  $m = n_p/n_m$ .

The calculations were done using Mie calculator software [12,23] for spherical particles. Input data for the calculations were: mass density of PMMA  $\rho_{\text{PMMA}} = 1.18 \text{ g/cm}^3$ , mass density of PS  $\rho_{\text{PS}} = 1.0 \text{ g/cm}^3$  and mass density of BGO  $\rho_{\text{BGO}} = 9.23 \text{ g/cm}^3$ . Based on those data the total volume fraction  $f_V$  of BGO in composite samples is calculated based on equation (1):

$$f_V = \frac{\rho_{\text{pol}} \cdot f_W}{(1 - f_W) \cdot \rho_{\text{BGO}} + \rho_{\text{pol}} \cdot f_W} \quad (1)$$

In the equation (1)  $\rho_{\text{pol}}$  denotes mass density of used polymer ( $\rho_{\text{PMMA}}$  or  $\rho_{\text{PS}}$ ) and  $f_W$  denotes mass fraction of BGO powder in the



**Table 2**  
Raman frequencies observed in single crystal BGO [13] and samples.

BGO single crystal wave number, cm <sup>-1</sup>	Symmetry type	Sample no.1 wave number, cm <sup>-1</sup>	Sample no.2 wave number, cm <sup>-1</sup>	Sample no.3 wave number, cm <sup>-1</sup>
168	A		166–170	
190	F (LO)	190s		
204	F (TO)		204	
234	E	234s		
268	A		269	269s
322	A	322s	322 wide peak	
454	E		454s	
486	F (TO + LO)	488s	488s	
538	A		538	538
619	E	620 s		620
677	F (TO)	676s	677s, 682s	
715	A			716s

s-small, hardly visible intensity peak.

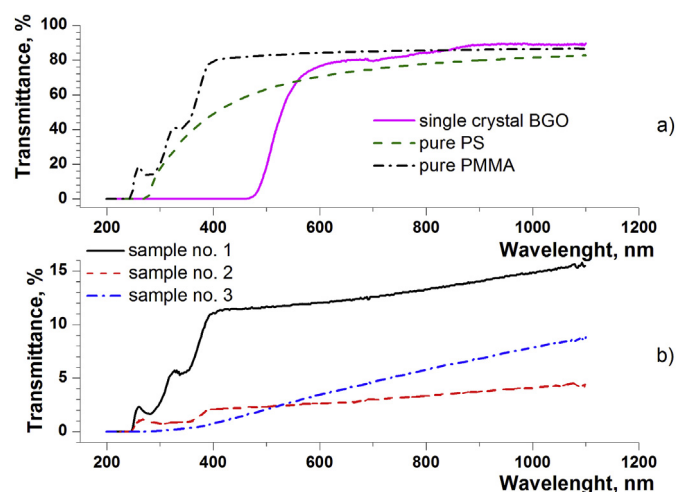


**Fig. 8.** Transmission spectra of: a) single crystal BGO, pure PMMA and pure PS, b) composite samples.

samples that was 0.01 (i.e. 1.0 wt%). Spectral dependences of index of refraction of the polymers and BGO were taken from the refractive index database [24]. Since the data for BGO are only available in the spectral range from 450 to 700 nm and the crystal is not or low transparent for wavelengths below 500 nm, the calculations of transmission of samples are derived for 500 nm, 600 nm and 700 nm.

The scattering cross sections  $\sigma_{iM}$  were calculated for spherical particles of diameter  $d_i$ , where  $d_i$  was taken in the range 100 nm - 0.8  $\mu\text{m}$  at 20 nm steps and in the range 0.8  $\mu\text{m}$ –10  $\mu\text{m}$  at 0.1  $\mu\text{m}$  steps for each of those three wavelengths.

Assumed that the number of particles with diameter  $d_i$  is  $N_i$ , the total volume of those particles was calculated as  $N_i V_i = N_i \cdot \pi \cdot \frac{d_i^3}{6}$ . Using total volume fraction of BGO in the sample from equation (1) the number concentration  $n_i$  of particles having diameter  $d_i$  is:

$$n_i = \frac{f_V \cdot N_i}{\sum_{i=1}^K (N_i \cdot V_i)} \quad (2)$$

where  $K$  is the number of different diameters of particles used in calculations. The scattering coefficient of the polymer composite sample at one wavelength  $\gamma_s$  is then obtained as:

$$\gamma_s = \sum_{i=1}^K n_i \sigma_{iM} \quad (3)$$

Since the imaginary parts of indices of refraction for BGO and polymers were zero, obtained scattering coefficients are the same as the extinction coefficients of the samples.

If two parallel planes, at distance  $L$ , inside a polymer composite are imagined and if  $I_0$  is the intensity of light incoming at first plane and  $I$  is intensity of transmitted light reaching the second plane, the transmission coefficient  $T$  can be calculated as:

$$T = \frac{I}{I_0} = e^{-\gamma_s \cdot L} \quad (4)$$

Thus obtained value  $T$  in equation (4) is the transmission or transmission coefficient of the composite sample normalized to the transmission of the pure polymer sample of the same width and for the same wavelength. In order to calculate the transmission spectra of a sample normalized to the air, calculated transmission  $T$  is multiplied with the measured transmission coefficient of corresponding pure polymer sample for that wavelength. In case of comparing composite samples based on the same polymer matrix it is more often to measure or calculate transmission normalized to transmission of pure polymer. Since our composite samples are based on different polymer matrices, their transmissions, normalized to the air, are compared.

The calculations based on the described procedure were applied to various PSD:

a) In order to evaluate the transmission coefficients in an "ideal" case, i.e. the case that particle size distribution in the polymer composite is the same as in the powder, the values for  $N_i$  and  $d_i$  were taken from the paragraph 3.1. The transmissions were calculated for  $L = 0.6$  mm thick plates and the results were presented also in Table 3. All calculated values were higher than measured since the particles were not ideally spherical and ideally dispersed. For the used mass fraction of 1 wt%, the maximum obtained values are around 17%, which means that input mass fraction of such BGO particles should be lower in order to get better transmissions. The measured transmission values for sample no.2 and no.3 (from Table 3) are five to six times lower from those maximums. Thus, to achieve sample the transmission of 50% of those samples, the number concentration of particles should be about five times lower (based on equations (3) and (4)) for both samples, which corresponds to particle mass fraction of 0.2 wt%.

b) The calculations based on PSD from SEM analysis of polymer samples (results presented in paragraph 3.2.) were calculated, too. In these calculations the measured longest dimension of a particle was assumed as a diameter  $d_i$  of the particle. The results are presented in Table 3. The obtained values for samples no.1 and no.3 differ significantly from measured values and those for sample no.2 show the best match, slightly higher than measured.

One of the reasons for this mismatch of measured and calculated

values is that PSD based on SEM analysis, which is in fact two-dimensional and relevant to the top of sample, was used as volume PSD. The PSD inside the sample could be different from that on the top. It seems from comparison of calculated and measured values that real partition of smaller particles (size up to 0.5  $\mu\text{m}$  diameter) is higher than from SEM analysis since their presence increases scattering volume and hence decreases transmission. The other reason for this mismatch is that in this type of modelling the aggregates are taken as spheres of pure crystal BGO, not as a group of very close connected particles. The light scattering process is more intensive on those particles group than on the homogeny sphere of the same diameter. For these reason, the aggregates have more significant influence on scattering loss, and some kind of their effective scattering cross sections are larger than obtained in this modelling.

The best match between calculated and measured results is for sample no.2 since the most of the powder volume in it is uniformly dispersed in small particles.

Sample no.1 has better measured transmission than sample no.2 because its real particle mass fraction is in fact less than 1 wt% due to filtering. On the other hand its larger particles and aggregates whose influence increases the transmission are not only round but sometimes with very complex structure. In calculations based on maximum particle length taken as a diameter of sphere, calculated volumes of large particles could be much higher than real and thus the calculated small particle size mass concentration based on (2) is lower than real. Since the input mass fraction of sample no. 1 is changed due to filtering during preparation procedure, the real mass fraction for the sample no.1 is not known, as well as, all the input values based on it. So with not known number concentrations of particles, as a main input data, the calculated influence of particle shape could not give valuable information for comparison with measuring data.

The dispersed particles in sample no.3 were mostly not spherical, so the concentration of smaller particles and their scattering cross sections were calculated with the errors. The scattering cross section calculations for non-spherical arbitrary shape particles are much more complicated than those based on Mie theory for spherical ones. There are lot of researches that compare the scattering cross sections of non-spherical and some kind of equivalent spherical particle [25–28]. They have presented their results through comparing graphs or by correction factors that show how to choose equivalent spherical particle that have similar scattering cross section as corresponding non-spherical one.

The dispersed particles and aggregates in sample no.3 could be in the first approximation taken as spheroids. The longest axis of such spheroids  $c_i$  equals the half of their measured longest dimension  $d_i$  and their perpendicular axis  $a_i$  is in average twice

shorter than  $c_i$  i.e.  $d_i = 2c_i = 4a_i$ . In this case the spheroid particle volume can be calculated as  $V_{iSRD} = \frac{\pi d_i^2}{24}$ . In literature [28] the scattering efficiency  $Q_{SRD}$  for spheroid and  $Q_S$  for related sphere, i.e. sphere whose radius equals the length the smaller axis of the spheroid were presented for different size parameters, and for different elongation factors  $\gamma = c_i/a_i$  of the spheroid. For the particles in sample no.3 this factor was taken as  $\gamma = 2$ . The size parameters for wavelengths  $\lambda_0 = 500, 600$  and  $700$  nm were calculated as  $\chi_i = \frac{2\pi \cdot n_{PS}(\lambda_0)}{\lambda_0} a_i$ , where  $n_{PS}(\lambda_0)$  was index of refraction of PS for the wavelength  $\lambda_0$ . From the PSD based on SEM analysis for the sample no.3 values of  $\chi_i$  were mostly bigger than 3 except for the particles that have  $d_i$  smaller than  $0.4 \mu\text{m}$ . The relation of scattering efficiencies for the spheroid and the sphere versus  $\chi_i$  taken from the literature (graph in Fig. 12b from Ref. [28]) was fitted with the curve

$$Q_{rel} = \frac{Q_{SRD}}{Q_S} = A \cdot \chi_i^{-B} \quad (5)$$

for  $0.1 \leq \chi_i \leq 4$ , where  $A = 1.59903$ , and  $B = 0.32823$ . For  $\chi_i > 4$ , based on the same literature [28],  $Q_{rel} = 1$ .

Since the cross section of the spheroid is two times bigger than the cross section of the sphere in the direction of the incident light and based on the definition of scattering efficiency [28] scattering cross section for the spheroid particle  $\sigma_{iSRD}$  was calculated as

$$\sigma_{iSRD} = 2 \cdot Q_{rel} \cdot \sigma_{iM} \quad (6)$$

The equations from (2)–(4) were applied for spheroids in a way that  $V_{iSRD}$  is used instead of  $V_i$ , and  $\sigma_{iSRD}$  instead of  $\sigma_{iM}$  for every wavelength. The transmissions of sample no.3 based on spheroid particles are presented in Table 3 too, and are much smaller than obtained for spherical particles, but still higher than measured, since real particle shape is more complex than spheroidal and the influence of aggregates is not taken into account, probably because the SEM analysis in the case of sample no.3 did not represent real PSD in the whole sample.

c) Another type of idealized backward calculation based on Mie scattering for spherical particle was done. It was supposed that the crystal BGO powder was ideally milled into spherical particles of the same diameter  $d_{eff}$ , and so the concentration of particles with the volume fraction  $f_V$  became  $n_{eff} = \frac{f_V}{\frac{\pi}{6} d_{eff}^3}$ . Scattering coefficient of

such material is  $\gamma_{Seff} = n_{eff} \cdot \sigma_{ieff}$  and using previously calculated scattering cross sections  $\sigma_{iM}$  for different diameters as  $\sigma_{ieff}$ , the dependence  $\gamma_{Seff}$  versus  $d_{eff}$  could be calculated based on (3) for each wavelength. Comparing those values with obtained  $\gamma_S$  from measured transmission using equation (4),  $d_{eff}$  for each sample

**Table 3**  
Measured and calculated optical transmission of the composite samples for three wavelengths.

Sample	Method of obtaining results	Transmission T,%		
		Wavelength $\lambda_0$ , nm		
		500	600	700
no.1	Measured	11.63	12.03	12.56
	Calculated (Mie-spheres)	16.91	16.86	17.42
no.2	Measured	42.6	42.5	42.1
	Calculated (Mie-spheres)	2.3	2.6	3.0
no.3	Measured	16.9	16.9	17.4
	Calculated (Mie-spheres)	4.46	3.9	3.96
no.3	Based on powder PSD Based on PSD from SEM Based on PSD from SEM and spheroid correction	3.3	4.6	6.2
		16.8	18.4	19.1
		31.9	34.7	37.3
		14.6	14.8	16.1

could be estimated for those three wavelengths. Averaging such obtained values over all wavelengths the calculated  $d_{\text{eff}}$  for sample no.1 is  $1.41 \pm 0.11 \mu\text{m}$ , for sample no.2 the corresponding value is  $0.87 \pm 0.11 \mu\text{m}$  and for sample no.3 is  $0.79 \pm 0.05 \mu\text{m}$ . The value of  $d_{\text{eff}}$  for sample no.2 is similar to its  $d(0.9)$  value from Table 1. In case of sample no.3 obtained  $d_{\text{eff}}$  is significantly smaller of its  $d(0.9)$  from SEM analysis (Table 1) and this could indicate that the volume fraction of small particles is higher than evaluated from SEM analysis or the scattering of aggregates is more similar to scattering at small particles.

#### 4. Conclusion

In this work it is shown that solution casting method is suitable for preparing polymer composites with milled BGO powder as filler. In such composites the BGO crystal structure should be preserved, the particles uniformly distributed and the samples enough transparent for potential electro-optical and magneto-optical applications.

The investigations of three prepared samples based on two polymer matrix (PMMA and PS) and two solvents (acetone and chloroform) pointed out that the dispersion of particles was very good in both PMMA and PS samples with chloroform as solvent but particles and agglomerate sizes were smaller in PMMA. The dispersed particles and agglomerates in PMMA are also more round than in PS. Two methods of dispersion and deaggregation of BGO powder were used in this study (filtration and sonication) and next research will be focused on the application of ultrasonic irradiation.

Powdered BGO particles keep their crystal characteristics in the composites and XRD measurements best recognize BGO characteristics in PS sample (no.3) while Raman spectroscopy was more efficient in detecting vibrational modes in the PMMA sample with chloroform as solvent.

Optical transmission of prepared samples was low since the BGO particles mass fraction was intentionally high (1 wt%) in order to have XRD and Raman measurements that clearly distinguish BGO particles in polymer matrix. The transmission of samples based on Mie theory scattering calculations for spherical particles was obtained based on PSD in the BGO powder, and on SEM analysis of the samples. In case of ideal powder particles dispersion when their PSD in the composite sample is the same as in the powder, it is shown that maximum obtained transmission would be 17%, when particle mass fraction is 1 wt % and in order to increase the transmission of such prepared samples the mass fraction of BGO particles should be lower. The real transmission values for sample no.2 and no.3 are five to six times lower from those maximum. To achieve the transmission of 50%, the number concentration of particles should be about five times lower for both samples, which corresponds to particle mass fraction of 0.2 wt%.

When the calculations are based on SEM analysis the obtained values of PMMA/chloroform composite have good match with measured because the particle sizes are the smallest and mostly round. On contrary, in the PS polymer composite particles have irregular shapes, and the approximation with spheroids with elongation factor 2 gave better results but still higher than measured.

The difference between calculated and measured transmission values is caused mainly because this type of modelling treats aggregates as pure crystal BGO spheres or spheroids, not as groups of very close connected particles. The light scattering process is more intensive on those multi-particles aggregates than on the homogenous crystal particles of the same dimension. So, comparing of calculating and measured transmission could be used to indicate level of agglomeration of particles in the samples.

The same Mie scattering calculations were used for some sort of

backward modelling in order to find the equivalent diameter of the identical BGO powdered spherical particles that would give the same transmission as prepared samples, with the same BGO mass fraction.

#### Acknowledgments

This work was supported by the Ministry of Science and Technological Development of the Republic of Serbia, Projects No. TR 34011 and III 45003.

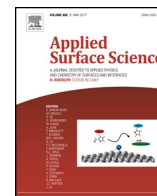
#### Appendix A. Supplementary data

Supplementary data related to this article can be found at <http://dx.doi.org/10.1016/j.jallcom.2016.10.140>.

#### References

- [1] V.M. Skorikov, Yu F. Kargin, A.V. Egorysheva, V.V. Volkov, M. Gospodinov, Growth of sillenite-structure single crystals, *Inorg. Mater.* 41 (1) (2005) S24–S46.
- [2] N.C. Deliolanis, I.M. Kourmoulis, G. Asimellis, A.G. Apostolidis, E.D. Vanidhis, N.A. Vainos, Direct measurement of the dispersion of the electrogyration coefficient of photorefractive  $\text{Bi}_{12}\text{GeO}_{20}$  crystals, *J. Appl. Phys.* 97 (2005) 023531.
- [3] R.A. Ganeev, A.I. Rysanyansky, B. Palpant, S. Debrus, Third-order nonlinearities of  $\text{Bi}_{12}\text{GeO}_{20}$  crystal measured by nanosecond radiation, *J. Appl. Phys.* 97 (2005) 104303.
- [4] E. Weidner, G. Pauliat, G. Roosen, Wavefront buffer memory based interferometric camera with a photorefractive crystal as the active medium, *J. Opt. A Pure Appl. Opt.* 5 (6) (2003) S529.
- [5] S. Sayuri Sato, J.C. Santos, Modeling residual thermal stress-induced integrated optical waveguides on  $\text{Bi}_{12}\text{GeO}_{20}$  substrate for electrooptic modulation application, in: SBMO/IEEE MTT-S International Microwave & Optoelectronics Conference (IMOC 2009), 2009, pp. 669–672.
- [6] O. Peña-Rodríguez, J. Olivares, I. Bányász, Optical properties of crystalline and ion-beam amorphous  $\text{Bi}_{12}\text{GeO}_{20}$ : relevance for waveguide applications, *Opt. Mater.* 47 (2015) 328–332.
- [7] P.M. Mihailovic, S.J. Petricevic, J.B. Radunovic, Compensation for temperature-dependence of the faraday effect by optical activity temperature shift, *IEEE Sens. J.* 13 (2) (2013) 832–837, <http://dx.doi.org/10.1109/JSEN.2012.2230322>.
- [8] L. Labrunie, G. Pauliat, G. Roosen, J. Launay, Simultaneous acquisition of  $\pi/2$  phase-stepped interferograms with a photorefractive  $\text{Bi}_{12}\text{GeO}_{20}$  crystal: application to real-time double-pulse holography, *Opt. Lett.* 20 (15) (1995) 1652–1654.
- [9] D.R. Paul, L.M. Robeson, Polymer nanotechnology: nanocomposites, *Polymer* 49 (2008) 3187–3204.
- [10] D. Stojanovic, A. Orlovic, S. Markovic, V. Radmilovic, Petar S. Uskokovic, R. Aleksic, Nanosilica/PMMA composites obtained by the modification of silica nanoparticles in a supercritical carbon dioxide-ethanol mixture, *J. Mater. Sci.* 44 (2009) 6223–6232.
- [11] R.M. Dukali, I. Radovic, D.B. Stojanovic, P.S. Uskokovic, N. Romcevic, V. Radojevic, R. Aleksic, Preparation, characterization and mechanical properties of  $\text{Bi}_{12}\text{SiO}_{20}$ -PMMA composite films, *J. Alloys Compd.* 583 (2014) 376–381.
- [12] D.B. Stojanović, L. Brajović, A. Orlović, D. Dramlić, V. Radmilović, P.S. Uskoković, R. Aleksić, Transparent PMMA/silica nanocomposites containing silica nanoparticles coating under supercritical conditions, *Prog. Org. Coat.* 76 (4) (2013) 626–631.
- [13] Z.Ž. Lazarević, P. Mihailović, S. Kostić, M.J. Romčević, M. Mitrić, S. Petricević, J. Radunović, N.Ž. Romčević, Determination of magneto-optical quality and refractive index of bismuth germanium oxide single crystals grown by Czochralski, *Opt. Mater.* 34 (11) (2012) 1849–1859.
- [14] R. Baskaran, S. Selvasekarapandian, N. Kuwata, J. Kawamura, T. Hattori, Conductivity and thermal studies of blend polymer electrolytes based on PVAc-PMMA, *Solid State Ionics* 177 (2006) 2679–2682.
- [15] N. Zhang, X. Yu, J. Hu, F. Xue, E. Ding, Synthesis of silver nanoparticle-coated poly(styrene-co-sulfonic acid) hybrid materials and their application in surface-enhanced Raman scattering (SERS) tags, *RSC Adv.* 3 (2013) 13740–13747.
- [16] B. Schneider, J. Štokr, P. Schmidt, M. Mihailov, S. Dirlikov, N. Peeva, Stretching and deformation vibrations of  $\text{CH}_2$ ,  $\text{C}(\text{CH}_3)$  and  $\text{O}(\text{CH}_3)$  groups of poly(methylmethacrylate), *Polymer* 20 (1979) 705–712.
- [17] X. Xingsheng, M. Hai, Z. Qijing, Z. Yunsheng, Properties of Raman spectra and laser-induced birefringence in polymethyl methacrylate optical fibres, *J. Opt. A Pure Appl. Opt.* 4 (2002) 237–242.
- [18] A. Palm, Raman spectrum of polystyrene, *J. Phys. Chem.* 55 (8) (1951) 1320–1324.
- [19] B. Jasse, L. Monnerie, Far-infrared and Raman spectra of polystyrene model molecules, *J. Phys. D. Appl. Phys.* 8 (1975), 863–861.

- [20] A. Serafim, R. Mallet, F. Pascaretti-Grizon, I-C. Stancu, D. Chappard, Osteoblast-like cell behavior on porous scaffolds based on poly(styrene) fibers, *Biomed. Res. Int.* 2014 (2014) 609319.
- [21] S. Venugopalan, A.K. Ramdas, Raman spectrum of bismuth germanium oxide\*, *Phys. Lett.* 34A (1971) 9–10.
- [22] R. Oberschmid, Absorption centers of  $\text{Bi}_{12}\text{GeO}_{20}$  and  $\text{Bi}_{12}\text{SiO}_{20}$  crystals, *Phys. Stat. Sol.(a)* 89 (1) (1985) 263–270.
- [23] Mie scattering by Scott Prah, [http://omlc.org/calc/mie\\_calc.html](http://omlc.org/calc/mie_calc.html), 2016 (accessed 14.03.2016).
- [24] Refractive index database, [www.refractiveindex.info](http://www.refractiveindex.info), 2015 (accessed 17.12.2015).
- [25] M.I. Mishchenko, Electromagnetic scattering by nonspherical particles: a tutorial review, *J. Quant. Spectrosc. Radiat. Transf.* 110 (2009) 808–832.
- [26] X. Li, Z. Chen, A. Taflove, V. Backman, Equiphasic - sphere approximation for analysis of light scattering by arbitrarily shaped nonspherical particles, *Appl. Opt.* 43 (2004) 4497–4505.
- [27] K. Muininen, T. Pieniluoma, Light Scattering by Gaussian random ellipsoid particles: first results with discrete dipole approximation, *J. Quant. Spectrosc. Radiat. Transf.* 112 (2011) 1747–1752.
- [28] V. Rysakov, M. Ston, Light scattering by spheroids, *J. Quant. Spectrosc. Radiat. Transf.* 69 (2001) 651–665.



# Nanospectroscopy of thiocyanine dye molecules adsorbed on silver nanoparticle clusters



Uroš Ralević<sup>a</sup>, Goran Isić<sup>a,\*</sup>, Dragana Vasić Anicijević<sup>b</sup>, Bojana Laban<sup>c</sup>, Una Bogdanović<sup>b</sup>, Vladimir M. Lazović<sup>d</sup>, Vesna Vodnik<sup>b</sup>, Radoš Gajić<sup>a</sup>

<sup>a</sup> Graphene Laboratory of Center for Solid State Physics and New Materials, Institute of Physics, University of Belgrade, Pregrevica 118, 11080 Belgrade, Serbia

<sup>b</sup> Vinča Institute of Nuclear Sciences, University of Belgrade, P.O. Box 522, Belgrade, Serbia

<sup>c</sup> Faculty of Natural Sciences and Mathematics, University of Priština, 38200 Kosovska Mitrovica, Serbia

<sup>d</sup> Institute of Physics, University of Belgrade, Pregrevica 118, 11080 Belgrade, Serbia

## ARTICLE INFO

### Article history:

Received 29 June 2017

Received in revised form 13 October 2017

Accepted 21 October 2017

Available online 25 October 2017

### Keywords:

Surface enhanced Raman scattering

Atomic force microscopy

Citrate capped silver nanoparticles

Thiocyanine dye

## ABSTRACT

The adsorption of thiocyanine dye molecules on citrate-stabilized silver nanoparticle clusters drop-cast onto freshly cleaved mica or highly oriented pyrolytic graphite surfaces is examined using colocalized surface-enhanced Raman spectroscopy and atomic force microscopy. The incidence of dye Raman signatures in photoluminescence hotspots identified around nanoparticle clusters is considered for both citrate- and borate-capped silver nanoparticles and found to be substantially lower in the former case, suggesting that the citrate anions impede the efficient dye adsorption. Rigorous numerical simulations of light scattering on random nanoparticle clusters are used for estimating the electromagnetic enhancement and elucidating the hotspot formation mechanism. The majority of the enhanced Raman signal, estimated to be more than 90%, is found to originate from the nanogaps between adjacent nanoparticles in the cluster, regardless of the cluster size and geometry.

© 2017 Elsevier B.V. All rights reserved.

## 1. Introduction

Dye coated metallic nanoparticles (NPs) exhibit interesting optical properties provided by the interaction between the metal core and dye shell. Depending on the interaction mechanism between the two, the optical properties of dye molecules and NPs can be changed separately or jointly within the adsorbate–NP complex [1]. For example, the NP surface plasmon frequency can be changed by the presence of adsorbate while the dye fluorescence can be quenched or enhanced by the NP [2,3]. Ultimately, under special conditions, these complexes can exhibit unique characteristics different than those of either isolated dye molecules or NPs. Owing to the variety of mechanisms by which dyes can interact with metallic NPs, dye–NP complexes can lead to applications ranging from nanoscale sensing [4] to advanced composite materials for novel active and nonlinear optical devices [5].

Many of the recent studies have been focused on dyes which are able to self-assemble in highly oriented structures called J-aggregates on the surface of the NPs [6–14]. J-aggregates have a

strong and narrow excitonic absorption band that is red-shifted with respect to the monomer absorption band [15]. The special way of molecular stacking, responsible for the formation of Frenkel excitons, has been extensively studied [16–24] as these aggregates are the most famous spectral sensitizers of silver halides for the photographic industry [25]. On the other hand, it has been shown that the combination of J-aggregates and silver or gold NPs provides a platform for the fundamental studies of excitons and their interaction with high electromagnetic fields, as well as a way to utilize optical properties of such a hybrid system for nanoscale optical devices.

A necessary condition for the interaction to occur is that the dye molecules are adsorbed on the surface of the NPs. Therefore, the adsorption process plays one of the key roles in these systems. The most common way in which the dye–NP hybrid systems are prepared is by mixing the appropriate colloid and dye solutions and letting the resulting mixture reach its metastable or stable state in which the NPs have dye molecules adsorbed on their surface. The dynamics of the adsorption process is quite complex as it depends on various factors including the target concentration of the constituents, affinity of the dye molecules to bind to the NP surface and the type of capping anions protecting the surface of the NPs. For instance, the spectrophotometric studies of thiocyanine (TC) dye coated silver nanoparticles (AgNPs) in Refs. [26,12–14]

\* Corresponding author.

E-mail address: [isicg@ipb.ac.rs](mailto:isicg@ipb.ac.rs) (G. Isić).

show that the capping anions can influence the mechanism of the adsorption process and therefore its efficiency.

The influence of capping anions on the adsorption process can be studied on a nanoscopic level by exploiting very strong localized plasmonic fields at the NP surface and employing surface-enhanced Raman scattering (SERS) [27,28]. SERS has already been used for identification of TC J-aggregates and for studying their dynamics on the surface NP clusters in solutions [29–36].

In view of the significance of the dye-to-NP adsorption mechanism, here the mechanism of TC dye adsorption on the surface of AgNP clusters with citrate anion stabilization is investigated. In order to probe the presence of TC dye molecules on the nanoscale (i.e. on individual AgNP clusters), Ag colloids are mixed with TC dye solutions, and subsequently drop-cast onto freshly cleaved mica or SiO<sub>2</sub> substrates and, after drying, investigated using colocalized Raman microspectroscopy and atomic force microscopy (AFM). The key mechanism used for the identification of a small amount of TC dye molecules adsorbed on AgNP clusters is SERS [32]. The measurements are complemented by rigorous numerical simulations of plane wave scattering on AgNP clusters, showing that the electromagnetic enhancement of the Raman signal originates dominantly from the nanogaps between adjacent AgNPs within the clusters. The analysis of the SERS spectra acquired at the AgNP clusters on mica substrate and the fact that the majority of the SERS signal comes from the nanogaps indicate that the citrate anions impede the efficient dye adsorption.

## 2. Materials and methods

### 2.1. Chemicals

Silver nitrate (AgNO<sub>3</sub>), potassium chloride (KCl), and sodium borohydride (NaBH<sub>4</sub>) trisodium citrate (Na<sub>3</sub>C<sub>6</sub>H<sub>5</sub>O<sub>7</sub> × 3H<sub>2</sub>O) of the highest purity were purchased from Sigma Aldrich and used as received.

Thiocyanine dye (3,3-disulfopropyl-5,5-dichlorothiocyanine sodium salt, TC) was purchased from Hayashibara Biochemical Laboratories, Okayama, Japan.

### 2.2. Samples

Aqueous solutions of borate- and citrate-capped AgNPs were synthesized by NaBH<sub>4</sub> reduction of AgNO<sub>3</sub>, as described in Refs. [12,14]. For the synthesis of citrate-capped AgNPs, Na<sub>3</sub>C<sub>6</sub>H<sub>5</sub>O<sub>7</sub> × 3H<sub>2</sub>O was used as a stabilizing agent. The solution of borate-capped AgNPs was prepared immediately before use as the colloid is stable only up to a few hours. Oppositely, the solution of citrate-capped AgNPs is stable for a longer period of time, measured in months, due to the protective citrate anion mantle. The average diameter of both borate- and citrate-capped AgNPs is around 10 nm (see Section S1 of the Supplementary information). The nominal concentration of citrate-capped AgNPs in water solution is  $c_{\text{Ag}} = 16 \text{ nM}$  (see Fig. S1 for the related absorption spectra).

Aqueous TC dye solution with nominal concentration  $c_{\text{TC}} = 50 \mu\text{M}$  of TC and 1 mM of KCl was prepared by dissolving the solid TC in water and by adding KCl afterwards. Water purified with a Millipore Milli-Q water system was used in all cases. The absorption spectra of the TC dye is given in Fig. S1 in the Supplementary information.

The Ag colloid and the TC dye solution are mixed, and the resulting mixture (see Fig. S1 in the Supplementary information for the related absorption spectra) is drop-cast on a substrate. The adsorption of TC molecules on the surface of borate-capped AgNPs happens almost instantaneously [13,12], and the mixture was therefore drop-cast on the substrate a few minutes after mix-

ing the two solutions. On the other hand, the adsorption of TC dye on the surface of citrate-capped AgNPs is a much slower process [26,14] and for that reason the mixture was left overnight and afterwards drop-cast on a substrate.

For the investigation of TC/citrate-capped AgNP clusters, as well as for initial characterization of pristine citrate-capped AgNP clusters, mica was used as a substrate. Mica has an atomically flat, hydrophilic surface on which the AgNPs are easily deposited, while its contribution to the total Raman signal is small (see Section S2 of the Supplementary information). In addition to mica, highly oriented pyrolytic graphite (HOPG) and SiO<sub>2</sub> substrates were used as their surfaces are hydrophobic and, therefore, facilitate the formation of large, closely spaced AgNP clusters as well as more efficient aggregation of the TC dye on their surface. In particular, HOPG is used for Raman characterization of concentrated TC dye, since the dye efficiently aggregates on its surface. The SiO<sub>2</sub> is used for the control study of AgNPs having dye/borate anions conformed to their surface, since the large closely spaced AgNP clusters are required for fast Raman/SERS characterization of the initially unstable borate-capped AgNPs. Raman spectra of the TC dye, Mica, Si and HOPG are shown in Fig. S2 in the Supplementary information.

### 2.3. Methods

The AgNP clusters on a substrate are investigated using colocalized Raman microspectroscopy and AFM. The two techniques are used simultaneously thus providing spatially resolved chemical information of the sample along with its surface topography at the same place. In this way one is able to identify and assert the size of the SERS active AgNP clusters while obtaining the chemical identity of the analyte adsorbed on the surface of AgNPs. The AFM is operated in tapping mode in order to minimize the lateral force between the tip and the sample induced by lateral movements of the tip across the sample. The cantilever-tip system is oscillated at the characteristic first order resonance which is usually in the 90–230 kHz range. For Raman spectroscopy and SERS measurements a linearly polarized semiconductor laser operating at a wavelength of 532 nm is used. The laser power was varied from 2 to 0.2 mW within the  $\sim 0.3 \times 0.3 \mu\text{m}$  sized focus. The experiments are performed using commercial NTegra Spectra system from NT-MDT.

To numerically solve the classical Maxwell equations we have used the finite element method implemented within the Comsol Multiphysics software package [37]. We consider clusters of AgNPs having a diameter of 10 nm on a substrate under plane wave illumination. The Ag dielectric constant is taken from Rakic et al. [38]. The substrate is assumed to be semi-infinite and isotropic with a dielectric constant of 2.25, which roughly corresponds to the dielectric constants of both mica and SiO<sub>2</sub> at visible frequencies. The surrounding medium is vacuum and its dielectric constant is 1. For purposes of efficient meshing, AgNPs are assumed to lie 1 nm above the substrate. The clusters are formed in the plane which is parallel to the substrate by allowing AgNPs to have random position but enforcing the following conditions: (i) there is a certain minimal allowed distance  $d$  between two AgNPs; two AgNPs separated by the minimal distance are said to be adjacent; (ii) each AgNP must be adjacent to at least one other AgNP, thus ensuring that each randomly generated cluster is connected. By imposing these two conditions, we were able to randomly generate various cluster geometries and mimic the lack of control over the clusters morphology in the experiment.

The absorption  $\sigma_a(\lambda)$ , scattering  $\sigma_s(\lambda)$  and extinction  $\sigma_{\text{ext}}(\lambda)$  cross sections are calculated as a function of wavelength  $\lambda$ , according to their well-known definition [39]. The electric-field enhancement  $f(\mathbf{r}, \lambda)$  is defined as the squared ratio of magnitudes of the local electric field  $\mathbf{E}_L(\mathbf{r}, \lambda)$  and the incoming electric field  $\mathbf{E}_0(\lambda)$ , with  $\mathbf{r}$  denoting the coordinate at which the former is evaluated.

Following Kerker et al. [40], the SERS enhancement factor is defined as  $F(\mathbf{r}, \lambda_{\text{inc}}, \lambda) = f(\mathbf{r}, \lambda_{\text{inc}}) / f(\mathbf{r}, \lambda)$  with  $\lambda_{\text{inc}}$  and  $\lambda$  denoting the laser and Stokes wavelength, respectively. Since the measured PL/Raman signal being reported in this paper originates from large (relative to a cluster), diffraction limited, spots of 300 nm approximate diameter, it cannot be directly related to the spatially-resolved field and SERS enhancement factors. Instead, we consider their integrals over the cluster surface  $S$  and the corresponding cluster-averaged SERS factor  $\langle F(\lambda_{\text{inc}}, \lambda) \rangle$  defined as

$$\langle F(\lambda_{\text{inc}}, \lambda) \rangle = \frac{1}{S} \int_S F(\mathbf{r}, \lambda_{\text{inc}}, \lambda) dS. \quad (1)$$

### 3. Results and discussion

#### 3.1. Surface-enhanced Raman spectroscopy of pristine citrate-capped AgNPs

Fig. 1(a) shows an AFM topograph of pristine AgNP clusters on mica surface. The corresponding PL/Raman map is shown in Fig. 1(b). The intensity of every pixel in the PL/Raman map is obtained by dividing the sum of PL/Raman intensities across the entire spectral range (100–2000  $\text{cm}^{-1}$ ) with the number of spectral points. The color bar in panel (b) thus enumerates the average photon count. Bright areas in Fig. 1(b) represent the regions of enhanced signal, henceforth referred to as hotspots. These regions coincide with AgNP clusters consisting of a large number of AgNPs (with diameters in the 10–50 nm range), as seen by comparing the PL/Raman map with the AFM topography image. In fact, we find that the hotspots are dominantly formed within larger AgNP clusters,

such as those in Fig. 1(a), regardless of the substrate which is used (mica,  $\text{SiO}_2$  or HOPG).

Fig. 1(d) and (e) shows two sets of consecutively acquired spectra with a 40 s time step taken at two hotspots from Fig. 1(b) using 532 nm laser with intensity of  $\approx 200 \mu\text{W}/\mu\text{m}^2$ . The spectra in panels (c) and (d) are similar, but cannot be quantitatively compared. Both sets feature a wide background which spreads over the entire spectral range, and a pronounced band blinking in the 1000–1800  $\text{cm}^{-1}$  range (shaded region) which hinders a quantitative analysis. Considering that citrate anions are used for stabilizing the AgNPs, our hypothesis is that the blinking spectra is the SERS signal from the citrate anion mantle, sensitive to local heating in hotspots due to the small size of citrate anions, while the wide background is PL coming from the AgNP clusters.

#### 3.2. Numerical simulations of light scattering on random AgNP clusters

In order gain an insight into hotspot formation and assess the Raman enhancement factors, we employ a numerical model to calculate the electromagnetic fields scattered on randomly generated AgNP clusters. The motivation for considering random AgNP clusters is to get an idea on the variability of the electric field enhancement upon changing the cluster geometry and to identify any invariants which could be used to interpret SERS measurements on clusters whose exact geometry is unknown. A typical cluster consisting of 20 AgNPs is shown in Fig. 2(a). In this example we set the minimal AgNP distance at  $d = 0.8 \text{ nm}$  while the adjacent AgNPs are indicated by solid (red) lines Fig. 2(a). The extinction cross-section of the AgNP cluster in panel (a) is plotted in Fig. 2(b),

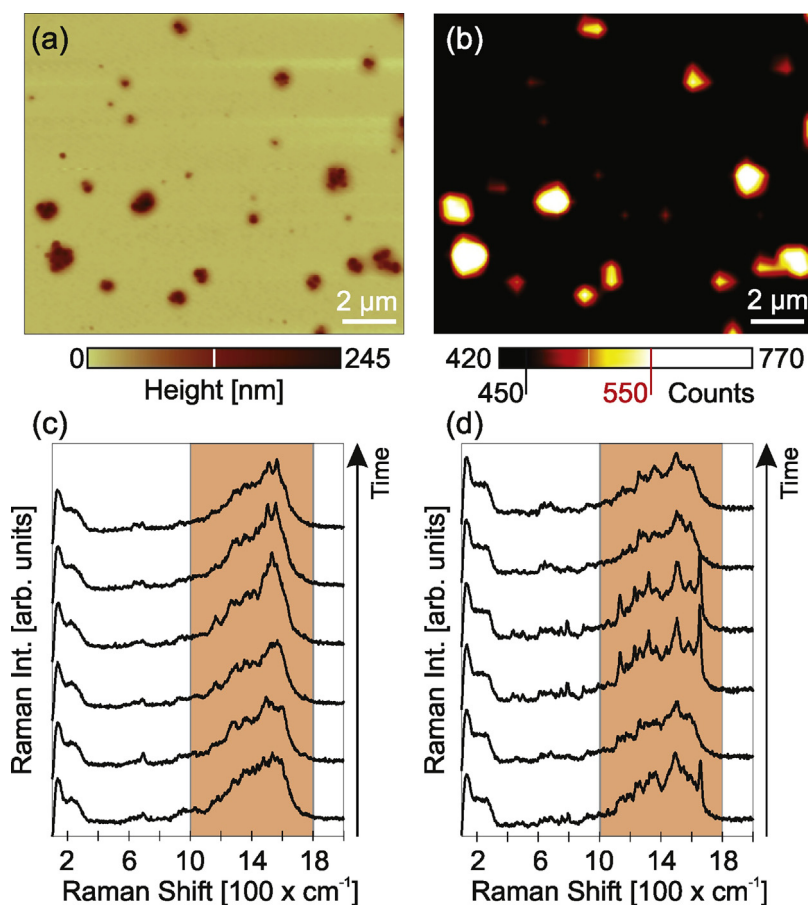
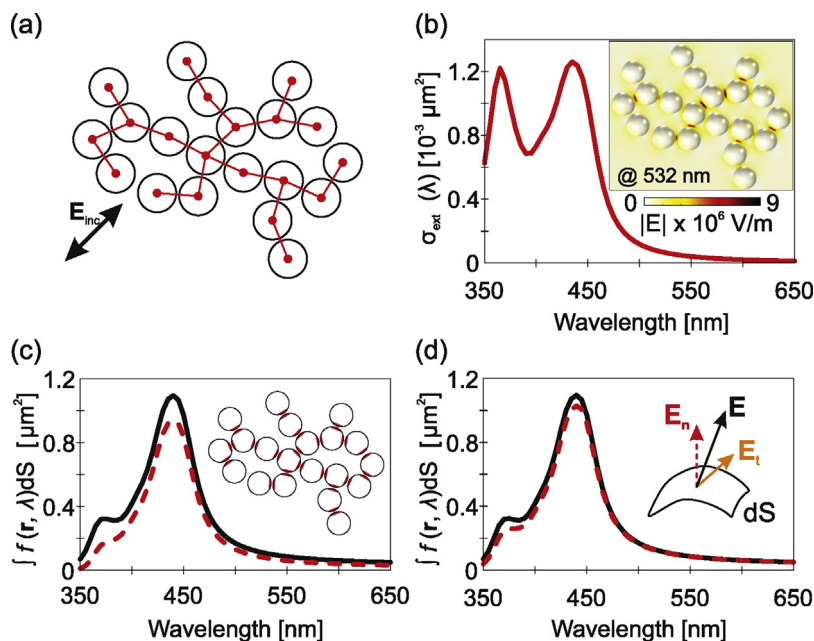


Fig. 1. (a) AFM topograph of pristine AgNP clusters drop-cast onto a freshly-cleaved mica substrate. (b) Corresponding PL/Raman map. (c), (d) Typical SERS spectra acquired within two hot spots in panel (b). The spectra were measured consecutively with a 40 s time step. The excitation laser wavelength is 532 nm.



**Fig. 2.** (a) Sketch of a typical cluster geometry used in the numerical model. Normal incidence is assumed for the incoming wave while its electric field is polarized parallel to the plane of the cluster and oriented as indicated by the arrow. The incident field intensity is set to  $200 \mu\text{W}/\mu\text{m}^2$ . (b) Extinction spectra of the cluster in panel (a). The inset shows the electric field magnitude distribution at 532 nm. (c) Surface integrals of the intensity enhancement over the entire cluster surface (solid black line) and over the entire gap area (dashed red line) plotted as the function of the wavelength. (d) Surface integrals of the total field enhancement (solid, black) and the ratio of the field component perpendicular to the AgNP surface (dashed, red) both taken over the entire cluster surface. (For interpretation of the references to color in this legend, the reader is referred to the web version of the article.)

as a function of the incident wavelength. For the considered cluster, the scattering cross-section is negligible with respect to the absorption cross-section and therefore  $\sigma_{\text{ext}} \approx \sigma_{\text{a}}$ . The two peaks observed at 365 and 435 nm, represent the single particle and cluster surface plasmon, respectively. Below we find that the wavelength of the former is virtually independent on the presence of other AgNPs, while the cluster plasmon wavelength redshifts with increasing cluster size. Upon the excitation of a cluster plasmon, the electric field is resonantly enhanced over the entire cluster. Although the distribution of resonant fields is highly dependent on the details of AgNP arrangement [41], the highest enhancement is known [42,43] to be invariably reached within the gaps between adjacent AgNPs, which is corroborated by our numerical simulations of many random AgNP arrangements.

The inset of Fig. 2(b) shows the spatial distribution of the electric field magnitude in the plane containing the NP centers, excited at 532 nm which is far from the cluster plasmon at 435 nm. This hints that the highest field enhancements are reached in NP gaps for any wavelength and not just for resonances. Fig. 2(c) shows the surface integral of the field enhancement evaluated over: (i) the entire cluster surface, consisting of the surfaces of all AgNPs and (ii) over the entire gap area, consisting of the sum of gap areas of individual AgNPs, defined as parts of the NP surface located very close to the adjacent AgNP, as indicated by the (red) shading in Fig. 2(c) inset. According to this definition, the surface over which the (ii) integral is evaluated is a small fraction of the (i) integral. However, the spectra in Fig. 2(c) show that these integrals have virtually the same value away from surface plasmon resonances. The difference around the cluster plasmon wavelength is also not significant, being of the order of 10%. This shows that regardless of the cluster geometry, the majority of the SERS signal of any species adsorbed uniformly on AgNPs is likely to come from the gap region (see also Fig. S3 in the Supplementary information).

Another important question regarding the fields on AgNP clusters is their orientation with respect to the AgNP surface, as

it determines the SERS cross section of vibrational modes of molecules adsorbed on the AgNP surface. To evaluate the extent to which the electric field is perpendicular to the local surface, in Fig. 2(d) we evaluate the surface integrals (taken over the entire cluster) of (i) the square of the normalized total electric field magnitude, which equals  $f(\mathbf{r}, \lambda)$  by definition (solid, black), and (ii) the square of the normalized magnitude of the electric field component perpendicular to the AgNP surface (dashed, red). The comparison of the two spectra in Fig. 2(d) shows that the contribution of the tangential component of the local electric field is negligible, indicating that in such clusters the perpendicular component of the electric field is the principal source of the SERS signal.

Having established that for an arbitrarily chosen AgNP cluster the large majority of the SERS signal comes from gaps between AgNPs and is associated with the perpendicular electric field component, we now focus on the cluster-averaged SERS enhancement factor  $\langle F(\lambda_{\text{inc}}, \lambda) \rangle$  and investigate how is it affected by the cluster size and geometry. The typical case is illustrated in Fig. 3(a) in which we consider a hierarchy of 3 NP clusters shown in the inset, each having twice as many AgNPs as the previous one. The first one represents a randomly chosen connected arrangement of 5 AgNPs with  $d = 0.8$  nm. The second is obtained by adding 5 more AgNPs so that each new AgNP is adjacent to one of the existing AgNPs. Finally, the third and largest cluster is obtained by adding 10 more AgNPs to the second one. The corresponding  $\langle F(\lambda_{\text{inc}}, \lambda) \rangle$  spectra in Fig. 3(a) shows two main effects of the cluster size increase. First, the enhancement peaks associated with the cluster plasmon undergoes a gradual redshift. Second, the surface-average enhancement  $\langle F(\lambda_{\text{inc}}, \lambda) \rangle$  increases, meaning that the actual SERS signal enhancement given by  $S \times \langle F(\lambda_{\text{inc}}, \lambda) \rangle$  will increase even more rapidly with adding new particles to the cluster. For example, a cluster having 5 AgNPs exhibits an average Raman enhancements of the order of 10 in the 532–600 nm range, whereas a cluster having 20 AgNPs yields 10 times higher values in the same range. In previous studies on AuNP chains [44], the increase of particle number has been found



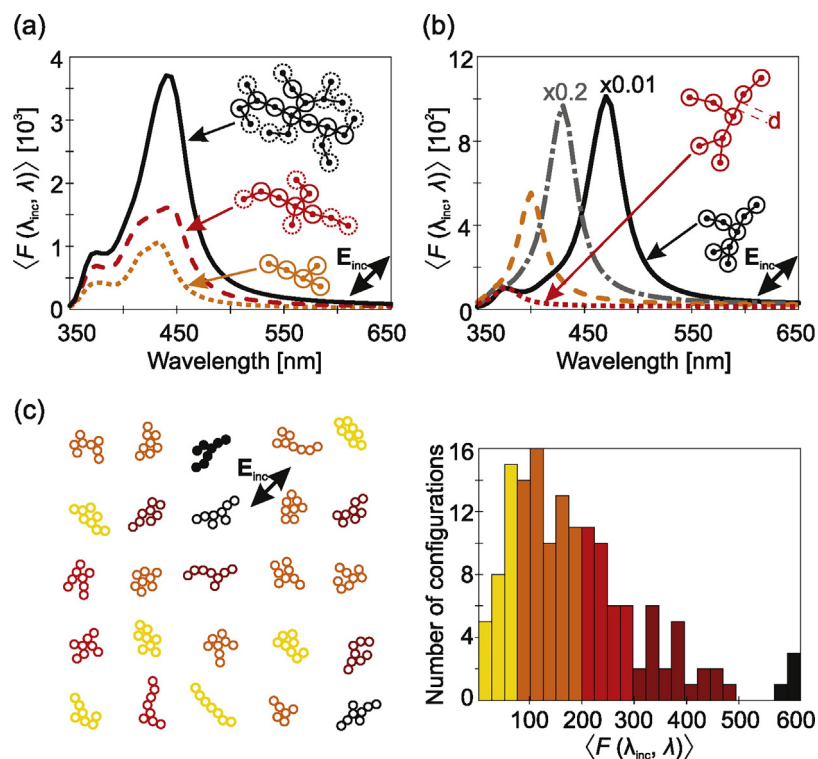


**Fig. 3.** (a) The average Raman enhancement calculated as a function of the emission wavelength for clusters having 5 particles (dotted orange line), 10 particles (dashed red line) and 20 particles (solid black line). (b) The average Raman enhancement calculated as a function of the emission wavelength for a cluster with 8 particles when the minimal distance between the particles is varied. Particles connected by lines, in the inset, are at the minimal distance  $d$  from each other. Solid (black) line corresponds to  $d = 0.5$  nm, whereas dash-dotted (gray) line, dashed (orange) line and dotted (red) line correspond to  $d = 1$  nm,  $d = 2$  nm and  $d = 5$  nm, respectively. (c) The left panel shows some of the 150 considered cluster variants and the electric field polarization direction. All the clusters have 8 particles, with the minimal distance  $d = 0.8$  nm. The right panel shows a histogram of the average Raman enhancement calculated at the emission wavelength 550 nm for all 150 cluster variants. In all calculations normal incidence at a wavelength 532 nm and the incident field intensity of  $200 \mu\text{W}/\mu\text{m}^2$  are assumed. (For interpretation of the references to color in this legend, the reader is referred to the web version of the article.)

to either increase or decrease the average Raman enhancement, depending on the relative position of the incident wavelength and the cluster (chain) plasmon.

In Fig. 3(b) we consider the role of the spacing  $d$  between adjacent AgNPs. For a cluster comprising 8 AgNPs decreasing  $d$  from 5 nm down to 0.5 nm is seen to result in drastic changes of  $\langle F(\lambda_{\text{inc}}, \lambda) \rangle$ . The cluster plasmon is rapidly blueshifted and approaches the single-particle plasmon as the AgNPs are moved further apart (see also panel (c) of Fig. S3 in the Supplementary information). Similar conclusions have been previously reported for the AuNP linear chains embedded in a dielectric medium [42,45]. Meanwhile, the peak values of  $\langle F(\lambda_{\text{inc}}, \lambda) \rangle$  are seen to decrease very rapidly since the gap field enhancement becomes less effective with increasing  $d$ . For example, the lowest considered minimal distance of 0.5 nm yields SERS enhancements as high as  $10^4$  in the 532–600 nm range.

Lastly, by evaluating the average Raman enhancement at the excitation and Stokes wavelengths of 532 nm and 550 nm, respectively, for a 150 randomly generated 8 AgNP clusters, we evaluate how the cluster morphology affects the non-resonant SERS enhancement value. The variety of clusters that have been considered in the 150 member ensemble, is represented by 25 typical members sketched in the left panel of Fig. 3(c). The histogram of  $\langle F(\lambda_{\text{inc}}, \lambda) \rangle$  values is shown in the right panel, where the column colors are selected so that they correspond to the color of the associated cluster in the left panel. The distribution is quite wide, spanning the range from 50 to 600. By comparing the two panels of Fig. 3(c), we see that the highest enhancements are reached in chain shaped clusters having the chain axis aligned with the incident electric field, such as the one illustrated in Fig. 3(c) by filled circles. The effect of disorder of the linear AuNP chain on the Raman

enhancement was studied in Ref. [43], where increasing disorder was found to diminish the Raman enhancement. In this case, the highest Raman enhancements were found for AuNP chains, when the incident electric field is oriented along the chain axis.

The brief numerical analysis of light scattering on random AgNP clusters made in this section shows that the overall SERS enhancement is highly dependent the cluster geometry and its orientation relative to the electric field polarization. The sensitivity of  $\langle F(\lambda_{\text{inc}}, \lambda) \rangle$  to fine details, such as the gap spacing, makes its exact evaluation very difficult even when electron microscopy is used for determining the AgNP arrangement with nanometer spatial resolution [46]. In the present case, the possibility of resonant enhancement cannot be excluded, since the cluster plasmon resonances are seen to redshift in elongated clusters with a larger number of particles than the ones considered here [42,43]. However, beside the well elaborated enormous Raman enhancements having a resonant origin [42], we have shown that in the non-resonant case enhancement factors in the range of  $10^2$ – $10^3$  are to be expected.

### 3.3. Surface-enhanced Raman spectroscopy of TC coated AgNPs I: influence of citrate capping anions on the TC dye adsorption

In the TC/AgNP mixture, the AgNPs may have the J-aggregates or dye monomers or dimers adsorbed on their surface, or even remain pristine. Therefore, it is expected that AgNP clusters drop-cast from the mixture would have a variety of SERS spectra corresponding to those of different dye conformations, citrate anions and even their combinations. To make a clear distinction between the non-aggregated and aggregated molecules one must have an

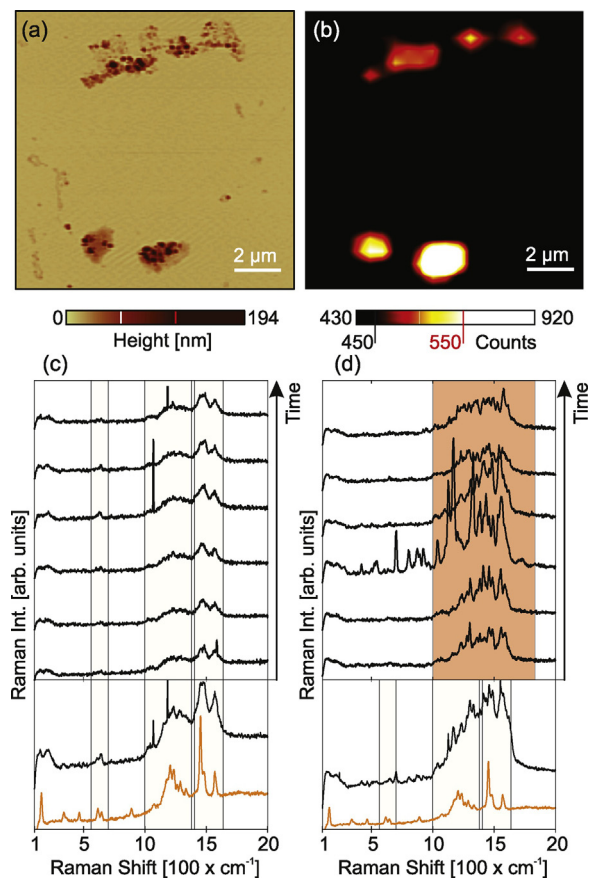


**Fig. 4.** (a) AFM topograph of TC dye coated Ag NP clusters which are drop-cast on mica. (b) Corresponding PL/Raman map. (c) and (d) Typical SERS spectra acquired within the hot spots, by consecutive measurements with 40 s time step. The excitation laser wavelength is 532 nm. In the lower parts of panels (c) and (d) shown are the SERS spectra obtained by summation of the corresponding consecutively acquired spectra, and the Raman spectra of the drop-cast TC dye. (For interpretation of the references to color in this legend, the reader is referred to the web version of the article.)

excitation resonant with the absorption of either aggregated or non-aggregated dye molecules [32,47]. Here we use a non-resonant laser line at 532 nm which does not allow identification of different dye conformations. However, AgNP clusters are very efficient enhancers at this wavelength, as it is shown in Section 3.1 and thus through the SERS effect alone we are able to determine if the TC dye molecules are adsorbed on AgNPs or not.

Comparison of the AFM topograph and the corresponding Raman map in Fig. 4(a) and (b) reveals that the hot spots are located within the larger AgNP clusters, as in the case of pristine AgNPs in Section 3.1. The SERS spectra acquired at these hot spots can be unambiguously categorized in two groups: one featuring stable Raman bands during successive measurements and the other having blinking Raman bands. The wide background from the AgNP clusters exists in this case as well. Fig. 4(c) and (d) shows the two distinct spectra types. The recording time step is 40 s and the laser intensity is  $\approx 200 \mu\text{W}/\mu\text{m}^2$ .

The consecutively measured SERS spectra having stable Raman bands are reminiscent of the drop-cast TC dye Raman spectrum. The similarity between the two becomes even more convincing after summation of ten consecutively measured spectra, six of which are displayed in Fig. 4(c). By applying markers to the three wave-number regions, I ( $300\text{--}1000 \text{ cm}^{-1}$ ), II ( $1050\text{--}1250 \text{ cm}^{-1}$ ), III ( $1400\text{--}1600 \text{ cm}^{-1}$ ), where the TC dye has its characteristic Raman bands (see Fig. S2 in the Supplementary information), we find that in region I around  $600 \text{ cm}^{-1}$  the summed SERS spectrum has

two bands matching those of a drop-cast TC dye, which is plotted again, for clarity, below the summed spectrum. The modes around  $400 \text{ cm}^{-1}$  and  $900 \text{ cm}^{-1}$  are, however, absent in the related TC dye SERS. In the remaining regions II and III the two spectra have, more or less, the same Raman bands and even similar backgrounds. Hence, our experiments corroborate the fact that the dye molecules are adsorbed on the surface of the AgNPs, and point out another interesting possibility – the dye molecules drop-cast on the surface of HOPG may be similarly organized as the dye molecules on the surface of the AgNPs.

Panel (d) in Fig. 4 displays SERS spectra characterized by a pronounced band blinking in the  $1000\text{--}1800 \text{ cm}^{-1}$  range, as indicated by gray (orange) region. The resemblance of the spectra in Fig. 4(d) and those of pristine AgNPs in Fig. 1(c) and (d) suggests that the TC dye molecules are not adsorbed on the surface of the AgNPs. However, the sum of the consecutive recordings, shown in the lower part of Fig. 4(d), reveals certain SERS bands in region II and III which are overlapping the drop-cast TC dye bands. Occasional emergence of Raman bands which could belong to the TC dye bands in regions I, II and III, however, is a common event even for the SERS spectra of pristine AgNPs. Having in mind that practically the entire enhanced Raman signal originates from the analyte located in the nanogaps, the blinking SERS signal can be interpreted as a consequence of mixing of the pristine AgNPs blinking SERS and the TC dye SERS which are collected at different nanogaps where the former has the dominant contribution. Consequently, we are unable to conclude whether the AgNP clusters exhibiting blinking SERS bands have the dye molecules adsorbed on their surface or not. However, the existence of the two distinct SERS spectra clearly points out that the AgNPs are partially covered by the TC dye molecules. This further indicates that during the adsorption process, the TC dye molecules are either competing with citrate anions in order to replace them on the surface of AgNPs or that the TC dye molecules have a difficulty conforming over the citrate anion mantle. Hence, we proceed further by changing the concentration of TC dye in the mixture while maintaining the concentration of AgNPs constant at  $c_{\text{Ag}} = 16 \text{ nM}$ .

The blinking and TC dye SERS spectra observed for  $0.01c_{\text{TC}} = 0.5 \mu\text{M}$ ,  $0.1c_{\text{TC}} = 5 \mu\text{M}$ , and  $0.5c_{\text{TC}} = 25 \mu\text{M}$  of TC, are shown in Fig. 5(a)–(c), respectively. By analyzing spectra at the hotspots within various Raman maps, we find that the AgNP clusters deposited from the solution with the lowest dye concentration yield no clear dye SERS spectra, whereas the AgNP clusters deposited from the solution with the two higher dye concentration provide a number of distinct TC dye SERS spectra at the hotspots, shown in Fig. 5. Comparison of the summed SERS spectra, in the lower parts of panels (a), (b) and (c) in Fig. 5, and the concentrated TC dye Raman spectra corroborates that the SERS spectra in panels (b) and (c) correspond to the one of the TC dye. As expected, using TC dye concentrations of  $0.01c_{\text{TC}} = 0.5 \mu\text{M}$ ,  $0.1c_{\text{TC}} = 5 \mu\text{M}$  in the final solution yields either pristine or partially covered AgNP clusters, a fact that concurs with the results in Ref. [14]. However, observation of the blinking type SERS within the AgNP clusters derived from the mixture with the highest TC dye concentration of  $0.5c_{\text{TC}} = 25 \mu\text{M}$ , for which all of the AgNPs in the solution should be covered by the dye molecules [14], further indicates that the citrate anion mantle impedes the adsorption of the TC dye molecules.

#### 3.4. Surface-enhanced Raman spectroscopy of TC coated AgNPs II: influence of borate and citrate capping anions on the TC dye adsorption

In order to examine if the citrate anions impede the TC dye adsorption, we have performed an additional set of measurements on a control sample – borate-capped AgNPs mixed with the TC dye and deposited on the surface of  $300 \text{ nm}$  thick  $\text{SiO}_2$ , which is thermally grown on the Si wafer. Meanwhile, the borate-capped AgNPs

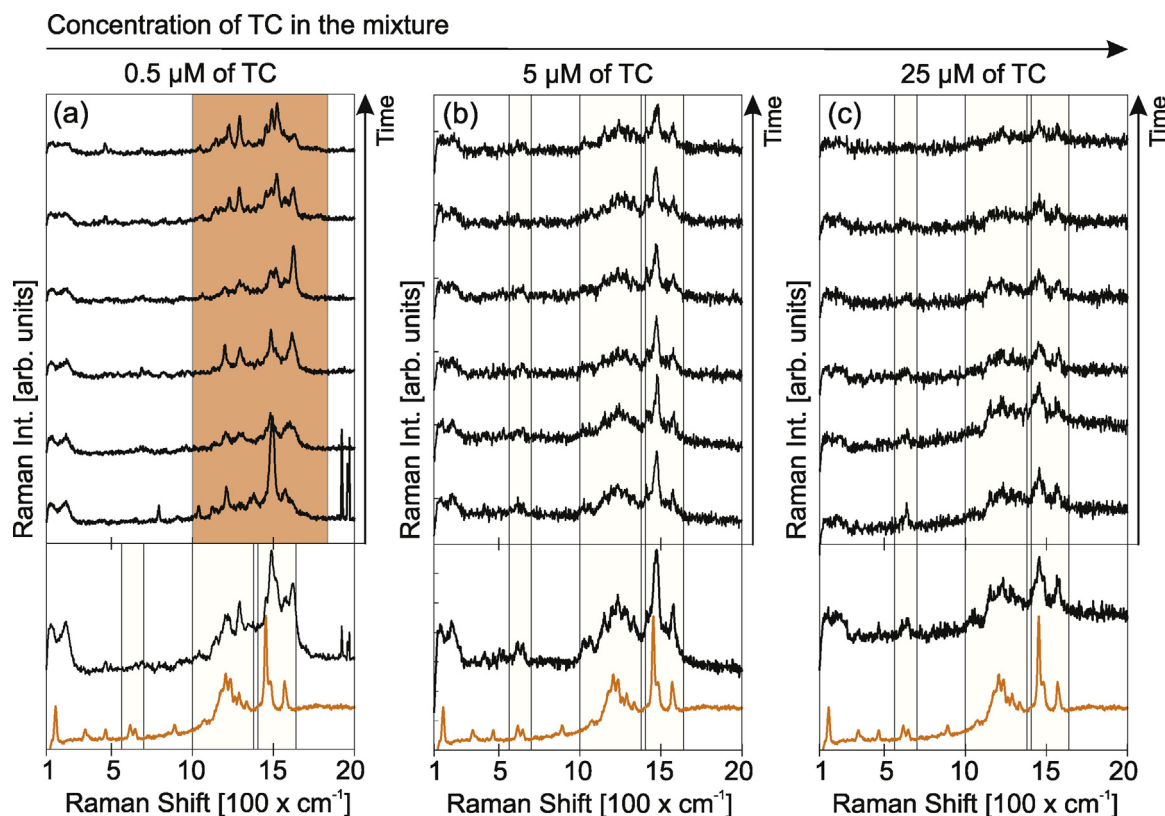


**Fig. 5.** Blinking and TC dye SERS spectra (acquired by consecutive measurements with 40 s time step) at hotspots on the samples made by varying the TC concentration in TC-Ag NP mixture: (a) 0.5  $\mu\text{M}$ , (b) 5  $\mu\text{M}$  and (c) 25  $\mu\text{M}$ . All shown spectra were taken under the same conditions using 532 nm laser with intensity of 200  $\mu\text{W}/\mu\text{m}^2$ .

are unstable with the average lifetimes of the order of couple of hours in the colloid dispersion and are usually stabilized by sodium citrate (or rather by the citrate anions which replace the borate anions while conforming to the surface of the AgNPs), as explained in Ref. [14]. The related lifetimes are much shorter upon deposition of these AgNPs on a substrate. The  $\text{SiO}_2$  surface is hydrophobic, and, therefore, promotes formation of closely spaced clusters larger than those observed on mica, since the droplet drop-cast of the former dries over a certain area rather than spreading all over the surface. Such an arrangement, along with the enhanced contrast between the  $\text{SiO}_2$  surface and the clusters, is absolutely necessary for fast acquisition of the SERS signal from the unstable, dye/borate-capped AgNP clusters.

Fig. 6(a)–(c) shows the three Raman maps corresponding to: (i) AgNP clusters deposited on mica from a solution having a (citrate-capped) AgNP to the TC dye concentration ratio of 22 nM/17  $\mu\text{M} \approx 1.3 \times 10^{-3}$ , (ii) AgNP clusters deposited on mica from a solution having a (citrate capped) AgNP to the TC dye concentration ratio of 16 nM/25  $\mu\text{M} \approx 0.64 \times 10^{-3}$ , (iii) AgNP clusters deposited on  $\text{SiO}_2/\text{Si}$  from a solution having a (borate-capped) AgNP to the TC dye concentration ratio of 10 nM/16  $\mu\text{M} \approx 0.63 \times 10^{-3}$ , respectively. The (red) diamonds mark the spatial positions within the hotspots where the blinking type of Raman spectra is observed, whereas the (green) squares mark the pixels having the TC dye type of Raman spectra. These maps share the color bar which is located below them. Panels (d), (e) and (f) of Fig. 6 display examples of the spectra collected at the hotspots within the corresponding maps in panels (a), (b) and (c), respectively. For comparison, the concentrated TC dye Raman spectra is plotted in each panel, below all the other spectra.

The dye/borate-capped AgNPs deposited on the  $\text{SiO}_2/\text{Si}$ , form a higher number of larger clusters than the dye/citrate-capped AgNPs on mica, as seen by comparing the Raman maps in panels (a), (b)

and (c), as expected. The SERS spectra acquired at these clusters is exclusively of the TC dye type, as seen in panel (c). In fact, we find this to be the case for every recorded Raman map. In contrast, the dye/citrate-capped AgNP clusters exhibit both the blinking and the TC dye SERS, even when the ratio of the citrate-capped AgNPs and the TC dye concentrations in solution is approximately the same as the one of the borate-capped AgNPs and the TC dye (compare panels (b) and (c) in Fig. 6). The adsorption of the TC dye seems to be more efficient if the AgNPs have borate anions initially conformed to their surface and, therefore, we conjecture that the citrate anions indeed interfere with the adsorption process of the TC dye molecules.

Our findings are in agreement with the previous spectrophotometric study of J-aggregation of TC dye on the surface of AgNPs [26,13,14,12], where is found that the capping anions (borate or citrate), as well as added KCl, have an important role in the adsorption and J-aggregation of the dye molecules. In case of borate-capped AgNPs, the J-aggregation is found to be a fast process ( $k_{\text{app}} = 4.97 \text{ s}^{-1}$ ) whose kinetics can be explained in terms of autocatalysis. Differently, kinetics measurements of J-aggregation on the surface of citrate-capped AgNPs has shown that the J-aggregation occurs via a two-step slower process (adsorption and aggregation,  $k_{\text{app1}} = 0.008 \text{ s}^{-1}$  and  $k_{\text{app2}} = 0.11 \text{ s}^{-1}$ ). Also, in the case of citrate-capped AgNPs was found that the quantity of added KCl has an important role in the adsorption of TC dye molecules.

This conclusion is further supported by the analysis of the DFT calculated adsorption energies of the TC dye, borate and citrate anions on the surface of Ag, reported in our previous work [26] (see also Section S4 of the Supplementary information).

#### 4. Summary

In summary, the analysis of SERS enhancement based on rigorous simulations of Maxwell equations for the case of plane wave

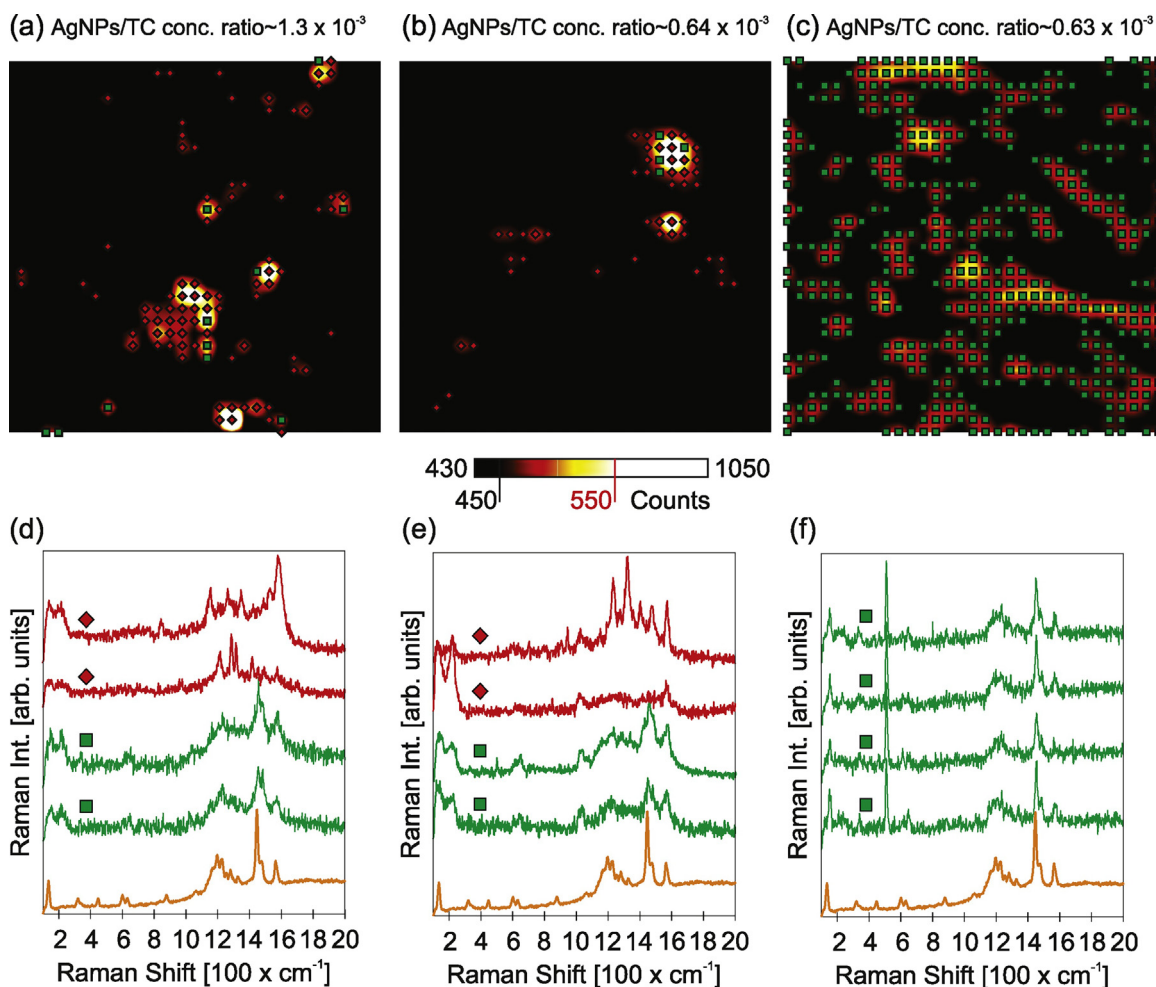


**Fig. 6.** Raman maps of (a) clusters deposited on mica from a solution having a (citrate capped) NP to the TC dye concentration ratio of  $22 \text{ nM}/17 \mu\text{M} \approx 1.3 \times 10^{-3}$ , (b) clusters deposited on mica from a solution having a (citrate capped) NP to the TC dye concentration ratio of  $16 \text{ nM}/25 \mu\text{M} \approx 0.64 \times 10^{-3}$  (c) clusters deposited on  $\text{SiO}_2/\text{Si}$  from a solution having a (borate capped) NP to the TC dye concentration ratio of  $10 \text{ nM}/16 \mu\text{M} \approx 0.64 \times 10^{-3}$ . (d)–(f) Examples of the blinking and dye SERS spectra observed in the Raman maps, displayed below the corresponding Raman maps.

scattering on random silver nanoparticle clusters on various substrates has shown that, for the investigated nanoparticles and the 532 nm excitation laser, typical enhancement factors in the range of  $10^2$ – $10^3$  can be expected. The highest field enhancement factors are reached at collective nanoparticle plasmon resonances, which lie in the 400–500 nm range for medium sized clusters (around 20 nanoparticles), and become redshifted in elongated clusters with an increasing number of particles. From an inspection of electromagnetic field distribution on nanoparticle surfaces, a conclusion is reached that at least 90% of the SERS total enhancement originates from nanogaps between adjacent nanoparticles, implying that the experiments are sensitive only to adsorbates located in these gaps.

Combined AFM and PL mapping of citrate-capped AgNP clusters with dye molecules adsorbed from solutions of variable TC concentration have shown that, even at highest TC concentrations, not all hotspots exhibit Raman signatures characteristic of TC dye molecules, indicating that the clusters are only partially covered by dye molecules. In contrast, the control experiment carried out with borate-capped AgNP clusters, with similar nanoparticle and dye concentrations, has shown a complete dye-coverage of AgNP clusters.

These results are a direct demonstration that the citrate anions, while useful for stabilizing the colloid, impede the efficient TC dye adsorption.

## Acknowledgements

The research reported in this article was supported by the Serbian Ministry of Education, Science and Technological Development through project Nos. ON171005, ON172023, III45016. This work was performed in the context of COST Action MP 1302 “Nanospectroscopy”.

## Appendix A. Supplementary data

Supplementary data associated with this article can be found, in the online version, at <https://doi.org/10.1016/j.apsusc.2017.10.148>.

## References

- [1] A. Manjavacas, F.J.G.d. Abajo, P. Nordlander, Quantum plexitronics: strongly interacting plasmons and excitons, *Nano Lett.* 11 (6) (2011) 2318–2323.
- [2] N.T. Fofang, T.-H. Park, O. Neumann, N.A. Mirin, P. Nordlander, N.J. Halas, Plexitonic nanoparticles: plasmon exciton coupling in nanoshell-J-aggregate complexes, *Nano Lett.* 8 (10) (2008) 3481–3487.
- [3] E. Dulkeith, A.C. Morteani, T. Niedereichholz, T.A. Klar, J. Feldmann, S.A. Levi, F.C.J.M. van Veggel, D.N. Reinhoudt, M. Möller, D.I. Gittins, Fluorescence quenching of dye molecules near gold nanoparticles: radiative and nonradiative effects, *Phys. Rev. Lett.* 89 (2002) 203002–203006.
- [4] J. Zhao, X. Zhang, Y.C. Ranjit, A.J. Haes, R.P. Van Duyne, Localized surface plasmon resonance biosensors, *Nanomedicine* 1 (2006) 219–228.

- [5] M.A. Noginov, G. Zhu, A.M. Belgrave, R. Bakker, V.M. Shalae, E.E. Narimanov, S. Stout, E. Herz, T. Suteewong, U. Wiesner, Demonstration of a spaser-based nanolaser, *Nature* 460 (2009) 1110–1112.
- [6] N. Kometani, M. Tsubonishi, T. Fujita, K. Asami, Y. Yonezawa, Preparation and optical absorption spectra of dye-coated Au, Ag, and Au/Ag colloidal nanoparticles in aqueous solutions and in alternate assemblies, *Langmuir* 17 (3) (2001) 578–580.
- [7] A. Yoshida, N. Kometani, Effect of the interaction between molecular exciton and localized surface plasmon on the spectroscopic properties of silver nanoparticles coated with cyanine dye J-aggregates, *J. Phys. Chem. C* 114 (7) (2010) 2867–2872.
- [8] V.S. Lebedev, A.S. Medvedev, D.N. Vasil'ev, D.A. Chubich, A.G. Vitukhnovskiy, Optical properties of noble-metal nanoparticles coated with a dye J-aggregate monolayer, *Quantum Electron.* 40 (3) (2010) 246.
- [9] Y. Kitahama, M. Kashihara, T. Itoh, Y. Ozaki, Surface-enhanced phosphorescence measurement by an optically trapped colloidal Ag nanoaggregate on anionic thiocarbocyanine H-aggregate, *J. Phys. Chem. C* 117 (6) (2013) 2460–2466.
- [10] A. Vujačić, V. Vasić, M. Dramićanin, S.P. Sovilj, N. Bibić, J. Hranisavljević, G.P. Wiederrecht, Kinetics of J-aggregate formation on the surface of Au nanoparticle colloids, *J. Phys. Chem. C* 116 (7) (2012) 4655–4661.
- [11] A. Vujačić, V. Vasić, M. Dramićanin, S.P. Sovilj, N. Bibić, S. Milonjić, V. Vodnik, Fluorescence quenching of 5,5-disulfofopropyl-3,3-dichlorothiacyanine dye adsorbed on gold nanoparticles, *J. Phys. Chem. C* 117 (13) (2013) 6567–6577.
- [12] B.B. Laban, V. Vodnik, A. Vujačić, S.P. Sovilj, A.B. Jokić, V. Vasić, Spectroscopic and fluorescence properties of silver-dye composite nanoparticles, *Russ. J. Phys. Chem. A* 87 (13) (2013) 2219–2224.
- [13] B. Laban, V. Vodnik, M. Dramićanin, M. Novaković, N. Bibić, S.P. Sovilj, V.M. Vasić, Mechanism and kinetics of J-aggregation of thiocyanine dye in the presence of silver nanoparticles, *J. Phys. Chem. C* 118 (40) (2014) 23393–23401.
- [14] B. Laban, V. Vodnik, V. Vasić, Spectrophotometric observations of thiocyanine dye J-aggregation on citrate capped silver nanoparticles, *Nanospectroscopy* 1 (2015) 54–60.
- [15] F. Würthner, T.E. Kaiser, C.R. Saha-Möller, J-aggregates: from serendipitous discovery to supramolecular engineering of functional dye materials, *Angew. Chem. Int. Ed.* 50 (15) (2011) 3376–3410.
- [16] M. Kawasaki, T. Sato, T. Yoshimoto, Controlled layering of two-dimensional J-aggregate of anionic cyanine dye on self-assembled cysteamine monolayer on Au(111), *Langmuir* 16 (12) (2000) 5409–5417.
- [17] R.W. Owens, D.A. Smith, Stm imaging of cyanine dye J-aggregates formed on carboxyl-terminated self-assembled monolayers, *Langmuir* 16 (2) (2000) 562–567.
- [18] H. Yao, S. Kitamura, K. Kimura, Morphology transformation of mesoscopic supramolecular J aggregates in solution, *Phys. Chem. Chem. Phys.* 3 (2001) 4560–4565.
- [19] N. Vranken, P. Foubert, F. Khn, R. Gronheid, I. Scheblykin, M. Van der Auweraer, F.C. De Schryver, Influence of the deposition method on the topography and spectroscopy of J-aggregates of a thiocarbocyanine dye adsorbed to a Langmuir film, *Langmuir* 18 (22) (2002) 8407–8417.
- [20] H. Yao, Y. Kagoshima, S. Kitamura, T. Isohashi, Y. Ozawa, K. Kimura, Superstructures of mesoscopic monomolecular sheets of thiocyanine J aggregates in solution, *Langmuir* 19 (21) (2003) 8882–8887.
- [21] H. Yao, T. Isohashi, K. Kimura, Large birefringence of single J-aggregate nanosheets of thiocyanine dye in solution, *Chem. Phys. Lett.* 396 (4–6) (2004) 316–322.
- [22] S. Özcelik, M.M. Demir, B. Birkan, Probing nanoscale domains of J-aggregates deposited on a mica surface, *J. Phys. Chem. B* 108 (15) (2004) 4679–4683.
- [23] H. Yao, K. Domoto, T. Isohashi, K. Kimura, In situ detection of birefringent mesoscopic H and J aggregates of thiocarbocyanine dye in solution, *Langmuir* 21 (3) (2005) 1067–1073.
- [24] V.V. Prokhorov, O.M. Pereyagina, S.I. Pozin, E.I. Mal'tsev, A.V. Vannikov, A.Y. Tsvadze, Tubular structure of J-aggregates of cyanine dye, *Dokl. Chem.* 460 (1) (2015) 1–4.
- [25] T.H. James, *The Theory of the Photographic Process*, 4th ed., Macmillan, New York, 1977.
- [26] B. Laban, I. Zeković, D. Vasić Aničijević, M. Marković, V. Vodnik, M. Luce, A. Cricenti, M. Dramićanin, V. Vasić, Mechanism of 3,3-disulfofopropyl-5,5-dichlorothiacyanine anion interaction with citrate-capped silver nanoparticles: adsorption and J-aggregation, *J. Phys. Chem. C* 120 (32) (2016) 18066–18074.
- [27] M. Kerker, O. Siiman, L.A. Bumm, D.-S. Wang, Surface enhanced Raman scattering (SERS) of citrate ion adsorbed on colloidal silver, *Appl. Opt.* 19 (19) (1980) 3253–3255.
- [28] O. Siiman, L.A. Bumm, R. Callaghan, C.G. Blatchford, M. Kerker, Surface-enhanced Raman scattering by citrate on colloidal silver, *J. Phys. Chem.* 87 (6) (1983) 1014–1023.
- [29] D.L. Akins, S. Zelik, H.-R. Zhu, C. Guo, Aggregation-enhanced Raman scattering of a cyanine dye in homogeneous solution, *J. Phys. Chem. A* 101 (18) (1997) 3251–3259.
- [30] Y. Kitahama, Y. Tanaka, T. Itoh, Y. Ozaki, Wavelength-dependent surface-enhanced resonance Raman scattering by excitation of a transverse localized surface plasmon, *J. Phys. Chem. C* 113 (27) (2009) 11877–11883.
- [31] Y. Kitahama, Y. Tanaka, T. Itoh, Y. Ozaki, Time-resolved surface-enhanced resonance Raman scattering spectra of thiocyanine molecules in water, *Chem. Lett.* 38 (1) (2009) 54–55.
- [32] Y. Kitahama, Y. Tanaka, T. Itoh, M. Ishikawa, Y. Ozaki, Identification of thiocyanine J-aggregates adsorbed on single silver nanoaggregates by surface-enhanced Raman scattering and emission spectroscopy, *Bull. Chem. Soc. Jpn.* 82 (9) (2009) 1126–1132.
- [33] Y. Kitahama, A. Ogawa, Y. Tanaka, S. Obeidat, T. Itoh, M. Ishikawa, Y. Ozaki, Difference in time dependence of surface-enhanced Raman scattering spectra of thiocarbocyanine J- and H-aggregates adsorbed on single silver nanoaggregates, *Chem. Phys. Lett.* 493 (4–6) (2010) 309–313.
- [34] Y. Kitahama, Y. Tanaka, T. Itoh, Y. Ozaki, Power-law analysis of surface-plasmon-enhanced electromagnetic field dependence of blinking SERS of thiocyanine or thiocarbocyanine adsorbed on single silver nanoaggregates, *Phys. Chem. Chem. Phys.* 13 (2011) 7439–7448.
- [35] C.R. Zamecnik, A. Ahmed, C.M. Walters, R. Gordon, G.C. Walker, Surface-enhanced Raman spectroscopy using lipid encapsulated plasmonic nanoparticles and J-aggregates to create locally enhanced electric fields, *J. Phys. Chem. C* 117 (4) (2013) 1879–1886.
- [36] Y. Kitahama, D. Araki, Y.S. Yamamoto, T. Itoh, Y. Ozaki, Different behaviour of molecules in dark SERS state on colloidal Ag nanoparticles estimated by truncated power law analysis of blinking SERS, *Phys. Chem. Chem. Phys.* 17 (2015) 21204–21210.
- [37] COMSOL MULTIPHYSICS v5.2, COMSOL, Inc.
- [38] A.D. Rakić, A.B. Djurišić, J.M. Elazar, M.L. Majewski, Optical properties of metallic films for vertical-cavity optoelectronic devices, *Appl. Opt.* 37 (22) (1998) 5271–5283.
- [39] C.F. Frontiers, D.R. Huffman, *Absorption and Scattering by an Arbitrary Particle*, Wiley-VCH Verlag GmbH, 2007, pp. 57–81.
- [40] M. Kerker, D.-S. Wang, H. Chew, Surface enhanced Raman scattering (SERS) by molecules adsorbed at spherical particles, *Appl. Opt.* 19 (19) (1980) 3373–3388.
- [41] L.O. Herrmann, V.K. Valev, J. Aizpurua, J.J. Baumberg, Self-sifting of chain plasmons: the complex optics of an nanoparticle clusters, *Opt. Express* 21 (26) (2013) 32377–32385.
- [42] C. Tserkezis, R.W. Taylor, J. Beitner, R. Esteban, J.J. Baumberg, J. Aizpurua, Optical response of metallic nanoparticle heteroaggregates with subnanometric gaps, *Part. Part. Syst. Char.* 31 (1) (2014) 152–160.
- [43] R. Esteban, R.W. Taylor, J.J. Baumberg, J. Aizpurua, How chain plasmons govern the optical response in strongly interacting self-assembled metallic clusters of nanoparticles, *Langmuir* 28 (24) (2012) 8881–8890.
- [44] R.W. Taylor, R. Esteban, S. Mahajan, J. Aizpurua, J.J. Baumberg, Optimizing SERS from gold nanoparticle clusters: addressing the near field by an embedded chain plasmon model, *J. Phys. Chem. C* 120 (19) (2016) 10512–10522.
- [45] N. Harris, M.D. Arnold, M.G. Blaber, M.J. Ford, Plasmonic resonances of closely coupled gold nanosphere chains, *J. Phys. Chem. C* 113 (7) (2009) 2784–2791.
- [46] Y. Ozaki, K. Kneipp, R. Aroca, *Frontiers of Surface-Enhanced Raman Scattering*, John Wiley & Sons Ltd, 2014.
- [47] D.L. Akins, Theory of Raman scattering by aggregated molecules, *J. Phys. Chem.* 90 (8) (1986) 1530–1534.

# Journal Pre-proof

The structural, electrical and optical properties of spark plasma sintered  $\text{BaSn}_{1-x}\text{Sb}_x\text{O}_3$  ceramics

Jelena Vukašinić, Milica Počuča-Nešić, Danijela Luković Golić, Vesna Ribić, Zorica Branković, Slavica M. Savić, Aleksandra Dapčević, Slavko Bernik, Matejka Podlogar, Matej Kocen, Željko Rapljenović, Tomislav Ivek, Vladimir Lazović, Biljana Dojčinović, Goran Branković



PII: S0955-2219(20)30532-X

DOI: <https://doi.org/10.1016/j.jeurceramsoc.2020.06.062>

Reference: JECS 13389

To appear in: *Journal of the European Ceramic Society*

Received Date: 4 February 2020

Revised Date: 21 June 2020

Accepted Date: 23 June 2020

Please cite this article as: Vukašinić J, Počuča-Nešić M, Golić DL, Ribić V, Branković Z, Savić SM, Dapčević A, Bernik S, Podlogar M, Kocen M, Rapljenović Ž, Ivek T, Lazović V, Dojčinović B, Branković G, The structural, electrical and optical properties of spark plasma sintered  $\text{BaSn}_{1-x}\text{Sb}_x\text{O}_3$  ceramics, *Journal of the European Ceramic Society* (2020), doi: <https://doi.org/10.1016/j.jeurceramsoc.2020.06.062>

This is a PDF file of an article that has undergone enhancements after acceptance, such as the addition of a cover page and metadata, and formatting for readability, but it is not yet the definitive version of record. This version will undergo additional copyediting, typesetting and review before it is published in its final form, but we are providing this version to give early visibility of the article. Please note that, during the production process, errors may be discovered which could affect the content, and all legal disclaimers that apply to the journal pertain.

© 2020 Published by Elsevier.

## The structural, electrical and optical properties of spark plasma sintered $\text{BaSn}_{1-x}\text{Sb}_x\text{O}_3$ ceramics

Jelena Vukašinić<sup>1\*</sup>, Milica Počuča-Nešić<sup>1</sup>, Danijela Luković Golić<sup>1</sup>, Vesna Ribić<sup>1</sup>, Zorica Branković<sup>1</sup>, Slavica M. Savić<sup>2</sup>, Aleksandra Dapčević<sup>3</sup>, Slavko Bernik<sup>4</sup>, Matejka Podlogar<sup>4</sup>, Matej Kocen<sup>4</sup>, Željko Rapljenović<sup>5</sup>, Tomislav Ivek<sup>5</sup>, Vladimir Lazović<sup>6</sup>, Biljana Dojčinović<sup>7</sup>, Goran Branković<sup>1</sup>

<sup>1</sup>Institute for Multidisciplinary Research, University of Belgrade, Kneza Višeslava 1a, 11030 Belgrade, Serbia

<sup>2</sup>BioSense Institute, University of Novi Sad, Zorana Đinđića 1, 21000 Novi Sad, Serbia

<sup>3</sup>Faculty of Technology and Metallurgy, University of Belgrade, Karnegijeva 4, 11120 Belgrade, Serbia

<sup>4</sup>Jožef Stefan Institute, Department for Nanostructured Materials, Jamova cesta 39, 1000 Ljubljana, Slovenia

<sup>5</sup>Institute of Physics, Bijenička cesta 46, HR-10001 Zagreb, Croatia

<sup>6</sup>Institute of Physics, University of Belgrade, Pregrevica 118, 11080 Belgrade, Serbia

<sup>7</sup>Institute of Chemistry, Technology and Metallurgy, Njegoševa 12, 11000 Belgrade, Serbia

\*Corresponding author:

*e-mail:* [jelena.vukasinovic@imsi.bg.ac.rs](mailto:jelena.vukasinovic@imsi.bg.ac.rs)

Tel.: +381 11 2085032; Fax: +381 11 2085 038

### Highlights

- Low Angle Grain Boundaries (LAGBs) present in Spark plasma sintered Sb-doped  $\text{BaSnO}_3$ .
- Loss of potential barrier at LAGBs drastically decreased electrical resistivity.
- Doping of  $\text{BaSnO}_3$  with Sb led to linearization of  $I-U$  characteristic.
- $\text{BaSn}_{0.92}\text{Sb}_{0.08}\text{O}_3$  can be used as linear resistor even at higher temperatures.

### Abstract



Antimony doped barium-stannate dense ceramic materials were synthesized using spark plasma sintering technique out of mechanically activated precursor powders. The influence of various Sb concentrations ( $x = 0.00 - 0.10$ ) on properties of  $\text{BaSn}_{1-x}\text{Sb}_x\text{O}_3$  ceramics was investigated. Relative densities of prepared samples were in the range of (79 – 96) %. TEM analysis revealed the presence of many dislocations in undoped  $\text{BaSnO}_3$ , and their significant reduction upon doping with Sb. All samples except  $\text{BaSn}_{0.92}\text{Sb}_{0.08}\text{O}_3$  exhibit non-linear  $I-U$  characteristic, typical for semiconductors with potential barrier at grain boundaries. Low angle grain boundaries found only in  $\text{BaSn}_{0.92}\text{Sb}_{0.08}\text{O}_3$  caused the loss of potential barrier at grain boundaries which was confirmed by AC impedance spectroscopy measurements. Consequently,  $\text{BaSn}_{0.92}\text{Sb}_{0.08}\text{O}_3$  showed the lowest electrical resistivity and linear  $I-U$  characteristic. UV-Vis analysis confirmed the increasing of band gap (Burstein–Moss shift) values in all doped samples.

Keywords:  $\text{BaSnO}_3$ ; Spark plasma sintering; Potential barrier; Low angle grain boundaries; Electrical conductivity

## 1. Introduction

In polycrystalline metal oxide ceramic materials common intrinsic defects are oxygen vacancies making these materials n-type semiconductors, while the grain boundary interfaces are p-type due to existence of trapping states. As a result, the potential barrier is formed at grain boundary, influencing the charge carrier transport and dominating the electrical properties of such semiconductor. In order to obtain highly conductive metal oxide ceramic material with linear  $I-U$  characteristic in a wide voltage range, the formation of potential barrier should be avoided [1].

The electroceramic materials with perovskite structure ( $AMO_3$ ) exhibit diverse physical properties such as superconductivity, colossal magnetoresistance, ferroelectricity, ferromagnetism and piezoelectricity [2, 3]. These properties offer many possible applications of perovskite materials in the fabrication of resistors, electrodes, components of heating devices [4], perovskite solar cells, photocatalysts or gas sensors [5 – 7].

Barium stannate,  $BaSnO_3$  (BSO), belongs to the perovskite-type alkaline earth stannates,  $ASnO_3$  ( $A = Ca, Sr, Ba$ ) [5, 6 – 9] and it crystallizes in an ideal cubic perovskite structure (space group:  $Pm\bar{3}m$ ). The larger  $Ba^{2+}$  cations coordinated with twelve  $O^{2-}$  anions form a cubic close-packed lattice, while smaller  $Sn^{4+}$  cations occupy octahedral holes formed by oxygen anions. As a result, the crystal structure of BSO consists of a 3D network of corner-sharing  $[SnO_6]$  octahedra with  $Ba^{2+}$  ions occupying the 12-fold coordination site formed in the middle of the cube of eight such octahedra [10 – 12]. Chemical and thermal stability at temperatures up to 1000 °C, optical transparency in the visible region [7, 13, 14], simple fabrication and non-toxicity make BSO suitable for many applications: as a photocatalyst, photoanode material for dye-sensitized solar cells [5, 13 – 16], dielectric capacitor [5, 6, 9, 15, 16], proton conductor [12,13], protective coating or catalyst support [5], gas sensor [5 – 7, 9, 13, 15 – 19] etc. Its high electron mobility enables the use of  $BaSnO_3$  in electronics, especially in Field-effect transistors as an active channel material [20]. For all aforementioned purposes,  $BaSnO_3$  has been synthesized in the forms of ceramic materials [2, 4, 6, 8, 9, 19, 21 – 26], single crystals [20, 27, 28] and thin films [29, 30], using various synthetic approaches such as solid state reaction [2, 4, 6, 9, 19, 21 – 24, 26], flux method [20, 27, 28], pulsed laser deposition [29], chemical solution deposition (CSD) [30] and molecular beam epitaxy [31, 32].

BSO is a wide band-gap semiconductor [5, 13, 19], but appropriate doping can alter its electrical characteristics. Replacement of tin with yttrium or indium (M-site doping) changes

BSO into a proton conductor [33]. On the other hand, after replacement of  $\text{Ba}^{2+}$  with  $\text{La}^{3+}$  (A-site doping) or  $\text{Sn}^{4+}$  with  $\text{Sb}^{5+}$ , BSO becomes n-type semiconductor with high electrical conductivity at 25 °C [2, 4, 8, 21].

The synthesis of the single phase Sb-doped BSO raises several problems. The electrical and optical properties of BSO are strongly correlated with the amount of antimony since these ions induce the formation of defects and local distortions within the BSO crystal lattice. According to the literature, the maximum solubility of Sb in BSO can reach 20 mol % [2, 4, 22, 23], whereas for the single crystals, the doping level is 10 mol% [27]. It is known that Sb ions can be segregated at the particle surface, forming Sb-rich secondary phase and inhibiting the grain growth [34]. High Sb concentration present in the system can also result in the formation of  $\text{BaSb}_2\text{O}_6$  and  $\text{SnO}$  as secondary phases, thus affecting the phase composition [4, 24, 27]. Another problem, which hinders the preparation of single phase BSO-based ceramics, is the formation of the tetragonal phase  $\text{Ba}_2\text{SnO}_4$ , with large band gap and high electrical resistivity [25, 35].

The major drawback of BSO-based ceramics is its low density [6, 9]. The conventional solid state procedure requires long thermal treatments with several intermittent grinding and heating steps at temperatures up to 1600 °C [6, 9]. Still, these conditions cannot sufficiently enhance the densification process of the ceramic material, even with the use of sintering aids like polyvinyl alcohol or  $\text{SiO}_2$  [4, 6, 9, 25]. In order to overcome these problems, an alternative sintering method should be used. The spark plasma sintering (SPS) technique, which includes simultaneous application of high pressure and heat during a short period of time, is known as an efficient method for the preparation of dense ceramic samples. SPS lowers the sintering temperature and shortens the overall processing time in comparison with the conventional sintering process [36]. It was successfully used in the preparation of various perovskite ceramic materials like  $\text{BiFeO}_3$ ,  $\text{BaTiO}_3$ ,  $\text{SrTiO}_3$  [36 – 38] including La-doped

BaSnO<sub>3</sub> [8], but, to the best of our knowledge, there are no literature reports about its use for the Sb-doped BaSnO<sub>3</sub>.

The attention has been previously focused on the structural, electrical or optical properties of BaSnO<sub>3</sub>-based ceramics, but with the lack of information about the microstructural properties, especially for the Sb-doped BaSnO<sub>3</sub> [2, 4, 8, 14, 16, 21 – 23]. The aim of this work was to prepare BaSn<sub>1-x</sub>Sb<sub>x</sub>O<sub>3</sub> ceramics with linear *I-U* characteristic, large electrical conductivity and higher density. The precursor powders obtained from mechanically activated BaCO<sub>3</sub>, SnO<sub>2</sub> and Sb<sub>2</sub>O<sub>3</sub> were sintered using SPS technique. In this process, the low melting point of Sb<sub>2</sub>O<sub>3</sub> (656 °C) [6] enabled sintering in the liquid phase, thus providing better contact between particles and improving material transport within the liquid phase. Structural, microstructural, electrical and optical characterizations of BaSn<sub>1-x</sub>Sb<sub>x</sub>O<sub>3</sub> ceramic samples were performed. For the first time, *I-U* characteristics of the obtained ceramics were observed at temperatures above 25 °C and the electrical conductivity of BaSn<sub>1-x</sub>Sb<sub>x</sub>O<sub>3</sub> ceramics was investigated. The correlation between structural, microstructural and electrical properties was established.

## 2. Materials and methods

The precursor powders of BaSn<sub>1-x</sub>Sb<sub>x</sub>O<sub>3</sub>, ( $x = 0.00, 0.04, 0.06, 0.08, \text{ and } 0.10$ ) were prepared by mechanical activation using BaCO<sub>3</sub> (99.95 %, Alfa Aesar), SnO<sub>2</sub> (99.9 %, Alfa Aesar) and Sb<sub>2</sub>O<sub>3</sub> (99 %, Merck) powders as starting reagents. The starting powders, weighed in appropriate stoichiometric ratios, were activated in a planetary ball mill (Fritsch Pulverisette 5) using isopropanol as the medium. The mixture of starting powders and tungsten carbide (WC) balls were placed in a WC cylindrical vial, with the 25:1 ball-to-powder weight ratio. The milling time was 8 h, and the rotational speed of disc was 120 rpm. Dried powders were calcined at 900 °C for 4 h in air.

Sintering was performed in a SPS furnace (FAST, Dr. Sinter FAST 515-S, Sumimoto FAST Syntex Ltd., Japan) under vacuum conditions using a graphite die with the diameter of 10 mm. The calcined powders were heated with the heating rate of 100 °C/min and sintered at 1200 °C for 5 minutes. Uniaxial pressure of 60 MPa was applied before the heating process and maintained until the sample was cooled to room temperature. For the characterization of ceramic materials thin slices of the sintered samples were cut from the both parallel sides. Afterwards, the surfaces were polished by sandpaper and annealed at 700 °C for 2 h in air in order to remove the surface carbon contamination and compensate the oxygen deficiency formed during sintering in reduction atmosphere [36, 37].

The X-ray powder diffraction (XRD) analysis was determined on Rigaku Ultima IV, Japan, with CuK $\alpha$  radiation ( $\lambda = 0.154$  nm) from 20 ° to 90 ° ( $2\theta$ ) with a step-width of 0.02 ° and scanning rate of 0.2 °/min. *PowderCell* (version 2.4) software was used for the phase composition and crystallite size analysis. The unit cell parameters were calculated by the least squares methods using the *LSUCRI* software [39]. The contents of Ba, Sb and Sn were determined by inductively coupled plasma optical emission spectrometry (ICP-OES). ICP-OES measurement was performed using Thermo Scientific iCAP 6500 Duo ICP (Thermo Fisher Scientific, Cambridge, United Kingdom). The digestion of samples was performed on Advanced Microwave Digestion System (ETHOS 1, Milestone, Italy) using HPR-1000/10S high pressure segmented rotor at temperature of 160 °C for 15 minutes. The microstructure was investigated by the Field Emission Scanning Electron Microscope (FESEM, MIRA3 FEG-SEM, Tescan), Scanning Electron Microscope (SEM, TESCAN Vega TS5130MM) equipped with the Energy dispersive spectroscopy (EDS, Oxford Instruments, model INCA PentaFETx3). FESEM analysis was examined on fractured cross-sections of sintered samples, while SEM and EDS analyses were performed on the polished cross-section of the pure sintered sample after thermal etching at 1100 °C for 20 minutes in the air atmosphere.

The average grain size was measured as the mean linear intercept method using the ImageJ software. For the Transmission Electron Microscopy (TEM) analysis pellets were cut into 3 mm discs using an ultrasonic cutter (SONICUT380, SBT, USA) and further mechanically thinned to 100  $\mu\text{m}$ . The discs were then dimpled down to 20  $\mu\text{m}$  in the center (Dimple grinder 656, Gatan Inc., USA), and finally ion-milled (PIPS 691, Gatan Inc., USA) using 4 kV  $\text{Ar}^+$  ions at an incidence angle of 8  $^\circ$  to obtain large transmissive areas for the TEM investigations. TEM, High Resolution Transmission Electron Microscopy (HRTEM) and Selected Area Electron Diffraction (SAED) analyses were performed using a 200 kV ultra-high-resolution field-emission gun (FEG) transmission electron microscope (JEM 2010F, Jeol, Japan).

The DC electrical conductivity of samples coated with Au electrodes was measured using Keithley 237 High Voltage Source Measure Unit. These measurements were performed in air in the temperature range of (25 – 150)  $^\circ\text{C}$ , with the step of 25  $^\circ\text{C}$ .

The AC impedance spectroscopy measurements were performed in the frequency range of 5 kHz – 5 MHz on the HIOKI 3532-50 impedance analyzer at 25  $^\circ\text{C}$  in air. EIS Spectrum Analyzer software was used for the fitting of experimental data collected for samples with  $x = 0.00$  and 0.04.

Hall effect measurements were performed at 290 K, in magnetic fields -5 T to 5 T perpendicular to the current through the sample. Samples were cut for the Hall-bar geometry with typical dimensions 10 mm  $\times$  2 mm  $\times$  1 mm. Two current contacts and three pairs of Hall contacts were made by applying DuPont 4929N silver paint. Hall signal was antisymmetrized,  $V_{yx} = [V_{yx}(+B) - V_{yx}(-B)]/2$ , in order to eliminate the possible mixing of the magnetoresistance component. Hall resistance,  $R_{yx} = V_{yx}/I$ , was found to be linear with magnetic field  $B$  for all samples and the Hall coefficient was obtained as  $R_H = V_{yx} t/(IB)$ , where  $I$  is the current and  $t$  the sample thickness.

Ultraviolet-Visible diffuse reflectance spectra (UV-Vis DRS) of pulverized pellets were measured using Shimadzu UV-2600 Spectrophotometer.

### 3. Results and discussion

#### 3.1. XRD and ICP-OES analyses

According to the XRD patterns, all calcined  $\text{BaSn}_{1-x}\text{Sb}_x\text{O}_3$  powders consist of cubic  $\text{BaSnO}_3$  (space group:  $Pm\bar{3}m$ , PDF # 89-2488), with the presence of small amounts of unreacted  $\text{SnO}_2$  (space group:  $P4_2/mnm$ , PDF # 88-0287) and  $\text{BaCO}_3$  (space group:  $Pm\bar{c}n$ , PDF # 71-2394) (Figure 1).

#### Fig.1.

After the sintering process, small soft silvery gray beads were observed on the top of the graphite die. ICP-OES analysis revealed that these are mainly composed of tin with traces of antimony and barium. Resulted molar ratio Sn : Ba : Sb in the beads (for the sample  $\text{BaSn}_{0.96}\text{Sb}_{0.04}$ ) was 5.6 : 0.6 : 0.03. The presence of these elements was also confirmed by BS-SEM and EDS analyses (see Supplementary material). During the SPS process the reaction between graphite die and oxygen from the sample can occur at temperatures lower than 600 °C [36], leading to the formation of CO phase. Vacuum atmosphere, high pressure and non-uniform temperature distribution from the center to the edge of sample together with created reduction atmosphere can cause the reduction of metal ion even to elementary state, *i.e.*  $\text{Sn}^{4+}$  can be reduced to  $\text{Sn}^{2+}$  or metallic Sn [40 – 43]. We can assume that Ba, Sn and Sb – cations in our samples are partially reduced to their elementary state. The low melting temperatures ( $T_m$  (Sn) = 232 °C,  $T_m$  (Sb) = 631 °C,  $T_m$  (Ba) = 727 °C) [44] of these metals enable the formation of the liquid phase while the vacuum atmosphere with high uniaxial pressure induces its partial evaporation and promotes the injection of the liquid phase out of

the die. Since tin has the highest vapor pressure, it was expected that tin would evaporate with the highest rate.

Figure 2 shows the XRD patterns for pulverized annealed  $\text{BaSn}_{1-x}\text{Sb}_x\text{O}_3$  ceramic samples after the SPS treatment. They reveal the presence of the cubic  $\text{BaSnO}_3$  (space group:  $Pm\bar{3}m$ , PDF # 89-2488) as a dominant phase, and tetragonal  $\text{Ba}_2\text{SnO}_4$  (space group:  $I4/mmm$ , PDF # 74-1349) as a secondary phase, with no reflections belonging to  $\text{SnO}_2$  or  $\text{BaCO}_3$ . Upon doping, the amount of secondary phase changes from 15 wt % in undoped samples to 7–8 wt % in doped ones (Table 1). However, the reduced content of tin in BSSO samples, due to its volatilization during SPS process led to the non-stoichiometry and enabled the formation of barium-rich phase  $\text{Ba}_2\text{SnO}_4$ .

**Fig. 2.**

In comparison with the undoped  $\text{BaSnO}_3$ , all reflections of doped samples are shifted towards lower  $2\theta$  angles as a consequence of the increased unit cell parameter  $a$  (Figure 2b, Table 1). The increase of the Sb concentration led to the expansion of unit cell, as was previously reported [2, 21, 24, 26]. Having in mind that in the six-coordinated geometry, the ionic radius of  $\text{Sn}^{4+}$  ( $r = 0.069$  nm) lies between the values of  $\text{Sb}^{3+}$  ( $r = 0.072$  nm) and  $\text{Sb}^{5+}$  ( $r = 0.060$  nm) ionic radii, one could assume that the unit cell expansion is a result of  $\text{Sb}^{3+}$  ions present in the crystal lattice. However, in this case it could not be explained only by consideration of ionic radii, but it should be correlated with the electronic band structure of  $\text{BaSn}_{1-x}\text{Sb}_x\text{O}_3$ . First-principles calculations along with the experimental data provided by Kim et al. [27] pointed out that this kind of unit cell expansion is a result of equilibrium ions' arrangement due to the achievement of the minimal Coulomb energy, because the electronic states in the antibonding conduction band of  $\text{BaSnO}_3$  cause repulsive forces between Sn and O upon Sb-doping [27].



The values of crystallite size for  $\text{BaSn}_{1-x}\text{Sb}_x\text{O}_3$  samples are in the range (37–57) nm (Table 1). The observed differences in crystallite size and unit cell parameter among doped samples are the result of lattice distortion and internal stress caused by Sb-doping.

### **Table 1.**

Taking into account densities of the samples and the results of preliminary electrical characterization, three samples ( $x = 0.00, 0.04$  and  $0.08$ ) were selected for ICP-OES analysis in order to determine the amount of antimony present and overall molar ratio of constituent cations. In all BSSO samples the content of Sn is significantly lower than experimentally targeted, as a result of its volatilization during SPS treatment (Table 2). Based on presented results it is expected that volatilization of all cations, together with the presence of  $\text{Ba}_2\text{SnO}_4$ , will affect properties of obtained ceramic samples. However, ICP results indicate that ratio between Ba and Sb is almost the same as experimentally defined, suggesting that the electrical properties of doped  $\text{BaSnO}_3$ , should be improved upon doping despite of partial material loss due to volatilization.

### **Table 2.**

## **3.2. Microscopy analyses**

### **3.2.1. FESEM and SEM analyses**

Relative densities of all  $\text{BaSn}_{1-x}\text{Sb}_x\text{O}_3$  ceramic samples were in the range of (79–96) % (Table 1). FESEM micrographs of the fractured cross-sections of undoped BSO showed well-densified microstructure, but non-homogeneous grain size distribution (Figure 3a). The Sb-doped ceramics showed more homogenous microstructure than the undoped one, with the decrease of the grain size upon increasing the dopant concentration (Figure 3b-e). The average grain size of all BSO samples is presented in Table 1. Even though the grain growth

inhibition could be correlated with the structure defects and Sb segregation on the surface of the grains [34], the latter was not confirmed by means of electron microscopy or XRD analyses.

**Fig. 3.**

In order to define location, morphology and composition of secondary phase, BS-SEM and EDS analyses were performed on the undoped BSO sample since it showed the highest content of the  $\text{Ba}_2\text{SnO}_4$  phase. This phase was not detected in fractured and polished sample, but thermal etching revealed the presence of secondary phase on the surface of the sample (Figure 4). Comparing the FE-SEM and BS-SEM micrographs we could conclude, that the  $\text{Ba}_2\text{SnO}_4$  phase was uniformly distributed through the sample's volume, and that thermal etching induced its diffusion to the sample's surface. EDS analysis of undoped BSO sample (Figure 4, Table 3, Spectra 1 and 2) showed the atomic ratio between constituent elements (Ba, Sn, and O) corresponding to the  $\text{BaSnO}_3$  phase. Still there are positions on the sample's surface having higher content of Ba in comparison to tin, indicating the presence of secondary phase (Figure 4, Table 3, Spectra 3 and 4).

**Fig. 4.**

**Table 3.**

**3.2.2. TEM, HRTEM and SAED analyses**

Additional microstructural analyses, using TEM and HRTEM techniques, were performed on  $\text{BaSn}_{1-x}\text{Sb}_x\text{O}_3$  ( $x = 0.00, 0.04$  and  $0.08$ ) ceramic samples with densities higher than 85 %. TEM analysis of the undoped  $\text{BaSnO}_3$  revealed the presence of many dislocations caused by the internal stress (dislocations are marked with white arrows on Figure 5a) and also a layer of amorphous phase (up to 2 nm thick) present in the grain boundary region. This amorphous phase is probably formed as a result of the changes in the grain orientations (Grain 1 and

Grain 2) and the formation of the high angle grain boundary (HAGB) between these differently oriented grains. HRTEM micrograph of the same sample, shows two grains, Grain 1 is oriented along [100] direction with visible (010) and (001) lattice planes, whereas the Grain 2 is not exactly, but close to [110] orientation with (1-10) and (001) planes (Figure 5b). The angle between the (001) planes of Grain 1 and Grain 2 is roughly  $27^\circ$  which makes the interface a high-angle tilt boundary. The interplanar distance of 0.292 nm, measured from the same HRTEM micrograph (Grain 2, Figure 5b) corresponds to the (1-10) crystal planes of BSO according to PDF card # 89-2488.

**Fig. 5.**

Sb-doping of BSO resulted in a more ordered microstructure with higher crystallinity. Also, the significant reduction of the grain size and the concentration of dislocations were observed in the  $\text{BaSn}_{0.96}\text{Sb}_{0.04}\text{O}_3$  sample (Figure 6a). HRTEM micrograph of  $\text{BaSn}_{0.96}\text{Sb}_{0.04}\text{O}_3$  sample showed Grain 1 oriented along [001] direction (Grain 1, Figure 6b) with diffractions from (200) and (110) crystal planes, and the Grain 2 with the only calculated  $d$ -spacing of 0.239 nm, corresponding to the (111) crystal planes of cubic BSO (space group  $Pm\bar{3}m$ ). Considering the facts that (111) crystal plane of the Grain 2 is almost parallel to the (200) crystal plane of the Grain 1 (Figure 6b), and that angle between these planes in space group  $Pm\bar{3}m$  is  $54.74^\circ$ , we can conclude that the angle between these two grains is close to  $54^\circ$ , forming the HAGB.

**Fig. 6.**

Figure 7 presents TEM micrograph of  $\text{BaSn}_{0.92}\text{Sb}_{0.08}\text{O}_3$  sample which revealed well-crystallized structure with the crystallite size in the range of (47–300) nm. All diffractions corresponding to cubic BSO phase were detected on the SAED pattern (Figure 7, Inset) and the most intense reflection (110) of cubic BSO appeared at  $d$ -spacing of 0.293 nm. Other,

weaker diffraction reflections (220), (211), (321), were also found and marked on SAED patterns. The overlapping of diffractions originates from the neighboring grains.

**Fig. 7.**

HRTEM micrograph of  $\text{BaSn}_{0.92}\text{Sb}_{0.08}\text{O}_3$  ceramic sample presented in Figure 8a revealed the presence of grains with [110] and [111] orientation. It also revealed the presence of Low Angle Grain Boundaries (LAGBs) between two grains oriented along [110] direction (Grain 1 and Grain 2), with the formed angle of  $\sim 4.43^\circ$ . In literature, LAGBs are described as series of dislocations stacked one above the other with a low tilt formed between the grains on the opposite sides of the grain boundary [45, 46]. However, the grain boundaries existing between two grains oriented along different directions, [110] and [111] (Figure 8a), cannot be described as LAGB since the angle between them is at least  $35^\circ$  [47]. The facets of interface between two grains on Figure 8b indicate that there is some special crystallographic relationship.

The lattice fringes in Grain 2 correspond to (110) planes of cubic BSO phase with  $d$ -spacing of 0.293 nm. LAGBs are also formed between two grains oriented along [111] direction with angle being  $\sim 7.11^\circ$ .

**Fig. 8.**

**3.3. Electrical characterization ( $I$ - $U$  characteristic), AC impedance spectroscopy and Hall effect**

Electrical measurements conducted on spark plasma sintered  $\text{BaSn}_{1-x}\text{Sb}_x\text{O}_3$  samples confirmed the assumption that Sb-doping can improve the electrical properties of BSO.

As mentioned previously, the  $\text{BaSn}_{1-x}\text{Sb}_x\text{O}_3$  ( $x = 0.00, 0.04$  and  $0.08$ ) samples were selected for further examination.

The undoped BaSnO<sub>3</sub> revealed non-linear  $I-U$  characteristic (Figure 9, Inset) typical for semiconductors with double Schottky barrier at grain boundaries. After doping with lower concentration ( $x = 0.04$ ) of Sb the electrical resistivity was decreased, but the sample retained non-linear  $I-U$  characteristic (Figure 9).

**Fig. 9.**

The change from non-linear to linear  $I-U$  characteristics was observed for the BaSn<sub>0.92</sub>Sb<sub>0.08</sub>O<sub>3</sub> sample, indicating the loss of potential barrier at grain boundaries (Figure 9). This change is primarily ascribed to the existence of LAGBs in this sample. The formed LAGBs do not possess potential barriers because of almost negligible change in the grains orientation. Owing to their low activation energy, they provide energetically more favorable path for the charge carriers' transport, having the highest impact on the electrical properties of BaSn<sub>0.92</sub>Sb<sub>0.08</sub>O<sub>3</sub> sample [45]. The DC electrical resistivity of all ceramic samples, measured at 25 °C, decreased with the increase of antimony concentration and these values are presented in Table 4. The sample with  $x = 0.08$  showed the lowest electrical resistivity of 1.09 Ωcm.

**Table 4.**

To the best of our knowledge, there are no literature reports about electrical characteristics of Sb-doped barium stannate at temperatures above 25 °C. Electrical resistivity of BaSn<sub>1-x</sub>Sb<sub>x</sub>O<sub>3</sub> ( $x = 0.00, 0.04$  and  $0.08$ ) samples observed in the temperature range of (25 – 150) °C is shown on Figure 10. It can be seen that Sb-doping also improves electrical properties of BaSnO<sub>3</sub> ceramics at higher temperatures. The introduction of Sb ( $x = 0.04$ ) into BaSnO<sub>3</sub> reduced the influence of temperature on sample's electrical resistivity (Figure 10b). Furthermore, BaSn<sub>0.92</sub>Sb<sub>0.08</sub>O<sub>3</sub> sample showed the lowest electrical resistivity, which remained almost constant in the specified temperature range (Figures 10b and 10c).

**Fig. 10.**

In order to confirm the absence of potential barrier at grain boundaries in some of the samples, and to separate the contribution of grains and grain boundaries on the electrical properties of  $\text{BaSn}_{1-x}\text{Sb}_x\text{O}_3$  samples ( $x = 0.00, 0.04$  and  $0.08$ ; at  $25\text{ }^\circ\text{C}$ ) the AC impedance spectroscopy was used, and the results are presented in Figure 11. The existence of one semicircle was confirmed in the case of undoped and  $\text{BaSn}_{0.96}\text{Sb}_{0.04}\text{O}_3$  samples. The equivalent circuit used for fitting consisted of two resistors ( $R_b$  and  $R_{gb}$ , where “b” and “gb” denote bulk and grain boundary region) and a constant phase element (CPE) (Figure 11, Inset). The obtained results of grain and grain boundary resistivity, capacitance and coefficient of CPE are shown in the Table 5.

**Fig. 11.**

**Table 5.**

We can assume that impedance results for the samples with  $x = 0.00$  and  $0.04$  originate mostly from the grain boundaries. The values of total electrical resistivity from AC impedance spectra are in agreement with the values of DC electrical resistivity obtained from  $I-U$  measurements (Table 4). On the other hand, the spectrum of  $\text{BaSn}_{0.92}\text{Sb}_{0.08}\text{O}_3$  could not be fitted since all measured resistivity values in the applied frequency region were almost identical, and amounted about  $1.12\ \Omega\text{cm}$ . This significant drop in the resistivity, noticed by DC measurements as well, originates from the loss of potential barrier at low angle grain boundaries. It manifested through the complete loss of semicircle in the impedance spectrum.

The results of Hall measurements are presented in Table 6. The negative value of the Hall coefficient at  $290\ \text{K}$  confirmed that prepared  $\text{BaSn}_{1-x}\text{Sb}_x\text{O}_3$  ceramic samples show n-type conductivity indicating the replacement of  $\text{Sn}^{4+}$  with  $\text{Sb}^{5+}$  in the  $\text{BaSnO}_3$  lattice. The magnitude of Hall coefficient at  $290\ \text{K}$  decreases monotonously with Sb concentration. Taking into account that oxygen vacancies intrinsically dope this system, in order to estimate charge carrier density and mobility we can assume a single n-type carrier is responsible for

electric transport. Its density  $n$  and mobility  $\mu$  can then be obtained from room temperature bulk resistivity  $\rho_b$ , Hall coefficient  $R_H$ , and electron charge  $e$  as  $n = 1 / |e R_H|$ ,  $\mu = |R_H / \rho_b|$  (Table 6). In this simplified picture the decreased resistivity of polycrystalline  $\text{BaSn}_{0.92}\text{Sb}_{0.08}\text{O}_3$  sample stems from increased mobility of charge carriers compared to the parent compound, but predominantly from the loss of potential barrier due to the presence of low angle grain boundaries.

The electrical resistivity of the  $\text{BaSn}_{0.92}\text{Sb}_{0.08}\text{O}_3$  polycrystalline ceramic sample is still higher than achieved in the BSSO thin films [29] and single crystals [20, 27], which showed the lowest electrical resistivity of  $2.43 \times 10^{-3} \text{ } \Omega\text{cm}$  and  $0.66 \times 10^{-3} \text{ } \Omega\text{cm}$ , respectively, measured at RT. Also, the values of charge carrier density and electrical mobility of the BSSO ceramic samples are lower than values achieved in the BSSO thin films [29] and single crystals [20, 27]. The highest charge carrier density of  $1.65 \times 10^{21} \text{ cm}^{-3}$  and electron mobility of  $1.75 \text{ cm}^2/\text{Vs}$  were found in the  $\text{BaSn}_{1-x}\text{Sb}_x\text{O}_3$  thin film with  $x = 0.07$  obtained by pulsed laser deposition (PLD) [29]. On the other hand, the charge carrier density and electron mobility of  $\text{BaSn}_{1-x}\text{Sb}_x\text{O}_3$  ( $x = 0.03$ ) single crystals obtained by molten flux [20, 27], reached  $1.02 \times 10^{20} \text{ cm}^{-3}$  and  $79.4 \text{ cm}^2/\text{Vs}$ , respectively.

#### **Table 6.**

### **3.4. UV-Vis spectroscopy**

UV-Vis Diffuse Reflectance Spectra of  $\text{BaSn}_{1-x}\text{Sb}_x\text{O}_3$  pulverized ceramic samples are shown in Figure 12 as a Tauc plot, which presents a modified Kubelka-Munk function  $[F(R)h\nu]^{1/2}$ , versus photon energy  $h\nu$ . (Kubelka-Munk function is given by  $F(R) = (1 - R)^{1/2}/2R$ , where  $R$  represents measured reflectance relative to a standard [48, 49]). For each

sample  $E_g$  value was obtained as the point of intersection of the tangent line on Tauc plot and the horizontal axis.

Based on literature data BSO has a clear absorption edge at approximately 400 nm, corresponding to the band gap of 3.1 eV [2]. In our case, the undoped sample showed the absorption edge at lower energy and the band gap was 2.92 eV, which is in accordance with some previously reported results [28, 50]. DRS of doped  $\text{BaSn}_{1-x}\text{Sb}_x\text{O}_3$  samples showed a reduction of slope, revealing that their absorption edge is moved to larger energies in comparison with BSO. This phenomenon known as a blue shift, or Burstein–Moss effect is noted in some other n-type doped  $\text{BaSnO}_3$ -based materials [2, 14, 27, 51]. Upon doping with Sb, the number of electrons filling the lower energy levels in the conduction band (CB) of BSO is increased, and more energy is needed for the electron transfer from the valence band (VB) to the higher unoccupied energy states in the CB [51]. As a result of this change in electronic states, the Fermi level energy ( $E_F$ ) moves to the higher energy values [51]. But, for the  $\text{BaSn}_{0.9}\text{Sb}_{0.1}\text{O}_3$  sample the Fermi level is shifted to the lower energies in comparison with the  $\text{BaSn}_{0.92}\text{Sb}_{0.08}\text{O}_3$ . Doping with the highest Sb concentration led to the formation of electrically inactive Sb, which behave like electron traps for the carriers showing a decrease in carrier density [29]. Furthermore, the created scattering centre originating from electrically inactive Sb can block the electron transport to the conduction band (CB) [29], which results in the decrease of electron mobility. This caused a decrease in the electrical conductivity of  $\text{BaSn}_{0.9}\text{Sb}_{0.1}\text{O}_3$  ceramic sample and the loss of linearity in its  $I$ - $U$  characteristic.

In our samples, as the Hall measurements confirmed, Sb-doping increased the carrier concentration and mobility of the charge carriers, which resulted in the band gap widening. The transparency of visible light for the undoped BSO sample was approximately 80 %, but doping with Sb resulted in a loss of transparency to the visible irradiation. We could conclude



that presented doped  $\text{BaSn}_{1-x}\text{Sb}_x\text{O}_3$  can't find application as a transparent conducting oxide. However, Sb-doping increased the electrical conductivity of  $\text{BaSn}_{1-x}\text{Sb}_x\text{O}_3$  samples, and it led to the linearity of  $I-U$  characteristic, making the  $\text{BaSn}_{1-x}\text{Sb}_x\text{O}_3$  samples good candidates for linear resistors.

**Fig. 12.**

#### 4. Conclusions

Spark plasma sintering method enabled the preparation of Sb-doped barium stannate ceramics in shorter times and at lower temperatures in comparison with the conventional sintering processes. Well densified polycrystalline samples of  $\text{BaSn}_{1-x}\text{Sb}_x\text{O}_3$  ( $x = 0.00, 0.04, 0.06, 0.08$  and  $0.10$ ) show homogeneous microstructure with reduction of the grain size with the increase of Sb concentration.

Sb-doping of SPS  $\text{BaSnO}_3$  proved to be useful for tailoring the presence of potential barrier at grain boundaries in ceramic materials. Samples with lower dopant concentration exhibited non-linear  $I-U$  characteristic typical for semiconductors having potential barriers at grain boundaries. On the other hand,  $\text{BaSn}_{0.92}\text{Sb}_{0.08}\text{O}_3$  sample ( $x = 0.08$ ) showed linear  $I-U$  characteristic in the whole temperature measurement range and significant drop in the electrical resistivity due to the loss of potential barriers at grain boundaries as a consequence of LAGBs present in this ceramic sample.

Sb-doping also increased n-type carrier concentration and charge carriers mobility in the ceramic samples, resulting in the increase of their electrical conductivity, especially for the  $\text{BaSn}_{0.92}\text{Sb}_{0.08}\text{O}_3$ . Doping with Sb increased the band gap values, revealing the Burstein–Moss shift (i.e., blue shift) in all doped samples. Hence,  $\text{BaSn}_{0.92}\text{Sb}_{0.08}\text{O}_3$  ceramic sample can be used as a linear resistor owing to its appropriate microstructural, electrical and optical properties.

### Declaration of interests

The authors declare that they have no known competing financial interests or personal relationships that could have appeared to influence the work reported in this paper.

### Acknowledgment

The authors acknowledge financial support of Ministry of Education, Science, and Technological Development of Republic of Serbia (Contract No. 451-03-68/2020-14/200053). S. Bernik, M. Podlogar and M. Kocen acknowledge support of Slovenian Research Agency (Program Contract No. P2-0084). The TEM work was conducted in the infrastructure of Centre for Electron Microscopy and Microanalysis (CEMM) in Jožef Stefan Institute, Ljubljana, Slovenia. Ž. Rapljenović and T. Ivek acknowledge the support of Croatian Science Foundation project IP-2018-01-2730. This work was done as a part of the project entitled "Zero-to Three-Dimensional Nanostructures for Application in Optics, Electronics and Energetics" under the bilateral collaboration between Institute for Multidisciplinary Research (University of Belgrade, Serbia) and Institute "Jožef Stefan" (Ljubljana, Slovenia).

### References

- [1] R. K. Pandey, Fundamentals of electroceramics: materials, devices, and applications, first ed., John Wiley & Sons, Inc., New Jersey, 2019.
- [2] H. Mizoguchi, P. Chen, P. Boolchand, V. Ksenofontov, K. Felser, P. W. Barnes, P. M. Woodward, Electrical and Optical Properties of Sb-Doped BaSnO<sub>3</sub>, Chem. Mater. 25 (19) (2013) 3858-3866.

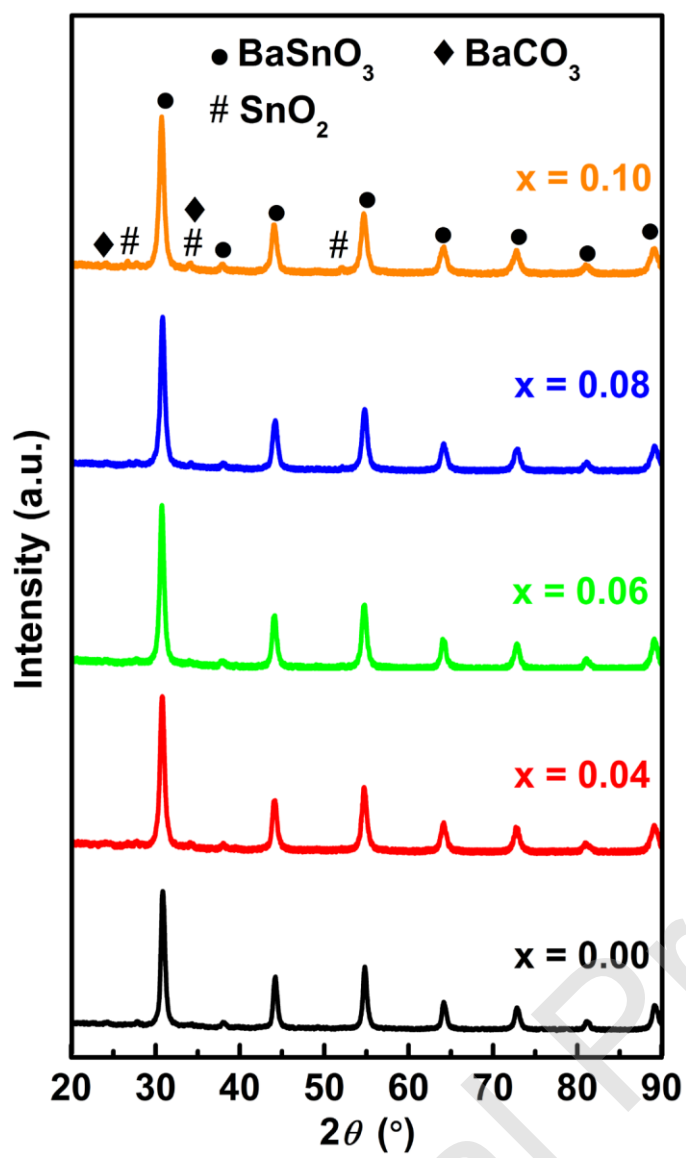
- [3] M. A. Peña, J. L. G. Fierro, Chemical Structures and Performance of Perovskite Oxides, *Chem. Rev.* 101 (2001) 1981-2017.
- [4] W. Lu, S. Jiang, D. Zhou, S. Gong, Structural and electrical properties of Ba(Sn,Sb)O<sub>3</sub> electroceramics materials, *Sens. Actuators* 80 (2000) 35-37.
- [5] Y. H. O. Muñoz, M. Ponce, J. E. R. Páez, Comparative study of two wet chemical methods of BaSnO<sub>3</sub> synthesis: Mechanism of formation of mixed oxide, *Powder Technol.* 279 (2015) 86-95.
- [6] A. M. Azad, N. C. Hon, Characterization of BaSnO<sub>3</sub>-based ceramics Part 1. Synthesis, processing and microstructural development, *J. Alloys Compd.* 270 (1998) 95-106.
- [7] J. Cerdà, J. Arbiol, G. Dezanneau, R. Díaz, J. R. Morante, Perovskite-type BaSnO<sub>3</sub> powders for high temperature gas sensor applications, *Sens. Actuators B* 84 (2002) 21-25.
- [8] M. Yasukawa, T. Kono, K. Ueda, H. Yanagi, S. W. Kim, H. Hosono, Thermoelectric properties and figure of merit of perovskite-type Ba<sub>1-x</sub>La<sub>x</sub>SnO<sub>3</sub> with  $x = 0.002-0.008$ , *Solid State Commun.* 172 (2013) 49-53.
- [9] A. M. Azad, L. L. W. Shyan, T. Y. Pang, C. H. Nee, Microstructural evolution in MSnO<sub>3</sub> ceramics derived via self-heat-sustained (SHS) reaction technique, *Ceram. Int.* 26 (2000) 685-692.
- [10] H. Mizoguchi, H. W. Eng, P. M. Woodward, Probing the Electronic Structures of Ternary Perovskite and Pyrochlore Oxides Containing Sn<sup>4+</sup> or Sb<sup>5+</sup>, *Inorg. Chem.* 43 (2004) 1667-1680.
- [11] C. Moure, Octavio Peña, Recent advances in perovskites: Processing and properties, *Prog. Solid State Chem.* 43 (2015) 123-148.
- [12] David O. Scanlon, Defect engineering of BaSnO<sub>3</sub> for high-performance transparent conducting oxide applications, *Phys. Rev. B* 87 (2013) 161201(R).

- [13] U. Kumar, Md. J. Ansaree, S. Upadhyay, Structural and optical characterizations of BaSnO<sub>3</sub> nanopowder synthesized by aqueous sol-gel method, *Process. Appl. Ceram.* 11 (3) (2017) 177-184.
- [14] A. Slassi, Ab initio study of a cubic perovskite: Structural, electronic, optical and electrical properties of native, lanthanum- and antimony-doped barium tin oxide, *Mat. Sci. Semicon. Proc.* 32 (2015) 100-106.
- [15] C. Huang, X. Wang, X. Liu, M. Tian, T. Zhang, Extensive analysis of the formation mechanism of BaSnO<sub>3</sub> by solid-state reaction between BaCO<sub>3</sub> and SnO<sub>2</sub>, *J. Eur. Ceram. Soc.* 36 (2016) 583-592.
- [16] M. Bilal Saddique, M. Rashid, A. Afzal, S. M. Ramay, F. Aziz, A. Mahmood, Ground state opto-electronic and thermoelectric response of cubic XSnO<sub>3</sub> (X = Ba, Sr) compounds, *Curr. Appl. Phys.* 17 (2017) 1079-1086.
- [17] P. Udawatte, M. Kakihana, M. Yoshimura, Preparation of pure perovskite-type BaSnO<sub>3</sub> powders by the polymerized complex method at reduced temperature, *Solid State Ion.* 108 (1998) 23-30.
- [18] G. Wang, J. Bai, C. Shan, D. Zhang, N. Lu, Q. Liu, Z. Zhou, S. Wang, C. Liu, Synthesis and ethanol gas sensing properties of mesoporous perovskite type BaSnO<sub>3</sub> nanoparticles interconnected network, *Mater. Lett.* 205 (2017) 169-172.
- [19] I. A. Alagdal, A. R. West, Oxygen stoichiometry, conductivity and gas sensing properties of BaSnO<sub>3</sub>, *J. Mater. Chem. C* 4 (2016) 4770-4777.
- [20] W.-J. Lee, H. J. Kim, J. Kang, D. H. Jang, T. H. Kim, J. H. Lee, K. H. Kim, Transparent Perovskite Barium Stannate with High Electron Mobility and Thermal Stability, *Annu. Rev. Mater. Res.* 47 (2017) 391-423.
- [21] M. G. Smith, J. B. Goodenough, A. Manthiram, Tin and Antimony Valence States in BaSn<sub>0.85</sub>Sb<sub>0.15</sub>O<sub>3-δ</sub>, *J. Solid State Chem.* 98 (1992) 181-186.

- [22] R. J. Cava, P. Gammel, B. Batlogg, J. J. Krajewski, W. F. Peck, Jr., L. W. Rupp, Jr., R. Felder, R. B. van Dover, Nonsuperconducting  $\text{BaSn}_{1-x}\text{Sb}_x\text{O}_3$ . The 5s-orbital analog of  $\text{BaPb}_{1-x}\text{Bi}_x\text{O}_3$ , *Phys. Rev. B.* 42 (7) (1990) 4815-4818.
- [23] M. G. Smith, J. B. Goodenough, Electronic structure of  $\text{BaSn}_{1-x}\text{Sb}_x\text{O}_3$  studied by photoemission spectroscopy, *Phys. Rev. B.* 47 (4) (1993) 1788-1793.
- [24] T. Huang, T. Nakamura, M. Itoh, Y. Inaguma, O. Ishiyama, Electrical properties of  $\text{BaSnO}_3$  in substitution of antimony for tin and lanthanum for barium, *J. Mater. Sci.* 30 (1995) 1556-1560.
- [25] G. Pfaff, Wet Chemical Powders Synthesis of  $\text{BaSnO}_3$  and  $\text{Ba}_2\text{SnO}_4$ , *J. Eur. Ceram. Soc.* 12 (1993) 159-164.
- [26] D. Yamashita, S. Takefuji, M. Tsubomoto, T. Yamamoto, Electronic structure analysis of Sb-doped  $\text{BaSnO}_3$ , *Mat. Sci. Eng. B* 173 (2010) 33-36.
- [27] H. J. Kim, J. Kim, T. H. Kim, W.-J. Lee, B.-Gu Jeon, J.-Y. Park, W. S. Choi, D. W. Jeong, S. H. Lee, J. Yu, T. W. Noh, K. H. Kim, Indications of strong neutral impurity scattering in  $\text{Ba}(\text{Sn,Sb})\text{O}_3$  single crystals, *Phys. Rev. B* 88 (2013) 125204.
- [28] Z. Galazka, R. Uecker, K. Irmscher, D. Klimm, R. Bertram, A. Kwasniewski, M. Naumann, R. Schewski, M. Pietsch, U. Juda, A. Fiedler, M. Albrecht, S. Ganschow, T. Markurt, C. Guguschev, M. Bickermann, Melt growth and properties of bulk  $\text{BaSnO}_3$  single crystals, *J. Phys.: Condens. Matter* 29 (2017) 075701.
- [29] Q. Liu, J. Dai, Z. Liu, X. Zhang, G. Zhu, G. Ding, Electrical and optical properties of Sb-doped  $\text{BaSnO}_3$  epitaxial films grown by pulsed laser deposition, *J. Phys. D: Appl. Phys.* 43 (2010) 455401
- [30] R. Wei, X. Tang, L. Hu, X. Luo, J. Yang, W. Song, J. Dai, X. Zhu, Y. Sun, Growth, Microstructures, and Optoelectronic Properties of Epitaxial  $\text{BaSn}_{1-x}\text{Sb}_x\text{O}_{3-\delta}$  Thin Films by Chemical Solution Deposition, *ACS Appl. Energy Mater.* 1 (4) (2018)1585-1593.

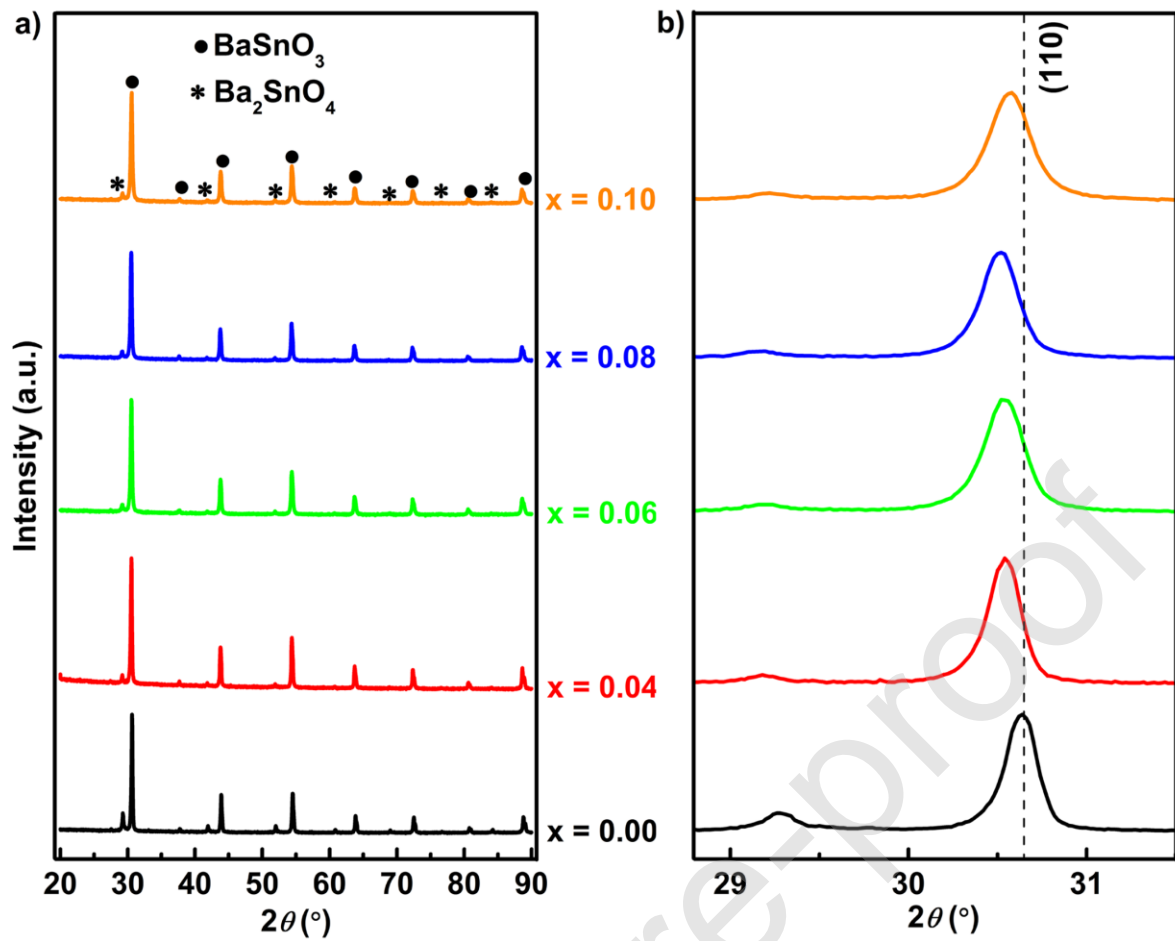
- [31] S. Raghavan, T. Schumann, H. Kim, J. Y. Zhang, T. A. Cain, S. Stemmer, High-mobility BaSnO<sub>3</sub> grown by oxide molecular beam epitaxy, *APL Mater.* 4 (2016) 016106.
- [32] A. Prakash, J. Dewey, H. Yun, J. S. Jeong, K. A. Mkhoyan, B. Jalan, Hybrid molecular beam epitaxy for the growth of stoichiometric BaSnO<sub>3</sub>, *J Vac Sci Technol A* 33 (2015) 060608.
- [33] Y. Z. Wang, E. Bevilion, A. Chesnaud, G. Geneste, G. Dezanneau, Atomistic Simulation of Pure and Doped BaSnO<sub>3</sub>, *J. Phys. Chem. C* 113 (2009) 20486-20492.
- [34] S. Liu, W. Ding, Y. Gu, W. Chai, Effect of Sb doping on the microstructure and optoelectrical properties of Sb-doped SnO<sub>2</sub> films prepared by spin coating, *Phys. Scripta* 85 (2012) 065601.
- [35] Y. Li, L. Zhang, Y. Ma, D. J. Singh, Tuning optical properties of transparent conducting barium stannate by dimensional reduction, *APL Materials* 3 (2015) 011102.
- [36] Z. Branković, D. Lukovic Golić, A. Radojković, J. Ćirković, D. Pajić, Z. Marinković Stanojević, J. Xing, M. Radović, G. Li, G. Branković, Spark plasma sintering of hydrothermally synthesized bismuth ferrite, *Process. Appl. Ceram.* 10 (4) (2016) 257-264.
- [37] R. Licheri, S. Fadda, R. Orrù, G. Cao, V. Buscaglia, Self-propagating high-temperature synthesis of barium titanate and subsequent densification by spark plasma sintering (SPS), *J. Eur. Ceram. Soc.* 27 (2007) 2245-2253.
- [38] N. Okinaka, L. Zhang, T. Akiyama, Thermoelectric Properties of Rare Earth-doped SrTiO<sub>3</sub> Using Combination of Combustion Synthesis (CS) and Spark Plasma Sintering (SPS), *ISIJ International* 50 (9) (2010) 1300-1304.
- [39] R.G. Garwey, *Computer Comments, Powder Diffract.* 1 (1986) 114-118.
- [40] F. Delorme, R. Dujardin, F. Schoenstein, B. Pintault, P. Belleville, C. Autret, I. Monot-Laffez, F. Giovannelli, Nanostructuring of dense SnO<sub>2</sub> ceramics by Spark Plasma Sintering, *Ceram. Int.* 45 (2019) 8313-8318.

- [41] H. Yoshida, K. Morita, B.-N. Kim, K. Soga, Low temperature spark plasma sintering of tin oxide doped with tantalum oxide, *J. Ceram. Soc. Jpn* 124 (9 (2016) 932-937.
- [42] B. Hadjarab, A. Bouguelia, M. Trari, Optical and transport properties of lanthanum-doped stannate  $\text{BaSnO}_3$ , *J. Phys. D: Appl. Phys.* (40) (2007) 5833-5839.
- [43] J. Wu, F. Chen, Q. Shen, J. M. Schoenung, L. Zhang, Spark Plasma Sintering and Densification Mechanisms of Antimony-Doped Tin Oxide Nanoceramics, *J. Nanomater.* (2013) ID 561895 (7 pages).
- [44] WebElements<sup>TM</sup>, The periodic table of the elements, <https://www.webelements.com/>.
- [45] Y. Furushima, A. Nakamura, E. Tochigi, Y. Ikuhara, K. Toyoura, K. Matsunaga, Dislocation structures and electrical conduction properties of low angle tilt grain boundaries in  $\text{LiNbO}_3$ , *J. Appl. Phys.* 120 (2016) 142107 1-10.
- [46] H. Li, G. Zhao, X. Zeng, G. Zhou, Z. Qian, S. Zhou, J. Xu, Study on cracking and low-angle grain boundary defects in  $\text{YAlO}_3$  crystal, *Mater. Lett.* 58 (2004) 3253-3256.
- [47] C. Wang, K. Du, K. Song, X. Ye, L. Qi, S. He, D. Tang, N. Lu, H. Jin, F. Li, H. Ye, Size-Dependent Grain-Boundary Structure with Improved Conductive and Mechanical Stabilities in Sub-10-nm Gold Crystals, *Phys. Rev. Lett.* 120 (2018) 186102.
- [48] P. Kubelka, F. Munk, An Article on Optics of Paint Layers, *Z. Tech. Phys.* 12 (1931) 593.
- [49] J. Tauc, R. Grigorovici, A. Vancu, Optical Properties and Electronic Structure of Amorphous Germanium, *Phys. Status Solidi* 15 (1966) 627-637.
- [50] R. Kurre, S. Bajpai, P. Kumar Bajpai, Synthesis, Characterization, Optical and Transport Properties of  $\text{BaSnO}_3$  Synthesized by Wet Chemical Route, *J. Mater. Sci.* 9 (2018) 92-110.
- [51] A. Sarkar, S. K. De, Defect and Optical Properties of Sb doped and hydrogenated  $\text{BaSnO}_3$ , *Semicond. Sci. Technol.* 33 (2018) 035018.

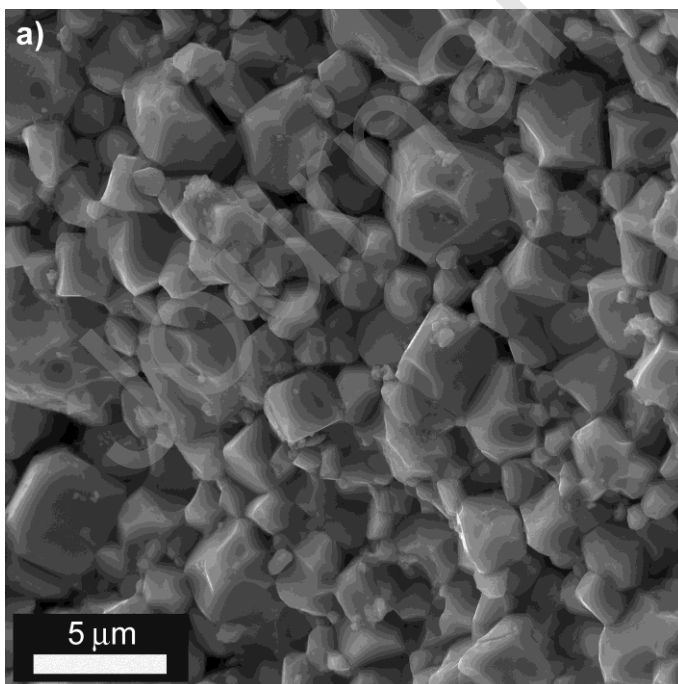


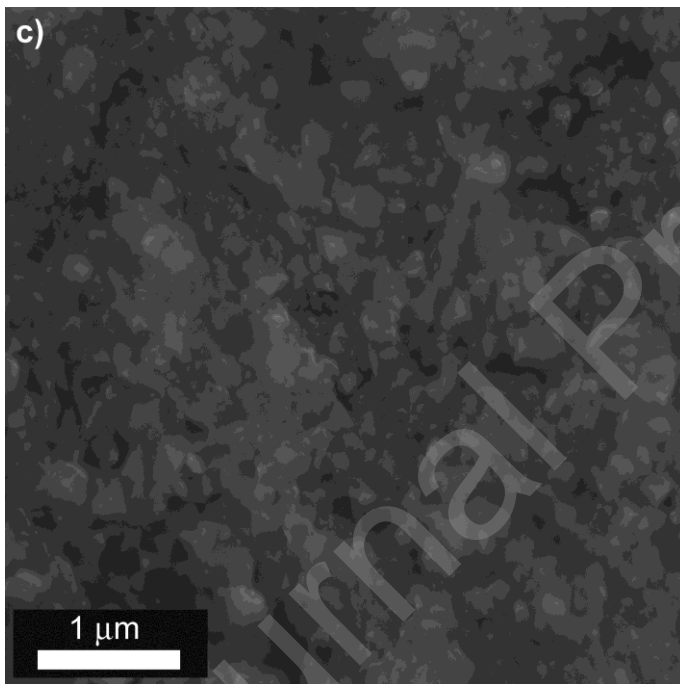
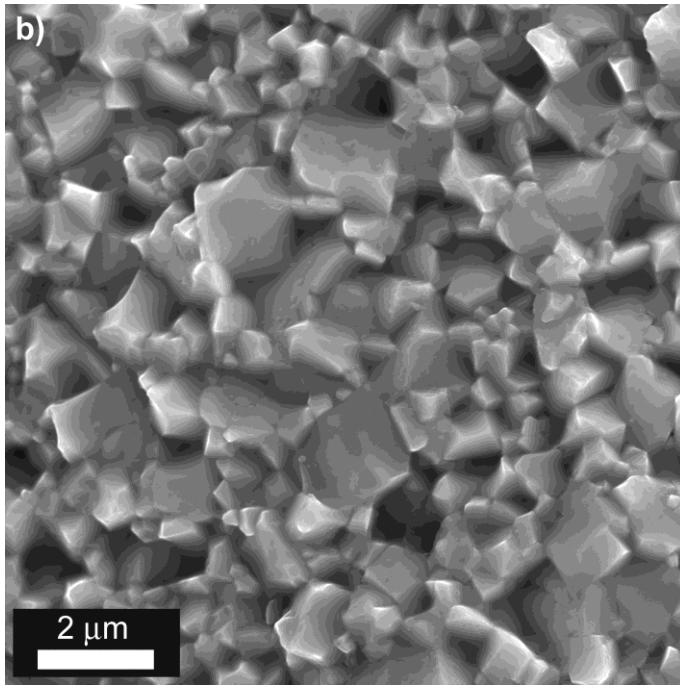
**Figure 1.** XRD patterns of BaSn<sub>1-x</sub>Sb<sub>x</sub>O<sub>3</sub> powders calcined at 900 °C for 4 h in air.





**Figure 2.** (a) XRD patterns of the pulverized  $\text{BaSn}_{1-x}\text{Sb}_x\text{O}_3$  ceramic samples after the SPS treatment; (b) Shifting of the strongest (110) reflection of  $\text{BaSn}_{1-x}\text{Sb}_x\text{O}_3$  ceramic samples.





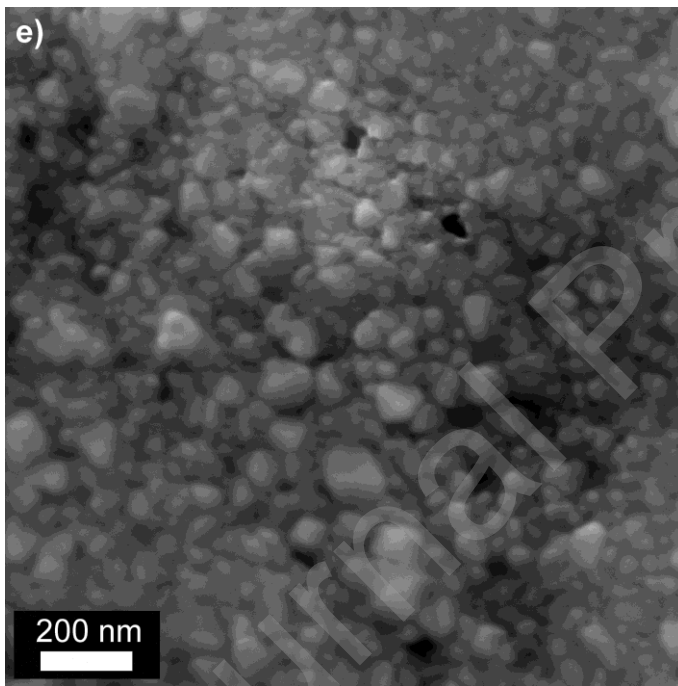
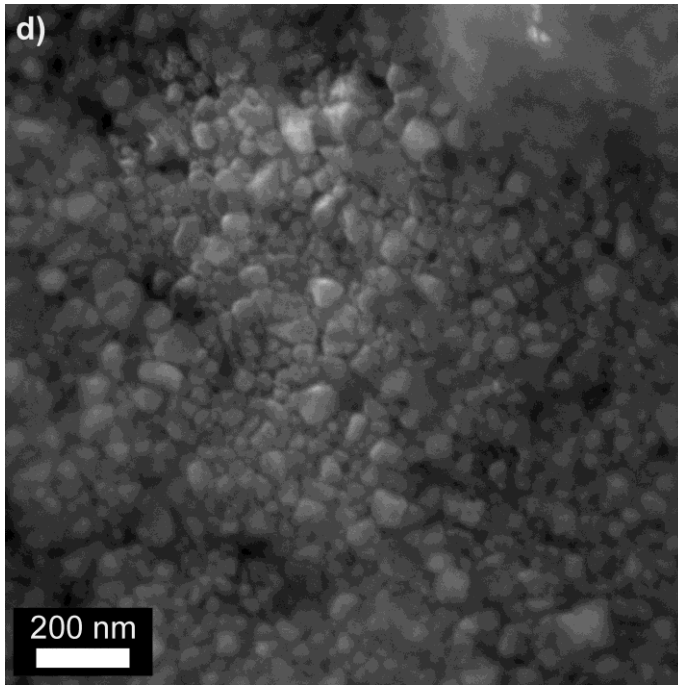


**Figure 3.** FESEM micrographs of the fractured cross-sections of  $\text{BaSn}_{1-x}\text{Sb}_x\text{O}_3$  ceramic samples: (a)  $x = 0.00$ , (b)  $x = 0.04$ , (c)  $x = 0.06$ , (d)  $x = 0.08$  and (e)  $x = 0.10$ .

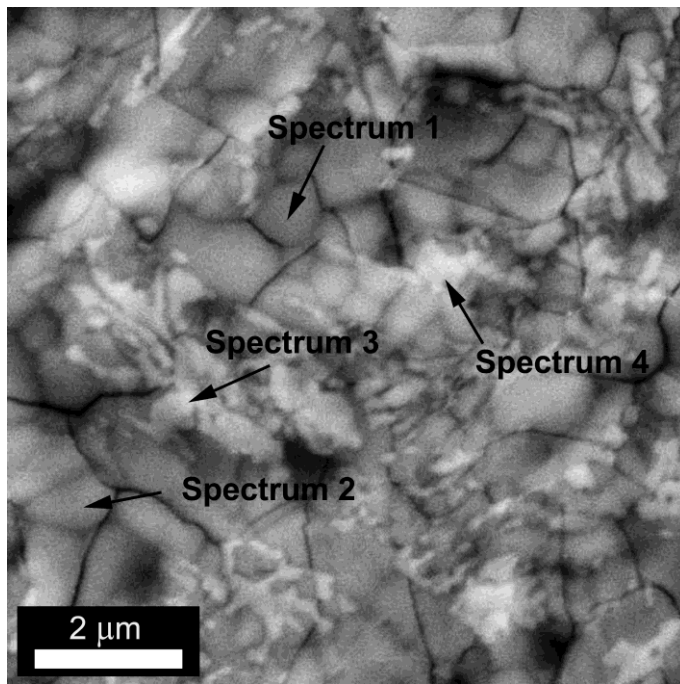


**Figure 4.** BS-SEM micrograph of the undoped BSO ceramic sample's polished surface thermally etched at 1100 °C/20 min.

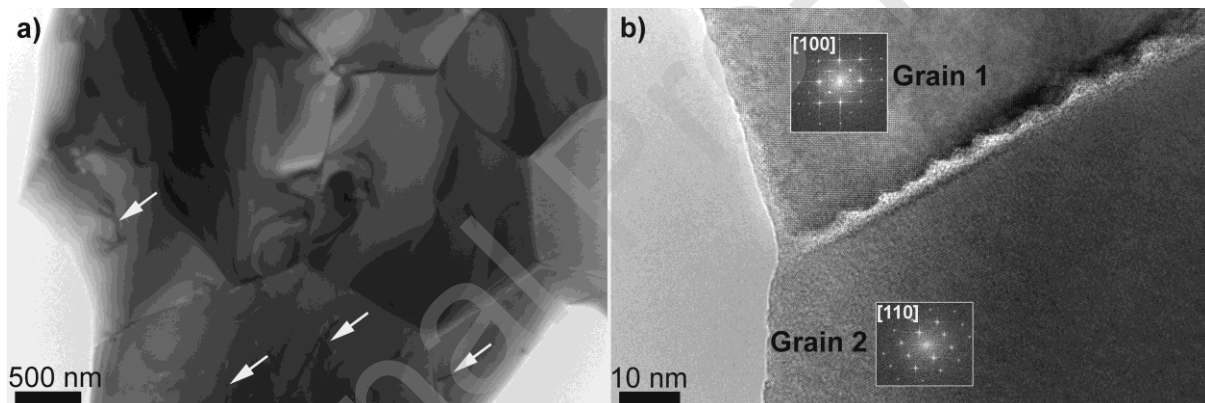


**Figure 5.** (a) TEM micrograph of the undoped BaSnO<sub>3</sub> pellet with marked dislocations (b) HRTEM micrograph of the undoped BaSnO<sub>3</sub> pellet (The insets present the fast Fourier transform (FFT) of micrographs of both grains tilted into zone axis).

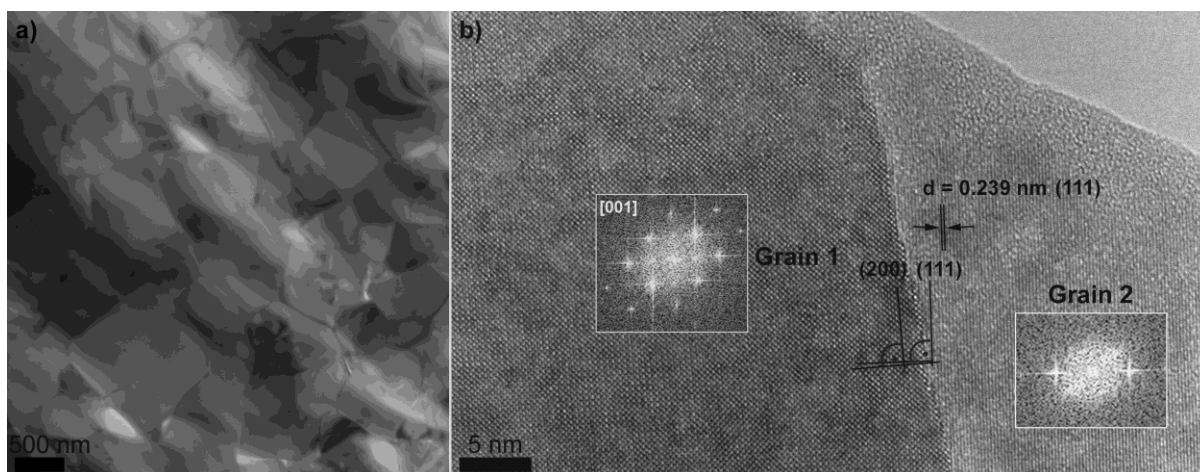


**Figure 6.** (a) TEM micrograph of the  $\text{BaSn}_{0.96}\text{Sb}_{0.04}\text{O}_3$  pellet, (b) HRTEM micrograph of the  $\text{BaSn}_{0.96}\text{Sb}_{0.04}\text{O}_3$  pellet (The insets present FFT, of Grain 1 oriented along [001] direction and Grain 2 out of zone axis).

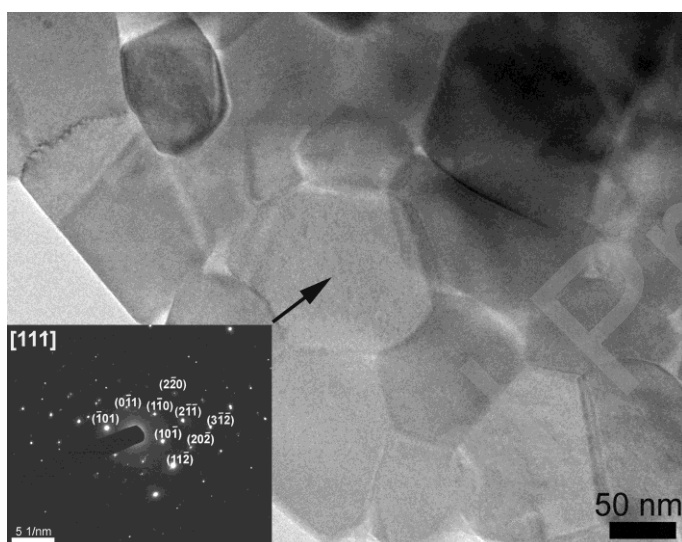


**Figure 7.** TEM micrograph of  $\text{BaSn}_{0.92}\text{Sb}_{0.08}\text{O}_3$  sample. The inset shows SAED pattern of grain oriented along [111] direction.

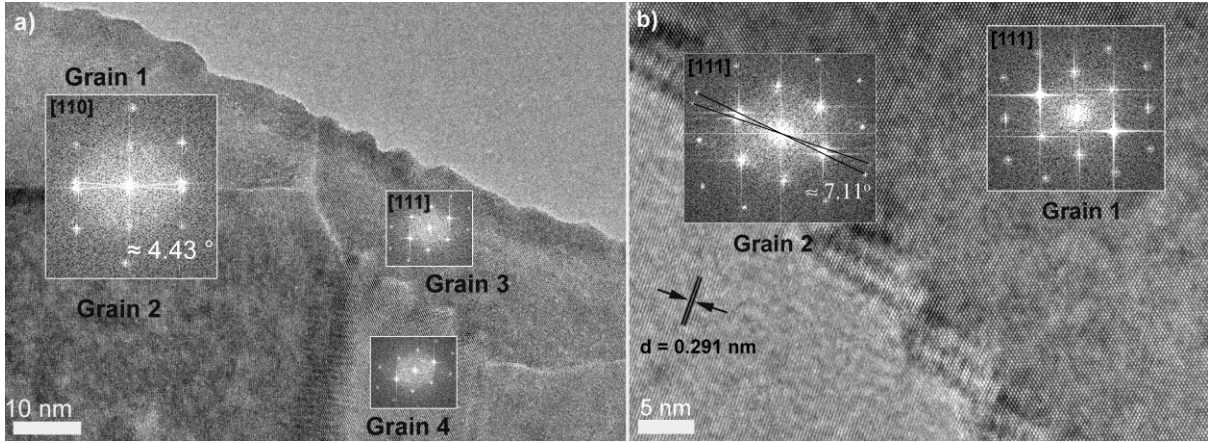


**Figure 8.** HRTEM micrographs of the  $\text{BaSn}_{0.92}\text{Sb}_{0.08}\text{O}_3$  ceramic sample showing LAGB formed between pairs of grains oriented along: (a) [110] and [111] direction; (b) [111] direction. (The insets present FFT of grains micrographs).

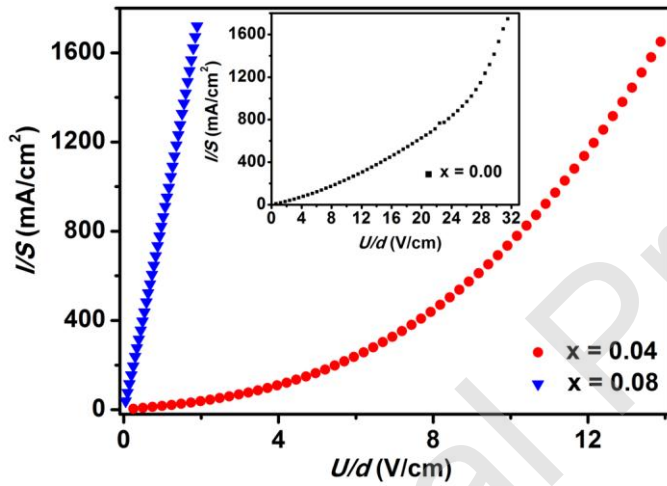


**Figure 9.**  $I$ - $U$  characteristic of  $\text{BaSn}_{1-x}\text{Sb}_x\text{O}_3$  ( $x = 0.04$  and  $0.08$ ) ceramic samples measured in air at  $25^\circ\text{C}$ . Inset:  $I$ - $U$  characteristic of undoped BSO ceramic sample measured under the same conditions.

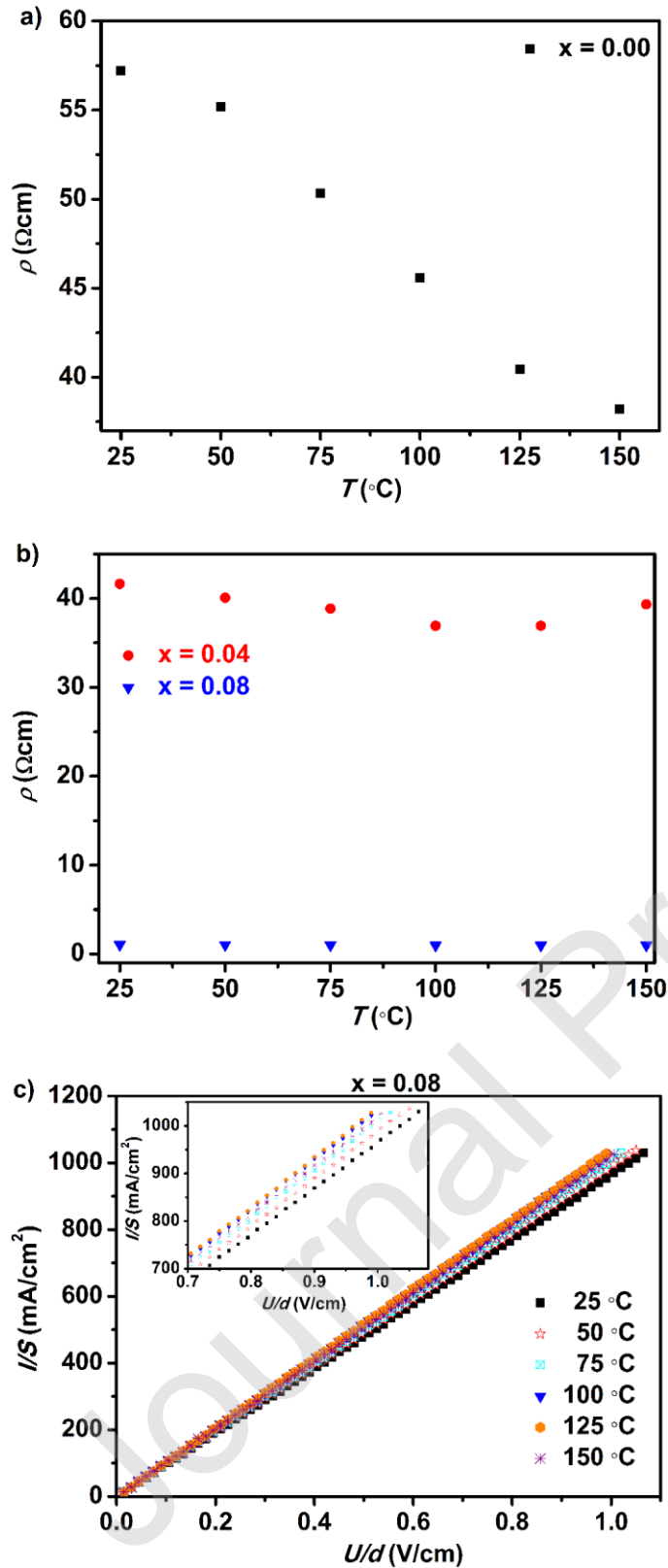


**Figure 10.** Electrical resistivity as a function of temperature for BaSn<sub>1-x</sub>Sb<sub>x</sub>O<sub>3</sub> samples: (a)  $x = 0.00$ ; (b)  $x = 0.04$  and  $0.08$ . (c)  $I$ - $U$  characteristic of BaSn<sub>0.92</sub>Sb<sub>0.08</sub>O<sub>3</sub> sample, measured in

the temperature range (25–150) °C. Inset graph:  $I$ - $U$  characteristic of  $\text{BaSn}_{0.92}\text{Sb}_{0.08}\text{O}_3$  sample in the range of (0.7-1.1) V/cm.

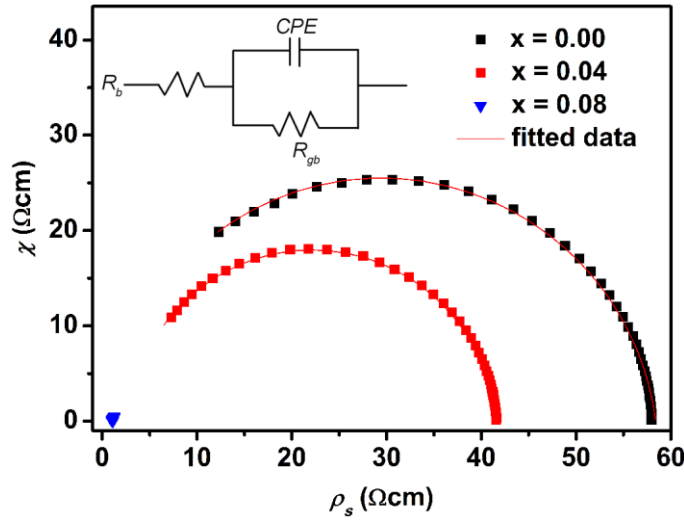


**Figure 11.** AC impedance data fitted to the circuit (shown as the inset) for the  $x = 0.00$ ,  $0.04$  and  $0.08$  samples measured at  $25$  °C.

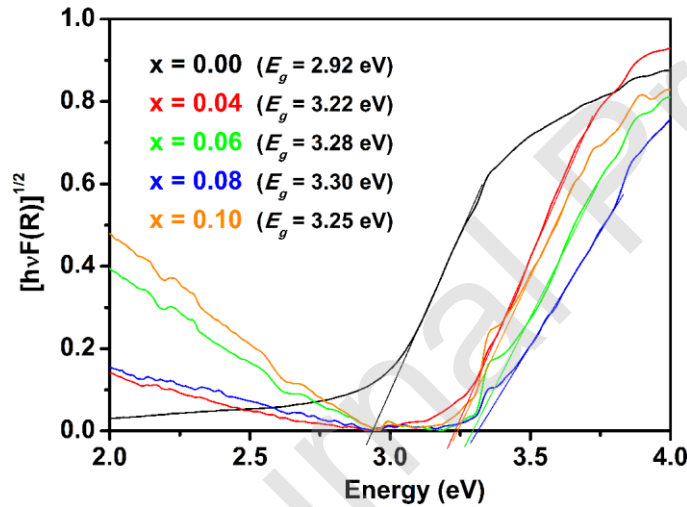


**Figure 12.** Tauc plots of pulverized  $\text{BaSn}_{1-x}\text{Sb}_x\text{O}_3$  ( $x = 0.00 - 0.10$ ) ceramic samples.

**Table 1.** The phase content of cubic  $\text{BaSnO}_3$  phase, unit cell parameter ( $a$ ), average crystallite size, grain size, and relative density for  $\text{BaSn}_{1-x}\text{Sb}_x\text{O}_3$  ceramic samples.

$\text{BaSn}_{1-x}\text{Sb}_x\text{O}_3$	$\text{BaSnO}_3$ phase content [wt %]	Unit cell parameter, $a$ [Å]	Crystallite size [nm]	Grain size [nm]	Rel. density [%TD*]
$x = 0.00$	85.00	4.1227(4)	57	1500	96
$x = 0.04$	93.10	4.1287(9)	49	650	95
$x = 0.06$	92.38	4.1301(9)	39	112	84



$x = 0.08$	92.21	4.1321(9)	43	44	86
$x = 0.10$	92.11	4.1302(4)	37	53	79

\*TD: theoretical density

**Table 2.** The comparison of theoretical and ICP experimental molar ratios of Ba, Sn and Sb in annealed ceramic  $\text{BaSn}_{1-x}\text{Sb}_x\text{O}_3$  samples.

$\text{BaSn}_{1-x}\text{Sb}_x\text{O}_3$	Ba : Sn : Sb molar ratio theor.	Ba : Sn : Sb molar ratio ICP
$x = 0.00$	1 : 1 : 0	1 : 0.79 : 0
$x = 0.04$	1 : 0.96 : 0.04	1 : 0.75 : 0.036
$x = 0.08$	1 : 0.92 : 0.08	1 : 0.72 : 0.08

**Table 3.** EDS analysis of undoped BSO sample.

Spectra	Atomic % of elements		
	Ba	Sn	O
<b>Spectrum 1</b>	20.35	20.74	58.91
<b>Spectrum 2</b>	19.17	19.85	60.98
<b>Spectrum 3</b>	19.72	15.51	64.77
<b>Spectrum 4</b>	20.17	17.24	62.59

**Table 4.** The dependence of DC electrical resistivity on the antimony concentration for  $\text{BaSn}_{1-x}\text{Sb}_x\text{O}_3$  ceramic samples.

$\text{BaSn}_{1-x}\text{Sb}_x\text{O}_3$	$x = 0.00$	$x = 0.04$	$x = 0.08$
DC electrical resistivity [ $\Omega\text{cm}$ ]	56.81	41.27	1.09

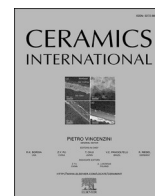
**Table 5.** The calculated values for bulk resistivity ( $\rho_b$ ), grain boundary resistivity ( $\rho_{gb}$ ), capacitance ( $P$ ), coefficient of constant phase element ( $p$ ) and total electrical resistivity ( $\rho$ ) for  $\text{BaSn}_{1-x}\text{Sb}_x\text{O}_3$  ceramic samples.

$\text{BaSn}_{1-x}\text{Sb}_x\text{O}_3$	Bulk resistivity $\rho_b$ [ $\Omega\text{cm}$ ]	Grain boundary resistivity $\rho_{gb}$ [ $\Omega\text{cm}$ ]	Capacitance $P$ [nF]	Coefficient of CPE CPE- $p$	Total electrical resistivity $\rho$ [ $\Omega\text{cm}$ ]
$x = 0.00$	5.1	52.79	1.4372	0.92	57.89
$x = 0.04$	2.77	38.89	2.8681	0.95	41.66

$x = 0.08$	-	-	-	-	1.12
------------	---	---	---	---	------

**Table 6.** The values of electrical bulk resistivity, Hall coefficient, charge carrier density and mobility for  $\text{BaSn}_{1-x}\text{Sb}_x\text{O}_3$  ceramic samples. (Charge carrier concentration and carrier mobility are shown in a single-carrier-type picture). For comparison, corresponding values for thin films [29] and single crystals [20, 27] are included in the Table.

	Ceramic materials			Thin films [29]	Single crystals [20, 27]
<b>Sb-content, <math>x</math> [mol]</b>	<b>0.00</b>	<b>0.04</b>	<b>0.08</b>	<b>0.07</b>	<b>0.03</b>
<b>Electrical bulk resistivity, <math>\rho_b</math> [<math>\Omega\text{cm}</math>]</b>	5.10	2.77	1.12	$2.43 \times 10^{-3}$	$0.66 \times 10^{-3}$
<b>Hall coefficient [<math>\text{cm}^3/\text{C}</math>]</b>	$-0.8 \pm 0.1$	$-0.64 \pm 0.02$	$-0.33 \pm 0.02$	-	-
<b>Carrier density [<math>\times 10^{18} \text{cm}^{-3}</math>]</b>	$8 \pm 1$	$9.7 \pm 0.3$	$19 \pm 1$	$1.65 \times 10^3$	102
<b>Carrier mobility [<math>\text{cm}^2/\text{Vs}</math>]</b>	$0.16 \pm 0.02$	$0.231 \pm 0.007$	$0.29 \pm 0.02$	1.75	79.4



# Influence of the addition of different radiopacifiers and bioactive nano-hydroxyapatite on physicochemical and biological properties of calcium silicate based endodontic ceramic

Djordje Antonijević<sup>a,b,c,\*</sup>, Ana Despotović<sup>d</sup>, Vladimir Biočanin<sup>e</sup>, Miloš Milošević<sup>f</sup>,  
Dijana Trišić<sup>c</sup>, Vladimir Lazović<sup>g</sup>, Nevena Zogović<sup>d</sup>, Jelena Milašin<sup>c</sup>, Dragan Ilić<sup>c</sup>

<sup>a</sup> Laboratory of Atomic Physics, "Vinča" Institute of Nuclear Sciences – National Institute of The Republic of Serbia, University of Belgrade, Serbia

<sup>b</sup> Laboratory for Anthropology, Institute of Anatomy, School of Medicine, University of Belgrade, Serbia

<sup>c</sup> School of Dental Medicine, University of Belgrade, Serbia

<sup>d</sup> Department of Neurophysiology, Institute for Biological Research "Siniša Stanković" – National Institute of The Republic of Serbia, University of Belgrade, Serbia

<sup>e</sup> Faculty of Dentistry, University of Business Academy, Novi Sad, Serbia

<sup>f</sup> Innovation Centre of Faculty of Mechanical Engineering, University of Belgrade, Serbia

<sup>g</sup> Institute of Physics Belgrade, University of Belgrade, Serbia

## ARTICLE INFO

### Keywords:

Endodontic surgery  
Strontium fluoride  
Bismuth oxide  
Zirconium dioxide  
Radiopacifier  
Hydroxyapatite

## ABSTRACT

The purpose of this study was to investigate the influence of different radiopacifiers on the physicochemical and biological properties of novel calcium silicate based endodontic ceramic enriched with bioactive nano-particulated hydroxyapatite – ECHA. Namely, ECHA was used as a basis for mixing with the following radiopacifiers: strontium fluoride (SrF<sub>2</sub>), zirconium dioxide (ZrO<sub>2</sub>) and bismuth oxide (Bi<sub>2</sub>O<sub>3</sub>). For comparison, Portland cement (PC) and mineral trioxide aggregate (MTA) were used. The following physicochemical characteristics were examined: the radiopacity, setting time, compressive strength, porosity, wettability and pH value. The biocompatibility of the cements was assessed by crystal violet, 3-(4,5-dimethylthiazol-2-yl)-2,5-diphenyl-tetrazolium bromide (MTT) and cell adhesion assays. The highest radiopacity was obtained for the ECHA + Bi<sub>2</sub>O<sub>3</sub> mixture and MTA that were statistically significant in comparison to other materials ( $p < 0.05$ ). Both initial and final setting times as well as compressive strengths were statistically lower for experimental cements than for PC and MTA ( $p < 0.05$ ). The lowest total porosity was observed in the ECHA + ZrO<sub>2</sub> group when compared with the other two experimental cements ( $p < 0.05$ ), but not when compared with PC and MTA ( $p > 0.05$ ). Experimental cements exhibited statistically higher contact angles of glycerol than PC and MTA ( $p < 0.05$ ). For blood plasma, a statistical difference was found only between ECHA + Bi<sub>2</sub>O<sub>3</sub> and PC ( $p < 0.05$ ). All investigated materials had alkalization ability. Cell viability assays revealed that the extracts of tested cements did not exhibit cytotoxic effect on L929 cells. Scanning electron microscopy had shown a high degree of cell proliferation and adhesion of cells from apical papilla on experimental cements' surfaces. Novel endodontic ceramics with nano-hydroxyapatite addition have satisfactory biological and physicochemical properties when compared to MTA and PC controls. Considerable lower setting time of experimental cements might present a huge advantage of these synthesized materials in clinical practice. SrF<sub>2</sub> presents a novel promising radiopacifying agent for dental cements manufacturing.

## 1. Introduction

The invention of calcium silicate (CS)-based endodontic ceramic (EC) has led to great progress in treatment of tooth diseases in

endodontics and root-end surgery [1]. The first CS-based dental EC – mineral trioxide aggregate (MTA) was developed at Loma Linda University in the early 1990s, received acceptance by the US Food and Drug Administration (FDA) and commercialized as ProRoot MTA by Tulsa

\* Corresponding author. "Vinča" Institute of Nuclear Sciences – National Institute of the Republic of Serbia, University of Belgrade, Mike Petrovića Alasa br. 12-14, 11001, Belgrade, Serbia.

E-mail address: [antonijevic@vin.bg.ac.rs](mailto:antonijevic@vin.bg.ac.rs) (D. Antonijević).

<https://doi.org/10.1016/j.ceramint.2021.07.052>

Received 5 March 2021; Received in revised form 12 June 2021; Accepted 5 July 2021

Available online 10 July 2021

0272-8842/© 2021 Elsevier Ltd and Techna Group S.r.l. All rights reserved.

Dental, OK, USA [2]. It is composed of type 1 ordinary Portland cement (PC) with a fineness in the range of 4500–4600 cm<sup>2</sup>/g and bismuth oxide (Bi<sub>2</sub>O<sub>3</sub>) added for radiopacity, in 4:1 proportion [3]. The main advantages over previously used pulp capping, retrograde root canal filling and perforation repair materials, i.e. calcium hydroxide (Ca(OH)<sub>2</sub>) and super ethoxybenzoic acid (Super EBA), are its bioactivity, increased mechanical resistance and low solubility [4,5]. However, MTA showed several drawbacks such as long setting time, decreased biocompatibility owing to presence of Bi and poor handling properties that cause discomfort to the practitioner and patient [5]. Attempts have been made to circumvent some of these downsides by replacing Bi<sub>2</sub>O<sub>3</sub> with alternative radiopacifiers such as barium sulphate (BaSO<sub>4</sub>) [6,7], titanium dioxide (TiO<sub>2</sub>) [6], gold (Au) [6,7], calcium tungstate (CaWO<sub>4</sub>) [8,9], zirconium dioxide (ZrO<sub>2</sub>) [8–10], ytterbium fluoride (YbF<sub>3</sub>) [11], tantalum pentoxide (Ta<sub>2</sub>O<sub>5</sub>) [12] and niobium pentoxide (Nb<sub>2</sub>O<sub>5</sub>) [8,9,13,14].

Despite the huge progress attained in this realm, lowering the setting time of CS and finding the most appropriate radiopacifying agent remain a major issue when it comes to design an EC composition able to satisfy all clinical needs. Recently, some products with short setting time have been developed in root-end surgery [15–17]. The problem with many radiopacifiers arises from the fact that their addition inhibits material setting reactions and bioactive behaviour [7]. Another undesirable issue related to the use of radiopacifiers is their possible toxicity in contact with human tissues [18]. Thus, the addition of radiopacifier has to be carefully balanced in order to obtain adequate radiopacity without negative influence to the CS's beneficial biological and mechanical characteristics. Our research group have demonstrated the satisfactory properties of two novel ECs formulations: one consisting of CS, nano-particulated hydroxyapatite (nano-hydroxyapatite, nHA) and BaSO<sub>4</sub> – ALBO MPC<sub>1</sub> and another composed of CS, calcium carbonate (CaCO<sub>3</sub>) and Bi<sub>2</sub>O<sub>3</sub> – ALBO MPC<sub>2</sub>. Their physicochemical suitability and *in vivo* safety, after both acute and subchronic administration, are documented previously [19–25]. The beneficial effects of nHA addition into EC include decreased setting time, increased pH value, good biocompatibility and enhanced neutralization of the bacterial biofilm [11,19,26,27]. In previous experiments, ECHA was associated with BaSO<sub>4</sub> and YbF<sub>3</sub> as radiopacifiers leading to adequate physicochemical and biological characteristics [11,25]. However, the issues of solubility of BaSO<sub>4</sub> and biological safety of Yb are still under discussion [28,29].

The current paradigm in EC manufacturing advocates that the added radiopacifier has to be inert in contact with human tissues [3,4]. The present paper raises the question whether a bioactive radiopacifier can be added into bioactive ceramics for improvement of regenerative capacity of the resulting mixture. It is hypothesised that strontium fluoride (SrF<sub>2</sub>) may simultaneously serve as a promising radiopacifying and biologically desirable agent in newly formulated EC. The hypothesis takes into account positive proofs of osteoproliferative and odontoproliferative effects of strontium (Sr) [30]. In addition, fluoride incorporation into ECs has contributed to their advantageous properties [11,31]. The assumption is also rooted in the observations that Sr stimulates bone formation and angiogenesis, inhibits cell differentiation and activity of osteoclasts and evokes human dental pulp stem cells by promoting their odontogenic differentiation, proliferation and mineralization [32,33]. The aim of this study was to investigate the influence of the following radiopacifiers on physicochemical and biological properties of nHA-enriched endodontic ceramic: SrF<sub>2</sub>, as potentially bioactive radiopacifier, ZrO<sub>2</sub>, as biologically inert ceramic material and Bi<sub>2</sub>O<sub>3</sub>, commonly used in many CS formulations.

## 2. Materials and methods

### 2.1. Synthesis of calcium silicates containing nano-hydroxyapatite

EC with the addition of bioactive nHA (ECHA) was used as a basis for mixing with radiopaque agents. For synthesis of CS-based EC, calcium

chloride pentahydrate (CaCl<sub>2</sub>·5H<sub>2</sub>O) (Merck, Germany) and silica sol obtained by hydrothermal treatment were used. The stoichiometric quantities of CaCl<sub>2</sub>·5H<sub>2</sub>O (42.41 g) and silica sol (15 g of 30% sol solution), corresponding to the ratio tricalcium/dicalcium silicate C<sub>3</sub>S/b-C<sub>2</sub>S = 2:1 (C=CaO, S=SiO<sub>2</sub>, C<sub>3</sub>S = 3CaO·SiO<sub>2</sub>, C<sub>2</sub>S = 2CaO·SiO<sub>2</sub>), were used to obtain silicate active phase (CS). Aluminium acetate (Al(CH<sub>3</sub>OO)<sub>3</sub>) was added to the mixture to provide the production of a small amount (3.01%) of active tricalcium aluminate (C<sub>3</sub>A) phase (C=CaO, A = Al<sub>2</sub>O<sub>3</sub>, C<sub>3</sub>A = 3CaO·Al<sub>2</sub>O<sub>3</sub>). The nHA was produced by a hydrothermal method from the shells of chicken eggs using a two solutions procedure: Ca(OH)<sub>2</sub> (solution 1) and diammonium hydrogen phosphate (NH<sub>4</sub>)<sub>2</sub>HPO<sub>4</sub> (solution 2). Detailed procedure of used CS and nHA synthesis is given in the Supplement 1 and elsewhere by Jokanović and colleagues [21,22]. The nHA was added into CS mixture using C<sub>3</sub>S to C<sub>2</sub>S ratio of 2:1 to produce the basis of each experimental endodontic ceramic mixture (ECHA). It was composed of 34% of CS and 66% of nHA.

### 2.2. Specimens preparation

Experimental cements were manufactured by replacing 30% of the cement powder by weight with the following radiopacifiers: SrF<sub>2</sub> (Sigma-Aldrich, St. Louis, Missouri, USA), ZrO<sub>2</sub> (Sigma-Aldrich) and Bi<sub>2</sub>O<sub>3</sub> (Alfa Aesar, Karlsruhe, Germany). PC (Aalborg, Denmark) and MTA+ (thereafter referred to as MTA) (Cerkamed, Stalowa Wola, Poland) served as controls. All experimental cements and PC were hand-mixed at a powder/liquid ratio of 1 g cement/0.3 ml distilled water, while MTA preparation was performed in accordance with manufacturer's instructions. A glass mixing pad and stainless steel spatula were used for hand mixing. The specimens were made using polytetrafluoroethylene (PTFE) ring moulds incorporating a cavity of various internal diameter and height depending on the test performed. Moulds were filled to a level surface with mixed cement.

### 2.3. Radiopacity

The radiopacity of the specimens was determined according to ISO 6876 standard [34]. The specimens (8 mm in diameter and 1 mm thick) were radiographed with a charge-coupled device (Trophy Radiology, Cedex, France) alongside an aluminium step-wedge, used as a reference. The step-wedge was made of aluminium plates graduated from 1 to 10 mm by 1 mm increments. The x-ray unit operated at 70 kV, 4 mA, distance of 33.5 mm and an exposure time of 0.077 s. Image J for Windows software (National Institutes of Health (NIH), Bethesda, MD, USA) was employed to calculate the grayscale values of each specimen and of each aluminium step-wedge thickness. The mean grey scale values of specimens were plotted against the number of aluminium steps and regressions were used to convert the grayscale values of the cements into millimeters of aluminium (mm Al) [35]. Five specimens per group were tested.

### 2.4. Setting time

Setting time was determined according to ISO 6876 standard using a Gilmore needle with a mass of 100 ± 1 g and an active tip of 2 ± 0.1 mm in diameter for measuring initial setting times and a needle with a mass of 400 ± 1 g and active tip of 1 ± 0.1 mm in diameter for measuring final setting times. The needles were vertically placed against the horizontal surface of the specimens (8 mm in diameter and 2 mm thick) every minute to observe indentations. The needles were cleaned between each test. The moment when the needle failed to create an indentation onto the surface of the material after being allowed to settle for 5 s was considered as an initial (100 g mass) and final (400 g mass) setting times. Three specimens per group were tested.

## 2.5. Compressive strength

The specimens (8 mm in diameter and 1 cm thick) were kept in phosphate buffer saline (PBS) (Sigma-Aldrich) for two weeks and thereafter placed vertically on the lower steel plate of a universal testing machine (AUTOGRAPH AG-IS, Shimadzu, Kyoto, Japan). The upper plate was moving at a distance of 1 mm per 1 min. Specimens were subjected to compression loads until fracture. The fracture load was recorded and compressive strength was calculated in terms of megapascals (MPa) using the following formula:

$$C = 4P/\pi D^2$$

where “P” represents the maximum load recorded in Newtons (N) and “D” represents the diameter of the specimens in millimeters. Five specimens per group were tested.

## 2.6. Porosity

The porosity of the cements was determined by scanning the specimens (5 mm in diameter and 1 mm thick) with a high-resolution micro-computed tomographic ( $\mu$ CT) system (SkyScan 1172 x-ray Microtomography; SkyScan, Kontich, Belgium) operated at 100 kV, 100 mA, an exposure time of 1150 ms with use of a copper/aluminium filter. Scanning was performed in 0.4° rotation steps, 10  $\mu$ m isotropic resolution and 2048  $\times$  2048 pixels per slice. The acquired images were reconstructed with NRecon v.1.6.9.8 software (SkyScan) using a ring artefact correction of 3%, beam hardening correction of 40% and no smoothing. Finally, images were analysed with CT. An 1.14.4.1 software (SkyScan) applying a global threshold of 23/255. The parameters calculated were as follows: porosity (total, open and closed), average pore size ( $\mu$ m) and the number of closed pores per volume (1/mm<sup>3</sup>). Five specimens per group were tested.

## 2.7. Wettability

The cements' wettability was assessed with a contact angle (CA) analyser (Vinča Institute, Belgrade, Serbia). The CAs of the glycerol and human blood plasma were measured by placing the 2  $\mu$ l liquid droplet on the specimens surface [36,37]. Since ISO 6876 does not stipulate the wettability measurements requirements, specimens measuring 10 mm in diameter and 2 mm in thickness provided enough space to successfully place reference liquids on the cements' surfaces. The CAs were calculated using ImageJ software (NIH, Bethesda, MD, USA) by fitting the contour of the droplet placed on the surface (tangent method). Six specimens per group were tested.

## 2.8. pH determination

The cylinder specimens (4 mm in diameter and 6 mm thick) were immersed in distilled water and maintained at 37 °C for 30 min, 1 h, 3 h, 6 h, 12 h, 24 h and 7 days. At each time point, specimens were removed from the flasks and put into a new flask with 7 ml distilled water. The pH of the solutions was measured using a calibrated pH meter (Hanna precision pH meter Model pH 211, Sigma-Aldrich). Five specimens per group were tested.

## 2.9. Cell viability analysis

**Preparation of the materials extracts.** Cell viability was carried out in accordance with the ISO Standard 10993-5/2005 [38]. All materials were manipulated under sterile conditions. Immediately after mixing, materials were placed into pre-sterilized PTFE moulds (5 mm in diameter and 3 mm thick) to set for 24 h in a humidified atmosphere. Subsequently, discs were sterilized by ultraviolet irradiation for 2 h, then immersed in 1 ml complete medium – Dulbecco's modified Eagle

medium (DMEM; Gibco, Thermo Fisher Scientific, Inc., Waltham, MA, USA) supplemented with 5% fetal bovine serum (FBS), 2 mM L-glutamine and penicillin/streptomycin (all from Capricorn Scientific, Ebsdorfergrund, Germany) and incubated for 24 h at 37 °C. Subsequently, the discs were discarded and the supernatants (extracts) were collected. To prepare eluents for treatment, extracts were diluted with complete culture medium which was used for cultivation of control/non-treated cells.

**Cell culture and treatment.** The mouse fibroblast L929 cell line (European Collection of Animal Cell Cultures, Salisbury, UK) was cultivated in complete medium and maintained at 37 °C, in a humidified atmosphere with 5% CO<sub>2</sub>. Cells were prepared for experiments using the conventional trypsinization procedure with trypsin/EDTA and seeded in 96-well flat-bottom plates (5  $\times$  10<sup>3</sup> cells/well) for the cell viability assessment. Cells were treated 24 h post-seeding with pure extract (1) and serial dilutions (1:2, 1:4, 1:8, 1:16 and 1:32 (v:v)). In order to evaluate a dose- and time-dependent response to potentially toxic soluble substances from investigated materials, cell viability was assessed after 24, 48 and 72 h treatment.

**Cell viability assessment.** The number of adherent cells and mitochondrial dehydrogenase activity was assessed using crystal violet (CV) and 3-(4,5-dimethylthiazol-2-yl)-2,5-diphenyl-tetrazolium bromide (MTT) tests, respectively. The CV assay is based on the inability of dead cells to remain adherent. After treatment, the adherent, viable cells were fixed with methanol and stained with 10% CV solution for 15 min at room temperature. CV dye was dissolved in 33% acetic acid after rigorous washing with water. MTT test measures mitochondrial-dependent reduction of MTT to formazan by metabolically viable cells. MTT solution was added to the cell cultures in final concentration of 0.5 mg/ml and cells were incubated for an additional hour. Thereafter, the solution was removed and cells were lysed by dimethyl sulfoxide. The absorbance of dissolved CV dye, corresponding to the number of adherent (viable) cells and the conversion of MTT to formazan, corresponding to the number of cells with an active mitochondria were measured in automated microplate reader at 570 nm (Sunrise; Tecan, Dorset, UK). The results were presented as percentage of viability relative to untreated control cultures, considered as 100% viable. The experiments were performed in triplicates.

## 2.10. Cell adherence on the materials' surface

The cell adhesion assay was performed in accordance with the approval of the Ethics Committee (School of Dental Medicine, University of Belgrade, number 36/19). The cell's attachment on apical dentine and cements surface was tested using human apical papilla stem cells as previously described [39]. Apical papilla tissue was obtained after signed informed consent from the patient (18 years of age) undergoing extraction of impacted third molar for orthodontic reasons. The tooth tissue was transferred into DMEM/F12 medium (Gibco; Thermo Fisher Scientific, Inc.), supplemented with 20% FBS (Gibco; Thermo Fisher Scientific, Inc.) and 1% antibiotic/antimycotic solution (Gibco, Thermo Fisher Scientific, Inc.). After 30 min of extraction, tooth tissue was rinsed in PBS and subjected to outgrowth isolation method. The specimens were prepared by filling up the root apical thirds of the upper central incisors with cements, as previously described [36]. Root specimens were obtained with signed informed consent from the patient undergoing extraction of mandibular central incisors for periodontal reasons. Before seeding, the sterilized specimens were immersed in a growth medium in 12 well plate for 24 h, at 37 °C in 5% CO<sub>2</sub>, avoiding the pH variation. The next day, the growth medium was discarded from wells containing root tops. Roots were positioned in the wells vertically with the apices up, enabling cells seeding on the roots' tops. On the apical tops of the roots filled with materials, 10  $\mu$ l of medium with 1  $\times$  10<sup>4</sup> cells was carefully placed. Plates containing roots with seeded apical papilla cells were cautiously placed in the CO<sub>2</sub> incubator for 30 min allowing cells to attach on the apical root surface, after which 500  $\mu$ l of growth

medium was added into wells. Half of specimens were further cultured in the growth medium, while the other half in the osteogenic medium containing growth medium supplemented with 10 nM dexamethasone disodium phosphate, 1.8 mM monopotassium phosphate, 10 mM  $\beta$ -glycerophosphate and 50  $\mu$ g/ml ascorbic acid (Sigma-Aldrich). The cells were cultured in growth and osteogenic medium for 21 days with the mediums being changed every 3 days. The specimens with cells grown on their surfaces were fixed with 2 vol% glutaraldehyde, dehydrated with increasing concentrations of ethanol (50 vol%, 60 vol%, 70 vol%, 80 vol%, 90 vol%, 95 vol%, and 100 vol%) and gold coated before scanning electron microscopic (SEM) evaluation (TESCAN, Mira3, XMU USA Inc.).

### 2.11. Statistical analysis

The SPSS software program (ver. 20, IBM Corp., Armonk, NY, USA) was employed for statistical analysis. The Shapiro-Wilk test was used to check the normality of data distribution. Afterwards, one-way ANOVA with Bonferroni post-hoc tests was employed to compare normally distributed data while Kruskal-Wallis test followed by series of pairwise Mann-Whitney tests with Bonferroni correction test was used to compare non-normally distributed outcomes ( $p < 0.05$ ).

## 3. Results

### 3.1. Radiopacity, setting time, compressive strength, porosity, wettability and pH determination

The Shapiro-Wilk test of normality found that the radiopacity, compressive strength, total porosity, open porosity, close porosity, pore size, number of closed pores per  $\text{mm}^3$ , CA of glycerol and human blood plasma and pH data for 30 min, 1 h, 3 h, 6 h, 12 h, 24 h and 7 days were normally distributed and thus they were subjected to one-way ANOVA analysis followed by Bonferroni test. On the contrary, initial and final setting time and pH values obtained after 24 h were not normally distributed and therefore they were subjected to a Kruskal-Wallis test followed by Mann-Whitney test with Bonferroni correction for non-parametric data ( $p < 0.005$ ). One way ANOVA have found statistical difference among tested cements' radiopacity, compressive strength, porosity (all parameters) and pH values obtained after 30 min, 1 h, 3 h, 6 h, 12 h and 7 days ( $p < 0.05$ ) while Kruskal-Wallis test showed significant difference among tested cements' initial and final setting times and pH values after 24 h evaluation ( $p < 0.05$ ).

The highest radiopacity values were observed for MTA ( $6.9 \pm 0.5$  mmAl) and ECHA +  $\text{Bi}_2\text{O}_3$  mixture ( $6.7 \pm 0.1$  mmAl) that were significantly higher than those in the other three groups of investigated cements ( $p < 0.05$ ), but without statistical difference among each other ( $p >$

0.05) (Fig. 1).

All experimental cements showed statistically much lower initial ( $p < 0.05$ ) and final ( $p < 0.05$ ) setting times as well as compressive strengths ( $p < 0.05$ ) than PC and MTA (Table 1).

The lowest total porosity was found for ECHA +  $\text{ZrO}_2$  ( $1.7 \pm 0.6\%$ ) that was statistically different compared to the other experimental cements ( $p < 0.05$ ), but not statistically different from those of PC and MTA ( $p > 0.05$ ). The highest value of open porosity was obtained for ECHA +  $\text{Bi}_2\text{O}_3$  ( $8 \pm 4\%$ ) that was statistically significant in comparison to ECHA +  $\text{ZrO}_2$  and MTA ( $p < 0.05$ ), but statistically insignificant in comparison to ECHA +  $\text{SrF}_2$  and PC ( $p > 0.05$ ). The lowest value of closed porosity was found for ECHA +  $\text{ZrO}_2$  ( $0.3 \pm 0.1\%$ ) that was statistically different only when compared to ECHA +  $\text{SrF}_2$  ( $3 \pm 2\%$ ) ( $p < 0.05$ ). Regarding the pore size, there were no significant differences among the investigated cements ( $p > 0.05$ ). The ECHA +  $\text{Bi}_2\text{O}_3$  group presented the greatest number of closed pores per  $\text{mm}^3$  ( $1.5 \pm 0.3$ )  $\times 10^7$

**Table 1**

Initial and final setting times, compressive strength and pH values of investigated cements. Results with different letters within the same row are statistically different (one-way ANOVA with Bonferroni post-hoc test was used for compressive strength and 30 min, 1 h, 3 h, 6 h, 12 h and 7 days pH reported data ( $p < 0.05$ ), while Kruskal-Wallis test ( $p < 0.05$ ) followed by Mann-Whitney test with Bonferroni correction ( $p < 0.005$ ) was used to compare setting time and 1 day pH data). ECHA, endodontic ceramic nano-hydroxyapatite;  $\text{ZrO}_2$ , zirconium dioxide;  $\text{Bi}_2\text{O}_3$ , bismuth oxide;  $\text{SrF}_2$ , strontium fluoride; MTA, mineral trioxide aggregate; PC, Portland cement.

		ECHA + $\text{SrF}_2$	ECHA + $\text{ZrO}_2$	ECHA + $\text{Bi}_2\text{O}_3$	PC	MTA
Setting time (min)	Initial	$7.7 \pm 0.6^a$	$5 \pm 0^b$	$8.3 \pm 0.6^a$	$46 \pm 7^c$	$41 \pm 4^c$
	Final	$33 \pm 1^a$	$33 \pm 7^a$	$35.3 \pm 1.2^a$	$190 \pm 10^b$	$107.3 \pm 1.6^c$
Compressive strength (MPa)		$2.5 \pm 0.9^a$	$2.7 \pm 1.3^a$	$3.8 \pm 1.9^a$	$27 \pm 8^b$	$23 \pm 17^b$
pH	30 min	$7.50 \pm 0.02^a$	$8.5 \pm 0.3^b$	$7.60 \pm 0.05^a$	$10.73 \pm 0.02^c$	$10.76 \pm 0.02^c$
	1 h	$8.38 \pm 0.09^a$	$8.73 \pm 0.17^b$	$8.18 \pm 0.02^a$	$10.58 \pm 0.07^c$	$10.83 \pm 0.06^c$
	3 h	$8.97 \pm 0.03^a$	$8.98 \pm 0.12^a$	$8.92 \pm 0.03^a$	$10.70 \pm 0.07^b$	$10.99 \pm 0.06^c$
	6 h	$9.33 \pm 0.06^a$	$9.47 \pm 0.05^a$	$9.67 \pm 0.03^a$	$10.57 \pm 0.12^b$	$10.82 \pm 0.19^b$
	12 h	$9.36 \pm 0.02^a$	$9.40 \pm 0.02^a$	$9.62 \pm 0.06^a$	$10.76 \pm 0.07^b$	$11.2 \pm 0.3^c$
	1 day	$9.24 \pm 0.11^a$	$9.67 \pm 0.11^a$	$9.78 \pm 0.05^a$	$10.6 \pm 0.3^a$	$10.84 \pm 0.13^a$
	7 days	$8.95 \pm 0.03^a$	$9.4 \pm 0.3^{b,c}$	$9.08 \pm 0.04^{a,c}$	$8.94 \pm 0.01^a$	$9.15 \pm 0.08^{a,c}$

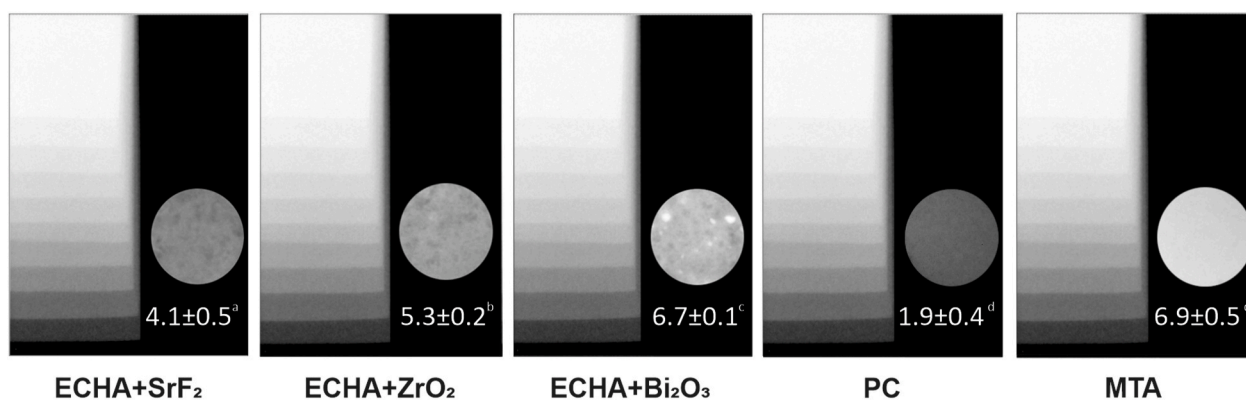


**Fig. 1.** Radiopacity of investigated cements as measured with digital radiography. Different letters mean statistical significance among cements' specimens (one-way ANOVA followed by Bonferroni post-hoc test,  $p < 0.05$ ). ECHA, calcium silicate hydroxyapatite;  $\text{SrF}_2$ , strontium fluoride;  $\text{ZrO}_2$ , zirconium dioxide;  $\text{Bi}_2\text{O}_3$ , bismuth oxide; PC, Portland cement; MTA, mineral trioxide aggregate.

and it was statistically higher than in other groups ( $p < 0.05$ ), among which the statistical difference was not noted ( $p > 0.05$ ) (Fig. 2).

Experimental cements exhibited statistically higher CA of glycerol than PC and MTA ( $p < 0.05$ ). Using blood plasma as a reference liquid,

the statistical difference was found only between ECHA + Bi<sub>2</sub>O<sub>3</sub> and PC ( $p < 0.05$ ), while other three investigated cements were not different neither among themselves nor from ECHA + Bi<sub>2</sub>O<sub>3</sub> and PC ( $p > 0.05$ ) (Fig. 2).

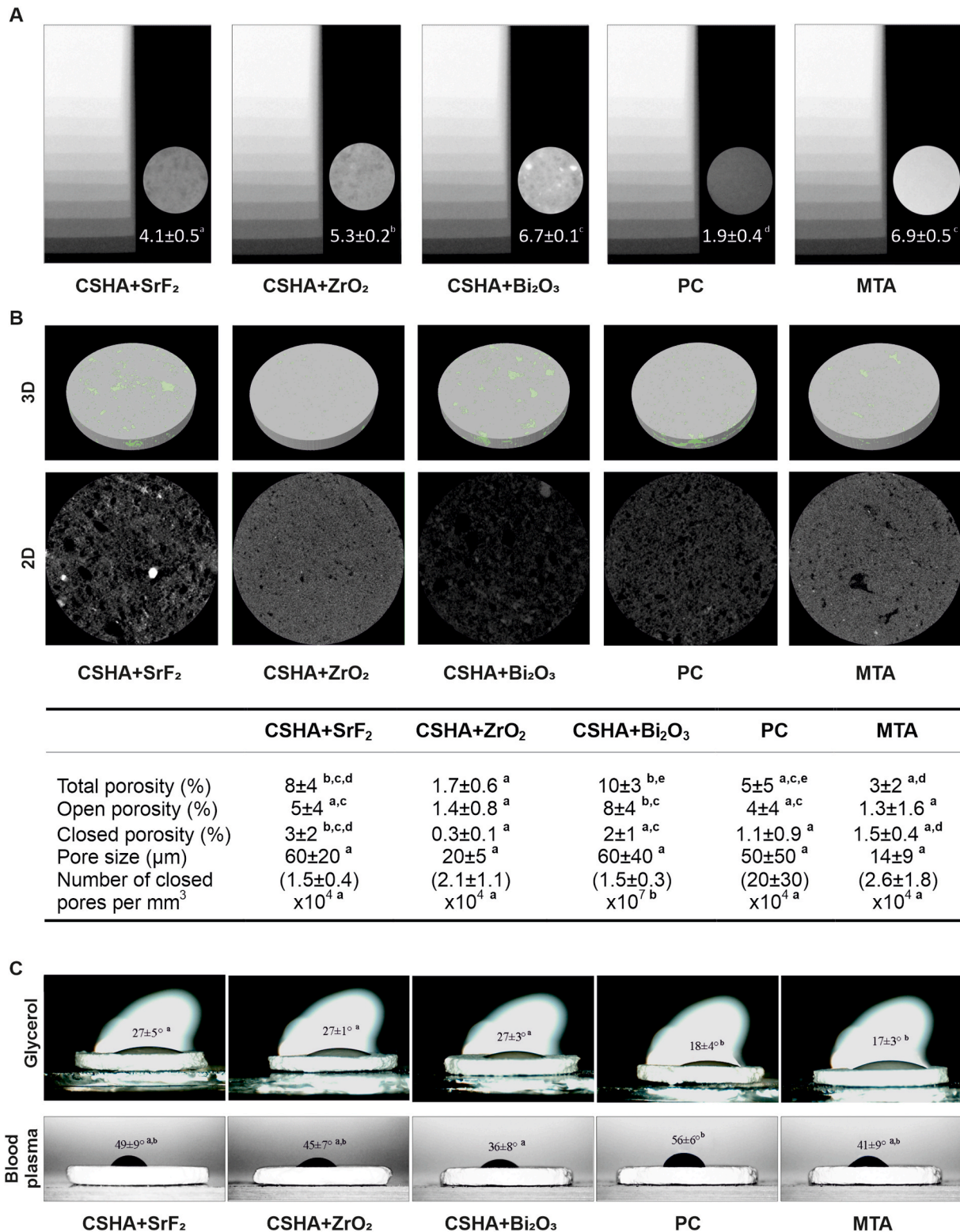


**Fig. 2.** Physicochemical properties of investigated materials. A) Porosity of investigated materials with three dimensional (3D) reconstructions and two dimensional (2D) presentations of representative specimens. B) Wettability of investigated materials expressed as glycerol and human blood plasma contact angles. Different letters mean statistical significance among cement specimens (one-way ANOVA followed by Bonferroni post-hoc test,  $p < 0.05$ ). ECHA, calcium silicate hydroxy-apatite; SrF<sub>2</sub>, strontium fluoride; ZrO<sub>2</sub>, zirconium dioxide; Bi<sub>2</sub>O<sub>3</sub>, bismuth oxide; PC, Portland cement; MTA, mineral trioxide aggregate.

All investigated materials had alkalization ability (Table 1). Experimental cements revealed statistically lower pH values than PC and MTA after 30 min, 1 h, 3 h, 6 h and 12 h ( $p < 0.05$ ). On the other hand, there was no significant difference between experimental cements on one side and PC and MTA on the other side neither after 24 h ( $p < 0.005$ ) nor after 7 days ( $p < 0.05$ ).

### 3.2. Cytotoxicity and cell adherence assay

Effects of experimental cements' eluents on L929 cell viability are presented in Fig. 3. Shapiro-Wilk test of normality revealed that results of CV assay after 24 h in pure extract, 1:2 and 1:4 eluents were not normally distributed and subsequently subjected to a Kruskal-Wallis test followed by Mann-Whitney test with Bonferroni correction for non-parametric data. All data obtained by MTT assay and the rest of the results obtained by CV assay were normally distributed and they were

subjected to one-way ANOVA analysis followed by Bonferroni test. For CV assay, one-way ANOVA showed the statistical difference among tested cements after 24 h (1:32), 48 h (pure extracts, 1:2 and 1:4) and 72 h (pure extracts and 1:2) ( $p < 0.05$ ). Kruskal-Wallis test showed significant difference of cell viability among tested cements after 24 h (pure extract, 1:2 and 1:4 eluents) ( $p < 0.05$ ). For MTT assay, one-way ANOVA showed the statistical difference for all time points/dilutions ( $p < 0.05$ ) except after 48 h (1:8) and 72 h (1:8, 1:16 and 1:32) ( $p > 0.05$ ).

Pure extracts of experimental cements had no effect on the cell viability after 24 h of exposure, measured by CV (Fig. 3A) and MTT (Fig. 3B) assays. Although longer incubation (48 h, 72 h) with ECHA + ZrO<sub>2</sub> and ECHA + Bi<sub>2</sub>O<sub>3</sub> extracts induced time-dependent decrease in cell viability, the number of adherent cells (Fig. 3A) and the activity of mitochondrial dehydrogenases (Fig. 3B) were significantly higher than in cultures incubated with pure extracts of MTA and PC which showed extremely high cytotoxic effect (>60–80%) at all time points. Further,

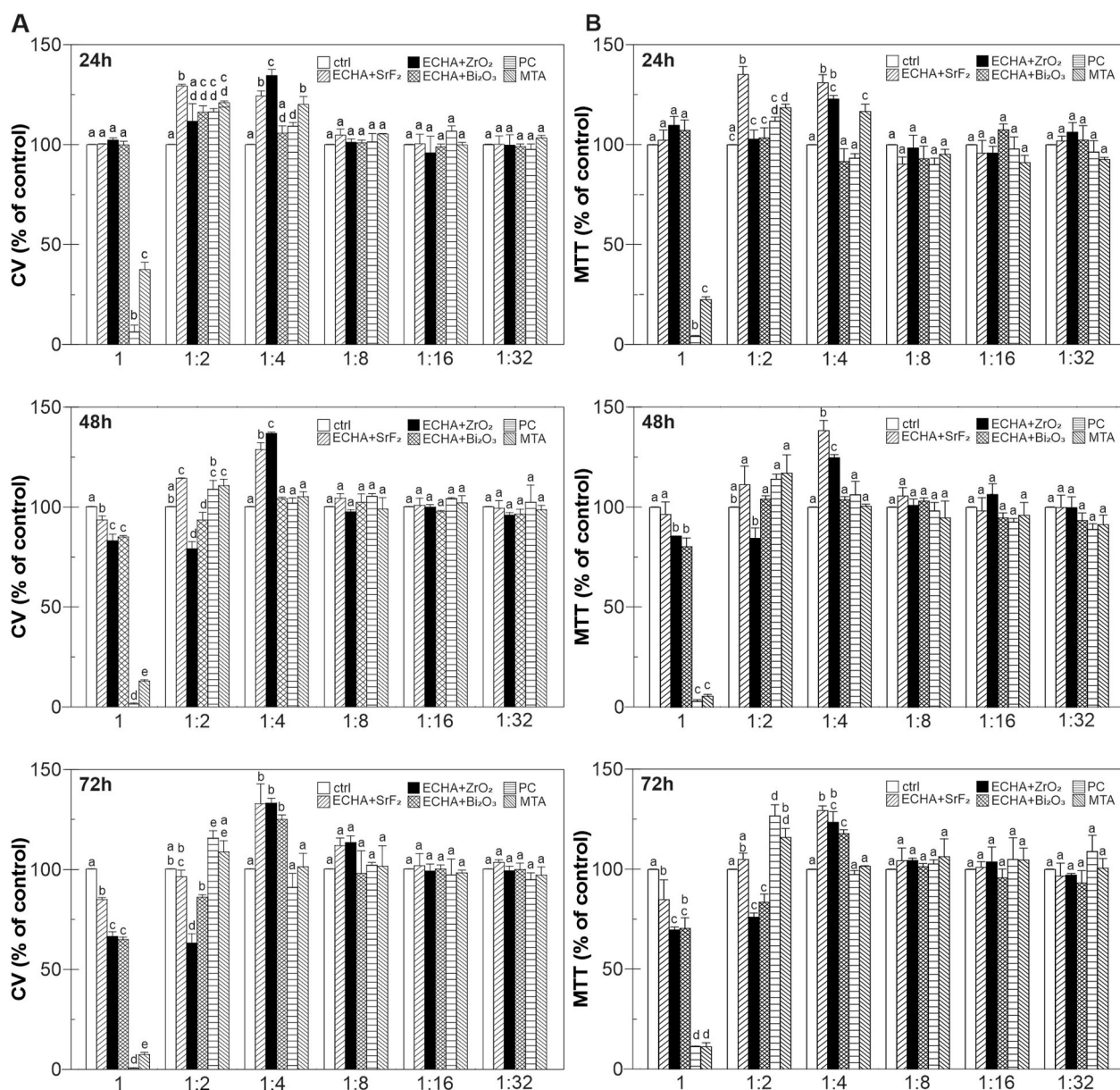


**Fig. 3.** Cell viability (%) evaluated by the crystal violet (CV) (A) and MTT (B) assays after 24 h, 48 h and 72 h exposure of L929 cells to the cements' eluents - pure extract (1) and different serial dilutions (1:2, 1:4, 1:8, 1:16, 1:32 (v:v)). The data are presented as mean  $\pm$  standard deviation (SD) values of triplicates from one representative of three independent experiments. Different letters mean statistical significance among cement specimens (one-way ANOVA followed by Bonferroni post-hoc test,  $p < 0.05$ , Kruskal-Wallis test ( $p < 0.05$ ) followed by Mann-Whitney test with Bonferroni correction ( $p < 0.005$ )). ECHA, calcium silicate hydroxyapatite; SrF<sub>2</sub>, strontium fluoride; ZrO<sub>2</sub>, zirconium dioxide; Bi<sub>2</sub>O<sub>3</sub>, bismuth oxide; PC, Portland cement; MTA, mineral trioxide aggregate.



the presence of ECHA + SrF<sub>2</sub> mixture eluent in 1:2 dilution potentiated proliferation of L929 cells – the number of viable (Fig. 3A) and metabolically active cells (Fig. 3B) was statistically higher than in all other treatments with experimental materials. Yet, in 1:2 dilution, ECHA + ZrO<sub>2</sub> reduced cell viability after 48 h and 72 h, while ECHA + Bi<sub>2</sub>O<sub>3</sub> manifested the same effect on cell viability after 72 h. The highest number of L929 cells (Fig. 3A) and mitochondrial dehydrogenase activity (Fig. 3B) was detected in cell culture treated with ECHA + SrF<sub>2</sub> and ECHA + ZrO<sub>2</sub> mixture eluent in 1:4 dilution at all time points, as well as in comparison with other dilutions. Higher dilutions of all tested extracts (1:8, 1:16 and 1:32) did not affect the L929 cell viability, at all time points.

SEM analysis of cell adhesion revealed that experimental cements had properties that were able to support apical papilla stem cells and osteoblasts adhesion and increase cell proliferation (100 × magnifications). Extended cytoplasmic processes and filopodia were observed to

spread between coronal dentine and cement material (2000 × magnification) (Fig. 4).

#### 4. Discussion

The choice of radiopacifier capable of contributing to the radio-visibility of CS-based dental ceramics is important since they should meet both the ISO standard of radiopacity and maintain adequate biological and physical properties of ECs. In the current study, novel ECs with incorporated nHA particles were used as a basis for mixing with radiopacifiers since it was previously demonstrated that the addition of such non-stoichiometric bioactive nHA significantly decreased CS's setting time [11]. All radiopacifiers were able to confer EC's ISO radiopacity requirements of 3 mmAl. The highest radiopacity value was observed in ECHA + Bi<sub>2</sub>O<sub>3</sub> (6.7 mmAl). This is expected as Bi absorbs x-rays much more efficiently than Zr and Sr due to its higher atomic

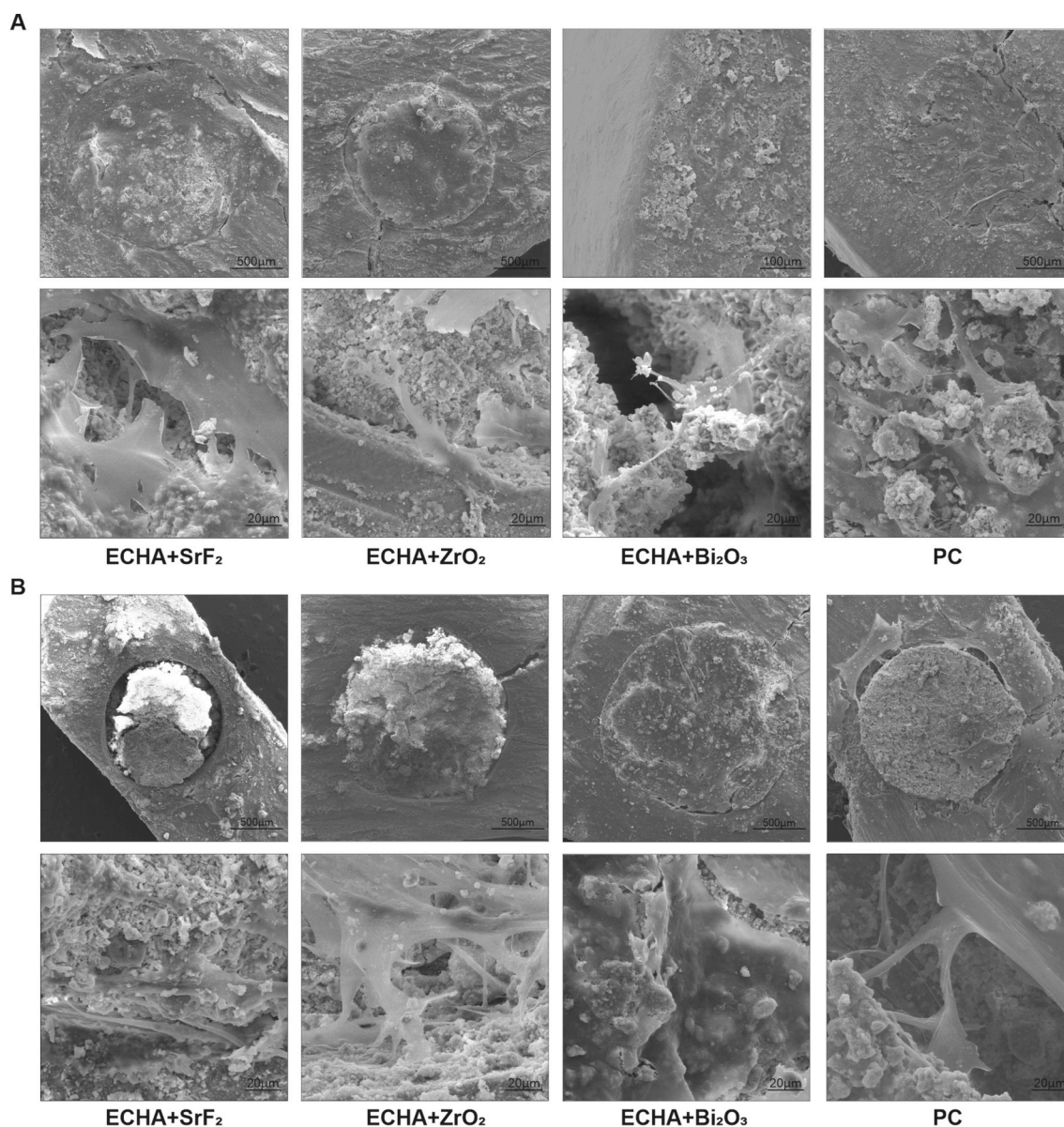


**Fig. 4.** Representative scanning electron microphotographs of cements' specimens seeded in A) control growth medium and B) osteogenic medium for 21 days. The morphological features of osteoblast-like cells observed at lower magnification (100x) have shown flattened cells proliferated on cement and dentine surface creating the multilayers covering their surfaces and bridges at a cement-dentine interface (upper rows). At higher magnification (2000x), numerous cell extensions that anchored well onto the cement surfaces can be observed (lower rows). ECHA, calcium silicate hydroxyapatite; SrF<sub>2</sub>, strontium fluoride; ZrO<sub>2</sub>, zirconium dioxide; Bi<sub>2</sub>O<sub>3</sub>, bismuth oxide; PC, Portland cement; MTA, mineral trioxide aggregate.

number ( $Z(\text{Bi}) = 83 > Z(\text{Zr}) = 40 > Z(\text{Sr}) = 38$ ) as absorption of x-rays is directly proportional to the third power of the atomic number of absorbing material [40]. The radiopacity of ECHA +  $\text{ZrO}_2$  (5.3 mmAl) was slightly higher than that found recently for CS with 30%  $\text{ZrO}_2$  added (4.2 mmAl) [9]. The radiopacity of ECHA +  $\text{Bi}_2\text{O}_3$  (6.7 mmAl) was lower than that previously found for CS+30% $\text{Bi}_2\text{O}_3$  (~11 mmAl) [6], but close to that of CS+25% $\text{Bi}_2\text{O}_3$  (6.9 mmAl) [41]. The result demonstrated for radiopacity of MTA (6.9 mmAl) favourably agrees with those reported previously: 4.86 [42], 6.74 [43], 7.0 [44], 7.5 [9] and 8.0 [41] mmAl. The PC did not meet the ISO radiopacity requirement which is in line with previous studies (~0.9 mmAl) [41,42]. The influence of  $\text{SrF}_2$  on the radiopacity of EC has not been previously mentioned in the literature.

Experimental cements have shown initial setting times varying from 5 to 8.3 min, significantly lower than those of PC and MTA (46 min and 41 min, respectively). The obtained results for experimental cements indicate their fast-setting property and corroborate the results found for fast-setting RetroMTA (2.5 min) [10], CS +  $\text{CaCO}_3$ +30% $\text{YbF}_3$  mixture (6 min) [11], Endocem (11.5 min) [40] and ECHA+30%  $\text{YbF}_3$  mixture (14 min) [11]. Literature data reported for MTA vary between 17.8 and 50 min for initial [9,42,43,46] and between 140 and 290 min for final setting times [43,47]. Fast-setting was achieved mainly by incorporation of nano-crystalline active nHA. Such desirable behavior is expected since lower particle size increases the active surface for cement reaction with water [4]. All experimental cements had low setting time values indicating that the choice of radiopacifying agent did not alter the nHA's capability to induce the fast setting of tested materials.

From a mechanical point of view, the compressive strength of tested cements (2.7–3.8 MPa) was considerably lower than that of MTA (23 MPa) and PC (27 MPa). The data observed for MTA was slightly lower than that of recent findings: 28 MPa [46], 33 MPa [48], 43 MPa [47] and 45 MPa [43] while that found for PC correlates with previous studies: 32 MPa [47] and 51 MPa [43]. The variation of results obtained in the present and other studies might be caused by the use of greater specimens size in the current research. Namely, specimens measuring 8 mm × 1 cm were rather employed than usually used 4 × 6 mm to adjust measurements with used universal testing machine force range. The reduced compressive strength of ECHA +  $\text{Bi}_2\text{O}_3$  mixture is in compliance with a previous study where  $\text{Bi}_2\text{O}_3$  was added into PC [48], but in contrast to another study where excluding/eliminating  $\text{Bi}_2\text{O}_3$  from MTA resulted in lower compressive strength [49]. Significant decrease of the compressive strength of mixtures is presumably not to a great extent the consequence of radiopacifier addition, but rather related to the addition of nHA in substantial portion (>60%). The nHA is an inert compound that affects the CS setting reaction by interposing among its particles. Low values of compressive strength in experimental cements are therefore not surprising and they go in line with previous studies where some other compounds replaced CS particles at high percentage:  $\text{CaCO}_3$  (60–80%) in RetroMTA or  $\text{ZrO}_2$  (43–46%) in Endocem [10,45]. The consequences were similar since, for instance, the addition of low-reactive/inert  $\text{ZrO}_2$  into CS decreased its compressive strength to 10.4 MPa in Endocem [45]. In the authors' opinion, lower values of compressive strength of experimental cements do not play a major role in the clinical practice since the cements are manufactured to fulfil the most important requirement in retrograde root-end surgery – fast setting time. The same holds true for porosity. Although it is known that cements' architectural properties are important, the challenge lies in the clinical interpretation of obtained porosity data. Namely, lower values of closed porosity (ECHA +  $\text{ZrO}_2$ ) mainly refers to the mechanical resistance of materials whereas lower values of open porosity (ECHA +  $\text{ZrO}_2$  and MTA) are more likely related to the ability of the material to prevent spreading of bacterial infection in the root canal system from the area where the bacteria are not totally eliminated during instrumentation [36]. It is observed that in all experimental mixtures open porosity is significantly higher than the closed one. The results compare moderately well with previously published values demonstrating the increase of CS porosity after HA addition as well as no influence of  $\text{ZrO}_2$

addition on CS porosity [50]. Results for radiopacifier additions to ECHA are also consistent with those reported for ECHA+30% $\text{YbF}_3$  (5.86%) [11]. The outcomes found for MTA total porosity coincide with some previous reports: 1.3% [36], 6.5% [51], 6.9% [52] and 9% [53], but are lower than those reported in other studies: 14.5% [54] and 50% [55]. The variability of the outputs obtained arises from different setting parameters among studies the scanning resolutions of which vary from 5  $\mu\text{m}$  to 20  $\mu\text{m}$  [52]. For porosity evaluation by micro-CT, specimens' size is not defined by ISO standard. The specimens' size of 5 × 1 mm was preferred since it provided the possibility to obtain high resolution (i.e. visualization of smaller pore sizes) having in mind that the size of the specimen directly influences the maximum scanning resolution [51–55].

The wettability experiments demonstrated the advantage of  $\text{SrF}_2$  over  $\text{ZrO}_2$  and  $\text{Bi}_2\text{O}_3$  for manufacturing EC due to the higher activity of the cement surface, which is expressed as a lower CA of glycerol. Indeed, ECHA +  $\text{SrF}_2$  and ECHA +  $\text{ZrO}_2$  resulted in superior wettability in comparison with MTA, PC and ECHA +  $\text{Bi}_2\text{O}_3$  after glycerol administration. Glycerol was used since researchers have documented that it mimics closely the viscosity of human blood plasma [11]. The innovative approach in this study is the use of human blood plasma for CAs calculations; here, it is the first time in the EC dental field. The higher CAs after blood plasma administration compared to glycerol administration may be related to the presence of non-polar components in the plasma, presumably proteins [37]. The wettability of dental materials has been poorly investigated and very limited contributions can be found in the literature. The CAs reported in the literature for different CS brands are as follows: Endocem = 12° [45], MTA = 17° [36], Biodentine = 22° [36] and 41° [56] using glycerol and CeraSeal = 18° [57], Bio-Root = 34.8° [57], Endoseal MTA = 35° [58] and Thera Cal = 62.3° [59] using water as a reference liquid. There are no reports for CA values of blood plasma on EC. Wettability is an important property of dental cement since it reflects the ability of the material surface to interact with surrounding biological tissues as well as the ability of body fluids to adhesively occupy the materials surface texture, i.e. osteoblasts in the interaction with cements surface irregularities [11]. Yet, higher wettability enhances the potential of the cement to penetrate into dentinal tubules [36].

Experimental cements revealed statistically lower pH values than PC and MTA up to 12 h of evaluation. However, after 24 h and especially after 7 days of soaking in distilled water their alkalinity matched the one found in PC and MTA, having the ECHA +  $\text{ZrO}_2$  mixture even reaching the highest pH value after 7 days of evaluation. It is noteworthy that in PC and MTA the pH values remain relatively unchanged from 30 min to 24 h time points and then decrease after 7 days of soaking. Conversely, experimental cements presented the lowest pH values after 30 min, 1 h and 3 h and then resulted in stable increase of pH values during the remaining measurements. The alkaline nature of the experimental cements is the consequence of the release of calcium ions and the formation of  $\text{Ca}(\text{OH})_2$  [5]. The slow and stable release of calcium ions and consequently increase of pH value in experimental cements might be of pertinent interest in clinical practice in those situations where long term alkalinity is desirable for complete pulp/bone healing [60]. The source of  $\text{Ca}(\text{OH})_2$  is still debatable. Some authors state that it is the product of tricalcium aluminate hydrolysis while other claim that dicalcium and tricalcium silicate in reaction with water form tobermorite ( $\text{Ca}_2[\text{Si}_2(\text{OH})_2]_2$ ) and  $\text{Ca}(\text{OH})_2$  [10,61,62]. Higher alkalinity of PC group solution is expected since it contains pure CS with higher percentage of calcium-releasing components. The specimens' size of 4 × 6 mm was chosen since the ISO 6876 does not propose the procedure for pH measurements. However, both experimental cements and control PC/MTA materials were made in uniform size thus providing conditions for their comparison. The pH values observed in the literature for MTA are 12.5 [43] after 30 min, 12.8 [43] after 1 h, 9.09 [19] and 10.5 [9] after 3 h, 9.9 [9] after 12 h, 8.26 [19] and 9.3 [9] after 24 h and 10.3 [9] after 7 days. The values reported for PC corroborate with present findings having the values found after 30 min (13.1) and 1 h (13.1) [43]

decreased to 10.24 after 12 h and 10.2 after 24 h [63]. The results found for ECHA + ZrO<sub>2</sub> are also in rough agreement to those observed for CS + ZrO<sub>2</sub> after 12 h – (10.0) [9] and (10.21) [63] as well as after 24 h – (9.0) [9] and (10.2) [63].

The effects of experimental cements, PC and MTA on cell viability/proliferation was evaluated on mouse fibroblast L929 cell line [38], since it is easily manipulated, provides reproducible results without the individual differences [64] and the most importantly, L929 cells are more sensitive to toxic products than other cell lines [65,66]. The last feature gives L929 cells advantage when it comes to evaluation of dental materials toxicity. It is especially important for EC to precisely determine their cytotoxic potential since, in clinical practice, they are placed in a direct contact with periapical tissue for many years [67].

Cytotoxicity analysis revealed that (biologically relevant) decrease in viability of L929 cells cultured with pure extract of ECHA + ZrO<sub>2</sub> and ECHA + Bi<sub>2</sub>O<sub>3</sub> was detected only after 72 h, while ECHA + SrF<sub>2</sub> did not affect cell viability at all. Opposite from the results gained with experimental cements, the PC and MTA pure extracts displayed a strong toxicity toward L929 cells in all time points. While ECHA + ZrO<sub>2</sub> eluent 1:2 reduced cell viability over time, 1:4 eluent showed proliferative potential. These results are in accordance with a recent study investigating the ZrO<sub>2</sub> addition to CS [9]. While the ECHA + Bi<sub>2</sub>O<sub>3</sub> 1:2 eluent reduced viability, 1:4 eluent showed excellent effect on L929 cell proliferation. As expected, effects of experimental cements and PC/MTA on cellular viability/proliferation diminished with dilution; no significant change in number of viable and metabolically active cells were detected in 1:8, 1:16, and 1:32 eluents. Presented results showed significantly lower percentage of viable cells in MTA/PC treatments than those found in some studies (80–150%) [9,14,68,69], but they are in accordance with other reports found for MTA after 24 h (7–37%) [58] and 72 h (20–80%) [63,69] and findings reported for PC after 24 h (10–25%) [69]. The differences could arise from variations in specimens size (5 × 3 mm [69,70], 5 × 2 mm [42], 5 × 1 mm [13], 10 mg/ml [68], 0.5 g/5 ml [9] and 1 g/50 ml [14]) and their form (powder vs. set materials). Specimens measuring 5 × 3 mm were used in the present investigation to allow comparison to other studies where the same specimen sizes were used [69,70]. For PC/MTA 1:2 and 1:4 eluents, the CV and MTT tests showed similar outcomes and are in rough agreement with data documented in the literature [9,70]. Overall, cytotoxicity experiments revealed that results obtained by CV and MTT assays are in concordance. Pure extracts of experimental cements revealed significantly lower cytotoxic potential than PC and MTA. The ECHA + SrF<sub>2</sub> and ECHA + ZrO<sub>2</sub> 1:4 eluents induced significant proliferation of L929 cells (>20%) after all time points. Finally, it should be pointed out, that ECHA + SrF<sub>2</sub> mixture had no toxic effect and showed the highest ability to induce the L929 cell proliferation among tested materials.

Further, since the number of cells needed for cell adhesion assay is considerably lower than necessitated for cytotoxicity assays, osteoblasts derived from human apical papilla stem cells were used for cell adhesion experiments. This experimental set up allows to analyze cells contact with tested materials *ex vivo* and their differentiation on these materials, thus providing more clinically relevant environment. Great osteoblasts adhesion on dentine and on the surface of specimens demonstrated by SEM evaluation contributes to cements' cytocompatibility and may be of special interest for efficient periapical healing after retrograde root canal surgery. Other studies have also documented that CS-based ECs are the excellent inductors of cell adhesion, migration and proliferation on the surface of experimental cements [11,42,71,72].

Regardless of advantages of cell-based methods, there are considerable limitations in mapping results gained in the cell culture to *in vivo* conditions, due to significant simplification of *in vitro* models compared to living systems. For example, freshly mixed cements are used in the clinic, while the set ones are commonly used in the cell-based assays. Similarly, in an *in vitro* system, it is not possible to determine whether tested materials maintain their cytotoxicity for a long period of time or if their initial toxic potential declines over time [73,74]. Having in mind

previous, it is not possible to assume with high certainty that absence of cytotoxicity, superior proliferative potential and good cell adhesion properties of investigated materials showed in the present study can be translated to *in vivo* system. However, obtained results undoubtedly represent a good starting point for further investigation of their benefits *in vivo*, and aftermath in long-term clinical studies.

The novelty of this study comprises the introduction of SrF<sub>2</sub> as a radiopacifier in CS-based EC. Sr may be, in traces, a normal constituent of dental tissues [75]. Sr incorporation into dental tissues is an endemic issue; it occurs in regions with high Sr concentration in drinking water [75]. In addition, it is a compound of dental dentifrices and restorative materials such as glass ionomer cements [76,77]. SrF<sub>2</sub> addition may be interesting for dental practitioners for two reasons. Firstly, Sr-associated EC formulations may be of special interest for periapical lesions treatment taking into account that investigators in orthopaedics have documented an abundance of promising evidences that Sr-enriched biomaterials accelerate the process of bone healing [32,33]. Additionally, researchers nowadays use Sr-doped HA to coat the surface of titanium implants in orthopaedic and dental surgery to increase their bioactivity [78]. Secondly, the potentially useful contribution of fluorides for strengthening of endodontically instrumented root canals and their ability to prevent bacterial growth is widely accepted [11]. For these reasons, investigators already addressed the possibility to dope CS with fluorides in the form of sodium fluoride or YbF<sub>3</sub> [11,31,79]. Current experiment served to document that CS-based EC doped with both Sr and F satisfies the basic physicochemical and biocompatibility needs. What deserves to be mentioned is that SrF<sub>2</sub> associated mixture was the only one of the investigated materials to meet ISO 10993-5 quantitative criteria of non-cytotoxicity (maximum reduction of cell viability by more than 30%) for both CV and MTT assays, for all time point and in all dilutions. In addition, lower CA values in ECHA + SrF<sub>2</sub> than in ECHA + ZrO<sub>2</sub> and ECHA + Bi<sub>2</sub>O<sub>3</sub> mixtures after glycerol and human blood plasma testing favour the use of SrF<sub>2</sub> as the radiopacifying agent. Further detailed and more sophisticated biological studies should be conducted to acknowledge the true value of promising initial outcomes.

## 5. Conclusion

Collective results of this study underscore the relevance of nHA addition into CS-based dental ceramics. All investigated radiopacifiers were able to increase the radio-visibility of the ECHA to meet ISO requirements. Fast setting time and excellent cell adherence as well as good biocompatibility features indicated by mitochondrial activity and the number of viable cells present valuable advantages of manufactured formulations. Further, all experimental cements exhibited satisfactory wettability and porosity. The downside of fabricated materials is their low compressive strength. This study supports the idea that SrF<sub>2</sub> can be a novel promising radiopacifying agent for manufacturing CS-based dental ceramics. The full spectrum of SrF<sub>2</sub>'s beneficial effects in EC formulations should be investigated in future studies.

## Declaration of competing interest

The authors declare that they have no known competing financial interests or personal relationships that could have appeared to influence the work reported in this paper.

## Acknowledges

This study was supported by the Ministry of Education and Science of the Republic of Serbia (Grant No. 451-03-68/2020-14/200017 and 451-03-9/2021-14/200007) and through a bilateral PPP grant provided jointly by the Ministry of Education, Science and Technological Development of the Republic of Serbia and Ministry of Science and Technology of The Peoples Republic of China (Grant No. 451-02-818/2021-09/20). The authors thank Aleksa Milovanović and Isaak Trajković for help

with compressive strength evaluation analysis. The authors' thanks are also extended to Dr Vukoman Jokanović for his useful comments and discussions.

## Appendix A. Supplementary data

Supplementary data to this article can be found online at <https://doi.org/10.1016/j.ceramint.2021.07.052>.

## References

- [1] M. Torabinejad, T.F. Watson, T.R.P. Ford, Sealing ability of a mineral trioxide aggregate when used as a root end filling material, *J. Endod.* 19 (1993) 591–595.
- [2] J. Camilleri, T.R. Pitt-Ford, Mineral trioxide aggregate: a review of the constituents and biological properties of the material, *Int. Endod. J.* 39 (2006) 747–754.
- [3] J. Camilleri, F.E. Montesin, K. Brady, R. Sweeney, R.V. Curtis, T.R.P. Ford, The constitution of mineral trioxide aggregate, *Dent. Mater. J.* 21 (2005) 297–303.
- [4] J. Camilleri, Hydration mechanisms of mineral trioxide aggregate, *Int. Endod. J.* 40 (2007) 462–470.
- [5] M. Parirokh, M. Torabinejad, Mineral trioxide aggregate: a comprehensive literature review-Part I: chemical, physical, and antibacterial properties, *J. Endod.* 36 (2010) 16–27.
- [6] J. Camilleri, M.G. Gandolfi, Evaluation of the radiopacity of calcium silicate cements containing different radiopacifiers, *Int. Endod. J.* 43 (2010) 21–30.
- [7] J. Camilleri, Hydration characteristics of calcium silicate cements with alternative radiopacifiers used as root-end filling materials, *J. Endod.* 36 (2010) 502–508.
- [8] R. Bosso-Martelo, J.M. Guerreiro-Tanomaru, R. Viapiana, F.L. Berbert, M. A. Duarte, M. Tanomaru-Filho, Physicochemical properties of calcium silicate cements associated with microparticulate and nanoparticulate radiopacifiers, *Clin. Oral Invest.* 20 (2016) 83–90.
- [9] M.B. Queiroz, F.F.E. Torres, E.M. Rodrigues, K.S. Viola, R. Bosso-Martelo, G. Chavez-Andrade, J.M. Guerreiro-Tanomaru, M. Tanomaru-Filho, Physicochemical, biological, and antibacterial evaluation of tricalcium silicate-based reparative cements with different radiopacifiers, *Dent. Mater. J.* S0109–5641 (20) (2020), 30334–1.
- [10] T. Dammashcke, A. Nowicka, M. Lipski, D. Ricucci, Histological evaluation of hard tissue formation after direct pulp capping with a fast setting mineral trioxide aggregate (RetroMTA) in humans, *Clin. Oral Invest.* 23 (2019) 4289–4299.
- [11] D. Antonijević, A. Jeschke, B. Colovic, P. Milovanovic, D. Jevremovic, D. Kasic, A. Scheidt, M. Hahn, M. Amlig, V. Jokanovic, B. Busse, M. Djuric, Addition of a fluoride-containing radiopacifier improves micromechanical and biological characteristics of modified calcium silicate cements, *J. Endod.* 41 (2015) 2050–2057.
- [12] I.M. Garcia, V.C.B. Leitune, C.J. Ferreira, F.M. Collares, Tantalum oxide as filler for dental adhesive resin, *Dent. Mater. J.* 37 (2018) 897–903.
- [13] L.B. Mestieri, A.L. Gomes-Cornélio, E.M. Rodrigues, G. Faria, J.M. Guerreiro-Tanomaru, M. Tanomaru-Filho, Cytotoxicity and bioactivity of calcium silicate cements combined with niobium oxide in different cell lines, *Braz. Dent. J.* 28 (2017) 65–71.
- [14] L.B. Mestieri, M. Tanomaru-Filho, A.L. Gomes-Cornélio, L.P. Salles, M.I. Bernardi, J.M. Guerreiro-Tanomaru, Radiopacity and cytotoxicity of Portland cement associated with niobium oxide micro and nanoparticles, *J. Appl. Oral Sci.* 22 (2014) 554–559.
- [15] S. Chen, L. Shi, J. Luo, H. Engqvist, Novel fast-setting mineral trioxide aggregate: its formulation, chemical-physical properties, and cytocompatibility, *ACS Appl. Mater. Interfaces* 10 (2018) 20334–20341.
- [16] D. Wang, Y. Zhang, Z. Hong, Novel fast-setting chitosan/ $\beta$ -dicalcium silicate bone cements with high compressive strength and bioactivity, *Ceram. Int.* 40 (2014) 9799–9808.
- [17] M. Wu, B. Tao, T. Wang, Y. Zhang, W. Wei, C. Wang, Fast-setting and anti-washout tricalciumsilicate/disodium hydrogen phosphate composite cement for dental application, *Ceram. Int.* 45 (2019) 24182–24192.
- [18] L.T.A. Cintra, F. Benetti, Í.O.A. Queiroz, J.M.A. Lopes, S.H. Penha de Oliveira, G. Sivieri Araújo, J.E. Gomes-Filho, Cytotoxicity, biocompatibility and biomineralization of the new high-plasticity MTA material, *J. Endod.* 43 (2017) 774–778.
- [19] B. Četenović, B. Čolović, S. Vasilijić, B. Prokić, S. Pašalić, V. Jokanović, Z. Tepavčević, D. Marković, Nanostructured endodontic materials mixed with different radiocontrast agents-biocompatibility study, *J. Mater. Sci. Mater. Med.* 29 (2018) 190.
- [20] B. Čolović, O. Janković, S. Živković, Ž. Žizak, I.B. Žizak, V. Jokanović, A new endodontic mixture based on calcium aluminate cement obtained by hydrothermal synthesis, *Ceram. Int.* 45 (2019) 9211–9218.
- [21] V. Jokanović, D. Izvonar, M. Damićanin, B. Jokanovic, V. Zivojinovic, D. Markovic, B. Dacic, Hydrothermal synthesis and nanostructure of carbonated calcium hydroxyapatite, *J. Mater. Sci. Mater. Med.* 17 (2006) 539–546.
- [22] V. Jokanović, B. Jokanović, D. Marković, V. Zivojinović, S. Pasalić, D. Izvonar, M. Plavšić, Kinetics and sintering mechanisms of hydro-thermally obtained hydroxyapatite, *Mater. Chem. Phys.* 111 (2008) 180–185.
- [23] S. Paraš, O. Janković, D. Trisić, B. Čolović, O. Mitrović-Ajtić, R. Dekić, I. Soldatovic, M. Živkovic-Sandic, S. Živkovic, V. Jokanovic, Influence of nanostructured calcium aluminate and calcium silicate on the liver: histological and unbiased stereological analysis, *Int. Endod. J.* 52 (2019) 1162–1172.
- [24] V. Opačić-Galić, V. Petrović, S. Živković, V. Jokanović, B. Nikolić, J. Knežević-Vukčević, D. Mitić-Culafic, New nanostructural biomaterials based on active silicate systems and hydroxyapatite: characterization and genotoxicity in human peripheral blood lymphocytes, *Int. Endod. J.* 46 (2013) 506–516.
- [25] B. Četenovic, B. Prokić, S. Vasilijić, B. Dojčinovic, M. Magic, V. Jokanovic, D. Markovic, Biocompatibility investigation of new endodontic materials based on nanosynthesized calcium silicates combined with different radiopacifiers, *J. Endod.* 43 (2017) 425–432.
- [26] J.M. Guerreiro-Tanomaru, F.A. Vázquez-García, R. Bosso-Martelo, M.I. Bernardi, G. Faria, M. Tanomaru-Filho, Effect of addition of nano-hydroxyapatite on physicochemical and antibiobiofilm properties of calcium silicate cements, *J. Appl. Oral Sci.* 24 (2016) 204–210.
- [27] W.C. Liu, H.Y. Wang, L.C. Chen, S.W. Huang, C. Wu, R.J. Chung, Hydroxyapatite/tricalcium silicate composites cement derived from novel two-step sol-gel process with good biocompatibility and applications as bone cement and potential coating materials, *Ceram. Int.* 45 (2019) 5668–5679.
- [28] B.C. Costa, J.M. Guerreiro-Tanomaru, R. Bosso-Martelo, E.M. Rodrigues, I. Bonetti-Filho, M. Tanomaru-Filho, Ytterbium oxide as radiopacifier of calcium silicate-based cements. Physicochemical and biological properties, *Braz. Dent. J.* 29 (2018) 452–458.
- [29] E. Wysłokińska, J. Cichos, E. Ziolo, A. Bednarkiewicz, L. Strządala, M. Karbowiak, D. Hreniak, W. Kalas, Cytotoxic interactions of bare and coated NaGdF<sub>4</sub>:Yb(3+):Er(3+) nanoparticles with macrophage and fibroblast cells, *Toxicol. Vitro* 32 (2016) 16–25.
- [30] M. Huang, R.G. Hill, S.C. Rawlinson, Strontium (Sr) elicits odontogenic differentiation of human dental pulp stem cells (hDPSCs): a therapeutic role for Sr in dentine repair, *Acta Biomater.* 38 (2016) 201–211.
- [31] P. Taddei, E. Modena, A. Tinti, F. Siboni, C. Prati, M.G. Gandolfi, Effect of the fluoride content on the bioactivity of calcium silicate-based endodontic cements, *Ceram. Int.* 40 (2014) 4095–4107.
- [32] Q. Wu, X. Wang, F. Jiang, Z. Zhu, J. Wen, X. Jiang, Study of Sr-Ca-Si-based scaffolds for bone regeneration in osteoporotic models, *Int. J. Oral Sci.* 12 (2020) 25.
- [33] K. Lin, L. Xia, H. Li, X. Jiang, H. Pan, Y. Xu, W.W. Lu, Z. Zhang, J. Chang, Enhanced osteoporotic bone regeneration by strontium-substituted calcium silicate bioactive ceramics, *Biomater* 34 (2013) 10028–10042.
- [34] International Organization for Standardization, ISO 6876, Dental Root Canal Sealing Materials, second ed., ISO, Geneva, 2001.
- [35] D. Ilić, Lj. Stojanović, Dj. Antonijević, S. Milutinović-Smiljanić, T. Savić-Stanković, Z. Milosavljević, Measuring of mandible bone density in dogs using digital/radiography/radiovisography, *Acta Vet.* 70 (2020) 285–295.
- [36] V. Biočanin, D. Antonijević, S. Poštić, D. Ilić, Z. Vuković, M. Milić, Y.Y. Fan, Z. Li, B. Brkovic, M. Djuric, Marginal gaps between 2 calcium silicate and glass ionomer cements and apical root dentin, *J. Endod.* 44 (2018) 816–821.
- [37] I. Schwarz, S. Zehnle, T. Hutzenlaub, R. Zengerle, N. Paust, System-level network simulation for robust centrifugal-microfluidic lab-on-a-chip systems, *Lab Chip* 16 (2016) 1873–1885.
- [38] International Organization for Standardization ISO 10993-5 Biological Evaluation of Medical Devices -Part 5: Tests for in vitro.Cytotoxicity, International Organization for Standardization, Geneva, Switzerland, 2009.
- [39] P. Hilkens, P. Gervois, Y. Fanton, J. Vanormelingen, W. Martens, T. Struys, C. Politis, I. Lambrechts, A. Bronckaers, Effect of isolation methodology on stem cell properties and multilineage differentiation potential of human dental pulp stem cells, *Cell Tissue Res.* 353 (2013) 65–78.
- [40] Z. Rakocevic, Fizika jonizujućeg zračenja, in: Z. Rakocevic (Ed.), 2nded. Osnovi Radiologije Dento-Maksilofacijalne Regije, Stomatološki fakultet Univerziteta u Beogradu, Beograd, 1998, pp. 15–18.
- [41] E.C. Kim, B.C. Lee, H.S. Chang, W. Lee, C.U. Hong, K.S. Min, Evaluation of the radiopacity and cytotoxicity of Portland cements containing bismuth oxide, *Oral. Surg. Oral. Med. Oral. Path. Radiol. Endod.* 105 (2008) e54–e57.
- [42] C.M.A. Ferreira, L.M. Sassone, A.S. Gonçalves, J.J. Carvalho, C.J. Tomás-Catalá, D. García-Bernal, R.E. Onate-Sanchez, F.J. Rodriguez-Lozano, E.J.N.L. Silva, Physicochemical, cytotoxicity and in vivo biocompatibility of a high-plasticity calcium-silicate based material, *Sci. Rep.* 9 (2019) 3933.
- [43] I. Islam, H.K. Cheng, A.U. Yap, Comparison of the physical and mechanical properties of MTA and portland cement, *J. Endod.* 32 (2006) 193–197.
- [44] A. Cutajar, B. Mallia, S. Abela, J. Camilleri, Replacement of radiopacifier in mineral trioxide aggregate; characterization and determination of physical properties, *Dent. Mater. J.* 27 (2011) 879–891.
- [45] J.S. Kwon, M.J. Lee, J.Y. Kim, D. Kim, J.H. Ryu, S. Jang, K.M. Kim, C.J. Hwang, S. H. Choi, Novel anti-biofouling bioactive calcium silicate-based cement containing 2-methylacryloyloxyethyl phosphorylcholine, *PLoS One* 14 (2019), e0211007.
- [46] P. Kogan, J. He, G.N. Glickman, I. Watanabe, The effects of various additives on setting properties of MTA, *J. Endod.* 32 (2006) 569–572.
- [47] Y.C. Hwang, D.H. Kim, I.N. Hwang, S.J. Song, Y.J. Park, J.T. Koh, H.H. Son, W. M. Oh, Chemical constitution, physical properties, and biocompatibility of experimentally manufactured Portland cement, *J. Endod.* 37 (2011) 58–62.
- [48] K.S. Coomaraswamy, P.J. Lumley, M.P. Hofmann, Effect of bismuth oxide radioopacifier content on the material properties of an endodontic Portland cement-based (MTA-like) system, *J. Endod.* 33 (2007) 295–298.
- [49] R. Grazziotin-Soares, M. H Nekoofar, T.E. Davies, A. Bafail, E. Alhaddar, R. Hübler, A.L.S. Busato, P.M.H. Dummer, Effect of bismuth oxide on white mineral trioxide aggregate: chemical characterization and physical properties, *Int. Endod. J.* 47 (2014) 520–533.
- [50] F.M. Saltarelli, G.B. Leoni, N.L.F. Aguiar, N.S. Faria, I.R. Oliveira, L. Bachmann, W. R. Neto, Apatite-like forming ability, porosity, and bond strength of calcium

- aluminate cement with chitosan, zirconium oxide, and hydroxyapatite additives, *Microsc. Res. Tech.* (2020), <https://doi.org/10.1002/jemt.23678>.
- [51] I. Milanovic, P. Milovanovic, D. Antonijević, B. Dzeletovic, M. Djuric, V. Miletic, Immediate and long-term porosity of calcium silicate-based sealers, *J. Endod.* 46 (2020) 515–523.
- [52] F.F.E. Torres, R. Jacobs, M. EzEldeen, K. Faria-Vasconcelos, J.M. Guerreiro-Tanomaru, B.C. Dos Santos, M. Tanomaru-Filho, How image-processing parameters can influence the assessment of dental materials using micro-CT, *Imag. Sci. Dent.* 50 (2020) 161–168.
- [53] F.F.E. Torres, R. Jacobs, M. EzEldeen, J.M. Guerreiro-Tanomaru, B.C.D. Santos, É. Lucas-Oliveira, T.J. Bonogamba, M. Tanomaru-Filho, Micro-computed tomography high resolution evaluation of dimensional and morphological changes of 3 root-end filling materials in simulated physiological conditions, *J. Mater. Sci. Mater. Med.* 31 (2020) 14.
- [54] F.F.E. Torres, J.M. Guerreiro-Tanomaru, R. Bosso-Martelo, G.M. Chavez-Andrade, M. Tanomaru-Filho, Solubility, porosity, dimensional and volumetric change of calcium silicate-based cements, *J. Appl. Oral Sci.* 26 (2018), e20170465.
- [55] F.F.E. Torres, J.M. Guerreiro-Tanomaru, R. Bosso-Martelo, C.G. Espir, J. Camilleri, M. Tanomaru-Filho, Solubility, porosity, dimensional and volumetric change of endodontic sealers, *Braz. Dent. J.* 30 (2019) 368–373.
- [56] S. Milutinović, D. Ilić, V. Danilović, Dj Antonijević, Advantages and downsides of biodentine, *Vojnosanit. Pregl.* (2020), <https://doi.org/10.2298/VSP.1912120.14M>.
- [57] N. Kharouf, Y. Arntz, A. Eid, J. Zghal, S. Sauro, Y. Haikel, D. Mancino, Physicochemical and antibacterial properties of novel, premixed calcium silicate-based sealer compared to powder-liquid bioceramic sealer, *J. Clin. Med.* 9 (2020) 3096.
- [58] S.B. Jo, H.K. Kim, H.N. Lee, Y.J. Kim, K.D. Patel, J.C. Knowles, J.H. Lee, Physical properties and biofunctionalities of bioactive root canal sealers in Vitro, *Nanomaterials* 10 (2020) 1750.
- [59] Y.K. Kim, M.H. Hong, T.Y. Kwon, Dentin bonding of TheraCallC calcium silicate containing an acidic monomer: an in vitro study, *Materials* 13 (2020) 293.
- [60] M. Parirokh, M. Torabinejad, Mineral trioxide aggregate: a comprehensive literature review - Part III: clinical applications, drawbacks, and mechanism of action, *J. Endod.* 36 (2010) 400–413.
- [61] T. Dammaschke, H.U. Gerth, H. Zuchner, E. Schafer, Chemical and physical surface and bulk material characterization of white ProRoot MTA and two Portland cements, *Dent. Mater. J.* 21 (2005) 731–738.
- [62] V. Jokanovic, B. Colovic, D. Markovic, S. Zivkovic, Highly active calcium-silicate phases for application in endodontics, *Serbian Dent. J.* 60 (2013) 210–217.
- [63] J.M.G. Tanomaru, A.L.G. Cornelio, C. Andolfatto, L.P. Salles, M.F. Tanomaru, pH and antimicrobial activity of Portland cement associated with different radiopacifying agents, *ISRN Dent* (2012), <https://doi.org/10.5402/2012/469019>.
- [64] J.E. Key, F.G. Rahemtulla, P.D. Eleazer, Cytotoxicity of a new root canal filling material on human gingival fibroblasts, *J. Endod.* 32 (2006) 756–758.
- [65] F. Chen, T. Wu, X. Cheng, Cytotoxic effects of denture adhesives on primary human oral keratinocytes, fibroblasts and permanent L929 cell lines, *Gerodontology* 31 (2014) 4–10.
- [66] F. Denizot, R. Lang, Rapid colorimetric assay for cell growth and survival. Modifications to the tetrazolium dye procedure giving improved sensitivity and reliability, *J. Immunol. Methods* 89 (1986) 271–277.
- [67] J. Camps, I. About, Cytotoxicity testing of endodontic sealers: a new method, *J. Endod.* 29 (2003) 583–586.
- [68] C. Slompo, C. Peres-Buzalaf, K.C. Gasque, C.A. Damante, R. Ordinola-Zapata, M. A. Duarte, R.C. de Oliveira, Experimental calcium silicate-based cement with and without zirconium oxide modulates fibroblasts viability, *Braz. Dent. J.* 26 (2015) 587–591.
- [69] A. Zakerzadeh, E. Esnaashari, S. Dadfar, In Vitro Comparison of cytotoxicity and genotoxicity of three vital pulp capping materials, *Iran. Endod. J.* 12 (2017) 419–425.
- [70] P. Yoshino, C.K. Nishiyama, K.C. Modena, C.F. Santos, C.R. Sipert, In vitro cytotoxicity of white MTA, MTA Fillapex® and Portland cement on human periodontal ligament fibroblasts, *Braz. Dent. J.* 24 (2013) 111–116.
- [71] Y. Jiang, Q. Zheng, X. Zhou, Y. Gao, D. Huang, A comparative study on root canal repair materials: a cytocompatibility assessment in L929 and MG63 cells, *Sci. World J.* 12 (2014) 463826.
- [72] H.M. Zhou, T.F. Du, Y. Shen, Z.J. Wang, Y.F. Zheng, M. Haapasalo, In vitro cytotoxicity of calcium silicate-containing endodontic sealers, *J. Endod.* 41 (2015) 56–61.
- [73] S. Arun, V. Sampath, S. Mahalaxmi, K. Rajkumar, A comparative evaluation of the effect of the addition of pachymic acid on the cytotoxicity of 4 different root canal sealers-an in vitro study, *J. Endod.* 43 (2017) 96–99.
- [74] D.A. Fonseca, A.B. Paula, C.M. Marto, A. Coelho, S. Paulo, J.P. Martinho, E. Carrilho, M.M. Ferreira, Biocompatibility of root canal sealers: a systematic review of in vitro and in vivo studies, *Materials* 12 (2019) 4113.
- [75] G. Goude, D.C. Salazar-García, R.C. Power, M. Rivollat, L. Gourichon, M. F. Deguilloux, M.H. Pemonge, L. Bouby, D. Binder, New insights on Neolithic food and mobility patterns in Mediterranean coastal populations, *Am. J. Phys. Anthropol.* 173 (2020) 218–235.
- [76] C. Grünberg, F. Bauer, A. Crispin, M. Jakob, R. Hickel, M.E. Draenert, Effectiveness of dentifrices with new formulations for the treatment of dentin hypersensitivity - a meta-analysis, *Am. J. Dent.* 30 (2017) 221–226.
- [77] H. Miyaji, K. Mayumi, S. Miyata, E. Nishida, K. Shitomi, A. Hamamoto, S. Tanaka, T. Akasaka, Comparative biological assessments of endodontic root canal sealer containing surface pre-reacted glass-ionomer (s-prg) filler or silica filler, *Dent. Mater. J.* 39 (2020) 287–294.
- [78] N. López-Valverde, J. Muriel-Fernández, R. Gómez de Diego, J.M. Ramírez, A. López-Valverde, Effect of strontium-coated titanium implants on osseointegration in animal models: a literature systematic review, *Int. J. Oral Maxillofac. Implants* 34 (2019) 1389–1396.
- [79] M.G. Gandolfi, P. Taddei, F. Siboni, E. Modena, M.P. Ginebra, C. Prati, Fluoride-containing nanoporous calcium-silicate MTA cements for endodontics and oral surgery: early fluorapatite formation in a phosphate-containing solution, *Int. Endod. J.* 44 (2011) 938–949.



## Thermal radiation management by natural photonic structures: *Morimus asper funereus* case

Darko Vasiljević<sup>a</sup>, Danica Pavlović<sup>a,\*</sup>, Vladimir Lazović<sup>a</sup>, Branko Kolarić<sup>a,c</sup>, Branislav Salatić<sup>a</sup>, Wang Zhang<sup>b</sup>, Di Zhang<sup>b</sup>, Dejan Pantelić<sup>a</sup>

<sup>a</sup> Institute of Physics, University of Belgrade, Pregrevica 118, 11080, Belgrade, Zemun, Serbia

<sup>b</sup> State Key Lab of Metal Matrix Composite, Shanghai Jiao Tong University, 800 Dongchuan Road, Shanghai, 200240, China

<sup>c</sup> Micro- and Nanophotonic Materials Group, University of Mons, Place du Parc 20, 7000, Mons, Belgium

### ARTICLE INFO

#### Keywords:

Photonic structures  
Infrared radiation  
Hyperuniformity  
Radiative energy exchange  
Longicorn beetle

### ABSTRACT

Convective, conductive and radiative mechanisms of thermal management are extremely important for life. Photonic structures, used to detect infrared radiation (IR) and enhance radiative energy exchange, were observed in a number of organisms. Here we report on sophisticated radiative mechanisms used by *Morimus asper funereus*, a longicorn beetle whose elytra possess a suitably aligned array of lenslets and blackbodies. Additionally, a dense array of microtrichia hyperuniformly covers blackbodies and operates as a stochastic, full-bandgap, IR-photonic structure. All these features, whose characteristic dimensions cover a range from several hundred down to a few micrometres, operate synergistically to improve the absorption, emission and, possibly, detection of IR radiation. We present a morphological characterization of the elytron, thermal imaging measurements and a theoretical IR model of insect elytron, uncovering a synergistic operation of all structures.

### 1. Introduction

Colouration in the living world serves multiple purposes, such as: camouflage, mimicry, warning or attraction (Doucet and Meadows, 2009; Kemp, 2007; Sweeney et al., 2003; Verstraete et al., 2019), and it sometimes affects the very existence of animals. Radiative heat exchange with the environment can also be influenced by colours, through absorption or reflection of the visible light. There is a delicate balance between colouration and other mechanisms of thermal regulation: convection, conduction, radiation emission and absorption, evaporation, perspiration, internal heat generation, behaviour (Bosi et al., 2008; Cossins, 2012).

Such mechanisms have also been observed in insects. Their exoskeleton (cuticle) serves many functions, such as: locomotion, providing a defence barrier (against mechanical stress, cold, hot or wet environment), a reservoir for the storage of metabolic waste products, mechano- and chemoreception, balancing radiant energy absorption in the visible and dissipation in the infrared (IR) part of the spectrum (Capinera, 2008; Gillott, 2005; Gullan and Cranston, 2004; Shi et al., 2015). The cuticle is usually patterned on micro- and nano-scale and produces striking optical effects. Such photonic structures (Vukusic and

Sambles, 2003) create structural colouration (Vukusic et al., 2001) in the visible, but can have an important role in the infrared part of the spectrum, participating in thermoregulation (Scoble, 1992; Shi et al., 2015).

Most insects are primarily ectothermic and rely on external heat sources, such as solar radiation (Nijhout, 1991). It is proven that butterflies use physiological mechanisms to regulate the heat gain by orientation and posture relative to the sun (Kingsolver, 1985). On the other hand, structures are developed during evolution to efficiently reflect the visible light, simultaneously dissipating infrared radiation directly into the atmospheric window at mid-infrared, as in the Saharan silver ant, *Cataglyphis bombycina* (Roger, 1859) (Shi et al., 2015). This clever mechanism enables an insect to efficiently regulate its body temperature in a hostile desert environment.

In addition, the insect cuticle can be a place where so-called extra-ocular photoreception occurs. Also known as “dermal light sense” and defined as a “widespread photic sense that is not mediated by eyes or eyespots and in which light does not act directly on an effector” (Millott, 1968), it has been reported in several orders of insects. Some butterflies have such photoreceptors located at the end of their abdomens to control copulation in males and oviposition in females (Arikawa and Takagi,

\* Corresponding author. Institute of Physics, University of Belgrade, Serbia Pregrevica 118, 11080, Belgrade, Zemun, Serbia.

E-mail address: [danica.pavlovic@ipb.ac.rs](mailto:danica.pavlovic@ipb.ac.rs) (D. Pavlović).

<https://doi.org/10.1016/j.jtherbio.2021.102932>

Received 19 November 2020; Received in revised form 5 March 2021; Accepted 29 March 2021

Available online 3 April 2021

0306-4565/© 2021 Elsevier Ltd. All rights reserved.

2001). In some cases, dermal light sensitivity has been confirmed from behavioural responses, mediated by light intensity and wavelength (Desmond Ramirez et al., 2011). For example the larvae of *Tenebrio molitor* avoid light even after decapitation (Tucolesco, 1933). Light sensitivity of the *Aphis fabae* antennae is responsible for the insect's photokinetic activity (Booth, 1963).

Here we highlight the specific architecture of *Morimus asper funereus* (Mulsant, 1863) (Insecta: Coleoptera: Cerambycidae) elytra, which implicates dermal detection of IR radiation, a feature not previously observed in any other species. We also study the radiative properties of the elytra. Electron and optical microscopy were used to reveal the external and internal morphology of elytra, and thermal imaging to establish its radiative properties in the thermal IR (7.5–13  $\mu\text{m}$ ) part of the spectrum. Theoretical analysis and 3D modelling were used to reveal the role of microstructures.

## 2. Materials and methods

### 2.1. Insect

*Morimus asper funereus* (Fig. 1) (family Cerambycidae, subfamily Lamiinae) is a large longicorn beetle inhabiting central and southern Europe. The species is characterized by grey elytra with four black patches and a body length of 15–40 mm (Parisi and Busetto, 1992). The colouration and velvety appearance of the elytra comes from the dense tomentum of the setae, grey hairs and black scales, embedded in the elytral surface, which is black and shiny. The hind wings (alae) of *M. asper funereus* are reduced and the species is flightless (Solano et al., 2013).

*M. asper funereus* is a saproxylic species (Carpaneto et al., 2015; Hardersen et al., 2017) and depends on decaying wood during larval development. This process takes place in tree trunks and stumps and lasts approximately three or four years (Stanić et al., 1985). We noticed that the insects evade direct sunlight. We never found them on trunks that were directly exposed to solar radiation: when we subjected an insect to sunlight, it hid in the shadow. This was confirmed by other research, which found that this species is active during the evening and at night (Polak and Maja, 2012; Romero-Samper and Bahülo, 1993). Hardersen et al. (2017) determined that the highest activity of the species was between 20:00 and 24:00. However, the authors stated that *M. asper funereus* individuals were seen during the day, but that the number was only 30% of the maximum recorded in the evening and at night.

The species is strictly protected in Europe (and Serbia) by Annex II of the Habitat Directive 92/43/CEE. In the IUCN Red List of Threatened Species, it is designated as vulnerable (A1c) (IUCN Red List of Threatened Species, 2018). We had ten, conserved and pinned, specimens at our disposal, collected during the summer of 2018 on Mt. Avala, near the city of Belgrade, with the permission of the Serbian Ministry of



Fig. 1. *Morimus asper funereus*: a longicorn beetle whose most prominent features are black body and greyish elytra with four prominent black patches.

Environmental Protection (N°:353-01 –1310/2018-04).

### 2.2. Microanalysis

A stereomicroscope (STEBA600, Colo Lab Experts, Slovenia) with maximum magnification up to 180X, eyepiece 20X, auxiliary objective 2X, working distance 100 mm, reflection and transmission mode, and equipped with a digital camera (Canon EOS 50D, Tokyo, Japan) was used to examine the anatomy of the whole insect.

The optical characteristics of the elytra and setae were analysed on a trinocular microscope (MET104, Colo Lab Experts, Slovenia) (maximum magnification 400X, polarization set, objectives Plan Achromatic POL Polarizing 10X/20X/40X).

Micro-computed tomography (micro-CT) was employed to view the overall anatomy of the beetle and measure the thickness of the elytra. We had at our disposal the Skyscan 1172 system (Bruker, USA). To ensure the optimum signal/noise ratio during micro-CT imaging, the specimens were scanned without filter, with scanning parameters set as follows: 40 kV, 244  $\mu\text{A}$ , 530 ms, rotation step 0.2° (pixel size 13.5  $\mu\text{m}$ ). For the purpose of this experiment, CT scanning was performed without any special preparation of a specimen.

A field emission gun scanning electron microscope (FEGSEM) (Mir-aSystem, TESCAN, Czech Republic) was used for ultrastructural analysis. Prior to analysis, insect elytra were removed and placed on an aluminium mount and coated with a thin layer (5–10 nm) of gold palladium (AuPd), using a SC7620 Mini Sputter Coater (Quorum Technologies Ltd., UK).

### 2.3. Thermal infrared (IR) analysis

Assessment of the thermal properties of insects is normally done by some kind of thermometry (Heinrich, 2013). With the advent of IR cameras, thermal imaging (TI) becomes a method of choice. It is a non-invasive and non-contact technique with applications in numerous fields (Vollmer and Möllmann, 2010). Recently, TI become an important sensing technology in biological investigations (Kastberger and Stachl, 2003). TI cameras are a relatively new tool in studying nocturnal flying animals: birds, bats and insects (Horton et al., 2015). So far, most TI studies of insects have focused on the thermoregulation of Hymenoptera species (Stabentheiner and Schmaranzer, 1987; Stabentheiner et al., 2012).

In this research, the emission of thermal radiation was analysed by an IR thermal camera corresponding to an atmospheric window at 7.5–13  $\mu\text{m}$  (FLIR A65, USA, 640 x 512 pixels, thermal resolution/NETD 50 mK). Thermal measurements were corrected for surface emissivity, and reflected temperature, while images were acquired without binning. Due to the smallness of the insect, we positioned the camera as close as possible (at a distance between 10 and 20 cm), and sometimes used an additional lens to further magnify the thermal image. Under these conditions, the Narcissus effect (radiation emitted by the camera itself) was pronounced. For this reason, we positioned the elytra outside the thermal beam emanating from the camera objective. The rest of the camera body was shielded by aluminium foil.

We manufactured an aluminium cavity and coated it with an absorbing, velvety material whose absorbance was measured at 0.996, in agreement with the calculated value (Prokhorov, 2012). It was used as a reference to measure elytra emissivities, as shown in Fig. 2.

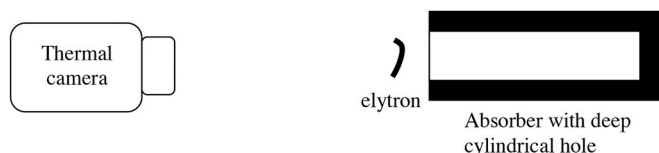


Fig. 2. A simple experimental setup for thermal measurements.

### 3. Results

#### 3.1. Morphological and optical characterization of photonic structures of *M. asper funereus*

The macroscopic anatomy of a dried specimen, visualized using micro-CT (Fig. 3), showed that the elytra of *M. asper funereus* are ellipsoidal, sclerotized and thick (between 200 and 350  $\mu\text{m}$ ). The hind wings of *M. asper funereus* are highly reduced and there is a large, air-filled space between the elytra and the insect body.

The elytra of *M. asper funereus* (Fig. 1) possess a hierarchical structure with a number of features ranging from macroscopic to micron and submicron levels.

The inner surface (facing the insect body) looks spongy (Fig. 4(a)), with an array of oval zones (approx. 0.2–0.4 mm in size – see Fig. 4(b)), surrounded by yellowish walls. If observed in transmission, it can be seen that the walls are actually a complex, connected network of channels that transport hemolymph (Fig. 4(c)) (Unruh and Chauvin, 1993; van de Kamp and Greven, 2010). Within each zone, there is a spherical-looking object with a circular opening at its centre that looks like a standard blackbody (BB) model found in textbooks. In transmission (Fig. 4(c)), BBs are deep red, doughnut-shaped features in the middle of each oval zone. It should be noted that the red colour is due to melanin, characterized by strong absorption in the blue-green part of the spectrum and good transmission in the red. By bleaching elytra using hydrogen peroxide ( $\text{H}_2\text{O}_2$ ) we were able to reveal a network of smaller channels, connecting the BB to the main microfluidic channels. (Fig. 4 (d)).

All the structures described above are protected by an optically transparent layer. This layer is electron-dense (Fig. 5) and hides all the structures observed optically. Microtrichia (thorn-like structures, approx. 5  $\mu\text{m}$  in height – inset in Fig. 5) are a dominant feature of the internal surface. As can be seen, the microtrichia are arranged in an ordered but not completely regular pattern (average mutual distance is 11  $\mu\text{m}$ ). In many other insects, such structures are used to lock the hind wings to the elytra, as in the Asian ladybeetle (Sun et al., 2018).

Outer surface of elytra is black and covered with two different types of microtrichiae (Fig. 6(a) and (b)). One type is transparent and covers most of the body, which looks greyish (grey zone) due to the scattered

radiation. The other type is pigmented and densely covers four distinct areas producing characteristic black patches. However, in thermal infrared, the whole body looks quite uniform.

On grey elytral zone there is also an array of shiny black, quite smooth, microlens-like protrusions, surrounded with hairs (compare optical and SEM images in Fig. 6(c), respectively). The microlenses and BBs have a well-defined mutual orientation, which was observed by simultaneously illuminating the elytron in transmission and reflection (Fig. 7). As observed before (Fig. 4), the BB occupies the centre of an oval zone, while the microlens is at its rim, directly facing a hemolymph-filled channel.

The elytron directly beneath the surface (procuticle 200- $\mu\text{m}$  thick) is well organized, as in all coleopteran (van de Kamp and Greven, 2010; van de Kamp et al., 2016). It is layered and possesses a number of laminae that envelope the BBs and microchannels (Fig. 8(a)). It is interesting to note a number of tiny hairs covering the internal surface of the blackbody (Fig. 8(b)). At the moment, we can only speculate about their biological function, because this can be revealed only by physiological investigation of live specimens, which we didn't have at our disposal. However, from purely physical point of view, we note that hairs increase the absorbance of the black body wall due to enhanced scattering and trapping of radiation.

#### 3.2. Radiative properties of *M. asper funereus*

We used thermal imaging to evaluate radiative properties of elytra. An elytron was placed in front of the reference cavity (with absorbance higher than 99% (Prokhorov, 2012)) and observed with a thermal camera (operating within the 8–14  $\mu\text{m}$  wavelength range). In thermal equilibrium (room temperature), the elytron completely disappears from thermal image (Fig. 9(a)) and becomes visible only when heated by the laser beam (Fig. 9(b)). The same is true for both the outer and inner sides, along the entire, highly curved, elytral surface. Thus, we may conclude that the high directional emissivity (higher than 99%) is constant along the surface and has the characteristics of a Lambertian source.

It is interesting to note that the emissivity of both black and grey areas of elytra is the same. This is because the wavelength of thermal radiation is close to characteristic dimensions of hairs covering the

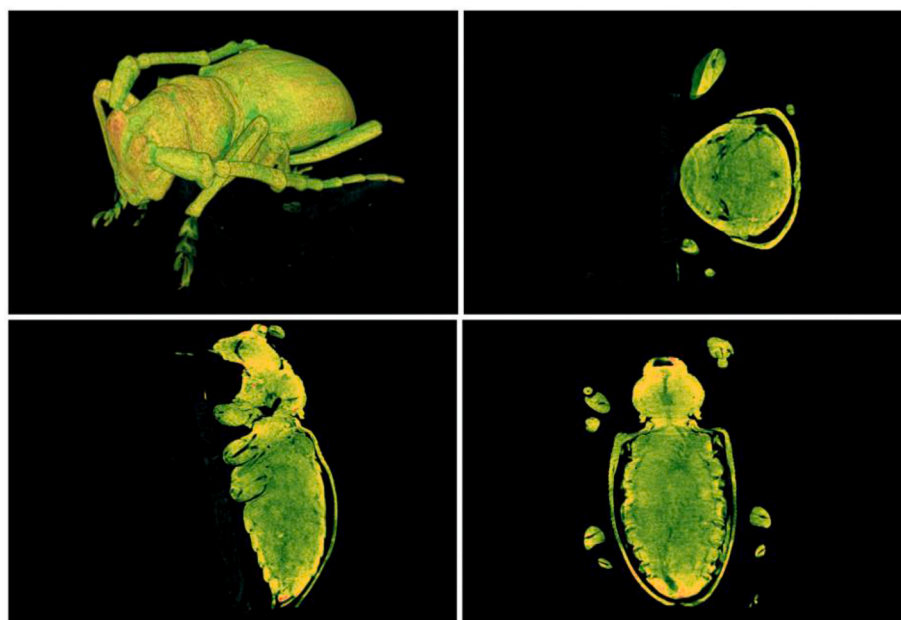
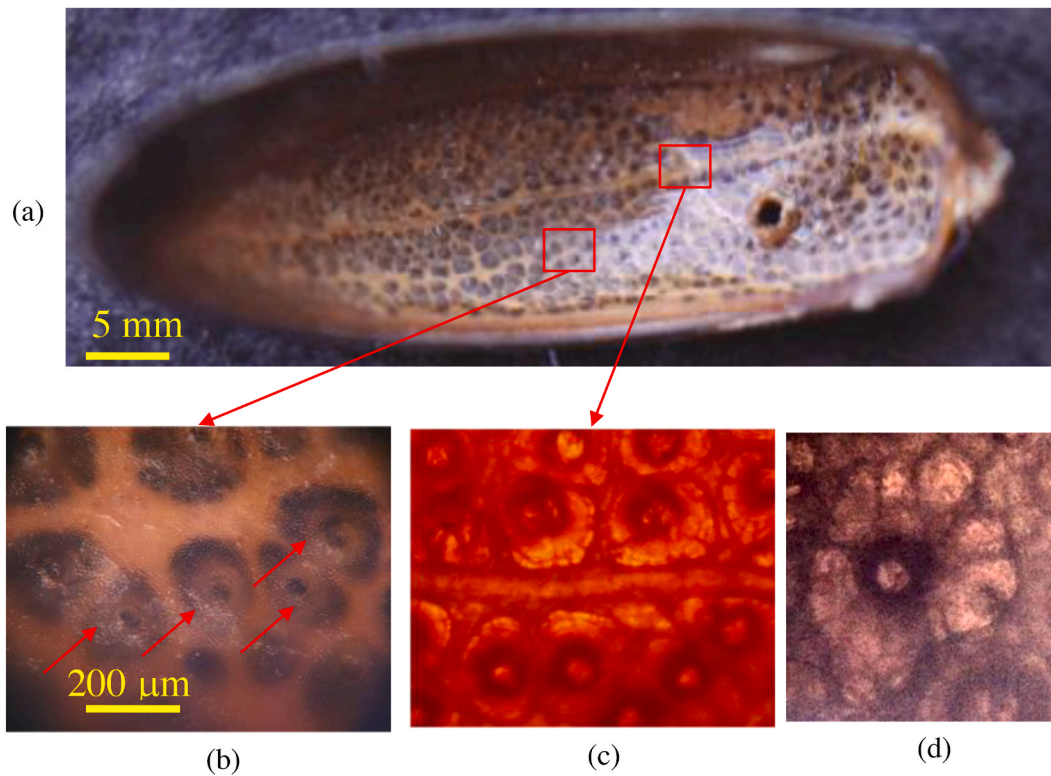
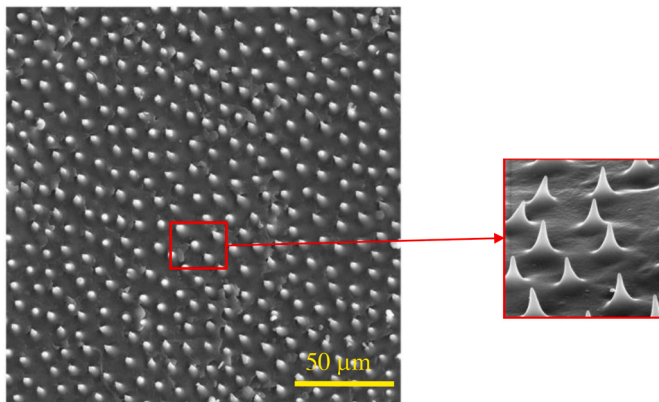


Fig. 3. (a) 3D reconstruction of *M. asper funereus* from a stack of MicroCT images. (b) frontal, (c) axial and (d) longitudinal cross sections of insect showing air filled space between elytra and the rest of the body.





**Fig. 4.** (a) Optical image of inner elytral surface of *M. asper funereus* in its natural state, exhibiting its original pigmentation. Enlarged portion in (b) shows blackbody-like (BB) structures (spherical-looking, with a black spot in the centre – red arrows). (c) Transmission optical image of elytron reveals a system of channels, branching from the central channel and surrounding each BB. (d) Elytron bleached in peroxide reveals a network of smaller channels, connecting the BB to the main microfluidic channels.



**Fig. 5.** SEM image of inner elytral surface of *M. asper funereus* with an array of microtrichia, enlarged in the inset.

elytra. That is why both types of hairs efficiently scatter the radiation and enhance the probability of radiation being absorbed.

### 3.3. Modelling of *M. asper funereus* elytron

#### 3.3.1. Blackbody array

Based on the anatomical features described in section 3.1, we were able to design a model of *M. asper funereus*. We took the oval zone of Fig. 4 as an elementary unit, composed of a layered blackbody surrounded by walls with microchannels. Blackbody is enclosed between two layers, one containing microlenses and the other covered by microtrichia.

We used 3D, open-source, computer graphics software (Blender, free

under GPL) to visualize the elementary unit of *M. asper funereus* elytra. Fig. 10(a) and (b) show two aspects of an elementary cell, so that the spatial relations between the microlenses, walls with microchannels and blackbody are clearly seen. Microlenses focus radiation directly into the elytron and microchannel filled with hemolymph (primarily water), as confirmed by ray tracing (Fig. 11) within a quite large angular range ( $-20^\circ$  to  $+20^\circ$ ).

We made a more exact finite element modelling of IR wave propagation in the cuticle. To do that, we needed complex refractive indices of hemolymph and insect cuticle at thermal infrared wavelengths. Hemolymph is mostly composed of water and we used the data from Hale and Querry (1973) – complex refractive index was averaged to  $n = 1.2 + i \cdot 0.0343$ , within 3–5  $\mu\text{m}$ , and  $n = 1.35 + i \cdot 0.13$ , within 8–12  $\mu\text{m}$ . Optical constants of insect cuticle at thermal infrared are not very well known and we used data extracted from Shi (2018) – within 3–5  $\mu\text{m}$  complex refractive index was  $n = 1.57 + i \cdot 0.005$  and within 8–12  $\mu\text{m}$ ,  $n = 1.57 + i \cdot 0.1$ . The absorption of melanin was not taken into account because it is found only in a thin superficial layer of elytra, its concentration is low, compared to that of chitin, and its absorption maximum is at UV.

Within the 8–12  $\mu\text{m}$  window, radiation is efficiently absorbed in the superficial layers of the cuticle due to the very high absorption coefficient of chitin (see Fig. 12(b)). The situation is more interesting within the 3–5  $\mu\text{m}$  window, where the absorption is an order of magnitude lower (Shi, 2018). There, the radiation is indeed focused onto the microchannels (Fig. 12(c)), while the multilayer structure of the BB efficiently reflects and expels the radiation from the central cavity. Within this spectral range, radiation penetrates deep and heats the internal structures of cuticle (Fig. 12(c)). If there is a constant flow of hemolymph through the cuticle (Unruh and Chauvin, 1993) heat will be convectively transferred to the central cavity of the blackbody. That is why we propose that tiny hairs lining the cavity might function as

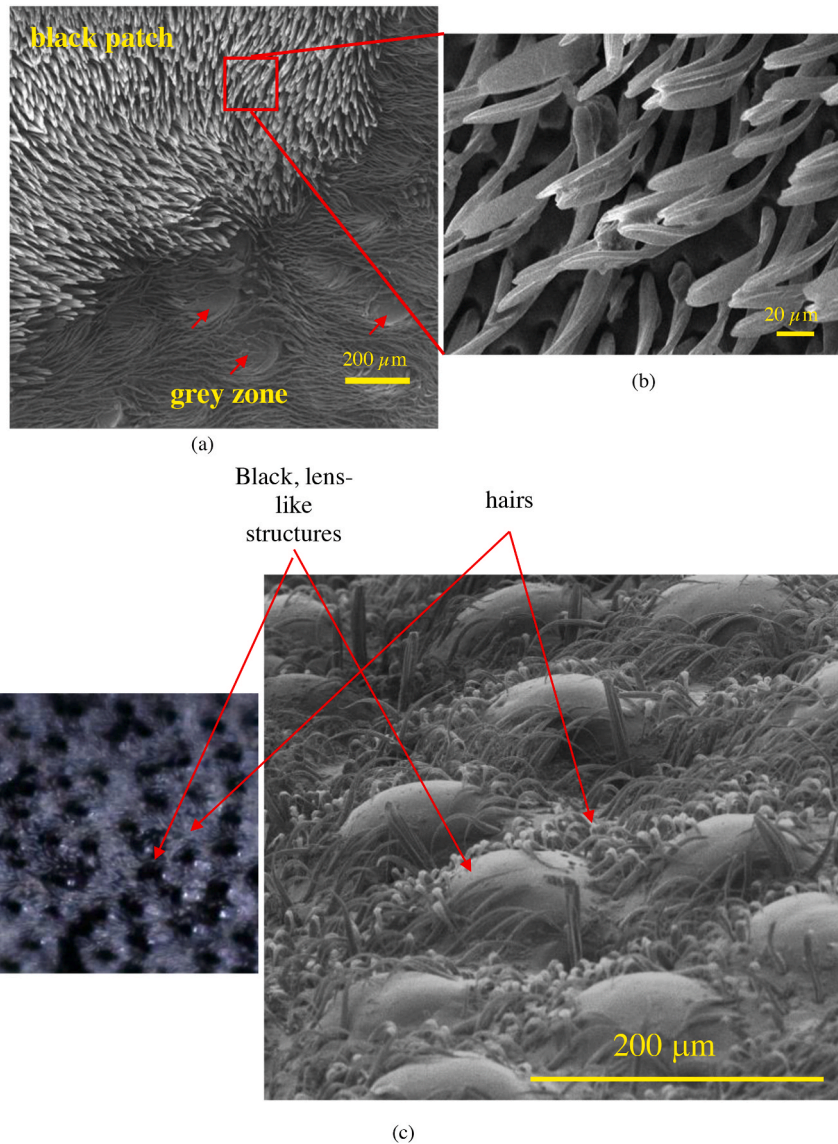


**Fig. 6.** SEM of the outer surface of the *M. asper funereus* elytra: (a) an edge between grey and black areas (red arrows indicate microlens-like protrusions); (b) enlarged SEM image of black scales. (c) Lens-like structures and hairs on the outer surface of *M. asper funereus*. Optical image is on the left and SEM image on the right. The captured area with lens-like structures is from the grey zone of the elytra.

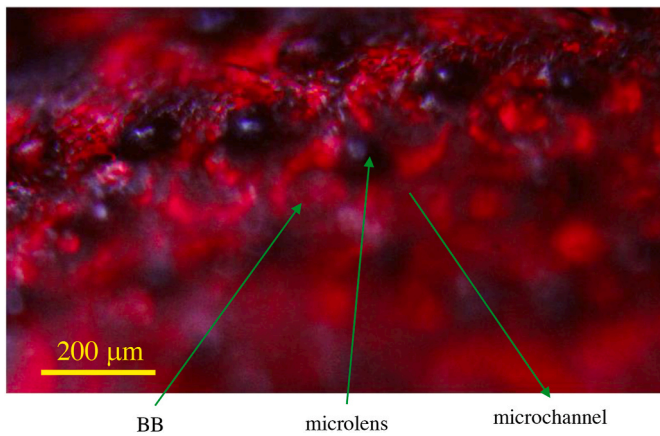


**Fig. 7.** Optical microscope image of elytron, simultaneously illuminated in reflection and transmission. Microlenses can be seen as black circular areas, blackbodies are doughnut-shaped zones within the network of channels.

sensilla, signalling the insect to search for a cooler place - which is a behavioural characteristic of this particular insect.

It seems that cuticular microlenses function like the cornea of an ommatidium, i.e. they focus radiation onto the sensitive layer. The architecture of *M. asper funereus* is well organized for the purpose.

### 3.3.2. Array of microtrichia

As can be seen from micro-CT images (Fig. 3), there is a thin (less than a millimetre) air-filled gap between the elytra and the insect body (see scheme at Fig. 13). Thermal energy is radiatively exchanged between those layers, thus filling the gap with infrared radiation. For the part of radiative energy propagating at grazing incidence, gap behaves as a hollow waveguide (such as those used for 10.6 μm CO<sub>2</sub> lasers – (Komachi et al., 2000)) with microtrichie as subwavelength scattering (diffractive) structures. In such waveguides, radiation propagates in a whispering-gallery manner.

In the following we will analyze their possible role in thermal radiation exchange of *M. asper funereus*. For the purpose of better understanding, we will treat microtrichie as a forest-like structure of almost conical protuberances on an otherwise flat surface. Each cone is 4.4 μm

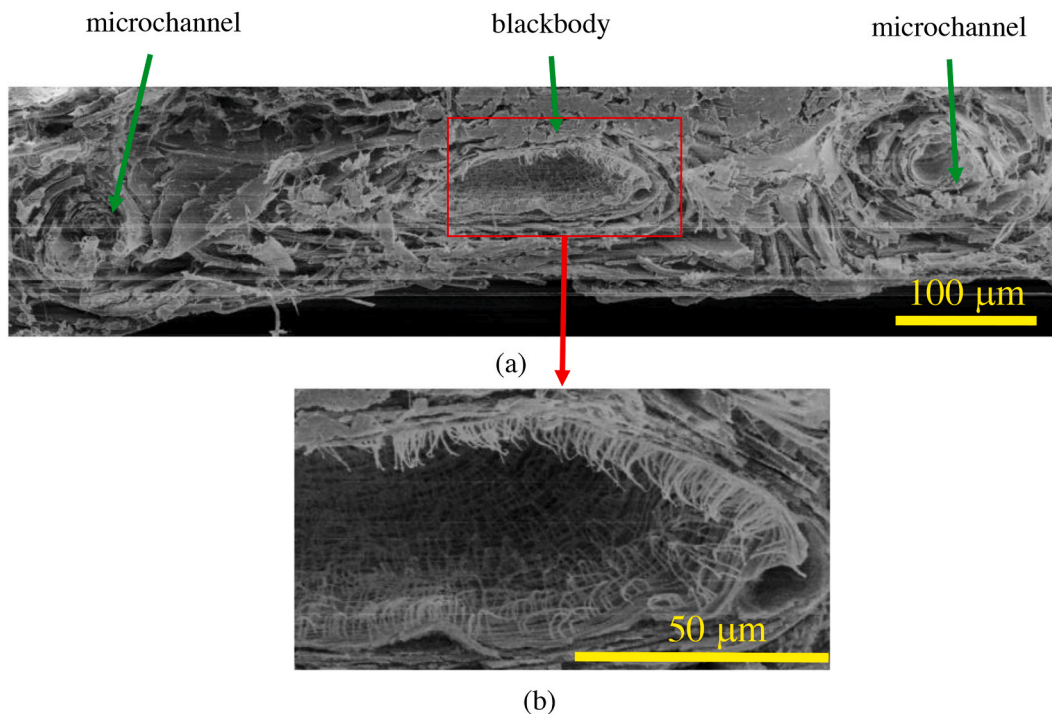


**Fig. 8.** (a) Cross section of *M. asper funereus* elytron with clearly visible blackbody with microchannels on both sides. (b) Enlarged image reveals the hair-like protrusions lining the internal surface of the blackbody.

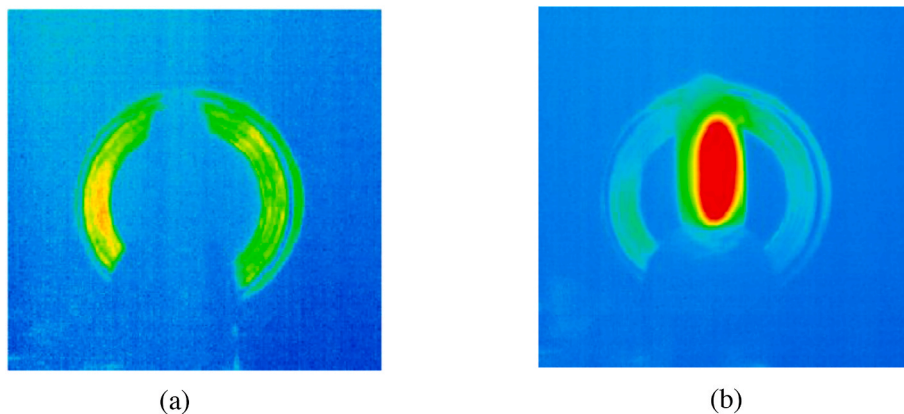


**Fig. 9.** (a) Thermal image of *M. asper funereus* elytra positioned in front of a blackbody. Emissivity is the same and they cannot be discerned. (b) When heated, the elytron becomes visible.

in diameter at its base and 3.8  $\mu\text{m}$  in height. An observer looking from above will see an arrangement like that in Fig. 14, schematically drawn using the section of Fig. 5 as a template. Looking from the side, as if sitting on the substrate, densely overlapping cone projections, even for a small number of microtrichia surrounding the central one, are observed. Thus, for the large number of microtrichia on the elytron, the radiation propagating close to the surface has a high chance of hitting a cone and being absorbed. This is a purely geometric optic analysis – in the following we will present a wave optics perspective.

Upon closer inspection of the spatial distribution of microtrichia (Fig. 5), we can see that it is neither regular nor completely random (rods in the chicken retina are arranged in a similar fashion (Jiao et al., 2014)). It is characterized by a ring-like Fourier transform, as in Fig. 15 (a). The spatial frequency of the prominent ring-like structure is 0.1/ $\mu\text{m}$ , corresponding to the average 10- $\mu\text{m}$  distance between microtrichia (Fig. 15(b)). The amplitude of the Fourier transform goes to zero as the spatial frequencies approach the central Fourier peak. This is a

characteristic of hyperuniform point distributions, which were shown to behave as a complete photonic bandgap structure (Florescu et al., 2009). The slight ellipticity of the Fourier transform observed here is possibly a consequence of the ellipsoidal profile of the elytron.

For thermal radiation entrapped between the elytra and the body, A 2-dimensional hyperuniform system behaves as a random full-bandgap photonic crystal. This can be inferred from the ring-like Fourier transform (Fig. 15(a)), which can be understood as a superposition of sinusoidal gratings with a 10- $\mu\text{m}$  period oriented in all directions along the plane substrate. Under grazing incidence, gratings behave as Bragg reflectors, blocking the propagation of radiation with the wavelength:

$$\lambda = 2d/N$$

where  $d$  is a grating period,  $N$  is an integer, assuming the normal angle of incidence. For the 10  $\mu\text{m}$  average period of microtrichia and  $N = 2$ , the Bragg wavelength is 10  $\mu\text{m}$ , right in the middle of an 8–12  $\mu\text{m}$  atmospheric window. Additionally, for  $N = 4$ , the Bragg wavelength

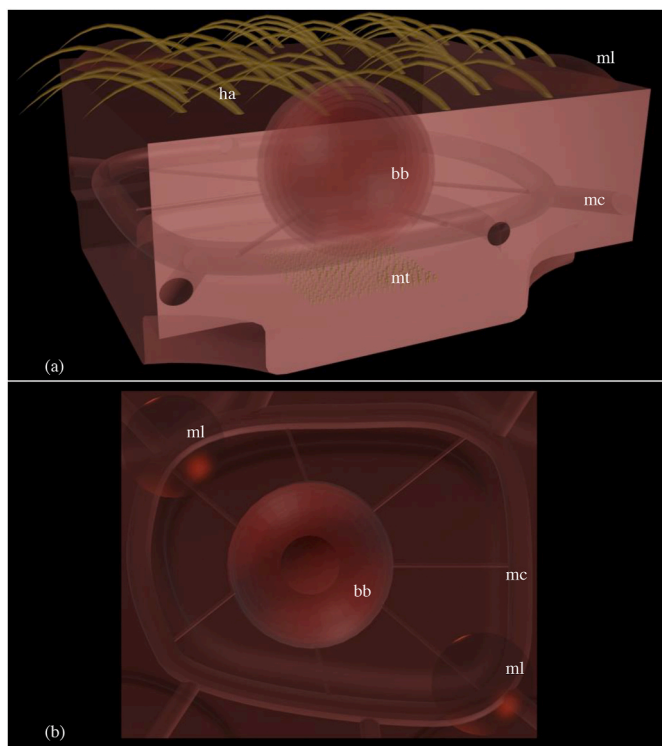


**Fig. 10.** (a) A semi-transparent 3D model of *M. asper funereus* elytron presenting internal structures hidden within the elytron (mt – microtrichia, mc – microchannels, ml – microlens, bb – black body, ha – hairs) (a) with microlenses and hairs clearly seen; (b) top view displaying alignment of microlenses and microchannels. The microchannel completely surrounds the blackbody and is connected to it via even smaller channels.

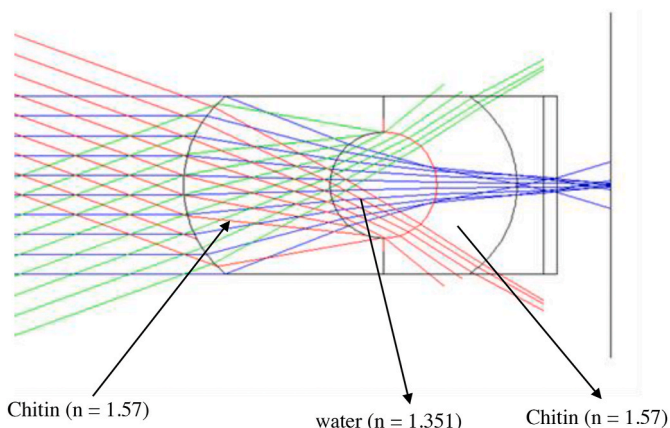


**Fig. 11.** Ray tracing through a microlens and microchannel (blue rays are incoming at normal incidence, while red and green rays obliquely, at  $+20^\circ$  and  $-20^\circ$ , illuminate the elytron). Calculations were done at  $3\ \mu\text{m}$ , where refractive indices are as indicated in figure.

corresponds to another window at  $3\text{--}5\ \mu\text{m}$ , but we were not able to check this experimentally.

#### 4. Discussion and conclusions

The search for highly absorbing structures is a long-standing one and many structured materials have been engineered so far (Mizuno et al., 2009), but only the vertically aligned nanotube array (VANTA black) (De Nicola et al., 2017) approaches the emissivity of a blackbody. In line with the research on silicon photonics for NIR silicon devices (Milošević

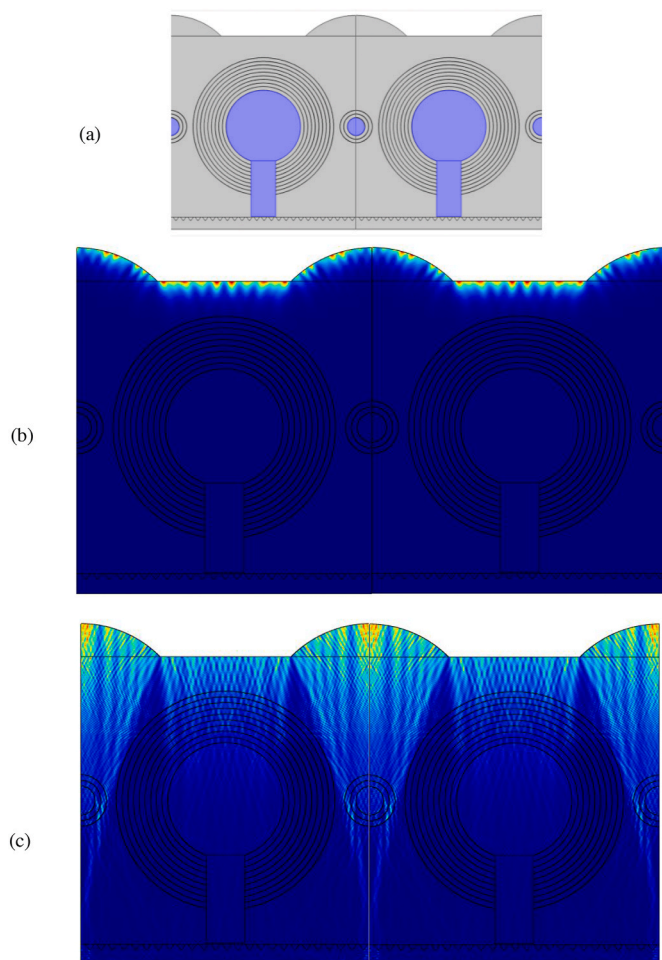


**Fig. 12.** (a) A model of *M. asper funereus* elytron used in FEM analysis (grey colour corresponds to chitin and purple to water). Distribution of thermal IR radiation inside *M. asper funereus* blackbody-like cuticular structure calculated by FEM. Two spectral windows were analysed: (b)  $8\text{--}12\ \mu\text{m}$  (image at  $10\ \mu\text{m}$  is shown) and (c)  $3\text{--}5\ \mu\text{m}$  (image at  $4\ \mu\text{m}$  is shown).

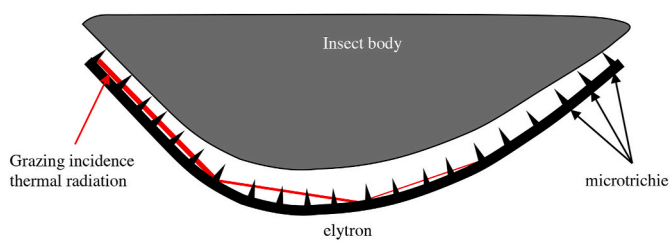


**Fig. 13.** *M. funereus* elytron and body with air filled gap acting as a hollow waveguide for grazing incidence thermal radiation.

et al., 2019), here we show that natural, less complex structures can achieve similar results owing to their forest-like structure and intrinsic curvature (Leonhardt and Tyc, 2009). A clever arrangement of hyper-uniform disordered structures efficiently competes with highly advanced nanotube structures. In contrast to artificial VANTA black material, which is fragile and complex to manufacture, the natural solution is robust and simple.

At this point, we are not able to estimate how important the role of microtrichie is. We must stress, however, that the amount of the radiation entrapped between elytra and the body is non-negligible due to Fresnel reflections and waveguiding. Simple calculation shows that, for the refractive index used in this study ( $n = 1.57$ ) and normal incidence,

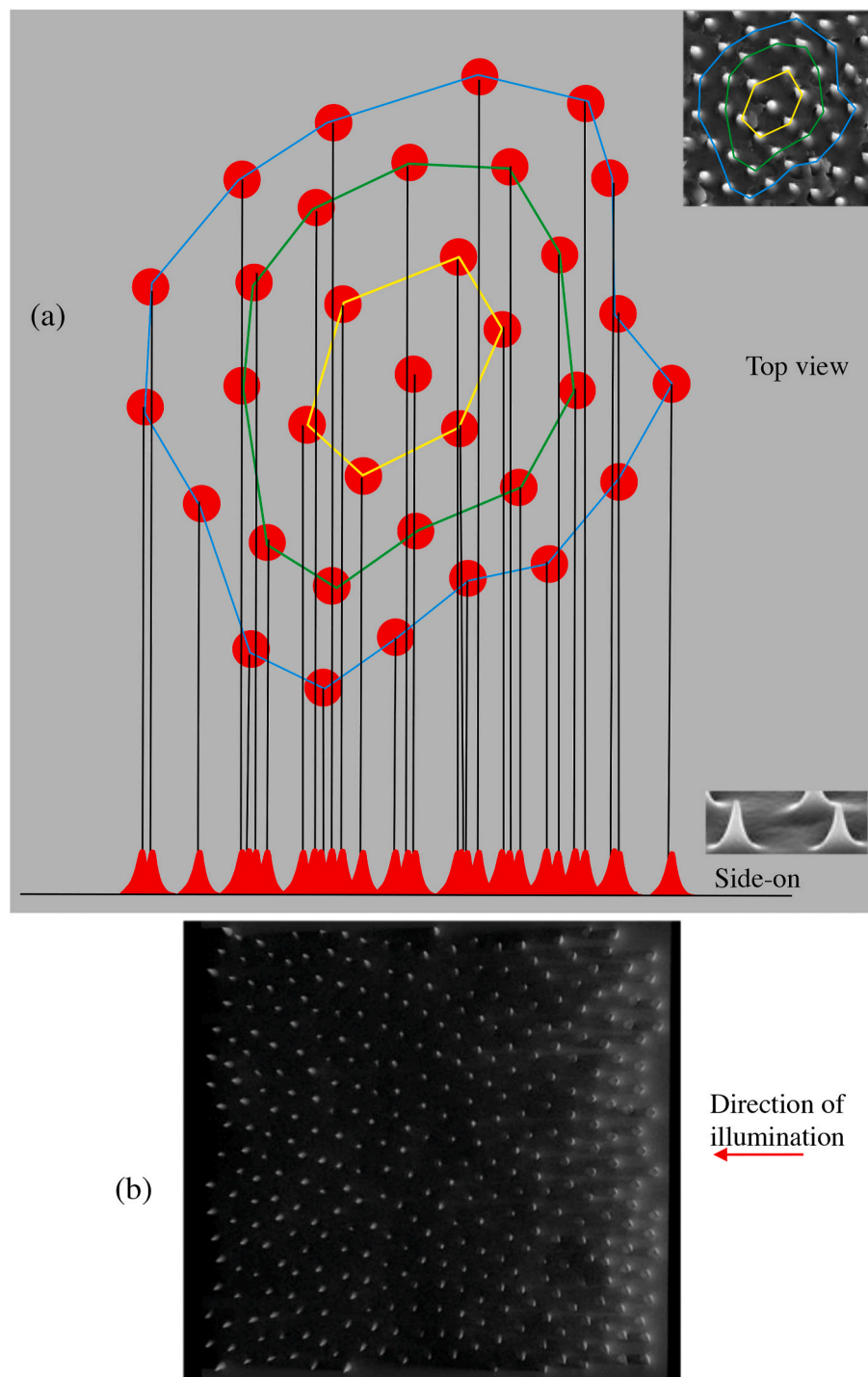


**Fig. 14.** (a) An arrangement of conical structures seen from above and drawn using Fig. 2 as a template. Inset in the upper right corner shows part of the SEM image used as a template. Side-on view is shown at the bottom of this figure. (b) Top view of a microtrichia 3D model illuminated obliquely from the right (red arrow) shows that microtrichia preclude the propagation of light.

4.99% of radiation is reflected, while for grazing incidence almost all radiation is reflected. Between those two extremes, due to uniform angular distribution of thermal radiation, it is clear that more than 4.99% of thermal radiation is entrapped and waveguided between body and elytra. More detailed answer to this question will be given in further studies.

In the interests of brevity and focus, several other elytral features that might be effective in thermal IR had to be left out of the scope of this paper. First of all, the chitinous lamellae of *M. asper funereus* have a

characteristic dimension of 4–5  $\mu\text{m}$  with the corresponding Bragg wavelength of 8–10  $\mu\text{m}$ . Each layer contains well-oriented microfibrils that certainly introduce birefringence, and the orientation of microfibrils is different in each layer (Supplement file). The exact value of the refractive index of chitinous structures is not very well known, in particular in the thermal infrared, and it is therefore difficult to make the correct theoretical calculations and numerical simulations. Thirdly, interfaces between each layer are rough and scatter radiation, so that the layers may act as planar waveguides to additionally absorb the

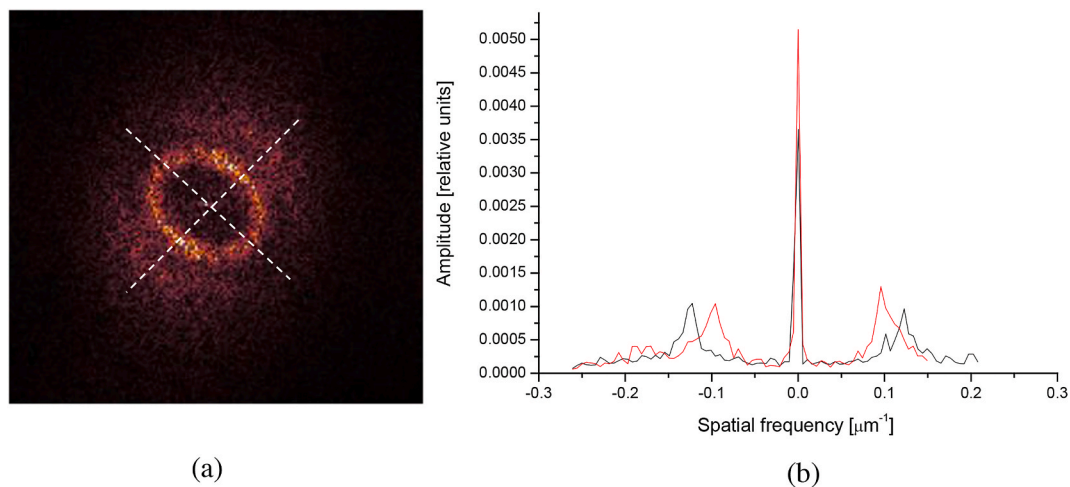


**Fig. 15.** (a) A Fourier transform of the image in Fig. 2 depicting the arrangement of microtrichia. Note the ring-like pattern with slight ellipticity. (b) Scanning along two orthogonal directions (see dotted lines in (a)) shows a pronounced peak at spatial frequency close to  $0.1/\mu\text{m}$ , corresponding to the average  $10\text{-}\mu\text{m}$  distance between microtrichia.

radiation. Finally, microtrichia can act as transmission gratings for non-obliquely impinging radiation and diffraction orders can be coupled into layers as planar waveguides.

From a theoretical point of view, it is quite difficult to treat inherently random structures (such as those of *M. asper funereus*) using exact methods like FEM, RCWA or FDTD. For large structures, periodic boundary conditions have to be introduced, thereby violating inherent randomness. If a random structure is to be simulated, computer memory requirements become extremely large and computational time intolerably long.

We performed other measurements that have revealed the excellent thermal insulation properties of this particular insect. By laser-heating one side of an elytron we observed that, in thermal equilibrium, the other side was approximately  $20\text{ }^{\circ}\text{C}$  lower in temperature. It is difficult to discern the contribution of radiative dissipation, with respect to other processes (convection and conduction) (Supplement file). However, the *M. asper funereus* elytron could be an excellent model to design similar thermally insulating materials.

Furthermore, taking into account that *M. asper funereus* lays its eggs in and emerging larvae feed on decaying wood (a saproxylic way of life), similarly to pyrophilous insects (Klocke et al., 2011), it is important for an insect to detect dead trees. Thermal fingerprint of a decaying wood is different, compared to healthy specimens, primarily due to the reduced amount of water. (Pitarma et al., 2019). Based on the structures and properties we have observed, we postulate that a number of infrared detectors on the elytron is used to detect the infrared fingerprint of wood and discriminate between healthy and decaying tree trunks. Even though the number of elytral IR detectors (approx. 400) is small, it is still a useable one, if compared to that of FLIR ONE Gen3 smart-phone, clip-on thermal cameras (60 x 80 IR pixels). By making this comparison we emphasize the “ingenuity” of evolution, in no way endorsing any particular IR camera.

It is well known that Coleoptera elytron has a complex layered structure with number of cavities, trabeculae, channels and pores (Sun and Bhushan, 2012). Research mostly dealt with mechanical significance of internal architecture of elytron (Du and Hao, 2018), and to a lesser degree with thermal effects (Le et al., 2019). By studying available literature we may say that many of structures might serve similar role in thermal radiation management, due to their characteristic dimensions being close to the wavelength of thermal radiation.

In conclusion, we have shown that a combination of micron-sized blackbodies and uniformly random microstructures possesses excellent properties to manage thermal radiation. The range of potential

applications is enormous and even might even extend from NIR to terahertz technology.

#### Funding

This work was supported by the Serbian Ministry of Education, Science and Technological Development, and the Science and Technology Development Programme – Joint Funding of Development and Research Projects of the Republic of Serbia and the People’s Republic of China: Mimetics of insects for sensing and security, No. I-2. BK acknowledges support from the F.R.S.- FNRS. DP acknowledges support from L’Oréal-UNESCO “For Women in Science”.

#### Ethical approval

All necessary permissions to collect the samples of *M. asper funereus* were obtained from the Ministry of Environmental Protection of the Republic of Serbia and the Institute for Nature Conservation of Serbia. The research did not include live insects.

#### Author statement

**Darko Vasiljević** : Formal analysis, Data Curation, Visualization.  
**Danica Pavlović**: Conceptualization, Formal analysis, Investigation, Resources, Writing-Original Draft Preparation.  
**Vladimir Lazović**: Formal analysis.  
**Branko Kolarić**: Project Administration, Writing Review and Editing.  
**Branislav Salatić**: Softwer, Formal analysis.  
**Wang Zhang**: Supervision, Validation.  
**Di Zhang**: Supervision, Validation.  
**Dejan Pantelić**: Conceptualization, Methodology, Investigation, Formal analysis, Writing-Original Draft Preparation.

#### Declaration of competing interest

The authors declare no conflict of interest.

#### Appendix A. Supplementary data

Supplementary data to this article can be found online at <https://doi.org/10.1016/j.jtherbio.2021.102932>.

## References

- Arikawa, K., Takagi, N., 2001. Genital photoreceptors have crucial role in oviposition in Japanese yellow swallowtail butterfly, *Papilio xuthus*. *Zool. Sci.* 18 (2), 175–179. <https://doi.org/10.2108/zsj.18.175>.
- Booth, C.O., 1963. Photocinetic function of aphid antennae. *Nature* 197, 265–266.
- Bosi, S.G., Hayes, J., Large, M.C.J., Poladian, L., 2008. Color, iridescence, and thermoregulation in Lepidoptera. *Appl. Opt.* 47, 5235–5241. <https://doi.org/10.1364/AO.47.005235>.
- Capinera, J.L., 2008. *Encyclopedia of Entomology*. Springer, New York.
- Carpaneto, G.M., Baviera, C., Biscaccianti, A.B., Brandmayr, P., Mazzei, A., Mason, F., Battistoni, A., Teofili, C., Rondinini, C., Fattorini, S., Audisio, P., 2015. A Red List of Italian Saproxyllic Beetles: taxonomic overview, ecological features and conservation issues (Coleoptera). *Fragm. Entomol.* 47, 53. <https://doi.org/10.4081/fe.2015.138>.
- Cossins, A., 2012. *Temperature Biology of Animals*. Springer Science & Business Media.
- De Nicola, F., Hines, P., De Crescenzi, M., Motta, N., 2017. Thin randomly aligned hierarchical carbon nanotube arrays as ultrablack metamaterials. *Phys. Rev. B* 96 (4), 045409. <https://doi.org/10.1103/PhysRevB.96.045409>.
- Desmond Ramirez, M., Speiser, D.I., Sabrina Pankey, M., Oakley, T.H., 2011. Understanding the dermal light sense in the context of integrative photoreceptor cell biology. *Vis. Neurosci.* 28, 265–279. <https://doi.org/10.1017/S0952523811000150>.
- Doucet, S.M., Meadows, M.G., 2009. Iridescence: a functional perspective. *J. R. Soc. Interface* 6 (Suppl. 1.2), S115–S132. <https://doi.org/10.1098/rsif.2008.0395.focus>.
- Du, J., Hao, P., 2018. Investigation on microstructure of beetle elytra and energy absorption properties of bio-inspired honeycomb thin-walled structure under axial dynamic crushing. *Nanomaterials* 8 (9), 667. <https://doi.org/10.3390/nano8090667>.
- Florescu, M., Torquato, S., Steinhardt, P.J., 2009. Designer disordered materials with large, complete photonic band gaps. *Proc. Natl. Acad. Sci. Unit. States Am.* 106 (49), 20658–20663. <https://doi.org/10.1073/pnas.0907744106>.
- Gillott, C., 2005. Food uptake and utilization. *Entomology (Tokyo)* 487–513. [https://doi.org/10.1007/1-4020-3183-1\\_16](https://doi.org/10.1007/1-4020-3183-1_16).
- Gullan, P.J., Cranston, P.S., 2004. *The Insects: An Outline of Entomology*. John Wiley & Sons.
- Hale, G.M., Querry, M.R., 1973. Optical constants of water in the 200-nm to 200- $\mu$ m wavelength region. *Appl. Opt.* 12 (3), 555–563. <https://doi.org/10.1364/ao.12.000555>.
- Hardersen, S., Bardiani, M., Chiari, S., Maura, M., Maurizi, E., Roversi, P.F., Mason, F., Bologna, M.A., 2017. Guidelines for the monitoring of *Morimus asper funereus* and *Morimus asper asper*. *Nat. Conserv.* 20, 205–236. <https://doi.org/10.3897/natureconservation.20.12676>.
- Heinrich, B., 2013. *The Hot-Blooded Insects: Strategies and Mechanisms of Thermoregulation*. Springer Science & Business Media, New York.
- Horton, K.G., Shriver, W.G., Buler, J.J., 2015. A comparison of traffic estimates of nocturnal flying animals using radar, thermal imaging, and acoustic recording. *Ecol. Appl.* 25 (2), 390–401. <https://doi.org/10.1890/14-0279.1.sm>.
- Jiao, Y., Lau, T., Hatzikirou, H., Corbo, J.C., Torquato, S., Mathematics, A., 2014. Avian photoreceptor patterns represent a disordered hyperuniform solution to a multiscale packing. *Phys. Rev.* 89 (2), 022721. <https://doi.org/10.1103/PhysRevE.89.022721>.
- Kastberger, G., Stachl, R., 2003. Infrared imaging technologies. *Behav. Res. Methods Instrum. Comput.* 35 (3), 429–439.
- Kemp, D.J., 2007. Female butterflies prefer males bearing bright iridescent ornamentation. *Proc. Biol. Sci.* 274 (1613), 1043–1047. <https://doi.org/10.1098/rspb.2006.0043>.
- Kingsolver, J.G., 1985. Butterfly thermoregulation: organismic. *J. Res. Lepid.* 24 (1), 1–20.
- Klocke, D., Schmitz, A., Soltner, H., Bousack, H., Schmitz, H., 2011. Infrared receptors in pyrophilous (“fire loving”) insects as model for new un-cooled infrared sensors. *Beilstein J. Nanotechnol.* 2 (1), 186–197. <https://doi.org/10.3762/bjnano.2.22>.
- Komachi, Y., Wakaki, M., Kanai, G., 2000. Fabrication of hollow waveguides for CO<sub>2</sub> lasers. *Appl. Opt.* 39 (10), 1555–1560. <https://doi.org/10.1364/ao.39.001555>.
- Le, V.T., Ha, N.S., Goo, N.S., 2019. Thermal protective properties of the allomyrina dichotoma beetle forewing for thermal protection systems. *Heat Tran. Eng.* 40, 1539–1549. <https://doi.org/10.1080/01457632.2018.1474603>.
- Leonhardt, U., Tyc, T., 2009. Broadband invisibility by non-Euclidean cloaking. *Science* 323 (5910), 110–112. <https://doi.org/10.1126/science.1166332>.
- Millott, N., 1968. The dermal light sense. In: *Symp. Zool. Soc. London*, pp. 1–36.
- Milošević, M.M., Man, W., Nahal, G., Steinhardt, P.J., Torquato, S., Chaikin, P.M., Amoah, T., Yu, B., Mullen, R.A., Florescu, M., 2019. Hyperuniform disordered waveguides and devices for near infrared silicon photonics. *Sci. Rep.* 9 (1), 1–11. <https://doi.org/10.1038/s41598-019-56692-5>.
- Mizuno, K., Ishii, J., Kishida, H., Hayamizu, Y., Yasuda, S., Futaba, D.N., Yumura, M., Hata, K., 2009. A black body absorber from vertically aligned single-walled carbon nanotubes. *Proc. Natl. Acad. Sci. Unit. States Am.* 106 (15), 6044–6047. <https://doi.org/10.1073/pnas.0900155106>.
- Nijhout, H.F., 1991. *The Development and Evolution of Butterfly Wing Patterns*, vol. 293. Smithsonian. Inst. Sch. Press.
- Parisi, V., Busetto, A., 1992. Revisione dei Coleotteri presenti nella collezione “A. Leosini”. Parte 2a. Scarabaeidae, Lucanidae, Cerambycidae. *Pubblicazioni del Museo di Storia naturale dell’Università di Parma* 5 (1), 1–93.
- Pitarma, R., Crisóstomo, J., Ferreira, M.E., 2019. Contribution to trees health assessment using infrared thermography. *Agriculture* 9 (8), 171. <https://doi.org/10.3390/agriculture9080171>.
- Polak, S., Maja, J., 2012. Phenology and mating behaviour of *Morimus funereus* (Coleoptera, Cerambycidae). *Saproxyllic beetles in Europe: monitoring, biology and conservation. Studia Forestalia Slovenica* 137, 43–52.
- Prokhorov, A., 2012. Effective emissivities of isothermal blackbody cavities calculated by the Monte Carlo method using the three-component bidirectional reflectance distribution function model. *Appl. Opt.* 51, 2322–2332. <https://doi.org/10.1364/AO.51.002322>.
- Romero-Samper, J., Bahülo, J., 1993. Algunas observaciones sobre la distribución y biología de *Morimus asper* Cerambycidae en la Península Ibérica. *Bol. Asoc. Esp. Entomol.* 17, 103–122.
- Scoble, M.J., 1992. *The Lepidoptera. Form, Function and Diversity*. Oxford University Press.
- Shi, N.N., 2018. *Biological and Bioinspired Photonic Materials for Passive Radiative Cooling and Waveguiding*. Doctoral dissertation. Columbia University.
- Shi, N.N., Tsai, C.C., Camino, F., Bernard, G.D., Yu, N., Wehner, R., 2015. Keeping cool: enhanced optical reflection and radiative heat dissipation in Saharan silver ants. *Science* 349 (6245), 298–301. <https://doi.org/10.1126/science.aab3564>.
- Solano, E., Mancini, E., Ciucci, P., Mason, F., Audisio, P., Antonini, G., 2013. The EU protected taxon *Morimus funereus* Mulsant, 1862 (Coleoptera: Cerambycidae) and its western Palaearctic allies: systematics and conservation outcomes. *Conserv. Genet.* 14 (3), 683–694. <https://doi.org/10.1007/s10592-013-0461-3>.
- Stabentheiner, S., Schmaranzer, A., 1987. Thermographic determination of body temperatures in honey bees and hornets: calibration and applications. *Thermology* 2, 563–572.
- Stabentheiner, A., Kovac, H., Hetz, S.K., Käfer, H., Stabentheiner, G., 2012. Assessing honeybee and wasp thermoregulation and energetics - new insights by combination of flow-through respirometry with infrared thermography. *Thermochim. Acta* 534, 77–86. <https://doi.org/10.1016/j.tca.2012.02.006>.
- Stanić, V., Ivanović, J., Janković-Hladni, M., Nenadović, V., Marović, R., 1985. Feeding habits, behavior, oviposition and longevity of the adult cerambycid beetle *Morimus asper funereus* Muls. (Col., Cerambycidae) under laboratory condition. *Acta Entomol. Jugosl.* 21, 87–94.
- Sun, J., Bhushan, B., 2012. Structure and mechanical properties of beetle wings: a review. *RSC Adv.* 2 (33), 12606–12623. <https://doi.org/10.1039/c2ra21276e>.
- Sun, J., Liu, C., Bhushan, B., Wu, W., Tong, J., 2018. Effect of microtrichia on the interlocking mechanism in the Asian ladybeetle, *Harmonia axyridis* (Coleoptera: Coccinellidae). *Beilstein J. Nanotechnol.* 9 (1), 812–823. <https://doi.org/10.3762/bjnano.9.75>.
- Sweeney, A., Jiggins, C., Johnsen, S., 2003. Polarized light as a butterfly mating signal. *Nature* 423, 31–32. <https://doi.org/10.1038/423031a>.
- Tucolesco, J., 1933. La dynamique de la larve de *Tenebrio molitor* et la théorie des tropismes. *Bull. Biol.* 4, 1–35.
- Unruh, T.R., Chauvin, R., 1993. Elytral punctures: a rapid, reliable method for marking Colorado potato beetle. *Can. Entomol.* 125 (1), 55–63.
- van de Kamp, T., Greven, H., 2010. On the architecture of beetle elytra. *Entomol. Heute* 22, 191–204.
- van de Kamp, T., Riedel, A., Greven, H., 2016. Micromorphology of the elytral cuticle of beetles, with an emphasis on weevils (Coleoptera: Curculionidae). *Arthropod Struct. Dev.* 45 (1), 14–22. <https://doi.org/10.1016/j.asd.2015.10.002>.
- Verstraete, C., Mouchet, S.R., Verbiest, T., Kolaric, B., 2019. Linear and nonlinear optical effects in biophotonic structures using classical and nonclassical light. *J. Biophot.* 12, 1–13. <https://doi.org/10.1002/jbio.201800262>.
- Vollmer, M., Möllmann, K.P., 2010. *Infrared Thermal Imaging: Fundamentals, Research and Applications*. John Wiley & Sons.
- Vukusic, P., Sambles, J.R., 2003. Photonic structures in biology. *Nature* 424 (6950), 852–855. <https://doi.org/10.1038/nature01941>.
- Vukusic, P., Sambles, J.R., Lawrence, C.R., Wootton, R.J., 2001. Now you see it - now you don't. *Nature* 410 (6824). <https://doi.org/10.1038/35065161>, 36–36.

## Agglomeration in core-shell structure of CuAg nanoparticles synthesized by the laser ablation of Cu target in aqueous solutions

This content has been downloaded from IOPscience. Please scroll down to see the full text.

2015 J. Opt. 17 025402

(<http://iopscience.iop.org/2040-8986/17/2/025402>)

View [the table of contents for this issue](#), or go to the [journal homepage](#) for more

Download details:

IP Address: 178.222.22.22

This content was downloaded on 12/03/2015 at 21:47

Please note that [terms and conditions apply](#).



# Agglomeration in core-shell structure of CuAg nanoparticles synthesized by the laser ablation of Cu target in aqueous solutions

S Petrović<sup>1</sup>, B Salatić<sup>2</sup>, D Milovanović<sup>1</sup>, V Lazović<sup>2</sup>, Lj Živković<sup>1</sup>,  
M Trtica<sup>1</sup> and B Jelenković<sup>2</sup>

<sup>1</sup>University of Belgrade, Institute of Nuclear Science-Vinča, POB 522, 11001 Belgrade, Serbia

<sup>2</sup>University of Belgrade, Institute of Physics, Pregrevica 118, 11080 Belgrade, Serbia

E-mail: [spetro@vinca.rs](mailto:spetro@vinca.rs)

Received 8 October 2014, revised 27 November 2014

Accepted for publication 10 December 2014

Published 9 January 2015



CrossMark

## Abstract

Metallic copper Cu and bimetallic copper–silver CuAg nanoparticles (NPs) are generated by the ablation of copper bulk target in water and aqueous Ag colloidal solution, respectively. The experiments were performed using nanosecond Nd:YAG laser operating at 1064 nm. The generated NPs are characterized by UV–vis absorption spectroscopy, laser-induced breakdown spectroscopy, dynamic light scattering and scanning electron microscopy. The conducted investigations can be summarized as follows: (i) CuAg NPs colloidal solution possess the absorption in UV–vis spectral region, which can be attributed to the Cu-component; (ii) the primary bimetallic CuAg NPs have near uniform dimensions with diameter of about 15 nm, and as a rule, they are grouped into larger agglomerates without defined morphology; (iii) the obtained Cu NPs have mainly spherical form with average diameters up to 20 nm. Both types of NPs show a tendency towards the formation of large agglomerates with different morphology. Bimetallic NPs show the plasmon resonance in the vicinity of 640 nm with a good coincidence with formation of the colloidal solution of pure Cu NPs. The results also demonstrate that the core–shell structure (Ag-rich core/Cu-rich shell) is important for the formation of the bimetallic NPs, also agreeing very well with theory.

Keywords: bimetallic nanoparticles, laser ablation in liquids, core-shell structure

(Some figures may appear in colour only in the online journal)

## Introduction

Nanoparticles (NPs) with a small size of several tens of nanometers have unique physical and chemical properties quite different from those of larger particles of the same material [1–3]. NPs have attracted a great interest in scientific research and industrial applications, owing to their unique large surface-to-volume ratios and quantum-size effects. Today, metal NP research is an area of intense scientific study due to a wide range of potential applications, from catalysis, biomedicine to electronics. Nanoparticle characteristics include shape, size, composition, crystallinity and structure, with the unusual dimensionally dependent optical and electronic properties [4, 5]. The surface of NPs is mostly

attractive for applications using their physico–chemical properties, such as those involving their functionalization with different molecules for biomedical or catalytic effects.

Besides the NPs of pure metals, particularly interest has attracted bimetallic NPs that involve alloying of metals as a way for developing new materials. Intermetallic compounds at nanometer scale have various structural and physical properties caused by the increase of the solubility of alloying components with decreasing particle size. Bimetallic NPs composed of the transition and noble metals have unique properties due to excellent thermodynamic stability, and therefore, different behaviour with temperature in functionality applications. Mostly, bimetallic NPs have a complicated structure, classified into a few classes based on the

capabilities of their mutual mixing (random, cluster-in-cluster, core-shell and nanoalloy) [6, 7]. In many cases, the specific properties of bimetallic NPs are enhanced because of the synergistic effects of the two distinct metals. Copper-based NPs may be useful in applications involving conductive thin films, lubrication and nanofluids, but also catalysis, semiconductors and electromagnetic wave shields. The Cu NPs incorporated into a dielectric environment (polymer) make this material suitable for nonlinear optical devices [8–11]. Bimetallic CuAg NPs are an effective antibacterial material, with improved antibacterial activity against gram-positive and gram-negative bacteria, even at a relatively low concentrations of less than  $0.3 \text{ mg l}^{-1}$ . On the other hand, CuAg NPs have proper adsorption strength to become a new generation of catalysts for the dissociation of oxygen [12–18].

The formation of NPs under the laser ablation of solids in a liquid environment has been studied to a much lesser extent compared to chemical techniques. The main advantage of this method is that it is simple and offers pure synthesis of NPs under ambient conditions, which do not require extreme pressures and temperatures [19]. The colloidal solutions of pure NPs are obtained easily and quickly and with high efficiency [20]. It has been proven that changing different parameters, such as laser wavelength, pulse duration, laser fluences, ablation time, the pH of the solution, temperature of solution and whether surfactants are added, one can control the size of synthesized NPs, which could lead to modification of the physical and chemical properties [21].

This paper reports on the possibilities of the synthesis of copper and bimetallic CuAg NPs by laser ablation in liquids. The copper targets placed in water or silver colloidal solution were irradiated by laser beam pulses in the nanoseconds time domain. We investigated the effect of a 1064 nm nanosecond-pulsed (Nd:YAG) laser on the composition and structural properties of NPs formed in different liquids. Multi-pulse action with a focused beam and relatively medium pulse energy was used to induce ablation/evaporation of material in the irradiation areas. Special attention was paid to the synthesis CuAg NPs using previously prepared Ag colloidal solution, as a starting liquid for processing Cu targets by laser ablation. Our emphasis was to study the experimental irradiation conditions for the formation of bimetallic CuAg NPs in a form of intermetallic and/or core-shell structures.

## Experimental

Colloidal metallic copper and bimetallic copper-silver NPs were prepared by pulsed laser ablation of a bulk copper target (figure 1). The cleaned target of copper plate with 3 mm thickness and purity of 99.9% was placed on the bottom of a glass vessel, filled with 5 ml of liquid, resulting in 3 mm of liquid above the target surface. In this experiment, water and colloidal silver solution with a concentration of 20 ppm were used as liquids. Aqueous colloidal Ag solution was prepared electrolytically using double-distilled water and two silver electrodes (one positive and one negative). Voltage between electrodes was 12 V; when the current starts to rise, the

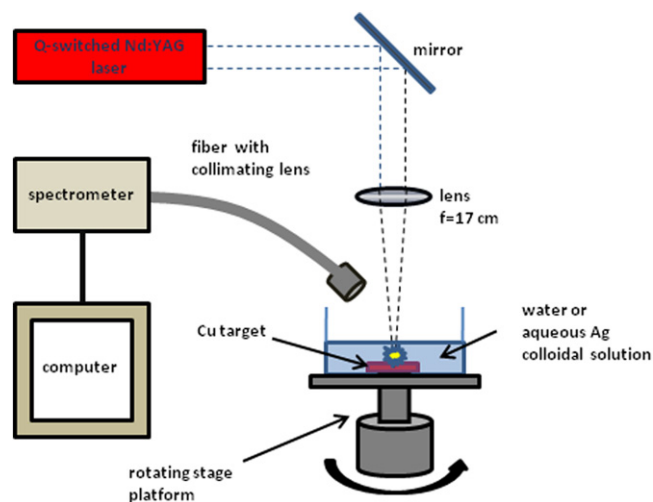


**Figure 1.** Schematic illustration of the experimental setup for synthesis of NPs by pulsed laser ablation in liquids.

process was stopped. A Nd:YAG laser pulse ( $\tau = 12 \text{ ns}$ ), operating at a repetition rate of 1 Hz and at the fundamental wavelength ( $\lambda = 1064 \text{ nm}$ ), was focused onto the target surface at normal incidence by means of a lens with a 17 cm focal length. The distance between the lens and the target was 16.5 cm, resulting in a quite large irradiated spot, and then in a large number of smaller particles. NPs were produced by using the laser pulse energy of 10 mJ, corresponding laser fluence was approximately  $6.8 \text{ J cm}^{-2}$  at the surface of Cu target. Each stage of NP production lasted 60 min, during which time the glass vessel was rotated and translated in order to prevent the effects of crater formation and fragment ejection.

Characteristic optical properties of metallic and bimetallic NPs were recorded using Perkin Elmer Lambda 35 UV-vis spectrophotometer. The size and shape of the NPs were determined by using a field emission (FE) scanning electron microscope (SEM) (TESCAN, MIRA 3) operating with secondary and backscattered electron detectors. The elemental composition of the irradiated areas was revealed by SEM (ZEISS Supra VP) equipped with an energy dispersive spectra analyzer (EDS, Oxford Instrument). The sample for SEM was prepared by putting several drops of the colloidal copper solution onto a conductive substrate and then drying under a UV lamp for 30 min. The particle-size distribution was measured using a dynamic light scattering (DLS) technique, applying backscatter detection ( $173^\circ$  detection optics), using a Zeta-sizer Nano ZS with 633 nm He-Ne laser (Malvern, UK). For compositional analysis and to monitor the process of NP formation during laser ablation, time-integrated, laser-induced breakdown spectrometry (LIBS) was used. The experimental set up for LIBS consisted of the optical system for focusing the laser beam and a fiber spectrometer. For collection of plasma emission, we used fiber with the 600 mm core diameter. The other end of the fiber is connected to a CCD spectrometer (Blue wave, Stellarnet), which covered a spectral range from 200–400 nm, with a resolution of 0.2 nm. This method relies on the fact that intense plasma background

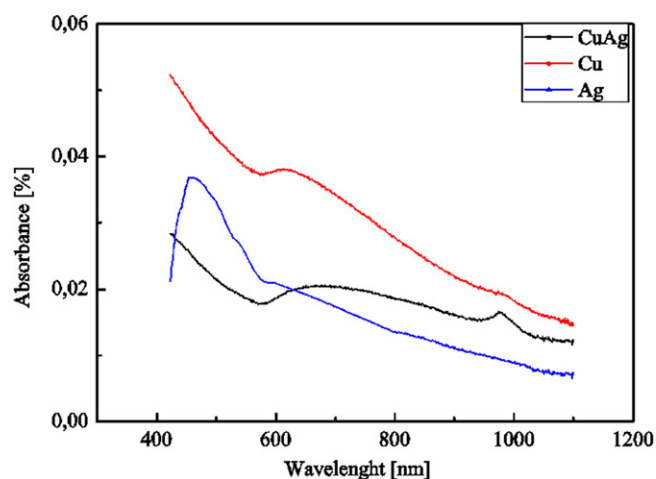


**Figure 2.** UV-vis absorbance spectra of copper, silver and CuAg-bimetal nanoparticles. Cu and Ag NPs are obtained in water whereas for CuAg NPs production the Ag-aqua's colloidal solution was used.

spectral continuum emission is mostly emitted from a region close to the sample surface, while in further-out regions of the plasma, the continuum emission is largely reduced. The time-integrated measurements provide average values in the different plasma spatial zones. At the beginning of the experiment, the copper target was covered with a very thin layer of water and Ag colloidal silver solution; subsequently, the LIBS spectra were recorded separately from the NP synthesis. Also, recording LIBS spectra under water is a complex process and requires the use of a double-pulse technique or a single-pulse technique with longer pulse duration (more than 100 ns). If the target is covered by a very thin layer of liquid, it is possible to obtain spectra with clear emission lines of elements (elemental emission line) [22].

## Results and discussion

After several minutes of laser irradiation, all the solutions have become blurred due to the generation of NPs. At the given pulse energy ( $\sim 10$  mJ), the formation of a plasma plume (primary plasma) in front of the target surface has occurred. However, with the increasing of number of accumulated laser pulses at the sample ( $\sim 100$  pulses,  $\sim 3$  min), another (secondary) plasma was created at the air-solvent interface. This plasma can reduce the level of incoming laser radiation to the sample surface, as well as reduce the primary plasma.

The formation of copper and bimetallic copper-silver NPs can be examined by optical spectroscopy. The absorption peaks arising from the localized surface plasmon resonance (SPR) were recorded in the UV-vis absorption spectra, as shown in figure 2. Copper NPs obtained by laser ablation of the Cu target in water are expected to have the SPR peak at wavelengths around 600 nm. As seen in figure 2, absorption spectra with Cu NPs show two SPR peaks, at 670 nm and 1000 nm. Shift of the peak towards a longer wavelength, to 670 nm, indicates that the NPs are somewhat larger. The shift

cannot be due to a high concentration of NPs, because of the low intensity of the SPR peak. From the appearance of the peak at 670 nm, one can conclude that NPs have a spherical shape, while the presence of another peak, at 1000 nm, indicates that some of the NPs also appear in an elliptical shape [10]. It is known that the Cu NPs are highly chemically active and can easily react with the vapour of surrounding liquid and/or with oxygen dissolved in the colloid solution. On the other hand, due to the Brownian motion of NPs in the solution, interaction between the particles is very likely, leading to their grouping. Cu-oxide NPs usually show enhanced absorption at lower wavelengths [8]. However, the pure Cu NPs possess an intense narrow SPR peak at a wavelength in the range of 590–620 nm. With the broadening of the registered SPR peak accompanied with red shift, it can be assumed to originate from the presence of a Cu-oxide shell surrounding the Cu metal core to form core-shell NPs. At room temperature,  $\text{Cu}_2\text{O}$  is the dominant product of oxidation with a few monolayers of CuO phase at the outside interface [23]. So, in our case, the interaction between Cu NPs is likely occur with partial oxidation at the surface of the agglomerated NPs with metal core and metal-oxide shell structure.

The UV-vis absorption spectrum of the solution obtained after laser ablation of the Cu target in previously prepared Ag colloidal solution shows the peak at 640 nm with strong resemblance to the colloidal solution of pure Cu NPs. By comparing the absorption spectra of Ag, Cu and CuAg NPs (figure 2), it is apparent that the peak corresponding to Ag (at  $\lambda = 450$  nm) does not exist in the spectrum of bimetallic NPs. This could mean that individual Ag particles are not present, while the predominant absorption arises from the Cu component in the colloidal solution of bimetallic NPs. However, the generated NPs in the form of nanoalloy do not exist, because there is no SPR peak at a wavelength between the peaks corresponding to individual Cu and Ag particles, such as the NPs prepared by microwave-assisted chemical reduction in an aqueous medium [14]. These results suggest that the formed NPs have a complex structure, such as a core-shell structure with the shell made from the Cu atoms and a very thin oxide layer.

Plasma generation near the Cu plate during irradiation, as well as the possibility of recording the emission spectrum of ejected excited species from the target and in liquids, means that the components and their chemical state can be identified during the process of NP formation. The elemental analysis is based on the emission spectra of the neutral and ionized excited species. Emission spectra of the Cu target irradiated in two different ambient conditions (water and a previously prepared Ag colloidal solution), in a narrow interval of wavelengths where both Cu and Ag species have corresponding lines, were recorded and presented in figure 3(a). In the LIBS spectrum, only lines (tabular values) corresponding to Cu and Ag neutral atoms and their ions were detected. The strongest copper lines appear at 324.7 nm and 327.4 nm, but the line at higher wavelength was overlapped with a very strong line of Ag at 328.1 nm, so only the Ag line at 338.3 nm was clearly recognizable in the spectrum [24]. It is assumed that during the ablation and the formation of the plasma

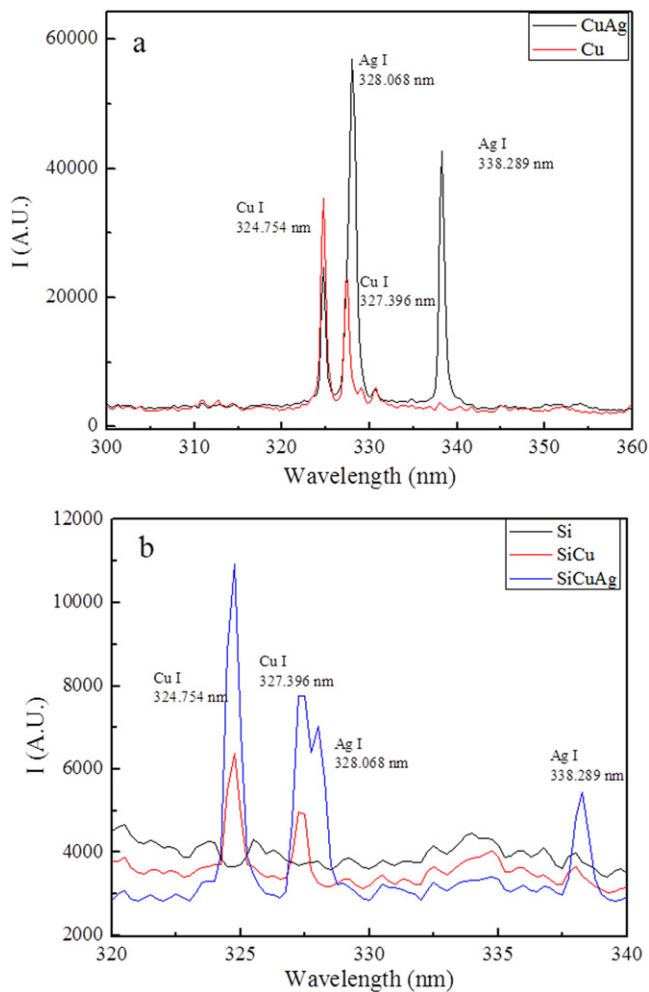


**Figure 3.** LIBS spectra recorded: (a) at synthesis of Cu and CuAg NPs and, (b) at generation of Cu and CuAg NPs upon placing of colloidal solution (an amount) on the Si substrate).

plume, many species exist, including electrons, ions, free atoms, clusters or small fragments in a liquid spread over the target, and all of them take part in NP formation [14]. Ejection of the material occurred due to lattice heat propagation, lattice expansion, thermally induced stress and shock-wave-induced mechanical vibration [25], which can be responsible for clearly visible surface ablation. A very small number of particles (several atoms or clusters) became the nucleation centres, and then interaction with other particles, or with the current upcoming species from the environment, can induce the formation of NPs [8].

The spectra of the pre-formed NPs, recorded after placing the appropriate amount of colloidal solution on the Si substrate (figure 3(b)), show close lying but clearly recognizable lines, originating from Cu (327.4 nm) and Ag (328.1 nm). The lines of the Cu and Ag species have significantly lower peak intensities compared to the lines observed in figure 3(a). This is additional evidence that the bimetallic CuAg NPs are formed during the laser ablation of the Cu target immersed in Ag colloidal solution: intensities of the Ag lines in the LIBS spectrum recorded during the formation of the NPs (figure 3(a)), are higher compared to intensities of these lines

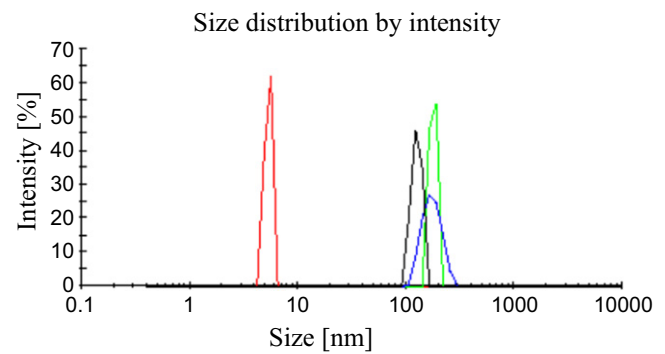


**Figure 4.** DLS NP size distribution analysis of copper, silver and copper-silver colloidal solution.

in figure 3(b). This is in contrast to the laser production of bimetallic CuAg NPs, when a laser beam, as it passed through a layer of colloidal Ag solution, is encountered with individual Ag particles, leading to a reduction of the intensity of Cu lines (figure 3(b)).

NP size distribution, observed by DLS method, is shown in figure 4. **Copper:** Size distribution of copper NPs in water (figure 4-red colour) exhibited high domination of NPs with a diameter in the range of 4–8 nm (maximum at ~5.5 nm). Also, some of them possess larger dimensions (maximum at ~200 nm) due to the agglomerate effect (figure 4-green colour). **Silver:** Size distribution of silver NPs in water (figure 4-blue colour) depicted the much higher dimensions with respect to the copper NPs. The diameter of silver NPs, i.e., the maximum is about 280 nm, while the lower dimensions are also presented, e.g. ~160 nm. The presence of these high-dimensions NPs, in one approximation, can be attributed to the intensive agglomeration. **Copper–Silver:** Size distribution of bimetallic CuAg NPs (figure 4-black colour) showed that the diameter distribution is in the range of 90–180 nm (maximum at ~125 nm). This distribution indicates that the size of Ag NPs was reduced by the action of laser radiation, before ejection of Cu species; thus, in the final step, the synthesized bimetallic CuAg NPs possessed smaller dimensions than the initial Ag NPs.

A comparative view of size, shape and morphology of metallic Cu and bimetallic CuAg NPs by SEM analysis is shown in figure 5. The size of primary-formed Cu NPs is in the range of 7–20 nm, and generally with a circular shape (figure 5(a)). However, the large Cu NPs are formed by the grouping of primary NPs, which have an elongated elliptical shape in the beginning, but with further agglomeration, these NPs become spherical with well-defined grain morphology (figure 5(a)). An intermediate elliptical form of the NPs was previously detected by the SPR at 1000 nm in the absorption spectrum (figure 2). It can be observed, though sporadically, that the initial formation of the usual icosahedron crystalline structure appears as an individual particle with a size of 50 nm (figure 5(b)) [26]. Primary bimetallic CuAg NPs are spherical with dimensions of about 10–20 nm, probably resulting from a growth of nucleus composed of a small number of atoms (figures 5(c)–(d)). The clustering of primary CuAg NPs generates large particles with smooth spherical shapes of over

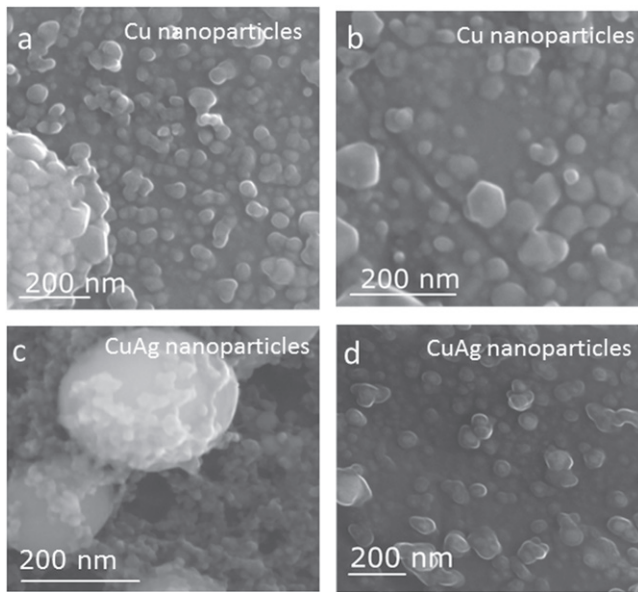


**Figure 5.** SEM microphotographs of: a, b-copper NPs; and c, d-bimetal CuAg NPs.

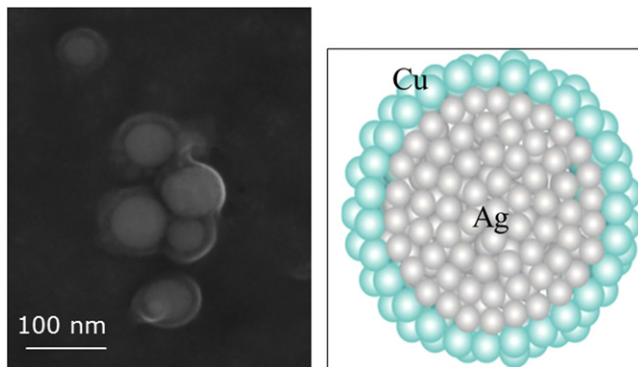


**Figure 6.** SEM microphotograph of CuAg-NPs with scheme/view of core-shell structure.

200 nm in diameter, and without specific grain morphology. EDS analysis was used to elucidate the composition of the NPs, and peak intensities of Cu, Ag and O were examined. The corresponding concentration of copper and oxygen are 36% and 64%, respectively, after the laser-assisted synthesis of Cu NPs. In contrast, the relative component concentrations for Cu (23%), Ag (18%) and O (59%) are obtained after laser ablation of the Cu target in aqueous Ag colloidal solution. This high content of oxygen can be attributed from oxidation process during the laser ablation in liquids, but also from air contamination at stage of the sample. The NPs were coated with oxide-shell, which is confirmed by a red shift in the UV-vis spectra (figure 3); thus, it can be explained by the existence of a shell-oxide phase around the metallic core. The oxide-shell formation may be reason for the exposure of NPs to dissolved oxygen in the water at the same point of time in the ablation process [27].

On the other hand, at higher magnification, it can be seen that bimetallic CuAg NPs possess specific core-shell structure (figure 6). Due to the differences in lattice parameter of

Ag (0.409 nm) and Cu (0.361 nm), and the large differences in the redox potentials of these two metals, the formation of intermetallic NPs (nanoalloy) is very unlikely. It is shown theoretically that the probability for the formation of a core-shell structure for the Ag and Cu combination is high; it was calculated that a stable configuration can be achieved for  $\text{Ag}_{212}\text{Cu}_{309}$  [24]. The existence of a theoretically predicted mechanism for the formation of a core-shell structure for bimetallic CuAg NPs implies that first the Cu cluster is formed which then reacts with a certain number of Ag atoms. Due to the surface segregation of smaller Cu atoms, a complete replacement of Cu by Ag atoms occurs, creating primary particles with a core-shell structure (Ag-rich core/Cu-rich shell) [28, 29]. In our case, initially Ag particles were present in the liquids only, and they became smaller by laser irradiation, followed by ejection of Cu atoms, ions and clusters from the Cu target. Ablated materials expand and disperse in liquid surrounding NPs, small clusters, free atoms and ions. First, NPs can be formed by fast condensation of ejected materials, collisions of plume species with one another, or the nucleation of small clusters from free atoms. The formation of a core-shell structure can be explained by preferential condensation and nucleation of small Cu clusters/particles onto sufficiently large Ag particles by reducing the interfacial free energy [8, 30].

## Conclusion

This study describes, to the best of our knowledge, for the first time, the effective production of bimetallic CuAg NPs by means of pulsed laser ablation of a Cu target in a previously prepared Ag colloidal solution. Pulsed nanosecond laser radiation was used for the ejection of Cu species in water and in a Ag colloidal solution. Synthesized pure metallic Cu NPs were used for comparison with the results obtained for CuAg NPs produced by laser interaction with the Cu sample in a previously prepared Ag colloidal solution. From UV-vis analysis of the appropriate colloidal solution of CuAg NPs, it was determined that the predominant absorption arises from the Cu component in the absence of Ag. The copper NPs are mainly spherical, and it has been found that their average diameters are up to 20 nm, with a strong tendency for the formation of agglomerates with a well-defined grain morphology. Primary bimetallic CuAg NPs have uniform dimensions of about 15 nm, typically grouped into larger agglomerates without a well-defined grain morphology. An important result was the formation of CuAg NPs with a specific core-shell structure, which agreed very well with the predicted mechanism for generation of NPs by laser ablation in liquids. This procedure provides a novel method to synthesize bimetallic CuAg NPs with a core-shell structure (Ag-rich core/Cu-rich shell). In the case of the antibacterial activity of these bimetallic CuAg NPs, it is desirable that copper atoms are located on the surface of NPs due to their greater inhibiting effect than Ag for certain types of bacteria.

## Acknowledgments

The research was sponsored by the Ministry of Education, Science and Technological Development of the Republic of Serbia through Project No. 45016. We also acknowledge the support from European Community, COST Action Project No. CM1104, 'Reducible oxide chemistry, structure and functions'.

## References

- [1] Ghatee M H and Shekoohi K 2013 *Fluid Phase Equilib.* **355** 114
- [2] Bardotti L, Tournus F, Pellarin M, Broyer M, Melinon P and Dopuis V 2012 *Surf. Sci.* **606** 110
- [3] Liu Y, Chi Y, Shan S, Yin J, Luo J and Zhong C J 2014 *J. Alloys Compd.* **587** 260
- [4] Barroso F and Tojo C 2011 *J. Colloid Interface Sci.* **363** 73
- [5] Nunokawa T, Onodera Y, Hara M, Kitamoto Y, Odawara O and Wada H 2012 *Appl. Surf. Sci.* **261** 118
- [6] Toshima N, Yan H and Shiraishi Y 2008 *Metal Nanoclusters in Catalysis and Materials Science: Recent Progress in Bimetallic NPs* ed B Corain, G Schmid and N Toshima (New York: Elsevier)
- [7] Duan S and Wang R 2013 *Prog. Nat. Sci.: Mater. Int.* **23** 113
- [8] Tilaki R M, Iraj Zad A and Mahdavi S M 2007 *Appl. Phys. A* **88** 415
- [9] Saito M, Yasukawa K, Umeda T and Aoi Y 2008 *Opt. Mater.* **30** 1201
- [10] Amikura K, Kimura T, Hamada M, Yokoyama N, Miyazaki J and Yamada Y 2008 *Appl. Surf. Sci.* **254** 6976
- [11] Suzuki K, Tanaka N, Ando A and Takagi H 2012 *J. NPs Res.* **14** 863
- [12] Shin K, Kim D H, Yeo S C and Lee H M 2012 *Catalysis Today* **185** 94
- [13] Zhang D and Liu X 2013 *J. Mol. Struct.* **1035** 471
- [14] Valodkar M, Modi S, Pal A and Thakore S 2011 *Mater. Res. Bull.* **46** 384
- [15] Langlois C T, Oikawa T, Bayle-Guillemand P and Ricolleau C 2008 *J. NPs Res.* **10** 997
- [16] Li W, Wang A, Liu X and Zhang T 2012 *Appl. Catalysis A* **433–434** 146
- [17] Singh M, Sinha I, Singh A K and Mandal R 2011 *Colloids Surface A* **384** 668
- [18] Tan K S and Cheong K Y 2013 *J. NPs Res.* **15** 1537
- [19] Sukhov I A, Shafeev G A, Voronov V V, Sygletou M, Stratakis E and Fotakis C 2014 *Appl. Surf. Sci.* **302** 79
- [20] Kabashin A V, Delaporte P, Pereira A, Grojo D, Torres R, Sarnet T and Sentis M 2010 *Nanoscale Res. Lett.* **5** 454
- [21] Itina T E, Gouriet K, Zhigilei L V, Noe S, Hermann J and Sentis M 2007 *Appl. Surf. Sci.* **253** 7656
- [22] Simileanu M, Radvan R and Puscas N 2010 *U.P.B. Sci. Bull., Series A* **72** 209–16
- [23] Chan G H, Zhao J, Hicks E, Schatz G C and Van Duyne R P 2007 *Nano Lett.* **7** 1947–52
- [24] NIST Atomic Spectra Database Lines Form (<http://physics.nist.gov/PhysRefData>)
- [25] Al-Mamun S A, Nakajima R and Ishigaki T 2012 *Thin Solid Films* **523** 46
- [26] Laasonen K, Panizon E, Bochicchio D and Ferrando R 2013 *J. Phys. Chem. C* **117** 26405
- [27] Schinca D C, Scaffardi L B, Videla F A, Torchia G A, Moreno P and Roso L 2009 *J. Phys. D: Appl. Phys.* **42** 215102
- [28] Bochicchio D and Ferrando R 2010 *Nano Lett.* **10** 4211
- [29] Barcaro G and Fortunelli A 2008 *Faraday Discuss.* **119** 433
- [30] Ganjali M, Ganjali M, Khoby S and Meshkot M A 2011 *Nano-Micro Letter* **3** 256

PAPER

# Graphene oxide improves the biocompatibility of collagen membranes in an *in vitro* model of human primary gingival fibroblasts

To cite this article: Patrizia De Marco *et al* 2017 *Biomed. Mater.* **12** 055005

View the [article online](#) for updates and enhancements.

## Related content

- [Fibronectin-tethered graphene oxide as an artificial matrix for osteogenesis](#)  
Ramesh Subbiah, Ping Du, Se Young Van et al.
- [3D porous collagen scaffolds reinforced by glycation with ribose for tissue engineering application](#)  
Natalia Gostynska, Gopal Shankar Krishnakumar, Elisabetta Campodoni et al.
- [Evaluation of 3D printed PCL/PLGA-TCP versus collagen membranes for guided bone regeneration in a beagle implant model](#)  
J-Y Won, C-Y Park, J-H Bae et al.

# Biomedical Materials



## PAPER

# Graphene oxide improves the biocompatibility of collagen membranes in an *in vitro* model of human primary gingival fibroblasts

RECEIVED  
21 March 2017

REVISED  
22 May 2017

ACCEPTED FOR PUBLICATION  
13 June 2017

PUBLISHED  
13 September 2017

Patrizia De Marco<sup>1</sup>, Susi Zara<sup>1</sup>, Marianna De Colli<sup>1</sup>, Milena Radunovic<sup>2</sup>, Vladimir Lazovic<sup>3</sup>, Valeria Ettore<sup>1</sup>, Antonello Di Crescenzo<sup>1</sup>, Adriano Piattelli<sup>4</sup>, Amelia Cataldi<sup>1,5</sup> and Antonella Fontana<sup>1,5</sup> 

<sup>1</sup> Department of Pharmacy, Università 'G. d'Annunzio', Via dei Vestini, I-66100 Chieti, Italy

<sup>2</sup> School of Dental Medicine, University of Belgrade, 11000, Belgrade, Serbia

<sup>3</sup> Institute of Physics, University of Belgrade, 11080 Zemun, Belgrade, Serbia

<sup>4</sup> Department of Medical, Oral and Biotechnological Sciences, Università 'G. d'Annunzio', Via dei Vestini, 66100 Chieti, Italy

<sup>5</sup> Author to whom any correspondence should be addressed.

E-mail: [amelia.cataldi@unich.it](mailto:amelia.cataldi@unich.it) and [antonella.fontana@unich.it](mailto:antonella.fontana@unich.it)

**Keywords:** graphene oxide, AFM analyses, human primary gingival fibroblasts

Supplementary material for this article is available [online](#)

## Abstract

Commercial collagen membranes are used in oral surgical procedures as scaffolds for bone deposition in guided bone regeneration. Here, we have enriched them with graphene oxide (GO) via a simple non-covalent functionalization, exploiting the capacity of oxygenated carbon functional moieties of GO to interact through hydrogen bonding with collagen. In the present paper, the GO-coated membranes have been characterized in terms of stability, nano-roughness, biocompatibility and induction of inflammatory response in human primary gingival fibroblast cells. The obtained coated membranes are demonstrated not to leak GO in the bulk solution, and to change some features of the membrane, such as stiffness and adhesion between the membrane and the atomic force microscopy (AFM) tip. Moreover, the presence of GO increases the roughness and the total surface exposed to the cells, as demonstrated by AFM analyses. The obtained material is biocompatible, and does not induce inflammation in the tested cells.

## Introduction

Barrier membranes are standardly used in oral surgical procedures exploiting guided tissue regeneration (GTR) and guided bone regeneration (GBR), for the treatment of periodontal bone defects and peri-implant defects, as well as for bone augmentation [1, 2]. The aim is to place the membrane in order to prevent the ingrowth of soft connective tissue into bone defects, and therefore create a secluded space into which only cells from the neighboring bone can migrate [3]. The muco-periosteal flap is then repositioned over the membrane and sutured. The membranes can be made of non-resorbable materials, such as expanded polytetrafluoroethylene (ePTFE), or resorbable materials, such as synthetic polyesters (polyglycolides, polylactides, or copolymers thereof) or collagen. In addition, resorbable membranes do not need a second intervention to be removed once bone

has been reformed, thus decreasing the risk of infection and the loss of some of the regenerated bone. Last but not least, the lack of a second intervention is desirable and cost-effective for the patient. Collagen membranes exhibit several advantages, compared to polymeric membranes, such as easy manipulation, weak immunogenicity [4], a direct effect on bone formation and chemotaxis of gingival and periodontal ligament fibroblasts [5, 6]. The source of the collagen is various, but typically it is obtained from bovine tendon, bovine dermis, calf skin, or porcine dermis [1]. In the attempt to improve the biocompatibility and promote the desired effect on the surrounding tissues, many modifications to collagen membranes have been proposed. Such modifications include cross-linking [7], the addition of heparan sulfate and fibronectin [8] or nanobioactive glass [9]. Here, we plan to improve the properties of collagen membranes by coating them with graphene oxide (GO).



Graphene is a flat monolayer of carbon atoms tightly packed into a two-dimensional (2D) honeycomb lattice and is a basic building block for graphitic materials with unique physical, chemical, and mechanical properties [10]. In particular, GO—an oxidized derivative of graphene—has been actively investigated in the biomedical field, due to its solubility in water and its reactive oxygen functional groups [11], which make it a good candidate for enzyme adsorption [12], cell imaging and drug delivery [13, 14]. However, in order to use GO as a biomaterial, its biosafety and biocompatibility has to be confirmed in both cell cultures and live biosystems. Many reports show that GO is a biocompatible material that discloses limited or no cytotoxicity, and allows the effective proliferation of human and mammalian cells. In fact, several reports have showed that, when grown on GO paper, the adhesion and proliferation of various cell types, such as L-929 cells [15], osteoblasts [16, 17], kidney cells, and embryonic cells [18] is promoted. In particular, Ferrari *et al* report that no cytotoxicity effects are evidenced when graphene is used as support for tissue regeneration or cell growth, suggesting that graphene is safe if it remains intact after cell growth [19]. These combined results support that GO materials are biocompatible and promote cell adhesion and proliferation. In particular, the dose-dependent cytotoxicity of GO is evident when cells are exposed to colloidal solutions of GO [20, 21], whereas it is minimal when GO flakes are used to cover different biomaterials [22].

The aim of this study was therefore to prepare collagen membranes enriched with GO. In particular, we were able to optimize the coating protocol, chemico-physically characterize the obtained coated membranes, and ascertain that the coating was stable and did not leak graphene oxide in the bulk medium. A relevant section of the paper is devoted to the superficial characterization of the coated membrane using atomic force microscopy (AFM). The following step was to investigate the biocompatibility of the obtained enriched collagen membranes with human primary gingival fibroblasts (HGFs), which are the first cells adhering to the membrane during healing. In particular, we evaluated the viability and metabolic activity, as well as the cytotoxic and the inflammatory response of HGFs grown on collagen membranes coated with two concentrations of GO, 2 and 10  $\mu\text{g ml}^{-1}$ . These two concentrations were chosen on consideration that GO-coated porcine bone granules treated using a concentration of 50  $\mu\text{g ml}^{-1}$  [22] have been demonstrated to release an appreciable amount of imperfectly adsorbed GO into the surrounding tissue.

## Methods

### Materials

Synthetic Graphite ~200 mesh, 99.9995% powder was purchased from Alfa Aesar. Collagen membranes

(Osteobiol Derma®, Tecnos), derived from porcine dermis after removal of the epithelial layer, were a gift of Tecnos Dental s.r.l. Pianezza (TO), Italy.

### Preparation of GO

GO was prepared by slightly modifying the Hummers method [23, 24]. A flask containing 0.2 g of graphite and 0.1 g of sodium nitrate in 4.6 ml of concentrated sulfuric acid was placed in an ice bath. To this mixture was added 0.6 g potassium permanganate, under continuous stirring. After 2 h, the reaction mixture was transferred to a water bath at 35 °C and stirred for 30 min. Deionized water (9.2 ml) was slowly added to the solution, and the flask was heated to 98 °C for 45 min; 27.8 ml of deionized water and 2.14 ml of 30% hydrogen peroxide were then poured into the mixture to stop the reaction. The light brown mixture obtained was filtered through a sintered-glass filter (pore size 15–40  $\mu\text{m}$ ), and rinsed three times with 5% HCl and then with deionized water. The solid was dried in an oven at 60 °C for 12 h. The obtained graphite oxide was redispersed in water, ultrasonicated for 45 min and centrifuged for 15 min at 9000 rpm. Rotary evaporation at 40 °C of the corresponding supernatant allowed to obtain exfoliated graphene oxide, GO. The quality of GO obtained was assessed using spectrophotometry, Fourier transform infra-red (FTIR) and Raman spectroscopies, dynamic light scattering,  $\zeta$ -potential, TEM and SEM techniques [22].

### Enrichment of collagen membranes

Different GO aqueous solutions were prepared by ultrasonating the proper amount of GO in water for 30 min and subsequently centrifugating the suspension at 5500 rpm for 15 min. The GO concentration in water was adjusted in order to obtain two diluted solutions: 2 and 10  $\mu\text{g ml}^{-1}$ . Then, the membranes (20 × 30 mm lateral dimensions) were cut with a cutter to obtain square pieces of membrane (5 × 5 mm lateral dimensions). Half of these samples were covered with 100  $\mu\text{l}$  of the 2  $\mu\text{g ml}^{-1}$  GO solution, while the other half were covered with 100  $\mu\text{l}$  of the 10  $\mu\text{g ml}^{-1}$  GO solution. The liquid was left to evaporate overnight under a fume hood. The rinsed pieces (see figure 1) were transferred in a 96 multiwell plate for the biocompatibility tests. We chose to cut the membranes in small pieces before wetting them with the GO solution, in order to avoid the edge rippling of the membrane during the drying process, and to have a more uniform distribution of the GO sheets on the surface and in the core of the membrane.

### Characterization of the GO-enriched material

The GO-enriched membranes obtained were characterized, using atomic force microscopy (AFM) and scanning electron microscopy (SEM) analyses. AFM measurements were performed using a Digital

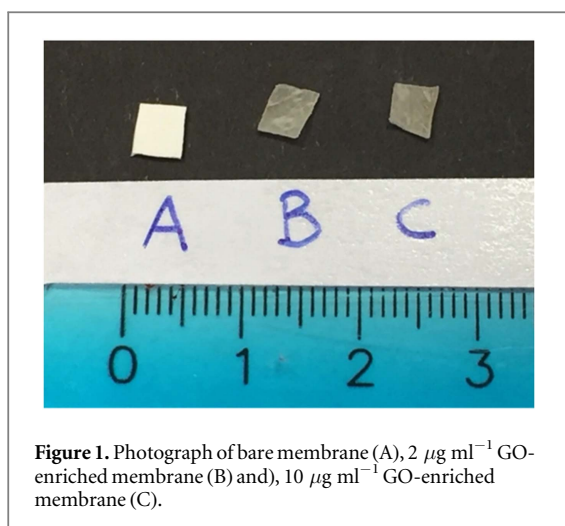


**Figure 1.** Photograph of bare membrane (A),  $2 \mu\text{g ml}^{-1}$  GO-enriched membrane (B) and,  $10 \mu\text{g ml}^{-1}$  GO-enriched membrane (C).

Multimode 8 Bruker AFM microscope with Nanoscope V controller, and using commercial silicon tips (cantilever resonance frequency of 75 kHz and nominal elastic constant of  $3 \text{ N m}^{-1}$ ) with a typical apex radius of 10 nm. In order to perform quantitative nanomechanical (QNM) investigations of height, deformation, dissipation energy and adhesion at each point across a  $1 \mu\text{m} \times 1 \mu\text{m}$  sized area of the prepared samples, the Peak Force QNM mode with ScanAsyst™ in air was used. The deflection sensitivity and tip radius were calibrated for each probe prior to use, against standard sapphire. AFM images were analyzed with the WSxM software [25].

Stability measurements were performed using a Cary 100 bio Varian spectrophotometer. Samples were investigated by SEM using a high resolution electron microscope, MIRA3 FEG-SEM, Tescan, at accelerating voltage 20 kV. In preparation, the surface of samples was coated with an ultrathin gold layer using an SC7620 Mini Sputter Coater, Quorum Technologies, to prevent the accumulation of static electric fields at the specimen due to the electron irradiation required during imaging.

#### Isolation and culture of HGFs

Donors subjected to the extraction of the third molar signed informed consent, according to Italian Legislation and the code of Ethical Principles for Medical Research involving Human Subjects of the World Medical Association (Declaration of Helsinki). The project obtained the approval of the Local Ethical Committee of the University of Chieti (approval number 1173, date of approval 31/03/2016). Donors, aged from 20 to 40 years, were not affected by any systemic conditions and did not take medication or tobacco. Gingival fragments were obtained from the retromolar area as a consequence of the surgical flap regularization before suture. Fragments of healthy gingival tissue were immediately placed in Dulbecco's modified Eagle's medium DMEM (Euroclone, Pero,

MI, Italy) for at least 1 h, rinsed three times in phosphate buffered saline solution (PBS), minced into small tissue pieces and cultured in DMEM containing 10% fetal bovine serum (FBS) and antibiotics (1% penicillin and streptomycin), 1% fungizone (all purchased from Euroclone, Pero, MI, Italy). After one week, fungizone was removed from the culture medium, and the gingival fragments were cultured until HGFs appeared (at least three weeks). All cells were maintained at  $37^\circ\text{C}$  in a humidified atmosphere of 5% (v/v)  $\text{CO}_2$ . Cells were processed after 4–8 passages. All the experiments were realized with cells obtained from two different donors and each assay was performed in triplicate. 24 h before cell seeding, membranes were immersed in medium. HGFs were seeded at  $7.5 \times 10^3 \text{ cm}^{-2}$  concentration in 48-well non-treated plates containing the membranes and cultured for one, three and seven days.

#### Sterilization of membranes

Both bare and GO-enriched membranes were UV irradiated (UV lamp 15 W) for 2 h in order to sterilize the samples. The stability of the irradiated membranes was monitored via spectrophotometric measurements in analogy to measurements performed on non-irradiated membranes.

#### Alamar blue cell viability assay

For the Alamar blue assay, three membranes for each experimental group at each time point were used. HGF viability was evaluated after 1, 3 and 7 d of culture by Alamar blue assay, based on the capability of viable cells to reduce Alamar blue reagent into a red product. At established time points the medium was replaced by a fresh one containing Alamar blue reagent (Thermo Scientific, Rockford, IL, USA) in 10% of the volume, probed with cells for 4 h at  $37^\circ\text{C}$  and read at 570 and 600 nm. Value obtained in the absence of cells was considered as negative control. The percentage reduction of Alamar blue reagent was calculated according to manufacturer's instructions.

#### Cytotoxicity assay (LDH assay)

To assess membrane integrity of HGFs, lactate dehydrogenase (LDH) leakage into the medium was quantified using 'CytoTox 96 non-radioactive cytotoxicity assay' (Promega, Madison, WI, USA), as suggested by the manufacturer, after 1, 3 and 7 d of culture on the different experimental membranes. In each well, the LDH leakage measured in the supernatant was normalized to the total intracellular LDH value obtained after cell lysis.

#### ELISA test of IL6 and PGE2 secretion

IL6 and PGE2 secretion in the culture medium at the different experimental times for all samples was

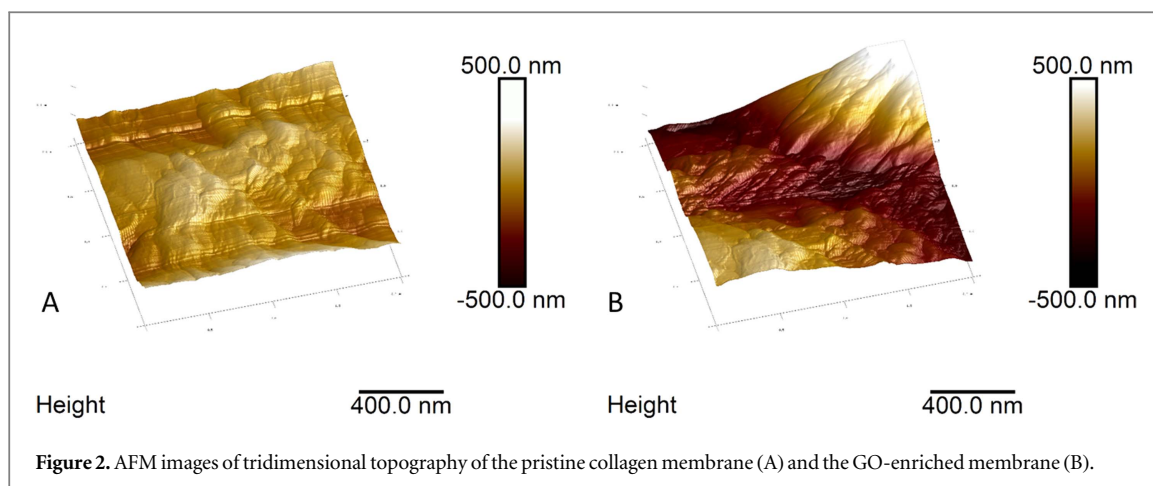


Figure 2. AFM images of tridimensional topography of the pristine collagen membrane (A) and the GO-enriched membrane (B).

detected, following the instructions provided by the manufacturer. EIA kit (Enzo Life Sciences, Farmingdale, NY, USA) was used to determine IL6 and PGE2 concentrations. Absorbance values were obtained by spectrophotometric reading at 450 and 405 nm respectively, by means of a Multiscan GO 96-well microplate spectrophotometer (Thermo Scientific, Rockford, IL, USA). Secretion levels of IL6 and PGE2 were measured in different wells, and normalized for percentage Alamar blue reduction values, as previously determined by Alamar blue assay.

## Results

The enrichment with GO was visually detected by comparing the bare pure membrane with GO-coated membranes enriched with different concentrations of GO. Figure 1 shows membranes coated with  $2 \mu\text{g ml}^{-1}$  and  $10 \mu\text{g ml}^{-1}$  GO solutions. The UV irradiation used for the sterilization of the membranes did not change the color of the coating from brown to black (the color of reduced GO) [26], thus confirming that GO did not reduce under the experimental conditions adopted. Indeed, reduction of GO has been obtained by Han *et al* by using a much higher lamp power (500 W) [27].

In most composite materials, an effective wetting and an uniform dispersion of components in a given matrix, as well as a strong interfacial adhesion between the coating and the underlying collagen membrane, are required to obtain an enriched material with satisfactory mechanical and biocompatibility properties.

AFM analyses allowed us to obtain molecular imaging (figure 2), as well as quantitative nanomechanical mapping of the coated membranes. In figure 2 the topographic map of the bare membrane and of the GO-coated membrane are displayed, showing the typical aspect of the pristine membrane in panel A, and that of the GO-covered material in panel B.

Peak force QNM provides images at a relatively high speed and a high resolution, quantifying the

mechanical features of the sample (see figures S1–S11, available online at [stacks.iop.org/BMM/12/055005/mmedia](https://stacks.iop.org/BMM/12/055005/mmedia) in the supplementary data). Peak force has been widely used to investigate mechanical effects on biological samples [28, 29]. Figure 3 reports the maps of peak force error (panels A and E), adhesion (panels B and F), dissipation (panels C and G) and deformation (panels D and H), respectively of bare collagen membrane (upper images) and  $10 \mu\text{g ml}^{-1}$  GO-coated membrane (lower images). The pure membrane (figure 2, panel A) appears quite corrugated, with a total thickness of at least 300 nm. In particular, the image indicates the presence of collagen fibers forming the membrane (see also figure 3, panel A). Panel E of figure 3 highlights the presence, in the upper right corner, of a different material, i.e. graphene oxide flake, that covers the membrane, rendering it different in terms of adhesion, dissipation and deformation.

The adhesion (figure 3, panels B and F) is determined by comparing the adhesion force region between tip approach and retracing during the surface scan of the sample. The data obtained highlight that the adhesion of the tip to the surface increases on coating the membrane with GO from  $1.9 \pm 0.2$  nN (figure S1 of the supplementary data) to  $2.3 \pm 0.9$  nN (figure S2 of the supplementary data), with values of  $2.4 \pm 1.2$  on the GO flake and  $1.3 \pm 0.6$  in the bottom region of the coated membrane (figures S3 and S4 of the supplementary data).

Panel C of figure 3 shows that the dissipation energy for the bare membrane ranges from 0.1 to 1 keV, with a mean value of  $120 \pm 30$  eV (figure S5 of the supplementary data). The dissipation energy measures the hysteresis between the loading and unloading curves of the cantilever, and therefore can give information on the elastic behavior of the sample, elastic samples being characterized by low dissipation energy values. In the present case the obtained dissipation energy is indicative of a non-perfectly elastic sample (i.e. viscoelastic behavior). In the presence of GO

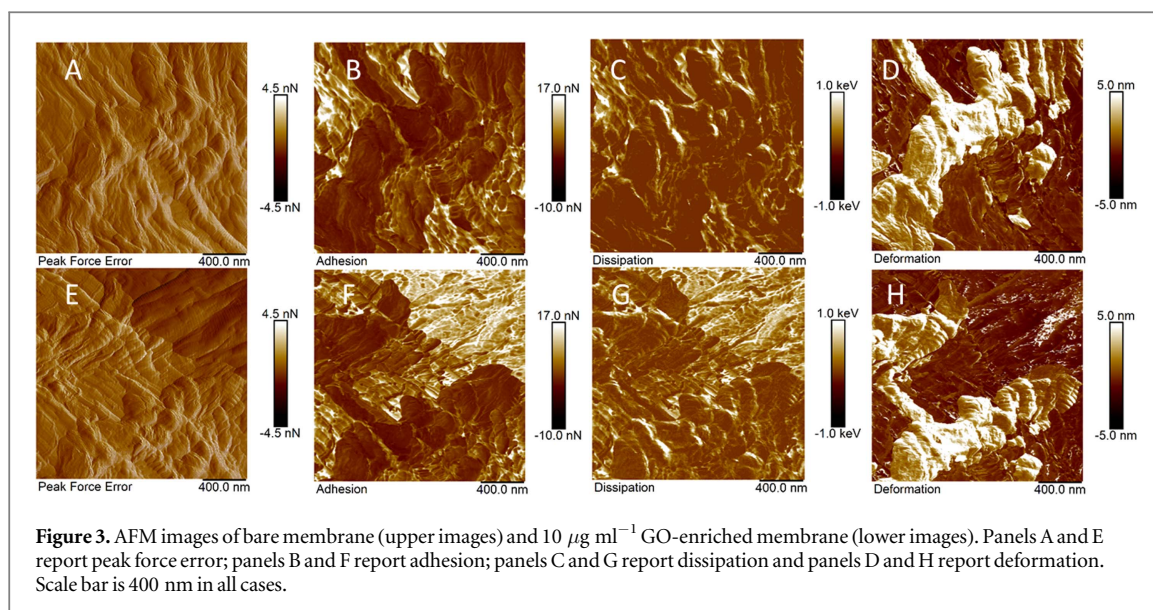


**Figure 3.** AFM images of bare membrane (upper images) and 10  $\mu\text{g ml}^{-1}$  GO-enriched membrane (lower images). Panels A and E report peak force error; panels B and F report adhesion; panels C and G report dissipation and panels D and H report deformation. Scale bar is 400 nm in all cases.

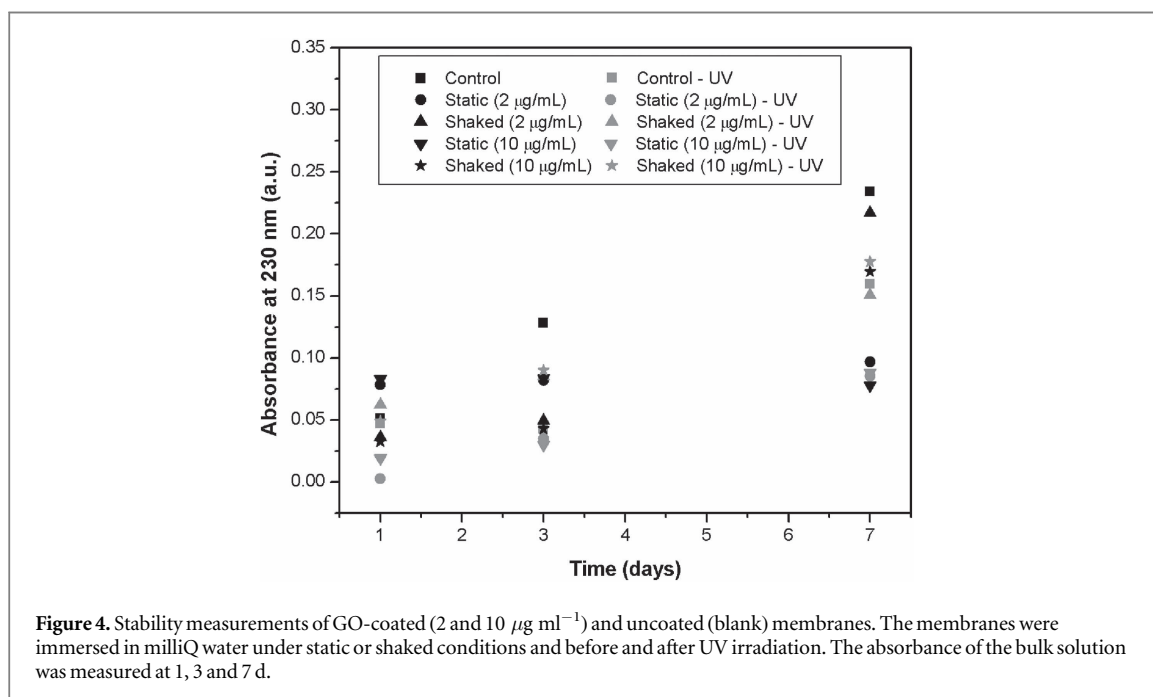


**Figure 4.** Stability measurements of GO-coated (2 and 10  $\mu\text{g ml}^{-1}$ ) and uncoated (blank) membranes. The membranes were immersed in milliQ water under static or shaken conditions and before and after UV irradiation. The absorbance of the bulk solution was measured at 1, 3 and 7 d.

(figure 3, panel G), the dissipation energy map splits the sample in two well defined regions: the top right region, with the recognizable GO flake, in which the dissipation energy increases to  $160 \pm 20$  eV (figure S6 of the supplementary data), and the lower region that keeps a relatively lower value of  $150 \pm 10$  eV (figure S7 of the supplementary data).

Panels D and H of figure 3 report the deformation data, i.e. the degree of indentation of the tip into the surface at the peak force. The bare membrane has a mean deformation of  $1.9 \pm 0.6$  nm (figure S8 of the supplementary data), whereas the coated membrane has a lower mean deformation of  $1.4 \pm 0.9$  nm (figure S9 of the supplementary data), with values of  $0.9 \pm 0.2$  nm and  $1.4 \pm 0.8$  nm for the GO flake region (upper right corner) and the bottom region respectively (see figures S10 and S11 of the supplementary data).

Nano-roughness evaluation was performed on the same instrument in peak force QNM operation mode (see figures S12 and S13 in the supplementary data).

Stability measurements (figure 4) were performed by keeping the membrane in contact with water under static or shaken conditions, before and after UV irradiation. The absorbance at 230 nm (the  $\lambda_{\text{max}}$  of GO) of the bulk aqueous solution was checked after 1, 3 and 7 d. No evidence of graphene oxide dissolution was observed being the absorbance of the bulk solution comparable with that recovered from the blank (a non-coated membrane). The increase of absorbance observed on passing from 1 to 7 days of immersion in the bulk solution is probably due to dissolution of collagen. As a matter of fact, the collagen membrane showed an absorbance spectrum in the 200–350 nm wavelength interval with a shoulder at 250 nm. It is

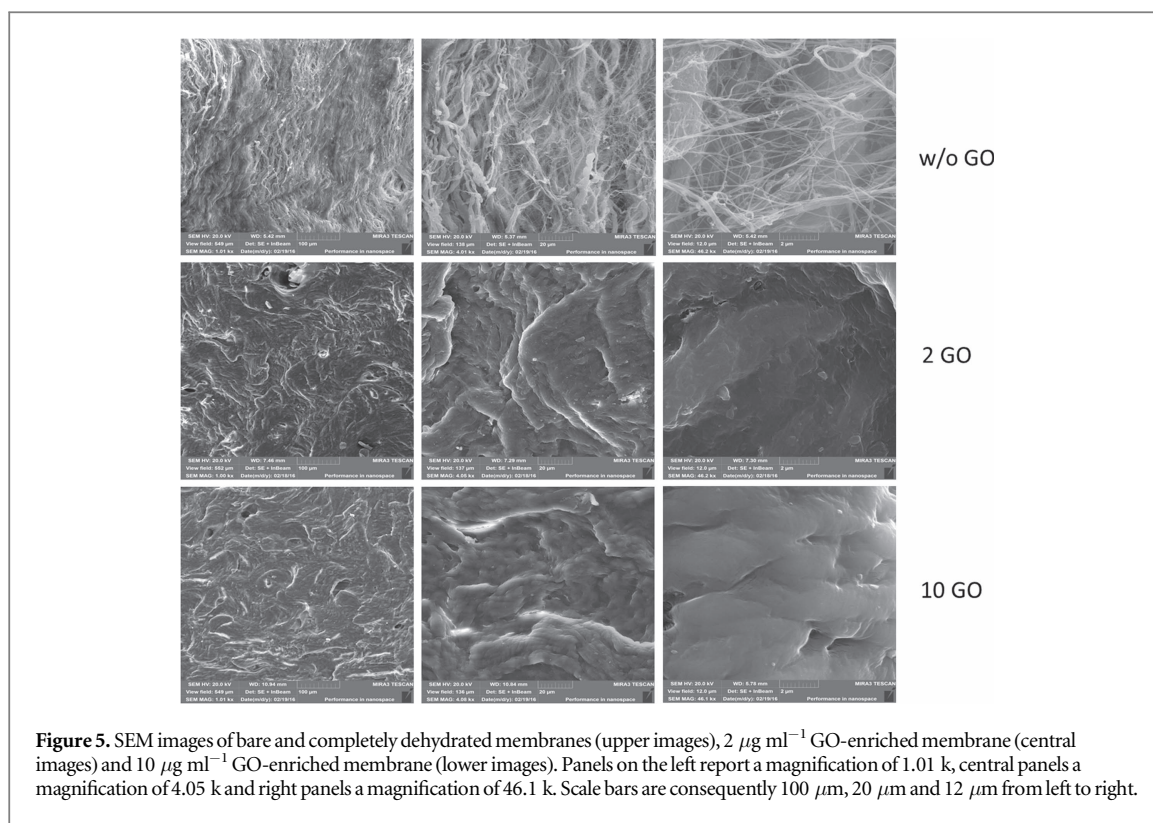


**Figure 5.** SEM images of bare and completely dehydrated membranes (upper images),  $2 \mu\text{g ml}^{-1}$  GO-enriched membrane (central images) and  $10 \mu\text{g ml}^{-1}$  GO-enriched membrane (lower images). Panels on the left report a magnification of 1.01 k, central panels a magnification of 4.05 k and right panels a magnification of 46.1 k. Scale bars are consequently  $100 \mu\text{m}$ ,  $20 \mu\text{m}$  and  $12 \mu\text{m}$  from left to right.

interesting to note that irradiation reduced the collagen's solubility in the bare membrane due to effective irradiation-induced cross-linking of collagen and subsequent reduction of solubility [30].

SEM analyses (figure 5) demonstrated, as well, the ability of graphene oxide to coat the membrane, although the lack of the network of collagen fibers in the coated samples is mainly due to the preparation protocol that implies a simple air drying of the samples rather than to a real GO coating. As a matter of fact, SEM is not the preferred method for the evaluation of the homogeneity of the GO coating. In order to obtain such a detailed visualization of collagen fibers, the coated samples should have been thoroughly dehydrated by performing several rinses with ethanol or heating at high temperatures, but both these processes could have altered the features of the final membrane.

HGFs were cultured on uncoated collagen membranes (control) and on  $2 \mu\text{g ml}^{-1}$  GO and  $10 \mu\text{g ml}^{-1}$  GO-coated collagen membranes for 1, 3 and 7 d. All the assays were performed at the three established experimental times.

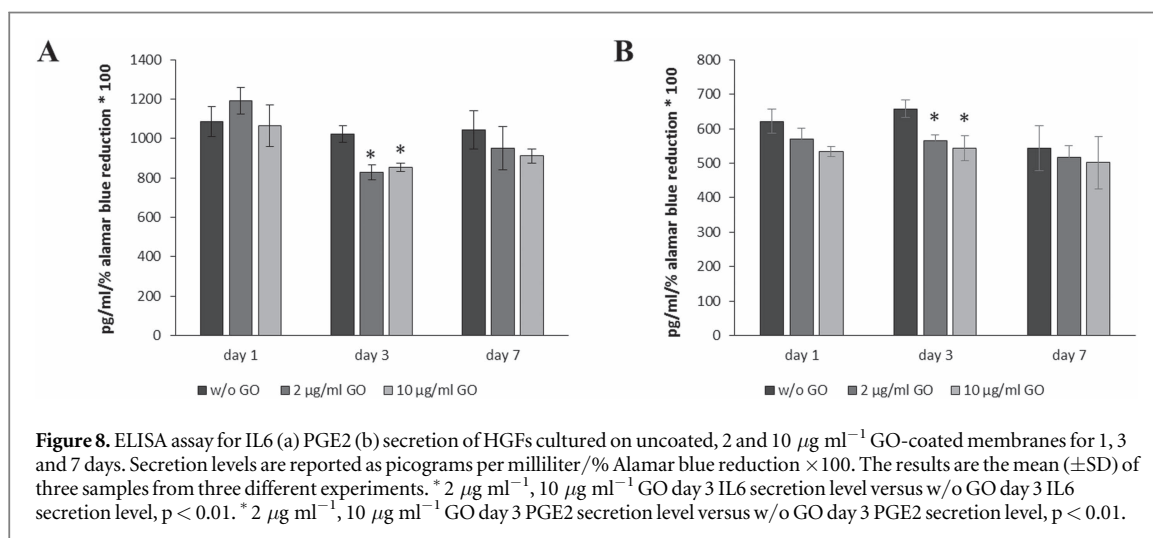
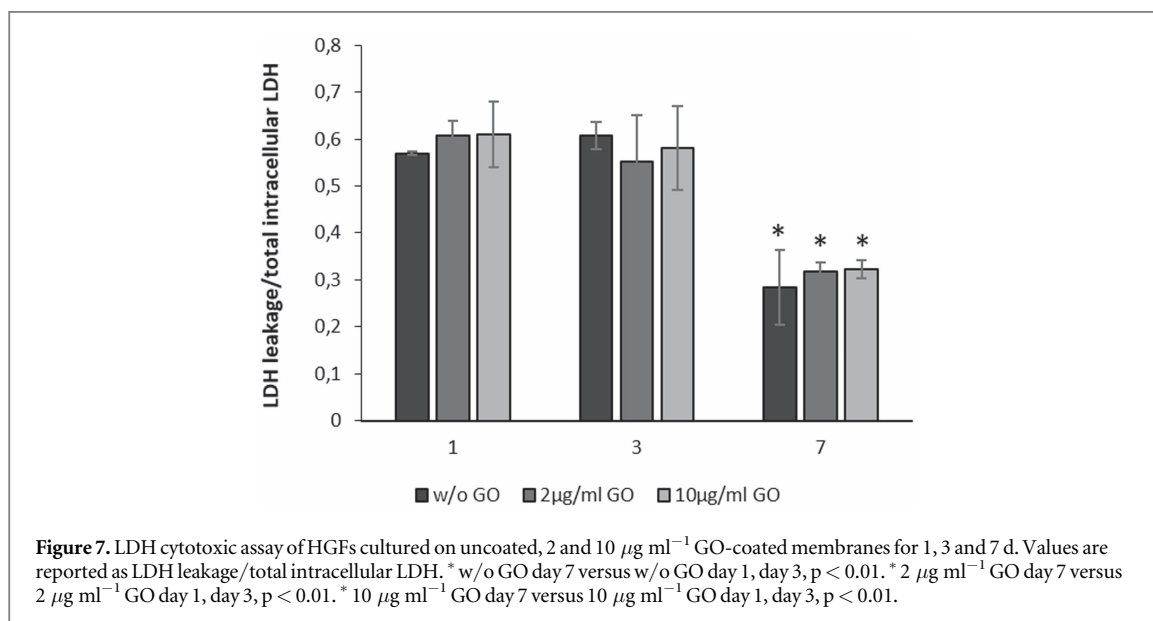
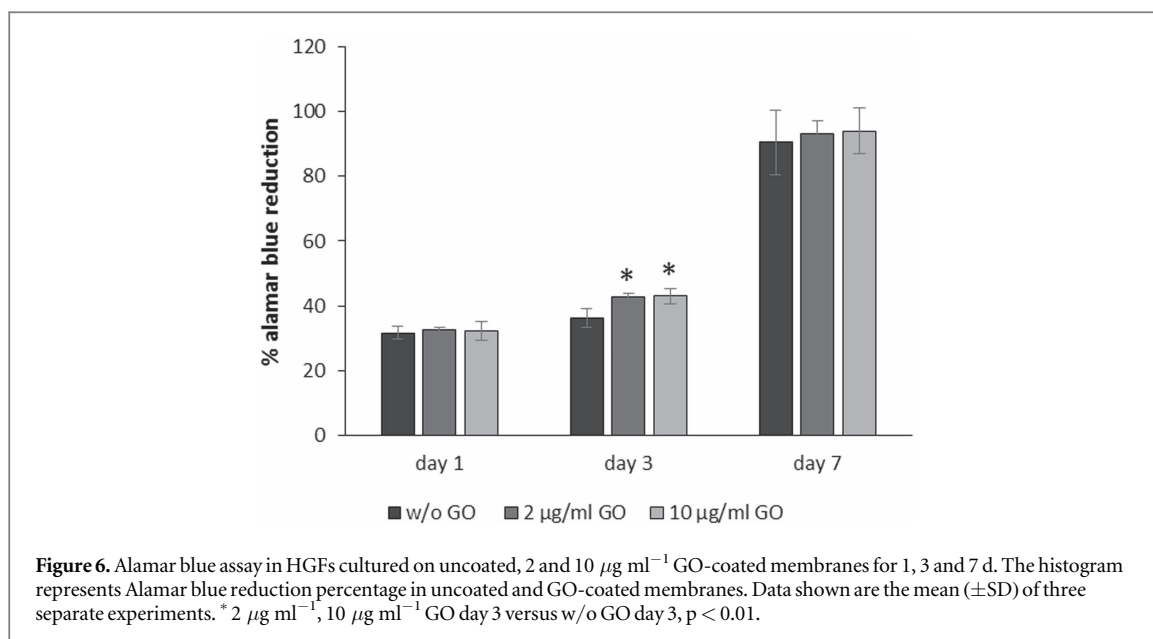
Alamar blue assay, performed in order to measure the cell metabolic activity, showed an expected increase over time due to cellular proliferation. At day 3 the metabolic activity of the cells grown on membrane coated with both  $2 \mu\text{g ml}^{-1}$  GO and  $10 \mu\text{g ml}^{-1}$  GO was significantly higher than that monitored on the control membrane, whereas no significant difference was recorded at other experimental times (figure 6).

In order to evaluate the biocompatibility of the membranes coated with GO, an LDH cytotoxicity assay was performed. A significantly lower LDH leakage by HGFs cultured on both test and control membranes on day 7 with respect to day 3 was shown, while no difference was observed between day 1 and day 3. Also, the presence of GO on the membranes did not affect LDH leakage at any experimental time (figure 7).

To investigate the occurrence of an inflammatory event, ELISA assay was performed in order to detect IL6 and PGE2 pro-inflammatory cytokine secretion levels in the culture medium. At day 3 the IL6 secretion level was significantly lower in cells cultured on membranes coated with both  $2 \mu\text{g ml}^{-1}$  and  $10 \mu\text{g ml}^{-1}$  GO with respect to those grown on control membranes, while at other experimental times no statistically significant difference was revealed (figure 8(a)). The secretion levels of PGE2 at day 1 and day 7 did not show a significant difference between the control membrane and both test membranes; however, at day 3 the control membrane showed a significantly higher secretion level than both test membranes. Although secretion levels of PGE2 through time showed a trend to decrease in the presence of all membranes, the only statistically significant decrease was observed between day 3 and day 7 in cells grown on membranes coated with  $2 \mu\text{g ml}^{-1}$  GO (figure 8(b)).

## Discussion

Collagen membranes were easily coated with GO by simply drop casting the aqueous GO solution of



proper concentration on the membrane. The GO demonstrated good distribution across the surface, although AFM analysis indicated that GO did not form a continuous film. SEM analyses highlighted the presence of some frustules on the surface of  $2 \mu\text{g ml}^{-1}$  GO-coated membrane, which disappeared in the  $10 \mu\text{g ml}^{-1}$  GO-coated one. A higher concentration of GO rendered the surface apparently more smooth, as already recently evidenced in the case of porcine bone granules [22]. This smoothness is only apparent because the calculated roughness indexes, although relative only to the imaged samples and therefore characterized by a high error, were  $R_q = 62.8 \text{ nm}$ ,  $R_a = 50 \text{ nm}$ , image  $R_{\text{max}} 401 \text{ nm}$ ,  $S_{\text{dq}} 40.6^\circ$ ,  $S_{\text{dr}} 32.3\%$  for the bare membrane (see figure S12 in the supplementary data) and  $R_q = 177 \text{ nm}$  and  $R_a = 141 \text{ nm}$ , image  $R_{\text{max}} 973 \text{ nm}$ ,  $S_{\text{dq}} 45^\circ$ ,  $S_{\text{dr}} 42.4\%$  for the GO-coated sample (see figure S13 in the supplementary data), where  $R_q$  is the roughness least square value;  $R_a$ , the average of the absolute values of the surface high deviations; image  $R_{\text{max}}$ , the maximum vertical distance between the highest and lowest data points in the image following the plane fit;  $S_{\text{dq}}$ , the root-mean-square of the surface slope, and  $S_{\text{dr}}$ , the developed interfacial area ratio. In terms of  $R_q$  and  $R_a$ , the non-coated membrane showed a lower roughness, as compared to the GO-coated sample, with slightly lower peaks, as confirmed by image  $R_{\text{max}}$  values. The surface indexes were in agreement with the previous data because  $S_{\text{dr}}$  and  $S_{\text{dq}}$ , which were expected to give the surface enlargement induced by the presence of roughness and an idea of the steepness of the peaks, showed more and steeper peaks in the coated sample.

GO-coated membranes have been characterized by peak force QNM. Despite adhesion, dissipation energy and deformation maps, reported in figure 3, indicate the presence of regions with different features on the coated sample (i.e. the upper right corner with the GO flakes and the bottom region); quantification of the obtained data should be performed with caution. Indeed, the adhesion force between the tip and the substrate, mainly associated with electrostatic and van der Waals interactions, may be affected by attractive capillary forces, especially when we consider that the collagen membrane is partially hydrated (i.e. measures are performed in air and not under controlled anhydrous conditions) [31]. The data obtained highlight that the adhesion of the tip to the surface increases on coating the membrane with GO. In particular, in the same membrane the top right region coated with GO shows a tip adhesion two times higher than that measured in the bottom region. The higher adhesion of the GO for the tip can be due to electrostatic interactions between the negative surface charge of GO [22] and the tip—although an adhesion increase, due the formation of a capillary meniscus, cannot be excluded.

The value of dissipation energy for the bare membrane (i.e.  $120 \pm 30 \text{ eV}$ ) is in agreement with the value previously measured for a hydrated collagen fiber [32]. Considering that an elastic sample is characterized by low dissipation energy values, the energy dissipation value obtained is indicative of a non-perfectly elastic sample (i.e. viscoelastic behavior). The dissipation energy measured for the GO-coated membrane is one third higher than that measured for the pure membrane—dissipation energy being higher on the GO flakes than in the bottom region. These data are difficult to explain; probably, they may be affected by water bridge formation [32] favored by the establishment of hydrogen bonds among acid, carbonyl and ether groups of GO and water, which hamper proper measurement of the viscoelastic properties.

Indeed, the small elastic deformability of GO-coated membranes may be the result of the stiffness conferred to the membrane by GO flakes. Since collagen fibers demonstrated an increase in their deformation on increasing hydration [32], the observed decrease of deformation of the GO-coated membrane may also be imputed to a reduction of collagen hydration due to the preference of collagen to form hydrogen bonds with GO rather than with water.

Stability measurements obtained by membrane immersion in water evinced no apparent dissolution of graphene oxide in solution after seven days of contact.

Collagen membranes coated with different GO concentrations were then tested in a human gingival fibroblast biological model, in order to check their early adhesion and proliferation on barrier membranes which switch on a healing process after surgical procedures.

During all the fibroblast culture period, GO addition did not negatively affect the biological parameters evaluated—thus indicating, at a glance, a good tolerability. In particular, GO coating, both at low and high concentration, enhanced the proliferation rate of fibroblasts, and at the same time ensured an appreciable control of inflammatory events (which appeared less pronounced in coated membranes). As expected, these evidences appeared statistically significant only after three days of culture, as the average doubling time of cultured fibroblasts is estimated to be  $33.2 \pm 10.4 \text{ h}$  *in vitro* [33]. For this reason, after 24 h of culture, gingival fibroblasts were still starting up their metabolism—thus proliferation and secretion events were scarcely appreciable. On the other hand, after 7 d of culture it could be easily expected that the cells reached a confluence condition on the available surface.

These results may be connected with the demonstrated ability of GO to favour protein adsorption [34], an essential step in regulating cell function and mediating cell adhesion and morphology [35]. This means that the presence of GO should favour cell adhesion

and subsequent cells growth. Analogously, by adsorption of IL6 and PGE2 pro-inflammatory cytokines, this same effect could affect their quantification in the culture medium. Nevertheless, this event seems unlikely because, during pro-inflammatory cytokines quantification, the GO-coated membrane was already covered, and therefore almost saturated, with proteins and cells. These preliminary conclusions pave the way for interesting discussions and further studies on the subject.

## Conclusions

This study demonstrated that the relatively homogeneous coating of commercial collagen membranes with GO was easy to obtain. No evidence of release of GO in the aqueous medium was observed in a time interval of seven days. The presence of GO on the membrane was shown to alter the mechanical features of the membrane, conferring a lower deformability—likely connected with a higher stiffness and reduced hydration—and increased roughness, with respect to the bare membrane. These changes were demonstrated to favor the proliferation rate of HGFs, avoiding inducing any inflammatory response—as checked by ELISA test of both IL6 and PGE2 secretion—probably due to the capacity of GO to adsorb proteins and promote cell adhesion. This study paves the way to the further investigation of these novel coated membranes in terms of promotion of osteoblast differentiation and/or bacteriostatic activity.

## Acknowledgments

The authors thank the Universities of Chieti-Pescara and MIUR (PRIN 2010-11, prot. 2010N3T9M4 and FIRB 2010, prot. RBAP1095CR) for financial supports.

## ORCID iDs

Antonella Fontana  <https://orcid.org/0000-0002-5391-7520>

## References

- [1] Bunyaratavej P and Wang H L 2001 *J. Periodontol.* **72** 215–29
- [2] Hämmerle C H F and Jung R 2003 *Periodontology 2000* **33** 36–53
- [3] Karring T, Isidor F, Nyman S and Lindhe J 1985 *J. Clin. Periodontol.* **12** 51–60
- [4] Schlegel A K, Möhler H, Busch F and Mehl A 1997 *Biomaterials* **18** 535–8
- [5] Locci P, Calvitti M, Belcastro S, Pugliese M, Guerra M, Marinucci L, Staffolani N and Becchetti E 1997 *J. Periodontol.* **68** 857–63
- [6] Rothamel D, Schwarz F, Sculean A, Herten M, Scherbaum W and Becker J 2004 *Clin. Oral. Implant. Res.* **15** 443–9
- [7] Brunel G, Piantoni P, Elharar F, Benque E, Marin P and Zahedi S 1996 *J. Periodontol.* **67** 1342–8
- [8] Pitaru S, Noff M, Grosskopf A, Moses O, Tal H and Savion N 1991 *J. Periodontol.* **62** 598–601
- [9] El-Fiqi A, Lee J H, Lee E J and Kim H W 2013 *Acta Biomater.* **9** 9508–21
- [10] Geim A and Novoselov K 2007 *Nat. Mater.* **6** 183–91
- [11] Sabourin J L, Dabbs D M, Yetter R A, Dryer F L and Aksay I A 2009 *ACS Nano* **3** 3945–54
- [12] Zhang J, Yang H, Shen G, Cheng P, Zhang J and Guo S 2010 *Chem. Commun.* **46** 1112–4
- [13] Sun X, Liu Z, Welsher K, Robinson J T, Goodwin A, Zaric S and Dai H 2008 *Nano Res.* **1** 203–12
- [14] Zhang W, Guo Z, Huang D, Liu Z, Guo X and Zhong H 2011 *Biomaterials* **32** 8555–61
- [15] Chen H, Muller M B, Gilmore K J, Wallace G G and Li D 2008 *Adv. Mater.* **20** 3557–61
- [16] Agarwal S, Zhou X, Ye F, He Q, Chen G C, Soo J, Boey F, Zhang H and Chen P 2010 *Langmuir* **26** 2244–7
- [17] Nishida E, Miyaji H, Kato A, Takita H, Iwanaga T, Momose T, Ogawa K, Murakami S, Sugaya T and Kawanami M 2016 *Int. J. Nanomed.* **11** 2265–77
- [18] Park S, Mohanty N, Suk J W, Nagaraja A, An J, Piner R D, Cai W, Dreyer D R, Berry V and Ruoff R S 2010 *Adv. Mater.* **22** 1736–40
- [19] Ferrari A C et al 2015 *Nanoscale* **7** 4598–810
- [20] Hu W, Peng C, Luo W, Lv M, Li X, Li D, Huang Q and Fan C 2010 *ACS Nano* **4** 4317–23
- [21] Liao K H, Lin Y S, Macosko C W and Haynes C L 2011 *ACS Appl. Mater. Interfaces* **3** 2607–15
- [22] Ettore V et al 2016 *Carbon* **103** 291–8
- [23] Hummers W S and Offeman R E 1958 *J. Am. Chem. Soc.* **80** 1339–1339
- [24] Rattana T, Chaiyakun S, Witit-anun N, Nuntawong N, Chindaudom P, Oaew S, Kedkeaw C and Limsuwan P 2012 *Procedia Eng.* **32** 759–64
- [25] Horcas I, Fernández R, Gómez-Rodríguez J M, Colchero J, Gómez-Herrero J and Baro A M 2007 *Rev. Sci. Instrum.* **78** 013705
- [26] Radunovic M, De Colli M, De Marco P, Di Nisio C, Fontana A, Piattelli A, Cataldi A and Zara S 2017 *J. Biomed. Mater. Res. A* **105** 2312–20
- [27] Han D-D, Zhang Y-L, Liu Y, Liu Y-Q, Jiang H-B, Han B, Fu X-Y, Ding H, Xu H-L and Sun H-B 2015 *Adv. Funct. Mater.* **25** 4548–57
- [28] Dufrene Y F, Martínez-Martín D, Medalsy I, Alsteens D and Müller D J 2013 *Nat. Methods* **10** 847–54
- [29] Alsteens D, Dupres V, Yunus S, Latgé J-P, Heinisch J J and Dufrene Y F 2012 *Langmuir* **28** 16738–44
- [30] Weadock K S, Miller E J, Bellincampi L D, Zawadsky J P and Dunn M G 1995 *J. Biomed. Mater. Res.* **29** 1373–9
- [31] Zitzel L, Herminghaus S and Mugele F 2002 *Phys. Rev. B* **66** 155436
- [32] Uhlig M R and Magerle R 2017 *Nanoscale* **9** 1244–56
- [33] Mio T, Nagai S, Kitaichi M, Kawatani A and Izumi T 1992 *Chest* **102** 832–7
- [34] Lee W C, Lim C H Y X, Shi H, Tang L A L, Wang Y, Lim C T and Loh K P 2011 *ACS Nano* **5** 7334–7341
- [35] Woo K M, Chen V J and Ma P X 2003 *J. Biomed. Mater. Res., Part A* **67A** 531–537



# Scattering-enhanced absorption and interference produce a golden wing color of the burnished brass moth, *Diachrysia chrysitis*

Dejan Pantelić,<sup>1,\*</sup> Svetlana Savić-Šević,<sup>1</sup> Dejan V. Stojanović,<sup>2</sup> Srećko Ćurčić,<sup>3</sup> Aleksandar J. Krmpot,<sup>1</sup> Mihailo Rabasović,<sup>1</sup> Danica Pavlović,<sup>1</sup> Vladimir Lazović,<sup>1</sup> and Vojislav Milošević<sup>1</sup>

<sup>1</sup>*Institute of Physics, University of Belgrade, Pregrevica 118, 11080 Zemun, Belgrade, Serbia*

<sup>2</sup>*Institute of Lowland Forestry and Environment, University of Novi Sad, Antona Čehova 13, 21000 Novi Sad, Serbia*

<sup>3</sup>*Institute of Zoology, University of Belgrade—Faculty of Biology, Studentski Trg 16, 11000 Belgrade, Serbia*

(Received 3 November 2016; published 8 March 2017)

Here we report how interference and scattering-enhanced absorption act together to produce the golden wing patches of the burnished brass moth. The key mechanism is scattering on rough internal surfaces of the wing scales, accompanied by a large increase of absorption in the UV-blue spectral range. Unscattered light interferes and efficiently reflects from the multilayer composed of the scales and the wing membranes. The resulting spectrum is remarkably similar to the spectrum of metallic gold. Subwavelength morphology and spectral and absorptive properties of the wings are described. Theories of subwavelength surface scattering and local intensity enhancement are used to quantitatively explain the observed reflectance spectrum.

DOI: [10.1103/PhysRevE.95.032405](https://doi.org/10.1103/PhysRevE.95.032405)

## I. INTRODUCTION

Fascinating “inventions” of evolution have been discovered in a large number of recent studies dealing with the biophysics of living creatures. In that respect, insects are an excellent research subject due to their diversity and abundance.

Biophotonics of insects is a particularly active subject which aims to explain function and imitate intricate micro- and nanostructures on their bodies. Several studies present a comprehensive overview of the current research [1–3]. Surprising results are still being published, such as the photonic system of a Saharan silver ant, enabling radiative dissipation of heat, directly through the IR atmospheric window [4]. This and a number of other studies suggest that nature has developed many technologies which can be used to solve everyday problems, if successfully imitated [5,6].

Optical photonic structures in the living world are diverse and have been classified by Land [7], based on their biological function, including tapeta (light-path doubling or image forming), camouflage, display, optical filters (e.g., corneal nipples of insect compound eyes), and anatomical accidents (features whose optical properties have no obvious biological function, e.g., mother-of-pearl in some mollusks).

More specifically, the biophotonics of Lepidoptera draws much attention, mostly due to the attractiveness of butterflies. Much less is known about moths (suborder Heterocera), which represent a group of Lepidoptera, characterized by the wings mostly having drab colors (gray or brown), and feathery or saw-edged antennae (vs club-shaped in butterflies). While moths are more numerous than butterflies, the number of structural coloration studies is significantly smaller. Only attractive and conspicuous moth species were explored, such as the Madagascan sunset moth [8]. The lack of interest is, possibly, due to the simpler wing-scale structure of moths, compared to really complex features present on the scales of day flying butterflies (e.g., Bragg gratings or photonic crystals).

Golden wing patches are prominent features of some noctuid moths. The patches might be just small marks as in *Autographa jota* (Linnaeus, 1758) and *A. bractea* (Denis & Schiffermüller, 1775), or large areas, as in *Diachrysia balluca* Geyer, 1832. The physics behind the golden moth color was previously analyzed using the diffraction theory of Stratton-Silver-Chu [9] in the case of *Thysanoplusia orichalcea* (Fabricius, 1775) (previously included in the genus *Trichoplusia* McDunnough, 1944) (Noctuidae family). However, a correspondence between theory and experimentally recorded spectra was qualitative, probably due to approximations of the mathematical formalism.

Other insects with a golden cuticle do exist, such as *Chrysin aurigans* (Rothschild & Jordan, 1894) (Coleoptera: Scarabaeidae) [10], whose broadband metallic reflection is due to a chirped Bragg mirror within the cuticle. Some species have a tunable color, which depends on atmospheric humidity [11] or stressful events [12], enabling the insects to change the color from red to golden.

Rothschild *et al.* [13] found that carotenoid pigments may also contribute to golden metallic areas of Danainae butterfly pupae. Similar results were obtained by Taylor [14] and Neville [15]. In contrast, Steinbrecht *et al.* [16] proved that golden reflections of *Euploea core* (Cramer, 1780) (Lepidoptera: Nymphalidae) pupae have an entirely physical nature. They showed that reflectance spectra of the cuticle (possessing multiple endocuticular thin alternating layers) and metallic gold are very similar, with a characteristic edge at 450–550 nm. The authors also emphasize that the carotenoids in the epidermis cannot contribute to the color effects because the cuticle practically does not transmit yellow light at all.

Scattering from an irregular surface is a secondary mechanism of structural coloration—interference and diffraction being dominant ones. For example, lycaenid butterflies (in particular, subfamily Polyommatae) scatter light from the internal, pepper-pot-like, Bragg layers (having holes of 100 nm average diameter). The wing-scale laminae are almost hollow and permit the blue radiation to escape [17]. Pieridae can also be mentioned due to the nanobeads (pigment granules), which fill the space between the laminae [18], where the scattering

\*pantelic@ipb.ac.rs

and fluorescence extend the reflection spectrum [19,20]. Scattering in the living world is sometimes accompanied by light trapping, as in diatoms [21]. This seems to be a significant mechanism for efficient light harvesting in photosynthetic organisms.

Here we describe how several optical mechanisms interact to produce the golden wing color of the burnished brass moth, *Diachrysis chrysitis* (Linnaeus, 1758). We have studied spectral properties of the golden wing patches, as well as the internal and external ultrastructure of the wing scales and wing membranes. It was found that the scattering from irregular internal surfaces of each scale suppresses the UV-blue reflection, while interference efficiently reflects the red-infrared spectral range. A theoretical model is proposed, which combines interference and scattering from the scale laminae. The finite element method (FEM) is used to confirm the trapping and local intensity enhancement of light inside the laminae, while the modified transfer matrix method is used to calculate the reflection spectrum.

## II. OPTICAL PROPERTIES AND STRUCTURE OF *D. CHRYSITIS* WING

The burnished brass moth (*D. chrysitis*; shown in Fig. 1) is a common species of the Noctuidae family (Insecta: Lepidoptera). It inhabits temperate climates in the Palearctic region [22]. *D. chrysitis* is a remarkable moth with big, golden (sometimes brassy-green) areas on each forewing. The wingspan is 28–35 mm, while the length of each forewing is 16–18 mm [23]. The burnished brass moth is usually found in marshy areas or in slightly moist forb communities. The larvae feed on plants such as *Urtica* spp., *Lamium* spp., or *Cirsium* spp. [24]. The moth flies from May to October depending on the location. It flies regularly in dusk, and was seen visiting flowers of various plants. Sometimes it can be noticed during the day, even sucking nectar. The species is widespread in Serbia [25].

It is supposed that irregular golden patches in the forewings of *D. chrysitis* are an example of disruptive coloring, as an excellent way of hiding oneself by breaking up the body contours [26]. Additionally, it was also postulated that specular



FIG. 1. Burnished brass moth (*D. chrysitis*) with golden areas on its forewings.

reflection of the sun's rays may imitate the glittering of dew droplets. Even more, it seems that the wing color is optimized to efficiently reflect the yellowish light of the sun. As a dusk species, the moth may emit a signal in the IR spectral range from the golden patches, which might be used as a signal for intraspecific recognition. Anatomical accidents seem unlikely because metallic areas on *D. chrysitis* forewings form species-specific patterns [27].

From the optical point of view, the most prominent features of the studied moth are golden-color wing patches, as seen in Fig. 1. The corresponding wing spectra were recorded in reflection using a fiber optic spectrometer (manufactured by Ocean Optics, HR2000CG-UV-NIR), with a 400- $\mu\text{m}$  core diameter fiber. A halogen lamp was used as a light source, and spectra were referenced to a standard white surface. The light collection angle was limited by the numerical aperture of the fiber ( $\text{NA} = 0.22$ , which is equivalent to an angular range of  $\pm 12.7^\circ$ ), positioned such that an approximately 40- $\text{mm}^2$  area is observed. This means that the spectra of individual scales are integrated both angularly and across the wing surface. This fact was accounted for in the numerical simulations.

The spectrum of *D. chrysitis* is broad, with a cutoff wavelength at approximately 500 nm. Its exact shape slightly depends on the angle between light source, wing, and detector. There is a close similarity with the spectrum of metallic gold, as shown in Fig. 2. The specular reflectance spectrum of gold is taken tabulated from Ref. [28], where it is treated as a reference standard.

Optical reflection microscopy of the *D. chrysitis* forewing reveals an almost uniform, intense golden sheen as shown in Fig. 3(a). In contrast, reflection from individual scales is yellowish, with occasional red and green bands, presented in Fig. 3(b). Overlapped scales show increased reflection and color bands, as can be observed in the same image. If observed in transmission, an individual scale in air [see Fig. 3(c)] is quite transparent, with a slight residual absorption. By immersing

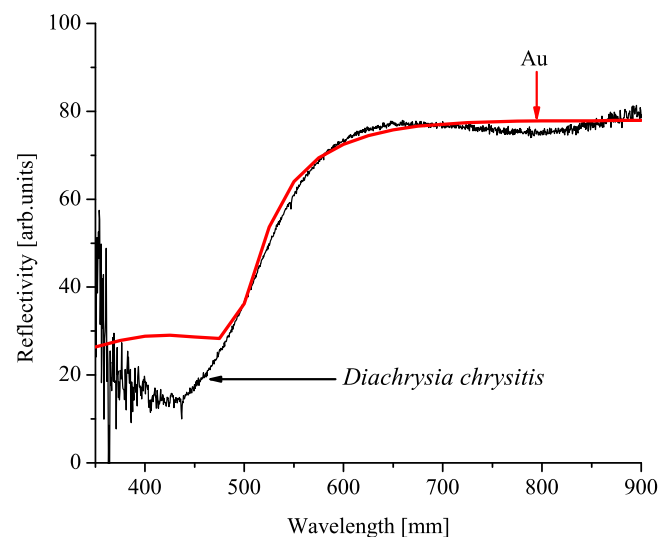


FIG. 2. Spectral reflectance of metallic gold (red curve) and golden wing patch of *D. chrysitis* forewings (black curve). Reflectance of *D. chrysitis* is scaled to emphasize the similarity with the gold.

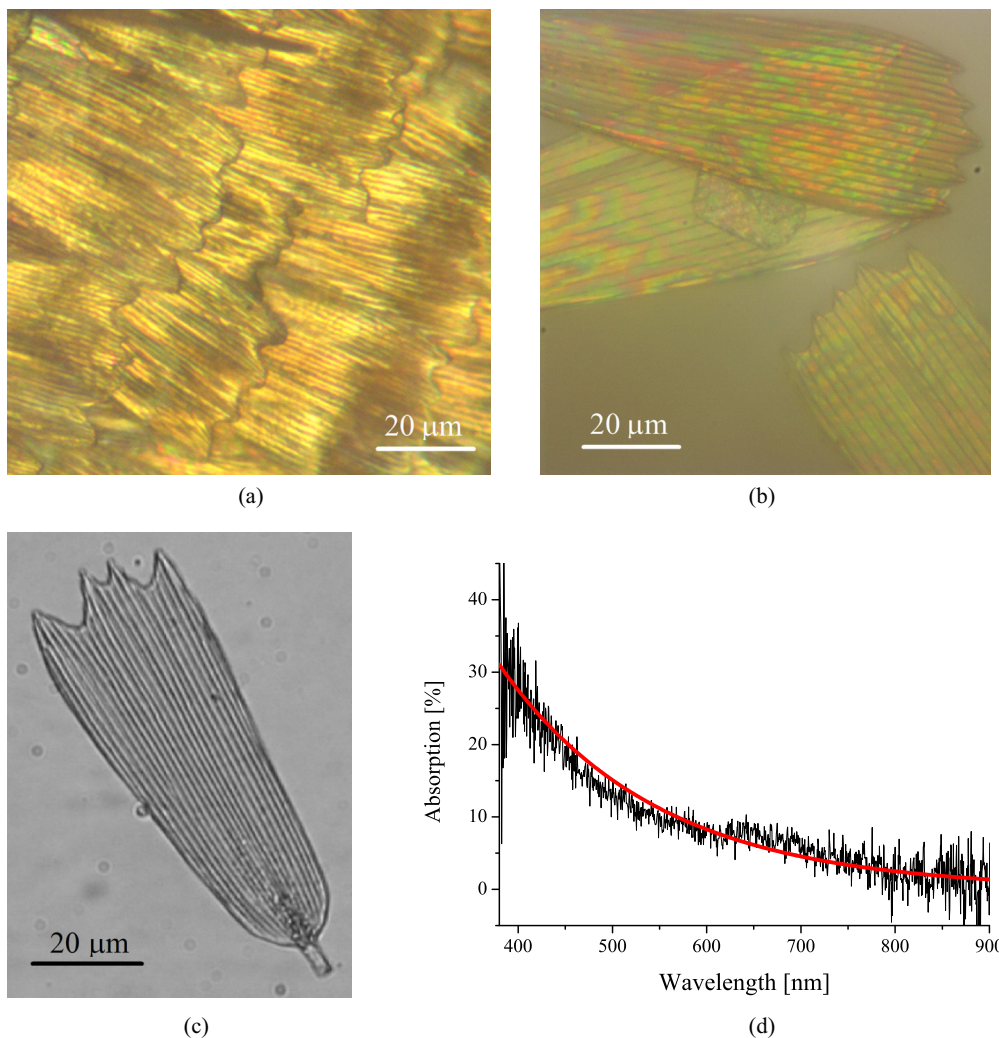


FIG. 3. Optical microscope images of *D. chrysitis*: (a) Scales on the forewing showing the uniformly golden reflection. (b) A microscope reflection image of two individual, overlapped scales. (c) A transmission image of an individual scale in air. (d) Absorption spectrum of a single scale placed in an immersion oil (black line) and the corresponding exponential fit (red line).

the scale in an index matching liquid (manufactured by Cargile, series A, with the certified refractive index  $1.5700 \pm 0.0002$ ) Fresnel reflection was suppressed. We measured the absorption spectrum [Fig. 3(d)], which is very similar to that of melanin [29], showing exponential decrease from the UV to the IR part of the spectrum. We were able to estimate the value of the absorption coefficient  $\alpha$  (or the imaginary part of the complex index of refraction  $k = \alpha\lambda/4\pi$ ), and use it in further calculations. We have found that  $k$  ranges between 0.081 (at 380 nm) and 0.0013 (at 800 nm).

A field-emission gun scanning electron microscope (FEGSEM) was used to study the fine anatomy of the moth scales. The *D. chrysitis* forewing possesses a number of overlapping scales [as in Fig. 4(a)], but we were not able to see a difference between cover and ground scales. At higher magnification, as in Fig. 4(b), we can see that the upper lamina is ornamented with very thin lamellar ridges (separated by approximately  $1.8 \mu\text{m}$ ). They are connected with herringbone shaped cross ribs, which constitute a subwavelength diffraction grating with the period of roughly 150 nm. A dual wing membrane seems to be an important optical component, too.

Its thickness is of the order of 500 nm and contains a number of 300-nm diameter, randomly dispersed, hemispherical protuberances [see inset in Fig. 4(a)].

Individual scales were prepared for scanning electron microscopy by the double transfer method, which was begun by detaching a scale with a low-surface-energy adhesive (adhesive layer of “Post-it” sticky note), followed by the transfer to a high-surface-energy tape (conductive carbon). By that means, the original scale orientation was preserved. Figure 5 shows one of the partially destroyed scales and its internal and external laminae structures. We see that the external side of the upper lamina (the one facing outwards) is strongly patterned, as explained above, while its internal surface is very irregular, with linear grooves directly beneath the ridges. The external side of the lower lamina (the one facing the wing membrane) is smooth, while its internal surface is completely irregular, similar to nanometer-sized “pebbles,” with a diameter less than 60 nm.

We have observed a strong autofluorescence of scales, which is enough for nonlinear (NL) fluorescence microscopy. We used a nonlinear microscope for laser processing and

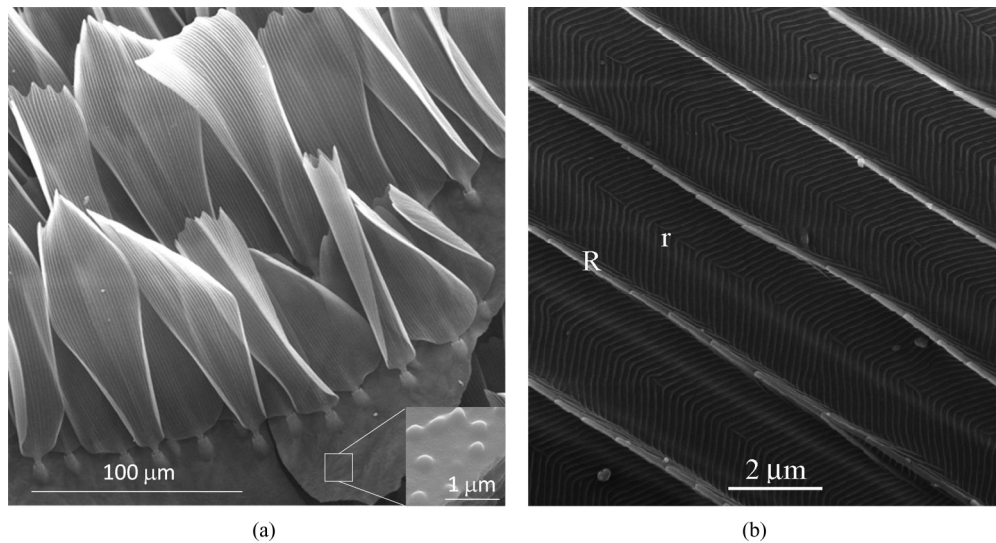


FIG. 4. (a) Scales of *D. chrysitis* in their natural position on the wing. The inset shows the enlarged part of the wing membrane with 300-nm-diameter protuberances. (b) Enlarged image of a single scale, showing lamellar ridges (R) and herringbone shaped cross ribs (r).

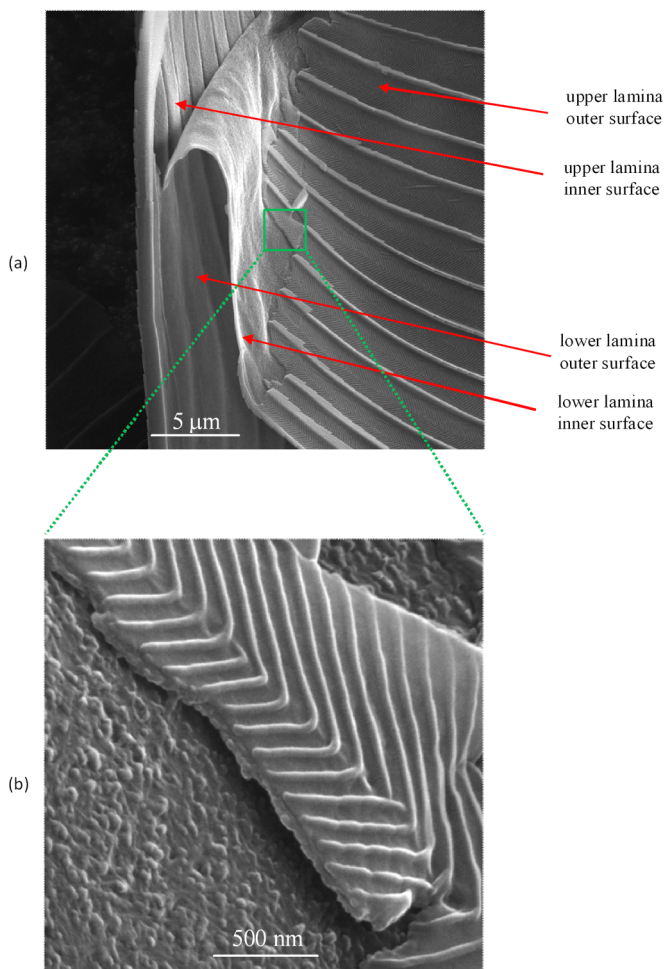


FIG. 5. FEGSEM images of a single *D. chrysitis* scale at two different magnifications. (a) This image reveals the internal and external structure of a single scale. (b) Enlarged zone of a scale showing rough internal surfaces.

cutting, too, which turned out to be a good tool for exposing otherwise hidden features. The beam power was increased above the threshold level and software was modified to enable drawing arbitrary shapes using vector images. At 840 nm and  $\sim 100$  fs pulse length we were cutting moth chitinous structures with as low as a few milliwatts of laser power. However, continuous wave (cw) radiation at the same wavelength required an order of magnitude higher power. It was interesting that the laser-cut lines were rather irregular in the case of *D. chrysitis*, in contrast to scales of other lepidopteran species, which produced clear, well defined, lines.

To further reveal the cross-sectional geometry of *D. chrysitis* moth scales, we cut them as explained above. A SEM image of a laser-cut scale is shown in Fig. 6. The internal space of the scale is not visible due to the welding of the upper and lower laminae, but we were able to estimate the thickness of the scale at 300 nm, and the height of the ridge at 400 nm. Based on the scanning electron microscope images we are able to draw a general scheme of an individual scale as presented in Fig. 7.

We emphasize that the external features of the wing scale (such as the distance between the ridges) can be measured accurately from FEGSEM images, because they are recorded at normal incidence. Other characteristics, such as laminae thickness, are more complicated to quantify due to difficulty in determining the exact relative position of the scale and the scanning electron microscope optics (see Fig. 6, where the scale is partially lifted from the substrate). In such cases, measurements were performed using external features as a reference—e.g., lamina thickness was determined at approximately 75 nm by observing that it is approximately one half of the distance between the cross ribs (150 nm). Anyway, such measurements served just as a starting point for a wing-scale model.

Variability of the moth scales is another source of uncertainty. We recorded a number of SEM images, measured relevant features at several positions, and were able to find that they vary between 15% and 20% (depending on the measured characteristics).

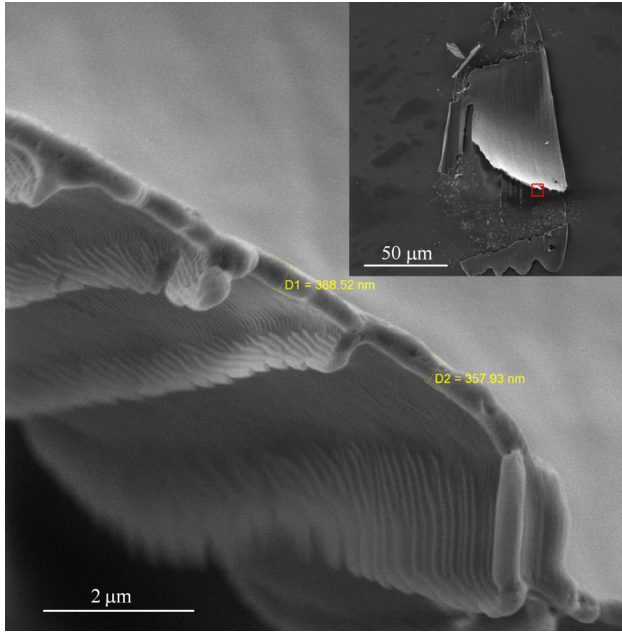


FIG. 6. A cross-sectional image of a femtosecond-laser-cut *D. chrysis* wing scale. The image of the whole, laser-cut scale is shown in the inset.

### III. OPTICAL MODELING OF THE *D. CHRYSITIS* WING SCALES

The transparency of *D. chrysis* scales and the apparent simplicity of their internal and external structure pose a problem in explaining the golden wing color. We show that all the wing components (a double layer of scales and a wing membrane, possibly also the pigmented scales on the wing underside) work together to produce the final effect. Several features operate synergistically: slight absorbance of each scale, scattering on internal scale surfaces, interference of light within the scale, reflection of light from the wing membrane, and diffraction on the upper lamina grating.

We first demonstrate that the scattering on the internal scale surfaces leads to significant dispersal of incident light. As shown in Fig. 5, the internal scale surfaces are highly irregular, with the root mean squared (RMS) roughness estimated between 10 and 30 nm. The wavelength of the incident visible light (inside material) is much larger than the roughness and

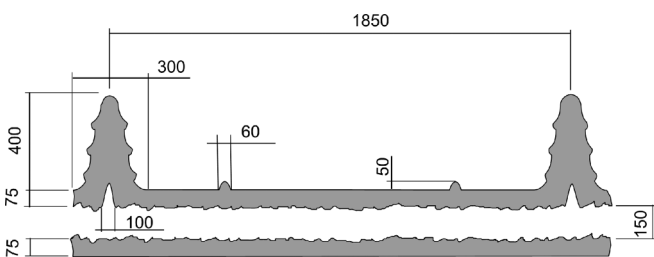


FIG. 7. A dimensional scheme of a *D. chrysis* scale cross section. All dimensions (expressed in nanometers) are estimated from SEM images and vary across the scales. Due to the variability of features in the living world, uncertainty of all the dimensions is between 15% and 20%.

the widely used scalar surface-scattering theory [30,31] is applicable. Under these circumstances, the light is split into two parts: one, regular, propagating as if the surface is perfectly flat, and the other diffusely scattered (haze).

Quantitatively, both components are described relative to transmittance  $T_0$  and reflectance  $R_0 = 1 - T_0$  of an ideally flat surface, when Fresnel equations hold. Accordingly, the haze transmittance  $T_H(\lambda)$  and reflectance  $R_H(\lambda)$  of a rough surface are described by [31]

$$T_H(\lambda) = T_0 \left( 1 - \exp \left\{ - \left[ \frac{2\pi\sigma}{\lambda} (n_i \cos \phi_i - n_t \cos \phi_t) \right]^2 \right\} \right), \quad (1)$$

$$R_H(\lambda) = R_0 \left\{ 1 - \exp \left[ - \left( \frac{4\pi\sigma}{\lambda} n_i \cos \phi_i \right)^2 \right] \right\}, \quad (2)$$

where  $T_0$  and  $R_0$  are the transmittance and the reflectance of a perfectly flat surface, respectively;  $\lambda$  is the wavelength in vacuum;  $\phi_i$  and  $\phi_t$  are the angles of incidence and refraction;  $n_i$  and  $n_t$  are corresponding refractive indices;  $\sigma$  is the surface RMS roughness.

A simple calculation, based on Eqs. (1) and (2), shows that between 1% and 3% of incident radiation is scattered at each interface, depending on the wavelength and assuming normal angle of incidence ( $\phi_i = 0$ ), RMS roughness  $\sigma = 20$  nm, and the refractive index of chitin  $n_i = 1.57$ . As expected, short wavelengths are scattered more than long ones. The scattered light has a tendency to be trapped inside chitin layers, in a manner similar to textured solar cells [32]. It was shown in [33] that the local light intensity is increased by  $2n^2$ , and absorption by  $4n^2$ , where  $n$  is the refractive index. This was verified for the *D. chrysis* moth by using the finite element method (FEM) with periodic boundary conditions, applied to the model simulating a double layer of scales, as shown in Fig. 8(a). The corresponding electromagnetic field distributions can be seen in Fig. 8(b) showing the strong electromagnetic field enhancement.

Local field enhancement due to scattering is accompanied by increased absorption as predicted by the model described in [33]. We made slight modifications to correctly describe the scales of *D. chrysis*.

The change of the beam cross section is ignored due to the thinness of the scales. This is justified by the following arguments: Assume that the angle of divergence is  $\theta = 40^\circ$  and scale laminae thickness is  $D = 75$  nm; then the beam spread is defined by  $2Dtg(\theta/2) = 55$  nm. This is insignificant for a beam width of approximately 7 mm, as used in our spectral measurement. The surface absorption was disregarded, too, because the residual melanin is expected to be distributed inside the laminae.

Under these assumptions, the absorption  $A_{int}$  inside the planar layer can be described by

$$A_{int} = \frac{4n^2 T_{inc}}{T_{esc} + 4n^2 \alpha l}, \quad (3)$$

where  $\alpha$  is absorption coefficient,  $n$  is the refractive index,  $I_{inc}$  is incident light intensity,  $l$  is the layer thickness, and  $T_{inc}$  is a fraction of light transmitted through the interface.  $T_{esc}$  is an

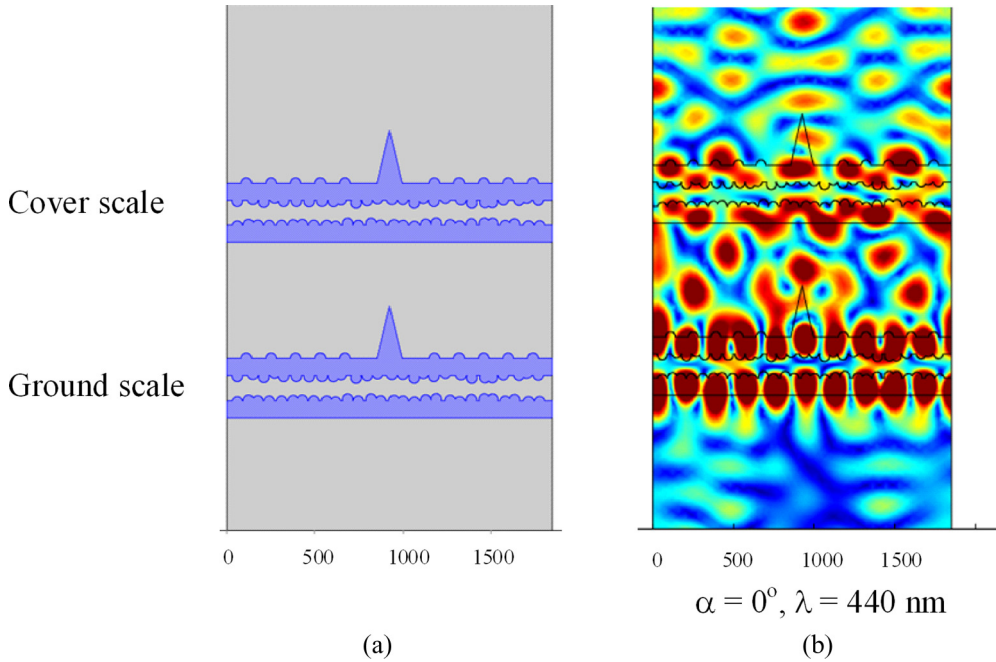


FIG. 8. (a) Geometry of the FEM model. (b) Intensity enhancement at 440 nm wavelength. The electromagnetic field is enhanced both in the ground and cover scales. Calculations were performed assuming that the angle of incidence is  $\alpha = 0$  and there is no absorption.

average transmission factor of the escaping radiation, due to partial (Fresnel) transmission at the interface. According to the same model, fraction of the incident radiation escaping the layer is described by

$$F_{\text{esc}} = \frac{T_{\text{inc}} T_{\text{esc}}}{T_{\text{esc}} + 4n^2 \alpha l}. \quad (4)$$

Now we have tools to treat the problem of the golden coloration of the burnished brass moth. Its geometry includes two layers of scales and two wing membranes as shown in Fig. 9(a). It is assumed that the outside surfaces of the scales are flat, which is strictly true only for the lower lamina. The upper lamina is structured with two gratings. The coarse one

will produce diffraction orders which will be treated similarly during the propagation through the scales, the only difference being the angle of incidence. The dense grating is incapable of generating any propagating modes and will not enter the calculations. The inside scale surfaces are rough with RMS roughness of 10–30 nm, and the wing membranes are treated as flat. Fresnel reflection and transmission will be taken into account at flat surfaces, while rough surfaces will also include haze in reflection and transmission as schematically shown in Fig. 9(b). In the latter case, haze  $R_H(\lambda)$  and  $T_H(\lambda)$  diminish Fresnel coefficients  $R_0$  and  $T_0$  by the amounts  $R_0 R_H(\lambda)$  and  $T_0 T_H(\lambda)$ . The resulting transmission and reflection coefficients are described by  $R_0 - R_0 R_H(\lambda)$  and  $T_0 - T_0 T_H(\lambda)$ .

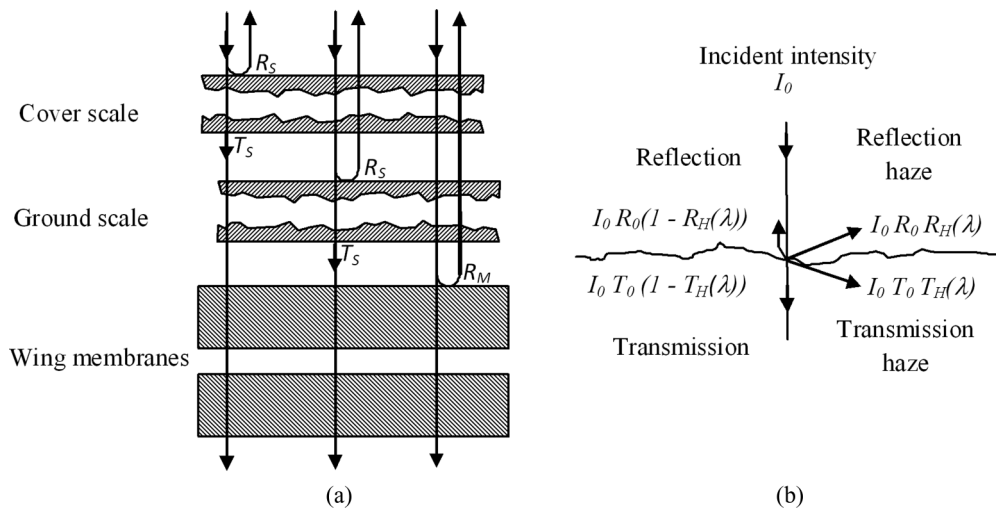


FIG. 9. (a) Geometry of the model used to simulate the wing of *D. chrysitis*.  $R_S$  and  $R_M$  are reflectance of a scale and a wing membrane, respectively.  $T_S$  is a transmittance of a single scale. (b) Reflection and transmission through the interface, as treated in a model. Incident intensity  $I_0$  is split into four components: Fresnel reflectance ( $R_0$ ), Fresnel transmittance ( $T_0$ ), reflection haze ( $R_H$ ), and transmission haze ( $T_H$ ).

TABLE I. Numerical values of the parameters used for modeling optical reflection from *D. chrysitis* moth scales.

Parameter	Meaning	Value
$N$	Refractive index of chitin	1.57
$\alpha_0$	Melanin absorption parameter, Eq. (5)	0.23 (1/nm)
$A$	Melanin absorption parameter, Eq. (5)	90 (nm)
$\lambda_0$	Melanin absorption parameter, Eq. (5)	380 (nm)
$\sigma$	RMS surface roughness	30 (nm)

The interference problem will be solved for an individual wing scale, as well as for the wing membranes, but not for the wing as a whole. This is a reasonable assumption, because the relative distances between the scales and the wing membrane are highly variable and the resulting effect is averaged across the wing surface. As a consequence, the resulting reflection spectral intensities of scales and membranes will be incoherently added.

Optical parameters of the model were estimated from the measurements performed on the scale embedded in an immersion liquid ( $n = 1.57$ ), as described in the previous section. Therefore, the refractive index was taken to be 1.57 (consistent with the results published in [34]). According to the same study [34], the refractive index dispersion is less than 4% within the wavelength range of interest (380–900 nm) and the resulting effects were found to be insignificant. The coefficient of absorption  $\alpha$  was modeled with an exponential function (assuming that the residual pigment is most probably melanin):

$$\alpha = \alpha_0 \exp\left(-\frac{\lambda - \lambda_0}{A}\right). \quad (5)$$

All parameters of the model are summarized in Table I.

Finding the exact solution to the multilayer interference is a problem requiring numerical tools. Here we adopt the transfer matrix method, described and used in [35] to analyze light scattering and trapping in silicon thin film solar cells. We divide incident light into two components: a scattered one, which is mostly absorbed and diffused, and an unscattered one, which interferes in wing scales and wing membranes. For the unscattered component we apply a transfer matrix method, where scattering from subwavelength rough surfaces is treated as a wavelength-dependent correction for Fresnel coefficients.

Reflection and transmission from a single scale are treated coherently using the transfer matrix method. As a result, the spectral reflectance  $R_S$  and transmittance  $T_S$  were found. Similarly, the reflection from the double wing membrane was treated coherently (with the resulting reflectance  $R_M$ ). Scattering from the wing membrane was not included in calculations due to the sparsity and large dimensions of scattering inclusions (as illustrated in Fig. 4). The resulting spectrum of the wing as a whole is composed of three components: one which is reflected from the cover scales, the other reflected from the ground scales, and the final one due to the wing membranes. We combine them incoherently, because the mutual position between scales and membranes is stochastic and highly variable. The final reflected spectral

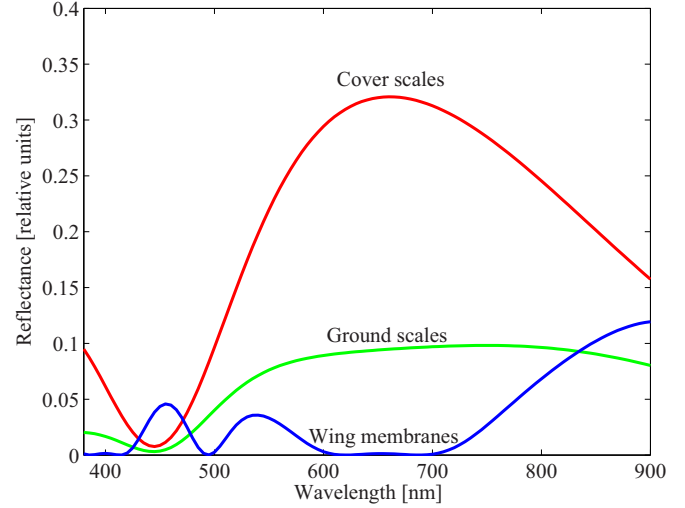


FIG. 10. Contributions of wing membranes, cover scales, and ground scales to the resulting wing spectrum. They are calculated using the transfer matrix method and normalized to the intensity of the incident light before being transmitted through the layers.

distribution of the whole wing is thus

$$R = R_S + T_S R_S T_S + T_S^2 R_M T_S^2. \quad (6)$$

The first term corresponds to the reflection from the cover scale, the second to the transmission through the cover scale, followed by the reflection from the ground scale and return path through the cover scale. The third term describes transmission through the cover and ground scales, followed by the reflection from the wing membrane, and return path through both layers of the scales. The calculated contribution of each term to the final spectrum is shown in Fig. 10 (normalized to the intensity of light before being transmitted through the layers).

Spectral contributions of wing components significantly depend on their geometry, i.e., scale laminae and wing membrane thicknesses. For some combination of dimensional parameters, even a single scale can quite faithfully reproduce an experimentally recorded spectrum (as in Fig. 11). However, there are slight modulations within the whole spectral range, due to thin film interference effects. They disappear when spatial and angular averaging is included, as further explained. As explained above, losses are much higher inside the blue-UV spectral range, as can be seen in Fig. 11. According to Eqs. (3) and (4), most of the light energy is absorbed, and the rest of the radiation is scattered. It is interesting to note that a significant amount of radiation is transmitted through the wing membranes (green curve in Fig. 11). However, the UV component of transmitted radiation is efficiently absorbed by the dark, pigmented scales, on the wing underside.

There is an important word of caution. In order to get a consistently golden wing color, the dimensional and optical parameters of each individual scale should be kept within quite tight tolerances—a task completely impossible in the living world. It is more realistic to expect significant variability of all the parameters. Thus they were varied in our simulations (according to the normal distribution) within  $\pm 15\%$  of the values producing fit in Fig. 11. The angle of incidence was also

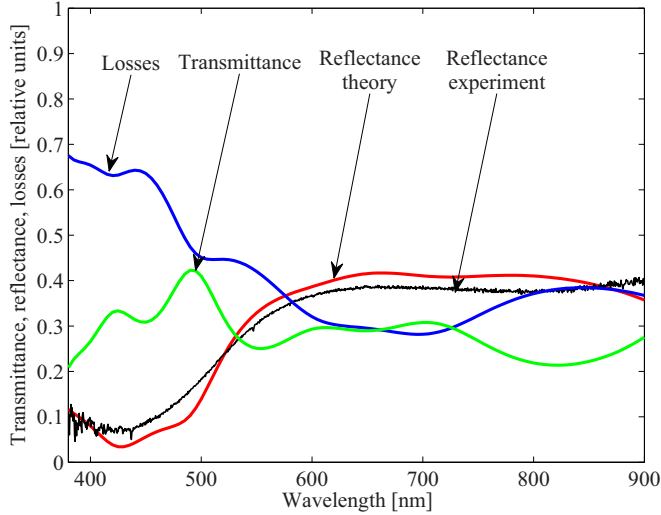


FIG. 11. A spectral reflectivity (red curve) of a *D. chrysitis* moth wing, calculated by the transfer matrix method is shown. The corresponding experimental curve (black curve) is added for reference. Losses (due to scattering and absorption, blue curve) and the wing transmittance (green curve) are displayed, too.

allowed to fluctuate within  $\pm 20^\circ$ , which imitates variability of scale orientations.

As a result, 100 different spectra were calculated (for clarity, only 25 of them are displayed in Fig. 12 as light blue curves). They were consequently averaged, in agreement with our experimental procedure where the light is collected from the wing area and within an angular range (the resulting curve is shown in blue). By comparing the calculated spectrum with the experimentally recorded one (red curve in the same figure), agreement appears remarkably good, except for the radiation above 800 nm.

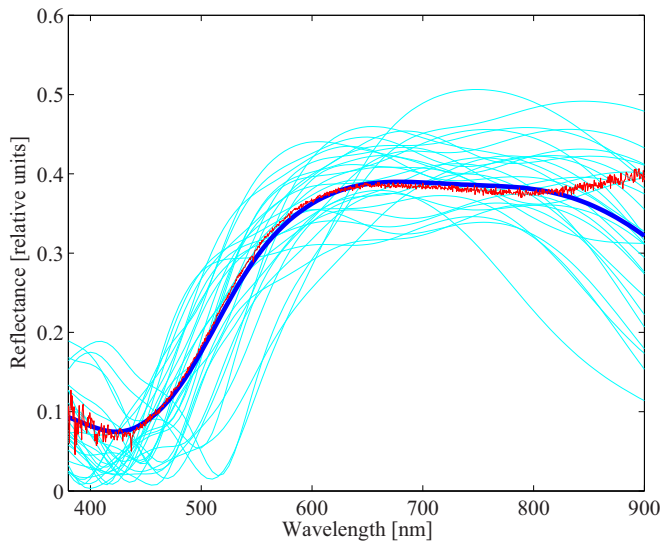


FIG. 12. Spectral averaging of light reflected from *D. chrysitis* wing, calculated by the transfer matrix method which includes scattering and local field enhancement. Light blue curves are individual spectra, blue curve is the averaged spectrum, and the red curve is the experimentally recorded spectrum.

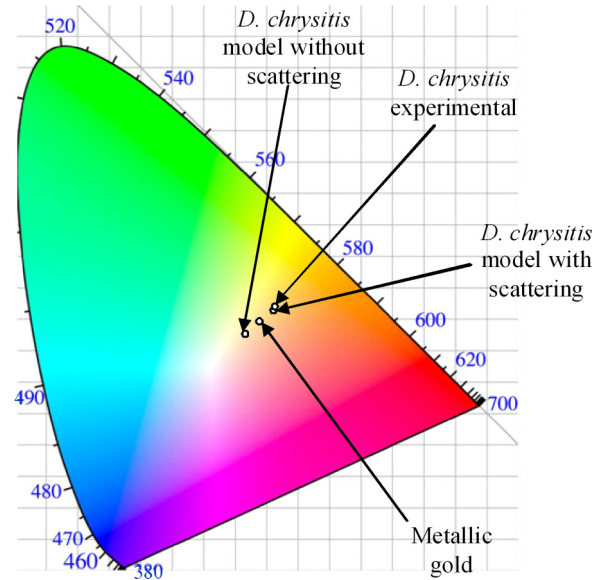


FIG. 13. CIE color coordinates of metallic gold and *D. chrysitis* forewing golden patches, with and without scattering.

The final shape of the spectrum is influenced by the layer thicknesses and the RMS surface roughness. They collectively influence the final calculated spectrum, but in general terms we have observed that increased thickness shifts the spectrum towards the red, while increased roughness depletes the blue part of the spectrum and decreases overall reflectivity.

All the computations are based on a transfer-matrix code, developed in [36] (declared free to use and made public at the URL provided therein). The program was modified by including scattering and local field enhancement effects [as defined by Eqs. (1)–(4)].

IV. DISCUSSION AND CONCLUSIONS

In contrast to most other lepidopteran species, each and every wing structure of *D. chrysitis* plays a certain role in iridescent color production. The same goes for the optical mechanisms—interference, diffraction, absorption, and surface scattering. They seem to be intricately intertwined in a synergistic manner—by omitting any of them, a significant change of the spectral profile would result. To demonstrate the fact, we calculated the resulting spectrum without taking into account scattering-enhanced absorption. As expected, reflection in the UV-blue spectral range is not attenuated. The corresponding CIE color coordinate testifies that the resulting color is whitish, as presented on a CIE 1931 diagram (Fig. 13). For reference, we have also displayed points corresponding to metallic gold, experimentally recorded spectrum, and full simulation of *D. chrysitis* wing. It is obvious that without scattering, the color coordinate would approach the achromatic center of the diagram—i.e., the wing will have only a slight coloration. It is interesting to note that the moth wing looks “yellow” than the gold.

As noted before, scattering stimulates confinement of light and increases the intensity by the  $2n^2$  factor. It seems that the ground scale layer further amplifies the confinement [see Fig. 8(b)]. One possible explanation is that the cover scales



diffuse the incoming light, while the ground scales additionally disperse it and make it amenable for wave guiding within the layer.

Angular variability of *D. chrysitis* wing coloration is noticeable, and the golden color is observable within the  $\pm 20^\circ$  from the specular direction. Beyond that, the color abruptly changes from golden to brown-gray. However, within the specular range, dependence of the reflected spectrum is slight for several reasons. On one hand, it results from irregular internal surfaces of the scale laminae and irregular mutual position of scales in ground and cover layers. The other reason is that the reflectivity at air-chitin interfaces is almost constant between  $0^\circ$  and  $30^\circ$ , as predicted by Fresnel equations. Therefore, the overall shape of the spectrum is not altered, but slightly shifted with the angle of incidence. Coarse diffraction grating on the upper lamina additionally diminishes angular dependence. From whichever direction light enters the scale, at least one of the diffraction orders is being reflected. This is what gives the notable stability of the optical effect with respect to the illumination direction (within the stated angular range).

We have not observed polarization sensitivity of the described reflection spectra, even though it certainly exists at the single wing-scale level. If observed macroscopically, across the whole wing, polarization effects cancel out due to strong variability of individual scale orientations with respect to incident radiation.

It is also interesting to note that the scales from brown-gray and golden areas of the wing have very similar morphology if observed under the scanning electron microscope. The most important difference is optical: while the golden area scales are almost transparent, the others contain a significant amount of absorbing pigment which leads to suppression of the specular component in the brown wing regions. Also, the brown scales are flatter, while the golden ones are slightly curled.

Calculations, according to Eqs. (3) and (4), have shown that approximately 70% of incoming radiation at 380 nm is scattered. Forty percent of the scattered component is absorbed, while the rest is uniformly dispersed all over the full solid angle. At the other end of the spectrum (above 800 nm), only 20% of light is scattered, without being absorbed to any significant extent. As a whole, the spectrum of unabsorbed light is quite flat from UV to IR. Its contribution to the wing

reflection is really small, because it is dispersed over the  $4\pi$  solid angle, while the reflected light is concentrated around the specular direction.

A dual wing membrane is densely covered with nanosized spherical inclusions, conveniently situated, just beneath the scales. It seems that this could be an additional mechanism to scatter light back through the layer of scales. Transmission of the membranes is high and light further propagates to underside scales. They are gray, most probably due to melanin, which will further absorb the UV-blue part of the spectrum. In the red-infrared range, melanin absorbance is insignificant, and scales are again capable of reflecting light back through all the previous layers. This might account for the increased reflectivity in the infrared, which is not predicted by the theory described in the previous section.

Insects with golden body parts are rare and interesting from the biological point of view. The roles of the golden color may be diverse and are related mostly to possible defense mechanisms. We suppose that in *D. chrysitis* the golden forewing patches may appear to predators as warning and/or they can facilitate the conspecific recognition [15].

To summarize: All the structures—cover and ground scales, wing membranes, and underside wing scales—contribute to the golden wing color of the burnished brass moth. Interference, scattering, and absorption enhancement are optical mechanisms responsible for the effect. In short, interference on the scales produces a broad reflection spectrum with a peak in the green part of the spectrum. The blue part of the spectrum is absorbed due to scattering-enhanced absorption on a residual pigment. The red part of the spectrum is transmitted to the wing membrane, where it reflects, goes back through the scales, and combines with the reflection from the scales. The resulting spectrum is strongly attenuated below 520 nm, being almost flat up to 800 nm. The forewings of the *D. chrysitis* moth seem to be a remarkable, finely tuned, optical filter.

#### ACKNOWLEDGMENTS

This research was supported by Projects No. ON171038, No. III45016, and No. ON173038 funded by the Ministry of Education, Science and Technological Development of the Republic of Serbia.

- 
- [1] J. Sun, B. Bhushan, and J. Tong, Structural coloration in nature, *RSC Adv.* **3**, 14862 (2013).
  - [2] J. Zi, B. Dong, T. Zhan, and X. Liu, in *Bioinspiration: From Nano to Micro Scales*, edited by X. Y. Liu (Springer, Berlin, 2012), pp. 275–329.
  - [3] T. Starkey and P. Vukusic, Light manipulation principles in biological photonic systems, *Nanophotonics* **2**, 289 (2013).
  - [4] N. N. Shi, C.-C. Tsai, F. Camino, G. D. Bernard, N. Yu, and R. Wehner, Keeping cool: Enhanced optical reflection and radiative heat dissipation in Saharan silver ants, *Science* **349**, 298 (2015).
  - [5] O. Karthaus, *Biomimetics in Photonics* (CRC Press, Boca Raton, FL, 2013).
  - [6] Z. Gan, M. D. Turner, and M. Gu, Biomimetic gyroid nanostructures exceeding their natural origins, *Sci. Adv.* **2**, e1600084 (2016).
  - [7] M. F. Land, The physics and biology of animal reflectors, *Prog. Biophys. Mol. Biol.* **24**, 75 (1972).
  - [8] S. Yoshioka, T. Nakano, Y. Nozue, and S. Kinoshita, Coloration using higher order optical interference in the wing pattern of the Madagascan sunset moth, *J. R. Soc., Interface* **5**, 457 (2008).
  - [9] D. J. Brink, J. E. Smith, M. E. Lee, and A. Möller, Optical diffraction by the microstructure of the wing of a moth, *Appl. Opt.* **34**, 6049 (1995).
  - [10] M. Hernández-Jiménez, D. E. Azofeifa, E. Libby, C. Barboza-Aguilar, Á. Solís, L. Arce-Marenco, I. García-Aguilar, A. Hernández, and W. E. Vargas, Qualitative correlation between structural chirality through the cuticle of *Chrysina aurigans* scarabs and left-handed circular polarization of the reflected light, *Opt. Mater. Express* **4**, 2632 (2014).

- [11] F. Liu, B. Q. Dong, X. H. Liu, Y. M. Zheng, and J. Zi, Structural color change in longhorn beetles *Tmesisternus isabellae*, *Opt. Express* **17**, 16183 (2009).
- [12] J. P. Vigneron, J. M. Pasteels, D. M. Windsor, Z. Vártesy, M. Rassart, T. Seldrum, J. Dumont, O. Deparis, V. Lousse, L. P. Biró, D. Ertz, and V. Welch, Switchable reflector in the Panamanian tortoise beetle *Charidotella egregia* (Chrysomelidae: Cassidinae), *Phys. Rev. E* **76**, 031907 (2007).
- [13] M. Rothschild, B. Gardiner, and R. Mummery, The role of carotenoids in the “golden glance” of danaid pupae (Insecta: Lepidoptera), *J. Zool.* **186**, 351 (1978).
- [14] R. L. Taylor, The metallic gold spots on the pupa of the monarch butterfly, *Entomol. News* **75**, 253 (1964).
- [15] A. C. Neville, Metallic gold and silver colours in some insect cuticles, *J. Insect Physiol.* **23**, 1267 (1977).
- [16] R. A. Steinbrecht, W. Mohren, H. K. Pulker, and D. Schneider, Cuticular interference reflectors in the golden pupae of danaine butterflies, *Proc. R. Soc. London, Ser. B* **226**, 367 (1985).
- [17] B. D. Wilts, H. L. Leertouwer, and D. G. Stavenga, Imaging scatterometry and microspectrophotometry of lycaenid butterfly wing scales with perforated multilayers, *J. R. Soc., Interface* **6**, S185 (2009).
- [18] N. I. Morehouse, P. Vukusic, and R. Rutowski, Pterin pigment granules are responsible for both broadband light scattering and wavelength selective absorption in the wing scales of pierid butterflies, *Proc. R. Soc. London, Ser. B* **274**, 359 (2007).
- [19] D. G. Stavenga, S. Stowe, K. Siebke, J. Zeil, and K. Arikawa, Butterfly wing colours: Scale beads make white pierid wings brighter, *Proc. R. Soc. London, Ser. B* **271**, 1577 (2004).
- [20] S. M. Luke, P. Vukusic, and B. Hallam, Measuring and modelling optical scattering and the colour quality of white pierid butterfly scales, *Opt. Express* **17**, 14729 (2009).
- [21] X. Chen, C. Wang, E. Baker, and C. Cun, Numerical and experimental investigation of light trapping effect of nanostructured diatom frustules, *Sci. Rep.* **5**, 11977 (2015).
- [22] A. Hille, M. A. Miller, and S. Erlacher, DNA sequence variation at the mitochondrial cytochrome oxidase I subunit among pheromotypes of the sibling taxa *Diachrysia chrysitis* and *D. tutti* (Lepidoptera: Noctuidae), *Zool. Scr.* **34**, 49 (2005).
- [23] A. Seitz, *The Macrolepidoptera of the World. A Systematic Description of the Known Macrolepidoptera. I Section. 3. Volume: The Palearctic Noctuidae. Plates* (Verlag des Seitz'schen Werkes, Stuttgart, 1914).
- [24] G. S. Robinson, P. R. Ackery, I. J. Kitching, G. W. Beccalon, and L. M. Hernández, *HOSTS—a Database of the World's Lepidopteran Hostplant* (Natural History Museum, London, 2010).
- [25] D. V. Stojanović and S. B. Čurčić, The diversity of noctuid moths (Lepidoptera: Noctuidae) in Serbia, *Acta Zool. Bulg.* **63**, 47 (2011).
- [26] M. Boardman, R. R. Askew, and L. M. Cook, Experiments on resting site selection by nocturnal moths, *J. Zool.* **172**, 343 (1974).
- [27] I. Svensson, P. Douwes, and B. O. Stille, Are *Diachrysia chrysitis* (L.) and *D. tutti* (Kostrowicki) different species? (Lepidoptera: Noctuidae), *Insect Syst. Evol.* **20**, 15 (1989).
- [28] A. D. Rakic, A. B. Djuricic, J. M. Elazar, and M. L. Majewski, Optical properties of metallic films for vertical-cavity optoelectronic devices, *Appl. Opt.* **37**, 5271 (1998).
- [29] D. G. Stavenga, H. L. Leertouwer, T. Hariyama, H. A. De Raedt, and B. D. Wilts, Sexual dichromatism of the damselfly *Calopteryx japonica* caused by a melanin-chitin multilayer in the male wing veins, *PLoS One* **7**, e49743 (2012).
- [30] H. Davies, The reflection of electromagnetic waves from rough surface, *Proc. IEE-Part IV: Inst. Monogr.* **101**, 209 (1954).
- [31] D. Domine, F.-J. Haug, C. Battaglia, and C. Ballif, Modeling of light scattering from micro- and nanotextured surfaces, *J. Appl. Phys.* **107**, 044504 (2010).
- [32] Y. A. Akimov, W. S. Koh, S. Y. Sian, and S. Ren, Nanoparticle-enhanced thin film solar cells: Metallic or dielectric nanoparticles? *Appl. Phys. Lett.* **96**, 073111 (2010).
- [33] E. Yablonovich and G. D. Cody, Intensity enhancement in textured optical sheets for solar cells, *IEEE Trans. Electron Devices* **29**, 300 (1982).
- [34] H. L. Leertouwer, B. D. Wilts, and D. G. Stavenga, Refractive index and dispersion of butterfly chitin and bird keratin measured by polarizing interference microscopy, *Opt. Express* **19**, 24061 (2011).
- [35] J. Springer, A. Porube, and M. Vanacek, Improved three-dimensional optical model for thin film silicon solar cells, *J. Appl. Phys.* **96**, 5329 (2004).
- [36] J. Junesch, T. Sannomiya, and A. B. Dahlin, Optical properties of nanohole arrays in metal-dielectric double films prepared by mask-on-metal colloidal lithography, *ACS Nano* **6**, 10405 (2012). Transfer matrix code can be found in <http://adahlin.com/onewebmedia/TransferMatrix3.m>.

# Author's Accepted Manuscript

Photonic structures improve radiative heat exchange of *Rosalia alpina* (Coleoptera: Cerambycidae)

Danica Pavlović, Darko Vasiljević, Branislav Salatić, Vladimir Lazović, Goran Dikić, Ljubiša Tomić, Srećko Ćurčić, Petar Milovanović, Dajana Todorović, Dejan V. Pantelić



PII: S0306-4565(18)30140-2  
DOI: <https://doi.org/10.1016/j.jtherbio.2018.07.014>  
Reference: TB2141

To appear in: *Journal of Thermal Biology*

Received date: 5 April 2018  
Revised date: 7 June 2018  
Accepted date: 22 July 2018

Cite this article as: Danica Pavlović, Darko Vasiljević, Branislav Salatić, Vladimir Lazović, Goran Dikić, Ljubiša Tomić, Srećko Ćurčić, Petar Milovanović, Dajana Todorović and Dejan V. Pantelić, Photonic structures improve radiative heat exchange of *Rosalia alpina* (Coleoptera: Cerambycidae), *Journal of Thermal Biology*, <https://doi.org/10.1016/j.jtherbio.2018.07.014>

This is a PDF file of an unedited manuscript that has been accepted for publication. As a service to our customers we are providing this early version of the manuscript. The manuscript will undergo copyediting, typesetting, and review of the resulting galley proof before it is published in its final citable form. Please note that during the production process errors may be discovered which could affect the content, and all legal disclaimers that apply to the journal pertain.

**Photonic structures improve radiative heat exchange of *Rosalia alpina* (Coleoptera: Cerambycidae)**

Danica Pavlović<sup>1\*</sup>, Darko Vasiljević<sup>1</sup>, Branislav Salatić<sup>1</sup>, Vladimir Lazović<sup>1</sup>, Goran Dikić<sup>2</sup>, Ljubiša Tomić<sup>3</sup>, Srećko Ćurčić<sup>4</sup>, Petar Milovanović<sup>5</sup>, Dajana Todorović<sup>6</sup>, Dejan V. Pantelić<sup>1</sup>

<sup>1</sup>Photonics Center, Institute of Physics, University of Belgrade, Pregrevica 118, 11080 Zemun, Belgrade, Serbia

<sup>2</sup>The School of Electrical and Computer Engineering of Applied Studies, Vojvode Stepe 283, 11010 Belgrade, Serbia

<sup>3</sup>Military Technical Institute, Ratka Resanovića 1, 11030 Belgrade, Serbia.

<sup>4</sup>Institute of Zoology, University of Belgrade - Faculty of Biology, Studentski Trg 16, 11000 Belgrade, Serbia

<sup>5</sup>Laboratory for Anthropology and Skeletal Biology, Institute of Anatomy, University of Belgrade – Faculty of Medicine, Dr Subotića 4/2, 11000 Belgrade, Serbia

<sup>6</sup>Department of Insect Physiology and Biochemistry, Institute for Biological Research “Siniša Stanković”, University of Belgrade, Despot Stefan Blvd. 142, 11060 Belgrade, Serbia

\*Corresponding author. Danica Pavlović Institute of Physics, University of Belgrade

Photonics Center Pregrevica 118, 11080 Zemun, Belgrade, Serbia danica.pavlovic@ipb.ac.rs

**Abstract**

The insect cuticle serves a multitude of purposes, including: mechanical and thermal protection, water-repelling, acoustic signal absorption and coloration. The influence of cuticular structures on infrared radiation exchange and thermal balance is still largely unexplored. Here we report on the micro- and nanostructured setae covering the elytra of the longicorn beetle *Rosalia alpina* (Linnaeus, 1758) (Coleoptera: Cerambycidae) that help the insect to survive in hot, summer environments. In the visible part of the spectrum, scale-like setae, covering the black patches of the elytra, efficiently absorb light due to the radiation trap effect. In the infrared part of the spectrum, setae of the whole elytra significantly contribute to the radiative heat exchange. From the biological point of view, insect elytra facilitate camouflage, enable rapid heating to the optimum body temperature and prevent overheating by emitting excess thermal energy.

**Keywords:** Longicorn beetle, behavioral thermoregulation, structural coloration, texture enhanced absorption.

**1. Introduction**

Environment affects the body temperature of animals through thermal energy exchange. Animals have adapted to thermal conditions in order to maintain the optimal temperature of their bodies necessary for survival. This is why evolution has developed many ways to control heat transfer, e.g. bird feathers [], mammalian fur [] or subcutaneous fat of marine animals [], to mention just a few.

Insects have developed diverse thermoregulatory adaptations by physiological or behavioral means []. Endothermic insects produce heat internally by physiological processes mostly associated with flying species, with moths and bees being the most common examples []. However, the majority of insects are primarily ectothermic [] and rely on external heat sources, such as solar radiation[]; for example, some butterflies regulate heat gain behaviorally, by orientation and posture relative to the sun [].

Insects exchange heat through the cuticle, whose color, structure and material properties determine the amount of absorbed and dissipated energy. The cuticle is, thus, evolutionarily adapted to use available mechanisms of heat transfer (convection, conduction, radiation, transpiration) [], depending on the environmental conditions and the insect's lifestyle. The cuticle is often patterned on the micro- and nano-scale levels, producing natural photonic structures that strongly interact with light and electromagnetic waves through absorption, interference, diffraction and scattering. The structures may have a variety of regular and stochastic architectures, such as diffraction gratings, layers, optical crystals that produce striking visual effects and act as selective optical filters, absorbers or antireflection coatings [, ].

Radiative transfer is an important, but often overlooked, mechanism used to heat or cool insects through the absorption [] and reflection of sunlight []. In this respect, visible light is usually absorbed by pigments and selectively reflected by photonic structures [, ]. Infrared (IR) radiation is important too [], and some insects use it to receive energy from the environment, while others dissipate heat by radiating in the IR atmospheric window [].

It was found that photonic structures of insects have an important function in this respect []. To better understand the interaction of infrared radiation and biological structures, appropriate mathematical models are necessary. These are based on Kirchhoff's law of radiation, which establishes the equality of emissivity (as a measure of how effectively a body emits radiation) and absorptance. It is therefore sufficient to calculate the absorptance and unequivocally determine the emissivity. To do this, standard methods for calculating electromagnetic wave propagation have been used, such as scattering matrix methods to analyze butterflies in the IR [], or a finite-difference time-domain technique to simulate the IR radiation transfer of Saharan silver ant [].

The grayish body of the longicorn beetle *Rosalia alpina*, (Linnaeus 1758) (Coleoptera: Cerambycidae), with several prominent black patches on its elytra, attracted our attention. We studied the effect of cuticular setae (scale- and hair-like structures) on the absorptive and emissive properties of the cuticle and the overall thermal balance of the insect. In our previous conference paper [] we performed pulsed thermal imaging of this insect and

presented the corresponding qualitative results. Here, our research is extended by (i) a new, well-controlled set of optical and thermal measurements, (ii) a detailed morphological analysis of photonic structures (elytral setae) and the development of a corresponding thermo-optical model, (iii) the contribution of biophotonic structures to the thermal balance of the insect under the high thermal load of direct, summer sunlight.

## 2. Materials and methods

### 2.1. Insect

*Rosalia alpina* is a longicorn beetle, characterized by a body length of 14-40 mm (antennae excluded), distinctive markings and coloration [1]. The hind wings and abdomen are protected by subcylindrical blue-gray elytra (hardened forewings), with several dominating black patches (Fig. 1). The long antennae and legs have the same blue-gray coloration, with striking black tufts of hair-like structures on the central segments of the antennae. The specific, velvety appearance is created by a large number of very fine setae—transparent hair-like structures (hairs in the further text) on the blue-grey areas (Fig. 1), and dark, scale-like structures (scales in the further text) in the black patches (Fig. 1). They form a dense tomentum, which covers the body [1, 2].

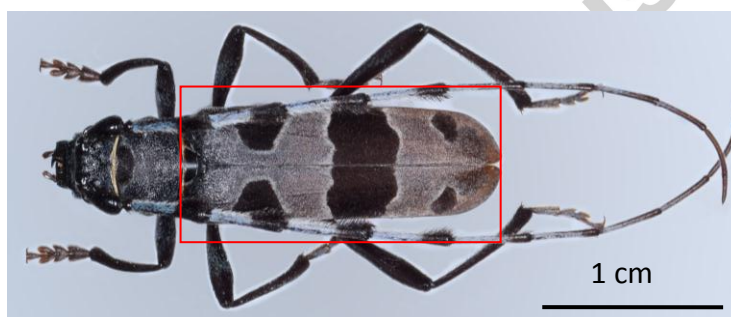


Fig. 1: *Rosalia alpina* is characterized by six prominent black patches and a blue-grey body. Elytra are shown within the red rectangle.

The species is strictly protected in Serbia and most of Europe by the Habitats Directive. Within the IUCN Red List of Threatened Species, it is designated as vulnerable (A1c) [1]. A limited number of insects was collected by the Faculty of Biology of the University of Belgrade during the summer of 2010 on Mt. Avala, near the city of Belgrade, with the permission of the Serbian Ministry of Environmental Protection (N<sup>o</sup>: 353-01-335/2010-03). We had five dry specimens at our disposal. The size of the insects was within the limits stated in [1]. All our samples possess a common dorsal pattern with six, almost symmetrical black spots. The hind spots are the smallest while the mid spots are the largest (Fig. 1). It is known that variability among individuals is due to the size and shape of the elytral patches[1]; however, the given variability is not important for the general thermal models in this study.

## 2.2. Microanalysis

We used reflection and transmission optical microscopy to study the optics of individual scales. A field emission gun scanning electron microscope (FEGSEM) (MiraSystem, manufactured by TESCAN) was used for ultrastructural analysis.

Micro-computed tomography (micro-CT) was employed to view the overall anatomy of the beetle and measure the thickness of the elytra. We had at our disposal the Skyscan 1172 system, manufactured by Bruker. To ensure the optimum signal/noise ratio during micro-CT imaging, the specimens were scanned without filter, with scanning parameters set as follows: 40 kV, 244  $\mu$ A, 530 ms, rotation step 0.2° (pixel size 13.5  $\mu$ m).

Microspectrometry was utilized to record spectral absorption due to pigmentary coloration. The device consisted of a fiberoptic spectrometer attached to an optical microscope.

## 2.3. IR analysis

Heat transfer was analyzed by two IR thermal cameras corresponding to atmospheric windows at 3-5  $\mu$ m (FLIR SC7200, 320 x 256 pixels, noise equivalent temperature difference better than 20 mK, spectral range 1.5-5.1  $\mu$ m) and 8-14  $\mu$ m (FLIR SC620, 640 x 480 pixels, 40 mK thermal resolution, spectral range 7.5-13  $\mu$ m). Thermal measurements were corrected for surface emissivity. To study radiative energy exchange, we used a xenon flashlamp (Bowens Gemini 1500Pro, pulse duration 0.9 ms, pulse energy 1.5 J) to uniformly irradiate the insect body. The elytra were also illuminated by a 405-nm wavelength laser in order to locally heat the black patch and study the thermal effects. Laser power was controlled by a variable beam splitter and the duration of irradiation by an Arduino microcontroller. A power-meter (Ophir, Nova, with photodiode sensor) was used to measure laser power. The IR spectral properties of the insect elytra were recorded by the Fourier transform infrared (FTIR) system Nicolet 6700 FT-IR, Thermo Scientific, USA and analyzed by the OMNIC, software package, Version 7.0.

## 3. Results

### 3.1. Photonic structures of *R. alpina*

The elytra of *R. alpina* are in the form of a thin elongated shell, with six prominent black patches on a blue-gray background. The anatomy of a dried specimen was visualized using micro-CT at 13.5  $\mu$ m resolution (see Fig. 2(a)), revealing an almost uniform thickness (30-40  $\mu$ m) of the elytra (Fig. 2(b)). There is a large space between the elytra and the abdomen, where the hindwings are folded and packed, which functions as a thermally-insulating layer.

FEGSEM images revealed that the scales on a black patch are bunched on the elytra, inclined towards each other and touching at the tips, thus forming a number of tent-like structures (Fig. 3(a)). The scales stand almost vertically to the surface, as can be seen in Fig. 2(b) and its inset. The cuticle beneath is rugged, with irregular, polygonal impressions (Fig. 3(b)). The periodicity of scale placement (and that of the corresponding polygonal impressions) is between 10 and 20  $\mu\text{m}$ , which is comparable to the wavelengths of environmental IR radiation.

In contrast to the black patches, the blue-gray areas of *R. alpina* elytra are covered with transparent, prostrated hairs (Fig. 3(c)), while the cuticle beneath is black and shiny. Together, the scales and cuticle present a velvety blue-gray appearance.

Grating-like structures are conspicuous features of the scales (Fig. 4), as observed at higher magnifications. A coarser grating (Fig. 4(a)), with a 1- $\mu\text{m}$  period, runs along the length of the scale. A much finer, irregular, sub-wavelength grating (with an approximately 100-nm period) extends diagonally between the coarse grating lines (Fig. 4(b)).

From the optical point of view, the structures on the gray and black areas of the elytra have completely opposite functions. The gray area is easily visible due to intense scattering (on the left in Fig. 5(a)), while the black area so strongly absorbs the light that only reflections from the polygonal impressions are partially visible (as revealed in optical microscope images in Fig. 5(a) and (b), at two magnifications). The scales themselves almost completely absorb the light and can be seen indirectly as dark shadows on the background, reflected from the cuticle beneath (Fig. 5(a)).

Individual scales are flattened (1-2  $\mu\text{m}$  thick, 20  $\mu\text{m}$  wide and 100  $\mu\text{m}$  long), asymmetrical and somewhat similar to butterfly-wing scales (Figs. 4(a) and 6(a)). They are strongly pigmented, with transmission gradually increasing from the blue to the red part of the spectrum, as can be verified by splitting the color image from Fig. 6(a) into its RGB components (see the three small images in Fig. 6(a)). The corresponding spectrum is shown in Fig. 6(b) and resembles that of melanin [], a pigment frequently encountered in the cuticles of dark insects.

Reflectance of the black elytral patches was measured through an optical microscope by detecting the reflected intensity. A measured value was referenced to a white diffuse standard and corrected for internal microscope objective scattering. We found that the reflectance in the blue and green parts of the spectrum is 2.6%, while in the red spectral range it is slightly higher, 3.5%.

The IR spectrum was between 2.5 and 15  $\mu\text{m}$  (using an FTIR spectrometer) and found to be completely in agreement with the one measured in [], showing two strong transmission minima at approximately 3 and 6  $\mu\text{m}$  (Fig. 6(c)), corresponding to the atmospheric infrared windows (3-5  $\mu\text{m}$  and 8-14  $\mu\text{m}$ ).



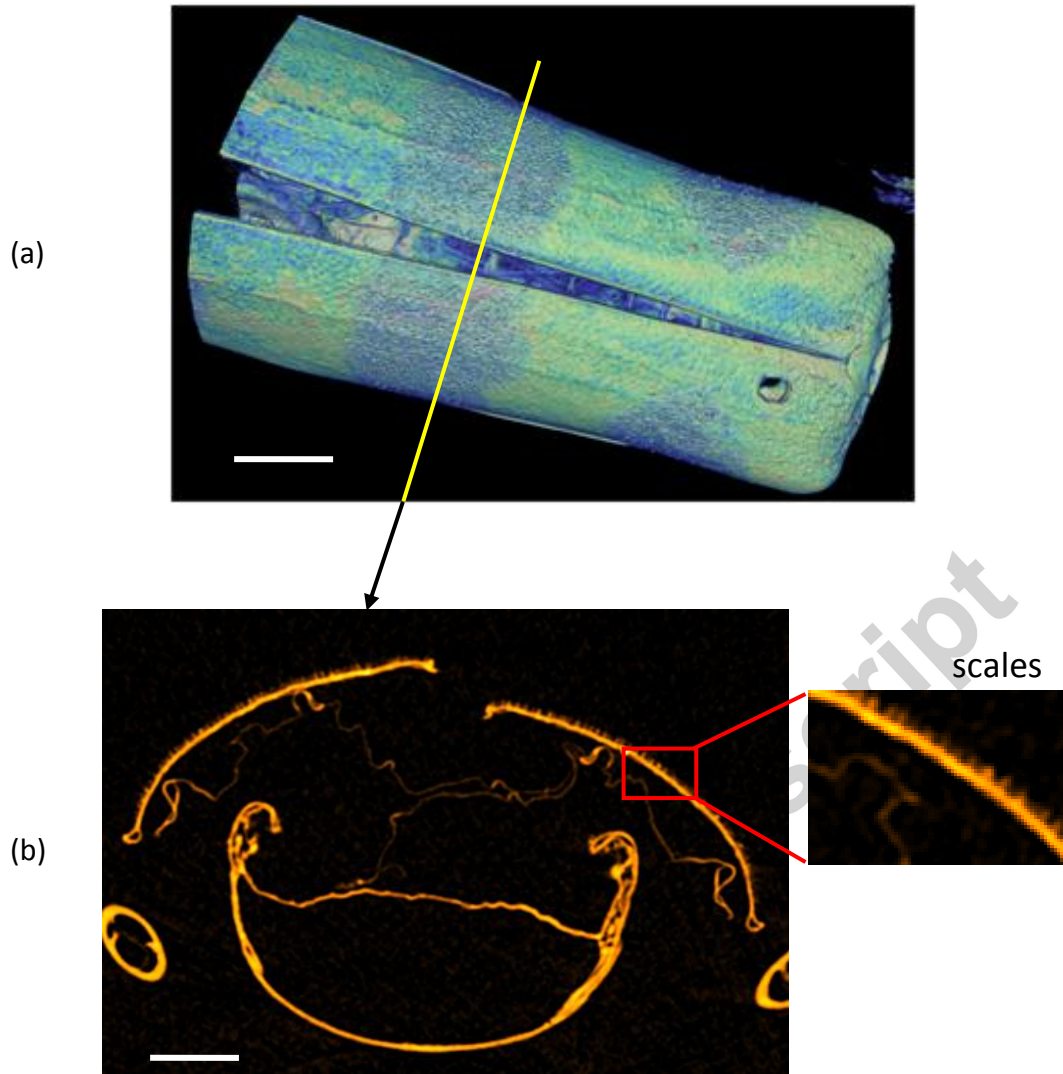
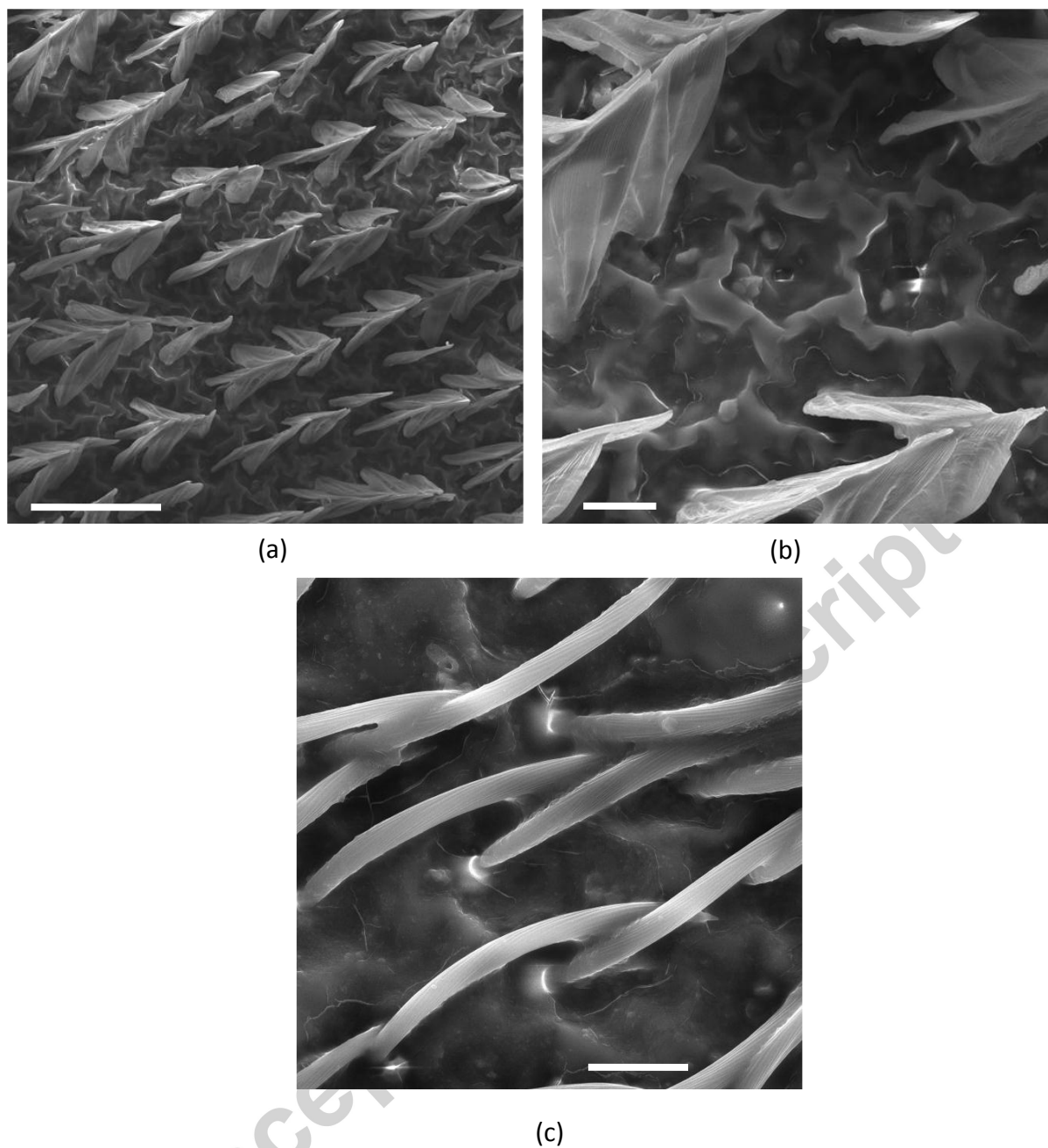
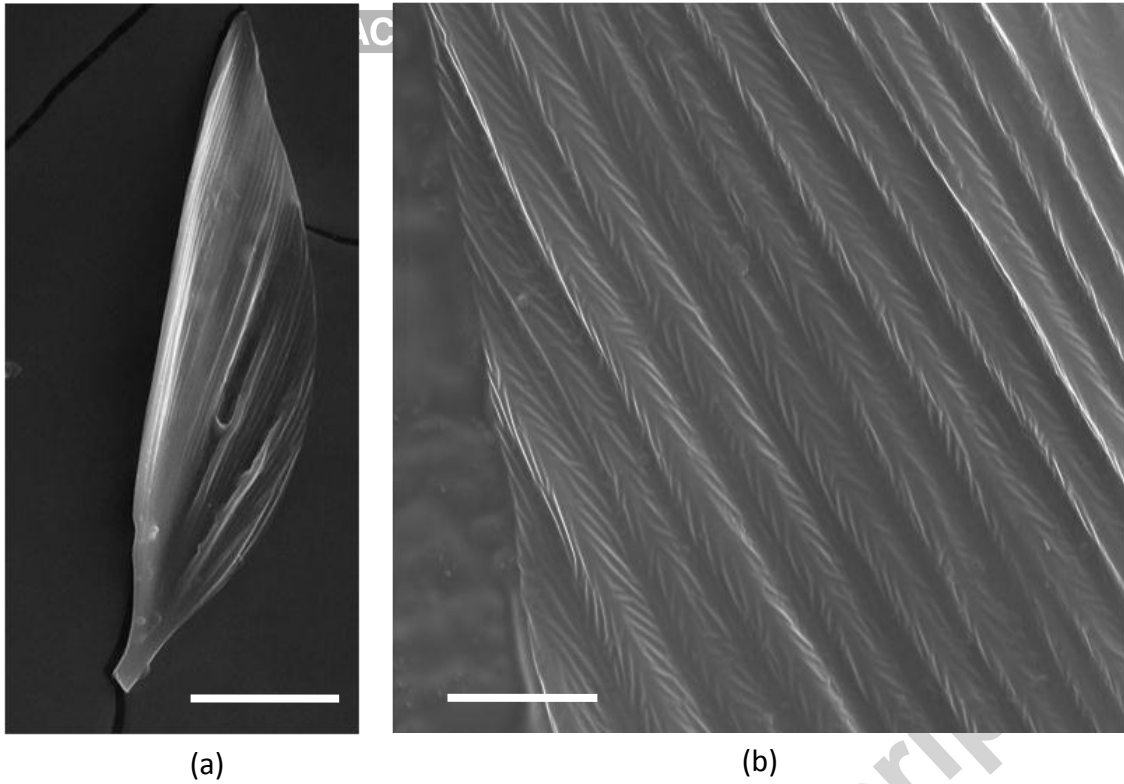


Fig. 2: (a) 3D reconstruction of *R. alpina* micro-CT image stack. (b) A single micro-CT slice through the black patch of *R. alpina* elytra (with scales visible on the enlarged portion of the slice).



*Fig. 3: FEGSEM images of R. alpina: (a) tent-like-organized scales concentrated in the black patch of elytra; (b) rugged elytral surface with polygonal depressions and dark scales; (c) hairs covering the blue-gray zone of elytra.*



*Fig. 4: (a) An individual scale of R. alpina, recorded on a FEGSEM. (b) 1- $\mu$ m period grating-like structure and a herringbone shaped sub-wavelength grating, observable on the R. alpina scale at higher magnification.*

Accepted manuscript

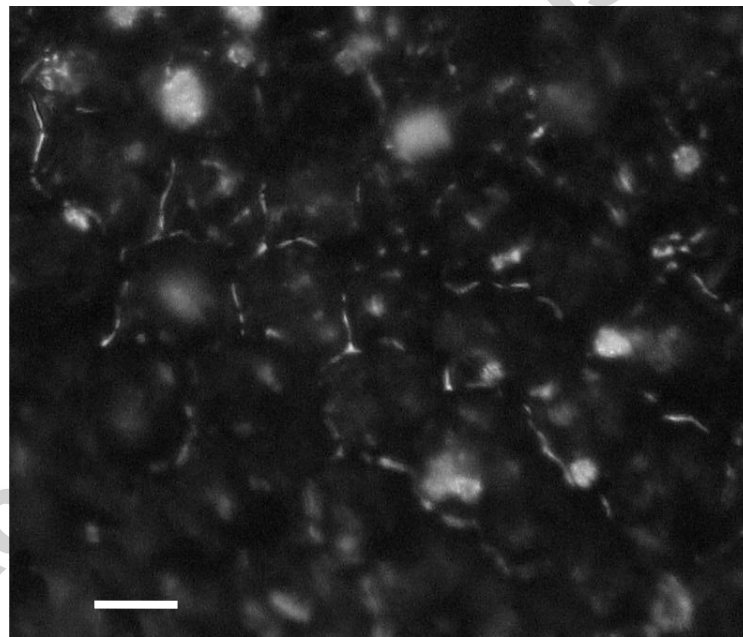
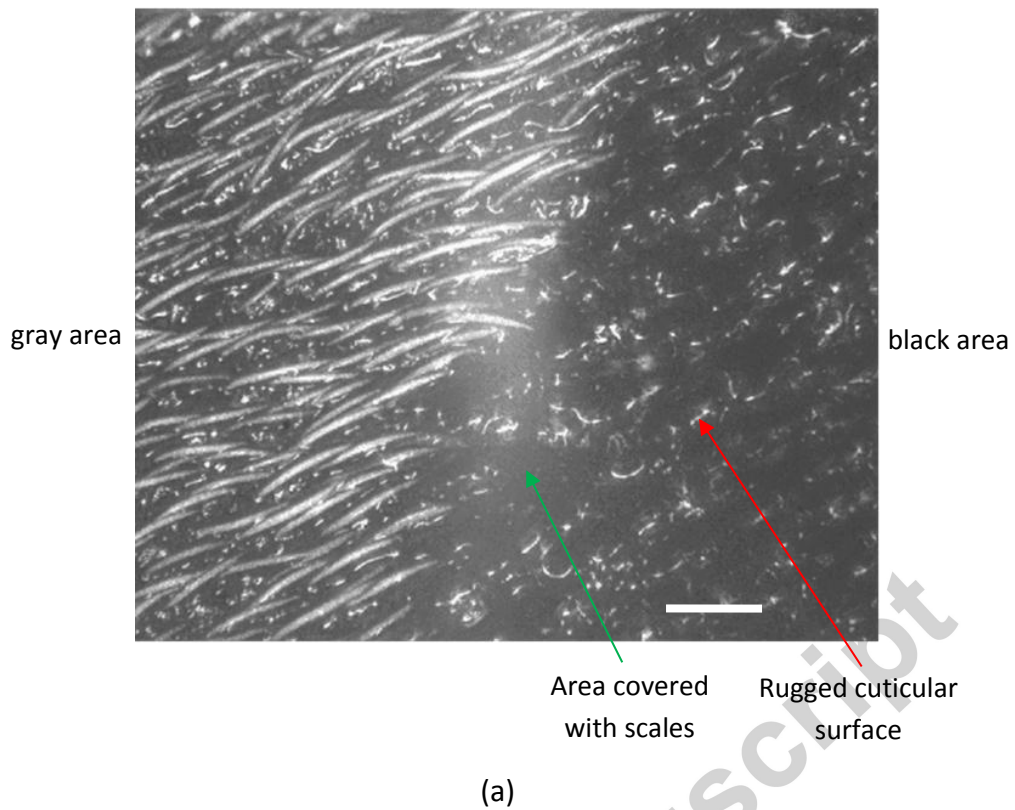


*Fig. 5: (a) Optical reflection microscope image of a boundary between gray (on the left) and black (on the right) areas of *R. alpina* elytra. In the black area, the scales are just a dark shadow (shown by green arrow) on the rugged cuticular surface (red arrow); (b) black elytral area devoid of scales, showing irregular reflections from the edges of polygonal depressions (see Fig. 3(b)).*

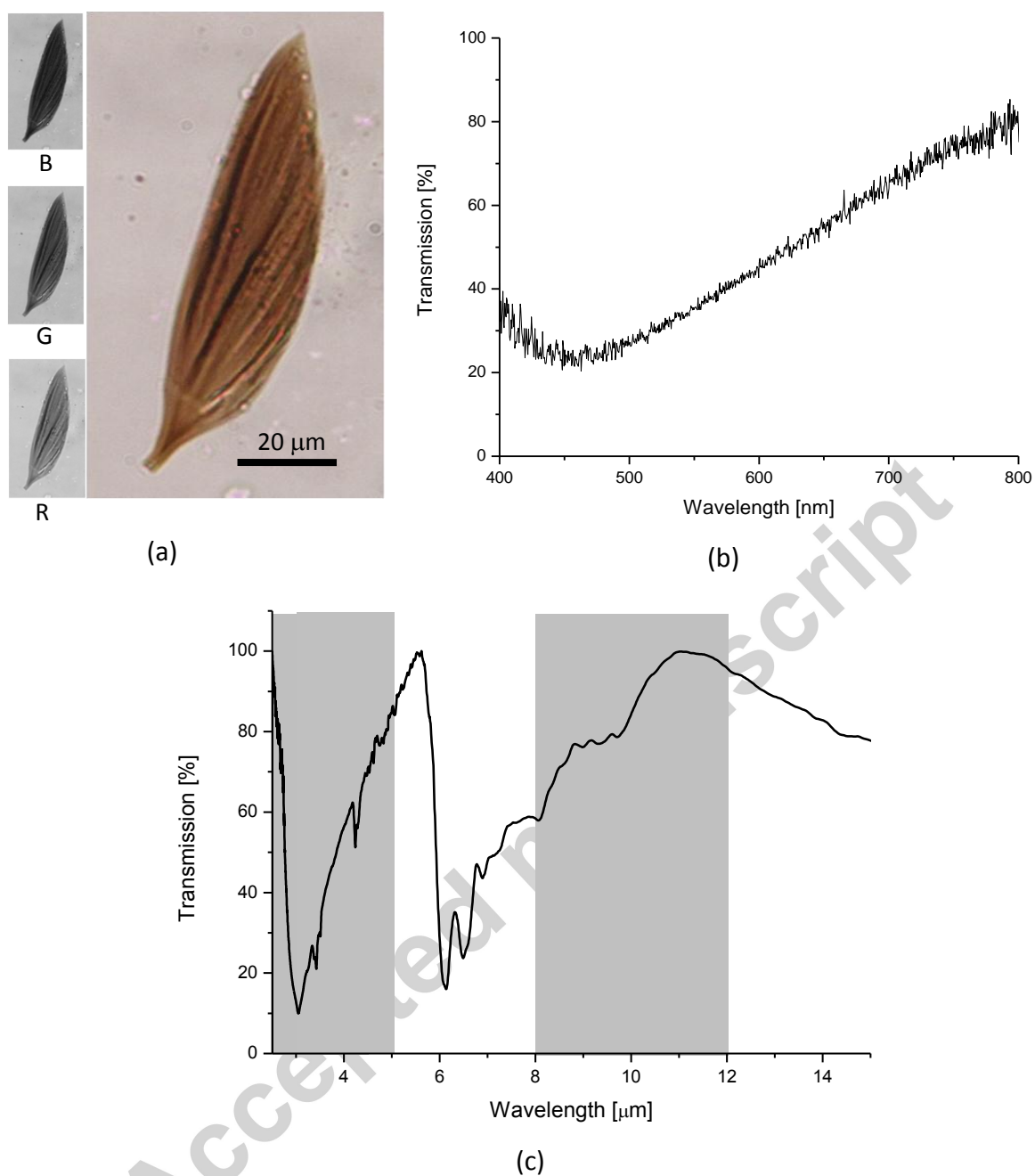


Fig. 6: (a) A single scale of *R. alpina* recorded in transmission (large image) and its RGB components shown on the left (three small images). Transmission gradually increases from blue to red channel. (b) Transmission spectrum of a single scale increases towards the red part of the spectrum (which is characteristic of melanin). (c) IR spectrum of a black patch of *R. alpina*. Gray areas show the sensitivity ranges of the IR cameras used in this research.

### 3.2. Measurement and modeling of thermal properties of *R. alpina* elytra

Two thermal cameras (sensitive within 1.5-5.1 $\mu\text{m}$  and 7.5-13 $\mu\text{m}$  ranges and corresponding to atmospheric windows) were used to monitor dried insect specimens mounted on the substrate whose temperature was measured. A tape with emissivity of 0.95 was used as a reference. The insect dorsal surface appeared uniform in thermal equilibrium (see Fig 7(a)), without any difference between the black spots and gray patches (both at 1.5-5.1 $\mu\text{m}$  and 7.5-13 $\mu\text{m}$  ranges). This is an interesting fact, showing that the gray and black areas contribute equally to the radiative energy exchange. However, there is a difference in emissivity between the two spectral ranges: average emissivity is 0.95 at 1.5-5.1 $\mu\text{m}$  (in line with [ ]), and 0.85 at 7.5-13 $\mu\text{m}$ .

To simulate environmental conditions, we used a flashlamp to uniformly irradiate the insect body. Here we analyzed the heating and cooling of the insect body using a thermal camera at 7.5-13  $\mu\text{m}$  (measurements at 1.5-5.1 $\mu\text{m}$  have a similar character and will not be shown). As expected, the black areas efficiently absorbed the light and converted it to heat (Fig. 7(b)), followed by a quick temperature rise of almost 7°C, while the temperature was lower for the gray area (see the corresponding graph in Fig. 7(b) representing temperature diagrams). This proves that the black areas absorbed the visible light more efficiently.

To measure the thermal properties of black elytral patches, we illuminated them with a 405-nm laser beam with an energy density of 1.67 mJ/mm<sup>2</sup>. An IR image of the laser-heated insect is shown in Fig. 7(c). Even though low power was used, the black patches efficiently absorbed the radiation and the temperature increase was up to 20°C (temperature variation is shown in a graph in Fig. 7(c)). The corresponding spatial variation of temperature was radially symmetrical (see the circular bright spot and the corresponding radial intensity distribution in Fig. 7(c)). Radial intensity distribution varied during irradiation and quickly reached a steady state (equilibrium) (Fig. 7(d)), without significant spreading of heat (which means that the thermal conductivity of elytra was small).

Further, we established a thermal model of *R. alpina* elytra to reveal the relative contribution of three basic thermal exchange mechanisms. This was done by fitting an experimentally recorded cooling curve to the theory based on radiation, convection and conduction [ , ]. The general, one-dimensional model includes all three mechanisms and is described by the following partial differential equation:

$$\frac{\partial T(z,t)}{\partial t} = -\frac{1}{\rho\tau c} \left[ \varepsilon\sigma(T(z,t)^4 - T_0^4) + h(T(z,t) - T_0) + k\nabla_z T(z,t) \right] \quad (1)$$

where  $T$  and  $T_0$  are material and environmental temperature, respectively,  $z$  is the spatial coordinate,  $t$  is the time variable and  $\sigma$  is a Stefan-Boltzmann constant. Material is described by its thickness  $\tau$  and several constants: material density  $\rho$ , specific heat  $c$ , surface emissivity  $\varepsilon$ , coefficient of thermal conductivity  $k$  and convection coefficient  $h$ . This is a partial differential equation that would be quite complicated if the exact morphology of the elytra is taken as a boundary condition.

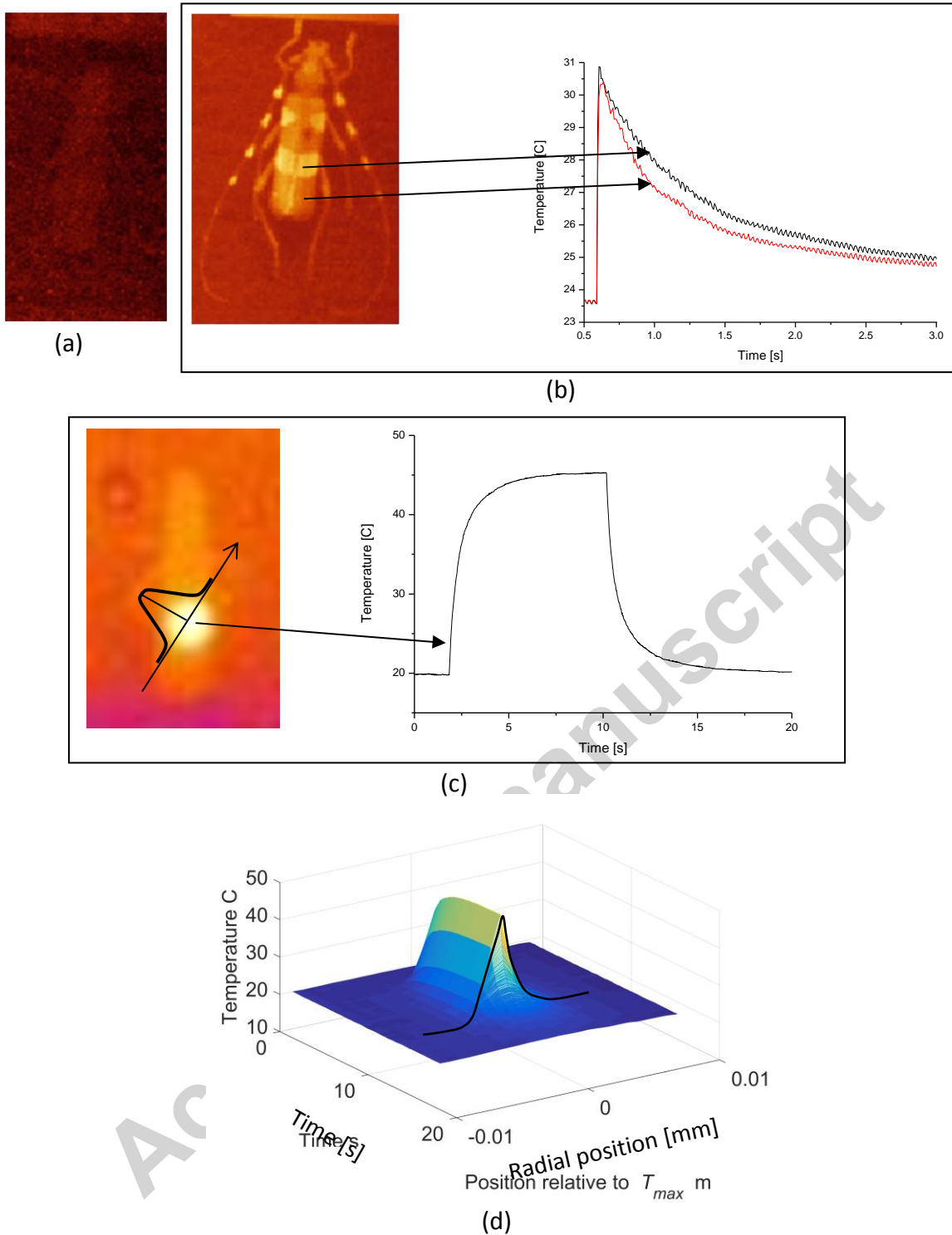


Fig. 7: (a) IR image of *R. alpina* in thermal equilibrium – black patches of elytra are not discernible. (b) IR image of *R. alpina* after irradiation with a flashlamp and the corresponding temperature variation of black (black diagram line) and grey (red diagram line) areas. (c) *R. alpina* heated by a laser beam (for 7.5 s) aimed at a black patch and the temperature variation at the center of the laser beam. (d) Temporal variation of radially symmetric temperature distribution of laser-heated *R. alpina* black patch. All images were recorded with a thermal camera sensitive within the range of 7.5-13  $\mu\text{m}$ .

We simplified the model by assuming that the temperature across the elytra is uniform (due to its thinness) and the thermal conduction along the elytra is so small that it can be neglected (as shown in the previous section). The only mechanisms of heat dissipation taken into account were therefore radiation and heat loss through the surrounding air (conduction and convection). Spatial distribution was assumed to be constant along the z-axis, with the jump at the air-elytra interface. The equation is simplified to:

$$\frac{dT(t)}{dt} = -\frac{1}{\rho\tau c} \left[ \varepsilon\sigma(T(t)^4 - T_0^4) + h(T(t) - T_0) + \frac{k}{\tau}(T(t) - T_0) \right] \quad (2)$$

The last two terms describe heat dissipation at the elytra-air interface due to conduction and convection in air (proportional to the corresponding temperature difference). Due to the small thermal conductivity of the elytra (revealed experimentally and described in the previous section), we assumed that the heated layer of the elytra is an order of magnitude smaller than the physical thickness of the elytra, and this value was taken as a thickness  $\tau$  in a model.

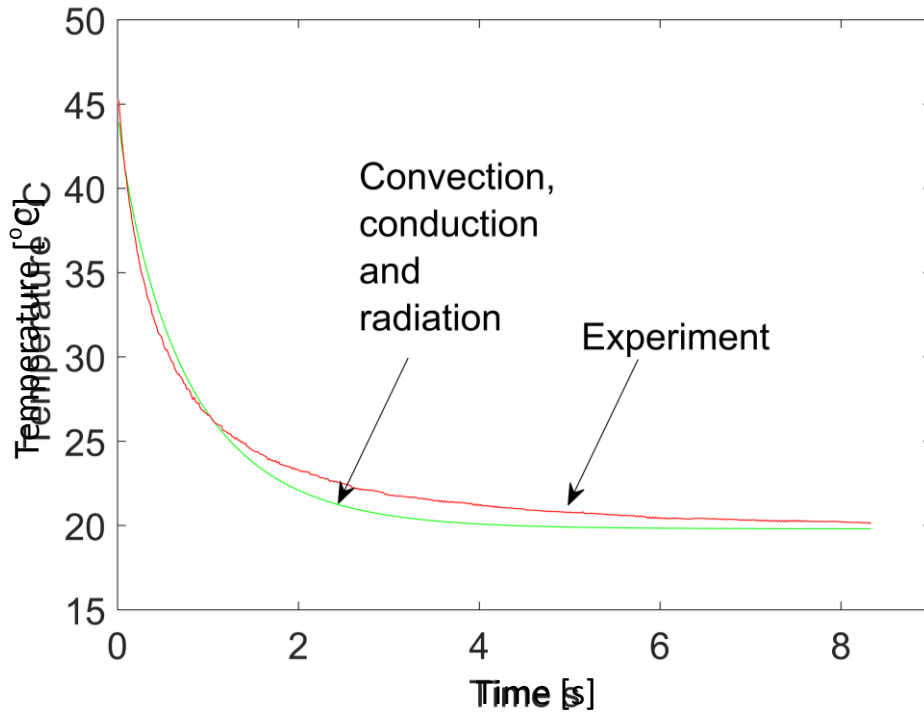
Chitin and cuticular proteins are the dominant constituents of the elytra [1]. Our measurements are based on literature data on the physical properties of cuticle [2] and chitin [3].

Table I: Parameter values used in a thermal model of *R. alpina*

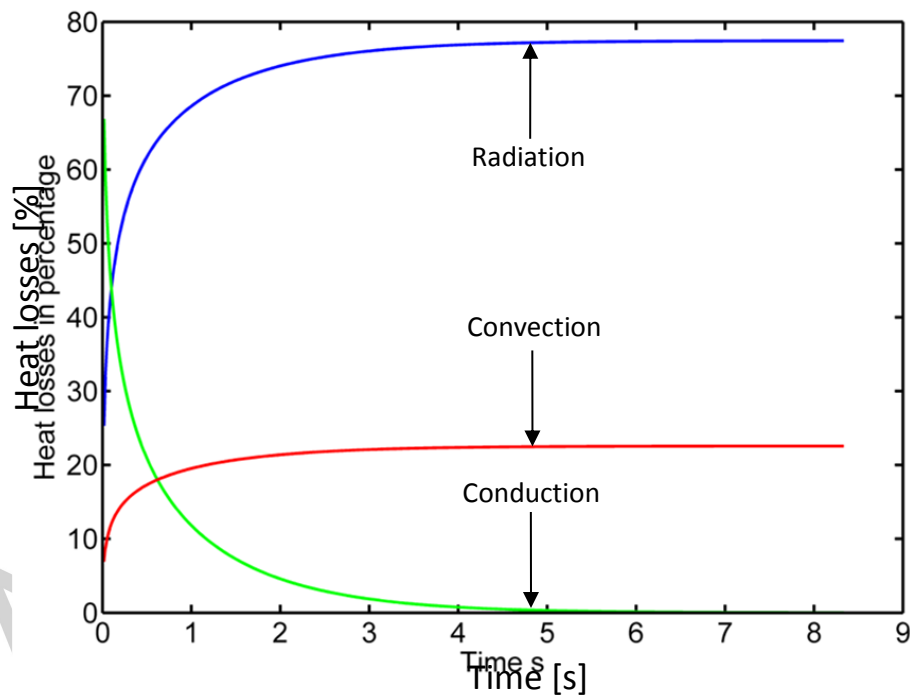
Parameters	Numerical value
conductivity of air, $k$	0.0257 W/m·K
convection coefficient of air, $h$	1.5 W/m <sup>2</sup> K (at 21°C)
surface emissivity $\varepsilon$	0.85
thickness $\tau$	3.25×10 <sup>-6</sup> m
density $\rho$ , [1]	1.560 g/cm <sup>3</sup>
specific heat $c$ [1]	1400 J/kg·K

Equation (1) was solved numerically by the Runge-Kutta method and we were able to fit the experimental cooling curve within  $\pm 1.5^\circ\text{K}$  (see Fig. 8(a)). We numerically separated the contributions of three basic dissipation mechanisms to the total losses. It was found that radiative cooling is the most important mechanism, because in less than a second, heat loss by radiation reached more than 50% (see Fig. 8(b)).





(a)



(b)

Fig.8: (a) Experimentally recorded temperature decay (red curve) is approximated using a model that includes convective, conductive and radiative losses (green curve).(b) Contribution of radiative (blue curve), convective (red curve) and conductive (green curve) losses to the total heat dissipation.

Here and in the previous sections we describe the experimentally measured and theoretically calculated thermal response of *R. alpina*. In the next sections we will show the contribution of underlying micro- and nanostructures to the observed thermal effects. Analysis will proceed by, first, calculating the absorptive properties of elytral structures of *R. alpina* in the visible part of the spectrum and will be concluded by calculating the emissive properties of the elytra. This is important, because the insect's lifestyle is such that the elytra must efficiently dissipate the light energy absorbed primarily through the black patches in order to maintain body temperature within tolerable limits.

### 3.3. Absorption of visible light by elytral structures of *R. alpina*

We have constructed an optical model of black elytral patches, based on SEM images (Figs. 3(a) and (b)) of *R. alpina*. A 2D model (shown in Fig. 9) imitates the tent-like arrangement of cuticular scales, which optically function as an optical beam dump. From the point of view of geometrical optics, beams entering the input aperture (within the  $134^\circ$  angular range, as estimated from SEM images; Figs. 3(a) and 4(a)) are being reflected several times from the wing scales, thus efficiently enhancing absorption. This is particularly true in the visible range, where the high concentration of melanin in the scales guarantees strong absorption.

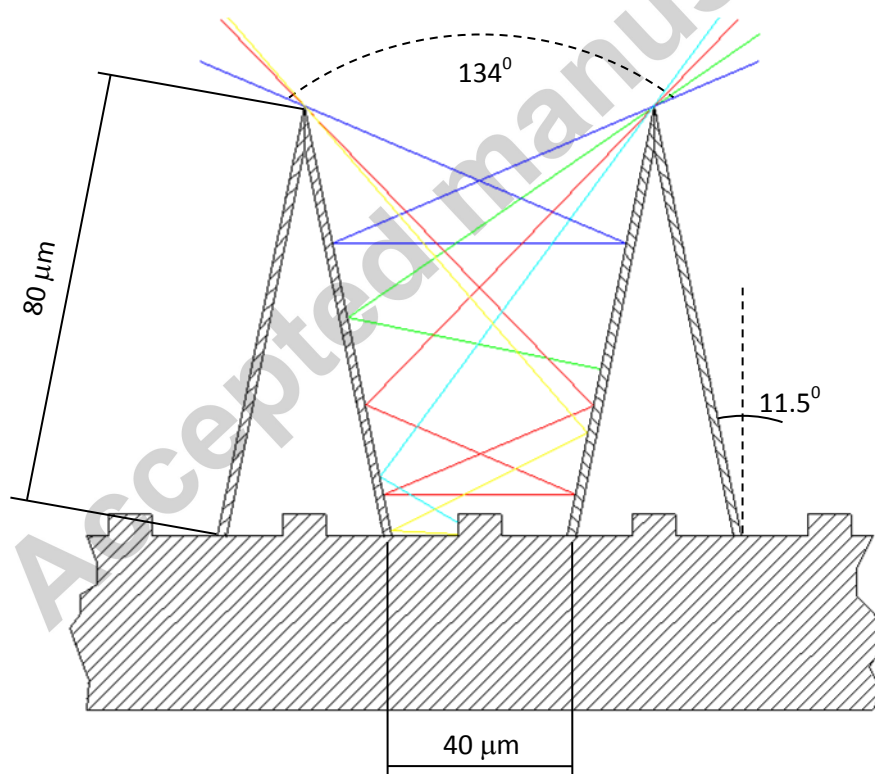
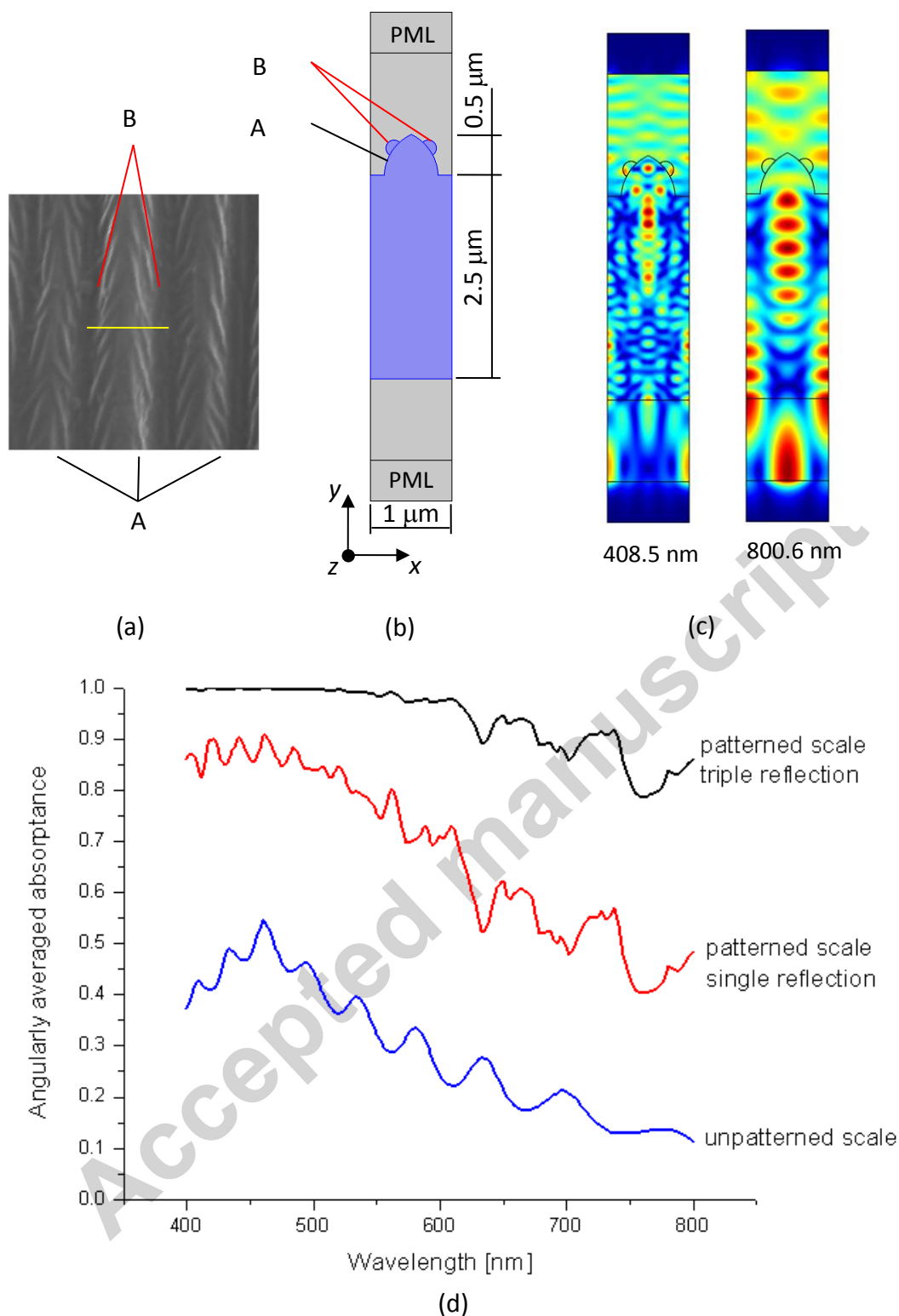


Fig. 9: An optical model of the *R. alpina* black patch operating as a beam dump in the visible part of the spectrum. Depending on the angle of incidence, beams (designated by different colors) may reflect 2-4 times.

To estimate the total absorption of the black patch, we must first calculate the absorption for a single reflection from a cuticular scale, which is a dominant elytral component of black patches. We noted that the scale surface was corrugated with high- and low-frequency gratings (Fig. 4(b)), above and below the wavelength of the visible light, respectively. At this point, we had to use wave optics to correctly model the interaction of light and the scale. Thus, small-scale morphology of the scale (Fig. 10(a)) is approximated by a two-dimensional elementary cell shown in Fig. 10(b). In the model, an elementary cell periodically repeats itself along the  $x$ -axis, it is infinite along the  $z$ -axis and bounded by perfectly matched layers (PML) along the  $y$ -axis. The feature (A) in Fig. 10(b) approximates the ridges of a low-period ( $1\ \mu\text{m}$ ) grating, while two smaller structures (B) approximate the high-frequency grating, sitting atop a low-frequency one. This model is used in a FEM to calculate the local electromagnetic field and spectral variation of absorbance.

The physical parameters were as follows. The refractive index of chitin is 1.57 and the extinction coefficient was determined from FTIR measurements (see the corresponding spectrum in Fig. 6(c)) and found to vary from 0.008 to 0.001 (within a 8-14 $\mu\text{m}$  range) and from 0.013 to 0.0016 (within a 3-5  $\mu\text{m}$  range). The corresponding reflection spectra were calculated for a range of angles of incidence and averaged to simulate the diffuse environmental radiation in the beetle's habitat. Averaged absorption spectra after single and triple reflections are shown in Fig. 10(d). Three reflections were chosen as an average between a minimum of two and a maximum of four possible reflections (see rays in Fig. 9). Both spectra are compared to the reflection spectrum of an unpatterned (flat-surface) scale, shown in the same graph. It is obvious that patterning doubles the amount of absorbed radiation. This is the consequence of the strong electromagnetic-field localization within the cuticular scale, as illustrated in Fig. 10(c). This makes this insect very efficient in capturing direct and diffused solar radiation and using it to heat its body.

Theoretical results are in agreement with the experiment showing 97.4% absorptance in the blue-green part of the spectrum. Discrepancy is greater in the red spectral range where theory predicts lower absorbance (80%) compared to the experiment (96.5%). This is certainly due to our inability to accurately model intricate cuticular structures – especially their randomness.



*Fig. 10: (a) Characteristic pattern on the *R. alpina* scale. The letter A designates the low-period (approximately 1  $\mu\text{m}$ ) grating, and B designates the high-period, herringbone-shaped grating. The yellow line corresponds to one grating period, used to design (b), a model of *R. alpina* scales used in FEM calculations (PML – perfectly matching layer). (c) A field distribution at two wavelengths showing strong electromagnetic-field localization within the scale. (d) Increase of scale absorbance due to surface pattern.*

### 3.4. Emission of IR radiation by elytral structures of *R. alpina*

After modeling the absorptive properties of *R. alpina*, we analyzed the IR properties of the same structures. We measured emissivity across beetle elytra in the IR and found it identical for both gray and black areas (see Section 4). To better understand the IR properties of elytra, we constructed models of black patch and blue-gray areas. Absorptance was calculated using FEM, at the same time giving us the value of emissivity according to Kirchhoff's law.

We used a model of black patch shown in Fig. 11(a) that simulates scales (Fig. 3(a)), together with the underlying, corrugated cuticular structure (Fig. 3(b)). To determine the emissivity of this structure, it is enough to calculate the absorptance (which is equal to emissivity, according to the Kirchhoff's law). It was averaged within an angular range of IR collected by the thermal camera lens (determined by its F-number), thus simulating the experimental situation of recording an infrared image of the insect.

FEM analysis shows that the light is localized within the elytra or scales (Fig. 11(b)), depending on the wavelength and morphology of the elytra. This significantly amplifies innate absorption of chitin (see its transmission spectrum in Fig. 6(c)) due to increased optical path length within the structure. In order to establish the influence of scales, we also calculated the absorption of the elytra alone (without scales – modeled as in Fig. 11 (c)). The corresponding graphs for elytra with and without scales, at 3-5  $\mu\text{m}$  and 8-14 $\mu\text{m}$  ranges, are shown in Fig. 11(d). Obviously, scales improve the absorptive/emissive characteristics of an insect by more than 20%.

The same line of reasoning was applied to the blue-gray elytral areas covered with hairs. Again, we found that the elytral hairs significantly improved the absorption and emissivity (Fig. 12(a) – (d)).

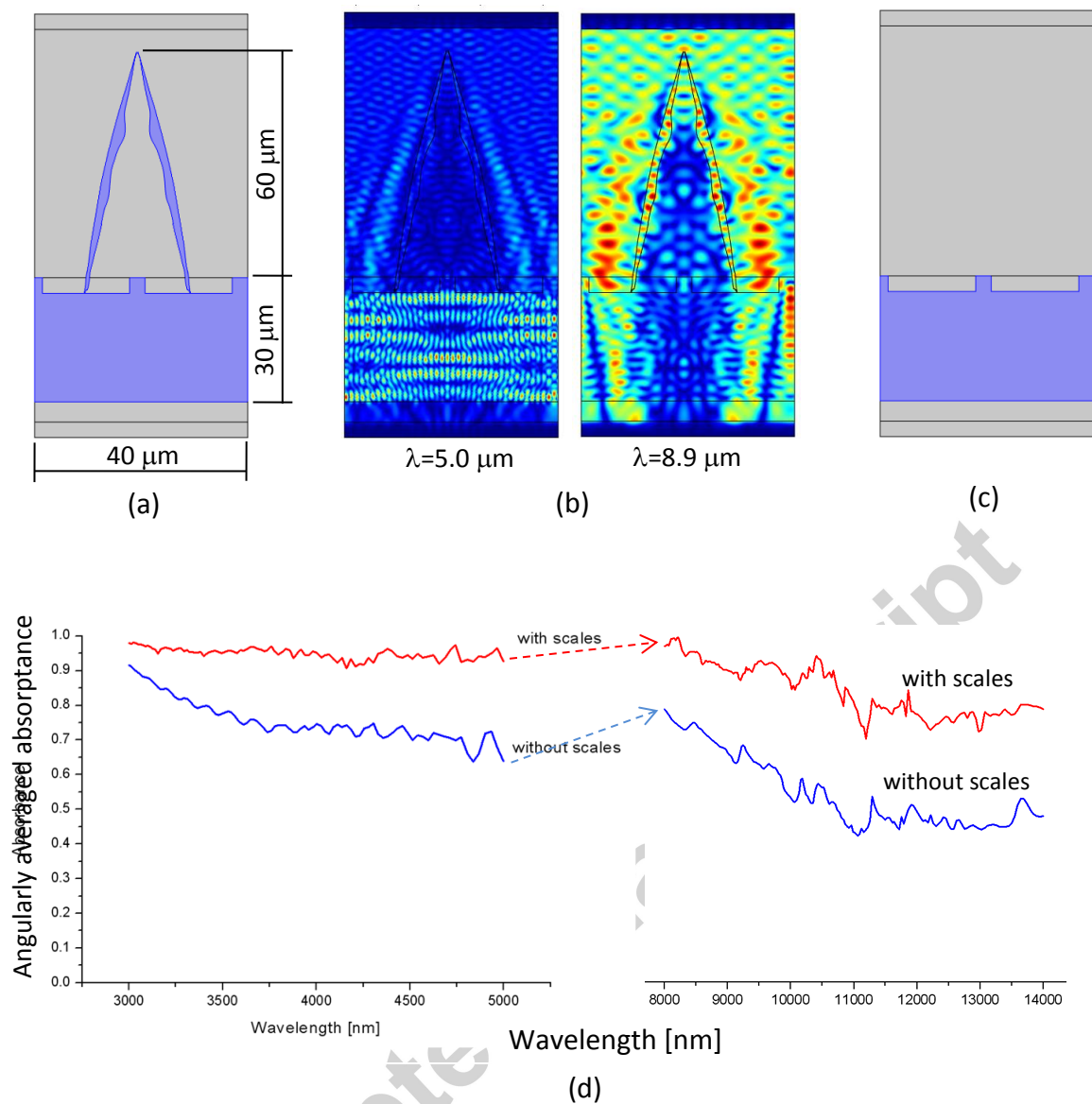


Fig. 11: IR properties of the *R. alpina* black patch. (a) A FEM model of a tent-like scale structure. (b) The corresponding EM field distribution at 5 μm and 8.9 μm. (c) A model of elytra without scales used to investigate the contribution of scales to total absorbance. (d) Angularly averaged absorptance of elytra with and without scales.

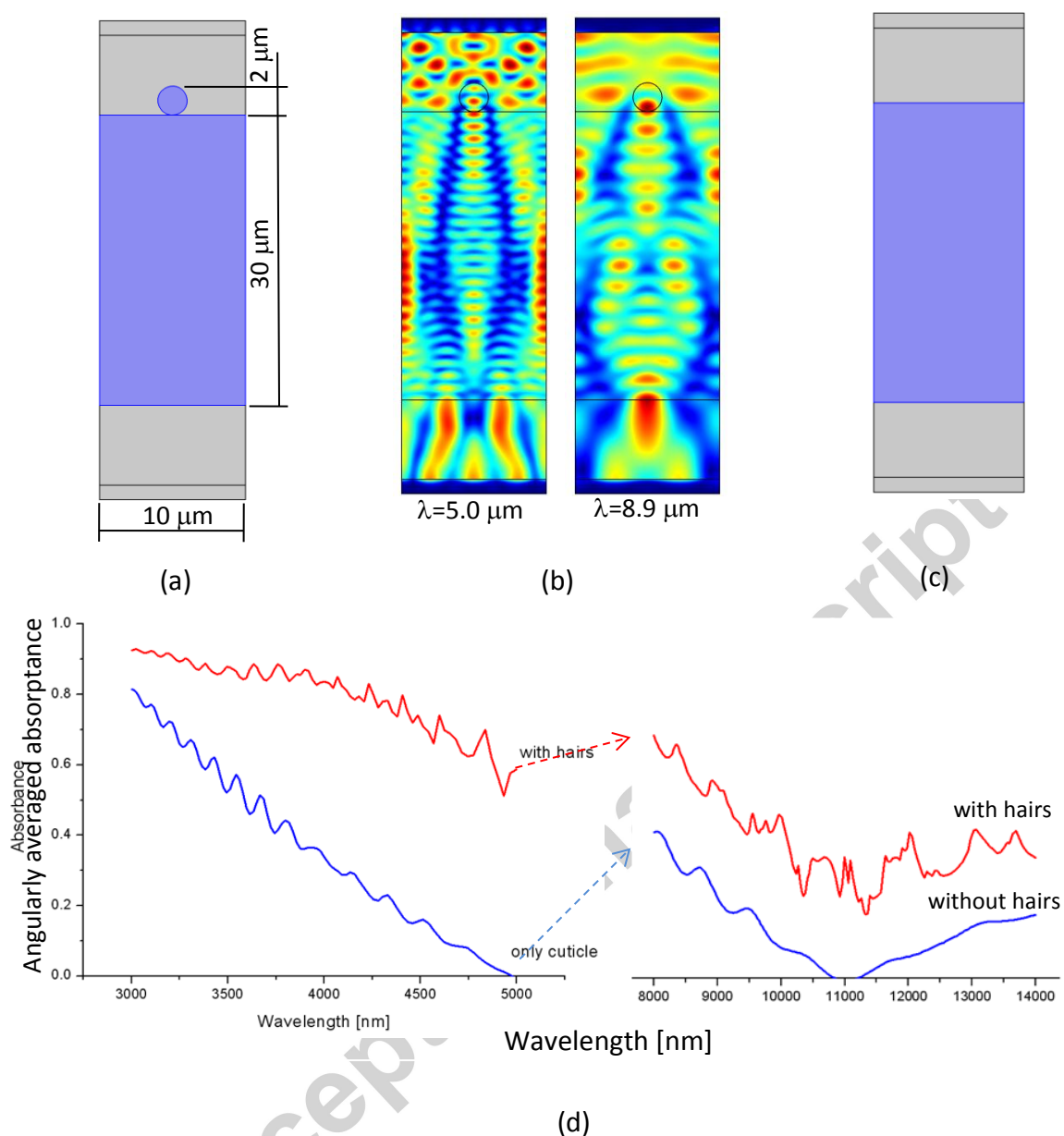


Fig. 12: IR properties of the blue-gray elytra of *R. alpina*. (a) A FEM model of the cuticle with hairs. (b) The corresponding EM field distribution at 5  $\mu\text{m}$  and 8.9  $\mu\text{m}$ . (c) A model of elytra without hairs used to investigate the contribution of hairs to total absorbance. (d) Angularly averaged absorptance of the elytra with and without hairs.

### 3.5. Radiative balance of *R. alpina*

Here we present a detailed energy balance, assuming the maximum insolation ( $1\text{kW/m}^2$ ) of an insect. Total visible light energy absorbed by the elytra of *R. alpina* is equal to:

$$P_A = P_S(A_B S_B + A_G S_G) \quad (3)$$

where  $P_A$  is the total absorbed power,  $P_S$  is the solar constant,  $A_B$  is the absorption coefficient of the black patch,  $S_B$  is the total area of black patches,  $A_G$  is the absorption coefficient of blue-gray areas, while  $S_G$  is the total area of the blue-gray-colored surface. On the other hand, IR energy emitted by the whole elytra is:

$$P_E = 2\pi S_T \left[ \varepsilon_M \int_M E(\lambda, T) d\lambda + \varepsilon_F \int_F E(\lambda, T) d\lambda \right] \quad (4)$$

where  $P_E$  is total energy emitted by the elytra within two IR atmospheric windows,  $S_T$  is the total area of the cuticle ( $S_T = S_B + S_G$ ),  $\varepsilon_M$  is the emissivity within the mid-infrared atmospheric window ( $M = 3-5 \mu\text{m}$ ),  $\varepsilon_F$  is the emissivity within the far-infrared atmospheric window ( $F = 8-14 \mu\text{m}$ ),  $\lambda$  and  $T$  are wavelength and absolute temperature, respectively, while  $E(\lambda, T)$  is the radiance of a black body.

As the next step, we found a temperature corresponding to the balance of radiative gain in the visible and radiative losses in the infrared (i.e.  $P_A = P_E$ ). By equating (3) and (4) we get:

$$P_S(A_B S_B + A_G S_G) = 2\pi S_T \left[ \varepsilon_M \int_M E(\lambda, T) d\lambda + \varepsilon_F \int_F E(\lambda, T) d\lambda \right] \quad (5)$$

and, after a slight rearrangement:

$$P_S \left( A_B \frac{S_B}{S_T} + A_G \frac{S_G}{S_T} \right) = 2\pi \left[ \varepsilon_M \int_M E(\lambda, T) d\lambda + \varepsilon_F \int_F E(\lambda, T) d\lambda \right] \quad (6)$$

We found that black patches occupy approximately one third of the whole elytral area ( $S_B/S_T=0.33$ ), while the rest of the elytra is gray ( $S_G/S_T=0.67$ ). Experimentally measured emissivities for the mid-infrared range and far-infrared were  $\varepsilon_M=0.95$  and  $\varepsilon_F=0.85$ , respectively, while the absorptance of the black patches was  $A_B=0.95$ , and that of the gray areas was  $A_G=0.12$ . We emphasize that the values of absorptance and emissivity are only averages and may vary across the insect elytra and between insect specimens.

Simple calculation, using Eq. (6), showed that the radiative balance between the visible and IR radiation was established somewhere between 300 K and 310 K, which is close to the maximum daily temperature in the summer months of the temperate areas where *R. alpina* lives []. This result was obtained by assuming the normal angle of incidence of radiation with respect to the insect's elytra – which is the worst-case condition. However, the mutual position of the sun and the insect varies during the day, establishing the radiation balance at lower temperatures in an average situation.

## 4. Discussion and conclusions



*R. alpina* is a saproxylic beetle present in Europe (except its northern parts), predominantly inhabiting thermophilic beech (*Fagus sylvatica*) forests [], but it is also found on other broadleaved trees []. The peculiar, visually attractive coloration is explained by the insect's need to camouflage itself within its habitat []. Nevertheless, an unavoidable question arises: why did nature create scales on the surface of the elytra? Why not just smooth, shiny black patches, without any cuticular appendages? Such black patches, without scales, would have the same camouflage role, without wasting life energy in producing a complicated nano-sized architecture on the elytral surface. The answer lies in the biology and ecology of the beetle and the optical properties of these surface nanostructures.

It was found that *R. alpina* adults search for decomposing beech wood on isolated trees and sun-exposed sites [, ]. The life cycle lasts about three years with the life span of an adult being just several weeks []. Adults are the most active during the hottest months of the year (from July till August) and during the hottest part of the day (12-14 h) [, ].

Despite the significance of this endangered species, little is known about its biology and ecology [,]. Some conclusions about the biology of the species can be made by comparison with related species [, ]. The related *R. coelestis*, Semenov 1911, as well as many other Cerambycidae species, require no food as adults. This is supported by [,] where no feeding was observed in *R. alpina* for 1500 adult capture events.

Adults are active and mobile, and they fly, but since they do not feed, their energy resources are very limited []. This could be the reason why *R. alpina* is always found on sun-exposed trunks and branches. In order to fly, it needs energy, to warm up its thoracic muscles, which run up the hindwings (alae). Like butterflies [] and other ectotherms, the insect relies on an external heat source – solar radiation. This is in complete correlation with research [,] proving that insect-occupied trees were not randomly distributed: insects were only found in open forests, while unmanaged forests were avoided. Only trees with a high sun index were selected. Occupied trees were always found in open sites with a low canopy closure and low or no undergrowth, allowing more sunlight to break through. Several other studies [,,] underline the importance of sun-exposed substrates for saproxylic beetles, which form a warm microclimate for the development of larvae.

Our research throws new light on the biology, ecology and evolution of *R. alpina*, proving that sun-exposed habitats are not just important for larvae development but also for the survival of adults. In order to maintain a temperature balance, heat gain and loss must be balanced. One of the possible mechanisms is regulation of heat exchange between the body and the external environment (behavioral mechanism). Here we show the significance of elytral setae (scales and hairs) of *R. alpina* for thermal regulation in adults. Direct solar radiation is efficiently absorbed by black patches, resulting in rapid heat gain. Additionally, excess heat is equally well dissipated by IR radiation through the whole surface of the elytra (both gray and black areas). Since *R. alpina* is a flying species, heat is produced during flight, but the above mentioned mechanism also helps in establishing the temperature balance.

It seems that evolution needed to solve two problems. The first one was to provide an efficient camouflage for the insect on the bark of a beech, which required the emergence of black patches similar to blemishes on the tree bark. The second problem is a consequence of the first: the efficient dissipation of thermal energy absorbed through the black patches. The solution was found by making the black areas serve a dual purpose. In the visible part of the spectrum they function as an efficient beam dump, absorbing almost all the radiation. In the IR, structures interchange radiation with the environment and quickly attain equilibrium. The rest of the body efficiently scatters the visible light and produces a uniform grayish color, very similar to the base color of beech bark. Simultaneously, the IR properties of the black and gray areas are almost the same. In this way, energy absorbed through the black patches is efficiently dissipated throughout the entire body surface. These effects not only reduce the possibility of overheating if exposed to direct solar radiation, but also enable radiative heating if insolation is diminished. Thus, the insect is capable of establishing a thermal balance under conditions of the highest thermal load (direct sunlight exposure), as well as under diffuse light irradiation (reduced insolation, at the end of the day or in cloudy weather).

In this study, a thermal model of *R. alpina* was constructed based on experiments with dry specimens, which contain only 1% of water (according to []). However, the contribution of water to radiation effects is unimportant, because the absorption of water is insignificant within the atmospheric windows used by the insect to dissipate the excess heat. On the other hand, even if wet, the elytra are a thermal insulator and the contribution of conduction to overall thermal properties is small compared to that of radiation and convection (see Fig. 7(b)). Lipids and waxes are present as a superficial layer and are of no significance. Therefore, our results also apply to live insects.

It is possible that temperature affects the flow of the hemolymph and air through the tracheoles. However, in this particular insect, micro-CT has revealed the presence of quite compact elytra, meaning that the amount of fluids is minute and incapable of significantly influencing the thermal balance of *R. alpina*.

Absorption enhanced by surface texture was previously established in solar radiation collection research [ , ]. In this respect, it seems that nature was well ahead of man. From a practical point of view, such structures observed in *R. alpina* could be used for photovoltaic conversion of solar energy to dissipate the fraction of light energy converted to heat. In this way, solar cells will remain within the optimal thermal limits.

## Acknowledgments

We express our gratitude to the Serbian Ministry of Education, Science and Technological Development for the financial support through projects, Nos. ON171038, III45016, III47029, III45005, ON173027 and 173038. The authors are grateful to Dr.Ljubodrag Vujisić and Dr.Boban Anđelković from the Faculty of Chemistry, University of Belgrade, Serbia, who measured the FTIR spectrum of *R. alpina* elytra. We also thank Dr.Zlatko Prolić and Dr.Dejan Stojanović for their support and useful comments.

### **Ethical approval**

All necessary permissions to collect the samples of *R. alpina* were obtained from the Ministry of Environmental Protection of the Republic of Serbia and the Institute for Nature Conservation of Serbia.

### **Author contributions**

D.T. observed the structural nature of black patches of certain Cerambycidae. D.V.P. initiated the thermal analysis study. P.M. performed the micro-CT analysis and V.L. performed the SEM analysis. B.S. calculated the optical and IR properties of the photonic structures, while G.D. made mathematical analyses of the thermal exchange mechanisms. Lj.T., D.P. and D.V. made the infrared measurements. D.P. and S.Ć. covered the biological, behavioral and environmental aspects of the work. D.V.P. supervised the research and performed the thermal balance calculations. D.P., D.V. and D.V.P. wrote the manuscript, taking into account the comments of the other coauthors.

This work was carried out as partial fulfillment of the requirements for the PhD degree of **Danica Pavlović** at the University of Belgrade –Faculty of Biology.

### **Conflict of interest**

The authors declare no conflict of interest.

### **References**

1. Torre-Bueno, J. R., Temperature regulation and heat dissipation during flight in birds. *Journal of Experimental Biology* **65** (2), 471-482 (1976).
2. Preciado, A. J. *et al.*, Radiative properties of polar bear hair. *ASME Proceedings of the International Mechanical Engineering Congress and Exposition*, 57-58 (2002).
3. Twiss, S. D. *et al.*, Behavioral evidences of thermal stress from overheating in UK breeding gray seals. *Marine Mammal Science* **18** (2), 455-468 (2002).
4. Heinrich, B., *The hot-blooded insects: strategies and mechanisms of thermoregulation* (Springer Science & Business Media, New York, 2013).
5. Heinrich, B., Thermoregulation in endothermic insects. *Science* **185**(4153), 747-756 (1974).

6. Angilletta Jr, M. J., Niewiarowski, P. H. & Navas, C. A., The evolution of thermal physiology in ectotherms. *Journal of Thermal Biology***27**, 249-268 (2002).
7. Nijhout, H. F., *The development and evolution of butterfly wing patterns* (Smithsonian Institution Press, Washington-London, 1991).
8. Kingsolver, J. G., Butterfly thermoregulation: organismic. *Journal of Research on the Lepidoptera***24(1)**, 1-20 (1985).
9. Church, N. S., Heat Loss and the Body Temperatures of Flying Insects, II Heat conduction within the body and its loss by radiation and convection. *Journal of Experimental Biology***37**, 186-212 (1960).
10. Vukusic, P. & Sambles, J. R., Photonic structures in biology. *Nature***454** (6950), 852 (2003).
11. Vukusic, P., Sambles, J. R., Lawrence, C. R. & Wootton, R. J., Structural colour: now you see it—now you don't. *Nature***410** (6824), 36 (2001).
12. Scoble, M. J., *The Lepidoptera. Form, function and diversity* (Oxford University Press, New York, 1992).
13. Shi, N. N. *et al.*, Keeping cool: enhanced optical reflection and radiative heat dissipation in Saharan silver ants. *Science***349(6245)**, 298-301 (2015).
14. Vukusic, P., Sambles, J. R. & Lawrence, C. R., Structurally assisted blackness in butterfly scales. *Proceedings of the Royal Society of London B: Biological Sciences***271(Suppl 4)**, S237-S239 (2004).
15. Biró, L. P. *et al.*, Role of photonic-crystal-type structures in the thermal regulation of a Lycaenid butterfly sister species pair. *Physical Review E***67(2)**, 021907 (2003).
16. Gallego, B., Verdú, J. R., Carrascal, L. M. & Lobo, J. M., A protocol for analysing thermal stress in insects using infrared thermography. *Journal of thermal biology*,**56**, 113-121 (2016).
17. Herman, A., Vandenberg, C., Deparis, O., Simonis, P. & Vigneron, J. P., Nanoarchitecture in the black wings of *Troides magellanus*: a natural case of absorption enhancement in photonic materials. *Proc. of SPIE Vol. 8094, Nanophotonic materials, 80940H-1* (2011).
18. Dikić, G. *et al.*, *The Thermographic Analysis of Photonic Characteristics of Rosalia alpina Surfaces*, presented at Proceedings of 3rd International Conference on Electrical, Electronic and Computing Engineering, Zlatibor, Serbia, 2016 (unpublished).
19. Campanaro, A. *et al.*, Guidelines for the monitoring of *Rosalia alpina*. *Nature Conservation***20**, 165–203 (2017).

20. Bense, U., *Bockkäfer. Illustrierter Schlüssel zu den Cerambyciden und Vesperiden Europas* (Margraf Verlag, Weikersheim, 1995).
21. Duelli, P. & Wermelinger, B., Der Alpenbock (*Rosalia alpina*). Ein seltener Bockkäfer als Flaggschiff Art. *Merkblatt für die Praxis***39**, 1-8 (2005).
22. The IUCN Red List of Threatened Species, Available at [www.iucnredlist.org](http://www.iucnredlist.org) (Version 2017-3).
23. Stavenga, D. G., Leertouwer, H. L., Hariyama, T., De Raedt, H. A. & Wilts, B. D., Sexual dichromatism of the damselfly *Calopteryx japonica* caused by a melanin-chitin multilayer in the male wing veins. *PLoS One***7** (11) (2012).
24. Stabentheiner, A. & Schmaranzer, S., Thermographic determination of body temperatures in honey bees and hornets: calibration and applications. *Thermology***2** (4), 563-572 (1987).
25. Levesque, L., Law of cooling, heat conduction and Stefan-Boltzmann radiation laws fitted to experimental data for bones irradiated by CO<sub>2</sub> laser. *Biomedical Optics Express***5**, 701-712 (2014).
26. Torres, J. H., Motamedi, M., Pearce, J. A. & Welch, A. J., Experimental evaluation of mathematical models for predicting the thermal response of tissue to laser irradiation. *Appl. Opt.***32**, 597-606 (1993).
27. Capinera, J. L., *Encyclopedia of entomology* (Springer, New York, 2008).
28. Gullan, P. J. & Cranston, P. S., *The insects: an outline of entomology*. (John Wiley & Sons, 2014).
29. Ishay, J. S. & Pertsis, V., The specific heat of the cuticle and the morphological differences between the brown and yellow cuticles of hornets. *Journal of electron microscopy***51** (6), 401-411 (2002).
30. Vincent, J. F. & Wegst, U. G., Design and mechanical properties of insect cuticle. *Arthropod structure & development***33** (3), 187-199 (2004).
31. Neville, A. C., *Biology of arthropode cuticle* (Springer Verlag, Berlin, Heidelberg, 1975).
32. Hammer, D. X. *et al.*, Investigation of the transduction mechanism of infrared detection in *Melanophila acuminata*: photo-thermal-mechanical hypothesis. *Comparative Biochemistry and Physiology, Part A***132**, 381-392 (2002).
33. Anders, I., Stagl, J., Auer, I. & Pavlik, D., in *Managing Protected Areas in Central and Eastern Europe Under Climate Change* (Springer, Dordrecht, 2014), pp. 17-30.
34. Cizek, L., Schlaghamerský, J., Bořucký, J., Hauck, D. & Helešic, J., Range expansion of an endangered beetle: Alpine Longhorn *Rosalia alpina* (Coleoptera: Cerambycidae) spreads to the lowlands of Central Europe. *Entomologica Fennica***20** (3), 200-206 (2009).

35. Starzyk, J. R., in *Polska czerwona księga zwierząt. Bezkręgowce. [Polish red data book of animals. Invertebrates.]* ( AR Poznan IOP PAN, Kraków, 2004), pp. 148-149.
36. Russo, D., Cistrone, L. & Garonna, A. P., Habitat selection by the highly endangered long-horned beetle *Rosalia alpina* in Southern Europe: a multiple spatial scale assessment. *Journal of Insect Conservation***15** (5), 685-693 (2011).
37. Drag, L., Hauck, D., Pokluda, P., Zimmermann, K. & Cizek, L., Demography and dispersal ability of a threatened saproxylic beetle: a mark-recapture study of the *Rosalia longicorn* (*Rosalia alpina*). *PLoS ONE***6** (6), e21345 (2011).
38. Tsherepanov, A. I., *Longicorn beetles of North Asia (Cerambycinae)*. (Nauka, Novosibirsk, 1981).
39. Ray, A. M. *et al.*, Male-produced aggregation pheromone of the cerambycid beetle *Rosalia funebris*. *Journal of Chemical Ecology***35** (1), 96-103 (2009).
40. Lachat, T., Ecker, K., Duelli, P. & Wermelinger, B., Population trends of *Rosalia alpina* (L.) in Switzerland: a lasting turnaround?. *Journal of Insect Conservation***17** (4), 653-662 (2013).
41. Lindhe, A., Lindelöw, Å. & Åsenblad, N., Saproxylic beetles in standing dead wood density in relation to substrate sun-exposed and diameter. *Biodiversity and Conservation***14** (12), 3033-3053 (2005).
42. Vodka, S., Konvicka, M. & Cizek, L., Habitat preferences of oak-feeding xylophagous beetles in a temperate woodland: implications for forest history and management. *Journal of Insect Conservation***13**, 553-562 (2009).
43. Buse, J., Schröder, B. & Assmann, T., Modelling habitat and spatial distribution of an endangered longhorn beetle—a case study for saproxylic insect conservation. *Biological Conservation***137** (3), 372-381 (2007).
44. Lomakin, J. *et al.*, Mechanical properties of the beetle elytron, a biological composite material. *Biomacromolecules***12** (2), 321-335 (2010).
45. Yablonovich, E. & Cody, G. D., Intensity enhancement in textured optical sheets for solar cells. *IEEE Trans. Electron Devices***29**, 300-305 (1982).
46. Niggemann, M., Riede, M., Gombert, A. & Leo, K., Light trapping in organic solar cells. *Phys. Stat. Sol. (A)***205**, 2862–2874 (2008).

**Highlights**

1. Photonic structures on insect elytra serve for camouflage and thermoregulation
2. In the visible part of the spectrum black patches absorb almost all the radiation
3. In the IR whole elytra efficiently dissipate radiation
4. We suggest biomimetic application in thermal management

Accepted manuscript

# Journal of Biomedical Optics

[SPIEDigitalLibrary.org/jbo](http://SPIEDigitalLibrary.org/jbo)

## **Nonlinear microscopy of chitin and chitinous structures: a case study of two cave-dwelling insects**

Mihailo D. Rabasović  
Dejan V. Pantelić  
Branislav M. Jelenković  
Srećko B. Čurčić  
Maja S. Rabasović  
Maja D. Vrbica  
Vladimir M. Lazović  
Božidar P. M. Čurčić  
Aleksandar J. Krmpot



# Nonlinear microscopy of chitin and chitinous structures: a case study of two cave-dwelling insects

Mihailo D. Rabasović,<sup>a</sup> Dejan V. Pantelić,<sup>a,\*</sup> Branislav M. Jelenković,<sup>a</sup> Srećko B. Čurčić,<sup>b</sup> Maja S. Rabasović,<sup>a</sup> Maja D. Vrbica,<sup>b</sup> Vladimir M. Lazović,<sup>a</sup> Božidar P. M. Curčić,<sup>b</sup> and Aleksandar J. Krmpot<sup>a</sup>

<sup>a</sup>University of Belgrade, Institute of Physics, Pregrevica 118, 11080 Zemun, Belgrade, Serbia

<sup>b</sup>University of Belgrade—Faculty of Biology, Institute of Zoology, Studentski Trg 16, 11000 Belgrade, Serbia

**Abstract.** We performed a study of the nonlinear optical properties of chemically purified chitin and insect cuticle using two-photon excited autofluorescence (TPEF) and second-harmonic generation (SHG) microscopy. Excitation spectrum, fluorescence time, polarization sensitivity, and bleaching speed were measured. We have found that the maximum autofluorescence signal requires an excitation wavelength below 850 nm. At longer wavelengths, we were able to penetrate more than 150- $\mu\text{m}$  deep into the sample through the chitinous structures. The excitation power was kept below 10 mW (at the sample) in order to diminish bleaching. The SHG from the purified chitin was confirmed by spectral- and time-resolved measurements. Two cave-dwelling, depigmented, insect species were analyzed and three-dimensional images of the cuticular structures were obtained. © 2015 Society of Photo-Optical Instrumentation Engineers (SPIE) [DOI: [10.1117/1.JBO.20.1.016010](https://doi.org/10.1117/1.JBO.20.1.016010)]

Keywords: nonlinear microscopy; fluorescence; two-photon excitation; second-harmonic generation; chitin; insect.

Paper 140595R received Sep. 23, 2014; accepted for publication Dec. 9, 2014; published online Jan. 9, 2015.

## 1 Introduction

Nonlinear microscopy (NLM) offers a unique insight into a variety of biological structures. Images are generated through multiphoton excited fluorescence, coherent anti-Stokes Raman spectroscopy (CARS), or nonlinear harmonic generation. Tissues and individual cells can be observed with excellent volume details<sup>1</sup>—i.e., lateral resolution is subdiffraction of the order of several hundred nanometers, while the axial resolution is of the order of 2 to 3  $\mu\text{m}$ . This technique is similar to confocal microscopy (in the sense of localized laser excitation and scanning), but with higher penetration depth, less photodamage, and without the need for specimen staining. Up until now, NLM was extensively used in biomedical research, but only marginally in entomology. It is well known that the chitin is a major constituent of the insect's (and arthropod) body and the goal of the study was to investigate the suitability of NLM for deep imaging of chitinous structures. We emphasize the following properties of chitin imaging: higher penetration depth, no need for staining due to efficient autofluorescence of chitin, possibility for *in vivo* imaging, and simultaneous multimodal imaging through harmonics generation.

The insect integument is composed of one live cell layer—epidermis, which produces a complex noncellular outer layer of the integument—cuticle. The cuticle serves as an insect exoskeleton, the site for muscle attachment, and a barrier against predators, parasites, and infection by pathogens.<sup>2</sup> Chitin is the major component of insect cuticle, with addition of proteins (such as resilin, sclerotin, and arthropodin),<sup>3</sup> lipids, waxes, mineral substances, and pigments (papiliochromes, pteridines, ommochromes, melanins, and flavonoids).<sup>4,5</sup> Chitin represents a water-insoluble polysaccharide whose molecules are long-chain sugars consisting of *N*-acetyl-glucosamines bonded with beta-glucosidic linkages.<sup>2</sup> It was extensively studied using a range of

techniques: scanning electron microscopy, atomic force microscopy, confocal fluorescent microscopy,<sup>6</sup> transmission electron microscopy,<sup>7</sup> and classical optical microscopy (polarizing interference and transmission).<sup>8</sup>

Traditionally, insect morphology was studied by bright field microscopy. Confocal fluorescence microscopy was also used to observe the structures and organs of insects,<sup>9,10</sup> while two-photon microscopy is still regarded as an emerging technique in entomology. Several papers have been published on the use of NLM in entomology (see Ref. 11 and references within). In Ref. 11, CARS and two-photon excited autofluorescence (TPEF) were used for visualization of *Drosophila melanogaster*, Meigen 1830.

The optical properties of chemically purified chitin have been studied previously. A complex refractive index was investigated in Ref. 12, while its Fourier transform infrared spectra were presented in Ref. 13. Absorption of thin chitin films was investigated in Ref. 14 and two peaks were found. The strong absorption peak was around 330 nm, and the other, much weaker, was identified at 1200 nm. It was found<sup>15</sup> that the fluorescence of the butterfly wings (consisting mostly of chitin) is caused mainly by natural pigments. They are efficiently excited by UV light (at 325-nm wavelength, in the case of various pteridines, 400 nm in papiliochrome, and 340 to 400 nm in melanin<sup>16</sup>). This was used for remote insect monitoring.<sup>17</sup>

Here, we study the nonlinear optical properties of chemically purified chitin and chitinous structures of insects. In the case of chemically purified chitin, we have explored two-photon fluorescence excitation efficiency, fluorescence spectrum, and the bleaching rate. The second-harmonic generation (SHG) was also confirmed. Chitinous structures of two cave-dwelling insect species were analyzed. The insects are adapted for life in underground habitats (trogllobites) and belong to two subclasses, Apterygota (wingless insects) and Pterygota (insects with

\*Address all correspondence to: Dejan V. Pantelić, E-mail: [pantelic@ipb.ac.rs](mailto:pantelic@ipb.ac.rs)

wings). They are depigmented or have a weak yellow color, transparent, and the cuticle is thinned, with homogeneous chitin.<sup>18</sup> These adaptations allow them to survive in the moisture-saturated atmosphere in caves.<sup>19</sup> By choosing depigmented insects, we largely avoid the fluorescence of pigments (mostly melanin) and other constituents of the insect cuticle.

Cave-dwelling insects, including the two species analyzed herein, are regarded as models for evolution and biogeography, as their reduced aboveground dispersal produces phylogenetic patterns of area distribution that largely matches the geological history of mountain ranges and cave habitats.<sup>20</sup> It should be mentioned that other model organisms have been analyzed using NLM: nematode *Caenorhabditis elegans* (Maupas 1900),<sup>21</sup> as a model in molecular and developmental biologies, and insect *D. melanogaster*<sup>22-24</sup>] as an important model in genetics.

Our results confirm the suitability of two-photon microscopy in entomology as a consequence of high penetration depth, negligible photodamage to the sample, and no need for specimen staining.<sup>25</sup> Measurements and imaging were performed by the homemade NLM with both modalities (TPEF and SHG) enabled.

## 2 Experimental Setup and Procedures

The experimental setup is shown in Fig. 1. We used two femtosecond lasers to generate two-photon excitation fluorescence and second harmonic images. The Ti-sapphire laser (Coherent Mira 900-F), pumped by a 10-W (Coherent Verdi V10) laser at 532 nm, generates 160-fs pulses at a 76-MHz repetition rate within the 700- to 1000-nm tuning range. We also used a 1040-nm Yb KGW femtosecond laser (Time-Bandwidth Products AG, Yb GLX) as the second excitation source. Galvanometer scanning mirrors (Cambridge Technologies, 6215H) were used to raster-scan the samples. The laser beam was expanded in order to fill the entrance pupil of a microscopic objective. A short-pass dichroic mirror (Thorlabs, DMSP805) directs the

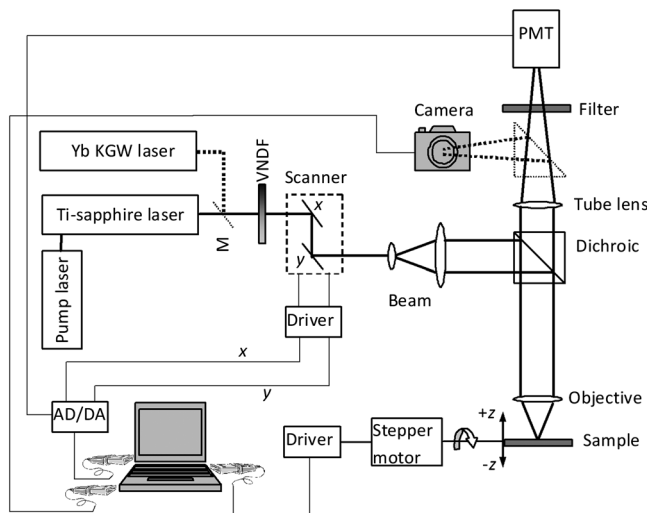


**Fig. 1** Scheme of the nonlinear microscope (NLM) experimental setup. PMT is the photomultiplier tube for two-photon excited autofluorescence (TPEF) and second-harmonic generation (SHG) signal detection and VNDF is the variable neutral-density filter for laser power adjustment, while AD/DA is a digital acquisition card. M is a mirror that can be inserted optionally in order to use 1040-nm laser beam from Yb laser. The laser beam path is drawn with thick lines, while electrical wiring is drawn with hair line style.

laser beam toward the microscopic objective. We were not able to use the full tuning range of the excitation laser due to 805-nm cut-off wavelength of the dichroic mirror. A photomultiplier tube (PMT) (RCA, PF1006) together with an appropriate blocking filter was used for detection of fluorescence and the second harmonic signal. An additional short-pass filter had to be used for the TPEF signal detection in order to reduce the parasitic laser light transmitted through the dichroic mirror. The signal was fed into a 1 MSample/s National Instruments acquisition card (NI USB-6351). The instrument is based on a modified JENAVAL microscopic frame (manufactured by Carl Zeiss). The sample was placed on the existing mechanical stage which was powered by the stepper motor, translating the sample vertically ( $z$ -axis in Fig. 1), with a 0.3- $\mu\text{m}$  resolution. Pixel size,  $z$ -sectioning step, signal-to-noise ratio (SNR), pixel size, and Nyquist criterion fulfillment depended on the sample itself and on a microscopic objective. The removable prism deflected the beam and enabled the capture of bright field images on a Canon EOS 50D digital camera. The control of the whole instrument and image processing was performed by the computer. VolView 3.4, open-source software (by Kitware, Inc.), was used for three-dimensional (3-D) visualization of a set of slices (either using volume rendering or maximum intensity projection algorithms).

We mostly used Carl Zeiss objectives: Planachromat, 40 $\times$ , 0.65 NA (with 815- $\mu\text{m}$  field-of view) and LD LCI Plan-Apochromat 25 $\times$ , 0.8 NA water/glycerin immersion. For large samples, Carl Zeiss Planachromat, 25 $\times$ , 0.5 NA (with 1200- $\mu\text{m}$  field-of-view), was used. The lateral and axial resolutions were measured using fluorescently labeled, nanometer-sized beads (Life Technologies, TetraSpeck<sup>TM</sup> fluorescent microspheres). For the 40 $\times$  microscopic objective, the lateral resolution was 630 nm by 915 nm (due to the excitation laser-beam ellipticity), while the axial resolution was 2100 nm [full-width at half-maximum (FWHM)].

We used a streak camera (Hamamatsu, C4334) coupled with a spectrograph (Princeton Instruments, SpectraPro 2300i) to study short light pulses due to autofluorescence and SHG. OPO-laser (Opotek, Inc., Vibrant 266-I) was used for single-photon excitation.

Chemically purified chitin and two insects (*Plusiocampa christiani* Condé & Bareth, 1996 and *Pheggomisetes ninae* S. Čurčić, Schönmann, Brajković, B. Čurčić & Tomić, 2004) were analyzed. We used commercially available chitin [poly ( $N$ -acetyl-1,4- $\beta$ -D-glucopyranosamine)] extracted from shrimp shells (Sigma Aldrich, practical grade powder) without further purification. It was used to study the intrinsic fluorescent properties and SHG ability of chitin.

Only natural autofluorescence of the insect specimens was detected. We have selected two depigmented, cave-dwelling species in which the fluorescence of other cuticular components is significantly reduced. This guarantees that the fluorescent signal of chitin is dominant, in contrast to other strongly colored insects.

*Plusiocampa christiani* is a cave-dwelling, eyeless, and wingless insect belonging to the family Campodeidae, Diplura order. It is endemic to several caves on Kučajske Planine Mts. in Eastern Serbia.<sup>26</sup> As with a majority of cavernicolous invertebrates, this species is without pigments.<sup>27,28</sup> The insect was kept in 70% ethyl alcohol due to its fragility if left to dry. All microscopic observations were done by immersing the insect into glycerin.

*Pheggomisetes ninae* is a cave-dwelling and blind insect as well, with a pair of coalesced forewings—elytra. Its hind wings are missing. It belongs to the family Carabidae, Coleoptera order. This endemic species inhabits several caves and pits on Mt. Vidlič in Southeastern Serbia.<sup>29</sup> The cuticle of this species is thin as in other troglolitic arthropods, chitinous, almost depigmented, and pale yellow.<sup>30</sup> The genitalia of *P. ninae* males were extracted from the bodies and then kept and observed in glycerin.

Both species prefer wet walls and the floor of caves, where they search for the food, mostly consisting of small invertebrates. They represent typical organisms adapted for life in underground habitats—troglolites. The specimens of both analyzed species are deposited in the collection of the Institute of Zoology, University of Belgrade—Faculty of Biology, Serbia.

### 3 Autofluorescence and Second-Harmonic Generation Properties of Chemically Purified Chitin

The second harmonic generation (SHG) signal of chemically purified chitin was detected using excitation with ultrashort laser pulses at 1040 nm and an 83-MHz repetition rate from Yb-KGW laser. We use a longer wavelength femtosecond laser in order to significantly reduce the two-photon autofluorescence. The detection system consisted of a streak camera coupled with a spectrograph.

The spectrum of chemically purified chitin exhibits a sharp peak at 520 nm—exactly one half of the excitation wavelength [Fig. 2(a)]. We also measured the temporal response of the signal at 520 nm [see Fig. 2(b)]. It is significantly shorter than the lifetime of TPEF (5.2 ns, as will be shown later) and is equal to the detector response time (approximately 260 ps). This additionally confirms the presence of the second harmonic signal. Two consecutive SHG signal pulses are shown, matching the period between excitation pulses (12 ns).

The intensity of TPEF was measured as a function of the laser wavelength (from 830 to 930 nm) and the laser power (from 3.4 to 13.6 mW at the sample). This particular power range was chosen in order to minimize the photodamage of the biological samples. Figure 3(a) shows that the TPEF signal decreases with the laser wavelength, indicating that the excitation maximum is slightly below 830 nm. Our results were not influenced by the possible spectral dependence of the femtosecond pulse length, because the laser excitation pulses are initially relatively long (more than 160 fs) and insensitive to the

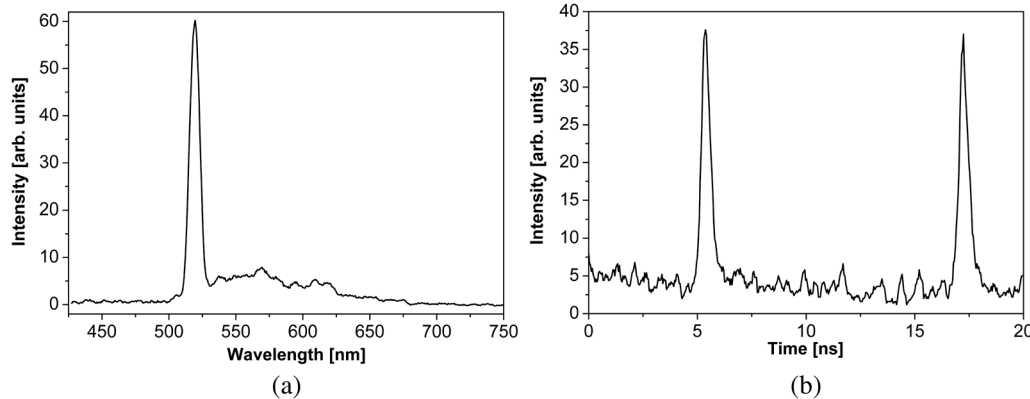


**Fig. 2** (a) Spectral and (b) temporal properties of nonlinear response of chemically purified chitin to the excitation by ultrashort pulses at 1040 nm. Pulse repetition rate is 83 MHz.

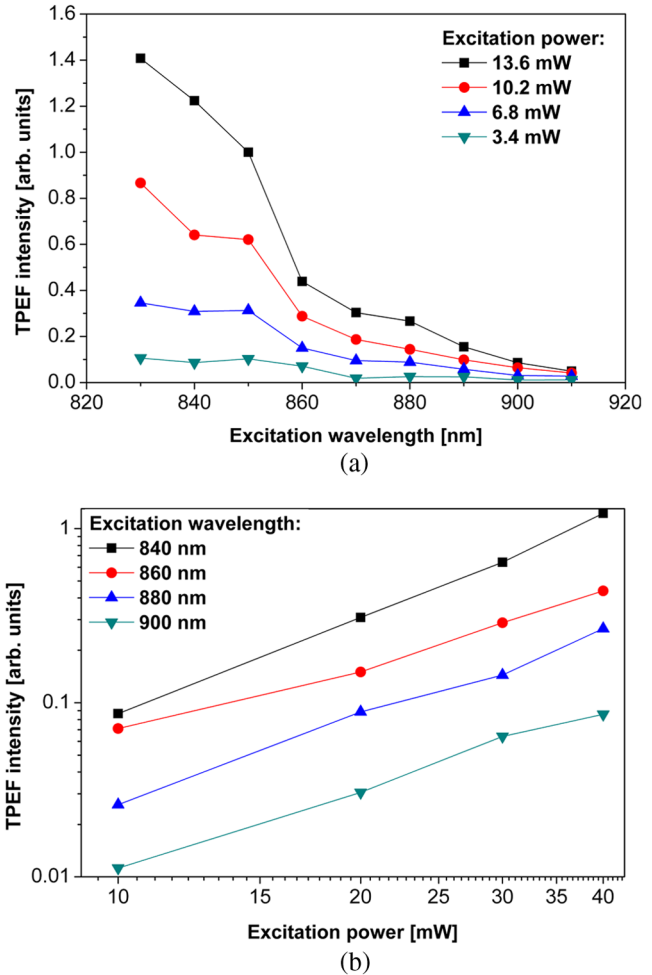


**Fig. 3** Intensity of TPEF of chemically purified chitin as a function of (a) laser wavelength (excitation efficiency) and laser power as a parameter; and (b) excitation power (presented in log-log scale) and the laser wavelength as a parameter.

operating wavelength, according to the manufacturer. We have always tried to maximize the spectral width of the laser at any particular wavelength, ensuring a constant pulse-width. Dispersion broadening of the optical system is constant and negligible (within the operating wavelength range) compared with the initial pulse-width.<sup>31</sup>

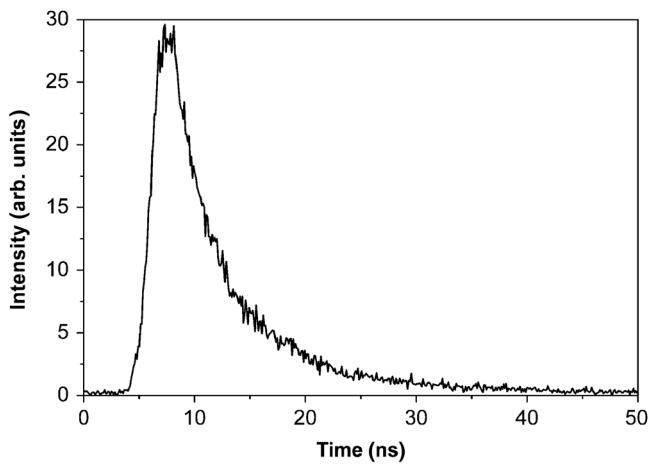


**Fig. 4** Fluorescence time of chemically purified chitin.

The intensity of TPEF as a function of excitation power is shown in Fig. 3(b). In order to emphasize the quadratic dependence, the logarithmic scales are chosen on both axes. The two-photon process is exactly quadratic,<sup>32</sup> but we have found the value of the power coefficient to be  $1.88 \pm 0.05$ . A slight deviation from the pure quadratic dependence can be explained by a relatively weak TPEF signal and averaging of the signal over a relatively large image area. Increased photobleaching at higher excitation intensities can also play a role in the departure from the quadratic dependence.

In order to measure the fluorescence decay time and the spectrum, we used a single-photon excitation with an OPO-laser and a streak camera coupled with a spectrograph. We have found that the fluorescence decay time of purified chitin is 5.2 ns (Fig. 4), while the fluorescence spectrum has a peak emission at 440 nm and a width of approximately 120 nm (FWHM) (Fig. 5).

We have measured the effects of prolonged irradiation of chitin (both chemically purified and insect) and the corresponding bleaching effects. The focused laser beam irradiated a single spot on a purified chitin sample, and the resulting signal was recorded. The laser power was 70 mW and the corresponding power density was  $5.3 \text{ MW/cm}^2$ . The decrease in signal intensity is shown in Fig. 6(a). The bleaching effect can be best observed in Fig. 6(b), where a darkened square remained

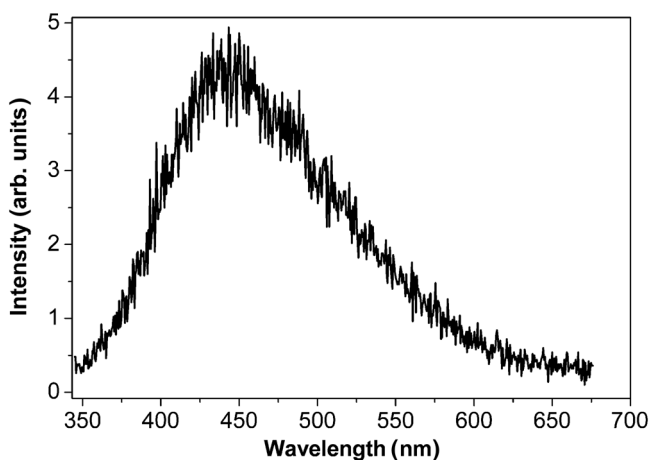


**Fig. 5** Autofluorescence spectrum of chemically purified chitin.

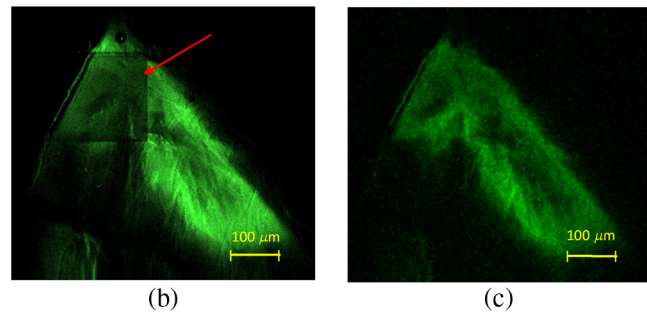
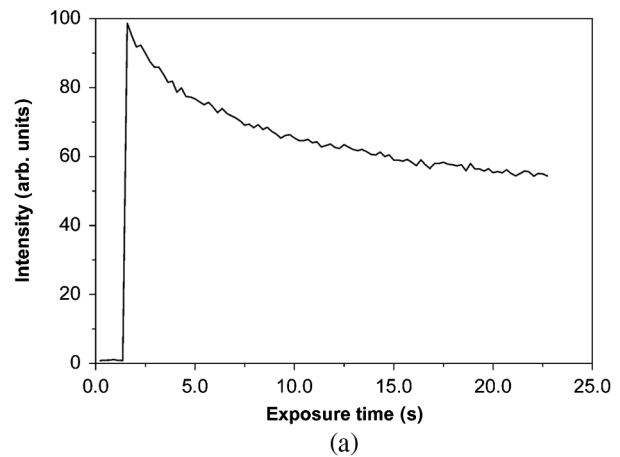


**Fig. 6** (a) Decrease of the TPEF signal due to chemically purified chitin photo-bleaching (at  $5.3 \text{ MW/cm}^2$  power density). (b) TPEF image of a chitin flake. Prolonged scanning of chemically purified chitin sample produces a rectangular region with reduced fluorescence intensity (red arrow). (c) Bleached square is not visible if sample is imaged using the SHG mode. Both images were taken by  $40\times/0.65$  objective.

after scanning at the higher magnification and 840-nm excitation. If observed using the second-harmonic signal (using narrow band detection filter at 420 nm), the square with reduced intensity could not be detected [Fig. 6(c)]. This is evidence that the purified chitin is not damaged—only its internal structure is permanently modified, diminishing autofluorescence. We have to add that, under normal scanning conditions (high-scanning speed and low-irradiation intensity), bleaching effects are minimal and do not obstruct high-quality image acquisition. Above a certain power level, photodisruption (with plasma formation) was observed. It was highly localized and could be used as another imaging modality.

#### 4 Two-Photon Excited Autofluorescence Microscopy of Cave-Dwelling Insects *Plusiocampa christiani* and *Pheggomisetes ninae*

Here, we present an NLM study of the two cave-dwelling insects: wingless *P. christiani* [Fig. 7(a)] and winged *P. ninae* [Fig. 7(b)]. The data on the morphology and anatomy were given in the descriptions.<sup>26,29</sup> The close correspondence of the evolution and geological record confirms cave-dwelling insects as an important study system for historical biogeography and molecular evolution.<sup>20</sup> They are best suited for testing many hypotheses concerning adaptation strategies during colonization of empty places on Earth.<sup>33</sup> These insects are very precious to the natural biodiversity of the world, because single species can

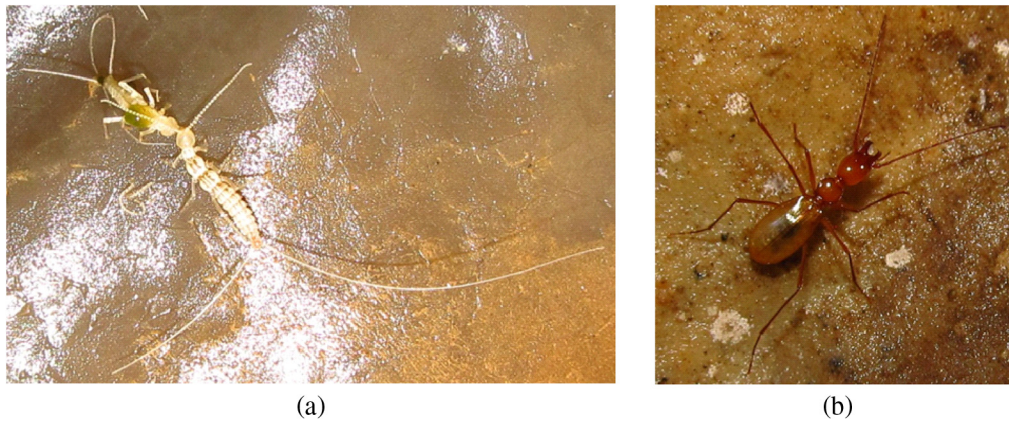


Fig. 7 (a) *Plusiocampa christiani*; and (b) *Pheggomisetes ninae* (photographs by Dragan Antić).

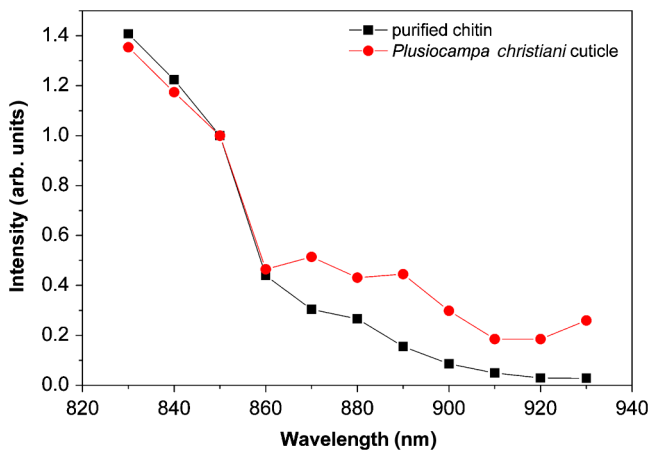


Fig. 8 TPEF spectra of *P. christiani* cuticle and chemically purified chitin.

populate one cave or mountain massif, so the degree of endemism is very high.

*Plusiocampa christiani* was chosen for its characteristic white appearance which is a consequence of the complete absence of pigments.<sup>28</sup> Apart from a certain amount of proteins, the outer nonliving layer of the insect (cuticle) is regarded as a highly chitinized (sclerotized) structure.<sup>34</sup> The autofluorescent signal comes almost exclusively from chitin, unobscured by the fluorescence of other constituents (i.e., pigments, proteins, and minerals) present in the insects living aboveground. This is supported by the comparison of excitation spectra of *P. christiani* cuticle and chemically purified chitin (Fig. 8). It can be seen that both curves have the same behavior between 830 and 860 nm. At longer wavelengths, the autofluorescence of the insect is higher, signifying the presence of other fluorescent materials in the cuticle (most probably proteins).

We demonstrate the importance of autofluorescence NLM in observing insect morphology by presenting the head of

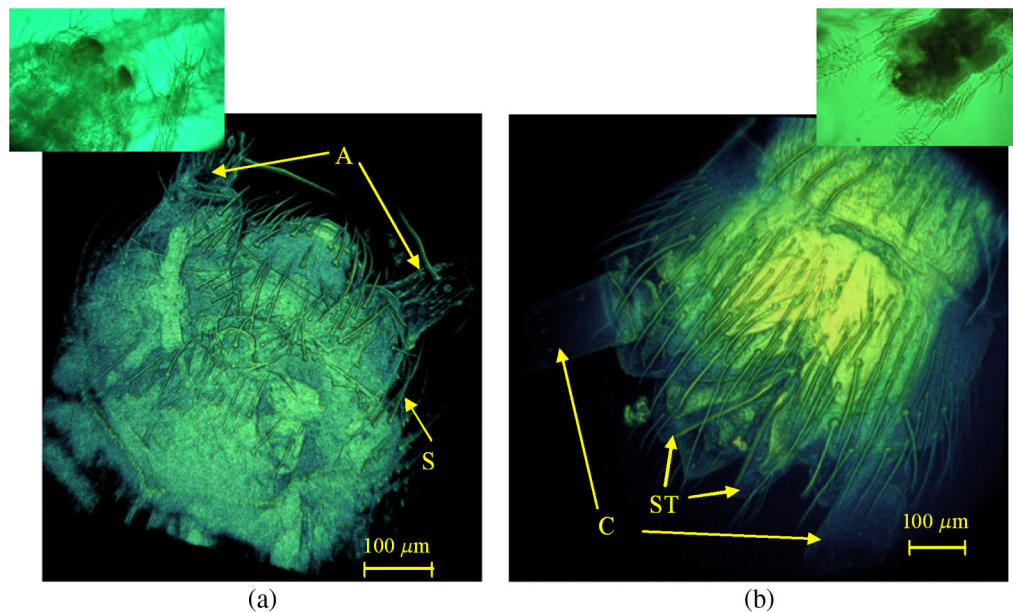
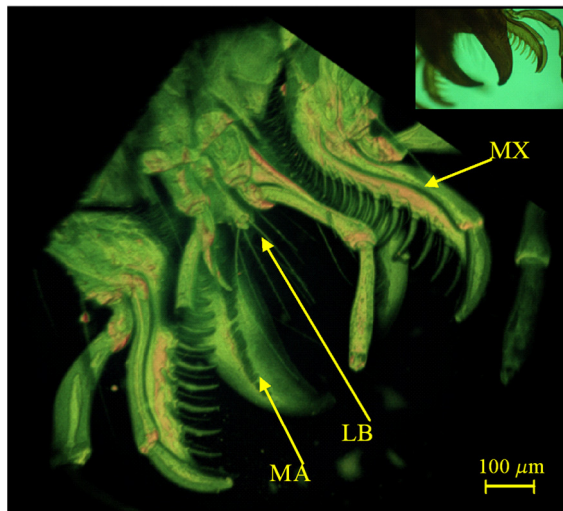


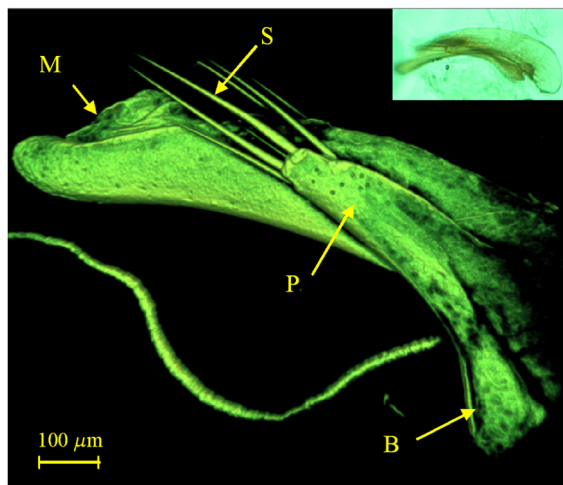
Fig. 9 TPEF images of *P. christiani*: (a) The head in dorsal view (proximal part of the antennae A and setae S). Field width is 654  $\mu\text{m}$ . (b) The posterior part of the abdomen in dorsal view (proximal part of the cerci C and styli ST). Both three-dimensional (3-D) images were obtained using a maximum intensity projection algorithm (from a set of 80 slices). The images were taken by 40 $\times$ /0.65 objective. Bright field microscopic images are in insets.

*P. christiani* in a dorsal view [Fig. 9(a)]. The antennae (seen partially), head sclerites, and sutures can be observed, along with the setation. It is interesting that the mouthparts, situated ventrally, may be seen as well. The laser beam, used to produce a stack of images, had a 12-mW power at the sample. The posterior part of the abdomen of the same insect in the dorsal view is shown in Fig. 9(b). Here, we clearly observe attached paired appendages: multisegmented cerci (seen partially) and shorter styli. The setation and segmentation are well distinguished.

*Pheggomisetes ninae* is slightly pigmented and its autofluorescence certainly has components stemming both from chitin and other cuticular components. Its apical part of the head in the ventral view is shown in Fig. 10(a), where the mouthparts



(a)



(b)

**Fig. 10** Two-photon autofluorescence images of cave-dwelling beetle *P. ninae*: (a) The apical part of the head with mouthparts in ventral view (mandible MA, maxillae MX, and labium LB). The image was taken by 25×/0.5 objective and rendered from a stack of 230 slices using VolView 3.4 (see also accompanying Video 1). (b) The male genitalia in lateral view (median lobe M, parameres P, parameral setae S, and basal bulb B). The image was taken by 40×/0.65 objective and rendered from a stack of 120 slices (see also accompanying Video 2). Bright field microscopic images are in insets. (Video 1, MPEG 7.1 MB) [URL: <http://dx.doi.org/10.1117/1.JBO.20.1.016010.1>]; (Video 2, MPEG 7.1 MB) [URL: <http://dx.doi.org/10.1117/1.JBO.20.1.016010.2>].

(mandibles, maxillae, and labium) are very visible, including the fine surface structure and setation.

Images of male genitalia of *P. ninae* are shown in Fig. 10(b). The features of the insect male copulatory organ (aedeagus) are of a great significance in species determination and are usually presented and imaged in taxonomical studies. We used 25× NA 0.8 water/glycerin immersion objective and 930-nm excitation wavelength. Longer wavelengths were used in order to avoid the autofluorescence of residual tissues that remained after insect dissection. At the same time, it was possible to penetrate deeper into the sample through the chitinous cuticle due to the reduced two-photon absorption of chitin. From the lateral view of *P. ninae* aedeagus, a fine relief can be observed on the surface, a complex teeth-like structure of the copulatory piece is visible, and both the inner sac and strongly sclerotized areas of the aedeagus are recognizable (see longitudinal and cross-sections in Figs. 11(a)–11(d)). All mentioned structures are seen in more detail compared with light or confocal microscopy. All parts of the male copulatory organ are well visible and delimited (median lobe, both parameres with the setae, basal bulb, copulatory piece, and inner sac). The penetration depth can be estimated to 200 μm for the given sample [see the scale bar in Fig. 11(b)].

## 5 Discussion

As shown above, the NLM is a valuable tool for observation of various insect body parts. In the current study, we have chosen cave-dwelling insects in order to separate the fluorescence of chitin from other cuticular components. During experiments, we have investigated a number of other insect species, such as *Apatura ilia* (Denis & Schiffermüller, 1775), *A. iris* (Linnaeus, 1758), and *Pieris rapae* (Linnaeus, 1758) butterflies, and found that each of them produced an autofluorescence signal. Its intensity ranged from good to excellent, depending on the investigated part of the body. The nature of autofluorescence was not always clear, since it depends on the cuticle structure. It is well known that the cuticle is secreted by epidermal cells as thin lamellae or sheets, like sheets of paper stacked on top of each other. The molecules of chitin both from exo- and endo-cuticles of insect integument can be visualized using multiphoton microscopy in the current study. With TPEF microscopy, even some chitinous structures that are lying beneath the integument (e.g., fine structure of the copulatory piece of the aedeagus) can be observed as well [Fig. 11(d)].

We emphasize that NLM is quite a universal tool, and its range of applicability is by no means limited to any particular insect group. We have found that by choosing the appropriate excitation wavelength (840 to 930 nm or 1040 nm), different components of cuticle could be observed with varying penetration depths. Figure 12 shows the image of the inner sac of *P. ninae* aedeagus, imaged using 1040-nm excitation and broadband detection. By comparing Figs. 11(d) and 12, different structures are emphasized at two wavelengths.

The presence of the second-harmonic signal and the SHG imaging of chitinous structures were barely mentioned in Refs. 35 and 36, but without strong experimental confirmation. In our study, the SHG signal of purified chitin was clearly detected (see Sec. 3), but its intensity was low compared with the autofluorescence. In spite of that, the SHG signal was used to image the naturally occurring chitin of insect cuticle, too. As an example, a part of the antenna of *P. christiani* was imaged under SHG and TPEF conditions (Fig. 13). Images were taken

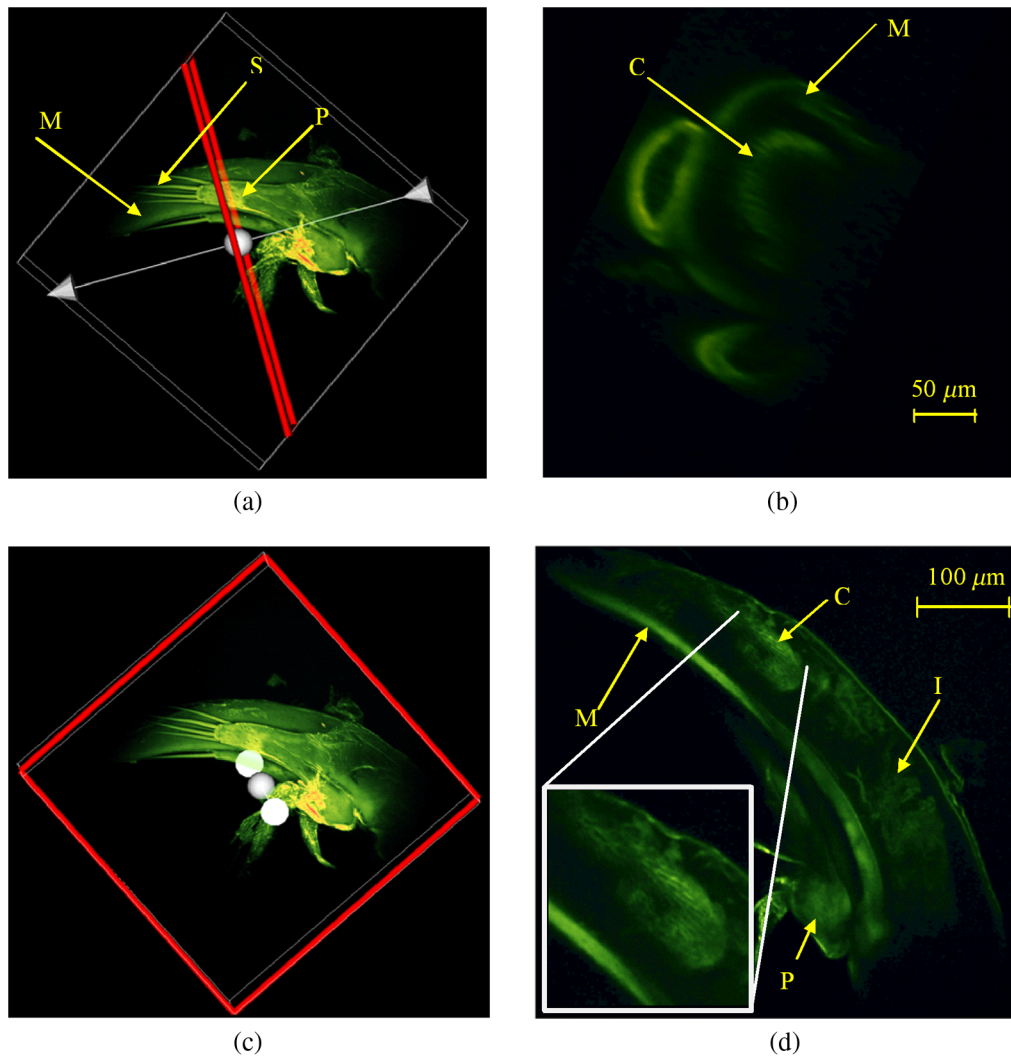


**Fig. 11** TPEF images of cave-dwelling beetle *P. ninae*: (a) The male genitalia with cross-sectional plane (red line), median lobe M, parameres P, and parameral setae S. (b) A corresponding cross-section of the genitalia showing median lobe M and copulatory piece C (yellow arrows). (c) The male genitalia with longitudinal section plane (red square). (d) A corresponding longitudinal section of the male genitalia showing the structure of median lobe M, paramere P, inner sac I, and copulatory piece C (yellow arrows). Inset (white square) in (d) is the enlarged copulatory piece with clearly visible teeth-like structure. The images were taken by 25 $\times$ /0.8 water/glycerin immersion objective.

using 840-nm excitation combined with either broadband [400 to 700 nm, see Fig. 13(a)] or narrowband [420 nm, see Fig. 13(b)] detection filters. From Fig. 13(a), it can be seen that the broadband detection produced fine details of the antenna, while narrow-band SHG conditions produced only an outline. A set of SHG slices was used to construct a 3-D-view of the antenna [Fig. 13(c)]. We emphasize that the SHG signal is much weaker compared with fluorescence which dominates in Fig. 13(a). Therefore, we did not need an additional filter to suppress SHG signal when observing fluorescence.

In order to study the polarization effects, we experimentally confirmed that our detection system is not sensitive to signal polarization. Also, the acquired polarization ellipticity in the excitation arm of the microscope is negligible.

It is well known that the dependence of the detected signal to the polarization state of excitation light may be regarded as a strong indication of the SHG.<sup>37,38</sup> However, we have found that the polarization effects were pronounced both under SHG (840-

nm excitation and 420-nm short-pass filter detection) and TPEF (840-nm excitation and broadband detection—between 400 and 700 nm) conditions. To further investigate this behavior, we fully suppressed the second-harmonic signal, using excitation at 850 nm and narrowband detection at  $450 \pm 5$  nm. Even then, the polarization sensitivity of the TPEF signal to the polarization of the excitation light was clearly seen (see Fig. 14 presenting a part of *P. christiani* antenna recorded at two orthogonal polarization states). We observed that the signal can be significantly altered, and the SNR can be affected by simply rotating the polarization plane. Such behavior is not frequently observed, and it is not clear why this happens. However, according to Refs. 39 and 40, this behavior can be used to discriminate between different features or processes.

In this and similar studies, high-power femtosecond lasers are used. In our case, only a fraction of the available laser power was necessary for NLM of chitinous structures. By simply increasing the laser power (above 20 to 30 mW at the

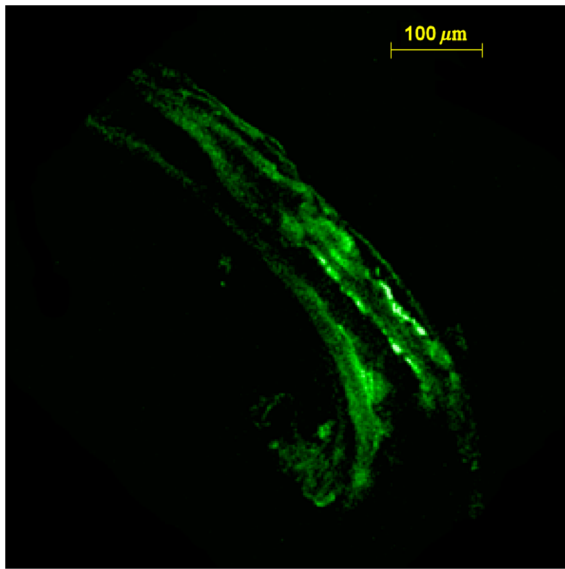


**Fig. 12** Image of the inner sac of *P. ninae* aedeagus obtained upon 1040-nm excitation and broadband detection. Different structures are seen, as compared with Fig. 11(d).

sample), we were able to vaporize certain sections of cuticle and reveal internal, otherwise invisible, structures. This kind of tissue surgery has to be done carefully in order to localize laser-induced damage. This will be the subject of our further investigations.

There are several experimental problems that should be carefully treated when imaging insects. Samples should be kept in a

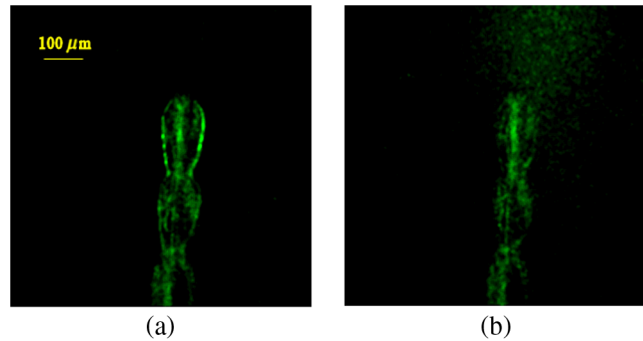


**Fig. 14** The tip of *P. Christiani* antenna recorded at two orthogonal polarization states. (a) Horizontal polarization, (b) vertical polarization of excitation light.

mounting medium which is free of autofluorescence. We found that glycerin is more appropriate than Canada balsam, which has a high level of autofluorescence. In order to increase the penetration depth of the laser light, insects like *P. ninae* were initially soaked in clove oil, which clears the tissues to some degree. We have found no significant autofluorescence of clove oil and we are not aware of altered autofluorescence properties of the sample after the treatment.

In this study, we used only dead insects, but it is possible to work with live specimens, too, as verified in our experiments. If the power density is properly controlled, we have found that the laser radiation is not harmful, even for such sensitive tissues as insect compound eyes. We have observed *in vivo* ommatidia of several insects without the damaging effects of the laser light. This will be the subject of our future research.

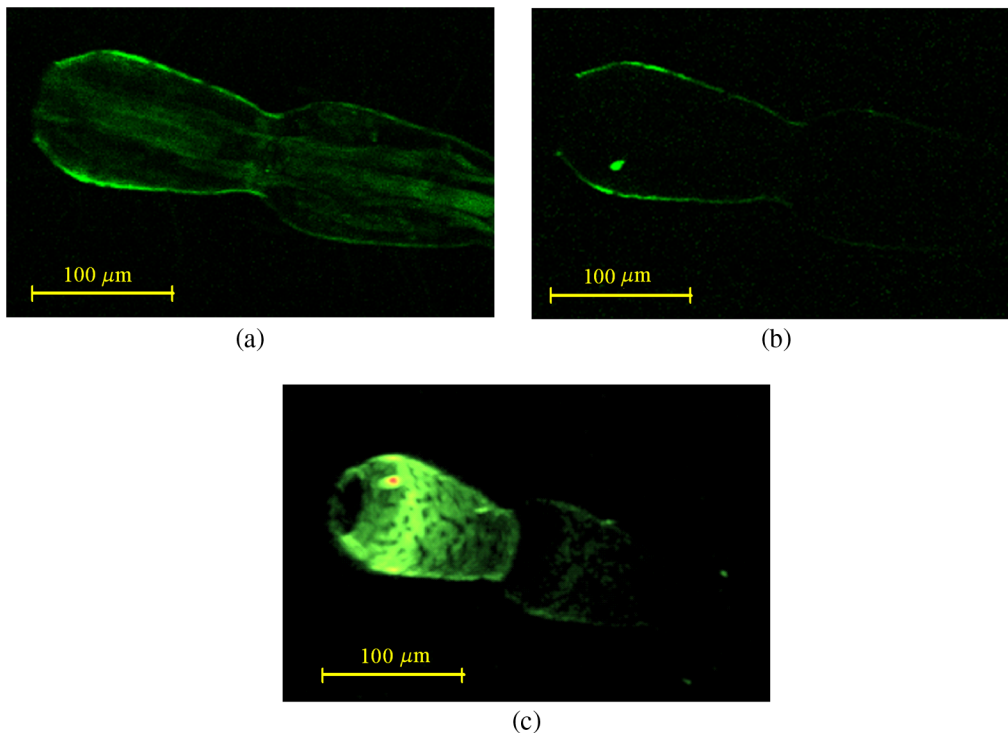


**Fig. 13** The tip of *P. christiani* antenna, recorded by: (a) excitation at 840 nm and broadband detection between 400 and 700 nm (single slice); (b) excitation at 840 nm and narrow-band detection at 420 nm (single slice); and (c) volume rendering of the stack recorded under 840 nm excitation and 420 nm detection conditions.



## 6 Conclusions

We have shown that NLM is an efficient tool to study the morphology and anatomy of chitinous insect structures. It is a powerful technique that does not require tissue staining (as in confocal microscopy) or special tissue clearing methods (e.g., in selective plane illumination microscopy). Biological samples can be observed both *in vivo* and *in vitro*, with high resolution, quickly and without complicated preparation procedures. The autofluorescence spectrum and fluorescence time of chemically purified chitin were measured and the SHG signal was detected. Strong, two-photon excited autofluorescence and weaker SHG signals were used for imaging the insects. Exterior (head and antenna) and interior (male genitalia) body parts of two selected, cave-dwelling, insect species were studied and results were presented. A set of slices was recorded with a penetration depth of up to 200  $\mu\text{m}$ . Many other insect species were analyzed, proving the universal applicability of the technique. We have found that almost any part of the insect body fluoresces. TPEF seems more suited to reflection analysis of whole insects, while SHG is more appropriate to transmission visualization of thin organs and structures like antennas and other appendages. NLM can also be used for dimensional metrology of an insect body and 3-D visualization of the body parts.

Apart from insects, the results of our study are applicable to a wide range of other biological taxa possessing chitin (algae, fungi, mollusks, other arthropods, and so on). Thanks to the high-penetration depth, NLM could enable studying of both morphological (external) and anatomical (internal) structures of a variety of living organisms. Such analyses are possible without any sample destruction or dissecting. The additional advantage of the technique is that either dead or living biological models could be experimentally observed.

## Acknowledgments

The study was financially supported by the Serbian Ministry of Education, Science, and Technological Development (Projects Nos. ON171038, III45016, and ON173038). We also acknowledge FNSNF Scopes project, JRP IZ7370\127942. We are indebted to Mr. Dragan Antić (Institute of Zoology, University of Belgrade—Faculty of Biology, Belgrade, Serbia), who kindly allowed us to include his two photographs in the current paper. We express our gratitude to Dr Dragutin Šević (Institute of Physics, University of Belgrade, Serbia) for his help in establishing fluorescence time and fluorescence spectrum of chemically purified chitin. We thank to the personnel of the Center for Laser Microscopy, University of Belgrade—Faculty of Biology, Belgrade, Serbia and Professor Pavle Andjus for enabling us to use their microscope objectives. Also, we would like to thank George Tserevelakis (Technical University of Munich, Germany and Institute of Electronic Structure and Lasers, Foundation for Research and Technology Hellas, Heraklion, Greece) for useful discussion and advices about the manuscript and the data processing.

## References

- P. T. C. So et al., "Two-photon excitation fluorescence microscopy," *Annu. Rev. Biomed. Eng.* **2**, 399–429 (2000).
- J. L. Capinera, *Encyclopedia of Entomology*, 2nd ed., Springer, Dordrecht (2008).
- J. Michels and S. N. Gorb, "Detailed three-dimensional visualization of resilin in the exoskeleton of arthropods using confocal laser scanning microscopy," *J. Microsc.* **245**, 1–16 (2012).
- H. F. Nijhout, "The developmental physiology of color patterns in Lepidoptera," *Adv. Insect Physiol.* **18**, 181–247 (1985).
- P. B. Koch et al., "Insect pigmentation: activities of  $\beta$ -alanine synthase in wing color patterns of wild-type and melanin mutant swallowtail butterfly *Papilio glaucus*," *Pigm. Cell Res.* **13**(Suppl 8), 54–58 (2000).
- H. Peisker, J. Michels, and S. N. Gorb, "Evidence for a material gradient in the adhesive tarsal setae of the ladybird beetle *Coccinella septempunctata*," *Nat. Commun.* **4**, 1661 (2013).
- G. Cárdenas et al., "Chitin characterization by SEM, FTIR, XRD, and  $^{13}\text{C}$  cross polarization/mass angle spinning NMR," *J. Appl. Polym. Sci.* **93**, 1876–1885 (2004).
- H. L. Leertouwer, B. D. Wilts, and D. G. Stavenga, "Refractive index and dispersion of butterfly chitin and bird keratin measured by polarizing interference microscopy," *Opt. Express* **19**, 24061–24066 (2011).
- B. de Campos Vidal, "Butterfly scale form birefringence related to photonics," *Micron* **42**, 801–807 (2011).
- J. Michels, "Confocal laser scanning microscopy: using cuticular autofluorescence for high resolution morphological imaging in small crustaceans," *J. Microsc.* **227**, 1–7 (2007).
- C.-H. Chien et al., "Label-free imaging of *Drosophila in vivo* by coherent anti-Stokes Raman scattering and two-photon excitation autofluorescence microscopy," *J. Biomed. Opt.* **16**, 016012 (2011).
- D. E. Azofeifa, H. J. Arguedas, and W. E. Vargas, "Optical properties of chitin and chitosan biopolymers with application to structural color analysis," *Opt. Mater.* **35**, 175–183 (2012).
- J. D. Schiffmann and C. L. Schauer, "Solid state physics characterization of  $\alpha$ -chitin from *Vanessa cardui* Linnaeus wings," *Mater. Sci. Eng. C* **29**, 1370–1374 (2009).
- G. Luna-Bárcenas et al., "FEMO modelling of optical properties of natural biopolymers chitin and chitosan," *Phys. Status Solidi (C)* **5**, 3736–3739 (2008).
- K. Kumazawa and H. Tabata, "A three-dimensional fluorescence analysis of the wings of male *Morpho sulkowskyi* and *Papilio xuthus* butterflies," *Zool. Sci.* **18**, 1073–1079 (2001).
- J. M. Gallas and M. Eisner, "Fluorescence of melanin-dependence upon excitation wavelength and concentration," *Photochem. Photobiol.* **45**, 595–600 (1987).
- M. Brydegaard et al., "Insect monitoring with fluorescence lidar techniques: feasibility study," *Appl. Opt.* **48**, 5668–5677 (2009).
- K. Christiansen, "Morphological adaptations," in *Encyclopedia of Caves*, W. B. White and D. C. Culver, Eds., 2nd ed., pp. 517–528, Elsevier, Amsterdam (2012).
- D. C. Culver and T. Pipan, *The Biology of Caves and Other Subterranean Habitats*, Oxford University Press, Oxford (2009).
- I. Ribera et al., "Ancient origin of a Western Mediterranean radiation of subterranean beetles," *BMC Evol. Biol.* **10**, 1–14 (2010).
- G. Filippidis et al., "Imaging of *Caenorhabditis elegans* neurons by second-harmonic generation and two-photon excitation fluorescence," *J. Biomed. Opt.* **10**, 024015 (2005).
- W. Supatto et al., "In vivo modulation of morphogenetic movements in *Drosophila* embryos with femtosecond laser pulses," *Proc. Natl. Acad. Sci. U. S. A.* **102**, 1047–1052 (2005).
- D. Debarre et al., "Imaging lipid bodies in cells and tissues using third-harmonic generation microscopy," *Nat. Methods* **3**, 47–53 (2006).
- C. Y. Lin et al., "Label-free imaging of *Drosophila* larva by multiphoton autofluorescence and second harmonic generation microscopy," *J. Biomed. Opt.* **13**, 050502 (2008).
- J.-A. Conchello and J. W. Lichtman, "Optical sectioning microscopy," *Nat. Methods* **2**, 920–931 (2005).
- B. Condé and C. Bareth, "Une évolution de *Stygiocampa*, sous-genre troglomorpe de *Plusiocampa* (Diplura Campodeidae), avec la description d'une nouvelle espèce de Serbie orientale," *Rev. Suisse Zool.* **103**, 369–381 (1996).
- J. Pages, "Remarks on the Japygidae (Insecta, Diplura) reported for the underground environment," *Int. J. Speleol.* **1**, 192–201 (1964).
- A. I. Camacho, *The Natural History of Biospeleology*, Monografias del Museo nacional de ciencias naturales, Consejo superior de investigaciones científicas, Madrid (1992).
- S. B. Čurčić et al., "On a new cave-dwelling beetle (Trechinae, Carabidae) from Serbia," *Arch. Biol. Sci.* **56**, 109–113 (2004).

30. M. Moseley, "Observations on the cave-associated beetles (Coleoptera) of Nova Scotia, Canada," *Int. J. Speleol.* **38**, 163–172 (2009).
31. J. B. Guild, C. Xu, and W. W. Webb, "Measurement of group delay dispersion of high numerical aperture objective lenses using two-photon excited fluorescence," *Appl. Opt.* **36**, 397–401 (1997).
32. W. Denk, J. H. Strickler, and W. W. Webb, "Two-photon laser scanning fluorescence microscopy," *Science* **248**, 73–76 (1990).
33. O. T. Moldovan, "Beetles," in *Encyclopedia of Caves*, W. B. White and D. C. Culver, Eds., 2nd ed., pp. 54–62, Elsevier, Amsterdam (2012).
34. P. J. Gullan and P. S. Cranston, *The Insects: An Outline of Entomology*, John Wiley & Sons, New York (2009).
35. B. Nie et al., "Multimodal microscopy with sub-30 fs Yb fiber laser oscillator," *Biomed. Opt. Express* **3**, 1750–1756 (2012).
36. E. J. Gualda et al., "In vivo imaging of anatomical features of the nematode *Caenorhabditis elegans* using non-linear (TPEF-SHG-THG) microscopy," *Proc. SPIE* **6630**, 663003 (2007).
37. R. Carriles et al., "Imaging techniques for harmonic and multiphoton absorption fluorescence microscopy," *Rev. Sci. Instrum.* **80**, 081101 (2009).
38. C. K. Chou et al., "Polarization ellipticity compensation in polarization second-harmonic generation microscopy without specimen rotation," *J. Biomed. Opt.* **13**, 014005 (2008).
39. T. Parasassi et al., "Two-photon microscopy of aorta fibers shows proteolysis induced by LDL hydroperoxides," *Free Radical Biol. Med.* **28**, 1589–1597 (2000).
40. Q. Yua and A. A. Heikal, "Two-photon autofluorescence dynamics imaging reveals sensitivity of intracellular NADH concentration and conformation to cell physiology at the single-cell level," *J. Photochem. Photobiol., B* **95**, 46–57 (2009).

**Mihailo D. Rabasović** is a research associate at the Institute of Physics, University of Belgrade, Serbia. He received his PhD degree in physics from the Physics Department of the University of Belgrade in 2007. His current research interests include photoacoustics, microscopy, and correlation spectroscopy.

**Dejan V. Pantelić** is a senior researcher at the Institute of Physics, University of Belgrade, Serbia. He received his PhD degree in optics from the Physics Department of the University of Belgrade in 1990. His current research interests include biophotonics, microscopy, and holography. He is a member of OSA.

**Branislav M. Jelenković** is a research professor at the Institute of Physics, University of Belgrade, Serbia. He received his PhD degree in atomic physics in 1983. His current research interests include laser

spectroscopy, quantum and nonlinear optics, and biophysics. He is current president of optical society of Serbia and the member of OSA.

**Srećko B. Čurčić** is an associate professor at the Institute of Zoology, University of Belgrade—Faculty of Biology, Serbia. He received his PhD degree in morphology, systematics, and phylogeny of animals from the Institute of Zoology, University of Belgrade—Faculty of Biology, in 2005. His current research interests include morphology, systematics, taxonomy, phylogeny, development and ecology of the Coleoptera order (Insecta), diversity and faunistics of both soil- and cave-dwelling invertebrates, and defensive secretion in ground beetles. He is a member of numerous scientific societies.

**Maja S. Rabasović** is a research associate at the Institute of Physics, Belgrade, Serbia. She received her PhD degree from the Physics Department of the University of Belgrade, in 2013. Her current research interests include electron atom collision processes, laser-induced fluorescence, and laser-induced breakdown spectroscopy.

**Maja D. Vrbica** is a research assistant at the Institute of Zoology, University of Belgrade—faculty of biology, Serbia. Her current research interests include morphology, taxonomy, systematic, and phylogeny of some ground beetles (Insecta, Coleoptera).

**Vladimir M. Lazović** is a research assistant at the Institute of Physics, University of Belgrade, Serbia. His research interests include electron microscopy, nonlinear microscopy, optics, and lasers.

**Božidar P. M. Čurčić** is a full professor at the Institute of Zoology, University of Belgrade—Faculty of Biology, Serbia. He received his PhD degree in morphology, systematics, phylogeny, and development of animals from the Department of Zoology, University of Belgrade—Faculty of Science, in 1976. His current research interests include morphology, systematics, taxonomy, phylogeny, and developmental biology of Arthropoda. He is the corresponding member of Bulgarian Academy of Sciences, member or fellow of 25 international societies, and president of MAB UNESCO Serbia.

**Aleksandar J. Krmpot** is a research associate at the Institute of Physics, University Belgrade, Serbia, and guest researcher at the Karolinska Institute, Stockholm, Sweden. He received his PhD degree in physics (quantum optics) from the Physics Department of the University of Belgrade. His current research interests are coherent laser spectroscopy and quantum optics, nonlinear microscopy, and correlation spectroscopy.



# The influence of oxygen vacancy concentration in nanodispersed non-stoichiometric $\text{CeO}_{2-\delta}$ oxides on the physico-chemical properties of conducting polyaniline/ $\text{CeO}_2$ composites

Bojana Kuzmanović<sup>a</sup>, Milica J. Vujković<sup>b,\*</sup>, Nataša Tomić<sup>c</sup>, Danica Bajuk-Bogdanović<sup>b</sup>, Vladimir Lazović<sup>c</sup>, Biljana Šljukić<sup>b</sup>, Nenad Ivanović<sup>a</sup>, Slavko Mentus<sup>b,d</sup>

<sup>a</sup> Institute of Nuclear Sciences “Vinča”, Mike Petrovića Alasa 12-14, 11001, Belgrade, University of Belgrade, Serbia

<sup>b</sup> Faculty of Physical Chemistry, University of Belgrade, Studentski trg 12-16, 11158, Belgrade, Serbia

<sup>c</sup> Institute of Physics Belgrade, University of Belgrade, Pregrevica 118, 11080, Belgrade, Serbia

<sup>d</sup> Serbian Academy of Sciences and Arts, Knez Mihajlova 35, 11000, Belgrade, Serbia

## ARTICLE INFO

### Article history:

Received 26 December 2018

Received in revised form

21 February 2019

Accepted 19 March 2019

Available online 22 March 2019

### Keywords:

Polyaniline

Oxygen deficient cerium oxide

PANI- $\text{CeO}_{2-\delta}$  interaction

Supercapacitors

## ABSTRACT

Cerium oxide ( $\text{CeO}_{2-\delta}$ ) ultrafine nanoparticles, with the lower ( $\text{CeO}_{2-\delta}$ -HT) and higher ( $\text{CeO}_{2-\delta}$ -SS) fraction of oxygen vacancies, were used as anchoring sites for the polymerization of aniline in acidic medium. As a result, polyaniline-emeraldine salt (PANI-ES)-based composites (PANI-ES@ $\text{CeO}_{2-\delta}$ -HT and PANI-ES@ $\text{CeO}_{2-\delta}$ -SS) were obtained. The interaction between  $\text{CeO}_{2-\delta}$  and PANI was examined by FTIR and Raman spectroscopy. The PANI polymerization is initiated via electrostatic interaction of anilinium cation and  $\text{Cl}^-$  ions (adsorbed at the protonated hydroxyl groups of  $\text{CeO}_{2-\delta}$ ), and proceeds with hydrogen and nitrogen interaction with oxide nanoparticles. Tailoring the oxygen vacancy population of oxide offers the possibility to control the type of PANI-cerium oxide interaction, and consequently structural, electrical, thermal, electronic and charge storage properties of composite. A high capacitance of synthesized materials, reaching  $\sim 294 \text{ F g}^{-1}$  (PANI-ES),  $\sim 299 \text{ F g}^{-1}$  (PANI-ES@ $\text{CeO}_{2-\delta}$ -HT) and  $\sim 314 \text{ F g}^{-1}$  (PANI-ES@ $\text{CeO}_{2-\delta}$ -SS), was measured in 1 M HCl, at a common scan rate of  $20 \text{ mV s}^{-1}$ . The high adhesion of PANI with cerium oxide prevents the oxide from its slow dissolution in 1M HCl thus providing the stability of this composite in an acidic solution. The rate of electrochemical oxidation of emeraldine salt into perigraniline was also found to depend on  $\text{CeO}_{2-\delta}$  characteristics.

© 2019 Elsevier Ltd. All rights reserved.

## 1. Introduction

The linkage of diverse metal oxides ( $\text{TiO}_2$ ,  $\text{CeO}_2$ ,  $\text{ZnO}$ , graphene oxide,  $\text{SiO}_2$ ,  $\text{Fe}_x\text{O}_y$ ,  $\text{MnO}_2$  ...) with one of the oldest conducting polymers such as polyaniline (PANI) has been shown as an effective strategy for improving mechanical, thermal, dielectric, electrical and optical properties of this polymer [1–5]. An easy synthesis, environmental stability, and fast doping/dedoping process, make PANI very suitable matrix for the facile further fabrication. On the other hand, inorganic oxides easily interact with PANI chains, resulting in the synergistic behaviour. The versatile properties of these hybrid materials, achieved either through the different

degree of PANI's protonation or different oxide structures (obtained through numerous synthesis procedures), make their study inexhaustable.

While the investigations of composites with  $\text{TiO}_2$  were quite diverse and numerous, the studies on PANI/ $\text{CeO}_2$  nano-composites have mostly directed to the development of sensor technology including  $\text{H}_2\text{O}_2$  sensors, humidity sensors, biosensors, gas sensing materials [6–11]. The positive influence of  $\text{CeO}_2$  particles, incorporated into PANI chains, has been recognized in many sensor properties. Besides, the binding of cerium oxide with the polyaniline was found to improve thermal [12,13], corrosion protection [14] and electrochemical properties [15–17]. Still, the studies regarding the Ce-oxide's influence to the charge storage properties of polyaniline are quite rare. Recently, Fei et al. [17] showed that an indirect chemical bonding of PANI to  $\text{CeO}_2$  surface via its  $-\text{OH}$  and  $-\text{NCO}$  functionalized groups improves both electrocatalytic and capacitive performance of PANI. By mixing  $\text{CeO}_2$  with 10% of PANI,

\* Corresponding author. University of Belgrade, Faculty of Physical Chemistry, Studentski trg 12–14, 11158, Belgrade, Serbia.

E-mail address: [milica.vujkovic@ffh.bg.ac.rs](mailto:milica.vujkovic@ffh.bg.ac.rs) (M.J. Vujković).

Maheswari et al. [15] have significantly improved charge storage properties of oxide in HCl, from a very high value of  $927 \text{ F g}^{-1}$  (for pure oxide) to the extremely high one amounting to  $1452 \text{ F g}^{-1}$  for the  $\text{CeO}_2/\text{PANI}$  composite. Also, Gong et al. [16], have recently prepared nickel doped cerium oxide nanospheres at PANI ( $\text{Ni-CeO}_2@\text{PANI}$ ) as an electrode material for supercapacitors, which provided a very high capacitance of  $894 \text{ F g}^{-1}$  (at  $1 \text{ A g}^{-1}$ ), thanks to the defective nature of  $\text{Ni-CeO}_2$ . The excess of reactive oxygen vacancies was achieved by doping  $\text{CeO}_2$  with nickel atoms, whereas the  $\text{Ni-CeO}_2@\text{PANI}$  nanocomposite was prepared by in situ chemical oxidative polymerization of aniline in presence of  $\text{Ni-CeO}_2$  particles. Herein, polyaniline-cerium oxide composites have been synthesized by typical chemical polymerization of aniline (under highly acidic conditions), adsorbed on the surface of cerium-oxide nanoparticles, in order to examine its charge storage ability. The idea was to use the two types of  $\text{CeO}_{2-\delta}$ , containing different fraction of oxygen vacancies (without metal doping), in order to compare how the O-vacancy population influences the PANI- $\text{CeO}_2$  interaction. The oxide's particles were synthesized by two different methods: i) the solid-state method, yielding cerium-oxide with higher concentration of oxygen vacancies and ii) the hydrothermal method yielding oxide with lower concentration of oxygen vacancies. The influence of vacancy concentration of  $\text{CeO}_{2-\delta}$  oxides, in their composites with highly conductive emeraldine form of PANI, on the thermal, vibrational and electrochemical properties of composites, was thoroughly examined. The mechanism of PANI- $\text{CeO}_{2-\delta}$  interaction is proposed and discussed.

## 2. Experimental

### 2.1. Synthesis procedure

#### 2.1.1. Synthesis of polyaniline emeraldine salt

Polyaniline, in the form of emeraldine salt (PANI-ES), was synthesized by typical chemical polymerization of aniline (Sigma Aldrich) in the presence of hydrochloric acid using ammonium persulfate (Sigma Aldrich) as an oxidant [18]. Briefly, 0.18 mL of two times distilled aniline monomer was injected into 7 mL of 2 M HCl solution. 0.45 g  $(\text{NH}_4)_2\text{SO}_4$  (previously dissolved in 2 mL of deionized water) was dropped to the solution and stirred magnetically at  $25^\circ\text{C}$ . After filtration, the precipitate was washed (with 2 M HCl and deionized water followed by ethanol) and dried at  $60^\circ\text{C}$  in the oven for 36 h.

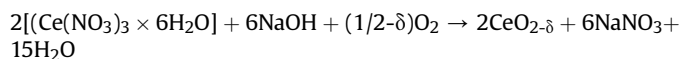
#### 2.1.2. Hydrothermally synthesis of $\text{CeO}_{2-\delta}$

The  $\text{CeO}_{2-\delta}$  nanoparticles with a lower amount of oxygen vacancies were prepared by the hydrothermal treatment ( $\text{CeO}_{2-\delta}\text{-HT}$ ), according to the procedure presented in Ref. [19]. In a typical synthesis, 2 g of polyvinylpyrrolidone (Sigma Aldrich) was dissolved in 40 mL of deionized water, continuously stirring on a magnetic stirrer (at room temperature  $T \approx 25^\circ\text{C}$ ) until a homogeneous solution was obtained. 6 mmol of  $\text{Ce}(\text{NO}_3)_3 \cdot 6\text{H}_2\text{O}$  (Acros Organics 99.5%), previously dissolved in deionized water  $V = 40 \text{ mL}$ , was slowly added to the resulting solution, with constant stirring. During the synthesis, the pH of the solution was not adjusted and value was  $\text{pH} \approx 4$ . The prepared solution was put into a Teflon-lined stainless steel autoclave (capacity  $\sim 80 \text{ mL}$ ), and hydrothermally treated at  $200^\circ\text{C}$  for 6 h. After synthesis, the autoclave was cooled down to room temperature naturally. The resulting precipitate was collected and washed several times with distilled water, and afterwards dried in a vacuum oven overnight at  $105.5^\circ\text{C}$ .

#### 2.1.3. Solid state synthesis of $\text{CeO}_{2-\delta}$

Solid-state reaction at room temperature was used for the

synthesis  $\text{CeO}_{2-\delta}$  ultrafine particles with a higher amount of oxygen vacancies [20,21]. Cerium nitrate hexahydrate (Acros Organics 99.5%) and sodium hydroxide (Carlo Erba) were used as starting materials for this procedure. Synthesis involves manual mixing of the starting chemicals in mortar ( $\sim 10 \text{ min}$ ) until the mixture becomes light brown. After exposure to the air (4 h), the sample was washed four times with distilled water and twice with ethanol to remove  $\text{NaNO}_3$ . The final product was transferred into petri dish using ethanol and dried at  $60^\circ\text{C}$  in a drying oven overnight. The final result of the synthesis obtained is a light yellow powder  $\text{CeO}_{2-\delta}$ .



#### 2.1.4. PANI@ $\text{CeO}_{2-\delta}$ synthesis procedure

The PANI@ $\text{CeO}_{2-\delta}$  composites were prepared in the same way as PANI-ES, in presence of cerium oxide. Namely, 0.18 mL of distilled aniline monomer was injected into an aqueous solution of 2 M HCl, containing 50 mg of  $\text{CeO}_{2-\delta}\text{-SS}$  or  $\text{CeO}_{2-\delta}\text{-HT}$  ultrafine nanoparticles. The acidic solutions of cerium-oxide nanoparticles were previously treated by ultrasound to prevent aggregation of nano- $\text{CeO}_2$  particles. The oxidizing agent  $(\text{NH}_4)_2\text{S}_2\text{O}_8$  (0.45 g), previously dissolved in 2 mL deionized water, was added to the solutions drop by drop. After mixing the solution for 6 h on a magnetic stirrer, at room temperature, the samples were filtered and washed. Afterwards, the obtained dark-green PANI@ $\text{CeO}_{2-\delta}$  composites, labelled as PANI-ES@ $\text{CeO}_{2-\delta}\text{-SS}$  and PANI-ES@ $\text{CeO}_{2-\delta}\text{-HT}$ , were dried in the oven at  $60^\circ$  for 36 h to achieve the constant weight.

For the sake of comparison, the similar experiments using 100 mg of  $\text{CeO}_{2-\delta}\text{-SS}$  and 9 mg, 50 mg and 100 mg of  $\text{TiO}_2$  anatase (Sigma Aldrich) were also performed.

### 2.2. Characterization

The obtained powdered samples were pressed into pellets and their conductivity was measured between two stainless pistons using an ac bridge (Wayne Kerr Universal Bridge B 224) at 1.0 kHz, at room temperature and pressure of 375 MPa.

Thermogravimetric and differential thermal analysis (TG/DTA) were carried out simultaneously by an SDT 2960 Simultaneous DSC-TGA thermal analyzer, in air atmosphere with a flowing rate of  $10 \text{ C min}^{-1}$ .

The morphology of synthesized samples was observed by field-emission scanning electron microscope (FESEM, Tescan MIRA3). PANI-based samples were clearly visible as such, while cerium oxide sample required vacuum decoration by gold.

The Raman spectra of samples were recorded on a DXR Raman microscope (Thermo Scientific) equipped with a research optical microscope and a CCD detector. A HeNe gas laser with an excitation wavelength of 633 nm was used for all measurements. The scattered light was analyzed by the spectrograph with a grating of 600 lines  $\text{mm}^{-1}$  and a spectrograph aperture of  $50 \mu\text{m}$  slit. The laser power was kept at 0.5 mW on the sample. Each spectrum was measured with an exposure time of 30 s and number of exposures of 20.

The Infrared transmission spectra (FTIR) of the samples in the form of pellets with KBr, were recorded using an Avatar System 370 spectrometer (Thermo Nicolet), with 64 scans per sample and  $2 \text{ cm}^{-1}$  resolution in the wavenumber range  $4000\text{--}400 \text{ cm}^{-1}$ .

### 2.3. Electrochemical measurements

Electrochemical measurements of examined samples were performed at Gamry PCI4/300 Potentiostat/Galvanostat, in the

typical three-electrode configuration. The reference electrode was a saturated calomel electrode (SCE), while the counter electrode was a wide Platinum foil (Pt). To prepare the working electrode the examined powder was mixed with the 5 wt% Nafion binder (Sigma Aldrich) in ethanol/water, in the 95:5 ratio. Several drops of ethanol were added in order to obtain the desired viscosity. After homogenization in an ultrasonic bath, the slurry was deposited over the rectangular glassy carbon support and dried at ambient temperature in order for ethanol to evaporate. The loading mass was  $1.7 \text{ mg cm}^{-2}$  for all examined electrodes. The electrolyte was  $1 \text{ mol dm}^{-3}$  HCl aqueous solution.

### 3. Results and discussion

#### 3.1. Conductivity measurements

The synthesized PANI-ES delivers a high value of electronic conductivity, amounting to  $\sim 0.6 \text{ S/cm}$ . The incorporation of semi-conducting cerium-oxide, into polymer matrix, decreases the conductivity to  $\sim 0.5 \text{ S/cm}$  and  $\sim 0.3 \text{ S/cm}$  for PANI-ES@CeO<sub>2- $\delta$</sub> -SS and PANI-ES@CeO<sub>2- $\delta$</sub> -HT, respectively.

#### 3.2. Thermal behavior

Thermal behavior of prepared samples was examined by simultaneous thermogravimetric/differential thermal analysis (TGA/DTA), in the temperature range 25–700 °C, under air atmosphere. The characteristic thermogram of conducting polymer [22], made of three separated weight loss steps, is observed (Fig. 1a). The first weight loss (about 7%) up to 100 °C, originates from desorption of adsorbed water molecules, while the second weight loss between 180 and 300 °C (about 13%) can be attributed to the elimination of protonating acid dopant (HCl) bound to the polymer chain. The third and the greatest weight loss (about 80% for pure PANI), within the temperature range 300–700 °C, corresponds to the structural degradation of the polymer backbone [22]. One can notice that both composites, unlike the pure PANI, did not lose the whole weight at 700 °C, but  $\sim 96.3\%$  (PANI-ES@CeO<sub>2- $\delta$</sub> -SS) and  $\sim 95.8\%$  (PANI-ES@CeO<sub>2- $\delta$</sub> -HT) of its initial weight. It is due to a high thermal stability of inorganic cerium oxide. Based on this, the fraction of cerium-oxide in the composite could be determined and, relative to the mass of dried sample (taking into account the amount of adsorbed water), was found to be  $\sim 4\%$  (PANI-ES@CeO<sub>2- $\delta$</sub> -SS) and  $4.5\%$  (PANI-ES@CeO<sub>2- $\delta$</sub> -HT). Somewhat higher content of hydrothermally synthesized oxide in the composite was obtained. This is in the correlation with the higher concentration of Ce<sup>4+</sup> ions i.e. higher fraction of oxygen atoms in the CeO<sub>2- $\delta$</sub> -HT crystal lattice.

It can be seen that weight loss of samples, up to 300 °C (removal of water molecules and dopant), is insensitive to the presence of oxide (it is governed by the type of dopant). However, above  $\sim 300$  °C, there are differences in the thermal decomposition of the polymer chain in examined samples, which are more visible in corresponding DTA curves (Fig. 1b). As our DTA curves show, two exothermic peaks follow the process of ES degradation within the temperature region 300–700 °C. The position of the first DTA peak (appearing at 384 °C) is the same for PANI-ES and PANI-ES@CeO<sub>2- $\delta$</sub> -SS, while its values for PANI-ES@CeO<sub>2- $\delta$</sub> -HT is slightly shifted towards higher temperature (393 °C). The second DTA peak, higher in the intensity, appears at  $\sim 489$  °C (PANI-ES),  $499$  °C (PANI-ES@CeO<sub>2- $\delta$</sub> -SS),  $512$  °C (PANI-ES@CeO<sub>2- $\delta$</sub> -HT). It can be concluded that the thermal resistance of PANI becomes higher by its binding with the cerium-oxide, especially when the chains grew on hydrothermally prepared oxide. This originates from its strong interaction with the oxide. The improved thermal stability of PANI in interaction with metal oxides has been already reported [12,13,17], but the opposite

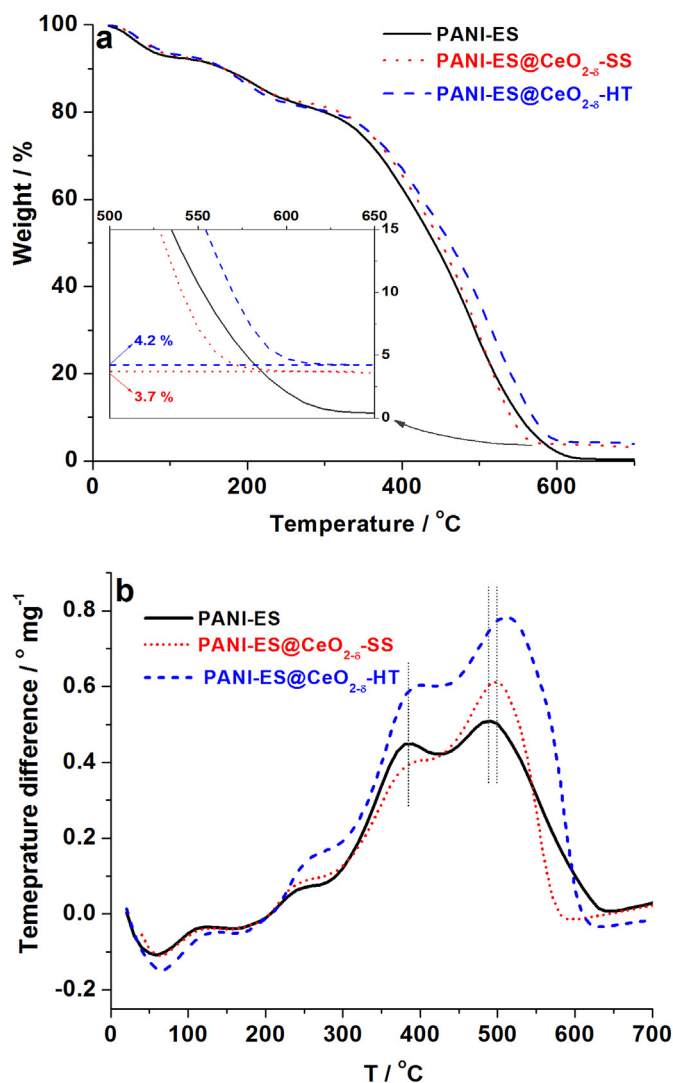
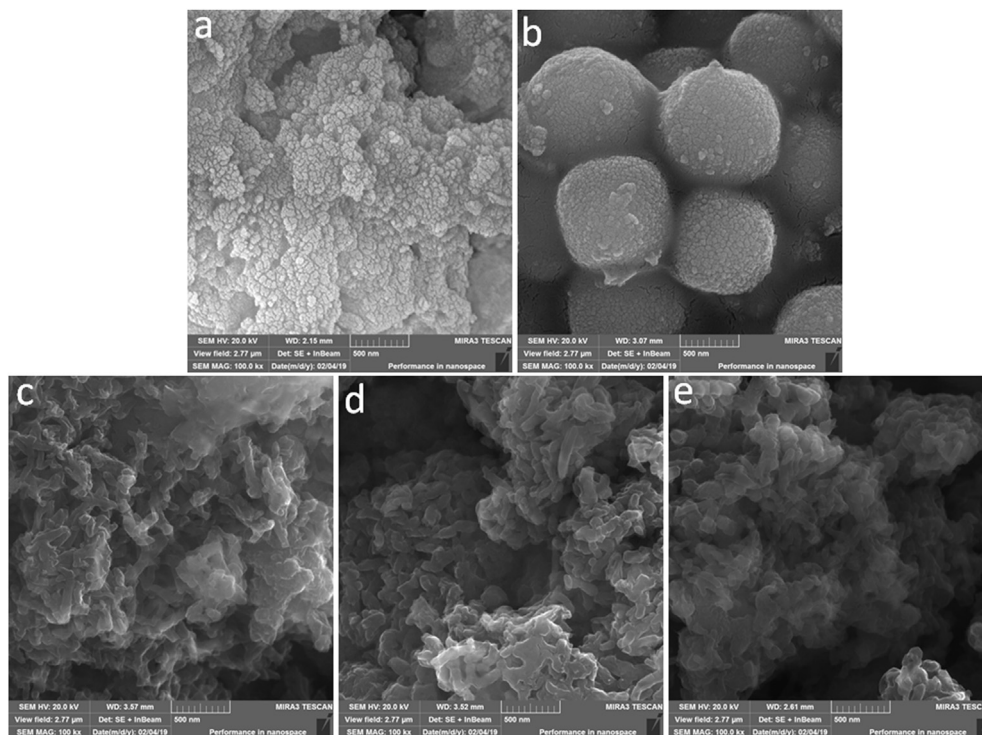


Fig. 1. TG (a) and DTA (b) curves of PANI-ES and PANI-ES@CeO<sub>2- $\delta$</sub>  samples.

behavior [17] was also found. These variations can be explained in the different interactions of cerium oxide with polyaniline chains, which can be influenced by the synthesis of oxide, the type of PANI dopant and the doping level. Here, higher thermal stability of PANI was obtained for the composite containing CeO<sub>2- $\delta$</sub>  with the lower fraction of oxygen vacancies. Furthermore, the declining slope of the PANI@CeO<sub>2- $\delta$</sub>  DTA curves is steeper than that of PANI-ES, which suggests that the cerium oxide acts as a catalyst of the combustion process of carbon, formed by the thermal decomposition of polymer.

#### 3.3. Morphology

Ultrafine nanoparticles of CeO<sub>2- $\delta$</sub> -HT and CeO<sub>2- $\delta$</sub> -SS are shown in Fig. 2a and b. Nanodispersed, nearly spherical particles, 20–40 nm in diameter, prevail on the CeO<sub>2- $\delta$</sub> -SS surface (Fig. 2a) while the CeO<sub>2- $\delta$</sub> -HT sample is composed of monodispersed spherical particles, 0.7–1.1  $\mu\text{m}$  in diameter (Fig. 2b). Interestingly, these sub-micron/micron CeO<sub>2- $\delta$</sub> -HT spheres are huge agglomerates of nanoparticles 20–40 nm in diameter, which are similar to CeO<sub>2- $\delta$</sub> -SS particles. Representative FE-SEM micrograph of PANI-ES sample shows that the short nanofibers ( $\sim 75$  nm in diameter) can be perceived (Fig. 2c). The FE-SEM micrographs of PANI-ES@CeO<sub>2-</sub>



**Fig. 2.** SEM micrographs of  $\text{CeO}_{2-\delta}$ -SS (a),  $\text{CeO}_{2-\delta}$ -HT particles (b), PANI-ES (c), PANI-ES@ $\text{CeO}_{2-\delta}$ -SS (d) and PANI-ES@ $\text{CeO}_{2-\delta}$ -HT (e).

$\delta$  composites (Fig. 2d and e) indicate that the presence of ultrafine nanodispersed  $\text{CeO}_{2-\delta}$  particles do not influence the original PANI-ES morphology.

### 3.4. Vibrational spectroscopy study

#### 3.4.1. Infrared spectroscopy

It is well known that FTIR spectrum of PANI is very sensitive to various experimental conditions such as humidity, temperature, pressure, storing and processing of samples and so on [23]. In order to avoid differences caused by the influence of the mentioned parameters we measured the spectra under the same conditions following recommendations by Trchova et al. [23].

Representative FTIR spectra of synthesized polyaniline-based samples are shown in Fig. 3. The characteristic spectrum of protonated emeraldine salt form can be recognized in all samples. The assignment of FTIR bands (well-documented in literature [23–30]), is presented in Supplementary Data. The spectrum of PANI-ES@ $\text{CeO}_{2-\delta}$  sample is almost the same as the spectrum of pure PANI-ES since the characteristic  $\text{CeO}_{2-\delta}$  vibrational modes (shown in inset of Fig. 3) cannot be distinguished. This can be associated to very intensive vibrational bands of protonated polyaniline as well as the low amount of cerium oxide in the composite. It can only be noticed that the intensity ratio of  $1306/1244\text{ cm}^{-1}$  bands (which are assigned to C–N stretching modes) changes in the presence of the oxide being 1.25, 1.28 and 1.29 for PANI-ES, PANI-ES@ $\text{CeO}_{2-\delta}$ -SS, and PANI-ES@ $\text{CeO}_{2-\delta}$ -HT, respectively. These changes are in correlation with the measured trend of electronic conductivity, and suggest the involvement of nitrogen from the polymer chain in the interaction with oxide.

#### 3.4.2. Raman spectroscopy

The molecular structure of samples was studied also by Raman spectroscopy. The obtained Raman spectrum of PANI-ES (Fig. 4a) is typical for protonated emeraldine form, and its assignment is well-

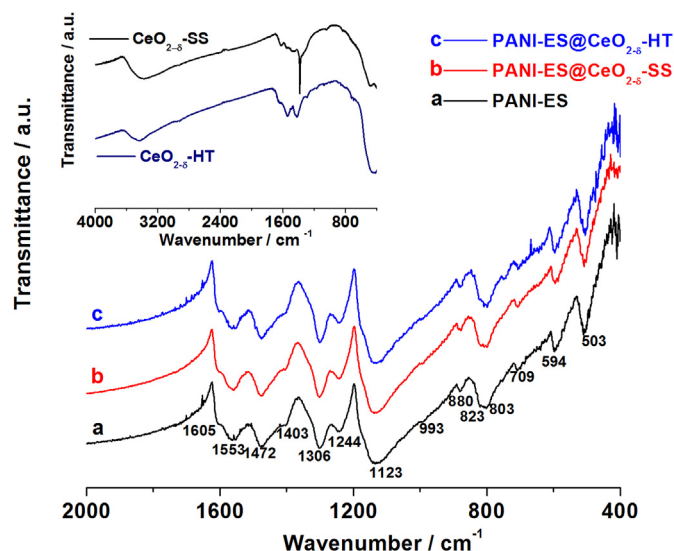


**Fig. 3.** FTIR spectrum of PANI-ES (a), PANI-ES@ $\text{CeO}_{2-\delta}$ -SS (b) and PANI-ES@ $\text{CeO}_{2-\delta}$ -HT (c). FTIR spectra of pure  $\text{CeO}_{2-\delta}$ -SS and  $\text{CeO}_{2-\delta}$ -HT are given in inset.

documented [27,31–36]. It can be seen in Supplementary Data.

Raman spectra of PANI@ $\text{CeO}_{2-\delta}$  composites (Fig. 4b and c) show all characteristic modes of PANI-ES, but  $\text{CeO}_{2-\delta}$  vibrations cannot be distinguished. The  $\text{CeO}_{2-\delta}$  spectra are measured under the same experimental conditions as that of PANI-ES and presented in the inset of Fig. 4. The high intensity Raman band at  $\sim 463\text{ cm}^{-1}$  corresponds to the  $F_{2g}$  vibrational mode of fluorite  $\text{CeO}_{2-\delta}$  structure. Interestingly, this high intensity mode is not visible in the spectra of composites. This confirms that the  $\text{CeO}_2$  is encapsulated into polymer chains thus forming the core-shell structure, via the polymerization of aniline adsorbed on the cerium oxide as a

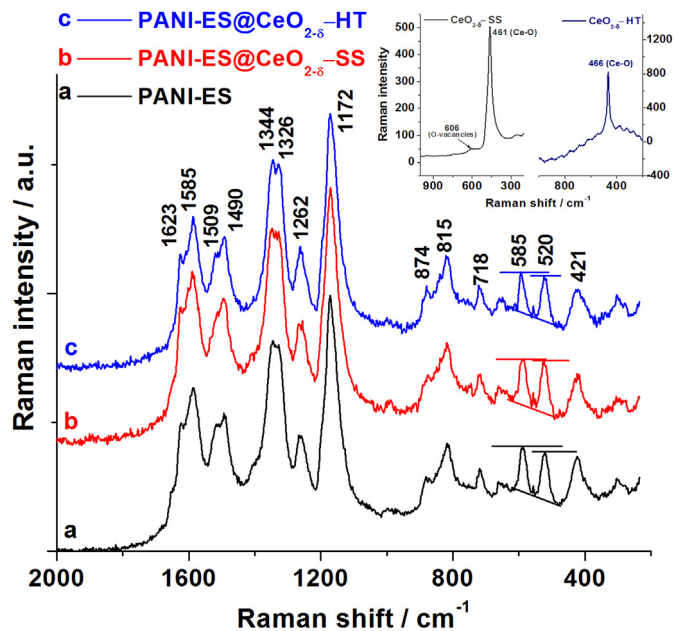


Fig. 4. Raman spectra of PANI-ES (a), PANI-ES@CeO<sub>2-δ</sub>-SS (b) and PANI-ES@CeO<sub>2-δ</sub>-HT in the normalized scale (c). Spectra of pure CeO<sub>2-δ</sub>-SS and CeO<sub>2-δ</sub>-HT oxides are given in inset.

nucleation core. A weak broadband (at  $\sim 606 \text{ cm}^{-1}$ ) in the spectrum of CeO<sub>2-δ</sub>-SS is related to the presence of oxygen vacancies. The use of more appropriate Raman conditions [35], provides more defined oxide modes, suggesting that both synthesized oxides investigated in this work actually possess a certain amount of vacancies, which is noticeable higher in the CeO<sub>2-δ</sub>-SS sample.

The changes of the PANI-ES mode positions due to the presence of CeO<sub>2-δ</sub> are not visible, but changes of the vibration modes intensity can be noticed. One can notice the CeO<sub>2-δ</sub> influence on the band corresponding to the C–N<sup>+</sup> stretching vibration of the delocalized polaronic structure, which is also identified by FTIR. Actually, the splitting of this band to  $\sim 1344 \text{ cm}^{-1}$  and  $\sim 1326 \text{ cm}^{-1}$  modes, which occurs in the pure PANI-ES, is more pronounced in the composites, especially in the PANI@CeO<sub>2-δ</sub>-HT sample with the lower concentration of vacancies, and consequently, a higher degree of Ce<sup>4+</sup> ions. It seems that the relative ratio of  $1344 \text{ cm}^{-1}/1326 \text{ cm}^{-1}$  bands decreases in the composite thus confirming the involvement of PANI's nitrogen in the interaction with cerium ions handing in electrons. By donating electrons to oxide, the C–N<sup>+</sup> stretching bonds became weaker thus appearing at low wavenumbers which is reflected in the decreased intensity of  $1344 \text{ cm}^{-1}$  band on account of the increase of  $1326 \text{ cm}^{-1}$  band intensity. The change in the  $1509 \text{ cm}^{-1}$  mode, corresponding to N–H deformation vibrations, upon PANI-CeO<sub>2-δ</sub> interaction, is also visible and is more pronounced in the composite containing CeO<sub>2-δ</sub>-SS.

The PANI-CeO<sub>2-δ</sub> interaction causes also pronounced changes of the vibrational modes intensity in the low-frequency region (in which the oxides modes appear). The relative intensity of the PANI's  $421 \text{ cm}^{-1}$  band (which is positioned in the vicinity of the most intensive CeO<sub>2-δ</sub> mode), is decreased in the composite. It can be correlated to the stronger F<sub>2g</sub> vibrational mode of fluorite structure of CeO<sub>2-δ</sub> which causes the strong interaction. Furthermore, the intensity ratio of bands at  $585 \text{ cm}^{-1}$  (positioned in the vicinity of oxygen vacancy band) and  $520 \text{ cm}^{-1}$  is decreased upon CeO<sub>2-δ</sub> action (as indicated in Fig. 4), thus following the trend PANI-ES, PANI@CeO<sub>2-δ</sub>-HT, PANI@CeO<sub>2-δ</sub>-SS. So, this decrease is more pronounced for PANI@CeO<sub>2-δ</sub>-SS, which could be related to the presence of higher concentration of oxygen vacancies. Also, the

change in the relative intensity of  $718 \text{ cm}^{-1}$ -assigned band to other bands follows this trend.

The observed changes in the Raman modes of polyaniline caused by the presence of cerium oxide indicates the existence of two types of PANI-CeO<sub>2-δ</sub> interactions including the nitrogen- (from radical cation) and hydrogen (from amine of polarons and bipolarons) bonding. Unlike the interaction involved nitrogen atoms, it seems that the hydrogen bonding interaction is facilitated by oxygen vacancies in the oxide lattice.

### 3.5. Electrochemical behavior

#### 3.5.1. Narrower voltage interval

The influence of the cerium oxide to the charge storage behavior of PANI was studied by Cyclic Voltammetry. Typical redox pair of PANI, corresponding to the transition of leucoemeraldine to emeraldine salt, was observed in the potential range from  $-0.2 \text{ V}$  vs. SCE to  $0.6 \text{ V}$  vs. SCE (Fig. 5a) [37]. This redox process is sensitive to the presence and relative fraction of CeO<sub>2-δ</sub> in the samples. As shown in Fig. 5a and Fig. S1, the current response of both cerium-oxides, in an acidic solution, is very poor, (below  $\sim 1 \text{ mA}$ ). On the other hand, PANI has more than twenty times higher current response. Theoretically, the ratio of active redox centers, such as Ce<sup>4+</sup>/Ce<sup>3+</sup> and the amino/imino centers in the composite (wt%/M for CeO<sub>2-δ</sub>: wt%/M for C<sub>6</sub>H<sub>5</sub>NH), corresponds exactly to the ratio of 1:22, respectively. However, taking into account the mass ratio of individual components in the composite, the current ratio of PANI and oxide (in the composite) would be even higher in favor of PANI. Therefore, the slightly depressed current response of PANI-ES could be expected if the certain fraction of PANI was replaced with CeO<sub>2-δ</sub>. However, the current response of PANI was somewhat increased after incorporation of cerium-oxide. This enhancement factor depends on the type of used oxide. Actually, the interaction of PANI with CeO<sub>2-δ</sub>-HT leads to the very small increase of its current (which is practically negligible), while this response became somewhat higher in the presence of CeO<sub>2-δ</sub>-SS (Fig. 5a and b). Charge/discharge capacitance expressed in  $\text{F g}^{-1}$ , were found to be  $296/294 \text{ F g}^{-1}$  for pure PANI,  $302/299 \text{ F g}^{-1}$  for PANI@CeO<sub>2-δ</sub>-HT and  $319/314 \text{ F g}^{-1}$  for PANI@CeO<sub>2-δ</sub>-SS, at a common scan rate of  $20 \text{ mVs}^{-1}$ .

Incorporation of CeO<sub>2-δ</sub> into PANI-ES provides a slightly higher coulombic capacity despite the fact that the conductivity of composite was decreased by CeO<sub>2-δ</sub> doping (although it decreased, the electronic conductivity of PANI-based composite is still very high). Therefore, the capability of polyaniline chains to attach/release electrolyte ions (without the charge transfer of protons) to compensate acceptance/liberation of electrons upon cycling can be limiting step. This process can be faster in the composite due to improved wettability caused by CeO<sub>2-δ</sub> presence [38]. Better charge behavior of PANI@CeO<sub>2-δ</sub>-SS than PANI@CeO<sub>2-δ</sub>-HT can be attributed to the differences in wettability. CeO<sub>2-δ</sub>-SS surface contains a higher amount of surface hydroxyl groups, compared to the one of CeO<sub>2-δ</sub>-HT surface (Fig. 3). The presence of these groups improves the wettability of both PANI's surface at its boundary with CeO<sub>2-δ</sub>.

To summarize, both investigated PANI@CeO<sub>2-δ</sub> composites present novel materials with a very large charge storage ability in an acidic solution. The synthesized PANI-ES@CeO<sub>2-δ</sub> composites are also stable in  $1 \text{ M HCl}$  solution. This is confirmed by the stability of the charge storage of PANI-ES@CeO<sub>2-δ</sub>-SS during the long cycling in this acidic electrolyte solution (Fig. S2, Supp.Data). Upon cycling, PANI@CeO<sub>2-δ</sub>-SS electrode is kept in the electrolyte overnight, after which the same charge storage behavior was measured. TG curve of such cycled electrode powder was identical to the one for the raw powder, thus confirming the same oxide fraction in the composite. It can be concluded that a strong adhesion of PANI with the cerium

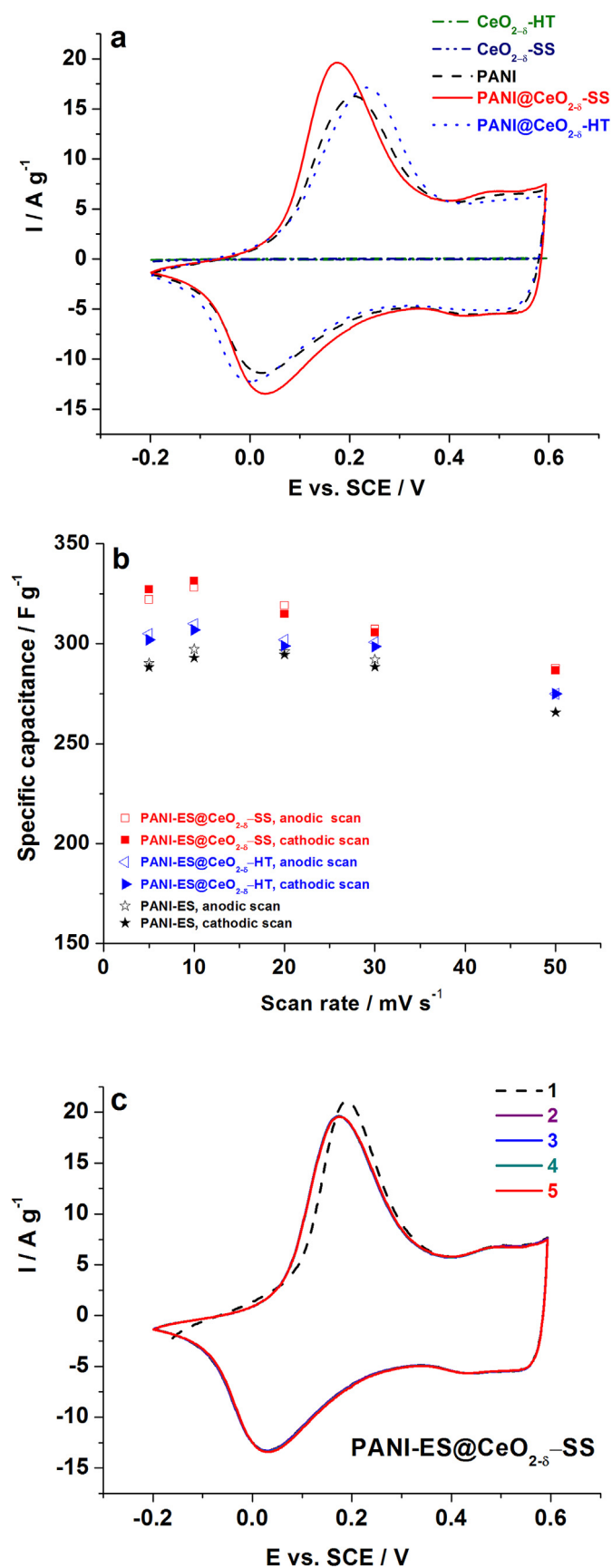


**Fig. 5.** a) Stabilized CVs of PANI-ES,  $\text{CeO}_{2-\delta}$ , and PANI-ES@ $\text{CeO}_{2-\delta}$  composites; b) Specific capacitance of PANI-ES, PANI-ES@ $\text{CeO}_{2-\delta}$ -HT, and PANI-ES@ $\text{CeO}_{2-\delta}$ -SS at different scan rates; c) The cyclic stability of PANI-ES@ $\text{CeO}_{2-\delta}$ -SS. The electrolyte was 1 M HCl. The voltage range was 0.2–0.6 V vs. SCE and the scan rate was  $20 \text{ mV s}^{-1}$ .

oxide surface prevents the oxide from its possible slow dissolution in 1 M HCl. The fact that the cerium oxide in the composite is encapsulated into the shell of polymer chains favors this assumption.

The higher capacitance was obtained for PANI-ES@ $\text{CeO}_{2-\delta}$ -SS, which makes this composite a very promising supercapacitor electrode. Its stable capacitance during consecutive cycling (Fig. 5c and Fig. S2) indicates the stable leucoemeraldine-emeraldine redox process. A small capacity decrease, with the increase of the scan rate, was measured (Fig. 5b).

### 3.5.2. Extended voltage interval

It is known that over-oxidation of PANI in an acidic solution by applying potentials above  $-0.6$ – $0.7$  V vs. SCE, results in its capacity decrease. Because of that, the cycling behavior in the deeper positive-going scan (beyond 0.6 V vs. SCE) was rarely examined [39]. Among other things, the idea of this work is to see how the presence of nonstoichiometric cerium-oxide influences the electrochemical over-oxidation of polyaniline.

CVs of all three samples, measured in an extended potential range from  $-0.2$ – $1$  V vs. SCE during ten consecutive cycles were shown in Fig. 6. In the first cycle, beside the main redox couple I (positioned at 0.22/0.01 V vs. SCE), which originates from the oxidation of leucoemeraldine base (LM) to emeraldine salt, one can see another main redox pair (labeled as III) at 0.8/0.65 V vs. SCE, corresponding to the emeraldine/parnigraniline (EM/PN) salt transition. A small redox pair II (0.55/0.45 V vs. SCE) positioned between these two main redox pairs can be also observed. Although the nature of this peak depends on the experimental details of polyaniline synthesis, electrolyte, and pH, this peak is generally attributed to the formation of benzoquinone degradation products and formation of cross-linked polyaniline chains by direct reaction between parts of the polyaniline chain itself [39]. One can see that the current of this middle redox couple increases during consecutive cycling of PANI within the extended water stability window, while the current of both LE-EM and EM-PN redox process decreases. Actually, over-oxidation of polyaniline leads to the irreversible formation of electrochemically inactive structures, which causes the current decrease throughout the consecutive cycling [37,39]. During experiments we noticed that the current of the second redox couple became more pronounced as soon as the current of the third peak has increased. One can conclude that the redox process corresponding to the second peak is still associated with the emeraldine-parnigraniline transformation.

Interestingly, some differences of the relative ratio of anodic peaks I and III can be observed between PANI and the  $\text{CeO}_{2-\delta}$ -modified PANI. A similar current response of these anodic peaks is observed for PANI and PANI@ $\text{CeO}_{2-\delta}$ -SS (Fig. 6a and b), indicating similar kinetics of the LE-EM and EM-PN redox processes in these samples. However, this is not the case for PANI-ES@ $\text{CeO}_{2-\delta}$ -HT (Fig. 6c) where the first anodic peak is noticeable higher than the third one. The process of the PN formation during PANI's oxidation is aggravated by  $\text{CeO}_{2-\delta}$ -HT action. The involvement of positively charged nitrogen in the interaction with cerium oxide impedes PANI-ES deprotonation, resulting in the lower fraction of formed PN upon the first anodic scan (Fig. 7a) and consequently the slower disappearance of the third peak after ten cycles (Fig. 7b). As a result, slightly better capacitance retention of PANI@ $\text{CeO}_{2-\delta}$ -HT (83.4% after 10 cycles or 64.4% after 30 cycles) was observed with respect to the pure PANI (80.8% after 10 cycles or 60.5% after 30 cycles) and PANI@ $\text{CeO}_{2-\delta}$ -SS (76.8% after 10 cycles and 55.6% after 30 cycles).

### 3.6. PANI- $\text{CeO}_{2-\delta}$ interaction

Polyaniline chains can change their redox state from a



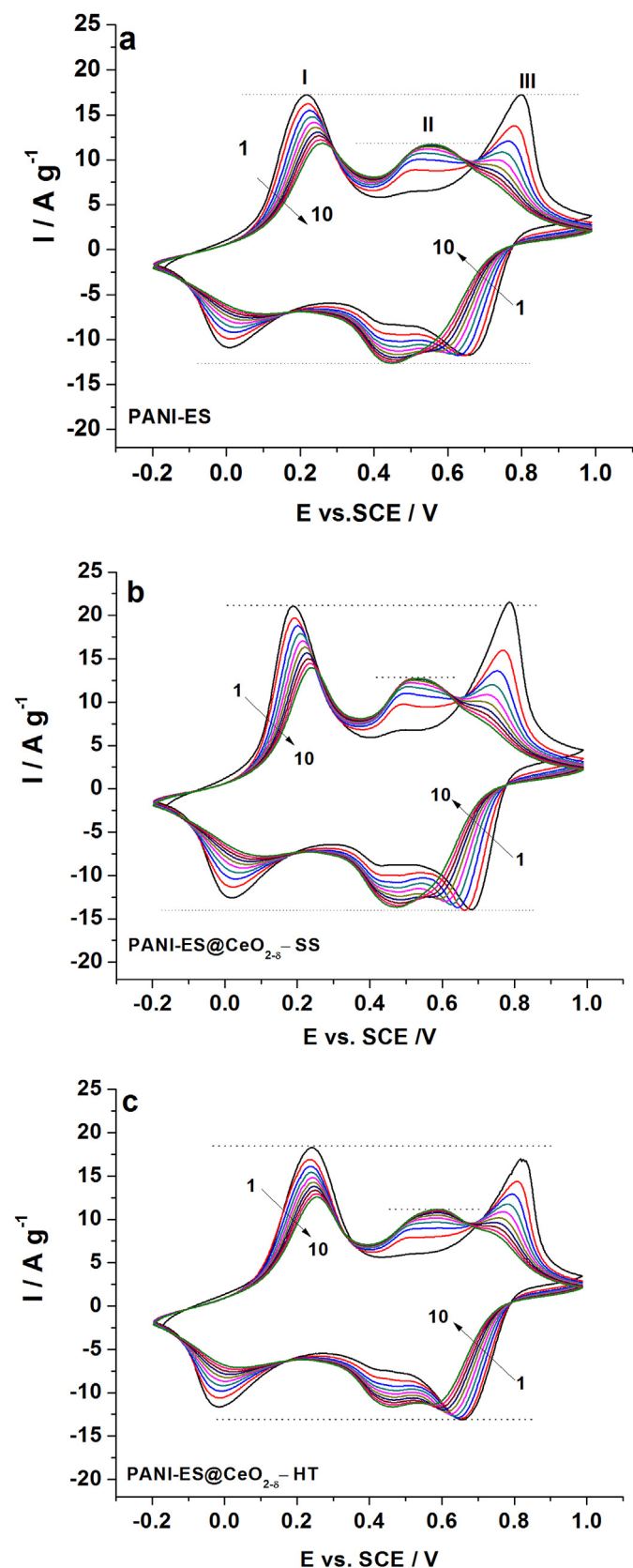


Fig. 6. CVs of PANI (a), PANI@CeO<sub>2-δ</sub>-SS (b) and PANI@CeO<sub>2-δ</sub>-HT (c) measured in wide potential interval from -0.2–1 V vs. SCE during 10 successive cycling, at a common scan rate at 20 mV s<sup>-1</sup>.

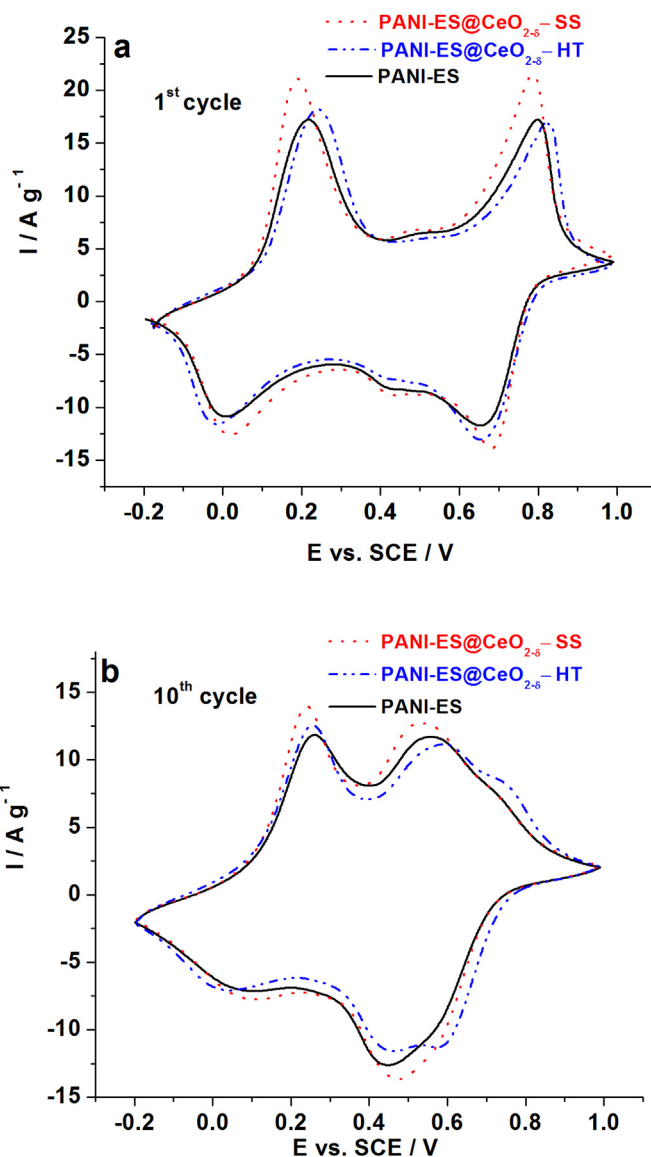


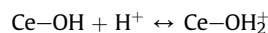
Fig. 7. CVs of PANI-ES, PANI-ES@CeO<sub>2-δ</sub>-SS and PANI-ES@CeO<sub>2-δ</sub>-HT samples measured in HCl at a common scan rate of 20 mV s<sup>-1</sup>: a) the 1st cycle and b) 10th cycle.

completely reduced form (leucoemeraldine), composed of benzenoid units containing amine nitrogen atoms –NH–, to a fully oxidized form (pernigraniline), composed of quinoid units containing imine nitrogen atoms –N=. A semi-oxidized form of polyaniline, known as emeraldine (either in the form of base or salt), is composed from equal numbers of reduced and oxidized polymer repeat units. The protonation of the emeraldine base, under acidic conditions, includes the addition of protons to imine nitrogen sites to generate radical cations (some amine nitrogen atoms can also be protonated to give NH<sub>2</sub><sup>+</sup> groups even if all the imines are not protonated), which can significantly increase the conductivity of polyaniline (up to 11 orders of magnitude) [25,40], reaching the metallic values.

On the other hand, cerium oxide crystallized in the fluorite type cubic crystal lattice where the Ce<sup>4+</sup> cation is surrounded by eight O<sup>2-</sup> anions, each of which is coordinated to four Ce<sup>4+</sup> cations. Both theoretical and experimental results revealed that in oxygen deficient cerium oxide the adsorbed water molecules prefer to dissociate near the oxygen vacancy sites thus forming surface hydroxyl

groups [41,42]. Therefore, both chemisorbed H<sub>2</sub>O and OH groups coexist at the reduced cerium oxide surface, so their presence can be expected at the surface of the CeO<sub>2-δ</sub>-SS and CeO<sub>2-δ</sub>-HT oxides, as confirmed by their FTIR spectra (inset in Fig. 3, O–H stretching vibrations around 3500 cm<sup>-1</sup>). Their lower content in the CeO<sub>2-δ</sub>-HT can be correlated to the lower reactivity of surface towards the water dissociation, due to the smaller fraction of oxygen vacancies.

The experimentally determined pH values of CeO<sub>2-δ</sub>-SS, at zero point of charge (pH<sub>ZPC</sub> = 6.3), showed that the oxide surface became positively charged in the reaction solution of HCl (Fig. 8). Namely, surface hydroxyl groups are protonated, according to the equation



Such formed positively charged cerium oxide nanoparticles can electrostatically attract Cl<sup>-</sup> ions from the acidic solution (Fig. 8a).

The adsorbed Cl<sup>-</sup> ions can easily attract the anilinium cation (formed by adding aniline into acidic solution) which undergoes further polymerization to the emeraldine salt when the oxidant is added in the acidic medium. Consequently, there is possibility that various oligomers with an active radical cation head (positive head) are adsorbed to the surface of CeO<sub>2-δ</sub> particles as well, but this possibility is reduced by the fact that the adsorption centers of cerium oxide were previously saturated with protonated aniline species. In this way, CeO<sub>2-δ</sub> particles become wrapped into PANI chains thus forming the "core-shell" nanostructure. This type of structure has been already recognized for polyaniline/cerium oxide system [6,7,12,43–45]. These data showed that the interaction of protonated form of polyaniline with CeO<sub>2-δ</sub> is usually achieved through the formation of hydrogen bond between surface hydroxyl (-OH) groups of oxide and hydrogen of the polymer chain [6,44–46]. Based on both Raman and FTIR measurements, the similar type of interaction is also identified in as-synthesized PANI@CeO<sub>2-δ</sub> composites. Namely, zeta potential-pH dependence, measured for oxygen deficient cerium oxide [21], revealed that the maximum positive charge, at the surface, was achieved for the pH solution of about 4–5. Besides, some of OH groups at the cerium-oxide surface can be found un-protonated, thus participating in the formation of hydrogen bonds, acting as the bridge between polymer and oxide (Fig. 8b). This type of interaction is more pronounced in the CeO<sub>2-δ</sub>-SS since the higher fraction of oxygen vacancies (relative to CeO<sub>2-δ</sub>-HT) results in the higher amount of hydroxyl groups. Besides, another type of oxide-polyaniline interaction (Fig. 8c), involving positively charged nitrogen (-N<sup>+</sup>H-), is identified by vibrational spectroscopy study. This interaction is found to be stronger in the case of composite with the hydrothermally synthesized oxide, which has the smaller oxygen vacancy population (i.e. higher concentration of Ce<sup>4+</sup> ions). Theoretical

study on CeO<sub>2-δ</sub> revealed that the electrons can be localized at cerium ions or oxygen vacancies [35]. Having in mind, that the nitrogen-involved interaction is more manifested in CeO<sub>2-δ</sub>-HT than in CeO<sub>2-δ</sub>-SS, and easier reduction of Ce<sup>4+</sup> to Ce<sup>3+</sup> ions, one can assume that delocalized π electrons of polymer chains became localized at 4f states of cerium ions. This may result in the decreased of the electronic conductivity of PANI when bonded to cerium oxide, following the trend PANI, PANI-ES@CeO<sub>2-δ</sub>-SS and PANI-ES@CeO<sub>2-δ</sub>-HT. Also, it could be responsible for the higher amount of bonded CeO<sub>2-δ</sub>-HT and consequently improved thermal stability of PANI-ES@CeO<sub>2-δ</sub>-HT composite. The mechanism of PANI-CeO<sub>2-δ</sub> interaction is illustrated in Fig. 9.

A small amount of oxide (about 4%wt), incorporated into the shell of conducting polymer, was found to decrease its conductive behavior (in the extent that depends on properties of the used oxides), but conversely to improve its charge storage capability. The interactions at the PANI@CeO<sub>2-δ</sub> interface weakened the polymer interchain bonds providing an easier attraction of electrolyte ions. Whether the higher amount of CeO<sub>2-δ</sub> can improve electrochemical performance even more is the main question which arises here? Our attempt to answer this question, by increasing the amount of doped CeO<sub>2-δ</sub> oxide during the synthesis, failed. Interestingly, PANI was not capable to bind a higher amount of CeO<sub>2-δ</sub> (under applied synthesis conditions) regardless to the increase of its initial amount into reaction medium. Actually, the doubling of the initial content of CeO<sub>2-δ</sub> (from 50 mg to 100 mg) for the aniline oxidation did not increase the content of bonded-CeO<sub>2-δ</sub> at all. Such behavior is opposite to the case of TiO<sub>2</sub> added upon aniline oxidation, under completely same experimental conditions. In a set of separated experiments we showed that the initial amounts of 9 mg, 50 mg and 100 mg of TiO<sub>2</sub> (under same synthesis conditions), resulted in the ~4 wt%, ~18 wt% and ~34 wt% of oxide (calculated per mass of dried sample), in the composites (Fig. S3), respectively, which is in agreement with results of Bian et al. [18]. We try to explain this peculiar behavior using TG analysis. It can be seen from TG curves of composites, doped with a small percent (3–4%) of either CeO<sub>2-δ</sub> (Fig. 1) or TiO<sub>2</sub> (Fig. S1), that the presence of such doped concentration did not change the final amount of internal dopant (HCl) in the composite. One can suggest that the type of interaction of these oxides in the case of their small doped fraction is similar i.e. both oxides coexist together with Cl<sup>-</sup> ions (some of the Cl<sup>-</sup> ions are adsorbed on the protonated hydroxyl groups) thus interacting also with hydrogen/nitrogen and weakening PANI's bonds with dopant. Furthermore, it can be seen that the amount of doped acid is noticeably decreased after mixing PANI with the higher percent (18% or 34%) of TiO<sub>2</sub> (Fig. 1). By competing with dopant ions for the positions of chains (close to the nitrogen atoms) during the synthesis, titanium oxide molecules (in higher concentration), are capable to eliminate some of dopant ions thus making complex

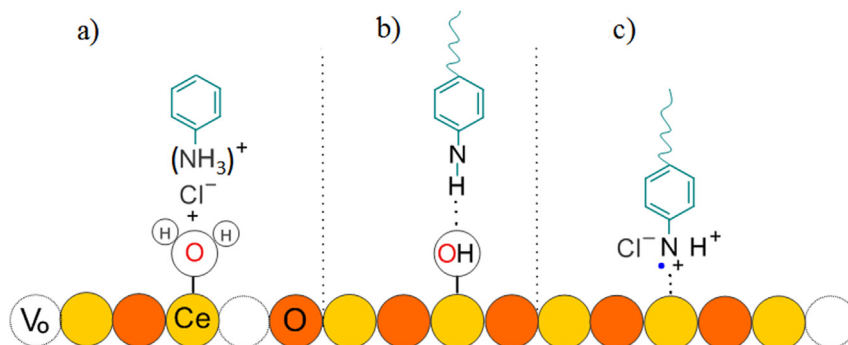
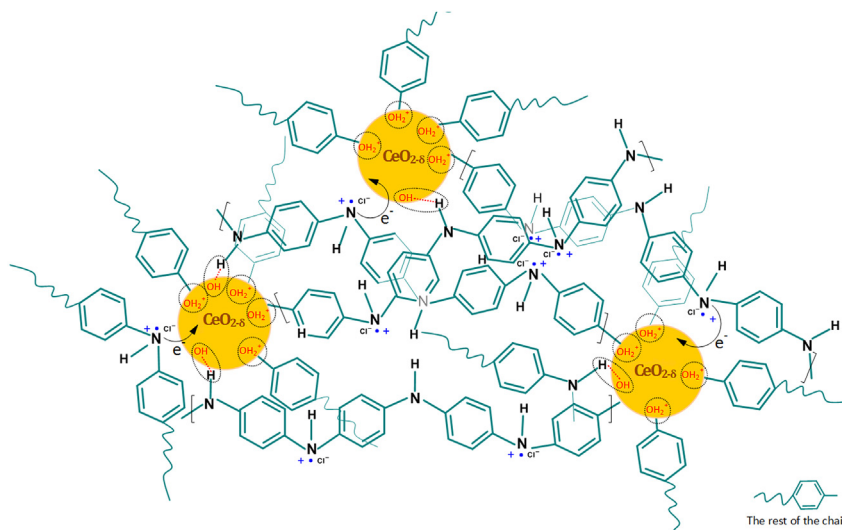


Fig. 8. The initial stage of polymerization (a) and hydrogen (b) and nitrogen-involved interactions (c).



**Fig. 9.** Schematic illustration of the formation of PANI chains on the surface of  $\text{CeO}_{2-\delta}$  nanoparticles (core-shell structure).

with nitrogen atoms of PANI. It could be related to a strong tendency of titanium to form coordination compounds with nitrogen [47]. On the other hand, nano- $\text{CeO}_{2-\delta}$ , in spite of the higher concentration in the reaction solution, does not show this capability under the same experimental conditions, which resulted in its unsuccessful high-level bonding.

#### 4. Conclusions

The use of non-stoichiometric cerium oxide as the adsorption center for the polymerization of aniline, in highly acidic conditions, influences thermal, electrical and charge storage properties of the formed emeraldine salt. These changes are the consequence of the strong interaction of polyaniline chains with cerium oxide ultrafine nanoparticles. The oxygen vacancies control indirectly the intensity of these interactions. A higher fraction of O-vacancies in  $\text{CeO}_{2-\delta}$  promotes the dissociation of chemisorbed  $\text{H}_2\text{O}$  to OH groups at the oxide's surface, which in the protonated form, play the role of chemically active sites for the growth of PANI chains. Besides, unprotonated hydroxyl groups of cerium oxide surface interact with the hydrogen of polymer chains through the formation of hydrogen bonds. A lower fraction of O-vacancies provides the higher concentration of  $\text{Ce}^{4+}$  ions into crystal lattice, thus intensifying the interaction of  $\text{Ce}^{4+}$  cation with the nitrogen of the polaron structure ( $\text{C} \sim \text{N}^{\bullet+}$ ), through the trapping of electrons into localized 4f states of cerium ions.

By encapsulating small weight percent of oxygen deficient cerium oxide, into highly conductive emeraldine salt, the improvement of both thermal stability and charge storage behavior is achieved. The highest and stable capacitance, amounting to  $314 \text{ F g}^{-1}$ , was obtained for the oxide with the higher degree of deficient oxygen (PANI-ES@ $\text{CeO}_{2-\delta}$ -SS), thus making this material promising as electrode for supercapacitors.

#### Acknowledgments

The Ministry of Education, Science and Technological Development of Republic of Serbia is acknowledged for funding support within projects III45014, III45003, III45018, OI172043, III45016 as well as through the bilateral projects Serbia-Slovenia entitled "Developments of novel materials for alkaline-ion batteries" and Serbia-Montenegro entitled "Development of ecological Li-ion

batteries". S.M. acknowledges Serbian Academy of Sciences and Arts for support of this investigation, too, through the project "Electrocatalysis in the contemporary process of energy conversion".

#### Appendix A. Supplementary data

Supplementary data to this article can be found online at <https://doi.org/10.1016/j.electacta.2019.03.135>.


#### References

- [1] H. Wang, J. Lin, Z.X. Shen, Polyaniline (PANI) based electrode materials for energy storage and conversion, *J. Sci. Adv. Mater. Dev.* 1 (2016) 225.
- [2] F.-Y. Chuang, S.-M. Yang, Cerium dioxide/polyaniline core-shell nanocomposites, *J. Colloid Interface Sci.* 320 (2008) 194.
- [3] S. Daikh, F.Z. Zeggai, A. Bellil, A. Benyoucef, Chemical polymerization, characterization and electrochemical studies of PANI/ZnO doped with hydrochloric acid and/or zinc chloride: differences between the synthesized nanocomposites, *J. Phys. Chem. Solids* 121 (2018) 78.
- [4] H. Wei, X. Yan, S. Wu, Z. Luo, S. Wei, Z. Guo, Electropolymerized polyaniline stabilized tungsten oxide nanocomposite films: electrochromic behavior and electrochemical energy storage, *J. Phys. Chem. C* 116 (2012) 25052.
- [5] C.-G. Wu, D.C. DeGroot, H.O. Marcy, J.L. Schindler, C.R. Kannewurf, Y.-J. Liu, W. Hirpo, M.G. Kanatzidis, Redox intercalative polymerization of aniline in V2O5 xerogel. The postintercalative intralamellar polymer growth in polyaniline/metal oxide nanocomposites is facilitated by molecular oxygen, *Chem. Mater.* 8 (1996) 1992.
- [6] C. Liu, H. Tai, P. Zhang, Z. Yuan, X. Du, G. Xie, Y. Jiang, A high-performance flexible gas sensor based on self-assembled PANI-CeO<sub>2</sub> nanocomposite thin film for trace-level NH<sub>3</sub> detection at room temperature, *Sens. Actuators B Chem.* 261 (2018) 587.
- [7] L. Wang, H. Huang, S. Xiao, D. Cai, Y. Liu, B. Liu, D. Wang, C. Wang, H. Li, Y. Wang, Q. Li, T. Wang, Enhanced sensitivity and stability of room-temperature NH<sub>3</sub> sensors using core-shell CeO<sub>2</sub> Nanoparticles@Cross-linked PANI with p-n heterojunctions, *Appl. Mater. Interfaces* 6 (2014) 14131.
- [8] A.A. Ansari, G. Sumana, R. Khan, B.D. Malhotra, Polyaniline-cerium oxide nanocomposite for hydrogen peroxide sensor, *J. Nanosci. Nanotechnol.* 9 (2009) 4679.
- [9] N. Parvatikar, S. Jain, S.V. Bhoraskar, M.V.N.A. Prasad, Spectroscopic and electrical properties of polyaniline/CeO<sub>2</sub> composites and their application as humidity sensor, *J. Appl. Polym. Sci.* 102 (2006) 5533.
- [10] M. Singh, N. Nesakumar, S. Sethuraman, U. Maheswari, Journal of Colloid and Interface Science Electrochemical biosensor with ceria – polyaniline core shell nano-interface for the detection of carbonic acid in blood, *J. Colloid Interface Sci.* 425 (2014) 52.
- [11] M.B. Gumpu, N. Nesakumar, S. Sethuraman, U.M. Krishnan, J.B.B. Rayappan, Electrochemical biosensor with ceria-PANI core-shell nano-interface for the detection of histamine, *Sens. Actuators B Chem.* 199 (2014) 330.
- [12] H. Huang, Z. Guo, Preparation and characterization of conductive polyaniline/cerium dioxide composites, *Mater. Sci. Forum* 663–665 (2011) 686.
- [13] S. Wang, Z. Huang, J. Wang, Y. Li, Z. Tan, Thermal stability of several

- polyaniline/rare earth oxide composites (I): polyaniline/CeO<sub>2</sub> composites, *J. Therm. Anal. Calorim.* 107 (2012) 1199.
- [14] B. Ramezanzadeh, G. Bahlakeh, M. Ramezanzadeh, Polyaniline-cerium oxide (PANI-CeO<sub>2</sub>) coated graphene oxide for enhancement of epoxy coating corrosion protection performance on mild steel, *Corros. Sci.* 137 (2018) 111.
- [15] N. Maheswari, G. Muralidharan, Fabrication of CeO<sub>2</sub>/PANI composites for high energy density supercapacitors, *Mater. Res. Bull.* 106 (2018) 357.
- [16] Q. Gong, Y. Li, H. Huang, J. Zhang, T. Gao, G. Zhou, Shape-controlled synthesis of Ni-CeO<sub>2</sub>@PANI nanocomposites and their synergetic effects on supercapacitors, *Chem. Eng. J.* 344 (2018) 290.
- [17] Y. Fei, H. Huang, S. Song, L. Jin, X. Zhang, Z. Guo, Preparation of thermostable and electroconductive PANI/TDI-CeO<sub>2</sub> composite by graft polymerization and its electrochemical properties, *Int. J. Electrochem. Sci.* 13 (2018) 1308.
- [18] C. Bian, Y. Yu, G. Xue, Synthesis of conducting polyaniline/TiO<sub>2</sub> composite nanofibres by one-step in situ polymerization method, *J. Appl. Polym. Sci.* 104 (2007) 21.
- [19] S. Phokha, S. Pinitsoontorn, P. Chirawatkul, Y. Poo-arporn, S. Maensiri, Synthesis, characterization, and magnetic properties of monodisperse CeO<sub>2</sub> nanoparticles prepared by PVP-assisted hydrothermal method, *Nanoscale Res. Lett.* 7 (2012) 425.
- [20] X. Yu, F. Li, X. Ye, X. Xin, Synthesis of cerium(IV) oxide ultrafine particles by solid-state reactions, *J. Am. Ceram. Soc.* 83 (2000) 964.
- [21] N. Tomić, Z.D. Dohčević-Mitrović, N.M. Paunović, D.Ž. Mijin, N.D. Radić, B.V. Grbić, S.M. Aškračić, B.M. Babić, D.V. Bajuk-Bogdanović, Nanocrystalline CeO<sub>2</sub>-δ as Effective Adsorbent of Azo Dyes 30 (2014) 11582.
- [22] Y. Wei, K.F. Hsueh, Thermal analysis of chemically synthesized polyaniline and effects of thermal aging on conductivity, *J. Polym. Sci., Part A: Polym. Chem.* 27 (1989) 4351.
- [23] M. Trchová, J. Stejskal, Polyaniline: the infrared spectroscopy of conducting polymer nanotubes, *Pure Appl. Chem.* 83 (2011) 1803–1817, <https://doi.org/10.1351/PAC-REP-10-02-01>.
- [24] M. Hasik, C. Paluszkiwicz, E. Bielńska, Reactions of Polyaniline with Transition Metal Ions in Nonaqueous Solutions, 2005, pp. 744–747, 677.
- [25] Z. Ping, In situ FTIR-attenuated total reflection spectroscopic investigations on the base-acid transitions of polyaniline, *J. Chem. Soc., Faraday Trans.* 92 (1996) 3063.
- [26] M. Lohrasbi, N. Hedayat, S.S.C. Chuang, In-situ infrared study of the synthesis of polyaniline under acid and neutral pH, *Top. Catal.* 57 (2014) 1570.
- [27] M. Trchová, Z. Morávková, I. Šeděnková, J. Stejskal, Spectroscopy of thin polyaniline films deposited during chemical oxidation of aniline, *Chem. Pap.* 66 (2012) 415.
- [28] M. Hasik, A. Drelinkiewicz, E. Wenda, C. Paluszkiwicz, S. Quillard, FTIR spectroscopic investigations of polyaniline derivatives-palladium systems, *J. Mol. Struct.* 596 (2001) 89.
- [29] M. Trchová, I. Šeděnková, E.N. Konyushenko, J. Stejskal, P. Holler, G. Čirić-Marjanović, Evolution of polyaniline nanotubes: the oxidation of aniline in water, *J. Phys. Chem. B* 110 (2006) 9461.
- [30] M.R. Devi, B. Lawrence, N. Prithvikumar, N. Jeyakumar, Synthesis and characterization of conducting polymer Polyaniline doped with Salicylic Acid, *Int. J. ChemTech Res.* 6 (2014) 5400.
- [31] G. Čirić-Marjanović, M. Trchová, J. Stejskal, The chemical oxidative polymerization of aniline in water: Raman spectroscopy, *J. Raman Spectrosc.* 39 (2008) 1375.
- [32] G.M. do Nascimento, V.R.L. Constantino, R. Landers, M.L.A. Temperini, Aniline polymerization into montmorillonite clay: a spectroscopic investigation of the intercalated conducting polymer, *Macromolecules* 37 (2004) 937.
- [33] M. Tagowska, B. Pałys, K. Jackowska, Polyaniline nanotubes - anion effect on conformation and oxidation state of polyaniline studied by, *Raman spectroscopy* 142 (2004) 223.
- [34] B.Z. Wei, M. Wan, T. Lin, L. Dai, Polyaniline nanotubes doped with sulfonated carbon nanotubes made via a self-assembly, *Adv. Mater.* 15 (2003) 136.
- [35] M. Radović, B. Stojadinović, N. Tomić, A. Golubović, B. Matović, I. Veljković, Z. Dohčević-Mitrović, Investigation of surface defect states in CeO<sub>2</sub>-y nanocrystals by Scanning-tunneling microscopy/spectroscopy and ellipsometry, *J. Appl. Phys.* 116 (2014) 234305.
- [36] A. Drury, S. Chauré, M. Kröll, V. Nicolosi, N. Chauré, W.J. Blau, Fabrication and characterization of silver/polyaniline composite nanowires in porous anodic alumina, *Chem. Mater.* 19 (2007) 4252.
- [37] E. Song, J.-W. Choi, Conducting polyaniline nanowire and its applications in chemiresistive sensing, *Nanomaterials* 3 (2013) 498.
- [38] S. Popescu, M. Mîndroiu, D. Cabuzu, C. Pîrvu, The Roll of NaPSS Surfactant on the Ceria Nanoparticles Embedding in Polypyrrole Films, 2016, 2016, p. 1.
- [39] R. Pauliukaite, C.M.A. Brett, A.P. Monkman, Polyaniline fibres as electrodes, *Electrochemical characterisation in acid solutions* 50 (2004) 159.
- [40] A.G. MacDiarmid, A.J. Epstein, *Conducting polymers: science and technology*, in: P.N. Prasad (Ed.), *Frontiers of Polymers and Advanced Materials*, Plenum Press, New York, 1994, p. 251.
- [41] Z. Yang, Q. Wang, S. Wei, D. Ma, Q. Sun, The effect of environment on the reaction of water on the ceria(111) surface: a DFT+U study, *J. Phys. Chem. C* 114 (2010) 14891.
- [42] Lj Kundakovic, D.R. Mullins, S.H. Overbury, Adsorption and reaction of H<sub>2</sub>O and CO on oxidized and reduced Rh/CeO<sub>x</sub>(111) surfaces, *Surf. Sci.* 457 (2000) 51.
- [43] E. Kumar, P. Selvarajan, D. Muthuraj, Preparation and characterization of polyaniline/cerium dioxide (CeO<sub>2</sub>) nanocomposite via in situ polymerization, *J. Mater. Sci.* 47 (2012) 7148.
- [44] Y. Sasikumar, A.M. Kumar, Z.M. Gasem, E.E. Ebenso, Hybrid nanocomposite from aniline and CeO<sub>2</sub> nanoparticles: surface protective performance on mild steel in acidic environment, *Appl. Surf. Sci.* 330 (2015) 207.
- [45] F. Liu, H. Yongjun-He, J.-S. Huh, Study on the synthesis and characterization of PANi/nano-CeO<sub>2</sub> composites, *Solid State Phenom.* 124–126 (2007) 287.
- [46] Y. He, Synthesis of polyaniline/nano-CeO<sub>2</sub> composite microspheres via a solid-stabilized emulsion route, *Mater. Chem. Phys.* 92 (2005) 134.
- [47] X. Li, G. Wang, X. Li, D. Lu, Surface properties of polyaniline/nano-TiO<sub>2</sub> composites, *Appl. Surf. Sci.* 229 (2004) 395.

**FULL ARTICLE**

# Naturally safe: Cellular noise for document security

Danica Pavlović<sup>1</sup> | Mihailo D. Rabasović<sup>1</sup> | Aleksandar J. Krmpot<sup>1</sup> | Vladimir Lazović<sup>1</sup> | Srećko Čurčić<sup>2</sup> | Dejan V. Stojanović<sup>3</sup> | Branislav Jelenković<sup>1</sup> | Wang Zhang<sup>4</sup> | Di Zhang<sup>4</sup> | Nenad Vukmirović<sup>1</sup> | Dimitrije Stepanenko<sup>1</sup> | Branko Kolarić<sup>1,5</sup>  | Dejan V. Pantelić<sup>1\*</sup>

<sup>1</sup>Institute of Physics, University of Belgrade, Belgrade, Serbia

<sup>2</sup>Institute of Zoology, University of Belgrade—Faculty of Biology, Belgrade, Serbia

<sup>3</sup>Institute of Lowland Forestry and Environment, University of Novi Sad, Novi Sad, Serbia

<sup>4</sup>State Key Lab of Metal Matrix Composite, Shanghai Jiao Tong University, Shanghai, China

<sup>5</sup>MNM Group, Department of Physics, UMONS, Mons, Belgium

**\*Correspondence**

Dejan V. Pantelić, Institute of Physics, University of Belgrade, Photonics Center, Pregrevica 118, 11080 Zemun, Belgrade, Serbia.

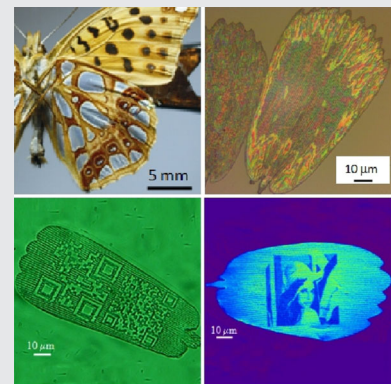
Email: pantelic@ipb.ac.rs

**Funding information**

Joint Funding of Development and Research Projects of the Republic of Serbia 407 and the People's Republic of China; Ministry of Education, Science and Technological 404 Development of the Republic of Serbia, Grant/Award Numbers: III45016, III43002, ON171038, ON173038, ON171017, ON171032; Institute of Physics; Innovation Fund; German Academic Exchange Service; Ministry of Education, Science and Technological Development of the Republic of Serbia

**Abstract**

Modern document protection relies on the simultaneous combination of many optical features with micron and submicron structures, whose complexity is the main obstacle for unauthorized copying. In that sense, documents are best protected by the diffractive optical elements generated lithographically and mass-produced by embossing. The problem is that the resulting security elements are identical, facilitating mass-production of both original and counterfeited documents. Here, we prove that each butterfly wing-scale is structurally and optically unique and can be used as an inimitable optical memory tag and applied for document security. Wing-scales, exhibiting angular variability of their color, were laser-cut and bleached to imprint cryptographic information of an authorized issuer. The resulting optical memory tag is extremely durable, as verified by several century-old insect specimens still retaining their coloration. The described technique is simple, amenable to mass-production, low cost and easy to integrate within the existing security infrastructure.


**KEYWORDS**

biophotonics, complexity, iridescence, optical document security, variability

## 1 | INTRODUCTION

Insects have been used more than any other living creatures as a blueprint for design of novel devices. Butterflies and moths (order: Lepidoptera) are particularly inspiring, due to vast number of species (nearly 180 000) [1] and peculiar

optical properties of their wings covered with large number (500–1000/mm<sup>2</sup>) of tiny, overlapping scales [2] (see section 1 of Appendix S1 for a short description of their properties). Some of them are structurally colored [3] that is, produce colors by interference, diffraction and scattering, rather than pigments. This is due to complex, regular or

irregular, micro/nanostructures, which can be classified in several groups according to their morphology [4]. Most frequently, iridescence (characterized by directionally dependent coloration [3]) can be observed.

Back into the XVIII century, Benjamin Franklin came up with an idea to reproduce the complexity of natural structures for document protection. He printed venation patterns of plant leaves on dollar bills to prevent counterfeiting [5]. Nowadays, his method was superseded by artificial security components, such as optically variable devices (OVDs) [6]. Diffractive optical elements (DOEs) are commonly exploited for the purpose, due to their, inherently complex microstructures, recognizable optical pattern and capability for mass-production by embossing. There is a significant drawback: for the specific type of document, all embossed copies of DOEs are identical. If a fake DOE is manufactured, counterfeited document can be made in large quantities, too. For that reason, an important goal is to invent a device which will provide unique and individual protection for each document. Protective elements should be highly complex, unique, difficult to reverse engineer and imitate. In the relevant literature, such objects are called physical one-way functions and can be realized by embedding randomly dispersed plastic, micron-sized spheres in a transparent medium and observing mesoscopic light scattering [7]. As another example, we mention using a randomized pattern of scattering from paper-based substrates [8].

Imprints of naturally occurring structures were proposed as security elements by Hamm-Dubischar [9], Biermann and Rauhe [10], and Rauhe [11], who presented the idea of document protection using biomineralized shells of radiolarians and diatoms. The protection is based on the structural complexity of their shells. The main problem is that optical effects are not particularly conspicuous, and the complexity can be assessed only at the morphological level, using scanning electron microscopy (SEM). Another problem is that structural variations among individuals of the same species seem to be small.

Whichever security element is used, it must be integrated in a security system relying on three inspection lines [6]: the first line is overt and can be visually inspected by anyone; the second is semi-covert and uses machine inspection; while the third one is covert and relies on forensic inspection with highly specialized equipment.

Here, we analyze the structural complexity, randomness, variability and uniqueness of the optical pattern of iridescent butterfly wing scales. We aim to establish their usefulness as inimitable OVDs for individualized, covert and overt, optical document security. Additionally, we investigate wing-scales as a memory medium for inscription of additional cryptographic information.

## 2 | STRUCTURE AND IRIDESCENCE OF *ISSORIA LATHONIA* BUTTERFLY WING-SCALES

In this section, we analyze morphological and optical features of scales belonging to the underside silver wing-patches of the Queen of Spain Fritillary, *Issoria lathonia* (Linnaeus, 1758), (see Figure 1A and section 2 of Appendix S1 for a short description of the butterfly's life history). This particular species was studied for the characteristic coloration of individual wing-scales, consisting of red, green and bluish spots randomly dispersed along a grating-like structure (see reflection microscope image in Figure 1B,C). The resulting silver color is produced by the local, additive spectral mixing [12].

Field-emission gun scanning electron microscope (FEGSEM) images reveal detailed structure of the scale's upper lamina (UL in Figure 1D). It consists of lamellar longitudinal ridges (R) regularly separated by a distance of 1.5  $\mu\text{m}$ . There is, also, a fish-bone-shaped sub-wavelength grating (SW) with period of 150 nm, radiating from ridges. The interior of the scale is hollow, filled only with nano-pillars, separating UL and lower lamina (LL).

Nonlinear optical microscopy was used to analyze three-dimensional (3D) structure of wing-scales using two-photon excited fluorescence (TPEF) of chitin. Nonlinear microscope was constructed in-house [13] (see Appendix S1 for details) and used to reveal that the wing scales have irregular, wavy shape (see Figure 1E). This significantly contributes to variability of the resulting optical pattern, together with variation of the thicknesses of upper and lower laminae and their mutual distance.

We have found that the individual wing scales are iridescent, that is, the color pattern strongly depends on illumination and observation directions. The pattern has maximum brightness and sharpness for orthogonal illumination, directly through the microscope objective (resulting in an image like in Figure 1C).

## 3 | VARIABILITY OF OPTICAL PATTERN AND UNIQUENESS OF BUTTERFLY WING-SCALES

In this section, we will establish a connection between the wing scale morphology and the resulting reflection spectrum. To do that, we have to make a numerical model, enabling us to calculate the reflection spectrum of a single wing scale, removed from the wing and attached to a transparent substrate (as in Figure 1C). For simplicity, each scale is represented by two, wavy thin plates, separated by the layer of air. To approximate waviness each scale is divided into a number of vertical sections with different positions

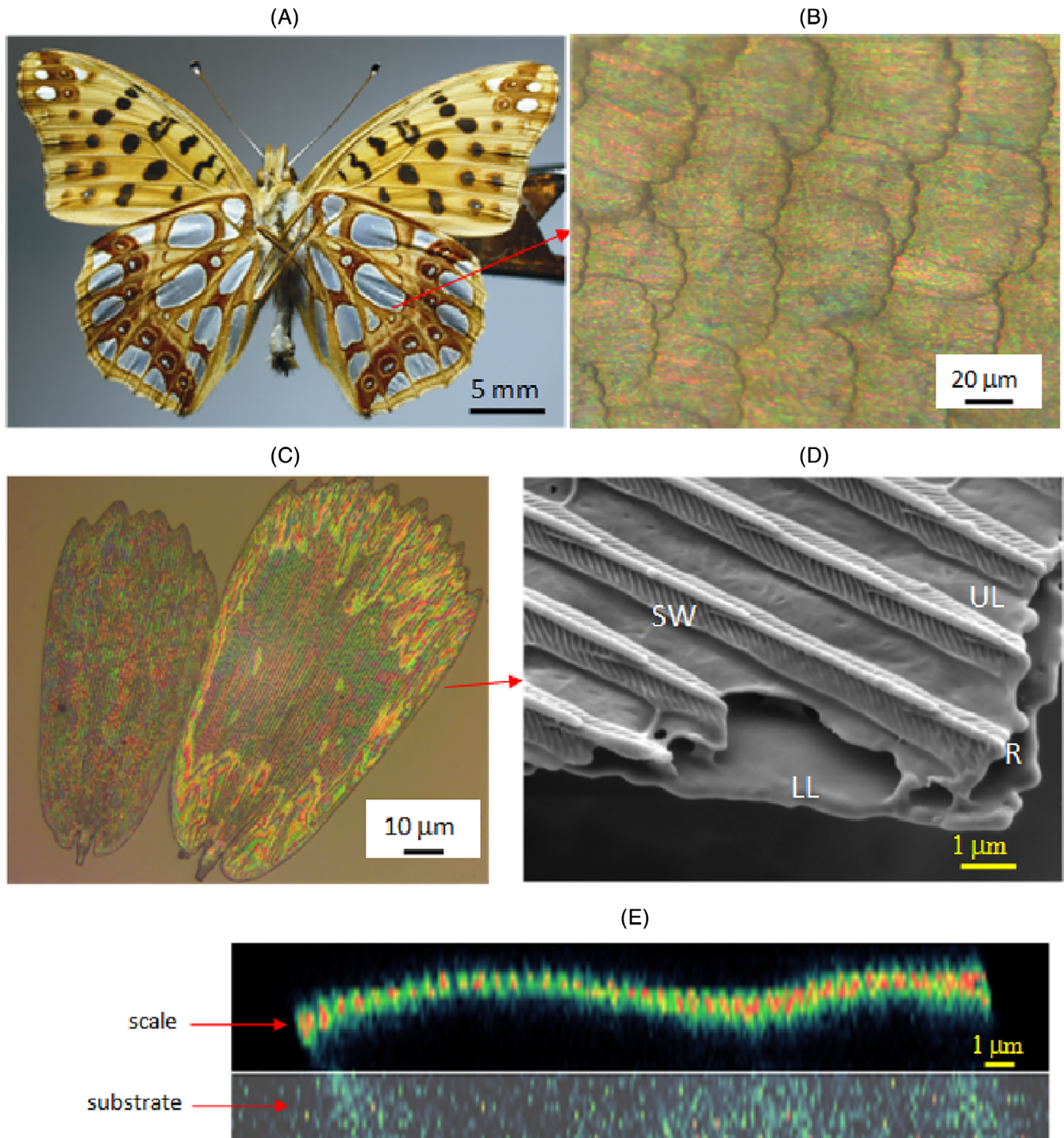


**FIGURE 1** A, Ventral side of *Issoria lathonia* butterfly. B, Reflection microscope (10 $\times$ , 0.25 NA) image of wing scales from the silver patch. C, Reflection microscope image (20 $\times$ , 0.4 NA) image of two isolated wing-scales, removed from the wing of *I. lathonia*. D Scanning electron microscope image of the *I. lathonia* wing scale. LL and UL are lower and upper lamina, respectively, R is a ridge, while SW is a, fishbone-shaped, sub-wavelength grating. E, Wavy cross-section of butterfly wing scale (as recorded on a nonlinear optical scanning microscope)

and thicknesses of layers (Figure 2A). Each section contains two layers of chitin, the first of which was regarded as a sub-wavelength scattering surface, due to its irregularity and presence of the subwavelength grating (Figure 1D). Both

layers are separated from the glass substrate by an additional air layer.

Reflection spectrum of each section was calculated using a transfer matrix method, modified to include the effects of

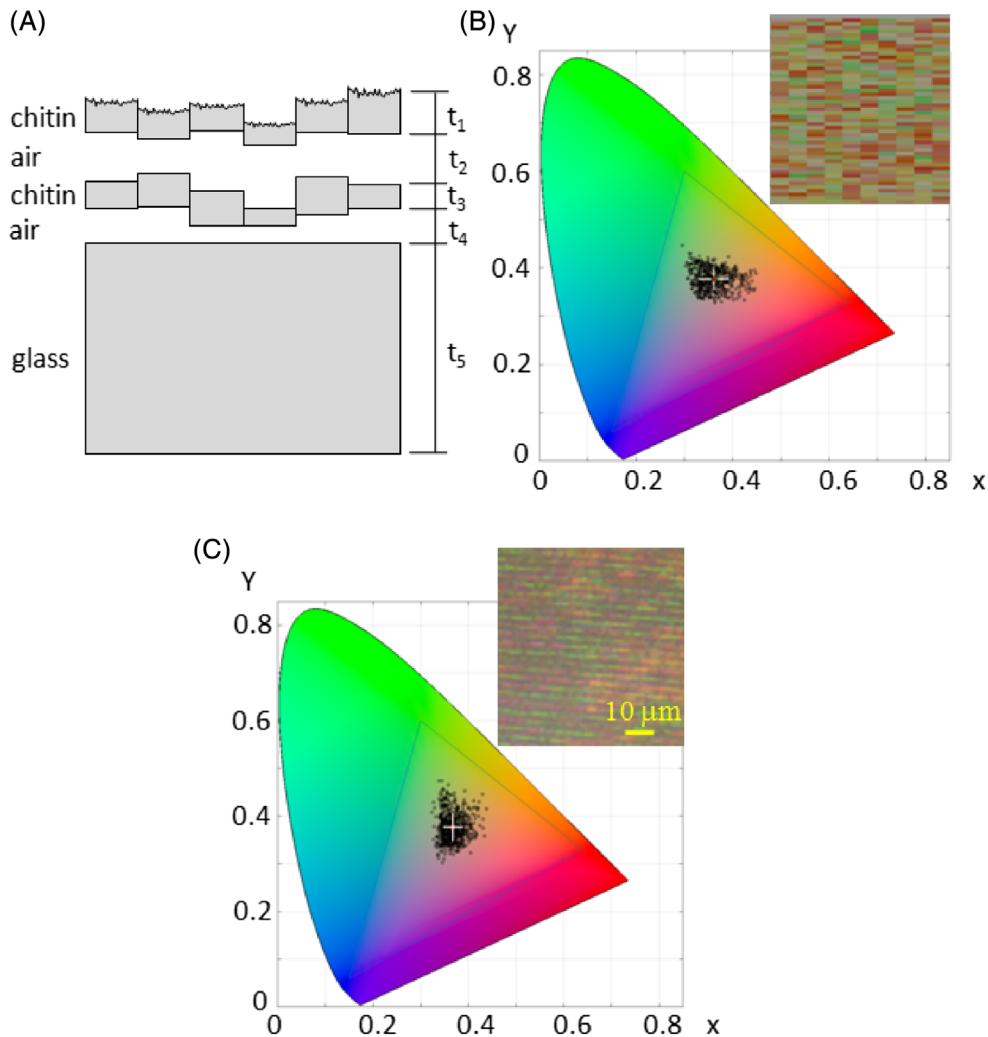


**FIGURE 2** A, A theoretical model of a wing scale on the glass substrate. B, Color coordinates of a modeled pattern are presented in a CIE 1931 diagram, together with the color pattern in the inset. C, Color coordinates of *Issoria lathonia* pattern are presented in a CIE 1931 diagram. A section of a *I. lathonia* wing scale pattern, used to calculate color coordinates, is presented in the inset. Crosses in B and C represent average color value and their lengths indicate SDs in  $x$ - and  $y$ -directions

scattering [14]. Layer thicknesses ( $t_1, t_2, \dots, t_5$  in Figure 2A) and their corresponding refractive indices were the parameters of the model, as well as the root mean square roughness (RMS) of the surfaces.

To simulate the wing scale as a whole, the same calculation was performed for each section. The starting point of our simulation was the layer thicknesses estimated from Figures 1D,E ( $\sim 100$  nm chitin,  $\sim 1000$  nm air layer thickness—see section 3 of Appendix S1 for the complete list of parameter values). Layer thicknesses were stochastically varied (according to normal distribution) with pre-defined SD  $\sigma = 15$  nm. Following the calculation of spectrum for each section,  $xyY$  color coordinates were calculated. They were presented in a CIE 1931 diagram (black dots in Figure 2B), which was designed to closely match human color perception (through three color-matching functions) [15]. It is, also, a useful tool to represent RGB values of color-camera images recorded through this research.

Calculated colors are, also, represented as a pattern of rectangular colored patches (see inset in Figure 2B). For

comparison, color coordinates of experimentally recorded pattern (inset in Figure 2C) were also computed and presented in CIE 1931 diagram (Figure 2C).

We were not able to obtain perfect match in CIE diagrams (Figures 2B,C), for the same reason which prevents a counterfeit to forge a wing scale—complexity of the problem. However, we were able to match the position of the mean color coordinate (small white crosses in CIE diagrams) of theoretical and experimental image. The shape of the color scattering distribution is different, but the SDs are similar.

The most important result is that the variation of layer thicknesses by only  $\pm 15$  nm leads to experimentally recorded variability of coloration. This means that one trying to copy the exact coloration pattern of the wing scale, has to maintain an extreme precision of manufacturing—at least one-tenth of the layer thickness variability ( $\sim 1.5$  nm). The task is well beyond practical limits of modern technology, and cellular noise precludes replication of identical wing-scales by natural means.



Wing-scales described above have a sufficient number of degrees of freedom (in terms of layer thicknesses and waviness) to enable significant variability. Here, we want to find how difficult would be to find two identical scales.

We first analyze the statistical properties of the wing-scales color patterns by decomposing an image into its RGB components and calculating two-dimensional (2D) autocorrelation function for each color channel separately—see details in section 4 of Appendix S1. It can be seen (Figure S1) that autocorrelation peak is asymmetrical, that is, its width along the wing-scale grating was estimated at 30  $\mu\text{m}$ , while in the orthogonal direction it is 1.5  $\mu\text{m}$ .

By taking into account that average dimensions of the scales are 50  $\times$  100  $\mu\text{m}$ , we can easily calculate that there are  $[50/1.5] \times [100/30] = 33 \times 3 = 99$  (numbers were rounded to the nearest integer) statistically independent, colored patches. We can discriminate intensity of a single color channel in, at least, 10 discrete levels—easily achievable for any low-cost or mobile phone camera. In that case, we may estimate that there are, at least theoretically,  $10^{99}$  wing-scales with different patterns per every channel. Thus, finding a scale exactly the same as another, previously chosen, one is impossible from any practical point of view.

Each wing-scale is a dead remnant of an individual cell and thus reflects intrinsic randomness of cellular development. This is a natural consequence of cellular noise [16], which is a well-established fact in biology, resulting in non-deterministic relation between genotype and phenotype. The important thing about butterfly wing scales is that they “freeze” the cellular noise, by leaving it in a state just before the cell died. Cellular noise cannot be switched-off and it is expected to be similar in all other butterfly species. In that sense, the similar level of randomness is expected on all wing-scales of all butterflies [17] including those of the *Issoria lathonia* species.

## 4 | OPTICAL DOCUMENT PROTECTION WITH WING SCALES

The main idea of this research is to use butterfly wing-scales as a natural, hologram-like, OVDs, permanently attached to a document (eg, a plastic credit card). In contrast to artificial OVDs, natural ones are unique (guaranteed by the cellular noise) and difficult to copy (due to their layered, micro- and nano-scale patterns).

We decided to use a near-field color pattern as a security feature of a document protection system and read it under the optical microscope. Practical inability to place a document at exactly the same position and orientation within the reading system requires shift- and rotation-invariant pattern recognition algorithm. We decided to use algorithm based

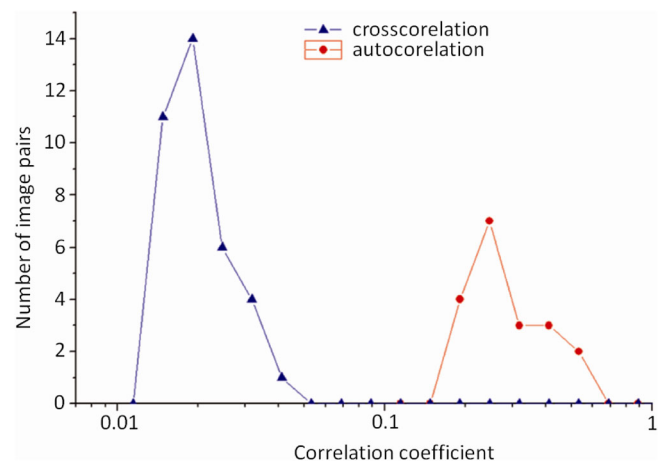
on Fourier-Mellin transform (FMT) [18] which fulfills the above requirements.

Nine *I. lathonia* wing-scales were attached to a glass substrate and their reflection microscope images were recorded at several positions and orientations (55 images in all). The recorded images were first decomposed into RGB components and the green one (G) was transformed using FMT. Correlations between corresponding FMT pairs were calculated and the corresponding statistical distribution is shown in Figure 3. The correlation coefficient, corresponding to the same wing-scale at displaced positions, had typical values around 0.4, while it never had values below 0.1. The most frequent values of correlation coefficient for two different wing-scales were around 0.02, and were never larger than 0.06. By placing validity threshold at 0.08, correct discrimination between wing scales is guaranteed.

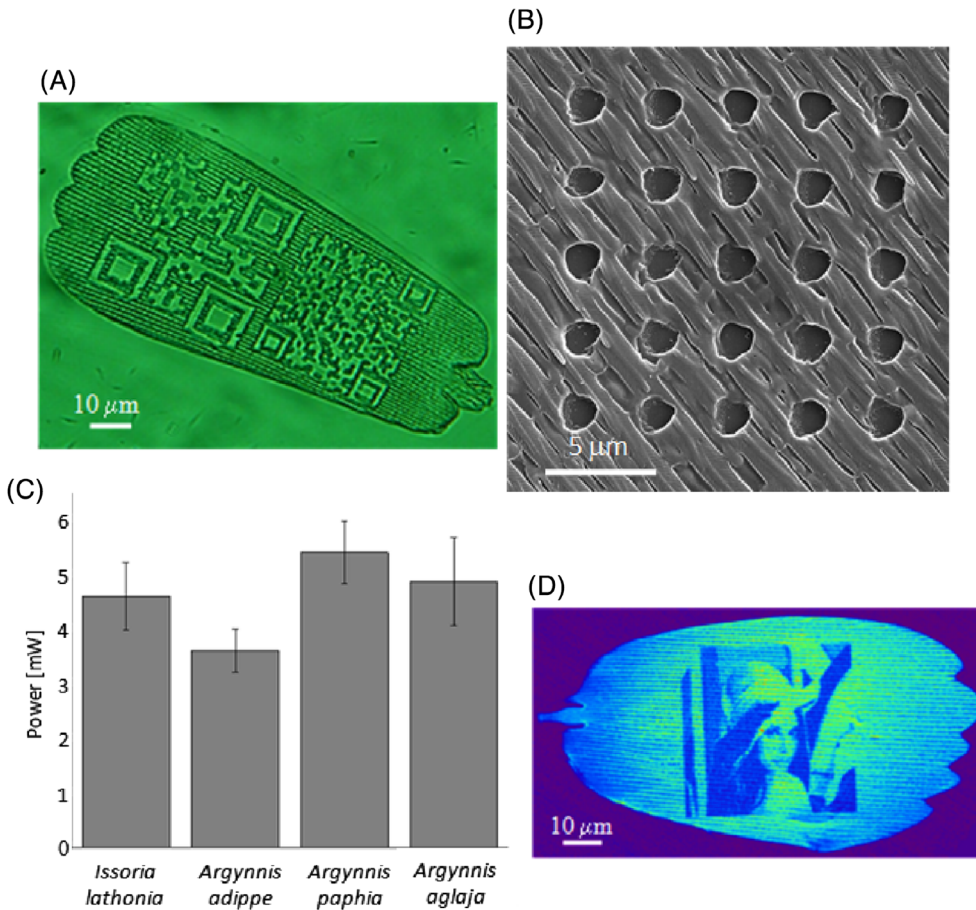
To correct for accidental tilt or defocusing of the wing scale image, we have recorded images at 3 to 4, closely spaced, focal positions. Consequently, focus stacking algorithm was used (using Picolay free software) to extract well-focused parts in each recorded image and combine them in a single, sharp image.

In order to build a strong security system, malicious party has to be prevented from picking any butterfly wing-scale and attaching it to a document. This can be performed by making a document self-verifying by using a digital signature of the document issuer, within the public key infrastructure (PKI) system [19]. Here, we show that the necessary authentication information can be written on the wing-scale itself.

We used femtosecond laser-processing to additionally modify butterfly wing scales and exploit them as a write-



**FIGURE 3** Cross- and auto-correlations of ensemble of 55 pairs of wing-scale images. Graph shows a number of image pairs vs the corresponding correlation coefficient. Maximum cross-correlation coefficient is at 0.02, while autocorrelation coefficient is always above 0.2

**FIGURE 4**

(A) Transmission microscope image of a femtosecond-laser-cut wing scale (QR-codes). (B) Array of holes on a *Issoria lathonia* wing-scale showing the minimum achievable diameter of a laser cut. (C) Thresholds for laser cutting of four butterfly species used throughout this research. (D) Selectively bleached wing scale with a Lena image observed by fluorescence modality of a nonlinear microscope

only memory. The software of a home-made nonlinear-microscope [13] was modified to enable vector and raster drawing of an arbitrary image (see section 5 of Appendix S1 for additional details). Depending on the average laser power, repetition rate and dwell time, wing scale can be cut (as in Figure 4A)). Minimal diameter of a laser cut achieved throughout this research is  $1.7 \mu\text{m}$ , as shown in Figure 4B. Damage threshold is  $4.5 \text{ mW}$  (using  $40 \times 1.3 \text{ NA}$  microscope objective) and  $8.0 \text{ mW}$  (with  $20 \times 0.8 \text{ NA}$  microscope objective). Three more butterfly species were analyzed in that respect, with similar damage thresholds (Figure 4C). In practice, we operated above threshold to enable reliable and repeatable laser-drawing. That is why we achieved the minimum cut width which is considerably above the lateral resolution of our femtosecond system [13]. Based on that and the average size of the wing-scale ( $\sim 50 \times 100 \mu\text{m}^2$ ), we estimated the information capacity of a single scale at about 3000 bits, providing that the damaged spot is treated as binary 1, and undamaged as binary 0.

Here, we point out that each bit, written on the wing-scale, reduces the number of statistically independent patches. We will assume that one half of the wing-scale surface is laser processed (reducing the original wing-scale area of  $50 \times 100 = 5000 \mu\text{m}^2$  to approximately  $35 \times 70 = 2450 \mu\text{m}^2$ ). That leaves approximately  $[35/1.5] \times [70/30] = 23 \times 2 = 46$  colored patches

(numbers are, again, rounded to the nearest integer). Thus, as in the previous section, we may estimate the number of different wing scales at  $10^{46}$  (per every RGB channel), each one being protected by 1500 bits of additional information.

By reducing the laser power below the damage threshold, we were able to bleach the autofluorescence of the wing-scale and use it to inscribe covert information (Figures 4D) as a gray level image.

## 5 | DISCUSSION AND CONCLUSIONS

While speaking of document protection, an important question immediately comes to mind: how difficult it is to counterfeit wing-scale? Forgeries can be produced by either (a) imitating the structure or (b) imitating the corresponding optical effect with another, possibly simpler, structure. The first approach is based on “reverse-engineering” and manufacturing of identical protective element structure, while the second one is based on imitating the optical effect.

Reverse engineering of butterfly wing-scales implies analysis of the 3D morphology and material properties (refractive index and absorption) followed by some-kind of lithographic copying of both the morphology and material properties. Even with the most advanced technologies

(microtomography, electron or X-ray holography), this approach will be extremely limited in terms of available resolution of 3D analytic and lithographic methods (of the order of 10 nm), duration and cost [20].

Imitating the optical effect requires careful analysis of iridescence across the whole visible spectrum and angular range, followed by finding a method to faithfully reproduce the optical wavefront. This also poses a fundamental question: is it possible to have identical wave-fields generated by different structures? The question goes into scattering theory, with a plethora of papers dealing with the uniqueness of the direct and inverse problems. There is no general answer to the question, because it depends on the nature of the scatterer (penetrable or non-penetrable), boundary conditions (conductive, dielectric, amplifying), wavelength and angular range of probing radiation [21]. There are more or less exotic situations where uniqueness is not guaranteed, such as amplifying medium or medium with optical cloaks [22]. But, for the range of problems relevant to this work, the answer is no—there are no two different scatterers producing the same scattered field (far or near) [23].

The wing-scales are best protected by their uniqueness implying necessity to counterfeit every single document time and again. Another point is that, both the material composition and morphology are unique, producing a plethora of optical effects: overall shape, iridescence, absorption, polarization, fluorescence, moiré, defects, far and near-field diffraction pattern, local spectra, etc. In addition, scales possess different optical properties on their upper and under side, which may be used to produce security features which can be read from both sides in perfect alignment (so-called see-through register). Simultaneous use of all or some of the mentioned effects vastly increases the capabilities of wing scale as a protective element.

An important question is whether wing scales can be copied by some of holographic methods. Up to now, volume and surface relief holograms have been copied using contact [24], non-contact [25] or scanning [26] methods. However, these techniques are not useful for copying step-index, layered structure of wing scales, because of the sinusoidal nature of holographic gratings. Additionally, subwavelength gratings of wing-scales ( $S$  in Figure 3) cannot be copied, due to evanescent fields obtained by diffraction. These tiny structures are essential for the final coloration of the wing scale, because they produce uniformly scattered radiation in the blue part of the spectrum (see blue component of the wing scale pattern in Figure 8A).

It should be emphasized that Lepidoptera species are not equally suitable for document protection. As already mentioned, these structures must have complex nanometer to micron-size features, with significant variability and must be difficult to analyze and reverse engineer. We preferred

nymphalid species, possessing silver patches on their wings. Other Lepidoptera species, with structurally colored scales have been tested. However, the scales of these species were not so easy to process and manipulate, with the equipment at our disposal.

There is a number of ways how insect scales can be manipulated and attached to documents, as described in the following patent applications [27–29]. Generally speaking, they have to be, either embedded within the transparent medium with large refractive index difference (compared to that of the scale), or placed in a recess with a transparent, protective, covering. The procedure can be performed by micromanipulation or by standard printing techniques (silk-screen, flexo-printing).

Once embedded, scale contents have to be read by some means, which depends on the insect species, type of the scales and the optical effect sought for. In addition to iridescence pattern detection described above, there are other choices: overall shape of the scale, near field color pattern, far-field diffraction pattern, moiré pattern, or pattern of defects (looking like minutia in a fingerprint), with many variations (such as phase and amplitude) and combinations (by recording simultaneously several effects). Reading devices can be based on far- or near-field detection, holography or scanning techniques using CD/DVD readout heads. In the context of document protection, strong variability of patterns with angular position of illumination and observation, as well as the polarization sensitivity are very important. This is what prevents malicious attacks by simple color laser-printing.

The document protection described here is limited to machine reading level. It can be extended to the forensic level, by reading electron microscope image (Figure 1D)), with, for example, cross-rib distances serving as a random feature. If visual protection is desired, a large number of scales can be transferred to another substrate, so to cover large area, visible with the naked eye. One of the scales can be chosen for machine and forensic protection, as described in Reference [28].

Practical implications of the proposed document protection method are numerous. There are thousands of wing scales on a single butterfly specimen suitable for document protection (we have estimated 40 000 iridescent wing scales on *I. lathonia* silver spots). With appropriate choice of butterfly species (eg, *Morpho* spp.) this number can be much larger. If commercially available dry butterfly specimens are used, we have estimated the cost of a single wing scale at  $85 \cdot 10^{-6}$  \$. Alternatively, butterfly species can be reared using well-established techniques of sericulture (silkworm raising). Wing-scales can be collected cheaply and applied using any of standard printing techniques (silk-screen, offset, ink-jet). Range of applications is huge: banknotes, credit-

cards, CD/DVDs, bonds, valuable goods. It is not even hard to imagine using wing-scales as a hardware lock for digital information security.

The base material of wing-scales is chitin, which is extremely and verifiably durable. Natural history museums have century-old butterfly specimens retaining their structural coloration and we have more than 30 years old specimens of *I. lathonia* with silver patches as shiny as in live insects. Even more, fossilized insects retain their iridescence after petrification and last for millions of years [30]. This should be compared to, recently described, five-dimensional optical memory [31], claiming “seemingly unlimited lifetime.”

Wing scales may reversibly change their dimensions in response to temperature variation [32], humidity and vapors [33]. As a consequence, there is a slight spectral shift, but it is too small to affect application of wing scales in document security, under normal atmospheric conditions. Systematic changes during extended periods of time are not expected due to hydrophobicity, insolubility and biological inertness of wing-scales [34]. However, we have not measured the long-term stability of wing scale patterns, we plan to perform accelerated aging tests in the near future and reveal details regarding the effect of aging on pattern stability.

Anyway, the validity period of most documents is less than 10 years, a period during which wing scales are expected to remain unaffected. Furthermore, taking into account the chemical and physical stability of chitin and the fact that optical response of the insects a hundred and more centuries-old (from museum) and from fossil samples exhibit extraordinary similarity with visual response measured from “the fresh” samples, suggest that corresponding patterns are very stable and could have long-term cryptographic applications.

## ACKNOWLEDGMENTS

We express our gratitude to the Ministry of Education, Science and Technological Development of the Republic of Serbia for supporting this research through the projects Nos. III45016, III43002, ON171038, ON173038, ON171017, ON171032 and by the Science and Technology Development Programme—Joint Funding of Development and Research Projects of the Republic of Serbia and the People's Republic of China: Mimetics of insects for sensing and security, No. I-2. This work was also partially supported by the projects: No 451-03-01038/2015-09/1 of bilateral collaboration program between Ministry of Education, Science and Technological Development of the Republic of Serbia and German Academic Exchange Service (DAAD); by the project: “Upscaling Teslagram technology based on variable and complex biological structures for security printing,” funded by the Innovation Fund of the Republic of Serbia.

B.K. warmly acknowledges the assistance of Ms. Bojana Bokic, Institute of Physics, University of Belgrade in design of graphical abstract for this publication.

## CONFLICT OF INTEREST

Institute of Physics Belgrade is the applicant and the owner of three pending patent applications given in a list of references [27–29] whose contents is partially described in this paper. Five authors (D.V.P., D.P., M.D.R., V.L. and A.J.K.) are also authors of abovementioned patent applications. Specific aspects of manuscript covered in patent applications are: laser cutting and bleaching of wing scales, as well as a partial list of butterfly species usable for this purpose.

## AUTHOR CONTRIBUTIONS

D.V.P. conceived the idea; M.D.R., A.J.K. and D.V.P. have constructed the nonlinear microscope used in this research. D.P., A.J.K., M.D.R. and V.L. performed experiments and measurements. D.V.P. designed an optical model of wing-scales, while N.V. and D.S. performed the theoretical analysis of uniqueness of butterfly wing-scales. B.J. D. Z., W. Z. and B. K were included in data analysis and supervised the research. D.S., S.Ć and D.P. made adequate choice of appropriate butterfly species used in this research, while D.V.P., D.P. and M.D.R. prepared the manuscript, based on comments of other authors. This work is performed in partial fulfillment of the requirements for the PhD degree of Vladimir Lazović at the University of Belgrade, Faculty of Physics. All authors gave final approval for publication and agree to be held accountable for the work performed therein.

## ETHICAL STANDARDS

Insects used in this research are NOT on the list of strictly protected and protected species defined in: By-law on proclamation and protection of strictly protected and protected wild species of plants, animals and fungi, Official gazette of the Republic of Serbia Nos. 5/2010 and 47/2011. All experiments were performed on dry specimens from the collection of Dejan Stojanović. The research did not include live insects.

## ORCID

Branko Kolarić  <https://orcid.org/0000-0003-0203-7897>

## REFERENCES

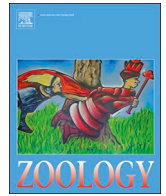
- [1] G. F. Robert, P. H. Adler, *Insect Biodiversity, Science and Society*, Chichester, UK: Willey-Blackwell, 2009.

- [2] X. Zhou, S. W. Applebaum, M. Coll, *Environ. Entomol.* **2000**, 29, 1289.
- [3] S. M. Doucet, M. G. Meadows, *J. R. Soc. Interface* **2009**, 6, S115.
- [4] W. Zhang, J. Gu, Q. Liu, H. Su, T. Fan, D. Zhang, *Phys. Chem. Chem. Phys.* **2014**, 16, 19767.
- [5] E. P. Newman, *Proc. Am. Philos. Soc.* **1971**, 115, 341.
- [6] R. L. Van Renesse, *Optical document security*, 3rd ed. Norwood, MA: Artech House, **2004**.
- [7] R. Pappu, B. T. J. Recht, N. Gershenfeld, *Science* **2002**, 297, 2026.
- [8] J. D. R. Buchanan et al., *Science* **2005**, 436, 475.
- [9] Hamm-Dubischar, C. Patent No. WO 2007031077 (A1), Inorganic marking particles for characterizing products for proof of authenticity method for production and use thereof (**2007**).
- [10] Biermann, N. & Rauhe, H., Method for Producing Security Markings. WO2004070667 A2 (**2004**).
- [11] Rauhe, H., Verfahren zur Herstellung von informationstragenden mikropartikelären Gemischen. Patent DE10238506 A1 (**2004**).
- [12] P. Vukusic, R. Kelly, I. Hooper, *J. Roy. Soc. Interface* **2009**, 6, S193.
- [13] D. M. Rabasović et al., *J. Biomed. Opt.* **2015**, 20(016010), 1.
- [14] D. Pantelić, S. Savić-Šević, D. V. Stojanović, S. Čurčić, A. J. Krmpot, M. Rabasović, D. Pavlović, V. Lazović, V. Milošević, *Phys. Rev. E* **2017**, 95, 032405.
- [15] J. e. Schanda, *Colorimetry: Understanding the CIE System*. Hoboken, NJ: John Wiley & Sons, **2007**.
- [16] I. G. Johnston et al., *PLoS Comput. Biol.* **2012**, 8, e1002416:1.
- [17] A. Dinwiddie, R. Null, M. Pizzano, L. Chuong, A. Leigh Krup, H. Ee Tan, N. H. Patel, *Dev. Biol.* **2014**, 392, 404.
- [18] J. Wood, *Pattern Recog.* **1996**, 29, 1.
- [19] L. O'Gorman, I. Rabinovich, *IEEE Trans. Pattern Anal. Mach. Intell.* **1998**, 20, 1097.
- [20] K. Watanabe, T. Hoshino, K. Kanda, Y. Haruyama, T. Kaito, S. Matsui, *J. Vac. Sci. Technol. B* **2005**, 23, 570.
- [21] D. Colton, R. Kress, *Inverse Acoustic and Electromagnetic Scattering Theory*, 2nd ed. New York, NY: Springer, **1998**.
- [22] F. Monticone, A. Alu, *Phys. Rev. X* **2013**, 3(041005), 1.
- [23] G. Bao, P. Li, J. Lin, F. Triki, *Inverse Probl* **2015**, 31, 093001.
- [24] S. Toxqui-López, A. Olivares-Pérez, I. Fuentes-Tapia, A. Quintero-Romo, *Opt. Mater.* **2007**, 29, 1604.
- [25] B. D. Chrysler, R. K. Kostuk, *Appl. Optics* **2018**, 57, 8887.
- [26] M. Okui, K. Wakunami, R. Oi, Y. Ichihashi, B. J. Jackin, K. Yamamoto, *Appl. Optics* **2018**, 57, 4117.
- [27] Pantelic, D., Rabasovic, M., Krmpot, A., Lazovic, V. & Pavlovic, D., Security device individualized with biological particles. PCT/EP2015/081398 (**2015**).
- [28] Pantelic, D., Rabasovic, M., Krmpot, A., Lazovic, V. & Pavlovic, D., Security tag containing a pattern of biological particles. PCT/EPO2015/081400 (**2015**).
- [29] Pantelic, D., Rabasovic, M., Krmpot, A., Lazovic, V. & Pavlovic, D., Security tag with laser-cut particles of biological origin. PCT/EP2015/081407 (**2015**).
- [30] M. E. McNamara et al., *PLoS Biol.* **2011**, 9, e1001200:1.
- [31] J. Zhang, M. Gecevičius, M. Beresna, P. G. Kazansky, *Phys. Rev. Lett.* **2014**, 112, 033901.
- [32] A. D. Pris, Y. Utturkar, C. Surman, W. G. Morris, A. Vert, S. Zalyubovskiy, T. Deng, H. T. Ghiradella, R. A. Potyrailo, *Nat Photon* **2012**, 6, 195.
- [33] R. A. Potyrailo, H. Ghiradella, A. Vertatchikh, K. Dovidenko, J. R. Cournoyer, E. Olson, *Nat photonics* **2007**, 1, 123.
- [34] H.-M. Hu, J. A. Watson, B. W. Cribb, G. S. Watson, *Biofouling* **2011**, 27, 1125.

## SUPPORTING INFORMATION

Additional supporting information may be found online in the Supporting Information section at the end of this article.

**How to cite this article:** Pavlović D, Rabasović MD, Krmpot AJ, et al. Naturally safe: Cellular noise for document security. *J. Biophotonics*. 2019; e201900218. <https://doi.org/10.1002/jbio.201900218>



## Chemistry and morphology of the pygidial glands in four Pterostichini ground beetle taxa (Coleoptera: Carabidae: Pterostichinae)

Sofija Vranić<sup>a</sup>, Srećko Ćurčić<sup>a</sup>, Nikola Vesović<sup>a</sup>, Boris Mandić<sup>b</sup>, Dejan Pantelić<sup>c</sup>, Marija Vasović<sup>a</sup>, Vladimir Lazović<sup>c</sup>, Wang Zhang<sup>d</sup>, Ljubodrag Vujisić<sup>b,\*</sup>

<sup>a</sup> Institute of Zoology, University of Belgrade - Faculty of Biology, Studentski Trg 16, 11000 Belgrade, Serbia

<sup>b</sup> University of Belgrade - Faculty of Chemistry, Studentski Trg 12-16, 11000 Belgrade, Serbia

<sup>c</sup> University of Belgrade - Institute of Physics, Pregrevica 118, 11080 Belgrade, Zemun, Serbia

<sup>d</sup> State Key Laboratory of Metal Matrix Composites, Shanghai Jiao Tong University, Dongchuan Road 800, 200240 Shanghai, China

### ARTICLE INFO

#### Keywords:

ground beetles  
Pterostichini  
pygidial glands  
gas chromatography-mass spectrometry  
morphology

### ABSTRACT

Morphology of the pygidial glands and chemical composition of their secretions in adults of four ground beetle representatives of the Pterostichini tribe (Coleoptera: Carabidae) were analysed. *Molops (Stenochoromus) montenegrinus*, *Pterostichus (Cophosus) cylindricus*, *P. (Feronidius) melas* and *P. (Pseudomaseus) nigrita* were chemically tested, while the latter three species were morphologically investigated. *Pterostichus (C.) cylindricus*, *P. (P.) nigrita* and *M. (S.) montenegrinus* were chemically studied for the first time. Altogether, 23 chemical compounds were isolated using gas chromatography-mass spectrometry (GC-MS), of which some are new for Pterostichini or even Carabidae. Methacrylic acid was present in all species analysed. It was predominant in the secretion extract of *P. (C.) cylindricus* and *P. (F.) melas*. Isobutyric and 2-methylbutyric acids were the major components in the secretion of *M. (S.) montenegrinus*. Undecane, methacrylic and tiglic acids were the main components in the secretion of *P. (P.) nigrita*. The simplest chemical mixture was found in *P. (C.) cylindricus* (two compounds), while the most complex one was detected in *P. (P.) nigrita* (15 compounds). No significant differences in the chemical composition of the pygidial gland secretions were evidenced in *P. (C.) cylindricus* sampled from the same area and in the same season in two different years. Morphology of the pygidial glands of the studied species was analysed for the first time. Morphological features of the pygidial glands were observed using bright-field microscopy and nonlinear microscopy and described in details.

### 1. Introduction

A great number of insect species use chemical defense (Dossey, 2011; Unkiewicz-Winiarczyk and Gromysz-Kałkowska, 2012; Gregorovičová and Černíková, 2015). All ground beetles (Carabidae) possess a pair of abdominal pygidial defensive glands, which are very similar among species in terms of general appearance. Each pygidial gland consists of secretory lobes, a collecting canal, a reservoir and an efferent duct (Forsyth, 1972). Morphology of these glands has been studied by several authors so far (Forsyth, 1970, 1972; Kanehisa and Shiraga, 1978; Bonacci et al., 2011; Di Giulio et al., 2015; Vesović et al., 2017; Muzzi et al., 2019; Vesović, 2019). Ground beetles can discharge their pygidial gland secretions in three ways: by oozing, spraying or crepitation (Moore, 1979). Chemical composition of secretions produced by these glands can differ between species considerably (Moore, 1979; Blum, 1981). All chemical compounds secreted by Carabidae can

be sorted into the following nine major groups: hydrocarbons, aliphatic ketones, saturated esters, formic acid, higher saturated fatty acids, unsaturated carboxylic acids, phenols, aromatic aldehydes and quinones (Moore, 1979; Will et al., 2000; Giglio et al., 2011). Recently, a sulfur-bearing isoprene derivative, 3-methyl-1-(methylthio)-2-butene, was reported for the first time in ground beetles in two species of the South American genus *Ceroglossus* Solier, 1848 (Xu et al., 2019).

A common feature of most of these compounds that are produced and released from the pygidial glands of ground beetles is, generally speaking, a negative sensory sensation in potential predators, and therefore their primary function is considered to be allomonic (Blum, 1981; Lečić et al., 2014; Vesović et al., 2017).

The pygidial gland secretions of ground beetles, as one of many natural products of insects that are subjects of scientific studies in the last few decades, might have multiple applications in biomedicine, while the structure of pygidial glands and mechanisms that stand

\* Corresponding author.

E-mail address: [ljubaw@chem.bg.ac.rs](mailto:ljubaw@chem.bg.ac.rs) (L. Vujisić).

<https://doi.org/10.1016/j.zool.2020.125772>

Received 1 November 2019; Received in revised form 20 February 2020; Accepted 22 February 2020

Available online 24 March 2020

0944-2006/ © 2020 Elsevier GmbH. All rights reserved.

behind discharge of the secretions can be used in the future pioneering biomimetic studies (Vesović, 2019).

Analyses of chemical composition of the pygidial gland secretions of European Pterostichinae were firstly conducted by Schildknecht and Weis (1962) and Schildknecht et al. (1964, 1968), who reported methacrylic and tiglic acids, as well as unidentified alkanes for 13 species of Pterostichini and two species of Zabrinini. A few years later, Schildknecht (1970) identified those alkanes as *n*-decane, *n*-undecane and *n*-tridecane. Balestrazzi et al. (1985) analysed *Pterostichus (Oreophilus) externepunctatus* (Dejean, 1828) and identified isobutyric and methacrylic acids, *n*-undecane and *n*-tridecane in the pygidial gland secretion. It has been almost 30 years since these pioneering studies with no refreshed data and publications on chemicals released by the pygidial glands of European Pterostichini. Then Lečić et al. (2014) reported isobutyric, crotonic, senecionic and propionic acids, in addition to dominant methacrylic and tiglic acids (previously reported by Schildknecht and Weis, 1962), in the pygidial gland secretion of *Abax (Abax) parallelepipedus* (Piller & Mitterpacher, 1783). Meanwhile, knowledge on pygidial gland chemicals has increased for non-European pterostichine taxa, mainly Japanese (Kanehisa and Murase, 1977) and North American (Attygalle et al., 2007).

Morphology of the pygidial glands and chemical composition of their secretions in the representatives of the tribe Pterostichini (Carabidae: Pterostichinae) have not been studied in detail so far. There are only a few studies dealing with morphology of the pygidial glands of European species of Pterostichinae. The most complete, a fully dedicated analysis is conducted by Forsyth (1970), in which all morpho-anatomical and histological aspects of these glands were presented on the example on *Pterostichus (Steropus) madidus* (Fabricius, 1775). Some of the later publications dealt more marginally with the morphological structure of the pygidial glands of European pterostichines (Forsyth, 1972; Dazzini Valcurone and Pavan, 1980; Balestrazzi et al., 1985; Vesović, 2019).

Bright-field microscopy (BFM) is most often used to study insect morphology, but recently nonlinear microscopy (NLM) has also been introduced as a method offering unique insight into a variety of biological structures (Vrbica et al., 2018). The latter method was rarely used in entomology in the past. It was recently confirmed that NLM can be used for deep imaging of chitinous structures in insects, including ground beetles (Rabasović et al., 2015), while only one study dealt with the anatomy of ground beetles (Vrbica et al., 2018). While giving microscopic images similar to confocal laser scanning microscopy (CLSM), NLM has several advantages. The most important fact is that the radiation used for excitation is mostly in the near-infrared (NIR) part of the spectrum, where the absorption and scattering are reduced. This increases penetration depth and reduces radiation bleaching and damage of the sample. With respect to CLSM, which is capable of observing only fluorescence (autofluorescence), NLM offers additional modalities of second and third harmonic excitation, giving additional information about noncentrosymmetric molecular structure and refractive index gradients. As a bonus, femtosecond radiation used in NLM can be used for precise cutting of entomological samples in order to reveal their internal structure. For these reasons, we decided to analyse four Pterostichini taxa chemically and three of those morphologically (using BFM and NLM). *Molops (Stenochoromus) montenegrinus nivalis* (Apfelbeck, 1890) is an endemic subspecies which inhabits high-altitude habitats in Montenegro and Bosnia and Herzegovina (Fig. 1A); *Pterostichus (Cophosus) cylindricus* (Herbst, 1784) inhabits moist to moderate moist leaf-litter in forests of lowlands in southeastern, eastern and central Europe (Fig. 1B); *P. (Feronidius) melas melas* (Creutzer, 1799) has similar habitat preferences as the former species and inhabits somewhat wider area in Europe than the preceding one (Fig. 1C); *P. (Pseudomaseus) nigrita nigrita* (Paykull, 1790) is a Palaearctic taxon which can be found almost everywhere in Europe, in shaded lowlands and hills, near rivers and in other moist habitats (Fig. 1D) (Trautner and Geigenmüller, 1987; Hürka, 1996).

Morphology of the pygidial glands of the mentioned taxa has not been studied so far. Chemical analyses previously conducted by Schildknecht et al. (1968) for *Pterostichus (Feronidius) melas* (Creutzer, 1799) are incomplete due to a low sensitivity of the formerly used techniques, while the three remaining pterostichine taxa have not been studied in terms of the chemical ecology. Our aims are: (i) to determine the chemical composition of the pygidial gland secretions of four Pterostichini taxa; and (ii) to characterize the pygidial glands of studied ground beetle taxa morphologically.

## 2. Materials and methods

### 2.1. Collection and handling of ground beetle specimens

Adult individuals of four taxa were collected manually at several locations both in Serbia and Montenegro. Two specimens of *Molops (Stenochoromus) montenegrinus* (Miller, 1866) were collected under stones on 28<sup>th</sup> June 2014 by S. Čurčić and D. Antić at 2,100 m a.s.l., at Sedlo pass, Mt. Durmitor, northern Montenegro. Individuals of *P. (C.) cylindricus* and *P. (F.) melas* were collected from leaf-litter on 15<sup>th</sup> April 2018 (three specimens of the former taxon and nine specimens of the latter taxon, leg. S. Čurčić, N. Vesović and M. Vasović) and individuals of the former species were additionally collected on 22<sup>nd</sup> April 2019 (two specimens, leg. S. Čurčić and S. Vranić) at the Čarapićev Brest site, village of Beli Potok, Mt. Avala, central Serbia, at 310 m a.s.l. Three specimens of *Pterostichus (Pseudomaseus) nigrita* (Paykull, 1790) were collected under stones on 14<sup>th</sup> April 2018 by N. Vesović on the embankment of the Sava River, Novi Beograd, central Serbia, at 71 m a.s.l.

The collected ground beetles were stored in laboratory-controlled conditions in a portable plastic climate chamber for a few days until further analyses. These conditions included constant temperature (10 °C) and presence of moisture. Moist soil was gathered from the collecting site. Water was sprayed into the chamber occasionally to maintain a high level of humidity. The insects were fed on earthworms.

### 2.2. Chemical extraction

Gas chromatography-mass spectrometry (GC-MS) sample preparation was performed in the laboratory at room temperature. Specimens of each ground beetle taxon analysed were milked into a 12-ml glass vial with dichloromethane (0.5 ml) (Merck, Darmstadt, Germany). The beetles were forced to discharge pygidial gland secretions by squeezing their abdominal tips. To avoid oxidation and degradation of compounds, a portion of the extracts was subjected to GC-MS analysis immediately after preparation.

### 2.3. Chemical analyses

A 7890A GC system equipped with a 5975C inert XL EI/CI mass selective detector (MSD) and a flame ionization detector (FID) (Agilent Technologies, Santa Clara, USA), connected by capillary flow technology through a two-way splitter, were used for analyses. A polar HP-INNOWax capillary column (30 m length, 0.32 mm inner diameter, 0.25 µm film thickness) (Agilent Technologies, Santa Clara, USA). The GC and GC-MS analyses were performed in splitless mode. The injection volume was 1 µl, the injector temperature was 220 °C and the transfer line temperature was 280 °C for all analyses. The carrier gas (He) flow rate was 2.0 ml min<sup>-1</sup> at 40 °C (constant pressure mode), and the column temperature was programmed linearly in the range of 40–240 °C at a rate of 10 °C min<sup>-1</sup>, with a final 10-min hold. The FID temperature was 300 °C. EI mass spectra (70 eV) were acquired in the range of 40–550 m/z, the ion source temperature being 230 °C, the quadrupole temperature was 150 °C, and solvent delay was 3.5 min for all analyses.

Library search and mass spectral deconvolution and extraction were performed using the NIST AMDIS (Automated Mass Spectral

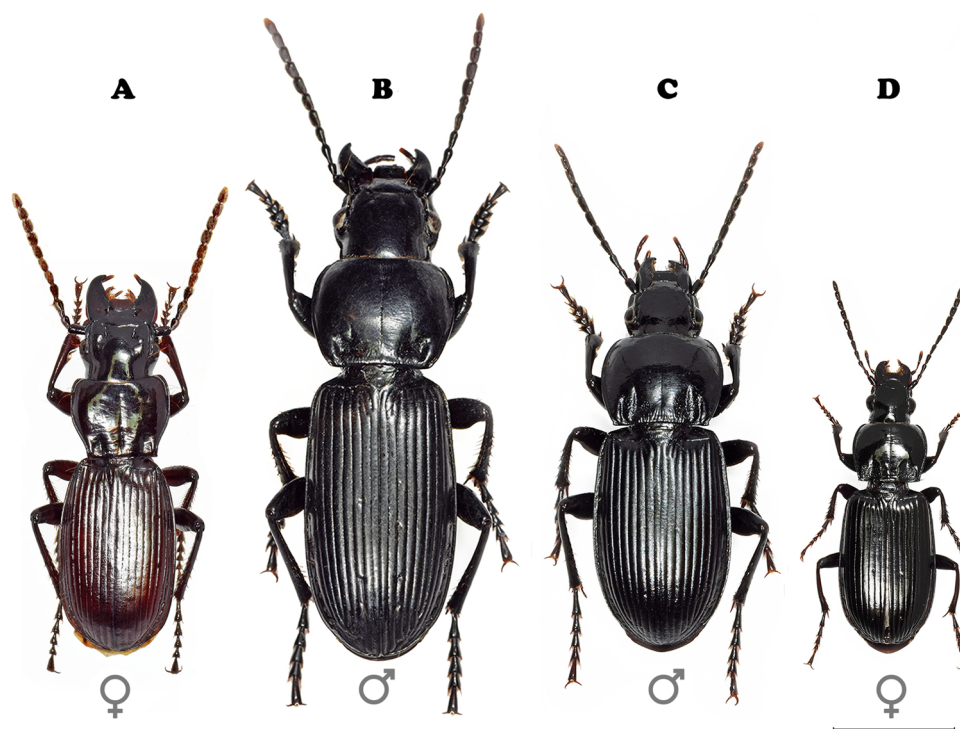


**Fig. 1.** Habitus (dorsal view) of the adult specimens of four analysed Pterostichini taxa: A – *M. (S.) montenegrinus*; B – *P. (C.) cylindricus*; C – *P. (F.) melas*; D – *P. (P.) nigrita*. Scale = 5 mm. Photo N. Vesović.

Deconvolution and Identification System) software, version 2.70, and the commercially available NIST11 and Wiley07 libraries containing approximately 500,000 spectra. Relative percentages of identified compounds were computed from the corresponding GC-FID peak areas using the MSD ChemStation software, version E02.02 (Agilent Technologies, Santa Clara, USA).

#### 2.4. Morphological analysis

The abdomens of adult individuals of all tested taxa except *M. (S.) montenegrinus* were dissected in 70% ethanol. Connective tissue was removed and pygidial glands were carefully extracted. The length of reservoirs was measured from the apical notch to the base of efferent duct, and the width was measured in the widest part. After analysis, the dry ground beetle specimens were deposited in the collection of the Institute of Zoology, University of Belgrade - Faculty of Biology, Belgrade, Serbia.

#### 2.5. Bright-field microscopy

A Zeiss SteREO Discovery.V8 stereomicroscope with a Zeiss AxioCam ICc 1 digital camera attached and the AxioVision microscope software were used for photographing morphological features of pygidial glands.

#### 2.6. Nonlinear microscopy

For NLM, morphological structures of pygidial glands were placed on microscope slides with glycerin as a medium, each covered with a slip. To obtain two-photon excitation fluorescence (TPEF) modality of NLM images, we used a multi-photon microscope with a Ti-sapphire laser Mira 900-F (Coherent, Inc., Santa Clara, USA), which can produce femtosecond pulses in the range of 700–1,000 nm at a repetition rate of 76 MHz (Rabasović et al., 2015). We varied the irradiation wavelength, and found that the best TPEF signal was at 840 nm. The duration of the lasers pulses was 160 fs. NLM was conducted in the laboratory of the

University of Belgrade - Institute of Physics, Belgrade, Serbia.

For better visualization of morphological features of pygidial glands, 3D video animations were made (Supplementary files S1–S6).

### 3. Results

#### 3.1. Chemical composition of secretion mixtures

Twenty-three chemical compounds were detected in the dichloromethane extracts of the pygidial gland secretions of four ground beetle taxa analysed. Twenty-two compounds were precisely identified, while one remained unidentified (Table 1, Fig. 2).

The extract of *M. (S.) montenegrinus* contained 11 compounds (Fig. 2A). All of them are carboxylic acids. The major components were 2-methylbutyric (31.2%), isobutyric (21.9%), methacrylic, *trans*-2-hexenoic (11.0% each), angelic (8.4%) and caproic acids (6.8%). In smaller amounts, we detected *trans*-3-hexenoic (3.1%), acetic (2.9%) and butyric acids (2.3%). The minor components were propionic (0.9%) and valeric acids (0.5%).

The extracts of *P. (C.) cylindricus* sampled in 2018 and 2019 contained only methacrylic and tiglic acids (Fig. 2B), which concentration slightly differed between the two years. In the sample from 2018, the concentration of methacrylic and tiglic acids was 93.2% and 6.8%, respectively, while in the sample from 2019, the concentration of methacrylic and tiglic acids was 91.7% and 8.3%, respectively.

The extract of *P. (F.) melas* contained nine compounds (Fig. 2C): six carboxylic acids, two medium-chain alkanes and one unidentified compound. The major component was methacrylic acid (81.3%), followed by tiglic acid (11.4%) and *n*-undecane (6.4%) in lesser amounts. The minor components were isobutyric acid, an unidentified compound (0.3% each), *n*-tridecane and 2-methylbutyric acid (0.1% each). Acetic and seneciolic acids were found in trace amounts (less than 0.1%).

The highest number of compounds was found in the extract of *P. (P.) nigrita* (Fig. 2D). It contained 15 compounds: nine hydrocarbons [two medium-chain ( $C_{11}$  and  $C_{13}$ ) and one long-chain ( $C_{21}$ ) alkanes, two long-chain ( $C_{21}$  and  $C_{23}$ ) alkenes, two long-chain ( $C_{21}$  and  $C_{23}$ ) dienes



**Table 1**  
Chemical composition of the pygidial gland secretions in four Pterostichini taxa analysed by GC-FID and GC-MS.

Peak	Rt (min) <sup>a</sup>	Compounds	Relative percentage (%) <sup>b</sup>				
			<i>M. (S.) montenegrinus</i>	<i>P. (C.) cylindricus</i> 2018	2019	<i>P. (F.) melas</i>	<i>P. (P.) nigrita</i>
1	4.18	<i>n</i> -Undecane	–	–	–	6.4	11.2
2	6.71	<i>n</i> -Tridecane	–	–	–	0.1	0.1
3	8.91	Acetic acid	2.9	–	–	<sup>d</sup>	0.6
4	10.09	Propionic acid	0.9	–	–	–	0.3
5	10.47	Isobutyric acid	21.9	–	–	0.3	0.6
6	11.25	Butyric acid	2.3	–	–	–	–
7	11.78	2-Methylbutyric acid	31.2	–	–	0.1	0.1
8	12.03	Methacrylic acid	11.0	93.2	91.7	81.3	65.3
9	12.62	Valeric acid	0.5	–	–	–	–
10	13.10	Angellic acid	8.4	–	–	–	–
11	13.28	Seneciolic acid	–	–	–	<sup>d</sup>	–
12	13.90	Caproic acid	6.8	–	–	–	–
13	13.94	Tiglic acid	–	6.8	8.3	11.4	17.4
14	15.17	<i>Trans</i> -3-hexenoic acid	3.1	–	–	–	–
15	15.29	<i>Trans</i> -2-hexenoic acid	11.0	–	–	–	–
16	16.64	Heneicosane	–	–	–	–	1.1
17	17.19	Heneicosene <sup>c</sup>	–	–	–	–	0.9
18	18.47	Heneicosadiene <sup>c</sup>	–	–	–	–	0.4
19	18.83	( <i>Z</i> )-9-Tricosene	–	–	–	–	0.7
20	19.27	Tricosadiene <sup>c</sup>	–	–	–	–	0.4
21	19.80	Tricosatriene isomer 1 <sup>c</sup>	–	–	–	–	0.6
22	19.88	Tricosatriene isomer 2 <sup>c</sup>	–	–	–	–	0.3
23	21.43	Unidentified compound	–	–	–	0.3	–

<sup>a</sup> Obtained from GC-MS data.

<sup>b</sup> Obtained from GC-FID peak areas.

<sup>c</sup> The exact positions of double bonds could not be determined.

<sup>d</sup> Trace amounts (< 0.1%).

and two long-chain (C<sub>23</sub>) trienes] and six short-chain carboxylic acids. The most dominant compound was methacrylic acid (65.3%). Tiglic acid (17.4%) and *n*-undecane (11.2%) were found in lesser amounts. The minor components were heneicosane (1.1%), heneicosene (0.9%), (*Z*)-9-tricosene (0.7%), acetic acid, isobutyric acid, tricosatriene isomer 1 (0.6% each), heneicosadiene, tricosadiene (0.4% each), propionic acid, tricosatriene isomer 2 (0.3% each), *n*-tridecane and 2-methylbutyric acid (0.1% each).

### 3.2. Morphology of pygidial glands

The pygidial glands were analysed in three *Pterostichus* species: *P. (C.) cylindricus*, *P. (F.) melas* and *P. (P.) nigrita*. Secretory lobes are more or less ellipsoid to spherical, whitish and composed of variable number of secretory units (Figs. 3 and 4, Supplementary files S1 and S2). Each unit is composed of elongated, flattened secretory cells, which are radially arranged around a central lumen (Fig. 4C), into which secretory products are released before reaching main collecting canal (Figs. 3 and 4). In *P. (C.) cylindricus*, secretory lobe units are almost spherical and their number is between 25 and 40 (Figs. 3A and 4A). The diameter of a single secretory unit is 200–260 µm. In *P. (F.) melas*, secretory lobe units are spherical, each about 210 µm in diameter (Figs. 3C, D and 4C). About 20–30 secretory units constitute a cluster. In *P. (P.) nigrita*, only 10 secretory units were present in a cluster (Fig. 3E). These are elongated, ellipsoid, and their diameter varies between 170 and 290 µm. Numerous tracheal tubes can be seen to surround the clusters of secretory lobes (Figs. 3A and 4A). One radial collecting canal emerges from each secretory unit (Figs. 3A, E, 4A and C). These canals merge into main collecting canal, with a continuous spiral ridge on its inner wall (Fig. 4B). Main collecting canal enters posterior, narrow part of reservoir, which then continues to efferent duct (Fig. 3B and D). The lumen of 2.2-mm long main collecting canal in *P. (C.) cylindricus* is 30 µm in diameter, while the diameter of entire main collecting canal is 60–70 µm (Fig. 4B, Supplementary files S3 and S4). In *P. (F.) melas*, the lumen of 3.50-mm long main collecting canal is 20 µm, while the

diameter of entire main collecting canal is about 60 µm. In *P. (P.) nigrita*, the length of main collecting canal is slightly over 2 mm, with the diameter of about 40 µm, while the diameter of its lumen is about 15 µm.

The reservoirs in all species studied herein are more or less heart-shaped, with differently expressed depth of the apical notch (Figs. 3B, D, F and 4D). The muscle wall of all reservoirs is thick, with interwoven muscle fibers. In *P. (C.) cylindricus*, reservoir is 1.20–1.45 mm long at its longest point and 1.02–1.35 mm wide at its widest point, with a highly expressed apical notch (Fig. 3B). In *P. (F.) melas*, reservoir is 0.80–1.58 mm long and 1.06–1.55 mm wide, with an expressed apical notch (Figs. 3D and 4D, Supplementary file S5). The upper part of reservoir of *P. (P.) nigrita* is almost completely flat, with a poorly expressed apical notch. Reservoir's wall in this species is transparent and a yellowish secretion is visible through the wall. The length of reservoir of *P. (P.) nigrita* is about 0.70 mm and the width is about 0.40 mm (Fig. 3F).

Efferent duct extends from reservoir. The lumen of efferent duct in its anterior part is surrounded by a muscle coat, with muscle fibers extending longitudinally (Fig. 3B, D and F). Efferent duct gradually narrows posteriorly and cannot be strictly anatomically separated from the posterior part of reservoir. In *P. (C.) cylindricus*, the diameter of efferent duct in its anterior and posterior parts is 0.35 mm and 0.10 mm, respectively (Supplementary file S6), while its length is about 1.50 mm. In *P. (F.) melas*, the anterior part of efferent duct is 0.30 mm in diameter, while the posterior part, before a broadened opening valve, is 70 µm in diameter (Fig. 3D). The length of efferent duct in *P. (F.) melas* is 1.70 mm. Efferent duct of *P. (P.) nigrita* is about 0.10 mm in diameter and 0.50 mm in length.

## 4. Discussion

### 4.1. Chemical survey

Methacrylic acid was found in all pterostichine taxa analysed in the current study. In three tested *Pterostichus* species, this compound was

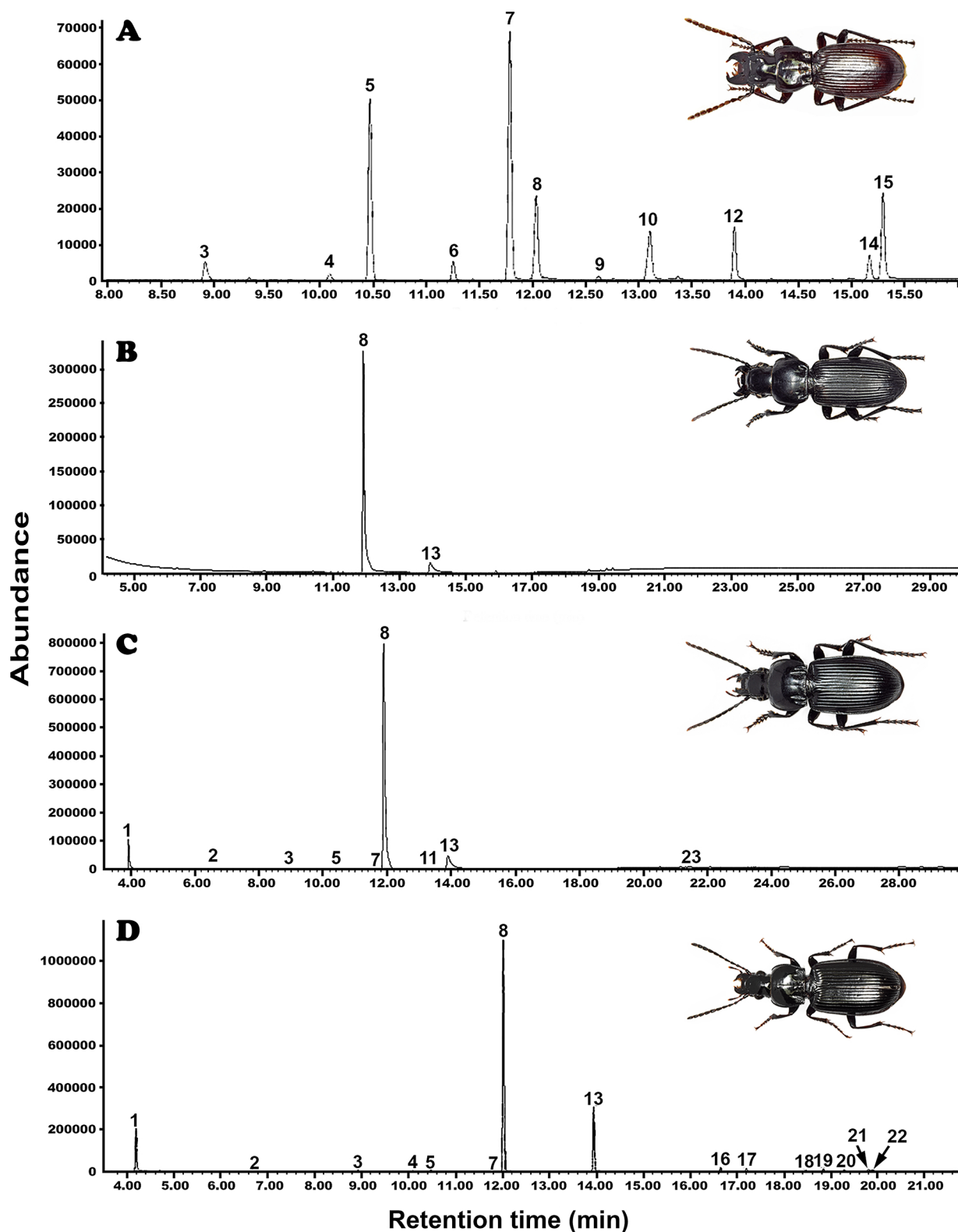
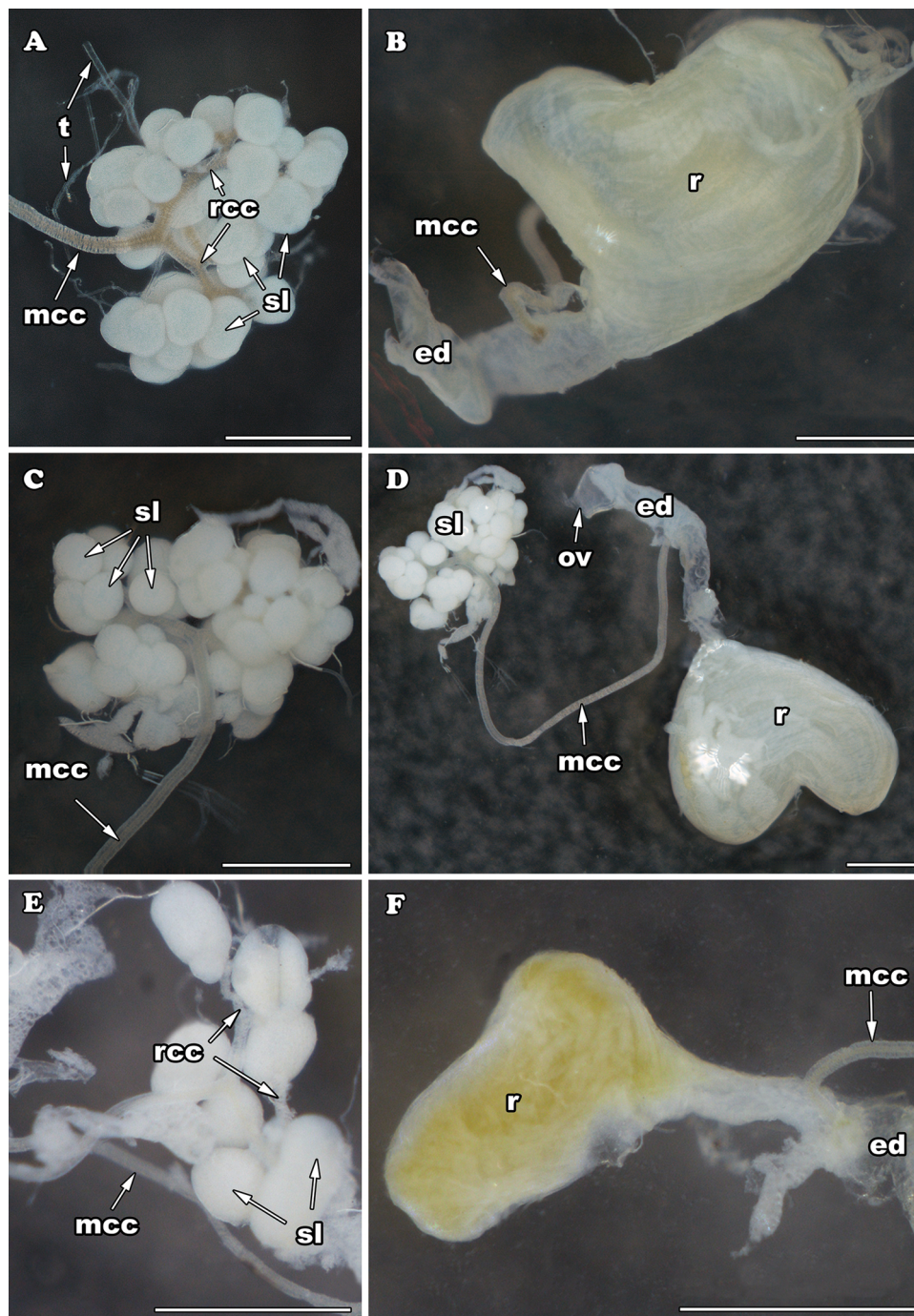


Fig. 2. GC-FID chromatograms of the dichloromethane pygidial gland secretion extracts from the adults of four analysed Pterostichini taxa: A – *M. (S.) montenegrinus*; B – *P. (C.) cylindricus*; C – *P. (F.) melas*; D – *P. (P.) nigrita*. Ordinal numbers of peaks correspond to the numbers in Table 1.

the major component in the secretion, with the lowest concentration in *P. (P.) nigrita* (65.3%) and the highest concentration in *P. (C.) cylindricus* (93.2%). The pygidial gland secretion of *M. (S.) montenegrinus* contained an unusually low concentration of methacrylic acid (11%). This was not expected, since the concentration of this compound, if present in the pygidial gland secretion of ground beetles, usually ranges from

75 to 90% (Blum, 1981). Tiglic acid was detected in three studied *Pterostichus* species, but not in *M. (S.) montenegrinus*. Furthermore, the combined presence of methacrylic and tiglic acids is one of the most common combinations in secretions of ground beetles (Blum, 1981; Lečić et al., 2014). This combination was found in almost all representatives of the subfamilies Carabinae and Pterostichinae (Lečić



**Fig. 3.** Morphology of the pygidial glands of three Pterostichini ground beetles observed with BFM: A – aggregation of secretory lobes in *P. (C.) cylindricus*; B – gland reservoir in *P. (C.) cylindricus*; C – aggregation of secretory lobes in *P. (F.) melas*; D – a whole pygidial gland in *P. (F.) melas*; E – aggregation of secretory lobes in *P. (P.) nigrita*; F – gland reservoir in *P. (P.) nigrita*. Abbreviations: ed – efferent duct; mcc – main collecting canal; ov – opening valve; r – reservoir; rcc – radial collecting canal; sl – secretory lobe; t – tracheal tubes. Scale bars = 0.5 mm.

et al., 2014; Vesović et al., 2017; Vesović, 2019). Absence of tiglic acid and a low concentration of methacrylic acid in *M. (S.) montenegrinus* might be due to the fact that this taxon inhabits high-altitude habitats (Trautner and Geigenmüller, 1987) with low temperatures, which might lead to different metabolic status of the individuals. When present together, tiglic acid is usually found in lower amounts (up to 25%) than methacrylic acid (Blum, 1981), what is in accordance with the results given in this study. Concentrations of methacrylic and tiglic acids in the secretion of *P. (C.) cylindricus* sampled from the same population during the spring of 2018 and 2019 showed that the two compounds maintain a stable ratio over multiple seasons within the

population (relative percentages of the two acids were only 1.5% different between samples). These minor differences are most probably just a usual intraspecific fluctuation in the secretion among individuals.

In *M. (S.) montenegrinus*, the major components were 2-methylbutyric (31.2%) and isobutyric acids (21.9%). Both compounds were detected in minor amounts in two tested *Pterostichus* species: *P. (F.) melas* and *P. (P.) nigrita*. Within Pterostichinae, isobutyric acid has been previously found only in two species: *A. (A.) parallelepipedus* (Lečić et al., 2014) and *P. (O.) externepunctatus* (Balestrazzi et al., 1985). Isobutyric acid is often accompanied by isovaleric or 2-methylbutyric acids (Lečić et al., 2014). Presence of 2-methylbutyric acid in pygidial

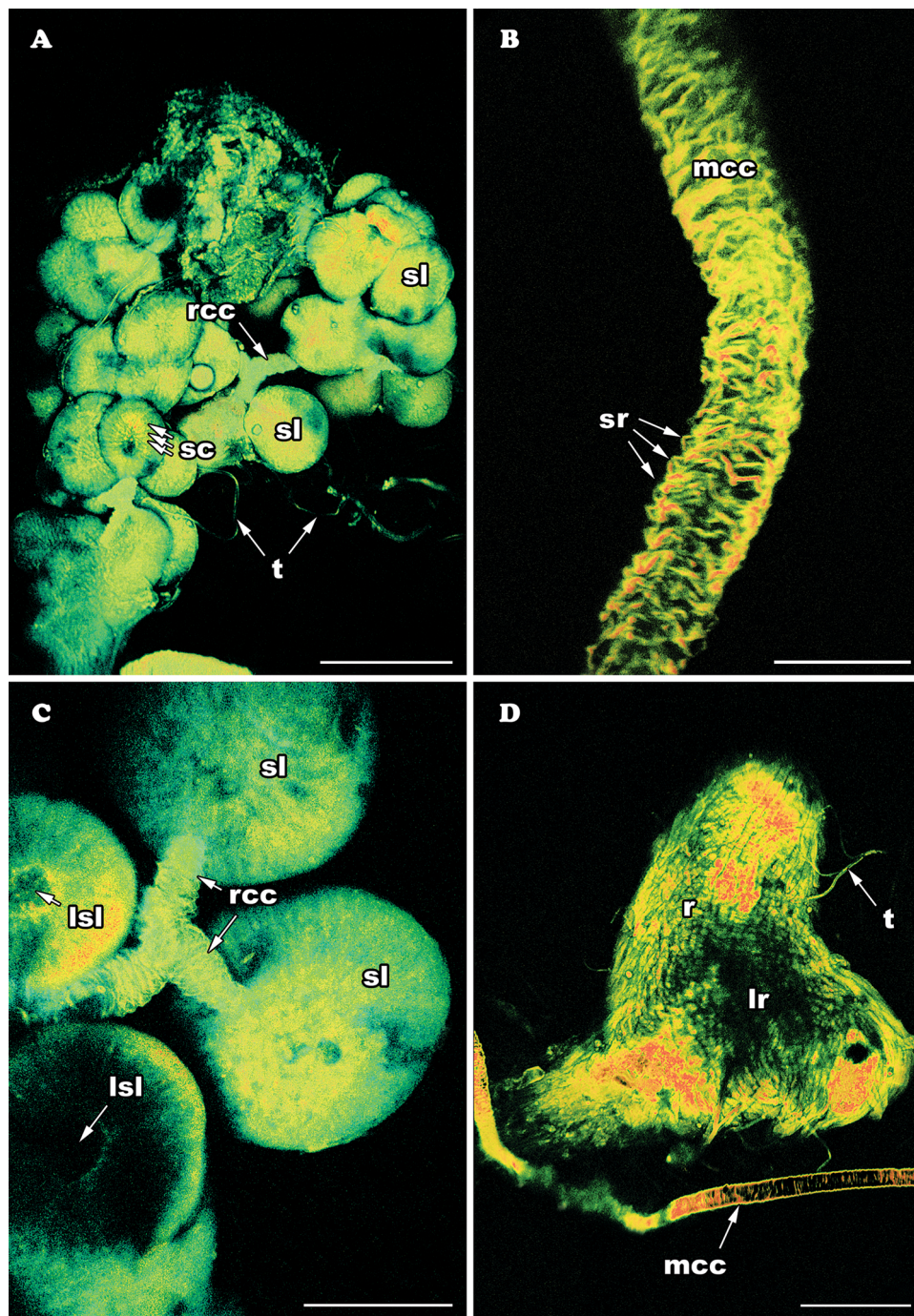


**Fig. 4.** Morphology of the pygidial glands of two Pterostichini ground beetles observed with TPEF modality of NLM: A – aggregation of secretory lobes in *P. (C.) cylindricus*; B – the structure of main collecting canal in *P. (C.) cylindricus*; C – a close-up view of several secretory lobes in *P. (F.) melas*; D – gland reservoir in *P. (F.) melas*. Abbreviations: lr – the lumen of reservoir; lsl – the lumen of secretory lobe; mcc – main collecting canal; r – reservoir; rcc – radial collecting canal; sc – secretory cells; sl – secretory lobes; sr – spiral ridge; t – tracheal tubes. Scale bars = 200  $\mu\text{m}$  (A, C and D) and 50  $\mu\text{m}$  (B).

gland secretions is characteristic only for the two species of the subfamily Pterostichinae: *Pterostichus (Argutor) sulcatoris* Morawitz, 1863 (Kanehisa and Kawazu, 1982) and *P. (Hyperpes) californicus* (Dejean, 1828) (Attygalle et al., 2007). Isobutyric acid is likely a byproduct of the biochemical synthesis of methacrylic acid from L-valine, while 2-methylbutyric acid is likely a byproduct in the conversion of L-isoleucine to tiglic acid (Attygalle et al., 1991a). Specifically, isobutyryl-CoA is an intermediate in the biosynthesis of methacrylyl-CoA from L-valine. Each of these thioesters is converted to its respective carboxylic acids, isobutyric acid and methacrylic acid, independently. Similarly, 2-methylbutyryl-CoA is an intermediate in the biosynthesis of tiglyl-CoA

from L-isoleucine. Each thioester again is converted to its respective carboxylic acids, 2-methylbutyric acid and tiglic acid, independently (Stark et al., 2003).

Acetic acid was detected in minor amounts in *M. (S.) montenegrinus* and *P. (P.) nigrita* and trace amounts in *P. (F.) melas*. This acid has been recorded in pygidial gland secretions of representatives of many different subfamilies of ground beetles (Vesović, 2019).

Propionic acid was the minor constituent of the secretions of *M. (S.) montenegrinus* and *P. (P.) nigrita*. Within Pterostichinae, this compound was detected only in the secretions of *A. (A.) parallelepipedus* (Lečić et al., 2014) and *P. (H.) californicus* (Attygalle et al., 2007), and within

other ground beetles, only in *Oodes americanus* Dejean, 1826 (Harpalinae) (Attygalle et al., 1991b) and *Pheggomisetes globiceps ninae* S. Čurčić, Schönmann, Brajković, B. Čurčić & Tomić, 2004 (Trechinae) (Vesović et al., 2015).

Butyric, valeric, angelic, caproic, *trans*-2-hexenoic and *trans*-3-hexenoic acids were found only in the secretion of *M. (S.) montenegrinus*. Butyric acid has been previously found in representatives of several ground beetles subfamilies, but most often in Carabinae, within which was detected in five species (Vesović, 2019). Within Pterostichinae, it has been found in the secretions of *A. (A.) parallelepipedus* (Lečić et al., 2014) and *P. (H.) californicus* (Attygalle et al., 2007).

Within ground beetles, valeric acid has only been detected in the secretions of *Archipatrobus flavipes* (Motschulsky, 1864) (Patrobiniae) and *Bembidion (Bembidion) quadrimaculatum* (Linnaeus, 1761) (Trechinae) (Schildknecht et al., 1968), making the presence in *M. (S.) montenegrinus* the first record of the compound in Pterostichinae.

Angelic acid has been previously identified in ground beetles chiefly in the secretions of Anthiinae (Scott et al., 1975), Carabinae (Lečić et al., 2014; Vesović, 2019) and Scaritinae (Moore and Wallbank, 1968; Kanehisa and Murase, 1977; Davidson et al., 1989; Attygalle et al., 1991a). Within Pterostichinae, it was detected only in the secretion of *Abacomorphus asperulus* Fauvel, 1882 (Moore and Wallbank, 1968). Questionable presence of this acid has been reported for subfamilies Broscinae and Trechinae (Kanehisa and Murase, 1977).

Caproic acid was also detected in a relatively high concentration (6.8%) in *M. (S.) montenegrinus* compared to other ground beetles (Attygalle et al., 1991b; Vesović et al., 2015). This is its first evidence in a representative of the tribe Pterostichini. Within other ground beetles, caproic acid has been recorded in species belonging to the subfamilies Broscinae, Carabinae, Oodinae, Platyninae, Scaritinae and Trechinae (two highly specialised troglitic representatives) (Moore and Wallbank, 1968; Moore, 1979; Attygalle et al., 1991b; Vesović et al., 2015).

2-Hexenoic acid has been found in a few ground beetle species: *Amara (Bradytus) ampliata* (Bates, 1873) (Harpalinae) (Kanehisa and Kawazu, 1982), *Schizogenius lineolatus* (Say, 1823) (Scaritinae) (Will et al., 2000) and *Carabus (Megodontus) caelatus* Fabricius, 1801 (Carabinae) (Vesović et al., 2020). However, in the mentioned cases, its *cis/trans* isomerism has remained unknown. In this study, we detected a *trans* isomer of hexenoic acid in *M. (S.) montenegrinus*. *Trans*-2-hexenoic acid has been previously found only in *O. americanus* (Harpalinae) (Attygalle et al., 1991b), *Carenum bonellii* Brullé, 1835 and *Lacopterum foveigerum* (Chaudoir, 1868) (Scaritinae) (Moore and Wallbank, 1968). In the latter species, it is the major component of the secretion (Blum, 1981). It is interesting to note that 2-hexenoic acid has been found in several high-altitude species of ground beetles [*C. (M.) caelatus* and *M. (S.) montenegrinus*] (Vesović et al., 2020), regardless of belonging to separate subfamilies. We are not certain about the reasons for this, but assume that specific sources of food or possible altitude-dependant alternations of physiological pathways might have some impact, but it was not verified. Within other insects, it was recorded in the defensive secretions of a few species of Blattodea (Blum, 1981).

The presence of *trans*-3-hexenoic acid in *M. (S.) montenegrinus* is the first record of the compound in semiochemicals of ground beetles. Previously, 3-hexenoic acid (with *cis/trans* isomerism unknown) had been detected only in *S. lineolatus* (Will et al., 2000).

Senecioic acid was detected in trace amount in *P. (F.) melas*. It was always detected in lesser amounts in a few ground beetle species belonging to the subfamilies Broscinae, Carabinae, Oodinae and Pterostichinae (Kanehisa and Kawazu, 1982; Will et al., 2000; Lečić et al., 2014; Vesović, 2019). *N*-undecane and *n*-tridecane, both detected in *P. (F.) melas* and *P. (P.) nigrita*, are common in the secretions of Pterostichinae, as well as for many other ground beetle subfamilies (Vesović, 2019). In some cases, these two alkanes can be found together (Will et al., 2000; Vesović et al., 2015). They represent the most common alkanes produced by the defensive glands of many different

insect groups, such as beetles, true bugs and ants (Blum, 1978, 1981). *N*-undecane in some insects may also act as an alarm pheromone (Blum, 1978).

Heneicosane was rarely detected in ground beetles so far. It was only found in the secretions of two ground beetle species: *Helluomorphoides clairvillei* (Dejean, 1831) (Anthiinae) (Attygalle et al., 1992) and *Anchomenus dorsalis* (Pontoppidan, 1763) (Bonacci et al., 2011). This alkane is far more common product of Dufour's gland of Hymenoptera (Blum, 1981).

The presence of (*Z*)-9-tricosene in *P. (P.) nigrita* in minor amount is the first record of the compound for Pterostichini and the second for Carabidae [after the record of Bonacci et al. (2011) for *A. dorsalis*]. This alkene was the first cuticular hydrocarbon which acts as a sex pheromone in some flies, bees and long-horned beetles (Blomquist and Bagnères, 2010; Francke and Schulz, 2010).

Heneicosene, heneicosadiene, tricosadiene and tricosatriene, found in the secretion of *P. (P.) nigrita*, have never been recorded before in other ground beetles. Although the exact positions of the double bonds could not be determined, some isomers of these hydrocarbons have been found in other insect groups. Heneicosadiene was suggested to be a sex attractant in moths (Blomquist and Bagnères, 2010), while different isomers of tricosadienes and tricosatrienes make an integral part of female sex pheromones in different insect groups (Francke and Schulz, 2010).

It is known that individuals of the same species may produce secretions which differ both in chemical composition and quantity. These may reflect genetic differences of populations on different habitats or seasonal variation (Pasteels et al., 1983). Analysing the secretion of *P. (C.) cylindricus* sampled in two different years, from the same area and in the same season, we realized that the samples from both years were qualitatively the same. Observed quantitative differences were very small and may be the result of the different metabolic status of analysed individuals.

Although organic acids are, in most cases, the main product of the pygidial glands in Pterostichini, hydrocarbons may also be a significant part of their secretions (Moore and Wallbank, 1968; Schildknecht et al., 1968; Will et al., 2000). If we compare pterostichine taxa analysed in this study, *P. (C.) cylindricus* had the simplest mixture of compounds, while the greatest number of compounds was found in the secretion of *P. (P.) nigrita*. In the latter taxon, a high number of hydrocarbons was found along with carboxylic acids, most of them being new for Pterostichini or even Carabidae. Compared with previously analysed Pterostichus taxa (Schildknecht et al., 1968; Kanehisa and Murase, 1977; Kanehisa and Kawazu, 1982; Balestrazzi et al., 1985; Will et al., 2000; Attygalle et al., 2007), *P. (P.) nigrita* had significantly more hydrocarbons, including unsaturated long-chain hydrocarbons which have never been found before in Carabidae. While medium-chain alkanes are common for Pterostichus species, long-chain alkanes were rarely found in ground beetles so far (Attygalle et al., 1992; Vesović et al., 2015).

Schildknecht et al. (1968) had already chemically analysed the secretion of *P. (F.) melas* (however, with no information provided which subspecies were analysed), while other three pterostichine species were studied for the first time in this study. The only compounds detected by Schildknecht et al. (1968) in the secretion of *P. (F.) melas* were *n*-alkanes, methacrylic and tiglic acids. The latter acids were found in *P. (F.) melas* in this study, as well as alkanes, which we identified as *n*-undecane and *n*-tridecane. Additionally, we detected four carboxylic acids and one unidentified compound, which were not reported by Schildknecht et al. (1968) for the same species. The same authors analysed the secretion of *Molops (Molops) elatus* (Fabricius, 1801), the only chemically studied *Molops* species so far, and detected only methacrylic and tiglic acids (Schildknecht et al., 1968). Since tiglic acid is almost always accompanied by methacrylic acid in ground beetles, the absence of the former compound in the secretion of *M. (S.) montenegrinus* in this study is a very rare phenomenon and sets the precedent of this acid not being detected in Pterostichini. In other ground beetles,

methacrylic acid sometimes may be present alone, without tiglic acid (Moore and Wallbank, 1968; McCullough, 1969, 1972; Benn et al., 1973; Will et al., 2000), but there are no available data on the presence of tiglic acid alone, without methacrylic acid. If we take into account that only one species of the genus *Molops* Bonelli, 1810 was previously analysed (Schildknecht et al., 1968), any chemotaxonomical comparison between species of the genus is currently not appropriate.

Further investigations should be directed toward analysing chemical composition of the pygidial gland secretions of ground beetle species that have not been studied yet. Re-analyses of previously examined species are also important since gas chromatography was less precise earlier, resulting in no possibility to detect minor constituents of the extracts. Identifying all constituents of the pygidial gland secretions (including the minor ones) is necessary in order to clarify the exact role. There are some assumptions that, along with defense against predators, they may act as alarm or sexual pheromones (Bonacci et al., 2011; Holliday et al., 2016). In addition, antimicrobial properties of the pygidial gland secretions released by adults were observed in a few ground beetle species (Nenadić et al., 2016a, b, 2017). Furthermore, minor or even trace constituents may significantly increase deterrent effect of the pygidial gland secretions (Blum, 1978). Usage of semi-chemical characters in taxonomy is still unreliable. Lack of information in that field makes it almost impossible to come to any conclusions. Nevertheless, indications exist that some compounds from the secretion mixtures in ground beetles can be used in chemotaxonomy at higher taxonomic levels (Will et al., 2000).

#### 4.2. Morphological survey

Pygidial glands in all taxa analysed herein were similar in structure and seem to follow the pattern of Pterostichini (Forsyth, 1970, 1972). All parts of the pygidial glands of ground beetles are closely associated with tracheoles, indicating their high aerobic metabolism (Giglio et al., 2011).

Secretory lobes in the tested *Pterostichus* taxa consist of a variable number of secretory units. Unlike most European species of the genus *Pterostichus* Bonelli, 1810, possessing 8-20 secretory units (Forsyth, 1972; Vesović, 2019), *P. (C.) cylindricus* has more secretory units (25-40). Such high number of secretory units is characteristic for *Pterostichus* species from Japan (Kanehisa and Shiraga, 1978). Single secretory units of the analysed *Pterostichus* taxa are more or less ellipsoid. This corresponds with the findings of Kanehisa and Murase (1977), who stated that such form of secretory lobes is characteristic for carboxylic acid-secreting species.

Long main collecting canal is present in all three studied *Pterostichus* species. Main collecting canal enters reservoir in its posterior, narrow part, which practically continues into efferent duct in all species analysed herein, similarly as in other representatives of Pterostichini which were previously studied (Forsyth, 1970, 1972; Balestrazzi et al., 1985).

The presence of two-notched reservoir is observed in *Pterostichus* taxa analysed in this study. The greatest difference in shape of reservoir between the analysed species is in depth of apical notch, which is almost absent in *P. (P.) nigrita* and poorly expressed in *P. (F.) melas*, while in *P. (C.) cylindricus*, reservoir is clearly divided in its apical region into two lobes, which gives reservoir a heart-shaped form. The muscle wall of reservoir is thicker in *P. (C.) cylindricus* and *P. (F.) melas* than in *P. (P.) nigrita*, where it is transparent and through which secretion can be seen. The muscle wall of reservoir is generally well-developed in Pterostichini, with the exception of the genera *Abax* Bonelli, 1810 and *Molops* (Forsyth, 1972; Vesović, 2019). In the studied *Pterostichus* taxa, reservoir narrows in its distal part and transitions to efferent duct, through which secretions are discharged outwards by spraying.

Considering the dimensions of individual pygidial gland components in three pterostichine species whose glands were analysed morphologically in the current study, most of the measurements generally were in positive correspondence with the beetle's body size. Namely, *P.*

*(C.) cylindricus* and *P. (F.) melas* had similar size, which were mainly considerably greater than those in *P. (P.) nigrita*. The diameters of secretory lobes in *P. (C.) cylindricus*, *P. (F.) melas* and *P. (P.) nigrita* were on average 230, 210 and 250  $\mu\text{m}$ , respectively. Contrary to other glandular parts, it can be observed that secretory lobes in *P. (P.) nigrita* were the largest due to the fact that they were the least numerous per cluster. In the three above-mentioned species, main collecting canal's length was 2.20, 3.50 and 2.00 mm, respectively. The width of this canal was 65, 60 and 40  $\mu\text{m}$ , respectively, while the diameter of its lumen was 30, 20 and 15  $\mu\text{m}$ , respectively. Similar values were obtained for measurements of reservoir. The length was 1.30, 1.30 and 0.70 mm, respectively, while its width was 1.20, 1.20 and 0.40 mm, respectively. Finally, efferent duct in the three Pterostichini taxa was 1.50, 1.70 and 0.70 mm long and 0.35, 0.30 and 0.10 mm wide, respectively.

Pygidial glands are universally present in Caraboidea. These are homologous morphological structures, which probably have been evolved early in the evolution of all Adephaga (Forsyth, 1972; Dettner, 1979). The form of reservoir and secretory lobes is the most informative feature for phylogenetic interpretation, while the form of main collecting canal and efferent duct is much more uniform and less significant for phylogenetic analyses (Vesović, 2019).

Different microscopy techniques allow us to see morphological structures in various and diverse ways. Classical approach using BFM is efficient to generally observe the pygidial glands of ground beetles and to conduct some measurements, but there are limitations regarding the examination of certain structures covered by chitin, such as central lumens of secretory lobes or lumens of various glandular ducts. Thus, usage of TPEF modality of NLM seems to be a highly promising additional way to study the morpho-anatomical features of pygidial glands. In comparison to BFM, TPEF modality of NLM enables a better visualization of morphological structures and a deeper insight into them (e.g., walls of collecting canals with spiral ridges, inner structures of secretory lobes and reservoirs). It is important to mention that the color on NLM images is due to signal processing and reflects the intensity of the collected radiation. As usual, "warmer" colors (such as red) correspond to more intense fluorescence. This reflects the autofluorescence properties of certain biological molecules, such as myosin or chitin.

#### Funding

This work was supported by the Serbian Ministry of Education, Science and Technological Development [grant numbers ON173038 (contract number 451-03-68/2020-14/200178), ON172053 (contract number 451-03-68/2020-14/200168), III45016 and ON171038]. It was additionally funded jointly by the Serbian Ministry of Education, Science and Technological Development and the Ministry of Science and Technology of the People's Republic of China (Grant "Mimetics of Insects for Sensing and Security", I-2).

#### Declaration of Competing Interest

The authors declare that they have no known competing financial interests or personal relationships that could have appeared to influence the work reported in this paper.

#### Acknowledgments

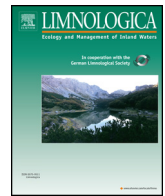
We are grateful to Dr. Dragan Antić (Institute of Zoology, University of Belgrade - Faculty of Biology, Belgrade, Serbia) for his help in collecting some ground beetle specimens during our fieldwork on Mt. Durmitor, northern Montenegro. We are grateful to an anonymous reviewer, whose constructive comments improved the quality of the paper.

## Appendix A. Supplementary data

Supplementary material related to this article can be found, in the online version, at <https://doi.org/10.1016/j.zool.2020.125772>.

## References

- Attygalle, A.B., Meinwald, J., Eisner, T., 1991a. Biosynthesis of methacrylic and isobutyric acids in a carabid beetle, *Scarites subterraneus*. *Tetrahedron Lett.* 32, 4849–4852. [https://doi.org/10.1016/S0040-4039\(00\)93477-4](https://doi.org/10.1016/S0040-4039(00)93477-4).
- Attygalle, A.B., Meinwald, J., Liebherr, J.K., Eisner, T., 1991b. Sexual dimorphism in the defensive secretion of a carabid beetle. *Experientia* 47, 296–299. <https://doi.org/10.1007/BF01958165>.
- Attygalle, A.B., Meinwald, J., Eisner, T., 1992. Defensive secretion of a carabid beetle, *Helluomorphoides clairvillei*. *J. Chem. Ecol.* 18, 489–498. <https://doi.org/10.1007/BF00994247>.
- Attygalle, A.B., Wu, X., Will, K.W., 2007. Biosynthesis of tiglic, ethacrylic and 2-methylbutyric acids in a carabid beetle, *Pterostichus (Hyperperes) californicus*. *J. Chem. Ecol.* 33, 963–970. <https://doi.org/10.1007/s10886-007-9276-3>.
- Balestrazzi, E., Dazzini Valcurone, M.L., De Bernardi, M., Vidari, G., Vita-Finzi, P., Mellerio, G., 1985. Morphological and chemical studies on the pygidial defence glands of some Carabidae (Coleoptera). *Naturwissenschaften* 72, 482–484. <https://doi.org/10.1007/BF00441073>.
- Benn, M.H., Lencucha, A., Maxie, S., Telang, S.A., 1973. The pygidial defensive secretion of *Carabus taedatus*. *J. Insect Physiol.* 19, 2173–2176. [https://doi.org/10.1016/0022-1910\(73\)90132-7](https://doi.org/10.1016/0022-1910(73)90132-7).
- Blomquist, G.J., Bagnères, A.G., 2010. Introduction: history and overview of insect hydrocarbons. In: Blomquist, G.J., Bagnères, A.G. (Eds.), *Insect Hydrocarbons: Biochemistry, and Chemical Ecology*. Cambridge University Press, New York, pp. 3–18. <https://doi.org/10.1017/CBO978051171909.002>.
- Blum, M.S., 1978. *Biochemical Defenses of Insects*. Academic Press, New York. <https://doi.org/10.1016/B978-0-12-591640-0.50016-9>.
- Blum, M.S., 1981. *Chemical Defenses of Arthropods*. Academic Press, New York. <https://doi.org/10.1016/B978-0-12-108380-9.X5001-7>.
- Bonacci, T., Brandmayr, P., Zetto, T., Perrotta, L.D., Guarino, S., Peri, E., Colazza, S., 2011. Volatile compounds released by disturbed and undisturbed adults of *Anchomenus dorsalis* (Coleoptera, Carabidae, Platynini) and structure of the pygidial gland. *ZooKeys* 81, 13–25. <https://doi.org/10.3897/zookeys.81.1122>.
- Davidson, B.S., Eisner, T., Witz, B., Meinwald, J., 1989. Defensive secretion of the carabid beetle *Pasimachus subsulcatus*. *J. Chem. Ecol.* 15, 1689–1697. <https://doi.org/10.1007/BF01012258>.
- Dazzini Valcurone, M., Pavan, M., 1980. Glandole pigdiali e secrezioni difensive dei Carabidae (Insecta Coleoptera). *Pubbl. Ist. entomol. Univ. Pavia* 12, 1–36.
- Dettner, K., 1979. Chemotaxonomy of water beetles based on their pygidial gland constituents. *Biochem. Syst. Ecol.* 7, 129–140. [https://doi.org/10.1016/0305-1978\(79\)90021-8](https://doi.org/10.1016/0305-1978(79)90021-8).
- Di Giulio, A., Muzzi, M., Romani, R., 2015. Functional anatomy of the explosive defensive system of bombardier beetles (Coleoptera, Carabidae, Brachininae). *Arthropod Struct. Dev.* 44, 468–490. <https://doi.org/10.1016/j.asd.2015.08.013>.
- Dossey, T.A., 2011. Chemical defenses of insects: a rich resource for chemical biology in the tropics. In: Vivanco, J.M., Weir, T. (Eds.), *Chemical Biology of the Tropics*. Springer-Verlag, Berlin-Heidelberg, pp. 27–57.
- Forsyth, D.J., 1970. The ultrastructure of the pygidial defence glands of the carabid *Pterostichus madidus* F. *J. Morphol.* 131, 397–416. <https://doi.org/10.1002/jmor.1051310404>.
- Forsyth, D.J., 1972. The structure of the pygidial defence glands of Carabidae (Coleoptera). *Trans. Zool. Soc. London* 32, 249–309. <https://doi.org/10.1111/j.1096-3642.1972.tb00029.x>.
- Francke, W., Schulz, S., 2010. Pheromones of terrestrial invertebrates. In: first edition. In: Mander, L., Liu, H.W. (Eds.), *Comprehensive Natural Products II: Chemistry and Biology Vol. 4*. Elsevier, Oxford, pp. 153–223. <https://doi.org/10.1016/b978-008045382-8.00095-2>.
- Giglio, A., Brandmayr, P., Talarico, F., Zetto, T., 2011. Current knowledge on exocrine glands in carabid beetles: structure, function and chemical compounds. *ZooKeys* 100, 193–201. <https://doi.org/10.3897/zookeys.100.1527>.
- Gregorovičová, M., Černíková, A., 2015. Reactions of green lizards (*Lacerta viridis*) to major repellent compounds secreted by *Graphosoma lineatum* (Heteroptera: Pentatomidae). *Zoology* 118, 176–182. <https://doi.org/10.1016/j.zool.2015.02.001>.
- Holliday, A.E., Mattingly, T.M., Toro, A.A., Donald, L.J., Holliday, N.J., 2016. Age- and sex-related variation in defensive secretions of adult *Chaenius cordicollis* and evidence for their role in sexual communication. *Chemoecology* 26, 107–119. <https://doi.org/10.1007/s00049-016-0210-4>.
- Hůrka, K., 1996. Carabidae of Czech and Slovak Republics. *Kabourek, Zlín.*
- Kanehisa, K., Kawazu, K., 1982. Fatty acid components of the defensive substances in acid-secreting carabid beetles. *Appl. Entomol. Zool.* 17, 460–466. <https://doi.org/10.1303/aez.17.460>.
- Kanehisa, K., Murase, M., 1977. Comparative study of the pygidial defensive systems of carabid beetles. *Appl. Entomol. Zool.* 12, 225–235. <https://doi.org/10.1303/aez.12.225>.
- Kanehisa, K., Shiraga, T., 1978. Morphological study of the pygidial defensive systems in carabid beetles. *Ber. Ohara Inst. landwirtsch. Biol., Okayama Univ.* 17, 83–94.
- Lečić, S., Čurčić, S., Vujisić, L., Čurčić, B., Čurčić, N., Nikolić, Z., Anđelković, B., Milosavljević, S., Tešević, V., Makarov, S., 2014. Defensive secretions in three ground-beetle species (Insecta: Coleoptera: Carabidae). *Ann. Zool. Fenn.* 51, 285–300. <https://doi.org/10.5735/086.051.0301>.
- McCullough, B.T., 1969. Chemical analysis of the scent fluid of *Pasimachus californicus* and *P. duplicatus* (Coleoptera: Carabidae). *Ann. Entomol. Soc. Am.* 62, 1492. <https://doi.org/10.1093/aesa/62.6.1492>.
- McCullough, B.T., 1972. Analysis of the defensive scent fluid of *Pasimachus elongatus* (Coleoptera: Carabidae). *Ann. Entomol. Soc. Am.* 65, 772. <https://doi.org/10.1093/aesa/65.3.772>.
- Moore, B.P., 1979. Chemical defense in carabids and its bearing on phylogeny. In: Erwin, T.L., Ball, G.E., Whitehead, D.R., Halpern, A.L. (Eds.), *Carabid Beetles: Their Evolution, Natural History and Classification*. Dr. W. Junk, London, pp. 193–203. [https://doi.org/10.1007/978-94-009-9628-1\\_9](https://doi.org/10.1007/978-94-009-9628-1_9).
- Moore, B.P., Wallbank, B.E., 1968. Chemical composition of the defensive secretion in carabid beetles and its importance as a taxonomic character. *Proc. R. Entomol. Soc. Lond., Ser. B* 37, 62–72. <https://doi.org/10.1111/j.1365-3113.1968.tb00199.x>.
- Muzzi, M., Moore, W., Di Giulio, A., 2019. Morpho-functional analysis of the explosive defensive system of basal bombardier beetles (Carabidae: Pausinae: Metriini). *Micron* 119, 24–38. <https://doi.org/10.1016/j.micron.2019.01.003>.
- Nenadić, M., Soković, M., Glamočlija, J., Čirić, A., Perić-Mataruga, V., Ilijin, L., Tešević, V., Vujisić, L., Todoršević, M., Vesović, N., Čurčić, S., 2016a. Antimicrobial activity of the pygidial gland secretion of three ground beetle species (Insecta: Coleoptera: Carabidae). *Sci. Nat.* 103, 34. <https://doi.org/10.1007/s00114-016-1358-z>.
- Nenadić, M., Soković, M., Glamočlija, J., Čirić, A., Perić-Mataruga, V., Tešević, V., Vujisić, L., Todoršević, M., Vesović, N., Čurčić, S., 2016b. Antimicrobial activity of the pygidial gland secretion of the troglomorphic ground beetle *Laemostenus (Pristonychus) punctatus* (Dejean, 1828) (Insecta: Coleoptera: Carabidae). *Bull. Entomol. Res.* 106, 474–480. <https://doi.org/10.1017/S0007485316000109>.
- Nenadić, M., Soković, M., Glamočlija, J., Čirić, A., Perić-Mataruga, V., Ilijin, L., Tešević, V., Todoršević, M., Vujisić, L., Vesović, N., Čurčić, S., 2017. The pygidial gland secretion of the forest caterpillar hunter, *Calosoma (Calosoma) sycophanta*: the antimicrobial properties against human pathogens. *Appl. Microbiol. Biotechnol.* 101, 977–985. <https://doi.org/10.1007/s00253-016-8082-7>.
- Pasteels, M.J., Gregoir, J.-C., Rowell-Rahier, M., 1983. The chemical ecology of defense in arthropods. *Ann. Rev. Entomol.* 28, 263–289. <https://doi.org/10.1146/annurev.en.28.010183.001403>.
- Rabasović, M.D., Pantelić, D., Jelenković, B., Čurčić, S., Rabasović, M.S., Vrbica, M., Lazović, V., Čurčić, B., Krmpot, A., 2015. Nonlinear microscopy of chitin and chitin structures: a case study of two cave-dwelling insects. *J. Biomed. Opt.* 20, 016010. <https://doi.org/10.1117/1.JBO.20.1.016010>.
- Schildknecht, H., 1970. The defensive chemistry of land and water beetles. *Angew. Chem. Int. Ed.* 9, 1–9. <https://doi.org/10.1002/anie.197000011>.
- Schildknecht, H., Weis, K.H., 1962. Die Abwehrstoffe einiger Carabiden insbesondere von *Abax ater*. XII. Mitteilung über Insektenabwehrstoffe. *Z. Naturforsch. B: Chem. Sci.* 17, 439–447. <https://doi.org/10.1515/znb-1962-0706>.
- Schildknecht, H., Holoubek, K., Weis, K.H., Krämer, H., 1964. Defensive substances of the arthropods, their isolation and identification. *Angew. Chem. Int. Ed.* 3, 73–82. <https://doi.org/10.1002/anie.196400731>.
- Schildknecht, H., Maschwitz, U., Winkler, H., 1968. Zur Evolution der Carabiden-Wehrdrüsensekrete. Über Arthropoden-Abwehrstoffe XXXII. *Naturwissenschaften* 55, 112–117. <https://doi.org/10.1007/BF00624238>.
- Scott, P.D., Hepburn, H.R., Crewe, R.M., 1975. Pygidial defensive secretions of some carabid beetles. *Insect Biochem.* 5, 805–811. [https://doi.org/10.1016/0020-1790\(75\)90024-4](https://doi.org/10.1016/0020-1790(75)90024-4).
- Stark, A., Brennecke, J., Russell, R.B., Cohen, S.M., 2003. Identification of *Drosophila* microRNA targets. *PLoS Biol.* 1, e60. <https://doi.org/10.1371/journal.pbio.0000060>.
- Trautner, J., Geigenmüller, K., 1987. *Illustrated Key to the Cicindelidae and Carabidae of Europe*. Josef Margraf, Aichtal.
- Unkiewicz-Winiarczyk, A., Gromysz-Kalkowska, K., 2012. Ethological defence mechanisms in insects. III. Chemical defence. *Ann. Univ. Mariae Curie-Skłodowska, Sect. C Biol.* 67, 63–74. <https://doi.org/10.2478/v10067-012-0021-0>.
- Vesović, N., 2019. Morphological Study of the Pygidial Glands and Analysis of the Chemical Composition of the Secretions of Selected Ground Beetle Species (Insecta: Coleoptera: Carabidae). *Doctoral Dissertation*. University of Belgrade - Faculty of Biology, Belgrade [in Serbian].
- Vesović, N., Čurčić, S., Todoršević, M., Nenadić, M., Zhang, W., Vujisić, L., 2020. Pygidial gland secretions of *Carabus Linnaeus, 1758* (Coleoptera: Carabidae): chemicals released by three species. *Chemoecology* 30, 59–68. <https://doi.org/10.1007/s00049-019-00298-w>.
- Vesović, N., Čurčić, S., Vujisić, L., Nenadić, M., Krstić, G., Perić-Mataruga, V., Milosavljević, S., Antić, D., Mandić, B., Petković, M., Vučković, I., Marković, Đ., Vrbica, M., Čurčić, B., Makarov, S., 2015. Molecular diversity of compounds from pygidial gland secretions of cave-dwelling ground beetles: the first evidence. *J. Chem. Ecol.* 41, 533–539. <https://doi.org/10.1007/s10886-015-0593-7>.
- Vesović, N., Vujisić, L., Perić-Mataruga, V., Krstić, G., Nenadić, M., Cvetković, M., Ilijin, L., Stanković, J., Čurčić, S., 2017. Chemical secretion and morpho-histology of the pygidial glands in two Palaearctic predatory ground beetle species: *Carabus (Tomocarabus) convexus* and *C. (Procrustes) coriaceus* (Coleoptera: Carabidae). *J. Nat. Hist.* 51, 545–560. <https://doi.org/10.1080/00222933.2017.1293183>.
- Vrbica, M., Petrović, A., Pantelić, D., Krmpot, A., Rabasović, M., Pavlović, D., Jovanić, S., Guéguen, B., Goranov, S., Vesović, N., Antić, Đ., Marković, Đ., Petković, M., Stanislavljević, L., Čurčić, S., 2018. The genus *Phegogmites* Knirsch, 1923 (Coleoptera: Carabidae: Trechinae) in Serbia: taxonomy, morphology and molecular phylogeny. *Zool. J. Linn. Soc.* 183, 347–371. <https://doi.org/10.1093/zoolinnean/zlx078>.
- Will, K.W., Attygalle, A.B., Herath, K., 2000. New defensive chemical data for ground beetles (Coleoptera: Carabidae): interpretations in a phylogenetic framework. *Biol. J. Linn. Soc.* 71, 459–481. <https://doi.org/10.1006/bjil.2000.0456>.
- Xu, S., Errabelli, R., Will, K., Arias, E., Attygalle, A.B., 2019. 3-Methyl-1-(methylthio)-2-butene: a component in the foul-smelling defensive secretion of two *Ceroglossus* species (Coleoptera: Carabidae). *Chemoecology* 29, 171–178. <https://doi.org/10.1007/s00049-019-00286-0>.



## First record of freshwater sponge *Trochospongilla horrida* Weltner, 1893 in Serbia – A morphological and genetic study



Stefan Andjus<sup>a,\*</sup>, Nadja Nikolic<sup>b</sup>, Ana Marjanovic<sup>c</sup>, Marija Brankovic<sup>c</sup>, Vladimir Lazovic<sup>d</sup>,  
Bojana Tubić<sup>a</sup>, Jelena Čanak Atlagić<sup>a</sup>, Vera Nikolić<sup>e</sup>, Momir Paunović<sup>a</sup>

<sup>a</sup> University of Belgrade, Institute of Biological Research “Sinisa Stanković”, Bul. despota Stefana 142, 11060, Belgrade, Serbia

<sup>b</sup> University of Belgrade, School of Dental Medicine, dr Subotica 8, 11000, Belgrade, Serbia

<sup>c</sup> University of Belgrade, School of Medicine, dr Subotica 8, 11000, Belgrade, Serbia

<sup>d</sup> University of Belgrade, Institute of Physics, Pregrevica 118, 11080, Belgrade, Serbia

<sup>e</sup> University of Belgrade, Faculty of Biology, Studentski trg 16, 11000, Belgrade, Serbia

### ARTICLE INFO

#### Keywords:

Porifera

*Trochospongilla horrida*

Serbian rivers

28S rDNA

### ABSTRACT

*Trochospongilla horrida* Weltner, 1893 (Spongillidae, Spongillida) has a relatively wide, though discontinuous, distribution in the Northern Hemisphere. The aim of this paper was to report the first finding of *T. horrida* in Serbia. During 2017, research was carried out on ten tributaries of the Sava and the Danube. *T. horrida* was identified at three localities in Tisa, Juzna Morava and Zapadna Morava rivers, out of 51 inspected sites. For the first time ribosomal 28S DNA was used for *T. horrida* identification.

The genus *Trochospongilla* Vejdovski, 1888 includes 21 species which can be found worldwide. Representatives of the genus have been reported in Europe, China, India, Central Africa, North and South America (Bonetto and De Drago, 1965; Pronzato and Manconi, 2001; Van Soest et al., 2018). Although found throughout the Holarctic area, the species *Trochospongilla horrida* Weltner, 1893 is considered a relatively rare species (Pronzato and Manconi, 2001; Richelle-Maurer et al., 1994). *T. horrida* can populate larger rivers and their deltas, canals, oxbow lakes, backwaters and lakes. It has been detected in the USA, Canada (Manconi and Pronzato, 2016) and Panama (Poirrier, 1990). European rivers and lakes have also been thoroughly investigated for the presence of Porifera (Pronzato and Manconi, 2001), and *T. horrida* has been found in Germany (Gugel, 2000), Belgium (Richelle-Maurer et al., 1994), Italy (Manconi and Pronzato, 2002; Pronzato and Manconi, 2001), Poland (Konopačka, 1983), the Czech Republic (Dorschner et al., 1993), Romania (Andjus et al., 2017). At present, there is no information about the distribution of *T. horrida* in Serbia. In the preliminary report on sponges in Serbia, only Sava and Danube rivers were included and in the Serbian stretches of these two rivers *T. horrida* was not detected (Andjus et al., 2017).

The morphology of the sponge skeleton spicules is commonly used for the identification of Porifera, complemented with molecular genetic analyses. Sequencing of 18S and 28S ribosomal RNA gene is usually performed in order to confirm the species. Interestingly, 28S ribosomal DNA has not been previously used in *T. horrida* identification.

The aims of the present study were to: (a) to present the first record of *T. horrida* in Serbian rivers (other than Sava and Danube); (b) use the 28S ribosomal DNA for further genetic characterization of *T. horrida*.

During September and October 2017, ten tributaries of the Sava and the Danube rivers (Velika Morava, Zapadna Morava, Juzna Morava, Tisa, Kolubara, Porecka River, Mlava, Beli Timok, Crni Timok and Nisava) were surveyed for the presence of freshwater sponges, so far very poorly studied in Serbia.

Samples were collected from hard substrate (stones, submerged wood or roots of aquatic vegetation) using hand nets, hand collection and breath-hold diving and preserved in 96% ethyl alcohol.

The following physico-chemical parameters were measured *in situ*: water temperature, pH, conductivity and dissolved oxygen, using appropriate instrumentation (HANNA HI 9126, HI 9146, and HI98130 instruments, and TFA EN 13,485 digital thermometer).

Spicules were isolated using the nitric acid technique (Manconi and Pronzato, 2016), as follows - pieces of sponge tissue (2–3 mm) were covered with 2–5 ml of concentrated nitric acid to decompose for 24 h; the acid was then removed with a pipette and the spicule pellet was rinsed and soaked in distilled water; finally, the spicules were rinsed with and resuspended in 96% ethanol.

For Light Microscopy (LM), a drop of suspension was placed on a cover slip and after the alcohol had dried the cover slip was placed over the microscope slide with Canada balsam. For Scanning Electron Microscopy (SEM), drops of spicule suspension in ethanol were placed

\* Corresponding author at: University of Belgrade, Institute for Biological Research “Siniša Stanković”, Bulevar despota Stefana 142, 11000, Belgrade, Serbia.

E-mail address: [stefan.andjus@ibiss.bg.ac.rs](mailto:stefan.andjus@ibiss.bg.ac.rs) (S. Andjus).

<https://doi.org/10.1016/j.limno.2019.03.004>

Received 4 December 2018; Received in revised form 31 March 2019; Accepted 31 March 2019

Available online 04 April 2019

0075-9511/ © 2019 Elsevier GmbH. All rights reserved.



on specimen holders and coated with gold in a gold sputter at 18 mA for 1 min.

The spicule suspensions were analyzed and photographed in a MIRA3 TESCAN, high vacuum mode using the SE detector with accelerating voltage.

A fragment of 340 base pairs (bp) corresponding to the D3 domain of sponge 28S rDNA together with the highly conserved region of 150 bp was amplified using the pair of primers as described previously (Lopp et al., 2007; Roovere et al., 2006) – forward 5'-GAC CCG TCT TGA AAC ACG GA-3' and reverse 5'-TCG GAG GGA ACC AGC TAC TA-3'. The PCR amplifications were performed in 25 µl reaction volumes containing about 100 ng of sponge DNA, 2.5 mM MgCl<sub>2</sub>, 200 µM each of dATP, dCTP, dGTP, and dTTP, 0.5 µM of each primer and one unit of Taq polymerase. The DNA was denatured at 95 °C for 1 min, followed by 35 cycles of denaturation at 94 °C for 45 s, annealing at 55 °C for 45 s, and extension at 72 °C, for 1 min, with a final extension at 72 °C for 5 min. The presence of PCR products was confirmed by electrophoresis in 8% polyacrylamide gel. The amplification products were directly sequenced in forward and reverse directions using the ABI Big Dye Terminator chemistry and an ABI 3500 instrument (Applied Biosystems, Foster City, CA). For the detection of defects and polymorphic sites on the ends of the sequences we used Sequencher 5.4.6. software (Free trial version). Comparison of the obtained sequences with sequences in the GenBank database was performed using the Basic Local Alignment Tool (BLAST), available at <http://www.ncbi.nlm.nih.gov>. Sequences were aligned using the program ClustalW with the parameters provided in the software package MEGA (Kumar et al., 2016).

*T. horrida* presence was recorded at three sites in three different rivers: Tisa, locality Kanjiza (46°04'28.4"N, 20°03'17.8"E), Juzna Morava, locality St. Roman (43°36'58.4"N, 21°30'56.8"E) and Zapadna Morava, locality upstream from Kraljevo (43°46'32.1"N, 20°37'45.7"E). Sponge populations were found on rocks in slowly flowing forested river stretches, rich in sediment, at a depth of about 0.5 m (Fig. 1a, b).

The average values of the measured parameters from the three localities where *T. horrida* was found were as follows: water temperature 15 °C, pH 7.7, dissolved oxygen level 8.69 mg/l and the conductivity 552 µs/cm.

*T. horrida* appeared as a thin encrustation of irregular shape, 2–3 cm in diameter, with visible pores, light green to grey. It was identified on the basis of its recognizable mineral spicules: megascleres (approximately 200 x 13 µm) are straight to slightly curved fusiform oxeas

covered with sharp spines (Fig. 2a); the gemmuloscleres are in the form of birotules with a short shaft (height of gemmulosclere shorter than rotule diameter) and two rotules with smooth edges, of approximately the same size (Fig. 2b, c). Microscleres are absent. Another typical characteristic are spherical gemmules 475–540 µm in diameter, located in the basal part of the sponge, grouped in carpets, or singly enveloped in pneumatic pseudo-cage armoured by acanthoxeas, as described by Pronzato and Manconi (2001).

Sequencing of the fragment of sponge 28S rDNA revealed differences and similarities between the 28S sequence of *T. horrida* and the sequences of the most frequent freshwater sponges in European rivers described by Roovere et al. (2006). Differences were present in eight hotspots, all situated between the 90<sup>th</sup> and 135<sup>th</sup> bp, as presented in Fig. 3. Previously, partial sequences of 28S rRNA gene were available only for two species of the genus *Trochospongilla* - *T. latouchiana* and *T. pennsylvanica* (accession numbers EF151955.1 and DQ178650.1, respectively). However, it was not possible to make any alignment between our sequence of *T. horrida* (accession number MH569483.1) and the two sequences mentioned above since the 28S gene regions were not overlapping.

Given the specific oxea megascleres and gemmuloscleres, the determination of *T. horrida* is accurate. Nowadays however, genetic confirmation is considered as a standard procedure (Addis and Peterson, 2005; Lopp et al., 2007; Nichols, 2005; Roovere et al., 2006). Surprisingly, only 18S was used for *T. horrida* genetic identification in previous studies. According to some authors 28S ribosomal DNA, which contains more variable sites than 18S rDNA, complemented with conserved sequences, is optimal for species level identification (Lopp et al., 2007; Roovere et al., 2006). The present study is the first report on *T. horrida* in Serbian rivers. The results are in general agreement with some previous findings about the relatively wide distribution of *T. horrida*, while showing discontinuity in the Northern Hemisphere in cold-temperate regions, along with its scarcity as previously described by Manconi and Pronzato (2016). Sponges were rare in Serbian rivers, although the abiotic factors, such as temperature and oxygen levels were favorable for zoobenthic diversity in general (Bashinskiy et al., 2018). Out of the five sponge species found in Serbian rivers during our survey (*T. horrida*, *Ephydatia fluviatilis* (Linnaeus, 1759), *Spongilla lacustris* Linnaeus, 1758, *Ephydatia muelleri* (Lieberkühn, 1856), and *Eunapius fragilis* (Leidy, 1851)), *T. horrida*, along with *E. fragilis* was the least frequently found Porifera. Out of 51 inspected localities on ten different rivers,

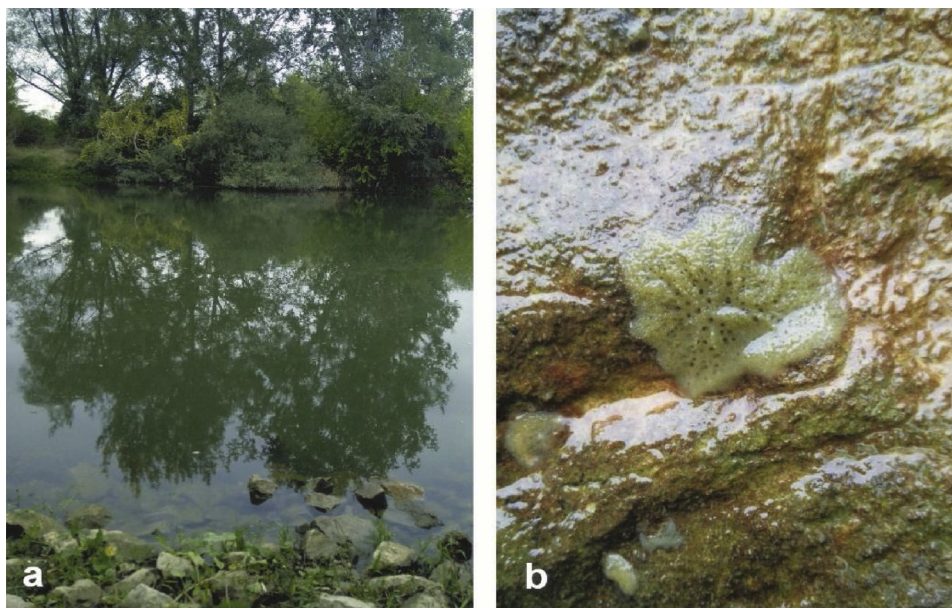


Fig. 1. a) The locality of Zapadna Morava River; b) a specimen of *T. horrida* attached to the underside of a rock found near the shore.

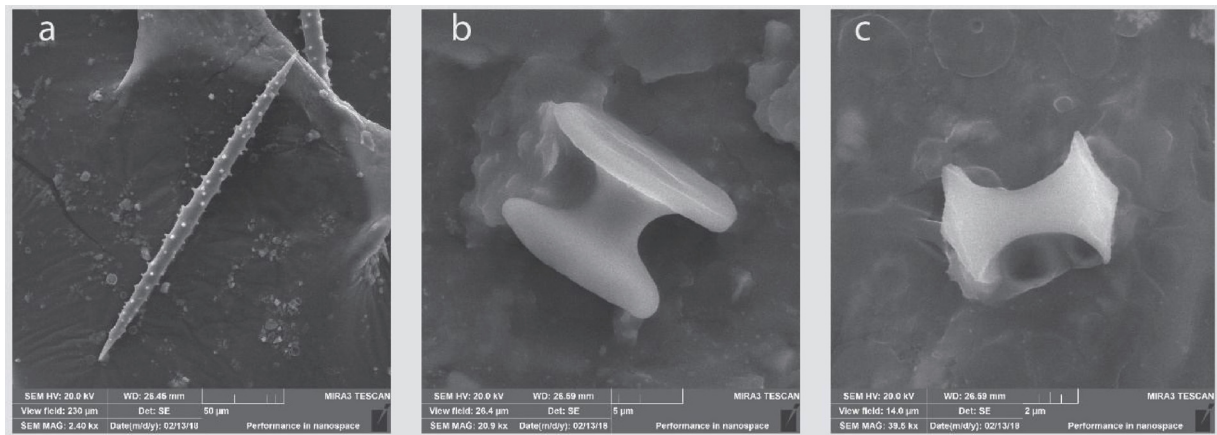


Fig. 2. a) Oxea (megasclere) with spines; b) fully formed gemmulosclere (axis length 9 µm, rotule width 15 µm); c) immature gemmulosclere (axis length 6 µm, rotule width 4 µm).

	10	20	30	40	50
<i>Ephydatia fluviatilis</i>	g a c c c g t c t t	g a a a c a c g g a	C C A A G G A G T G	C A A C A T G C G C	G C G G A G T C T T T
<i>Spongilla lacustris</i>	.	.	.	.	.
<i>Ephydatia muelleri</i>	.	.	.	.	.
<i>Eunapius fragilis</i>	.	.	.	C	.
<i>Trochospongilla horrida</i>	.	.	.	.	.
	60	70	80	90	100
<i>Ephydatia fluviatilis</i>	G G G T G A G A C G	A A A A G C C C T G	T G G C G C A A T G	A A A G T G A A G C	G T C G G C T T G -
<i>Spongilla lacustris</i>	.	.	.	.	C . . . . .
<i>Ephydatia muelleri</i>	.	.	.	.	.
<i>Eunapius fragilis</i>	.	.	.	.	.
<i>Trochospongilla horrida</i>	.	.	.	C . . . . .	C . . . . . T
	110	120	130	140	150
<i>Ephydatia fluviatilis</i>	C C G A C G C G A G	G C G G A G A G C -	C C T C T T C G C G	G G G G C C C A T C	G T C G A C C G A T
<i>Spongilla lacustris</i>	. . . G . . . . .	. . . C . . . . .	. . . A . . . . .	. . . T . . . . .	. . . . .
<i>Ephydatia muelleri</i>	.	. . . C . . . . .	. . . G . . . . .	. . . T . . . . .	. . . . .
<i>Eunapius fragilis</i>	.	. . . A T . . . . .	. . . . .	. . . T . . . . .	. . . . .
<i>Trochospongilla horrida</i>	A . . G . . . . .	. . . . . A C . . . . .	. . . . .	. . . T . . . . .	. . . . .
	160	170	180	190	200
<i>Ephydatia fluviatilis</i>	C C T A T T C A C T	T G T G A A G G G A	T T C G A G T G A G	A G C G T G C C T G	T T G C G A C C C G
<i>Spongilla lacustris</i>	.	.	.	.	.
<i>Ephydatia muelleri</i>	.	.	.	.	.
<i>Eunapius fragilis</i>	.	.	.	.	.
<i>Trochospongilla horrida</i>	.	.	.	.	.
	210	220	230	240	250
<i>Ephydatia fluviatilis</i>	A A A G A T G G T G	A A C T A T G C C T	G A G T A G G G T G	A A G C C A G A G G	A A A C T C T G G T
<i>Spongilla lacustris</i>	.	.	.	.	.
<i>Ephydatia muelleri</i>	.	.	.	.	.
<i>Eunapius fragilis</i>	.	.	.	.	.
<i>Trochospongilla horrida</i>	.	.	.	.	.
	260	270	280	290	300
<i>Ephydatia fluviatilis</i>	G G A A G C T C G T	A G C G A T T C T G	A C G T G C A A A T	C G A T C G T C A A	A C T T G G G T A T
<i>Spongilla lacustris</i>	.	.	.	.	.
<i>Ephydatia muelleri</i>	.	.	.	.	.
<i>Eunapius fragilis</i>	.	.	.	.	.
<i>Trochospongilla horrida</i>	.	.	.	.	.
	310	320	330	340	
<i>Ephydatia fluviatilis</i>	A G G G G C G A A A	G A C T A A T C G A	A C C A T C t a g t	a g c t g g t t c c	c t c c g a
<i>Spongilla lacustris</i>	.	.	.	.	.
<i>Ephydatia muelleri</i>	.	.	.	.	.
<i>Eunapius fragilis</i>	.	.	.	.	.
<i>Trochospongilla horrida</i>	.	.	.	.	.

Fig. 3. 28S rDNA sequence of *T. horrida* compared with four common European freshwater sponges previously sequenced by Roovere et al. (2006), with emphasized base difference.

only three localities harbored this species. Its abundance was also very low. Namely, only 4 specimens were found, one in Juzna Morava, one in Zapadna Morava and 2 in Tisa River. There are also opposite reports. For instance, Gugel found that *Trochospongilla* was the most frequent sponge in the river Rhine in the period 1992–1995 (Gugel, 2000). In agreement with other studies, *T. horrida* was found in Serbian rivers with slightly alkaline waters and slower flows (Gugel, 2000; Ricciardi and Reiswig, 1993).

The Balkan Peninsula is well known for its remarkable biodiversity, and since endemic species of Porifera have been found, for instance *Spongilla stankovici* Arndt, 1938 and *Ochridospongia routunda* Arndt, 1938 in large Macedonian/Albanian lakes (Bănărescu, 2004), other regions with yet unexplored habitats, including Serbia should also be more extensively investigated and mapped for the presence of freshwater sponges.

### Conflict of interest

The authors declare no competing interests.

### Acknowledgment

The study was supported by the Ministry of Education, Science and Technological Development of the Republic of Serbia, Grants No.176018.

### References

- Addis, J.S., Peterson, K.J., 2005. Phylogenetic relationships of freshwater sponges (Porifera, Spongillina) inferred from analyses of 18S rDNA, COI mtDNA, and ITS2 rDNA sequences. *Zool. Scr.* 34, 549–557. <https://doi.org/10.1111/j.1463-6409.2005.00211.x>.
- Andjus, S., Nikolic, N., Dobricic, V., Marjanovic, A., Gacic, Z., Brankovic, G., Rakovic, M., Paunovic, M., 2017. Contribution to the knowledge on the distribution of freshwater sponges—the Danube and Sava rivers case study. *J. Limnol. Balkan Biodiversity*. Springer, pp. 203–217.
- Bănărescu, P.M., 2004. Distribution pattern of the aquatic fauna of the Balkan Peninsula. *Balkan Biodiversity*. Springer, pp. 203–217.
- Bashinskiy, I.V., Senkevich, V.A., Stoyko, T.G., Katsman, E.A., Korkina, S.A., Osipov, V.V., 2018. Forest-steppe oxbows in limnophase—abiotic features and biodiversity. *Limnologia* 74, 14–22.
- Bonetto, A.A., De Drago, I.E., 1965. El Genero *Trochospongilla* Vajdovsky el alto Paraná Argentino (Porifera, Spongillidae). *Physis* 25, 95–98.
- Dorschner, J., Dreyer, U., Gugel, J., Guhr, H., Kinzelbach, R., Meister, A., Seel, P., 1993. Der Gewässerzustand der Elbe 1991. Ergebnisse einer Bereisung mit dem Hess. Meß- und Laborschiff 'Argus' zwischen Veletov und Geestthacht. *Umweltplanung. Arbeits- und Umweltschutz* 153, 99.
- Gugel, J., 2000. High abundance of *Trochospongilla horrida* (Porifera, Spongillidae) in the Rhine (Germany) 1992–1995. *Hydrobiologia* 421, 199–207. <https://doi.org/10.1023/a:1003946604832>.
- Konopacka, A., 1983. 84. Morphological analysis of skeleton elements in freshwater sponges. *Acta Hydrobiol* 2, 157–164.
- Kumar, S., Stecher, G., Tamura, K., 2016. MEGA7: molecular evolutionary genetics analysis version 7.0 for bigger datasets. *Mol. Biol. Evol.* 33, 1870–1874. <https://doi.org/10.1093/molbev/msw054>.
- Lopp, A., Reintamm, T., Vallmann, K., Päre, M., Mikli, V., Richelle-Maurer, E., Kelve, M., 2007. Molecular identification, characterization and distribution of freshwater sponges (Porifera: Spongillidae) in Estonia. *Fundam. Appl. Limnol. für Hydrobiol.* 168, 93–103.
- Manconi, R., Pronzato, R., 2002. Suborder Spongillina subord. nov.: freshwater sponges. In: Hooper, J.N.A., Van Soest, R.W.M., Willenz, P. (Eds.), *Systema Porifera: A Guide to the Classification of Sponges*. Springer US, Boston, MA, pp. 921–1019. [https://doi.org/10.1007/978-1-4615-0747-5\\_97](https://doi.org/10.1007/978-1-4615-0747-5_97).
- Manconi, R., Pronzato, R., 2016. Phylum porifera. In: James, T.H., Christopher, R.D. (Eds.), Thorp and Covich's *Freshwater Invertebrates: Ecology and General Biology*, fourth edition. Academic Press, pp. 133–157. <https://doi.org/10.1016/B978-0-12-385026-3.00008-5>.
- Nichols, S.A., 2005. An evaluation of support for order-level monophyly and inter-relationships within the class Demospongiae using partial data from the large subunit rDNA and cytochrome oxidase subunit I. *Mol. J. Phylogenet. Evol. Biol.* 34, 81–96.
- Poirrier, M.A., 1990. Freshwater sponges (Porifera: Spongillidae) from Panama. *Hydrobiologia* 194, 203–205.
- Pronzato, R., Manconi, R., 2001. Atlas of European freshwater sponges. *Ann. del Mus. Civ. di Stor. Nat. di Ferrara* 4, 3–64.
- Ricciardi, A., Reiswig, H.M., 1993. Freshwater sponges (Porifera, Spongillidae) of eastern Canada: taxonomy, distribution, and ecology. *Can. J. Zool.* 71, 665–682.
- Richelle-Maurer, E., Degoudenne, Y., de Vyver, G., Dejonghe, L., 1994. Some Aspects of the Ecology of Belgian Freshwater Sponges. *Sponges Time Sp.* pp. 341–350.
- Roovere, T., Lopp, A., Reintamma, T., Kuuskalua, A., Richelle-Maurer, E., Kelve, M., 2006. Freshwater sponges in Estonia: genetic and morphological identification. *Proceedings of the Estonian Academy of Sciences, Biology and Ecology* 216–227.
- Van Soest, R.W.M., Boury-Esnault, N., Hooper, J.N.A., Rützler, Kde, De Voogd, N.J., Alvarez de Glasby, B., Hajdu, E., Pisera, A.B., Manconi, R., Schoenberg, C., 2018. World Porifera Database. World Regist. Mar. Species (WoRMS). Available online <http://www.marinespecies.org/porifera/> (Accessed 25 October 2018).



## A new troglobitic species of the genus *Leptomeson* Jeannel, 1924 (Coleoptera: Leiodidae: Cholevinae: Leptodirini) from the Island of Šolta (middle Dalmatia, Croatia)

SREĆKO ĆURČIĆ<sup>1,4</sup>, NIKOLA VESOVIĆ<sup>1</sup>, VLADIMIR LAZOVIĆ<sup>2</sup>, DEJAN PANTELIĆ<sup>2</sup> & TONČI RAĐA<sup>3</sup>

<sup>1</sup>Institute of Zoology, University of Belgrade—Faculty of Biology, Studentski Trg 16, 11000 Belgrade, Serbia

E-mail: [srecko@bio.bg.ac.rs](mailto:srecko@bio.bg.ac.rs)

<sup>2</sup>Institute of Physics, University of Belgrade, Pregrevica 118, 11080 Zemun, Belgrade, Serbia

<sup>3</sup>Špiljar Speleological Society, Varaždinska 53, 21000 Split, Croatia

<sup>4</sup>Corresponding author

*Leptomeson* Jeannel, 1924, originally treated as a subgenus of *Anthroherpon* Reitter, 1889 (Jeannel, 1924), was erected to a distinct genus by Guéorguiev (1990). It currently includes 13 endemic taxa (nine species and four subspecies) (Perreau, 2015), of which five species are recently described (Giachino *et al.*, 2011). All *Leptomeson* taxa are troglobitic, montane or insular, and are distributed in a narrow Dinaric area in the proximity to the Adriatic Sea coast belonging to Croatia and Bosnia and Herzegovina (Perreau, 2000; Giachino *et al.*, 2011) (Fig. 1).

In the recent Catalogue of Palaearctic Coleoptera, within the chapter on the family Leiodidae, Perreau (2015) has reported a few erroneous and inaccurate data on the distribution of certain *Leptomeson* taxa. Namely, *Leptomeson dombrowskii pubipenne* (Müller, 1941) inhabits Mt. Midena in Bosnia and Herzegovina [close to but not in the Duvanjsko Polje (= Duvno field), as reported by Perreau (2015), who claimed the locality is situated in Croatia] (Perreau, 2000). *Leptomeson leonhardi* (Reitter, 1902) lives on Mts. Vran and Čvrsnica in Bosnia and Herzegovina [Perreau (2015) reported it from Mts. Vran and Muharnica, the latter being indeed the northern plateau of Mt. Čvrsnica]. *Leptomeson loreki* (Zoufal, 1904) inhabits a cave in the vicinity of the town of Nevesinje in Bosnia and Herzegovina [not Nevesinje, as reported by Perreau (2015)] (Perreau, 2000). *Leptomeson radjai* Giachino, Bregović & Jalžić, 2011 lives in the vicinity of the cities of Šibenik and Split in Croatia [not on Mali Šibenik, a peak of Mt. Biokovo in Croatia, as reported by Perreau (2015)] (Giachino *et al.*, 2011). Additionally, *Leptomeson svircevi knirschi* Guéorguiev, 1990 inhabits Lisac peak, Mt. Crna Gora, Prenj massif in Bosnia and Herzegovina [not Mt. Prenj in Montenegro, as reported by Perreau (2015)] (Guéorguiev, 1990; Perreau, 2000) (Fig. 1).

The following five taxa are known from the territory of Croatia so far: *Leptomeson biokovenski* Giachino, Bregović & Jalžić, 2011 (from Mt. Biokovo), *L. bujasi* Giachino, Bregović & Jalžić, 2011 (from the Island of Brač), *L. dalmatinus* Giachino, Bregović & Jalžić, 2011 (from the Island of Čiovo), *L. dombrowskii dombrowskii* (Apfelbeck, 1907) (from Mts. Biokovo and Mosor) and *L. radjai* (from the vicinity of the cities of Šibenik and Split) (Giachino *et al.*, 2011) (Fig. 1).

Based on the current distribution of the genus *Leptomeson*, we have supposed that some new species to science may be discovered in the surrounding areas of the Dinaric Alps in the proximity to the Adriatic Sea coast. Špiljar Speleological Society organized a number of field trips in Dalmatia (Croatia) in the last few years led by one of the authors of this study (T.R.), especially on some Adriatic islands close to type localities of other known species of this genus. Eventually, a sample of leptodirine leiodid beetles was recently collected in a pit on the Island of Šolta by the aforementioned author and a few other members of the Špiljar Speleological Society. The specimens enabled us to describe a new species of the genus *Leptomeson*.

**Abbreviations of collections.** IZFB—collection of the Institute of Zoology, University of Belgrade—Faculty of Biology, Belgrade, Serbia; NHMS—collection of the Natural History Museum, Split, Croatia.

**Abbreviations of collector names.** AB—leg. Ana Buklijaš; DA—leg. Dragan Alajbeg; DK—leg. Dejan Kalebić; IB—leg. Ivana Birčić; TR—leg. Tonči Rađa.

**Abbreviations of measures.** AM/BA—ratio of anterior pronotal margin length to pronotal base length; AN/AL—percentage length of antennomeres (ratio of each antennomere length x 100 to antennal length measured from the base of antennal scape to the apex of terminal antennal segment); A2/A1—ratio of antennomere 2 length to antennomere 1 length;

A11/A10—ratio of antennomere 11 length to antennomere 10 length; BO/AL—ratio of body with no head included (pronotum + elytra) length to antennal length measured from the base of antennal scape to the apex of terminal antennal segment; EL/EW—ratio of length of elytra (as linear distance measured along suture from elytral base to apex) to maximum width of elytra; M—mean value for certain measurements; MP/BA—ratio of mesothoracic peduncle length to pronotal base length; PW/PL—ratio of maximum width of pronotum (as greatest transverse distance) to length of pronotum; R—range of total measurements performed; TL—maximum body length measured from the apex of mandibles to the apex of elytra.

**Abbreviations of types.** HT—holotype; PT—paratype; TT—topotype.

**Other abbreviations used in the text.** MI—middle; Mt.—mountain; No.—number.

**Other examined taxa.** *Leptomeson raguzi* Giachino, Bregović & Jalžić, 2011: one TT male, Majića Ponor Cave, village of Drinovci, near Grude, Bosnia and Herzegovina, 20.vii.2000, TR (IZFB).

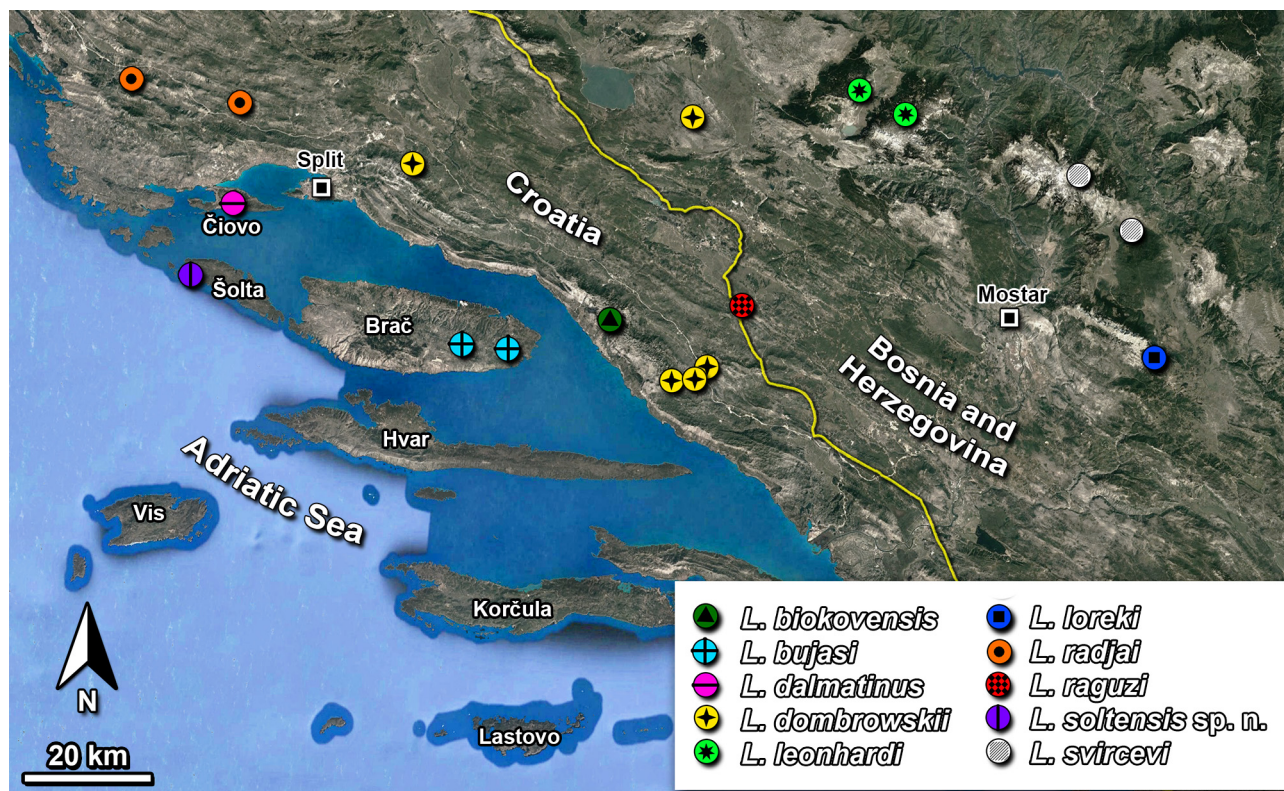


FIGURE 1. The distribution of a new leptodirine species from Croatia and other species of the genus *Leptomeson*.

### *Leptomeson soltensis* Ćurčić & Rađa, sp. n. (Figs. 2–16)

**Type material.** HT male labelled as follows: “Jama na Idrenici Pit, village of Maslinica, Island of Šolta, MI Dalmatia, Croatia, 23.vii.2016 (hand collecting), TR & AB” (white label, printed) / Holotypus *Leptomeson soltensis* sp. n. Ćurčić & Rađa det. 2017 (red label, printed) (NHMS) (Fig. 2). PTs: four females, same data as for HT (IZFB); five males and nine females labelled as follows: “Jama na Idrenici Pit, village of Maslinica, Island of Šolta, MI Dalmatia, Croatia, 09.vii.2017 (pitfall trapping), DK, DA & IB” (IZFB). All PTs are labelled with white, printed locality labels and with red printed labels “Paratypus *Leptomeson soltensis* sp. n. Ćurčić & Rađa det. 2017”.

**Description.** TL R 4.65–5.05 mm, M 4.89 mm, males (M 4.725 mm) smaller than females (M 4.95 mm) (HT 4.65 mm) (Table 1). Integument shiny, of testaceous color, while legs, palps and antennae somewhat lighter. With leptodiroid and elongate body, narrow and elongate pronotum, convex physogastric and scaphoid elytra and wingless (Figs. 2 and 8). Head wider than pronotum, eyeless. Microsculpture weakly expressed, almost absent dorsally (Figs. 2, 11 and 14), developed ventrally (Fig. 10), nearly isodiametric, pentagonal and hexagonal. Head and pronotum almost glabrous (Figs. 2, 9 and 11), while elytra with sparsely distributed hairs (Figs. 15 and 16).

Head hypognathous, elongate, with no eyes and occipital carina, widened anteriorly, broader than pronotum, with an impressed vertex (Figs. 2 and 9). Mandibles concave apically, maxillary palps elongate, penultimate palpomere sub-conical, broadened distally, terminal palpomere conical and elongate. Antennae extremely long (BO/AL R 0.58–0.66, M 0.62, in males M 0.58, while in females M 0.64), thin, antennomere 2 shorter than antennomere 1 (A2/A1 R 0.71–0.82, M 0.77),

distalmost antennomere longer than preceding (A11/A10 R 1.10–1.31, M 1.17) (Table 1). Both dorsal and ventral surfaces smooth, shiny, with a few sparsely distributed short, erect hairs and small punctures. No microsculpture developed.

Values of AN/AL M R for all specimens, males and females are presented in Table 1.

**TABLE 1.** Linear measurements and morphometric ratios in *Leptomeson soltensis* sp. n. Numerical values out of parentheses represent mean values, while those in parentheses are ranges (\* - values in mm).

	All specimens	Males	Females
No. of examined specimens	12	4	8
TL*	4.89 (4.65–5.05)	4.725 (4.65–4.80)	4.95 (4.70–5.05)
BO/AL	0.62 (0.58–0.66)	0.58 (0.58–0.59)	0.64 (0.62–0.66)
A2/A1	0.77 (0.71–0.82)	0.79 (0.76–0.82)	0.76 (0.71–0.815)
A11/A10	1.17 (1.10–1.31)	1.26 (1.21–1.31)	1.14 (1.10–1.17)
A1/AL	5.46 (5.23–5.78)	5.505 (5.23–5.78)	5.43 (5.27–5.53)
A2/AL	4.27 (4.065–4.38)	4.34 (4.30–4.38)	4.22 (4.065–4.30)
A3/AL	10.21 (9.77–10.98)	10.03 (9.96–10.09)	10.33 (9.77–10.98)
A4/AL	10.01 (9.53–10.57)	9.85 (9.53–10.16)	10.12 (9.84–10.57)
A5/AL	12.50 (12.15–13.09)	12.15 (12.15)	12.73 (12.50–13.09)
A6/AL	10.285 (10.09–10.57)	10.13 (10.09–10.16)	10.39 (10.25–10.57)
A7/AL	10.52 (10.28–10.74)	10.42 (10.28–10.56)	10.59 (10.45–10.74)
A8/AL	9.05 (8.37–9.375)	8.76 (8.37–9.16)	9.25 (9.15–9.375)
A9/AL	9.28 (8.54–9.72)	9.44 (9.16–9.72)	9.18 (8.54–9.57)
A10/AL	10.035 (9.35–10.96)	10.80 (10.65–10.96)	9.52 (9.35–9.84)
A11/AL	8.38 (8.13–8.785)	8.58 (8.37–8.785)	8.245 (8.13–8.40)
PW/PL	0.32 (0.31–0.33)	0.32 (0.32–0.325)	0.325 (0.31–0.33)
AM/BA	1.22 (1.15–1.30)	1.23 (1.20–1.26)	1.22 (1.15–1.30)
MP/BA	0.89 (0.80–0.95)	0.87 (0.84–0.90)	0.90 (0.80–0.95)
EL/EW	1.94 (1.82–2.08)	1.98 (1.87–2.08)	1.93 (1.82–2.05)

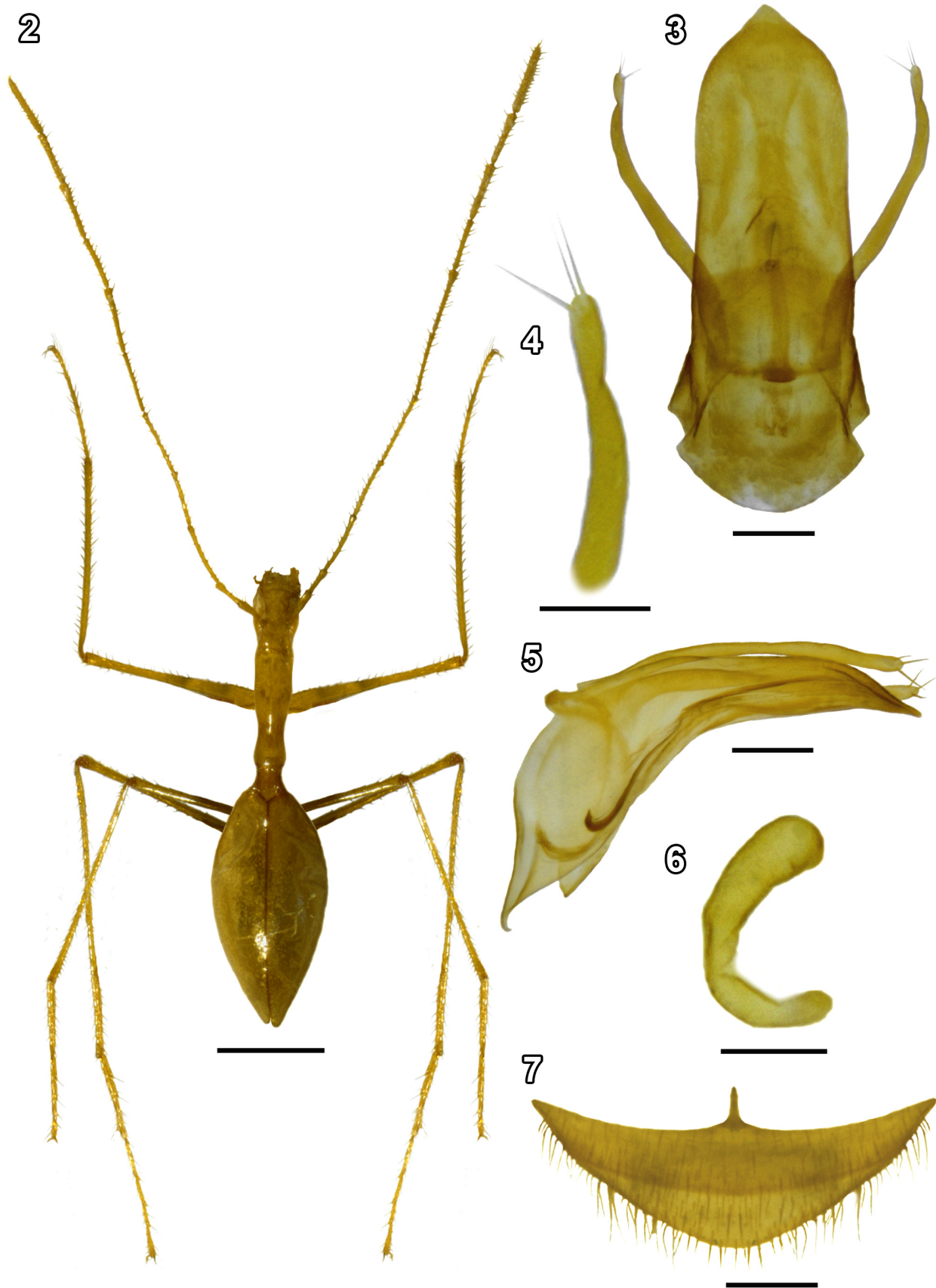
Pronotum very narrow and elongate, approximately three times as long as wide (PW/PL R 0.31–0.33, M 0.32, in males M 0.32, while in females M 0.325), constricted in posterior half and very gently prior to 1/3 of its length, widest at anterior margin, at base distinctly narrower, narrowest between 2/3 and 3/4 of its length, AM/BA R 1.15–1.30, M 1.22 (Figs. 2, 9 and 11; Table 1). Lateral margins strongly sinuate basally, slightly concave anteriorly, very finely bordered in basal 2/3 of pronotal length. Hind angles obtuse and blunt, while fore angles obtuse and rounded. Base convex, not bordered. Disc convex both basally (more pronouncedly) and anteriorly, with a concavity between the latter regions. Dorsal surface smooth, shiny, with a few sparsely distributed short hairs and small punctures. No microsculpture developed.

Mesothoracic peduncle elongate, somewhat shorter than pronotal base (MP/BA R 0.80–0.95, M 0.89) (Table 1). Lateral margins slightly concave. Scutellum elongate, sub-triangular, with pronounced polygonal microsculpture and slightly concave dorsal surface (Figs. 12 and 13).

Prosternum narrow, elongate, with a long sharp sagittal carina, with pronounced microsculpture. Mesosternum sub-triangular, elongate, slightly angled ventrally, with pronounced microsculpture (Figs. 8 and 10), without carina. Mesocoxal cavities widely confluent. Mesosternal process short, sub-triangular. Metasternum huge, slightly wider than long, covered with densely distributed short hairs and punctures, with pronounced microsculpture (Fig. 10). Metacoxal cavities separated. Abdominal ventrites transverse, covered with densely distributed short hairs and punctures, with pronounced microsculpture (Fig. 10).

Elytra elongate, physogastric, scaphoid (EL/EW R 1.82–2.08, M 1.94, in males M 1.98, while in females M 1.93), thick in lateral view (Fig. 8), widest slightly prior to middle, with lateral margins rounded, separated and briefly rounded apically (Figs. 2 and 14) (Table 1). Elytral suture evident. No sutural stria present. Disc strongly convex, smooth, shiny, with sparse and superficial puncturation. No microsculpture developed. Hairs short, sparsely distributed, yellow, erect, slightly denser around elytral median suture and basally, near scutellum (Figs. 15 and 16).

Legs elongate and narrow (Fig. 2). Femora broadened basally, gradually narrowing distally. Tibiae straight and thin both basally and distally. Tarsi not dilated. Protarsomeres pentamerous in males and tetramerous in females. Tarsal claws slightly widened medially, long.



**FIGURES 2–7.** *Leptomeson soltensis* sp. n. from the Jama na Idrenici Pit, village of Maslinica, Island of Šolta, MI Dalmatia, Croatia. 2—holotype male, habitus (dorsal view); 3—holotype male, aedeagus (dorsal view); 4—holotype male, left paramere apex (dorsal view); 5—holotype male, aedeagus (lateral view); 6—paratype female, spermatheca (lateral view); 7—paratype female, abdominal segment VIII. Scales = 1 mm (Fig. 2), 100  $\mu$ m (Figs. 3, 5 and 7) and 50  $\mu$ m (Figs. 4 and 6).

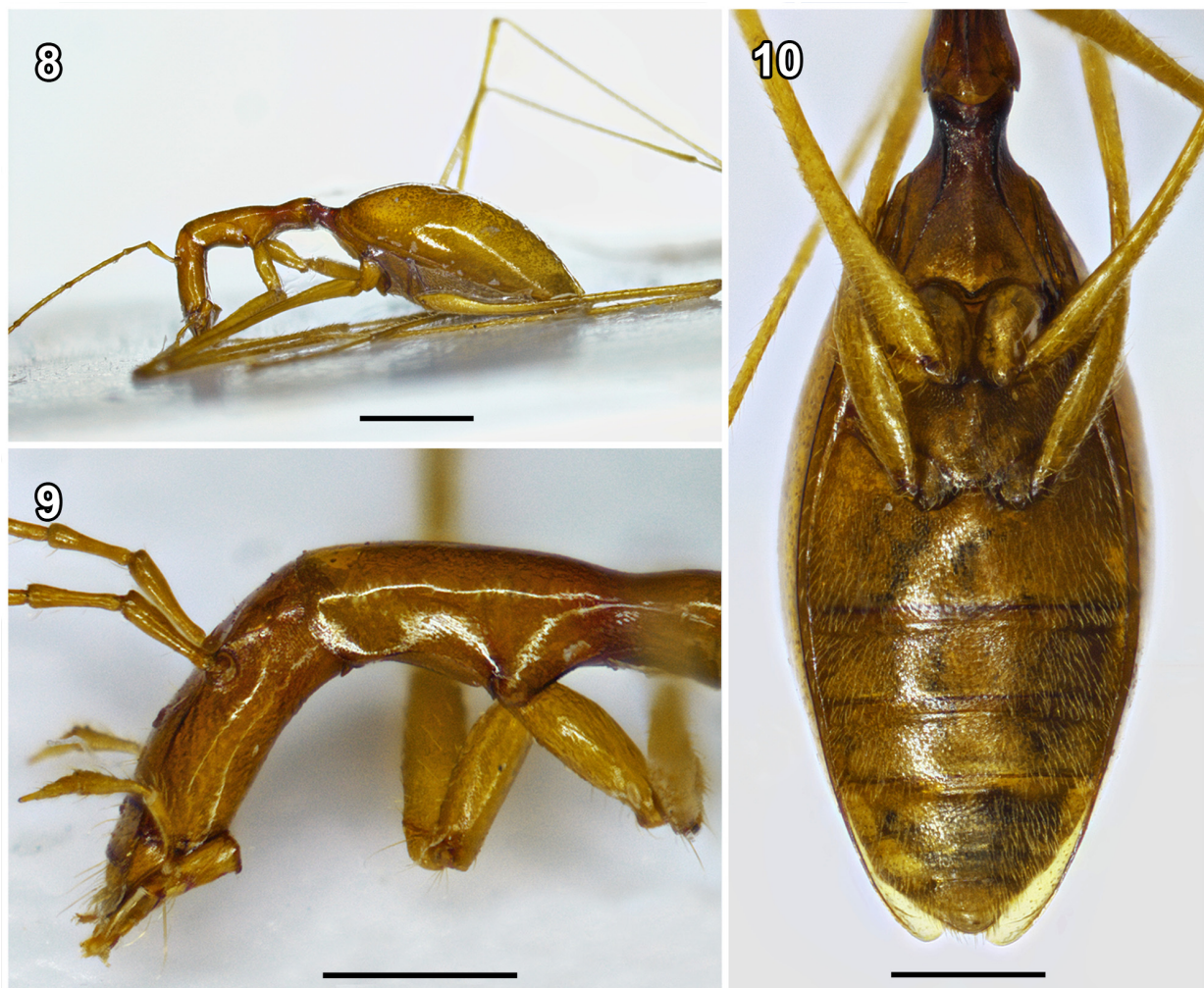
Aedeagus short, robust, almost straight (Figs. 3 and 5). Median lobe in dorsal aspect weakly broadened sub-basally, with a sub-triangular apex, basal bulb short and rounded (Fig. 3). Median lobe in lateral aspect gradually narrowing apically, with a straight pointed apex; basal bulb long and widened (Fig. 5). Parameres elongate, shorter than median lobe, each with three apical setae, in dorsal view curved inwards, gradually narrowing apically, spoon-like and twisted at apex (Figs. 3 and 4), while in lateral view weakly curved, not narrowing apically (Fig. 5). Inner sac with a long chitinized median phanera in the form of a stylet (Fig. 3).

Spermatheca tiny, weakly chitinized, strongly curved, rounded at top (Fig. 6).

Female abdominal sternite VIII large, transverse, with a narrow anterior process, pubescent (Fig. 7).

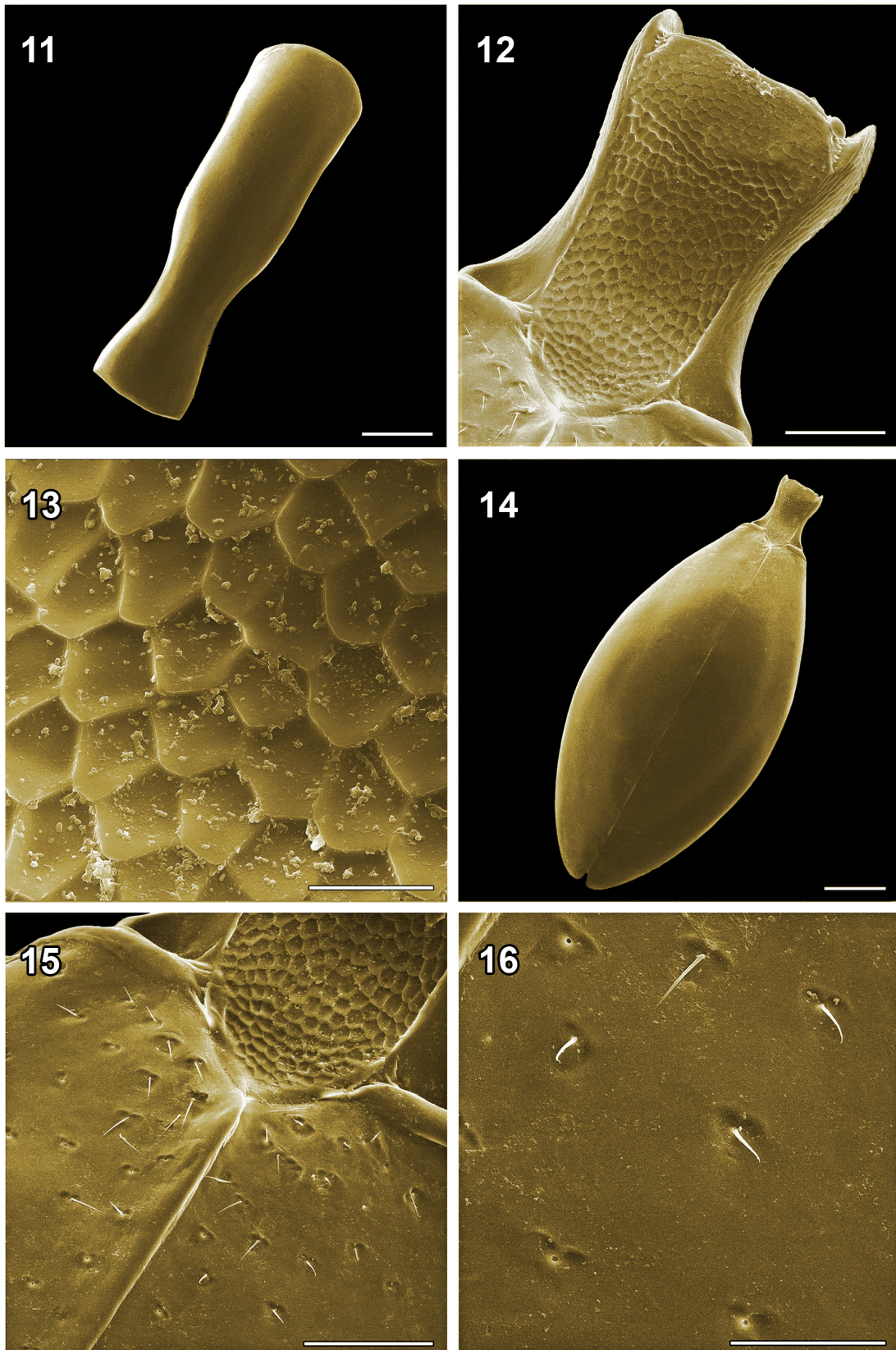
**Differential diagnosis.** *L. soltensis* **sp. n.** is most closely related to *L. dalmatinus* and *L. bujasi*, which inhabit two Croatian Adriatic islands in the surroundings of the Island of Šolta (Čiovo and Brač, respectively) (Giachino *et al.*, 2011). The three mentioned taxa share the following features: presence of pronotum with weakly expressed microsculpture or without microsculpture, elytral disc with short pubescence, parameres bearing three apical setae each and median lobe of aedeagus of similar shape (Giachino *et al.*, 2011).

The new species differs from *L. dalmatinus* in the BO/AL M in males and females (0.58 and 0.64, respectively *vs.* 0.64 and 0.69, respectively), degree of expression of anterior pronotal constriction (barely distinguished *vs.* well expressed), PW/PL M in females (0.325 *vs.* 0.37), MP/BA (mesothoracic peduncle somewhat shorter than pronotal base *vs.* mesothoracic peduncle about as long as pronotal base), EL/EW M in males and females (1.98 and 1.93, respectively *vs.* 2.18 and 2.00, respectively), position of maximum width of elytra (slightly prior to middle *vs.* around at middle), shape of median lobe apex in dorsal aspect (sub-triangular, not protruding *vs.* not sub-triangular, largely rounded and strongly protruding beak-wise), length of parameres (shorter than median lobe *vs.* as long as median lobe) and shape of spermatheca (more curved *vs.* less curved) (Giachino *et al.*, 2011) (Table 2).



**FIGURES 8–10.** *Leptomeson soltensis* **sp. n.** from the Jama na Idrenici Pit, village of Maslinica, Island of Šolta, MI Dalmatia, Croatia. 8—paratype female, habitus (lateral view); 9—paratype female, head and pronotum (lateral view); 10—paratype female, mesosternum, metasternum and abdomen (ventral view). Scales = 1.0 mm (Fig. 8) and 0.5 mm (Figs. 9 and 10).





**FIGURES 11–16.** *Leptomeson soltensis* sp. n. from the Jama na Idrenici Pit, village of Maslinica, Island of Šolta, MI Dalmatia, Croatia. 11—paratype female, pronotum (dorsal view); 12—paratype female, mesothoracic peduncle (dorsal view); 13—paratype female, microsculpture of scutellum (dorsal view); 14—paratype female, elytra (dorsal view); 15—paratype female, basal part of elytra (dorsal view); 16—paratype female, elytral hairs (dorsal view). Scales = 250  $\mu$ m (Fig. 14), 200  $\mu$ m (Fig. 11), 100  $\mu$ m (Figs. 12 and 15), 50  $\mu$ m (Fig. 16) and 20  $\mu$ m (Fig. 13).

It differs from *L. bujasi* in the BO/AL M in females (0.64 vs. 0.80), A11/A10 in females (antennomere 11 longer than antennomere 10 vs. antennomere 11 shorter than antennomere 10), degree of expression of anterior pronotal constriction (barely distinguished vs. well expressed), PW/PL M in males (0.32 vs. 0.28), shape of pronotal base (convex vs. almost straight), MP/BA (mesothoracic peduncle somewhat shorter than pronotal base vs. mesothoracic peduncle about as long as pronotal base), EL/EW M in females (1.93 vs. 1.82), position of maximum width of elytra (slightly prior to middle vs. just beyond middle), shape of median lobe apex in dorsal aspect (not protruding vs. slightly protruding beak-wise), length of parameres (shorter than median lobe vs. as long as median lobe), shape of parameral apex in dorsal aspect (spoon-like, twisted vs. simple, narrow) and shape of spermatheca (less widened distally vs. more widened distally) (Giachino *et al.*, 2011) (Table 2).

**TABLE 2.** Main morphological differences between *Leptomeson soltensis* sp. n. and the most related species *L. dalmatinus* and *L. bujasi*. Source of data: Giachino *et al.* (2011), current paper.

Character	<i>Leptomeson soltensis</i> sp. n.	<i>L. dalmatinus</i>	<i>L. bujasi</i>
BO/AL M in males and females	0.58 and 0.64, respectively	0.64 and 0.69, respectively	0.55 and 0.80, respectively
A11/A10 in females	Antennomere 11 longer than antennomere 10	Antennomere 11 longer than antennomere 10	Antennomere 11 shorter than antennomere 10
Degree of expression of anterior pronotal constriction	Barely distinguished	Well expressed	Well expressed
PW/PL M in males and females	0.32 and 0.325, respectively	0.30 and 0.37, respectively	0.28 and 0.30, respectively
Shape of pronotal base	Convex	Convex	Almost straight
MP/BA	Mesothoracic peduncle somewhat shorter than pronotal base	Mesothoracic peduncle about as long as pronotal base	Mesothoracic peduncle about as long as pronotal base
EL/EW M in males and females	1.98 and 1.93, respectively	2.18 and 2.00, respectively	2.00 and 1.82, respectively
Position of maximum width of elytra	Slightly prior to middle	Around at middle	Just beyond middle
Shape of median lobe apex in dorsal aspect	Sub-triangular, not protruding	Not sub-triangular, largely rounded and strongly protruding beak-wise	Slightly protruding beak-wise
Length of parameres	Shorter than median lobe	As long as median lobe	As long as median lobe
Shape of parameral apex in dorsal aspect	Spoon-like, twisted	Spoon-like, twisted	Simple, narrow
Shape of spermatheca	More curved, less widened distally	Less curved	More widened distally

**Etymology.** The species is named after the Island of Šolta, MI Dalmatia, Croatia, on which is situated the type locality.

**Type locality.** Jama na Idrenici Pit, village of Maslinica, Island of Šolta, MI Dalmatia, Croatia.

**Distribution.** The new species currently inhabits solely the Jama na Idrenici Pit.

**Habitat.** The type specimens were collected by hand and pitfall trapping with rotten meat as bait in the deepest, totally dark part of the Jama na Idrenici Pit, on vertical limestone walls with a high level of humidity (presence of trickling water).

## Acknowledgements

The study was financially supported by the Serbian Ministry of Education, Science and Technological Development [Grants Nos. ON173038, ON171038, III45016 and I-2 (Mimetics of Insects for Sensing and Security) (Science and Technology Development Programme—Joint Funding of Development and Research Projects of the Republic of Serbia and the People's Republic of China)]. We are thankful to Dejan Kalebić, Dragan Alajbeg, Petra Baleta, Ivana Birčić, Ana Buklijaš and Ivana Buklijaš, members of the Špiljar Speleological Society, who helped in field research and collecting scientific samples. We express special gratitude to Dr. Pier Mauro Giachino (Settore Fitosanitario Regionale, Turin, Italy), Dr. Borislav Guéorguiev (National Museum of Natural History, Sofia, Bulgaria), Prof. Dr. Snežana Pešić (University of Kragujevac—Faculty of Science, Kragujevac, Serbia) and an anonymous reviewer for their constructing comments in the manuscript.

## References

- Giachino, P.M., Bregović, P. & Jalžić, B. (2011) Five new species of the genus *Leptomeson* Jeannel, 1924 from Croatia and Bosnia and Herzegovina (Coleoptera, Cholevidae, Leptodirinae). *Natura Croatica*, 20 (2), 355–374.
- Guéorguiev, V.B. (1990) Recherches sur les Bathysciinae (Coleoptera: Catopidae) de Yougoslavie. I. Antroherponini. *Acta Entomologica Musei Nationalis Pragae*, 43, 237–273.
- Jeannel, R. (1924) Monographie des Bathysciinae. *Biospeologica L. Archives de Zoologie expérimentale et générale*, 63, 1–436.
- Perreau, M. (2000) Catalogue des Coléoptères Leiodidae Cholevinae et Platypsyllinae. *Mémoires de la Société entomologique de France*, 4, 1–461.
- Perreau, M. (2015) Family Leiodidae Fleming, 1821. In: Löbl, I. & Löbl, D. (Eds.), *Catalogue of Palaearctic Coleoptera. Vol. 2/1. Hydrophiloidea—Staphylinoidea. Revised and Updated Edition*. Brill, Leiden-Boston, pp. 180–291.



This work is licensed under a Creative Commons Attribution License (CC BY 4.0).

## Research article

[urn:lsid:zoobank.org/pub:B4BE1ABB-A27F-4985-A330-C3352A1147A6](https://zoobank.org/pub:B4BE1ABB-A27F-4985-A330-C3352A1147A6)

# On the diversity of subterranean beetles of the Dinarides: new leiodid taxa (Coleoptera: Leiodidae) from Serbia

Srećko ĆURČIĆ<sup>1,\*</sup>, Dragan PAVIĆEVIĆ<sup>2,11</sup>, Nikola VESOVIĆ<sup>3</sup>, Maja VRBICA<sup>4</sup>,  
Miloš KURAICA<sup>5</sup>, Đorđe MARKOVIĆ<sup>6</sup>, Matija PETKOVIĆ<sup>7</sup>, Vladimir LAZOVIĆ<sup>8</sup>,  
Dejan PANTELIĆ<sup>9</sup> & Fabrizio BOSCO<sup>10</sup>

<sup>1,3,4,5,7</sup>Institute of Zoology, University of Belgrade - Faculty of Biology,  
Studentski Trg 16, 11000 Belgrade, Serbia.

<sup>2</sup>Serbian Biospeleological Society, Trg Dositeja Obradovića 2, 21000 Novi Sad, Serbia.

<sup>6</sup>School of Zoology, George S. Wise Faculty of Life Sciences, Tel-Aviv University,  
P.O. Box 39040, Tel Aviv 6997801, Israel.

<sup>8,9</sup>Institute of Physics Belgrade, University of Belgrade, Pregrevica 118, 11080 Belgrade, Serbia.

<sup>10</sup>A.F. Linder Association for the Study of Karst, Via Fratelli Cervi 9/G,  
34077 Ronchi dei Legionari, Italy.

<sup>11</sup>Krunska 15, 11000 Belgrade, Serbia.

\* Corresponding author: [srecko@bio.bg.ac.rs](mailto:srecko@bio.bg.ac.rs)

<sup>2</sup>Email: [dragan.pavicevic@hotmail.com](mailto:dragan.pavicevic@hotmail.com)

<sup>3</sup>Email: [nikola.vesovic@bio.bg.ac.rs](mailto:nikola.vesovic@bio.bg.ac.rs)

<sup>4</sup>Email: [maja.vrbica@bio.bg.ac.rs](mailto:maja.vrbica@bio.bg.ac.rs)

<sup>5</sup>Email: [kuraica@gmail.com](mailto:kuraica@gmail.com)

<sup>6</sup>Email: [djordje.markovic@zoho.com](mailto:djordje.markovic@zoho.com)

<sup>7</sup>Email: [matija.petkovic@bio.bg.ac.rs](mailto:matija.petkovic@bio.bg.ac.rs)

<sup>8</sup>Email: [lazovicv@ipb.ac.rs](mailto:lazovicv@ipb.ac.rs)

<sup>9</sup>Email: [pantelic@ipb.ac.rs](mailto:pantelic@ipb.ac.rs)

<sup>10</sup>Email: [fbosco1959@libero.it](mailto:fbosco1959@libero.it)

<sup>1</sup>[urn:lsid:zoobank.org/author:D495B4D6-C13B-4604-BA20-FB91AC31395A](https://zoobank.org/author:D495B4D6-C13B-4604-BA20-FB91AC31395A)

<sup>2</sup>[urn:lsid:zoobank.org/author:15893469-3368-4566-AF88-170CDF3DD072](https://zoobank.org/author:15893469-3368-4566-AF88-170CDF3DD072)

<sup>3</sup>[urn:lsid:zoobank.org/author:AA52F4F6-C952-4887-B257-FDBED464C5DA](https://zoobank.org/author:AA52F4F6-C952-4887-B257-FDBED464C5DA)

<sup>4</sup>[urn:lsid:zoobank.org/author:47E4BA55-887B-4BDB-A6BF-C8490ACE633A](https://zoobank.org/author:47E4BA55-887B-4BDB-A6BF-C8490ACE633A)

<sup>5</sup>[urn:lsid:zoobank.org/author:D08B8433-4F2B-4C1C-A741-6840F2B18B88](https://zoobank.org/author:D08B8433-4F2B-4C1C-A741-6840F2B18B88)

<sup>6</sup>[urn:lsid:zoobank.org/author:8D3E0F6F-E182-480B-908C-373DC331E3EE](https://zoobank.org/author:8D3E0F6F-E182-480B-908C-373DC331E3EE)

<sup>7</sup>[urn:lsid:zoobank.org/author:EBAC2E4C-D69A-407B-9FE1-3587DA21628E](https://zoobank.org/author:EBAC2E4C-D69A-407B-9FE1-3587DA21628E)

<sup>8</sup>[urn:lsid:zoobank.org/author:DC9A3926-6CBF-41B9-9A25-3B5AED053BCA](https://zoobank.org/author:DC9A3926-6CBF-41B9-9A25-3B5AED053BCA)

<sup>9</sup>[urn:lsid:zoobank.org/author:CE4DAE64-D33D-48CC-88CF-E6F35501B922](https://zoobank.org/author:CE4DAE64-D33D-48CC-88CF-E6F35501B922)

<sup>10</sup>[urn:lsid:zoobank.org/author:918BD686-1CA3-45BA-8D22-A7C6FF81E4D3](https://zoobank.org/author:918BD686-1CA3-45BA-8D22-A7C6FF81E4D3)

**Abstract.** Three subterranean leptodirine leiodid taxa, viz., *Bozidaria* Ćurčić & Pavićević gen. nov., *Bozidaria serbooccidentalis* Ćurčić & Pavićević gen. et sp. nov. and *Proleonhardella* (*Proleonhardella*) *tarensis* Ćurčić & Pavićević sp. nov., are described and diagnosed. *Bozidaria* Ćurčić & Pavićević

gen. nov. belongs to the phyletic series of “*Leonhardella*”. The new beetle taxa differ from their closest relatives in numerous morphological characters. They most likely belong to phyletic lineages of Pliocene age. The new leiodid taxa are endemic to the Dinaric mountain chain of western Serbia. Keys to the leptodirine leiodid genera of the phyletic series of “*Leonhardella*” and to the taxa of the genus *Proleonhardella* Jeannel, 1910 are included.

**Keywords.** New genus, new species, endogean and cave-dwelling, Cholevinae, Leptodirini.

Ćurčić S., Pavićević D., Vesović N., Vrbica M., Kuraica M., Marković Đ., Petković M., Lazović V., Pantelić D. & Bosco F. 2021. On the diversity of subterranean beetles of the Dinarides: new leiodid taxa (Coleoptera: Leiodidae) from Serbia. *European Journal of Taxonomy* 782: 55–81. <https://doi.org/10.5852/ejt.2021.782.1589>

## Introduction

A moderately rich endogean and a relatively poor cave-dwelling fauna of leiodid beetles occur in Serbia. This diversity is highest in the western and southwestern parts of the country (Jeannel 1924; Perreau 2000; Ćurčić 2005; Ćurčić *et al.* 2006, 2008b, 2015, 2018). Most subterranean leptodirine taxa from Serbia are either bathyscioid (*Magdelainella* spp., *Proleonhardella* spp., *Pavicevicia* spp., *Bathyscia montana apfelbecki* Ganglbauer, 1899 and *Pseudobathyscidius serbicus* (Karaman, 1964)) or pholeuonoid (*Pholeuonopsis* spp.) (Jeannel 1924; Nonveiller 1983; Moldovan *et al.* 2018; Perreau 2019). Highly-evolved scaphoid taxa are the representatives of the genus *Remyella* Jeannel, 1931, which are distributed in a narrow Dinaric area in southwestern Serbia and northeastern Montenegro (Njunjić *et al.* 2017). Interestingly, no highly-evolved leptodiroid taxa are known from Serbia so far, although some species of *Anthroherpon* Reitter, 1889 inhabit certain areas close to the country’s border (Njunjić *et al.* 2015). Most leiodid taxa from Serbia are associated with the Central Dinarides, a smaller amount with the Inner Dinarides, while the Carpathian-Balkan mountain system is characterized by only a few taxa (e.g., the endemic genus *Pseudobathyscidius* Karaman, 1964 and the endemic *Magdelainella* subgenus *Derveniella* Pavićević & Perreau, 2008) (Perreau 2015; Hlaváč *et al.* 2017).

The genus *Proleonhardella* Jeannel, 1910 currently includes 10 endemic taxa (eight species and two subspecies) (Perreau 2000, 2015; Hlaváč *et al.* 2017), which were all described in the first half of the twentieth century. *Proleonhardella* taxa are distributed in a narrow Dinaric area belonging to Bosnia and Herzegovina, Serbia, and Montenegro (Perreau 2000; Pavićević *et al.* 2012). The genus is divided into two subgenera: *Proleonhardella* Jeannel, 1910 and *Pholeuonillus* Breit, 1913. The former subgenus includes seven species and two subspecies inhabiting caves in the montane areas of central, eastern and southeastern Bosnia and Herzegovina, southwestern Serbia and northern Montenegro (Perreau 2000; Pavićević *et al.* 2012). The latter subgenus contains only one endogean montane species from southern Bosnia and Herzegovina (Perreau 2000). Two species of *Proleonhardella* occur in Serbia: *Proleonhardella* (*Proleonhardella*) *hirtella* Jeannel, 1934 (described from the Popova Pećina Cave, village of Seljane, near the town of Prijepolje, southwestern Serbia) and *P. (P.) remyi* Jeannel, 1934 (described from the Bjeloševačka (= Dvostruka) Pećina Cave, village of Bjeloševina, near the town of Pljevlja, northern Montenegro) (Fig. 9) (Perreau 2000).

In the chapter on the family Leiodidae in the recent Catalogue of Palaearctic Coleoptera, Perreau (2015) reported the presence of both species of *Proleonhardella* solely for Serbia (Pešter Plateau). In reality, the type localities of both species are not situated on the Pešter Plateau, but in its surroundings. Additionally, they inhabit the territory of Montenegro, as documented by Pavićević *et al.* (2012) and Hlaváč *et al.* (2017). Namely, *P. (P.) hirtella*, besides its type locality, is known to inhabit three caves and pits near the towns of Prijepolje and Priboj (southwestern Serbia) and one pit near the town of Pljevlja (northern

Montenegro) (Pavićević *et al.* 2012). On the other hand, *P. (P.) remyi*, besides its type locality, lives in numerous caves and pits in the area of Kamena Gora and near the towns of Prijepolje and Priboj (southwestern Serbia), as well as in two caves and one pit near the town of Pljevlja (northern Montenegro) (Pavićević *et al.* 2012). The two species cohabit in some caves and pits (five such localities are known), where the populations of the latter are more abundant (Pavićević *et al.* 2012). Additionally, the type locality of *P. (P.) remyi* in northern Montenegro is erroneously reported by Perreau (2000) to be situated in Serbia.

On the basis of the current distribution of Serbian endogean and cave-dwelling leioidid taxa, we assumed that some taxa new to science (genera and species) might be discovered in certain karstic areas of the Dinaric Alps of Serbia, which were so far not investigated and from which no taxa of leioidids from the underground have been documented.

Several field surveys conducted by the staff of the Institute of Zoology, University of Belgrade - Faculty of Biology and the Institute for Nature Conservation of Serbia at a few speleological sites in western Serbia, as well as by the late Prof. Guido Nonveiller on Mt Bobija in western Serbia, resulted in the discovery of a new leptodirine genus, viz., *Bozidaria* Ćurčić & Pavićević gen. nov., and two new leptodirine species, *B. serbooccidentalis* Ćurčić & Pavićević gen. et sp. nov. and *Proleonhardella (Proleonhardella) tarensis* Ćurčić & Pavićević sp. nov., the descriptions and diagnoses of which are given in the current study.

#### **Material and methods**

The material of *Bozidaria serbooccidentalis* gen. et sp. nov. is comprised of a large series of individuals: four males and five females collected in traps for endogean fauna baited with rotten meat during 1980 on Mt Bobija, near the town of Ljubovija, western Serbia, as well as 30 males and 44 females collected by pitfall trapping during 2010 and 2017 in the Simina Jama Pit, village of Gornje Košlje, Debelo Brdo saddle, Mt Povlen, near the town of Ljubovija, western Serbia. That of *Proleonhardella (Proleonhardella) tarensis* sp. nov. includes four males and four females collected by pitfall trapping during 2014 in Pit 4-1-3-27, village of Kaluderske Bare, Mt Tara, near the town of Bajina Bašta, western Serbia, as well as three males and five females collected by pitfall trapping during 2003 in the Sovljačka Pećina Cave, village of Šljivovica, Mt Tara, near the town of Bajina Bašta, western Serbia.

Type specimens were studied in the laboratories of the Institute of Zoology, University of Belgrade - Faculty of Biology, Belgrade, Serbia. The beetles were dissected, analysed in detail and photographed. Dry individuals were glued onto rectangular paper mounting cards. Extracted genitalia were fixed in a medium composed of Canada balsam and toluene and put onto rectangular transparent plastic mounting cards placed on the same entomological pin together with the mounting card of the dry individual.

Observations were conducted with a Carl Zeiss-Stemi 2000 binocular stereo microscope. A Nikon SMZ 18 stereo microscope combined with a Nikon DS-Fi1c digital camera, as well as a Leica DMLS light microscope combined with a Leica DC 300 camera, were used to photograph morphological details of the whole specimens and genitalia of new beetle taxa. The detailed morphology of the new taxa was imaged using scanning electron microscopy (SEM) at the Photonics Center, Institute of Physics Belgrade, University of Belgrade. SEM micrographs were made using a MIRA3 FEGSEM field-emission scanning electron microscope (FESEM) (Tescan, Brno, Czech Republic) in high vacuum mode, at a voltage of 15 kV. All samples were sputter coated with gold/palladium for 30 seconds. The index of intensity of the electron beam was 15.00. Pressure in the column was about 127 MPa.

### Abbreviations of measurements

A1/A2	=	ratio of length of antennomere I to length of antennomere II
A3/A2	=	ratio of length of antennomere III to length of antennomere II
A3/A5	=	ratio of length of antennomere III to length of antennomere V
A7/A6	=	ratio of length of antennomere VII to length of antennomere VI
A7/A8	=	ratio of length of antennomere VII to length of antennomere VIII
A8LW	=	ratio of length to width of antennomere VIII
A9LW	=	ratio of length to width of antennomere IX
A9/A8	=	ratio of length of antennomere IX to length of antennomere VIII
A10LW	=	ratio of length to width of antennomere X
A11LW	=	ratio of length to width of antennomere XI
A11/A9+A10	=	ratio of length of antennomere XI to length of antennomeres IX and X combined
EL/EW	=	ratio of length of elytra (as linear distance between base to apex of elytra along median suture) to maximum width of elytra
EL/PL	=	ratio of length of elytra (as linear distance between base to apex of elytra along median suture) to length of pronotum
HL/HW	=	ratio of length of head (as linear distance between anterior margin of clypeus to occipital carina) to maximum width of head
M	=	mean value for certain measurements
P1LW	=	ratio of length to width of protarsomere I
PB/AM	=	ratio of length of pronotal base to length of anterior pronotal margin
PL/PW	=	ratio of length of pronotum to maximum width of pronotum
PL+EL/AL	=	ratio of length of pronotum and elytra combined (as linear distance between anterior pronotal margin to apex of elytra along median suture) to total antennal length
R	=	range of measured values
TL	=	maximum body length from anterior margin of clypeus to apex of elytra along median suture

### Repositories

CDP	=	collection of Dragan Pavićević, Belgrade, Serbia
IZFB	=	Institute of Zoology, University of Belgrade - Faculty of Biology, Belgrade, Serbia
SBS	=	Serbian Biospeleological Society, Novi Sad, Serbia

### Other abbreviations used in the text

Ma	=	million years
Mt	=	Mountain/Mount

### Other material examined

#### *Proleonhardella (Proleonhardella) hirtella* Jeannel, 1934

SERBIA • 1 ♂; southwestern Serbia, municipality of Priboj, village of Krnjača, Tmuša Gorge, Goveda Pećina Cave; 17 Jul. 2013; Dragan Antić leg.; IZFB.

#### *Proleonhardella (Proleonhardella) remyi* Jeannel, 1934

SERBIA • 6 ♂♂, 8 ♀♀; southwestern Serbia, municipality of Priboj, village of Krnjača, Tmuša Gorge, Goveda Pećina Cave; 17 Jul. 2013; Dragan Antić leg.; IZFB • 8 ♂♂, 18 ♀♀; southwestern Serbia, municipality of Prijepolje, Kamena Gora, village of Kamena Gora, Bezdán Pit; 20 May–5 Nov. 2017; Miloš Kuraica leg.; pitfall traps; IZFB.

## Results

Subphylum Hexapoda Latreille, 1825  
Class Insecta Linnaeus, 1758  
Order Coleoptera Linnaeus, 1758  
Suborder Polyphaga Emery, 1886  
Family Leiodidae Fleming, 1821  
Subfamily Cholevinae Kirby, 1837  
Tribe Leptodirini Lacordaire, 1854

Genus *Bozidaria* Ćurčić & Pavićević gen. nov.

[urn:lsid:zoobank.org:act:8CF69930-741E-4484-9F09-5E8C1FBC86AA](https://zoobank.org/act:8CF69930-741E-4484-9F09-5E8C1FBC86AA)

### Type species

*Bozidaria serbooccidentalis* Ćurčić & Pavićević gen. et sp. nov., by monotypy.

### Diagnosis

*Bozidaria* gen. nov. is most closely related to the following Dinaric genera of the group Théléomorphes belonging to the phyletic series of “*Leonhardella*” (Jeannel 1924): *Proleonhardella*, *Blattochaeta* Reitter, 1910, *Augustia* Zariquiey, 1927 and *Pholeuodromus* Breit, 1913. These genera share a similar body form, the presence of tetramerous tarsi in males, the absence of a comb on anterior tibiae, the first antennomere clearly shorter than the second antennomere, apically widened distal antennomeres, the absence of sutural striae, and the presence of a similar type of aedeagus.

The new genus differs from its closest relatives in the body shape (elliptical, elongate vs bathyscioid, oval/ovoid, mostly wide in *Proleonhardella*), TL (R 2.51–2.80 mm vs R 4.0–5.5 mm in *Blattochaeta* and R 3.8–4.6 mm in *Pholeuodromus*), body pubescence (short, recumbent vs long, erect in *Blattochaeta*), shape of antennae (elongate, thin, including distal antennomeres vs short, distal antennomeres wide, barely longer than wide in *Proleonhardella*), length of antennae (exceeding the middle of the body vs reaching, but not exceeding the middle of the body in *Augustia* and not reaching the middle of the body in *Pholeuodromus*), presence/absence of mesosternal carina (present vs absent in *Augustia*), shape of mesosternal carina (with no concavity on its anterior border, not atrophied vs with a concavity on its anterior border in *Blattochaeta* and atrophied posteriorly in *Pholeuodromus*), shape of lateral pronotal margins (arcuate vs weakly convex in *Augustia*), position of maximum pronotal length (sub-basally vs at base in *Pholeuodromus*), ratio of pronotum width to elytral width (pronotum slightly narrower than elytra vs pronotum as wide as elytra in *Blattochaeta* and *Pholeuodromus* and pronotum clearly narrower than elytra in *Augustia*), shape of elytra (more rounded, gradually narrowed distally vs less rounded, more pronouncedly attenuated distally in *Augustia*), shape of aedeagus (long, elongate vs short, wide in *Blattochaeta* and *Augustia* and mostly wide in *Proleonhardella*), shape of basal bulb (elongate, narrow vs short, rounded in *Proleonhardella*, *Blattochaeta* and *Augustia*) and its basal projection (long vs short in *Proleonhardella* and *Augustia*), and shape of parameral apex (narrow vs widened in *Blattochaeta*) (Jeannel 1910, 1924, 1930, 1931, 1934; Reitter 1910; Breit 1913; Zariquiey 1927; Knirsch 1928; Guéorguiev 1976).

### Etymology

This genus is named after the late Academician Božidar Ćurčić, a well-known Serbian biospeleologist and zoologist.



## Description

**HABITUS.** A small-sized elliptical leptodirine with short and wide head, transverse pronotum and elongate obovoid elytra. Blind, reddish-brown, body shiny, densely pubescent, dorsoventrally convex, finely punctate. Pubescence composed of short yellow hairs, on pronotum and elytra recumbent, while on head erect. Legs and antennae long and slender, densely pubescent. Microsculpture composed of isodiametric meshes.

**HEAD.** Anophthalmous, of almost equal length and width. Antennae inserted medially on head, elongate, thin, apically widened and flattened, exceeding middle of body, reaching basal third of elytral length. Antennomere I shorter than antennomere II. Antennomere III shorter than antennomere II and longer than antennomere IV. Antennomeres IV–VI of similar length. Antennomere VII elongate, apically widened. Antennomere VIII short, elongate, oval. Ultimate antennomere slender, ovoid, about as long as antennomeres IX and X combined. Occipital carina present.

**THORAX.** Pronotum almost twice as wide as long, with arcuate and well-rounded lateral margins, slightly narrower than elytra, widest slightly prior to pronotal base. Mesosternal carina well-developed, with no furrow, high, obtuse-angled, with an apical tooth.

**ELYTRA.** Elongate, much longer than pronotum, rounded medially, regularly arcuate distally, not attenuated. Scutellar striae absent. A part of pygidium not covered by elytra.

**LEGS.** Extended and slender. Fore tarsi tetramerous. Male protarsi dilated. Tibiae with spines on external edges. No comb on external edges or apical parts of protibiae. Meso- and metatibiae with no apical baskets.

**ABDOMEN.** Median lobe of aedeagus slender, rounded sub-terminally, with an elongate triangular apex. Basal bulb elongate, narrow, with a long sub-triangular basal projection. Each paramere longer than median lobe, thin, sub-terminally widened, with three apical setae.

**GONOSTYLI.** Elongate, slender, almost straight.

## Distribution

The new genus is currently known to inhabit deep soil on Mt Bobija and the Simina Jama Pit on Mt Povlen in the surroundings of the town of Ljubovija, western Serbia. It is probable that it might be present both in the soil and caves of the adjacent areas.

## Key to the leptodirine leiodid genera of the phyletic series of “*Leonhardella*”

(modified after Guéorguiev 1976) (Fig. 1)

1. Body of bathyscioid form, oval or ovoid, wide and short ..... 2  
– Body of elliptical or pholeuonoid form ..... 6
2. Mesosternal carina absent (Fig. 1A). Cavernicolous, Mt Čvrsnica, southwestern Bosnia and Herzegovina ..... *Augustia* Zariquiey, 1927  
– Mesosternal carina present (Fig. 1B) ..... 3
3. Antennae short, not reaching middle of body ..... 4  
– Antennae much longer, reaching middle of body ..... 5
4. Pubescence fine and recumbent, except in both lateral exterior border of elytra and apical elytral half, where long hairs occur. Antennae very short, barely exceeding pronotal base. Longer species

- (TL 2.5 mm). Mesosternal carina rounded. Basal lamina of tegmen of aedeagus without tooth. Cavernicolous, region of Kuči, vicinity of the city of Podgorica, eastern Montenegro ..... *Weiratheria* Zariquiey, 1927
- Pubescence entirely normal and recumbent. Antennae somewhat longer, but not reaching middle of body. Shorter species (TL 1.85 mm). Mesosternal carina triangular. Basal lamina of tegmen of aedeagus with a pronounced tooth basally. Cavernicolous, vicinity of the town of Karystos, island of Euboea, southern Greece ..... *Henrotiella* Perreau, 1999
5. Pubescence short and recumbent. Anterior border of mesosternal carina without concavity (Fig. 1C). Protarsi weakly dilated in males. Shorter species (TL 1.3–3.5 mm). Cavernicolous and endogean, central, eastern and southern Bosnia and Herzegovina, southwestern and western Serbia and eastern Montenegro ..... *Proleonhardella* Jeannel, 1910
- Pubescence long and erect. Anterior border of mesosternal carina with a deep concavity (Fig. 1D). Protarsi not dilated in males. Longer species (TL 4.0–5.5 mm). Cavernicolous, western, southwestern and eastern Montenegro, southern Bosnia and Herzegovina and southern Croatia ..... *Blattochaeta* Reitter, 1910
6. Body of elliptical form (Fig. 1E). Pronotum regularly or almost regularly arcuate, slightly narrower than elytra or as wide as elytra ..... 7
- Body of pholeuonoid form (Fig. 1F). Pronotum campanuliform or strongly sinuated backwards, clearly narrower than elytra ..... 11
7. Body shorter (TL 1.8–2.0 mm). Antennae almost reaching middle of body. Elytra very attenuated apically, with sparse pubescence. Ventral border of mesosternal carina triangular and deeply grooved. Endogean and cavernicolous, southern Croatia and western Bosnia and Herzegovina ..... *Anisoscapa* Müller, 1917
- Body longer (TL 2.5–5.2 mm). Antennae reaching middle of body. Elytra regularly arcuate apically, with dense pubescence. Ventral border of mesosternal carina not grooved ..... 8
8. Body shorter (TL 2.5–3.0 mm). Mesosternal carina not atrophied. Protarsi dilated in males (Fig. 1G) ..... 9
- Body longer (TL 3.8–5.2 mm). Mesosternal carina atrophied posteriorly. Protarsi not dilated in males (Fig. 1H) ..... 10
9. Body very elongate and narrower. Pubescence long and erect. Median lobe more elongate, thin. Basal bulb small, with a short rounded basal projection (Fig. 1I). Paramerae distally widened. Cavernicolous, southern and southeastern Bosnia and Herzegovina and western Montenegro ..... *Anillocharis* Reitter, 1903
- Body less elongate and wider. Pubescence short and recumbent. Median lobe less elongate, wide. Basal bulb elongate, with a long sub-triangular basal projection (Fig. 1J). Paramerae distally narrow. Endogean and cavernicolous, Mts Bobija and Povlen, western Serbia ..... *Bozidaria* Ćurčić & Pavićević gen. nov.
10. Body shorter (TL 3.8–4.6 mm). Pronotum as wide as elytra. Lateral pronotal margins regularly arcuate. Anterior border of mesosternal carina with no concavity. Paramerae with three setae. Endogean, central and southern Bosnia and Herzegovina ..... *Pholeuodromus* Breit, 1913
- Body longer (TL 5.0–5.2 mm). Pronotum slightly narrower than elytra. Lateral pronotal margins weakly sinuate in basal third. Anterior border of mesosternal carina with a deep concavity. Paramerae with four setae. Cavernicolous, southeastern Bosnia and Herzegovina and northern Montenegro ... *Blattodromus* Reitter, 1904

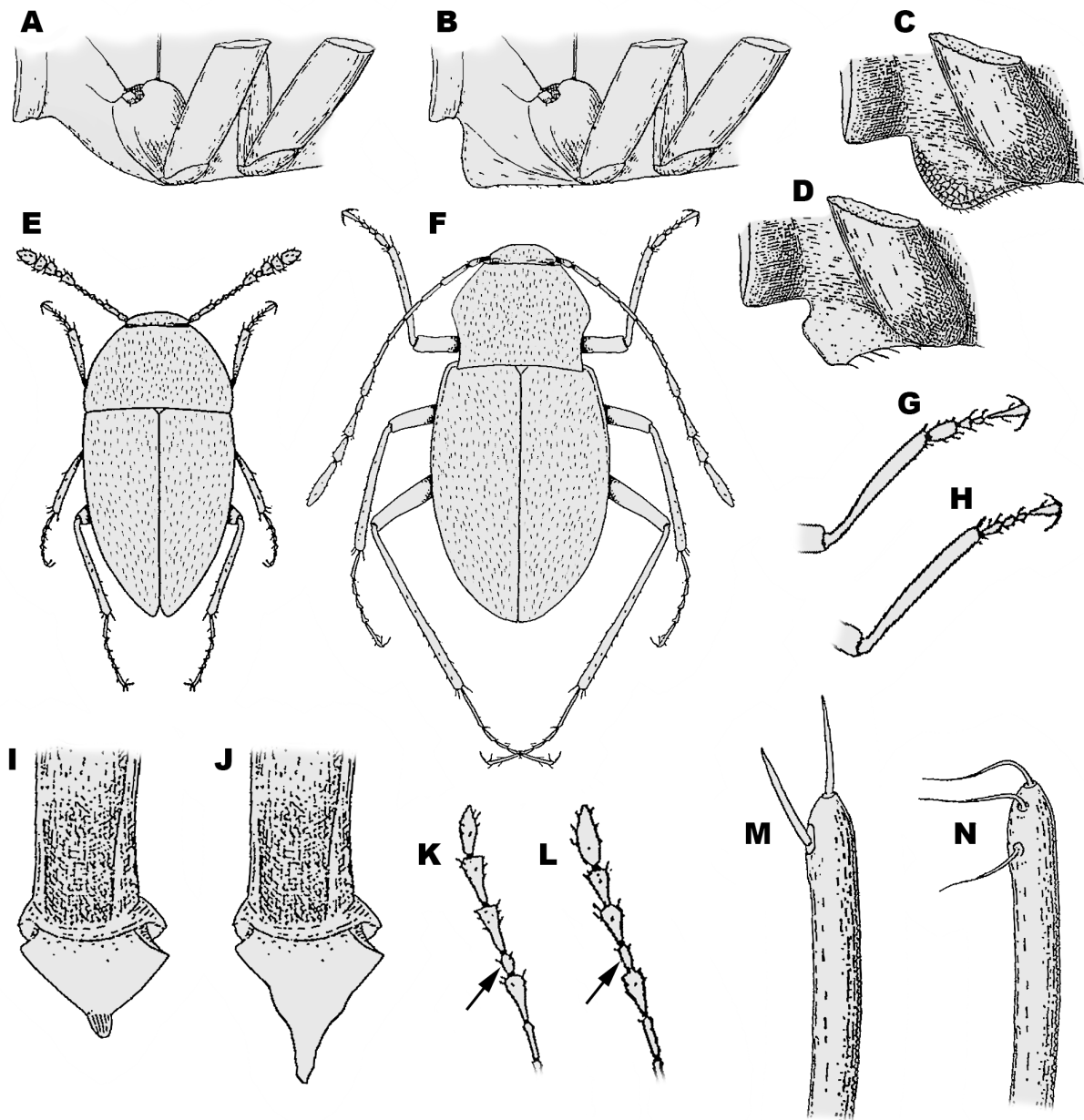


**Fig. 1.** Illustrations of morphological characters presented in the Key to the leptodirine leiodid genera of the phyletic series of “*Leonhardella*” (after Jeannel 1911, 1924; Ćurčić *et al.* 2008a). **A.** Absence of mesosternal carina. **B.** Presence of mesosternal carina. **C.** Absence of a concavity on mesosternal carina. **D.** Presence of a deep concavity on mesosternal carina. **E.** Presence of elliptical body shape. **F.** Presence of pholeuonoid body shape. **G.** Presence of dilated protarsi in males. **H.** Presence of undilated protarsi in males. **I.** Presence of a short rounded basal projection on basal bulbus. **J.** Presence of a long sub-triangular basal projection on basal bulbus. **K.** Presence of subglobular antennomere VIII. **L.** Presence of elongate antennomere VIII. **M.** Presence of paramerae with two setae. **N.** Presence of paramerae with three setae.

11. Antennomere VIII subglobular (Fig. 1K). Elytral punctuation strong and deep. Pubescence long, usually double, with bristle-like setae. Cavernicolous and endogean, western Serbia, southern, southeastern, central, western and eastern Bosnia and Herzegovina and northwestern Montenegro ..... *Pholeuonopsis* Apfelbeck, 1901  
– Antennomere VIII elongate (Fig. 1L). Elytral punctuation fine and shallow. Pubescence short, with no bristle-like setae ..... 12
12. Body shorter (TL 2.0 mm). Pronotum elongate, very narrow basally. Mesosternal carina low. Paramerae with two setae (Fig. 1M). Cavernicolous, vicinity of the town of Ključ, western Bosnia and Herzegovina ..... *Deelemaniella* Perreau, 2002  
– Body longer (TL 3.2–4.5 mm). Pronotum as long as wide or transverse, wider basally. Mesosternal carina high or atrophied. Paramerae with three setae (Fig. 1N) ..... 13
13. Mesosternal carina high. Protarsi somewhat dilated in males. Tibiae with no external spur. Cavernicolous, northwestern, western and northern Montenegro and southeastern and southern Bosnia and Herzegovina ..... *Leonhardella* Reitter, 1903  
– Mesosternal carina atrophied. Protarsi not dilated in males. Tibiae with external spur. Cavernicolous, Mt Durmitor, northern Montenegro ..... *Tartariella* Nonveiller & Pavićević, 1999

*Bozidaria serbooccidentalis* Ćurčić & Pavićević gen. et sp. nov.

[urn:lsid:zoobank.org:act:A2B51421-4CD9-4696-BF46-7EACBC395C4E](https://zoobank.org/act:A2B51421-4CD9-4696-BF46-7EACBC395C4E)

Figs 2–3

### Diagnosis

The genus is currently monotypic and therefore a differential diagnosis for *Bozidaria serbooccidentalis* gen. et sp. nov. cannot be provided.

### Etymology

The species is named after western Serbia, where its type locality and known localities are situated.

### Type material

#### Holotype

SERBIA • ♂; western Serbia, town of Ljubovija, Mt Bobija; alt. 1000 m; 19 Apr. 1980; Guido Nonveiller leg.; traps for endogean fauna baited with rotten meat; IZFB-21/1.

#### Paratypes

SERBIA • 1 ♂, 2 ♀♀; same collection data as for holotype; SBS-21/1 to 21/3 • 1 ♀; same collection data as for holotype; IZFB-21/2 • 2 ♂♂, 2 ♀♀; same collection data as for holotype; CDP-21/1 to 21/4 • 10 ♂♂, 14 ♀♀; western Serbia, town of Ljubovija, Mt Povlen, Debelo Brdo saddle, village of Gornje Košlje, Simina Jama Pit; 44°08'32.2" N, 19°37'40.4" E; 20 May–5 Nov. 2017; Miloš Kuraica leg.; pitfall trapping; IZFB-21/3 to 21/26 • 2 ♂♂, 1 ♀; same locality as for preceding; 31 Dec. 2010; Iva Njunjić leg.; pitfall trapping; SBS-21/4 to 21/6 • 18 ♂♂, 39 ♀♀; same collection data as for preceding; CDP-21/5 to 21/61 (Fig. 2).

### Description

**HABITUS.** Body elliptical, TL R 2.51–2.80 mm (R 2.51–2.73 mm in males, R 2.67–2.80 mm in females), reddish-brown in colour, shiny, pubescent, with a fine punctuation (Fig. 2A).

**HEAD.** Short, wide, slightly wider than long (HL/HW M 0.97), without eyes (Fig. 2A). Antennae long and slender, apically gradually widened and flattened, ending slightly after basal third of elytra in males

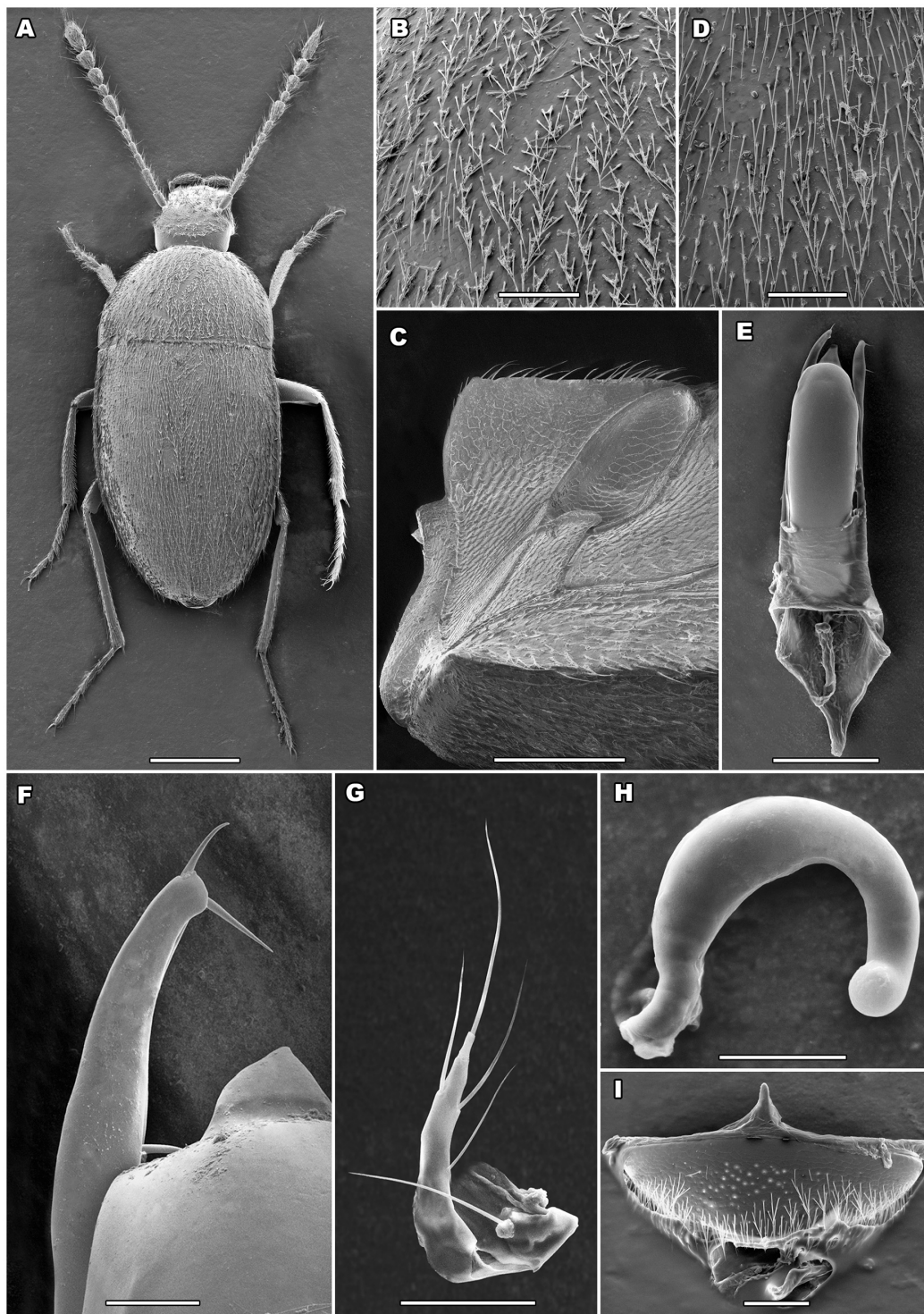


**Fig. 2.** *Bozidaria serbooccidentalis* Ćurčić & Pavićević gen. et sp. nov. from the Simina Jama Pit, village of Gornje Košlje, Debelo Brdo saddle, Mt Povlen, near the town of Ljubovija, western Serbia. A–F. Paratype male (IZFB-21/3). A. Habitus (dorsal view). B. Surface of pronotum (dorsal view). C. Mesosternal carina (lateral view). D. Surface of elytra (dorsal view). E. Aedeagus (dorsal view). F. Left paramere apex (dorsal view). G–I. Paratype female (IZFB-21/4). G. Left gonostylus (dorsal view). H. Spermatheca (lateral view). I. Abdominal segment VIII (ventral view). Scale bars: A = 500  $\mu\text{m}$ ; B, D, G, I = 100  $\mu\text{m}$ ; C, E = 200  $\mu\text{m}$ ; F = 25  $\mu\text{m}$ ; H = 50  $\mu\text{m}$ .

or slightly prior to basal third of elytra in females. Antennomere II longer than antennomere I (A1/A2 M 0.795). A3/A2 M 0.67. A3/A5 M 1.24. Antennomeres IV–VI of similar length, of which IV narrowest and VI widest. Antennomere VII apically widened. A7/A6 M 1.56. Antennomere VIII slightly longer than half of antennomere VII (A7/A8 M 1.53), oval, somewhat elongate (A8LW M 1.52). Antennomere IX somewhat elongate, gradually widened distally (A9LW M 1.47). A9/A8 M 1.52 in males, M 1.42 in females. Antennomere X slightly longer than wide (A10LW M 1.24), more widened apically. Antennomere XI slender, ovoid, apically pointed, more elongate in males (A11LW M 2.45) than in females (A11LW M 1.97), as long as preceding two antennomeres combined or slightly shorter than the latter. Occipital carina present. Hairs yellow, erect. Microsculpture composed of small isodiametric meshes.

**THORAX.** Pronotum transverse, widest sub-basally, almost twice as wide as long (PL/PW M 0.59) (Fig. 2A). Lateral pronotal margins arcuate, rounded medially, sub-parallel prior to hind pronotal angles. Pronotal base more than twice as long as anterior pronotal margin (PB/AM M 2.13). Both anterior pronotal margin and pronotal base convex medially, the latter less pronouncedly. PL+EL/AL M 1.63 in males, M 1.89 in females. Fore angles prominent, obtuse, rounded, hind angles sharp, rounded, prominent, directed backwards. Microsculpture of pronotum composed of large isodiametric meshes. Hairs yellow, recumbent (Fig. 2B). Pronotal disc weakly convex. Mesosternal carina high, obtuse-angled, anterior margin strongly convex, posterior margin barely convex, almost straight, with hairs and teeth (Fig. 2C). Mesosternal carina with an apical tooth. Ventral border of mesosternal carina not grooved.

**ELYTRA.** Elongate (EL/EW M 1.38 in males, M 1.40 in females), more than 2.5 times as long as pronotum (EL/PL M 2.65), obovoid, sub-parallel below humeral angles, weakly narrowed basally, rounded medially, narrowed apically (Fig. 2A). Apex rounded. Sutural striae absent. Scutellum small, triangular. Elytra widest between basal third and mid-length. Microsculpture composed of large isodiametric meshes. Hairs yellow, recumbent (Fig. 2D). Elytral disc convex. Pygidium not completely covered by elytra.

**LEGS.** Elongate and thin, with hairs (Fig. 2A). Tibiae with a few spines laterally. Anterior tarsi tetramerous in both genders, somewhat dilated in males (P1LW M 1.825 in males, M 1.88 in females).

**ABDOMEN.** Median lobe of aedeagus elongate, thin, sub-parallel, sub-apically rounded (Figs 2E, 3A). Apex elongate, triangular. Basal bulb relatively narrow, elongate, with a sub-triangular basal projection. Copulatory piece weakly chitinised, consisting of a basal phanera, median paired stripes and apical paired sclerotizations. Median lobe proximally straight, distally relatively curved, gradually narrowed distally in lateral view (Fig. 3B). Basal bulb narrow in lateral view. Parameres slender, thin, longer than median lobe, sub-terminally widened, terminally narrowed, apex slightly dilated, proximally arcuate and distally straight in lateral view, with three setae: one apical terminal, one apical inner and one sub-apical inner (Fig. 2F). Two apical parameral setae close-set. Parameral apices directed inwards. Parameres basally slightly curved, distally relatively straight in lateral view, sub-terminally widened, terminally narrowed in lateral view (Fig. 3B).

**GONOSTYLI.** Almost straight, elongate, thin, with one apical seta, three inner setae and one outer seta (Fig. 2G).

**SPERMATHECA.** Small, curved, widest in proximal third, apically sub-spherical (Fig. 2H).

**FEMALE ABDOMINAL STERNITE VIII.** Large, transverse, setose both medially and distally, with a narrow, pointed anterior process. Microsculpture consisting of transverse polygonal meshes (Fig. 2I).

**Bionomy, distribution and type locality**

The type specimens were collected in traps for endogean fauna (cans) baited with rotten meat placed in the deep soil on Mt Bobija, near the town of Ljubovija, western Serbia, as well as by pitfall trapping with rotten meat as bait in the deep, totally dark parts of the Simina Jama Pit, village of Gornje Košlje, Debelo Brdo saddle, Mt Povlen, near the town of Ljubovija, western Serbia (Fig. 9). The type locality on Mt Bobija is located on its northern slope, at an altitude of 1000 m a.s.l., in a beech forest, close to several



**Fig. 3.** *Bozidaria serbooccidentalis* Ćurčić & Pavićević gen. et sp. nov. from the Simina Jama Pit, village of Gornje Košlje, Debelo Brdo saddle, Mt Povlen, near the town of Ljubovija, western Serbia. Holotype male (IZFB-21/1), aedeagus. **A.** Dorsal view. **B.** Lateral view. Scale bar = 200  $\mu$ m.

streams. The entrance of the Simina Jama Pit is situated at 920 m a.s.l., the total length of its investigated channels is 270 m, while its depth is 56 m. It starts with a 31-m long vertical passage, which splits into two horizontal channels – left and right (Andelić *et al.* 2011). Beetle specimens were found at the end and in the middle of the left horizontal channel with a clay muddy substrate and rocks, on the vertical limestone walls and floor with a high level of humidity (presence of trickling water). The places where the specimens were found in the pit are shown in Fig. 4. It is assumed that the species is actually endogean, as is the case with some other leiodid taxa (e.g., *Magdelainella* spp.), which inhabit the soil beneath deeply sunken rocks and forest detritus, but can also be found in caves and pits (Pavićević *et al.* 2012).

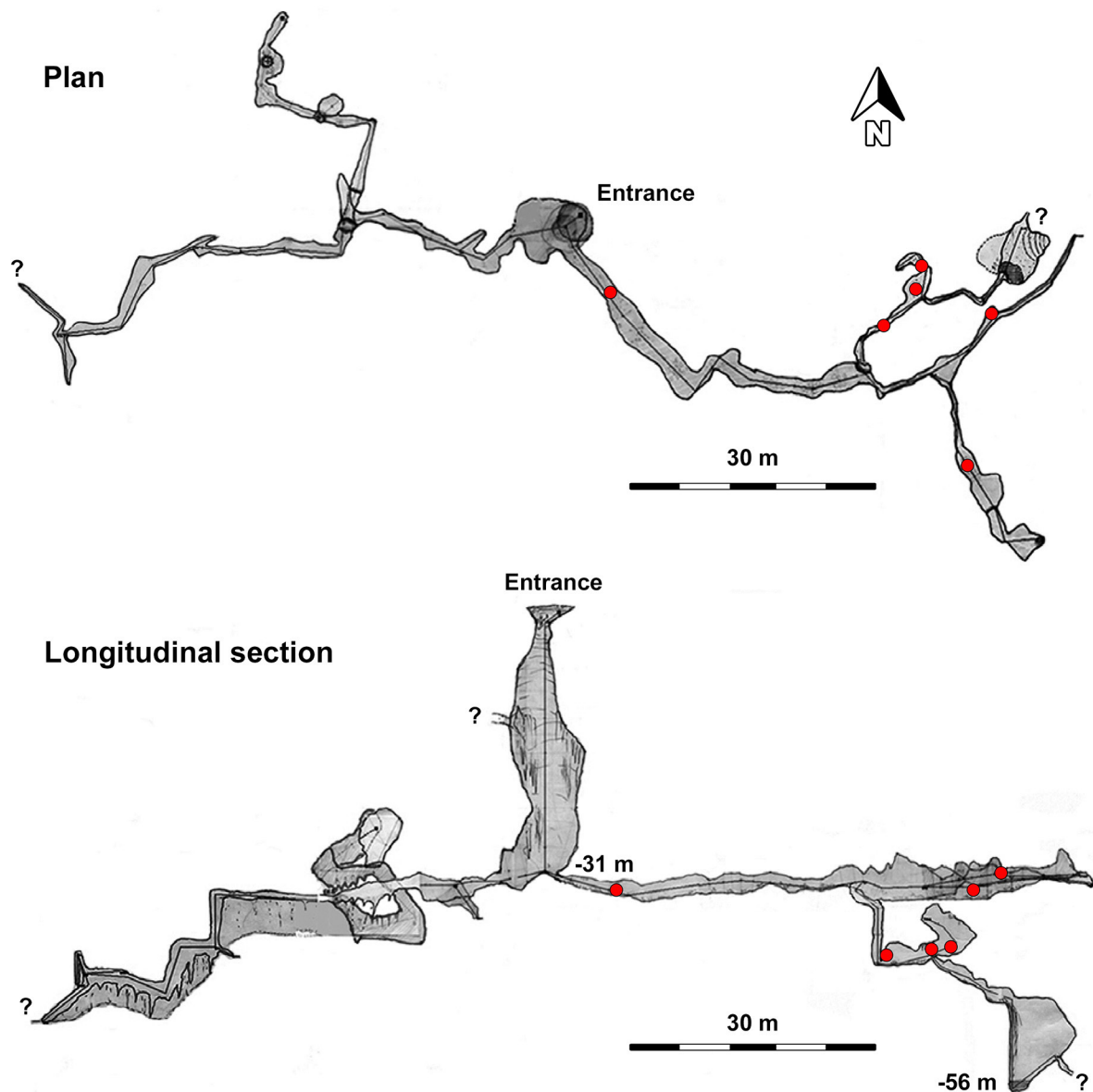


**Fig. 4.** A plan and a longitudinal section of the Simina Jama Pit, village of Gornje Košlje, Debelo Brdo saddle, Mt Povlen, near the town of Ljubovija, western Serbia (modified after Andelić *et al.* 2011). The red circles indicate the places where specimens of *Bozidaria serbooccidentalis* Ćurčić & Pavićević gen. et sp. nov. were found.



Genus *Proleonhardella* Jeannel, 1910

*Proleonhardella (Proleonhardella) tarensis* Ćurčić & Pavićević sp. nov.  
[urn:lsid:zoobank.org:act:E1B53D50-0C09-4E5C-AFB1-AC9F6EBBD426](https://doi.org/10.21203/rs.3.rs-10000000)

Figs 5–6

### Diagnosis

*Proleonhardella (Proleonhardella) tarensis* sp. nov. is most closely related to *P. (P.) hirtella* (from several caves and pits near the towns of Prijepolje (southwestern Serbia) and Pljevlja (northern Montenegro)), *P. (P.) weiratheri* (Reitter, 1913) (from the Vrteljka Cave, village of Đipi, Mt Sjemeć, near the town of Višegrad, eastern Bosnia and Herzegovina) and *P. (P.) neumanni* (Apfelbeck, 1901) (from a small unnamed cave, village of Podromanija, near the town of Sokolac, eastern Bosnia and Herzegovina) (Fig. 9) (Perreau 2000; Pavićević *et al.* 2012). Another congener from Serbia, *P. (P.) remyi* (from caves and pits in the area of Kamena Gora and near the towns of Prijepolje, Priboj (southwestern Serbia) and Pljevlja (northern Montenegro)), is of bathyscioid shape (*P. (P.) tarensis* sp. nov. is more elongate and of oval shape), it is significantly longer than the new species (TL R 3.0–3.5 mm vs 2.185–2.435 mm in *P. (P.) tarensis* sp. nov.) and has a quite different shape of aedeagus (stout, with a rounded apex, longer than parameres vs elongate, with a pointed apex, shorter than parameres in *P. (P.) tarensis* sp. nov.), indicating that these two species are not closely related (Jeannel 1934; Ćurčić *et al.* 2008a).

The new species differs from its closest congeners in the TL R (2.185–2.435 mm vs 1.6–1.8 mm in *P. (P.) hirtella* and 1.6–2.0 mm in *P. (P.) weiratheri*), antennal length (ending prior to basal third of elytra vs reaching only basal quarter of elytra in *P. (P.) hirtella* and exceeding middle of body in *P. (P.) weiratheri*), A1/A2 M (0.76 vs 0.80 in *P. (P.) neumanni*), A7/A6 M (1.66 vs 1.50 in *P. (P.) hirtella*), A7/A8 R (1.75–2.00 vs 3.00 in *P. (P.) hirtella*), A11/A9+A10 M (0.90 vs 1.00 in *P. (P.) weiratheri*), shape of antennomere VIII (oval and slightly longer than wide in males and spherical in females vs as long as wide in males and almost transverse in females in *P. (P.) weiratheri*), shape of antennomeres IX and X (slightly longer than wide vs as long as wide in *P. (P.) hirtella*), position of maximum width of pronotum (sub-basally vs at base in *P. (P.) hirtella* and *P. (P.) weiratheri*), shape of mesosternal carina (obtuse-angled vs almost right-angled in *P. (P.) neumanni*), shape of elytra (narrowed basally vs parallel basally in *P. (P.) hirtella* and *P. (P.) weiratheri* and clearly sinuate basally in *P. (P.) neumanni*), EL/EW (R 1.31–1.39 vs M 1.75 in *P. (P.) weiratheri*), position of maximum width of elytra (slightly after basal third vs prior to middle in *P. (P.) neumanni*), and shape of aedeagus (less elongate, with wider apex and larger basal bulb vs more elongate, with narrower apex and smaller basal bulb in *P. (P.) hirtella*) (Apfelbeck 1901; Reitter 1913; Jeannel 1924, 1934).

### Etymology

The species is named after Mt Tara in western Serbia, where its type locality is situated.

### Type material

#### Holotype

SERBIA • ♂; western Serbia, town of Bajina Bašta, Mt Tara, village of Kaluderske Bare, Pit 4-1-3-27; 43°54'30.712" N, 19°33'11.585" E; 5 Jul. 2014; Fabrizio Bosco leg.; pitfall trapping; IZFB-21/27.

#### Paratypes

SERBIA • 3 ♂♂, 3 ♀♀; same collection data as for holotype; IZFB-21/28 to 21/33 • 1 ♀; same collection data as for holotype; SBS-21/7 • 1 ♂, 2 ♀♀; western Serbia, town of Bajina Bašta, Mt Tara, village of Šljivovica, Sovljačka Pećina Cave; 43°52'39.7" N, 19°30'56.3" E; 7 May 2003; Dragan Pavićević leg.; pitfall trapping; SBS-21/8 to 21/10 • 2 ♂♂, 3 ♀♀; same collection data as for preceding; CDP-21/62 to 21/66 (Fig. 5).

## Description

**HABITUS.** Body oval, relatively elongate, TL R 2.185–2.435 mm (R 2.185–2.32 mm in males, 2.435 mm in females), colour brownish-red (one teneral female specimen yellowish), shiny, pubescent and with a fine punctuation (Fig. 5A).

**HEAD.** Short, wide, slightly longer than wide (HL/HW R 1.00–1.06), anophthalmous (Fig. 5A). Antennae long and narrow, ending prior to basal third of elytra, apically widened and flattened. Antennomere II longer than antennomere I (A1/A2 M 0.76). Antennomeres III–VI small, narrow, of similar shape and length. A3/A2 M 0.58. A3/A5 M 1.19. Antennomere VII apically widened, obovoid. A7/A6 M 1.66. Antennomere VIII half as long as antennomere VII, oval and slightly longer than wide in males (A8LW M 1.31), while somewhat shorter (A7/A8 M 1.75), nearly as long as wide (A8LW M 1.04) and spherical in females. Antennomeres IX and X slightly longer than wide (A9LW M 1.28 and A10LW M 1.21, respectively), apically widened. A9/A8 M 1.60 in males, 2.00 in females. Antennomere XI ovoid, twice as long as wide in males, somewhat shorter in females (A11LW M 1.92), slightly shorter than two preceding antennomeres combined (A11/A9+A10 M 0.90). Occipital carina present. Hairs yellow, erect. Microsculpture composed of small isodiametric meshes.

**THORAX.** Pronotum transverse, almost twice as wide as long (PL/PW M 0.59), widest sub-basally (Fig. 5A). Lateral pronotal margins arcuate, most rounded medially, almost sub-parallel prior to hind pronotal angles. Anterior pronotal margin somewhat convex medially, base almost straight, around twice as long as anterior pronotal margin (PB/AM M 1.985). PL+EL/AL M 1.685 in males, 1.94 in females. Fore angles prominent, obtuse, rounded, hind angles sharp, rounded, prominent, directed backwards. Microsculpture of pronotum composed of large isodiametric meshes. Hairs yellow, recumbent (Fig. 5B). Pronotal disc weakly convex. Mesosternal carina high, obtuse-angled, anterior margin convex, posterior margin straight, setose and with unpronounced teeth (Fig. 5C). Mesosternal carina with an apical tooth.

**ELYTRA.** Elongate (EL/EW M 1.39 in males, 1.31 in females), more than twice as long as pronotum (EL/PL M 2.46), obovoid, sub-parallel below humeral angles, conspicuously narrowed basally, rounded medially, attenuated apically (Fig. 5A). Apex rounded. Sutural striae absent. Scutellum small, triangular. Elytra widest slightly after basal third. Microsculpture composed of large isodiametric meshes. Hairs yellow, recumbent (Fig. 5D). Elytral disc gently convex apically, more steeply distally. Pygidium completely covered by elytra.

**LEGS.** Moderately elongate and thin, with hairs (Fig. 5A). Tibiae with a few spines. Anterior tarsi tetramerous in both genders, dilated in males (P1LW M 1.50 in males, 2.00 in females).

**ABDOMEN.** Median lobe of aedeagus elongate, thin, sub-parallel, sub-terminally somewhat widened, then narrowed apically (Figs 5E, 6A). Apex triangular. Basal bulb large, elongate, with a sub-triangular basal projection. Copulatory piece weakly chitinised, consisting of a basal phanera, median paired stripes and distal paired sclerotizations. Median lobe proximally weakly curved, distally more curved, gradually narrowed distally in lateral view (Fig. 6B). Basal bulb relatively narrow in lateral view. Parameres slender, thin, longer than median lobe, sub-terminally widened, terminally narrowed, basally arcuate and distally straight in lateral view, with three setae: one apical terminal, one apical inner and one sub-apical inner (Fig. 5F). Two apical parameral setae close-set. Parameral apices directed inwards. Parameres basally slightly curved, distally relatively straight, sub-terminally widened, terminally narrowed, apically directed downwards in lateral view (Fig. 6B).

**GONOSTYLI.** Straight, elongate, thin, with one apical seta, three inner setae and one outer seta (Fig. 5G).

**SPERMATHECA.** Small, hook-like, widest in middle, apically sub-spherical (Fig. 5H).

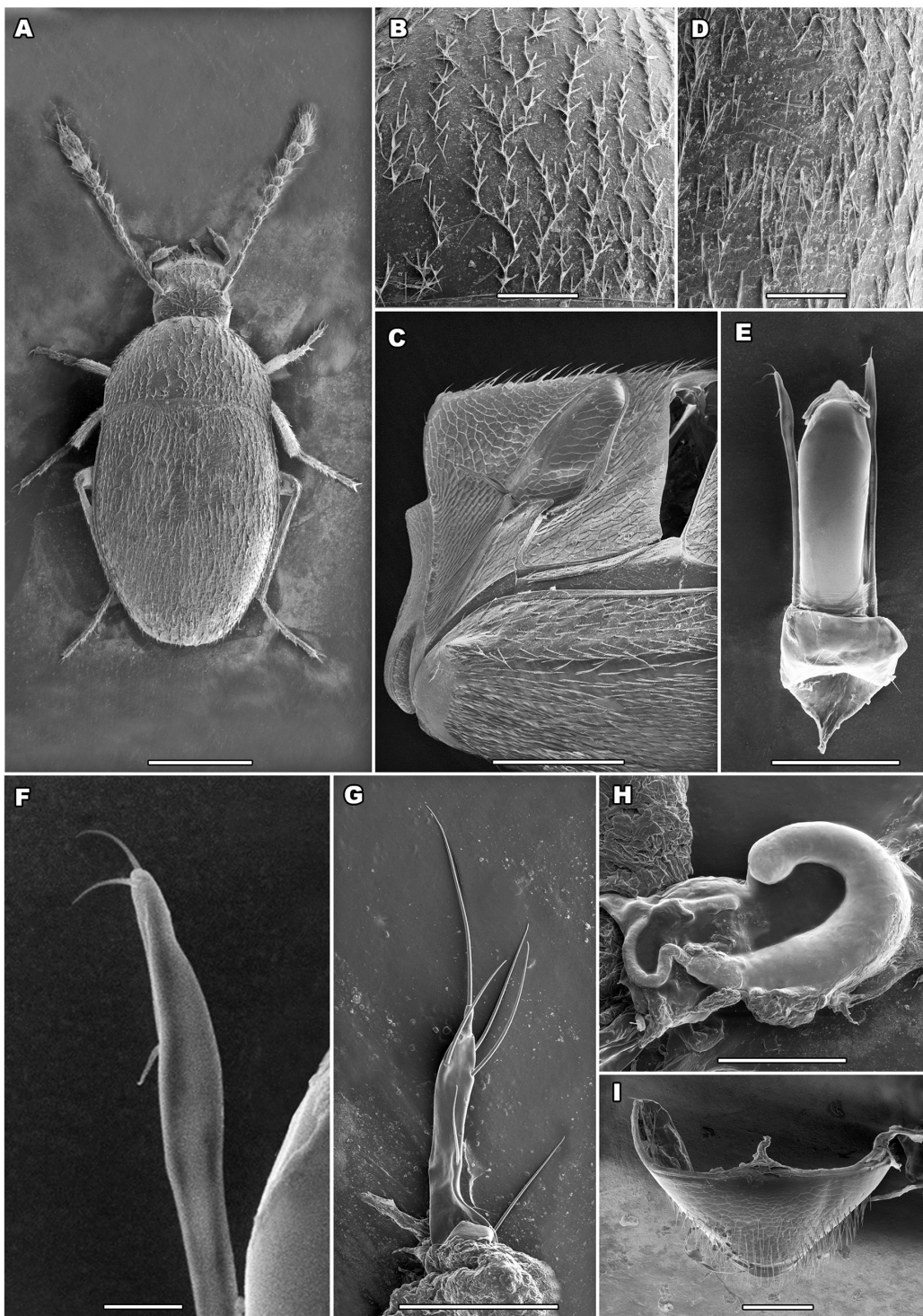


**Fig. 5.** *Proleonhardella (Proleonhardella) tarensis* Ćurčić & Pavićević sp. nov. from Pit 4-1-3-27, village of Kaluderske Bare, Mt Tara, near the town of Bajina Bašta, western Serbia. **A–F.** Paratype male (IZFB-21/28). **A.** Habitus (dorsal view). **B.** Surface of pronotum (dorsal view). **C.** Mesosternal carina (lateral view). **D.** Surface of elytra (dorsal view). **E.** Aedeagus (dorsal view). **F.** Left paramere apex (dorsal view). **G–I.** Paratype female (IZFB-21/29). **G.** Left gonostylus (dorsal view). **H.** Spermatheca (lateral view). **I.** Abdominal segment VIII (ventral view). Scale bars: A = 500  $\mu\text{m}$ ; B, D, G, I = 100  $\mu\text{m}$ ; C, E = 200  $\mu\text{m}$ ; F = 25  $\mu\text{m}$ ; H = 50  $\mu\text{m}$ .

FEMALE ABDOMINAL STERNITE VIII. Large, transverse, setose in distal half, with a small, narrow anterior process. Microsculpture consisting of transverse polygonal meshes (Fig. 5I).

### Comparisons

*Proleonhardella* (*P.*) *hirtella*, *P.* (*P.*) *weiratheri* and *P.* (*P.*) *tarensis* sp. nov. are somewhat elongate and their aedeagus is narrower than in the remaining congeners, suggesting their specific position within the genus. Based on these features, they are similar to *Bozidaria* gen. nov., but are much shorter (TL R 1.6–1.8 mm in *P.* (*P.*) *hirtella*, 1.6–2.0 mm in *P.* (*P.*) *weiratheri* and 2.185–2.435 mm in *P.* (*P.*) *tarensis* sp. nov.



**Fig. 6.** *Proleonhardella* (*Proleonhardella*) *tarensis* Ćurčić & Pavićević sp. nov. from Pit 4-1-3-27, village of Kaluderske Bare, Mt Tara, near the town of Bajina Bašta, western Serbia. Holotype male (IZFB-21/27), aedeagus. **A.** Dorsal view. **B.** Lateral view. Scale bar = 200  $\mu$ m.

vs 2.51–2.80 mm in *B. serbooccidentalis* gen. et sp. nov.), share other characteristics of *Proleonhardella* and additionally differ from the new genus in the shape of the antennae, the median lobe of the aedeagus, the basal bulb and its basal projection.

*Proleonhardella* (*P.*) *tarensis* sp. nov. and its closest relatives (*P.* (*P.*) *hirtella*, *P.* (*P.*) *weiratheri* and *P.* (*P.*) *neumanni*) share the presence of elongate, somewhat convex elytra, which are more than twice as long as the pronotum. Furthermore, the new species, *P.* (*P.*) *hirtella* and *P.* (*P.*) *weiratheri* have a somewhat elongate body shape, while the body shape in the remaining *Proleonhardella* taxa

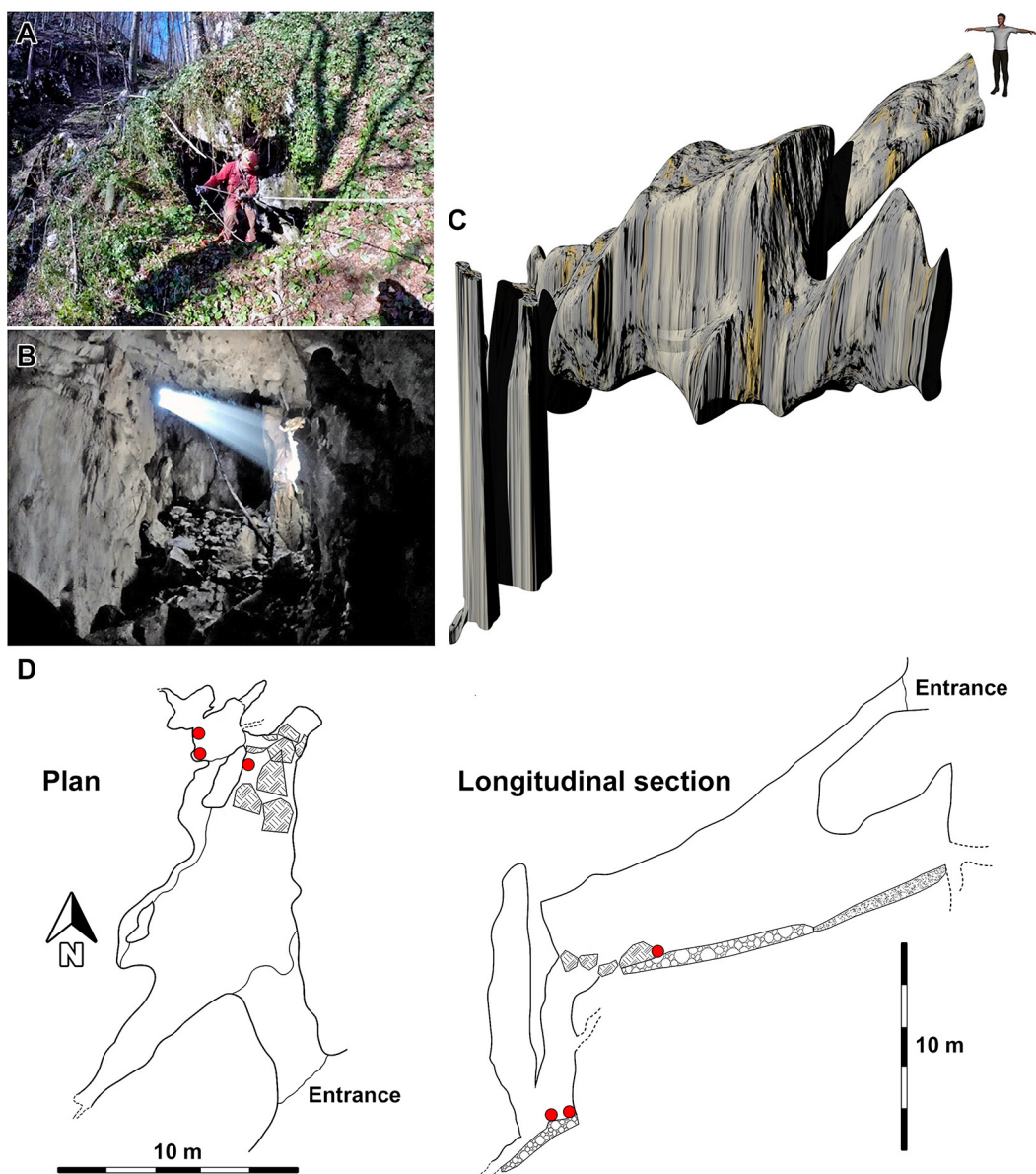


**Fig. 7.** Pit 4-1-3-27, village of Kaluderske Bare, Mt Tara, near the town of Bajina Bašta, western Serbia (modified after Bosco 2016). **A.** Entrance. **B.** A chamber in which one type specimen of *Proleonhardella* (*Proleonhardella*) *tarensis* Ćurčić & Pavićević sp. nov. was collected. **C.** A 3D view. **D.** A plan and a longitudinal section. The red circles indicate the places where specimens of *P.* (*P.*) *tarensis* Ćurčić & Pavićević sp. nov. were found.

is more or less bathyscioid. These three species have an elongate aedeagus, contrary to other known congeners, in which the aedeagus is more or less short (Jeannel 1924, 1934). The shape of the aedeagus of *P. (P.) neumanni* wasn't mentioned in the description of the species or elsewhere (Apfelbeck 1901; Jeannel 1924).

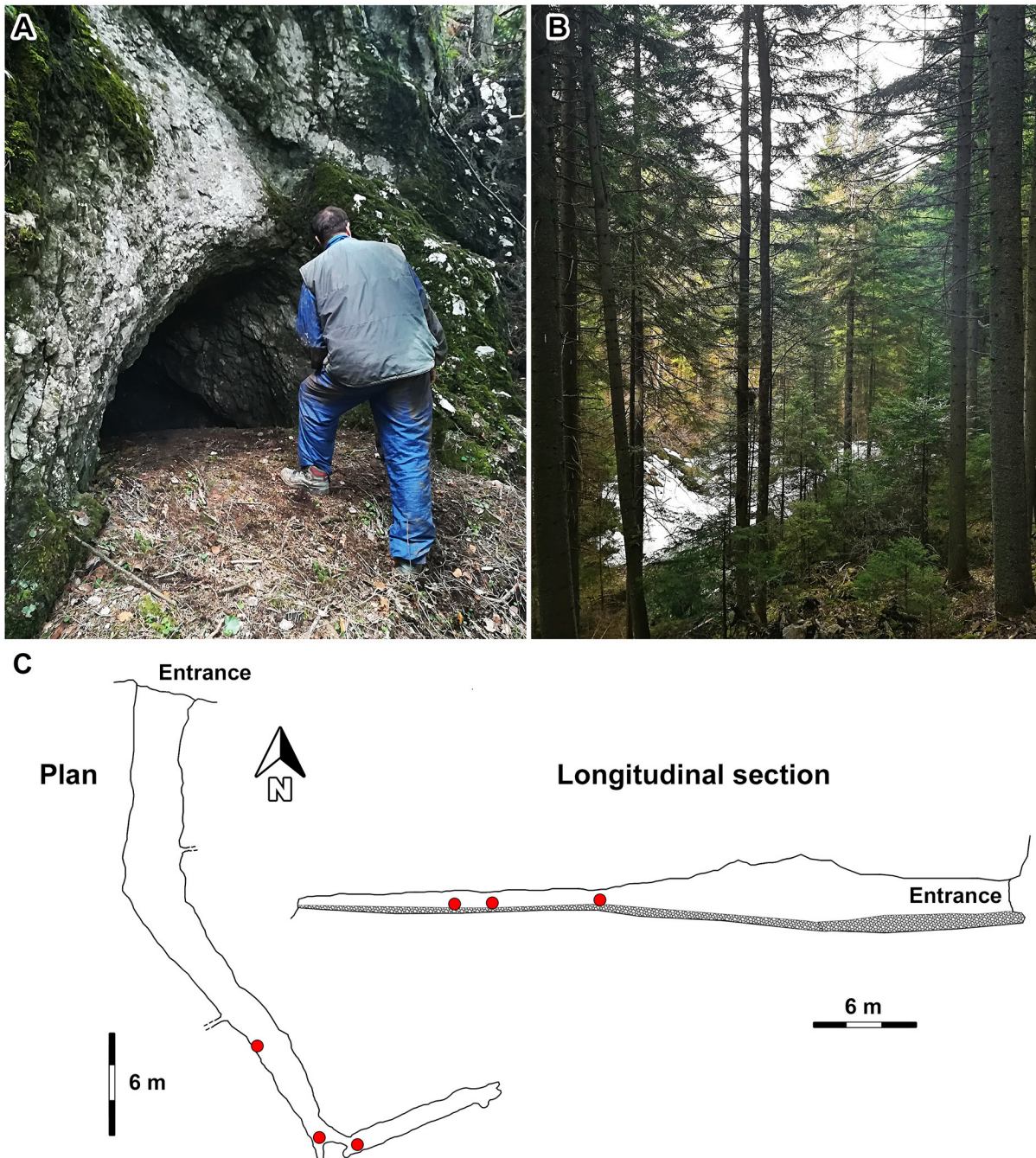


**Fig. 8.** Sovljačka Pećina Cave, village of Šljivovica, Mt Tara, near the town of Bajina Bašta, western Serbia (modified after Bosco 2016). **A.** Entrance. **B.** Immediate surroundings (a coniferous forest and view of the Sovljak stream). **C.** A plan and a longitudinal section. The red circles indicate the places where specimens of *P. (P.) tarensis* Ćurčić & Pavićević sp. nov. were found.

### Bionomy, distribution and type locality

The type specimens were gathered using pitfall traps with rotten meat as bait in Pit 4-1-3-27 in the village of Kaluđerske Bare, as well as in the Sovljačka Pećina Cave in the village of Šljivovica (Fig. 9). Both localities are situated on Mt Tara, near the town of Bajina Bašta, western Serbia. Beetles were found in the inner (from the middle to the innermost point), totally dark parts of the cave sites. The entrance of Pit 4-1-3-27 is situated at 868 m a.s.l., the total length of its investigated channels is 28 m, while its depth is 22 m. After a short vertical passage, the pit opens into a large chamber which contains big rocks at its lowest part. At this point another vertical passage starts, at the end of which is situated a small, moist semicircular chamber with a clay substrate and rocks (Bosco 2016). Beetle specimens were found in the inner part of the larger chamber, among rocks, and in the smaller chamber with a clay substrate and rocks, on the floor and vertical limestone walls with a high level of humidity (presence of trickling water). The entrance of the Sovljačka Pećina Cave is situated at 1080 m a.s.l. and its total length is 43 m (Bosco 2016). The cave is located in a coniferous forest in a valley where the Sovljak stream runs. It is entirely horizontal and consists of a single channel which is oriented to the left. Its height is slightly decreasing towards the end. Beetle individuals were found in the inner

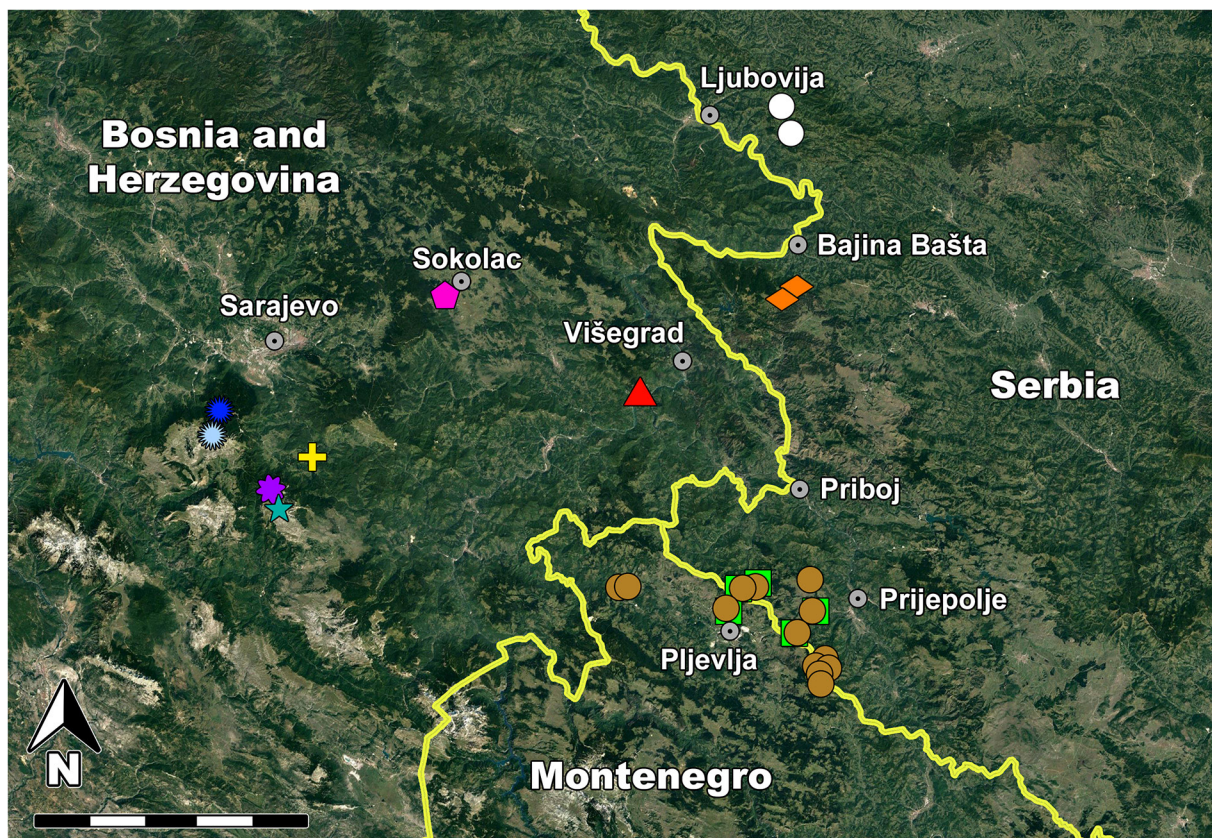


**Fig. 9.** Map of the distribution of taxa of the genera *Bozidaria* Ćurčić & Pavićević gen. nov. and *Proleonhardella* Jeannel, 1910. White circles: *B. serbooccidentalis* Ćurčić & Pavićević gen. et sp. nov. Turquoise star: *P. (Pholeuonillus) adolfi* (Reitter, 1911). Light blue sun: *P. (Proleonhardella) matzenaueri matzenaueri* (Apfelbeck, 1907). Dark blue sun: *P. (P.) matzenaueri ottonis* Müller, 1917. Purple flower: *P. (P.) leonhardi* (Breit, 1913). Yellow cross: *P. (P.) apfelbecki* Jeannel, 1924. Brown circles: *P. (P.) remyi* Jeannel, 1934. Green squares: *P. (P.) hirtella* Jeannel, 1934. Pink pentagon: *P. (P.) neumanni* (Apfelbeck, 1901). Red triangle: *P. (P.) weiratheri* (Reitter, 1913). Orange rhombuses: *P. (P.) tarensis* Ćurčić & Pavićević sp. nov. Scale bar = 50 km.

part of the cave, on the floor among rocks, both on limestone and clay substrate, where a high level of humidity (presence of trickling water) was evident. Images of the cave localities and the places where the specimens were found in the caves are shown in Figs 7–8. The new species is most probably endogean and is likely to be found outside caves as well – in the deep soil strata and other speleological sites in the surroundings.

**Key to the taxa of the genus *Proleonhardella* Jeannel, 1910**

(modified after Jeannel 1924) (Figs 9–10)

1. Body more elongate, elliptical. Pronotum as wide as elytra, well constricted basally. Pronotal lateral margins well-rounded backwards. Mesosternal carina very low. Elytral punctuation rough and deep (subgenus *Pholeuonillus* Breit, 1913). Endogean, Mt Treskavica, southern Bosnia and Herzegovina ..... ***P. (Pholeuonillus) adolfi*** (Reitter, 1911)
  - Body less elongate, oval. Pronotum narrower than elytra, weakly constricted basally. Pronotal lateral margins weakly rounded backwards. Elytral punctuation fine. Mesosternal carina elevated, angled (subgenus *Proleonhardella* Jeannel, 1910) ..... 2
2. Elytra shorter, more convex, less than twice as long as pronotum (Fig. 10A) ..... 3
  - Elytra longer, less convex, more than twice as long as pronotum (Fig. 10B) ..... 6
3. Body of oval shape, longer (TL 1.8–2.2 mm). Antennae short, not reaching middle of body. Antennomere III not longer than antennomere V. Antennomere VIII globular in males (Fig. 10C). Cavernicolous, Mts Bjelašnica and Igman, central Bosnia and Herzegovina [*P. (Proleonhardella) matzenaueri* (Apfelbeck, 1907)] ..... 4
  - Body of subglobular shape, shorter (TL less than 1.8 mm). Antennae long, reaching middle of body. Antennomere III longer than antennomere V. Antennomere VIII slightly elongate in males (Fig. 10D) ..... 5
4. Body of almost regular oval shape, longer (TL 2.0–2.2 mm). Elytra not widened towards middle. Cavernicolous, Mt Bjelašnica, central Bosnia and Herzegovina .....
  - ..... ***P. (Proleonhardella) matzenaueri matzenaueri*** (Apfelbeck, 1907)
  - Body narrower anteriorly, shorter (TL 1.8–2.0 mm). Elytra clearly widened medially. Cavernicolous, Mt Igman, central Bosnia and Herzegovina .....
    - ..... ***P. (Proleonhardella) matzenaueri ottonis*** Müller, 1917
5. Body more elongate and convex, longer (TL 1.5 mm). Elytral punctuation finer and denser. Antennae shorter, with apical antennomeres thicker. Antennomere VIII barely longer than wide, antennomere IX as long as wide and antennomere X transverse in females. Cavernicolous, Mt Treskavica, southern Bosnia and Herzegovina ..... ***P. (Proleonhardella) leonhardi*** (Breit, 1913)
  - Body less elongate and convex, shorter (TL 1.3 mm). Elytral punctuation stronger and less dense. Antennae longer, with apical antennomeres less thick. Antennomeres VIII, IX and X longer than wide in females. Cavernicolous, village of Trnovo, vicinity of the city of Sarajevo, central Bosnia and Herzegovina ..... ***P. (Proleonhardella) apfelbecki*** Jeannel, 1924
6. Body longer (TL 3.0–3.5 mm). Cavernicolous, Kamena Gora and vicinity of the towns of Prijepolje, Priboj and Pljevlja, southwestern Serbia and northern Montenegro .....
  - ..... ***P. (Proleonhardella) remyi*** Jeannel, 1934
  - Body shorter (TL less than 2.435 mm) ..... 7
7. Elytra parallel in basal half (Fig. 10E) ..... 8
  - Elytra narrowed in basal half (Fig. 10F) ..... 9



8. Pubescence long. Punctuation less fine. Apical antennomeres more widened. Pronotum less rounded. Apex of median lobe of aedeagus less bent ventrally. Elytral apex wide, obtuse and oblique. Cavernicolous, vicinity of the towns of Prijepolje and Priboj (southwestern Serbia) and Pljevlja (northern Montenegro) ..... *P. (Proleonhardella) hirtella* Jeannel, 1934  
 – Pubescence short. Punctuation finer. Apical antennomeres less widened. Pronotum more rounded. Apex of median lobe of aedeagus more bent ventrally. Elytral apex attenuated. Cavernicolous, Mt Sjemeć, eastern Bosnia and Herzegovina ..... *P. (Proleonhardella) weiratheri* (Reitter, 1913)
9. A1/A2 M 0.80. Mesosternal carina almost right-angled. Elytral lateral margins below humeral angles clearly sinuate. Maximum width of elytra prior to middle. Cavernicolous, village of Podromanija, near the town of Sokolac, eastern Bosnia and Herzegovina .....  
 ..... *P. (Proleonhardella) neumanni* (Apfelbeck, 1901)  
 – A1/A2 M 0.76. Mesosternal carina obtuse-angled. Elytral lateral margins below humeral angles sub-parallel. Maximum width of elytra slightly after basal third. Cavernicolous, Mt Tara, western Serbia ..... *P. (Proleonhardella) tarensis* Ćurčić & Pavićević sp. nov.

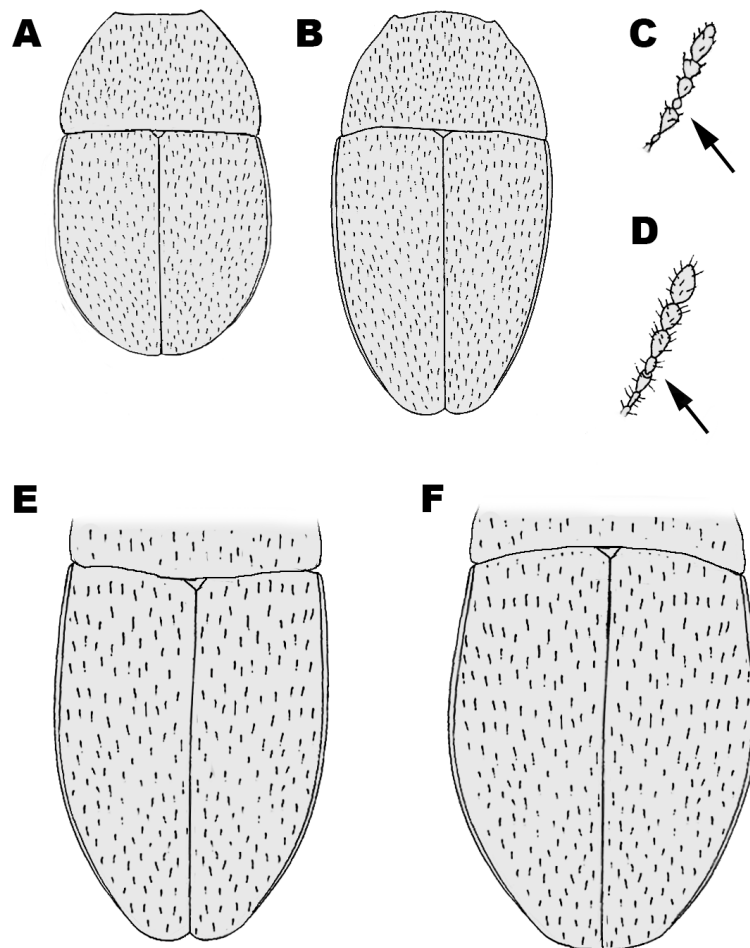


**Fig. 10.** Illustrations of morphological characters presented in the Key to the taxa of the genus *Proleonhardella* Jeannel, 1910 (after Jeannel 1924; Ćurčić *et al.* 2008a). **A.** Short elytra, less than twice as long as pronotum. **B.** Long elytra, more than twice as long as pronotum. **C.** Globular antennomere VIII in males. **D.** Slightly elongate antennomere VIII in males. **E.** Elytra parallel in basal half. **F.** Elytra narrowed in basal half.

## Discussion

It should be noted that a new genus of leptodirines belonging to the phyletic series of “*Leonhardella*” was recently established. Ćurčić *et al.* (2008a) considered the status of *P. (P.) remyi* and described a new genus, *Serboleonhardella* S. Ćurčić & Schönmann, 2008, based on this taxon. Numerous differences between *P. (P.) remyi* and other members of the genus *Proleonhardella*, some of which are quite significant (body size and form, antennal length, shape of certain antennomeres, form of median lobe and shape of parameral apex), indicated a need to separate *P. (P.) remyi* as a distinct genus or at least to a specific position within the genus *Proleonhardella*. This genus was not reported in the catalogues of Perreau (2015) and Hlaváč *et al.* (2017), nor has it been synonymized so far. Even Jeannel (1934) recognised that *P. (P.) remyi* is quite remarkable for its large size compared to other congeners, which barely exceed 2 mm in length. The occurrence together of several congeners is a rare phenomenon in caves. Such is the case with *P. (P.) remyi* and *P. (P.) hirtella*, which were recorded together at five speleological sites in southwestern Serbia and northern Montenegro (Pavićević *et al.* 2012). This might also suggest that these taxa are indeed not congeneric. Additionally, Ćurčić *et al.* (2008a) proposed a new status for *Pholeuonillus* – as a full genus instead of a subgenus. Interestingly, *Pholeuonillus* was established by Breit (1913), who gave it generic rank. Later on, Jeannel (1924) treated it as a subgenus of *Proleonhardella* – a status that was maintained until now. It is recommended to study the taxa in question and other members of the genus *Proleonhardella* using molecular analyses in order to illuminate their phylogenetic relationships and to have their taxonomic status reconsidered and changed, if needed.

A series of high fluvial plateaus of the Inner Dinarides occur in western and southwestern Serbia (Zlatibor, Jabuka-Babine, etc.). According to their position in the area’s relief, these plateaus are presumed to be of Pliocene age (Cvijić 1924, 1926). The palaeokarst in the areas of Mts Povlen and Tara was most probably formed at the same time as the Zlatibor plateau, in the second half of the Pliocene. Based on chronostratigraphic criteria by the International Commission on Stratigraphy (Gibbard *et al.* 2010; Gaudenyi & Jovanović 2012), it is estimated that the palaeokarst in question is around 3–3.5 Ma old. It is likely that the karstic areas of Mts Povlen and Tara were connected with other karstic regions in their vicinity, favouring links between their subterranean faunas in old geological times, as evidenced by the occurrence of two new endogean and cavernicolous leptodirine taxa and their closest relatives in the surrounding areas.

The tribe Leptodirini has a Palaearctic distribution with its highest diversity located in the Mediterranean (Perreau 2000, 2015). It has undergone extensive diversification in the subterranean environment (Ribera *et al.* 2010). In their comprehensive molecular approach to the phylogeny of western Mediterranean Leptodirini, including the fauna of the Iberian Peninsula, Ribera *et al.* (2010) revealed that the main subterranean lineages of the tribe were separated before the Early Oligocene.

The Dinaric mountain chain has provided suitable conditions for subterranean life for millions of years, which resulted in the presence of a rich and diverse cave-dwelling fauna (Zagmajster *et al.* 2008; Kozel *et al.* 2020; Sendra & Reboleira 2020). The leioidid beetle tribe Leptodirini is among the richest groups in the subterranean habitats (Sket 2005), comprising 175 species and 50 genera, most of which are endemic to the Dinarides. This mountain range is recognized for having the world’s greatest species richness of subterranean fauna (Sket 2004; Culver *et al.* 2006; Deharveng *et al.* 2012). A very few studies dealing with phylogenetic relationships of certain subtribes within Dinaric Leptodirini exist. These studies were based only on morphology (Jeannel 1930; Perreau & Pavićević 2008; Perreau 2019) and in most cases they have not been tested with molecular data. Only recently, Njunjić *et al.* (2018) commented on the suprageneric classification of eastern Mediterranean Leptodirini based on molecular phylogeny data. The clade comprising the subtribes Bathysciina Horn, 1880 and Bathysciotina V. Guéorguiev, 1974 was estimated to have originated in the Oligocene (ca 30 Ma ago), while the tested genera of Bathysciina

belonging to the phyletic series of “*Leonhardella*” (*Leonhardella* and *Proleonhardella*) separated more recently – in the Miocene (ca 20 Ma ago) (Njunjić *et al.* 2018).

As in the study of Njunjić *et al.* (2018) only two taxa belonging to the subtribe Bathysciina (phyletic series of “*Leonhardella*”) were subjected to molecular characterization (*Leonhardella* (*Leonhardellina*) *antennaria* Apfelbeck, 1907 and *P. (P.) remyi*), more Dinaric genera of Bathysciina should be included in future molecular analyses to establish their phylogenetic relationships and to understand their origin and the colonization of the region by the subterranean representatives of the group. Discoveries of fascinating new genera of Bathysciina in the underground of the Dinaric karst in the last few decades (Nonveiller & Pavićević 1999; Perreau 1999), including the one described herein, suggest that further investigations of the caves of the area are needed.

## Acknowledgements

This study was financially supported by the Serbian Ministry of Education, Science and Technological Development (Contract No. 451-03-9/2021-14/200178), as well as by the Serbian Ministry of Education, Science and Technological Development and the Ministry of Science and Technology of the People’s Republic of China (project “Mimetics of Insects for Sensing and Security”, Grant I-2). The authors also acknowledge funding provided by the Institute of Physics Belgrade, through the grant by the Ministry of Education, Science and Technological Development of the Republic of Serbia. We are thankful to Assist. Prof. Dr Dragan Antić (Institute of Zoology, University of Belgrade - Faculty of Biology, Belgrade, Serbia) and Dr Iva Njunjić (Naturalis Biodiversity Center, Leiden, the Netherlands), who collected some of the scientific samples of Leptodirini that we used in this study. We are grateful to Assoc. Prof. Dr Borislav Guéorguiev (National Museum of Natural History, Bulgarian Academy of Sciences, Sofia, Bulgaria), Mr Max Barclay (Natural History Museum, London, UK) and an anonymous reviewer, whose constructive comments greatly improved the manuscript.

## References

- Anđelić M., Njunjić I., Jovanović J. & Pavićević D. 2011. Rezultati interdisciplinarnih istraživanja Simine jame, selo Gornje Košlje, opština Ljubovija. In: Čalić J. (ed.) *Proceedings of the 7<sup>th</sup> Symposium on Karst Protection (Bela Palanka, Serbia, 21–22.5.2011)*: 143–148. Student Speleologic and Alpinistic Club & Municipality of Bela Palanka, Belgrade-Bela Palanka, Serbia.
- Apfelbeck V. 1901. Drei neue Höhlenkäfer aus Bosnien. *Verhandlungen der Kaiserlich-Königlichen Zoologisch-Botanischen Gesellschaft in Wien* 51: 14–16.
- Bosco F. 2016. *180 Grotte per Raccontare il Fenomeno Carsico in Serbia*. Società di Studi Carsici “A.F. Lindner”, Ronchi dei Legionari, Italy.
- Breit J. 1913. Wissenschaftliche Ergebnisse der Bearbeitung von O. Leonhard’s Sammlungen. 5. Beiträge zur Blindkäferfauna von Bosnien und der Herzegowina. *Entomologische Mitteilungen* 2 (11): 351–358.
- Culver D.C., Deharveng L., Bedos A., Lewis J.J., Madden M., Reddell J.R., Sket B., Trontelj P. & White D. 2006. The mid-latitude biodiversity ridge in terrestrial cave fauna. *Ecography* 29: 120–128. <https://doi.org/10.1111/j.2005.0906-7590.04435.x>
- Ćurčić S.B. 2005. *Uporedno-morfološka svojstva, razviće i filogenija nekih zemljišnih i pećinskih tvrdokrilaca (Carabidae i Cholevidae = Leiodidae, Coleoptera) u Srbiji*. PhD thesis, Faculty of Biology, University of Belgrade, Belgrade, Serbia.
- Ćurčić S.B., Brajković M.M., Ćurčić B.P.M. & Ćurčić N.B. 2006. A new cave-dwelling and endemic species of the genus *Pholeuonopsis* (Coleoptera, Leiodidae) from Serbia. *Biologia, Bratislava* 61 (5): 497–501. <https://doi.org/10.2478/s11756-006-0082-0>

- Ćurčić S.B., Schönmann H., Brajković M.M. & Ćurčić B.P.M. 2008a. *Serboleonhardella* gen. n., based on *Proleonhardella remyi* Jeannel (Leptodirini, Leiodidae, Coleoptera), from a cave in southwestern Serbia. In: Makarov S.E. & Dimitrijević R.N. (eds) *Advances in Arachnology and Developmental Biology. Papers Dedicated to Prof. Dr. Božidar Ćurčić*: 463–473. Institute of Zoology, Faculty of Biology, University of Belgrade, Committee for Karst and Speleology, Serbian Academy of Sciences and Arts, Institute of Zoology, Bulgarian Academy of Sciences, Faculty of Life Sciences, University of Vienna & UNESCO MAB Committee of Serbia, Vienna-Belgrade-Sofia, Austria-Serbia-Bulgaria.
- Ćurčić S., Waitzbauer W., Zolda P., Brajković M.M. & Ćurčić B.P.M. 2008b. New cave-dwelling species of the genus *Remyella* Jeannel (Leptodirini, Leiodidae, Coleoptera) from Serbia. *Archives of Biological Sciences, Belgrade* 60 (1): 109–115. <https://doi.org/10.2298/ABS0801109C>
- Ćurčić S., Vrbica M., Vesović N., Antić D., Petković M., Bosco F. & Ćurčić B. 2015. A new troglotic species of the genus *Pholeuonopsis* (Coleoptera: Leiodidae: Cholevinae: Leptodirini) from western Serbia, with a key to the species from Serbia. *Zootaxa* 3937 (2): 393–400. <https://doi.org/10.11646/zootaxa.3937.2.10>
- Ćurčić S., Pavićević D., Vesović N., Mulaomerović J., Rađa T., Antić D., Bosco F., Marković Đ. & Petković M. 2018. Seven new taxa of Leptodirini (Coleoptera: Leiodidae: Cholevinae) from the Balkan Peninsula. *Zootaxa* 4483 (3): 523–548. <https://doi.org/10.11646/zootaxa.4483.3.6>
- Cvijić J. 1924. *Geomorfologija I*. Serbian Royal State Printing Office, Belgrade, Serbia.
- Cvijić J. 1926. *Geomorfologija II*. Serbian Royal State Printing Office, Belgrade, Serbia.
- Deharveng L., Gibert J. & Culver D.C. 2012. Diversity patterns in Europe. In: White W.B. & Culver D.C. (eds) *Encyclopedia of Caves. Second Edition*: 219–228. Academic Press, Amsterdam, the Netherlands.
- Gaudenyi T. & Jovanović M. 2012. Quaternary stratigraphy – recent changes. *Bulletin of the Serbian Geographical Society* 92 (4): 1–16. <https://doi.org/10.2298/GSGD1204001G>
- Gibbard P.L., Head M.J., Walker M.J.C. & the Subcommission on Quaternary Stratigraphy 2010. Formal ratification of the Quaternary System/Period and the Pleistocene Series/Epoch with a base at 2.58 Ma. *Journal of Quaternary Science* 25 (2): 96–102. <https://doi.org/10.1002/jqs.1338>
- Guéorguiev V.B. 1976. Recherches sur la taxonomie, la classification et la phylogénie des Bathysciinae (Coleoptera Catopidae). *Dissertationes Academiae Scientiarum et Artium Slovenicae, Ljubljana* 19 (4): 91–147.
- Hlaváč P., Perreau M. & Čeplík D. 2017. *The Subterranean Beetles of the Balkan Peninsula: Carabidae, Leiodidae, Staphylinidae, Scarabaeidae, Bothrideridae, Zopheridae, Salpingidae, Brachyceridae, Curculionidae*. Faculty of Forestry and Wood Sciences, Czech University of Life Sciences Prague, Prague, Czech Republic.
- Jeannel R. 1910. Essai d'une nouvelle classification des Silphides cavernicoles. *Archives de Zoologie expérimentale et générale* 45 (1): 1–48.
- Jeannel R. 1911. *Revision des Bathysciinae (Coléoptères Silphides): Morphologie, Distribution Géographique, Systématique*. Librairie A. Schulz, Paris, France. <https://doi.org/10.5962/bhl.title.63151>
- Jeannel R. 1924. Monographie des Bathysciinae. *Biospeologica L. Archives de Zoologie expérimentale et générale* 63: 1–436.
- Jeannel R. 1930. Revision des genres *Blattochaeta* et *Antroherpon* (Bathysciinae). *L'Abeille* 34: 123–148.
- Jeannel R. 1931. Bathysciinae nouveaux recueillis par P. Rémy dans les grottes du Novi-Pazar. *Bulletin de la Société zoologique de France* 56: 258–266.

- Jeannel R. 1934. Bathysciinae recueillis par M. M. Rémy et R. Husson dans le Sandjak de Novi-Pazar et la Macédoine grecque. *Revue française d'entomologie* 1: 89–103.
- Knirsch E. 1928. Coleoptera nova subterranea. *Časopis Československé společnosti entomologické* 25 (5–6): 81–98.
- Kozel P., Delić T. & Novak T. 2020. *Nemaspela borkoae* sp. nov. (Opiliones: Nemastomatidae), the second species of the genus from the Dinaric Karst. *European Journal of Taxonomy* 717: 90–107. <https://doi.org/10.5852/ejt.2020.717.1103>
- Moldovan O.T., Kováč L. & Halse S. (eds) 2018. *Cave Ecology. Ecological Studies, Volume 235*. Springer, Cham, Switzerland.
- Njunjić I., Perreau M. & Pavićević D. 2015. Two new species of the genus *Anthroherpon* Reitter, 1889 from northern Montenegro with notes on the “*A. ganglbaueri*” species group (Coleoptera: Leiodidae: Cholevinae: Leptodirini). *Zootaxa* 3915 (3): 403–412. <https://doi.org/10.11646/zootaxa.3915.3.5>
- Njunjić I., Schilthuizen M., Pavićević D. & Perreau M. 2017. Further clarifications to the systematics of the cave beetle genera *Remyella* and *Rozajella* (Coleoptera: Leiodidae: Cholevinae: Leptodirini). *Arthropod Systematics & Phylogeny* 75 (1): 141–158.
- Njunjić I., Perrard A., Hendriks K., Schilthuizen M., Perreau M., Merckx V., Baylac M. & Deharveng L. 2018. Comprehensive evolutionary analysis of the *Anthroherpon* radiation (Coleoptera, Leiodidae, Leptodirini). *PLoS ONE* 13 (6): e0198367. <https://doi.org/10.1371/journal.pone.0198367>
- Nonveiller G. 1983. Endogejska i troglobiontska fauna tvrdokrilaca Srbije (Insecta, Coleoptera). I. Istraživanja od 1976. do 1982. *Zbornik radova o Fauni SR Srbije* 2: 267–299.
- Nonveiller G. & Pavićević D. 1999. *Tartariella durmitorensis* n. gen. et n. sp., troisième Leptodirini de la chaîne Dinarique à mœurs hadésiennes (Coleoptera, Leiodidae). *Bulletin de la Société entomologique de France* 104 (4): 307–318.
- Pavićević D., Popović M., Komnenov M. & Njunjić I. 2012. Diversity of arthropod fauna in caves and pits of Kamena Gora (Serbia) and its surroundings. In: Pavićević D. & Perreau M. (eds) *Fauna Balkana. Volume 1*: 151–176. Department of Biology and Ecology, Faculty of Sciences, University of Novi Sad, Novi Sad, Serbia.
- Perreau M. 1999. Nouveaux genres et nouvelles espèces de Leptodirini (Coleoptera, Leiodidae). *Bulletin de la Société entomologique de France* 104 (4): 399–406.
- Perreau M. 2000. Catalogue des Coléoptères Leiodidae Cholevinae et Platypsyllinae. *Mémoires de la Société entomologique de France* 4: 1–461.
- Perreau M. 2015. Family Leiodidae Fleming, 1821. In: Löbl I. & Löbl D. (eds) *Catalogue of Palaearctic Coleoptera. Volume 2/1. Hydrophiloidea - Staphylinoidea. Revised and Updated Edition*: 180–291. Brill, Leiden-Boston, the Netherlands-USA.
- Perreau M. 2019. Phylogeny of Bathysciotina Guéorguiev, 1974, based on morphology with a special emphasis to Italian genera and with the description of a new species of *Halbherria* (Coleoptera Leiodidae Cholevinae Leptodirini). *Zootaxa* 4590 (3): 367–381. <https://doi.org/10.11646/zootaxa.4590.3.3>
- Perreau M. & Pavićević D. 2008. The genus *Hadesia* Müller, 1911 and the phylogeny of Anthroherponina (Coleoptera, Leiodidae, Cholevinae, Leptodirini). In: Pavićević D. & Perreau M. (eds) *Advances in the Studies of the Fauna of the Balkan Peninsula. Papers Dedicated to the Memory of Guido Nonveiller*: 215–239. Institute for Nature Conservation of Serbia, Belgrade, Serbia.
- Reitter E. 1910. Eine neue *Bathyscia* aus Dalmatien. *Wiener entomologische Zeitung* 29 (5–6): 164. <https://www.biodiversitylibrary.org/page/12086245>

- Reitter E. 1913. Sechs neue von Herrn Weirather in Bosnien entdeckte Höhlensilphiden. *Koleopterologische Rundschau* 10: 153–157.
- Ribera I., Fresneda J., Bucur R., Izquierdo A., Vogler A.P., Salgado J.M. & Cieslak A. 2010. Ancient origin of a western Mediterranean radiation of subterranean beetles. *BMC Evolutionary Biology* 10: 29. <https://doi.org/10.1186/1471-2148-10-29>
- Sendra A. & Reboleira A.S.P.S. 2020. Euro-Mediterranean fauna of Campodeinae (Campodeidae, Diplura). *European Journal of Taxonomy* 728: 1–130. <https://doi.org/10.5852/ejt.2020.728.1181>
- Sket B. 2004. Dinaric karst: biospeleology. In: Gunn J. (ed.) *Encyclopedia of Caves and Karst Science*: 595–598. Taylor & Francis, New York, USA.
- Sket B. 2005. Dinaric karst, diversity. In: Culver D.C. & White W.B. (eds) *Encyclopedia of Caves*: 158–165. Elsevier, Amsterdam, the Netherlands.
- Zagmajster M., Culver D.C. & Sket B. 2008. Species richness patterns of obligate subterranean beetles (Insecta: Coleoptera) in a global biodiversity hotspot – effect of scale and sampling intensity. *Diversity and Distributions* 14: 95–105. <https://doi.org/10.1111/j.1472-4642.2007.00423.x>
- Zariquiey R. 1927. Nuevos Bathysciinae de los Balcanes (Col. Silphidae). *Butlletí de l'Institutió Catalana d'Història Natural* 27: 152–158.

*Manuscript received: 3 March 2021*

*Manuscript accepted: 13 October 2021*

*Published on: 1 December 2021*

*Topic editor: Nesrine Akkari*

*Section editor: Max Barclay*

*Desk editor: Pepe Fernández*

Printed versions of all papers are also deposited in the libraries of the institutes that are members of the *EJT* consortium: Muséum national d'histoire naturelle, Paris, France; Meise Botanic Garden, Belgium; Royal Museum for Central Africa, Tervuren, Belgium; Royal Belgian Institute of Natural Sciences, Brussels, Belgium; Natural History Museum of Denmark, Copenhagen, Denmark; Naturalis Biodiversity Center, Leiden, the Netherlands; Museo Nacional de Ciencias Naturales-CSIC, Madrid, Spain; Real Jardín Botánico de Madrid CSIC, Spain; Zoological Research Museum Alexander Koenig, Bonn, Germany; National Museum, Prague, Czech Republic.



Cite this: *Soft Matter*, 2021, 17, 6477

## Synergy of interference, scattering and pigmentation for structural coloration of *Jordanita globulariae* moth

Danica Pavlović,<sup>a</sup> Svetlana Savić-Šević,<sup>a</sup> Branislav Salatić,<sup>a</sup> Vladimir Lazović,<sup>a</sup> Wang Zhang,<sup>b</sup> Di Zhang<sup>b</sup> and Dejan Pantelić<sup>a</sup>

Structural and pigment colorations are omnipresent in insects, producing a range of colors for camouflage, warning, mimicry and other strategies necessary for survival. Structural coloration has attracted a lot of attention due to its significance in biophotonics, biomimetics and even esthetic appeal. The coupling of structural and pigment colorations has been largely unnoticed. Herein we show how pigments, scattering and interference work together in two-dimensional waveguiding structures to produce the coloration of *Jordanita globulariae* (Huebner, 1793), a moth whose forewings sparkle with slightly iridescent green scales. We show that subwavelength structures scatter and couple light into a concave multilayered structure to enhance the absorption of pigments. A finite element method (FEM) model, adequately describing the photonic properties of *J. globulariae*, was developed based on the nanoscale architecture of the insect's wing scales. The principle of absorption enhanced by scattering and waveguiding is present in many insect species and might be imitated to tailor the spectral properties of optical devices.

Received 29th January 2021,  
Accepted 25th May 2021

DOI: 10.1039/d1sm00157d

[rsc.li/soft-matter-journal](http://rsc.li/soft-matter-journal)

### 1. Introduction

Animals produce colors in two fundamentally different ways: by pigments and structurally. Most animals have pigmentary coloration that is based on the selective absorption of a certain range of wavelengths. However, the most intense and brightest colors are structural. They result from the interaction of light with micro- and nanostructures comparable with visible wavelengths.<sup>1</sup>

Pigment coloration is prevalent, except for blue and green, which seem to be rare, but nonetheless can be found in some vertebrates,<sup>2</sup> the most notable being the green coloration of frogs.<sup>3</sup> The same is true for insects, whose blue-green colors can be produced by bile pigments such as pterobilin, phorbabilin and sarpodobilin. Some butterfly species have a bluish- or greenish-pigmented hue obtained by bile pigments (seen in two Papilionidae genera: *Papilio* and *Graphium*). Pigmented blue has not been found in other insects.<sup>4</sup> Structural coloration seems to be an alternative, evolutionarily developed, way to generate shiny, pronounced shades of arbitrary colors, including blues and greens.

There are many different studies and advanced techniques dealing with structural coloration.<sup>5,6</sup> The genesis of green coloration is particularly interesting because of its significance in camouflage. Structural green sometimes arises solely from photonic structures<sup>7,8</sup> or due to color mixing within concave structures (as in the wing scales of some Papilionidae species (Lepidoptera) and Cicindelidae (Coleoptera)).<sup>9,10</sup> It is worth noting that green may be a result of the color-mixing of structural blue and pigmentary yellow.<sup>11,12</sup>

Such a peculiar coloration is even more interesting if it is found on the wings of moths (Heterocera: Lepidoptera). Moths are mostly nocturnal, and therefore, generally drab in color (brown or grey). However, there are some moth species that possess attractive coloration such as the tropical Madagascan sunset moth.<sup>13</sup> There is also a whole group of colorful, day-flying moths of the Zygaenidae family. The majority of zygaenids are tropical, but they are nevertheless quite well represented in temperate regions. The species *Jordanita globulariae* (subfamily Procrinae) caught our attention because of the dull, slightly iridescent green coloration of its forewings.

In this study we reveal the structure and function of the scales of the *Jordanita globulariae* moth through morphological characterization, spectral measurement and numerical simulation. The synergistic operation of structure and pigments is analyzed. We also discuss the role of this particular coloration in the moth's lifestyle.

<sup>a</sup> Institute of Physics Belgrade, Pregrevica 18, 11080 Zemun, Belgrade, Serbia.  
E-mail: danica.pavlovic@ipb.ac.rs

<sup>b</sup> State Key Lab of Metal Matrix Composite, Shanghai Jiao Tong University, 800 Dongchuan Road, Shanghai 200240, China

## 2. Materials and methods

### 2.1 Specimen details

*Jordanita globulariae* (Fig. 1) is a day-flying moth (fam. Zygaenidae, subfam. Procridinae). The species is widespread from the Iberian Peninsula in the west to the Urals in the east of Europe. The forewing's length is 10.5–17 mm in males and 7.7–10.1 mm in females. It flies during the sunny days from May to August, usually in limestone pastures.<sup>14</sup> Larvae are fed on species from the genera *Centaurea* L., *Cirsium* and *Globularia* L. On very hot days, the moth usually perches on flowers and other vegetation. Males occasionally fly at night.<sup>15</sup> Adults of this moth have green forewings, while the hind ones are grey-brown. When at rest, the hindwings are completely obscured under the green forewings, enabling the insect to hide in foliage. Several species within this family have similar morphological characteristics [e.g. *Adscita statices* (Linnaeus, 1758)]. We had three, conserved and pinned *J. globulariae* specimens at our disposal, collected during May and June of 2011 on Mt. Fruška Gora, near the city of Novi Sad, Serbia (leg. D. Stojanović).

### 2.2 Microscopy and spectroscopy

Field-emission gun scanning electron microscope (FEGSEM) (MiraSystem, TESCAN) was used to study the fine anatomy of the moth scales. Dried insect forewings were mounted and sputter-coated with 5–10 nm of Au/Pd in preparation for SEM. We used an Au/Pd target because it has a smaller grain size and it is the recommended metal coating for a wide range of sample types.

Individual scales were prepared for SEM by the double transfer method: a scale was detached with a low-surface-energy adhesive ("Post-it" sticky note), followed by transfer to a high-surface-energy tape (conductive carbon). In this way, the original scale orientation was preserved. During this process some of the scales were mechanically broken, revealing the inner structure and cross section of the scales.

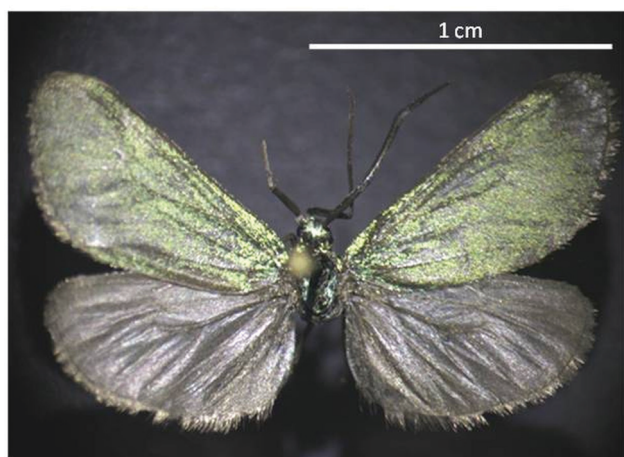


Fig. 1 *Jordanita globulariae* with structurally green dorsal sides of the forewings.

Optical characteristics of the wings and scales were analyzed on a trinocular microscope MET104 (Colo Lab Experts) with a Plan Achromatic POL Polarizing objective lens (10X/20X/40X).

To record reflectance spectra, we used a fiber optic spectrometer (Ocean Optics, HR2000CG-UV-NIR) with a 400  $\mu\text{m}$  core diameter fiber. A halogen lamp was used as a light source and spectra were referenced to a standard white surface. Angular variation of the reflectance spectra was measured with a stationary sample illuminated by the light source at normal incidence. The spectrometer fiber was rotated within the angular range from  $10^\circ$  to  $50^\circ$ .

### 2.3 Optical modeling

A finite element method (FEM) was used to model the interaction of visible light with wing pigmented scale nanostructures. The model is two-dimensional because it saves computation time, which was approximately 20 min on our PC. It would be difficult to model the exact shape of photonic structures that are certainly not spherical, but somewhat irregular, rather oval and elongated along one axis (Fig. 2(b) and 3(a)). Thus, a 2D model (which is equivalent to a 3D infinite cylinder) is a satisfactory approximation, as the photonic structure studied here departs significantly from cylindrical only at its edges. The arrayed structure of wing scales is modeled using one unit cell with periodic boundary conditions. Perfectly matched layers (PMLs) are placed above and below the structure in order to minimize any reflected signal. In the model, the average mesh size was manually set to one-fifth

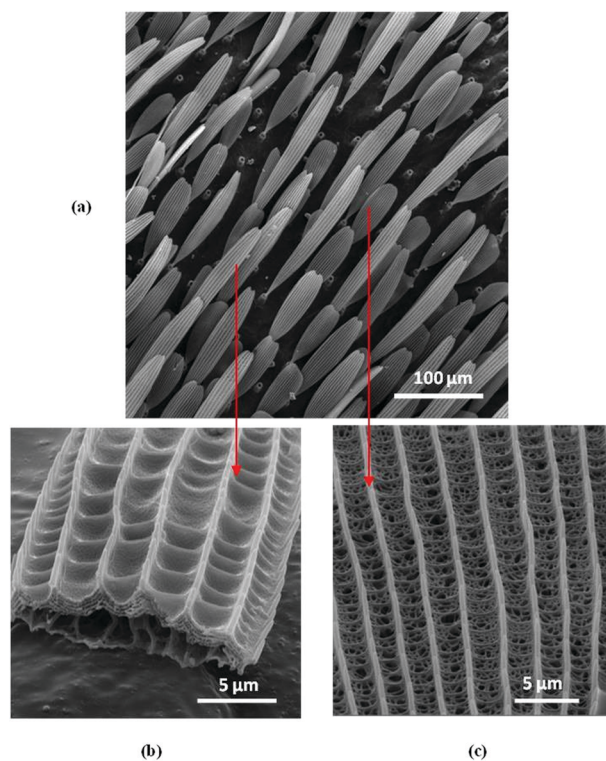


Fig. 2 (a) A SEM image of the *J. globulariae* forewing with two types of scales. Magnified SEM images of: (b) a long scale covered with several cup-shaped dips and (c) a short scale with a random, sponge-like structure.



of the minimum incident wavelength, which was 400 nm in our case. However, mesh density was adaptively adjusted to correctly model the tiniest structures of the model. To create a numerical simulation, it is necessary to know the complex refractive index of the biological structure. It is difficult to know the exact value, but we found that modest variation ( $\Delta n \sim \pm 0.03$ ) of the refractive index has only a slight impact on simulations. The real part of the complex refractive index was taken from the literature:  $n = 1.57$ .<sup>16,17</sup>

The extinction coefficient was determined experimentally by measuring the transmission of light through the structure and applying Beer–Lambert's law. We assumed that the structures analyzed here had a subwavelength size and could be regarded within the effective medium approximation. Imaginary part  $k$  of the refractive index was 0.011 at 400 nm, 0.019 at 500 nm and 0.01 at 800 nm.

### 3. Results

#### 3.1 Morphological and optical analysis of *J. globulariae* wing structures

The dorsal side of *J. globulariae* forewings is covered with scales that seem to be randomly distributed (Fig. 2(a)). The scales are either long with a regular internal architecture (Fig. 2(b)), or short with an irregular, sponge-like structure (Fig. 2(c)).

Long scales (with characteristic dimensions of approximately  $20 \mu\text{m} \times 150 \mu\text{m}$ ) seem to be more elaborate. At higher magnification (Fig. 3(a)), we can see that their upper lamina is ornamented with thin, lamellar ridges (separated by approximately  $3 \mu\text{m}$ ) connected by cross ribs. Together, ridges and cross ribs produce a sequence of concave dips (cup-like structures,  $0.5\text{--}3 \mu\text{m}$  deep) whose surface has a large number of tiny pores ( $20\text{--}50 \text{ nm}$ ). The interior of the whole scale is hollow, supported by large,  $1.5 \mu\text{m}$  high, trabeculae (Fig. 3(a)) connecting the upper and lower lamina (which is irregular, single-layered and about  $100 \text{ nm}$  thick).

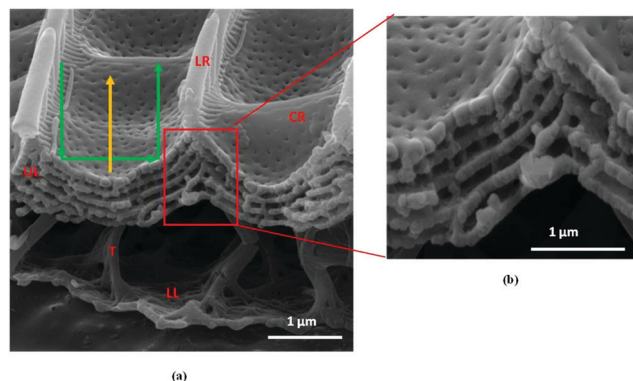


**Fig. 3** SEM image of *J. globulariae* long wing-scale structure. (a) A cross section of the scale showing concave, multilayered upper lamina and single-layer lower lamina separated by trabeculae (LR – lamellar ridges; CR – cross ribs; T – trabeculae; UL – upper lamina; LL – lower lamina). Green and yellow arrows indicate different wavelengths for radiation hitting the structure at its center or its edges. (b) A concave multilayer of the upper lamina with five chitin layers.

The cross section of the scale (Fig. 3(b)) shows the concave upper lamina with five chitin layers whose thickness is approximately  $110 \text{ nm}$ . They are mutually separated by tiny, pillar-like structures, producing  $90 \text{ nm}$ -thin, air-filled, voids. This arrangement will be further considered as a curved multilayer serving as a specific, spectrally selective, filter.

On the other hand, short scales (whose approximate size is  $40 \mu\text{m} \times 80 \mu\text{m}$ ) are quite different. They are almost hollow, filled with an intricate, irregular, sponge-like structure (Fig. 4(a) and (b)), but surface ridges and cross ribs can be seen as well.

From an optical point of view, the green color of the insect is diffuse, dim and slightly iridescent (Fig. 1) – *i.e.* we were able to observe a significant color shift only for large, almost grazing, angles of observation. If observed through an optical microscope, long scales reflect, while short ones absorb light (Fig. 5). If the image of a long scale is further magnified (inset in Fig. 5), a number of discrete blue-green and yellow dots can be seen.

Comparing SEM and optical images, we can see accurate matching between the morphology of long scales and the observed optical pattern. It is well known that the spectral reflection of a layered structure is influenced by the distance between the layers, the refractive index and the angle of incidence. In this case, reflection is strongly affected by the concave shape of the layers. We can see that light falling on the center of the concavity has a different angle of incidence compared to off-center zones. This is why we observe differently colored spots in the inset of Fig. 5. Macroscopically, colors are mixed to produce the insect's green color.

Apart from structural coloration, scales are slightly pigmented, as can be seen from the transmission optical image (Fig. 6(a) – scales were immersed in an index matching fluid to suppress Fresnel reflections). Interestingly, the long (structurally colored) scale has significantly higher (0.25) absorption than the short (nonstructural) one (0.16).

Absorption is much higher in the blue part of the spectrum and decreases towards the green-red part (as can be seen in Fig. 6(b)). We found that the average coefficient of absorption is between  $0.35 \text{ 1}/\mu\text{m}$  in the blue part of the spectrum and  $0.1 \text{ 1}/\mu\text{m}$  in the red. All the above facts signify that the effect of pigments cannot be disregarded, as we will further show.

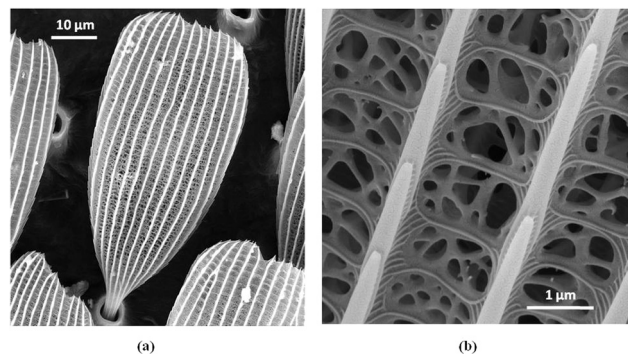


**Fig. 4** SEM images of (a) a short wing scale of *J. globulariae* and (b) its hollow, sponge-like internal structure.

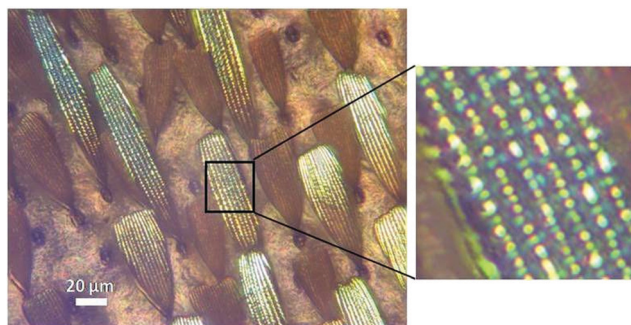
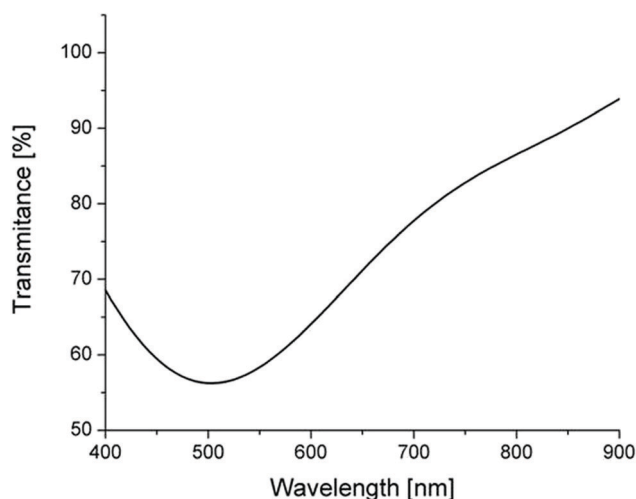


Fig. 5 Optical micrograph of *J. globulariae* wing scales. An enlarged part of a structurally colored one is shown on the right (with yellow and blue-green dots).



(a)



(b)

Fig. 6 *J. globulariae* moth: (a) Transmission optical image of long (L) and short (R) scales. (c) Transmittance spectrum of the long, structurally colored scale.

We measured the angular variation of the spectrum by rotating the detector (spectrometer fiber) and keeping the wing and illuminator positions fixed. Illumination was at normal incidence with respect to the wing. The reflection was recorded within the angular range of 10–50 degrees. Under these conditions we observed a slight spectral shift of 40 nm (Fig. 7(a)). This corresponds to the perception of unsaturated green color,

irrespective of the angle of observation. As a final remark, we emphasize that the spectrum fits nicely into the spectrum of foliage (Fig. 7(b)), enabling the insect to hide effectively in its natural environment.

### 3.2 Optical modeling of *J. globulariae* wing scales

Here we present an optical model of structurally colored scales (Fig. 8(a)) designed to simulate all the characteristic features observed in SEM images (Fig. 3):

- concave dip (1.5  $\mu\text{m}$  radius) with five chitin layers, 110 nm thick, and refractive index 1.57;
- layers separated by (20 nm  $\times$  90 nm) producing 90 nm air spaces;
- outer surface with a number of 10 nm-diameter holes.

On this basis, we will establish a link between the architecture and the optical response of wing scales.

In a simplified model and before going into more detail, we will approximate the structure with a collection of Bragg gratings with different orientations. According to Bragg's law:

$$\lambda = 2nd \cos \theta \quad (1)$$

where  $\lambda$  is the wavelength of multilayer reflectance maximum,  $d$  is the grating period,  $n$  is the effective refractive index of the grating, and  $\theta$  is the angle of incidence of radiation. Observe that the incident plane wave irradiates the concave structure within the range of angles – 0 degrees in the center and 50 degrees at the edges. At the center of a concave dip (angle of incidence  $\theta = 0^\circ$ ) the Bragg wavelength can be estimated at 520 nm (assuming a grating period of 200 nm and an effective refractive index of 1.3). Towards the edge, the Bragg resonance drops to 370 nm. Due to only five Bragg layers, the reflection maxima are broad (Fig. 8(b)) and the resulting spectra cover the UV-blue part of the spectrum.

We can conclude that, without an additional mechanism, *J. globulariae* wings will evenly reflect visible light, making the insect appear to be bluish. Absorption alone is not enough to modify the reflection spectrum due to the thinness of individual scales and small amount of pigment (Fig. 6). In the following we will prove that scattering amplifies absorption in accordance with the theory of Yablonovitch described in ref. 18. It was shown that rough surfaces amplify the radiation intensity within planar layers by  $2n^2$  factor, where  $n$  is the refractive index of the material. This leads to increased absorption of up to  $4n^2$  times compared to ideally flat layers. For chitinous structures of scales ( $n = 1.57$ ), absorption may thus increase up to 9.9 times.

The Yablonovitch theory is universally applicable to layers of any thickness, as it is based on the basic laws of radiation. For subwavelength multilayer structures, as is the case here, the effects of evanescent waves certainly lead to radiation being redistributed among the layers. However, the total thickness of all layers taken together is significantly larger than the wavelength and the radiation stays entrapped and waveguided. Here we add that the theory is limited to randomly distributed (Lambertian) incoming radiation. This is usually the case for the environmental, solar, irradiation omnipresent in most natural surroundings. We have previously used the theory to

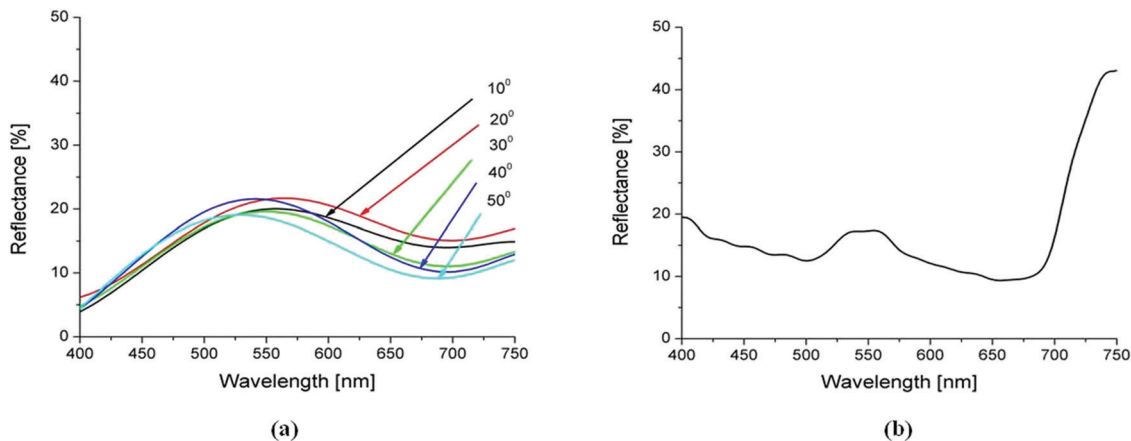


Fig. 7 (a) A slight angular variation (within a 10–50° range) of the *J. globulariae* wing reflectance spectrum. (b) A reflectance spectrum of the green leaves of Hibiscus.

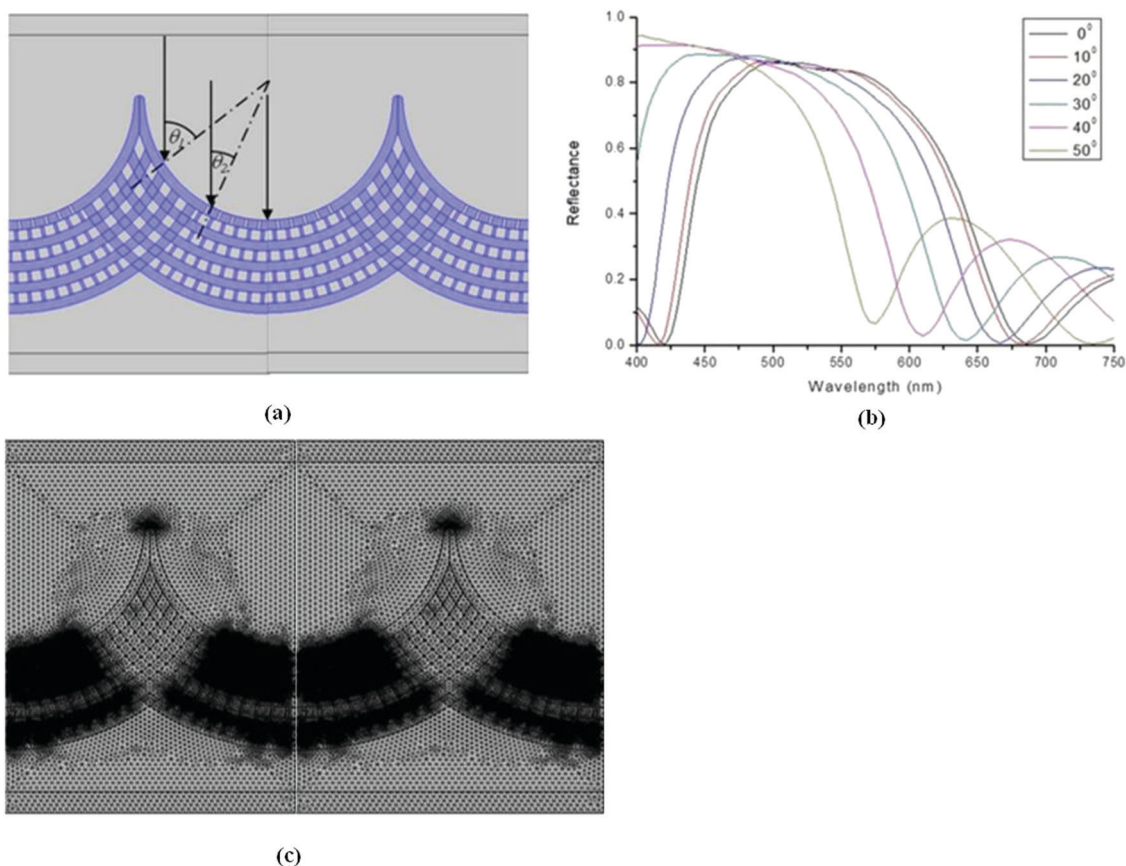


Fig. 8 (a) Geometry of a concave multilayer model used in FEM. Arrows indicate the radiation direction and  $\theta$  is the angle of incidence. (b) Strong spectral shift for different angles of incidence. (c) A model, depicted in (a), is adaptively meshed for correct FEM analysis of the smallest features.

explain a golden coloration of rather simple wing scales of *Diachrysis chrysitis* moths.<sup>19</sup>

In the case of *J. globulariae* wing scales, scatterers are numerous and include nanometer scale pits on the surface, nanopillars between the layers and many of the other defects of otherwise regular structures. The whole problem is too

complicated to be analyzed analytically because it includes the effects of scattering on subwavelength structures, spectrally dependent absorption, waveguiding and radiation localization, as well as interference effects on a very specific concave Bragg grating. This is why we had to use FEMs to calculate the reflection spectrum of the scales. A model in Fig. 8(a) was

adaptively meshed (*i.e.* finer structures were meshed more densely – Fig. 8(c)) in order to obtain the correct results.

First, we calculated the electromagnetic intensity distribution (square of the amplitude) without taking into account absorption (Fig. 9(a)). We clearly observed the localization of the field within the concave Bragg structure due to wave-guided modes. They were introduced into the structure because of scattering on subwavelength structures (pillars and pits) in accordance with the Yablonovitch theory. Resulting spectra are wide and independent on the angle of incidence (Fig. 9(b)).

If absorption is introduced into the model, in accordance with the characteristics of real scales, we can clearly see that waveguided modes are strongly absorbed (Fig. 9(c)) and the resulting spectra are narrowed (Fig. 9(d)) and independent on the angle of illumination, to match those observed experimentally (Fig. 7(a)). This is in stark contrast to the completely flat Bragg grating – its reflectance is very high (up to 90%) but its angular dependence is significant (the shift is larger than 150 nm).

It seems that natural evolution has brought about a nicely balanced set of features: concave structures to induce angular insensitivity of coloration, residual pigments to absorb light and subwavelength structures to enhance scattering and waveguiding. As a result, *J. globulariae* becomes quite inconspicuous within its environment.

We can note that theoretical spectra have a number of local minima and maxima, resulting from a very complex structure with many resonances (Fig. 9(b) and (d)). In reality, the resulting spectrum is obtained by reflection from a large number of scales. They are not identical, and the resonances are averaged to produce a smooth curve as in Fig. 7(a).

To further refine the model, we sliced a spherical multilayer into 8 planar cross-sections and approximated each one as a collection of cylindrical layers (as shown in Fig. 10(a)). Due to symmetry of the structure, there were only 4 different sections (designated 1–4 in Fig. 10(a)) to which we applied an FEM technique in the manner described above. By averaging spectral distributions of all cross sections, we obtained the resulting spectrum in Fig. 10(b), which is comparable to the experimentally recorded curves in Fig. 7(a).

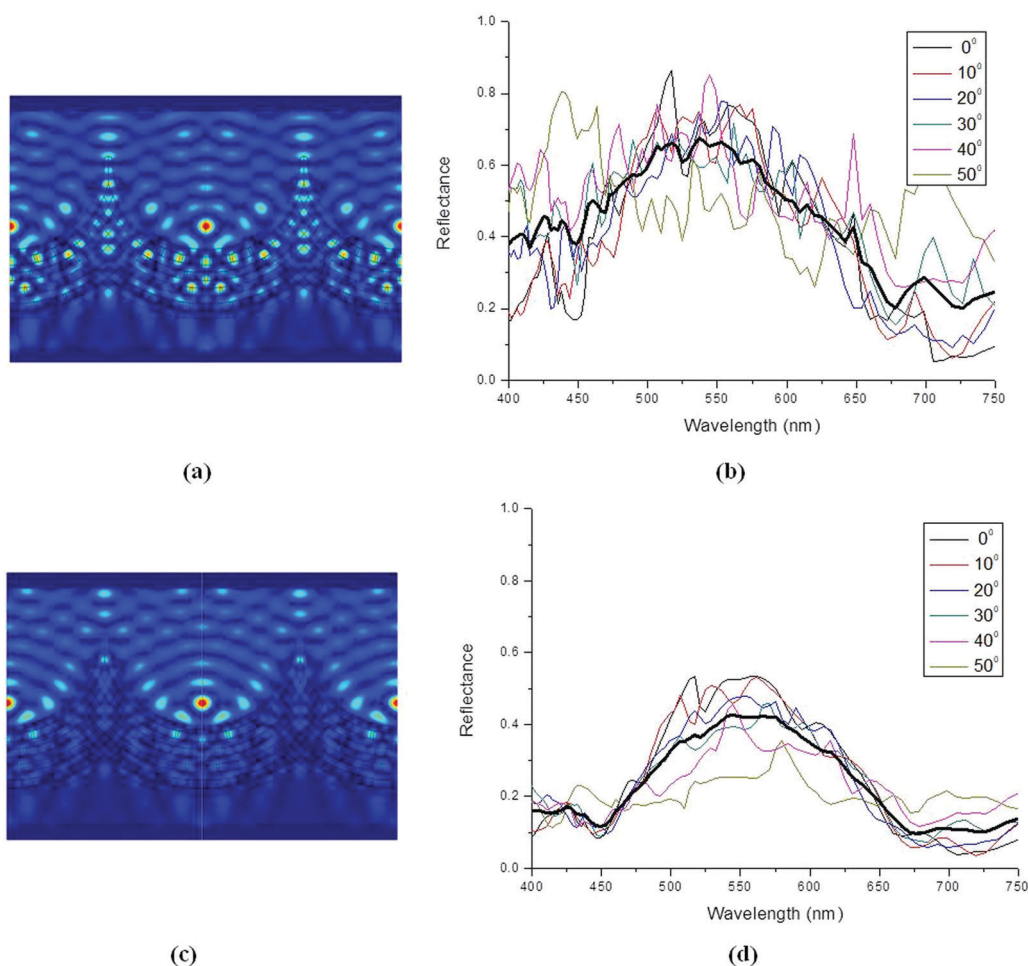


**Fig. 9** (a) Strong localization of the electromagnetic field ( $\lambda = 479$  nm) inside the structure (WITHOUT pigmentation taken into account), and (b) the corresponding spectra at different angles of incidence. (c) Absorption of a localized electromagnetic field ( $\lambda = 479$  nm) inside the structure (WITH pigmentation taken into account), and (d) the corresponding spectra at different angles of incidence.

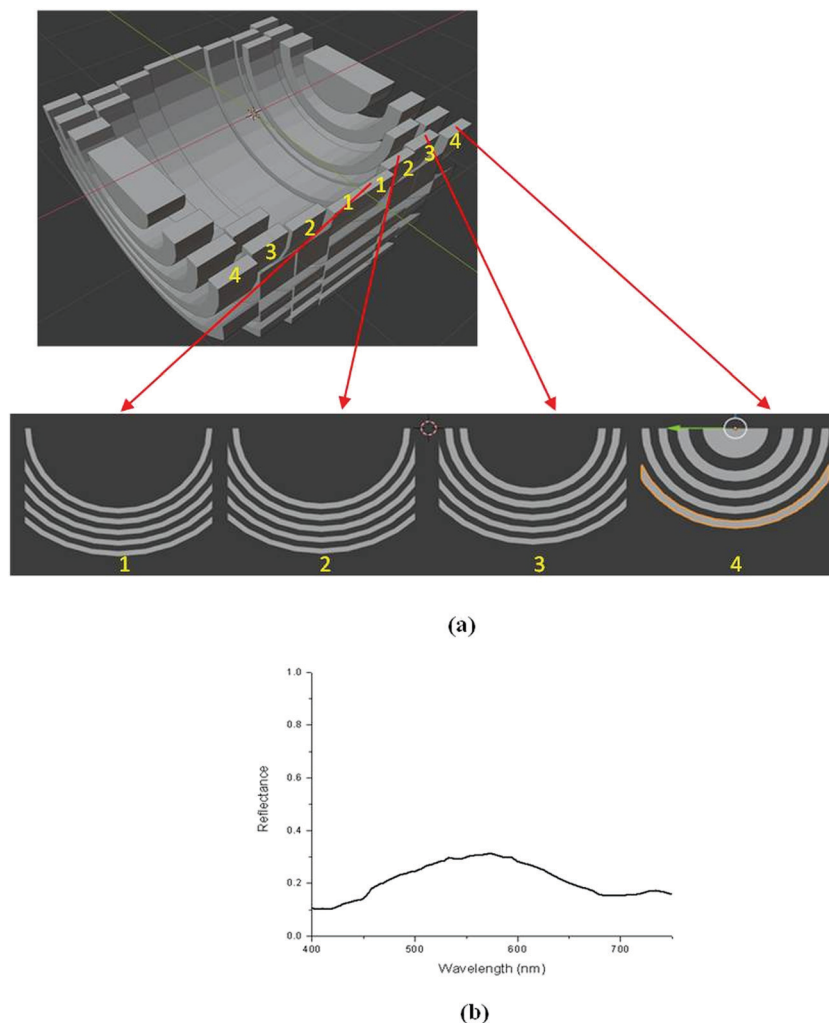


Fig. 10 (a) A characteristic multilayer dip of *J. globulariae* wing scale is modeled as a collection of cylindrical cross-sections designated by numbers 1–4. (b) The resulting spectral distribution, obtained by angular averaging spectra of cross-sections 1–4.

## 4. Discussion

We have shown that the wings of the *J. globulariae* moth possess a set of structural features that produce a slightly iridescent (*i.e.* observable only at grazing incidence) green structural color. This is important for a day-flying insect to remain unseen on the green background of vegetation. To do this, wings evolved with low angular variation and reflectance comparable to that of green surroundings.

Similar structural coloration was also observed in other insects. It was found that *Papilio palinurus* produces its green coloration as a result of color mixing between reflected and retroreflected light from a concave multilayer structure.<sup>10</sup> There, the effects of scattering and pigmentation were not analyzed, and the coloration was explained solely by the multilayer interference.

The question of adequate modeling is an important (and still open) problem for understanding the interaction of light with biophotonic structures. Three-dimensional modeling is extremely demanding, with respect to execution time and

memory requirements. Massively parallel computers are used with computational time of the order of several hours (for a single 3D geometry and single wavelength) and tens (even hundreds) of gigabytes of working memory.<sup>7</sup>

Overall architecture of *J. globulariae* structures is variable – ranging from almost spherical to cylindrical, with several layers and a number of randomly distributed nano-pillars and holes. Such complexity is beyond the capability of most computers. Even the fastest ones are incapable of calculating irregular, stochastically distorted, nano-patterned geometries on a reasonable timescale. Here, we used 2D, cylindrical models of essentially three-dimensional structures. This is quite sufficient for oblong structures, while for those closer to spherical symmetry, a dip was sectioned in order to make the approximation more adequate. Anyway, optical microscopy (Fig. 5) shows that the overall optical effect is quite tolerant to random variation of size, shape and nanostructure. The computational results presented here confirm that slightly absorbing nanostructures restrict the radiation to the green-red part of the spectrum

(compare Fig. 9(b) and (d)) in accordance with the theory of absorption enhancement by scattering.

The role of pigments was analyzed in ref. 20. The authors described the *Eudocima materna* moth whose cover scales act as an interference mirror (not the multilayer one), while ground scales are strongly pigmented. For certain angles of observation, cover scales mirror the incoming radiation, thereby making underlying pigmented scales invisible. For other angles, radiation is redirected by the mirror scales outside the viewing direction, making the underlying pigmented scales visible. Again, interference, scattering and absorption are not interlinked and enhanced.

A somewhat different analysis of the interplay between wing coloration and visual pigments was performed in ref. 21. It was found that additional visual pigment in the photoreceptors of Lycaenidae is well tuned to the characteristic structural coloration of butterflies within this family.

A good overview of photonic structures has been given in ref. 22. The authors remark that green pigments are absent in butterfly wing scales and analyze blackness and fluorescence enhancement caused by structures.

Structures at all dimensional scales are included and work in synergy to produce the coloration of *J. globulariae*. At the molecular level, dark pigments (melanin) are needed to selectively absorb the blue part of the spectrum. However, in this particular insect there is only a small amount of pigment, which is not enough to significantly absorb the blue part of the spectrum as shown in Fig. 9(b). Therefore, nanoscales, pillars, pits and other subwavelength structures are necessary to preferentially scatter blue light and enhance its absorption. Micron-sized concave multilayers selectively filter the red part of the spectrum while making it angularly independent.

On a higher scale (in the order of hundreds of micrometers and millimeters), the wing as a whole must be accounted for. Our model shows that the reflectivity of a single structural scale is in the order of 40% (Fig. 9(d)). However, the reflectivity of the wing is much lower (20–25%, Fig. 7) as a result of sparse scale population, attenuation by nonstructural scales and the wing membrane. The resulting value corresponds well to the reflectivity of vegetation, making the insect almost invisible in its environment. We have calculated the CIE xy color coordinates of the green leaves of *Hibiscus*.<sup>23,24</sup> *J. globulariae* and our model show how well nature has “adjusted” the insect to the environment (Fig. 11). Here, a CIE diagram is used as a simple way to compare complex spectra, not as a measure of human color perception, which is certainly quite different compared to that of insects.

For reference, we have shown the color coordinates of a model without scattering and absorption. In this case, the insect's color would have been blue, making it highly visible.

In this paper we had no space to analyze the “nonstructural” scales, but it seems that there are structural effects too. By looking closely at Fig. 6(a), we can see that the absorption of a nonstructural scale is lower than that of the structural one, yet it is highly absorbing on the wing (Fig. 5). It seems that scattering enhances the absorption of the rather hollow structure of a “nonstructural” scale as well.

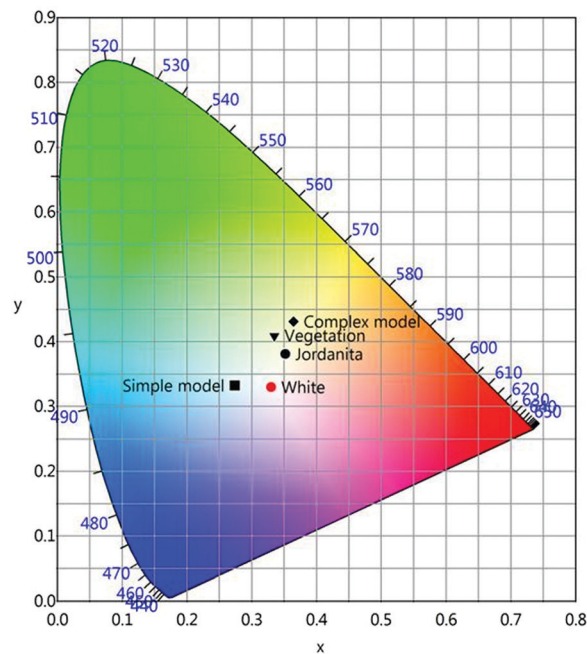


Fig. 11 A CIE diagram showing the xy chromatic coordinates of vegetation, *J. globulariae* and a complex model (concave layer with scattering structures and absorption). Coordinates of achromatic white and a simple, flat, layer model have been shown for reference.

From a biological point of view, the color green usually has a cryptic role in insects,<sup>25–27</sup> providing very effective camouflage among leaves. This greenish color, which is not highly reflective, indicates a primary defensive role in *J. globulariae*. Slight iridescence and color contrast, which are very important in communication between species, further speak in favor of the protective role of such an optical signal.<sup>28</sup>

On the other hand, species of this family (including *J. globulariae*) also possess a chemical defense mechanism. All Zygaenidae<sup>15</sup> contain hydrogen cyanide (HCN), taken from plants or synthesized from plant glucose.<sup>29</sup> Therefore, they are poisonous or, at least, distasteful to potential predators. Sending a warning is another reason why the species of this family may have such coloration. The color green becomes highly visible during feeding on flowers<sup>14</sup> when it acquires its second, aposematic role.<sup>30</sup> Other examples are also known among Lepidoptera where warning and camouflage coloration are not contradictory.<sup>31</sup> We can therefore assume that the role of *J. globulariae* can be cryptic, when resting, hidden in leaves, and aposematic, during nectar feeding.

In most moths, the dorsal side of the front wings is visible during rest.<sup>32</sup> Given that all Zygaenidae are diurnal species, evolution has ensured that they have structural coloration only on the dorsal surface of their forewings.<sup>15</sup>

## 5. Conclusion

This paper reveals the delicate combination of interference, scattering, absorption and color mixing, all working together,

to facilitate the survival of *J. globulariae*. The fine tuning of many structural factors, from submicron to macroscopic levels, is amazing and its imitation provides a new way to control the spectral content of light.

## Conflicts of interest

There are no conflicts to declare.

## Acknowledgements

The authors acknowledge funding provided by the Institute of Physics, Belgrade, through a grant from the Ministry of Education, Science and Technological Development of the Republic of Serbia and the Science and Technology Development Program – Joint Funding of Development and Research Projects of the Republic of Serbia and the People's Republic of China: Mimetics of insects for sensing and security, No. I-2. DP acknowledges support from L'Oréal-UNESCO "For Women in Science". We express our gratitude to Dejan Stojanović from the Institute of Lowland Forestry and Environment, Novi Sad, Serbia, who donated *J. globulariae* specimens from his insect collection.

## References

- 1 J. Sun, B. Bhushan and J. Tong, *RSC Adv.*, 2013, **3**, 14862–14889.
- 2 J. T. Bagnara, P. J. Fernandez and R. Fujii, *Pigment Cell Res.*, 2007, **20**, 14–26.
- 3 C. Taboada, A. E. Brunetti, M. L. Lyra, R. R. Fitak, A. F. Soverna, S. R. Ron, M. G. Lagorio, C. F. B. Haddad, N. P. Lopes, S. Johnsen, J. Faivovich, L. B. Chemes and S. E. Bari, *Proc. Natl. Acad. Sci. U. S. A.*, 2020, **117**, 18574–18581.
- 4 P. Simonis and S. Berthier, How nature produces blue color. in *Photonic Crystals – Introduction*, ed. A. Massaro, Applications and Theory, InTech, Rijeka, 2012, pp. 3–24.
- 5 P. Kaspar, D. Sobola, P. Sedláč, V. Holcman and L. Grmela, *Microsc. Res. Tech.*, 2019, **82**, 2007–2013.
- 6 D. Sobola, S. Talu, P. Sadvovskiy, N. Papez and L. Grmela, *Adv. Electr. Electron. Eng.*, 2017, **15**, 569–576.
- 7 K. Michielsen, H. De Raedt and D. G. Stavenga, *J. R. Soc., Interface*, 2010, **7**, 765–771.
- 8 B. D. Wilts, K. Michielsen, J. Kuipers, H. De Raedt and D. G. Stavenga, *Proc. R. Soc. B*, 2012, **279**, 2524–2530.
- 9 S. Berthier, *Iridescences, les couleurs physiques des insectes*, Springer Science & Business Media, 2007.
- 10 P. Vukusic, J. R. Sambles and C. R. Lawrence, *Nature*, 2000, **404**, 457.
- 11 D. L. Fox, *Animal biochromes and structural colours: physical, chemical, distributional & physiological features of coloured bodies in the animal world*, University of California Press, 1976.
- 12 D. G. Stavenga, M. A. Giraldo and H. L. Leertouwer, *J. Exp. Biol.*, 2010, **213**, 1731–1739.
- 13 S. Yoshioka, T. Nakano, Y. Nozue and S. Kinoshita, *J. R. Soc., Interface*, 2008, **5**, 457–464.
- 14 K. A. Efetov and G. M. Tarmann, *Forester Moths: The genera Theresimima Strand, 1917, Rhagades Wallengren, 1863, Jordanita Verity, 1946, and Adscita Retzius, 1783 (Lepidoptera: Zygaenidae, Procridinae)*, Apollo Books, 1999.
- 15 C. M. Naumann, G. M. Tarmann and W. G. Tremewan, *The Western Palaearctic Zygaenidae (Lepidoptera)*, Apollo Books, 1999.
- 16 N. N. Shi, C. C. Tsai, F. Camino, G. D. Bernard, N. Yu and R. Wehner, *Science*, 2015, **349**, 298–301.
- 17 H. L. Leertouwer, B. D. Wilts and D. G. Stavenga, *Opt. Express*, 2011, **19**, 24061.
- 18 E. Yablonovitch and G. D. Cody, *IEEE Trans. Electron Devices*, 1982, **29**, 300–305.
- 19 D. Pantelić, S. Savić-Šević, D. V. Stojanović, S. Curčić, A. J. Krmpot, M. Rabasović, D. Pavlović, V. Lazović and V. Milošević, *Phys. Rev. E*, 2017, **95**, 032405.
- 20 J. L. Kelley, N. J. Tatarnic, G. E. Schröder-Turk, J. A. Endler and B. D. Wilts, *Curr. Biol.*, 2019, **29**, 2919–2925.
- 21 Z. Bálint, K. Kertész, G. Piszter, Z. Vértesy and L. P. Biró, *J. R. Soc., Interface*, 2012, **9**, 1745–1756.
- 22 L. P. Biró and J. P. Vigneron, *Laser Photonics Rev.*, 2011, **5**, 27–51.
- 23 C. Buschmann and E. Nagel, *Int. J. Remote Sens.*, 1993, **14**, 711–722.
- 24 C. Buschmann, S. Lenk and H. K. Lichtenthaler, *Isr. J. Plant Sci.*, 2012, **60**, 49–64.
- 25 F. Liu, H. Yin, B. Dong, Y. Qing, L. Zhao, S. Meyer, X. Liu, J. Zi and B. Chen, *Phys. Rev. E: Stat., Nonlinear, Soft Matter Phys.*, 2008, **77**, 1–4.
- 26 A. R. Parker, D. R. McKenzie and M. C. J. Large, *J. Exp. Biol.*, 1998, **201**, 1307–1313.
- 27 D. G. Stavenga, Surface Colors of Insects: Wings and Eyes, in *Functional Surfaces in Biology. Little Structures with Big Effects*, ed. S. N. Gorb, Springer, The Netherlands, 2009, vol. 1, 285–306.
- 28 P. Vukusic, J. R. Sambles, C. R. Lawrence and R. J. Wootton, *Proc. R. Soc. B*, 1999, **266**, 1403–1411.
- 29 O. Niehuis, S. H. Yen, C. M. Naumann and B. Misof, *Mol. Phylogenet. Evol.*, 2006, **39**, 812–829.
- 30 C. Wiklund and B. Sillen-Tullberg, *Evolution*, 1985, **39**, 1155.
- 31 K. L. Prudic, A. K. Skemp and D. R. Papaj, *Behav. Chem. Ecol.*, 2007, **18**, 41–46.
- 32 N. P. Kristensen, *Handbook of Zoology, Vol. IV, Part 3.: Lepidoptera: Moths and Butterflies. Morphology, Physiology, and Development*, Walter DeGruyter Press, Berlin, 2004.



## Size–strain line-broadening analysis of anatase/brookite (TiO<sub>2</sub>)-based nanocomposites with carbon (C): XRPD and Raman spectroscopic analysis

**Aleksandar Kremenović, Mirjana Grujić-Brojčin, Nataša Tomić, Vladimir Lazović, Danica Bajuk-Bogdanović, Jugoslav Krstić and Maja Šćepanović**

*Acta Cryst.* (2022). **B78**, 214–222



**IUCr Journals**

CRYSTALLOGRAPHY JOURNALS ONLINE

Author(s) of this article may load this reprint on their own web site or institutional repository provided that this cover page is retained. Republication of this article or its storage in electronic databases other than as specified above is not permitted without prior permission in writing from the IUCr.

For further information see <https://journals.iucr.org/services/authorrights.html>





# Size–strain line-broadening analysis of anatase/brookite (TiO<sub>2</sub>)-based nanocomposites with carbon (C): XRPD and Raman spectroscopic analysis

Aleksandar Kremenović,<sup>a\*</sup> Mirjana Grujić-Brojčin,<sup>b</sup> Nataša Tomić,<sup>b</sup> Vladimir Lazović,<sup>c</sup> Danica Bajuk-Bogdanović,<sup>d</sup> Jugoslav Krstić<sup>e</sup> and Maja Šćepanović<sup>b</sup>

Received 4 August 2021

Accepted 15 February 2022

Edited by R. Černý, University of Geneva, Switzerland

**Keywords:** anatase; brookite; TiO<sub>2</sub>; size-strain line broadening; XRPD; Raman spectra; phonon confinement model.

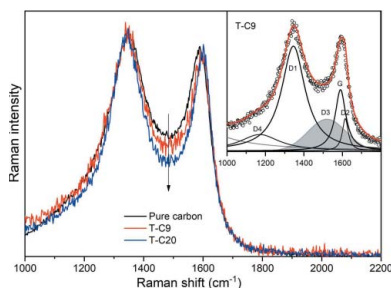
**Supporting information:** this article has supporting information at journals.iucr.org/b

<sup>a</sup>Faculty of Mining and Geology, University of Belgrade, Đušina 7, Belgrade 11000, Serbia, <sup>b</sup>Center for Solid State Physics and New Materials, Institute of Physics, University of Belgrade, Pregrevice 118, Belgrade 11000, Serbia, <sup>c</sup>Photonics Center, Institute of Physics, University of Belgrade, Pregrevice 118, Belgrade 11000, Serbia, <sup>d</sup>Faculty of Physical Chemistry, University of Belgrade, Studentski Trg 12-16, Belgrade 11000, Serbia, and <sup>e</sup>Department of Catalysis and Chemical Engineering, Institute of Chemistry, Technology and Metallurgy, University of Belgrade, Njegoševa 12, Belgrade 11000, Serbia. \*Correspondence e-mail: akremenovic@rgf.bg.ac.rs

A size–strain line-broadening analysis of the XRPD patterns and Raman spectra for two anatase/brookite (TiO<sub>2</sub>)-based nanocomposites with carbon (C) was carried out and the results compared with those of a similar sample free of carbon. The crystal structures and microstructures of anatase and brookite, as well as their relative abundance ratio, have been refined from XRPD data by the Rietveld method (the low amount of carbon is neglected). The XRPD size–strain analysis resulted in reliable structure and microstructure results for both anatase and brookite. The experimental Raman spectra of all the samples in the region 100–200 cm<sup>-1</sup> are dominated by a strong feature primarily composed of the most intense modes of anatase (*E<sub>g</sub>*) and brookite (*A<sub>1g</sub>*). The anatase crystallite sizes of 14–17 nm, estimated by XRPD, suggest the application of the phonon confinement model (PCM) for the analysis of the anatase *E<sub>g</sub>* mode, whereas the relatively large brookite crystallite size (27–29 nm) does not imply the use of the PCM for the brookite *A<sub>1g</sub>* mode. Superposition of the anatase *E<sub>g</sub>* mode profile, calculated by the PCM, and the Lorentzian shape of the brookite *A<sub>1g</sub>* mode provide an appropriate simulation of the change in the dominant Raman feature in the spectra of TiO<sub>2</sub>-based nanocomposites with carbon. Raman spectra measured in the high-frequency range (1000–2000 cm<sup>-1</sup>) provide information on carbon in the investigated nanocomposite materials. The results from field-emission scanning electron microscope (SEM), thermogravimetric analysis (TGA), Fourier transform infrared (FTIR) spectroscopy and nitrogen physisorption measurements support the XRPD and Raman results.

## 1. Introduction

Titanium dioxide (TiO<sub>2</sub>) is the most commonly used photocatalyst because of its high efficiency, nontoxicity, chemical and biological stability, and low cost. Among the three natural crystalline modifications (anatase, rutile and brookite) of TiO<sub>2</sub>, anatase and rutile are the most common and have been extensively investigated due to their excellent photoactivity. However, little has been reported for the brookite modification. Investigation of the properties and applications was limited due to the difficulty in producing pure brookite (Di Paola *et al.*, 2008, 2013; Xie *et al.*, 2009; Iliev *et al.*, 2013; Lee *et al.*, 2006; Bhavé & Lee, 2007; Lee & Yang, 2006). It was also reported that hydrothermal synthesis is necessary to obtain brookite as a major phase (Bhavé & Lee, 2007). The control of pH is very important, as high basicity is required for the



formation of brookite (Yanqing *et al.*, 2000; Zheng *et al.*, 2000; Okano *et al.*, 2009). Also, the control of the synthesis parameters, such as the hydrothermal temperature and reaction time, is of great importance (Nguyen-Phan *et al.*, 2011; Lin *et al.*, 2012; Tomić *et al.*, 2015).

Modifications of metal oxide nanoparticles with carbonaceous materials have attracted much attention over the past decade. Carbon materials, such as graphene, carbon nanotubes and carbon black, having unique structures, morphology, good conductivity and large surface area appear to be good candidates to be involved in the synthesis procedure with nanomaterials (Zhang, Lv *et al.*, 2010; Zhong *et al.*, 2010; Xie *et al.*, 2010; Cong *et al.*, 2015). This kind of composite is showing improvement in different application areas, such as water splitting for hydrogen generation and the degradation of various pollutants in wastewater, as well as air purification (Fan *et al.*, 2011; Sun *et al.*, 2014; Zhang, Tang *et al.*, 2010; Xie *et al.*, 2010). In this regard, it is beneficial to design composites that can provide higher adsorptivity, extended light absorption and good charge separation and transportation (Zhang, Lv *et al.*, 2010). Among the mentioned materials, carbon is easily affordable due to its low cost (Cong *et al.*, 2015).

This article is devoted to an investigation of the features and distinctions of XRPD and Raman scattering in the microstructure characterization of nanomaterials. XRPD and Raman spectroscopy results have been analysed and compared for pure TiO<sub>2</sub> and TiO<sub>2</sub> nanocomposites with carbon. The results of scanning electron microscopy (SEM), thermogravimetric analysis (TGA), Fourier transform infrared (FTIR) spectroscopy and nitrogen physisorption measurements support the XRPD and Raman results, and provide additional insight into the microstructure of the samples and their carbon content.

## 2. Materials synthesis

TiO<sub>2</sub> nanoparticles based on the brookite phase were synthesized using the sol-gel hydrothermal method. In a typical procedure, an appropriate amount of TiCl<sub>4</sub> (99.9% pure, Acros Organic) was dissolved in distilled water (150 ml) in an ice bath. In order to obtain the hydrogel, an aqueous solution of NaOH was added after careful control of the pH of the solution (pH ~ 9). After aging in the mother liquor for 5 h, the hydrogel was placed in a steel pressure vessel (autoclave, V = 50 ml) at a controlled temperature. After treatment at 200°C for 24 h, filtration and washing (rinsing) with distilled water until complete removal of chloride ions were carried out. The last step was drying at 105.5°C for 72 h. For the purposes of preparing the composites of TiO<sub>2</sub> with carbon, a different amount of carbon black was added together with the hydrogel to an autoclave. As well as the pure TiO<sub>2</sub> sample (T-AB), samples with 9 and 20 wt% carbon black in the nanocomposite were prepared and are denoted T-C9 and T-C20, respectively. The carbon black content in these nanocomposites was estimated using thermogravimetric analysis (TGA) (see §1 of the supporting information).

## 3. Experimental methods

X-ray powder diffraction (XRPD) measurements were carried out on a Philips PW1710 diffractometer employing Cu K $\alpha_{1,2}$  radiation. Data were collected every 0.06° in the 10–110° 2 $\theta$  angular range in step scan mode using a counting time of 12.5 s per step. The instrumental resolution function was obtained by parameterizing the profiles of the diffraction pattern of an LaB<sub>6</sub> (NIST SRM660a) standard specimen. Details of the XRPD line-broadening analysis are presented in §S2.1 of the supporting information.

Raman scattering measurements were performed using the TriVista TR557 triple spectrometer system equipped with a nitrogen-cooled CCD detector. The samples were excited in backscattering micro-Raman configuration by a Coherent Verdi G optically pumped semiconductor laser operating at 532 ± 2 nm with a minimal output laser power of about 20 mW. The Raman scattering measurements of nanopowders pressed into pellets were performed in the air, at room temperature, using an objective lens with 50× magnification and a 0.75 numerical aperture to focus the laser to a spot size of around 2 µm. To avoid local heating of the sample surface due to laser irradiation, neutral density filters transmitting 10 or 1% of the incident light were used to additionally reduce the laser power at the entrance of the optical system of the Raman spectrometer to less than 1 mW. To reveal the local heating effects on the Raman spectra of the investigated samples with a high carbon content, the output laser power was varied from 20 to 400 mW. In order to record the spectra with relatively high resolution in a lower frequency range, a 1800/1800/2400 grooves/mm diffraction grating combination was used in the TriVista system, whereas for the measurements in a wide wavenumber range with lower resolution, a 300/300/500 grooves/mm grating combination was used. In order to analyze the experimental results, the Raman spectra are fitted by the sum of the Lorentzian profiles and the profile obtained by Phonon Confinement Method (PCM) (see §S3.1 in the supporting information).

The morphologies of the synthesized nanopowders were studied on a Tescan MIRA3 field emission gun scanning electron microscope (FESEM) at 20 kV in a high vacuum. Powdered samples were sonicated in ethanol for 10 min, then a drop of the solution was applied to 'kish' graphite (crystals of natural graphite) and the sample was degassed in a low vacuum for an hour.

The loading percentage of C in TiO<sub>2</sub> was checked by TGA in air by scanning the temperature from 30 to 700°C at a rate of 10°C min<sup>-1</sup> on an SDT 2960 TA instrument.

The IR transmission spectra of T-AB, T-C9 and T-C20 pellets before and after the introduction of carbon black were measured on a Thermo Nicolet 6700 FTIR spectrophotometer at room temperature in the range from 4000 to 400 cm<sup>-1</sup>.

The textural properties of the nanocomposites were analyzed by nitrogen physisorption at -196°C using a Sorptomatic 1990 Thermo Finnigan device. Prior to adsorption, the samples were outgassed for 1 h in a vacuum at room temperature and, additionally, at 110°C and the same residual

pressure for 16 h. The specific surface areas ( $S_{\text{BET}}$ ) of the samples were calculated from the linear part of the adsorption isotherm by applying the Brunauer–Emmet–Teller (BET) equation (Brunauer *et al.*, 1938).

#### 4. Results and discussion

Results concerning composite materials of similar composition,  $\text{TiO}_2\text{:Fe}$ , are reported in Kremenović *et al.* (2011, 2013). In relation to the  $\text{TiO}_2\text{:C}$  composite materials presented in this article, the amount of Fe in  $\text{TiO}_2\text{:Fe}$  was significantly lower than the amount of C in  $\text{TiO}_2\text{:C}$ . Heterogeneity (phase and spatial), disorder, morphology and crystal structure were investigated for  $\text{TiO}_2\text{:Fe}$ . Only phase heterogeneity and not spatial heterogeneity is shown in  $\text{TiO}_2\text{:C}$ . The presence of three polymorphic modifications of  $\text{TiO}_2$  (rutile, anatase and brookite), as well as amorphous  $\text{TiO}_2$ , was confirmed in  $\text{TiO}_2\text{:Fe}$ . The presence of Fe in  $\text{TiO}_2\text{:Fe}$  composites was confirmed only by SQUID magnetic measurements, but was not located in  $\text{TiO}_2$  (rutile, anatase, brookite or amorphous) by XRPD (WPPF and PDF fit), high-resolution transmission electron microscopy (HRTEM) or Raman spectroscopy. SQUID magnetic measurements defined only the type of Fe distribution in the composite material. In the composite materials  $\text{TiO}_2\text{:C}$ , the presence of only two polymorphic modifications of  $\text{TiO}_2$  (brookite and anatase) was confirmed, as well as amorphous C, but not amorphous  $\text{TiO}_2$ . The effect of Fe on the heterogeneity and disorder of  $\text{TiO}_2\text{:Fe}$  composites has not been studied, but the effect of C on  $\text{TiO}_2\text{:C}$  composites has been investigated. The aim of the study of  $\text{TiO}_2\text{:C}$  composite materials presented in this article is focused primarily on comparing the results of diffraction line/vibration mode broadening analysis using XRPD and Raman spectroscopic techniques. Also, during the investigation of  $\text{TiO}_2\text{:Fe}$  composite materials, the XRPD and Raman results were analyzed routinely. The XRPD and Raman results for  $\text{TiO}_2\text{:C}$  composite materials presented here have been analyzed and compared in much more detail. Such an analysis is necessary to determine the agreement/mutual support of the XRPD and Raman results. In this way, these two methods show a common/synergistic series of effects, which the individual methods alone cannot completely resolve.

##### 4.1. XRPD

The XRPD patterns of the investigated samples are presented in Fig. S2 (see §S2.2 of the supporting information). In all three samples, the most intense diffraction peaks in the XRPD patterns can be ascribed to the two polymorph phases of  $\text{TiO}_2$  brookite (PDF card 29-1360) and anatase (PDF card 78-2486). For the carbon-containing samples (T-C9 and T-C20), low-intensity diffraction peaks that correspond to carbon, *i.e.* the graphite 2H pattern (PDF card 89-7213), could be hardly distinguished due to extensive peak overlap with peaks from the brookite and anatase patterns. However, the 101 reflection at  $\sim 44.5^\circ 2\theta$  that corresponds to the graphite 2H pattern could be recognized if the  $y$  axis is represented as a

**Table 1**

Refined unit-cell, structure and microstructural parameters (average apparent crystallite size and average maximal strain), quantitative phase analysis results, *i.e.* contents of anatase and brookite, as well as reliability factors of the refinements for T-AB, T-C9 and T-C20.

Sample	T-AB	T-C9	T-C20
Brookite (space group $Pbca$ , No. 61)			
$a$ (°)	9.1747 (2)	9.1850 (3)	9.1837 (2)
$b$ (°)	5.4518 (1)	5.4579 (2)	5.4568 (1)
$c$ (°)	5.1428 (1)	5.1488 (1)	5.1472 (1)
$\alpha=\beta=\gamma$ (°)	90	90	90
$V$ (Å <sup>3</sup> )	257.24 (1)	258.11 (1)	257.94 (1)
$\langle\text{Ti—O}\rangle$ (Å)	1.963 (5)	1.967 (6)	1.965 (5)
Average appar. size (nm)	29 (3)	27 (6)	29 (4)
Average max. strain $\times 10^{-4}$	11 (1)	7(2)	9(1)
%	74 (1)	83 (1)	77 (1)
$R_{\text{B}}$ (%)	1.95	2.71	2.27
Anatase (space group $I4_1/amd$ , No. 141)			
$a$ (°)	3.7898 (2)	3.7939 (3)	3.7930 (2)
$c$ (°)	9.4954 (6)	9.508 (1)	9.5089 (7)
$\alpha=\beta=\gamma$ (°)	90	90	90
$V$ (Å <sup>3</sup> )	136.38 (1)	136.86 (2)	136.81 (1)
$\langle\text{Ti—O}\rangle$ (Å)	1.955 (2)	1.962 (4)	1.957 (3)
Average appar. size (nm)	17 (2)	14 (5)	15 (7)
Average max. strain $\times 10^{-4}$	27 (3)	17 (6)	11 (5)
%	26 (1)	17 (1)	23 (1)
$R_{\text{B}}$ (%)	1.79	3.10	1.74
Reliability factors of the refinements			
$R_{\text{wp}}$ (%)	6.51	8.41	6.96
$R_{\text{p}}$ (%)	4.71	6.52	5.36
$R_{\text{exp}}$ (%)	4.70	4.63	4.41
$\chi^2$	1.97	3.38	2.55

logarithm of diffraction intensity (insets of Fig. S2 in §S2.2 of the supporting information). The XRPD patterns indicate the microcrystalline to amorphous character of carbon black (see Fig. S3 in §S2.3 of the supporting information). The above-mentioned 101 reflection that corresponds to the graphite 2H pattern indicates a slight change of the carbon black crystalline structure during synthesis.

Structure models for the Rietveld (1969) refinements are taken from Meagher & Lager (1979) for brookite and from Horn *et al.* (1972) for anatase. Some of the results from the Rietveld refinements are presented in Table 1 and Fig. 1. Refined values of the atomic coordinates and the corresponding interatomic distances and angles are in good agreement with the literature data. For all three samples, the refined values of the interatomic Ti—O distances for brookite and anatase are in excellent agreement with the values obtained by Meagher & Lager (1979) and Horn *et al.* (1972) (Table 1). The same is true for the refined unit-cell parameters when compared to the values obtained by Meagher & Lager (1979) for brookite and Horn *et al.* (1972) for anatase. This is clear evidence that C atoms did not enter in significant amounts into the brookite and anatase crystal structures.

The contents of the brookite phase in the samples T-AB, T-C9 and T-C20 are 74 (1), 83 (1) and 77 (1)%, respectively (values in parentheses represent estimated standard deviations). A somewhat higher brookite content in the  $\text{TiO}_2$ -based nanocomposite samples (T-C9 and T-C20) in comparison to pure  $\text{TiO}_2$  (T-AB) indicates that the presence of carbon may

have an influence on the brookite/anatase phase ratio. The quantity of crystalline carbon could not be refined due to its low abundance (probably less than 2%) and large diffraction peak overlap.

The refined average apparent crystallite size and average maximal strain in brookite are similar for all samples, indicating that the average crystallite size radius is about 30 nm and the average maximal strain is about  $1 \times 10^{-3}$  (Table 1).

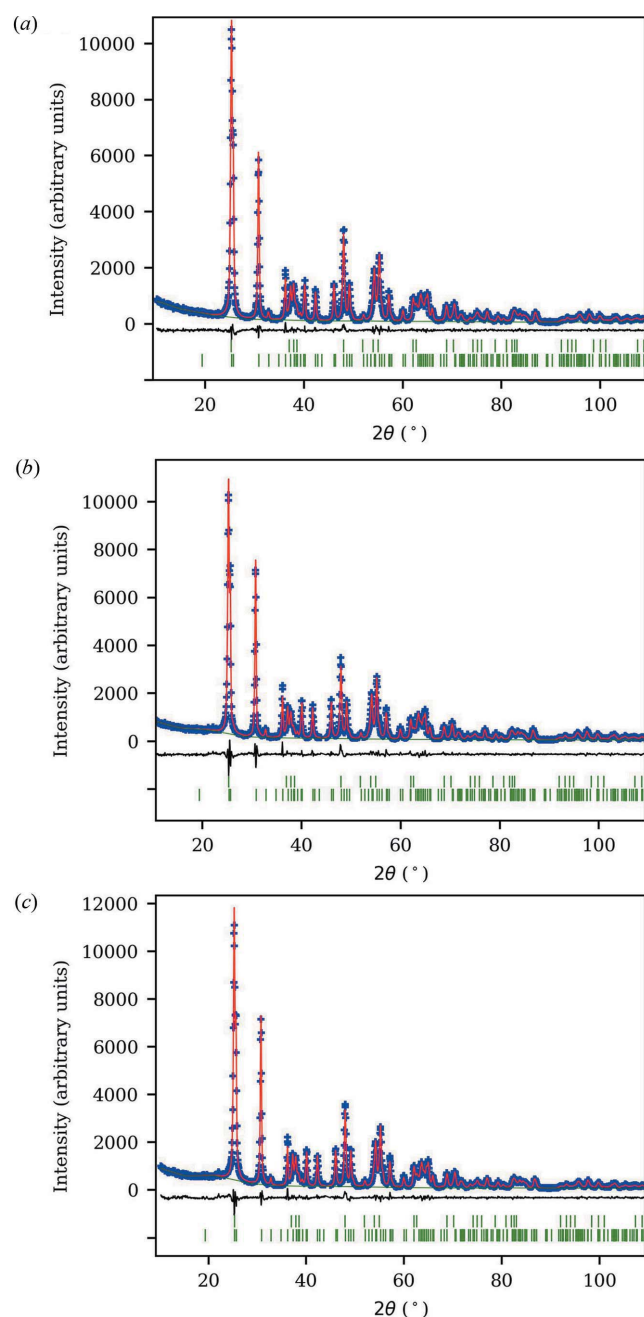


**Figure 1**

Final Rietveld plots for (a) T-AB, (b) T-C9 and (c) T-C20. Blue crosses denote observed step intensities and the red line represents the corresponding calculated values. The difference curve between the observed and calculated values is given at the bottom (black line). Vertical green bars represent diffraction line positions; the upper bars correspond to brookite and the lower bars to anatase.

The refined average apparent crystallite size and average maximal strain in anatase are similar for all samples, with the exception of the strain in T-AB ( $27 \times 10^{-4}$ ), indicating that the average crystallite size radius is about 15 nm and the average strain is about  $15 \times 10^{-4}$  (Table 1).

#### 4.2. Raman scattering

The Raman spectra of all the synthesized samples are dominated by the features of anatase and brookite (shown and assigned in §S3.2 of the supporting information). The spectra taken in the region from 100 to  $230 \text{ cm}^{-1}$ , usually used as a reliable titania fingerprint (Tomić *et al.*, 2015), are shown in Fig. 2. Characteristic Raman modes at  $\sim 126 [A_{1g}(B)]$ , 130  $[B_{1g}(B)]$ , 143  $[E_g(A)]$ , 153  $[A_{1g}(B)]$ , 160  $[B_{1g}(B)]$ , 172  $[B_{1g}(B)]$ , 197  $[E_g(A) + A_{1g}(B)]$  and  $212 \text{ cm}^{-1} [A_{1g}(B)]$  are assigned to the anatase (A) and brookite (B) phases (Iliev *et al.*, 2013; Ohsaka *et al.*, 1978; Tomić *et al.*, 2015; Šćepanović *et al.*, 2007), as denoted in Fig. 2. Since the average crystallite sizes in anatase are estimated by XRPD to be from  $\sim 14$  to  $\sim 17$  nm (Table 1), it is expected that phonon confinement and other effects relevant for nanomaterials may have an impact on the most intense anatase  $E_g$  mode (Šćepanović *et al.*, 2007;

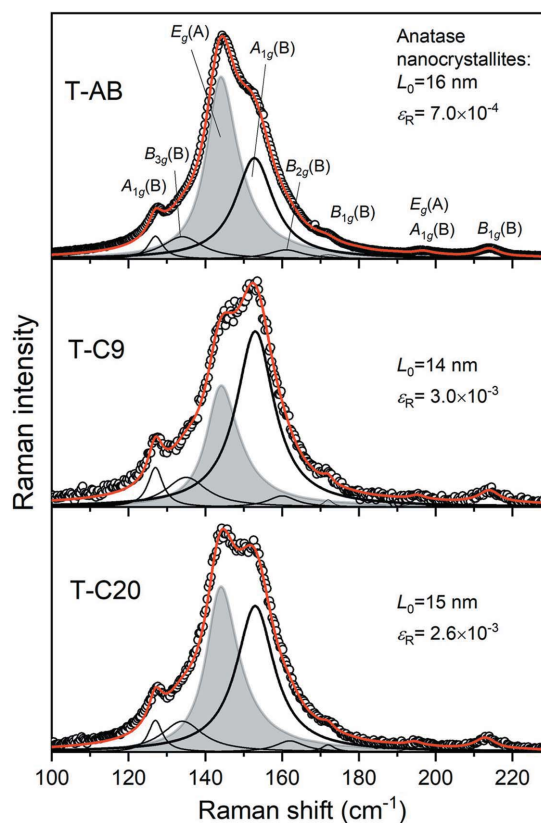


**Figure 2**

Experimental Raman spectra of T-AB, T-C9 and T-C20 in the titania fingerprint region ( $100\text{--}230 \text{ cm}^{-1}$ ), with the modes assigned, together with the corresponding calculated results, given as the sum of the most intense anatase mode,  $E_g(A)$ , obtained by the PCM, other anatase (A) and all brookite (B) modes fitted by the Lorentzians. The values of the reduced chi-squared ( $\chi^2$ ) and adjusted  $R$ -squared ( $R^2$ ) parameters: T-AB ( $\chi^2 = 1.98 \times 10^{-5}$ ,  $R^2 = 0.9964$ ), T-C9 ( $\chi^2 = 4.55 \times 10^{-4}$ ,  $R^2 = 0.9928$ ) and T-C20 ( $\chi^2 = 1.24 \times 10^{-4}$ ,  $R^2 = 0.9982$ ).

Kremenović *et al.*, 2013). On the other hand, for the crystallite size of brookite, estimated to be close to 29 nm (Table 1), the effect of phonon confinement (shift and broadening of the Raman mode) on the  $A_{1g}$  mode is not expected, as can be seen in previous work related to mixed-phase titania (Kremenović *et al.*, 2013; Tomić *et al.*, 2015). Therefore, all the modes shown in Fig. 2 are fitted by the Lorentzian profiles, except the most intense anatase  $E_g$  mode, which is simulated by the PCM (defined in §S3.1 of the supporting information).

The phonon confinement due to the nanosize effect causes asymmetrical broadening and a shift of the most intense anatase  $E_g$  mode to higher frequencies (blue-shift) in comparison to the corresponding bulk values. The influence of strain on the mode position is simulated in the PCM by Equations S11 and S12 (see §S3.1 in the supporting information), proposed by Gouadec & Colombari (2007) and Kibasomba *et al.* (2018). The values of the average correlation length  $L_0$  and the so-called Raman strain ( $\epsilon_R$ ) in anatase, both obtained as fitting parameters in the numerical adjustment of the spectrum calculated by PCM to the experimental spectrum, are shown in Fig. 2. A good agreement between the

simulated and experimental  $E_g$  mode, with a similar Raman shift ( $\sim 144\text{ cm}^{-1}$ ) and broadening ( $\sim 10\text{--}11\text{ cm}^{-1}$ ) in all the investigated samples, could be obtained by using a parameter choice reflecting the compensation of the blue-shift due to a decrease of nanocrystallite size and the red-shift due to tensile Raman strain (see §S3.1 in the supporting information). Namely, the effects of tensile strain partially compensate for the effect of phonon confinement in such a way as to produce similar Raman positions in the spectra of all the samples in spite of their different correlation lengths.

The brookite modes are simulated by Lorentzian profile, with the position  $\sim 153\text{ cm}^{-1}$  and linewidth  $\sim 12\text{ cm}^{-1}$  of the most intense brookite  $A_{1g}$  mode similar for all the samples, which relies on the similar crystalline structure of brookite (Table 1). Therefore, the proposed fitting procedure is appropriate for an analysis of the changes in the position and shape of the dominant Raman features with C content in  $\text{TiO}_2$ -based nanocomposites.

The strong impact of different laser powers (1–400 mW) during the Raman measurements on the spectra of  $\text{TiO}_2$ -based nanocomposites with carbon has been noticed and analyzed for sample T-C20. The Raman feature shown in Fig. 3(a) is blue-shifted and becomes more symmetric with increasing laser power. The decomposition of the spectra with a procedure similar to that described above shows that the anatase  $E_g$  mode is blue-shifted (from 144.0 to 148.8  $\text{cm}^{-1}$ ) and broadened (from 10.5 to 18  $\text{cm}^{-1}$ ) with increasing laser power, whereas the brookite  $A_{1g}$  mode is less influenced; it is slightly red-shifted (by less than 1  $\text{cm}^{-1}$ ) and less broadened (by 12 to 16.5  $\text{cm}^{-1}$ ) in comparison to the anatase  $E_g$  mode [Fig. 3(b)]. This is in accordance with literature data (Šćepanović *et al.*, 2007, 2019; Du *et al.*, 2006) and indicates the increase of the local temperature at the sample surface up to 277°C at maximal laser power (400 mW) (Du *et al.*, 2006). This analysis also reveals that the Raman spectrum of the  $\text{TiO}_2$  nanopowder

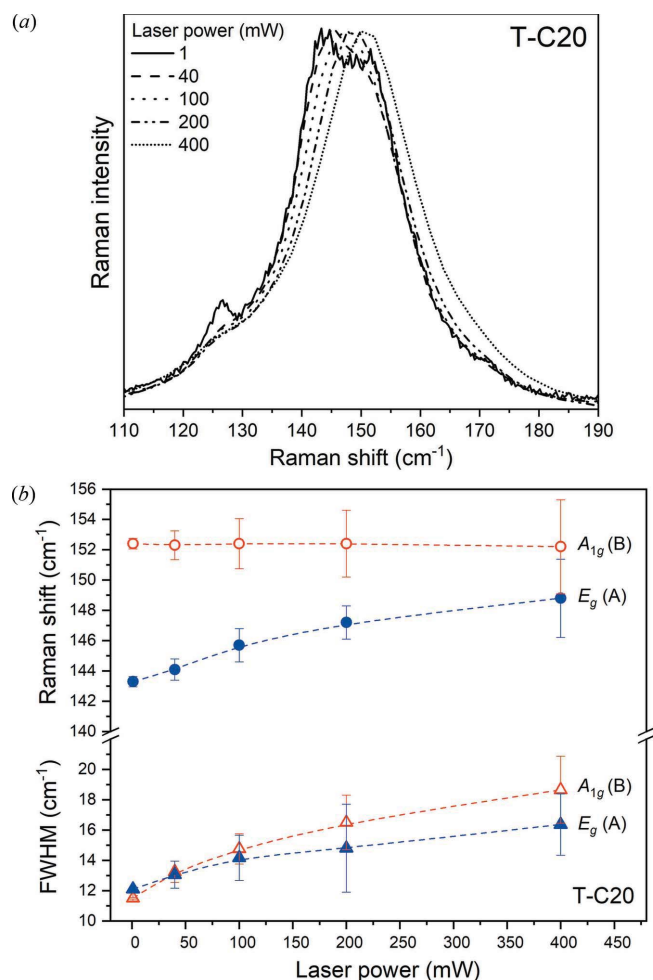


**Figure 3**  
(a) Normalized Raman spectra of the  $\text{TiO}_2$ -based nanocomposite with 20% C (T-C20) taken at different laser powers in the range 1–400 mW. (b) The dependence of the Raman shift and the FWHM of the most intense anatase  $E_g$  (A) and brookite  $A_{1g}$  (B) modes on laser power.

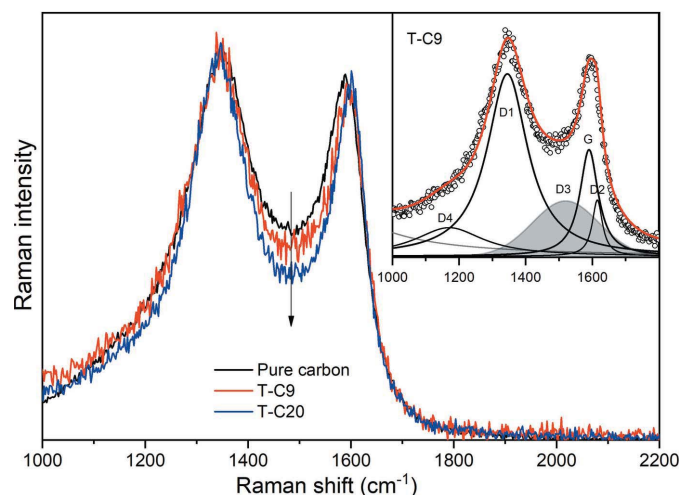


**Figure 4**  
The Raman spectra of pure carbon and  $\text{TiO}_2$ -based nanocomposites T-C9 and T-C20, taken in the fingerprint carbon region and normalized to the G mode. Inset: the Raman spectra of nanocomposite sample T-C9, fitted by the sum of the corresponding Lorentzian and Gaussian profiles.

Table 2

The frequencies of the first-order Raman modes of carbon, together with relevant mode intensity ratios and the statistics of fit.

The intensities are denoted as: *vs* = very strong, *s* = strong, *m* = medium and *w* = weak. FWHM is full width at half maximum.

Band	Vibrational mode (Sadezky <i>et al.</i> , 2005)	Pure C		T-C9		T-C20	
		Raman shift (cm <sup>-1</sup> )	FWHM (cm <sup>-1</sup> )	Raman shift (cm <sup>-1</sup> )	FWHM (cm <sup>-1</sup> )	Raman shift (cm <sup>-1</sup> )	FWHM (cm <sup>-1</sup> )
G	<i>E</i> <sub>2g</sub> Graphitic structure ( <i>s</i> )	1582	68	1590	67	1596	60
D1	<i>A</i> <sub>1g</sub> Disordered graphitic lattice ( <i>vs</i> )	1343	193	1345	148	1345	140
D2	<i>E</i> <sub>2g</sub> Disordered graphitic lattice ( <i>s</i> )	1610	39	1615	37	1615	37
D3	Amorphous carbon (Gaussian shape) ( <i>m</i> )	1513	220	1520	200	1530	160
D4	<i>A</i> <sub>1g</sub> Disordered graphitic lattice ( <i>w</i> )	1177	318	1170	255	1170	300
Mode intensity ratio							
<i>I</i> (D1)/ <i>I</i> (G)		2.3		3.6		3.9	
<i>I</i> (D3)/ <i>I</i> (G)		1.8		1.2		0.8	
Goodness-of-fit							
Reduced $\chi^2$		$3.40 \times 10^{-4}$		$8.82 \times 10^{-4}$		$4.91 \times 10^{-4}$	
Adjusted <i>R</i> <sup>2</sup>		0.9958		0.9906		0.9943	

composed of anatase and brookite phases, in the spectral range presented in Fig. 3(a), is mostly influenced by the behaviour of the anatase *E*<sub>g</sub> mode.

Besides the TiO<sub>2</sub> modes discussed above, in the Raman spectra of the TiO<sub>2</sub>-based nanocomposites (T-C9 and T-C20), features related to carbon are detected. In Fig. 4, the variations of the Raman spectra of pure carbon black and TiO<sub>2</sub>-based nanocomposite samples are shown in the carbon fingerprint range (1000–2200 cm<sup>-1</sup>). It can be seen that the central part of the normalized spectrum (around 1500 cm<sup>-1</sup>) decreases from the pure carbon sample to T-C20. To relate the observed variations in the spectra to variations of the carbon structure due to hydrothermal synthesis conditions, the spectra have been fitted by the sum of the Lorentzians (denoted D1, D2 and G) and Gaussian (D3), according to the methodology optimized by Sadezky *et al.* (2005) and Pawlyta *et al.* (2015). The decomposed spectrum of T-C9 is given in the inset as an example, and the results are summarized in Table 2.

The D1 band, ascribed to the disordered graphitic lattice (Sadezky *et al.*, 2005), is located at a similar position in pure carbon and the TiO<sub>2</sub> nanocomposites. However, the G band, related to the graphitic structure (Sadezky *et al.*, 2005), is shifted in T-C9 and T-C20 towards higher frequencies in comparison to pure carbon. Such a shift, together with the narrowing of the D1 and G bands (see Table 2), indicates a decrease of the amorphous carbon content in the nanocomposite samples (Ferrari *et al.*, 2000; Pawlyta *et al.*, 2015). Also, the narrowing and shift to higher frequencies of the D3 band, related to amorphous carbon (Merlen *et al.*, 2017; Sadezky *et al.*, 2005; Pawlyta *et al.*, 2015), supports the conclusion that the content of amorphous carbon decreases when carbon is subjected to a hydrothermal procedure, which is more pronounced in the nanocomposites with a higher carbon content.

Note that bands D3 and D4 (related to the disordered graphite lattice) may also originate from hydrogenation (CH)

and oxidation (CO), respectively (Karlin *et al.*, 1997; Merlen *et al.*, 2017), but in the nanocomposite samples investigated here, we have not detected CH and CO vibrations in the relevant regions of the FTIR spectra (see §S5 in the supporting information).

The ratios of the integrated intensities of the different Raman bands in the first-order spectral region have been used to perform further analysis of carbon crystalline and amorphous phases (Sadezky *et al.*, 2005; Pawlyta *et al.*, 2015). The increase of the integrated intensity ratio *I*<sub>D1</sub>/*I*<sub>G</sub> and the decrease of *I*<sub>D3</sub>/*I*<sub>G</sub> (Table 2) both point to a slightly higher content of the crystalline carbon phase and a lower amount of the amorphous carbon phase in the nanocomposites (especially in sample T-C20) than in pure carbon.

Although the refined unit-cell parameters obtained from XRPD analysis have shown that C atoms did not enter in significant amounts into the brookite and anatase crystal structures, the results of both characterization methods imply that carbon could influence the formation of brookite and anatase phases in TiO<sub>2</sub>-based nanocomposites synthesized by the hydrothermal method. This is also supported by our wider research, where we have investigated the influence of carbon content in the range from 0.3 to 20% on the formation of titania phases by this synthesis method. The Raman results, presented in §S3.2 in the supporting information, show that the addition of a small amount of carbon suppresses the formation of brookite, so that the synthesized sample with a low carbon content is dominated by the anatase phase. An increase in the carbon content is followed by the formation of brookite in preference to the anatase phase. However, it seems that this transformation may be partially suppressed at a higher percent of carbon (as in sample T-C20), which may be a consequence of a different manner of formation of the composite with the highest carbon content (for an analysis of nitrogen physisorption, see §S7 of the supporting information). Recent research shows that the influence of carbon

content on the brookite-to-anatase ratio in  $\text{TiO}_2$ -based nanomaterials depends on the carbon source, the type of synthesis and the starting  $\text{TiO}_2$  phase (Li *et al.*, 2013; Cano-Casanova *et al.*, 2021), but this subject still needs further study.

#### 4.3. XRPD versus Raman scattering

Both XRPD and Raman scattering analyses have shown that  $\text{TiO}_2$  consists of a combination of anatase and brookite phases in all samples investigated in this work. This is also supported by the SEM measurements (see §S6 in the supporting information), revealing two different types of particles: spherical, ascribed to anatase, and spindle-like, characteristic for brookite (Tomić *et al.*, 2015). The spindle-like particles of brookite in sample T-AB are elongated by up to  $\sim 200$  nm, with the shorter dimension estimated at less than 40 nm. By comparing size values for brookite obtained from XRPD (Table 1) and SEM measurements, one can conclude that on average one particle is composed from 6–7 crystallites.

It is known that the Raman modes in nanocrystalline oxide materials are very sensitive to disorder, caused by nonstoichiometry due to the nanometric crystallite size or thermal effects. In that sense, the correlation length is introduced in the PCM to define the mean size of the homogeneous regions in a material (Kosacki *et al.*, 2002). The correlation length may be influenced by many factors, such as the level of disorder due to the presence of point defects, dislocations and voids, as well as a disturbance in the long-range order, due to doping or the creation of solid solutions, so the PCM analysis of the Raman spectra may provide important information about lattice disorder (Šćepanović *et al.*, 2010). Having in mind that in this work the correlation lengths of the anatase phase used in the PCM simulations match the anatase crystallite size estimated by XRPD, the crystallites are suggested to have little disorder.

The analysis of the Raman spectra, performed in §4.2, has shown that the most intense brookite Raman  $A_{1g}$  mode is not significantly shifted and broadened in comparison to the bulk values (Iliev *et al.*, 2013). This fact, together with the brookite crystallite size (according to XRPD) being too big for phonon confinement effects, excludes the PCM analysis in the case of the brookite phase.

Regarding the amorphous  $\text{TiO}_2$  phase, the Raman and XRPD analyses have given similar results. Namely, an analysis of the Raman spectra, decomposed by the combination of the PCM and Lorentzian profiles (§4.2), did not show the presence of modes which could be assigned to this phase (Kremenović *et al.*, 2013), either in pure  $\text{TiO}_2$  or in the nanocomposites.

Besides giving insight into the nanocrystalline structures of the anatase and brookite phases in pure  $\text{TiO}_2$  and nanocomposites, XRPD and Raman scattering may also provide information on their content ratio (see §S4 in the supporting information).

The carbon content, which contributes to the very dark colour of the sample (in comparison to the white of pure  $\text{TiO}_2$ ), has little influence on the XRPD measurements, but in the Raman scattering causes a significant increase in the

absorption of laser energy, which can induce local heating. This makes the nanocomposites with carbon extremely sensitive to laser power, which requires additional attention during the Raman measurements (careful choice of parameters and equipment). However, this allows an investigation of the behaviour of the Raman spectra of complex materials with local heating. The observed variation of the Raman spectra with increasing laser power (see Fig. 3) may even be used to estimate the level of heating and local temperature.

It appears that XRPD is not very useful for the investigation of carbon in the crystalline and especially amorphous state when it is present in small amounts. The intensities of the diffraction maxima depend on the number of electrons of the atoms that make up the crystal and XRPD barely detects carbon (carbon has only six electrons; we had to show the diffraction intensity on a logarithmic scale in order for the strongest carbon reflection to be visible) in samples T-C9 and T-C20. Note also that the results of XRPD analysis show that initial carbon is mostly amorphous (see §S2.3 of the supporting information). In contrast, the intensity of Raman scattering is proportional to the change in the polarizability of molecules; the atoms in carbon are tightly bound by strong covalent bonds and the Raman spectra show clearly defined carbon bands which do not overlap with the anatase and brookite modes. This allows a detailed analysis to be made of the variation of carbon structure due to hydrothermal synthesis by Raman scattering measurements (presented in Fig. 4 and Table 2). These results show that, during hydrothermal synthesis, the amorphous carbon phase is reduced in the nanocomposites in comparison to this phase in initial carbon. This is even more pronounced in sample T-C20, which may indicate that higher carbon content probably enhances the carbon crystallization during the hydrothermal process.

## 5. Conclusions

The compatibility, synergy and limits of XRPD and Raman scattering measurements have been established by investigating pure  $\text{TiO}_2$  nanopowder and two  $\text{TiO}_2$ -based nanocomposites with different amounts of carbon, fabricated by the sol-gel hydrothermal method. To assure proper correlation between the XRPD and Raman results, several analytical techniques (TGA, SEM, FTIR and nitrogen physisorption) have also been used. Both XRPD and Raman scattering, together with SEM results, have shown that, in all the samples, brookite is a major phase with good crystallinity. Matching anatase crystallite sizes were determined by XRPD and PCM analysis of the anatase Raman  $E_g$  mode, confirming the low disorder of this phase. Amorphous  $\text{TiO}_2$  has not been detected by either Raman scattering or XRPD. XRPD analysis could not detect whether significant amounts of carbon had been incorporated into the brookite and anatase crystal structures, whereas the Raman results revealed a decreasing content of amorphous carbon when subjected to the hydrothermal procedure, which is more pronounced in the nanocomposite with the higher carbon content. The brookite-to-anatase ratios estimated by the XRPD and Raman measurements imply that

carbon could influence the formation of the brookite phase in preference to the anatase phase in the TiO<sub>2</sub>-based nanocomposites synthesized by the hydrothermal method.

## 6. Related literature

The following references are cited in the supporting information: Barrett *et al.* (1951); Campbell & Fauchet (1986); Dubinin (1975); Gregg & Sing (1982); Grujić-Brojčdin *et al.* (2009); Hearne *et al.* (2004); Mikami *et al.* (2002); Richter *et al.*, 1981; Rodríguez-Carvajal (1993, 2001, 2016); Spanier *et al.* (2001); Stokes & Wilson (1944); Thompson *et al.* (1987); Wang *et al.* (2007).

## Acknowledgements

The authors acknowledge funding provided from the Faculty of Mining and Geology, Faculty of Physical Chemistry, University of Belgrade, Institute of Physics Belgrade, Institute of Chemistry, Technology and Metallurgy, and Ministry of Education, Science and Technological Development of the Republic of Serbia. The authors appreciate advice given by Ljiljana Karanović, Professor Emeritus since 2016, and Predrag Dabić, Faculty of Mining and Geology, University of Belgrade.

## Funding information

Funding for this research was provided by: Faculty of Mining and Geology, University of Belgrade, Serbia (contract No. 451-03-68/2022-14/200126).

## References

- Barrett, E. P., Joyner, L. G. & Halenda, P. P. (1951). *J. Am. Chem. Soc.* **73**, 373–380.
- Bhave, R. C. & Lee, B. I. (2007). *Mater. Sci. Eng. A*, **467**, 146–149.
- Brunauer, S., Emmett, P. H. & Teller, E. (1938). *J. Am. Chem. Soc.* **60**, 309–319.
- Campbell, I. H. & Fauchet, P. M. (1986). *Solid State Commun.* **58**, 739–741.
- Cano-Casanova, L., Amorós-Pérez, A., Ouzzine, M., Román-Martínez, M. C. & Lillo-Ródenas, M. A. (2021). *J. Environ. Chem. Eng.* **9**, 104941.
- Cong, Y., Li, X., Dong, Z., Yuan, G., Cui, Z. & Zhang, J. (2015). *Mater. Lett.* **138**, 200–203.
- Di Paola, A., Bellardita, M. & Palmisano, L. (2013). *Catalysts*, **3**, 36–73.
- Di Paola, A., Cufalo, G., Addamo, M., Bellardita, M., Campostri, R., Ischia, M., Ceccato, R. & Palmisano, L. (2008). *Colloids Surf. A Physicochem. Eng. Asp.* **317**, 366–376.
- Du, Y. L., Deng, Y. & Zhang, M. S. (2006). *J. Phys. Chem. Solids*, **67**, 2405–2408.
- Dubinin, M. M. (1975). *Prog. Surface Membrane Sci.* **9**, 1–70.
- Fan, W., Lai, Q., Zhang, Q. & Wang, Y. (2011). *J. Phys. Chem. C*, **115**, 10694–10701.
- Ferrari, A. C. & Robertson, J. (2000). *Phys. Rev. B*, **61**, 14095–14107.
- Gouadec, G. & Colomban, Ph. (2007). *Prog. Cryst. Growth Charact. Mater.* **53**, 1–56.
- Gregg, S. J. & Sing, S. J. (1982). *Adsorption, Surface Area and Porosity*. London: Academic Press.
- Grujić-Brojčdin, M., Šćepanović, M. J., Dohčević-Mitrović, Z. D. & Popović, Z. V. (2009). *Acta Phys. Pol.* **A116**, 51–54.
- Hearne, G. R., Zhao, J., Dawe, A. M., Pischedda, V., Maaza, M., Nieuwoudt, M. K., Kibasomba, P., Nemraoui, O., Comins, J. D. & Witcomb, M. J. (2004). *Phys. Rev. B*, **70**, 134102.
- Horn, M., Schweddtfefer, C. F. & Meagher, E. P. (1972). *Z. Kristallogr. Cryst. Mater.* **136**, 273–281.
- Iliev, M. N., Hadjiev, V. G. & Litvinchuk, A. P. (2013). *Vib. Spectrosc.* **64**, 148–152.
- Karlin, S. & Colomban, Ph. (1997). *J. Raman Spectrosc.* **28**, 219–228.
- Kibasomba, P. M., Dhlamini, S., Maaza, M., Liu, C.-P., Rashad, M. M., Rayan, D. A. & Mwakikunga, B. W. (2018). *Results Phys.* **9**, 628–635.
- Kosacki, I., Suzuki, T., Anderson, H. U. & Colomban, Ph. (2002). *Solid State Ionics*, **149**, 99–105.
- Kremenović, A., Antić, B., Blanuša, J., Čomor, M., Colomban, Ph., Mazerolles, L. & Bozin, E. S. (2011). *J. Phys. Chem. C*, **115**, 4395–4403.
- Kremenovic, A., Grujic Brojcin, M., Welsch, A.-M. & Colomban, P. (2013). *J. Appl. Cryst.* **46**, 1874–1876.
- Lee, B. I., Wang, X., Bhave, R. & Hu, M. (2006). *Mater. Lett.* **60**, 1179–1183.
- Lee, J. H. & Yang, Y. S. (2006). *J. Mater. Sci.* **41**, 557–559.
- Li, K., Xiong, J., Chen, T., Yan, L., Dai, Y., Song, D., Lv, Y. & Zeng, Z. (2013). *J. Hazard. Mater.* **250–251**, 19–28.
- Lin, H., Li, L., Zhao, M., Huang, X., Chen, X., Li, G. & Yu, R. (2012). *J. Am. Chem. Soc.* **134**, 8328–8331.
- Meagher, E. P. & Lager, G. A. (1979). *Can. Mineral.* **17**, 77–85.
- Merlen, A., Buijnsters, J. G. & Pardanaud, C. (2017). *Coatings*, **7**, 153.
- Mikami, M., Nakamura, S., Kitao, O. & Arakawa, H. (2002). *Phys. Rev. B*, **66**, 155213.
- Nguyen-Phan, T.-D., Kim, E. J., Hahn, S. H., Kim, W.-J. & Shin, E. W. (2011). *J. Colloid Interface Sci.* **356**, 138–144.
- Ohsaka, T., Izumi, F. & Fujiki, Y. (1978). *J. Raman Spectrosc.* **7**, 321–324.
- Okano, S., Yamamuro, S. & Tanaka, T. (2009). *Sci. China Ser. E-Technol. Sci.* **52**, 190–192.
- Pawlyta, M., Rouzaud, J.-N. & Duber, S. (2015). *Carbon*, **84**, 479–490.
- Richter, H., Wang, Z. P. & Ley, L. (1981). *Solid State Commun.* **39**, 625–629.
- Rietveld, H. M. (1969). *J. Appl. Cryst.* **2**, 65–71.
- Rodríguez-Carvajal, J. (1993). *Physica B*, **192**, 55–69.
- Rodríguez-Carvajal, J. (2001). *IUCr Commission on Powder Diffraction Newsletter*, **26**, 12–19.
- Rodríguez-Carvajal, J. (2016). *FullProf* computer program (<https://www.ill.eu/sites/fullprof/>)
- Sadezky, A., Muckenhuber, H., Grothe, H., Niessner, R. & Pöschl, U. (2005). *Carbon*, **43**, 1731–1742.
- Šćepanović, M., Grujić-Brojčdin, M., Lazarević, N. & Popović, Z. V. (2019). *Phys. Status Solidi A*, **216**, 1800763.
- Šćepanović, M., Grujić-Brojčdin, M., Vojisavljević, K., Bernik, S. & Srećković, T. (2010). *J. Raman Spectrosc.* **41**, 914–921.
- Šćepanović, M. J., Grujić-Brojčdin, M., Dohčević-Mitrović, Z. D. & Popović, Z. V. (2007). *Appl. Phys. A*, **86**, 365–371.
- Spanier, J. E., Robinson, R. D., Zhang, F., Chan, S.-W. & Herman, I. P. (2001). *Phys. Rev. B*, **64**, 245407.
- Stokes, A. R. & Wilson, A. J. C. (1944). *Proc. Phys. Soc.* **56**, 174–181.
- Sun, H., Liu, S., Liu, S. & Wang, S. (2014). *Appl. Catal. Environ.* **146**, 162–168.
- Thompson, P., Cox, D. E. & Hastings, J. B. (1987). *J. Appl. Cryst.* **20**, 79–83.
- Tomić, N., Grujić-Brojčdin, M., Finčur, N., Abramović, B., Simović, B., Krstić, J., Matović, B. & Šćepanović, M. (2015). *Mater. Chem. Phys.* **163**, 518–528.



- Wang, D., Chen, B. & Zhao, J. (2007). *J. Appl. Phys.* **101**, 113501.
- Xie, J., Lü, X., Liu, J. & Shu, H. (2009). *Pure Appl. Chem.* **81**, 2407–2415.
- Xie, Y., Heo, S. H., Yoo, S. H., Ali, G. & Cho, S. O. (2010). *Nanoscale Res. Lett.* **5**, 603–607.
- Yanqing, Z., Erwei, S., Suxian, C., Wenjun, L. & Xingfang, H. (2000). *J. Mater. Sci. Lett.* **19**, 1445–1448.
- Zhang, H., Lv, X., Li, Y., Wang, Y. & Li, J. (2010). *ACS Nano*, **4**, 380–386.
- Zhang, Y., Tang, Z.-R., Fu, X. & Xu, Y.-J. (2010). *ACS Nano*, **4**, 7303–7314.
- Zheng, Y., Shi, E., Cui, S., Li, W. & Hu, X. (2000). *J. Am. Ceram. Soc.* **83**, 2634–2636.
- Zhong, J., Chen, F. & Zhang, J. (2010). *J. Phys. Chem. C*, **114**, 933–939.

## Additional information on the distribution and ecology of the recently described diatom species *Geissleria gereckeii*

by

Danijela Vidakovic\*, Marco Cantonati,  
Marcella Mogna, Olga Jakovljević,  
Sanja Šovran, Vladimir Lazović, Katarina  
Stojanović, Jelena Đorđević, Jelena  
Krizmanić

DOI: [10.1515/ohs-2017-0002](https://doi.org/10.1515/ohs-2017-0002)

Category: **Original research paper**

Received: **May 03, 2016**

Accepted: **July 08, 2016**

University of Belgrade, Faculty of Biology,  
Institute of Botany and Botanical Garden  
„Jevremovac“, Belgrade, Takovska 43,  
11000 Belgrade, Serbia

### Abstract

The main objective of this paper is to report new information about the distribution and ecology of a recently described diatom species, *Geissleria gereckeii*. The opportunity for updating the information on the distribution and ecology of the species was provided by the finding of well-developed *G. gereckeii* populations on the lithic material and bryophytes in the Raška and Mlava rivers (Serbia). For several years after the first description, *G. gereckeii* has been known only from the type locality and from another spring in the Dolomiti Bellunesi National Park (the south-eastern Alps). After accurate LM and SEM observations, we provide evidence for the occurrence of the species also in the two above-mentioned rivers in Serbia, as well as in the south-western and south-eastern Alps. After an extensive literature search, it appears that the species is known with certainty only from these sites. Our observations and details from the literature suggest that the species is able to occupy a much broader ecological niche than the very-specific one observed at the time of discovery. The two main determinants for the species' occurrence appear to be the carbonate nature of the catchments or aquifers, and the ability of the species to be competitive in habitats or microhabitats exposed to seasonal desiccation.

**Key words:** diatom, distribution, ecology, *Geissleria gereckeii*, rivers, Serbia, south-eastern Alps

\* Corresponding author: [daca.vidakovic@yahoo.com](mailto:daca.vidakovic@yahoo.com)

## Introduction

The genus *Geissleria* was originally described in 1996 by Lange-Bertalot & Metzeltin and is characterized by the presence of an annulus, groups of subterminal openings. *Geissleria* comprises species formerly included in the *Annulatae* section of *Navicula* s.l. According to Lange-Bertalot (2001), this genus belongs to naviculoid diatoms. However, recent studies have shown that the characteristics of the genus *Geissleria* are more related to cymbelloid diatoms (Nakov et al. 2014; Kulikovskiy et al. 2014). Species of the genus *Geissleria* are widespread in oligo- to eutrophic waters but generally occur with low abundance (Spaulding & Edlund 2009).

According to Lange-Bertalot, in 2001 about 30 species were known from the genus *Geissleria*, many still undescribed or included within other genera (in particular *Navicula* s.l.). Currently, the genus comprises 71 taxa, widely distributed in Europe, Asia, South and North America, and the Maritime Antarctic and sub-Antarctic regions. *Geissleria* species were recorded in different freshwater habitats, such as rivers, lakes, springs, waterfalls, and in soils (Novais et al. 2013).

*Geissleria gereckeii* was described by Cantonati & Lange-Bertalot (2009) from a typical limestone/dolostone area. The type locality was Val-Lovatel Spring (Dolomiti Bellunesi National Park, the south-eastern Alps). At the time of its first description, this diatom was also found in the second spring (Casera-Maiolera Spring) in the same geographic area. In these two special freshwater habitats, the species was observed to be associated with the specific microhabitat of leaf-litter covered stones in shaded, forest springs emerging on the carbonate substrate. These low-elevation, small-discharge springs are likely to be affected by seasonal desiccation.

There is relatively little literature available on diatoms of the Raška River (Vidaković 2013; Vidaković et al. 2014), and there are no published data on the diatom microflora of the Mlava River. So far only five *Geissleria* species have been reported from Serbia: *G. decussis*, *G. ignota*, *G. schoenfeldii*, *G. similis*, and *G. thingvallae* (Krizmanić 2009; Andrejić 2012; Vidaković 2013).

The aim of this contribution was to collect and review information on the distribution and ecology of *Geissleria gereckeii* in the period between the first description of the taxon and the present day in order to obtain a more comprehensive database and consequently a better description of its ecological preferences in nature.

## Materials and methods

### ***G. gereckeii*: The new riverine sites and their characterization. Diatom sampling and analysis**

The Raška River and the Mlava River belong to the Black Sea drainage basin. The Raška River is a tributary of the Ibar River in the southwestern part of Serbia. The Mlava River is a tributary of the Danube in eastern Serbia (Marković 1980). The rivers have a carbonate bedrock and run through trout ponds. Samples were collected at the sites located downstream and upstream of the trout ponds. Some of the sites are exposed to seasonal desiccation when the discharge drops.

Diatoms were sampled from 5 localities in the Raška and Mlava rivers in April, June, August, and November 2011, and March and May 2012. Epilithon and epibryon were considered in the Raška River, while only epilithon was sampled in the Mlava River. Samples were immediately fixed with formaldehyde to a final concentration of 4%. Conductivity, oxygen, pH, and water temperature were measured in the field. Hydrochemical analyses were carried out at the Institute of General and Physical Chemistry, University of Belgrade, following standard methods (APHA 1998). Diatom samples were treated according to standard methods to obtain permanent slides (Krammer & Lange-Bertalot 1986). Permanent slides, prepared material, and aliquots of the samples were deposited in the diatom collection of the University of Belgrade, Faculty of Biology.

Slides from the Raška (14 samples) and Mlava (8 samples) rivers were used for microscope observations. Light microscope observations and micrographs were made using a Zeiss AxiolmagerM.1 microscope with DIC optics and AxioVision 4.8 software. SEM observations were made at the Institute of Physics, University of Belgrade, using a TESCAN MIRA 3 scanning electron microscope with maximum accelerating voltage of 30 kV. Sample surfaces were sputtered with gold using QUORUM TECHNOLOGIES MINI SPUTTERCOATER SC7620 for enhanced conductivity.

### ***G. gereckeii*: Further sites of occurrence found after the species description**

Trying to gather as much data on the distribution of *Geissleria gereckeii* as possible, the following databases were carefully checked: Pesio and Tanaro Valleys Nature Park (Ligurian Alps, the south-western extreme of the Alps; Mogna et al. 2015), central to eastern Switzerland and the Jura (the north-western/

central Alps; Taxböck, L., Karger, D.N., Kessler, M. & Cantonati, M. 2016 submitted paper), CRENODAT (Trentino, the south-eastern Alps; Cantonati et al. 2012), CESSPA (Province of Verona, Veneto Region, Italy; Cantonati et al. 2016), Berchtesgaden National Park (Bavaria, Germany; Cantonati & Lange-Bertalot 2010), Gesäuse National Park (Styria, Austria; MC unpublished data), Julian Pre-Alps Nature Park (Friuli Venezia Giulia Autonomous Region, Italy) (the south-eastern Alps; Cantonati 2003). In the case of the database established before the description of *G. gerecke*, also direct inspection of the permanent mounts was carried out to check for possible occurrence of the species. Finally, repeated literature searches were carried out ("\*Geissleria\*gerecke") in the Web of Science (WOS) and Google Scholar.

## Results

### *Geissleria gerecke* populations found in the two rivers in Serbia

**Main morphological characteristics.** Valve outline linear-elliptic to elliptic. Ends subcapitate and protracted. Length 9.9-18.5  $\mu\text{m}$ , breadth 5.0-7.1  $\mu\text{m}$ ; length/width ratio 2.0-2.8. Raphe filiform; axial area narrow, linear; central area characterized by longer and shorter striae. Single stigma placed in the center of the valve. Striae 13-17/10  $\mu\text{m}$ , radiate throughout (Fig. 1a-g).

SEM: external view (Fig. 2b): Proximal ends of the raphe expanded and moderately deflected whilst distal ends are hooked. Striae uniseriate throughout. Areolae apertures as short slits (55-60 in 10  $\mu\text{m}$ ). Annulus

evident as three rows of areolae larger than in stria areolae, apically elongated. In each row, from 3 to 6 apically elongated areolae are present.

SEM: internal view (Fig. 2 a and c): Distal raphe ends slightly deflected in a small, aureole-shaped helictoglossa, central raphe endings straight. Annulus structure with warty outgrowths.

**Distribution.** The Raška and Mlava River. *G. gerecke* was found both in the epilithon and in the epibryon. Relative abundance in epilithic diatom communities of the Raška River ranged from 0.5 to 3%. Only one specimen of *G. gerecke* was recorded in epiphytic diatom assemblages of the Raška River and in epilithic diatom assemblages of the Mlava River.

**Associated diatoms.** The most frequent diatoms which were found together with *G. gerecke* (Raška River epilithon) were: *Achnantheidium affine* (1.2-18%), *A. minutissimum* (9.2-48%), *Amphora pediculus* (11-32%), *Cocconeis lineata* (0.5-32%), *Diatoma vulgaris* (0.2-20%), *Gomphonema parvulum* (0.2-2.8%), *G. tergestinum* (0.3-39%), *Navicula cryptotenella* (0.2-4.2%), and *Nitzschia dissipata* (0.5-5%).

**Ecology.** The Raška and Mlava rivers are small mountain rivers, running at altitudes between 296 and 557 m a.s.l. Samples were collected at the sites located downstream and upstream of the trout ponds, which explains the high nutrient values. Conductivity values are consistent with the carbonate bedrock (Table 1). The highest abundance of *G. gerecke* was observed at microhabitats (river wetted surface and bryophytes) exposed to seasonal desiccation.

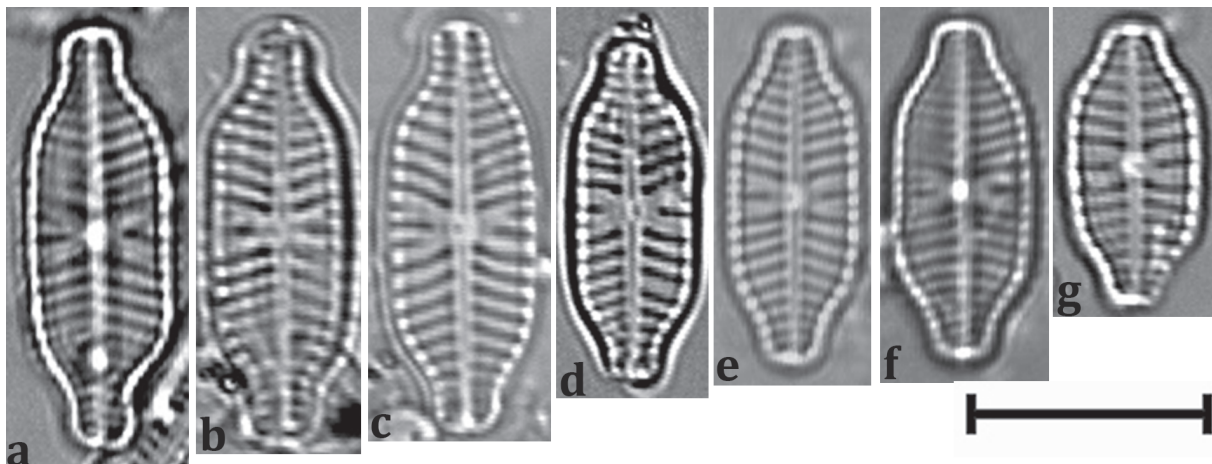


**Figure 1**

(a-g) Light microscopy (LM) micrographs of *Geissleria gerecke* Cantonati et Lange-Bertalot. Scale bar = 10  $\mu\text{m}$

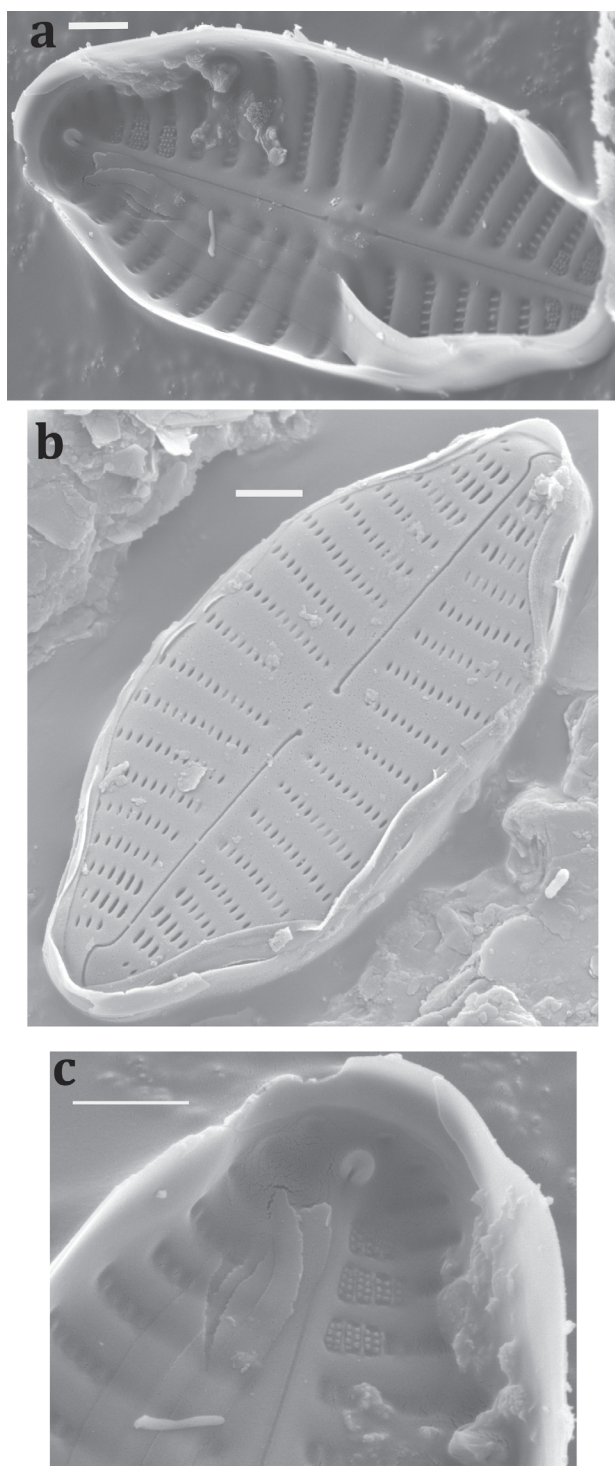


**Figure 2**

Scanning electron microscopy (SEM) micrographs of *Geissleria gerecke*. (a) Inside view of the valve. (b) Valve outside view of the frustule; apically elongated areolae (annulus). (c) Distal ends (internally) and helictoglossa; annulus structure with warty outgrowths. Scale bar = 1  $\mu\text{m}$

### Further occurrence of *Geissleria gerecke*

*G. gerecke* was also found in one spring in the south-eastern Alps (Ziola Bassa, AT0756, Vigolana Upland), in springs Alpine foothills (Verona Province, Lessinia, ML0622) and in eight springs of the south-western Alps (Table 1). These springs are small, with low discharge (probably  $<0.5 \text{ l s}^{-1}$  in most cases), and likely to be affected by periodic desiccation. All of these springs are fed by carbonate aquifers, and have medium conductivities ( $200\text{--}400 \mu\text{S cm}^{-1}$ ).

### Discussion

The morphological features of the *Geissleria gerecke* populations observed during this study correspond with those reported at the time of the species description (Cantonati & Lange-Bertalot 2009). However, our observations, based on the populations in the two rivers in Serbia, advance the knowledge about the size range of the species.

Our data increase the number of known sites of the species from 2 to 13, and the populations are no longer limited to the Alpine area.

The ecological characteristics of the new sites revealed that *G. gerecke* can also successfully colonize sites where light intensity is not a limiting factor. The niche described at the time of the species description (carbonate stones covered by leaf litter in small shaded springs in broadleaf forests) must therefore be considered an extreme situation that shows that the species has the capability to be competitive also in microhabitats with very low light availability.

Our data and observations provide insights into the niche of *G. gerecke* in terms of nutrient concentrations, suggesting that although the species thrives well and is frequent at oligotrophic sites, it can colonize places with high nutrient (in particular P) concentrations. The spring and river sites also reveal that above-average sulfate values are well tolerated by the species.

A preference for carbonate stony substrate is confirmed, although it is shown that the species can thrive on bryophytes substrate as well.

The two main determinants for the species occurrence appear to be the carbonate nature of the catchments or aquifers of the environments colonized, and the ability of the species to be competitive in habitats (small springs) or microhabitats (river wetted surface and bryophytes) exposed to seasonal desiccation because of fluctuating and low discharge values.

Table 1

Value ranges of physical and chemical parameters of the sites with *Geissleria gereckeii*

Parameters/Sampling sites	Rivers in Serbia		Spring SE Alps (Trentino)	Springs Alpine foothills (Verona Province, Lessinia)	Springs in the south-western Alps							
	Raška River	Mlava River	AT0756	ML0622	DC1620	RF1477	MT1300	SB1050	MC1650	MC1652	MC1655	RP1800
Shading (1-5 scale)			2	1	1	1	4	3	1	1	1	2
Temperature (°C)	7.5-14	9.1-14.6	9.4	11	8.4	8.1	5.8	7	4	3.4	3.2	2
pH	7.02-8.23	6.95-7.95	7.6	7.3	8.4	7.39	8.33	8.31	8.48	8.56	8.43	8.9
Conductivity ( $\mu\text{S cm}^{-1}$ )	305-420	389-490	356	411	200	105	125	175	198	200	201	170
Alkalinity (as mg $\text{CaCO}_3 \text{ l}^{-1}$ )	7-120.8	12.6-120.6	195	240	25	15.2	17.7	26	23	23	24	18.4
$\text{N-NH}_4^+$ ( $\mu\text{g l}^{-1}$ )	<18.9-473.8	<18.9-355.8	<20	<100	<10	<10	<10	<10	<10	<10	<10	<10
$\text{N-NO}_3^-$ ( $\mu\text{g l}^{-1}$ )	6300-7900	6900-9500	224	3160	45	147	481	565	361	373	230	319
TP ( $\mu\text{g P l}^{-1}$ )	13.5-104.2	8.7-112.8	4	-	-	-	-	-	-	-	-	-
SRP ( $\mu\text{g P l}^{-1}$ )	5.2-51.7	3.7-46.8	2	-	-	-	-	-	-	-	-	-
Cl ( $\text{mg l}^{-1}$ )	1.2-2.2	0.9-2	1.0	8.0	0.4	0.4	0.3	0.3	0.5	0.5	0.4	0.2
$\text{SO}_4^{2-}$ ( $\text{mg l}^{-1}$ )	1.4-3.4	5.5-22.4	21.0	10.0	-	1.6	1.8	4.3	-	-	-	-
% <i>Geissleria gereckeii</i>	0.5-3	-	<0.2	4.5	1.0	2.3	0.2	0.5	1.0	0.8/0.5	0.5	0.8
Substrate	epil./epib.	epilithon	epilithon	epilithon	epilithon	epilithon	epilithon	epilithon	epilithon	epil./epib.	epilithon	epilithon

- No data

Data from the springs in the Alps were provided by Marco Cantonati.

## Acknowledgments

Financial support was provided by the Ministry of Education and Science of the Republic of Serbia (Projects No. TR 037009). MC was partially funded by the Autonomous Province of Trento while contributing to this paper.

## References

- Andrejić, J., Krizmanić, J. & Cvijan, M. (2012). Diatom species composition of the Nišava river and its tributaries Jerma and Temska rivers (southern Serbia). *Archives of Biological Sciences* 64(3): 1127-1140. DOI:10.2298/ABS1203127A.
- APHA. (1998). Standard Methods for the Examination of Water and Wastewater, 20th ed. American Public Health Association, Washington, DC.
- Cantonati, M. (2004). Le diatomee di tre sorgenti del Parco Naturale delle Prealpi Giulie (Italia nord-orientale). *Gortania – Atti Museo Friul. di Storia Nat.* 25: 95-108.
- Cantonati, M. & Lange-Bertalot, H. (2009). *Geissleria gereckeii* sp. nov. (Bacillariophyta) from leaf-litter covered stones of very shaded carbonate mountain springs with extremely low discharge. *Phycological Research* 57: 171-177. DOI: 10.1111/j.1440-1835.2009.00536.x.
- Cantonati, M. & Lange-Bertalot, H. (2010). Diatom biodiversity of springs in the Berchtesgaden National Park (northern Alps, Germany), with the ecological and morphological characterization of two species new to science. *Diatom Research* 25: 251-280. DOI: 10.1080/0269249X.2010.9705849
- Cantonati, M., Angeli, N., Bertuzzi, E., Spitale, D. & Lange-Bertalot, H. (2012). Diatoms in springs of the Alps: spring types, environmental determinants, and substratum. *Freshwater Science* 31: 499-524. DOI: 10.1899/11-065.1.
- Cantonati, M., Angeli, N., Spitale, D. & Lange-Bertalot, H. (2016). A new *Navicula* (Bacillariophyta) species from low-elevation carbonate springs affected by anthropogenic disturbance. *Fottea* 16(2): 255-265. DOI: 10.5507/fot.2016.013.
- Krammer, K. & Lange-Bertalot, H. (1986). Bacillariophyceae. 1. Teil: Naviculaceae. In H. Ettl, J. Gerloff, H. Heynig & D. Mollenhauer (Eds.), *Süßwasserflora von Mitteleuropa*. 2/1. (pp. 1-876). Jena: G. Fischer Verlag.
- Krizmanić, J. (2009). *Floristic, taxonomical and ecological investigations of diatoms (Bacillariophyceae, Bacillariophycidae, Bacillariophyta) in Serbia*. Unpublished doctoral dissertation, University of Belgrade, Belgrade.
- Lange-Bertalot, H. (2001). *Navicula* sensu stricto. 10 genera separated from *Navicula* sensu lato. *Frustulia*. In H. Lange-Bertalot (Ed.), *Diatoms of Europe: diatoms of the European inland waters and comparable habitats*. Vol. 2. (pp. 1-526). Ruggell: A.R.G. Gantner Verlag. K.G.
- Lange-Bertalot, H. & Metzeltin, D. (1996). Indicators of oligotrophy - 800 taxa representative of three ecologically distinct lake types, carbonate buffered - Oligodystrophic - weakly buffered soft water. In H. Lange-Bertalot (Ed.), *Iconographia Diatomologica. Annotated Diatom*

- Micrographs. Vol.2. Ecology, Diversity, Taxonomy.* (pp. 1-390). Königstein: Koeltz Scientific Books.
- Marković, J. (1980). *Regionalna geografija SFR Jugoslavije* (in serbian). Beograd: Građevinska knjiga.
- Mogna, M., Cantonati, M., Andreucci, F., Angeli, N., Berta, G. et al. (2015). Diatom communities and vegetation of springs in the south-western Alps. *Acta Bot. Croat.* 74(2): 265–285. DOI: 10.1515/botcro-2015-0024.
- Novais, M.H., Wetzel, C.E., Van de Vijver, B., Morais, M.M, Hoffmann, L. et al. (2013). New species and combinations in the genus *Geissleria* (Bacillariophyceae). *Cryptogamie Algologie* 34(2): 117-148. DOI: 10.7872/crya.v34.iss2.2013.117.
- Spaulding, S. & Edlund, M. (2009). *Geissleria*. In *Diatoms of the United States*. Retrieved August 12, 2015, from <http://westerndiatoms.colorado.edu/taxa/genus/Geissleria>
- Taxböck, L. (2015). *Diatom biodiversity, distribution patterns and spring types in near-natural Swiss springs*. Unpublished doctoral dissertation, University of Zurich.
- Vidaković, D. (2013). *Assessment of the ecological status of Raška River based on epilithic diatoms*. Unpublished master Thesis, University of Belgrade, Belgrade.
- Vidaković, D., Krizmanić, J. & Šovran, S. (2014). New taxa of the genus *Navicula* (Bacillariophyceae) in the diatom flora of Serbia. *Oceanol. Hydrobiol. St.* 43(2): 185-190. DOI: 10.2478/s13545-014-0132-0.

See discussions, stats, and author profiles for this publication at: <https://www.researchgate.net/publication/320785817>

# An updated list of Serbian diatom flora: New recorded taxa

Article in Archives of Biological Sciences · November 2017

DOI: 10.2298/ABS170606043V

CITATIONS

0

READS

123

7 authors, including:



[Danijela Vidakovic](#)

University of Belgrade, Faculty of Biology, Ins...

16 PUBLICATIONS 16 CITATIONS

[SEE PROFILE](#)



[Dragana Predojević](#)

University of Belgrade

22 PUBLICATIONS 10 CITATIONS

[SEE PROFILE](#)



[Gordana V. Subakov Simic](#)

University of Belgrade

59 PUBLICATIONS 187 CITATIONS

[SEE PROFILE](#)



[Jelena Krizmanic](#)

University of Belgrade

44 PUBLICATIONS 107 CITATIONS

[SEE PROFILE](#)

Some of the authors of this publication are also working on these related projects:



Monitoring of algae in 5 selected ponds within the project “Protecting Europe’s Lifeline - The creation of a Trans-Boundary Biosphere Reserve along the Danube, Drava and Mura Rivers”. with WWF. [View project](#)



Managing the effects of multiple stressors on aquatic ecosystems under water scarcity - GLOBAQUA [View project](#)

All content following this page was uploaded by [Danijela Vidakovic](#) on 03 November 2017.

The user has requested enhancement of the downloaded file.



# An updated list of Serbian diatom flora: new recorded taxa

Danijela P. Vidaković<sup>1,\*</sup>, Olga S. Jakovljević<sup>1</sup>, Dragana D. Predojević<sup>1</sup>, Sanja M. Radovanović<sup>1</sup>, Gordana V. Subakov-Simić<sup>1</sup>, Vladimir M. Lazović<sup>2</sup> and Jelena Ž. Krizmanić<sup>1</sup>

<sup>1</sup>University of Belgrade, Faculty of Biology, Institute of Botany and Botanical Garden "Jevremovac", 43 Takovska, 11000 Belgrade, Serbia

<sup>2</sup>University of Belgrade, Institute of Physics, 118 Pregrevica, 11080 Belgrade, Serbia

\*Corresponding author: [daca.vidakovic@bio.bg.ac.rs](mailto:daca.vidakovic@bio.bg.ac.rs)

**Received:** June 6, 2017; **Revised:** September 15, 2017; **Accepted:** October 13, 2-2017

**Abstract:** Diatoms are a widespread group of organisms with well-known ecological preferences. Knowledge of their diversity is of great importance for assessing the environmental status of different aquatic ecosystems. The present study was based on 55 different localities that included rivers, streams, channels, accumulations and salt marshes throughout Serbia. The results of this study expanded the diatom checklist by 80 taxa, including two new recorded genera (*Fistulifera* and *Microfissurata*) for Serbia. The data were obtained by combining light microscopy (LM) and scanning electron microscopy (SEM) that provided reliable identification, which is very important in diatom diversity studies.

**Key words:** *Fistulifera*; *Microfissurata*; light microscopy; scanning electron microscopy; new records

## INTRODUCTION

Species diversity is one of the main factors in assessing the environmental state of various aquatic ecosystems. It also has an important role in ecosystem processes and functioning, food chains and ecosystem integrity [1]. Widespread in different environments, well-known ecological preferences and standardized identification methods point to diatoms as an important group of algae for species diversity studies that can serve to evaluate ecosystems health and environmental changes [2,3].

Diatom diversity have been relatively well studied across Europe and is presented in various books [4-9], monographs [10,14] and articles [11-13,15]. Compared to previously cited data, diatom records and literature in Serbia are scattered. The first diatom data in Serbia date from 1883 [16]. However, it was only in the second half of the 20<sup>th</sup> century that extensive research into diatoms began [17-21], and in the last twenty years the number of new recorded diatom taxa for Serbian flora has increased [20-24]. The aim of this paper was to report new records of diatom taxa from different sites throughout Serbia in order to supplement the diatom checklist.

## MATERIALS AND METHODS

### Study area

The study areas were located in different parts of Serbia (Fig. 1). Samples of diatoms were collected at different localities, in rivers, streams, channels, accumulations and salt marshes. The list of the 55 localities is presented in Table 1.

### Sample preparation

Diatoms were collected from different types of substrate (mosses, macrophytes, mud, stones) and communities (benthos, plankton) and poured into 100-mL bottles. Epiphytic and epilithic diatom samples were collected by squeezing out and scraping off the surface with a toothbrush,

respectively. Epipellic diatom samples were collected from the sediment surface using a corer ( $\varnothing$  1 cm), and phytoplankton samples were collected using a plankton net ( $\varnothing$  25  $\mu$ m) drawn through open water. All samples were fixed with formaldehyde to a final concentration of 4%.

### Sample analysis

In the laboratory, the algological samples were treated with a standard method with concentrated acid ( $\text{H}_2\text{SO}_4$ ) and a  $\text{KMnO}_4$  solution in order to remove organic matter; the samples were then washed several times with distilled water until pH 7 [25]. Permanent slides were prepared by air-drying of the material on cover glasses and mounting in Naphrax<sup>®</sup> mounting medium. Microscopic examinations were done using a Zeiss AxioImagerM.1 light microscope (LM) with DIC optics and AxioVision 4.8 software. Scanning electron microscopy (SEM) observations were made at the Institute of Physics, University of Belgrade, using a TESCAN MIRA 3 scanning electron microscope with maximum accelerating voltage of 30 kV. Sample surfaces were sputtered with gold using Quorum Technologies Mini Sputtercoater SC7620 for enhanced conductivity.

The terminology of valve morphology is based on Krammer and Lange-Bertalot [25] and Hofmann et al. [26]. Taxa were identified according to different literature sources, indicated next to each type.

## RESULTS

A total of 80 diatom taxa belonging to 33 genera have been noted for the first time in Serbian diatom flora. Among the 33 genera, two, *Microfissurata* and *Fistulifera*, are new to Serbian diatom flora. Species names as well as their dimensions and distribution in Serbia are given below.

***Achnantheidium caledonicum*** Lange-Bertalot (Fig. 4(30,31))

Basionym: *Achnanthes caledonica* Lange-Bertalot

Reference: Hofmann et al. [26] (p. 23, Figs. 51–55: 79)

Dimensions: Valve length 15.06-20.4  $\mu$ m, breadth 2.63-3.1  $\mu$ m, striae 27-33/10  $\mu$ m.

Distribution in Serbia: CP95 Krnda 2, CP95 Cvetića zaliv and CP95 Zaliv pritoke streams, CP66 Batarski Rzav and CP76 Kruščica rivers (Fig. 1, Table 1).

***Achnantheidium crassum*** (Hustedt) Potapova and Ponader (Fig. 4(34, 35))

Basionym: *Achnanthes crassa* Hustedt

Reference: Potapova and Ponader [27] (Figs. 19-27, 44-49)

Dimensions: Valve length 8.37-10.25  $\mu$ m, breadth 3.04-3.86  $\mu$ m, striae of raphe valve 22-26/10  $\mu$ m, striae of rapheless valve 23-24/10  $\mu$ m.

Distribution in Serbia: EN48 Rasina and CP86 Rača rivers (Fig. 1, Table 1).

***Achnantheidium druartii*** Rimet and Couté (Fig. 4(24, 25))

Basionym: *Achnantheidium druartii* Rimet and Couté

Reference: Rimet et al. [28] (pl. 1, Figs. 1-38, 188)

Dimensions: Valve length 20.92-4.32  $\mu$ m, breadth 3.04-3.86  $\mu$ m, striae 21/10  $\mu$ m.

Distribution in Serbia: CP95 Jovac stream and CP95 Đetinja River (Fig. 1, Table 1).

***Achnantheidium eutrophilum*** (Lange-Bertalot) Lange-Bertalot (Fig. 4(32, 33))

Basionym: *Achnanthes eutrophila* Lange-Bertalot

Reference: Hofmann et al. [26] (p. 23, Figs. 30-35: 80)

Dimensions: Valve length 9.91-13.17  $\mu$ m, breadth 3.45-4.53  $\mu$ m, striae of raphe valve 24-27/10  $\mu$ m, striae of rapheless valve 27/10  $\mu$ m.

Distribution in Serbia: CP86 Rača, CP95 Đetinja and DQ31 Kolubara rivers (Fig. 1, Table 1).

***Achnantheidium latecephalum*** Kobayasi (Fig. 4(26-29); Fig. 5(3, 4))

Basionym: *Achnantheidium latecephalum* Kobayasi

Reference: Potapova [29]

Dimensions: Valve length 10.46-18.84  $\mu\text{m}$ , breadth 3.78-5.26  $\mu\text{m}$ , striae of raphe valve 20-22/10  $\mu\text{m}$ , striae of rapheless valve 19-21/10  $\mu\text{m}$ .

Distribution in Serbia: EN48 Rasina, CP86 Rača, DN79 Raška and CP95 Đetinja rivers, CP95 Krnda 2 and CP95 Ročnjak streams (Fig. 1, Table 1).

***Achnanthidium straubianum*** Lange-Bertalot (Fig. 4(36, 37))

Basionym: *Achnanthes straubiana* Lange-Bertalot

Reference: Hofmann et al. [26] (p. 23, Figs 36-39: 87)

Dimensions: Valve length 6.62  $\mu\text{m}$ , breadth 3.72  $\mu\text{m}$ , striae of raphe valve 23/10  $\mu\text{m}$ .

Distribution in Serbia: DN79 Raška River and CP95 Vrutci tributary 10 (Fig. 1, Table 1).

***Adlafia aqueductae*** (Krasske) Lange-Bertalot (Fig. 3(17))

Basionym: *Navicula pseudopupula* var. *aquaeductae* Krasske

Reference: Lange-Bertalot [7] (p. 105, Figs. 19-21: 142)

Dimensions: Valve length 19.57-23.82  $\mu\text{m}$ , breadth 4.05-4.99  $\mu\text{m}$ , striae 23-24/10  $\mu\text{m}$ .

Distribution in Serbia: CP95 Cvetića zaliv stream (Fig. 1, Table 1).

***Adlafia minuscula*** (Grunow) Lange-Bertalot (Fig. 3(13, 14))

Basionym: *Navicula minuscula* Grunow

Reference: Lange-Bertalot [7] (p. 106, Figs. 5-8; p. 108, Figs. 4-10: 143)

Dimensions: Valve length 10.86-15.22  $\mu\text{m}$ , breadth 3.51-4.79  $\mu\text{m}$ .

Distribution in Serbia: EN48 Rasina, EQ40 Mlava, FN02 Vrla, EP75 Radovanska, CP76 Vrelo rivers, CP95 Krnda 2, CP95 Cvetića zaliv, CP95 Cvetića potok, CP95 Simića potok and CP95 Jasik streams (Fig. 1, Table 1).

***Adlafia minuscula* var. *muralis*** (Grunow) Lange-Bertalot (Fig. 3(15))

Basionym: *Navicula muralis* Grunow

Reference: Lange-Bertalot [7] (p. 106, Fig. 9; p. 108, Figs. 1-3: 144)

Dimensions: Valve length 9.41-11.87  $\mu\text{m}$ , breadth 4.05-5.22  $\mu\text{m}$ .

Distribution in Serbia: EN48 Rasina, DN79 Raška, CQ87 Zasavica, EQ40 Mlava and EP75 Radovanska rivers (Fig. 1, Table 1).

***Adlafia suchlandtii*** (Hustedt) Lange-Bertalot (Fig. 3(16))

Basionym: *Navicula suchlandtii* Hustedt

Reference: Lange-Bertalot [7] (p. 105, Figs. 33-39; p. 106, Fig. 4: 145)

Dimensions: Valve length 10.39-15.18  $\mu\text{m}$ , breadth 2.36-3.24  $\mu\text{m}$ , striae 26-28/10  $\mu\text{m}$ .

Distribution in Serbia: EN48 Rasina, FN02 Vrla and EP75 Radovanska rivers (Fig. 1, Table 1).

***Amphora lange-bertalotii* var. *tenuis*** Levkov and Metzeltin (Fig. 4(15))

Basionym: *Amphora lange-bertalotii* var. *tenuis* Levkov and Metzeltin

Reference: Levkov [30] (p. 53, Figs. 1-12; p.163: 73, 288)

Dimensions: Valve length 37.58  $\mu\text{m}$ , valve breadth 7.22  $\mu\text{m}$ , striae 13/10  $\mu\text{m}$ .

Distribution in Serbia: CP95 Cvetići zaliv stream (Fig. 1, Table 1).

***Amphora meridionalis*** Levkov (Fig. 4(13, 14))

Basionym: *Amphora meridionalis* Levkov

Reference: Levkov [30] (p.55, Figs. 18-30; p. 166, Figs. 1-6; p.167, Figs. 1-5; p. 196, Fig. 5: 81, 289)

Dimensions: Valve length 15.72-34.27  $\mu\text{m}$ , valve breadth 4.12-6.21  $\mu\text{m}$ , frustule breadth 9.45-12.46  $\mu\text{m}$ , dorsal striae 14-17 /10  $\mu\text{m}$ , ventral striae 14-18/10  $\mu\text{m}$ .

Distribution in Serbia: CP86 Rača, CP95 Đetinja, EQ40 Mlava and EP75 Radovanska rivers, CP95 Jasik, CP95 Jovac and CP95 Ročnjak streams (Fig. 1, Table 1).

***Amphora micra*** Levkov (Fig. 4(12))

Basionym: *Amphora micra* Levkov

Reference: Levkov [30] (p. 78, Figs. 1-11; p. 189, Figs. 1-5; p. 190, Figs. 1-5; p. 195, Fig. 2: 83, 289)

Dimensions: Valve length 18.28  $\mu\text{m}$ , valve breadth 3.78  $\mu\text{m}$ , dorsal striae 18/10  $\mu\text{m}$ , ventral striae 17/10  $\mu\text{m}$ .

Distribution in Serbia: CP95 Krnda 2 and CP95 Cvetići zaliv streams (Fig. 1, Table 1).

***Chamaepinnularia muscicola*** (J.B.Petersen) Kulikovskiy, Lange-Bertalot and A.Witowski (Fig. 2(18))

Basionym: *Pinnularia muscicola* J.B.Petersen

Reference: Hofmann et al. [26] (p. 50, Figs. 29,30: 129)

Dimensions: Valve length 12.48  $\mu\text{m}$ , breadth 3.37  $\mu\text{m}$ , striae 19/10  $\mu\text{m}$ .

Distribution in Serbia: CP95 Cvetići zaliv stream (Fig. 1, Table 1).

***Cocconeis pseudothumensis*** Reichardt (Fig. 2(20))

Basionym: *Cocconeis pseudothumensis* Reichardt

Reference: Hofmann et al. [26] (p. 20, Figs. 1-4: 134)

Dimensions: Valve length 11.4-12.56  $\mu\text{m}$ , breadth 8.03-8.58  $\mu\text{m}$ , striae 10-12/10  $\mu\text{m}$ .

Distribution in Serbia: EN48 Rasina and EQ40 Mlava rivers (Fig. 1, Table 1).

***Craticula molestiformis*** (Hustedt) Mayama (Fig. 3(11))

Basionym: *Navicula molestiformis* Hustedt

Reference: Lange-Bertalot [7] (p. 93, Figs. 19-28: 116)

Dimensions: Valve length 9.5-16.5  $\mu\text{m}$ , breadth 3.5-5  $\mu\text{m}$ , striae 25-26/10  $\mu\text{m}$ .

Distribution in Serbia: EQ40 Mlava, DN79 Raška and DQ31 Kolubara rivers, DR44 Jaruge salt marsh (Fig. 1, Table 1).

***Cymbella lange-bertalotii*** Krammer (Fig. 2(21))

Basionym: *Cymbella lange-bertalotii* Krammer

Reference: Krammer [8] (p. 179, Figs. 1-6; p. 180, Figs. 1-8; p. 181, Figs. 1-6, 8; p. 182, Figs. 1-9: 152, 174)

Dimensions: Valve length 52.46-90.02  $\mu\text{m}$ , breadth 12.52-15.11  $\mu\text{m}$ , dorsal striae 8-11/10  $\mu\text{m}$ , ventral striae 10-11/10  $\mu\text{m}$ , puncta 19-23/10  $\mu\text{m}$ .

Distribution in Serbia: CP95 Đetinja, CP66/76 Karaklijski Rzav and CP66/76 Batuski Rzav rivers, DQ50 Garaši, DP76/86 Gruža, CP93 Zlatibor and DP18 Divčibare accumulations (Fig. 1, Table 1).

***Diatoma problematica*** Lange-Bertalot (Fig. 4(6))

Basionym: *Diatoma problematica* Lange-Bertalot

Reference: Hofmann et al. [26] (p. 2, Figs. 26-30: 175)

Dimensions: Valve length 15.18-26.93  $\mu\text{m}$ , breadth 4.52-5.75  $\mu\text{m}$ , striae 5-10/10  $\mu\text{m}$ .

Distribution in Serbia: EN48 Rasina, CP86 Rača, EQ40 Mlava and DN79 Raška rivers (Fig. 1, Table 1).

***Encyonema brevicapitatum*** Krammer (Fig. 2(17))

Basionym: *Encyonema brevicapitatum* Krammer

Reference: Krammer [31] (p. 27, Figs. 1-9, 17; p. 34, Figs. 1-7: 92)

Dimensions: Valve length 11.66-23.53  $\mu\text{m}$ , breadth 4.38-6.81  $\mu\text{m}$ , striae 14-18/10  $\mu\text{m}$ .

Distribution in Serbia: EQ40 Mlava, EP75 Radovanska and FN02 Vrla rivers (Fig. 1, Table 1).

***Encyonema procerum*** Krammer (Fig. 2(15))

Basionym: *Encyonema procerum* Krammer

Reference: Krammer [31] (p. 32, Figs. 9-19: 169)

Dimensions: Valve length 24.22-26.34  $\mu\text{m}$ , breadth 6.01-3.37  $\mu\text{m}$ , dorsal striae 13-15/10  $\mu\text{m}$ , ventral striae 13-16/10  $\mu\text{m}$ .

Distribution in Serbia: EN48 Rasina River (Fig. 1, Table 1).

***Encyonema subminutum*** Krammer and Lange-Bertalot (Fig. 2(16))

Basionym: *Encyonema subminutum* Krammer and Lange-Bertalot

Reference: Krammer [31] (p. 19, Figs. 17-24; p. 25, Figs. 28-34: 56)

Dimensions: Valve length 18.08-26.38  $\mu\text{m}$ , breadth 4.72-6.48  $\mu\text{m}$ , dorsal striae 14-17/10  $\mu\text{m}$ , ventral striae 14-16/10  $\mu\text{m}$ .

Distribution in Serbia: EN48 Rasina, EQ40 Mlava and EP75 Radovanska rivers (Fig. 1, Table 1).

***Encyonopsis cesatii*** (Rabenhorst) Krammer (Fig. 2(23))

Basionym: *Navicula cesatii* Rabenhorst

Reference: Krammer [32] (p. 182, Figs. 1-13; p. 183, Figs. 10-12; p. 184., Figs. 4-7; p. 185, Figs. 1-7, 11-13; p. 186, Figs. 10, 11; p. 187 Figs. 1-7: 152).

Dimensions: Valve length 17.07-43.96  $\mu\text{m}$ , breadth 4.59-7.88  $\mu\text{m}$ , striae 17-21/10  $\mu\text{m}$ .

Distribution in Serbia: EN48 Rasina, CP87 Rača, CP95 Đetinja, CP79, CP87, CQ66 Drina and CP82, CP90 Lim rivers, CP95 a 2, CP95 Cvetića zaliv, CP95 Cvetića potok, CP95 Simića potok, CP95 Jasik and CP95 Jovac streams, DP18 Divčibare, CP93 Zlatibor, EP50 Bresnica, EN29 Pridvorica and CP95 Vrutci accumulations, DR43 Okanj bara salt marsh (Fig. 1, Table 1).

***Encyonopsis krammeri*** Reichardt (Fig. 2(24))

Basionym: *Encyonopsis krammeri* Reichardt

Reference: Krammer [32] (p. 144, Figs. 12-15, 21; p. 145, Figs. 1-18; p. 147., Figs. 4-6; p. 150, Figs. 1-3, 5, 6, 11-14; p. 193, Figs. 1, 4, 6: 99)

Dimensions: Valve length 12.28-14.37  $\mu\text{m}$ , breadth 3.17-3.24  $\mu\text{m}$ , striae 28-30/10  $\mu\text{m}$ .

Distribution in Serbia: EQ40 Mlava River (Fig. 1, Table 1).

***Fallacia insociabilis*** (Krasske) D.G.Mann (Fig. 3(18))

Basionym: *Navicula insociabilis* Krasske

Reference: Hofmann et al. [26] (p. 46, Figs. 21-25: 244)

Dimensions: Valve length 10.04-15.25  $\mu\text{m}$ , breadth 5.18-6.14  $\mu\text{m}$ , striae 22-23/10  $\mu\text{m}$ .

Distribution in Serbia: DN79 Raška, EQ40 Mlava and FN02 Vrla rivers (Fig. 1, Table 1).

***Fallacia lange-bertalotii*** (Reichardt) Reichardt (Fig. 3(20))

Basionym: *Navicula lange-bertalotii* Reichardt

Reference: Hofmann et al. [26] (p. 46, Fig. 18: 242)

Dimensions: Valve length 9.78-11.47  $\mu\text{m}$ , breadth 3.24-3.31  $\mu\text{m}$ , striae 29-31.5/10  $\mu\text{m}$ .

Distribution in Serbia: CP95 Krnda 2 stream (Fig. 1, Table 1).

***Fallacia lenzii*** (Hustedt) Lange-Bertalot (Fig. 3(19))

Basionym: *Navicula lenzii* Hustedt

Reference: Hofmann et al. [26] (p. 46, Figs. 3-7: 243)

Dimensions: Valve length 10.25-15.98  $\mu\text{m}$ , breadth 3.42-4.97  $\mu\text{m}$ , striae 27/10  $\mu\text{m}$

Distribution in Serbia: CP95 Ročnjak stream, CP66/76 Karaklijski Rzav, CP66/76 Baturski Rzav and DQ31 Kolubara rivers (Fig. 1, Table 1).

***Fallacia sublucidula*** (Hustedt) D.G.Mann (Fig. 3(21))

Basionym: *Navicula sublucidula* Hustedt

Reference: Hofmann et al. [26] (p. 46, Figs. 1,2: 243)

Dimensions: Valve length 7.02-10.52  $\mu\text{m}$ , breadth 3.71-4.59  $\mu\text{m}$ , striae 23-28/10  $\mu\text{m}$ .

Distribution in Serbia: CP86 Rača, DN79 Raška, EQ40 Mlava and EP75 Radovanska rivers, CP95 Ročnjak stream (Fig. 1, Table 1).

***Fistulifera pelliculosa*** (Kützing) Lange-Bertalot (Fig. 3(12); Fig. 5(2))

Basionym: *Synedra minutissima* var. *pelliculosa* Kützing

Reference: Lange-Bertalot [7] (p. 110, Figs. 1-11; p. 112, Fig. 1: 148)

Dimensions: Valve length 9.2-11.04  $\mu\text{m}$ , breadth 4.52-5.75  $\mu\text{m}$ .

Distribution in Serbia: CP87 Rača River, CP95 Jasik, CP95 Bioštanska Banja and CP95 Ročnjak streams, CP95 Vrutci tributary 12 and 13 (Fig. 1, Table 1).

***Fragilaria pararumpens*** Lange-Bertalot, G.Hofmann and Werum (Fig. 4(5))

Basionym: *Fragilaria pararumpens* Lange-Bertalot, G.Hofmann and Werum

Reference: Hofmann et al. [26] (p. 8, Figs. 4-10: 269)  
Dimensions: Valve length 23.08-46.42  $\mu\text{m}$ , breadth 2.09-4.59  $\mu\text{m}$ , striae 17-19/10  $\mu\text{m}$ .  
Distribution in Serbia: EN48 Rasina, DN79 Raška, EQ40 Mlava and EP75 Radovanska rivers (Fig. 1, Table 1).

***Fragilaria radians*** (Kützing) D.M. Williams and Round (Fig. 4(4))

Basionym: *Synedra radians* Kützing

Reference: Hofmann et al. [26] (p. 7, Figs. 21-25: 274)

Dimensions: Valve length 33.19-47.22  $\mu\text{m}$ , breadth 3.44-4.25  $\mu\text{m}$ , striae 10-11/10  $\mu\text{m}$ .

Distribution in Serbia: EN48 Rasina, CP86 Rača and DN79 Raška rivers (Fig. 1, Table 1).

***Geissleria ignota*** (Krasske) Lange-Bertalot and Metzeltin (Fig. 3(25))

Basionym: *Navicula ignota* Krasske

Reference: Lange-Bertalot [7] (p. 97, Figs. 25-30; p. 98, Figs. 1, 2: 125)

Dimensions: Valve length 18.42  $\mu\text{m}$ , breadth 5  $\mu\text{m}$ , striae 12/10  $\mu\text{m}$ .

Distribution in Serbia: CP95 Simića potok stream (Fig. 1, Table 1).

***Geissleria paludosa*** (Hustedt) Lange-Bertalot and Metzeltin (Fig. 3(26))

Basionym: *Navicula paludosa* Hustedt

Reference: Lange-Bertalot [7] (p. 97, Figs. 16-20; p. 98, Fig. 3: 126)

Dimensions: Valve length 13.09-19.83  $\mu\text{m}$ , breadth 4.45-6.69  $\mu\text{m}$ , striae 13-17/10  $\mu\text{m}$ .

Distribution in Serbia: EQ40 Mlava, EP75 Radovanska and FN02 Vrla rivers (Fig. 1, Table 1).

***Gomphonema acidoclinatum*** Lange-Bertalot and Reichardt (Fig. 2(5))

Basionym: *Gomphonema acidoclinatum* Lange-Bertalot and Reichardt

Reference: Hofmann et al. [26] (p. 98, Figs. 28-32: 294)

Dimensions: Valve length 24.61-37.13  $\mu\text{m}$ , breadth 6.26-7.45  $\mu\text{m}$ , striae 14-16/10  $\mu\text{m}$ .

Distribution in Serbia: FN02 Vrla and CQ87 Zasavica rivers, CP95 Zaliv pritoke stream (Fig. 1, Table 1).

***Gomphonema calcifugum*** Lange-Bertalot and Reichardt (Fig. 2(11))

Basionym: *Gomphonema calcifugum* Lange-Bertalot and Reichardt

Reference: Levkov et al. [9] (p. 199, Figs. 29-53: 39)

Dimensions: Valve length 16.19  $\mu\text{m}$ , breadth 4.52  $\mu\text{m}$ , striae 12/10  $\mu\text{m}$ .

Distribution in Serbia: EQ40 Mlava River (Fig. 1, Table 1).

***Gomphonema clavatum*** Reichardt (Fig. 2(4))

Basionym: *Gomphonema clavatum* Reichardt

Reference: Hofmann et al. [26] (p. 97, Figs. 7-9: 300)

Dimensions: Valve length 21-32.28  $\mu\text{m}$ , breadth 5.72-6.6  $\mu\text{m}$ , striae 11-12/10  $\mu\text{m}$ .

Distribution in Serbia: CP95 Cvetića zaliv stream, DQ58 Velika Slatina, DR43 Okanj bara and DR54 Novo Ilje I salt marshes (Fig. 1, Table 1).

***Gomphonema cymbelliclinum*** Reichardt and Lange-Bertalot (Fig. 2(7); Fig. 5(1))

Basionym: *Gomphonema cymbelliclinum* Reichardt and Lange-Bertalot

Reference: Reichardt [33] (p. 39, Figs. 11-14, 24-26; p. 40; p. 41: Figs. 10-17: 36)

Dimensions: Valve length 19.97-36.81  $\mu\text{m}$ , breadth 5.18-6.88  $\mu\text{m}$ , striae 10-15/10  $\mu\text{m}$ .

Distribution in Serbia: EN48 Rasina, CP86 Rača, DN79 Raška, CP95 Đetinja, EQ40 Mlava, FN02 Vrla, EP75 Radovanska, CP66/76 Karaklijski Rzav, CP66/76 Batarski Rzav and CP79. CP87 Drina rivers, CP95 Cvetića potok, CP95 Simića potok, CP95 Jasik, CP95 Jovac, CP95 Konjski potok, and CP95 Ročnjak streams, CP95 Vrutci tributary 10, 12 and 13, DP18 Divčibare, EP50 Bresnica and DQ60 Bukulja accumulations (Fig. 1, Table 1).

***Gomphonema drutelingense*** Reichardt (Fig. 2(6))

Basionym: *Gomphonema drutelingense* Reichardt

Reference: Reichardt [33] (p. 39, Figs. 21-23; p. 42: 38)

Dimensions: Valve length 19.32-40.26  $\mu\text{m}$ , breadth 6.48-8.96  $\mu\text{m}$ , striae 10-14/10  $\mu\text{m}$ .

Distribution in Serbia: EN48 Rasina, CP86 Rača, EQ40 Mlava, FN02 Vrla, CP76 Vrelo rivers, CP95 Jasik, CP95 Bioštanska Banja and CP95 Ročnjak streams, CP95 Vrutci tributary 13 (Fig. 1, Table 1).

***Gomphonema extentum*** Reichardt and Lange-Bertalot (Fig. 2(3))

Basionym: *Gomphonema extentum* Reichardt and Lange-Bertalot

Reference: Hofmann et al. [26] (p. 97, Figs. 21, 22: 306)

Dimensions: Valve length 21.37-40.04  $\mu\text{m}$ , breadth 6.15-8.2  $\mu\text{m}$ , striae 11-13/10  $\mu\text{m}$ .

Distribution in Serbia: CP95 Đetinja and FN02 Vrla rivers, CP95 Zaliv pritoke stream (Fig. 1, Table 1).

***Gomphonema lagenula*** Kützing (Fig. 2(14))

Basionym: *Gomphonema lagenula* Kützing

Reference: Levkov et al. [9] (p. 102, Figs. 39-47: 71)

Dimensions: Valve length 18.89-34.37  $\mu\text{m}$ , breadth 5.61-9.92  $\mu\text{m}$ , striae 11-14/10  $\mu\text{m}$ .

Distribution in Serbia: EN48 Rasina, FN02 Vrla, EQ40 Mlava, DP39 Toplica, DQ50 Kačer and DQ31 Kolubara rivers, CR62 Danube-Tisa-Danube Canal (Bač), DP76/86 Gruža accumulation (Fig. 1, Table 1).

***Gomphonema lippertii*** Reichardt and Lange-Bertalot (Fig. 2(2))

Basionym: *Gomphonema lippertii* Reichardt and Lange-Bertalot

Reference: Hofmann et al. [26] (p. 98, Figs. 1-5: 295)

Dimensions: Valve length 36.63-53.1  $\mu\text{m}$ , breadth 9.19-10.32  $\mu\text{m}$ , striae 11-13/10  $\mu\text{m}$ , punctae 24/10  $\mu\text{m}$ .

Distribution in Serbia: DN79 Raška River (Fig. 1, Table 1).

***Gomphonema procerum*** Reichardt and Lange-Bertalot (Fig. 2(8))

Basionym: *Gomphonema procerum* Reichardt and Lange-Bertalot

Reference: Hofmann et al. [26] (p. 96, Fig. 27: 313)

Dimensions: Valve length 37.91-40.14  $\mu\text{m}$ , breadth 5-6.44  $\mu\text{m}$ , striae 10-11/10  $\mu\text{m}$ .

Distribution in Serbia: CP86 Rača, DN79 Raška and EQ40 Mlava rivers (Fig. 1, Table 1).

***Gomphonema saprophilum*** (Lange-Bertalot and Reichardt) Abraca, R.Jahn, J.Zimmermann and Enke (Fig. 2(12))

Basionym: *Gomphonema parvulum* f. *saprophilum* Lange-Bertalot and Reichardt

Reference: Levkov et al. [9] (p. 104, Figs. 25-33: 116)

Dimensions: Valve length 11.66-34  $\mu\text{m}$ , breadth 5.4-8  $\mu\text{m}$ , striae 9-16/10  $\mu\text{m}$ .

Distribution in Serbia: EN48 Rasina, EP75 Radovanska, FN02 Vrla, EP17 Belica, EP33 Zapadna Morava, DQ75 Ponjavica (Omoljica), DQ85 Ponjavica (Brestovac), DQ31 Kolubara and DR22 Jegrička rivers, CR57 Danube-Tisa-Danube (Sombor) and DR24 Danube-Tisa-Danube (Bačko Gradište) canals, DQ58 Velika Slatina, DQ58 Gergina Slatina, DR28 Kerekszék and DR54 Novo Ilje I salt marshes (Fig. 1, Table 1).

***Gomphonema sphenovortex*** Lange-Bertalot and Reichardt (Fig. 2(13))

Basionym: *Gomphonema sphenovortex* Lange-Bertalot and Reichardt

Reference: Hofmann et al. [26] (p. 98, Figs. 26, 27: 315)

Dimensions: Valve length 16.62-19.84  $\mu\text{m}$ , breadth 4.79-5.94  $\mu\text{m}$ , striae 13-14/10  $\mu\text{m}$ .

Distribution in Serbia: DN79 Raška and EQ40 Mlava rivers (Fig. 1, Table 1).

***Gomphonema zellense*** Reichardt (Fig. 2(1))

Basionym: *Gomphonema zellense* Reichardt

Reference: Reichardt [33] (p. 5: 11)

Dimensions: Valve length 41.57-61.39  $\mu\text{m}$ , breadth 9.58-11.54  $\mu\text{m}$ , striae 8-10/10  $\mu\text{m}$ , areolae 22-26/10  $\mu\text{m}$ .

Distribution in Serbia: CP86 Rača River (Fig. 1, Table 1).

***Hantzschia calcifuga*** Reichardt and Lange-Bertalot (Fig. 3(1))

Basionym: *Hantzschia calcifuga* Reichardt and Lange-Bertalot

Reference: Werum and Lange-Bertalot [34] (p. 96, Figs. 1-6; p. 97, Figs. 1-4: 63)  
Dimensions: Valve length 81.4 µm, breadth 6.44 µm, fibulae 6/10 µm, striae 22/10 µm.  
Distribution in Serbia: CP95 Krnda 2 stream (Fig. 1, Table 1).  
***Halumphora normanii*** (Rabenhorst) Levkov (Fig. 2(27, 28))  
Basionym: *Amphora normanii* Rabenhorst  
Reference: Levkov [30] (p. 94, Figs. 1-8, 28-32: 208)  
Dimensions: Valve length 26.73-38.21 µm, frustule breadth 13.63-15.92 µm, striae 18-26/10 µm.  
Distribution in Serbia: EN48 Rasina, CP86 Rača and DN79 Raška rivers, CP95 Jasik stream and CP95 Vrutci tributary 13 (Fig. 1, Table 1).  
***Halumphora veneta*** (Kützing) Levkov (Fig. 2(25, 26))  
Basionym: *Amphora veneta* Kützing  
Reference: Levkov [30] (p. 94, Figs. 9-19; p. 102, Figs. 17-30; p. 217, Figs. 1-5; p. 218, Figs. 1-5: 242)  
Dimensions: Valve length 21.18-31.3 µm, valve breadth 4.75-5.29 µm, frustule breadth 10.47-13.63 µm, striae 20-23/10 µm.  
Distribution in Serbia: CQ87 Zasavica River, CP95 Zaliv pritoke stream (Fig. 1, Table 1).  
***Humidophila brekkaensis*** (Petersen) Lowe, Kociolek, Johansen, Van de Vijver, Lange-Bertalot and Kopalová (Fig. 3(30))  
Basionym: *Navicula brekkaensis* J.B.Petersen  
Reference: Werum and Lange-Bertalot [34] (p. 58, Figs. 1-13; p. 62, Figs. 30-32: 135)  
Dimensions: Valve length 19.63 µm, breadth 3.51 µm, striae 24-25/10 µm.  
Distribution in Serbia: CP95 Simića potok stream (Fig. 1, Table 1).  
***Humidophila irata*** (Krasske) Lowe, Kociolek, Johansen, Van de Vijver, Lange-Bertalot and Kopalová (Fig. 3(29))  
Basionym: *Navicula irata* Krasske  
Reference: Werum and Lange-Bertalot [34] (p. 62, Figs. 39, 40: 137)  
Dimensions: Valve length 14.98-23.07 µm, breadth 3.24-3.92 µm, striae 28-32/10 µm.  
Distribution in Serbia: EN48 Rasina River, CP95 Krnda 2 stream (Fig. 1, Table 1).  
***Humidophila paracontenta*** (Lange-Bertalot and Werum) Lowe, Kociolek, Johansen, Van de Vijver, Lange-Bertalot and Kopalová (Fig. 3(27, 28))  
Basionym: *Diadesmis paracontenta* Lange-Bertalot and Werum  
Reference: Werum and Lange-Bertalot [34] (p. 59, Figs. 1-11; p. 62, Figs. 15-17: 138)  
Dimensions: Valve length 9.98-10.25 µm, breadth 2.43-2.6 µm.  
Distribution in Serbia: EN48 Rasina River, CP95 Jasik and CP95 Konjski potok streams (Fig. 1, Table 1).  
***Kurtkammeria recta*** (Krammer) L.Bahls (Fig. 2(22))  
Basionym: *Encyonopsis recta* Krammer  
Reference: Krammer [32] (p. 165, Figs. 12-14; p. 166, Figs. 4-12: 132)  
Dimensions: Valve length 32.05 µm, breadth 5.67 µm, striae 15/10 µm.  
Distribution in Serbia: EN48 Rasina River (Fig. 1, Table 1).  
***Luticola acidoclinata*** Lange-Bertalot (Fig. 3(39))  
Basionym: *Luticola acidoclinata* Lange-Bertalot  
Reference: Levkov et al. [35] (p. 18, Figs. 1-46; p. 19, Figs. 1-7: 52)  
Dimensions: Valve length 10.12-28.6 µm, breadth 5.61-8.74 µm, striae 19-23/10 µm.  
Distribution in Serbia: EQ40 Mlava, FN02 Vrla and EP75 Radovanska rivers, CP95 Cvetića zaliv stream (Fig. 1, Table 1).  
***Luticola paramutica*** (W.Bock) D.G.Mann (Fig. 3(38))  
Basionym: *Navicula paramutica* W.Bock  
Reference: Levkov et al. [35] (p. 12, Figs. 17-23; p. 32, Figs. 23-39: 182)



Dimensions: Valve length 16.54-16.73  $\mu\text{m}$ , breadth 5.83-6.68  $\mu\text{m}$ , striae 19-20/10  $\mu\text{m}$ .  
Distribution in Serbia: CP95 Zaliv pritoke stream, CP93 Zlatibor accumulation (Fig. 1, Table 1).

***Luticola triundulata*** Levkov, Metzeltin and A.Pavlov (Fig. 3(37))

Basionym: *Navicula paramutica* W.Bock

Reference: Levkov et al. [35] (p. 178, Figs. 19-30; p. 180, Figs. 5-8: 240)

Dimensions: Valve length 24  $\mu\text{m}$ , breadth 7.29  $\mu\text{m}$ , striae 17/10  $\mu\text{m}$ .

Distribution in Serbia: EQ40 Mlava River (Fig. 1, Table 1).

***Luticola ventriconfusa*** Lange-Bertalot (Fig. 3(36))

Basionym: *Luticola ventriconfusa* Lange-Bertalot

Reference: Levkov et al. [35] (p. 190, Figs. 1-57; p. 191, Figs. 1-6: 250)

Dimensions: Valve length 15.87-22.94  $\mu\text{m}$ , breadth 6.48-7.69  $\mu\text{m}$ , striae 19-21/10  $\mu\text{m}$ , areolae 15/10  $\mu\text{m}$ .

Distribution in Serbia: DN79 Raška River, CP95 Jovac stream (Fig. 1, Table 1).

***Mayamaea fossalis*** (Krasske) Lange-Bertalot (Fig. 2(19))

Basionym: *Navicula fossalis* Krasske

Reference: Lange-Bertalot [7] (p. 104, Figs. 25-30: 138)

Dimensions: Valve length 9.78  $\mu\text{m}$ , breadth 3.64  $\mu\text{m}$ , striae 23/10  $\mu\text{m}$ .

Distribution in Serbia: CP95 Krnda 2 stream (Fig. 1, Table 1).

***Microfissurata australis*** Van de Vijver and Lange-Bertalot (Fig. 2(9, 10))

Basionym: *Microfissurata australis* Van de Vijver and Lange-Bertalot

Reference: Cantonati et al. [36] (Fig. 2: 735)

Dimensions: Valve length 15.28  $\mu\text{m}$ , breadth 3.3  $\mu\text{m}$ .

Distribution in Serbia: CP95 Ročnjak stream (Fig. 1, Table 1).

***Naviculadicta absoluta*** (Hustedt) Lange-Bertalot (Fig. 3(24))

Basionym: *Navicula absoluta* Hustedt

Reference: Hofmann et al. [26] (p. 42, Figs. 62-66: 411)

Dimensions: Valve length 17  $\mu\text{m}$ , breadth 4.59  $\mu\text{m}$ , striae 22/10  $\mu\text{m}$ .

Distribution in Serbia: EN48 Rasina River (Fig. 1, Table 1).

***Naviculadicta vitabunda*** (Hustedt) Lange-Bertalot (Fig. 3(22, 23))

Basionym: *Navicula vitabunda* Hustedt

Reference: Hofmann et al. [26] (p. 42, Figs. 67-71: 412)

Dimensions: Valve length 13.44  $\mu\text{m}$ , breadth 5.81  $\mu\text{m}$ , striae 27/10  $\mu\text{m}$ .

Distribution in Serbia: DN79 Raška River (Fig. 1, Table 1).

***Nitzschia acidoclinata*** Lange-Bertalot (Fig. 3(7))

Basionym: *Nitzschia acidoclinata* Lange-Bertalot

Reference: Hofmann et al. [26] (p. 112, Figs. 50-54: 431)

Dimensions: Valve length 14.25-20.96  $\mu\text{m}$ , breadth 2.56-3.02  $\mu\text{m}$ , fibulae 11-12/10  $\mu\text{m}$ , striae 11/10  $\mu\text{m}$ , fibulae 24/10  $\mu\text{m}$ .

Distribution in Serbia: CP95 Zaliv pritoke stream, FN02 Vrla River, CP93 Zlatibor accumulation (Fig. 1, Table 1).

***Nitzschia bryophila*** (Hustedt) Hustedt (Fig. 3(8))

Basionym: *Nitzschia frustulum* var. *bryophila* Hustedt

Reference: Krammer and Lange-Bertalot [37] (p. 74, Figs. 27-29; 103)

Dimensions: Valve length 12.2-21.37  $\mu\text{m}$ , breadth 3.44-4.5  $\mu\text{m}$ , fibulae 8-13/10  $\mu\text{m}$ , striae 30/10  $\mu\text{m}$ .

Distribution in Serbia: EQ40 Mlava, CP79 Drina and CP82 Lim rivers, DP18 Divčibare accumulation (Fig. 1, Table 1).

***Nitzschia draveillensis*** Coste and Ricard (Fig. 3(3))

Basionym: *Nitzschia draveillensis* Coste and Ricard

Reference: Hofmann et al. [26] (p. 106, Fig. 13: 463)

Dimensions: Valve length 34.34-64.36  $\mu\text{m}$ , breadth 2.23-2.7  $\mu\text{m}$ , fibulae 21/10  $\mu\text{m}$ .

Distribution in Serbia: EN48 Rasina and FN03 Vlasina rivers (Fig. 1, Table 1).

***Nitzschia palea* var. *debilis*** (Kützing) Grunow (Fig. 3(6))

Basionym: *Synedra debilis* Kützing

Reference: Hofmann et al. [26] (p. 111, Figs. 10-13: 455)

Dimensions: Valve length 16.53-27.94  $\mu\text{m}$ , breadth 2.43-3.72  $\mu\text{m}$ , fibulae 12-17/10  $\mu\text{m}$ .

Distribution in Serbia: EN48 Rasina River, CP93 Zlatibor accumulation (Fig. 1, Table 1).

***Nitzschia palea* var. *tenuirostris*** Grunow (Fig. 3(4))

Basionym: *Nitzschia palea* var. *tenuirostris* Grunow

Reference: Hofmann et al. [26] (p. 111, Figs. 14-20: 455)

Dimensions: Valve length 31.41-39.5  $\mu\text{m}$ , breadth 3.24-4.64  $\mu\text{m}$ , fibulae 15-16/10  $\mu\text{m}$ .

Distribution in Serbia: EN48 Rasina, FN02 Vrla, DP26 Zapadna Morava, DQ75 Ponjavica (Omoljica) and DQ85 Ponjavica (Brestovac) rivers, DQ58 Gergina Slatina and DR44 Jaruge salt marshes (Fig. 1, Table 1).

***Nitzschia solgensis*** Cleve-Euler (Fig. 3(9))

Basionym: *Nitzschia solgensis* Cleve-Euler

Reference: Hofmann et al. [26] (p. 117, Figs. 21-25: 461)

Dimensions: Valve length 9.99-12.64  $\mu\text{m}$ , breadth 3.17-3.24  $\mu\text{m}$ , fibulae 8-10/10  $\mu\text{m}$ .

Distribution in Serbia: EN48 Rasina River (Fig. 1, Table 1).

***Nitzschia suchlandtii*** Hustedt (Fig. 3(5))

Basionym: *Nitzschia suchlandtii* Hustedt

Reference: Krammer and Lange-Bertalot [37] (p. 66, Figs. 12-16; 93)

Dimensions: Valve length 22.74-33.46  $\mu\text{m}$ , breadth 3.46-3.59  $\mu\text{m}$ , fibulae 11-16/10  $\mu\text{m}$ .

Distribution in Serbia: EN48 Rasina River (Fig. 1, Table 1).

***Nitzschia vermicularoides*** Lange-Bertalot (Fig. 3(2))

Basionym: *Nitzschia vermicularoides* Lange-Bertalot

Reference: Hofmann et al. [26] (p. 115, Figs. 4-6: 468)

Dimensions: Valve length 77.53-78.08  $\mu\text{m}$ , breadth 4.5  $\mu\text{m}$ , fibulae 14/10  $\mu\text{m}$ .

Distribution in Serbia: EQ40 Mlava River (Fig. 1, Table 1).

***Pinnularia grunowii*** Krammer (Fig. 4(2))

Basionym: *Pinnularia grunowii* Krammer

Reference: Krammer [38] (p. 77, Figs. 7-14; p. 81, Figs. 10-17; p. 82, Fig. 7,8: 100, 222)

Dimensions: Valve length 33.46-53  $\mu\text{m}$ , breadth 8.31-10.59  $\mu\text{m}$ , striae 12-14/10  $\mu\text{m}$ .

Distribution in Serbia: EQ40 Mlava, FN02 Vrla and DQ31 Kolubara rivers (Fig. 1, Table 1).

***Pinnularia isselana*** Krammer (Fig. 4(3))

Basionym: *Pinnularia isselana* Krammer

Reference: Krammer [38] (p. 103, Figs. 1-20: 132)

Dimensions: Valve length 33.6-46.3  $\mu\text{m}$ , breadth 7.15-8.63  $\mu\text{m}$ , striae 12-13/10  $\mu\text{m}$ .

Distribution in Serbia: FN02 Vrla and EP75 Radovanska rivers, CP95 Krnda 2 and CP95 Zaliv pritoke streams (Fig. 1, Table 1).

***Pinnularia peracuminata*** Krammer (Fig. 4(1))

Basionym: *Pinnularia peracuminata* Krammer

Reference: Krammer [38] (p. 142, Figs. 1-10: 157)

Dimensions: Valve length 54-61.32  $\mu\text{m}$ , breadth 11-12.96  $\mu\text{m}$ , striae 10-11/10  $\mu\text{m}$ .

Distribution in Serbia: DN79 Raška River, DQ58 Aleksića Slatina salt marsh (Fig. 1, Table 1).

***Placoneis hambergii*** (Hustedt) K.Bruder (Fig. 4(7))

Basionym: *Navicula hambergii* Hustedt

Reference: Krammer and Lange-Bertalot [25] (p. 50, Figs. 9-13: 146)

Dimensions: Valve length 14.91-19.05  $\mu\text{m}$ , breadth 6.68-7.56  $\mu\text{m}$ , striae 16-17/10  $\mu\text{m}$ .

Distribution in Serbia: EN48 Rasina River (Fig. 1, Table 1).

***Planothidium biporomum*** (Hohn and Hellerman) Lange-Bertalot (Fig. 4(8, 9))

Basionym: *Achnanthes biporoma* Hohn and Hellerman

Reference: Wetzel et al. [39] (Figs. 1-18, 37-50: 45)

Dimensions: Valve length 16.42-18.24  $\mu\text{m}$ , breadth 5.2-5.83  $\mu\text{m}$ , striae 14-15/10  $\mu\text{m}$ .

Distribution in Serbia: EN48 Rasina, EQ40 Mlava and FN02 Vrla rivers (Fig. 1, Table 1).

***Planothidium reichardtii*** Lange-Bertalot and Werum (Fig. 4(10, 11))

Basionym: *Planothidium reichardtii* Lange-Bertalot and Werum

Reference: Werum and Lange-Bertalot [34] (p. 15, Figs. 9-18: 172)

Dimensions: Valve length 11.94-14.03  $\mu\text{m}$ , breadth 5.06-5.8  $\mu\text{m}$ , striae 14-18/10  $\mu\text{m}$ .

Distribution in Serbia: DN79 Raška river (Fig. 1, Table 1).

***Psammothidium bioretii*** (H.Germain) Bukhtiyarova and Round (Fig. 4(16, 17))

Basionym: *Achnanthes bioretii* H.Germain

Reference: Hofmann et al. [26] (p. 26, Figs. 12-16: 519)

Dimensions: Valve length 12.08-18.35  $\mu\text{m}$ , breadth 5.46-8.85  $\mu\text{m}$ , striae 23-27/10  $\mu\text{m}$ .

Distribution in Serbia: EN48 Rasina, EP75 Radovanska and FN02 Vrla rivers, CP95 Zaliv pritoke stream (Fig. 1, Table 1).

***Psammothidium grischunum*** (Wuthrich) L.Bukhtiyarova and Round (Fig. 4(18, 19))

Basionym: *Achnanthes grishuna* Wuthrich

Reference: Hofmann et al. [26] (p. 26, Figs. 33-37: 521)

Dimensions: Valve length 8.1-13.57  $\mu\text{m}$ , breadth 3.51-5.18  $\mu\text{m}$ , striae of raphe valve 21-28/10  $\mu\text{m}$ , striae of rapheless valve 24-26/10  $\mu\text{m}$ .

Distribution in Serbia: EN48 Rasina and CP76 Vrelo rivers, CP95 Cvetića potok stream (Fig. 1, Table 1).

***Psammothidium lauenburgianum*** (Hustedt) Monnier, Lange-Bertalot (Fig. 4(20-23))

Basionym: *Achnanthes lauenburgiana* Hustedt

Reference: Hofmann et al. [26] (p. 26, Figs. 55-59: 522)

Dimensions: Valve length 7.22-17.47  $\mu\text{m}$ , breadth 3.91-6.07  $\mu\text{m}$ , striae of raphe valve 23-29/10  $\mu\text{m}$ .

Distribution in Serbia: EQ40 Mlava River, Vrutci tributary 12 (Fig. 1, Table 1).

***Reimeria uniseriata*** (W.Gregory) Kociolek and Stoermer (Fig. 3(32, 33))

Basionym: *Cymbella sinuata* W.Gregory

Reference: Sala et al. [40] (Figs. 2-10: 445)

Dimensions: Valve length 11.2-26.24  $\mu\text{m}$ , breadth 3.92-6.21  $\mu\text{m}$ , striae 7-16/10  $\mu\text{m}$ , areolae 20-24/10  $\mu\text{m}$ .

Distribution in Serbia: EN48 Rasina, CP86 Rača, DN79 Raška, CP95 Đetinja and EP75 Radovanska rivers, CP95 Cvetića zaliv, CP95 Cvetića potok, CP95 Simića potok, CP95 Jasik, CP95 Jovac, CP95 Bioštanska Banja, CP95 Konjski potok and CP95 Ročnjak streams, Vrutci tributary 12 and 13 (Fig. 1, Table 1).

***Sellaphora mutatoides*** Lange-Bertalot and Metzeltin (Fig. 3(34, 35))

Basionym: *Sellaphora mutatoides* Lange-Bertalot and Metzeltin

Reference: Hofmann et al. [26] (p. 42, Figs. 1-4: 535)

Dimensions: Valve length 23.22-23.27  $\mu\text{m}$ , breadth 7.48-8.71  $\mu\text{m}$ , striae 19-21/10  $\mu\text{m}$ .

Distribution in Serbia: EN48 Rasina and CQ87 Zasavica rivers (Fig. 1, Table 1).

***Simonsenia delognei*** (Grunow) Lange-Bertalot (Fig. 3(10))

Basionym: *Nitzschia delognei* Grunow

Reference: Hofmann et al. [26] (p. 117, Figs. 47-50: 540)

Dimensions: Valve length 8.98-14.23  $\mu\text{m}$ , breadth 2.16-3.11  $\mu\text{m}$ , striae 16-19/10  $\mu\text{m}$ .

Distribution in Serbia: CP86 Rača and EP75 Radovanska rivers (Fig. 1, Table 1).

***Surirella terricola*** Lange-Bertalot and E.Alles (Fig. 3(31))

Basionym: *Surirella terricola* Lange-Bertalot and E. Alles

Reference: Lange-Bertalot and Metzeltin [6] (p. 77, Figs. 15-19; p. 106, Fig. 16:107)

Dimensions: Valve length 17.61-22.34  $\mu\text{m}$ , breadth 7.17-8.16  $\mu\text{m}$ , striae 4.5-8/10  $\mu\text{m}$ .

Distribution in Serbia: CP86 Rača River and CP95 Krnda 2 stream (Fig. 1, Table 1).

## DISCUSSION

On the territory of Serbia, c. 800 diatom taxa have been recorded to date (unpublished database of Serbian diatom flora, Krizmanić). The diversity of diatoms in Serbia is relatively low as compared to other European countries, e.g. only in two lakes in Macedonia (Lakes Ohrid and Prespa) 919 taxa were recorded [14]. The number of diatom taxa in Serbia is very similar to the number of recorded taxa in Turkey (more than 800), although Turkey is much larger than Serbia [41]. The highest number of recorded taxa in Serbia is widespread and common in European, Asian, North and South American freshwaters [7,41-43]. The results of this study are based on 55 different localities (rivers, streams, channels, accumulations and salt marshes) and have expanded the diatom checklist with 80 new recorded taxa. The reasons for the constant increase in the number of recorded diatom taxa are numerous, such as improved light microscope resolution and digital cameras with accompanying software, and the increasing use of scanning electron microscopy (SEM), which have enabled the description of a great number of new taxa as well as the separation of new taxa from *sensu lato* species.

One third of our identified taxa are diatoms with a small cell size, and belong to the genera *Achnantheidium*, *Adlafia*, *Fistulifera*, *Humidophila*, *Mayamaea* and *Psammothidium*. The recently described new taxa, *Achnantheidium crassum* and *Achnantheidium druartii* [27,28], are separated from the *A. pyrenaicum* group. *A. pyrenaicum* was described *Achnantheidium* for the first time by Obušković [44], but it is only now these taxa have provided new records. This example illustrates how a better understanding of SEM is important in diatom diversity investigations. Also, SEM has led to a marked distinction of the genus *Humidophila* from *Diademsis* and the description of new taxa, *H. irata* and *H. brekkaensis* [45], which are new records for Serbian diatom flora.

The small-sized genus, *Microfissurata*, with its unique combination of morphological characteristics, was described using both light and SEM. It includes only two species, *M. paludosa* and *M. australis* [36]. *M. australis* was recorded at Ročnjak stream in an epilithic community, a small-discharge stream affected by seasonal desiccation. However, literature data indicate epiphytic and epipellic as the community types, but not epilithic [36]. Distinguishing between the *Fistulifera pelliculosa* form and *F. saprophila* is hardly possible without the use of SEM due to its very small dimensions (8.9-12.5  $\mu\text{m}$ , breadth 4-6.2  $\mu\text{m}$ ) and specific morphological valve features (numerous copulae of the girdle) [7]. Our findings of *Fistulifera* correlate with literature data.

In almost all investigated Serbian freshwaters from 1984 to 2016, *Reimeria sinuata* has been recorded [22,44,46,47]. Although more than 15 years ago a related species, *R. uniseriata*, was identified [40], it has not been recorded on the territory of Serbia until now. The widespread use of high-resolution light microscopes in Serbia is probably the reason leading to an increased insight into the main characteristics of this species, its uniseriate striae, in contrast to *R. sinuata*, which has biseriata striae.

This study has contributed a diatom checklist and provides a fuller insight of diatom diversity in Serbia. As the potential diversity of diatoms in Serbia is probably higher, this type of research is very important. Also, further detailed investigation, especially with SEM, may identify new interesting taxa for the diatom flora of Serbia.

**Acknowledgments:** Financial support was provided by the Ministry of Education, Science and Technological Development of the Republic of Serbia (Project No. TR 037009).

**Authors' contribution:** All authors have contributed to the fieldwork, elaboration of the data, the writing process and the discussion of the results.

**Conflict of interest disclosure:** The authors declare no conflict of interest.

## REFERENCES

1. Borics G, Görgényi J, Grigorszky I, László-Nagy Zs, Tóthmérész B, Krasznai E, Várbíró G. The role of phytoplankton diversity metrics in shallow lake and river quality assessment. *Ecol Indic.* 2014;45:28-36.
2. Ács É, Szabó K, Tóth B, Kiss KT. Investigation of benthic algal communities, especially diatoms of some Hungarian streams in connection with reference conditions of the Water Framework Directives. *Acta Bot Hung.* 2004;46:255-77.
3. Solak CN, Kaleli A, Baytut Ö. The Distribution of Cymbelloid Diatoms in Yalova Runningwaters. *Turk J Fish Aquat Sc.* 2016;16(4):953-9.
4. Thomé O. Flora von Deutschland, Österreich und der Schweiz in Wort und Bild. Band VI. Kryptogamen-Flora: Moose, Algen, Flechten und Pilze (die Farne befinden sich in Band I) ca. 30000 Arten und Varietäten bearbeitet von Dr. W. Migula. Bd. II Algen. 1. Teil. *Cyanophyceae, Diatomaceae, Chlorophyceae.* Gera: Friedrich von Zetzschwitz Verlag für Botanik „Flora von Deutschland“; 1907. 918 p.
5. Hustedt F. Bacillariophyta (Diatomae). In: Pascher A, editor. Die Süßwasser-Flora Mitteleuropas 10. Jena, Germany: Verlag von Gustav Fischer; 1930. 466 p.
6. Lange-Bertalot H, Metzeltin D. Indicators of oligotrophy. 800 taxa representative of three ecologically distinct lake types, carbonate buffered-Oligodystrophic-weakly buffered soft water. *Iconographia Diatomologica* 2. Königstein, Germany : Koeltz Scientific; 1996. 390 p.
7. Lange-Bertalot H. *Navicula* sensu stricto. 10 genera separated from *Navicula* sensu lato. *Frustulia.* In: Lange-Bertalot H, editor. Diatoms of Europe: diatoms of the European inland waters and comparable habitats Vol. 2. Ruggell: A.R.G. Gantner Verlag. K.G.; 2001. 526 p.
8. Krammer K. *Cymbella.* In: Lange-Bertalot H, editor. Diatoms of Europe, diatoms of the European inland waters and comparable habitats Vol. 3. Ruggell: A.R.G. Gantner Verlag K.G.; 2002. 584 p.
9. Levkov Z, Mitic-Kopanja D, Reichardt E. The diatom genus *Gomphonema* in the Republic of Macedonia. In: Lange-Bertalot H, editor. Diatoms of Europe. Diatoms of the European inland waters and comparable habitats. Vol. 8. Oberreifenberg: Koeltz Botanical Books; 2016. 552 p.
10. Pavlov A, Levkov Z. Diversity and distribution of taxa in the genus *Eunotia* Ehrenberg (Bacillariophyta) in Macedonia. *Phytotaxa.* 2013;86(1):1-117.
11. Van Dam H, Mertens A, Sinkeldam J. A coded checklist and ecological indicator values of freshwater diatoms from the Netherlands. *Aquat Ecol.* 1994;28(1):117-33.
12. Wojtal AZ. The Diatoms of Kobylanka Stream Near Kraków (Wyżyna Krakowsko-Częstochowska Upland, S Poland). *Pol Bot J.* 2009;54(2):129-330.
13. Cantonati M, Corradini G, Juettner I, Cox EJ. Diatom assemblages in high mountain streams of the Alps and the Himalaya. *Nova Hedwigia.* 2001;123:37-61.
14. Levkov Z, Williams DM. Checklist of diatoms (Bacillariophyta) from Lake Ohrid and Lake Prespa (Macedonia), and their watersheds. *Phytotaxa.* 2012;45(1):1-76.
15. Kókai Z, Bácsi I, Török P, Buczkó K, Krasznai E, Balogh C, Tóthmérész B, Béres V. Halophilic diatom taxa are sensitive indicators of even short term changes in lowland lotic systems. *Acta Bot Croat.* 2015;74:1-16.
16. Schaarschmidt J. *Fragmenta Phycologiae Bosniaco-Serbicae.* Magyar Növénytani Lapok. 1883;75(7):33-9.
17. Cvijan M, Laušević R. Floristical study of algae of Vlasinsko Lake (Yugoslavia). *Bull Nat Hist Mus.* 1991;46:57-69.
18. Laušević R. Floristical composition of algae in the Samokovska river. *Arch Biol Sci.* 1993;45(3-4):125-36.
19. Laušević R, Nikitović J. Floristical composition of algae of Borsko jezero lake (Yugoslavia). *Bull Nat Hist Mus.* 1993-1994;48:73-81.
20. Jurišić I. Benthic algal community structure and water quality of the Zapadna Morava River Basin near Cacak. *Acta Agric Serb.* 2004;9:13-33.
21. Simić S. Algae from the Trgoviški Timok river (Serbia, Yugoslavia). *Glasnik Instituta za botaniku i botaničke bašte Univerziteta u Beogradu.* 1996;XXX:107-18.
22. Andrejić J, Krizmanić J, Cvijan M. Diatom species composition of the Nišava River and its tributaries Jerma and Temska Rivers (Southern Serbia). *Arch Biol Sci.* 2012;64:1127-40.

23. Vidaković D, Krizmanić J, Šovran S, Stojanović K, Đorđević J. Diatom species composition of the Raška River (Southwestern Serbia). *Matica Srpska J Nat Sci.* 2015;128:29-40.
24. Krizmanić J, Ilić M, Vidaković D, Subakov-Simić G, Petrović J, Cvetanović K. Diatoms of the Dojkinci River (Stara Planina Nature Park, Serbia). *Acta Bot Croat.* 2015;74:317-31.
25. Krammer K, Lange-Bertalot H. Bacillariophyceae. 1. Teil: Naviculaceae. In: Ettl H, Gerloff J, Heynig H, Mollenhauer D, editors. Süßwasserflora von Mitteleuropa 2/1, Jena: G. Fischer Verlag; 1986. 876 p.
26. Hofmann G, Werum M, Lange-Bertalot H. Diatomeen im Süßwasser – Benthos von Mitteleuropa. Bestimmungsflora Kieselalgen für die ökologische Praxis. Königstein: Koeltz Scientific Books; 2013. 908 p.
27. Potapova MG, Ponader KC. Two common North American diatoms, *Achnantheidium rivulare* sp. nov. and *A. deflexum* (Reimer) Kingston: morphology, ecology and comparison with related species. *Diatom Res.* 2004;19(1):33-57.
28. Rimet F, Couté A, Piuz A, Berthon V, Druart JC. *Achnantheidium druartii* sp. nov. (Achnanthes, Bacillariophyta), a new species invading European rivers. *Vie Milieu.* 2010;60(3):185-95.
29. Diatoms of the United States [Internet]. Boulder (USA): University of Colorado; c2007. *Achnantheidium latecephalum*; 2010 [cited 2017 Apr 25]; [about 3 screens]. Available from: [http://westerndiatoms.colorado.edu/taxa/species/achnantheidium\\_latecephalum](http://westerndiatoms.colorado.edu/taxa/species/achnantheidium_latecephalum)
30. Levkov Z. *Amphora* sensu lato. In: Lange-Bertalot H, editor. Diatoms of Europe: Diatoms of the European Inland Waters and Comparable Habitats Vol. 5. Ruggell: A.R.G. Gantner Verlag KG; 2009. 916 p.
31. Krammer K. Die cymbelloiden Diatomeen. Eine Monographie der weltweit bekannten Taxa. Teil 1. Allgemeines und *Encyonema* Part. *Bibliotheca Diatomologica* 36. Berlin-Stuttgart: J. Cramer; 1997. 382 p.
32. Krammer K. Die cymbelloiden Diatomeen. Eine Monographie der weltweit bekannten Taxa. Teil 2: *Encyonema* part., *Encyonopsis* und *Cymbellopsis*. *Bibliotheca Diatomologica* 37. Berlin-Stuttgart: J. Cramer; 1997. 469 p.
33. Reichardt E. Zur Revision der Gattung *Gomphonema*. Die Arten um *G. affine/insigne*, *G. angustatum/micropus*, *G. Acuminatum* sowie gomphonemoide Diatomeen aus dem Oberoligozän in Böhmen. *Iconographia Diatomologica* 8. Ruggell: A.R.G. Gantner Verlag KG; 1999. 203 p.
34. Werum M, Lange-Bertalot H. Diatoms in springs from Central Europe and elsewhere under the influence of hydrogeology and anthropogenic impacts. *Iconographia Diatomologica* 13. Ruggell: A.R.G. Gantner Verlag KG; 2004. 417 p.
35. Levkov Z, Metzeltin D, Pavlov A. *Luticola* and *Luticolopsis*. In: Lange-Bertalot H, editor. Diatoms of Europe. Diatoms of the European inland waters and comparable habitats. Volume 7. Königstein: Koeltz Scientific Books; 2013. 698 p.
36. Cantonati M, Van de Vijver B, Lange-Bertalot H. *Microfissurata* gen. nov. (Bacillariophyta), a new diatom genus from dystrophic and intermittently wet terrestrial habitats. *J Phycol.* 2009;45(3):732-41.
37. Krammer K, Lange-Bertalot H. Bacillariophyceae. 2. Teil: *Bacillariaceae*, *Epithemiaceae*, *Surirellaceae*. In: Ettl H, Gerloff J, Heynig H, Mollenhauer D, editors. Süßwasserflora von Mitteleuropa 2/2. G. Stuttgart, Jena: Fischer Verlag; 1998. 596 p.
38. Krammer K. The genus *Pinnularia*. In: Lange-Bertalot H, editor. Diatoms of the European inland waters and comparable habitats. Volume 1. Ruggell: A.R.G. Gantner Verlag KG; 2000. 703 p.
39. Wetzel CE, Van De Vijver B, Hoffmann L, Ector L. *Planothidium incuriatum* sp. nov. a widely distributed diatom species (Bacillariophyta) and type analysis of *Planothidium biporumum*. *Phytotaxa.* 2013;138(1):43-57.
40. Sala SE, Guerrero JM, Ferrario ME. Redefinition of *Reimeria sinuata* (Gregory) Kociolek and Stoermer and recognition of *Reimeria uniseriata* nov. spec. *Diatom Res.* 1993;8(2):439-46.
41. Solak CN, Kulikovskiy MS, Kaleli A, Gönülol A. Rare and new records of diatoms in Turkey from Kütahya flowing waters. *Oceanol Hydrobiol Stud.* 2016;45(4):564-87.
42. Stoermer EF, Kreis RG, Andresen NA. Checklist of diatoms from the Laurentian Great Lakes. II. *J Great Lakes Res.* 1999;25(3):515-66.
43. Metzeltin D, Lange-Bertalot H, García-Rodríguez F. Diatoms of Uruguay compared with other taxa from South America and elsewhere. *Iconographia Diatomologica* 15. Ruggell: A.R.G. Gantner Verlag KG; 2005. 736 p.
44. Obušević Lj. Saprobiološke karakteristike u ekosistemima tekućih voda. [dissertation]. [Novi Sad]: Faculty of Sciences, University of Novi Sad. 1984. 116 p.
45. Lowe RL, Kociolek P, Johansen JR, Vijver BVD, Lange-Bertalot H, Kopalová K. *Humidophila* gen. nov., a new genus for a group of diatoms (Bacillariophyta) formerly within the genus *Diademesmis*: species from Hawai'i, including one new species. *Diatom Res.* 2014;29(4):351-60.

46. Nikitović J, Laušević R. Benthic algae in the River Vlasina (Serbia, Yugoslavia). *Ekologija*. 1999;34(1-2):19-26.
47. Jakovljević O, Popović S, Vidaković D, Stojanović K, Krizmanić J. The application of benthic diatoms in waterquality assessment (Mlava River, Serbia). *Acta Bot Croat*. 2016;75(2):199-205.

**Table 1.** Investigated localities with UTM coordinate.

Localities	UTM coordinates	
Rasina River		EN48
Raška River		DN79
Rača River		CP87
Vrla River		FN02
Mlava River		EQ40
Radovanska River		EP75
Baturski Rzav River		CP66/76
Kolubara River		DQ31
Zapadna Morava River		DP26, EP33
Karaklijski Rzav River		CP66/76
Drina River		CQ64, CQ66, CP79, CP87
Jegrička River		DR22
Toplica River		DP39
Kačer River		DQ50
Lim River		CP82, CP90
Đetinja River		CP95
Vrelo River		CP76
Zasavica River		CQ87
Belica River		EP17
Ponjavica River (Omoljica)		DQ75
Ponjavica River (Brestovac)		DQ85
Vlasina River		FN03
Krnda 2 stream		CP95
Konjski potok stream		CP95
Cvetića zaliv stream		CP95
Cvetića potok stream		CP95
Zaliv pritoke stream		CP95
Simića stream		CP95
Jasik stream		CP95
Jovac stream		CP95
Bioštanska Banja stream		CP95
Ročnjak stream		CP95
Vrutci tributary 10		CP95
Vrutci tributary 12		CP95
Vrutci tributary 13		CP95
Garaši accumulation		DQ50
Kruščica accumulation		CP76
Bresnica accumulation		EP50
Gruža accumulation		DP76/86
Zlatibor accumulation		CP93
Divčibare accumulation		DP18
Vrutci accumulation		CP95
Pridvorica accumulation		EN29
Bukulja accumulation		DQ60
Danube-Tisa-Danube (Sombor)	Canal	CR57
Danube-Tisa-Danube (Bač)	Canal	CR62
Danube-Tisa-Danube (Novo Miloševo)	Canal	DR46
Danube-Tisa-Danube (Bačko Gradište)	Canal	DR24
Jaruge salt marsh		DR44
Okanj bara salt marsh		DR43
Velika Slatina salt marsh		DQ58
Novo Ilje I salt marsh		DR54
Gergina Slatina salt marsh		DQ58
Kerekszék salt marsh		DR28
Aleksića Slatina salt marsh		DQ58



## Figure Legends

**Fig. 1.** UTM map of Serbia with new recorded diatom taxa localities.

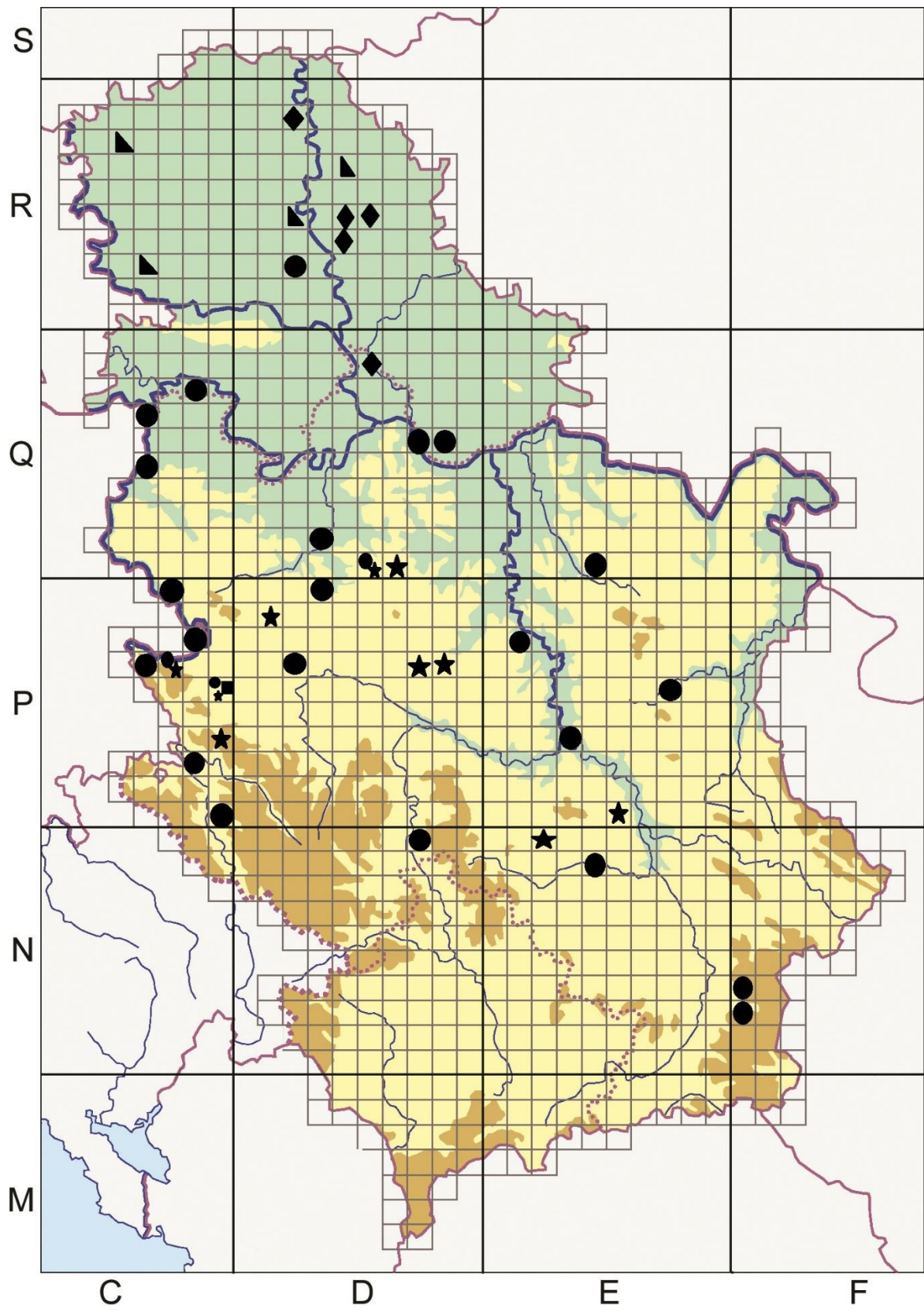
● – river; ■ – stream; ★ – accumulation; ▲ – canal; ◆ – salt marsh

**Fig. 2.** Light microscopy (LM) micrographs (x1600): 1 *Gomphonema zellense*; 2 *G. lippertii*; 3 *G. extentum*; 4 *G. clavatum*; 5 *G. acidoclinatum*; 6 *G. drutelingense*; 7 *G. cymbelliclinum*; 8 *G. procerum*; 9, 10 *Microfissurata australis*; 11 *G. calcifugum*; 12 *G. saprophilum*; 13 *G. sphenovortex*; 14 *G. lagenula*; 15 *Encyonema procerum*; 16 *E. subminutum*; 17 *E. brevicapitatum*; 18 *Chamaepinnularia muscicola*; 19 *Mayamaea fossalis*; 20 *Cocconeis pseudothumensis*; 21 *Cymbella lange-bertalotii*; 22 *Kurtkrammeria recta*; 23 *Encyonopsis cesatii*; 24 *E. krammeri*; 25, 26 *Halamphora veneta*; 27, 28 *H. normanii*. Scale bar=10 µm.

**Fig. 3.** Light microscopy (LM) micrographs (x1600): 1 *Hantzschia calcifuga*; 2 *Nitzschia vermicularoides*; 3 *N. draveillensis*; 4 *N. palea* var. *tenuirostris*; 5 *N. suchlandtii*; 6 *N. palea* var. *debilis*; 7 *N. acidoclinata*; 8 *N. bryophila*; 9 *N. solgensis*; 10 *Simonsenia delognei*; 11 *Craticula molestiformis*; 12 *Fistulifera pelliculosa*; 13, 14 *Adlafia minuscula*; 15 *A. minuscula* var. *muralis*; 16 *A. suchlandtii*; 17 *A. aquaeductae*; 18 *Fallacia insociabilis*; 19 *F. lenzii*; 20 *F. lange-bertalotii*; 21 *F. sublucidula*; 22, 23 *Naviculadicta vitabunda*; 24 *N. absoluta*; 25 *Geissleria ignota*; 26 *G. paludosa*; 27, 28 *Humidophila paracontenta*; 29 *H. irata*; 30 *H. brekkaensis*; 31 *Surirella terricola*; 32, 33 *Reimeria uniseriata*; 34, 35 *Sellaphora mutatooides*; 36 *Luticola ventriconfusa*; 37 *L. triundulata*; 38 *L. paramutica*; 39 *L. acidoclinata*. Scale bar=10 µm.

**Fig. 4.** Light microscopy (LM) micrographs (x1600): 1 *Pinnularia peracuminata*; 2 *P. grunowii*; 3 *P. isselana*; 4 *Fragilaria radians*; 5 *F. pararumpens*; 6 *Diatoma problematica*; 7 *Placoneis hambergii*; 8, 9 *Planothidium biporum*; 10, 11 *P. reichardtii*; 12 *Amphora micra*; 13, 14 *A. meridionalis*; 15 *A. lange-bertalotii* var. *tenuis*; 16, 17 *Psammothidium bioretii*; 18, 19 *P. grischunum*; 20-23 *P. lauenburgianum*; 24, 25 *Achnantheidium druartii*; 26-29 *A. latecephalum*; 30, 31 *A. caledonicum*; 32, 33 *A. eutrophilum*, 34, 35 *A. crassum*; 36, 37 *A. straubianum*. Scale bar=10 µm.

**Fig. 5.** Scanning electron microscopy (SEM) micrographs: 1 *Gomphonema cymbelliclinum*; 2 *Fistulifera pelliculosa*; 3, 4 *Achnantheidium latecephalum*. Scale bar=2 µm.



● – river; ■ – stream; ★ – accumulation; ▲ – canal; ◆ – salt marsh

**Fig. 1.**

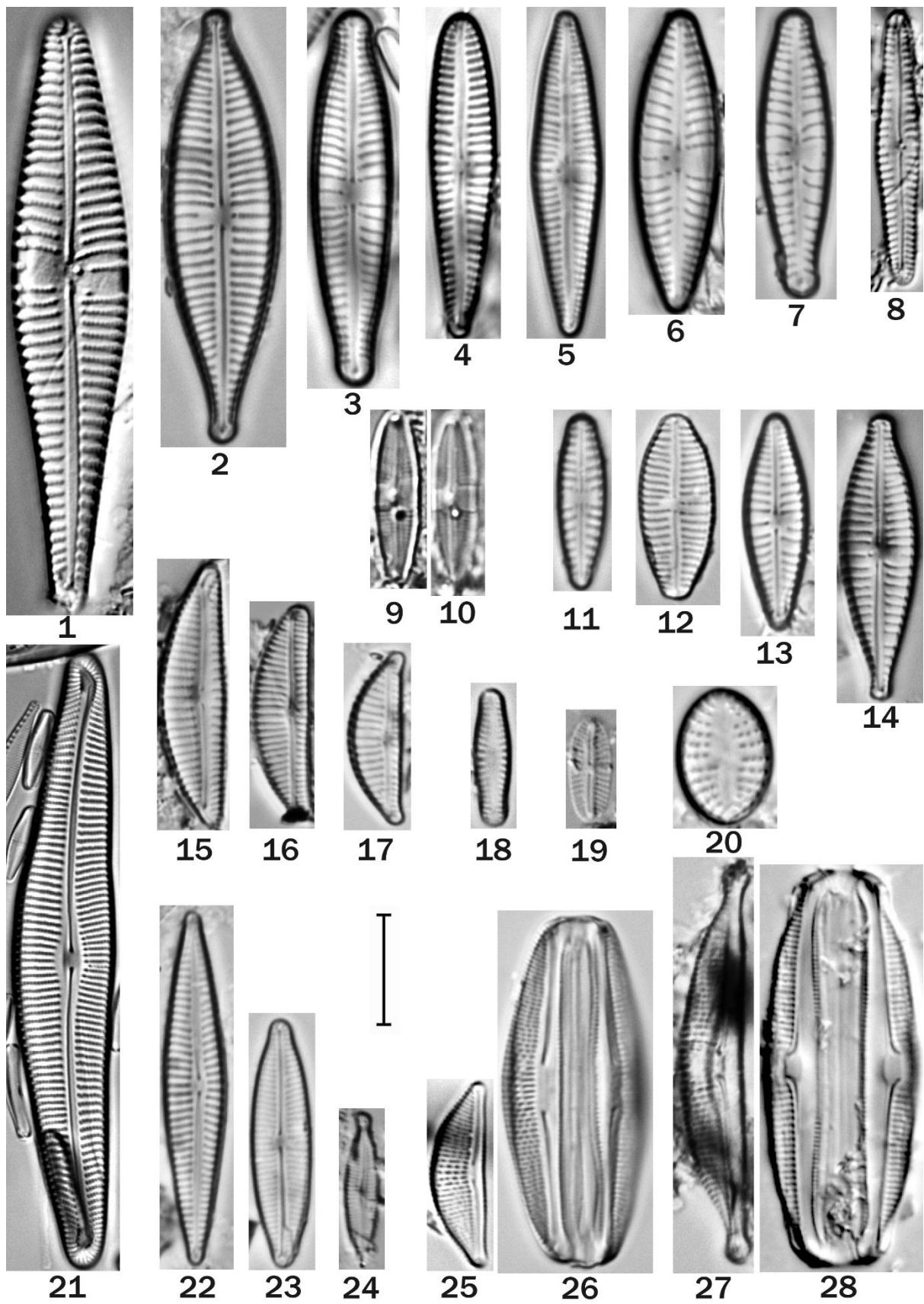


Fig. 2.

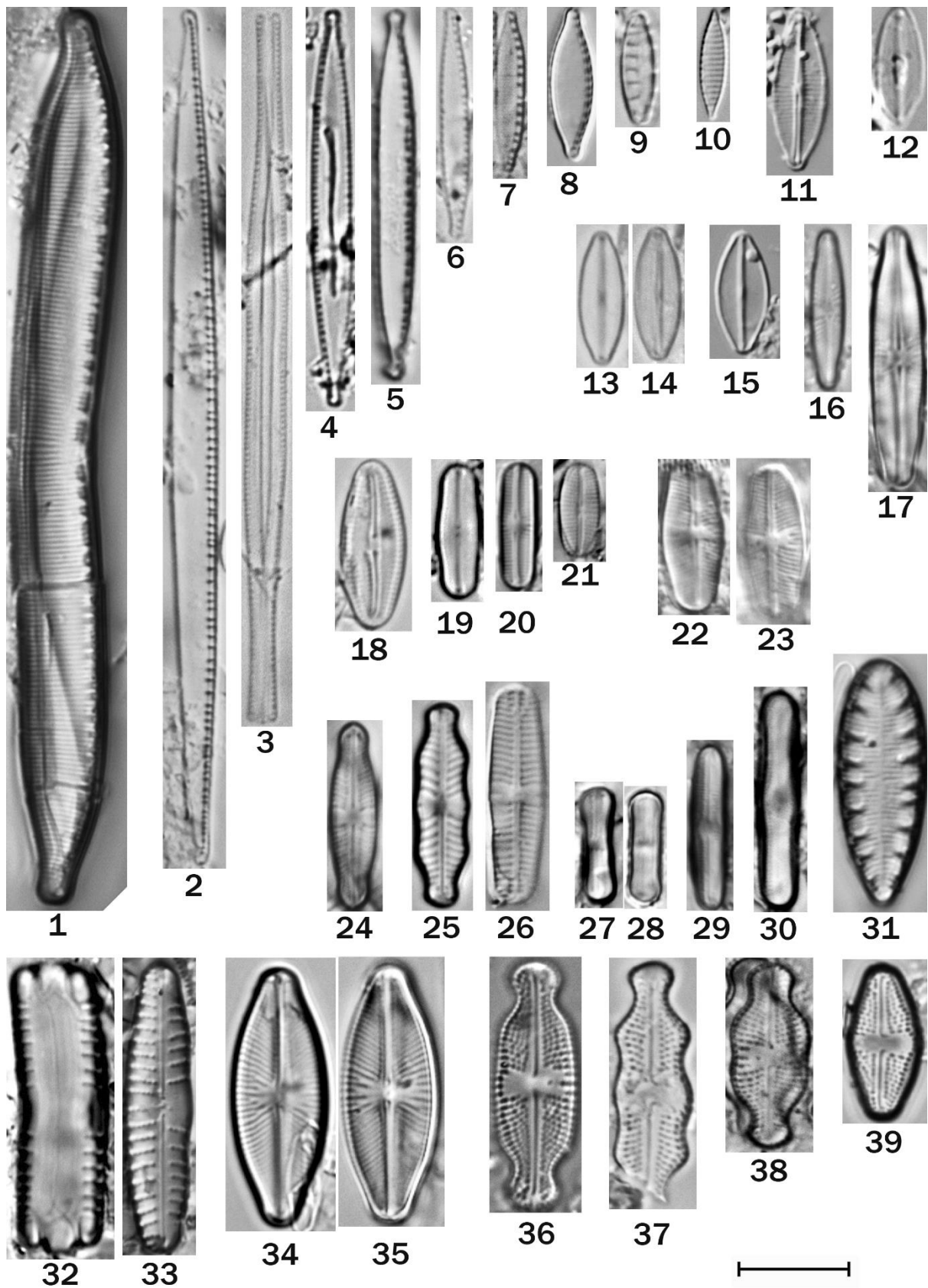


Fig. 3.

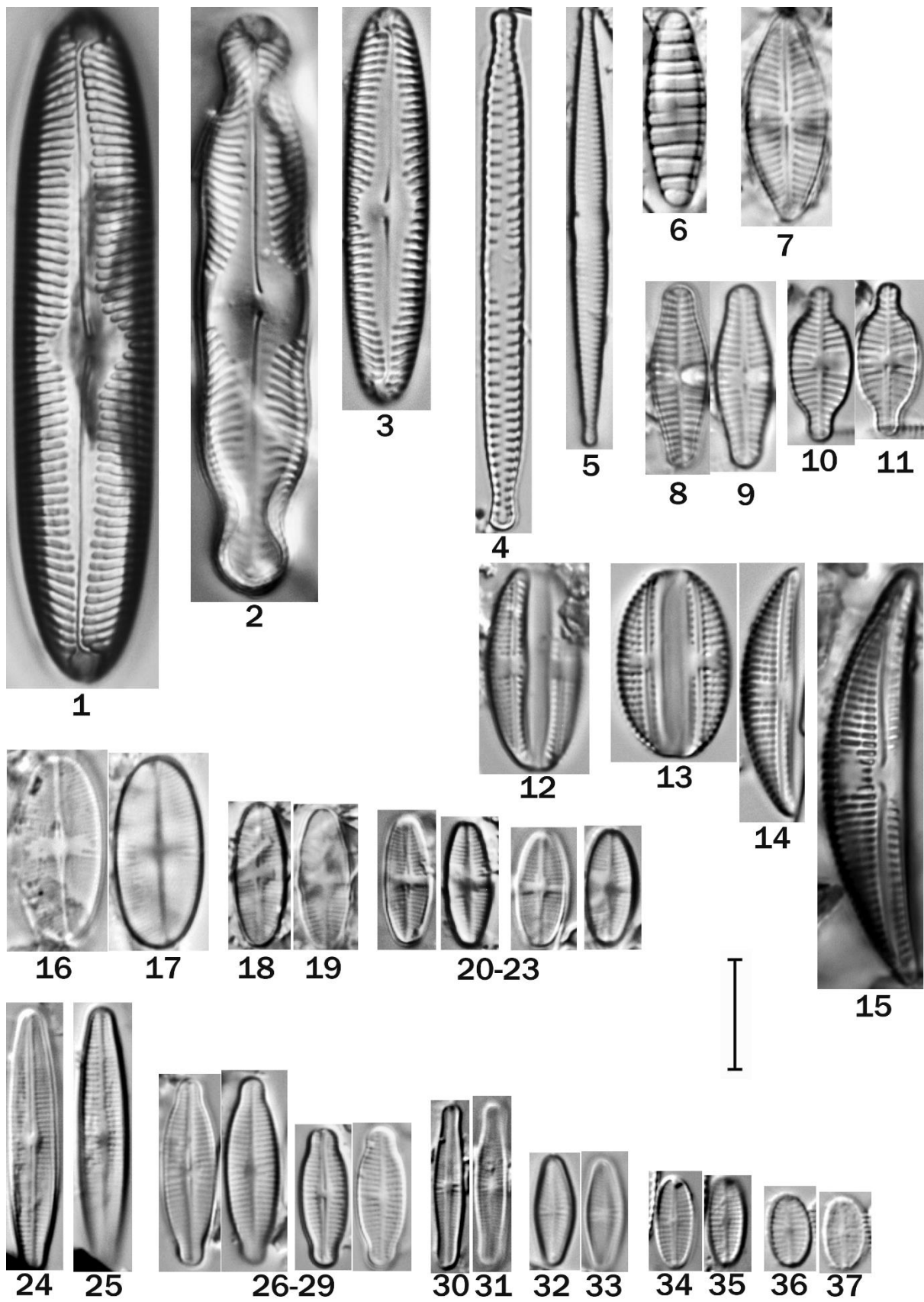
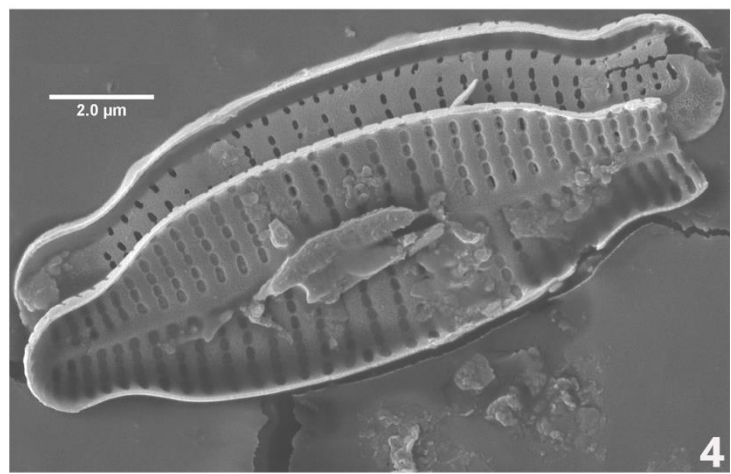
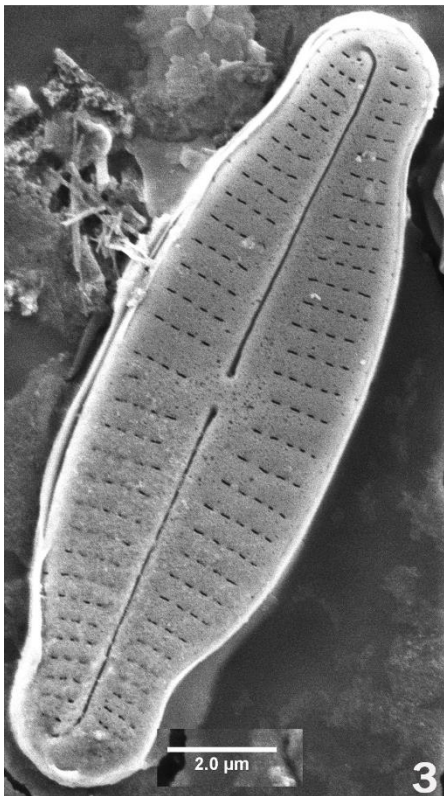
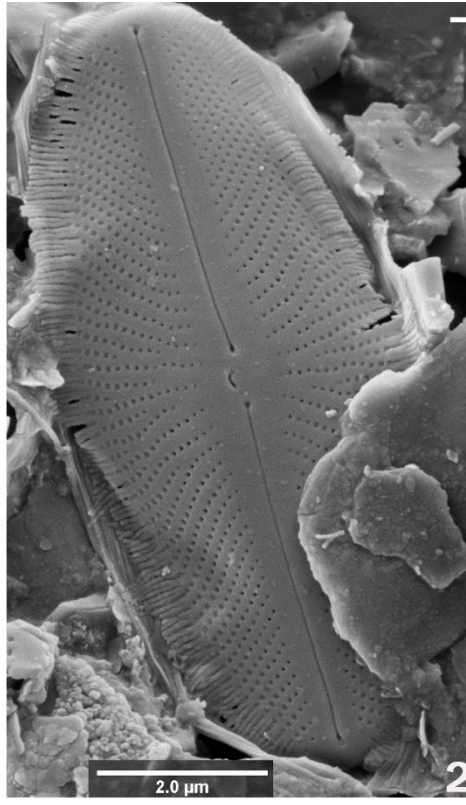
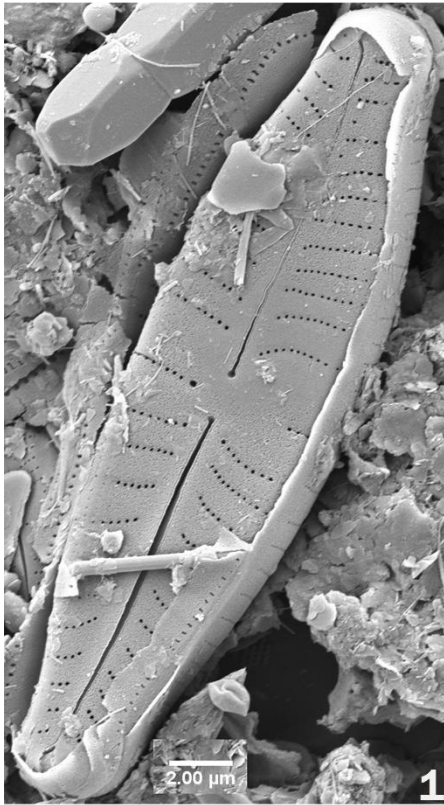



Fig. 4.



**Fig. 5.**

# Laser induced mixing in multilayered Ti/Ta thin film structures

Marko Obradović<sup>1</sup>  · Janez Kovač<sup>2</sup> · Suzana Petrović<sup>1</sup> · Vladimir Lazović<sup>3</sup> · Branislav Salatić<sup>3</sup> · Jovan Ciganović<sup>1</sup> · Dejan Pjević<sup>1</sup> · Momir Milosavljević<sup>1</sup> · Davor Peruško<sup>1</sup>

Received: 12 October 2017 / Accepted: 1 June 2018  
© Springer Science+Business Media, LLC, part of Springer Nature 2018

**Abstract** The possibility of interlayer mixing in a Ti/Ta multilayer system, induced by laser irradiation, was the main purpose of these experiments. Ti/Ta multilayer system, consisting of ten alternating Ti and Ta thin films and covered by slightly thicker Ti layer, was deposited on Si (100) wafers to a total thickness of 205 nm. Laser irradiation was performed in air by picoseconds Nd:YAG laser pulses in defocused regime with fluences of 0.057 and 0.11 J cm<sup>-2</sup>. Laser beam was scanned over the 5×5 mm surface area with different steps along y-axes. Structural and compositional characterisation was done by auger electron spectroscopy, X-ray photoelectron spectroscopy, atomic force microscopy, and scanning electron microscopy. Laser processing at lower fluence caused only oxidation of the top Ti layer, despite of the number of applied laser pulses. Interlayer mixing was not observed. Application of laser pulses at fluence of 0.11 J cm<sup>-2</sup> caused partial and/or complete ablation of deposited layers. In partially ablated regions considerable mixing between Ti and Ta films was registered.

**Keywords** Thin films · Multilayers · Laser irradiation · Mixing

---

This article is part of the Topical Collection on Focus on Optics and Bio-photonics, Photonica 2017

---

Guest Edited by Jelena Radovanovic, Aleksandar Krmpot, Marina Lekic, Trevor Benson, Mauro Pereira, Marian Marciniak

---

✉ Marko Obradović  
mbradovic@vin.bg.ac.rs

<sup>1</sup> VINČA Institute of Nuclear Sciences, University of Belgrade, P.O. Box 522, Belgrade 11001, Serbia

<sup>2</sup> Jožef Stefan Institute, Jamova 39, 1000 Ljubljana, Slovenia

<sup>3</sup> Institute of Physics Belgrade, University of Belgrade, Pregrevica 118, Zemun 11080, Serbia

## 1 Introduction

During the last few decades great attention is being devoted to the development of new materials for biomedical applications. Currently metallic biomaterials (stainless steels, Co–Cr alloys, Ti and its alloys) are the most widely used materials in this field, especially for orthopedic implants. An ideal metallic biomaterial should satisfy the criteria such as biocompatibility, high corrosion resistance, high strength and low elastic modulus close to that of human bones. Physical and particularly chemical characteristics of the material are to a large extent defined by their surface, so because of that, examination of thin films and coatings of biomaterials requires more attention.

Some previous investigations show that the Ti–Ta alloys are promising materials for biomedical applications due to excellent corrosion resistance and better mechanical characteristics than pure Ti (Zhou et al. 2004a, b, 2005; Zhou and Niinomi 2009; Kesteven et al. 2015; Liu et al. 2015). Multilayered metallic thin film structures are very useful for wide applications due to their properties, such as enhanced hardness or unusual phase composition, compared to single component systems (Sproul 1996). Ti/Ta multilayers belong to the so-called immiscible materials, in which chemical driving forces can prevent radiation induced atomic mixing at their interface. The absence of interlayer mixing was shown during the  $\text{Ar}^+$  ion irradiation of this system up to relatively high fluence of  $2 \times 10^{16}$  ions  $\text{cm}^{-2}$  (Milosavljević et al. 2011).

It is generally accepted that creating an appropriate porous structure on the Ti-based implant surface is very important when biocompatibility is of great concern. Chemical and thermal treatments have usually been used for creating such porous structures (Yang and Huang 2010; Nishiguchi et al. 2003; Fujibayashi et al. 2004). However, these roughening procedures induce contamination of implants. On the other hand laser irradiation provides contamination free roughening process because it enables surface treatments without direct contact and easy control of the surface roughness (Jeong et al. 2011).

Surface modification of biomaterials by ultrafast laser processing is considered an innovative technique, which contributes to improved cell integration and inhibits bacterial growth. Different types of the novel surface motives (ripples, groves, spikes) with sub-micron sized features are produced by ultrafast laser processing, while the chemical and physical properties of semiconductor, dielectric and metallic surfaces are significantly modified. Laser-assisted changes of chemistry, charge, topography and wettability of the surface can improve the degree of biocompatibility in terms of promoting cell adhesion, spreading and proliferation (Stratakis et al. 2009; Simitzi et al. 2015, 2017).

This article presents the results of structural and compositional investigations of the laser beam induced effects in Ti/Ta multilayer system. A defocused Nd:YAG laser beam was used, with two different energies. Beam was scanned over the sample surfaces. The aim of these experiments was to investigate the possibility of interlayer mixing in this system caused by irradiation with picoseconds laser pulses.

## 2 Experiment

Ti/Ta multilayer structure consisted of 10 alternate Ti and Ta thin films, with individual thickness of  $\sim 18$  nm each, covered with slightly thicker Ti film ( $\sim 27$  nm). Total thickness of deposited structure, measured with a talystep profilometer, was  $\sim 205$  nm.



Samples were deposited in a Balzers Sputtron II system, using 1.2 keV argon ions and 99.9% pure Ti and Ta targets. The base pressure in the chamber was  $\sim 2 \times 10^{-6}$  mbar, and the partial pressure of Ar during deposition was  $1 \times 10^{-3}$  mbar. Complete multilayer structure was deposited in a single vacuum run, at an average deposition rate of  $\sim 0.13$  nm  $s^{-1}$  for both materials onto (100) Si wafers at ambient temperature. The first layer deposited on the silicon substrate was titanium. Si wafers were cleaned by standard HF etch and a dip in deionised water before being mounted in the chamber.

The samples were irradiated by a defocused Nd:YAG laser beam with energies of 4 and 8 mJ. Nd:YAG laser (model EKSPLA SL212P) was operated in the fundamental transverse mode (TEM00 mode). Distribution of energy over the spots was near Gaussian with energy maximum in the centre of the laser spot. All irradiations were performed in air, and laser beam was perpendicular to the sample surface. The laser beam output characteristics were: wavelength 1064 nm, pulse duration  $\sim 150$  ps and linearly polarised. The pulse-to-pulse energy variation was  $\sim 10\%$  with typical pulse repetition rate of 10 Hz. Diameter of the laser spot on the sample surface was 3 mm, so that laser pulse fluences were 0.057 and 0.11 J  $cm^{-2}$  for energies of laser beam of 4 and 8 mJ, respectively. Laser beam was scanned over the sample surfaces with different steps along y-axes covering an area of  $5 \times 5$  mm<sup>2</sup>. Description of the analysed samples is shown in Table 1.

Compositional and structure analyses were done by auger electron spectroscopy (AES), X-ray photoelectron spectroscopy (XPS), atomic force microscopy (AFM) and scanning electron microscopy (SEM).

The depth distribution of elements in as deposited and laser treated samples was analysed by auger electron spectroscopy in the PHI SAM 545 spectrometer. For electron excitation a primary electron beam of 3 keV and 0.5  $\mu A$ , with a diameter of 40  $\mu m$ , was used. During AES depth profiling, the samples were sputtered by two symmetrically inclined Ar ion beams of 1 keV. The sputtering area was  $6 \times 6$  mm<sup>2</sup>. The quantitative composition was determined using the relative sensitivity factors provided by the instrument manufacturer.

XPS analyses were carried out on the PHITFA XPS spectrometer manufactured by physical electronics Inc. XPS spectra were excited by X-ray radiation from an Al monochromatic source. The changes of surface morphology, induced by laser treatment, were examined by atomic force microscopy (Solver PRO47) in oscillating mode. SEM analyses of samples surface and fracture cross section of sample 4 (irradiated with laser beam energy of 8 mJ) was performed by MIRA3 TESCAN microscopy.

**Table 1** Samples description

Sample	Laser beam energy (mJ)	Laser pulse fluence (J $cm^{-2}$ )	Scan speed along x-axis ( $\mu m$ $s^{-1}$ )	Step distance along y-axis ( $\mu m$ )	Total number of applied laser pulses
1	–	–	–	–	–
2	4	0.057	300	300	2670
3	4	0.057	300	200	4170
4	8	0.11	300	300	2670

### 3 Results and discussion

AES depth concentration profiles of elements in the as deposited and laser treated Ti/Ta samples are presented in Fig. 1. The surface of as deposited sample (1) is contaminated with oxygen and carbon. Concentrations of O and C are 41.7 and 42.5 at.% respectively, and they decrease very fast to a few atomic percent inside the top titanium layer. Ti and Ta layers are well separated in the whole multilayered structure. Due to small thickness (~18 nm) of individual layers and limited depth resolution of AES method, some overlapping between Ti and Ta curves is visible. This phenomenon can be assigned to limitations of the AES analytical method rather than mixing of the layers. Enhanced concentration of oxygen (about 7 at.%) was registered in the first Ti layer deposited on silicon substrate. This is a consequence of degassing of the vacuum system at the beginning of thin film deposition process and high reactivity of titanium.

In the case of lower energy of applied laser pulses (samples 2 and 3) laser irradiation induces oxidation of the top Ti layer. Oxygen signal spreads within this layer up to interface with Ta. All other layers beneath remain unaffected, and Ta and Ti signals are still well separated. Enhanced concentration of oxygen in the near surface region originates from the fact that laser irradiation was performed in air. Reason for observed increased incorporation of oxygen is the high temperature on the sample surface during the laser interaction and great reactivity of titanium. It also can be seen that time necessary for completely removing of deposited layers is higher for laser treated samples compared

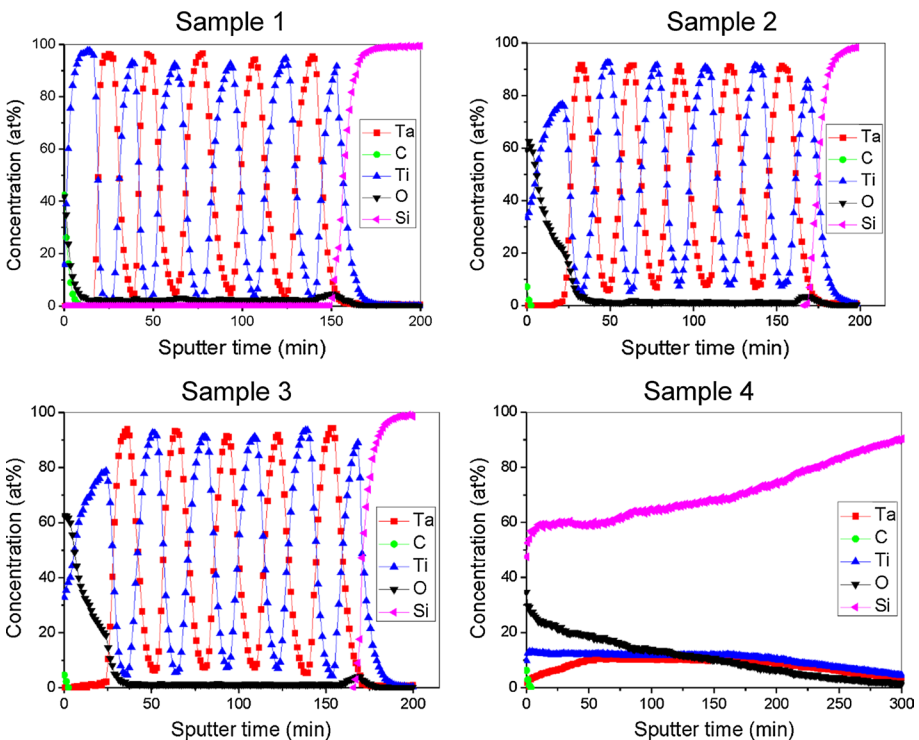


**Fig. 1** AES depth profiles of as deposited (1) and laser treated (2–4) samples

to as deposited. This phenomenon can be explained by formation of Ti–O oxides which have lower sputtering coefficients than those of pure titanium and tantalum.

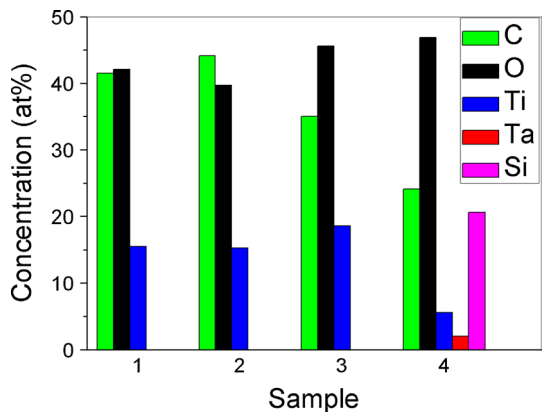
Multilayered structure was completely destroyed by applying the laser beam with higher energy (sample 4). Signals of Ti and Ta are practically equalised and spread deep into the sample, but their concentrations are considerably lower (about 10 at.%). High concentration of Si (~60 at.% at the sample surface) and lack of concentrations of Ti and Ta may be the result of inhomogeneous ablation of deposited layers. Laser spot overlapping was the greatest in the central part of irradiated sample and induced their complete removal, while at the peripheral areas, layers have not completely ablated, some still remained. It may be presumed that AES depth concentration profiles represent some average values of elements concentration that include both ablated and not fully ablated parts of the sample.

The results of surface composition of as deposited and laser treated samples, performed by XPS, are shown in Fig. 2. The aim of this analysis was to deduce whether Ta occurs at the sample surface as a result of laser irradiation. Its appearing would indicate intermixing of layers. Presence of titanium and contaminants, carbon and oxygen, was registered on the surface of as deposited sample (1). These contaminants appear on the surface of all samples due to their adsorption from atmosphere. Tantalum does not appear on the surface in the cases of laser treated samples at lower energy of laser beam despite on the number of applied laser pulses (samples 2 and 3). It occurs only for sample treated with laser beam at higher energy (sample 4). In that case a large amount of silicon was also registered on the sample surface.

XPS analysis show that titanium appeared at the sample surface in the oxide but not metal state in all analysed samples (1–4). Tantalum and silicon are in oxide state at the surface of sample 4 as well. It is well known that clean surfaces of many materials (Ti, Al, Si, etc.) spontaneously react with air, even at room temperature, to form a thin native oxide layer. These layers are usually very dense and can prevent further oxidation. Laser irradiation caused additional oxidation and oxide layer became wider, as can be seen in AES analysis for samples 2 and 3.

AES and XPS analysis show that, except the phenomenon of oxidation of the top Ti layer, multilayered Ti/Ta structure is very stable upon the laser irradiation for laser pulse fluence of  $0.057 \text{ J cm}^{-2}$  (laser beam energy 4 mJ). Appliance of higher laser pulse fluence ( $0.11 \text{ J cm}^{-2}$ ) leads to the complete destruction of this thin film structure.

**Fig. 2** XPS surface composition of as deposited (1) and laser irradiated (2–4) samples



The results of AFM analysis of as deposited and laser treated samples are shown in Fig. 3. Average surface roughness, measured over an area of  $5 \times 5 \mu\text{m}$  for all samples, is presented on the same figure.

It is obvious that laser irradiation induces enhancing of surface roughness. This increase is particularly pronounced for sample irradiated with laser pulses with higher energy (sample 4). Application of laser beam with lower energy (samples 2 and 3) causes the formation of a mesh of micro-cracks, which contributes increasing of surface roughness. This effect is more pronounced for sample irradiated with larger number of laser pulses (sample 3 compared to sample 2).

The results of SEM analysis of as deposited and laser treated samples are presented in Fig. 4. As deposited Ti/Ta sample has a flat, mirror-like surface. As was shown in AFM analysis, irradiation with lower laser pulse fluence of  $0.057 \text{ J cm}^{-2}$  causes the formation of micro-cracks on the top Ti layer.

SEM micrographs of sample 4, treated with higher laser pulse fluence, confirm the assumption about full and/or partial removing of deposited layers. Completely ablated areas are visible on the left micrograph of the sample 4. Magnified area with residual layers is shown on the right micrograph of the sample 4. Dark and bright sections within residual layered structure indicate possible mixing between Ti and Ta. Bright parts correspond to tantalum and dark to titanium.

Formation of micro-cracks may be explained by the fact that short processing cycles permit material transformations within thin films and surfaces without a significant influence on the substrate or underlying bulk material (Bäuerle 2000; Mondal et al. 2008; Petrović et al. 2012). As was mentioned earlier, on the surface of the cover Ti layer a very thin amorphous oxide film (thickness of a few nm) was formed. This formation is a consequence of high reactivity of titanium (Peruško et al. 2015). According to XPS analysis, this surface oxide layer is mainly  $\text{TiO}_2$  and it cannot follow the fast heating and quenching processes caused by laser pulses. This leads to cracking of this oxide film and enables

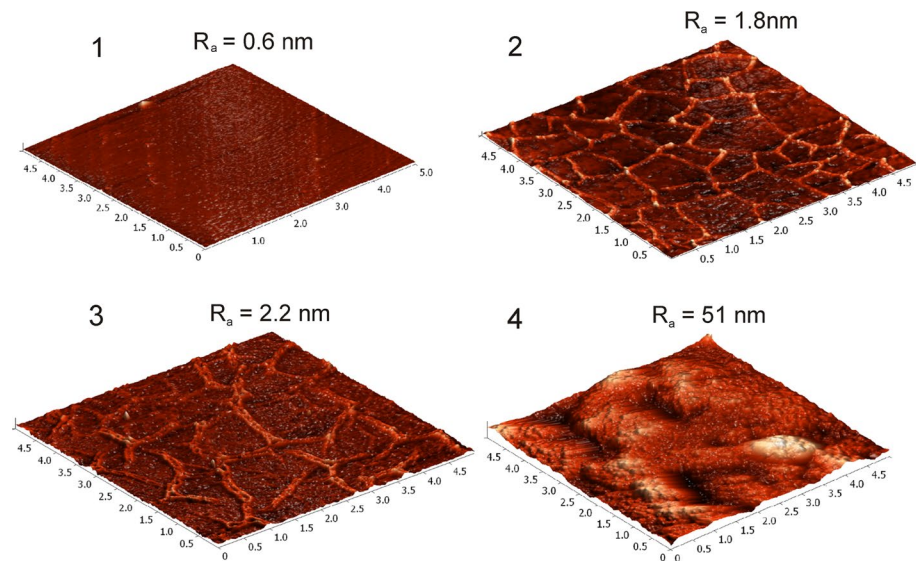


**Fig. 3** AFM images and average surface roughness of as deposited (1) and laser irradiated (2–4) samples

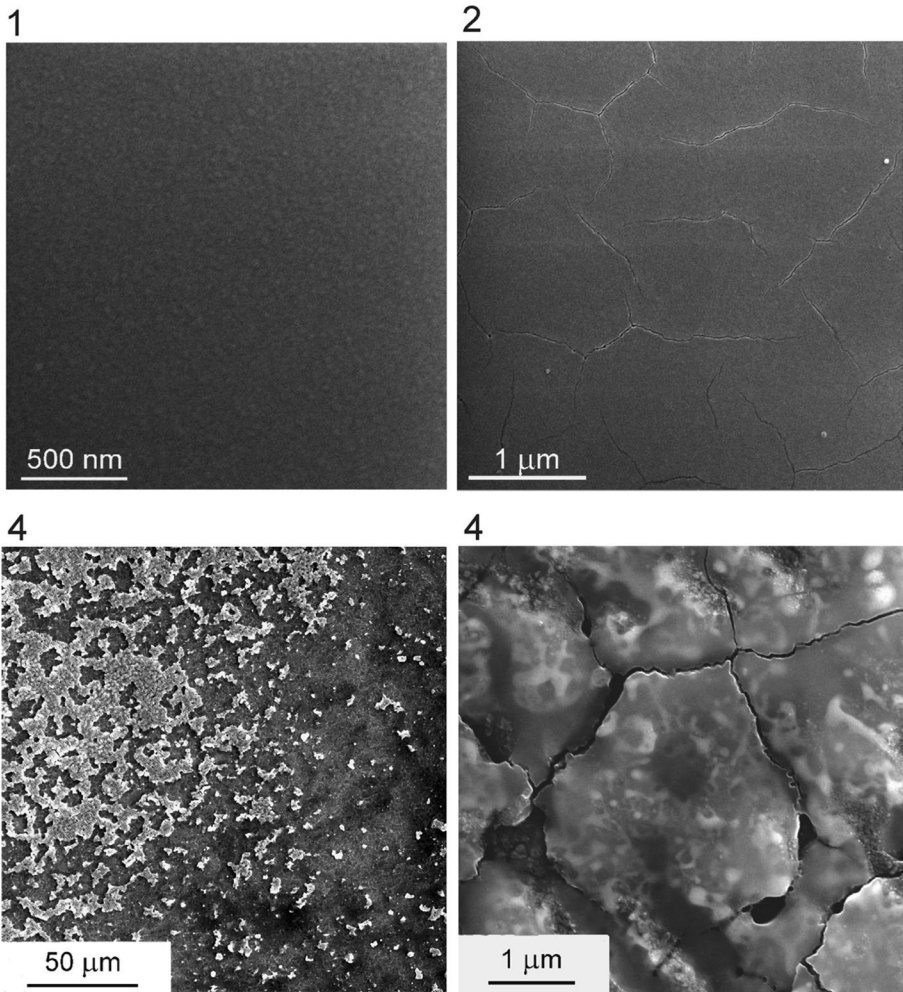


**Fig. 4** SEM analysis of surfaces of as deposited (1) and laser treated (2–4) samples

further oxidation of underlying Ti layer. AES analyses show that this process is limited to the cover layer only, for lower value of laser pulse energy. Approximate calculation of surface temperature, for laser pulse fluence of  $0.057 \text{ J cm}^{-2}$ , gives the value of 1550 K. Since the melting temperature of Ti is 1941 K, it is probably the reason for absence of melting and ablation of cover layer. For fluence of  $0.11 \text{ J cm}^{-2}$  the surface temperature reaches the value of 2280 K and in this case melting and ablation of titanium layer can be expected to appear. The melting temperature for tantalum is 2744 K and its coefficient of thermal expansion is about 30% lower compared to that of titanium. Ta thin film cannot follow the expansion of melted titanium and cracks into small fragments that are trapped and fused into Ti. Ablation of titanium includes the ablation of trapped tantalum fragments. Confirmation of this assumed mechanism for ablation could be seen in the SEM micrograph of surface of sample 4 (Fig. 4). In solidified titanium there can be seen some isolated Ta fragments.

SEM analysis of fracture cross section of sample 4 (Fig. 5) explicitly show that laser treatment with higher energy of laser pulses induces partial mixing between Ti and Ta layers. Fracture cross section of part of sample that is not affected by laser beam is present in Fig. 5a. Well separated Ti and Ta layers are clearly visible.

Micrographs shown in Fig. 5b, c are taken from the parts of sample close to boundary with unaffected zone. The layers close to Si substrate (five or six of them) stay well separated, while the upper part of multilayered structure is completely mixed.

Due to Gaussian distribution of energy over the laser spot, energy (and laser pulse fluence) is lower in this zone. Also, overlapping of laser spots near the border is smaller compared to central part of irradiated zone. Mixing between Ti and Ta layers is less pronounced immediately next to the boundary (Fig. 5b).

Moving away from the border interlayer mixing becomes more expressed (Fig. 5c). Surface roughness increases, deposited layers accumulate in the form of hills in some places and their height overcomes the total thickness of deposited layers. In other places deposited material is almost completely removed. Probably, these effects are responsible for laser induced ablation visible in Fig. 4.

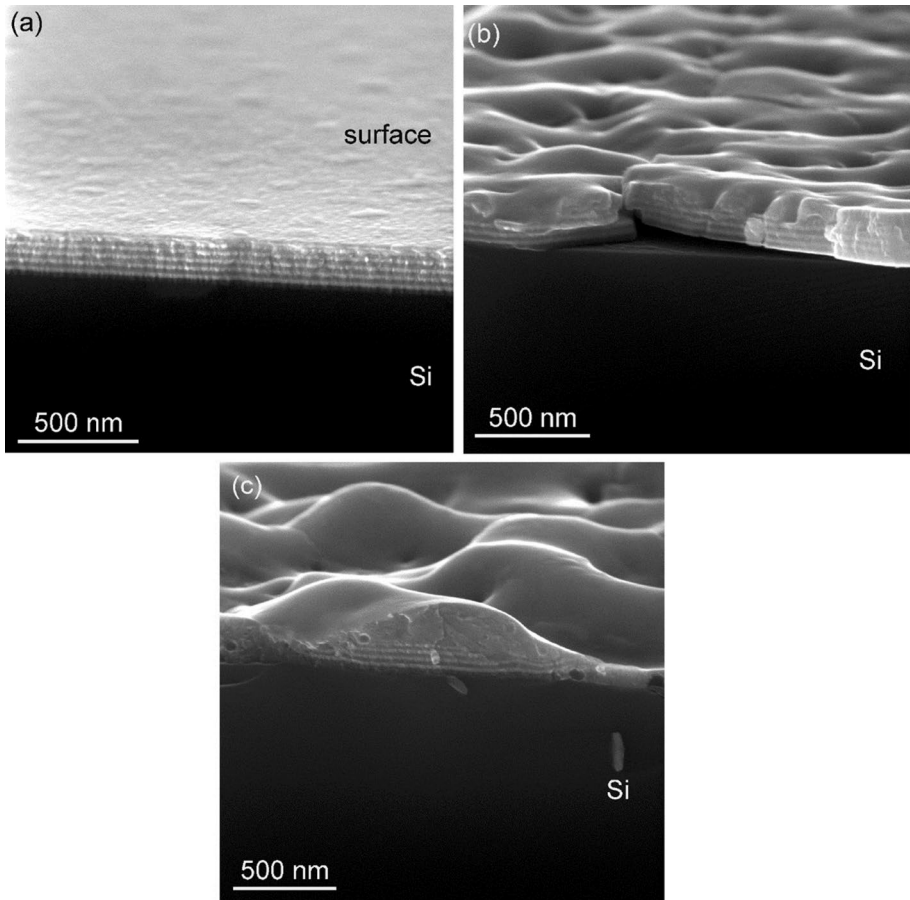


**Fig. 5** Fracture cross section of sample (4) irradiated with laser pulse fluence of  $0.11 \text{ J cm}^{-2}$

Laser induced modification of materials is based on the high temperature created at the surface during very short laser pulses. If the pulse duration is longer than a few tenths of picoseconds, laser–material interaction can be considered as thermally activated (Bäuerle 2000). It has been shown that irradiation of multilayered thin film systems by pico-seconds laser pulses induces mixing of constituent films incorporated within heat-affected zone (HAZ; Peruško et al. 2012, 2013). Approximate calculation of the HAZ (Bäuerle 2000) for this Ti/Ta multilayered system and applied laser beam parameter (duration of laser pulse of 150 ps) gives the value of 68 nm. This result coincides fairly well with observed intermixed layers shown in Fig. 5b. However, formula for HAZ contains only laser pulse duration and thermal diffusivity of materials. In that case the amount of mixed material, incorporated within HAZ, should be the same regardless of the laser pulse fluence. But, for fluence of  $0.057 \text{ J cm}^{-2}$  mixing between Ti and Ta layers was not observed. Probably, the process of interlayer mixing in this case is related to the energy of laser pulses, which must be sufficient to overcome the activity of chemical driving forces.

## 4 Conclusions

Irradiation of Ti/Ta multilayer structure, performed in air by defocused Nd:YAG picoseconds laser pulses at fluence of  $0.057 \text{ J cm}^{-2}$ , did not induce interlayer mixing regardless on the number of applied laser pulses. Only oxidation of the top Ti layer was observed under these conditions.

Appliance of the laser pulses with fluence of  $0.11 \text{ J cm}^{-2}$  leads to partial or complete ablation of multilayered structure, mixing between Ti and Ta films and large increase in surface roughness. Incomplete mixing of layers appeared in the vicinity of boundary with untreated part of sample.

Obtained results indicate that the use of picoseconds laser pulses with fluences in interval ( $0.057\text{--}0.11$ )  $\text{J cm}^{-2}$  can be very useful for mixing of titanium and tantalum layers and fabrication of a new material for medical implants. Suitable choice of films thicknesses, laser pulse fluence and scan speed over the sample surface would lead to the desired composition of this alloy.

**Acknowledgements** This research was supported by the Ministry of Education, Science and Technological Development of the Republic of Serbia, Contract No. OI 171023, and Slovenian Research Agency, Research Program P2-0082.


## References

- Bäuerle, D.: Laser Processing and Chemistry, 3rd edn. Springer, Berlin (2000)
- Fujibayashi, S., Neo, M., Kim, H.M., Kokubo, T., Nakamura, T.: Osteoinduction of porous bioactive titanium metal. *Biomaterials* **25**, 50–443 (2004)
- Jeong, Y.H., Son, I.B., Choe, H.C.: Formation of surface roughness on the Ti–35Nb–xZr alloy using femto-second laser for biocompatibility. *Proc. Eng.* **10**, 2393–2398 (2011)
- Kesteven, J., Kannan, M.B., Walter, R., Khakbaz, H., Choe, H.C.: Low elastic modulus Ti–Ta alloys for load-bearing permanent implants: enhancing the biodegradation resistance by electrochemical surface engineering. *Mater. Sci. Eng. C* **46**, 226–231 (2015)
- Liu, Y., Li, K., Wu, H., Song, M., Wang, W., Li, N., Tang, H.: Synthesis of Ti–Ta alloys with dual structure by incomplete diffusion between elemental powders. *J. Mech. Behav. Biomed.* **51**, 302–312 (2015)

- Milosavljević, M., Milinović, V., Peruško, D., Grce, A., Stojanović, M., Pjević, D., Mitrić, M., Kovač, J., Homewood, K.P.: Stability of nano-scaled Ta/Ti multilayers upon argon ion irradiation. *Nucl. Instrum. Method B* **269**, 2090–2097 (2011)
- Mondal, A.K., Kumar, S., Blawert, C., Dahotre, N.B.: Effect of laser surface treatment on corrosion and wear resistance of ACM720 Mg alloy. *Surf. Coat. Technol.* **202**, 3187–3198 (2008)
- Nishiguchi, S., Fujibayashi, S., Kim, H.M., Kokubo, T., Nakamura, T.: Biology of alkali and heat-treated titanium implants. *J. Biomed. Mater. Res. A* **67**, 26–35 (2003)
- Peruško, D., Petrović, S., Kovač, J., Stojanović, Z., Panjan, M., Obradović, M., Milosavljević, M.: Laser-induced formation of intermetallics in multilayered Al/Ti nano-structures. *J. Mater. Sci.* **47**(10), 4488–4495 (2012)
- Peruško, D., Čizmović, M., Petrović, S., Siketić, Z., Mitrić, M., Pelicon, P., Dražić, G., Kovač, J., Milinović, V., Milosavljević, M.: Laser irradiation of nano-metric Al/Ti multilayers. *Laser Phys.* **23**, 036005 (2013)
- Peruško, D., Kovač, J., Petrović, S., Dražić, G., Mitrić, M., Milosavljević, M., Ciganović, J.: Intermixing and phase transformations in Al/Ti multilayer system induced by picosecond laser beam. *Thin Solid Films* **591**, 357–362 (2015)
- Petrović, S., Peruško, D., Kovač, J., Panjan, M., Gaković, B., Radak, B., Janković-Mandić, L., Trtica, M.: Laser treatment of nanocomposite Ni/Ti multilayer thin films in air. *Surf. Coat. Technol.* **211**, 93–97 (2012)
- Simitzi, C., Efstathopoulos, P., Kourgiantaki, A., Ranella, A., Charalampopoulos, I., Fotakis, C., Athanasakis, I., Stratakis, E., Gravanis, A.: Laser fabricated discontinuous anisotropic microconical substrates as a new model scaffold to control the directionality of neuronal network outgrowth. *Biomaterials* **67**, 115–128 (2015)
- Simitzi, C., Ranella, A., Stratakis, E.: Controlling the morphology and outgrowth of nerve and neuroglial cells: the effect of surface topography. *Acta Biomater.* **51**, 21–52 (2017)
- Sproul, W.D.: New routes in the preparation of mechanically hard films. *Science* **273**, 889–892 (1996)
- Stratakis, E., Ranella, A., Farsari, M., Fotakis, C.: Laser-based micro/nanoengineering for biological applications. *Prog. Quantum Electron.* **33**, 127–163 (2009)
- Yang, W.E., Huang, H.H.: Improving the biocompatibility of titanium surface through formation of a TiO<sub>2</sub> nano-mash layer. *Thin Solid Films* **518**, 50–7545 (2010)
- Zhou, Y.L., Niinomi, M.: Ti–25Ta alloy with the best mechanical compatibility in Ti–Ta alloys for biomedical applications. *Mater. Sci. Eng. C* **29**, 1061–1065 (2009)
- Zhou, Y.L., Niinomi, M., Akahori, T.: Effects of Ta content on Young's modulus and tensile properties of binary Ti–Ta alloys for biomedical applications. *Mater. Sci. Eng. A* **371**, 283–290 (2004a)
- Zhou, Y.L., Niinomi, M., Akahori, T.: Decomposition of martensite  $\alpha$  during aging treatments and resulting mechanical properties of Ti–Ta alloys. *Mater. Sci. Eng. A* **384**, 92–101 (2004b)
- Zhou, Y.L., Niinomi, M., Akahori, T., Fukui, H., Toda, H.: Corrosion resistance and biocompatibility of Ti–Ta alloys for biomedical applications. *Mater. Sci. Eng. A* **398**, 28–36 (2005)



# Oxidation behaviour of composite CrN/(Cr,V)N coatings with different contents of vanadium induced by UV nanosecond laser pulses

Suzana Petrović<sup>1</sup> · B. Gaković<sup>1</sup>  · P. Panjan<sup>2</sup> · J. Kovač<sup>2</sup> · V. Lazović<sup>3</sup> · C. Ristoscu<sup>4</sup> · I. Negut<sup>4,5</sup> · I. N. Mihailescu<sup>4</sup>

Received: 17 October 2017 / Accepted: 16 April 2018  
© Springer Science+Business Media, LLC, part of Springer Nature 2018

**Abstract** The oxidation behaviour and morphological modification of CrN/(Cr,V)N coatings on Si wafers were studied after UV nanosecond laser (wavelength 248 nm, pulse duration 25 ns) processing in ambient air. The evolution of the surface composition and microstructure with the number of accumulated/subsequent pulses was systematically analysed depending on the initial content of vanadium in the as-deposited coatings. Irradiation of CrN/(Cr,V)N coatings with different content of vanadium was carried out at a fluence of  $0.17 \text{ J cm}^{-2}$  with different number of pulses. The concentration of metallic components was fairly homogeneous distributed throughout the sample. However, on surface and in sub-surface regions the contents of Cr and V are diminished due to laser-induced oxidation. The composition and thickness of forming oxides mixture,  $\text{Cr}_2\text{O}_3$  and  $\text{V}_2\text{O}_5$ , are depending on the number of applied laser pulses and the initial vanadium content. The asymmetric progress of surface morphology is characterized by the formation of grainy structures at peripheries and the appearance of cracks and irregular closed shapes in the centre of the irradiation area.

**Keywords** Hard-protective coatings · Surface oxidation · Laser modification

---

This article is part of the Topical Collection on Focus on Optics and Bio-photonics, Photonica 2017.

---

Guest Edited by Jelena Radovanovic, Aleksandar Krmpot, Marina Lekic, Trevor Benson, Mauro Pereira, Marian Marciniak.

---

✉ B. Gaković  
biljagak@vin.bg.ac.rs

<sup>1</sup> Vinča Institute of Nuclear Sciences, University of Belgrade, P. O. Box 522, Belgrade 11001, Serbia

<sup>2</sup> Jožef Stefan Institute, Jamova 39, 1000 Ljubljana, Slovenia

<sup>3</sup> Institute of Physics Belgrade, University of Belgrade, Pregrevica 118, Belgrade 11080, Serbia

<sup>4</sup> National Institute for Lasers, Plasma and Radiation Physics, Magurele, Ilfov, P. O. Box MG-36, 077125, Romania

<sup>5</sup> Faculty of Physics, University of Bucharest, 077125 Magurele, Ilfov, Romania

## 1 Introduction

Transition metal nitrides are widely applied as hard protective coatings. Simple binary (TiN and CrN) and ternary (TiCrN, TiAlN and CrVN) nitride systems are used, due to their high hardness, wear resistance, thermal stability, oxidation resistance, and chemical inertness (Yongqiang et al. 2013; Polcar et al. 2007; Uglov et al. 2005; Panjan et al. 2015). For cutting and forming tools, marine and machinery components, aerospace and automotive parts, new protective coatings have been intensively investigated, including ternary components, multilayer and nanocomposite structures (Shi et al. 2013; Drnovšek et al. 2015). The original idea with ceramic CrN coatings has been to prevent corrosion, but its high coefficient of friction hinders the application as wear protection (Uchida et al. 2004; Perfilyev et al. 2013). Adding a third element is an effective method to further improve the mechanical properties and oxidation resistance of the CrN coatings, obtaining ternary nitrides in form of nanocomposite or single-phase (solid solution) coatings (Rapoport et al. 2014). Addition of vanadium to form CrVN coating has improved the tribological and lubricious properties with roughly the same hardness and toughness as the CrN coating. The existence of vanadium in form of VN is particularly interesting because of easy oxidation in Magneli-phase with the specific property that planes can slide leading to self-lubricating (Wua et al. 2013; Qiu et al. 2014). The sliding performance of CrVN is highly superior as compared to CrN, especially in the case of motor oil environment at 373 K (Qiu et al. 2014).

Material laser processing can be used as heat treatment, welding and processes based on material removal (Gaković et al. 2012; Iordanova and Antonov 2008). Laser processing without material removal is important for alloying, cladding, hardening etc., when the purpose is to improve the surface properties by changing the chemical composition or/and structure (Baurle 2000; Dumitru et al. 2005). When metallic sample irradiated by different laser pulses in an oxidizing atmosphere, oxide layers are formed on the metal surface. The oxide layers majorly change the surface properties in two aspects: (1) the surface absorptivity effected by the increase in thickness of oxide layers and (2) the colour of surface varied by the colour of the oxide layers. The following advantages of laser-induced oxidation with respect to other methods are limitation of the process to a small area with a resolution down to laser wavelength, high precision spatial–temporal control, short processing time, high repeatability and formation of new types of oxides (Stefanov et al. 2006; Mondal et al. 2008). The surface structure, mechanical, corrosion and optical properties after laser processing can be modified by formation of relatively thin oxide layers (Petrović et al. 2014; Cui et al. 2008).

Studies of specific and complex samples, such as thin films or coatings deposited on a substrate, are highly desirable nowadays, primarily due to the existence of new, improved properties of the systems which are different from the bulk material (Ramos et al. 2006; PalDey and Deevi 2003). The combination of a nanolayer of binary CrN and ternary CrVN exhibits remarkable physical–chemical and mechanical characteristics, among which high corrosion resistance (Qiu et al. 2014). The goal of this work was to study laser-assisted surface oxidation with morphological changes induced by an UV nanosecond excimer laser source emitting at 248 nm on complex CrN/(Cr,V)N coating deposited on silicon substrate. The influence of different content of vanadium in the CrVN coatings on the laser-induced surface oxidation by various numbers of irradiation pulses was investigated. This research should contribute to a better understanding of the oxidation process of this complex CrN/(Cr,V)N system in extreme conditions such as nanosecond UV laser pulses.

## 2 Experimental

### 2.1 Sample preparation

The samples in form of multi-layered coatings were prepared by DC magnetron sputtering in a CC800/9 (Ceme Con) industrial unit. The nanolayer CrN/(Cr,V)N coatings were deposited from one pair of chromium and one pair of Cr/V triangular targets with target power of 9.5 kW. Ion etching with bias on a turntable of 650 V was conducted for 75 min in mixed argon (flow rate 120 ml min<sup>-1</sup>) and krypton (flow rate 90 ml min<sup>-1</sup>) atmosphere under a pressure of 0.35 Pa. In this way a set of samples with a composition gradient along the chamber's vertical axis were deposited in a single process. The vanadium concentration in the (Cr,V)N layers was varied in the range (1.0–11.5) at% (Panjan et al. 2015). As substrate, silicon wafers were mounted on a one-, two- and threefold rotating substrate holder. By using double rotation it was possible to produce nanolayered coatings with a uniform thickness of the constituent layers. The total operating pressure was maintained at 0.6 Pa, with the flow rates of nitrogen, argon and krypton being 100, 160 and 110 ml min<sup>-1</sup>, respectively. Prior to the deposition, the chamber was heated to 450 °C. The multilayer system composed of two different layers, i.e. CrN/Cr<sub>x</sub>V<sub>1-x</sub>N was prepared in single vacuum run at the deposition rate ~ 1.7 μm h<sup>-1</sup>. Thickness of particular layer was about 40 nm. For the study reported here, two samples with different vanadium concentration (6 at% (sample I) and 12 at% (sample II)) and total coating thickness of ~ 6.5 and 5.7 μm, respectively, were chosen.

### 2.2 Laser irradiation

The CrN/(Cr,V)N multilayer coatings were irradiated by nanosecond laser beam in ambient air. The laser source (Compex Pro 205) employed in the research was an excimer laser system emitting at 248 nm wavelength. The temporal pulse width was of 25 ns and a frequency repetition rate of 3 Hz. The laser beam was focused on the samples through a mask with dimension of 2 mm<sup>2</sup>. The used energy per pulse (Ep) was 100 mJ, corresponding to a laser fluence of 0.17 J cm<sup>-2</sup>. Multi-pulse irradiation was performed with 5 and 10 pulses.

### 2.3 Sample characterization

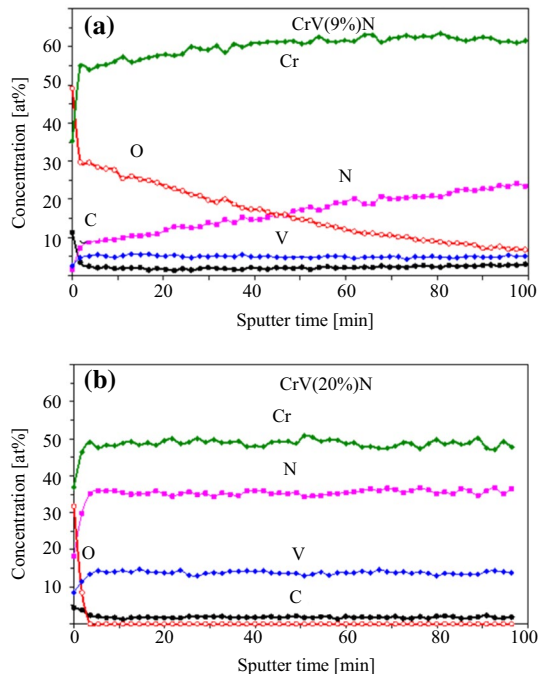
The depth profile in the non-treated and laser-treated areas of the CrN/(Cr,V)N coatings was analysed by Auger electron spectroscopy (AES) in a PHI SAM 545 spectrometer. Compositional analysis of the CrN/(Cr,V)N coatings was done by X-ray photoelectron spectroscopy (XPS) using the PHI-TFA XPS spectrometer. XPS spectra were excited by X-ray radiation from an Al standard and an Al-monochromatic source. The relative sensitivity factors were used for the calculation of surface concentrations (Moulder et al. 1995), and they were provided by an instrument producer. Detailed characterization of the morphological changes of the sample surface after laser irradiation was performed by confocal microscopy and scanning electron microscopy (SEM). SEM micrographs were obtained with the field emission (FE) SEM (TESCAN, MIRA 3) operating with secondary and backscattered electron detectors.

### 3 Results and discussion

Laser-induced modification was done under the same experimental conditions for both chosen samples, CrN/(Cr,V)N coatings with different content of vanadium. The changes in composition and depth distribution of components after laser irradiation with 5 pulses of CrN/(Cr,V)N system were recorded by AES. The depth profile of components through the samples almost 200 nm from the surface, are presented in Fig. 1a, b. The sample I refers to nanolayer CrN/(Cr,V)N coatings with a lower content of vanadium (6%). Its depth profile after laser treatment shows that the concentration of metallic components was rather homogeneous distributed throughout the sample with the following concentrations: chromium ~60% and vanadium ~6% (Fig. 1a). Depth profile for sample II with higher vanadium content shows the same uniform distribution but with different values of chromium (~48%) and vanadium (~12%) concentrations (Fig. 1b). Wavy shape of the concentration profile for chromium can be associated with the change of chromium content in the alternately deposited CrN and (Cr,V)N layers. At surface and in sub-surface region, the contents of Cr and V are reduced due to the surface oxidation. In the sample I, the oxidation process was prolonged in the depth of coating, where the nitrogen atoms are replaced by oxygen atoms. Oxygen atoms have penetrated the coating, wherein the concentration of oxygen on the surface of about 30% (without surface contamination with CO<sub>2</sub>) and gradually reduces to a depth of 200 nm (Fig. 1a). In the sample II with higher content of V, the penetration of oxygen included only sub-surface region to a depth of 8 nm, without noticeable replacement with nitrogen atoms (Fig. 1b).

Analysis of the binding energy in the corresponding XPS spectra was used for the determination of chemical states of the constituents (Cr, V, O and N) after laser processing of CrN/(Cr,V)N coatings with accumulated 5 pulses. For sample I, the changes in binding

**Fig. 1** AES depth profile of CrN/(Cr,V)N multilayer coatings: **a** sample I with 6% at of vanadium, **b** sample II with 11% at of vanadium, after nanosecond laser processing with fluence  $F=0.17 \text{ J cm}^{-2}$  with 5 pulses irradiation



energies are presented at the surface (red lines in Fig. 2) and in the depth of 6 nm (blue lines in Fig. 2). Both metallic constituents (Cr and V) formed oxides phases mostly at the surface than in the sub-surface layer. The concentration of V-oxide in form of  $V_2O_5$ , with the binding energy of 517 eV (Fig. 2a), was about 40% while  $Cr_2O_3$  oxide, with the binding energy 577 eV (Fig. 2b), had the concentration on the surface close to 60% (<http://xpsimplified.com/periodictable.php>). The relative concentration of V-oxide phase is drastically decreased in the depth of the sample, reaching only 5% at 6 nm. However, only 10% of Cr-oxide has remained in sub-surface region at 6 nm depth. Nitride states of V and Cr are dominant phases in sub-surface region, at a depth of 6 nm. The binding energy for metallic V (512.3 eV) is very close to V-nitride state (514.2 eV) while the V 2p peak was asymmetrical shifted towards higher values of binding energy, which is indicative for the presence of both chemical states (Fig. 2a) (Wang et al. 2016). The same situation was observed for Cr species, metallic Cr (574.3 eV) and Cr-nitride (575 eV), which had close binding energies and also an asymmetrical Cr 2p peak moved to higher values (Fig. 2b) (Wang et al. 2016). The N 1s peak was appearing at the binding energy of 397 eV, which is attributed to nitride state. During the laser-induced surface oxidation, an ultra-thin layer, composed from mixture  $Cr_2O_3$  and  $V_2O_5$  was preferentially formed on the surface. The laser action is likely to cause diffusion of elements between layers. Since the top-surface layer is CrN, vanadium can reach the surface by diffusion and react with oxygen from the air to form V-oxide phase. In the depth, the Cr-oxide phase was majority in comparison with V-oxide, due to the initial higher content of Cr species in the as-deposited CrN/(Cr,V)N coating.

The laser-induced composition modification in surface and sub-surface region for sample II (with higher content of vanadium) after cumulative action with 5 pulses have shown very similar results as in sample I. The same chemical phases ( $Cr_2O_3$  and  $V_2O_5$ ) were formed in the ultra-thin oxide layer, while both metallic constituents and/or nitride states were observed at 6 nm depth of the modified CrN/(Cr,V)N coating (Fig. 3a, b). However, the concentration of corresponding oxide phases were different, namely the surface concentrations were about 25% for V oxide and 75% for Cr oxide. Surface concentrations of Cr oxide for sample II had higher values in comparison with sample I under the same experimental conditions. At the depth of 6 nm, both components (Cr and V) appeared in a very small percentage as oxides (~5%), which is consistent with AES analysis proving that the sample II undergone a lower degree of laser-assisted surface oxidation.

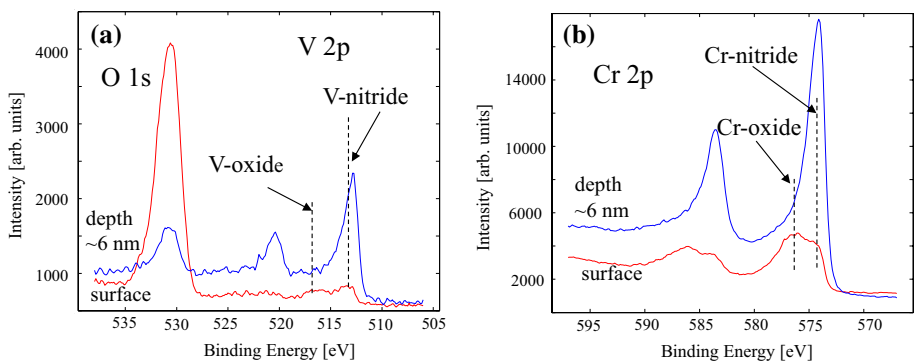


**Fig. 2** XPS spectra of **a** V 2p and **b** Cr 2p regions of sample I (low content of V) obtained on the surface and in the depth of 6 nm after laser treatment with five pulses at fluence of  $F=0.17 \text{ J cm}^{-2}$ . (Color figure online)

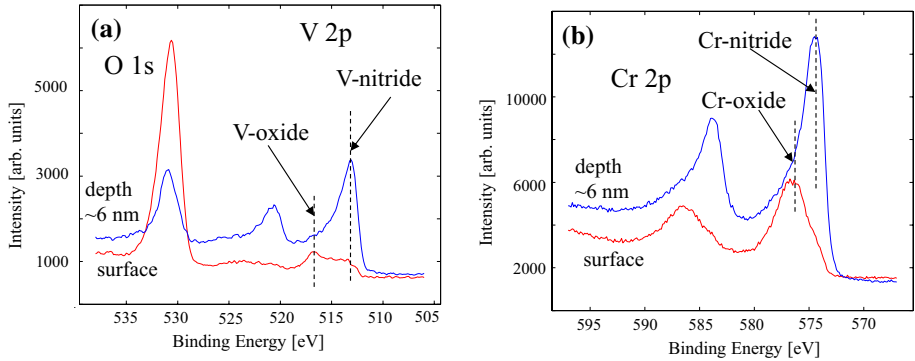


**Fig. 3** XPS spectra of **a** V 2p and **b** Cr 2p regions of sample II (high content of V) obtained on the surface and in the depth of 6 nm after laser treatment with five pulses at fluence of  $F=0.17 \text{ J cm}^{-2}$

The changes in surface and sub-surface composition are also accompanied with changes morphological modification of irradiated surface. In the central part of the modified area, the separation of the different oxide phases at the surface based on the regions with different reflectivity is observed (regions with different colours in Fig. 4). The absorptivity of the irradiated surface changed considerably with change of

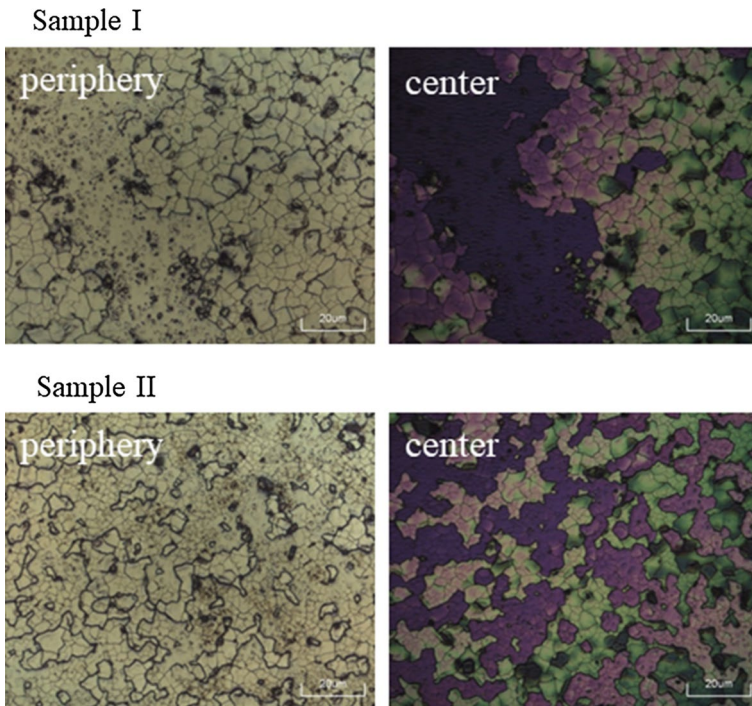


**Fig. 4** Confocal images of the central modified zones of the CrN/(Cr,V)N multilayer coatings, after nano-second laser processing with fluence  $F=0.17 \text{ J cm}^{-2}$  with five pulses irradiation

thickness of the oxide layers as result of molecular absorption and interference effect (Li et al. 2009). Also, different types of oxides have different spectral reflectance during the illumination by light, resulting in showing of various colours. The different colours of the irregular closed shapes with cracks can be associated with different oxide phases ( $\text{Cr}_2\text{O}_3$  and  $\text{V}_2\text{O}_5$ ), which are segregated on the irradiated surface for both samples (Fig. 4). Unmodified areas for both samples did not show changes in colours, which can be attributed to the presence of the one phase on the surface.

The dominant morphology characteristic was the occurrence of the cracks with dimensions (length and depth) gradually increasing from periphery to centre of irradiated areas for both samples (Fig. 5A1–B2). Locally removal/exfoliation of surface layer (probably CrN) was recorded at the surface of the sample I (Fig. 5A2), which could point to the formation of V-oxide phase with specific property to easy sliding the planes.

This further enables the presence of  $\text{V}_2\text{O}_5$  phase on the surface because the (Cr,V)N layer become the surface layer in contact with air. In very small regions of the order of 100 nm, the surface melting was recognized/observed in the top layer and in the opened layer created by the previous exfoliated surface layer (Fig. 5A3, A4). Hydrodynamic feature of these surface melting are appearing as cone-like forms or spikes. At the surface of the sample II, the cracks were quite densely arranged, generating some netting-mosaic structure with irregular shapes contoured by cracks. However, at the surface is not observed the removal/exfoliation of the top layer, and also no noticeable locally surface melting as for the sample I (with lower vanadium content). The surface between cracks seems rather smooth (Fig. 5B3), only an initial melting very rarely occurs in the form of small circular cavities (Fig. 5B4).

Laser-induced morphological modification of CrN/(Cr,V)N samples with different content of vanadium was reported after cumulative action with 10 pulses (Fig. 6). The SEM images have shown that the exfoliation of surface layer was occurring for both

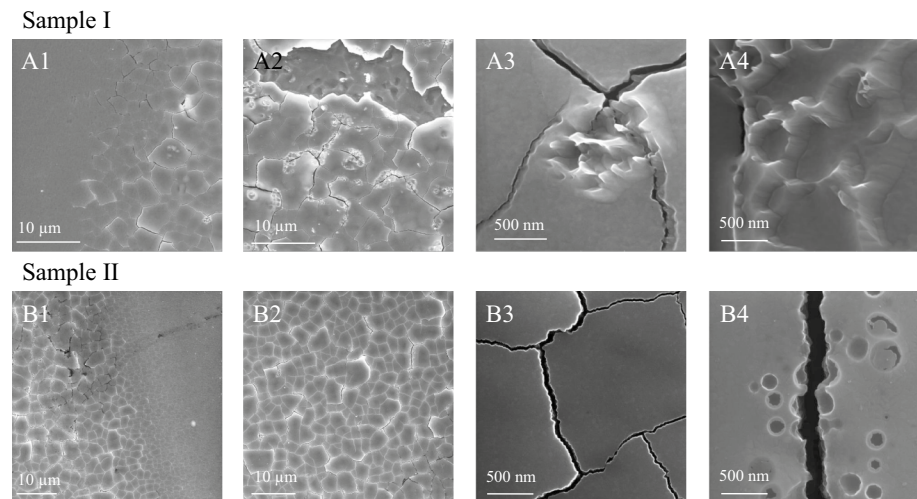


**Fig. 5** SEM analyses of the CrN/(Cr,V)N multilayer coatings, after nanosecond laser processing of both sample I (low content of V) and sample II (high content of V) at fluence  $F=0.17 \text{ J cm}^{-2}$  with five pulses irradiation

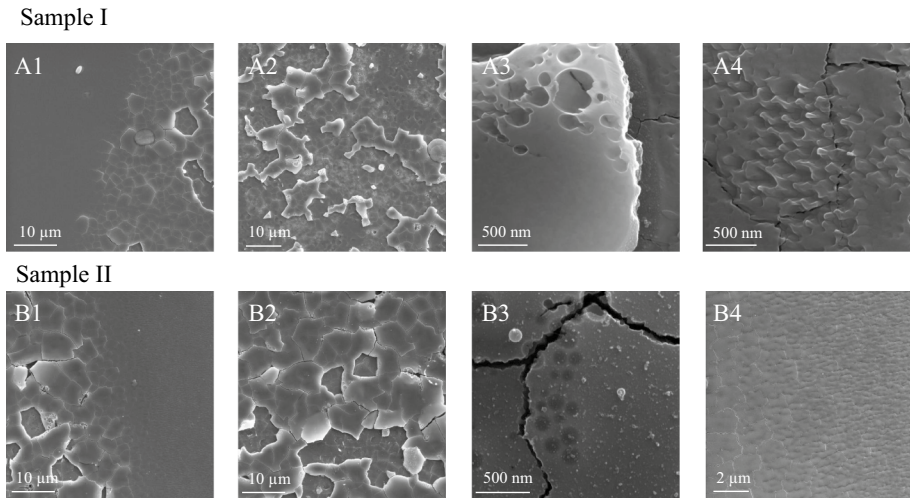


**Fig. 6** SEM analyses of the CrN/(Cr,V)N multilayer coatings, after nanosecond laser processing of both sample I (low content of V) and sample II (high content of V) at fluence  $F=0.17 \text{ J cm}^{-2}$  with 10 pulses irradiation

samples (Fig. 6A1–B2). The exfoliation is more pronounced in the sample I, which is consistent with the changes obtained in the case of the laser processing with 5 pulses.

At the same time, the formation of cracks was recorded at the top layer. Regions covered by surface melting are larger for the sample I, cavities were formed on the surface layer and the cone-like structure was induced in the bottom layer (Fig. 6A3, A4). A local surface melting was not observed in the sample II, in accordance with the higher melting point of the sample with larger vanadium content. Laser treatment of the sample II with accumulated 10 pulses induced the formation of a parallel periodic structure at the periphery of irradiated area. The width of periods decreased (from 800 nm to 300 nm) with the distance from the centre of the irradiated zone to the far periphery. The origin of these periodic structures can be associated with the wrinkling of softened material, because the periodicity of these ripples is not comparable with the applied wavelength.

The oxides start to nucleate and growth through chemical reaction between oxygen and metallic component (Cr and V) at the gas-nitride surface. The oxidation reactions were spontaneous process for Cr and V due to the corresponding Gibbs free energy values ( $\Delta G = -1053.10 \text{ kJ mol}^{-1}$  for  $\text{Cr}_2\text{O}_3$  and  $\Delta G = -1421.15 \text{ kJ mol}^{-1}$  for  $\text{V}_2\text{O}_5$ ) were negative (Vaz et al. 2013). The more negative  $\Delta G$  for  $\text{V}_2\text{O}_5$  than for  $\text{Cr}_2\text{O}_3$  at the same temperature suggesting the greater affinity with oxygen is vanadium. On the other hand, thermodynamics strongly prefers the formation of oxides to nitrides ( $\text{V}_2\text{O}_5$ ,  $\Delta G = -1421 \text{ kJ mol}^{-1}$ ; VN,  $\Delta G^\circ = -191 \text{ kJ mol}^{-1}$ ), the oxidation process is extremely sensitive to the presence of oxygen even in trace amounts (Galesic and Kolbesen 1999). However, on the irradiated surface for the both samples, the concentration of  $\text{Cr}_2\text{O}_3$  had higher values. The top/surface layer was CrN causing higher initial concentration of Cr on the surface in compare to vanadium surface concentration. Appearance of vanadium atoms on the surface may be consequence of thermal activated diffusion and/or exfoliation of top CrN layer during the laser treatment. The oxidation mechanism can be assumed to be controlled by diffusion of component at the surface and in depth of samples. The formation of oxides at the high



temperature and atmospheric pressure mainly depends on the thermodynamic and kinetic factors, as well as the initial concentration. One of additional reasons why vanadium prevents the replacement of nitrogen by oxygen in the sample II, can be good performance of VN and V<sub>2</sub>O<sub>5</sub> as diffusion barriers (Galesic and Kolbesen 1999).

## 4 Conclusion

Multi-pulse irradiation provided enough input energy for laser induced surface oxidation and interaction between the sample constitutive components and oxygen. For the selected experimental conditions, the CrN/(Cr,V)N multilayer coatings are oxidized. They actually consist mostly of a mixture of oxides, Cr<sub>2</sub>O<sub>3</sub> and V<sub>2</sub>O<sub>5</sub> depends on the components which are brought on the surface either by diffusion of components or exfoliation. The composition and thickness of this ultra-thin oxide layer correlates with the applied number of laser pulses. The penetration depth of oxygen largely depends on the concentration of vanadium, which is blocking the replacement of nitrogen by oxygen inside coating with beneficial results on corrosion deceleration and stopping. This is demonstrated by SEM evidence showing an increased degradation by exfoliation and cracking in case of sample with 6% at V, which is prone to an enhanced corrosion. This is expected to result in a significant increase of the protective role of substrate by the applied, laser modified CrN/(Cr,V)N coating.

**Acknowledgements** The research was sponsored by the Ministry of Education, Science and Technological Development of the Republic Serbia through Projects Nos. III 45016 and OI 172019. Romanian co-authors acknowledge the financial support of the work by the National Authority for Research and Innovation in the frame of Nucleus programme—contracts ID 304/2011 and 4N/2016. We also acknowledge the support from European Community, COST Action. Project No. MP1208.

## References

- Baurle, D.: Laser Processing and Chemistry. Springer, Berlin (2000)
- Cui, C., Hu, J., Liu, Y., Gao, K., Guo, Z.: Morphological and structural characterizations of different oxides formed on the stainless steel by Nd: YAG pulsed laser irradiation. *Appl. Surf. Sci.* **254**, 6537–6542 (2008)
- Drnovšek, A., Panjan, P., Panjan, M., Paskvale, S., Buh, J., Čekada, M.: The influence of surrounding atmosphere on tribological properties of hard protective coatings. *Surf. Coat. Technol.* **267**, 15–20 (2015)
- Dumitru, G., Luscher, B., Krack, M., Hermann, J., Gerbig, Y.: Laser processing of hardmetals: physical basics and applications. *Int. J. Refract. Met. Hard Mater.* **23**, 278–286 (2005)
- Gaković, B., Radak, B., Radu, C., Zamfirescu, M., Trtica, M., Petrović, S., Stašić, J., Panjan, P., Mihailescu, I.N.: Selective single pulse femtosecond laser removal of alumina (Al<sub>2</sub>O<sub>3</sub>) from a bilayered Al<sub>2</sub>O<sub>3</sub>/TiAlN/steel coating. *Surf. Coat. Technol.* **206**, 5080–5084 (2012)
- Galesic, I., Kolbesen, B.O.: Analysis of oxide formation induced by UV laser coloration of stainless steel. *Fresenius J. Anal. Chem.* **365**, 199–202 (1999)
- Jordanova, I., Antonov, V.: Surface oxidation of low carbon steel during laser treatment, its dependence on the initial microstructure and influence on the laser energy absorption. *Thin Solid Films* **516**, 7475–7481 (2008)
- Li, Z.L., Zheng, H.Y., Teh, K.M., Liu, Y.C., Lim, G.C., Seng, H.L., Yakovlev, N.L.: Analysis of oxide formation induced by UV laser coloration of stainless steel. *Appl. Surf. Sci.* **256**, 1582–1588 (2009)
- Mondal, A.K., Kumar, S., Blawert, C., Dahotre, N.B.: Effect of laser surface treatment on corrosion and wear resistance of ACM720 Mg alloy. *Surf. Coat. Technol.* **202**, 3187–3198 (2008)
- Moulder, J.F., Stickle, W.F., Sobol, P.E., Bomben, K.D.: Handbook of X-ray Photoelectron Spectroscopy. Physical Electronics Inc., Eden Prairie (1995)

- PalDey, S., Deevi, S.C.: Properties of single layer and gradient (Ti, Al) N coatings. *Mater. Sci. Eng. A* **361**, 1–8 (2003)
- Panjan, P., Drnovšek, A., Kovač, J., Gselman, P., Bončina, T., Paskvale, S., Čekada, M., Kek Merl, D., Panjan, M.: Oxidation resistance of CrN/(Cr, V) N hard coatings deposited by DC magnetron sputtering. *Thin Solid Films* **591**, 323–329 (2015)
- Perfilyev, V., Moshkovich, A., Lapsker, I., Laikhtman, A., Rapoport, L.: The effect of vanadium content and temperature on stick–slip phenomena under friction of CrV (x) N coatings. *Wear* **307**, 44–51 (2013)
- Petrović, S., Peruško, D., Kovač, J., Siketić, Z., Radović-Bogdanović, I., Gaković, B., Radak, B., Trtica, M.: Laser-induced surface oxidation of (Ni/Ti)/Si system with picosecond laser pulses. *Mater. Chem. Phys.* **143**, 530–535 (2014)
- Polcar, T., Parreira, N.M.G., Novak, R.: Friction and wear behaviour of CrN coating at temperatures up to 500 C. *Surf. Coat. Technol.* **201**, 5228–5235 (2007)
- Qiu, Y., Li, B., Lee, J., Zhao, D.: Self-lubricating CrVN coating strengthened via multilayering with VN. *J. Iron Steel Res.* **21**(5), 545–550 (2014)
- Ramos, A.S., Calinas, R., Vieira, M.T.: The formation of  $\gamma$ -TiAl from Ti/Al multilayers with different periods. *Surf. Coat. Technol.* **200**, 6196–6200 (2006)
- Rapoport, L., Moshkovich, A., Perfilyev, V., Lapskera, I., Kugler, M., Kailer, A., Renz, A., Hollstein, T.: High temperature friction behavior of CrVxN coatings. *Surf. Coat. Technol.* **238**, 207–215 (2014)
- Shi, P.Z., Wang, J., Tian, C.X., Li, Z.G., Zhang, G.D., Fu, D.J., Yang, B.: Structure, mechanical and tribological properties of CrN thick coatings deposited by circular combined tubular arc ion plating. *Surf. Coat. Technol.* **228**, S534–S537 (2013)
- Stefanov, P., Minkovski, N., Belchev, I., Avramova, I., Sabotinova, N., Marinova, T.S.: XPS studies of short pulse laser interaction with copper. *Appl. Surf. Sci.* **253**, 1046–1050 (2006)
- Thermo scientific XPS website: <http://xpssimplified.com/periodictable.php>
- Uchida, M., Nihira, N., Mitsuo, A., Toyoda, K., Kubota, K., Aizawa, T.: Friction and wear properties of CrAlN and CrVN films deposited by cathodic arc ion plating method. *Surf. Coat. Technol.* **177–178**, 627–630 (2004)
- Uglov, V.V., Anishchik, V.M., Zlotski, S.V., Abadias, G., Dub, S.N.: Stress and mechanical properties of Ti–Cr–N gradient coatings deposited by vacuum arc. *Surf. Coat. Technol.* **200**, 178–181 (2005)
- Vaz, F., Martin, N., Fenker, M.: *Metallic Oxynitride Thin Films by Reactive Sputtering and Related Deposition Methods, Process, Properties and Applications*. Bentham Science Publisher (2013)
- Wang, S., Yu, X., Zhang, J., Wang, L., Leinenweber, K., He, D., Zhao, Y.: Synthesis, hardness, and electronic properties of stoichiometric VN and CrN. *Cryst. Growth Des.* **16**, 351–358 (2016)
- Wua, Z.T., Qib, Z.B., Zhua, F.P., Liua, B., Wang, Z.C.: Influences of Y addition on mechanical properties and oxidation resistance of CrN coating. *Physics Procedia* **50**, 150–155 (2013)
- Yongqiang, W., Xiaoya, Z., Zhongzhen, W., Xiubo, T., Chunzhi, G., Shiqin, Y., Zhiqiang, J., Liangji, C.: Effects of modulation ratio on microstructure and properties of TiN/TiAlN multilayer coatings. *Surf. Coat. Technol.* **229**, 191–196 (2013)



# Distribution of freshwater sponges in Serbia

Stefan Andjus<sup>1</sup>, \*, Vladimir Lazović<sup>2</sup>, Nadja Nikolić<sup>3</sup>, Bojana Tubić<sup>1</sup>, Vera Nikolić<sup>4</sup>  
and Momir Paunović<sup>1</sup>

With 4 figures and 1 table

**Abstract:** As data on the distribution of freshwater sponges (Porifera, Demospongiae, Spongillida) in Serbia are extremely scarce, we investigated the main Serbian rivers and lakes with respect to Porifera occurrence, for which 17 lotic and 11 lentic water bodies were selected. Sponges were found in 11 of 17 rivers (62 specimens in total) and in 3 of 11 lakes/reservoirs (seven specimens in total). Classical morphological spicule analysis was coupled with polymerase chain reaction (PCR) and gene sequencing for species identification. Among the 69 collected specimens, five sponge species of the family Spongillidae have been identified: *Ephydatia fluviatilis* (Linnaeus, 1759), *Spongilla lacustris* (Linnaeus, 1759), *Ephydatia muelleri* (Lieberkühn, 1856), *Trochospongilla horrida* Weltner, 1893, and *Eunapius fragilis* (Leidy, 1851). The most frequently found sponge in Serbian rivers was *E. fluviatilis* (45 % of all specimens), while the least frequent was *E. fragilis* (6 % of all specimens). The Tisa river has the highest sponge diversity (four species). In lentic water bodies, only *E. fluviatilis* (four specimens) and *S. lacustris* (three specimens) were found. In general, sponges were infrequent and their abundance was low in Serbian fresh waters. While sponges seem to tolerate significant variations of physical and chemical parameters, some optimal values can be established.

**Keywords:** Serbian lotic and lentic waters; Porifera; spicule morphology; physical and chemical parameters

## Introduction

Freshwater sponges, which are ubiquitous benthic organisms, are widely distributed, live at all latitudes (Manconi & Pronzato 2007; Manconi & Pronzato 2008; Manconi & Pronzato 2015), and are predominantly marine, with the exception of the family Spongillidae, an extant of freshwater demospongia whose fossil record begins in the Permo-Carboniferous era (Schindler et al. 2008; Pronzato et al. 2017). Six families with 48 known genera colonize a variety of flowing and stagnant water habitats (Manconi & Pronzato 2002; Manconi & Pronzato 2015). Sponges are sessile organisms with an outstanding filtering

potential and the capacity to capture high amounts of bacteria present in the water, making them an important element in the purification process of freshwater ecosystems (Manconi & Pronzato 2008). Sponges also represent fine microhabitats for other species, and can be found associated with unicellular algae, protists, hydrozoans, nematodes, worms, turbellarians and several other invertebrates and vertebrates (Pronzato & Manconi 2001; Manconi & Pronzato 2008; Manconi & Pronzato 2015). They can be found attached to rocks and logs in a variety of habitats with different levels of pollution, and hence they may be used as water-quality indicators (Venkateswara Rao et al. 2009).

---

### Authors' addresses:

<sup>1</sup> University of Belgrade, Institute for Biological Research “Siniša Stanković” – National Institute of the Republic of Serbia, Bul. despota Stefana 142, 11060 Belgrade, Serbia

<sup>2</sup> University of Belgrade, Institute of Physics, Pregrevica 118, 11080 Belgrade, Serbia

<sup>3</sup> University of Belgrade, School of Dental Medicine, dr Subotica 8, 11000 Belgrade, Serbia

<sup>4</sup> University of Belgrade, Faculty of Biology, Studentski trg 16, 11000 Belgrade, Serbia

\* Corresponding author: stefan.andjus@ibiss.bg.ac.rs

## New records of *Navicula* sensu stricto from Serbia with taxonomic notes and autecological characterization of *Navicula splendicula* and *N. moskalii*

by

Danijela Vidakovic<sup>1,\*</sup>,  
Olga Jakovljević<sup>2</sup>,  
Vladimir Lazović<sup>3</sup>,  
Sanja Šovran<sup>2</sup>,  
Jelena Krizmanić<sup>2</sup>

DOI: [10.1515/ohs-2020-0006](https://doi.org/10.1515/ohs-2020-0006)

Category: **Original research paper**

Received: **March 18, 2019**

Accepted: **June 24, 2019**

<sup>1</sup>University of Belgrade, Institute of Chemistry, Technology and Metallurgy, Department of Chemistry, Njegoseva 12, 11000 Belgrade, Serbia

<sup>2</sup>University of Belgrade, Faculty of Biology, Institute of Botany and Botanical Garden "Jevremovac" Takovska 43, 11000 Belgrade, Serbia

<sup>3</sup>University of Belgrade, Institute of Physics, Pregrevica 118, 11000 Belgrade, Serbia

\* Corresponding author: [daca.vidakovic@yahoo.com](mailto:daca.vidakovic@yahoo.com)

### Abstract

A total of 15 *Navicula* taxa were recorded in epilithic communities occurring in seven rivers of Serbia, all of which are new to the diatom flora of Serbia. The most interesting of them are *N. splendicula* and *N. moskalii*. When observing *N. splendicula* specimens under SEM, we noticed a characteristic silicate tongue in the center of raphe ends, which had not been previously reported in the available literature. The insufficiently researched distribution of *N. moskalii* and scarce autecological information on the taxon prompted us to provide new details about the species in this study. These findings clearly indicate the need for further comprehensive research that would provide new information on rare taxa.

**Key words:** diatoms, ecological preferences, *Navicula splendicula*, *Navicula moskalii*, SEM, silicate tongue

## Introduction

*Navicula*, one of the most species-rich freshwater genera, was originally described in 1822 by Bory de St. Vincent. Its typification has been changed several times (Patrick 1959; Cox 1979) and species were organized into 15 sections (Hustedt 1961–1966; Van-Landingham 1975). Only members of the section *Lineolatae* Cleve (1895: 10), which comprises the neotypus generis *Navicula tripunctata* (O.F. Müller) Bory, were included in *Navicula sensu stricto* (Cox 1979). *Navicula sensu stricto* includes a group of species with boat-shaped valves characterized by different shapes of apices, uniseriate striae composed of slit-like areolae and two plate-like, girdle-appressed plastids (Round et al. 1990; Lange-Bertalot 2001). Central pores of the raphe can be deflected toward the primary side (section *Alinea*) or toward the secondary side, where the Voigt fault is located (section *Navicula*).

To date, the order Naviculales includes 5003 taxa, the family Naviculaceae – 1944 species, and the genus *Navicula* – 1344 species (Guiry 2018). *Navicula sensu stricto* has been recorded throughout Europe from different types of freshwater habitats, e.g. springs, rivers, lakes (Lange-Bertalot 2001; Miho et al. 2004; Werum, Lange-Bertalot 2004; Levkov et al. 2007; Van de Vijver et al. 2010; 2011; Beauger et al. 2015; Cantonati et al. 2016). In Serbia, the genus is also widespread and has so far been recorded in rivers (Laušević 1993; Andrejić et al. 2012a,b; Vidakovic et al. 2014; 2015a; Krizmanić et al. 2015a; Jakovljević et al. 2016a,b), peat bogs (Vidakovic et al. 2015b), salt marshes (Krizmanić et al. 2008), lakes (Zlatković et al. 2010; Trbojević et al. 2017) and reservoirs (Cvijan & Laušević 1997; Simić 2004; Gavrilović et al. 2016).

The main objectives of this study were as follows: (1) to describe *Navicula* taxa new to the territory of Serbia, (2) to describe in detail morphological characteristics of *N. splendidula* and *N. moskalii*, and (3) to provide ecological preferences of *N. splendidula* and *N. moskalii*.

## Materials and methods

Epilithic diatom samples were collected from seven rivers in Serbia: the Rasina, the Rača, the Raška, the Studenica, the Mlava, the Vrla, and the Radovanska Reka. The Rača, the Raška and the Studenica are located in the southwestern part of Serbia, the Rasina is located in the central part, while the Mlava, the Vrla and the Radovanska Reka are located in the eastern part of Serbia (Fig. 1). The rivers have a carbonate bedrock substrate and run through trout farms.



**Figure 1**

Map of Serbia with an indication of the surveyed rivers. RČ – Rača; ST – Studenica; RŠ – Raška; RA – Rasina; ML – Mlava; RD – Radovanska Reka; VR – Vrla

Samples were collected in 2011 and 2012 by scraping the upper surface of rocks with a stiff brush (a total of 234 samples were collected). The analyzed chemical and physical factors include water temperature, pH, conductivity, oxygen, total phosphorus, ammonium and nitrate ions. Water temperature, pH, conductivity and oxygen were measured at each sampling site using a PCE-PHD device. Concentrations of total phosphorus, ammonium ions and nitrate ions were determined at the Institute of General and Physical Chemistry, University of Belgrade. Diatom samples were processed in the laboratory according to the permanent slide preparation method described by Krammer, Lange-Bertalot (1986).

A Zeiss AxiomagerM.1 microscope with DIC optics and AxioVision 4.8 software were used to carry out light microscope observations and to prepare micrographs. Abundance was estimated by counting 400 valves of each taxon present on a slide. SEM observations were made at the Institute of

Physics, University of Belgrade, using a TESCAN MIRA 3 scanning electron microscope with a maximum accelerating voltage of 30 kV. Surfaces of samples were sputtered with gold using a Quorum Technologies SC7620 Mini Sputter Coater for enhanced conductivity.

## Results

*Navicula* is one of the most species-rich genera in Serbian rivers. To date, 61 *Navicula* taxa have been recorded in Serbia (Table 1, Supplementary material). During the field research conducted in seven rivers, we recorded 15 *Navicula* taxa new to the diatom flora of Serbia (Table 1, Fig. 2).

Water in these rivers is alkaline, oligo- to  $\alpha$ -mesosaprobic, characterized by low to moderate electrolyte content, poor in total phosphorus, rich in ammonium and nitrate ions (Table 2).

Of all the recorded taxa, *N. splendidula* and *N. moskalii* are the most interesting ones. Their detailed morphological characteristics with ecological preferences are presented below.

***Navicula splendidula*** Van Landingham (Fig. 3. 1–17; Fig. 4. 1–6)

**Reference.** Lange-Bertalot 2001 (p. 6, Figs 1–7; p. 65, Fig. 4; p. 69, Fig. 1)

**Morphological characteristics (LM).** Valve outline narrowly to broadly lanceolate. Ends broadly protracted and obtusely rounded. Length 23.2–45.9  $\mu\text{m}$ , breadth 6.8–9.0  $\mu\text{m}$ . Raphe filiform; axial area narrow, central area small, characterized by longer and

shorter striae. Striae radiate in the middle and parallel at the ends, 14–17/10  $\mu\text{m}$  (Fig. 3. 1–17).

**Morphological characteristics (SEM).** Axial and central areas flat without ornamentation (Fig. 4. 1, 3, 5). Raphe branches straight with deflected central pores toward the secondary side and elongated, drop-like (Fig. 4. 1–5). A characteristic silicate tongue appears in the center of raphe ends (Fig. 4. 2, 4). Terminal raphe fissures arising from the terminal pores running almost straight to the valve mantle (Fig. 4. 6). Striae composed of slit-like lineolae, 25–29/10  $\mu\text{m}$ .

**Distribution in Serbia.** *Navicula splendidula* was recorded in the Rasina, the Rača, the Studenica and the Vrla. In the Rasina River, it occurred with relative abundance of 0.2–1.73%, in the Rača River – 0.44–0.99% and in the Vrla River – 0.3%; whereas in the Studenica River only the presence of the species was noted, without estimating its abundance.

**Ecology:** *Navicula splendidula* was recorded in epilithic diatom communities in small rivers, at altitudes between 273 and 1142 m a.s.l. The substrate consisted of carbonate bedrock, which is consistent with conductivity values. The proximity of sampling sites to trout farms explains the elevated concentrations of ammonium and nitrate ions. Waters were alkaline, oligo- to  $\alpha$ -mesosaprobic (Table 2).

***Navicula moskalii*** Metzeltin, Witkowski & Lange-Bertalot (Fig. 2. 1–10; Fig. 5. 1–5)

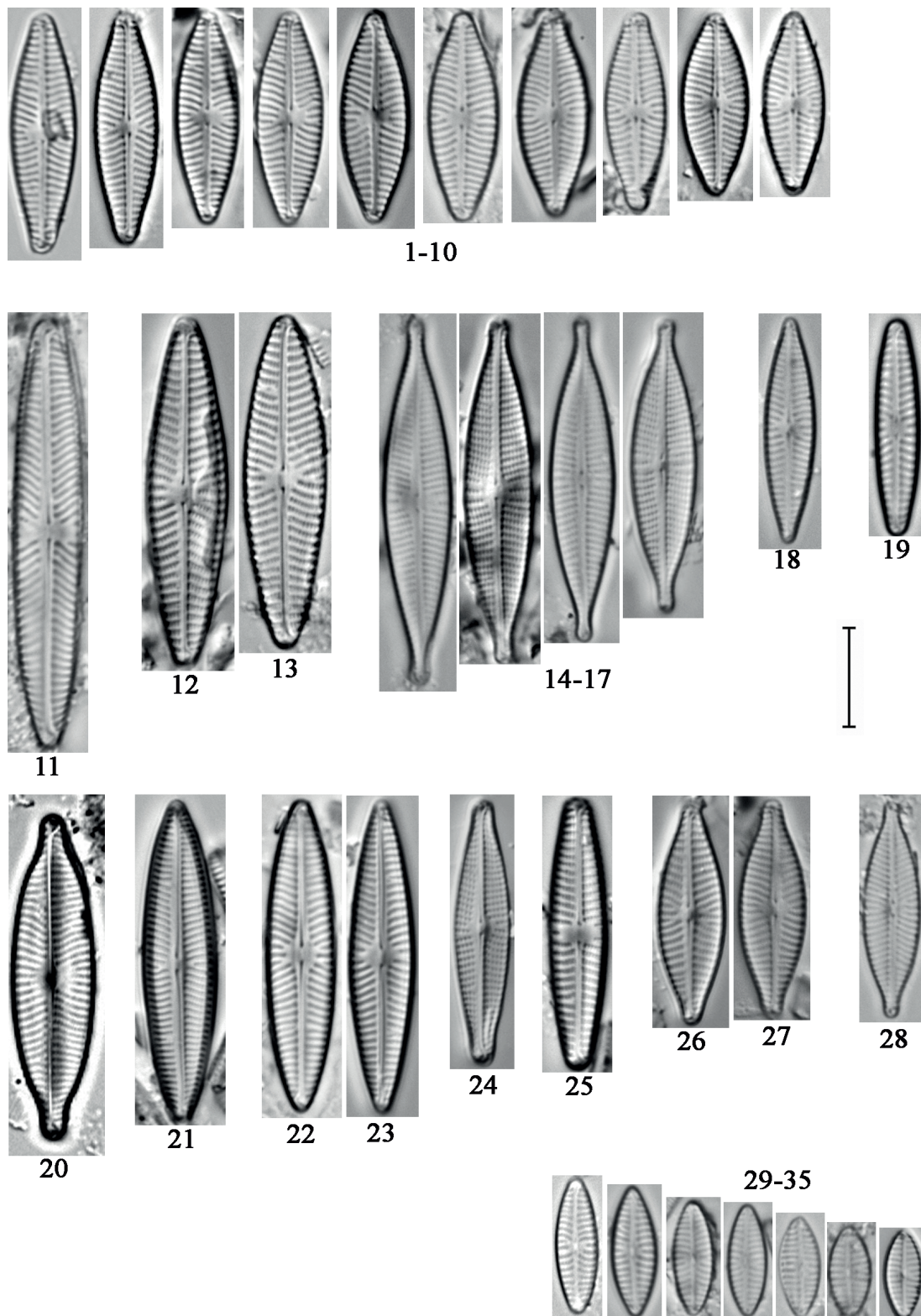
**Reference.** Lange-Bertalot 2001 (p. 14, Figs 1–14; p. 64, Fig. 8)

**Table 1**

List of *Navicula* species new to the diatom flora of Serbia

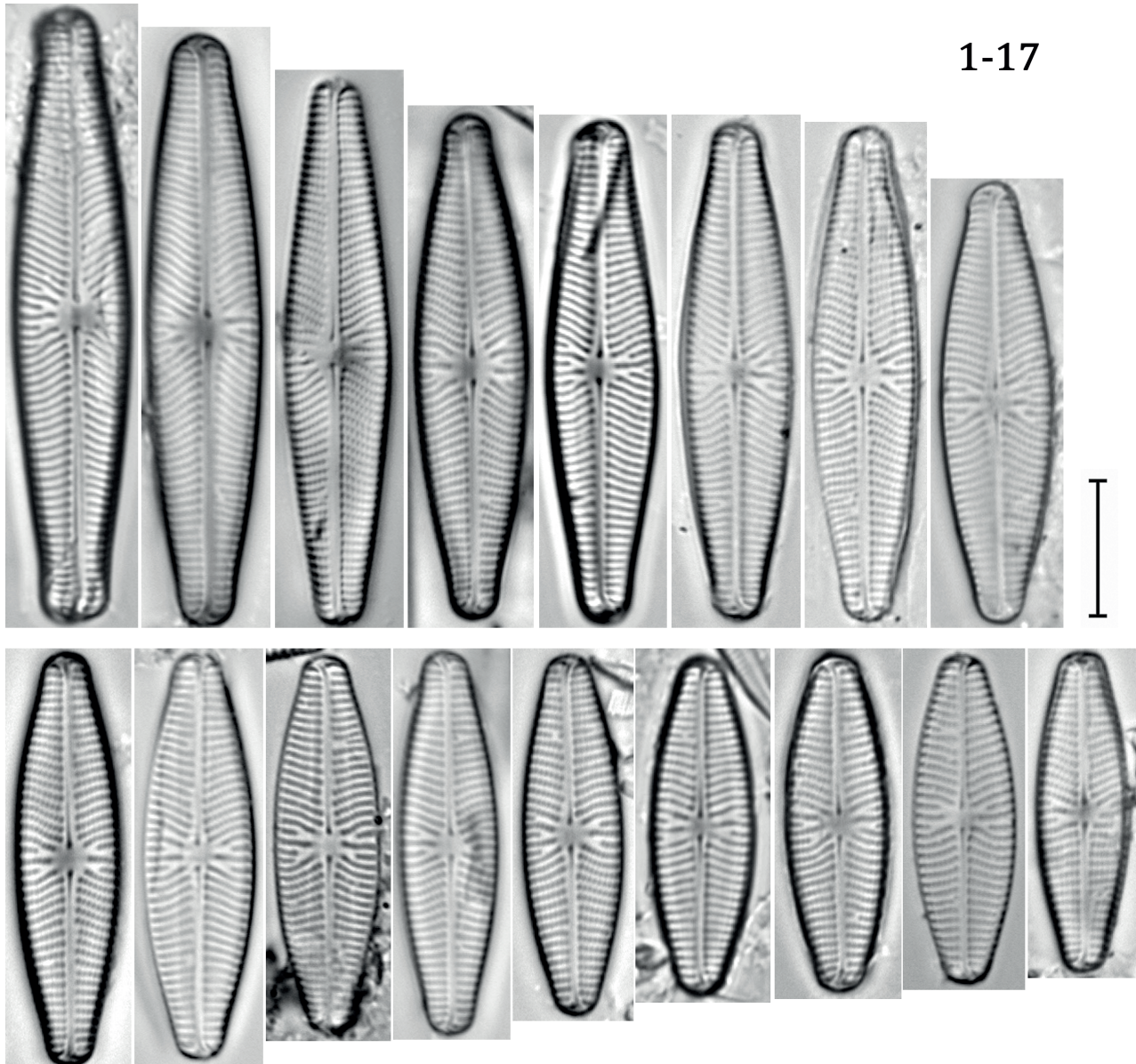
Taxon	River	Figure
<i>N. aquaedurae</i> Lange-Bertalot	ML	Fig. 2. 18
<i>N. associata</i> Lange-Bertalot	ML, RD	Fig. 2. 26, 27
<i>N. cariocincta</i> Lange-Bertalot	ML	Fig. 3. 11
<i>N. cataracta-rheni</i> Lange-Bertalot	VR	Fig. 2. 22, 23
<i>N. cryptotenelloides</i> Lange-Bertalot	RA, RČ, ST, ML, RD, VR	Fig. 2. 29–35
<i>N. germainii</i> J.H.Wallace	VR	Fig. 2. 20
<i>N. libonensis</i> Schoeman	RA, RŠ	Fig. 2. 25
<i>N. moskalii</i> Metzeltin, Witkowski & Lange-Bertalot	RA, RŠ, RČ, ST, ML, RD,	Fig. 2. 1–10, Fig. 5. 1–5
<i>N. oppugnata</i> Hustedt	RA, RŠ, ML, RD	Fig. 2. 12, 13
<i>N. praeterita</i> Hustedt	ST, ML	Fig. 2. 14–17
<i>N. splendidula</i> VanLandingham	RA, RČ, ST, VR	Fig. 3. 1–17, Fig. 4. 1–6
<i>N. stankovicii</i> Hustedt	RA	Fig. 2. 21
<i>N. subalpina</i> Reichardt	RŠ, ML	Fig. 2. 28
<i>N. vandamii</i> Schoeman & Archibald	ML	Fig. 2. 24
<i>N. wiesneri</i> Lange-Bertalot	RA, RŠ, VR	Fig. 2. 19

RČ – Rača; ST – Studenica; RŠ – Raška; RA – Rasina; ML – Mlava; RD – Radovanska Reka; VR – Vrla



**Figure 2**

Light microscopy (LM) micrographs. 1–10 *N. moskalii*; 11 *N. cariocincta*; 12, 13 *N. oppugnata*; 14–17 *N. praeterita*; 18 *N. aquaedurae*; 19 *N. wiesneri*; 20 *N. germainii*; 21 *N. stankovicii*; 22, 23 *N. cataracta-rheni*; 24 *N. vandamii*; 25 *N. libonensis*; 26, 27 *N. associata*; 28 *N. subalpina*; 29–35 *N. cryptotenelloides*. Scale bar = 10 µm

**Figure 3**

Light microscopy (LM) micrographs. 1–17 *N. splendicula*. Scale bar = 10  $\mu\text{m}$

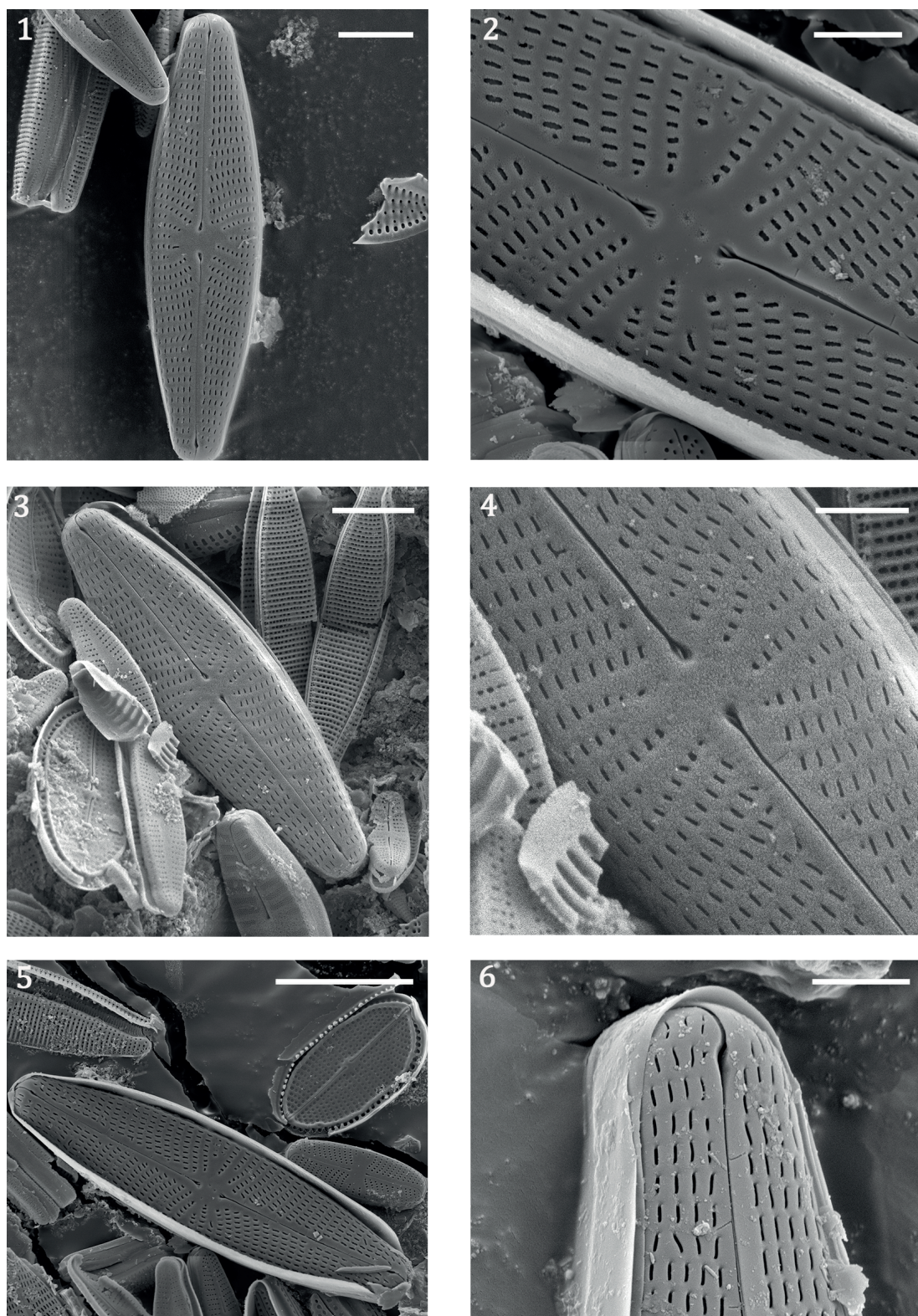
**Table 2**

Mean values of physical and chemical parameters of water from seven rivers in Serbia

Parameters	Unit	Rivers						
		Rasina	Rača	Studenica	Raška	Mlava	Vrla	Radovanska
T	$^{\circ}\text{C}$	2.5–18.7	5.7–17.3	1.4–19.1	9.9–13.5	6.4–16.8	2–15	6.4–15.4
pH		7.32–8.41	7.9–8.68	7.6–8.72	7.02–8.23	7.14–8.12	7.5–8.43	7.18–8.34
DO	$\text{mg l}^{-1}$	9.2–14.4	9.5–12.5	9.2–16.4	7–12.6	7.5–12.2	8.8–15.1	7.5–12.8
BOD		1.3–8.8	2.2–7.5	2.45–9	2.05–8.3	1.4–7.8	< 0.2–6.7	1.25–7.2
$\text{N-NH}_4^+$		0.02–0.33	0.04–0.41	0.02–0.30	0.01–0.52	0.04–0.56	0.005–0.26	0.02–1.1
$\text{N-NO}_3^-$		1.41–6.7	1.39–7.3	0.93–2.21	6.3–7.9	3.62–7.6	0.60–3.4	4.23–9
Con.	$\mu\text{S cm}^{-1}$	120–345	247–384	146–257	305–423	340–506	58–115.6	278–540
TP	$\mu\text{g P l}^{-1}$	11–61.6	6.7–86.5	11.5–73	13.5–97.6	8.7–115.1	22.1–91	16–66.5

T – Temperature, DO – Dissolved oxygen, TP – Total phosphorus, Con. – Conductivity



**Figure 4**

Scanning electron microscopy (SEM) micrographs of *N. splendida* (1–6). 1–6 External valve view of the frustule; 6 Terminal raphe fissures; 2, 4 Center of raphe ends with the silicate tongue. Scale bar = 5  $\mu\text{m}$  for 1, 3; 2  $\mu\text{m}$  for 2, 4, 6; 10  $\mu\text{m}$  for 5

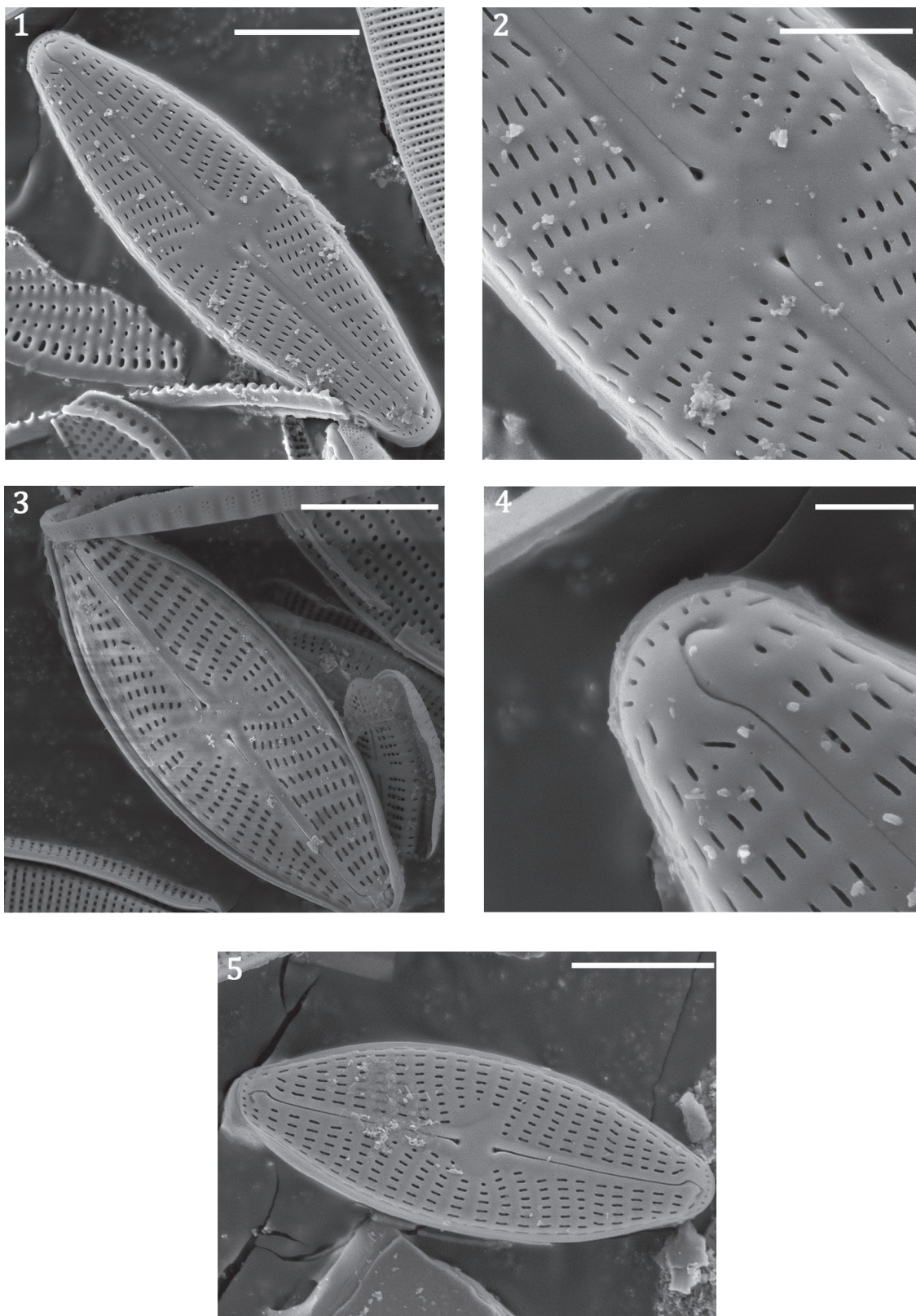


**Figure 5**

Scanning electron microscopy (SEM) micrographs of *N. moskalii* (1–5). Scale bar = 5  $\mu\text{m}$  for 1, 3, 5; 2  $\mu\text{m}$  for 2; 1  $\mu\text{m}$  for 4

**Morphological characteristics (LM).** Valve outline broadly lanceolate. Ends slightly protracted and obtusely rounded. Length 16.1–31.7  $\mu\text{m}$ , breadth 5.8–8.5  $\mu\text{m}$ . Raphe filiform, axial area linear, central area moderately large, rectangular to elliptic and asymmetric. Striae radiate and sometimes curved at the center, parallel to slightly convergent at the ends, 13–16/10  $\mu\text{m}$ ; lineolae 29–34/10  $\mu\text{m}$  (Fig. 2. 1–10).

**Morphological characteristics (SEM).** Sternum elevated relief-like, interrupted in the center (Fig. 5. 1, 2, 5). On the strongly tilted valve, the sternum appears scarcely elevated (Fig. 5. 3). Central pores expanded drop-like and the central area almost asymmetric (Fig. 5. 2). Terminal raphe fissures slightly curved, with one row of terminal pores visible (Fig. 5. 4).

**Distribution in Serbia.** *Navicula moskalii* was recorded in the Rača, the Raška, the Rasina, the Studenica, the Mlava and the Radovanska Reka. In the Rača River, it occurred with relative abundance of 0.42–0.49%, in the Rasina River – 0.49%, in the Studenica River – 0.5% and in the Radovanska Reka – 0.24%; whereas in the Raška and the Mlava only the presence of *N. moskalii* was noted, without estimating its abundance.

**Ecology:** The species was recorded in epilithic diatom communities in small, alkaline, oligo- to  $\alpha$ -mesosaprobic mountain rivers, at altitudes between 273 and 701 m a.s.l. The substrate was carbonate bedrock, which is consistent with conductivity values. The proximity of the sampling sites to trout farms explains the elevated concentrations of ammonium and nitrate ions (Table 2).

## Discussion

The first diatom taxa were recorded in Serbia by Schaarschmidt (1883). However, extensive research on diatoms did not begin until the second half of the 20th century (Blaženčić et al. 1985; Blaženčić 1986). Several papers have been published so far (e.g. Andrejić et al. 2012a,b; Krizmanić et al. 2015a,b; 2016; Vidaković et al. 2014; 2015a,b; 2017; 2018; Jakovljević et al. 2016a,b), which have resulted in the extension of the diatom checklist to about 900 taxa (Krizmanić et al. unpubl. data). The main reason for the continuous increase in the number of new diatom taxa in the flora of Serbia is most likely insufficient research on different types of habitats and under-reporting.

Detailed descriptions of *Navicula splendidula* morphology are provided in Diatoms of Europe (Lange-Bertalot 2001) and Freshwater Benthic Diatoms

of Central Europe (Cantonati et al. 2017). The only available SEM micrographs are presented in Diatoms of Europe, where Lange-Bertalot gives the following description: “central area almost symmetric; central pores apically elongated drop-like” (Lange-Bertalot 2001: 374, Fig. 1). The SEM micrographs presented in our paper clearly show a silicate tongue in the center of raphe ends. The silicate tongue was observed in other taxa, e.g. *N. tipunctata* (Lange-Bertalot 2001: 370, Figs 3, 4), *N. concentrica* (Lange-Bertalot 2001: 380, Fig. 6) and *N. jakovljevicii* (Lange-Bertalot 2001: 378, Fig. 6), which suggests that this may be an important taxonomic character. This character is not mentioned in the description of *N. splendidula* probably due to possible corrosion of the described material. In several papers, *N. splendidula* was just listed with information about the community in which it was found, without details about ecological preferences. It was recorded in small numbers in epipelagic (Atici & Obali 2010), epiphytic (Millie, Lowe 1981; Atici and Obali 2010), epilithic (Battagazzore et al. 2003; Atici & Obali 2010; Noga et al. 2014) and plankton communities (Ziller, Economou-Amilli 1998; Bolgovics et al. 2015). Known facts about its ecological preferences indicate that the taxon prefers oligo-mesotrophic to eutrophic calcium-rich waters with average electrolyte content and oligo- to  $\beta$ -mesosaprobic characteristics (Lange-Bertalot 2001; Cantonati et al. 2017). *Navicula splendidula* belongs to the group of diatoms tolerant of a wide spectrum of oligo- to eutrophic conditions, but intolerant of higher saprobity levels (Lange-Bertalot 2001). According to our results, it occurs at sites with elevated concentrations of ammonium and nitrate ions. According to Lange-Bertalot (2001), *N. splendidula* was recorded in Southern and Central Europe. The exception is the type locality (Drinkuellen – St. Naum Springs), which is located near Lake Ohrid. In recent years, it was recorded in Italy in the Argentino and Abatemarco rivers (Battagazzore et al. 2003), in streams of the central Apennine mountains (Dell’Uomo & Torrisi 2009), in Lake Ohrid in Albania (Miho & Tase 2004), in the San River in southeastern Poland (Noga et al. 2014) and in the Sajó River in Slovakia and Hungary (Bolgovics et al. 2015). The taxon was recorded outside Europe, in the Asartepe Dam Lake in Turkey (Atici & Obali 2010), in Lake Erie and the Laurentian lakes in North America (Millie & Lowe 1981), and in the Niger Delta system in Nigeria (Ziller & Economou-Amilli 1998).

The distribution of *Navicula moskalii* is still insufficiently explored and autecological data on the species are still scarce, which prompted us to present details about this species. According to Cantonati et al. (2017), *N. moskalii* is more or less characteristic

of calcium-rich and meso- to eutrophic lotic waters and lakes. Our results confirm that the taxon occurs in calcium-rich lotic waters, but also supplement the available ecological data with the information about its presence in oligo- to  $\alpha$ -mesosaprobic waters with low to moderate electrolyte content, low concentrations of total phosphorus and elevated concentrations of ammonium and nitrate ions. According to Szczepocka & Rakowska (2015), *N. moskalii* is an indicator species characteristic of waters with good ecological status as well as calcareous and silicate waters, which contradicts the statement that it is “apparently absent from nutrient-poor freshwater habitats of siliceous regions” (Cantonati et al. 2017). After the first finding on the Arctic Bear Island, *N. moskalii* was also found in the Kinzig River in Germany (Lange-Bertalot 2001), in a peat bog in the Eastern Carpathians and in the Apuseni Mountains in Transylvania (Szigyártó et al. 2017, only mentioned in the text), in the Kobylanka stream and the Czarna Staszowska River in Poland (Wojtal 2009: 174, Fig. 30, 15; Szczepocka & Rakowska 2015, only mentioned in the text), and in a peat bog in the Novgorod region of Russia (Kulikovskiy 2009: 96, Fig. 1, 13). Wojtal (2009) and Szczepocka & Rakowska (2015) found *N. moskalii* only in the epipelagic community, while in our samples it was present in the epilithic community. The valve dimensions reported by Lange-Bertalot (2001) are: length 24–27  $\mu\text{m}$ , breadth 6.8–8  $\mu\text{m}$ , with 11.5–15 striae per 10  $\mu\text{m}$ . Kulikovskiy (2009) found a single specimen, which was 21.8  $\mu\text{m}$  long, 6.4  $\mu\text{m}$  wide, with 12 striae per 10  $\mu\text{m}$ . Our population shows a broader dimension range, with a length of 16.1–31.7  $\mu\text{m}$  and a breadth of 5.8–8.5  $\mu\text{m}$ .

These findings clearly indicate the need for further extensive research to provide new information on insufficiently known and rare taxa.

## Acknowledgements

Financial support was provided by the Ministry of Education and Science of the Republic of Serbia (Project No. TR 037009).

## References

- Andrejić, J., Krizmanić, J. & Cvijan, M. (2012a). Three new records for diatoms from the Nišava River and its tributary, the Jerma River (Southern Serbia). *Oceanol. Hydrobiol. St.* 41(3): 17–23. DOI: 10.2478/s13545-012-0021-3.
- Andrejić, J.Z., Krizmanić, J. & Cvijan, M. (2012b). Diatom species composition of the Nišava river and its tributaries Jerma and Temska rivers (southern Serbia). *Arch. Biol. Sci.* 64(3): 1127–1140. DOI: 10.2298/ABS1203127A.
- Atici, T. & Obali, E.O. (2010). The diatoms of Asartepe Dam Lake (Ankara), with environmental and some physicochemical properties. *Turk. J. Botany* 34(6): 541–548. DOI: 10.3906/bot-0912-271.
- Battegazzore, M., Gallo, L., Lucadamo, L. & Morisi, A. (2003). Quality of the main watercourses in the Pollino National Park (Apennine Mts, S Italy) on the basis of the diatom benthic communities. *Studi. Trent. Sci. Nat., Acta Biol.* 80: 89–93.
- Beauger, A., Voldoire, O., Mertens, A., Le Cohu, R. & Van de Vijver, B. (2015). Two new *Navicula* species (Bacillariophyceae) from Western Europe. *Phytotaxa* 230(2): 172–182. DOI: 10.11646/phytotaxa.230.2.4.
- Blaženčić, J. (1986). Pregled razvoja algologije u Srbiji od 1883. do 1983. godine. *Glasnik Instituta za botaniku i Botaničke bašte Univerziteta u Beogradu XX*: 99–108. (In Serbian).
- Blaženčić, J., Martinović-Vitanović, V., Cvijan, M. & Filipi-Matutinović, S. (1985). Bibliografija radova o algama i algoškim istraživanjima u SR Srbiji od 1947. do 1980. godine. *Glasnik Instituta za botaniku i Botaničke bašte Univerziteta u Beogradu XIX*: 233–266. (In Serbian).
- Bolgovics, Á., Ács, É., Várbíró, G., Kiss, K.T., Lukács, B.A. et al. (2015). Diatom composition of the rheoplankton in a rhithral river system. *Acta Bot. Croat.* 74(2): 303–316. DOI: 10.1515/botcro-2015-0028.
- Cantonati, M., Angeli, N., Spitale, D. & Lange-Bertalot, H. (2016). A new *Navicula* (Bacillariophyta) species from low-elevation carbonate springs affected by anthropogenic disturbance. *Fottea* 16(2): 255–265. DOI: 10.5507/fot.2016.013.
- Cantonati, M., Kelly, M.G. & Lange-Bertalot, H. (2017). *Freshwater benthic diatoms of Central Europe: over 800 common species used in ecological assessments. English edition with updated taxonomy and added species.* Schmitten-Oberreifenberg: Koeltz Botanical Books.
- Cleve, P.T. (1895). Synopsis of the Naviculoid Diatoms, Part II. *Kongliga Svenska-Vetenskaps Akademiens Handlingar* 27(3): 1–219.
- Cox, E. (1979). Taxonomic studies on the diatom genus *Navicula* Bory: the typification of the genus. *Bacillaria* 2: 137–153.
- Cvijan, M. & Laušević, R. (1997). Floristički sastav algi Vlasinskog jezera u periodu 1949–1993. godine. In J. Blaženčić (Ed.), *Vlasinsko jezero – hidrobiološka studija* (pp. 61–90). Beograd: Biološki fakultet.
- Dell’Uomo, A. & Torrisi, M. (2009). Freshwater algae and their use for safeguarding the Mediterranean basin. *Bocconea* 23: 93–105.
- Gavrilović, B., Popović, S., Čirić, M., Subakov-Simić, G., Krizmanić, J. et al. (2016). Qualitative and quantitative composition of the algal community in the water column of the Grlšte reservoir (Eastern Serbia). *Botanica Serbica* 40(2): 129–135. DOI: 10.5281/zenodo.162209.

- Guiry M.D. (2018). *AlgaeBase*. Retrieved July 19, 2018, from <http://www.algaebase.org>
- Husted F. (1961–1966). Die Kieselalgen Deutschlands, Osterreichs und der Schweiz unter Berücksichtigung der übrigen Länder Europas sowie der angrenzenden Meeresgebiete. In L. Rabenhorsts (Ed.), *Kryptogamen Flora von Deutschland, Österreich und der Schweiz* 7, 3. Teil (pp. 1–815). Leipzig: Akad. Verl.-Ges.
- Jakovljević, O.S., Popović, S.S., Vidaković, D.P., Stojanović, K.Z. & Krizmanić, J.Ž. (2016a). The application of benthic diatoms in water quality assessment (Mlava River, Serbia). *Acta Bot. Croat.* 75(2): 199–205. DOI: 10.1515/botcro-2016-0032.
- Jakovljević, O., Popović, S., Živić, I., Stojanović, K. & Krizmanić, J. (2016b). Benthic diatoms of the Vrla River (Serbia) and their application in the water ecological status assessment. *Oceanol. Hydrobiol. St.* 45(3): 304–315. DOI: 10.1515/ohs-2016-0029.
- Krammer, K. & Lange-Bertalot, H. (1986). Bacillariophyceae. 1. Teil: Naviculaceae. In H. Ettl, J. Gerloff, H. Heynig & D. Mollenhauer (Eds.), *Süßwasserflora von Mitteleuropa* 2/1 (pp. 1–876). Jena: G. Fischer Verlag.
- Krizmanić, J., Subakov-Simić, G., Cvijan, M. & Karadžić, V. (2008). Diatoms of the Three Salt Marshes in Vojvodina (Serbia). In 20<sup>th</sup> International Diatom Symposium, 7–13 September 2008 (pp. 108–108). Dubrovnik, Croatia.
- Krizmanić, J., Ilić, M., Vidaković, D., Subakov-Simić, G., Petrović, J. et al. (2015a). Diatoms of the Dojkinci River (Stara Planina Nature Park, Serbia). *Acta Bot. Croat.* 74(2): 317–331. DOI: 10.1515/botcro-2015-0022.
- Krizmanić, J., Ilić, M., Vidaković, D., Subakov-Simić, G., Cvetanović, K. et al. (2015b). New records and rare taxa of the genus *Eunotia* Ehrenberg (Bacillariophyceae) for the diatom flora of Serbia. *Botanica Serbica* 39(1): 35–44.
- Krizmanić, J., Jakovljević, O., Vidaković, D. & Jovanović, J. (2016). The first record of the genus *Decussata* (Patrick) Lange-Bertalot (Bacillariophyta) in Serbia – description, distribution and ecology of the rare species *D. hexagona* (Torka) Lange-Bertalot. *Botanica Serbica* 40(2): 161–165.
- Kulikovskiy, M.C. (2009). Виды рода *Navicula* Bory s. str. (Bacillariophyta) в сфагновых болотах Приволжской возвышенности и Полистово-Ловатском массиве (Россия). *Альгология* 19(1): 92–102.
- Lange-Bertalot, H. (2001). *Navicula* sensu stricto. 10 genera separated from *Navicula* sensu lato. Frustulia. In H. Lange-Bertalot (Ed.), *Diatoms of Europe: diatoms of the European inland waters and comparable habitats Vol. 2* (pp. 1–526). Ruggell: A.R.G. Gantner Verlag. K.G.
- Laušević, R. (1993). Floristical composition of algae in the Samokovska river. *Arch. Biol. Sci.* 45(3–4): 125–136.
- Levkov, Z., Krstić, S., Metzeltin, D. & Nakov, T. (2007). *Diatoms of lake Prespa and Ohrid*. Iconographia Diatomologica 16. Ruggell: A.R.G. Gantner Verlag KG.
- Millie, D.F. & Lowe, R.L. (1981). Diatoms new to Ohio and the Laurentian Great Lakes. *Ohio J. Sci.* 81(5): 195–206.
- Miho, A., Tase, D. & Lange-Bertalot, H. (2004). Overview on diatoms from Ohrid Lake. In Proceedings of BALWOIS, 25–29 May 2004 (pp. 1–9). Ohrid, FY Republic of Macedonia.
- Noga, T., Stanek-Tarkowska, J., Pajczek, A. & Kochman, N. (2014). Ecological assessment of the San River water quality on the area of the San Valley Landscape Park. *Journal of Ecological Engineering* 15(4): 12–22. DOI: 10.12911/22998993.1125453.
- Patrick, R.M. (1959). New species and nomenclatural changes in the genus *Navicula* (Bacillariophyceae). Proceedings of the Academy of Natural Sciences of Philadelphia. 111: 91–108.
- Round, F.E., Crawford, R.M. & Mann, D.G. (1990). *The diatoms: Biology and Morphology of the genera*. Cambridge: Cambridge University Press.
- Schaarschmidt, J. (1883). Fragmenta Phycologiae Bosniaco-Serbicae. *Magyar Növénytani Lapok.* 75(7): 33–39.
- Simić, S. (2004). Changes in structure of the phytoplankton in the Barje reservoir (Serbia). *Kragujevac J. Sci.* 26: 53–64.
- Szczepocka, E. & Rakowska, B. (2015). Diatoms in the biological assessment of the ecological state of waters using the Czarna Staszowska River as an example. *Oceanol. Hydrobiol. St.* 44(2): 254–266. DOI: 10.1515/ohs-2015-0024.
- Szigyártó, I.L., Buczkó, K., Rákossy, I., May, Z., Urák, I. et al. (2017). Contrasting diatom diversity in lentic and lotic habitats of Romanian peat bogs and the relation to environmental variables. *Fundamental and Applied Limnology/Archiv für Hydrobiologie* 189(2): 137–151. DOI: 10.1127/fal/2016/0943.
- Trbojević, I., Jovanović, J., Kostić, D., Popović, S., Krizmanić, J. et al. (2017). Structure and succession of periphyton in an urban reservoir: artificial substrate specificity. *Oceanol. Hydrobiol. St.* 46(4): 379–392. DOI: 10.1515/ohs-2017-0038.
- Van de Vijver, B., Jarlman, A. & Lange-Bertalot, H. (2010). Four new *Navicula* (Bacillariophyta) species from Swedish rivers. *Cryptogamie, Algologie* 31: 355–367.
- Van de Vijver, B., Zidarova, R., Sterken, M., Verleyen, E., de Haan, M., et al. (2011). Revision of the genus *Navicula* s.s. (Bacillariophyceae) in inland waters of the Sub-Antarctic and Antarctic with the description of five new species. *Phycologia* 50(3): 281–297. DOI: 10.2216/10-49.1.
- Vanlandingham, S.L. (1975). *Catalogue of the Fossil and Recent Genera and Species of Diatoms and their Synonyms*. Germany: J. Cramer Verlag, Lehre.
- Vidaković, D., Krizmanić, J. & Šovran, S. (2014). New taxa of the genus *Navicula* (Bacillariophyceae) in the diatom flora of Serbia. *Oceanol. Hydrobiol. St.* 43(2): 185–190. DOI: 10.2478/s13545-014-0132-0.
- Vidaković, D.P., Krizmanić, J.Ž., Šovran, S.I., Stojanović, K.Z. & Đorđević, J.D. (2015a). Diatom species composition in the Raška river (Southwestern Serbia). *Matica Srpska Journal for Natural Sciences* 128: 29–40.
- Vidaković, D., Krizmanić, J., Šovran, S. & Cvijan, M. (2015b). Diatoms from a peat bog on the Pešter plateau

(southwestern Serbia): New records for diatom flora of Serbia. *Arch. Biol. Sci.* 68(1): 107–116. DOI: 10.2298/ABS150512132V.

- Vidaković, D., Cantonati, M., Mogna, M., Jakovljević, O., Šovran, S. et al. (2017). Additional information on the distribution and ecology of the recently described diatom species *Geissleria gereckeii*. *Oceanol. Hydrobiol. St.* 46(1): 18–23. DOI: 10.1515/ohs-2017-0002.
- Vidaković, D., Jakovljević, O., Predojević, D., Radovanović, S., Subakov-Simić, G. et al. (2018). An updated list of Serbian diatom flora – new recorded taxa. *Arch. Biol. Sci.* 70(2): 259–275. DOI: 10.2298/ABS170606043V.
- Ziller, S. & Economou-Amilli, A. (1998). Freshwater algae from lakes in the lower Niger Delta system (Nigeria). *Hydrobiologia* 368(1–3): 217–229.
- Zlatković, S., Šabić, D., Milinčić, M., Knežević-Vukčević, J. & Stanković, S. (2010). Geographical and biological analysis of the water quality of Bovan Lake, Serbia. *Arch. Biol. Sci.* 62(4): 1083–1089. DOI: 10.2298/ABS1004083Z.
- Werum, M. & Lange-Bertalot, H. (2004). *Diatoms in springs, from Central Europe and elsewhere under the influence of hydrogeology and anthropogenic impacts*. Iconographia Diatomologica 13. Ruggell: A.R.G. Gantner Verlag KG.
- Wojtal, A.Z. (2009). The Diatoms of Kobylanka Stream Near Kraków (Wyżyna Krakowsko-Częstochowska Upland, S Poland). *Polish Botanical Journal* 54(2): 129–330.

## Supplementary material

Checklist of the recorded *Navicula* taxa in Serbia (from the unpublished database of Serbian diatom flora compiled by Dr Jelena Krizmanić, University of Belgrade, Faculty of Biology)

No.	Taxon
1.	<i>Navicula amphiceropsis</i> Lange-Bertalot & U.Rumrich
2.	<i>Navicula angusta</i> Grunow
3.	<i>Navicula antonii</i> Lange-Bertalot
4.	<i>Navicula aquaedurae</i> Lange-Bertalot
5.	<i>Navicula bourrellyivera</i> Lange-Bertalot, Witkowski & Stachura
6.	<i>Navicula broetzii</i> Lange-Bertalot & E.Reichardt
7.	<i>Navicula capitatoradiata</i> H.Germain ex Gasse
8.	<i>Navicula cari</i> Ehrenberg
9.	<i>Navicula catalanogermanica</i> Lange-Bertalot & G.Hofmann
10.	<i>Navicula cincta</i> (Ehrenberg) Ralfs
11.	<i>Navicula cryptocephala</i> Kützing
12.	<i>Navicula cryptofallax</i> Lange-Bertalot & G.Hofmann
13.	<i>Navicula cryptotenella</i> Lange-Bertalot
14.	<i>Navicula dealpina</i> Lange-Bertalot
15.	<i>Navicula digitoradiata</i> (W.Gregory) Ralfs
16.	<i>Navicula erifuga</i> Lange-Bertalot
17.	<i>Navicula exilis</i> Kützing
18.	<i>Navicula exilissima</i> Grunow
19.	<i>Navicula gregaria</i> Donkin
20.	<i>Navicula jakovljevicii</i> Hustedt
21.	<i>Navicula lanceolata</i> Ehrenberg
22.	<i>Navicula lundii</i> E.Reichardt
23.	<i>Navicula hasta</i> Pantocsek
24.	<i>Navicula hintzii</i> Lange-Bertalot
25.	<i>Navicula margalithii</i> Lange-Bertalot
26.	<i>Navicula menisculus</i> Schumann
27.	<i>Navicula microdigitoradiata</i> Lange-Bertalot
28.	<i>Navicula novaesiberica</i> Lange-Bertalot
29.	<i>Navicula oblonga</i> (Kützing) Kützing
30.	<i>Navicula oligotrappenta</i> Lange-Bertalot & G.Hofmann
31.	<i>Navicula peregrine</i> (Ehrenberg) Kützing
32.	<i>Navicula perminuta</i> Grunow
33.	<i>Navicula phyllepta</i> Kützing
34.	<i>Navicula pseudolanceolata</i> Lange-Bertalot
35.	<i>Navicula pseudosilicula</i> Hustedt
36.	<i>Navicula pseudotenelloides</i> Krasske
37.	<i>Navicula radiosa</i> Kützing
38.	<i>Navicula recens</i> (Lange-Bertalot) Lange-Bertalot
39.	<i>Navicula reinhardtii</i> (Grunow) Grunow
40.	<i>Navicula reichardtiana</i> Lange-Bertalot
41.	<i>Navicula rhynchotella</i> Lange-Bertalot
42.	<i>Navicula rostellata</i> Kützing
43.	<i>Navicula salinarum</i> Grunow
44.	<i>Navicula salinarum</i> var. <i>rostrate</i> (Hustedt) Lange-Bertalot
45.	<i>Navicula semen</i> Ehrenberg
46.	<i>Navicula slesvicensis</i> Grunow
47.	<i>Navicula subrhynchocephala</i> Hustedt
48.	<i>Navicula symmetrica</i> R.M.Patrick
49.	<i>Navicula staffordiae</i> L.L.Bahls
50.	<i>Navicula streckeriae</i> Lange-Bertalot & Witkowski
51.	<i>Navicula rhynchocephala</i> Kützing
52.	<i>Navicula tenelloides</i> Hustedt
53.	<i>Navicula tripunctata</i> (O.F.Müller) Bory
54.	<i>Navicula trivialis</i> Lange-Bertalot
55.	<i>Navicula trophicatrix</i> Lange-Bertalot
56.	<i>Navicula veneta</i> Kützing
57.	<i>Navicula viridula</i> (Kützing) Ehrenberg
58.	<i>Navicula viridulacalcis</i> Lange-Bertalot
59.	<i>Navicula vulpine</i> Kützing
60.	<i>Navicula upsaliensis</i> (Grunow) M.Peragallo
61.	<i>Navicula wildii</i> Lange-Bertalot



*J. Serb. Chem. Soc.* 88 (2) 183–197 (2023)  
JSCS–5619

## Influence of N doping on structural and photocatalytic properties of hydrothermally synthesized TiO<sub>2</sub>/carbon composites

MARINA M. MALETIĆ<sup>1\*#</sup>, ANA M. KALIJDIS<sup>2</sup>, VLADIMIR LAZOVIĆ<sup>3</sup>,  
SNEŽANA TRIFUNOVIĆ<sup>4</sup>, BILJANA M. BABIĆ<sup>3</sup>, ALEKSANDRA DAPČEVIĆ<sup>5#</sup>,  
JANEZ KOVAC<sup>6</sup> and MARIJA M. VUKČEVIĆ<sup>5#</sup>

<sup>1</sup>Innovation Center of the Faculty of Technology and Metallurgy, Karnegijeva 4, 11000 Belgrade, Serbia, <sup>2</sup>Department of Materials, „Vinča” Institute of Nuclear Sciences – National Institute of the Republic of Serbia, University of Belgrade, Mike Petrovića Alasa 12–14, 11000 Belgrade, Serbia, <sup>3</sup>Institute of Physics – National Institute of the Republic of Serbia, University of Belgrade, Pregrevica 118, 11080 Belgrade, Serbia, <sup>4</sup>Faculty of Chemistry, University of Belgrade, Studentski trg 12–16, 11000 Belgrade, Serbia, <sup>5</sup>Faculty of Technology and Metallurgy, University of Belgrade, Karnegijeva 4, 11000 Belgrade, Serbia and <sup>6</sup>Department of Surface Engineering, Institute Jožef Stefan, Jamova cesta 39, 1000 Ljubljana, Slovenia

(Received 8 June, revised 11 October, accepted 15 October 2022)

**Abstract:** N-doped TiO<sub>2</sub>/carbon composites (TiO<sub>2</sub>/CN) with different nitrogen content, were obtained starting from titanium isopropoxide and glucose, and by varying the amount of melamine, added to starting reaction mixture. For comparison, an undoped sample (TiO<sub>2</sub>/C) was also prepared. Structural and surface characteristics were determined through scanning electron microscopy, thermogravimetric analysis, elemental analysis, Fourier transform infrared spectroscopy, X-ray photoelectron spectroscopy, X-ray diffraction and nitrogen adsorption–desorption isotherms. The photocatalytic activity of TiO<sub>2</sub>/CN composites was examined via photocatalytic degradation of methylene blue and multiclass pharmaceuticals from water solution. It was found that N doping of TiO<sub>2</sub>/carbon composites induced changes in structural and surface characteristics of TiO<sub>2</sub>/CN composites, improving their adsorption, but decreasing photocatalytic efficiency. Nevertheless, TiO<sub>2</sub>/CN<sub>0.05</sub> composite obtained by the hydrothermal synthesis in the presence of glucose and 0.05 g melamine showed the highest efficiency for removing selected pharmaceuticals and methylene blue from aqueous solutions through the combined processes of adsorption in the dark, and photocatalytic degradation under UV and visible irradiation.

\* Corresponding author. E-mail: mvukasinovic@tmf.bg.ac.rs

# Serbian Chemical Society member.

<https://doi.org/10.2298/JSC220608079M>



*Keywords:* TiO<sub>2</sub>/carbon composites; N-doping; surface properties; photocatalytic properties; pharmaceuticals.

## INTRODUCTION

Photocatalysis represents a clean, green and sustainable technology that is constantly being studied and improved for its effective application in removing organic pollutants from the environmental water. Titanium dioxide is one of the most widely used photocatalytic materials in the fields of environmental purification, due to its advantages of good chemical stability, low cost and nontoxicity.<sup>1</sup> However, it is photocatalytically active only under UV light, due to its relatively high band gap energy.<sup>2</sup> Reduction of the band gap energy, which can be achieved by doping TiO<sub>2</sub> with non-metal elements, such as C, B, S and N,<sup>2-6</sup> spread the spectral response of TiO<sub>2</sub> into the visible region. Also, it was found<sup>7</sup> that N-doping of TiO<sub>2</sub> enhances the photocatalytic performance under UV irradiation by increasing the specific surface area of a photocatalyst.

To obtain highly reactive photocatalysts, in addition to TiO<sub>2</sub> doping with nitrogen, photocatalysts can be combined with different carbon materials that play the role of catalysts.<sup>1,8-10</sup> It was found that nitrogen doping combined with some carbon material as a carrier lead to an increase in the specific surface area of the material, as well as its photocatalytic activity under visible irradiation.<sup>1</sup>

Previously,<sup>8</sup> we have used a simple method of hydrothermal synthesis to obtain highly reactive TiO<sub>2</sub>/carbon composites for photocatalytic degradation of selected organic pollutants, under UV irradiation. In this work, the hydrothermal method was applied to synthesize the material, photocatalytically active under visible light. N-doped TiO<sub>2</sub>/carbon composites (TiO<sub>2</sub>/CN), with different nitrogen content, were obtained starting from titanium isopropoxide and glucose, and by varying the amount of melamine, added to starting reaction mixture. Obtained composites were characterized by the means of structural and surface properties. Their photocatalytic activity was tested through the degradation of methylene blue (MB) and selected pharmaceuticals, belonging to classes of antibiotics, painkillers, sedatives and cardiovascular. Additionally, it is important to highlight that some of the examined pharmaceuticals (diclofenac, azithromycin, and erythromycin) were included in the watch list of substances for union-wide monitoring in the field of water policy,<sup>11</sup> since their presence may pose a significant risk to the aquatic environment.

## EXPERIMENTAL

TiO<sub>2</sub>/carbon composites doped with nitrogen (TiO<sub>2</sub>/CN) were obtained by hydrothermal synthesis. Starting reaction mixture containing: 37 cm<sup>3</sup> glucose solution (30 g dm<sup>-3</sup>), 3 cm<sup>3</sup> 35 % hydrochloric acid, 6 cm<sup>3</sup> of titanium isopropoxide, and different amounts of melamine (0.05, 0.1 and 0.5 g), was placed in the Teflon lined stainless steel autoclave (50 cm<sup>3</sup>), and carbonized at a temperature of 160 °C and self-generated pressure for 12 h. The resulting suspension, obtained after the carbonization, was filtered and the precipitate was washed with

distilled water and ethanol and dried at 60 °C overnight. Obtained samples were denoted as TiO<sub>2</sub>/CN<sub>0.05</sub>, TiO<sub>2</sub>/CN<sub>0.1</sub> and TiO<sub>2</sub>/CN<sub>0.5</sub>, respectively, based on the amount of melamine used. For the purpose of comparison, the undoped sample (TiO<sub>2</sub>/C) was prepared according to the same procedure, without melamine adding.

Scanning electron microscopy (Mira Tescan 3X, Tescan Orsay Holding, Czech Republic) was used to examine the structure and morphology of prepared carbon composites.

The thermogravimetric analysis (TGA, SDT Q600, TA Instruments) was performed in the O<sub>2</sub> atmosphere (flow rate: 100 cm<sup>3</sup> min<sup>-1</sup>) from room temperature up to 800 °C, with a heating rate of 20 °C min<sup>-1</sup>.

Elemental analysis (Vario EL III Element Analyzer, Elementar, Shimadzu Europe) was performed to determine the nitrogen content in the synthesized composite materials.

Fourier transform infrared spectroscopy (FTIR, Bomem MB-Series, Hartmann Braun) was used for qualitative analysis of surface functional groups. FTIR spectra were obtained in the wavenumber range from 400 to 4000 cm<sup>-1</sup>.

X-Ray photoelectron spectroscopy (XPS) measurements were performed on the PHI-TFA XPS spectrometer produced by Physical Electronics Inc. and equipped with the monochromatic X-ray source with the Al anode. Wide energy range XPS spectra were taken with pass energy of 187 eV to identify present elements and high-energy resolution XPS spectra were taken with pass energy 29 eV to identify chemical bonds of elements on the surface. Low-energy electron gun was used for neutralization of possible charging effects.

The specific surface area and the pore size distribution (PSD) of carbon composites were analyzed using the Surfer (Thermo Fisher Scientific, USA). PSD was estimated by applying Barrett–Joyner–Halenda (BJH) method<sup>12</sup> to the desorption branch of isotherms and mesopore surface ( $S_{\text{meso}}$ ) and micropore volume ( $V_{\text{micro}}$ ) were estimated using the *t*-plot method.<sup>13</sup>

X-ray diffraction (XRD) patterns were performed by Philips PW1710 diffractometer with CuK $\alpha$  radiation at a scanning speed 1 °C min<sup>-1</sup> in the range of  $2\theta$  of 20–60°. Based on obtained X-ray diffraction patterns, crystalline phases have been identified, and approximate share of the individual phases in the product and the crystallite size was calculated by computer program Powder Cell.<sup>14</sup>

The photocatalytic activity of TiO<sub>2</sub>/CN composites, as well as undoped TiO<sub>2</sub>/C composite, was evaluated by photocatalytic degradation of methylene blue (MB) and selected pharmaceuticals from multicomponent solution. Experiments were carried out at room temperature and atmospheric pressure with constant shaking on a magnetic stirrer. The starting concentration of the MB solution was 25 mg dm<sup>-3</sup>, while the concentration of composite material was 2 g dm<sup>-3</sup>. The suspension was held for 60 min in the dark until an adsorption–desorption equilibrium is reached, after which the suspension was exposed to UV irradiation. Process of photocatalytic degradation was monitored by periodic sampling (60, 75, 90, 105, 120, 150 and 180 min), and measuring of MB concentration. To compare the photocatalytic activity of examined samples under visible irradiation, MB solution with an initial concentration of 10 mg dm<sup>-3</sup> was used. As a source of UV irradiation, 125 W high-pressure mercury lamp, Philips, HPLN was used, while visible irradiation was obtained by 150 W tungsten halogen lamp with a 400 nm cut off glass optical filter.

Also, TiO<sub>2</sub>/CN composites were used as photocatalysts for degradation of the selected pharmaceuticals: diclofenac (painkillers); bromazepam (sedatives); atorvastatin, amlodipine, cilazapril and clopidogrel (cardiovascular); azithromycin, doxycycline and erythromycin (antibiotics). The initial concentration of each of the selected pharmaceuticals from the multicomponent solution was 5 mg dm<sup>-3</sup>. The concentration of composite photocatalysts was 1 g

dm<sup>-3</sup>, while experimental conditions were the same as for degradation of MB under UV irradiation. The solution samples were taken after 180 min of the removal process, which included 60 min of adsorption in the dark, followed by photocatalytic degradation. Samples were filtered through 0.45 µm PVDF syringe filters, and the concentration of selected pharmaceuticals was assessed by high-performance liquid chromatography–tandem mass spectrometry (LC–MS/MS Thermo Scientific). LC–MS/MS method conditions are given in the Supplementary material to this paper.

## RESULTS AND DISCUSSION

The morphological characteristics of TiO<sub>2</sub>/CN samples were examined by scanning electron microscopy (Fig. 1). Compared to the undoped sample (Fig. 1d), the addition of melamine in the reaction mixture does not lead to any important differences in the morphology of obtained composites. SEM photographs showed that all N-doped TiO<sub>2</sub>/carbon composites were characterized by a similar and homogenous structure, regardless of the amount of melamine added to the reaction mixture.

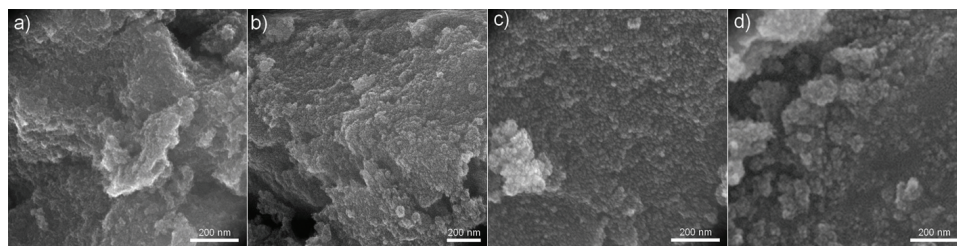


Fig. 1. SEM photographs of samples: a) TiO<sub>2</sub>/CN<sub>0.5</sub>; b) TiO<sub>2</sub>/CN<sub>0.1</sub>, c) TiO<sub>2</sub>/CN<sub>0.05</sub> and d) TiO<sub>2</sub>/C.

The contents of nitrogen, carbon phase and TiO<sub>2</sub> in examined composites were obtained by elemental and thermogravimetric analysis. The TGA, DTG, and DTA curves of the TiO<sub>2</sub>/CN composites, as well as undoped TiO<sub>2</sub>/C, are shown in Fig. 2a–c, respectively. For all examined samples, according to the DTG curves, the first mass loss was observed in the temperature range from 40 to 120 °C, which originates from physically and chemically adsorbed water. The second mass loss observed in the range 250–450 °C, is a consequence of hydrothermal carbon oxidation during TG analysis. Sample TiO<sub>2</sub>/CN<sub>0.05</sub> has an additional mass loss in the temperature range 550–650 °C, which origin is not fully understood.

According to the literature<sup>15</sup> the mass loss in this region can be the consequence of the decomposition of residual melamine, which is unlikely because samples obtained with a higher amount of melamine do not display the mass loss in this temperature region. Also, it is suggested that the mass loss in the temperature region from 350–800 °C can be a result of carbon residue degradation, as well as TiO<sub>2</sub> crystal phase transformation.<sup>16</sup> The content of TiO<sub>2</sub>, carbon

phase (obtained from TGA), and nitrogen (from elemental analysis) in examined composites are presented in Table I. Percentage contents of TiO<sub>2</sub> and carbon phase, shown in Table I, were calculated taking the content of hydrothermally obtained TiO<sub>2</sub> on 800 °C as 100 %.

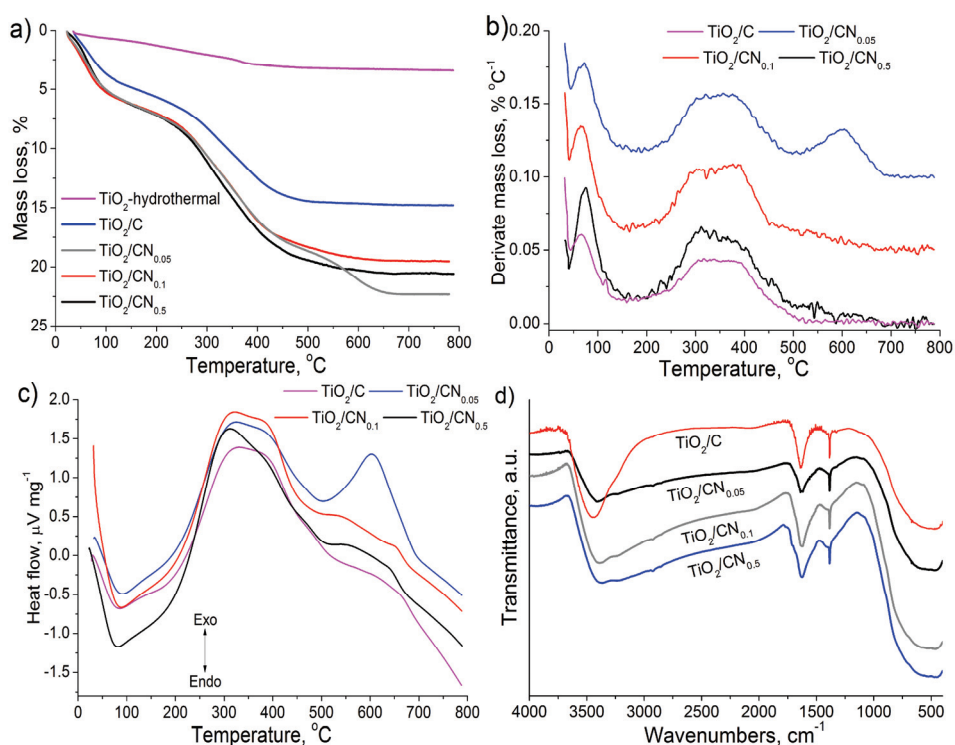


Fig. 2. TGA (a), DTG (b) and DTA (c) curves, and FTIR spectra (d) of TiO<sub>2</sub>/C and TiO<sub>2</sub>/CN composites.

Table I. TiO<sub>2</sub>, carbon phase and nitrogen content in TiO<sub>2</sub>/CN composites (wt. %)

Sample	Component		
	TiO <sub>2</sub>	Carbon phase	N
TiO <sub>2</sub> /C	88.17	11.83	0
TiO <sub>2</sub> /CN <sub>0.05</sub>	80.45	19.33	0.221
TiO <sub>2</sub> /CN <sub>0.1</sub>	83.27	16.61	0.156
TiO <sub>2</sub> /CN <sub>0.5</sub>	82.23	17.48	0.292

Obtained results showed that adding the melamine to the reaction mixture led to nitrogen incorporation into TiO<sub>2</sub>/CN composites in the range from 0.156 to 0.292 wt. %. However, nitrogen content in TiO<sub>2</sub>/CN composites is not directly dependent on the amount of melamine added to the reaction mixture since both, the lowest and the highest amount of melamine, led to similar nitrogen content in

the TiO<sub>2</sub>/CN composites. It has been observed that the lowest concentration of melamine in the reaction mixture resulted in increased content of the organic carbonaceous phase at the expense of the TiO<sub>2</sub> inorganic phase.

FTIR spectra of undoped and doped composites are shown in Fig. 2d. The broad band in the range of 400–1000 cm<sup>-1</sup> is derived from the stretch vibration of Ti–O and Ti–O–Ti bonds.<sup>17,18</sup> The peak at 3400 cm<sup>-1</sup> originates from the stretching vibration of the OH bond in Ti–OH and in water adsorbed on the TiO<sub>2</sub> surface, indicating the presence of hydroxyl groups on the surface of the material.<sup>18</sup> Another peak that may correspond to bending vibrations of the O–H bond in water molecules appears around 1625 cm<sup>-1</sup> for all tested samples.<sup>18</sup> Two weak peaks at 2850 and 2920 cm<sup>-1</sup> can be ascribed to characteristic stretching vibrations of aliphatic C–H, which indicate the formation of carbon layers.<sup>17</sup> The addition of melamine leads to a broadening of the peak at 3400 cm<sup>-1</sup>. It is necessary to highlight that there are no distinct differences between the FTIR spectra of TiO<sub>2</sub>/CN composites. Nevertheless, a small shoulder at around 1715 cm<sup>-1</sup>, was observed for sample TiO<sub>2</sub>/CN<sub>0.5</sub>. This peak may originate from stretching vibration of –C=O from carbonyl and carboxyl groups, indicating that N-doping with the highest amount of melamine induced their formation. Although the peak at 1385 cm<sup>-1</sup> can be related to C=C and O–H bond,<sup>19</sup> it may also be induced by the C–N bond. However, this observation could not confirm the presence of nitrogen in obtained composite materials, since undoped TiO<sub>2</sub>/C spectra displayed peaks at the same wavenumber.

XPS analysis was conducted to confirm the nitrogen incorporation into TiO<sub>2</sub>/CN composites and to identify the valence state of the doping nitrogen. Fig. 3a shows the very similar spectra of undoped TiO<sub>2</sub>/C and TiO<sub>2</sub>/CN samples, doped with various nitrogen amounts, taken in the binding energy range from 0 to 1200 eV. In the high-resolution spectra of Ti 2p (Fig. 3b), peaks at 458.8 and 464.4 eV correspond to Ti 2p<sub>3/2</sub> and Ti 2p<sub>1/2</sub>, respectively.<sup>20</sup> Binding energy difference between these two peaks is 5.6 eV. Binding energy 458.8 eV of Ti 2p<sub>3/2</sub> confirms the presence of the Ti<sup>4+</sup> states in TiO<sub>2</sub>. Fig. 3c shows the high resolution XPS spectra of O 1s, deconvoluted in three peaks at 530.1, 531.7 and 532.8 eV that are ascribed to lattice oxygen (Ti–O–Ti), surface hydroxyl groups (Ti–O–H) and adsorbed water.<sup>21,22</sup>

The C 1s spectrum (Fig. 3d) was fitted with four peaks. The main peak at 284.8 eV corresponds to C–C and C–H bonds,<sup>23</sup> while the peak at 289.6 eV corresponds to O=C–O. Peaks at 286.4 and 288.4 eV can be assigned to nitrogen-doped sp<sup>2</sup> carbon (C–N) and nitrogen-doped sp<sup>3</sup> carbon (C=N),<sup>20</sup> although, these peaks may be related to the C–O, C–OH and C=O, due to much higher concentration of oxygen, compared to nitrogen. Furthermore, the high-resolution N 1s spectra display a peak of around 400 eV (Fig. 3e). Emission in the 399–400 eV region can originate from nitriles (N triple-bonded to only one carbon), graphitic

N (bonded to three carbons),<sup>24</sup> or adsorbed nitrogen, but also from the interstitial integration of nitrogen into TiO<sub>2</sub> lattice.

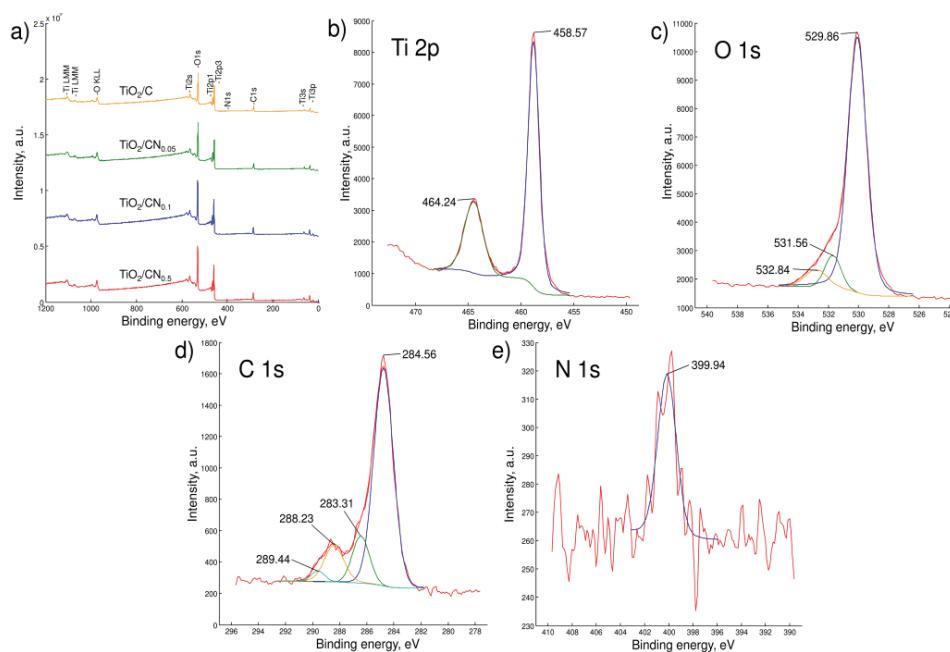


Fig. 3. XPS survey spectra of TiO<sub>2</sub>/C and TiO<sub>2</sub>/CN samples with various nitrogen content (a), the high-resolution spectra of Ti 2p (b), O 1s (c), C 1s (d) and N 1s (e) of TiO<sub>2</sub>/CN<sub>0.5</sub>.

Nitrogen adsorption isotherms obtained for undoped and TiO<sub>2</sub>/CN samples are given in Fig. 4a, as the dependence of the adsorbed amount of N<sub>2</sub> ( $n$  / mmol g<sup>-1</sup>) and relative pressure ( $P/P_0$ ) at the temperature of liquid nitrogen. Obtained isotherms are type IV of IUPAC classification,<sup>25</sup> containing a hysteresis loop, which indicates a mesoporous material. The observed hysteresis loop of type H2 is typical for the pores of undefinable shape.

Additionally, non-limiting adsorption at high  $P/P_0$ , observed for N-doped samples indicates the presence of slit-shaped pores at non-rigid aggregates of plate-like particles.<sup>26</sup> Pore size distribution (Fig. 4b) for all samples is very narrow and close to the limiting value between micro and mesopores (2 nm). This means that these materials can be considered microporous with a small fraction of mesoporousness. Values for the average pore width ( $r_p$ ), for all samples, along with the calculated porosity parameters ( $S_{BET}$ ,  $S_{meso}$ ,  $S_{mic}$ ,  $V_{mic}$ ) are given in Table II. The mesoporous TiO<sub>2</sub>/C sample showed an  $S_{BET}$  of 174.08 m<sup>2</sup> g<sup>-1</sup> and an average pore width of 3.78 nm.

On the other hand, all TiO<sub>2</sub>/CN composites are mainly microporous, with a maximum pore radius of about 2.2 nm. Also, it was found that the  $S_{BET}$  of

N-doped samples, ranging from 186 to 239  $\text{m}^2 \text{g}^{-1}$ , increase with nitrogen content. Consideration of the obtained results indicates that melamine addition in reaction mixture leads to the decrease of average pore width, and drastically increases the microporosity, as well as  $S_{\text{BET}}$  values of obtained  $\text{TiO}_2/\text{CN}$  samples. As it was reported previously,<sup>27</sup> these changes in specific surface area and average pore width may be the consequence of the substitution of carbon atoms, most likely located on the reactive edges, with nitrogen atoms during hydrothermal synthesis. These incorporated N atoms could act as a catalyst for porosity development.

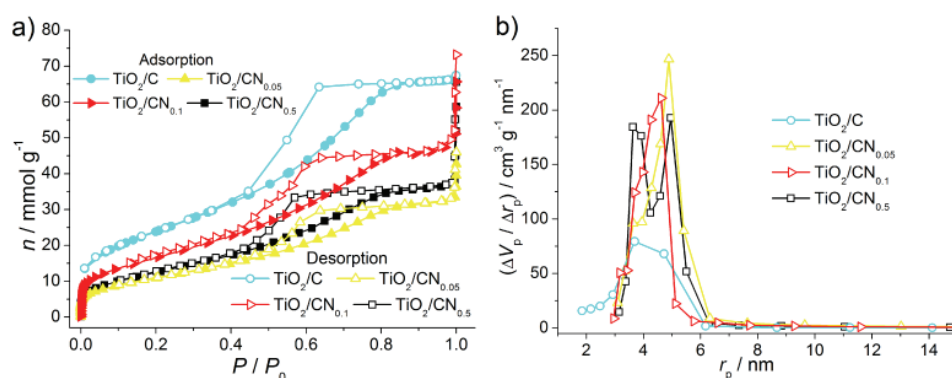


Fig. 4. Nitrogen adsorption isotherms (a) and pore size distribution (b) for  $\text{TiO}_2/\text{C}$  and  $\text{TiO}_2/\text{CN}$  samples.

TABLE II. Porous properties of  $\text{TiO}_2/\text{CN}$  samples

Sample	$S_{\text{BET}} / \text{m}^2 \text{g}^{-1}$	$S_{\text{meso}} / \text{m}^2 \text{g}^{-1}$	$S_{\text{mic}} / \text{m}^2 \text{g}^{-1}$	$V_{\text{mic}} / \text{cm}^3 \text{g}^{-1}$	$r_p / \text{nm}$
$\text{TiO}_2/\text{C}$	174	168	6	0.048	3.78
$\text{TiO}_2/\text{CN}_{0.05}$	231	32	199	0.231	2.37
$\text{TiO}_2/\text{CN}_{0.1}$	186	17	169	0.194	2.11
$\text{TiO}_2/\text{CN}_{0.5}$	239	22	217	0.246	2.38

XRD analysis was performed to determine the content of crystalline  $\text{TiO}_2$  phases in  $\text{TiO}_2/\text{C}$  and  $\text{TiO}_2/\text{CN}$  composites, as well as the crystallite size. XRD diffraction pattern for all tested samples (Fig. 5) showed the presence of a characteristic peak for anatase (101) ( $2\theta = 25.6^\circ$ ) crystalline phase, as well as peaks at  $2\theta$  38.2 (112), 48.3 (200) and  $54.6^\circ$  (105) also arising from anatase crystalline modification.<sup>10,28</sup> The presence of a low-intensity peak at  $2\theta = 27.7^\circ$  (110), originating from rutile crystal modification, was observed for the undoped sample  $\text{TiO}_2/\text{C}$  (Fig. 5).<sup>28</sup> However, no distinguish peaks characteristic for the rutile phase were displayed on XRD diffraction patterns of  $\text{TiO}_2/\text{CN}$  composites. A shoulder appearing at  $2\theta = 26^\circ$  (110), visible on the XRD diffraction pattern of all  $\text{TiO}_2/\text{CN}$  composites, may originate from the photocatalytically inactive crys-

talline phase of brookite, as well as from titanium nitride.<sup>29</sup> The presence of these phases may affect the photocatalytic activity of the examined composites, especially of sample TiO<sub>2</sub>/CN<sub>0.5</sub> which shows the shoulder of higher intensity. Although XPS analysis showed that nitrogen was most likely incorporated in carbon lattice, the addition of melamine to the starting reaction mixture affected the structure of N-doped composites by favoring the formation of the anatase phase and suppressing the formation of the rutile phase.

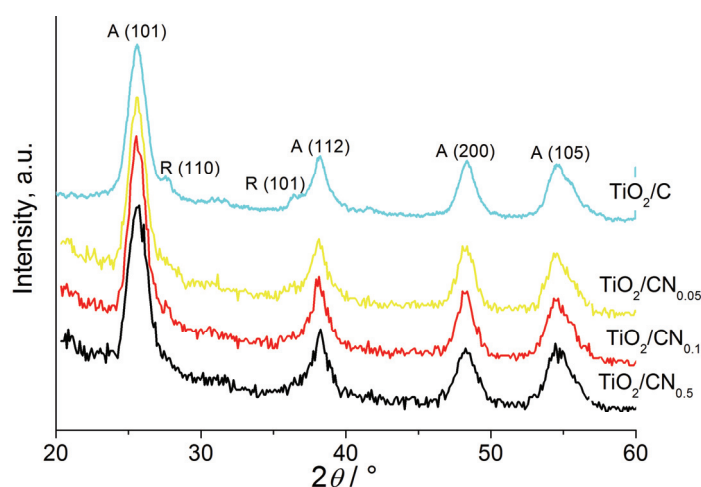


Fig. 5. XRD patterns of examined samples.

The calculated approximate values of the fraction of TiO<sub>2</sub> crystalline phases and the size of the crystallite are shown in Table III. The undoped sample, TiO<sub>2</sub>/C, contains 24 % of the rutile phase, while N doping significantly decreased the content of the rutile phase. The observed increase of the anatase phase content should favorably affect the photocatalytic characteristics of TiO<sub>2</sub>/CN composites. It can be noticed that N-doping leads to a decrease in the average grain size, which is dependable on nitrogen content in TiO<sub>2</sub>/CN composites. The addition of melamine increases the content of amorphous carbon (Table I), which inhibits the growth of TiO<sub>2</sub> grains and thus N-doping leads to a decrease in the grain size. Obtained values for grain size and average pore width (Table II), suggest that these pores most likely represent interparticle spaces.

The photocatalytic activity of TiO<sub>2</sub>/CN composites was investigated in the process of removing methylene blue from aqueous solutions under UV and visible irradiation. Fig. 6a shows the photocatalytic decomposition of MB as a decrease in the MB concentration during the time. The entire process of MB removal lasted 180 min and it was performed in two steps. The first step is related to the establishment of an adsorption/desorption equilibrium for 60 min in the dark, and the second step implied the degradation of organic pollutants in the



presence of UV or visible irradiation. Fig. 6b summarized the removal efficiency after the first adsorption step in the dark, the second step of photocatalytic degradation under UV irradiation, and total removal efficiency. At the end of the first step, TiO<sub>2</sub>/CN samples showed higher adsorption capacity (removing 44–70 % of MB) than sample TiO<sub>2</sub>/C, which adsorbed about 35 % of the initial amount of MB. According to the results shown in Fig. 6b and Table II, adsorption efficiency increases with specific surface area, although, a direct relationship between  $S_{\text{BET}}$  and the amount of MB adsorbed cannot be established. N-doped samples had higher adsorption capacity, but lower photocatalytic efficiency since N-doped samples showed lower removal efficiency during the irradiation step than the undoped sample. However, according to Fig. 6b, samples TiO<sub>2</sub>/CN<sub>0.5</sub> and TiO<sub>2</sub>/CN<sub>0.05</sub> showed the highest level of adsorption and total removal efficiency, due to the high specific surface area, which is the result of the highest content of carbon. Photocatalytic characteristics of examined materials are not directly influenced by nitrogen content. TiO<sub>2</sub>/C showed better photocatalytic activity than N-doped samples, most likely because increased carbon content in N-doped samples had a negative effect on photocatalytic activity by preventing light penetration to the TiO<sub>2</sub>.

TABLE III. Anatase and rutile phase content and grain sizes of TiO<sub>2</sub>/C and TiO<sub>2</sub>/CN composites

Sample	Crystallite size, nm	Phase content, wt. %	
		Anatase	Rutile
TiO <sub>2</sub> /C	9.76	76.0	24.0
TiO <sub>2</sub> /CN <sub>0.05</sub>	7.15	98.0	2.0
TiO <sub>2</sub> /CN <sub>0.1</sub>	7.26	99.0	1.0
TiO <sub>2</sub> /CN <sub>0.5</sub>	6.52	95.0	5.0

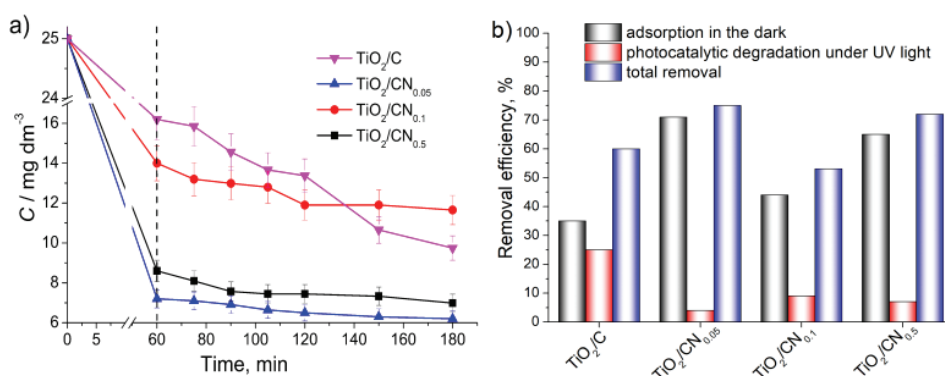


Fig. 6. Photocatalytic decomposition (a) and removal efficiency (b) of MB in the presence of TiO<sub>2</sub>/C and TiO<sub>2</sub>/CN composites.

Undoped and N-doped samples showed a similar trend in the photocatalytic activity in the process of methylene blue removal under visible irradiation (Fig. 7a). Samples obtained by adding a larger amount of melamine to the reaction mixture (TiO<sub>2</sub>/CN<sub>0.1</sub>, TiO<sub>2</sub>/CN<sub>0.5</sub>) show lower photocatalytic activity in the visible region than the undoped sample. Only the sample obtained with a small amount of melamine (TiO<sub>2</sub>/CN<sub>0.05</sub>) shows a better efficiency than the undoped sample. As was already mentioned, due to the large specific surface area and the highest carbon content, sample TiO<sub>2</sub>/CN<sub>0.05</sub> displayed the best efficiency in the MB removal process. Also, its photocatalytic activity in the decomposition of MB under visible radiation ( $\lambda > 400$  nm) was followed by the recording of the absorption spectra. According to the spectra shown (Fig. 7b), no new absorption bands appear in the visible or UV area, which confirms the disappearance of the dye chromophore structure.<sup>30</sup> Even though the absorption peak at 663 nm decreases with the increase in reaction time, the MB is not degraded after 24 h.

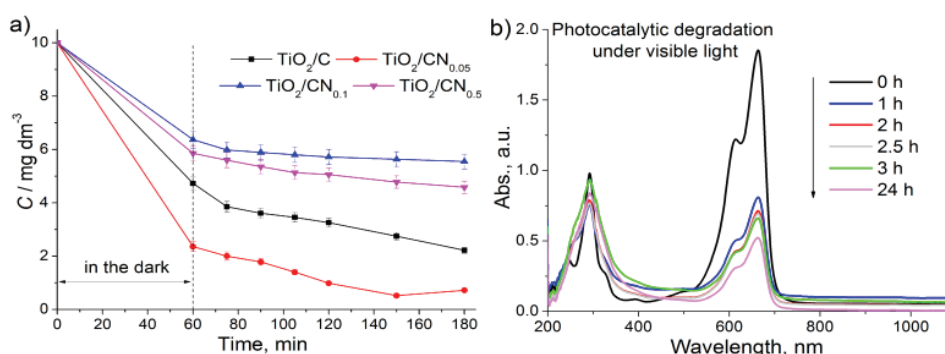


Fig. 7. Photocatalytic decomposition of MB in the presence of undoped and N-doped samples (a) and absorption spectra of MB on TiO<sub>2</sub>/CN<sub>0.05</sub> (b).

The possibility of removing selected pharmaceuticals from a multi-component solution by TiO<sub>2</sub>/CN composites under UV irradiation was also examined. For the purpose of comparison, results obtained by undoped TiO<sub>2</sub>/C composite were also presented. Fig. 8 summarized the percentage of removed pharmaceuticals by adsorption in the dark, followed by the photocatalytic degradation under UV irradiation after 180 min, and total removal efficiency.

Generally, all tested materials better adsorb pharmaceuticals of decreased polarity (higher values of retention time in Table S-II of the Supplementary material), except in the case of doxycycline. The higher specific surface area of N-doped samples, compared to the undoped sample, positively affects the pharmaceutical adsorption, except for amlodipine adsorption where the undoped sample showed the highest removal efficiency in the dark. Samples TiO<sub>2</sub>/CN<sub>0.1</sub> and TiO<sub>2</sub>/CN<sub>0.5</sub> show a lower efficiency of pharmaceuticals removal under UV

irradiation (Fig. 8b), compared to the undoped sample and  $\text{TiO}_2/\text{CN}_{0.05}$ . Nevertheless, all tested composites demonstrate high efficacy in the total removal (Fig. 8c) of diclofenac, doxycycline, atorvastatin, amlodipine and clopidogrel, which were completely removed after the adsorption in the dark, followed by photocatalytic degradation under UV irradiation.

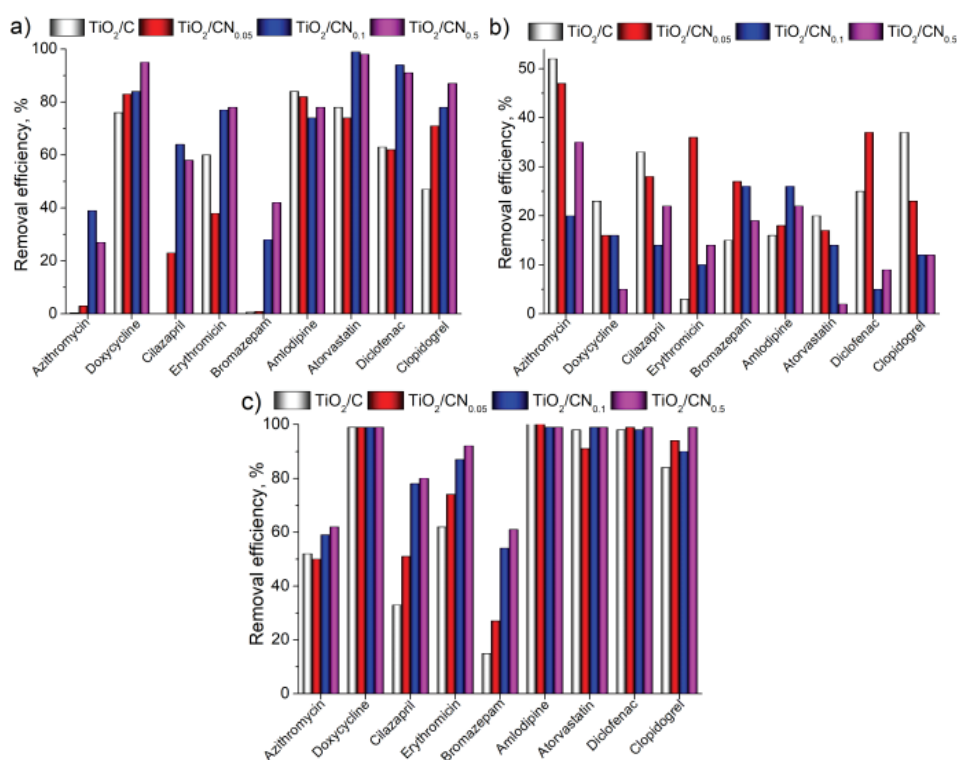


Fig. 8. Removal of pharmaceuticals from a multi-component solution by  $\text{TiO}_2/\text{C}$  and  $\text{TiO}_2/\text{CN}$  composites: a) adsorption in the dark, b) under UV irradiation and c) total removal.

The percentage of totally removed pharmaceuticals increases with the higher amount of melamine introduced in the starting reaction mixture, most likely due to the increased specific surface area and adsorption efficiency. In that way, the composite obtained with the highest amount of melamine,  $\text{TiO}_2/\text{CN}_{0.5}$ , showed the highest efficiency for removing selected pharmaceuticals from aqueous solutions.

#### CONCLUSION

N-doped  $\text{TiO}_2/\text{carbon}$  composites were obtained by hydrothermal synthesis using melamine, as a source of nitrogen, though the nitrogen content in  $\text{TiO}_2/\text{CN}$  composites was not directly proportional to the amount of melamine added to the

reaction mixture. The incorporation of nitrogen affected the structural and surface characteristics of composite photocatalysts, by increasing the specific surface area and microporosity, as well as the content of the photocatalytically active anatase phase. N-doping affected the efficiency of these composites to remove methylene blue and selected pharmaceuticals, by increasing their adsorption efficiency and decreasing photocatalytic activity under UV irradiation. Nevertheless, TiO<sub>2</sub>/CN<sub>0.05</sub> composite, obtained by the hydrothermal synthesis in the presence of glucose and 0.05 g melamine, showed the highest efficiency for removing selected pharmaceuticals and methylene blue from aqueous solutions through the combined processes of adsorption in the dark and photocatalytic degradation under UV and visible irradiation.

#### SUPPLEMENTARY MATERIAL

Additional data and information are available electronically at the pages of journal website: <https://www.shd-pub.org.rs/index.php/JSCS/article/view/11912>, or from the corresponding author on request.

*Acknowledgements.* The research was funded by the Ministry of Education, Science and Technological Development of the Republic of Serbia (Contract Nos. 451-03-68/2022-14/200135, 451-03-68/2022-14/200287 and 451-03-9/2021-14/200017).

#### ИЗВОД

#### УТИЦАЈ ДОПИРАЊА АЗОТОМ НА СТРУКТУРНЕ И ФОТОКАТАЛИТИЧКЕ КАРАКТЕРИСТИКЕ ХИДРОТЕРМАЛНО СИНТЕТИСНИХ TiO<sub>2</sub>/КАРБОН КОМПЗИТА

МАРИНА М. МАЛЕТИЋ<sup>1</sup>, АНА М. КАЛИЈАДИС<sup>2</sup>, ВЛАДИМИР ЛАЗОВИЋ<sup>3</sup>, СНЕЖАНА ТРИФУНОВИЋ<sup>4</sup>,  
БИЉАНА М. БАБИЋ<sup>3</sup>, АЛЕКСАНДРА ДАПЧЕВИЋ<sup>5</sup>, JANEZ KOVAČ<sup>6</sup> и МАРИЈА М. ВУКЧЕВИЋ<sup>5</sup>

<sup>1</sup>Иновациони Центар Технолошко–металуршког факултета, Карнегијева 4, 11000 Београд,  
<sup>2</sup>Лабораторија за материјале, Институт за нуклеарне науке Винча – Институт од националног значаја, Универзитет у Београду, Мике Пешировића Аласа 12–14, 11000 Београд, <sup>3</sup>Институт за физику – Институт од националног значаја, Универзитет у Београду, Преобрадица 118, 11080 Београд, <sup>4</sup>Хемијски факултет, Универзитет у Београду, Студентски тир 12–16, 11000 Београд,  
<sup>5</sup>Технолошко–металуршког факултета, Универзитет у Београду, Карнегијева 4, 11000 Београд и  
<sup>6</sup>Department of Surface Engineering, Institute Jožef Stefan, Jamova cesta 39, 1000 Ljubljana, Slovenia

TiO<sub>2</sub>/карбон композити допирани азотом (TiO<sub>2</sub>/CN) добијени су хидротермалном карбонизацијом смеше титан изопропоксида и глукозе, у присуству различитих количина меламина као прекурсора азота. Извршена је површинска и структурна карактеризација материјала, а добијени резултати су упоређени са карактеристикама недопираниог TiO<sub>2</sub>/карбон композита. Фотокаталитичка активност добијених композита испитана је фотокаталитичком разградњом метиленско плавог и лекова из мултикомпонентног воденог раствора. Утврђено је да допирање азотом TiO<sub>2</sub> карбон композита доводи до промена у структурним и површинским карактеристикама TiO<sub>2</sub>/CN композита, побољшавајући њихову адсорпциону ефикасност, али смањујући фотокаталитичку активност. Показано је да се примењеном методом хидротермалне карбонизације могу добити ефикасни композити за уклањање одабраних лекова и метиленског плавог из водених раствора, применом процеса адсорпције у мраку, праћеног фотокаталитичком разградњом под UV и видљивим зрачењем.

(Примљено 8. јуна, ревидирано 11. октобра, прихваћено 15. октобра 2022)

## REFERENCES

1. N. C. T. Martins, J. Ângelo, A.V. Girão, T. Trindade, L. Andrade, A. Mendes, *Appl. Catal., B* **193** (2016) 67 (<http://dx.doi.org/10.1016/j.apcatb.2016.04.016>)
2. B. Farkas, P. Heszler, J. Budai, A. Oszkó, M. Ottosson, Z. Geretovszky, *Appl. Surf. Sci.* **433** (2018) 149 (<https://doi.org/10.1016/j.apsusc.2017.09.181>)
3. R. Asahi, T. Morikawa, H. Irie, T. Ohwaki, *Chem. Rev.* **114** (2014) 9824 (<https://dx.doi.org/10.1021/cr5000738>)
4. Y.T. Lin, C.H. Weng, Y.H. Lin, C.C. Shiesh, F.Y. Chen, *Sep. Purif. Technol.* **116** (2013) 114 (<http://dx.doi.org/10.1016/j.seppur.2013.05.018>)
5. K. Siuzdak, M. Szkoda, A. Lisowska-Oleksiak, K. Grochowska, J. Karczewski, J. Ryl, *Appl. Surf. Sci.* **357** (2015) 942 (<http://dx.doi.org/10.1016/j.apsusc.2015.09.130>)
6. K. Pathakoti, S. Morrow, C. Han, M. Pelaez, X. He, D. D. Dionysiou, H. M. Hwang, *Environ. Sci. Technol.* **47** (2013) 9988 (<https://dx.doi.org/10.1021/es401010g>)
7. N. X. Qian, X. Zhang, M. Wangb, X. Sun, X. Y. Sun, C. Liu, R. Rao, Y. Q. Ma, *J. Photochem. Photobiol., A* **386** (2020) 112127 (<https://doi.org/10.1016/j.jphotochem.2019.112127>)
8. M. Maletić, M. Vukčević, A. Kalijadis, I. Janković-Častvan, A. Dapčević, Z. Laušević, M. Laušević, *Arab. J. Chem.* **12** (2019) 4388 (<http://dx.doi.org/10.1016/j.arabjc.2016.06.020>)
9. M. Maletić, M. Vukčević, A. Kalijadis, Z. Laušević, M. Laušević, *Adv. Mater. Sci. Eng.* (2015) 803492 (<http://dx.doi.org/10.1155/2015/803492>)
10. H. Belayachi, B. Bestani, N. Benderdouche, M. Belhakem, *Arab. J. Chem.* **12** (2019) 3018 (<http://dx.doi.org/10.1016/j.arabjc.2015.06.040>)
11. Commission implementing Decision (EU) 2015/495, *Off. J. Eur. Union* **L78(58)** (2015) 40 ([https://eur-lex.europa.eu/legal-content/EN/TXT/?uri=uriserv%3AOJ.L\\_.2015.078.01.0040.01.ENG&toc=OJ%3AL%3A2015%3A078%3ATOC](https://eur-lex.europa.eu/legal-content/EN/TXT/?uri=uriserv%3AOJ.L_.2015.078.01.0040.01.ENG&toc=OJ%3AL%3A2015%3A078%3ATOC))
12. E.P. Barrett, L.G. Joyner, P.P. Halenda, *J. Am. Chem. Soc.* **73** (1951) 373 (<https://doi.org/10.1021/ja01145a126>)
13. B.C. Lippens, B.G. Linsen, J.H. De Boer, *J. Catal.* **3** (1964) 32 ([https://doi.org/10.1016/0021-9517\(64\)90089-2](https://doi.org/10.1016/0021-9517(64)90089-2))
14. W. Kraus, G. Nolze, *Powder Cell for Windows*, V.2.4, Federal Institute for Materials Research and Testing, Berlin (<https://powdercell-for-windows.software.informer.com/2.4/>)
15. M. Sathish, B. Viswanathan, R. P. Viswanath, *Appl. Catal., .* **74** (2007) 307 (<https://doi.org/10.1016/j.apcatb.2007.03.003>)
16. J. Zhang, Y. Li, L. Li, W. Li, C. Yang, *ACS Sustain. Chem. Eng.* **6** (2018) 12893 (<https://doi.org/10.1021/acssuschemeng.8b02264>)
17. H. He, H. Wang, D. Sun, M. Shao, X. Huang, Y. Tang, *Electrochim. Acta* **236** (2017) 43 (<http://dx.doi.org/10.1016/j.electacta.2017.03.104>)
18. K. Kalantari, M. Kalbasia, M. Sohrabi, S. J. Royae, *Ceram. Int.* **43** (2017) 973 (<http://dx.doi.org/10.1016/j.ceramint.2016.10.028>)
19. H. Safardoust-Hojaghan, M. Salavati-Niasari, *J. Clean. Prod.* **148** (2017) 31 (<http://dx.doi.org/10.1016/j.jclepro.2017.01.169>)
20. W. Ji, Y.G. Mei, M. Yang, H. Liu, S. Wang, Z. Shan, F. Ding, X. Liu, X. Gao, X. Li, *J. Alloys Compd.* **806** (2019) 946 (<https://doi.org/10.1016/j.jallcom.2019.07.225>)
21. Y. Li, H. Li, X. Lu, X. Yu, M. Kong, X. Duan, G. Qin, Y. Zhao, Z. Wang, D. D. Dionysiou, *J. Colloid Interface Sci.* **596** (2021) 384 (<https://doi.org/10.1016/j.jcis.2021.03.140>)

22. X. Chen, D. H. Kuo, D. Lu, *Chem. Eng. J.* **295** (2016) 192 (<http://dx.doi.org/10.1016/j.cej.2016.03.047>)
23. A. Kalijadis, J. Đorđević, T. Trtić-Petrović, M. Vukčević, M. Popović, V. Maksimović, Z. Rakočević, Z. Laušević, *Carbon* **95** (2015) 42 (<http://dx.doi.org/10.1016/j.carbon.2015.08.016>)
24. N. Hellgren, R.T. Haasch, S. Schmidt, L. Hultman, I. Petrov, *Carbon* **108** (2016) 242 (<http://dx.doi.org/10.1016/j.carbon.2016.07.017>)
25. K.S.W. Sing, D.H. Everett, R.A.W. Haul, L. Moscou, R.A. Pierotti, J. Rouquerol, T. Siemieniowska, *Pure Appl. Chem.* **57** (1985) 603 (<https://doi.org/10.1351/pac198557040603>)
26. S. Lowell, J.E. Shields, M.A. Thomas, M. Thommes, *Characterization of Porous Solids and Powders: Surface Area, Pore Size and Density*, Kluwer Academic Publishers, Dordrecht, 2004 (<https://doi.org/10.1007/978-1-4020-2303-3>)
27. A. Kalijadis, N. Gavrilov, B. Jokić, M. Gilić, A. Krstić, I. Pašti, B. Babić, *Mater. Chem. Phys.* **239** (2020) 122120 (<https://doi.org/10.1016/j.matchemphys.2019.122120>)
28. E. Kordouli, K. Bourikas, A. Lycourghiotis, C. Kordulis, *Catal. Today* **252** (2015) 128 (<http://dx.doi.org/10.1016/j.cattod.2014.09.010>)
29. A.D. Paola, M. Bellardita, L. Palmisano, *Catalysts* **3** (2013) 36 (<http://doi:10.3390/catal3010036>)
30. G. Dai, S. Liu, Y. Liang, H. Liu, Z. Zhong, *J. Mol. Catal., A* **368–369** (2013) 38 (<http://dx.doi.org/10.1016/j.molcata.2012.11.014>).



US010406847B2

(12) **United States Patent**  
**Pantelic et al.**

(10) **Patent No.:** **US 10,406,847 B2**

(45) **Date of Patent:** **Sep. 10, 2019**

(54) **SECURITY TAG CONTAINING A PATTERN OF BIOLOGICAL PARTICLES**

(58) **Field of Classification Search**

None

See application file for complete search history.

(71) Applicant: **Institute of Physics Belgrade, University of Belgrade, Belgrade (RS)**

(56) **References Cited**

U.S. PATENT DOCUMENTS

4,011,308 A \* 3/1977 Giaever ..... B82Y 5/00  
435/5

4,279,200 A 7/1981 Newcomb  
(Continued)

FOREIGN PATENT DOCUMENTS

DE 10 238 506 3/2004  
DE 10 2007 052 009 12/2008

(Continued)

OTHER PUBLICATIONS

Buchanan et al., "Fingerprinting' documents and packaging," Nature, vol. 436, 2005, p. 475.

(Continued)

*Primary Examiner* — Christle I Marshall

(74) *Attorney, Agent, or Firm* — Grüneberg and Myers PLLC

(57) **ABSTRACT**

A security tag can be used to identify or authenticate a substrate that has the security tag. The security tag includes a pattern of inimitable biological particles, a transparent adhesive layer, a substrate, and a transparent superstrate, where the pattern of inimitable biological particles is directly transferred from an organism to the transparent adhesive layer on the substrate, and where said biological particles are covered with the transparent superstrate, such that said inimitable biological particles are encapsulated between said substrate and said superstrate.

**11 Claims, 13 Drawing Sheets**

(\* ) Notice: Subject to any disclaimer, the term of this patent is extended or adjusted under 35 U.S.C. 154(b) by 0 days.

(21) Appl. No.: **16/067,283**

(22) PCT Filed: **Dec. 30, 2015**

(86) PCT No.: **PCT/EP2015/081400**

§ 371 (c)(1),

(2) Date: **Jun. 29, 2018**

(87) PCT Pub. No.: **WO2017/114570**

PCT Pub. Date: **Jul. 6, 2017**

(65) **Prior Publication Data**

US 2019/0023055 A1 Jan. 24, 2019

(51) **Int. Cl.**

**G09F 3/02** (2006.01)

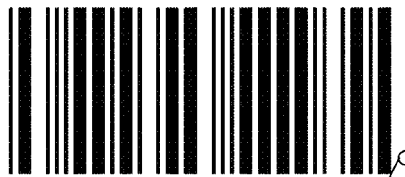
**B42D 25/36** (2014.01)

(Continued)

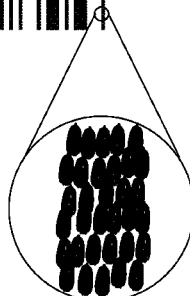
(52) **U.S. Cl.**

CPC ..... **B42D 25/36** (2014.10); **B42D 25/45** (2014.10); **G06K 7/10366** (2013.01);

(Continued)



0123452



- (51) **Int. Cl.**  
*B42D 25/45* (2014.01)  
*G06K 7/10* (2006.01)  
*G09F 3/00* (2006.01)  
*G09F 3/10* (2006.01)
- (52) **U.S. Cl.**  
 CPC ..... *G09F 3/0297* (2013.01); *G09F 3/10*  
 (2013.01); *G09F 3/0292* (2013.01); *G09F*  
*2003/0208* (2013.01)

(56) **References Cited**

U.S. PATENT DOCUMENTS

8,189,247 B2 \* 5/2012 Winterbottom ..... G03H 1/0011  
 359/2  
 8,408,470 B2 4/2013 Komatsu et al.  
 2010/0075858 A1 \* 3/2010 Davis ..... C12Q 1/6813  
 506/4  
 2014/0037158 A1 \* 2/2014 McNulty ..... G06K 9/00013  
 382/125  
 2017/0038353 A1 \* 2/2017 Zografos ..... G01N 33/025

FOREIGN PATENT DOCUMENTS

WO 2007/031077 3/2007  
 WO WO-2017114569 A1 \* 7/2017

OTHER PUBLICATIONS

Pappu et al., "Physical One-Way Functions," *Science*, vol. 297, 2002, pp. 2026-2030.

Grubb, "Benjamin Franklin and the birth of the paper money economy," published essay given by lecture on Mar. 30, 2006, published by the Federal Reserve Bank of Philadelphia.  
 Berthier et al., "Butterfly inclusions in Van Schrieck masterpieces. Techniques and optical properties," *Appl. Phys. A*, vol. 92, 2008, pp. 51-57.  
 Cowan, "Butterfly wing-prints," *J. Soc. Bibliophy. Nat. Hist.*, vol. 4, 1968, pp. 368-369.  
 Edwards, "A receipt for taking figures of butterflies on thin gummed paper," in *Essays upon Natural History and other Miscellaneous Subjects*, London, 1770, pp. 117-119.  
 Sun et al., "Structural coloration in nature," *RSC Adv.*, vol. 3, 2013, pp. 14862-14889.  
 Yoon et al. "Recent functional material based approaches to prevent and detect counterfeiting," *J. Mater. Chem. C*, vol. 1, 2013, pp. 2388-2403.  
 Biro et al., "Photonic nanoarchitectures in butterflies and beetles: valuable sources for bioinspiration," *Laser & Photonics Review*, vol. 5, No. 1, 2011, pp. 27-51.  
 Sotiropoulou et al., "Biotemplated Nanostructured Materials," *Chem. Mater.* vol. 20, 2008, pp. 821-834.  
 di Francia, "Degrees of Freedom of an Image", *JOSA*, vol. 59, No. 7, 1969, pp. 799-804.  
 International Search Report mailed in PCT/EP2015/081400 dated Sep. 2, 2016, filed in this application dated Jun. 29, 2018.  
 Written Opinion of the International Searching Authority, mailed in PCT/EP2015/081400 dated Sep. 2, 2016, filed in this application dated Jun. 29, 2018.  
 International Preliminary Report on Patentability mailed in PCT/EP2015/081400, dated Jul. 3, 2018.

\* cited by examiner



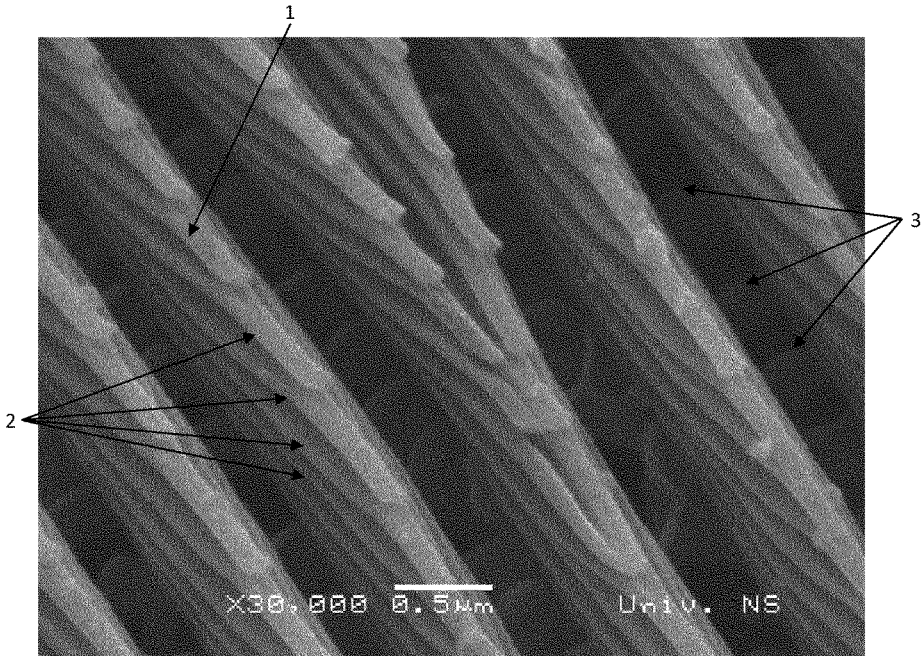


Fig. 1

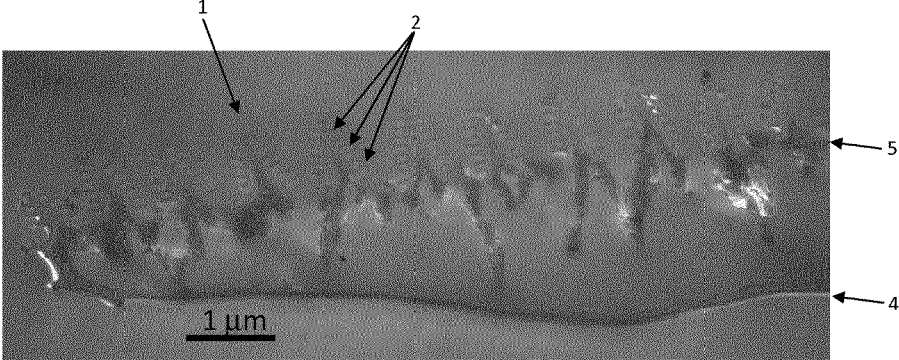


Fig. 2

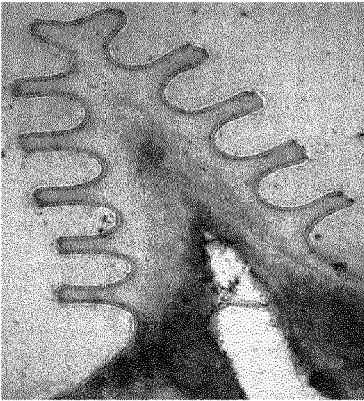


Fig. 3



Fig. 4



Fig. 5

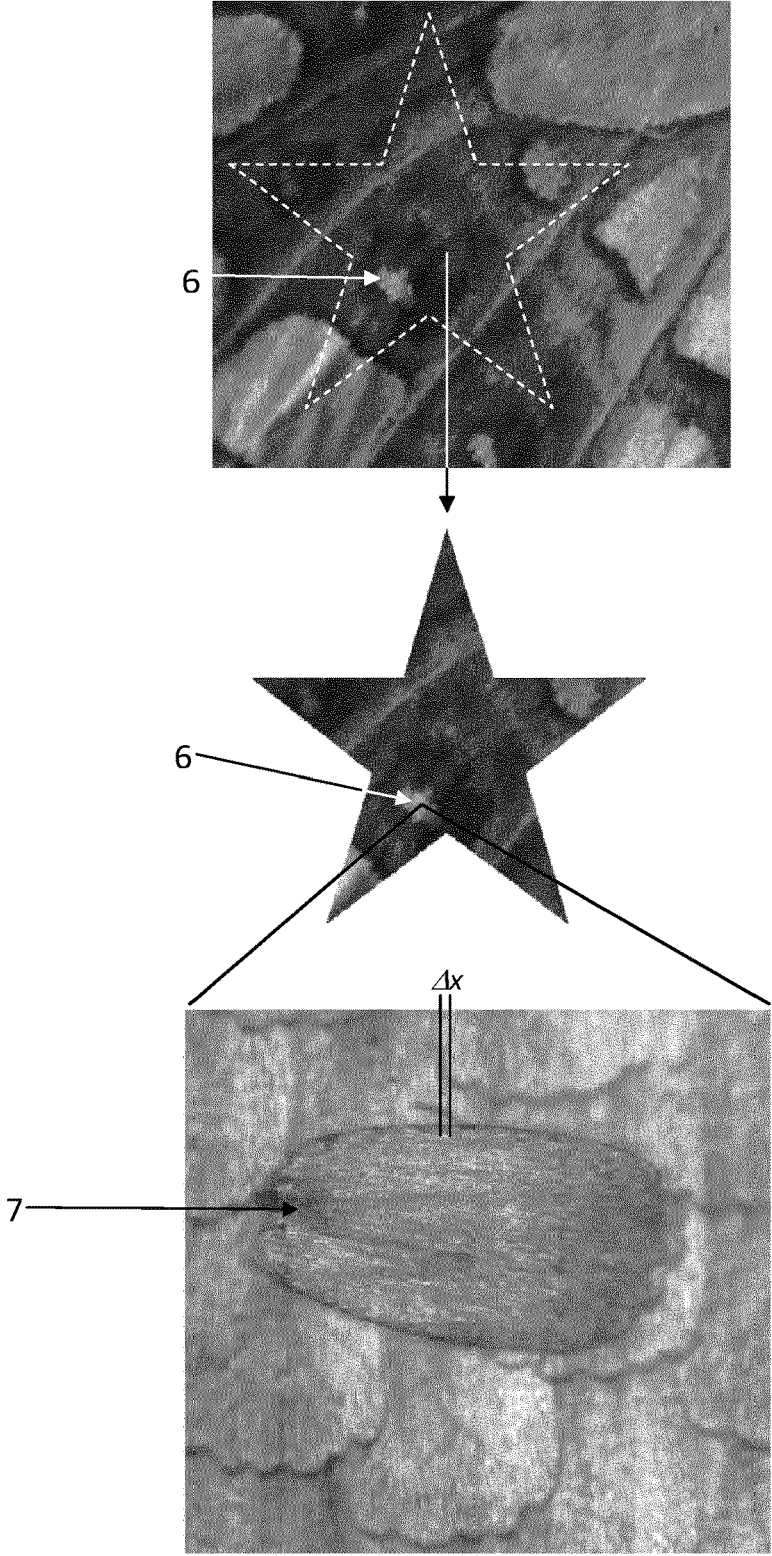


Fig. 6

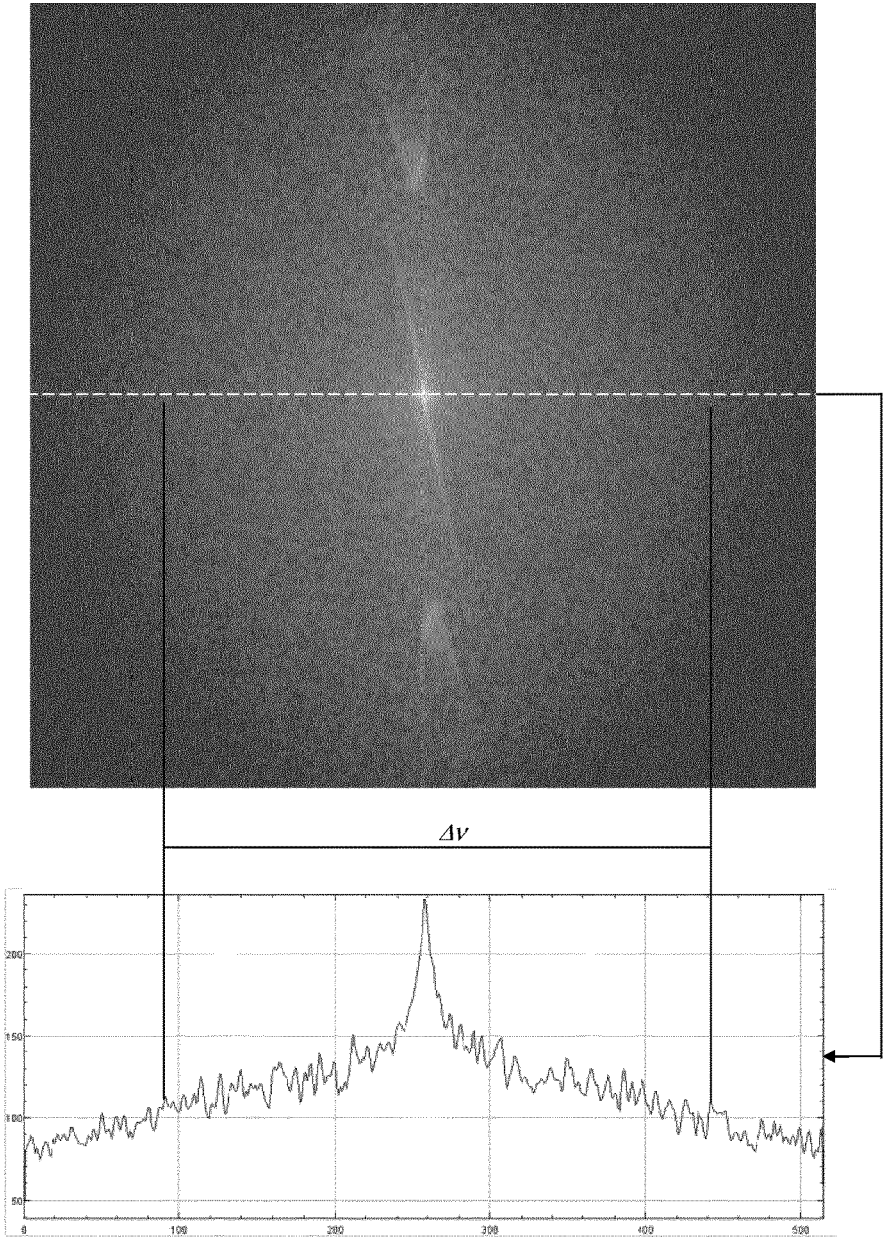


Fig. 7

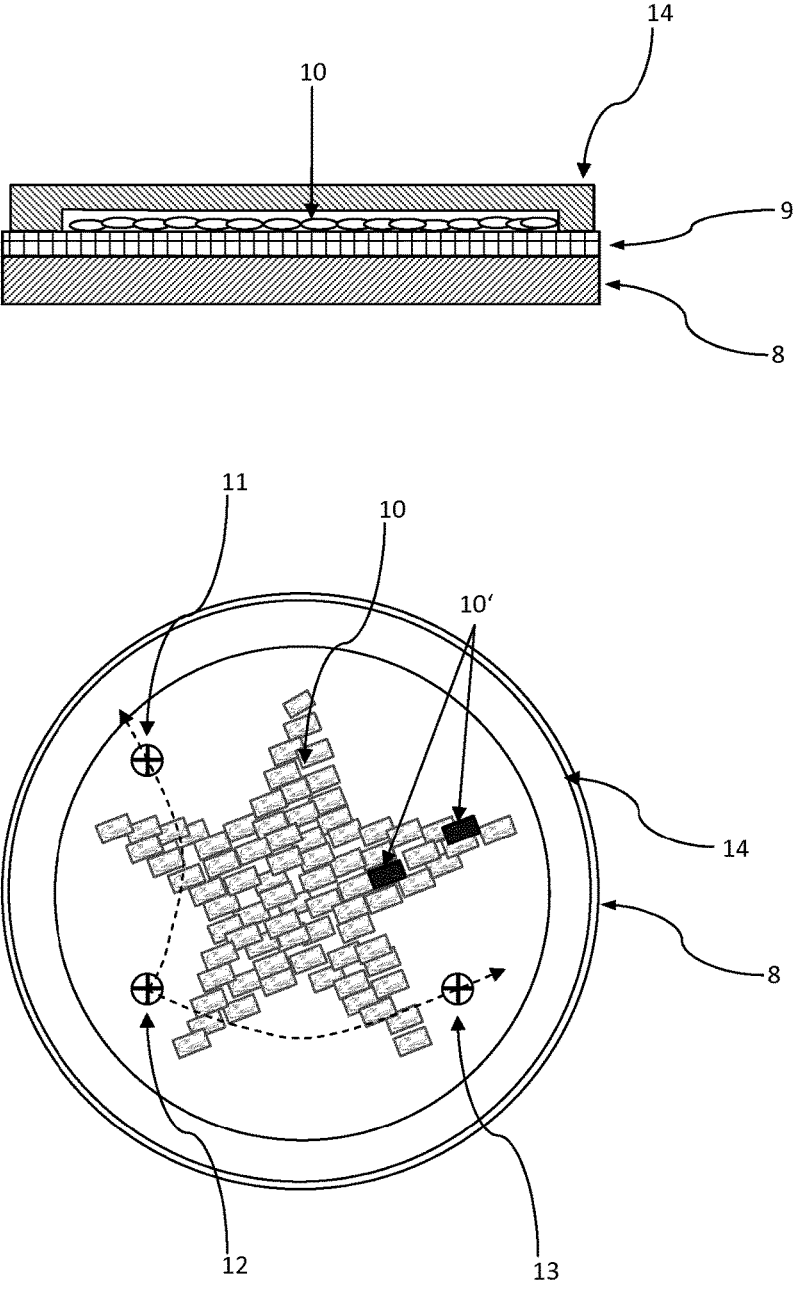


Fig. 8

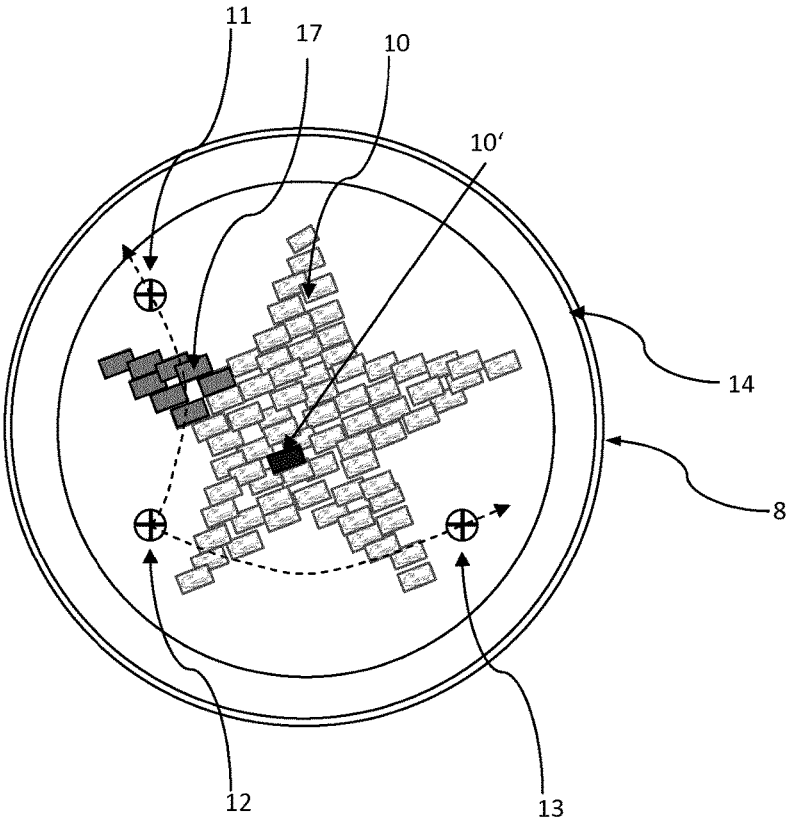
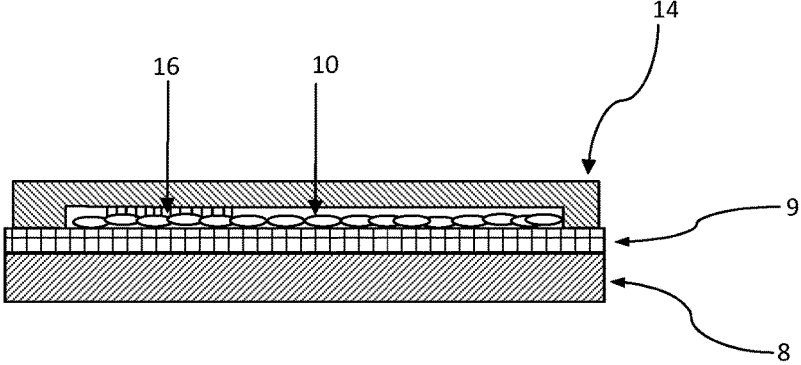


Fig. 9

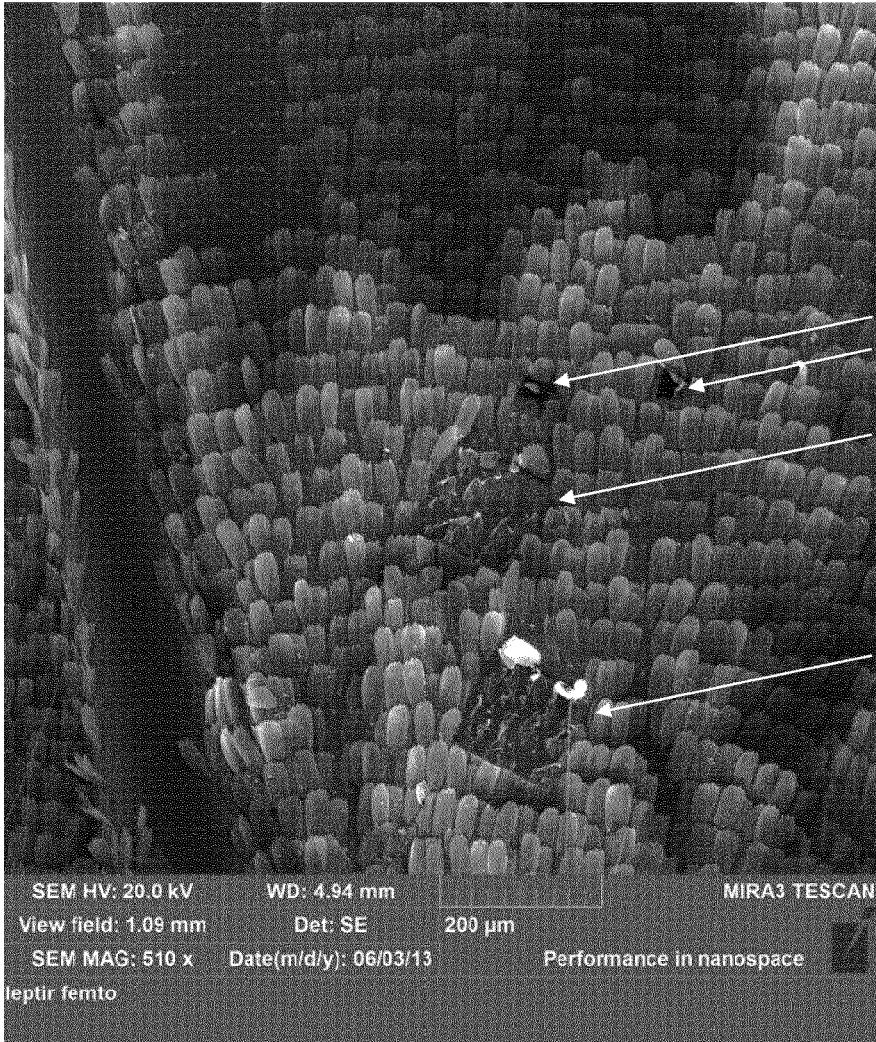


Fig. 10

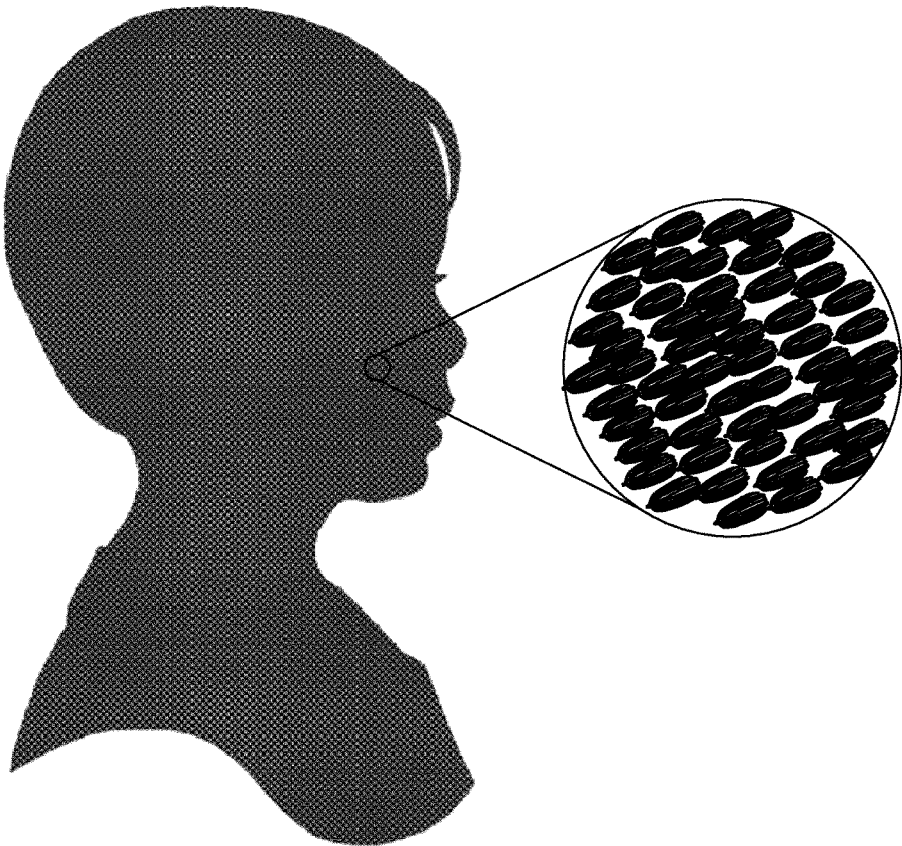


Fig. 11



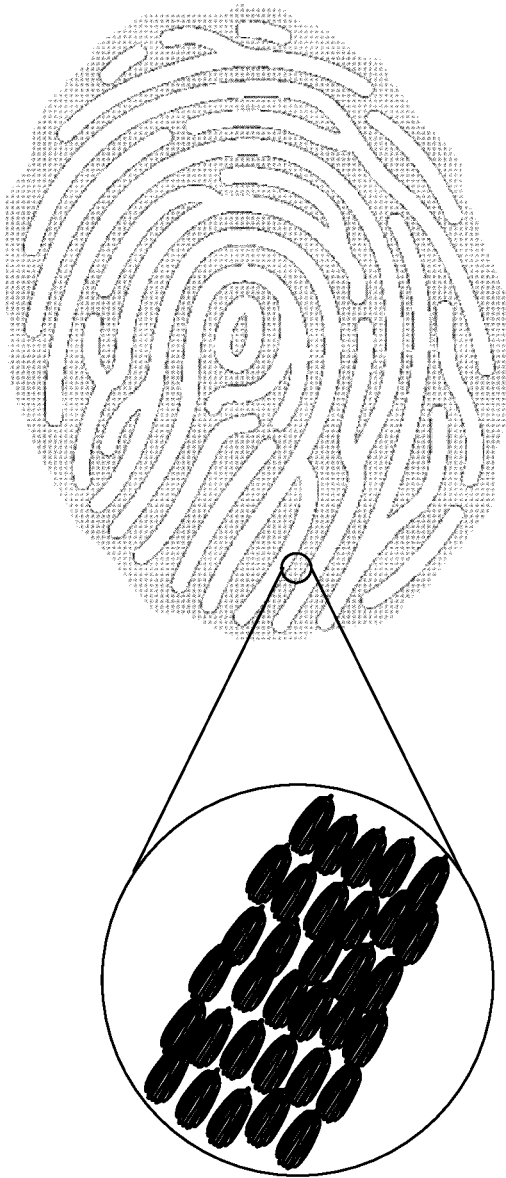


Fig. 12



Fig. 13

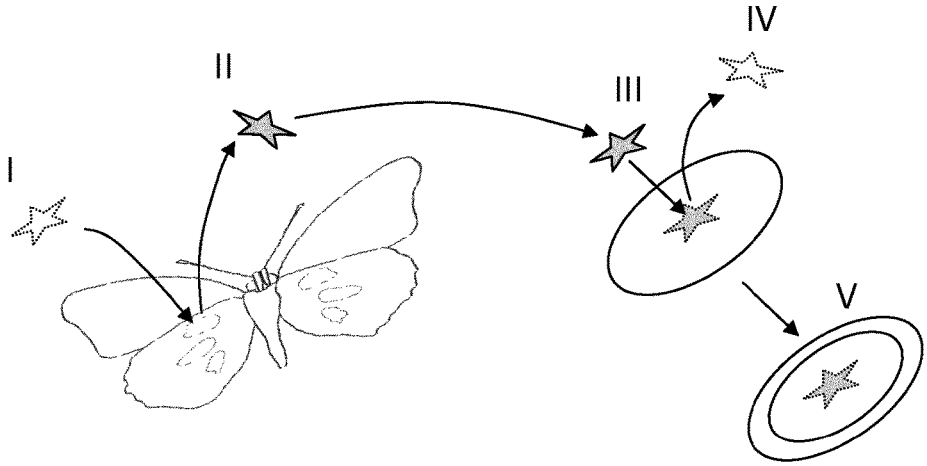


Fig. 14

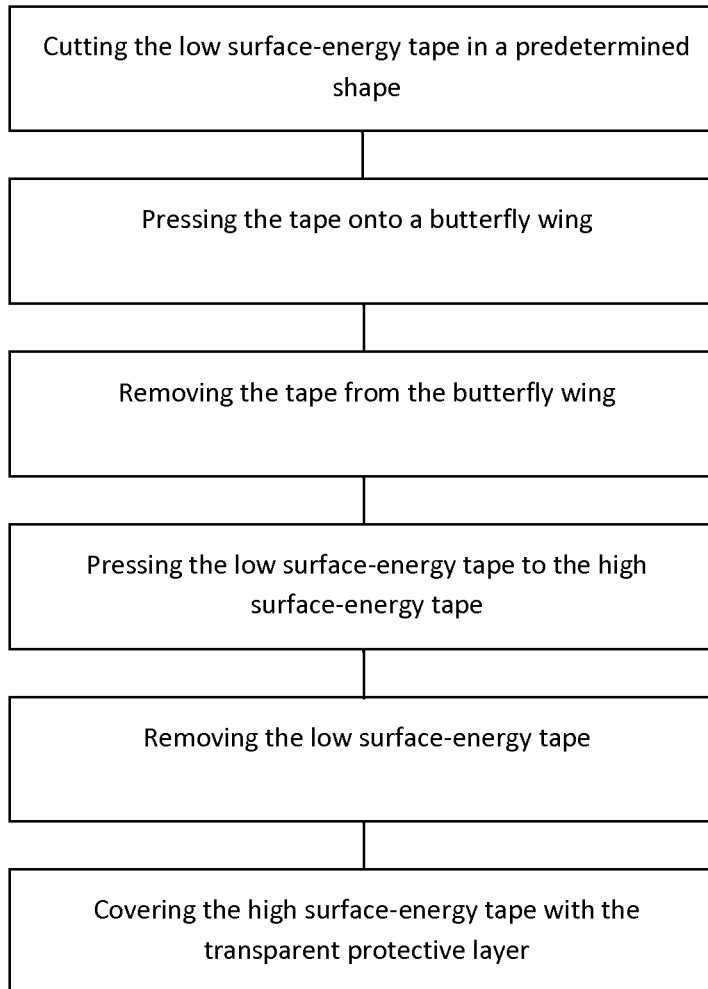


Fig. 15

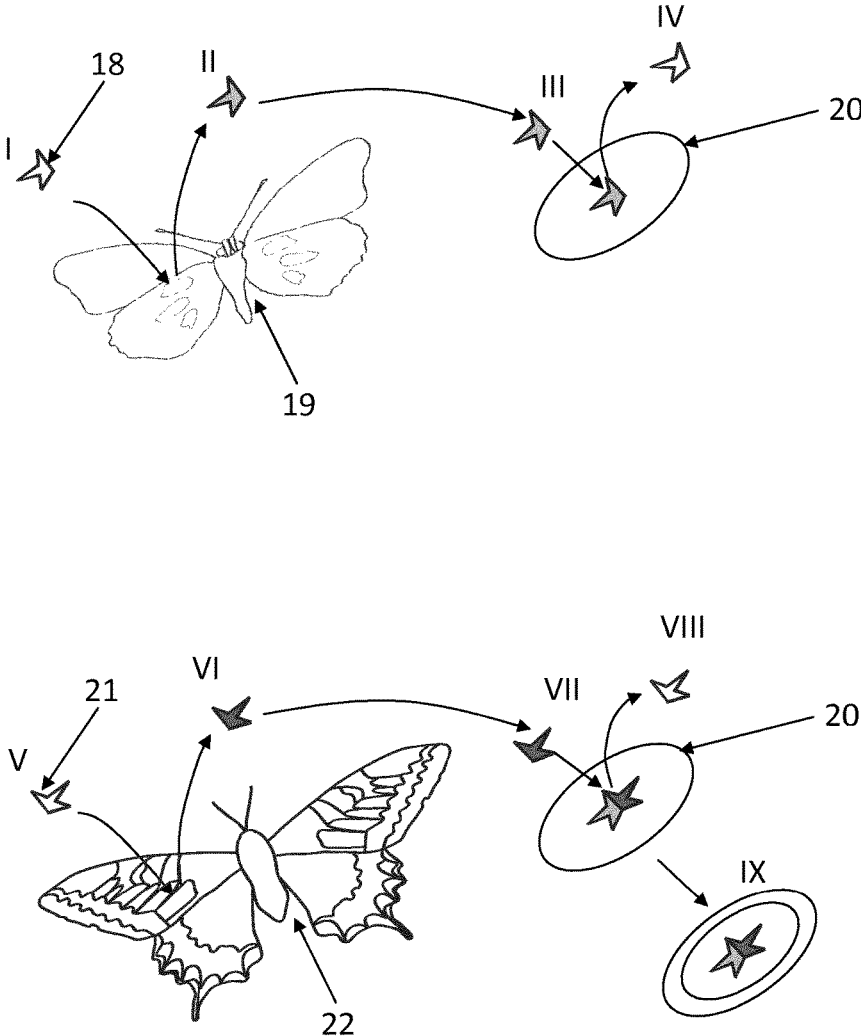


Fig. 16

## SECURITY TAG CONTAINING A PATTERN OF BIOLOGICAL PARTICLES

This application is a National Stage entry under § 371 of International Application No. PCT/EP2015/081400, filed on Dec. 30 2015.

### FIELD OF INVENTION

The present invention relates to security tags for identification and authentication of goods, articles and documents.

### BACKGROUND OF INVENTION

Optically variable devices (OVD) are a common protective element on various types of documents (e.g. identity cards, passports, visas, bank cards)—see the book “Optical Document Security”, ed. by R. L. Van Renesse, Artech House, (1998). Holograms and other diffractive elements are mainly used, because their protective value is based on complexity of micron and submicron structures. Manufacturing is a complicated and expensive process whose final result is a master hologram—a single, unique prototype. To make protection commercially acceptable, the master hologram is copied and multiplied, resulting in a replica shim used for embossing into a plastic foil, which is then integrated into a document using a hot tool. The final result is a series of documents possessing exactly the same protective OVD. This is a significant drawback, because, if the OVD is counterfeited, a large number of fake documents can be manufactured.

As a result, there is ongoing research for a simple and affordable document individualization method. This makes counterfeit much harder, because each and every document has to be copied individually, i.e. large scale production of false documents becomes impossible. However, the trivial individualization by simply printing numbers will not work, because it is too simple and affordable, if using modern printing technologies (e.g. laser printing). Therefore the individualization-bearing features must possess a significant amount of complexity together with strong, unrepeatable, individual properties. They have to be comparable in its uniqueness with biometric characteristics, such as: fingerprints, iris and retina pattern, but significantly more complex and miniscule. Currently used OVD security methods are not well suited for individualization (fingerprinting), as this will significantly increase the production prices.

Attempts to obtain “fingerprint” documents are based on the idea of physical one-way functions (C. Boehm, M. Hofer, “Physically unclonable functions in theory and practice”, Springer, 2013)—which are physical devices simple to manufacture, yet extremely difficult to reverse engineer and copy. Random structures can be highly significant for document security, because they offer simple and cheap production, almost impossible re-origination and unique features. It was proposed to tag documents with randomly dispersed objects such as metal, fluorescent or optical fibers (van Renesse book, and references therein).

Natural fibrous structure of paper-based substrates was used (J. D. R. Buchanan, R. P. Cowburn, A.-V. Jausovec, D. Petit, P. Seem, G. Xiong, D. Atkinson, K. Fenton, D. A. Allwood, M. T. Bryan, “‘Fingerprinting’ documents and packaging”, *Nature* 436, (2005) 475). Laser beam was scattered from the paper surface and its statistics was observed and recorded. This however requires a large scale

scanning of the document surface which is a slow process, and paper structure may be strongly affected by printing and everyday usage.

Yet another technique was described in R. Pappu, B. Recht, J. Taylor, N. Gershenfeld, “Physical One-Way Functions,” *Science* 297, (2002) 2026-2030, where mesoscopic scattering from disordered array of plastic spheres embedded in a transparent substrate was used to construct physical one-way function. The response of the system strongly depends on the illumination direction, again producing unique individual characteristics. The proposed method is limited by the physical requirements for the mesoscopic scattering, resulting in a 10 mm×10 mm sized tag, with 2.5 mm thickness, which is unsuitable for the modern plastic card technology. Furthermore, the dimension of scattering particles is rather large—500-800 μm in diameter, with 100 μm average spacing—resulting in a bulky system which can be reverse engineered by techniques like micro-tomography.

It is a common knowledge that certain natural characteristic of living creatures are essentially complex and hard to reproduce. This was first realized by Benjamin Franklin who used this for document protection (Farley Grubb, “Benjamin Franklin and the birth of the paper money economy”, Essay based on Mar. 30, 2006 lecture, published by Federal Reserve Bank of Philadelphia). He made casts of plant leaves (correctly recognizing the uniqueness of their venation) and used them to print the first dollar bills. Due to further technological advancements, Franklin’s method became obsolete, and was replaced with different printing techniques, such as: intaglio, guilloche, watermark, holograms, etc.

Complexity of natural structures was observed in art, too. Japanese painters used fish printing (gyotaku) to directly transfer fish features, instead of painting them. Later, Leonardo Da Vinci directly printed leaf venation on the paper, while Dutch painter Otto Marseus Van Schrieck transferred butterfly wing scales to his canvases (S. Berthier, J. Boulanguez, M. Menu, B. Mottin, “Butterfly inclusions in Van Schrieck masterpieces. Techniques and optical properties”, *Appl. Phys. A*, 51-57, (2008)). Today, all the techniques have the common name: nature printing (R. Newcomb, “Method for producing nature prints”, U.S. Pat. No. 4,279, 200 A, (1981), C. F. Cowan, “Butterfly wing-prints”, *J. Soc. Bibliophy. Nat. Hist.*, 4 (1968) 368-369, D. G. Edwards, “A receipt for taking figures of butterflies on thin gummed paper”, in *Essays upon natural history and other miscellaneous subjects*, pg. 117).

Patents WO 2007031077 (A1) March 2007, C. Hamm-Dubischar, “Inorganic marking particles for characterizing products for proof of authenticity method for production and use thereof” and DE10238506 A1, 3/2004, H. Rauhe, “Producing information-bearing micro-particulate mixtures involves defining code that can be implemented using natural or subsequently applied particle characteristics selected from e.g. morphology”, disclosed an idea for document protection which uses natural complexity of aquatic organism inorganic shells (like diatoms and radiolarians) according to characteristics of their surfaces. The practicing method is, however, not disclosed. Another problem is that the optical effects are not very pronounced, and the complexity can be observed only at the sub-wavelength levels, using electron microscopy. Technique for estimating the degree of complexity was not described, either. Variation among the specimens of the same species is rather small. In that respect, the method can be used only for the forensic level of document authentication.

Recently, there was a significant amount of research aimed at using the principles of optics in nature for document protection—biomimetics (J. Sun, B. Bhushanand J. Tong, “Structural coloration in nature”, RSC Adv., 2013, 3, 14862-14889, B. Yoon, J. Lee, I. S. Park, S. Jeon, J. Lee, J-M. Kim, “Recent functional material based approaches to prevent and detect counterfeiting”, J. Mater. Chem. C 1, (2013) 2388-2403). Variability of biological structures was also observed (L. P. Biro and J-P. Vigneron, “Photonic nanoarchitectures in butterflies and beetles: valuable sources for bioinspiration”, Laser Photonics Rev. 5, No. 1, 27-51 (2011)). Biotemplating was used to manufacture butterfly scale-like structures using metals (S. Sotiropoulou, Y. Sierra-Sastre, S. S. Mark, and C. A. Batt, “Biotemplated Nanostructured Materials”, Chem. Mater. 2008, 20, 821-834).

The randomized systems described above must be machine-inspected, based on radiation scattering with consequent optical or microwave detection (in the case of metal inclusions). Recorded pattern is encrypted and stored in a central repository or on the document, itself. Public key encryption method is used, as described in the report: “Counterfeit deterrent features for the next generation currency design”, Committee on Next-Generation Currency Design, National Materials Advisory Board, Commission on Engineering and Technical Systems, National Research Council, Publication NMAB-472, (1993), Section: Random Pattern/Encryption Counterfeit-Deterrence Concept, pg. 74-75, and Appendix E: “Methods for authentication of unique random”, pg. 117-119. A technique is based on two keys: a secret one, used for encryption, and a public one, used for the decryption.

All the methods used a complexity of natural structures but their variability remained completely unused in the context of the document protection. Document variability was rather attained by randomly dispersing particle- or thread-like entities across the document, as described in the patent literature (U.S. Pat. No. 8,408,470B2, 2013, N. Komatsu, S-I. Nanjo, “Object for authentication verification, authentication verifying chip reading device and authentication judging method”).

#### SUMMARY OF THE INVENTION

This invention solves the problem of identicalness of, presently used, document security features (e.g. holograms and other OVDs), making them vulnerable to counterfeiting. Presently, security elements are identical on the same type of document (passport, visa, credit card), without variability between the individual documents. This eases the counterfeiting process because, once the counterfeit is made, it can be applied to any number of documents. The invention uses naturally occurring biological particles, whose variability is guaranteed by the large number of degrees of freedom of biological processes. They are used to manufacture a tag, which can be further applied to a document or a product, thus making it unique.

A security tag and a manufacturing method are disclosed.

The security tag of the present invention is characterized by a pattern of inimitable biological particles, directly transferred from an organism to a transparent adhesive layer on a substrate, covered with a transparent superstrate, such that said biological particles are encapsulated between said substrate and said superstrate.

In one embodiment of the present invention, the pattern of biological particles is in the shape of a bar-code or QR-code.

In another embodiment of the present invention, the pattern of biological particles is in the shape of a silhouette of a human head or, alternatively, in the shape of a fingerprint.

Preferably, the biological particles are overtly inscribed with information by mechanical or laser cutting.

Alternatively, the biological particles are covertly inscribed with information by permanently bleaching their fluorescence.

Preferably, the biological particles are selected from Lepidoptera scales, hairs or bristles, Coleoptera scales, Trichoptera hairs or bristles, and Arachnides scales.

More preferably, the biological particles are taken from several different species, and assembled on the substrate in a predetermined pattern.

In one embodiment of the present invention, selected parts of the superstrate are covered with a transparent layer of adhesive, which permanently adheres to the biological particles.

Furthermore, the invention is directed to the use of a security tag according to the present invention for identification and authentication of goods, articles and documents.

Finally, the invention is directed to a method of manufacturing a security tag according to the present invention, comprising the following steps:

- (1) providing for at least one biological particle on a surface;
- (2) cutting an optically transparent tape, with a low surface energy adhesive layer, in a predetermined shape to form a first pre-cut tape;
- (4) pressing the first pre-cut tape onto the surface with the biological particles;
- (5) removing the first pre-cut tape from the surface with the biological particles, with a majority of the biological particles being attached to the first pre-cut tape;
- (6) bringing in contact the first pre-cut tape with attached biological particles (10) with a second, high surface energy, optically transparent, adhesive tape, such that the adhesive layers face each other;
- (7) lifting-off the first pre-cut tape from the second tape;
- (8) covering the second tape with a third optically transparent tape, which is smaller than the second tape to form the security tag ready to be attached to goods, articles or documents.

A tag according to the present invention comprises a multiplicity of selected, micron-sized, parts of an insect body (biological particles), attached on a substrate surface within the predetermined area having well defined, easily recognizable, shape. Biological particles are directly transferred to the substrate, retaining their original physical characteristics and spatial arrangement. Said biological particles are selected according to a high level of complexity and variability of their optical properties, observable under different image magnifications. Overall tag size is such that it enables visual inspection and easy recognition by the user, as well as machine inspection at the microscopic level.

Complexity is measured by the statistically averaged volume to surface ratio of the biological particle (FIG. 1 and FIG. 2 show the typical complexity of insect body-scales found on the cuticle of some insects). Preferably, the volume/surface ratio is less than 50 nm. Variability is defined through the number of degrees of freedom (G. T. di Francia, “Degrees of freedom of an image”, JOSA 59, (1969) 799-804) of the observed biological particle image at the defined magnification (FIG. 6 presents optical patterns of insect

body-scales 7 recorded at different magnifications). Preferably, the number of degrees of freedom should be larger than 1000.

It is required that the observed optical effects are strongly localized, variable and individual and the result of interference, diffraction and scattering (including their polarization and angular dependence) from a complex three-dimensional structure. Additionally, tissues and cells are chosen to be durable, with permanent optical properties and capable of being transferred to the substrate and processing prior, during and after attachment to the substrate. A substrate which receives the biological structure thus becomes unique and unrepeatable. The resulting tag can be further attached on various types of objects demanding individualization and secure identification.

A tag substrate may contain three printed markers, which are used as a reference to generate a local coordinate system. Selected features of insect body parts attached to the tag are used as the machine-readable security code (second line of protection).

Tag manufacturing process consists of several stages, which use adhesive tapes with varying surface energy. The first tape is used to lift off the biological particles from the organism. They are transferred to a higher surface energy tape, where they remain permanently affixed and protected by an additional protective layer.

#### BRIEF DESCRIPTION OF THE DRAWINGS

FIG. 1: Butterfly scale observed under the scanning electron microscope (SEM).

FIG. 2: Cross-section of the butterfly scale observed under the transmission electron microscope (TEM).

FIG. 3: Magnified cross-section of the butterfly scale ridge, observed under the TEM microscope.

FIG. 4: Gamma corrected image of the butterfly scale from FIG. 3, where edges are emphasized.

FIG. 5: Thresholded version of the image in FIG. 3, enabling calculation of the enclosed surface area.

FIG. 6: Part of the butterfly wing is star-shaped cut, such that an iridescent patch is included, whose magnified image reveals individual scales with number of dots of different intensity and spectral content.

FIG. 7: A Fourier transform of the scale in FIG. 6 is used to calculate signal bandwidth  $\Delta\nu$ .

FIG. 8: A tag with transferred biological particles.

FIG. 9: A tag with transferred biological particles and superstrate having an adhesive layer which changes the iridescence color.

FIG. 10: Square-shaped cuts in a butterfly wing (designated with white arrows), as observed under the scanning electron microscope.

FIG. 11: A silhouette made of biological particles.

FIG. 12: A fingerprint made of biological particles.

FIG. 13: A bar-code made of butterfly scales.

FIG. 14: A manufacturing process of a tag with biological particles.

FIG. 15: A flow chart of the manufacturing process of a tag with biological particles.

FIG. 16: A manufacturing process of a tag with biological particles belonging to different biological species.

#### DETAILED DESCRIPTION OF THE INVENTION

In cooperation with the attached drawings, the technical contents and detailed embodiments of the present invention

are described hereinafter, however, not limiting its scope of protection, which is exclusively defined by the claims. Any equivalent variation and modification made according to the appended claims is to be included into their scope of protection.

An optical tag is disclosed which contains a number of biological particles selected according to their complexity and variability. Before describing the construction of a tag and its various embodiments, we assign concrete meaning to notions of complexity and variability. This is necessary in order to select the best species and biological particles, which guarantee the anti-counterfeit properties of a tag.

In reference to FIG. 1, the typical complexity of biological particles can be observed, e.g. Lepidoptera scales. Structure consists of two types of gratings: a volume grating which is characterized by ridges 1 having a number of lamellas 2, and a surface grating consisting of cross-ribs 3 connecting the ridges. By observing the cross-section of the scale (FIG. 2), it can be seen that the scale has two membranes: a lower one 4, which is unstructured, and an upper one 5, which contains ridges, lamellas and cross-ribs. By using magnified cross-section of a complex part of the butterfly scale in FIG. 3, the complexity can be quantified by determining the contour length to contour enclosed-surface ratio. Contour length is determined by first digitally emphasizing object edges (see FIG. 4) and calculating the total number of black pixels— $L_b$ . Surface area is determined by digitally thresholding image in FIG. 3 (the result of the operation is shown in FIG. 5), and integrating the total number of black pixels  $S_b$ . Complexity  $C$  is thus  $C=S_b/L_b$ .

Natural variation in the internal structure of the biological particles, e.g. Lepidoptera scale (as shown in FIGS. 1, 2 and 3), leads to variability of resulting optical effects. FIG. 6 shows a star-shaped part of the butterfly wing transferred on another substrate. Concrete Lepidoptera species and cut position are chosen such that the resulting piece contains at least one iridescent spot 6. Its magnified image reveals scales 7 having a number of dots of varying intensity and spectral content. Their position, optical spectrum and intensity are unpredictable and define degrees of freedom. Their number  $N$  is used as a measure of variability. This can be estimated by calculating the ratio of the individual scale surface area  $S$  (easily calculated from an image) to the average dimension of a dot  $\Delta x$  (FIG. 6). The last feature is connected to spectral width of the signal via relation:

$$\Delta x \Delta \nu = 1 / (4\pi)$$

(see FIG. 7, where Fourier transform of the Lepidoptera scale image is shown). By measuring the spectral width  $\Delta\nu$ , average dot dimension  $\Delta x$  can be calculated. Finally, the number of the degrees of freedom is calculated as  $N=S/\Delta x$

In reference to FIG. 8, a preferred embodiment of an optical security tag according to the invention is shown by presenting it in two orthogonal projections. A substrate 8 is covered with a thin, transparent, adhesive layer 9. Biological particles 10 firmly adhere to the said adhesive layer, producing an easily recognizable pattern (e.g. a symbol, a letter, a barcode, a silhouette, etc.). Adhesion of the biological particles 10 is such that the attempt of removal destroys their submicron-sized structure. Three visible marks 11, 12 and 13 (e.g. crosses) are printed on the substrate 8, and are used for positioning the tag in a well defined position, with respect to the optical reading system. They also define a local coordinate system which can be curvilinear and non-orthogonal (designated with dashed lines). The exact mathematical nature of the coordinate system is known only to the issuer of the tag. The biological particles 10 are protected



by a transparent cover **14**. One or several particles **10'** are randomly selected as bearers of individualization pattern. Their position with respect to markers **11**, **12** and **13** is determined and memorized. In addition, their optical pattern (7 in FIG. 6) is recorded and memorized, too.

In another embodiment (FIG. 9) the superstrate **14** comprises a patterned adhesive layer **16** which permanently affixes to the biological particles. This serves a dual purpose. First, the refractive index of the layer changes the refractive index above the biological particles and alters the iridescent color of one part of the pattern **17**. As in the previous embodiment, one or several scales **10'**, are randomly selected as bearers of individualization pattern. In addition, any attempt to disassemble the tag results in separation of biological particles—some of them remain on the substrate and others are lifted with the superstrate, thus producing a tamper sensitive tag.

In another embodiment, the substrate **8** is transparent, thus enabling two-sided observation of the biological particle **10**. For some Lepidoptera species, the iridescence pattern is different on each side of the scale. In this embodiment, the optical pattern can be observed both in transmitted and reflected light. The pattern can be a result of diffraction, interference, iridescence, scattering and fluorescence of coherent or incoherent light. Angular, focal and polarization changeability of the pattern is recorded and used as an authentication signal.

In yet another embodiment, transferred biological particles **10** are further patterned by mechanical means. A mechanical tool is engraved with the desired pattern, producing a system of raised and recessed portions. It is pressed onto the pattern, thus crushing the biological particles and changing their optical properties (e.g. iridescence, scattering), producing visually observable pattern.

In yet another embodiment, transferred biological particles are macroscopically patterned by laser cutting or engraving (e.g. square shaped areas designated with white arrows in FIG. 10). A beam from an ultrafast laser is introduced in a system with a computer-controlled galvanometer-mirror scanner, which is used to angularly deflect a beam according to programmed trajectory. The beam is then expanded and focused to the tag with biological particles, using an f-theta lens, which enables flat scanning field and linear relation between the deflection angle and the focal beam position. The laser wavelength, scanning speed and power are chosen such that cutting or engraving is enabled. It is used to draw a personalized, biometric, pattern (e.g. silhouette as in FIG. 11, fingerprint as in FIG. 12, retinal blood vessel pattern, signature, or iris image) onto the surface of a tag with biological particles. In this manner an overt pattern is produced, which can be used for visual and machine authentication.

A further embodiment is characterized by a bar-code or QR-code pattern made from biological particles (FIG. 13).

In another embodiment, fluorescence of transferred biological particles is selectively bleached using high intensity UV radiation. This can be done using an UV projection system consisting of a UV lamp and an objective. A mask, containing transparent and opaque areas which comprise an image, is inserted into the system such that an image is produced directly on a tag with biological particles. Bleaching action is controlled by the intensity of the illuminating beam and the illumination time. Alternatively, a beam from a continuous wave (CW) or ultrafast laser is introduced in a system with a computer-controlled galvanometer-mirror scanner, which is used to angularly deflect a beam according to programmed trajectory. The beam is then expanded and

focused to the tag with biological particles, using an f-theta lens, which enables flat scanning field and linear relation between the deflection angle and the focal beam position. Wavelength of a laser is chosen such that the bleaching action is enabled via single-photon process (in the case of a CW laser), or two-photon process (in the case of an ultrafast laser). The laser power and its scanning speed determine the intensity of the bleaching. The pattern is observable using low intensity UV radiation as a covert security feature.

The tag manufacturing process consists of several stages depicted in FIG. 14. First, a tape having an adhesive layer (pressure sensitive) with low peel strength (preferably, the surface energy of the order of 0.5 N/cm) is laser- or die-cut in the required shape. A tape is pressed on the surface covered with biological particles (e.g. a butterfly wing), with their iridescent surface facing up, and they adhere to the tape (phase I) in FIG. 14). The tape is peeled, lifting-off cells or tissues (phase II) in FIG. 14). Next, a tape is transferred to a second optically transparent tape having high peel strength and, preferably, surface energy of the order of 2.5 N/cm (phase III) in FIG. 14). Tapes are pressed together with the adhesive layers facing each other, biological particles being trapped between the layers. After a certain dwell time, the tapes are separated (phase IV) in FIG. 14). Due to the higher surface energy of the second tape, biological particles from the first plate remain on the second tape. The third, optically transparent, non-adhesive tape is used to cover the biological particles, protecting them from external influences (phase V) in FIG. 14). The third tape is smaller than the second tape, thus exposing the remaining adhesive layer, which will be used for attachment to an object requiring individualization. A flow chart of the whole process is shown in FIG. 15.

In another embodiment, a tag and associated manufacturing process use biological particles of several species. The final pattern is assembled from two or more sub-patterns transferred from several insect species belonging to e.g. Lepidoptera order, as described in FIG. 16. First, a tape **18** having an adhesive layer (pressure sensitive) with low peel strength (preferably, with a surface energy of the order of 0.5 N/cm) is laser- or die-cut in the required shape. A tape is pressed on the surface **19** covered with biological particles (e.g. a Lepidoptera wing) belonging to one biological species, with their iridescent surface facing up. Biological particles adhere to the tape (phase I) in FIG. 16). The tape is peeled, lifting off cells or tissues (phase II) in FIG. 16). Next, a tape is transferred to a second optically transparent tape **20** having high peel strength and, preferably, a surface energy of the order of 2.5 N/cm (phase III) in FIG. 16). Tapes are pressed together with the adhesive layers facing each other, biological particles being trapped between the layers. After a certain dwell time, the tapes are separated (phase IV) in FIG. 16). Due to the higher surface energy of the second tape, biological particles from the first plate remain on the second tape. Another tape **21**, having an adhesive layer (pressure sensitive) with a low peel strength (preferably, with a surface energy of the order of 0.5 N/cm) is laser- or die-cut in the required shape, complementary to the one described in Phase I of the process. A tape is pressed on the surface **22** covered with biological particles (e.g. a Lepidoptera wing) belonging to another biological species, with their iridescent surface facing up. Biological particles adhere to the tape (phase V) in FIG. 16). The tape is peeled, lifting off cells or tissues (phase VI) in FIG. 16). Next, a tape is transferred to, previously manufactured, transparent tape **20** having high peel strength and, preferably, a surface energy of the order of 2.5 N/cm (phase VII) in FIG. 16).

Tapes are pressed together with the adhesive layers facing each other such that patterns defined by tapes **18** and **21** complement each other. Consequently biological particles are trapped between the layers. After a certain dwell time, the tapes are separated (phase (VIII) in FIG. **16**). Due to the higher surface energy of the second tape, biological particles from the first tape remain on the second tape.

In the next phase (IX in FIG. **16**) the third, optically transparent, non-adhesive tape is used to cover the biological particles, protecting them from external influences. The third tape is smaller than the second tape, thus exposing the remaining adhesive layer, which will be used for attachment to an object requiring individualization.

The method described in the previous embodiment can be further extended to any number of different biological species.

The invention claimed is:

1. A security tag, comprising:
  - a pattern of inimitable biological particles,
  - a transparent adhesive layer,
  - a substrate, and
  - a transparent superstrate,
 wherein the pattern of inimitable biological particles is directly transferred from an organism to the transparent adhesive layer on the substrate, and
  - wherein said biological particles are covered with the transparent superstrate, such that said inimitable biological particles are encapsulated between said substrate and said superstrate.
2. The security tag according to claim 1, wherein the pattern of inimitable biological particles is in the shape of a bar-code or a QR-code.
3. The security tag according to claim 1, wherein the pattern of inimitable biological particles is in the shape of a silhouette of a human head.
4. The security tag according to claim 1, wherein the pattern of inimitable biological particles is in the shape of a fingerprint.
5. The security tag according to claim 1, wherein the biological particles are overtly inscribed with information by mechanical or laser cutting.
6. The security tag according to claim 1, wherein the biological particles are covertly inscribed with information by permanently bleaching a fluorescence thereof.

7. The security tag according to claim 1, wherein the inimitable biological particles are particles of at least one member selected from the group consisting of a Lepidoptera scale, hair, a bristle, a Coleoptera scale, Trichoptera hair, a Trichoptera bristle, and an Araneae scale.

8. The security tag according to claim 7, wherein the inimitable biological particles are particles of at least two members selected from the group consisting of a Lepidoptera scale, hair, a bristle, a Coleoptera scale, Trichoptera hair, a Trichoptera bristle, and an Araneae scale, and

wherein the inimitable biological particles are assembled on the substrate in a predetermined pattern.

9. The security tag according to claim 7, wherein at least one part of the superstrate is covered with a transparent layer of adhesive, which permanently adheres to the biological particles.

10. A method of identifying or authenticating a good, an article, or a document comprising the security tag according to claim 1, the method comprising: scanning the security tag with a scanning device.

11. A method of manufacturing a security tag, comprising:

- (1) providing biological particles on a surface;
- (2) cutting an optically transparent tape, with a low surface energy adhesive layer, in a predetermined shape to form a first pre-cut tape;
- (3) pressing the first pre-cut tape onto the surface with the biological particles provided thereon;
- (4) removing the first pre-cut tape from the surface with the biological particles present thereon, with a majority of the biological particles being attached to the first pre-cut tape;
- (5) bringing into contact the first pre-cut tape with attached biological particles with a second, high surface energy, optically transparent, adhesive tape, such that the adhesive layers face each other;
- (6) lifting-off the first pre-cut tape from the second tape; and
- (7) covering the second tape with a third optically transparent tape, which is smaller than the second tape to form the security tag ready to be attached to goods, articles or documents.

\* \* \* \* \*

See discussions, stats, and author profiles for this publication at: <https://www.researchgate.net/publication/314154328>

# THERMAL AND CAMOUFLAGE PROPERTIES OF *Rosalia alpina* LONGHORN BEETLE WITH STRUCTURAL COLORATION

Conference Paper · October 2016

CITATIONS

3

READS

1,001

9 authors, including:



**Danica Pavlović**

Institute of Physics Belgrade

16 PUBLICATIONS 60 CITATIONS

[SEE PROFILE](#)



**Vladimir Lazovic**

Institute of Physics Belgrade

25 PUBLICATIONS 204 CITATIONS

[SEE PROFILE](#)



**Dragan Knežević**

30 PUBLICATIONS 123 CITATIONS

[SEE PROFILE](#)



**Goran Dikic**

School of Electrical and Computer Engineering of Applied Studies

30 PUBLICATIONS 82 CITATIONS

[SEE PROFILE](#)

Some of the authors of this publication are also working on these related projects:



Thermography [View project](#)



Generation and characterization of nano-photonic structures in biomedicine and informatics [View project](#)



## THERMAL AND CAMOUFLAGE PROPERTIES OF *Rosalia alpina* LONGHORN BEETLE WITH STRUCTURAL COLORATION

IVANA KOSTIĆ

Technical Test Center, Belgrade, [kostic.ici@gmail.com](mailto:kostic.ici@gmail.com)

DANICA PAVLOVIĆ

Photonics Center Institute of Physics, University of Belgrade, [danica.pavlovic@ipb.ac.rs](mailto:danica.pavlovic@ipb.ac.rs)

VLADIMIR LAZOVIĆ

Photonics Center Institute of Physics, University of Belgrade, [vladimir.lazovic@ipb.ac.rs](mailto:vladimir.lazovic@ipb.ac.rs)

DARKO VASILJEVIĆ

Photonics Center Institute of Physics, University of Belgrade, [darko@ipb.ac.rs](mailto:darko@ipb.ac.rs)

DEJAN STOJANOVIĆ

Fruška Gora National Park, Sremska Kamenica, [dejanstojanovic021@yahoo.co.uk](mailto:dejanstojanovic021@yahoo.co.uk)

DRAGAN KNEŽEVIĆ

Military Technical Institute, Belgrade, [dragankn@gmail.com](mailto:dragankn@gmail.com)

LJUBIŠA TOMIĆ

Military Technical Institute, Belgrade, [ljubisa.tomic@gmail.com](mailto:ljubisa.tomic@gmail.com)

GORAN DIKIĆ

Military Academy, University of Defence in Belgrade, [goran.dikic@mod.gov.rs](mailto:goran.dikic@mod.gov.rs)

DEJAN PANTELIĆ

Photonics Center Institute of Physics, University of Belgrade, [pantelic@ipb.ac.rs](mailto:pantelic@ipb.ac.rs)

---

**Abstract:** *Rosalia alpina* is a longhorn beetle possessing distinctive gray body with several black spots. They serve as a camouflage within its environment (beech forest) and we suppose that insect also uses them to control the body temperature. We have studied the optical properties of this particular insect, ranging from the visible to far infrared part of the spectrum. Optical analysis has shown strong absorption in the visible, while thermal camera (operating in the spectral range from 7.5 to 13  $\mu\text{m}$ ) has shown quite uniform emissivity of the whole body. Numerical ray tracing was used to explain the exact optical mechanism of strong absorption of black spots. Possible military applications of the natural camouflage and absorption mechanism are outlined.

**Keywords:** Infrared imaging, natural photonics, camouflage.

### 1. INTRODUCTION

Coloration has multiple purposes in the living world: to hide, attract or warn. It can be also used for heat energy exchange with the environment [1]. Thermoregulation can be improved using natural photonic processes. In that respect, we have analyzed antennas and elytra (modified forewings of Coleoptera, which are used as a hard shield for their body) of *Rosalia alpina* (Linnaeus, 1758) (see photograph in Picture 1).

This is a large longhorn beetle (family *Cerambycidae*) with flat, blue-gray elytra with large, dominating black spots. It is 15-38 mm long, with the long antennas and striking black tufts of hair on the central segments of the

antenna [2]. Such coloration serves as a good camouflage with their preferred habitat, the European Beech [3].

The largest part of the beetles' body is covered with a dense tomentum, consisting of very fine, light blue, blue gray and dark blue hairs. The black spots on the elytra and pronotum are also covered with dense black hairs which give the spots their velvety appearance [2,4]. Picture 1 shows the photography of *Rosalia alpina* (test sample).

Natural photonic structures have the main purpose of producing colors that would have been impossible to generate by the pigments alone. In the insect world this is particularly true for blue colors (generated by pepper-pot structures found in many Polyommatae [5]) and green colors (produced by chiral photonic structures in *Calophrys rubi* (Linnaeus, 1758), [6]).

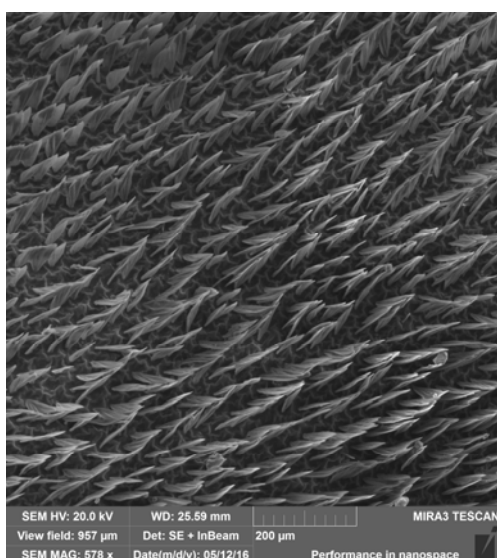


**Picture 1.** The photography of *Rosalia alpina*.

Sometimes photonic structure enhances the pigment color as observed in some snakes [7] or butterflies [8]. Micro and nano-structures localize light, and increase the average path length within the structure thus increasing absorption. The biological purpose of such structures might be the camouflage or thermoregulation, as in Lycaenid butterflies [9].

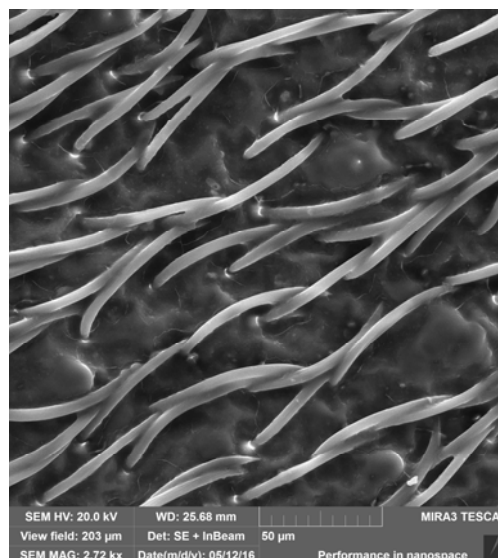
More advanced structures have dual purpose as in Saharan silver ant (*Cataglyphis bombycina* (Roger, 1859) [1]): to reflect maximum amount of the visible light, and to simultaneously dissipate infrared radiation directly into the atmospheric window at mid-infrared. This enables insect to efficiently regulate its body temperature in very hostile desert environment.

Four prominent black spots on the elytra of *Rosalia alpina* have attracted our attention. We have found, that the light absorption is not the sole consequence of dark pigments (most probably melanin), but that it is strongly influenced by the underlying structure [10]. We have been using Scanning Electron Microscope to examine the structure of *Rosalia alpina* hairs within the black spot (Picture 2). In adjacent grey zones hairs have completely different structure, as shown in Picture 3.

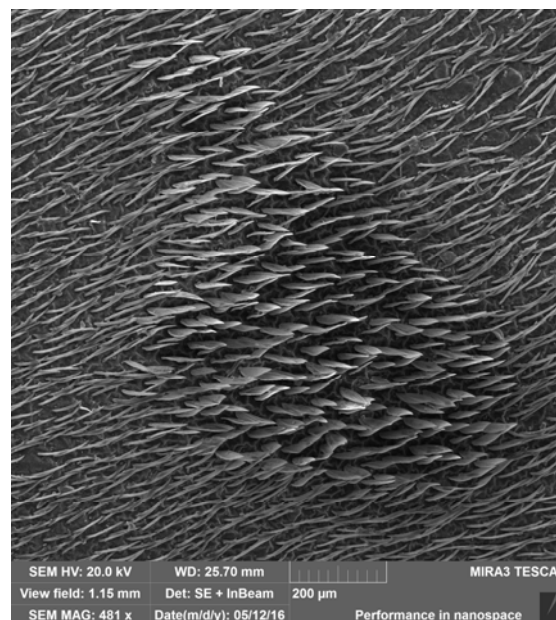


**Picture 2.** The hairs in black spots area of *Rosalia alpina*.

Both structures can be viewed, in the same scale, in picture 4. The different structure of hairs can be very easy notified in this picture.



**Picture 3.** The hairs in gray zones of *Rosalia alpina*.



**Picture 4.** The black spot area of *Rosalia alpina* surrounded by hairs with different structure.

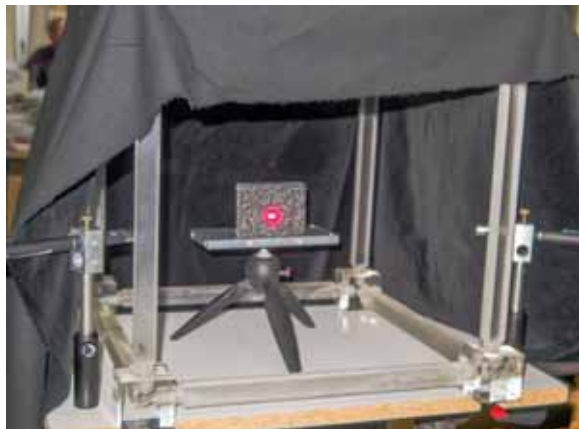
Materials developed by nature during the evolution, have a significant impact on search for artificial materials having useful absorptive properties, especially for solar energy collection, thermal energy dissipation and camouflage.

Bearing in mind possible military application we have been examining cooling process in the area of black spots of *Rosalia alpina*. The first results have been obtained using thermographic analysis based on pulse thermography [10]. This method involves the analysis of images that have been recorded by an infrared (IR) camera irradiating the test sample with infrared radiation. We have found that the light absorption is not the sole consequence of dark pigments (most probably melanin), but that it is strongly influenced by the underlying structure.

Here we analyze spectral absorption of black spots using several laser wavelengths.

## 2. EXPERIMENTAL SETUP

The test equipment comprised a set of laser pointers, a thermal camera and a personal computer (PC), which recorded digital data in real time. The surface of test sample (*Rosalia alpina*) was heated using the red, green and blue laser pointers (650 nm, 532 nm and 405 nm), positioned at a distance of 50 cm from the sample. Picture 5 shows the experimental setup.



**Picture 5.** The experimental setup.

Cooling of the test sample, previously heated by means of a short laser pulse, was monitored using a commercial thermal camera "FLIR SC620", operating in the spectral range from 7.5 to 13  $\mu\text{m}$  with FLIR T197189 macro lens. This type of camera has a focal plane matrix of 640x480 consisting of semiconductor detector (Vanadium Oxide - VOx). Each detector measures the intensity of infrared radiation. These values can be represented on a monitor as a thermal image coded in shades of gray or in color and can be converted to temperature values using the appropriate table.

In order to obtain optimal experimental results zoom has been set manually. After that, the all other parameters (ambient temperature, emissivity, the distance of the object from the thermal imaging camera, humidity, etc) have been found. Measurements, presented in this paper, have been carried out at short distances, (about 50 cm) and are not affected by atmospheric absorption.

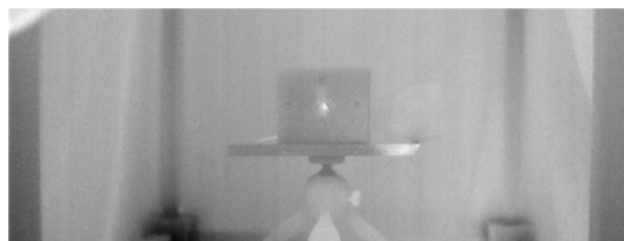
Thermal imaging camera allows conversion of spatially inhomogeneous distribution of radiation flux of scene, due to differences in the distribution of temperature and/or emissivity, in the visible image. The right choice of measuring geometry and correct interpretation of the results is based on the knowledge of the spatial and temperature resolution (sensitivity) of thermal imaging cameras.

## 3. EXPERIMENTAL RESULTS

Experiments have been organized in two ways. In the first case laser has been pointed to the black spot. In the second it has been used to irradiate the gray area near the black spot. During the short time (several seconds) laser pulse has been heating the irradiated place. Complete process has been recorded by IR camera and analyzed later using MATLAB software.

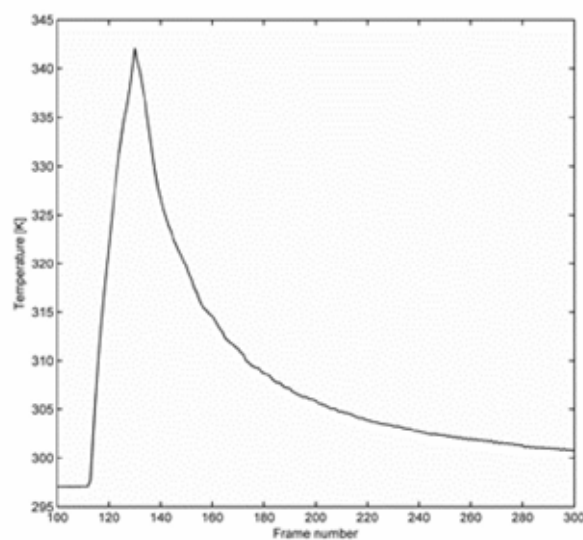
Energy emitted by laser, during irradiation of black spot, was 49.632 mJ (red light), 5.73 mJ (green light) and 176.305 mJ (blue light). It is followed by temperature increase of 44.226  $^{\circ}\text{C}$  (in case of red light), 23.512  $^{\circ}\text{C}$  (in case of green light) and 4.531  $^{\circ}\text{C}$  (in the case of blue light). It can be noticed that approximately 10 times less energy had been emitted in case of green light but temperature increase was only 2 times less than in case of red light. In addition, 3.5 times more energy had been emitted in case of blue light but temperature increase was nearly 10 times less than in case of red light.

Picture 6 shows a thermal image during the experiments with red laser in case of frame number 700. This frame is chosen because the temperature difference between maximal and minimal temperature is small enough that both, details of the target and the background can be visible.



**Picture 6.** Thermal image recorded during the 700<sup>th</sup> frame in case when red laser has been pointed at black spot.

Picture 7 shows a typical temperature change during the experiments.



**Picture 7.** Temperature change in case when red laser had been pointed at black spot.

Here we try to establish the dominant cooling mechanism: convection, conduction or radiation. We have started with analysis based on the Newton's law of cooling.

This law states that the rate of heat loss of a body is proportional to the difference in temperatures between the body and its surroundings. This means that the heat transfer coefficient, which mediates between heat losses and temperature differences, is a constant. This condition

is true in thermal conduction, but approximately true in conditions of convective heat transfer.

Newton's law of cooling is described by equation

$$\frac{dT}{dt} = k(T_t - T_a) \tag{1}$$

Whose solution is

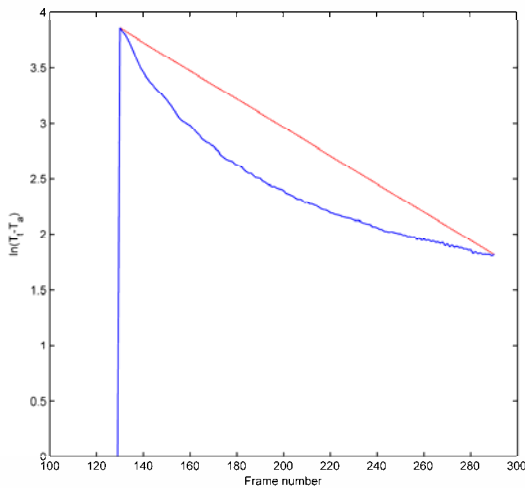
$$T_t = T_a + (T_0 - T_a)e^{-kt} \tag{2}$$

In these equation  $T_t$  is the temperature at time  $t$  and  $T_a$  is the ambient temperature,  $T_0$  is the initial temperature of the body, and  $k$  is a constant.

From equation 2 it follows that

$$\ln \frac{(T_t - T_a)}{(T_0 - T_a)} = -kt \tag{3}$$

We can see that appropriate curve, in ideal case of cooling, should be the straight line. In picture 8 we can see slightly displacement of real process (blue line) comparing to the ideal case (red line)

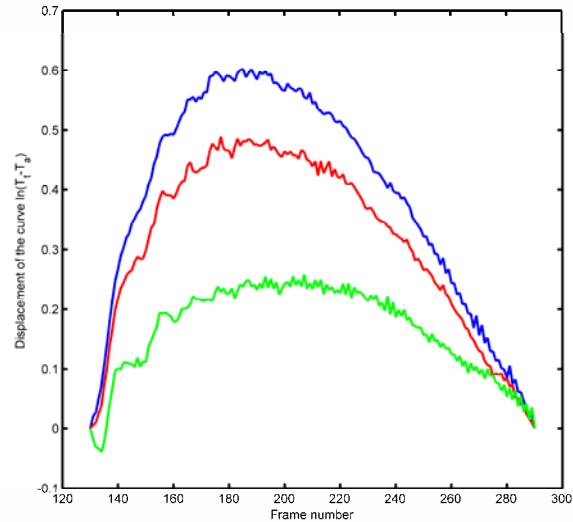


**Picture 8.** Natural logarithm of temperature difference in case of red laser; blue line real; red line in accordance with the Newton's law of cooling

Picture 9 shows the temperature difference in case when laser with red light has been pointed to the black spot. The blue line represents results obtained at the position of pixel with maximal temperature obtained during irradiation. The red line represents the results for the pixel in the same colon but one row below. Line marked by green colour represents the results in the same colon two row below. The similar results has been obtained in case of laser with the green and blue light.

Obviously the cooling process not coincide ideally with the Newton's law of cooling. There is a process of heat conduction in space that surround the irradiated point. The existence of negative values in case of green curve is clear evidence of that. Maximal temperature is achieved later than in case of red curve, after conducting of energy from the space with higher temperature.

During experiments the radiation time of laser has not controlled precisely. The next experiments will be organized with possibility for strictly control of radiation time. Also, with intention to have more comparable results, more attention will be paid to the positioning of the laser beam. During the last experiments irradiation of the object has been realized pointing laser from the hand. In addition, a couple of lasers with different wavelengths will be used for better covering of radiation spectra.



**Picture 9.** Displacement of real curve comparing to the curve obtained by the Newton's law of cooling; blue in position of maximal temperature; red in the same colon but one row below, and green in the same colon but two rows below.

#### 4. CONCLUSION

Our experiments are in progress. The results we have up to now show the existence of different photonic structure in the area of black spots. It is confirmed by the scanning electronic microscope but we want to confirm comparing the results of irradiation of the black spots and area outside of them.

In this paper we present the preliminary results of thermal analysis of *Rosalia alpina*. Insect was irradiated with laser radiation at three wavelengths, spanning the whole visible spectrum (405 nm, 532 nm and 650 nm). Significant departure from the Newton's law of cooling indicates that the thermal dissipation is regulated by radiation from the photonic structures. It seems that the structure is optimized such that it maximizes absorption in the visible part of the spectrum and simultaneously minimizes thermal losses due to radiation. More experimental and theoretical research is needed to better assess the thermal effects.

If proven true, the described effect could be used in construction of military personnel and arms clothes, which will diminish thermal dissipation through radiation. The effect could be important from the military point of view, because it can help the soldier to survive in cold weather, while reducing its thermal trace.

## References

- [1] Norman Nan Shi, Cheng-Chia Tsai, Fernando Camino, Gary D. Bernard, Nanfang Yu, Rüdiger Wehner: *Keeping cool: Enhanced optical reflection and heat dissipation in silver ants*, Science, Vol. 349, pp. 298-301, 2015.
- [2] Bense, U.: *Bockkäfer*, illustrierter Schlüssel zu den Cerambyciden und Vesperiden Europas, Margraf Verlag, 512 p., 1995.
- [3] Starzyk, J.R.: *Rosalia alpina* (LINNAEUS, 1758), *Nadobnica alpejska*.- In: *Głowacinski, Z. & Nowacki, J. (eds), Polsak czerwona księga zwierząt. Bezkręgowce: 148-149. IOP PAN Kraków, AR Poznań, 448 p., 2004.*
- [4] Duelli, P., Wermelinger, B.: *Der Alpenbock (Rosalia alpina)*, Ein seltener Bockkäfer als Flaggschiff-Art, Eidg. Forschungsanstalt WSL, CH-8903 Birmensdorf, 2005.
- [5] Vertesy, Zs., Balint, K., Kertész, J.P., Vigneron, V., Lousse, L.P. Biro, *Wing scale microstructures and nanostructures in butterflies – natural photonic crystals*, J. Microsc., 224, pp. 108-110, 2006.
- [6] Schröder-Turk, G.E., Wickham, S., Averdunk, H., Brink, F., Fitz Gerald, J.D., Poladian, L., Large, M.C.J., Hyde, S.T.: *The chiral structure of porous chitin within the wing-scales of Callophrys rubi*, J. Struct. Biol. 174, pp. 290-295, 2011.
- [7] Spinner, M., Kovalev, A., Gorb, S.N., Westhoff, G.: *Snake velvet black: Hierarchical micro- and nanostructure enhances dark colouration in Bitis rhinoceros*, Scientific Reports 3, Article number: 1846, 2013.
- [8] Vukusic, P., Sambles, J.R., Lawrence, C.R. : *Structurally assisted blackness in butterfly scales*, Proc. Roy. Soc. Vol. 271, S237-S239, May, 2004.
- [9] Biró, L.P., Bálint, Zs., K. Kertész, Z. Vértesy, G. I. Márk, Z. E. Horváth, Balázs, J., Méhn, D., Kiricsi, I., Lousse, V., Vigneron, J.-P.: *Role of photonic-crystal-type structures in the thermal regulation of a Lycaenid butterfly sister species pair*, Phys. Rev. E 67, 021907, Feb. 2003.
- [10] Dikić, G., Pavlović, D., Tomić, Lj., Pantelić, D., Vasiljović, D.: *The thermographic analysis of photonic characteristics of Rosalia Alpina Surfaces*, Symposium IcETRAN, Zlatibor, Serbia, 13.-16. June 2016.



### 3D imaging of micro objects by nonlinear laser scanning microscopy

Mihailo Rabasović<sup>1</sup>, Dejan Pantelić<sup>1</sup>, Branislav Jelenković<sup>1</sup>, Srećko Ćurčić<sup>2</sup>, Maja Rabasović<sup>1</sup>, Aleksandra Dimić<sup>1,3</sup>, Vladimir Lazović<sup>1</sup>, and Aleksandar Krmpot<sup>1</sup>

(1) *Institute of Physics, University of Belgrade, Pregrevica 118, 11080 Belgrade, Serbia*

(2) *Institute of Zoology, University of Belgrade - Faculty of Biology, Studentski Trg 16, 11000 Belgrade, Serbia*

(3) *University of Belgrade - Faculty of Physics, Studentski Trg 12, 11000 Belgrade, Serbia*

**Contact:** A. Krmpot ( [krmpot@ipb.ac.rs](mailto:krmpot@ipb.ac.rs) )

**Abstract.** The state of the art investigations in the laser scanning microscopy and its application is enabled mainly by new optical devices, laser sources and microscopic objectives. Advanced microscopic techniques, that give different and mutually compatible information about the sample, enable full characterization of the micro objects. Nonlinear microscopy enables obtaining the information on oriented structures, refraction index variation, and fluorescent properties deeply from the volume of the sample. The information are obtained by detecting nonlinear optical effects Two Photon Excitation Fluorescence (TPEF), Second Harmonic Generation (SHG) and Third Harmonic Generation (THG) during the scanning of the laser beam through the sample [1]. The nonlinear optical effects are efficiently produced only in the focus of the laser beam where the intensity is high enough. High intensity is achieved by tight focusing using high numerical aperture objectives and ultra short laser pulses. In this way it is possible to slice the sample, in optical manner, into tiny layers, and to use those layers for 3D reconstruction of the object. We present the images of chitinous structures of the specimens of endemic cave-dwelling insects *Pheggomisetes ninae* and *Plusiocampa christiani* from Southeast and East Serbia [2]. The results are obtained using home made experiental setup for nonlinear microscopy. We also present results of compound eyes of the Small White butterfly (*Pieris rapae*) and some other species of butterflies (Lepidoptera) (Fig. 1).

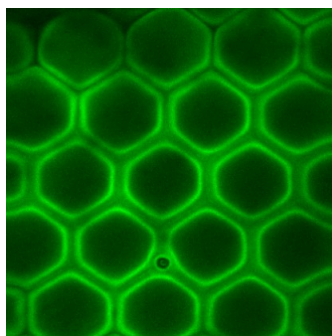


Figure 1. A slice of compound eye of *Pieris rapae* consisting of ommatidia obtained by TPEF modality of nonlinear microscopy.

**Acknowledgements.** We are thankful for financial support by the Ministry of education and science of Republic of Serbia, under grants III45016 and OI171038, and SNF-Scopes Grant IZ 76Z0 147548/1.

#### REFERENCES

- [1] R. Carriles, D. N. Schafer et al, *Rev Sci Inst* **80** (2009), 081101.  
 [2] S. B. Ćurčić, H. Schönmann et al, *Arch. Biol. Sci. Belgrade* **56** (2004), 109-113.

## Analysis of human healthy dentin microstructure by using two photon excitation fluorescence microscopy and second harmonic generation

Tijana Lainović<sup>1</sup>, Mihailo Rabasović<sup>2</sup>, Larisa Blažić<sup>1,3</sup>, Dejan Pantelić<sup>2</sup>,  
Aleksandar Krmpot<sup>2</sup>, Vladimir Lazović<sup>2</sup>, Branislav Jelenković<sup>2</sup>

<sup>1</sup>Faculty of Medicine, School of Dentistry, University of Novi Sad, Novi Sad, Serbia

<sup>2</sup>Institute of Physics, University of Belgrade, Belgrade, Serbia

<sup>3</sup>Clinic of Dentistry of Vojvodina, Novi Sad, Serbia

e-mail: tijana.lainovic@gmail.com

Human dentin is an organized hard, mineralized tissue of a tooth, composed of 70 wt% calcified tissue (hydroxyapatite), 20 wt% the organic phase (mostly composed of collagen type 1 and the other fibrils, glycosaminoglycans and proteoglycans), and 10 wt% water [1]. Dentin has a specific tubular structure containing tubules, peritubular and intertubular parts, biologically arranged to meet the specific mechanical, nutritional, sensory and reparative needs of a tooth [2].

The aim of this study was to analyze the microstructure of human dentin with the advanced microscopy tools, in order to get better insight into the architecture of healthy dentin.

The healthy premolar teeth were extracted for the orthodontic reasons, and collected in accordance with the ethical requirements for ex-vivo investigations, which was approved by the Ethical Committee of the Clinic of Dentistry of Vojvodina. The teeth were cleaned, and kept in 0.5 % Chloramine solution until the examination. The slices of teeth were prepared using a hard tissues microtome. The images of dentinal microstructures were obtained by the homemade nonlinear microscopy setup [3]. Ti-sapphire laser, adjusted at 730 nm wavelength, was used as an excitation source for two-photon excitation fluorescence (TPEF), while 840 nm excitation was used for the second harmonic generation (SHG).

The dentinal tubular, peritubular and intertubular structures were clearly presented. Natural human dentin enables the label-free and fixation-free visualization of its architectural content by the TPEF microscopy, owing to its intrinsic autofluorescence. The SHG can be detected due to the presence of collagen type I in dentin, which is a triple helical molecule, assembled in organized, non-centrosymmetric directional fibrils [4]. Images of healthy dentin could serve as a reference point for comparison and investigation of internal structural changes in dentin, affected by caries or non-caries lesions, or changed after the use of various restorative materials and procedures.

**Acknowledgments.** Research was supported by the Ministry of Education, Science and Technological Development of the Republic of Serbia (Projects. III 46010, ON 171038 and TR 035020)

### REFERENCES

- [1] M. Goldberg, A.B. Kulkarni, M. Young, A. Boskey, *Front. Biosci. (Elite Ed)*. 3, 711 (2011).
- [2] S.R. Stock, A.C. Deymier-Black, A. Veis, A. Telsler, E. Lux, Z. Cai, *Acta Biomater.* 10, 3969 (2014).
- [3] K. Bukara, S. Jovanić, I.T. Drvenica, A. Stančić, V. Ilić, M.D. Rabasović, D. Pantelić, B. Jelenković, B. Bugarski, A.J. Krmpot, *J Biomed Opt* 22, 026003 (2017).
- [4] R. Elbaum, E. Tal, A.I. Perets, D. Oron, D. Ziskind, Y. Silberberg, H.D. Wagner, *J. Dent.* 35, 150 (2007).

Универзитет у Београду

Физички Факултет

Владимир М. Лазовић

**Оптичке и флуоресцентне особине хитина и  
хитинских микроструктура биолошког порекла**

Докторска дисертација

Београд, 2022.

University of Belgrade

Faculty of Physics

Vladimir M. Lazović

**Optical and fluorescent properties of chitin and  
chitinous structures of biological origins**

Doctoral Dissertation

Belgrade, 2022.

**Ментор:**

Др Дејан Пантелић, научни саветник, Институт за физику, Универзитет у Београду

**Чланови комисије:**

Проф. др Ђорђе Спасојевић, редовни професор, Физички факултет, Универзитет у Београду

Проф. др Горан Попарић, редовни професор, Физички факултет, Универзитет у Београду

Др Бранко Коларић, научни саветник, Институт за физику, Универзитет у Београду

**Датум одбране:**

*Ова докторска дисертација је урађена у Институту за физику, у Центру за фотонику којим руководи др Жељка Никитовић.*

*Изражавам велику захвалност свом ментору др Дејану Пантелићу, научном саветнику Института за физику, на непосредном руковођењу израде докторске дисертације, као и на изузетно корисним саветима и консултацијама у току писања дисертације. Захваљујем се и др Брани Јеленковићу на корисним саветима.*

*Захвалност дугујем професорима др Ђорђу Спасојевићу, др Горану Попарићу и др Бранку Коларићу на прегледу и оцени ове докторске дисертације.*

*Највећу захвалност дугујем својој породици на великом разумевању и подршци.*

*Владимир Лазовић*

# Оптичке и флуоресцентне особине хитина и хитинских микроструктура биолошког порекла

## Резиме

Предмет истраживања ове докторске дисертације су оптичке, флуоресцентне и термалне радијативне особине хитина и хитинских микро и наноструктура биолошког порекла. Хитин је, после целулозе, најзаступљенији полисахарид у природи и добија се прерадом одбачених љуштура морских шкољки и ракова, и има многобројне технолошке примене. Хитин је такође и главни састојак тела инсеката. Поједини делови тела ових инсеката су често структурисани на микро и нано нивоу па се могу анализирати као сложени оптички системи биолошког порекла и приликом интеракције упадне светлости са овим хитинским структурама испољавају се различити физички механизми (интерференција, дифракција, различите врсте расејања светлости) који синергијски дају значајан допринос рефлексији, трансмисији и апсорпцији светлости.

У оквиру ове докторске дисертације експериментално и теоријски су истражене поједине нелинеарне оптичке особине хемијски пречишћеног хитина применом двофотонски побуђене флуоресценције и генерисањем другог хармоника. Ови резултати су употребљени за анализу оптичких и флуоресцентних особина појединих хитинских микро и наноструктура биолошког порекла, и за истраживање контролисане модификације ових особина ласерском радијацијом. Анализирани су и термалне особине природне хитинске микроструктуре.

Добијени резултати су искоришћени за технолошку примену – сложене хитинске наноструктуре су, у изворној и ласерски модификованој форми, употребљене као варијабилни оптички елемент у заштити од фалсификовања докумената, хартија од вредности, новчаница итд. Показана је и примена у ентомологији, за високо-квалитетно површинско и дубинско осликавање делова тела организама који се доминантно састоје од хитина.

**Кључне речи:** иридесценција, дво-фотонски побуђена флуоресценција, хитин, природне хитинске наноструктуре, ласерска модификација хитинских наноструктура

**Научна област:** Физика

**Ужа научна област:** Биофотоника

**УДК број:**

# Optical and fluorescent properties of chitin and chitinous structures of biological origins

## Abstract

The main subject of this doctoral thesis are optical, fluorescent and thermal radiative properties of chitin and chitinous micro and nanostructures of biological origins. Chitin is the most prevalent polysaccharide after cellulose and it is made by processing of the dumped seashells and sea crawfish shells, and it has numerous technological applications. Chitin is also a main body ingredient of insects. Some body parts of these insects are often micro and nanostructured so that many of them represent complex optical systems of biological origins and many physical mechanisms (interference, diffraction, different forms of scattering) appear during the interaction of incident light with these chitinous structures. These physical mechanisms act in synergy and have significant contribution to the reflection, transmission and absorption of light.

In this doctoral thesis, nonlinear optical properties (two-photon excited fluorescence, second harmonic generation) of chemically purified chitin powder are experimentally and theoretically investigated. These results are used for the analysis of the optical and fluorescent properties of biological chitinous micro and nanostructures and for the investigation of the controlled modification of these properties by laser irradiation. Thermal properties of natural chitinous microstructure are also analyzed.

Results are used for technological application – complex chitinous nanostructures are used, in natural and laser-modified form, for variable optical element whose optical and fluorescent properties have central spot in its function, which is prevention of counterfeiting of documents, stocks, paper money etc. Additional application, in entomology, is demonstrated, for high quality surface and deep imaging of insect's body parts which are dominantly built of chitin.

**Key words:** iridescence, two-photon excited fluorescence, chitin, natural chitinous nanostructures, laser modification of chitinous nanostructures

**Scientific field:** Physics

**Scientific subfield:** Biophotonics

**UDK number:**



# Садржај

<b>1. Увод .....</b>	<b>1</b>
1.1. Фотоника и биофотоника .....	1
1.1.1. Структурна и пигментна обојеност .....	2
1.1.2. Хитин и хитинске наноструктуре биолошког порекла .....	5
1.2. Природне фотонске наноструктуре.....	7
1.2.1. Периодичне природне фотонске наноструктуре .....	7
Танки филмови .....	7
Дводимензионе (2Д) природне фотонске наноструктуре .....	12
Тродимензионе (3Д) природне фотонске наноструктуре .....	17
1.2.2. Хиралне нано-структуре биолошког порекла.....	20
1.2.3. Неуређене природне фотонске наноструктуре.....	22
1.3. Флуоресценција и природне наноструктуре.....	28
<b>2. Материјали и методе.....</b>	<b>30</b>
2.1. Експериментални методи и уређаји .....	30
2.1.1. Оптичка микроанализа .....	30
2.1.2. Сканирајућа електронска микроскопија .....	30
"Double transfer" метод.....	31
2.1.3. Нелинеарни ласерски микроскоп.....	32
2.1.4. Streak камера .....	33
2.1.5. Компјутеризована микро-томографија .....	34
2.1.6. Радијативна термографија .....	35
2.1.7. Фурије трансформ инфр-црвена спектроскопија („FTIR“) .....	37
2.1.8. Усаглашавање индекса преламања .....	38
2.2. Математичко моделовање .....	39
2.2.1. Метод коначних елемената.....	39
2.2.2. Метод преносне матрице („Transfer matrix method“) .....	40
2.2.3. Ray tracing метод.....	40
2.2.4. Фурије-Мелинова трансформација .....	41
2.3. Алгоритми и софтверски пакети.....	42
Алгоритам пројекције максималног интензитета .....	42
Запремински приказ .....	43
"Focus stacking" алгоритам.....	43

Софтверски пакети .....	44
2.4. Колориметрија .....	44
<b>3. Нелинеарне оптичке особине хитина .....</b>	<b>45</b>
3.1. Двофотонски побуђена флуоресценција .....	45
3.2. Двофотонски побуђена флуоресценција хитина .....	47
3.3. Други хармоник хитина.....	51
<b>4. Оптичке особине хитинских нано-структура биолошког порекла и њихове примене .....</b>	<b>53</b>
4.1. Оптичке особине и наноструктура крилних љуспица одабраних врста инсеката .....	54
4.2. Оптички модел крилних љуспица одабраних врста инсеката.....	58
4.3. Варијабилност и јединственост оптичког одзива крилних љуспица одабраних врста инсеката. ....	66
4.4. Оптичка заштита са крилним љуспицама одабраних врста инсеката. ....	68
4.5. Флуоресцентне особине крилних љуспица одабраних врста инсеката и ласерска обрада.....	71
4.6. Разматрање оптичко-заштитне функције крилних љуспица одабраних врста инсеката.....	76
<b>5. Радијативне термалне особине хитинских наноструктура биолошког порекла .....</b>	<b>79</b>
5.1. Радијативне особине наноструктуре инсекта <i>Morimus asper funereus</i> .....	84
5.2. Термални модел наноструктуре инсекта <i>Morimus asper funereus</i> .....	85
5.3 Хипер-униформност хитинских микроструктура .....	90
5.4. Завршна разматрања термалних особина анализираних хитинских микроструктура .....	96
<b>6. Закључак .....</b>	<b>97</b>
<b>Литература .....</b>	<b>99</b>
<b>Прилог А.....</b>	<b>121</b>
<b>Биографија .....</b>	<b>134</b>

# 1. Увод

## 1.1 Фотоника и биофотоника

Фотоника је област физике која проучава активну и пасивну контролу светлости кроз генерисање, детекцију и контролисање светлости самом светлошћу (нелинеарни ефекти) [1,2]. Фотоника највећим делом истражује радијацију из оптичког и блиско инфра-црвеног дела спектра. Настанку фотонике претходиле су прве практичне примене полупроводничких извора светлости, раних 1960.-их година, и развој оптичких влакана 1970.-их година. Биофотоника је огранак фотонике који проучава интеракцију светлости и биолошких система. Многи биолошки системи интерагују са светлошћу на веома сложен и још увек не у потпуности истражен начин. Ови системи често имају веома сложену структуру, на нанометарском нивоу. Због тога, приликом интеракције светлости са њима долази до различитих оптичких ефеката који настају комбинацијом интерференције, дифракције, различитих типова расејања светлости... Оптичке особине ових биолошких система – организама помажу и омогућавају организму да преживи. Са становишта оптике, они представљају сложене оптичке системе са сложеним оптичким одзивом. Због многобројних примена, биолошки системи се могу имитирати, и на различите начине модификовати, чиме се додатно повећава број оптичких механизма који одређују интеракцију светлости и ових система. Огранак биофотонике који се бави имитирањем, модификацијом и функционализацијом природних система се назива биомиметика.

Друга, такође значајна област биофотонике се бави развојем и применом оптичких техника, првенствено осликавања, са циљем проучавања биолошких молекула, ћелија и ткива [3]. У оквиру ове тезе, под осликавањем се подразумева микроскопско осликавање узорака биолошког порекла, применом различитих микроскопских техника. При томе, многе оптичке технике развијене у биофотоници не оштећују ткива и ћелије [4], што је значајна предност у односу на многе друге методе (флуоресцентна конфокална микроскопија, опто-акустичко осликавање, термографија...) које се користе у „живим наукама“. У овом смислу, биофотоника проучава апсорпцију, емисију, модификацију и детекцију радијације код биолошких материјала – ћелија, ткива, па и читавих организама. Ово има значајне примене у медицини, биологији, пољопривреди, примене као што су терапија и хирургија, где се радијација користи као преносилац енергије. Међутим, биофотоника се бави и дијагностиком ћелија и ткива, при чему радијација побуђује материју која онда приликом релаксације у основно стање „емитује“ одређену информацију о ткиву, у форми радијације измењених особина.

Почеци биофотонике као науке датирају још од времена Исака Њутна, који је, између осталог, проучавао и обојеност у живом свету и претпоставио да интензивна обојеност пауновог перја потиче од биолошког материјала који има форму танког филма [5]. На прелазу из 19.-ог у 20.-и век настављена су истраживања феномена структурне обојености [6-15]. У тим почетним истраживањима, један од најистраживанијих објеката су била крила иридесцентних лептира. Међутим, пошто тада није постојала електронска микроскопија, узрок иридесценције није било лако одредити. Теорије из тог времена се зато могу сврстати у следеће категорије [16]: 1) дифракција светлости на набораној површини природних структура, 2) интерференција светлости на танким филмовима, 3) расејање светлости, 4) селективна рефлексација светлости као у случају метала и обојених кристала.

Савремена биофотоника представља веома атрактивну научну дисциплину, како са аспекта фундаменталних истраживања физике и оптике природних фотонских микроструктура, тако и са аспекта многобројних технолошких примена. На пример, недавно је откривено да спољашњи хитински омотач (хитин је доминантни градивни елемент инсеката и о њему ће бити више речи у наставку ове дисертације, у подпоглављу 1.1.2.) инсекта *P. c. Pavonius* има структуру 3Д фотонског кристала са елементарном ћелијом „једноструког“ дијаманта (*single diamond network morphology*) [17]. О научном и технолошком значају оваквих природних 3Д фотонских наноструктура ће бити речи у наставку ове дисертације. Оно што оптику ове структуре разликује од осталих оваквих 3Д фотонских кристала откривених код инсеката је велика спектрална варијабилност рефлексије – у зависности од упадног угла светлости, рефлексија може да има максимум на било којој таласној дужини из оптичког дела спектра. Изузетна спектрална подесивост је омогућена структуром 3Д фотонског кристала који је изграђен од хитина и ваздушних шупљина, и у којој постоје адекватне варијације константе кристалне решетке и варијације односа запремине хитин/ваздух.

Настављају се истраживања нових биофотонских система, са акцентом на хитин-ваздух наноструктуре. Имитирање оваквих наноструктура вештачким материјалима са бољим оптичким и осталим особинама и адекватна модификација и функционализација оваквих структура представљају плодно тло за примене у биоинжењерству, соларним ћелијама, различитим сензорима, комуникационим технологијама, обради података [23]. Упоредо са тим, откривају се и нови физички и оптички механизми интеракције електро-магнетне радијације са сложеним хитинским наносистемима, који се заснивају на оптичкој синергији различитих хитинских микро и наноелемената.

Веома су активна и истраживања примене биофотонице у медицини, у развоју нових биомедицинских оптичких уређаја за осликавање, дијагнозу и терапију различитих обољења [18-22].

### 1.1.1. Структурна и пигментна обојеност

Обојеност у природи је најчешће последица присуства пигмената и она се назива пигментна обојеност. Међутим, поједини организми имају веома сложене, нано-структурисане делове тела. Приликом интеракције упадне светлости са овим структурама, долази до комбиновања низа оптичких ефеката (интерференција, дифракција, различите врсте расејања светлости...) који синергијски одређују оптичке особине оваквих структура. Оваква обојеност се назива структурна обојеност. Није редак случај да се пигменти налазе у сложеној природној нано-структури, и онда је рефлексија радијације са овакве структуре комбинација утицаја нано - структуре и пигмената. За разлику од пигментне обојености, структурна обојеност показује јаку угаону зависност. Дакле рефлексионни спектар се мења са променом угла посматрања или осветљавања структуре и ова појава се у биофотоници назива иридесценција. Структурне, иридесцентне боје су такође интензивније од пигментне обојености (рефлектована светлост има већу амплитуду), јер се не заснивају на селективној апсорпцији електро-магнетних таласа од стране пигментних молекула него на суперпозицији великог броја парцијално рефлектованих таласа.

Поред кохерентних процеса као што су интерференција и дифракција, за структурну обојеност је веома значајно и некохерентно, дифузно расејање светлости. Поједине природне структуре су оптимизоване за овај процес. Оне расејавају таласне дужине из одређеног подопсега оптичког дела спектра у пуном просторном углу и на тај начин елиминишу ове таласне дужине из кохерентне и високо-амплитудске иридесцентне рефлексije. Уколико је материјал транспарентан, расејана светлост се појављује и унутар материјала због чега се, захваљујући дифузном расејању, повећава време боравка ових фотона унутар материјала. Овде је у питању ефекат локалног таласовода који је праћен повећањем апсорпције светлости унутар материјала услед чега поново имамо елиминацију ових таласних дужина из иридесцентне, структуром узроковане рефлексije.

Постоје различите врсте расејања радијације у материјалној средини, у зависности од односа таласне дужине радијације и величине честица на којима се расејање одиграва. Рејлијево расејање се дешава када је пречник честице за ред величине (или више од тога) мањи од таласне дужине радијације. Ако се ради о радијацији из оптичког дела спектра, то значи да пречник честице треба да буде  $\sim 50 \text{ nm}$  или мањи. Значајна особина овог расејања је да је интензитет расејања обрнуто пропорционалан четвртој степену таласне дужине радијације која се расејава ( $I \sim 1/\lambda^4$ ), па се таласне дужине из „плавог дела спектра“ ( $\lambda \sim 400\text{-}500 \text{ nm}$ ) расејавају веома интензивно у свим правцима, док је расејање преосталих таласних дужина из оптичког дела спектра скоро занемарљиво [24]. Лорд Рејли је дошао до израза за расејање које је добило назив по њему анализирајући расејање радијације на дипол-расејавачима чије су димензије бар за ред величине мање од таласне дужине радијације која се расејава:

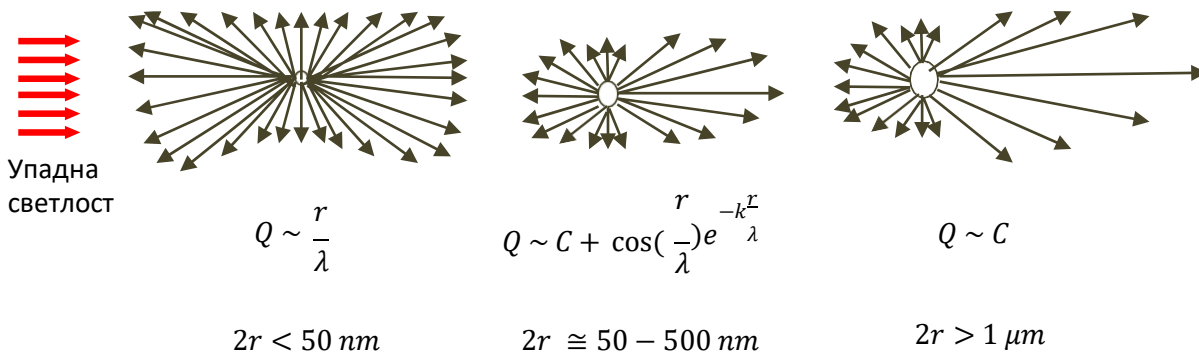
$$(1.1) \quad I = I_0 \frac{8\pi^4 N \alpha^2}{\lambda^4 R^2} (1 + \cos^2 \theta)$$

где је  $I$  - интензитет расејане радијације на дипол-расејавачу,  $I_0$  - интензитет упадне радијације,  $N$  - број расејавача,  $\alpha$  – поларизабилност,  $\lambda$  - таласне дужина радијације,  $R$  - растојање између расејавача и детектора радијације,  $\theta$  - угао између правца упадне светлости и правца дуж кога се детектује расејана радијација. На пример, молекули  $O_2$  и  $N_2$  који су веома заступљени у Земљиној атмосфери имају ове димензије па се Рејлијевим расејањем може објаснити плава боја неба и наранцасто-црвена боја излазака и залазака Сунца [24]. Рејлијево расејање значајно утиче на оптичке особине многих биолошких система [25-28].

Широкопојасна рефлексija многих биофотонских система објашњава се Миеевим расејањем (слика 1.1) [142, 143, 153-155]. Оно се испољава на честицама чије димензије одговарају таласној дужини упадне светлости. Миеево расејање представља решење Максвелових једначина за расејање равнoг електро-магнетног таласа на хомогеној сфери. Упадни равни талас, као и расејано поље, приказују се преко низа радијалних сферних векторских таласних функција. Електро-магнетно поље унутар честице се приказује преко низа регуларних сферних векторских таласних функција. Применом одговарајућих граничних услова на површини сфере, могу се израчунати коефицијенти пропагације расејаног електро-магнетног поља. Решење има облик бесконачног реда сферних парцијалних таласа. Ипак, не постоји горњи лимит за величину сфере, јер у случају веома великих честица Миеево решење конвергира ка решењу геометријске оптике [29].

Миево расејање је најинтензивније у правцу побудне светлости, јер су у овом правцу најмање релативне фазне разлике између радијације која је расејана са различитих делова честице. На пример, ово доприноси белој боји млека где се расејање дешава на капљицама масти унутар воде. Такође, облаци се састоје од капљица воде које су већих димензија од таласне дужине светлости и због тога се дешава Миево расејање – све таласне дужине из оптичког дела спектра се расејавају приближно једнако, што ствара утисак беле боје облака. Миево расејање је такође одговорно за белу боју шећера, соли, магле итд. Оно је заступљено и у нижим слојевима атмосфере, где се налазе сферичне честице чији су пречници приближно једнаки таласним дужинама упадне радијације [30].

Код појединих биолошких материјала заступљено је Тиндалово расејање [31, 32]. Оно је слично Рејлијевом расејању, јер је и овде интензитет расејане светлости обрнуто пропорционалан четвртој степену таласне дужине светлости, па се „плава“ светлост ( $\lambda \sim 400\text{-}500\text{ nm}$ ) расејава знатно интензивније од „црвене“ светлости ( $\lambda \sim 600\text{-}700\text{ nm}$ ), али се дешава на честицама већих димензија у односу на Рејлијево расејање (због чега се светлост интензивније расејава у случају Тиндаловог расејања). У оптички транспарентним срединама у којима се дешава Тиндалово расејање, веће таласне дужине се трансмитују кроз материјал, док се краће таласне дужине дифузно рефлектују због Тиндаловог расејања. Ово расејање се дешава када се у оптички транспарентној средини налазе честице пречника  $\sim 500\text{ – }900\text{ nm}$ .



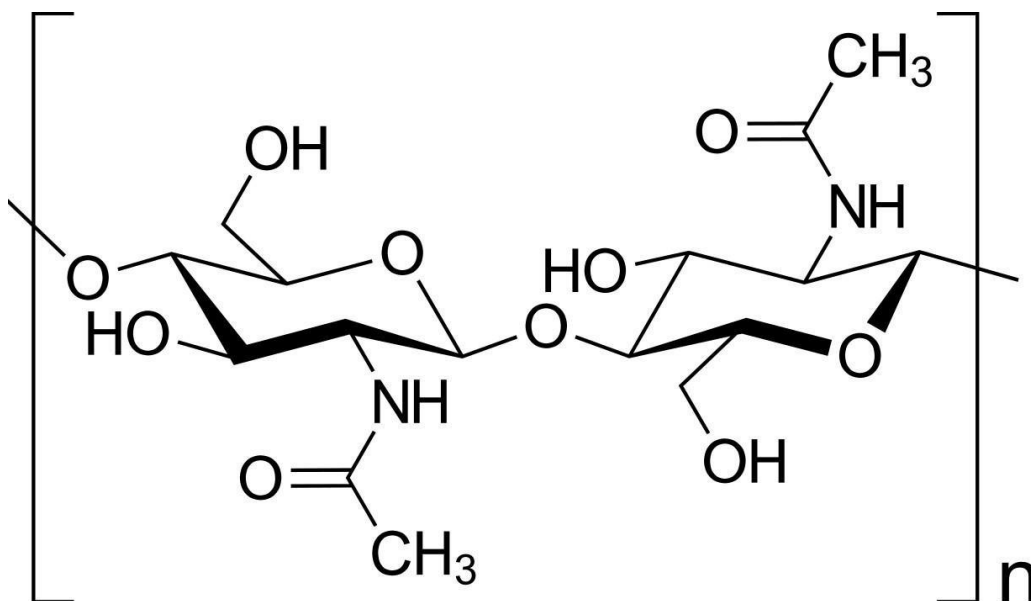
**Слика 1.1.** Различите врсте расејања светлости. С лева на десно: Рејлијево расејање, које се дешава када је пречник честице на којој се радијација расејава мањи од 50 nm (овој групи припадају, на пример, молекули  $O_2$  и  $N_2$ , веома заступљени у Земљиној атмосфери); Миево расејање: величина честице је 50 – 500 nm; Када је пречник честице већи од оптичких таласних дужина, Миево расејање конвергира ка решењу геометријске оптике за расејање светлости на крупним честицама.  $Q$  - коефицијент атенуације надлазеће светлости,  $r$  – полупречник честице на којој се светлост расејава,  $\lambda$  – таласна дужина светлости,  $C$  – константа.

У оквиру ове дисертације су проучаване оптичке, флуоресцентне и термалне особине сложених нано-структура инсеката. Доминантан градивни састојак ових структура је хитин.

## 1.1.2. Хитин и хитинске наноструктуре биолошког порекла

Постоје многи материјали који су свеprisутни у живом свету (ДНК, протеини, полисахариди...). Међу најзаступљенијима су полисахариди целулоза (градивни елемент биљака) и хитин (градивни елемент инсеката).

Хитин је полимер који се налази у егзоскелету и у унутрашњим структурама бескичмењака. То је други најзаступљенији полимер на Земљи, после целулозе [5]. Производи се од одбачених љуштура шкољки и морских ракова (љуштуре садрже 20 – 30% хитина) [33, 34]. Хитин је природно обилан и обновљив полимер са одличним особинама као што су: биоразградивост, биокомпатибилност, нетоксичност.



Слика 1.2. Хемијска структура молекула хитина

Хитин је доминантан градивни елемент инсеката. Хитинске наноструктуре се налазе на крилима и другим деловима тела инсеката а истражују се због откривања нових оптичких механизма и због различитих примена као што су:

- сензори малих (нанометарских) помераја и деформација које могу бити различитог порекла: термалног, акустичког, механичког па чак и нуклеарног [35-39].
- текстилна индустрија – иридесцентна одећа [40].
- медицина – где се користе као повољна подлога за раст различитих ћелијских култура што доводи до примена у регенеративној медицини, инжењерингу ткива, контроли облика ћелија [41]...
- биохемија – анализа молекулских интеракција [42].

Због ових примена истражују се физичке и оптичке особине хитинских наноструктура у природном облику, проучавају се могућности њихове модификације и функционализације због побољшања ових особина, и развија се нова област чија је улога да имитира природне структуре вештачким материјалима ради побољшања њихових својстава (биомиметика).

Љуспице лептира, које биофотоника препознаје као сложене нано-структурисане оптичке микро-објекте, састоје се највећим делом од хитина и класификоване су у две основне категорије – љуспице чији је типичан представник „*Morpho*“ фамилија лептира и други тип љуспица чији је типичан представник „*Urania*“ фамилија лептира [65, 203], у зависности од тога да ли су равнoг облика или конвексне (облик љуспице утиче на оптичке ефекте). Обе категорије садрже одређени број подкатегија које се разликују у наноструктури [204]. Веома честа појава код оваких структура је иридесценција – промена рефлексионог спектра са променом угла посматрања или осветљавања љуспице. Љуспице се могу делимично преклапати, а код појединих врста инсеката постоје два слоја љуспица – базне и покровне, које су постављене једне преко других и могу имати исту или веома различиту нано-структуру и оптичке особине.

Због своје сложене нано-структуре и резултујућих оптичких особина, љуспице лептира имају многобројне технолошке примене. На пример, користе се као подлога за Раманову спектроскопију појачану површинском структуром („*surface enhanced Raman scattering - SERS*“) [205-207]. Такође, у развоју сензора малих (нанометарских) помераја и деформација које могу бити различитог порекла: термалног, механичког, акустичког, па чак и нуклеарног. Структурисање фото-анодe соларних ћелија по узору на љуспице лептира доводи до повећања ефикасности соларних ћелија [208]. Овде се примењују особине љуспица појединих врста лептира и мољаца да „заробљавају“ светлост [95]. У скорије време, локализована површинска плазмонска резонанца („*localized surface plasmon resonance (LSPR)*“) остварена је плазмонским ефектима на металима са површином нано-структурисаном по узору на горњу површину љуспица лептира [209]. Ово има потенцијалну примену у производњи водоника фотокатализом воде. У појединим применама, на пример у текстилној индустрији, предложено је да се љуспице лептира користе у изворном облику, уклоњене са крила инсекта. За сложеније примене („*SERS*“, „*LSPR*“, гасни, термални, механички сензори...) сложена нано-структура љуспица се имитира – од различитих метала и легура се генеришу копије љуспица, допирају се нано-честицама итд. Ове технике се примењују у биомиметици, области биофотонике која истражује могућности имитирања природних нано-структура другим материјалима, као и побољшање оптичких, механичких и других особина ових „копија“ контролисаном модификацијом и функционализацијом (придруживање нових елемената структури ради побољшања већ постојеће или додавања нове функције структури, на пример, поједини оптички апсорбери се функционализују допирањем карбонским наноцевима, чиме се значајно повећава њихова апсорпција у оптичком делу спектра) њихове наноструктуре [210-212, 238].



## 1.2. Природне фотонске наноструктуре

У природи постоји велика разноврсност сложених фотонских структура и оптичких ефеката који настају у интеракцији светлости са њима. Поједине структуре су периодичне и њихов период је реда величине таласне дужине радијације из оптичког дела спектра па се на њима испољавају кохерентни ефекти (као што су интерференција, дифракција...). Постоје и насумичне структуре чија је примарна оптичка функција расејање светлости из одређеног опсега таласних дужина у широком просторном углу, што има централно место у рефлексiji али може бити значајно и за апсорпцију светлости, што ће касније бити објашњено. Присутна је и псеудо-уређеност, где структуре биолошког порекла показују различит степен уређености на различитим физичким скалама – нпр. биолошки поликристал, материјал који се састоји од великог броја периодичних области, при чему је међусобна оријентација тих под-области насумична (тзв. „*short range order – long range disorder*“).

Природне структуре се могу састојати од два различита материјала код којих постоји разлика у индексу преламања потребна да се добију резултујући оптички ефекти. То су нпр. меланин и кератин код птица, гуанин и цитоплазма код водених организама...Али периодичност се у природи може постићи и у форми рељефа, као нпр. код инсеката где је периодичност обезбеђена хитином и ваздушним шупљинама унутар хитина, па су главне компоненте оваквих система хитин и ваздух. О свим поменутих структурама и оптичким механизмима интеракције светлости са њима биће речи у наставку овог поглавља, са посебним акцентом на хитинске фотонске структуре.

### 1.2.1. Периодичне природне фотонске нано-структуре

У зависности од броја просторних димензија у којима постоји периодичност, овакве структуре се могу поделити у 3 основне категорије: танки филмови (код којих периодичност постоји у једној просторној димензији), дифракционе решетке и фотонски кристали, где периодичност постоји у две и три просторне димензије, респективно.

#### *Танки филмови*

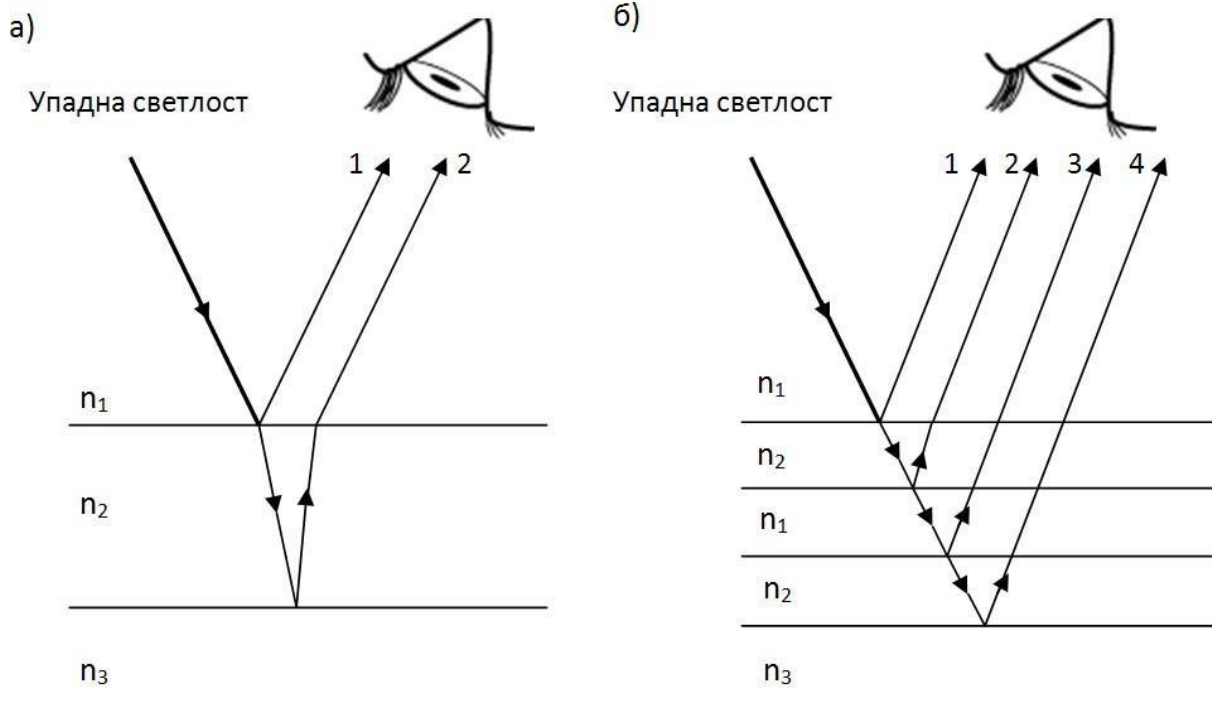
Танки филмови имају периодичну промену индекса преламања у једној димензији. Пошто је главна оптичка функција хитинских танких филмова до сада откривених у природи рефлексija (спектрално уско-појасна или широко-појасна, и угаоно-зависна рефлексija), они су познати и под називом вишеслојни рефлектори. Уколико се светлост простире кроз овакав материјал, на свакој граничној површини унутар материјала на којој постоји дисконтинуитет индекса премања долази до рефлексije једног дела упадне светлости. Уколико је физичка дебљина слојева од којих се материјал састоји реда величине таласне дужине светлости, долази до интерференције парцијално рефлектованих таласа. Када два електро-магнетна таласа интерферирају, резултујући интензитет електро-магнетног поља је једнак:

$$I = I_1 + I_2 + 2\sqrt{I_1 I_2} \cos \delta \quad (1.2)$$

где су  $I_1$  и  $I_2$  интензитети појединачних електро-магнетних таласа а  $\delta$  је њихова фазна разлика у одређеној тачки у простору.

У различитим тачкама у простору, резултујући интензитет  $I$  може да буде већи, мањи или једнак збиру  $I_1 + I_2$ , што зависи од вредности фазне разлике  $\delta$ , а исти принцип важи и када у материјалу постоји већи број граничних површина, па због тога долази до интерференције већег броја парцијалних рефлектованих таласа, слика 1.3 б. У различитим областима у простору, електромагнетни таласи одређене таласне дужине слабе или се појачавају у различитој мери, у зависности од њихове фазне разлике у датој области. Из тог разлога, рефлексioni спектар једнодимензионих периодичних материјала се мења са променом угла посматрања (или угла осветљавања) материјала.

Слојеви од којих се састоји вишеслојни оптички рефлектор могу имати константну дебљину – сви слојеви индекса преламања  $n_1$  имају исту физичку дебљину, а слојеви индекса преламања  $n_2$  имају неку другу (или исту) вредност дебљине и тада овакав рефлектор рефлектује узак интервал таласних дужина које задовољавају услов за конструктивну интерференцију у рефлексiji. Овакви рефлектори се, због ширине њиховог рефлексionoг спектра, називају уско-појасно рефлектори. Међутим, рефлектори који имају велики број слојева, могу имати и варијабилну дебљину слојева. У том случају, повећава се број таласних дужина које испуњавају услов за конструктивну интерференцију у рефлексiji па због тога овакви рефлектори имају шири рефлексioni спектар од уско-појасних рефлектора и, уколико је он значајно шири, називају се широко-појасни рефлектори. Оптички механизми уско-појасне и широко-појасне рефлексije на хитинским 1Д вишеслојним рефлекторима откривени су у живом свету, код многобројних врста инсеката [49-60].



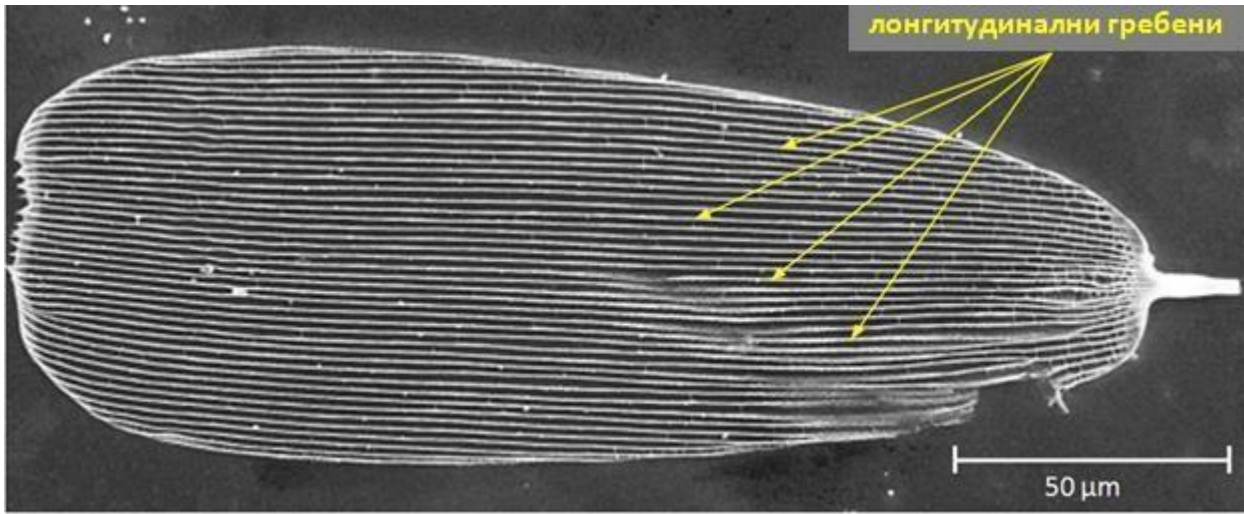
**Слика 1.3.** Интерференција светлости: а) Интерференција на танком слоју, два делимично рефлектована таласа (таласи означени бројевима 1 и 2) интерферирају. б) интерференција на вишеслојној структури са периодичном променом индекса преламања – већи број граничних површина узрокује већи број делимично рефлектованих таласа (на слици су означени бројевима 1, 2, 3 и 4) који интерферирају. Ради једноставности приказа, таласи су приказани правим линијама – зрацима.

### Ускопојасни хитински 1Д рефлектори биолошког порекла

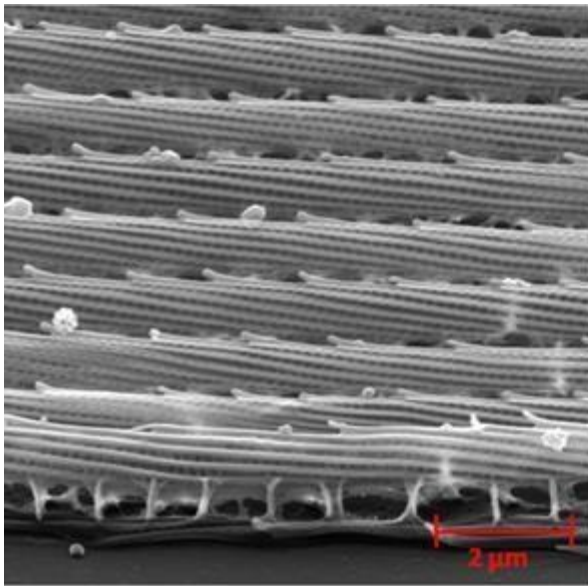
Уско-појасна рефлексија на хитинским 1Д вишеслојним рефлекторима откривена је у природи код различитих врста инсеката [43-54]. На пример, Вукушић и сарадници [55] истраживали су оптичке особине појединачних љуспица (микро-објекти којима су прекривена крила различитих врста инсеката, често имају сложену структуру и оптичку функцију) *Morpho rhetenor* лептира и показали да се ове љуспице могу успешно моделовати као 1Д вишеслојни рефлектори изузетних оптичких особина. Наиме, мерења су показала да је оптичка дебљина слојева оптимизована за интензивну рефлексију „плаве“ светлости ( $\sim 400\text{-}500\text{ nm}$ ) – љуспице рефлектују 75% упадне плаве светлости и то у великом просторном углу што је далеко више него што се може постићи пигментацијом. Дакле, ови лептири су развили вишеслојне рефлекторе са довољним бројем слојева који им омогућавају веома интензивну рефлексију у поменутом спектралном опсегу, и који у комбинацији са другим компонентама овог сложеног биофотонског микро-система показују рефлексивност у широком просторном углу, поништавајући дакле, у одређеној мери, угловну зависност рефлексије карактеристичну за вишеслојне рефлекторе. Али не само то, него и друге оптичке особине као што су интензивна рефлексија у УВ области и различити поларизациони ефекти. Ништа од овога се не може постићи само пигментима.

Уско-појасна рефлексија је карактеристична и за хитинске 1Д вишеслојне рефлекторе који се налазе на дорзалној површини крила лептира *Morpho aega*, слика 1.4. Она је прекривена љуспицама просечних димензија  $200 \times 75\ \mu\text{m}$ . Електронски микрограф типичне љуспице је приказан на слици 1.4а. Она се састоји од лонгитудиналних гребена, који се простиру целом дужином љуспице. Структура је отвореног типа, састоји се од слојева хитина између којих се налази празан простор испуњен ваздухом, просечна дебљина хитинских слојева је  $\sim 700\text{ nm}$ , а ваздушних шупљина  $\sim 1\ \mu\text{m}$ . Дакле сваки лонгитудинални гребен представља вишеслојни рефлектор који се састоји од 5 слојева хитина и 5 ваздушних слојева (слика 1.4в). Захваљујући малом растојању између суседних гребенова, љуспица се може моделовати као вишеслојни рефлектор чији су компоненте хитин и ваздух (слика 1.5). Оваква љуспица представља природан оптички микро-систем чије су дебљине слојева оптимизоване за иридесценцију – интензивну рефлексију која показује угаону зависност. Код многих врста међутим, угаона зависност је значајно смањена услед „колективног ефекта“ (рефлексија је креирана од стране великог броја љуспица чије међусобне оријентације имају благе природне варијације што доводи до ширења резултујућег рефлексионог спектра крила инсекта и смањења његове угаоне зависности). Код појединих врста, изнад слоја иридесцентних љуспица, налази се слој транспарентних љуспица чија је оптичка функција дифракција светлости рефлектоване са иридесцентног слоја љуспица. Захваљујући дифракцији, може се значајно повећати просторни угао у коме се простире светлост рефлектована са иридесцентног слоја љуспица. Код оваквих сложених нано-

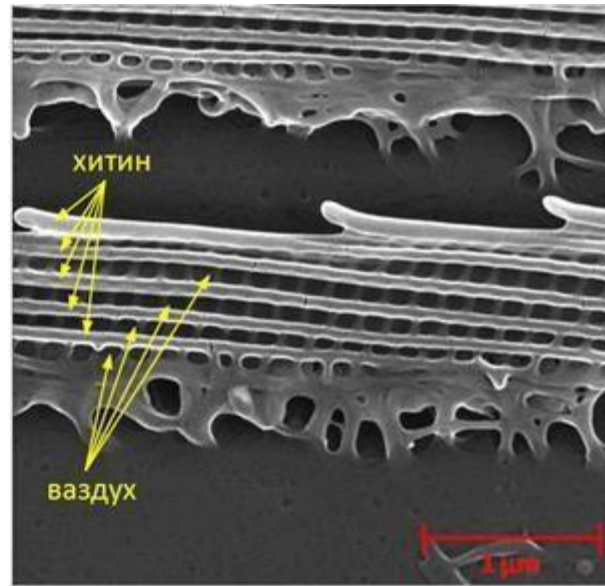
структурисаних система, сви природни оптички елементи (високо транспарентан горњи „дифракциони“ слој љуспица, нано-структурисан доњи иридесцентни слој љуспица, крилна мембрана испод љуспица богата пигментима који апсорбују радијацију која је прошла кроз горње слојеве љуспица...) синергијски утичу на рефлексioni спектар.



(a)

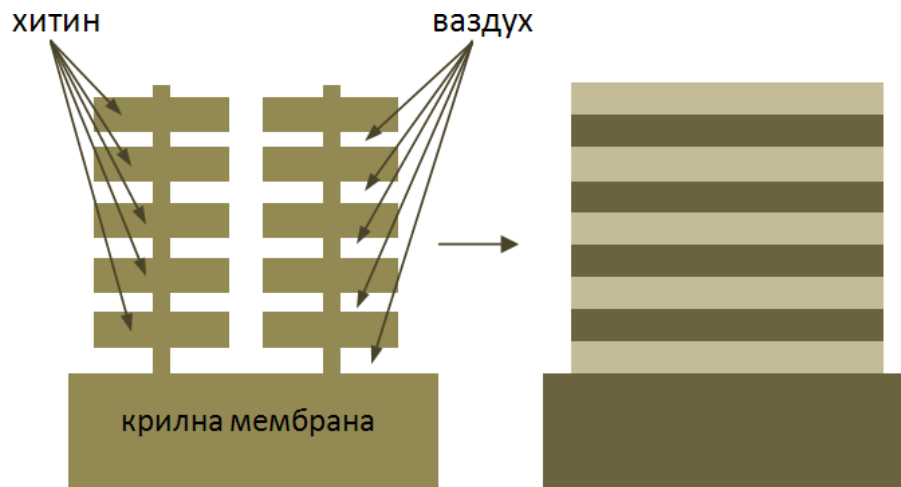


(б)



(в)

**Слика 1.4.** а) електронски микрограф љуспице *Morpho aega* лептира; б) бочни снимак љуспице при већем микроскопском увећању. Уочава се слојевита структура лонгитудиналних гребена.



**Слика 1.5.** Растојање између лонгитудиналних гребена је код *Morpho aega* лептира довољно мало па се љуспица може моделовати као 1Д вишеслојни рефлектор применом теорије ефективне средине [56].

Иридесценција услед вишеслојних рефлектора је откривена и код појединих припадника реда вилинских коњица (лат. *Odonata*) [57], као и код других копнених организама (нпр. паукова (који нису инсекти и спадају у класу *Arachnidae*) [58].

1Д периодичне нано-структуре су откривене и код водених организама. На пример, истраживањем високо-рефлексивних структура појединих риба и других водених организама откривено је да се оне састоје од наизменично поређаних слојева високог и ниског индекса преламања (код водених организама, то су гуанин и цитоплазма). Слојеви гуанина (један од четири главна састојка нуклеинских киселина ДНК и РНК) имају облик плочица, а између њих се налази течност – цитоплазма. Оптичка дебљина гуанинских плочица и цитоплазме је у опсегу 100 – 200 nm. Многе од ових рефлектујућих структура су интензивно обојене и код њих је откривена добра корелација између спектралног опсега који се најинтензивније рефлектује и дебљине слојева - структура тежи да буде идеалан рефлектор.

### *Широко-појасни 1Д рефлектори биолошког порекла*

Међутим, код водених организама су откривене комплексније структуре и оптички механизми, као што су неидеалан систем – вишеслојни рефлектор где дебљина слојева показује значајно одступање од  $\frac{1}{4}$  таласне дужине максимума рефлексије, или вишеслојни рефлектор са широко-појасном рефлексијом [59].

Јордан и сарадници анализирају поларизационо независну оптичку рефлексију откривену у широко-појасном „сребрном“ вишеслојном рефлектору код трију врста риба [60]. Овај природни механизам генерисања спектрално широко-појасне и неполаризоване рефлексије може имати примену у генерисању синтетичких оптичких компонената. Широко-појасни неполаризујући диелектрични вишеслојни рефлектори су важне оптичке компоненте и саставни су делови

оптичких фибера [61], диелектричних таласовода [62] и светлосно-емитујућих диода [63]. Високо двојно-преламајући полимери са индексима преламања сличним као код риба су већ коришћени у производњи вишеслојних огледала [64].

Ови рефлектори обезбеђују рибама камуфлажу тако што изједначавају сопствену рефлексију са зрачењем из спољашње средине [65]. Због адекватне камуфлаже, рефлектујуће структуре морају да генеришу спектрално широко-појасно, интензивно и неполаризовано (под овим се подразумева да рефлектор не мења поларизацију упадне светлости) зрачење за све упадне углове надлазеће радијације. На пример, неки водени предатори имају поларизационо осетљив вид, па овакве структуре не мењају поларизацију упадне светлости – дакле у великом интервалу упадних углова поларизација светлости је иста пре и после рефлексије.

Неполаризујући рефлектори су значајни зато што код њих не долази до опадања рефлективности са приближавањем упадног угла светлости Брустеровом углу. Начин на који вишеслојни рефлектори код риба производе спектрално широко-појасну рефлексију су добро познати [66, 67]. То су насумична варијација у дебљини слојева и систематска варијација у дебљини слојева. Ово прво је биолошки аналогон неуређених синтетичких диелектричних огледала [68].

### *Дводимензионе (2Д) природне фотонске нано-структуре*

За разлику од 1Д и 3Д периодичних фотонских система, биофотонски системи са периодичном варијацијом индекса преламања у две димензије су мање истраживани [69]. То су дифракционе решетке са периодичношћу у две просторне димензије.

Дифракционе решетке су оптичке компоненте које се састоје од периодичног низа структура (то су најчешће удубљења или испупчења) при чему је растојање између свака два суседна елемента константно и назива се периодом решетке. Ако је период дифракционе решетке упоредив са таласном дужином надлазеће радијације, решетка има способност да упадни снап радијације „подели“, дифрактује, на већи број снопова. Различите таласне дужине из упадног снопа се, после интеракције са решетком, простиру у различитим правцима. Угао под којим се, у односу на нормалу на решетку, простиру различите таласне дужине после рефлексије (или трансмисије) са решетке одређен је односом периода решетке и таласне дужине упадне радијације. Једначина која повезује ове параметре (упадни угао и таласну дужину надлазеће радијације, угао дифракције и период решетке) је једначина дифракционе решетке:

$$(\sin \theta_i - \sin \theta_m) = m\lambda \quad (1.3)$$

где је  $d$  период решетке,  $\theta_i$  је упадни угао радијације у односу на нормалу на решетку,  $\theta_m$  је угао под којим се радијација таласне дужине  $\lambda$  простира после дифракције (ова радијација се назива и дифракциони максимум на таласној дужини  $\lambda$ ), у односу на нормалу на решетку, а  $m$  је целобројна вредност – дифракциони ред. Ова једначина, када радијација долази у правцу нормале на решетку ( $\theta_i = 0^\circ$ ), узима следећи облик:

$$d \sin \theta_m = m\lambda \quad (1.4)$$

На основу једначине (1.3) може се израчунати угао под којим се, после дифракције, у односу на нормалу на решетку, простире дифракциони максимум таласне дужине  $\lambda$ :

$$\theta_m = \arcsin\left(\frac{m\lambda}{d}\right) \quad (1.5)$$

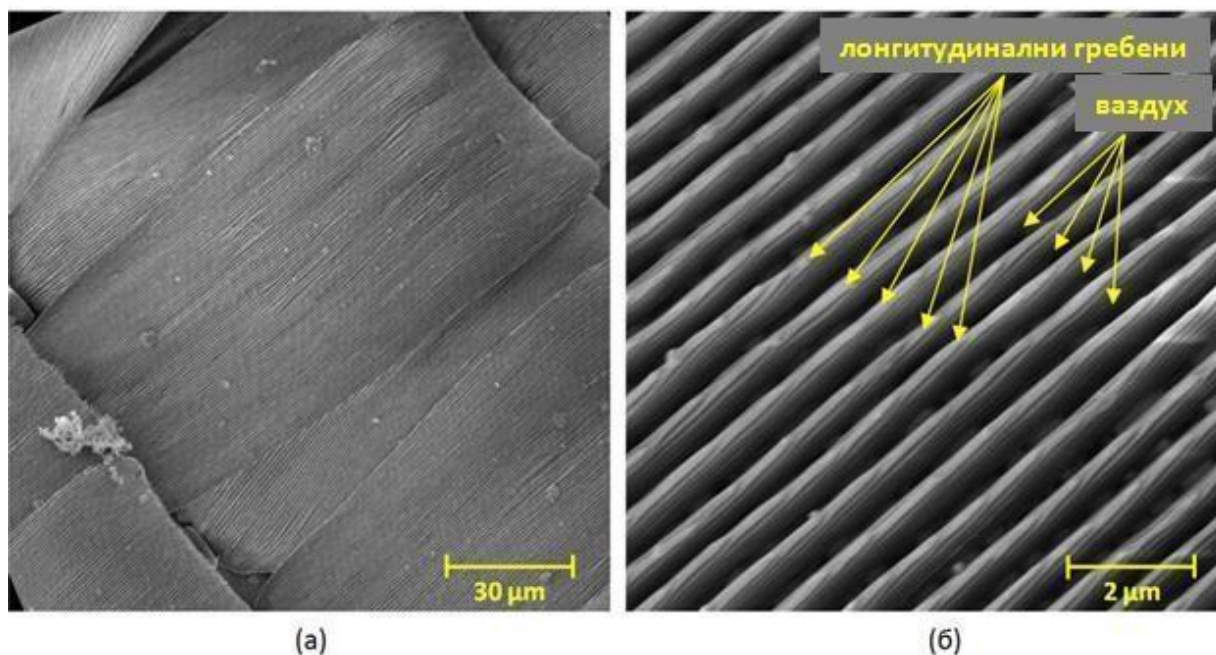
Пошто дифракциона решетка функционише као дисперзни оптички елемент, она је саставни део појединих оптичких уређаја: спектрометара, монохроматора...

Постоје и дифракционе решетки чији је период значајно (за један ред величине или више) мањи од таласне дужине надлазеће радијације (енгл. „*subwavelength diffraction grating*“) [70]. Када се на ову ситуацију примени једначина дифракционе решетки за упад радијације у правцу нормале на решетку (једначина 1.4), показује се да је дифракција сузбијена за  $m < \frac{d}{\lambda}$ , јер је тада угао дифракције  $\theta_m$  имагинаран број за сваки дифракциони ред  $m$ . Дакле, због малог периода, код оваквих решетки су немогући сви дифракциони редови осим основног, нултог реда који се односи на радијацију која се рефлектује и трансмитује у складу са Снеловим законом. Овакве решетки се могу теоријски третирати теоријом ефективне средине [56] или скаларном теоријом површинског расејања [231, 232] (која је примењена у овој дисертацији, погледати 4.2.). У складу са тим, оваква решетка се теоријски приказује као локална хомогена ефективна средина кроз коју се радијација простире и чије су оптичке особине одређене геометријом решетки. Овакве решетки су присутне на површинским деловима тела многих инсеката и тада су то најчешће хитинске „*subwavelength*“ дифракционе решетки које имају оптичку улогу дифузног расејавача упадне светлости који у веома различитом степену расејава радијацију из различитих под-опсега оптичког дела спектра.

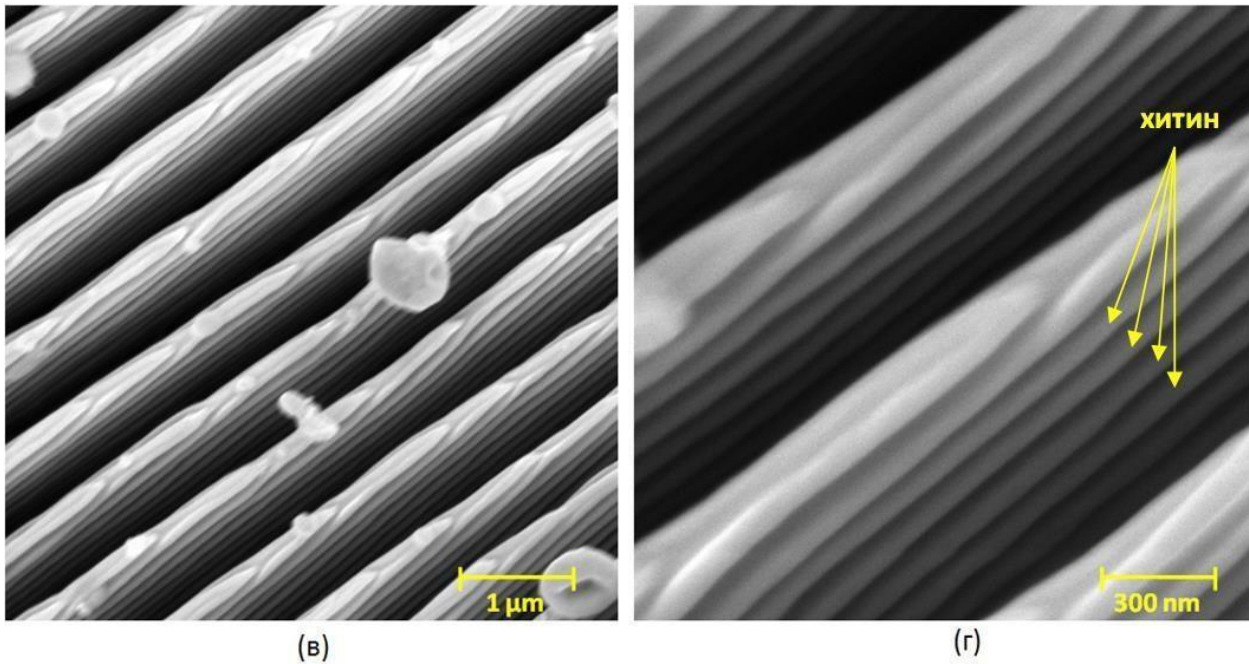
Услед постојања виших дифракционих редова светлост се са дифракционих решетки рефлектује у знатно ширем просторном углу у односу на обичну огледалску рефлексију са равних површина. Дифракцију светлости у широком просторном углу инсекти су развили због међусобне комуникације или камуфлаже. На пример, лептир *Saskia charonda* поседује на својим крилима лонгитудиналне гребене који се простиру целом дужином крила и који се састоје од већег броја хитинских и ваздушних слојева (слика 1.6). За разлику од поменутог *Morpho aega* лептира, овде се гребени не налазе на блиском међусобном растојању па се структура не може моделовати као 1Д вишеслојни рефлектор, већ се поред слојевите структуре појединачних гребена (која формира периодичност у једној димензији) мора узети у обзир и дифракциона решетка коју формирају гребени (то је периодичност у другој просторној димензији). Оптичка функција овакве дифракционе решетки је ширење просторног угла рефлексије иридесценте светлости која се рефлектује са вишеслојних рефлектора.

Код инсекта су откривене и дифракционе решетки изузетно велике моћи разлагања. На пример, паукови *Maratus robinsoni* и *M. chrysomelas* поседују нанодифракционе решетки (енгл. *subwavelength*) на конвексним испупчењима на површини свог тела. Спектрометар чији је саставни део оваква нанодифракциона решетка конвексног облика има 2 пута већу моћ разлагања од спектрометра са стандардном (планарном) дифракционом решетком истог периода. За разлику од иридесценције узроковане интеракцијом светлости са вишеслојним рефлекторима или 3Д фотонским кристалима, која обухвата узак регион оптичког дела спектра, у рефлексији са хитинских нанодифракционих решетки уочава се тзв. широкопојасна иридесценција: постепеном променом угла посматрања (или угла просветљавања) овакве структуре уочавају се све таласне дужине из оптичког дела спектра. Показано је да оваква

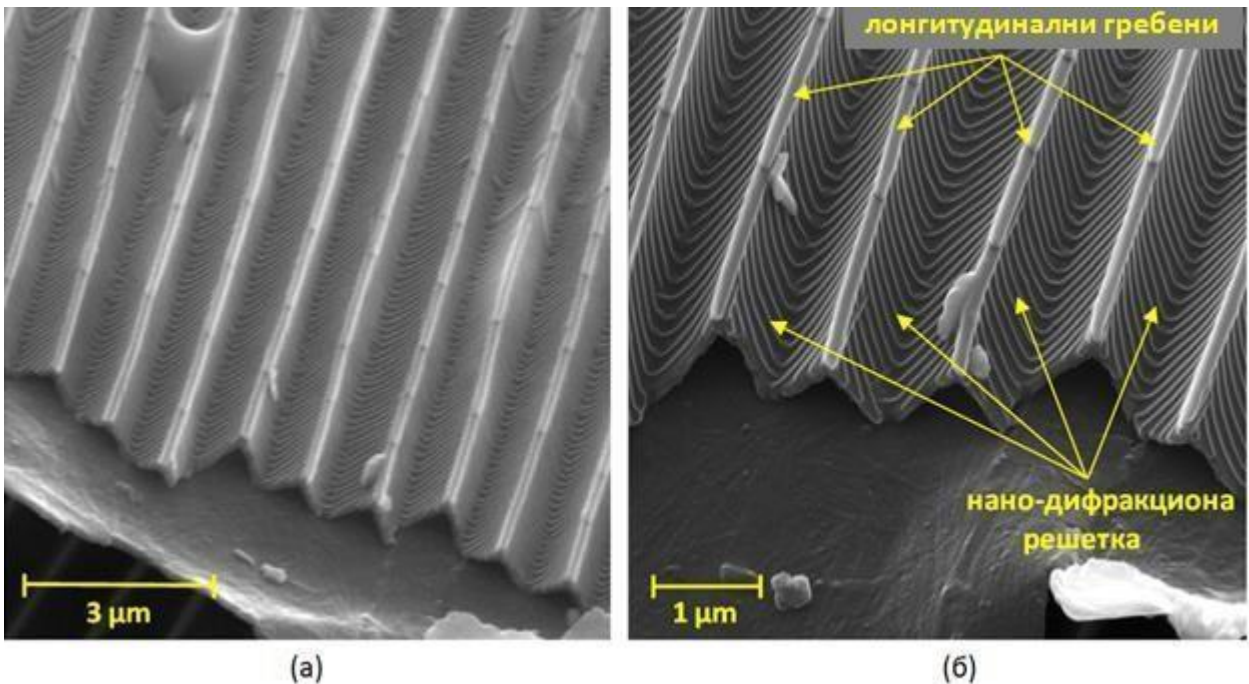
широкопојасна иридесценција има биолошку функцију сигнализирања. Комбинацијом одговарајућег периода решетке и текстуре на којој се она налази, што могу да буду микронска удубљења или испупчења адекватног облика, омогућена је велика моћ разлагања, велика спектрална чистоћа иридесценте светлости, па се разматра употреба оваквих дифракционих решетки у минијатурним супер-резулционим спектрометрима следеће генерације. На слици 1.7 су приказани електронски микрографи љуспица лептира *Autographa bractea* који такође има непланарну дифракциону решетку. У правцу нормале на њу, може се приметити додатна дифракциона решетка са периодом мањим од таласне дужине светлости (период ове решетке је  $\sim 200$  nm), тзв. површинска дифракциона решетка. Површинске дифракционе решетке са периодом мањим од таласне дужине светлости су откривене на крилима појединих инсеката. Због малог периода, оне много интензивније расејавају краће таласне дужине („плави део“ спектра) из оптичког дела спектра и њихова оптичка функција је расејање тих таласних дужина у широком просторном углу.



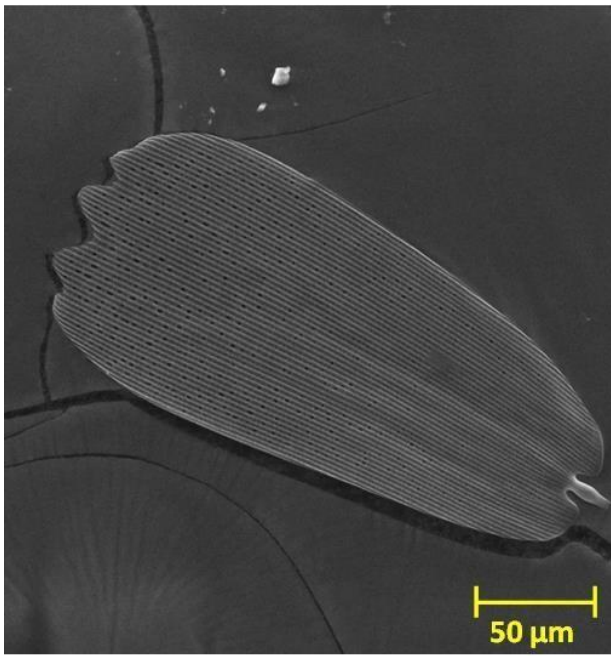




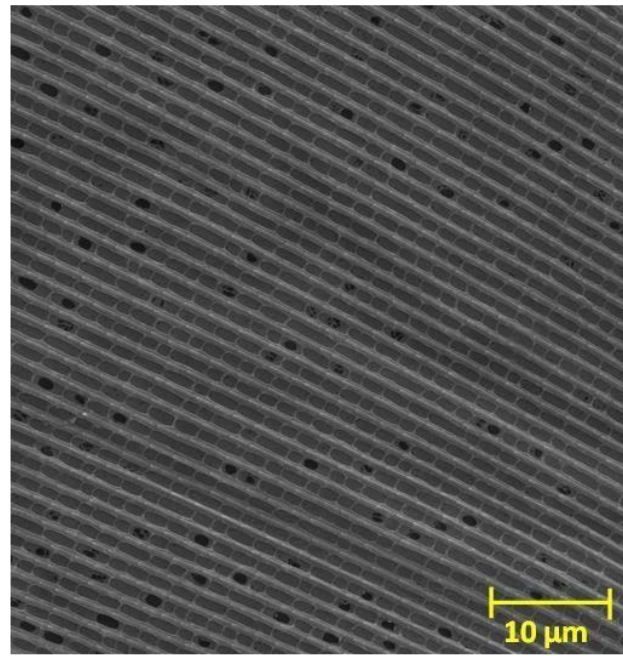
**Слика 1.6.** Електронски микрографи: а) љуспице на крилима лептира *Saskia charonda*, електронски микрограф; б) лонгитудинални гребени који се налазе на површини љуспице образују дифракциону решетку; в) при већим увећањима уочава се слојевита структура гребена; г) сваки гребен представља вишеслојни 1Д рефлектор чији су слојеви хитин и ваздух.



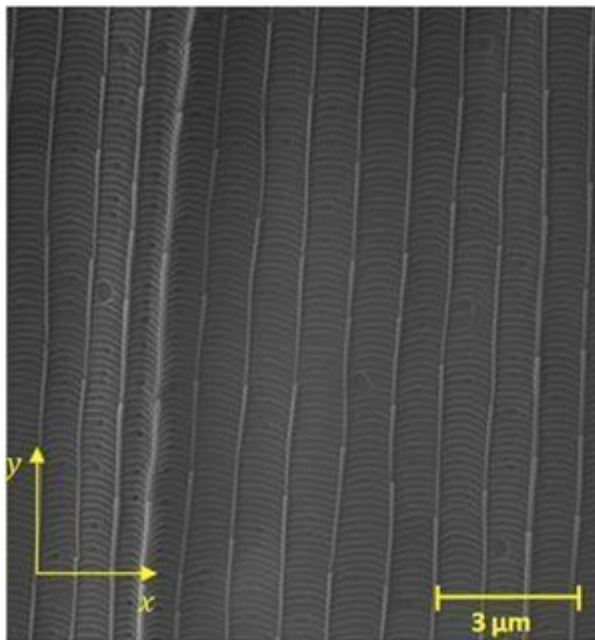
**Слика 1.7.** Електронски микрографи: љуспица лептира *Autographa bractea* је преломљена што омогућава осликавање њеног попречног пресека. Уочава се површинска дифракциона решетка периода  $\sim 1 \mu\text{m}$ , као и знатно ужа дифракциона решетка периода  $\sim 200 \text{ nm}$ .



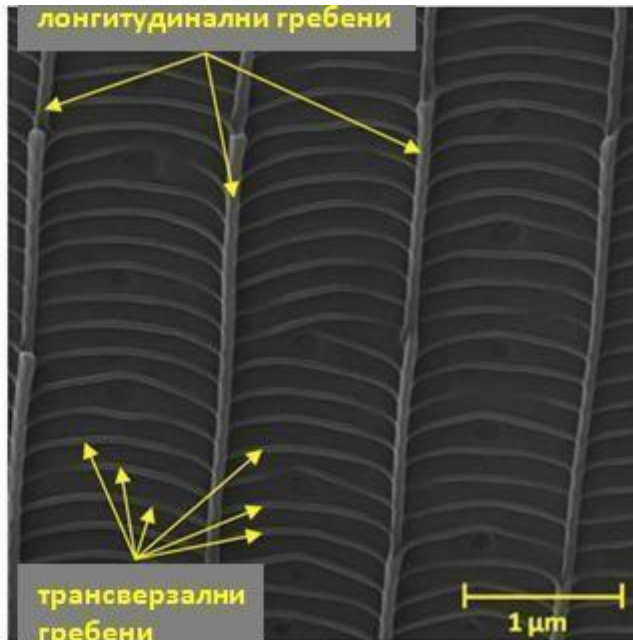
(a)



(б)



(в)



(г)

**Слика 1.8.** Електронски микрографи, љуснице мољца *Cydalima perspectalis* (у нашим крајевима познатог под називом шимширов мољац). Планарни 2Д систем са периодичношћу у правцу  $x$  и  $y$  осе .

Велики број откривених дифракционих решетки у природи је пронађен у перју птица. Ове наноструктуре су изграђене од цилиндричних гранула меланина распоређених у матрици од кератина. Дакле меланин и кератин су основне компоненте које овде обезбеђују периодичну варијацију индекса преламања. Меланин је назив групе пигмената браон или тамне боје који су

саставни део великог броја организама. Постоји 5 основних типова меланина [71]. Најчешћи је еумеланин који се јавља у два облика – браон и црни еумеланин. Меланин интензивно апсорбује УВ радијацију, а има значајну апсорпцију и у оптичком делу спектра. Он такође дисипира 99,9% апсорбоване УВ радијације [72]. Кератин је протеин и кључни састојак човекове косе и ноктију, перја птица, канци различитих животиња итд. Меланинске грануле могу бити на правилан начин распоређене у кератинској матрици, формирајући тако дифракциону решеку. Дифракција светлости која се одиграва на оваквим структурама је одговорна за обојеност пауновог перја. Код појединих организама димензије меланинских гранула (најчешће нешто краће од 800 nm) омогућавају Тиндалово расејање светлости на њима [75].

Пауново перје је један од најпознатијих примера структурне обојености у живом свету. Прво научно запажање оптике пауновог перја вероватно потиче од Исака Њутна који је у 18.-ом веку закључио да рефлексија светлости са пауновог перја показује значајну сличност са рефлексијом светлости са танких филмова [5]. Почетком 20.-ог века, Мејсон [73, 74] је истраживао обојеност перја многих птица и закључио да је та обојеност веома слична иридесцентним бојама танких филмова. Касније, истраживања уз помоћ електронске микроскопије су открила овакве фотонске нано-структуре у перју појединих врста птица: колибрија [75], свраке [76] итд. 2Д периодична сунђераста нано-структура је такође откривена код многих других птица и анализирана 2Д Фуријеовим трансформом [77-80].

До сада су у природи откривене хексагоналне [81, 82], правоугаоне [84, 75] и квадратне дифракционе решетке [83]. Решетке хексагоналног уређења су, осим код инсеката, откривене и код појединих водених организама [81, 84], као и код копнених сисара [85].

### *Тродимензионе (3Д) природне фотонске наноструктуре*

Фотонски кристали су у различитим формама проучавани још од 1887. године [86], али термин *фотонски кристал* први пут је употребљен готово 100 година касније – када су објављена два пионирска рада на ту тему [87, 88]. Од тада, они су били предмет опсежних експерименталних и теоријских истраживања због својих погодних карактеристика [89-92].

Фотонски кристали су материјали који имају периодичну промену индекса преламања у три просторне димензије, и код којих је период промене индекса преламања упоредив са таласном дужином светлости [93, 94]. Периодична варијација индекса преламања утиче на простирање светлости кроз фотонски кристал на исти начин као што периодична варијација потенцијала утиче на пропагацију електрона кроз полупроводник. Кристална решетка полупроводника узокује постојање и одређује особине електронске забрањене зоне, док начин на који се индекс преламања мења у фотонским кристалу одређује особине фотонске забрањене зоне – оптичког еквивалента електронске забрањене зоне.

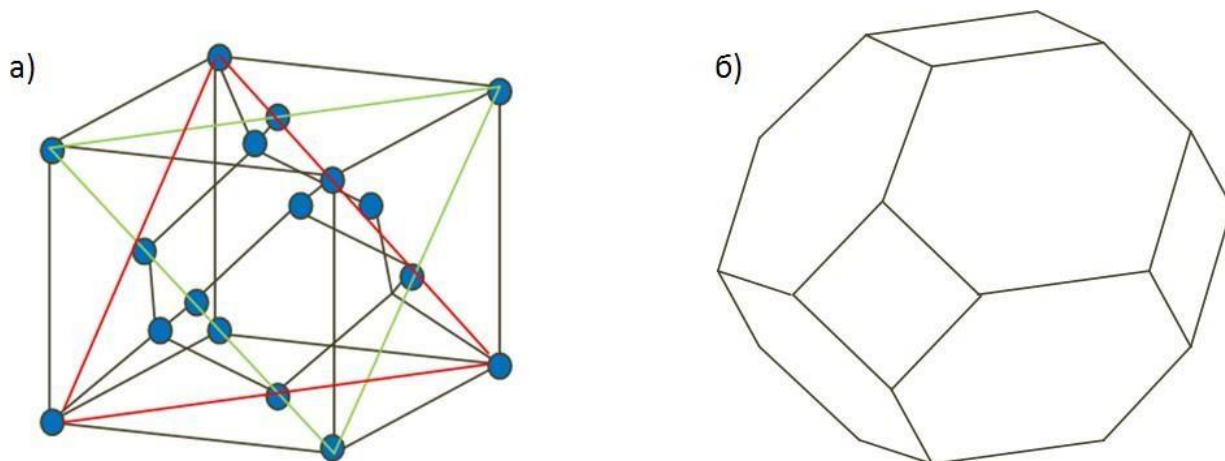
Фотонска забрањена зона је скуп фреквенција на којима је забрањено простирање светлости кроз фотонски кристал и због тога светлост на овим фреквенцијама бива рефлектована са фотонског кристала [93]. Постоје потпуна и делимична забрањена зона. Када је пропагација радијације забрањена за било који правац и поларизацију упадне светлости, забрањена зона је потпуна. Код делимичне забрањене зоне светлост може да се простира кроз фотонски кристал у одређеним правцима и за поједина поларизациона стања.

Постојање 3Д фотонских забрањених зона у периодичним структурама је предложио Јаблоневич 1987 [87], један век пошто је Рејлеј описао 1Д фотонску забрањену зону [96]. Ово је енергијски интервал у коме оптички модови, спонтана емисија, и флукуације нулте - тачке нису присутни [103]. Поједине оптичке примене захтевају забрањену зону која је широка и потпуна у одређеном спектралном опсегу [93, 97], а понекад је потребно и да фотонски кристал буде релативно великих физичких димензија [98]. Потпуна фотонска 3Д забрањена зона је изузетно важна за контролу светлост – материја интеракције и за многобројне примене: оптички и опто-електронски уређаји који раде на радио и оптичким фреквенцијама [93], високо – ефикасне соларне ћелије [99], контролисање локалне густине фотонских стања са циљем сузбијања спонтане емисије флуорофора [100-102], интерференциони рефлектори [94]...Да би фотонски кристали имали потпуну фотонску забрањену зону они морају имати велики контраст у индексу преламања између периодично постављених материјала који их сачињавају [93]. Ова особина је најважнија за фотонске кристале али има велику цену: ограничена величина узорка, скупа техника производње, потреба за материјалима ултра - високог индекса преламања, нанометраска резолуција (у производњи). Потпуне фотонске забрањене зоне највеће ширине су предвиђене за све потпуно-диелектричне 3Д фотонске кристале са структуром дијаманта [93]. Из тог разлога, ово је једна од најатрактивнијих структура за истраживање. Састоји се од две адекватно преклапајуће површински – центриране кубне Бравеове решетке [104].

Структура дијаманта има приближно сферичну прву Брилионову зону [105], слика 1.9. Генерално, површине прве Брилионове зоне задовољавају Брегов закон и због тога апроксимативно одређују таласну дужину максимума рефлектоване светлости или, прецизније, централну таласну дужину фотонске забрањене зоне [106]. Прва Брилионова зона представља примитивну ћелију 3Д фотонског кристала у инверзном простору и због тога је директно повезана са симетријом јединичне ћелије у основном простору [93]. Фотонски кристал са структуром дијаманта има површински центрирану кубну јединичну ћелију у реалном простору и због тога површине његове прве Брилионове зоне формирају окрњени октаедар који поседује осам хексагоналних и шест мањих квадратних површина са просторно – центрираном кубном симетријом.

Производња 3Д фотонских кристала са структуром дијаманта је веома компликована и неусавршена, али алтернативе се могу пронаћи у природи. На пример, комплексни 3Д распоред ваздушних шупљина и хитина у спољашњем омотачу тврдокрилца *Entimus imperialis* формира 3Д фотонски кристал са структуром дијаманта [107] и због тога представља идеалан модел за конструисање материјала са широком потпуном фотонском забрањеном зоном који рефлектује у видљивој области спектра.

Галуша и сарадници [92] су предложили коришћење кутикуларних структура врста *Papilionidae* и *Lycaenidae* као модела за производњу фотонских кристала са потпуном фотонском забрањеном зоном у оптичком делу спектра. Предлаже се и наношење материјала који има већи индекс преламања од хитина на овај биолошки модел што би довело до ширења потпуне фотонске забрањене зоне. Постојање оваквих природних фотонских кристала који су оперативни у оптичком делу спектра је веома значајно јер отвара могућности и за производњу напредних оптичких материјала путем имитирања (биомиметике) природних материјала [108].



**Слика 1.9.** а) елементарна ћелија дијаманта; б) прва Брилионова зона елементарне ћелије дијаманта

Многе примене фотонских кристала су на таласним дужинама у видљивом и ИЦ (инфрацрвеном) делу спектра. Због тога је веома важно, са становишта примена, откривање природних фотонских кристала са широком потпуном фотонском забрањеном зоном у видљивом или ИЦ делу спектра, који су погодни за масовну производњу.

У природним фотонским системима периодичност се може постићи специфичном запреминском структуром - такви системи се састоје од само једног материјала (нпр. хитин) који је испуњен одговарајућим шупљинама. Шупљине су испуњене ваздухом, па је он компонента која заједно са примарним материјалом омогућава периодичну модулацију индекса преламања и резултујуће оптичке ефекте. Међутим, постоје и структуре које комбинују два (или више) различита биолошка материјала (на пример, кератин и меланин код птица, гуанин и цитоплазма код риба) и на тај начин обезбеђују поменути периодичност. Постоје структуре које поред два различита биолошка материјала имају и ваздушне шупљине обезбеђујући тако још сложеније оптичке ефекте (код птица – меланин, кератин и ваздушни канали).

3Д фотонски кристали откривени у спољашњем омотачу инсеката су у потпуности изграђени од хитина испуњеног ваздушним шупљинама, и могу да имају различите структуре: структура минерала опала [109] и инверзна структура опала [110], жироидни хирални кристали [111-113], кристали са структуром дијаманта [114-117], фотонски кристали са тетрадарском структуром [93, 118]. Хитински фотонски кристали, откривени у спољашњем омотачу инсеката, у интеракцији са упадном светлошћу производе низ оптичких ефеката: иридесценција, углавно независна рефлексија, циркуларни дихроизам, поинтилистичко мешање таласних дужина [119]...

Термин поинтилизам је преузет из истоименог правца у сликарству, где се од мноштва малих области велике спектралне чистоће формира слика [120]. Поинтилистичко мешање таласних дужина у оптици је појава карактеристична за материјале који се састоје од великог броја насумично оријентисаних области – домена, који имају веома уређену структуру. Због уређене периодичне структуре, у овим областима долази до интерференције упадне светлости па се материјал састоји од великог броја области са високим интензитетом спектрално ускопојасне рефлексије, тзв. „интерференционих центара“. Интензитет и спектрални опсег рефлексије се разликују за различите интерференционе центре, услед њихове различите

оријентације у односу на детектор. Када се овакав материјал посматра, у оку долази до мешања таласних дужина рефлектованих са различитих интерференционих центара, што материјалу даје загасит, мат изглед. На пример, љуспице тврдокрилца *Pachyrrhynchus congestus pavonius* (Heller 1921) су по својој структури 3Д фотонски поликристали густо-пакованог хексагоналног уређења, веома слично структури минерала опала [121]. Овај природни фотонски кристал се састоји од великог броја различито и насумично оријентисаних кристалних домена - монокристала. Сваки монокристал има веома уређену, правилну кристалну решетку која приликом интеракције са упадном светлосћу показује иридесценцију - узак рефлексциони максимум високе амплитуде са јаком угаоном зависношћу од таласне дужине. Међутим, пошто се љуспица састоји од великог броја насумично оријентисаних монокристала, њихове појединачне рефлексije се сабирају што резултира значајним спектралним ширењем рефлексивног спектра уз задржавање његове високе амплитуде, и значајно смањење његове угаоне зависности. Овде дакле говоримо о феномену високе уређености на малом растојању и неуређености на великом растојању („short range order - long range disorder effect“). Донекле слично као код широко-појасних вишеслојних рефлектора, оптичка функција је елиминисање иридесценције уз задржавање високе амплитуде рефлексije. Код *Pachyrrhynchus* тврдокрилца монокристали у његовим љуспицама се састоје од правилно распоређених хитинских сфера (200 - 250 nm полупречника). Структура инверзна овој, сферичне шупљине у хитинској матрици, производи исти оптички ефекат. Галуша и сарадници [92] су овакву структуру описали као „хексагонално распоређени ваздушни цилиндри“. Код појединих инсеката, да би се смањило интензитет рефлектованог сигнала, високо уређена поликристална структура се појављује у комбинацији са неуређеним расејавајућим структурама, које интензивну рефлексiju са поликристала расејавају у ширем просторном углу и тако смањују интензитет рефлексije у појединачним правцима. Биолошка функција оваквих оптичких механизма је најчешће камуфлажа.

### 1.2.2. Хиралне наноструктуре биолошког порекла

У природи су откривени и оптички активни рефлектори који утичу на стање поларизације упадне светлости – тз. хирални вишеслојни рефлектори. Хиралност је особина асиметричности материјала (или његове унутрашње структуре). Објекат је хиралан уколико не може бити мапиран на своју огледалску слику произвољним бројем ротација и транслагација [122]. Хиралност се дакле, може схватити као одсуство огледалске симетрије. Хирални кристали различито реагују на различита поларизациона стања упадне светлости. За њих су карактеристичне појаве као што су: ротација равни поларизације линеарно поларизоване светлости (појава позната под називом оптичка активност), линеарни и циркуларни дихроизам. Циркуларни дихроизам је појава која означава апсорпцију циркуларно поларизованог таласа једне оријентације и трансмисију (као и рефлексiju) циркуларно поларизованог таласа супротне оријентације. Дакле, ако се лево циркуларно поларизован талас апсорбује, онда десно циркуларно поларизован талас може да се креће кроз материјал и да се рефлектује се њега. Узрок ове појаве је хирална микроструктура материјала.

Природни хитински хирални материјали, који су саставни делови тела појединих инсеката, су изложени упадној, неполаризованој Сунчевој светлости. Оваква, неполаризована светлост, може се приказати преко једнаких доприноса лево и десно кружно поларизоване светлости. Једна од ове две компоненте, чија је ротација електричног поља иста као оријентација хиралних структура, доводи до осциловања електронског омотача молекула и бива мање или више (у зависности од односа фреквенције електро-магнетне радијације и природне фреквенције осциловања електронског омотача датог молекула) апсорбована у материјалу, док се друга компонента неометано креће кроз хирални кристал и бива апсорбована по изласку из њега у унутрашњим органима инсекта [155]. Међутим, један део ове компоненте се такође и рефлектује са спољашњег хиралног омотача па је једна од оптичких особина оваквих материјала рефлексија циркуларно поларизоване светлости. Показано је да ови инсекти имају вид осетљив на циркуларну поларизацију светлости па се сматра да је примарна биолошка функција оваквих рефлектора сигнализација. У спољашњем хитинском омотачу појединих инсеката налазе се шупљине испуњене ваздухом. На свакој граничној површини хитин-ваздух долази до рефлексије и, ако су хитински и ваздушни слојеви адекватно распоређени и имају адекватне дебљине, долази до конструктивне интерференције парцијално рефлектованих таласа. Хитински слојеви могу да имају хиралну структуру услед чега се у рефлектованој светлости поред иридесценције уочавају и различити поларизациони ефекти (на пример, иридесцентна, угловно-зависна, циркуларно поларизована рефлексија) [123-126].

Хирални вишеслојни рефлектори су откривени код одређеног броја инсеката, углавном тврдокрилаца [127-140]. На пример, истраживање оптичких особина иридесцентног спољашњег омотача тврдокрилца *Plusiotis boucardi* показало је да спољашњи омотач има специфичну наноструктуру која одређује таласну дужину и поларизацију рефлектоване светлости [132].

Овај инсект се такође одликује и специфичном рефлексијом у широком просторном углу, која настаје због текстурисаности површине његовог спољашњег омотача. Ова особина је аналогна рефлексији светлости са низа сребрних сферних конкавних микро-огледала сличних димензија која су развијена за примене у фотоници [141]. Уколико се на овакав низ микро-огледала усмери сноп колимисане светлости, светлост се рефлектује у различитим правцима који зависе од тачке на закривљеној површини на коју светлост пада. Ово се такође дешава на конкавним удубљењима на елитри поменутог инсекта. Елитра је модификован предњи пар крила појединих редова инсеката (највећим делом тврдокрилаца), који представља својеврстан тврди оклоп. У овом случају дубинска микроструктура додатно доприноси комплексности рефлексије обезбеђујући зависност рефлексије од таласне дужине упадне светлости. Репликацијом овакве структуре могу се произвести хирална микро-огледала са ускопојасном рефлексијом која би омогућила контролу кружно-поларизоване светлости у различитим оптичким применама [132].

### 1.2.3. Неуређене природне фотонске наноструктуре

#### *Оптичка широкопојасна рефлексивност*

Интензивна бела боја на деловима тела различитих организама и биљака је структурна. У питању је некохерентно, дифузно и у свим правцима истоветно расејање свих таласних дужина из оптичког дела спектра које човек перцепира као белу боју. Овакво расејање се може објаснити Миевом теоријом, а настаје приликом интеракције светлости са специфичним, веома неуређеним нано-структурама које се најчешће састоје од мреже влакана одговарајућих димензија, уз одсуство апсорбујућих пигмената.

Вукушић и сарадници [142, 143] истраживали су изузетно интензивну широко-појасну рефлексiju тврдокрилца *Cyphochilus* spp. Откривено је да је су узрок овакве рефлексije љуспице микрометарских димензија које се налазе на површини тела овог инсекта. Љуспице целом својом запремином имају аморфну структуру – састоје се од неуређене мреже хитинских влакана чије су димензије оптимизоване за ресејање свих таласних дужина из оптичког дела спектра. Са становишта оптике, ове љуспице су широко-појасни дифузни рефлектор за оптички део спектра. Оно што је посебно фасцинантно и занимљиво са становишта примена је веома мала дебљина ових оптичких елемената којима се постиже интензивно расејање. Наиме, љуспице су дебеле само око 5  $\mu\text{m}$ . Упоредивањем са синтетичким белим или сребрним материјалима које је човек направио, долази се до закључка да ове љуспице представљају знатно ефикаснији широко-појасни дифузни рефлектор. Веома сличне структуре су откривене и код других инсеката, као што је на пример вилински коњиц *Calopteryx splendens* (Harris, 1780). Овај инсект на својим крилима поседује светле и тамне регионе који су структурно идентичне високо-расејавајуће структуре, при чему тамни региони имају велику концентрацију апсорбујућег пигмента, слика 1.10.

Квалитет широкопојасне рефлексije (у даљем тексту: белине) и сјаја (интензитет рефлектоване оптичке радијације) љуспица тврдокрилца *Cyphochilus* spp је квантификован у складу са Интернационалном организацијом за стандардизацију (ISO). Белина и сјај су основне колориметријске карактеристике објеката. Колориметрија је наука која описује и квантификује човекову перцепцију боје [144]. Квалитет белине је квантификован у складу са ISO 11475, а квалитет сјаја у складу са ISO 2470 стандардом, употребом D65 осветљавача у фотоспектрометру калибрисаном у складу са ISO/IR3 стандардом. Белина и сјај су дефинисани су на следећи начин:

$$W_{CIE} = Y + 800(x_0 - x) + 1700(y_0 - y) \quad (1.6)$$

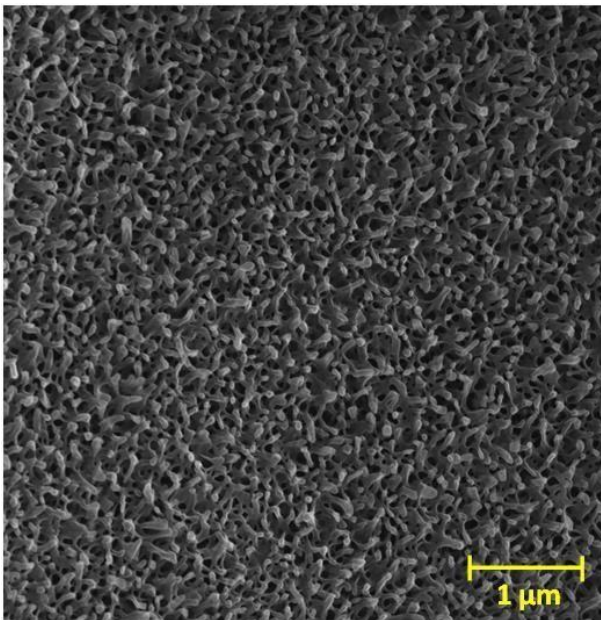
где је  $W_{CIE}$  белина, тј. оптичка широкопојасна рефлексивност објекта,  $Y$  је његов сјај, а  $x, y$  и  $x_0, y_0$  су координате хроматичности објекта и осветљавача, респективно, у CIE 1964 простору боја (у Материјалима и Методама је дат опис колориметрије и CIE простора боја) [145, 146]. Сјај  $Y$  дефинисан је на следећи начин:

$$Y = 100 \frac{\int E_{\lambda} R_{\lambda} \bar{y} d\lambda}{\int E_{\lambda} \bar{y} d\lambda} \quad (1.7)$$

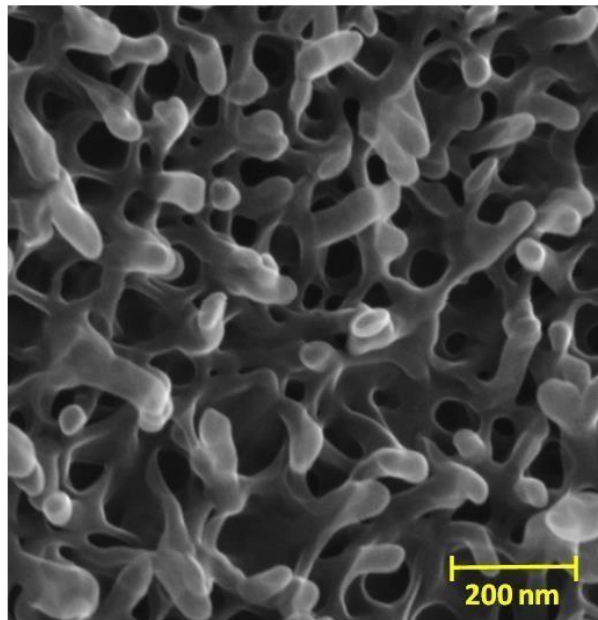


где је  $E_\lambda$  функција осветљивача (интензитет електричног поља радијације осветљивача-емитера, на таласној дужини  $\lambda$ ),  $R_\lambda$  је рефлексијност посматраног објекта на таласној дужини  $\lambda$ ,  $\bar{\rho}$  је луминозност на тал. дужини  $\lambda$  [147].

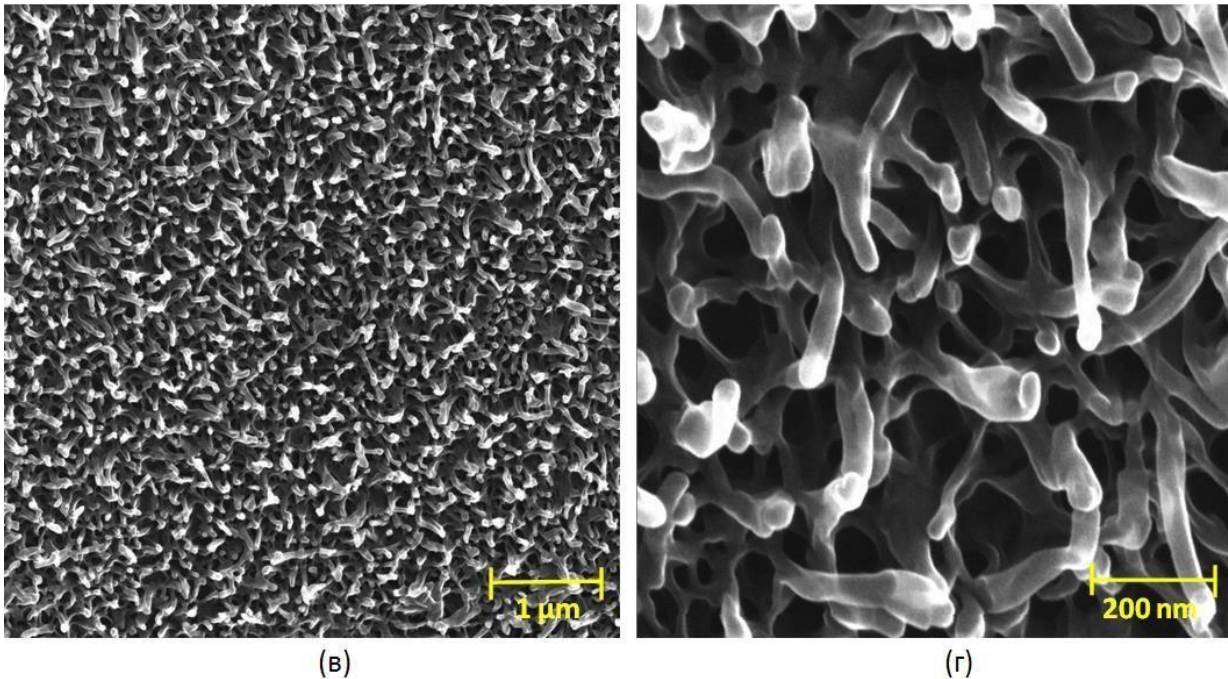
Широкопојасна рефлексијност и сјај просечне љуспице тврдокрилца *Cyphochilus* spp имају вредности 60 и 65, респективно [148] што указује на изузетан мулти-расејавајући (расејање се дешава у широком опсегу таласних дужина) систем чија је дебљина само 5  $\mu\text{m}$ . Нпр. бели папир, који се састоји од насумичне мреже избељених влакана целулозе, је до 25 пута дебљи (дебљина му је око 100  $\mu\text{m}$  [149]) од љуспица овог тврдокрилца а опет производи белу боју која је само 8% квалитетнија (има за 8% већи сјај). У процесу проиводње папира, да би се повећао квалитет његове беле боје, на површину папира се, у форми танког премаза, додају кристали калцијум карбоната и материјали који повећавају одсјај. Међутим, појединачни изоловани слој калцијум карбоната дебљине 5  $\mu\text{m}$  има веома слаб сјај (40 - 50) у поређењу са љуспицама бубе а транспарентност му је толико велика да рачунање белине нема смисла. Даље, белина човекових зуба настаје због мулти-расејања светлости на напакованим кристалима хидрокси-апатита који се простиру до дубине од 2 mm унутар зуба. Њихова максимална природна вредност белине и сјаја су релативно мале: белина просечног човековог зуба је око 40 а ниво сјаја око 53 услед тога што материјали од којих се зуб састоји имају мали контраст у индексу преламања и велику апсорптивност у „плавом“ делу спектра [143].



(a)



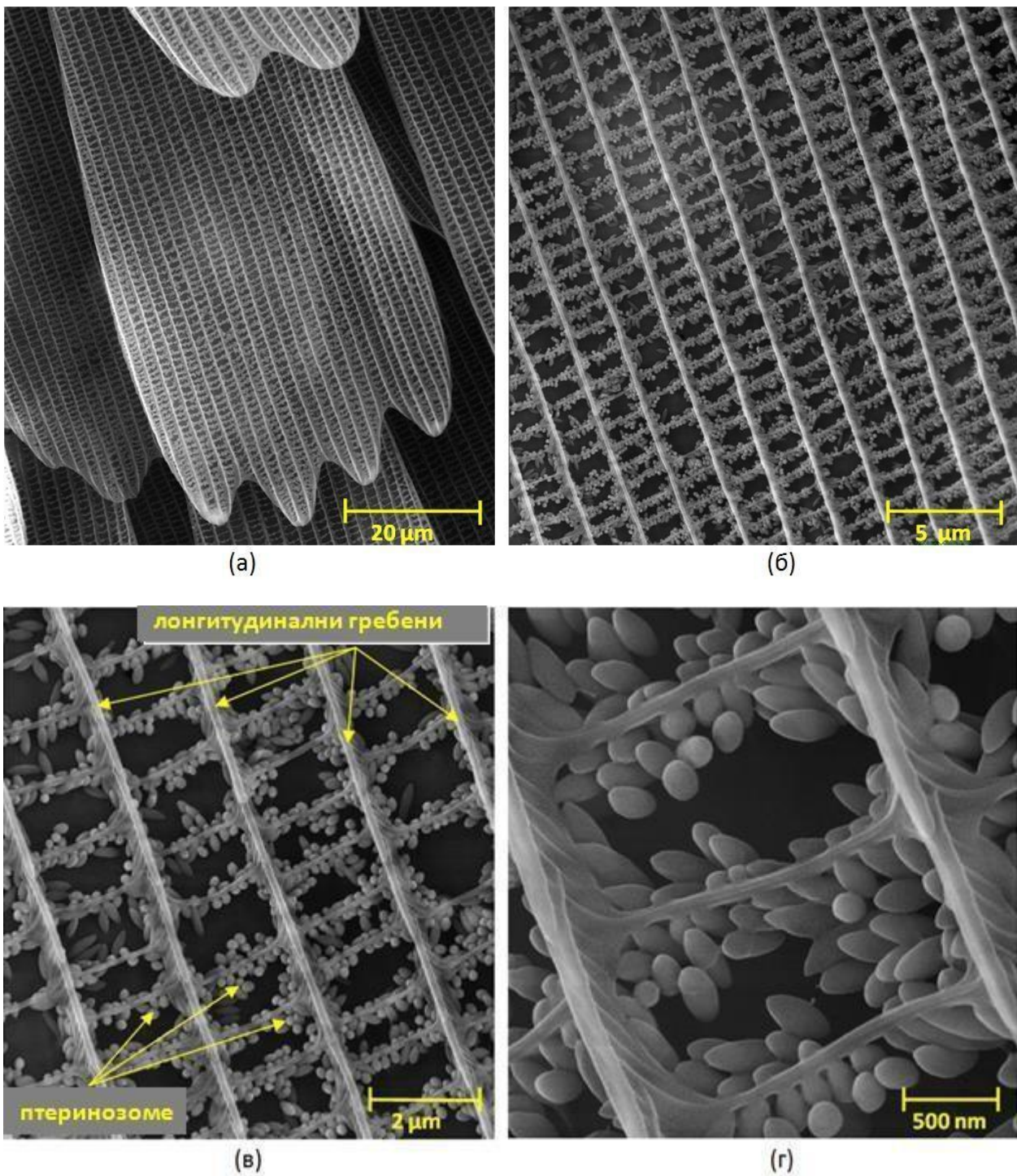
(б)



**Слика 1.10.** Електронски микрографи дорзалне стране љуспица *Calopteryx splendens m* (*Odonata*) инсекта, при великом микроскопском увећању (увећање на сликама а) и в) је 90 000 X, а на сликама б) и г) 216 000 X). Микрографи а) и б) су са светлог дела крила а микрографи в) и г) су са тамног дела крила. У оба случаја је уочљива високо-неуређена структура хитинских влакана чије су димензије оптималне за расејање светлости. Таман регион крила поседује велику концентрацију апсорбујућег пигмента меланина.

У многим оптичким системима, где је квалитет широкопојасне оптичке рефлексије важан, додавање фотонске нано-структуре коју поседују љуспице бубе *Cyphochilus* би довело до тога да бисмо имали незнатно, готово занемарљиво мало повећање у дебљини материјала а значајан пораст у квалитету широкопојасне рефлексије. Овај природни нано-фотонски систем се одликује и значајном хемијском пермеабилношћу и могао би да има примену у белим светлосно емитујућим диодама (ОЛЕД) велике површине и у контроли правца њихове емисије, као и различите друге технолошке примене [150-152].

Високо-ефикасни широко-појасни дифузни рефлектори откривени су и код других врста инсеката [153-155], као и код биљака [29], и за све њих је карактеристична неуређена структура. На пример, код лептира *Pieridae* (фамилија лептира која садржи 1100 врста, домаћи назив: белци) постоје насумично распоређене шупље честице елипсоидног облика, ткз. птеринозома, чија је величина (неколико стотина нанометара) оптимизована за дифузно расејање светлости [153]. Оне дају највећи допринос широкопојасној оптичкој рефлексији крила овог лептира (слика 1.11).



**Слика 1.11.** Електронски микрограф љуспице белог лептира *Pieris rapae*. У простору између лонгитудиналних гребена уочава се велики број насумично распоређених шупљих гранула – птеринозома (пречника неколико стотина нанометара) које омогућавају интензивно расејање радијације из оптичког дела спектра и омогућавају лептировим крилима његову белу обојеност.

## *Оптичка широкопојасна апсорптивност*

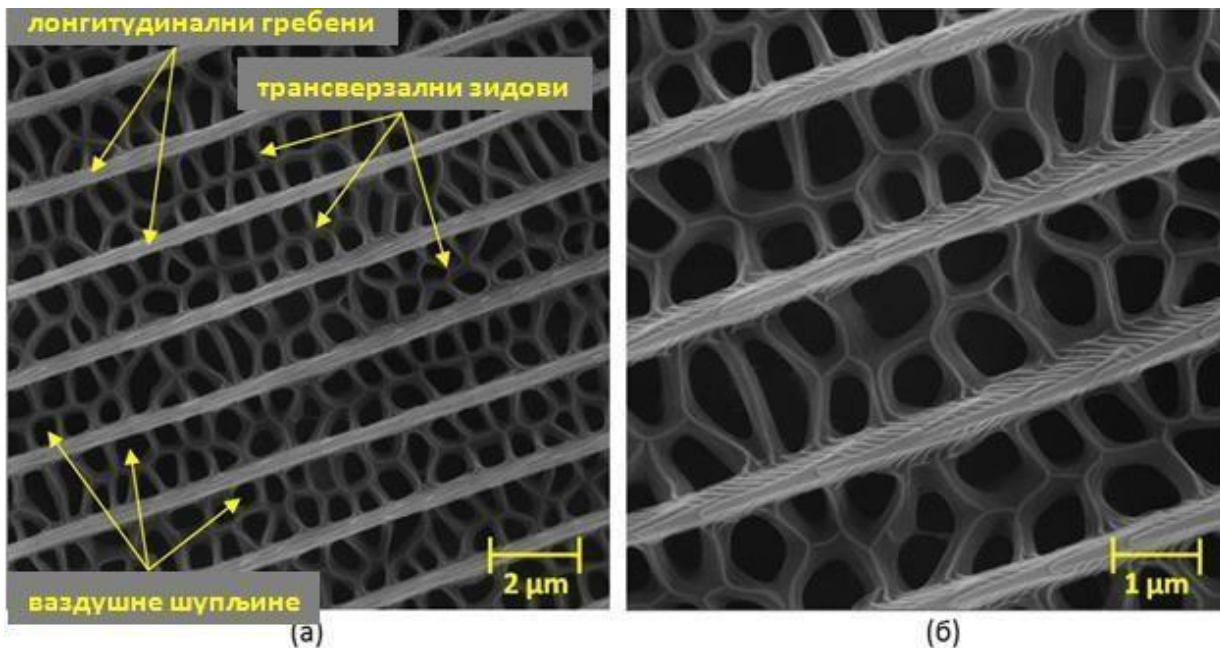
Широкопојасна апсорптивност, карактеристична за поједине природне материјале, је углавном објашњавана великом концентрацијом апсорбујућих пигмената. Међутим, у новије време је показано да поред апсорбујућих пигмената, и сложене нано-структуре значајно доприносе великој апсорптивности. Постоје природни оптички системи чија нано-структурисаност значајно повећава њихову апсорпцију. Њихова основна карактеристика је високо неуређена структура у којој су густо распоређени апсорбујући пигменти. Оптичка функција нано-структуре је расејање светлости и повећање времена боравка фотона у нано-структури услед чега се повећава вероватноћа да ће фотон наићи на пигмент и бити апсорбован. Поред оваквих, запреминских неуређених структура, постоје и површинске неуређене структуре. То су храпаве граничне површине између ваздуха и биолошког материјала (а то је хитин, код инсеката). На оваквој граничној површини хитин-ваздух долази до расејања упадне светлости чији један део пролази кроз овакву храпаву граничну површину, доспева у хитински слој и проводи унутар овог слоја више времена (средње време живота фотона је дуже) него у случају равне граничне површине, јер се фотони у просеку крећу дужом путањом (унутар хитинског слоја). Дакле, светлост има тенденцију да буде заробљена унутар хитинског слоја, слично као код текстурисаних соларних ћелија [157]. Јаблонич је показао да када радијација пада на оптичке, транспарентне танке филмове са неравним површинама, као поседица дифузног расејања радијације са овакве површине у материјал, долази од пораста интензитета радијације унутар материјала за фактор  $2n^2$ , где је  $n$  индекс преламања материјала, и као последица повећања овог „локалног“ интензитета електро-магнетне радијације долази до повећања апсорпције за фактор  $4n^2$  [158]. При томе, геометријске карактеристике храпаве површине нису важне, докле год површина има довољан ниво храпавости. До ових резултата дошао је статистичким приступом али је показао и да се исти резултат може добити и применом геометријске оптике уколико се поштују њена поједина ограничења. Ова теорија је превасходно развијена са циљем повећања ефикасности соларних ћелија заменом равних граничних површина силиконских танких слојева унутар ћелија храпавим површинама [158]. Међутим, теорија објашњава читав низ појава и у биофотоници [95].

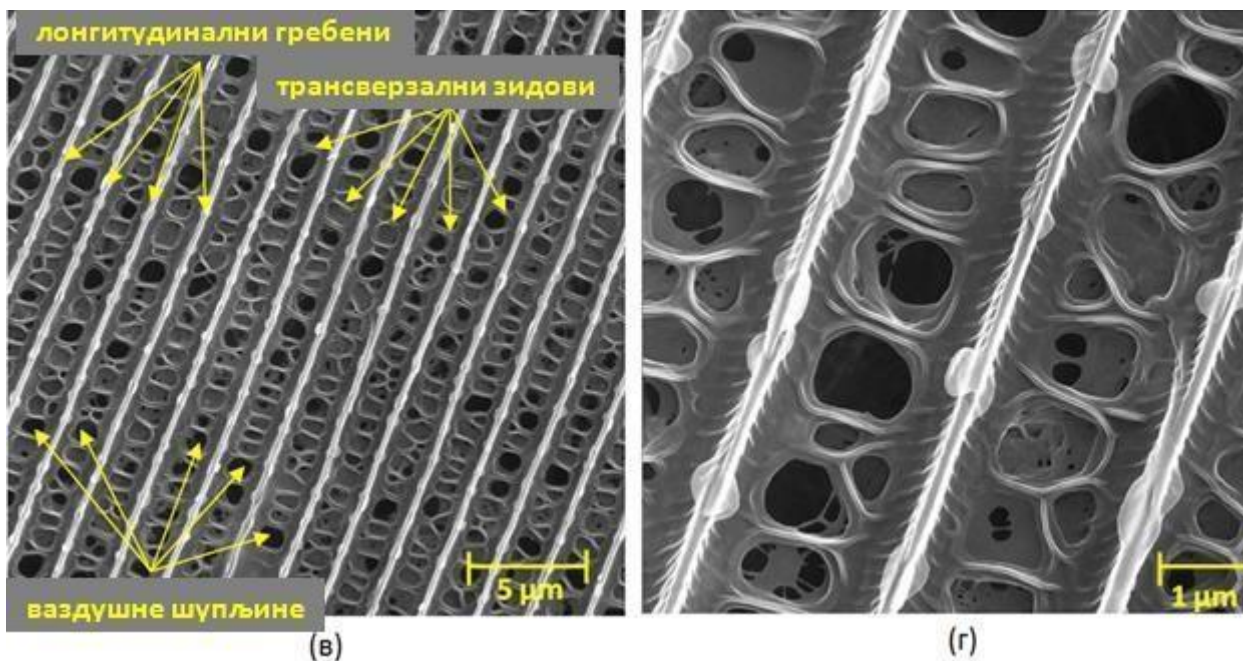
Један од примера запреминске неуређене биофотонске структуре је густа, неуређена мрежа апсорбујућих влакана. Поједини инсекти на површинским деловима тела (крила, елитра...) имају, из биолошких разлога, високо-специјализоване нано-структуре чија је оптичка функција иридесценција – генерисање високо амплитудске и спектрално уско-појасне рефлексије која, у зависности од осталих карактеристика нано-структуре, може али и не мора да показује угаону зависност. Апсорпција у површинским структурама је занемарљива и таласне дужине које се не рефлектују су трансмитоване дубље у тело инсекта. Испод слоја високо-рефлективних нано-структура – љуспица, налази се слој тзв. тамних љуспица. Тамне љуспице су оптички елементи специјализовани за максималну апсорпцију одређених таласних дужина – апсорпција се максимизира њиховом нано-структуром (запреминска неуређена мрежа хитинских влакана нанометарског пречника, на којој се светлост интензивно расејава), унутар које се налазе апсорбујући пигменти (најчешће меланин). Дакле у питању су веома ефикасни широко-појасни апсорбери. Када слој тамних љуспица не би постојао, овај оптички систем би давао веома другачији одзив – таласне дужине које се апсорбују унутар тамних љуспица биле би расејане на унутрашњим деловима тела инсекта па би један део те радијације био враћен у спољашњу средину кроз горњи слој високо-рефлективних љуспица. Рефлексионни спектар би био значајно проширен и овај оптички систем више не би представљао уско-појасни

рефлексионни филтер. На пример, Вукушић и сарадници су показали да веома тамним зонама на крилима *Papilio ulysses* лептира значајно доприносе љуспице високо специјализоване за апсорпцију светлости (слика 1.12) [156]. Ово истраживање је показало повезаност између структуре љуспица и високе оптичке апсорптивности, и како се адекватном нано-структуром љуспица значајно повећава ефикасност апсорпције.

Материјали велике апсорптивности су свеprisутни у живом свету. Могу имати различите биолошке функције. Нпр. контролисана апсорпција Сунчеве радијације је главни метод за терморегулацију код многих инсеката [159]. С обзиром да терморегулацију одређују закони апсорпције и емисије црног тела [24], квалитет апсорпције одређује температуру крила и тела инсекта. Поред утицаја на терморегулацију, апсорпција је веома важна и за изглед. На изглед многих интензивно обојених инсеката веома утичу тамне регије које се налазе око обојених. Нејасан прелаз између црних и обојених делова чини инсекта мање уочљивим за предаторе [160].

Оваква ултра-црна боја је технолошки јако значајна за оптичке инструменте (минимизација нежељене, паразитске рефлексије) а има и многе друге технолошке примене. У скорије време, имитирањем биофотонских система, произведене су нетранспарентне синтетичке површине које апсорбују 99,6 % упадне светлости [161].





**Слика 1.12.** Електронски микрографи: „Структурно црно“, лептир *Papilio ulysses*, а) и в) – електронски микрографи љуспица са црног и сивог региона крила, респективно. Између лонгитудиналних гребена, уочава се неуређен распоред зидова чија је оптичка функција расејање надоласеће радијације, и по том основу повећање времена боравка фотона унутар љуспице чиме се повећава вероватноћа за апсорпцију фотона од стране пигмената. „Црне“ љуспице имају мрежу веће густине што резултира интензивнијом апсорпцијом светлости. На микрографима б) и г) су приказане увећане зоне са микрографа а) и в), респективно.

### 1.3. Флуоресценција и природне наноструктуре

Флуоресценција означава ексцитацију атома или молекула апсорпцијом фотона одређене таласне дужине, а затим деексцитацију на другој таласној дужини. Апсорпцијом фотона молекула прелази у побуђено стање и флуоресценција настаје уколико се повратак молекула у основно стање одиграва синглет – синглет електронском релаксацијом. Типично време живота побуђеног стања молекула (што одговара флуоресцентном одговору молекула у функцији времена) је реда величине наносекунди. Уколико се прелазак молекула из побуђеног у основно стање одиграва триплет – триплет електронском релаксацијом, та појава се назива фосфоресценција и типично време живота побуђеног триплетног стања молекула је реда величине микросекунди или дуже. У природи постоје молекули, флуоресцентни пигменти, који апсорбују радијацију из одређеног спектралног опсега и приликом релаксације емитују радијацију из неког другог дела спектра. Човек перцепира материјале богате оваквим пигментима као обојене, при чему боја зависи од емисионог флуоресцентног спектра пигмента.

Флуоресценција је веома присутна у живом свету. Досадашња истраживања показују да је код неких организама она само нуспроизвод структуре пигмената, а код неких има одређену биолошку функцију. На пример, папагај *Melopsittacus undulatus* има флуоресцентно перје. Показано је да ова флуоресценција има јасну биолошку функцију тј. да служи као сигнал у доба парења [162]. Биохемијски процес у коме настају флуоресцентни пигменти је веома комплексан и биолошки захтеван (што значи да у процесу формирања флуоресцентних пигмента организм

троши доста енергије и осталих ресурса). Из тог разлога, немају све јединке ове врсте пигменте а и оне које их поседују, не поседују их у једнаким количинама, па је присуство овог пигмента (које се детектује његовом флуоресценцијом) показатељ индивидуалног квалитета јединке. Флуоресцентно перје је откривено и код других врста птица [163-166], а флуоресценција је откривена и код инсеката [167], зглавкара [168]...

Ако се молекул пигмента налази у нано-структурисаном материјалу (при чему материјал има периодичну промену индекса преламања у једној или више просторних димензија), флуоресцентне особине пигмента могу бити веома измењене. Материјал – фотонски кристал може да утиче на време флуоресценције и на правац емитовања флуоресцентне светлости. Ако се таласна дужина максимума флуоресценције налази у забрањеној зони фотонског кристала онда долази до значајног повећања времена флуоресценције. Пошто фотонски кристал мења локалну густину оптичких стања, флуоресценција је сузбијена у једном правцу али је зато поспешена у другим правцима па се на овакав начин постиже и контрола правца флуоресценције – просторног угла флуоресценције. Овакве појаве су откривене у природи, код појединих организама, код којих се флуоресцентни пигменти налазе распоређени у нано-структурисаним биофотонским материјалима. На пример Вукушић и сарадници су описали природан фотонски систем у коме се налазе и пигменти чије су флуоресцентне особине веома измењене услед фотонске нано-структуре [167]. У питању су љуспице лептира *Swallowtail* (*Papilio*) које су по својој структури квази-периодични 2Д фотонски кристали.

Истраживања флуоресценције у биофотоници, а поготову модификоване и контролисане флуоресценције (у смислу контроле времена и правца-просторног угла флуоресценције) имају значајне технолошке примене. На пример, код појединих оптичких емитера као што су флуоресцентне светлосно-емитујуће диоде, велика количина светлости остаје заробљена у њиховој унутрашњости што значајно смањује њихову ефикасност. У скоријој прошлости развијени су ефикаснији уређаји који су нано-структурисани - користе 2Д фотонске кристале у сврху ефикасније екстракције светлости из уређаја а такође користе и Брегове рефлекторе за контролу правца емитовања флуоресцентне светлости, по узору на природне биофотонске системе [167].

## 2. Материјали и методе

### 2.1. Експерименталне методе и уређаји

#### 2.1.1. Оптичка микроанализа

За оптичку микроскопску анализу хитинских објеката природног порекла коришћени су следећи оптички микроскопи:

Стере микроскоп (СТЕВА600, Colo Lab Experts, Словенија) са максималним увећањем 180X, објективом 20X, 0.35 NA, помоћним објективом 2X, радним растојањем 100 mm. Микроскоп може да ради у рефлексноном и трансмисионом моду.

Тринокуларни микроскоп (МЕТ104, Colo Lab Experts, Словенија), максимално увећање 400X. Микроскоп поседује поларизациони мод. Објективи: Plan Achromatic POL Polarizing 10X, 0.25 NA, 20X, 0.4 NA, 40X, 0.65 NA.

Рефлексни и трансмисиони спектри хитинских наноструктура и макроскопских хитинских објеката измерени су оптичким фибер спектрометром (Ocean Optics, HR2000CG-UV-NIR) са пречником фибера од 400  $\mu\text{m}$ . Као извор светлости је коришћена халогена лампа. Спектри су калибрисани помоћу стандардне беле површине.

#### 2.1.2. Сканирајућа електронска микроскопија

Сканирајући електронски микроскоп (СЕМ) се користи за микроскопско снимање и карактеризацију површине узорака на великом увећању. Када се електронски сноп усмери на узорак, услед сударних процеса долази до емисије валентних електрона из електронског омотача атома који се налазе унутар узорка (ови електрони се у електронској микроскопији називају секундарни електрони). Поред секундарних електрона, приликом интеракције електронског снопа и узорка долази до емисије и Auger-ових електрона, X-зрака, катодолуминисценције. Ови процеси се такође могу користити за карактеризацију узорака, али у истраживањима у оквиру ове дисертације су претежно коришћени секундарни електрони. Топографија површине узорка се снима сканирањем површине узорка електронским снопом и аквизицијом слике добијене детектовањем секундарних електрона.

Основне компоненте стандардног СЕМ-а су електронско-оптички систем који управља електронским снопом, веома прецизан луз координатни сто на који се монтира узорак, детектор секундарних електрона, јединица за приказ слике, операциони систем за извођење различитих операција и систем за обезбеђивање високог вакуума. Електронско-оптички систем се састоји од извора електрона, кондензаторског електронског сочива и објектива који производе електронски сноп и сканирајућих система који контролишу позицију електронског снопа на површини узорка [214]. Електронско-оптички систем и узорак се налазе у вакууму ( $10^{-3} - 10^{-4}$  Pa). Извор



електрона је танко волфрамско влакно (пречника  $\sim 0.1$  nm). Загревањем овог влакна (до температуре од 2800 K) долази до емисије електрона (термо-електронска емисија). За формирање и контролу електронског снопа СЕМ користи магнетна сочива – пропуштањем електричне струје кроз (металне) калемове долази до формирања ротационо-симетричног електричног поља које функционише као сочиво за електронски снап.

У оквиру ове дисертације, коришћен је „*field emission*“ СЕМ (FE – SEM, MIRA 3, TESCAN), са максималном резолуцијом од 1 nm. Пошто је пречник електронског снопа  $\sim 1000$  пута мањи у односу на стандардан електронски микроскоп, квалитет слике је значајно бољи. Због овако уског електронског снопа „*field emission*“ микроскоп захтева високу вредност вакуума у колони ( $10^{-5} - 10^{-6}$  Pa). Напон између катоде и аноде се може подешавати у опсегу 0.5 – 30 kV.

### „*Double transfer*“ метод

Овај метод је развијен у оквиру експерименталног дела ове тезе, за припрему узорака за електронску микроскопију. Припрема узорака игра важну улогу у сканирајућој електронској микроскопији и од квалитета припреме узорака зависи квалитет осликавања узорка и максимално увећање. Метод је такође коришћен и у реализацији варијабилног оптичког елемента описаног у трећем делу ове дисертације.

Биофотонски објекти истраживани у оквиру ове дисертације су хитинске љуспице инсеката које су у природном стању кумулативно распоређене на деловима тела инсеката. Да би се испитале њихове оптичке и термалне особине и креирали одговарајући теоријски модели, потребно је имати детаљне податке о наноструктури објеката, и у ову сврху се користи сканирајућа електронска микроскопија. За анализу на СЕМ-у, објекте је потребно изоловати и при том не нарушити њихову нано-структуру, што није једноставно, имајући у виду да су ови објекти веома осетљиви.

„*Double transfer*“ метод омогућава да објекти у неизмењом стању и оријентацији (онако како су оријентисани на деловима тела инсеката) буду припремљени за анализу сканирајућом електронском микроскопијом.

Метод се састоји од одвајања љуспице са крила инсекта применом лепљиве траке мале површинске енергије после чега се љуспица пребацује директним контактом на лепљиву траку веће површинске енергије (нпр. то може бити лепљива карбонска трака која се у електронској микроскопији стандардно користи за фиксацију узорака). На овај начин, задржава се оригинална оријентација љуспице (иста оријентација као на крилу инсекта) а, ако се процедура обави пажљиво, очувана је наноструктура љуспице.

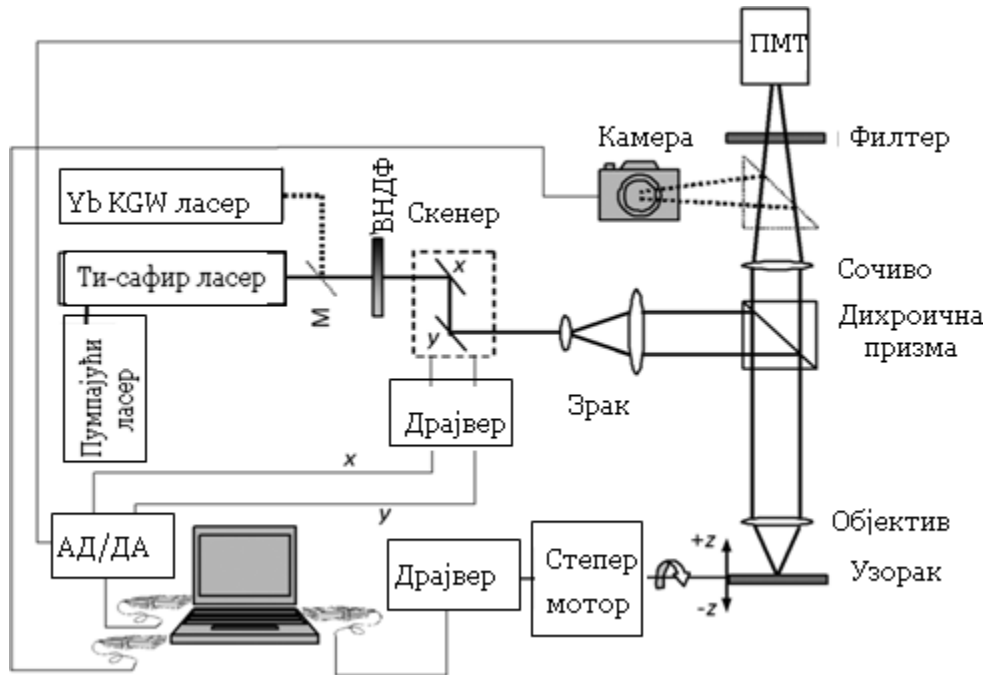
### 2.1.3. Нелинеарни ласерски микроскоп

Ласер креира високо-кохерентно зрачење које по изласку из ласера улази у оптички систем у коме се могу додатно подешавати поједини параметри ласерског зрачења (снага, поларизација...). Ласерски сноп затим доспева у микроскоп где је усмерен на узорак. Услед интеракције ласерског снопа и узорка долази до мулти-фотонских процеса (у оквиру ове дисертације истраживани су дво-фотонски побуђена флуоресценција и други хармоник хитина). Радијација која настаје као резултат ових процеса долази на детектор (фотомултипликатор) и рачунар затим обрађује сигнал и приказује слику узорка на екрану. Основне компоненте нелинеарног ласерског микроскопа су: побудни ласер, микроскоп, и детекторско – рачунарски систем. Истраживања у оквиру ове дисертације су урађена на нелинеарном ласерском микроскопу који је конструисан у Центру за Фотонику, у Институту за Физику у Београду. Шематски приказ је дат на слици 2.1.

Два фемто-секундна ласера су коришћена за генерисање дво-фотонски побуђене флуоресценције и другог хармоника на узорку. Један од њих је титанијум-сафир ласер Coherent Mira 900-F који је побуђиван Coherent Verdi V10 ласером који производи зрачење на 532 nm, снаге 10 W. Овај титанијум-сафирни ласер производи фемто-секундне импулсе (време трајања импулса је 160 fs) при репетицији од 76 MHz, у спектралном опсегу од 700-1000 nm. Други ласер који је коришћен за нелинеарну побуду узорака је Yb KGW фемто-секундни ласер (Time-Bandwidth Products AG, Yb GLX) који генерише зрачење на 1040 nm. Галванометарска сканирајућа огледала (Cambridge Technologies, 6215H) се користе за рестерско сканирање узорака ласерским снопом. Сноп је адекватно проширен да би попунио улазну пушилу микроскопског објектива. Дихроично огледало (Thorlabs, DMSP805) које пропушта таласне дужине < 805 nm а рефлектује таласне дужине > 805 nm усмерава ласерски сноп ка микроскопском објективу. Део операционог опсега побудног Титанијум - сафир ласера није могао да буде искоришћен због граничне таласне дужине дихроичног огледала. За детекцију флуоресценције и другог хармоника са узорка користи се фотомултипликатор (RCA, PF1006) у комбинацији са одговарајућим блокирајућим филтером. За детекцију дво-фотонски побуђене флуоресценције са узорка користи се и додатни филтер да би се редуковала паразитска ласерска светлост која пролази кроз дихроично огледало. Са фотомултипликатора сигнал се уводи у аквизициону карту (NI USB-6351, 1 Msample/s, National Instruments). Оптички део микроскопа је базиран на модификованом JENVAL микроскопу (произвођач Carl Zeiss). Узорак се поставља на механичко постоље чије се померање контролише степер - мотором. Степер - мотор омогућава вертикално померање постоља (z-оса на слици) са кораком од 2  $\mu\text{m}$ . Покретна призма омогућава скретање ласерског снопа и осликавање узорка у светлом пољу помоћу Canon EOS 50D дигиталне камере. Рачунар контролише цео инструмент и обраду слике. Vol View 3.4 слободан софтвер (Kitware, Inc.) омогућава формирање 3Д модела узорака на основу низа 2Д попречних пресека (тзв. „слајсова“), употребом алгоритма пројекције максималног интензитета или запреминским изоштравањем („*volume rendering*“).

За микроскоп су коришћени Carl Zeiss објективи: Planachromat, 40X, 0.65 NA (са видним пољем од 815  $\mu\text{m}$ ) и LD LCI Planapochromat 25X, 0.8 NA вода/глицерин имерзиони објектив. За узорке већих димензија коришћен је Carl Zeiss Planachromat, 25X, 0.5 NA, са видним пољем од 1200  $\mu\text{m}$ . Попречна и осна резолуција нелинеарног микроскопа су одређене употребом флуоресцентних нанометаских гранула (Life Technologies, TetraSpeck<sup>TM</sup> флуоресцентне микросфере). За микроскопски објектив са увеличањем 40X, измерена је латерална резолуција

од 630 nm X 915 nm (услед елиптичности побудног ласерског снопа), док је вертикална резолуција 2100 nm.



**Слика 2.1.** Шема нелинеарног сканирајућег ласерског микроскопа. ПМТ- фотомултипликатор који се користи за детекцију дво-фотонски побуђене флуоресценције и другог хармоника, VNDФ – варијабилни неутрални филтер за подешавање снаге ласерске радијације, АД/ДА – дигитална аквизициона карта, М – огледало које се уноси у систем због коришћења побудног ласерског снопа на 1040 nm из Yb KGW ласера. Путања ласерског снопа је приказана подебљаном линијом, електрични каблови су приказани танком линијом.

## 2.1.4. Streak камера

Streak камера је уређај који служи за временску и спектралну карактеризацију ултра брзих светлосних импулса. Ова врста камере има најбољу резолуцију у поређењу са осталим уређајима који мере ултра брзе импулсе.

Светлост пролази кроз процеп на улазу у камеру и затим бива фокусирана на фото-катоду. Светлост се на фото-катоди конвертује у одрђени број електрона који је пропорционалан интензитету упадне светлости. Затим, електрони пролазе кроз пар убрзавајућих електрода, где долази до повећања њихове брзине и после тога доспевају на фосфоресцентни екран. Док електрони, који су првобитно „настали“ интеракцијом светлосних импулса и фото-катоде, пролазе кроз пар убрзавајућих електрода, на електроде се примењује висок напон који је временски синхронизован са упадним светлосним импулсима. Ово узрокује просторно размештање електрона. Током овог процеса, електрони, који доспевају у простор између убрзавајућих електрода у различитим временским тренуцима, излазе одатле под различитим угловима у вертикалном правцу и доспевају на мултипликатор електрона. Овде бивају

умножени неколико хиљада пута и затим доспевају на фосфорни екран, где се поново конвертују у светлост. На фосфоресцентном екрану, слике које одговарају различитим упадним светлосним импулсима се налазе на различитим вертикалним позицијама. Дакле, вертикална оса фосфоресцентног екрана служи као временска оса за разликовање оптичких импулса у времену. Сјај (*brightness*) различитих слика на фосфоресцентном екрану је пропорционалан интензитету одговарајућих улазних оптичких импулса.

На овај начин, Streak камера конвертује временску и просторну варијацију интензитета светлости у одговарајућу расподелу тачака различитог сјаја на фосфорном екрану. Информација о интензитету упадне светлости је корелисана са сјајем слике на фосфорном екрану, а време доласка (на Streak камеру) и позиција упадне светлости је корелисана са локацијом слике на фосфорном екрану.

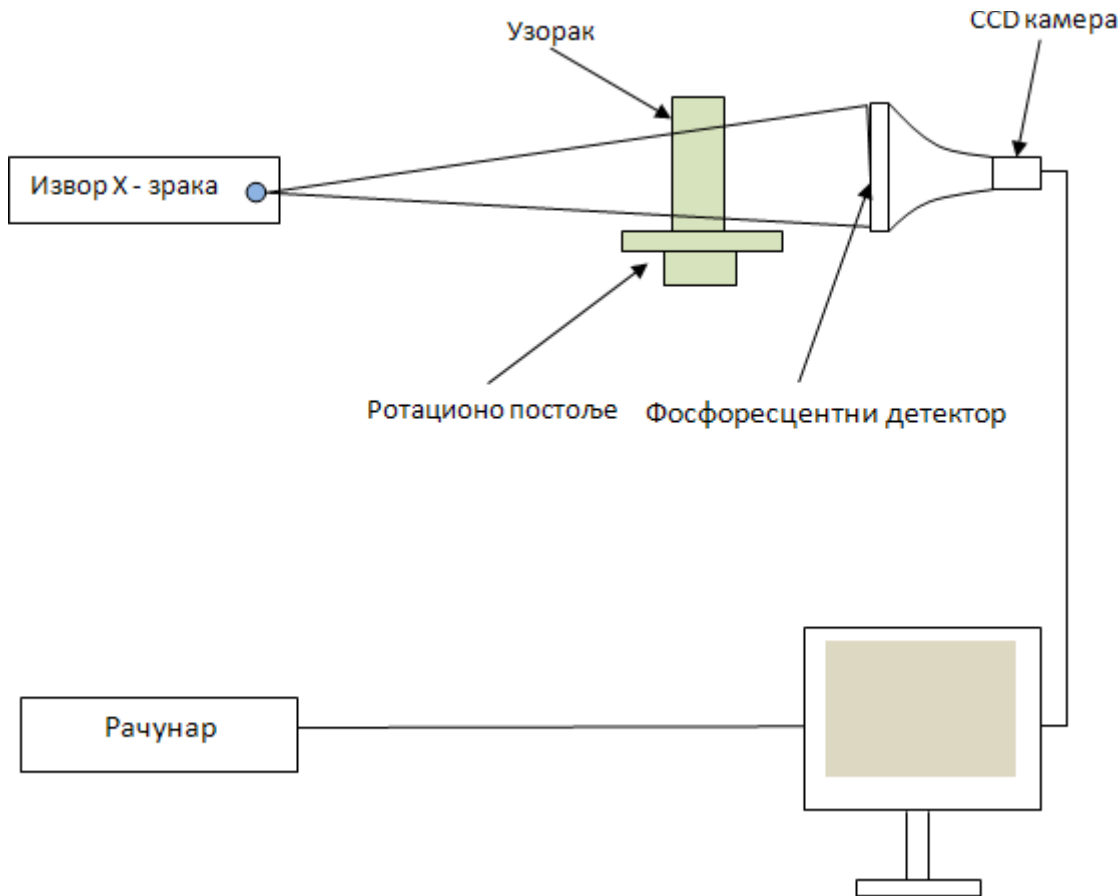
У комбинацији са спектроскопом Streak камера може да мери временску промену интензитета светлосног импулса на одређеним таласним дужинама (*time resolved spectroscopy*). На овај начин је, у оквиру ове дисертације, показано постојање другог хармоника хитина (поглавље 3.3). У комбинацији са одговарајућим оптичким системом могуће је мерити и временску зависност упадне светлости у зависности од позиције (*time and space-resolved measurement*).

## 2.1.5. Компјутеризована микро – томографија

Компјутеризована микро-томографија је 3Д осликавајућа техника у којој се користе X-зраци за осликавање унутрашњости узорка [335]. Уз специфичне уређаје може се постићи резолуција од  $\sim 100$  nm. Микро-томографијом се може направити серија 2Д планарних снимака унутрашњости објекта, и обрадом ових снимака добијају се 3Д модели ових објеката. У питању је неинванзивна техника која пружа информацију о унутрашњости објекта.

X-зраци пролазе кроз посматрани објекат и доспевају на детектор X-зрака, где бивају детектовани као 2Д пројекција („радиограф“). Узорак се тада заротира за веома мали угао ( $< 1^\circ$ ) и у тој позицији се такође детектује 2Д пројекција X-зрака. Овај процес се понавља до укупног угла ротације од  $180^\circ$  или  $360^\circ$ , у зависности од врсте узорка. Применом Радонове трансформације добијају се фотографије различитих попречних пресека објекта. Од овог низа фотографија се може формирати 3Д модел узорка, а од њега се може направити физички модел узорка методом штампања.

Ова техника се може користити за проучавање унутрашње структуре узорака, без потребе за сечењем. Ово омогућава проучавање порозности, физичке дебљине, запремине, густине, анализу дефеката, одређивање величине честица унутар узорка, оријентацију влакана...



Слика 5.4. Скица експерименталне поставке за компјутерску микро-томографију

### 2.1.6. Радијативна термографија

За експерименталну карактеризацију термалних особина биофотонских структура користе се термометријске методе. Једна од тих метода је термално осликавање, које омогућавају савремене ИЦ камере [291]. Ово је неинванзивна и бесконтактна техника са применама у различитим областима науке [321]. ИЦ камере могу да детектују различите делове ИЦ спектра. Термалне камере су оне које могу да детектују радијацију у опсегу 8 – 10  $\mu\text{m}$ , а неке су оперативне у опсегу 3 – 5  $\mu\text{m}$ . Ови спектрални опсежи одговарају, апроксимативно, термалним атмосферским прозорима (то су спектрални опсежи у којима атмосферски гасови показују веома малу апсорпцију инфрацрвене радијације [322]).

Теоријска основа радијационе термографије је Планков закон зрачења црног тела који показује колики је интензитет електро-магнетног зрачења које емитује црно тело, у зависности од температуре црног тела и таласне дужине радијације (формула 2.1).

$$I(\lambda, T) = \frac{2hc^2}{\lambda^5} \frac{1}{e^{\frac{hc}{\lambda kT}} - 1} \quad (2.1)$$

где је  $I$  – интензитет електро-магнетне радијације таласне дужине  $\lambda$  коју црно тело на температури  $T$ , по јединици површине и у јединичном просторном углу,  $\lambda$  - таласна дужина емитоване радијације,  $T$  - температура црног тела,  $h$  - Планкова константа,  $c$  - брзина светлости,  $k$  - Болцманова константа.

Реални материјали емитују само део енергије коју зрачи црно тело, што је описано емисивношћу материјала  $\varepsilon$ . Емисивност је коефицијент којим се мери способност материјала да емитује енергију у форми термалне радијације. По дефиницији, за црно тело у термалној равнотежи важи  $\varepsilon = 1$ . Извор који има нижу емисивност се назива сиво тело [323]. Укупна енергија коју емитује сиво тело је једнака производу његове емисивности и енергије коју емитује црно тело на истој температури.

Сви објекти међусобно размењују топлотну енергију помоћу три механизма: конвекција, кондукција и радијација. ИЦ камера (позната и под називом термална камера) детектује и мери ИЦ радијацију коју посматрани објекат емитује, и конвертује ову радијацију у „термалну“ фотографију објекта на којој је приказана температура на површини објекта. ИЦ камера се састоји од оптичког система који фокусира ИЦ радијацију на детекторски чип (низ сензора) који се састоји од хиљада детекторских пиксела распоређених у растер. Сваки пиксел реагује на фокусирану ИЦ радијацију и производи електрични сигнал. Процесор ИЦ камере преузима сигнале од свих пиксела и математичким прорачуном креира термалну фотографију објекта. На термалној фотографији, различите температуре су приказане различитим бојама. За разлику од оптичких камера, сочива код ИЦ камере не могу да буду направљена од стакла зато што стакло има веома малу трансмисију у области  $\lambda \sim > 4 \mu\text{m}$ . Зато се користе други материјали: германијум, калцијум флуорид, кристални силицијум...Изузев калцијум флуорида, ови материјали имају висок индекс преламања (нпр, за германијум  $n = 4$ ) што доводи до интензивне рефлексije (> 30% упадне радијације се рефлектује). Из овог разлога већина сочива за ИЦ камере има антирефлексионе слојеве.

У оквиру ове дисертације, емисија термалне радијације је анализирана следећим ИЦ камерама чији операциони опсези одговарају блиском ( $\lambda = 3\text{-}5 \mu\text{m}$ ) и далеком ( $\lambda = 8\text{-}14 \mu\text{m}$ ) атмосферском прозору:

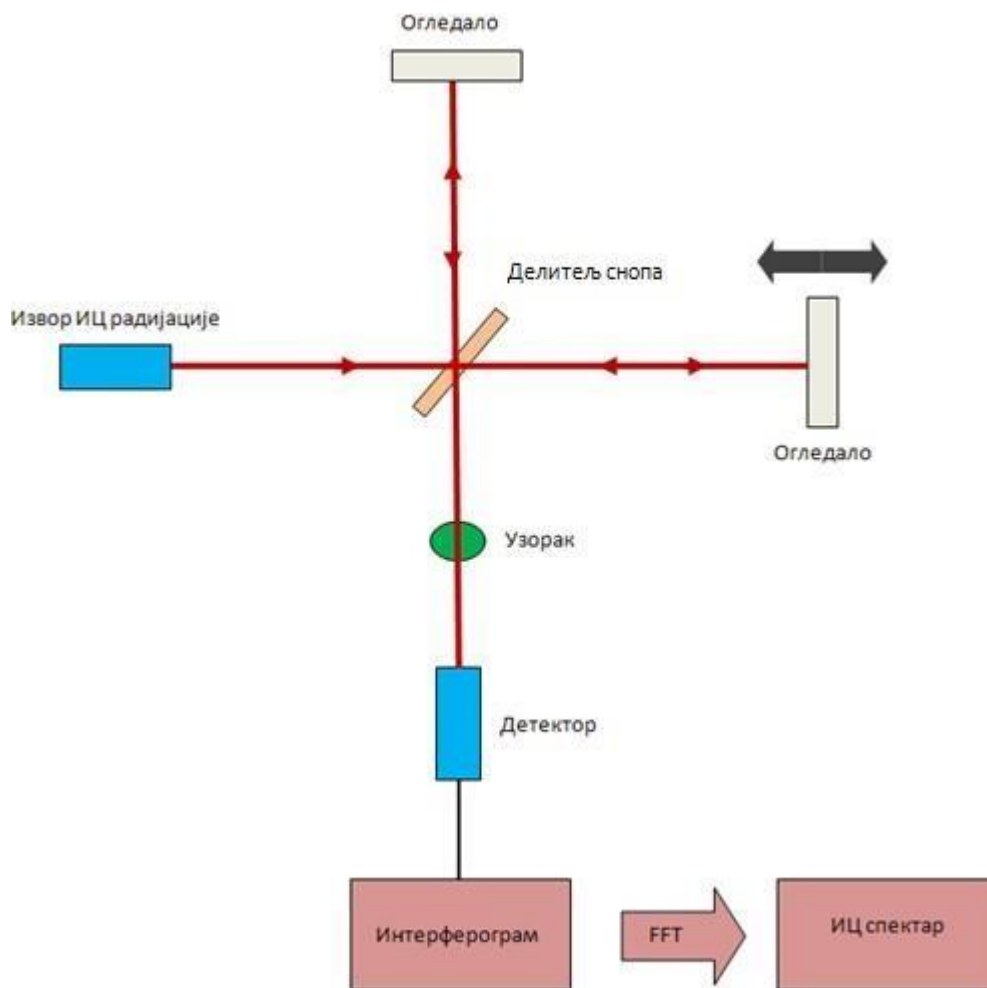
- 1) FLIR A65, USA, 640 x 512 пиксела, термална резолуција 50 mK, спектрални опсег 7.5-13  $\mu\text{m}$
- 2) FLIR SC7200, 320 x 256 пиксела, термална резолуција 20 mK, спектрални опсег 1.5 – 5.1  $\mu\text{m}$
- 3) FLIR SC620, 640 x 480 пиксела, термална резолуција 40 mK, спектрални опсег 7.5 – 13  $\mu\text{m}$

Због малих димензија инсекта, камера је позиционирана што је могуће ближе инсекту (на растојање 10-20 cm), а повремено је коришћено и додатно сочиво за додатно увећање. У оваквим условима постаје изражен „Narcissus“ ефекат (радијација коју емитује сама камера). Због тога су анализиране биофотонске структуре постављене изван термалног снопа који излази из објектива камере. Остатак камере је био прекривен алуминијумском фолијом.

Као референца за мерење термалне емисивности коришћена је алуминијумска шупљина на коју је нанесен апсорбујући материјал. Његова апсорптивност је теоријски израчуната и добијена је вредност од 0.996 [292].

## 2.1.7. Фурије трансформ инфра-црвена спектроскопија („FTIR“)

Када се инфрацрвена радијација усмери на узорак, један део те радијације се апсорбује у узорку, а други део пролази кроз узорак. FTIR је техника која захваљујући интеракцији ИЦ радијације са узорком омогућава мерење ИЦ спектра узорка [293]. FTIR спектрометар се састоји од извора ИЦ радијације, интерферометра, детектора ИЦ радијације, појачавача сигнала и рачунара (слика 2.2). Извор генерише ИЦ радијацију која пада на узорак претходно пролазећи кроз интерферометар са једним помичним огледалом и затим доспева на детектор. У детектору се сигнал појачава и конвертује у дигитални сигнал (интерферограм) аналогно-дигиталним конвертором. ИЦ спектар се добија применом брзог Фуријеовог трансформа на интерферограм [293].



Слика 2.2. Шематски приказ експерименталне поставке за Фурије трансформ инфра-црвену спектроскопију („FTIR“).

FTIR спектроскопија има многобројне примене: користи се у анализи различитих материјала са комплексним хемијским саставом [294-297]. FTIR је универзална алатка за карактеризацију материјала [298, 299] а посебно у идентификацији непознатих материјала [300]. FTIR техника је коришћена у идентификацији супстанци [301] и њихових мешавина [302], и

нечистоћа [303, 304]. Такође и у анализи структурних промена и у контроли процеса производње [304-306, 315], у анализи заразних болести [307-310], за карактеризацију структуре протеина [309]. Затим, у анализи полимера и биополимера: анализа процеса полимеризације, карактеризација структуре полимера, површине полимера, деградације и модификације полимера [309-311], анализа танких филмова [312], контрола квалитета прехранбених производа [313, 314].

FTIR спектар носи информацију о врсти хемијских веза, и о ротационим и вибрационим нивоима у комплексним молекулима [316-318].

FTIR спектроскопија је коришћена у анализи апсорпције инфрацрвеног зрачења сложених хитинских микроструктура инсекта *Rosalia Alpina*. Коришћен је систем Nicolet 6700 FT-IR, Thermo Scientific, USA.

### 2.1.8. Усаглашавање индекса преламања

У оптици, материјал који се користи у техници усаглашавања индекса преламања је супстанца (најчешће течност или гел) чији се индекс преламања веома мало разликује од индекса преламања неког другог објекта (сочиво, призма...).

У биофотоници, ова техника се користи да би се смањиле Френелове рефлексије на граници два материјала. Ови материјали могу имати сложену микро и нано-структуру која значајно утиче на њихове оптичке особине. Међутим, на оптичке особине материјала такође утичу и концентрација, просторни распоред и врста пигмената, уколико су пигменти присутни у материјалу. У том случају, оптичке особине су последица комбинованог утицаја пигмената присутних у материјалу и нано-структуре материјала. Сузбијањем Френелове рефлексије на граници различитих материјала техника усаглашавања индекса преламања смањује утицај наноструктуре и на тај начин омогућава раздвајање оптичких утицаја наноструктуре и пигмената.

Нано-структурисани биофотонски материјали чије су оптичке и термалне особине истраживане у оквиру ове дисертације се састоје од хитина и шупљина испуњених ваздухом. Пошто су ово структуре отвореног типа, техником усаглашавања индекса преламања се шупљине унутар материјала испуњавају течношћу чији је индекс преламања једнак индексу преламања хитина. Овај поступак елиминише преламање и рефлексију светлости на граничним површинама хитин-ваздух и на тај начин омогућава да се елиминише утицај нано-структуре на оптичке особине материјала. На овакав начин се може истражити да ли су у материјалу присутни пигменти и, ако јесу, који је њихов допринос резултујућим оптичким особинама материјала. Процедура се састоји од мерења оптичког рефлексионог спектра истраживаног биофотонског материјала а затим се он урања у течност за усаглашавање индекса преламања и поново се мери рефлексиони спектар. У првом случају, ако су у материјалу присутни пигменти, рефлексија настаје комбинованим утицајем пигмената и микроструктуре материјала. У другом случају, поменута течност минимизира утицај микроструктуре (сузбијањем Френелових рефлексија на граничним површинама) па измерени рефлексиони спектар потиче од пигмената. Одузимањем „пигментног“ рефлексионог спектра од укупне рефлексије добија се „структурни“



рефлексиони спектар који је последица интеракције упадне светлости са микро и наноструктуром биофотонског материјала.

## 2.2. Математичко моделовање

### 2.2.1. Метод коначних елемената

Метод коначних елемената је нумерички метод за решавање проблема који се могу описати скупом парцијалних диференцијалних једначина. Заснива се на подели моделованог система на већи број мањих, једноставнијих делова, дискретизацијом простора. Ово се постиже креирањем тзв. „мреже“ објекта. Дискретизацијом диференцијалних једначина на целокупну „мрежу“ објекта добија се систем алгебарских једначина. На овај начин, метод апроксимира непознату функцију која описује проблем [319]. Процедура примене овог нумеричког метода се састоји од следећих корака:

- 1) *Дискретизација континуума.* У овој фази, посматрани проблем се дели на већи број елемената. Ови елементи су, због погодности, једноставни геометријски облици (као што су нпр. четвороугао или троугао у случају 2Д моделирања. У 3Д случају, то су призме, тетраедри... ). На овај начин, посматрани објекат се трансформише у „мрежу“ (енгл. „*mesh*“).
- 2) *Избор интерполационих функција.* Интерполационе функције се користе за интерполацију варијабли физичког поља по површини коначних елемената. Најчешће се користе полиноми, где степен полинома зависи од броја чворова додељених елементу.
- 3) *Одређивање особина коначних елемената.* У овој фази се формира матрична једначина за коначни елемент и она повезује нодалне вредности непознате функције (вредности функције у чворовима локалног коначног елемента) са осталим параметрима.
- 4) *Формирање скупа једначина коначних елемената.* Од свих једначина којима се описују сви коначни елементи формира се глобални систем једначина који описује цео проблем. Другим речима, комбинују се једначине свих локалних елемената којима је проблем дискретизован. У овој фази се задају и гранични услови (који се не налазе у једначинама локалних коначних елемената).
- 5) *Решавање глобалног система једначина.* Примењују се директне или итеративне методе. Решења глобалног система једначина су нодалне вредности непознате функције која описује цео проблем.
- 6) *Прорачун додатних резултата.* У многим случајевима потребно је израчунати додатне параметре. На пример, код решавања механичких проблема, поред прорачуна помераја, често је важно израчунати и механичка напрезања.

У оквиру ове дисертације метод коначних елемената је коришћен за анализу простирања упадне термалне ИЦ радијације (у спектралним опсезима који одговарају атмосферским прозорима 3-5  $\mu\text{m}$  и 8-12  $\mu\text{m}$ ) кроз хитински, микро-структурисани омотач *Morimus asper funereus* инсекта.

## 2.2.2. Метод преносне матрице („Transfer matrix method“)

Овај метод се користи у оптици и акустици за анализу простирања електро-магнетних и акустичних таласа у вишеслојним срединама [320]. На пример, овај метод се користи у дизајну анти-рефлексионих слојева и диелектричних огледала.

Рефлексија и трансмисија електро-магнетне радијације на граничној површини између две материјалне средине је описана Френеловим једначинама. Када се материјал састоји од већег броја слојева, онда постоји већи број граничних површина на које радијација наилази (под условом да радијација може да се простире кроз дати материјал). На свакој граничној површини између слојева долази до рефлексије и трансмисије радијације. У зависности од односа између таласне дужине радијације и дужине путање радијације између две узастопне рефлексије, рефлектована радијација (тзв. парцијални рефлектовани таласи) може да интерферира. Укупна, резултујућа рефлексија вишеслојног објекта је збир коначног броја парцијалних рефлексија са свих граничних површина на које је радијација наишла приликом простирања кроз објекат.

Метод преносне матрице се базира на чињеници да, у складу са Максвеловим једначинама, постоје гранични услови за понашање електричног поља на граничној површини између две материјалне средине. Приликом пропагације електро-магнетне радијације кроз вишеслојни материјал, ако је електрично поље познато на улазу у слој, онда поље на излазу из датог слоја, може да буде израчунато једноставном матричном операцијом. Вишеслојни материјал се може приказати преко система матрица, где сваком слоју одговара по једна матрица, и резултујућа рефлексија и трансмисија материјала се одређују множењем матрица појединачних слојева. Ово омогућава да се одреде коефицијенти рефлексије и трансмисије вишеслојног материјала.

У оквиру ове дисертације, метод преносне матрице је коришћен за анализу иридесцентне рефлексије светлости са љуспица лептира *Issoria lathonia*, која је описана у трећем делу дисертације. Метод је претходно модификован применом скаларне теорије површинског расејања, да би се узео у обзир ефекат расејања светлости на неравним површинама.

## 2.2.3. Ray tracing метод

*Ray tracing* метод се користи за прорачун путање простирања електро-магнетне радијације и базира се на апроксимацији решења Максвелових једначина која је исправна докле год је таласна дужина радијације много мања од физичких димензија објекта кроз које се радијација простире па се могу занемарити дифракциони ефекти [323]. Дакле, овај метод се заснива на геометријској оптици и Снеловом закону преламања и не може се примењивати на таласне феномене као што су на пример интерференција и дифракција (где фаза електро-магнетне радијације постаје важан параметар). С тим у вези, *Ray tracing* метод представља добру прву апроксимацију путање простирања електро-магнетне радијације кроз материјалну средину која има градијент индекса преламања, различитих апсорпционих особина и која такође садржи и дисконтинуитете у индексу преламања на којима долази до рефлексије. У оваквим условима,

радијација се рефлектује на дисконтинуитетима индекса преламања унутар материјала, или може континуално да мења правац свог простирања (одступање од праволинијске путање).

У оквиру ове дисертације, *Ray tracing* метод је коришћен као прва апроксимација простирања ИЦ радијације (у атмосферским прозорима 3-5  $\mu\text{m}$  и 8-12  $\mu\text{m}$ ) кроз спољашњи, микро-структурисани омотач *Morimus asper funereus* инсекта.

## 2.2.4. Фурије-Мелинова трансформација

Ова трансформација представља комбинацију Фуријеове и Мелинове трансформације, и инваријантна је на translацију и ротацију. Фуријеов трансформ функције  $(x)$ ,  $x \in R$ , дат је следећом једначином:

$$z(w) = \int_{-\infty}^{\infty} (x)^{-2\pi i w x} dx \quad (2.2)$$

Модуо Фуријеове трансформације  $(w)$  у било којој тачки  $w$  је инваријантан на translацију функције  $(x)$ . Такође, постоји и циркуларна Фуријеова трансформација [241], дефинисана за периодичну функцију  $(r, \theta)$ , изражена у полярним координатама  $r$  и  $\theta$  са периодом  $2\pi$ :

$$f(r) = \frac{1}{2\pi} \int_0^{2\pi} (r, \theta)^{-i\theta} d\theta \quad (2.3)$$

Модуо циркуларне трансформације је инваријантан на translацију функције  $(r, \theta)$ , што је у овом случају заправо ротација функције за угао  $\theta$ .

Мелинова трансформација [243-245] функције  $(x)$ ,  $x \in R$ , је дата следећом једначином:

$$(u) = \int_0^{\infty} (x) x^{u-1} dx \quad (2.4)$$

где је  $u$  комплексан број ( $u \in C$ ). Када је  $u$  имагинаран број ( $u = iw$ ), једначина 2.4 постаје [69,73]:

$$(w) = \int_0^{\infty} (x) x^{iw-1} dx \quad (2.5)$$

где је  $w \in R$ . Уколико се у једначини 2.5 изврши замена променљиве  $x$  променљивом  $a$  тако да важи:  $x = e^{-2\pi a}$ , ова једначина добија следећи облик:

$$(w) = \int_0^{\infty} f(a)^{-2\pi i a w} da \quad (2.6)$$

где је  $f_1(a) = -2\pi f(e^{-2\pi a})$ . Дакле, овакво мапирање координата трансформише Мелинову трансформацију у Фуријеову трансформацију и у овом случају може се рећи да Мелинова трансформација представља Фуријеову трансформацију примењену на експоненцијалној скали [249]. Примена скалирајућег фактора  $K$  на функцију, у случају описаног мапирања координата, резултира translацијом функције  $f_1$  за вредност пропорционалну  $\ln K$ . Ово за последицу има инваријантност на translацију овог облика Мелинове трансформације у тачки  $w$ , на основу инваријантности Фуријеове трансформације на translацију функције  $f$  [250, 251]. Мелинова трансформација функције двају променљивих  $(x_1, x_2)$  [233] дат је једначином:

$$(w_1, w_2) = \int_0^\infty \int_0^\infty f(x_1, x_2) x_1^{iw_1-1} x_2^{iw_2-1} dx_1 dx_2 \quad (2.7)$$

где је  $w_1 \in R$  и  $w_2 \in R$ . Мапирањем координата  $x_1 = e^{-2\pi a_1}$ ,  $x_2 = e^{-2\pi a_2}$  поново се добија Фуријеова трансформација. Магнитуда 2Д Мелинове трансформације је дакле инваријантна на скалирање функције  $f$  по једној оси.

Нека је  $(r, \theta)$  функција у 2Д равни, изражена у поларним координатама. Ако на њену циркуларну Фуријеову трансформацију применимо Мелинову трансформацију у облику који је дат једначином 2.7, добијамо Фурије-Мелинову трансформацију:

$$(l, w) = \int_0^\infty \int_0^{2\pi} (r, \theta) e^{-il\theta} r^{iw-1} d\theta dr \quad (2.8)$$

Логаритамско-поларним мапирањем координата  $(r, \theta) \rightarrow (\ln r, \theta)$  ова трансформација добија облик 2Д Фуријеове трансформације. Модуло Фурије-Мелинове трансформације је дакле инваријантан и на ротацију и на транслацију функције [248, 252-255].

У оквиру ове дисертације, Фурије-Мелинова трансформација је коришћена у реализацији технолошке примене оптичких особина љуспица *Issoria lathonia* лептира (поглавље 4, подпоглавље 4.4).

## 2.3. Алгоритми и софтверски пакети

### Алгоритам пројекције максималног интензитета

Алгоритам пројекције максималног интензитета се заснива на пројекцији воксела са највећом вредношћу сигнала, по свакој праволинијској путањи дубинског (вертикалног) сканирања узорка, на 2Д слику [337]. Назив воксел (енгл. *voxel*) је настао комбиновањем две енглеске речи: „*volume*“ и „*element*“ и означава 3Д еквивалент пиксела. Он представља појединачни елемент 3Д матрице која представља дискретизацију простора. Применом алгоритма пројекције максималног интензитета, свака ХУ координата 2Д слике представља пиксел који показује највећу вредност сигнала по Z оси (која одговара датој ХУ координати, тј. у геометријском смислу, пролази кроз тачку са датом ХУ координатом). Овај алгоритам омогућава да се на основу низа 2Д слика (хоризонтални пресеци објекта са константним растојањем између свака 2 узастопна пресека) формира 3Д модел објекта.

У оквиру ове дисертације, алгоритам пројекције максималног интензитета је коришћен у склопу VolView 3.4 софтверског пакета за 3Д визуализацију објеката осликаних на нелинеарном ласерском микроскопу. На тај начин је показана примена нелинеарних оптичких особина хитина (поглавље 3) у високо-квалитетном осликавању објекта биолошког порекла чији је доминантан састојак хитин.

## Запремински приказ

Запремински приказ (енгл. *volume rendering*) је назив за методе које се користе у визуализацији и компјутерској графици за приказ 2Д пројекције 3Д објекта (један од тих метода је алгоритам пројекције максималног интензитета, описан на претходној страни). 3Д објекат се осликава употребом скупа 2Д хоризонталних пресека објекта (ткз. „слајсова“, енгл. *slice*). Ово може бити урађено техникама попут компјутеризоване томографије, магнетне резонанце, микротомографије X зрацима. У оквиру ове дисертације су коришћене технике нелинеарне ласерске микроскопије које се заснивају на двофотонски побуђеној флуоресценцији хитина и генерисању другог хармоника. Формирани су 2Д пресеци објекта (нпр. један 2Д пресек за сваки милиметар дуж вертикалне осе објекта) и број пиксела свих осликаних 2Д пресека је константан. Овакав скуп 2Д пресека представља регуларну запреминску решетку где је сваки запремински елемент представљен бројном вредношћу која се добија узорковањем запремине коју дати елемент обухвата.

Да би се реализовала 2Д пројекција 3Д објекта, прво је потребно дефинисати позицију камере (детектора сигнала) у односу на објекат који се осликава. Затим се дефинише непрозирност (величина којом се мери немогућност простирања електро-магнетне радијације кроз елемент запремине, ова величине описује апсорпцију и расејање радијације) и боја сваког воксела употребом *RGBA* трансфер функције (*RGBA* је назив модела који се у компјутерској графици користи за приказ боје и састоји се од 4 канала: *red* (*R*), *green* (*G*), *blue* (*B*) и *alpha* (*A*), где *R*, *G* и *B* канали означавају количину радијације из „црвеног“ ( $\lambda \sim 600-700$  nm), „зеленог“ ( $\lambda \sim 500-600$  nm) и „плавог“ појаса ( $\lambda \sim 400-500$  nm оптичког дела спектра, а *alpha* канал означава непрозирност пиксела). Ова трансфер функција придружује *RGBA* бројну вредност сваком вокселу. Када је сваком вокселу у 3Д репрезентацији осликаног објекта придружена *RGBA* вредност, употребљава се један од неколико нумеричких метода којима се од овакве 3Д репрезентације објекта креира његова 2Д пројекција.

У оквиру ове дисертације, запреминским приказом су формиран 3Д модели хитинских објеката осликаних на нелинеарном ласерском микроскопу.

### „*Focus stacking*“ алгоритам

„*Focus stacking*“ алгоритам, познат и под називима „*focal plane merging*“ и „*z-stacking*“ [210] алгоритам, се користи у дигиталној обради слике. Заснива се на комбиновању неколико фотографија које су снимљене при различитим фокалним растојањима у једну фотографију. На различитим фокалним растојањима различити делови фотографисаног објекта се налазе у фокусу. Овим алгоритмом се најбоље изфокусирани делови фотографија спајају у једну фотографију која онда има већу дубину фокуса од појединачних фотографија од којих је формирана [206, 207].

Алгоритам је коришћен у оквиру *Picolay* слободног софтвера, у четвртом поглављу ове дисертације (под-поглавље 4.4) за квалитетно осликавање хитинских љуспица. Алгоритам је било потербно користити јер су хитинске љуспице у природном стању неравног облика и имају запреминску структуру.

## Софтверски пакети

Софтверски пакети који су коришћени у изради ове дисертације: COMSOL, VolView 3.4, Picolay, Blender.

## 2.4. Колориметрија

Колориметрија описује квантитавну и квалитативну повезаност између расподеле таласних дужина радијације у оптичком делу спектра и човекове физиолошке перцепције боје [219,220]. CIE дијаграм приказује човекову перцепцију спектра светлости на релативно једноставан и визуелно схватљив начин. Њиме се читав комплексни спектар приказује једном тачком. Ово је у већој мери метод упоређивања спектара и доношења квалитативних закључака о њиховој међусобној различитости, него што је егзактан приказ. Овакав приступ, помоћу CIE дијаграма, се користи и за спектралне прорачуне и приказ свих боја на екранима рачунара, мобилних телефона као и код камера и мерних уређаја.

У основи колориметрије су човекови рецептори за вид који могу бити три врсте ћелија које се налазе у очима и свака од ових врста ћелија има максималну осетљивост у одређеном спектралном опсегу из оптичког дела спектра (ти опсежи су: 420-440 nm, 530-540 nm, 560-580 nm). Човекова перцепција боје се заснива на комбинованом одговору ових трију врста рецептора на спољашњи надражај (светлост која је емитована из извора или рефлектована са објекта). У математичком смислу, свакој од трију врста ћелија се придружује функција осетљивости која показује колика је осетљивост ћелије за сваку таласну дужину из оптичког дела спектра и одговор човековог видног апарата на спољашњу побуду (тј. боја коју човек региструје посматрајући спољашњи објекат) је дат комбинованим дејством ових трију функција, при чему, ако је позната вредност двају функција осетљивости, онда вредност коју има трећа функција може да буде једнозначно одређена. Из тог разлога, у CIE дијаграму се користе три координате за квантитавно и квалитативно одређивање боје коју просечно људско око детектује: две координате боје  $x$  и  $y$  које дефинишу спектрални одзив човекових трију рецептора за вид и луминанса  $Y$  која се односи на интензитет радијације која доспева у човеков апарат за вид. Ове три координате једнозначно дефинишу тачку на CIE дијаграму и на тај начин се читав комплексни оптички спектар може приказати једном тачком. CIE дијаграм је у истраживањима у оквиру ове дисертације коришћен у приказу и моделовању рефлексионих спектара сложених биофотонских наноструктура – љуспица лептира *Issoria lathonia*.

У наредна три поглавља су представљени научни резултати у оквиру ове дисертације.

### 3. Нелинеарне оптичке особине хитина

У овом делу истраживања су испитане нелинеарне оптичке особине хемијски пречишћеног хитина и хитинских структура два пећинска инсекта. За хемијски чист хитин, истражене су ефикасност дво-фотонске побуде, флуоресцентни спектар за дво-фотонску побуду, степен фото-избелјивања и поларизациона осетљивост дво-фотонске побуде. Потврђено је генерисање другог хароника. Мерења су извршена на нелинеарном ласерском микроскопу конструисаном у Институту за физику у Београду, Центар за фотонику. Коришћен је комерцијално доступан хитин (поли – N – ацетил – 1,4-β-D-глукопираносамин) добијен из одбачених шкољки ракова (Sigma Aldrich, practical grade powder), без додатног пречишћавања. Резултати су омогућили да се у наредном делу дисертације изврши карактеризација и контролисана модификација оптичких и флуоресцентних особина фотонских структура биолошког порекла.

#### 3.1. Двофотонски побуђена флуоресценција

Двофотонски побуђена флуоресценција означава побуду атома или молекула приближно симултаном ( $10^{-16}$  s) апсорпцијом два фотона, а затим релаксацију атома или молекула емисијом фотона на другој таласној дужини [169]. Први фотон побуђује молекул на виртуелно стање док други фотон доводи до прелаза са виртуелног стања на побуђено стање. Било која комбинација два фотона чији је збир енергија једнак разлици енергија основног и побуђеног стања молекула може да изврши двофотонску побуду молекула. Из практичних разлога најчешће се користе фотони једнаких енергија при чему сваки од два фотона има приближно половину енергије и двоструко већу таласну дужину од фотона потребног за једнофотонску побуду датог молекула. На пример, два фотона у црвеном делу спектра ( $\approx 700$  nm) могу да се удруже и да побуде молекул који их апсорбује као да је у питању један фотон у ултраљубичастом делу спектра ( $\approx 350$  nm).

Оптималне таласне дужине за двофотонску побуду не могу се одредити простим скалирањем таласних дужина на којима су максимуми за једнофотонску апсорпцију, јер се квантно механичка селекциона правила разликују за једнофотонску и двофотонску апсорпцију [169-171].

Једначина која описује слабљење интензитета светлосног снопа услед апсорпције, приликом простирања светлости кроз материјал, је:

$$\frac{\partial I}{\partial z} = -\alpha_1 I - \alpha_2 I^2 - \dots - \alpha_n I^n \quad (3.1)$$

где је  $I$  интензитет светлости,  $z$  је дужина пређеног пута који је светлост прешла у материјалу,  $\alpha_n$  је апсорпциони коефицијент за симултану апсорпцију  $n$  фотона. У класичним условима осветљења, као што су Сунчева светлост или светлост лампе, само  $\alpha_1$ , коефицијент за апсорпцију једног фотона је незанемарљив, и доминантан процес је једнофотонска апсорпција. Међутим, при већим густинама фотонског флукса, које су могуће са ласерском радијацијом, и остали

коэффициенти постају незанемарљиви и тада до изражаја долазе мултифотонски процеси апсорпције. Апсорпциони коефицијент за симултану апсорпцију 2 фотона је

$$\alpha_2 = \sigma_2 N_0 \quad (3.2)$$

где је  $\sigma_2$  ефикасни пресек за двофотонску апсорпцију, а  $N_0$  је густина популације молекула у основном стању. Уколико побуђени молекул може само радијативним прелазом (флуоресценцијом) да се врати у основно стање, онда је интензитет двофотонски побуђене флуоресценције једнак:

$$I_{2PE} = 2I^2 = \sigma_2 N_0 I^2 \quad (3.3)$$

Дакле, интензитет двофотонски побуђене флуоресценције се карактерише квадратном зависношћу од интензитета побудне ласерске радијације. У процесу двофотонске побуде флуорофора апсорбује два фотона и прелази из основног у побуђено стање. Пошто су два фотона потребна за сваку двофотонску побуду, вероватноћа да флуорофора апсорбује фотонски пар је пропорционална квадрату интензитета светлости. Из тог разлога, уколико локални фотонски флукс није веома велики, вероватноћа за двофотонску апсорпцију је веома мала. Адекватан фотонски флукс се постиже конценрисуњем фотона временски користећи фемтосекундне импулсе и просторно фокусирајући светлост кроз објектив микроскопа. На тај начин се у фокалној запремини постиже довољан број фотона који могу симултано да интерагују са флуорофором и добије се значајна количина двофотонске побуде. Изван фокалне запремине, густина фотона није довољно велика да омогући симултану апсорпцију фотонског пара и не долази до побуде, што је значајна разлика у односу на стандардну конфокалну флуоресцентну микроскопију (која се заснива на једнофотонској побуди узорка).

Вероватноћа за двофотонску апсорпцију од стране молекула је изузетно мала, о томе сведочи следећи пример. При Сунчевој светлости флуоресцентни молекул Родамин Б апсорбује просечно један фотон за једну секунду једнофотонским процесом апсорпције. Међутим, исти молекул апсорбује фотонски пар (процесом двофотонске апсорпције) једном у десет милиона година [169]. Из тог разлога, иако је двофотонску апсорпцију предвидела Maria Görrert - Mauey у својој докторској дисертацији још 1931.-е године [170], први експериментални рад на овом феномену је омогућен тек појавом ласера као извора довољно светлости велике снаге. Данас се углавном импулсни ласери користе за ефикасну двофотонску побуду. Титанијум-сафирни ласер је стандардан избор [171].

Нелинеарна ласерска микроскопија која се заснива на двофотонски побуђеној флуоресценцији има значајне предности у односу на више коришћену конфокалну флуоресцентну микроскопију (која се заснива на једнофотонској побуди молекула):

- већа дубина продирања побудне ласерске радијације због веће таласне дужине и мањег расејања [172, 173]
- ефикаснија детекција флуоресцентног сигнала јер се таласне дужине побуде и сигнала значајно разликују [173-175]
- мање оштећење узорка због ниже енергије побудне радијације [176]
- одсуство паразитске (изван-фокусне) флуоресценције, јер се двофотонска побуда одиграва само у фокалној запремини унутар узорка [174, 177]
- бољи контраст услед смањеног расејања побудне радијације [178]



- нема потребе за употребом више од једног ласера када се ради мулти-модално флуоресцентно осликавање (симултана побуда већег броја флуорофора које имају различит апсорпциони спектар) [179,180]

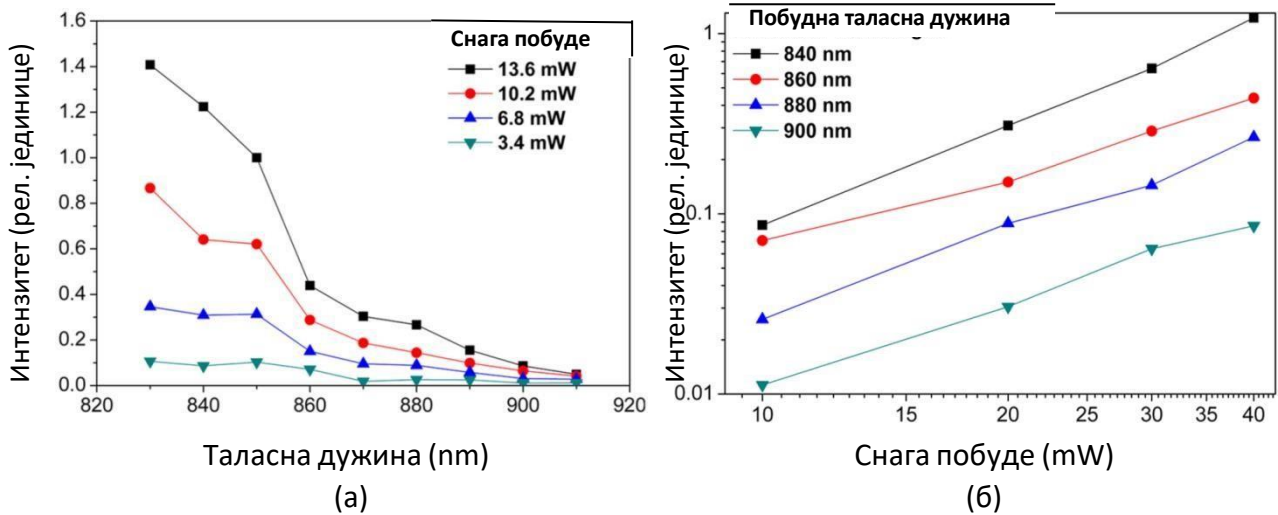
Због ових предности, ова метода има многобројне примене у: медицини (за снимање попречног пресека ћелија) [181, 182], биологији [183, 184], фармацији [185-188], хемији (за одређивање оријентације молекула) [189]... У наставку ове дисертације, биће показане примене у биофотоници, за карактеризацију и контролисану модификацију хитинских структура.

## 3.2. Двофотонски побуђена флуоресценција хитина

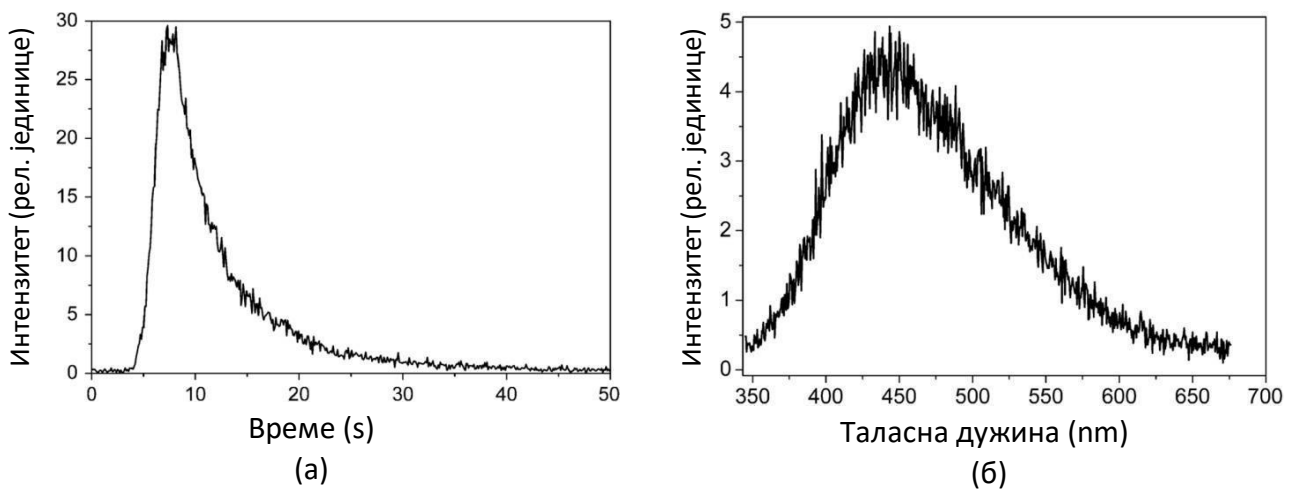
У почетном делу истраживања, измерен је интензитет двофотонски побуђене флуоресценције хитина у функцији таласне дужине (у опсегу 830 – 930 nm) и средње снаге побудног фемтосекундног ласерског зрачења (у опсегу 3,4 – 13,6 mW), добијеног из Ti-Sapphire ласера (Coherent Mira 900-F). Мале вредности снаге су изабране да би се минимизирало фото-оштећење узорка. Резултати показују да интензитет двофотонски побуђене флуоресценције опада са порастом таласне дужине побудне ласерске радијације у поменутом опсегу и да флуоресценција има максималан интензитет када је побудна таласна дужина  $\sim 830$  nm (слика 3.1a).

Зависност интензитета дво-фотонски побуђене флуоресценције од снаге побудног ласерског зрачења је приказана на слици 3.1б. Да би се нагласила квадратна зависност, обе осе су приказане у логаритамској скали. Коефицијент зависности дво-фотонски побуђене флуоресценције од интензитета побудне радијације је  $1.88 \pm 0.05$ . Мало одступање сигнала од строге квадратне зависности објашњава се релативно slabим сигналом и усредњавањем сигнала преко велике површине узорка. При већим интензитетима побуде долази и до већег фотоизбељивања (фотохемијска реакција услед које молекул флуорофоре трајно губи способност флуоресцирања. Ово је изазвано цепањем ковалентних веза и хемијским реакцијама између флуорофоре и околних молекула [324, 325]) што такође доприноси одступању сигнала од строге квадратне зависности.

За мерење једно-фотонски побуђеног флуоресцентног спектра и средњег времена флуоресценције коришћена је једно-фотонска побуда са ОПО („optical parametric oscillator“) - ласера и “streak“ камера (уређај који мери временску и спектралну зависност интензитета ултра – брзих светлосних импулса [190, 336], у Материјалима и Методама дат је детаљан опис уређаја) са спектрографом. Измерен је флуоресцентни одговор чистог хитина у функцији времена (што представља средње време побуђеног стања молекула) и добијена вредност од 5,2 ns (слика 3.2a). Флуоресцентни спектар показује максимум на 440 nm и спектралну ширину од 120 nm (слика 3.2б).



**Слика 3.1.** Интензитет двофотонски побуђене флуоресценције хемијски чистог хитина у функцији (а) таласне дужине побудног зрачења и снаге побудног зрачења као параметра; и (б) снаге побудног зрачења (приказане у  $\log\text{-}\log$  скали) и таласне дужине побудног зрачења као параметра.

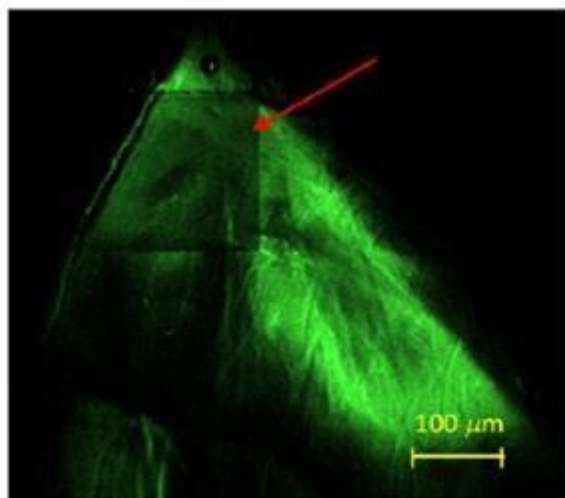


**Слика 3.2.** а) Флуоресцентни одговор хемијски чистог хитина у функцији времена; б) флуоресцентни спектар хемијски чистог хитина.

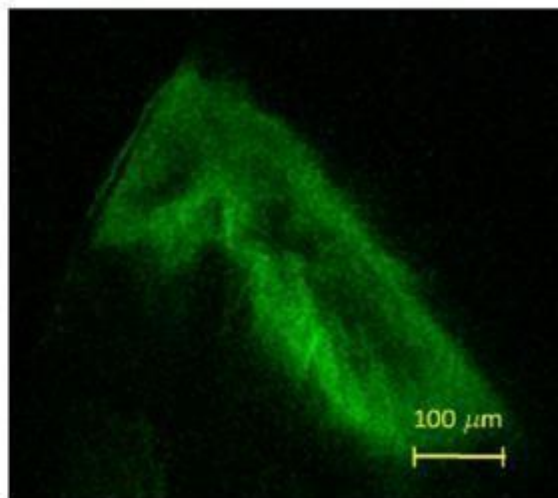
Због истраживања описаних у наставку ове дисертације, анализирани су и ефекти фото-избељивања који настају услед продуженог озрачивања хитина ласерским зрачењем. Опадање интензитета сигнала је приказано на слици 3.3а. Ови ефекти су истражени на хемијски чистом хитину и на хитину из кутикуле (спољашњи тврд омотач) пећинских инсеката. Фокусирани ласерски снап озрачува место на узорку и мери се повратни сигнал. Средња снага ласера је 70 mW, а одговарајућа густина снаге  $5,3 \text{ mW}/\text{cm}^2$ .



(a)



(б)



(в)

**Слика 3.3.** а) опадање дво-фотонски побуђене флуоресценције хемијски чистог хитина услед фото-избељивања (густина снаге ласерског зрачења од  $5,3 \text{ mW/cm}^2$ ,  $\lambda = 840 \text{ nm}$ ); б) 2PEF слика једне грануле од хитина – продужено ласерско озрачивање хитина производи квадратни регион са смањеним интензитетом флуоресценције (означен црвеном стрелицом); в) “избељени” регион није уочљив приликом осликавања узорка помоћу другог хармоника. За обе слике је коришћен  $40\times / 0.65$  микроскопски објектив. Сlike су добијене при једнакој побудној снази ласера ( $70 \text{ mW}$ ), на слици в) се уочава слабији интензитет другог хармоника хитина у односу на двофотонски побуђену флуоресценцију (слика 3.3 б).

Ефекат фото-избелјивања је веома уочљив. На слици 3.3б, прво је ласерском радијацијом озрачен цео узорак хитина (који се види на слици, у зеленој боји) а затим је при непромењеном интензитету ласерске радијације озрачен само део првобитног узорка. Густина радијације је већа на том делу узорка, и довољна да изазове процес фото-избелјивања. Услед тога, када се цео узорак поново третира ласерском радијацијом (њена снага је током целог експеримента константна) део узорка на коме је изазвано делимично фото-избелјивање слабије флуоресцира, што се може приметити као потамнели квадрат на слици 3.3б. Када се исти узорак снима користећи други хармоник као сигнал (уз помоћ ускопојасног пропусног филтера који се поставља у детекциону грану микроскопа, и који пропушта зрачење на 420 nm, јер је побудна таласна дужина у овом експерименту 840 nm), тамни квадрат је неуочљив. С обзиром да други хармоник постоји само код материјала са нецентросиметричном симетријом, ово је доказ да хитин није оштећен ласерским зрачењем, само је његова унутрашња структура перманентно промењена тако да умањује интензитет флуоресценције. Пажљивом контролом интензитета побуде ефекти фото-избелјивања су мали и не утичу на висок квалитет слике. Узорак се осликава контролисаним померањем ласерског снопа по површини узорка (сканирање узорка ласерским снопом), или унутар узорка (када се осликавају дубинске структуре материјала или биолошких организама). Контрола померања ласерског снопа на узорку обавља се галванометарским огледалима у склопу нелинеарног ласерског микроскопа (погледати Матријале и Методе за детаљно објашњење принципа функционисања нелинеарног ласерског микроскопа). Изнад одређеног нивоа снаге побудног зрачења долази до уништавања узорка, и формирања плазме. Уништавање узорка је веома локализовано и може се користити као алтернативни модалитет осликавања, што је један од праваца будућих истраживања.

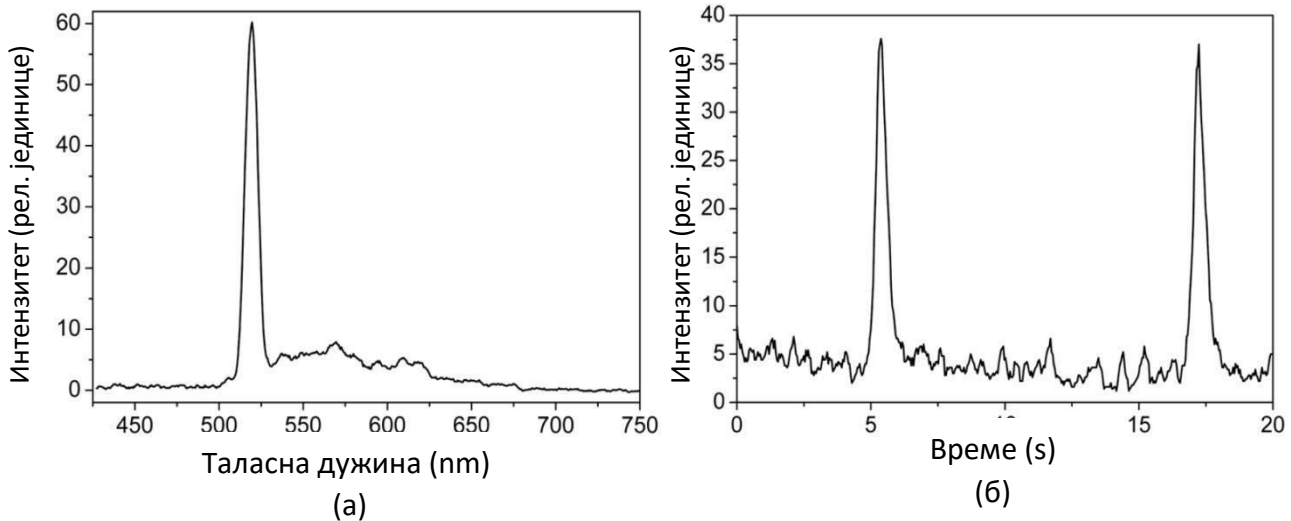
На свим побудним таласним дужинама, у свим експериментима који су у вези са нелинеарним оптичким особинама хитина, спектрална ширина ласерског импулса је максимизирана, чиме је обезбеђена минимална временска ширина импулса за све побудне таласне дужине. Дисперзионо ширење унутар оптичког система је константно и занемраљиво у датом спектралном опсегу, у поређењу са почетном ширином импулса [191].

У овом делу истраживања одређени су, дакле, оптимални параметри за употребу нелинеарне ласерске микроскопије у истраживању хитинских структура, које су веома присутне код великог броја организама. У наставку ове дисертације је истражена, између осталог, и двофотонски побуђена флуоресценција нано-структурисаних хитинских микро-објеката биолошког порекла. Ови микро-објекти, због своје нано-структуре, имају сложене оптичке особине. У интеракцији са упадном светлошћу, они испољавају низ оптичких механизма који синергијски формирају сложен оптички одзив. Нелинеарна ласерска микроскопија омогућава осликавање оваквих структура коришћењем двофотонски побуђене флуоресценције хитина и затим модификацију њихових оптичких особина ласерском модификацијом структуре (контролисано ласерско сечење и бушење структуре). Такође, може се контролисано мењати и њихова флуоресценција. Као што ће бити показано, ово има значајне примене. На тај начин демонстрирана је примена нелинеарне ласерске микроскопије и анализираних нелинеарних оптичких особина хитина у биофотоници.

### 3.3. Други хармоник хитина

Минималном модификацијом нелинеарног ласерског микроскопа омогућено је и истраживање другог хармоника хитина. Приликом истраживања способности хитина да генерише други хармоник, хитин је озрачиван ултра кратким ласерским импулсима таласне дужине 1040 nm и репетиције 83 MHz који су добијени из Yb-KGW ласера. Ова таласна дужина је коришћена да би се минимизирала дво-фотонски побуђена флуоресценција хитина. Детекциони систем се састоји од „streak“ камере и спектрографа (као што је описано у Материјалима и Методама).

Спектар другог хармоника хемијски чистог хитина показује оштар максимум на 520 nm, што је тачно једна половина од побудне таласне дужине (слика 3.4а). Измерен је и временски одзив сигнала на 520 nm (слика 3.4б) и показало се да је знатно краћи у односу на време флуоресценције хитина (5.2 ns, слика 3.2а) и близак је времену одзива детектора (приближно 260 ps). Ово је додатан доказ постојања другог хармоника за хемијски чист хитин. Два узастопна импулса другог хармоника су приказана на слици 3.4б, време између побудних ласерских импулса је 12 ns. Други хармоник хемијски чистог хитина има знатно мањи интензитет у односу на двофотонски побуђену флуоресценцију.



**Слика 3.4.** (а) спектралне и (б) временске карактеристике другог хармоника хитина. Таласна дужина побудне ласерске радијације је 1040 nm, а репетиција 83 MHz.

Други хармоник настаје услед површинске или запреминске нелинеарности другог реда, мада ова два фактора могу и симулатано да делују ако су оба присутна у материјалу. Запреминска нелинеарност је повезана са симетричношћу материјала и посебно је изражена у нецентросиметричним материјалима који показују одсуство инверзионе симетрије. У центросиметричним материјалима, запреминска нелинеарност другог реда није присутна у дипол апроксимацији, и само чланови виших редова мултипол апроксимације доприносе настанку другог хармоника.

Површинска нелинеарност другог реда настаје на граничној површини материјала услед дисконтинуитета у структури и у нормалној компоненти електричног поља упадне електромагнетне радијације, што доводи до великог градијента електричног поља по површини материјала. Чак и у центросиметричним материјалима, инверзиона симетрија је нарушена на граничној површини материјал – спољашња средина, што доводи до изражене дипол нелинеарности другог реда. Због овога, површинско генерисање другог хармоника је доминантно у нелинерном одзиву центросиметричних материјала, што се може употребити за осликавање и наализу површине оваквих материјала.

Детекцијом другог хармоника су у овом делу истраживања добијени резултати који одговарају полимерној структури хитина која није центросиметрична. Такође, у наредном делу истраживања је показана примена нелинерне ласерске микроскопије у осликавању хитинских структура природног порекла. За ову примену су кључне нелинеарне оптичке особине хитина. Експериментално је утврђено да употреба двофотонски побуђене флуоресценције и употреба другог хармоника хитина представљају комплементарне технике осликавања – када се као сигнал користи двофотонски побуђена флуоресценција, унутрашњост објекта је осликана са већим квалитетом у односу на ивице објекта, док је ситуација обрнута када се као сигнал користи други хармоник (погледати на пример, слику 3.13). Дакле, комбиновање ове две технике омогућава да се добију микроскопске фотографије са потпунијом информацијом.

## 4. Оптичке особине хитинских наноструктура биолошког порекла и њихове примене

Инсекти су доста коришћени у технологији, на пример у производњи свиле, меда, кармина (пигмент). Међутим, и многи принципи еволутивно развијени код инсеката могу наћи своју примену. Поједине врсте које припадају фамилији *Cicadoidea* (ови инсекти имају дугачка транспарентна крила, налик на домаћу мушицу) поседују природан звучник који им служи за појачање звука који њихова крила производе током летења [192]. Лептири са „стакленим“ крилима (*glasswing butterflies*) имају готово потпуно транспарентна крила што ствара утисак невидљивости [193, 194]. Поједини инсекти имају специфичну структуру на површинским деловима својих тела која их чини супер-хидрофобним [195-197]. Инсект *Melanophila acuminata* полаже своја јајашца у остацима од спаљених стабала, после шумских пожара. Овом инсекту је веома важно да може благовремено и на великој удаљености да детектује шумски пожар, и он због тога поседује сензор за инфра-црвену радијацију који може да детектује пожар до на удаљеност од 5 km [198, 199].

Лептири и мољци (ред: *Leptodoptera*) су посебно занимљиви због веома великог броја врста (око 180 000) [200] и јединствених оптичких особина њихових крила која су прекривена великим бројем (500-1000 по  $\text{mm}^2$ ) минијатурних елемената – тзв. љуспица [201, 202]. Љуспице имају корен у крилној мембрани, постављене су хоризонтално уз крило, често прекривају целу површину крила густо прибијене једна уз другу, слика 4.16. Њихов доминантан градивни састојак је хитин. Могу бити различитог облика који се разликује од врсте до врсте. Просечне димензије љуспица су 50 X 100  $\mu\text{m}$ , са веома малом дебљином од 1 – 2  $\mu\text{m}$ .

Стандардна љуспица лептира или мољца се састоји од две паралелне плоче које су повезане микростубовима – тзв. трабекулама. Доња плоча, која лежи директно на крилној мембрани је равна, док горња хитинска плоча има сложену микро и нано-структуру (слика 4.26). Она се састоји од лонгитудиналних гребена који су повезани трансверзалним микро-гребенима и на овај начин је формирана мрежа правоугаоних отвора који повезују спољашњу средину са унутрашњошћу љуспице. Код различитих врста лептира и мољаца, делови љуспице (горња хитинска плоча, уздужни и попречни гребени...) могу бити различито нано-структурисани – високо специјализовани за различите оптичке (али такође и УВ и ИЦ) ефекте који настају у интеракцији упадне радијације са овим структурама. На пример, лонгитудинални гребени на горњој површини горње хитинске плоче се могу састојати од већег или мањег броја делимично или потпуно преклапајућих ламела (на пример, слике 1.3 и 1.5). У зависности од броја ламела, степена и начина преклапања ламела и међусобног растојања између суседних лонгитудиналних гребена, може се фаворизовати интерференција или дифракција упадне радијације (оптички одзив оваквих структура је најчешће комбинација интерференције, дифракције, и других оптичких ефеката), уз присуство различитих поларизационих ефеката, при чему структура може имати различите особине у оптичком, УВ и ИЦ делу спектра. Код појединих врста унутрашњост љуспице (простор између горње и доње хитинске плоче) није шушља већ је испуњена уређеним (фотонски кристал) или неуређеним хитинским структурама.

Љуспице могу имати различите улоге у опстанку организма, а једна од њих је оптичка функција – њихова сложена нано-структура узрокује њихову структурну обојеност [204] – рефлексија радијације са љуспица није узрокована пигментима већ је последица различитих

оптичких механизма којима упадна светлост интерагује са њима: интерференција, дифракција, различите врсте расејања светлости, поларизациони ефекти, мешање таласних дужина, локални таласоводи са функцијом повећања апсорпције...Доказано је да лептири имају поларизационо осетљив вид, и да могу да детектују и радијацију из УВ дела спектра, за разлику од човека, па се код појединих врста ефекти присутни у оптичком, УВ и ИЦ делу спектра међусобно разликују. Код појединих врста су присутни и пигменти, па је рефлексија комбинација доприноса пигмената и сложене нано-структуре.

У овом делу истраживања је експериментално и теоријски анализирана наноструктура иридесцентних љуспица лептира *Issoria lathonia*, (Linnaeus, 1758), оптички механизми којима оне интерагују са упадном светлошћу, варијабилност и јединственост њиховог оптичког одзива (у овом истраживању, оптички одзив је рефлексиони оптички спектар). Ова врста је истраживана због специфичног рефлексионог спектра појединачних љуспица, које се састоје од великог броја иридесцентних региона различитог спектралног садржаја насумично распоређених по површини љуспице (слике 4.1б и 4.2а). Показано је да љуспице поседују адекватне оптичке особине које их квалификују као потенцијалне оптички варијабилне елементе (сличне холограмима). Истражене су и могућности контролисане промене оптичких и флуоресцентних особина љуспица и уписивања додатних криптографских информација на љуспице, применом ласерске технологије. Истраживање флуоресцентних особина љуспица и могућности њихове модификације, због технолошких примена, обухватило је још три врсте лептира: *Argynnis adippe*, *Argynnis paphia*, *Argynnis aglaja*. Нано-структура њихових љуспица је слична нано-структури љуспица *Issoria lathonia*, љуспице су иридесцентне и у рефлексији у блиском пољу показују велики број области са независним спектралним садржајем. Услед сличности у структури и у резултујућим оптичким ефектима који су од кључног значаја за потенцијалну технолошку примену, љуспице ових трију врста су такође анализирани да би се утврдило која врста је најпогоднија за ласерску обраду и технолошку примену. Резултати истраживања су искоришћени за реализацију варијабилног оптичког елемента који је базиран на хитинским љуспицама.

## **4.1. Оптичке особине и наноструктура крилних љуспица одабраних врста инсеката**

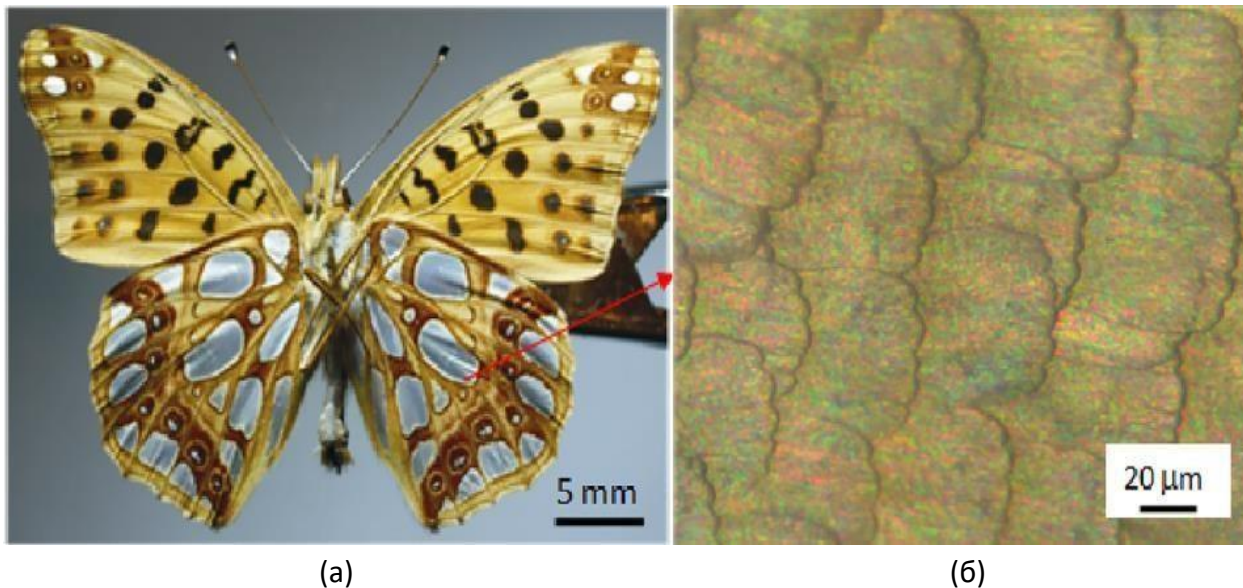
У почетном делу истраживања урађена је анализа оптичких и морфолошких особина љуспица са сребрних дорзалних делова на крилима лептира *Issoria lathonia*, (Linnaeus, 1758) који је приказан на слици 4.1. Сребрнасте зоне су изабране зато што љуспице са ових делова крила имају сложену нано-структуру и њихов резултујући рефлексиони спектар настаје приликом интеракције упадне светлости са оваквом структуром. Други делови крила, као и љуспице које се налазе на вентралној страни крила, су пигментисани, што значајно смањује интерференционе ефекте. Из тог разлога они нису били предмет овог истраживања. Оптичке особине лептирових крила и љуспица су анализирани оптичким трансмисионим и рефлексионим микроскопом и нелинеарним ласерским микроскопом. Слика љуспица у оптичкој рефлексији се добија при ортогоналном осветљењу, директно кроз објектив микроскопа. Йуспице су ручно уклоњене са крила и причвршћене на стаклени супстрат. Оне су неравне површине и поседују запреминску структуру што захтева снимање више фотографија на различитим позицијама фокуса, уз каснију рачунарску обраду („focus stacking“ алгоритам, објашњен у Материјалима и Методама), да би се добила јасна микроскопска слика. Проблем фокусираности се може решити



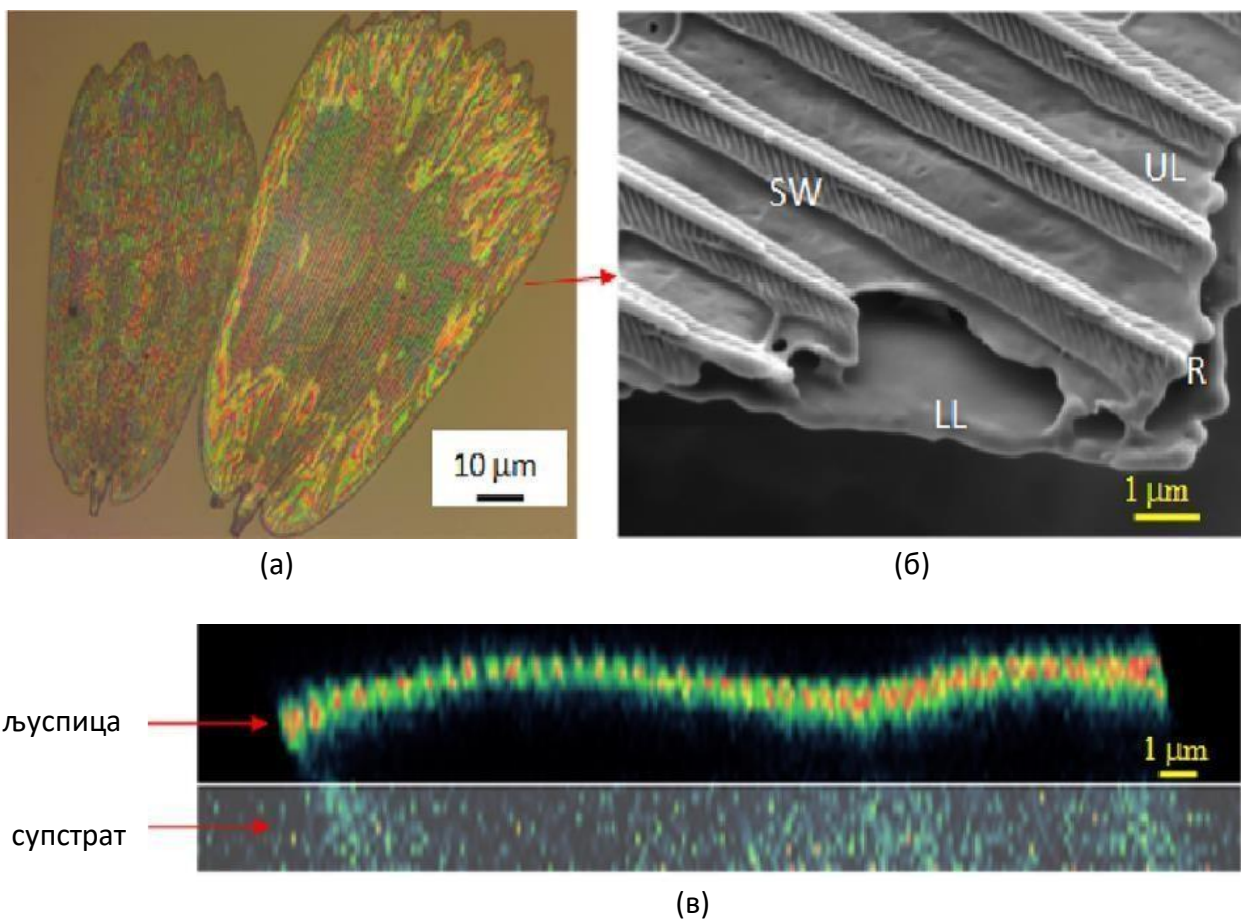
и кондензацијом водене паре која се поставља између љуспице и супстрата услед чега долази до поравњања љуспице због површинског напона. После испаравања водене паре, љуспица остаје равна и причвршћена целом својом доњом површином за супстрат услед адхезивних сила.

Лептир *Issoria lathonia* (као и остали испитивани лептири: *Argynnis adippe*, *Argynnis raphia*, *Argynnis aglaja*) поседује два слоја љуспица (тзв. базне и покровне љуспице) на дорзалној површини крила. Анализирани су љуспице из оба слоја, иако не постоје значајне разлике у њиховој структури. Поједини региони љуспице имају висок интензитет рефлексije која настаје у интеракцији (интерференција, дифракција, расејање) упадне светлости са сложеном наноструктуром љуспице. Љуспице су иридесцентне, рефлексioni спектар појединачних региона, као и целе љуспице, интензивно се мења са променом угла посматрања или осветљења. Резултујућа сребрна боја крила лептира се добија ефектом локалног спектралног мешања [213].

Детаљна, нанометарска структура љуспица је анализирана сканирајућим електронским микроскопом (Mira3, Tescan). Љуспице су пажљиво одвојене од крила и постављене на микроскопско стакло које је затим залепљено за микроскопски носач узорка. Пошто су љуспице веома фрагилне, понекад је у току процеса одвајања љуспица од крила долазило до насумичних прелома љуспица што се показало као одлична прилика да се истражи њихова унутрашња структура и попречни пресек. Други, много контролисанији, прецизнији и поузданији начин да се ово уради је употребом ласера, у оквиру нелинеарног ласерског микроскопа – уколико се ласерски сноп помера по узорку на адкватан, контролисан начин, долази до сечења узорка и откривања његове унутрашње структуре.



**Слика 4.1.** а) лептир *Issoria lathonia*, дорзална страна, б) фотографија сребрног региона на рефлексionoм оптичком микроскопу (објектив 10X / 0.25). Уочава се слој покровних љуспица са областима различитог спектралног садржаја. Сребрна боја на слици а) настаје ефектом локалног спектралног мешања.

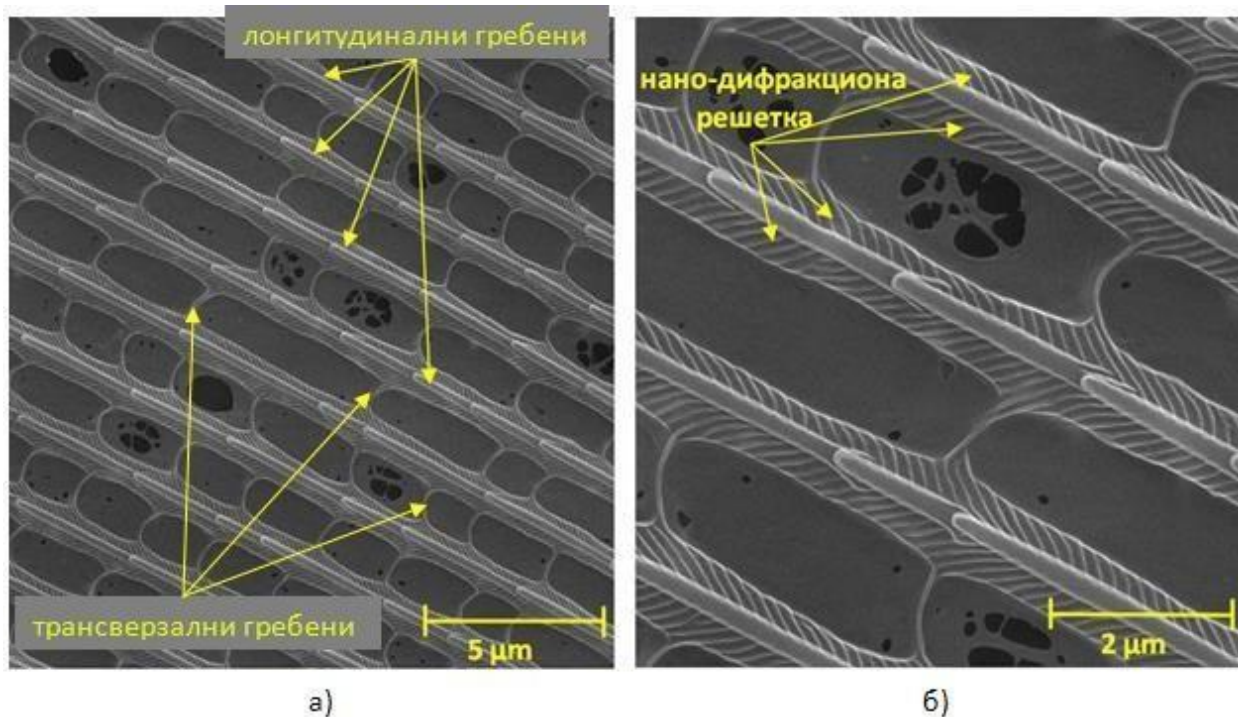


**Слика 4.2.** а) фотографија две љуспице *Issoria lathonia* лептира на оптичком рефлексионом микроскопу (објектив 20X / 0.4). Љуспице су изоловане са дорзалне површине крила (слика 4.1б). Уочава се насумичан распоред области са различитим спектралним садржајем, б) слика покривне љуспице *Issoria lathonia* лептира, са сканирајућег електронског микроскопа; LL – доња хитинска плоча, UL – горња хитинска плоча, R –лонгитудинални гребен, SW – дифракциона решетка са периодом мањим од таласне дужине светлости, у облику „рибље кости“, в) профил љуспице на нелинеарном сканирајућем микроскопу, уочава се таласаст облик љуспице.

Електронски микрограф љуспице лептира *Issoria lathonia* је приказан на слици 4.2б. Љуспица је делимично преломљена, што омогућава да се види и њена унутрашња, запреминска структура. Љуспица се састоји од две паралелне хитинске плоче, које се налазе једна изнад друге и спојене су стубовима – тзв. трабекулама. Доња плоча има равну горњу и доњу површину. Горња плоча такође има равну доњу површину, али њена горња површина (која је окренута ка спољашњој средини и на коју долази светлост из спољашње средине) има сложену нано-структуру и на њој се уочавају три дифракционе решетке: запреминска решетка која се састоји од лонгитудиналних гребена (који се простиру целом дужином љуспице) и површинска решетка која се састоји од трансверзалних гребена (који повезују лонгитудиналне гребене). Трећа дифракциона решетка, са периодом мањим од таласне дужине светлости (њен период је ~ 150 nm), у облику ребље кости, налази се на површини сваког лонгитудиналног гребена. Ово је уочљиво и на електронским микрографима љуспице који су приказани на сликама 4.2б и 4.3б. Међусобна удаљеност лонгитудиналних гребена је око 1.5 μm. Код *Issoria lathonia* лептира,

број ламела од којих се лонгитудинални гребени састоје је мали и степен преклапања ламела је занемарљив, па због тога нису изражени оптички ефекти запреминске (Брагове) дифракционе решетке. Ово је значајна разлика у односу на поједине друге врсте лептирова код којих су лонгитудинални гребенови знатно „згуснутији“ (растојање између њих је знатно мање од  $1,5 \mu\text{m}$ ) и са већим бројем слојева (већи број ламела са значајним степеном преклапања ламела – оне стоје једне изнад других и њихове дебљине су приближно једнаке), што омогућава моделовање гребенова као вишеслојних уско-појасних 1Д рефлектора (на пример, љуспице *Morpho rhetenor* и *Morpho aega* лептирова, о којима је било речи у уводном делу ове дисертације). Унутрашњост љуспице је шупља, испуњена ваздухом, и у њој се налазе само нано-стубови који повезују доњу и горњу плочу љуспице.

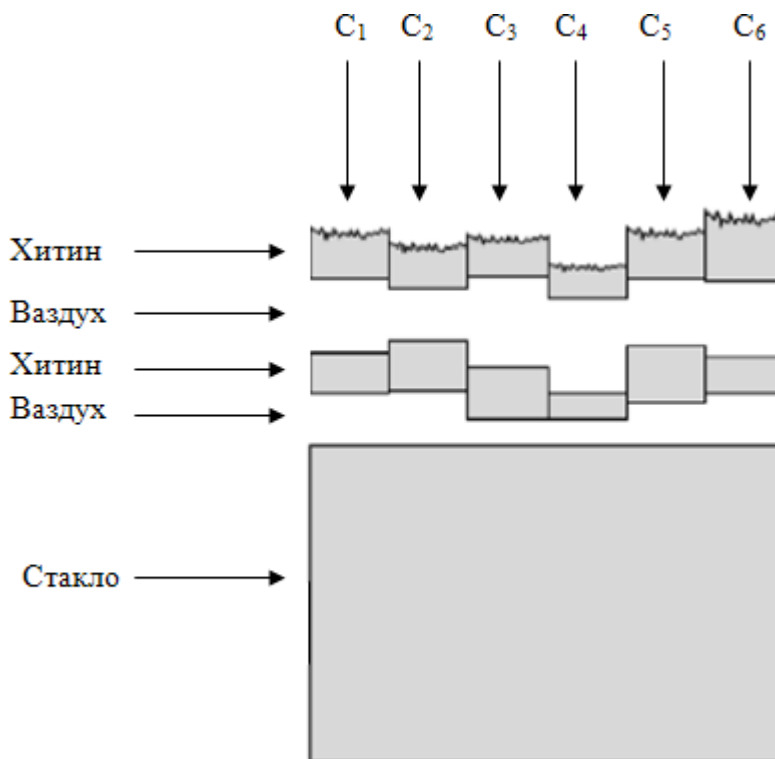
Доминантан састојак љуспица *Issoria lathonia* лептира је хитин [326]. Резултати истраживања описаног у претходном делу ове дисертације, који се односи на нелинеарне оптичке особине хитина, омогућили су да љуспице лептира *I.Lathonia* буду осликане, анализирани а затим и ласерски обрађене нелинеарном ласерском микроскопијом. Захваљујући дво-фотонској флуоресценцији хитина, нелинеарним ласерским микроскопом је потврђено је да љуспица има нерегуларан таласати облик (слика 4.2в). Ова особина веома доприноси варијабилности иридесцентног оптичког одзива, у комбинацији са варијацијама у дебљини горње и доње ламеле, варијацијама у њиховој међусобној удаљености, и осталим параметрима, што ће бити показано у теоријском моделу љуспице.



**Слика 4.3.** Електронски микрографи љуспице лептира *Issoria lathonia*. На слици а) се виде лонгитудинални и трансверзални гребени; б) сваки лонгитудинални гребен представља осу симетрије за нано-дифракционе решетке периода  $\sim 150 \text{ nm}$ .

## 4.2. Оптички модел крилних љуспица одабраних врста инсеката

У овом делу је истражена повезаност између нано-структуре љуспица и њиховог оптичког одзива – рефлексије. Са тим циљем је направљен теоријски модел, који омогућава да се израчуна рефлексиони спектар појединачне љуспице, уклоњене са крила лептира и причвршћене на транспарентан супстрат. Основни елемент модела је приказан на слици 4.4.



**Слика 4.4.** Модел покровне љуспице *Issoria lathonia* лептира. Приказан је само део модела који се састоји од 6 вертикалних региона. Цео модел се састојао од 500 региона. У даљем тексту је показано да су спектрални садржаји региона некорелисани.  $C_1, C_2, \dots, C_6$  – вертикални региони хитинске љуспице. Модел је објашњен у даљем тексту.

Да би се симулирао таласаст облик љуспице, прво је узето у обзир да је, приликом експерименталног мерења рефлексионог спектра на оптичком микроскопу, љуспица постављена на стаклени супстрат и да је због њеног облика дебљина ваздушног слоја између љуспице и супстрата варијабилна. Електронском микроскопијом је утврђено да се љуспица састоји од две хитинске плоче између којих се налази слој ваздуха. Доња плоча има равну горњу и доњу површину. Горња плоча има равну доњу (унутрашњу) површину, али њена горња површина (окренута ка спољашњој средини, и ова површина је први део љуспице са којим се сусреће упадна радијација) је, услед сложене структуре, моделована као неравна површина одређеног степена храпавости. Ова површина, дакле, улази у модел као расејавајућа структура и на тај начин се узима у обзир њена сложена микро и наноструктура која се састоји од лонгитудиналних и трансверзалних гребена и дифракционе решетке са периодом мањим од

таласне дужине светлости која се налази на површини сваког од лонгитудиналних гребена. Претпоставка је да дифракционе решетке које чине лонгитудинални и трансверзални гребени не дају значајан допринос оптичкој рефлексији, с обзиром на њихов период (период лонгитудиналне решетке је  $\sim 1.5 \mu\text{m}$ , а растојање између трансверзалних гребена је веома варијабилно, у опсегу  $3\text{-}5 \mu\text{m}$ ). Међутим, дифракциона решетка са периодом мањим од таласне дужине светлости (период ове решетке је  $\sim 150 \text{ nm}$ ) би могла да делује као високо расејавајућа структура која дифузно расејава краће таласне дужине из оптичког дела спектра. На основу оваквих разматрања, љуспица је моделована одређеним бројем вертикалних региона, слика 4.4. Сваки регион се састоји од два хитинска и два ваздушна слоја и стакленог слоја супстрата константне дебљине. Горња хитинска плоча је први хитински слој, затим следи: слој ваздуха између горње и доње хитинске плоче, доња хитинска плоча, слој ваздуха између доње хитинске плоче и стакленог супстрата, и последњи слој је стаклени супстрат (микроскопско стакло) на коме се љуспица налази током микроскопске анализе на оптичком микроскопу. Електронском микроскопијом је утврђено да различити региони имају различите дебљине хитинских и ваздушних слојева. Узимајући у обзир природан таласаст облик љуспице, као и насумичну расподелу региона различитог спектралног садржаја (што је уочљиво на оптичким микрографима, слике 4.1б, 4.2а и 4.8а), претпоставка је да су дебљине хитинских слојева различитих региона потпуно накорелисане (а биолошки узрок насумичних варијација дебљине слојева би могао да буде ћелијски шум, што ће касније бити објашњено).

За теоријски модел је изабрано да се симулира део љуспице који се састоји од 500 вертикалних региона (на слици 4.4 је приказано 6 региона). Рефлексиони спектар сваког вертикалног региона у моделу је израчунат методом преносне матрице („*transfer matrix*“ метод, који је објашњен у Материјалима и Методама), који је модификован да би се узели у обзир ефекти расејања светлости на горњој (спољашњој) површини горње хитинске плоче [213]. С обзиром да је таласна дужина упадне светлости знатно већа од храпавости горње површине љуспице (са електронских микрографа је средње квадратно одступање храпавости горње површине љуспице процењено на  $50 - 70 \text{ nm}$ ), понашање упадне светлости на овој површини се може објаснити применом скаларне теорије површинског расејања [217, 218]: светлост се на храпавој граничној површини дели на две компоненте. Једна компонента се простире као да је гранична површина идеално равна, а друга компонента („одбљесак“ – енгл. *haze*) се дифузно расејава у великом просторном углу. Обе компоненте се квантитативно дефинишу у односу на трансмитивност  $T_0$  и рефлексивност  $R_0 = 1 - T_0$  идеално равне површине, где важе Френелове једначине. Дифузна трансмитивност  $T(\lambda)$  и дифузна рефлексивност  $R_H(\lambda)$  су, у складу са скаларном теоријом површинског расејања, дефинисане на следећи начин [217]:

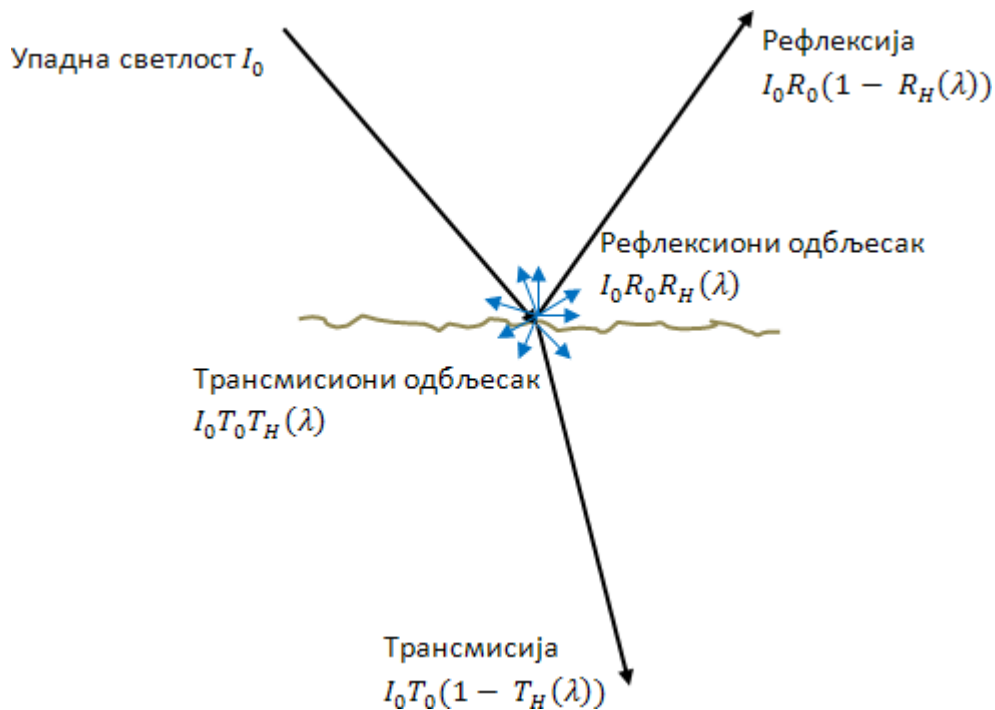
$$T(\lambda) = T_0 \left( 1 - \exp \left\{ - \left[ \frac{2\pi\sigma}{\lambda} (n_i \cos\phi_i - n_t \cos\phi) \right]^2 \right\} \right) \quad (4.1)$$

$$R_H(\lambda) = R_0 \left\{ 1 - \exp \left[ - \left( \frac{4\pi\sigma}{\lambda} (n_i \cos\phi_i)^2 \right) \right] \right\} \quad (4.2)$$

где су  $T_0$  и  $R_0$  трансмитивност и рефлексивност идеално равне површине, респективно;  $\lambda$  је таласна дужина светлости у вакуму;  $\phi_i$  и  $\phi_t$  су упадни угао светлости и угао преламања,  $n_i$  и  $n_t$  су одговарајући индекси преламања;  $\sigma$  је храпавост површине (средње квадратно одступање од

идеално равне површине). Понашање светлости на храпавој граничној површини приказано је на слици 4.5.

На основу оваквих разматрања, формиран је оптички модел појединачног вертикалног региона хитинске љуспице приказаног на слици 4.6. На равним граничним површинама, рачуна се Френелова трансмисија и рефлексија. На храпавој граничној површини (горња површина горње плоче љуспице), узима се у обзир и дифузно расејана светлост у рефлексији и трансмисији, која је описана коефицијентима  $R_H(\lambda)$  и  $T_H(\lambda)$ , респективно, у складу са скаларном теоријом површинског расејања, као што је шематски приказано на слици 4.5. Ово доводи до умањења Френелових коефицијената  $R_0$  и  $T_0$  за  $R_0(\lambda)$  и  $T_0 T_H(\lambda)$ , респективно.



**Слика 4.5.** Рефлексија и трансмисија на храпавој граничној површини, упадна светлост  $I_0$  је подељена на 4 компоненте: Френелова рефлексија ( $R_0$ ), Френелова трансмисија ( $T_0$ ), рефлексиони „одбљесак“ – дифузно расејана светлост у рефлексији ( $R_H$ ), и трансмисиони „одбљесак“ – дифузно расејана светлост у трансмисији ( $T_H$ ).

Дакле, резултујући рефлексиони и трансмисиони коефицијенти на храпавој површини,  $R_s$  и  $T_s$ , респективно, су једнаки:

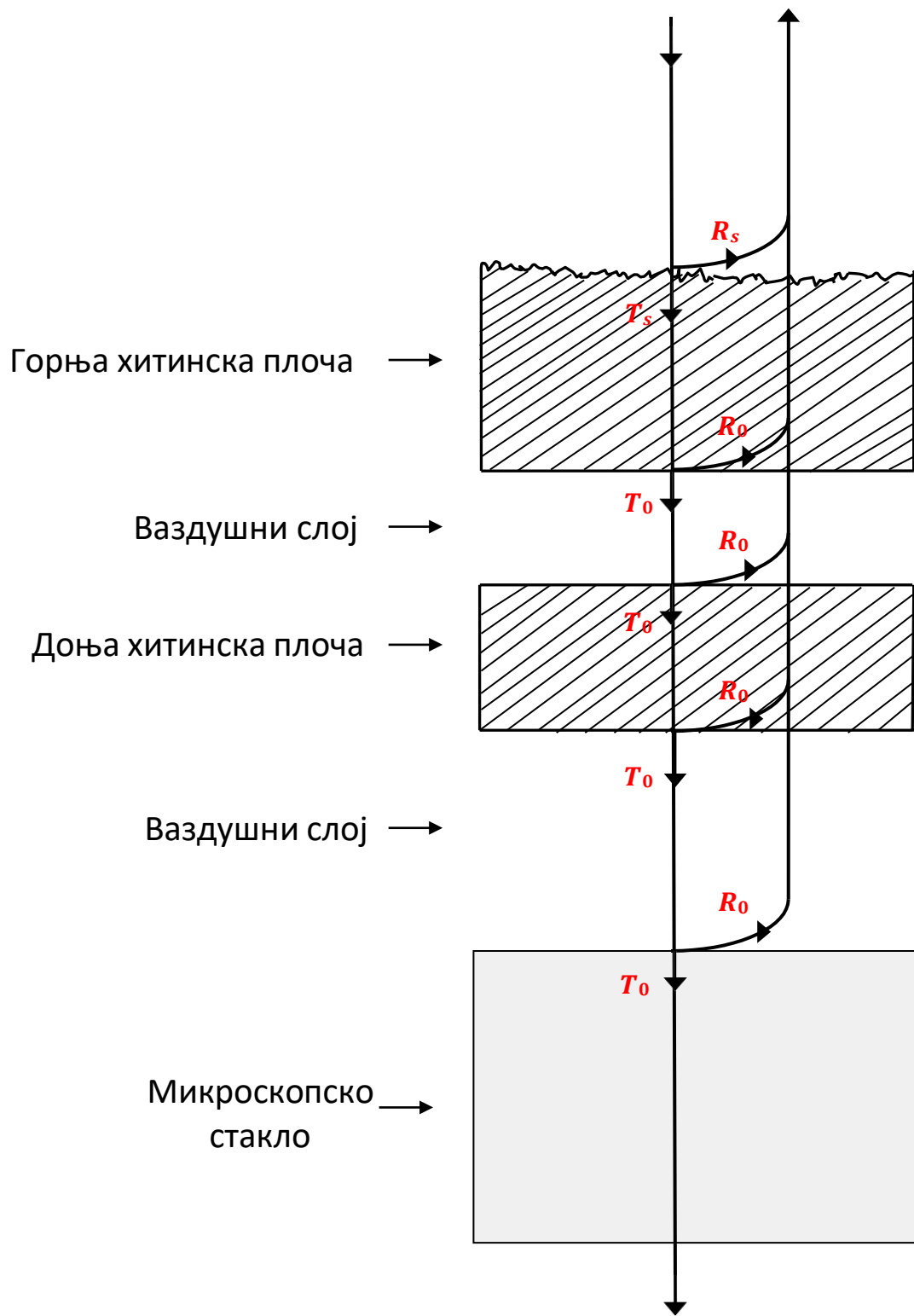
$$R_s = R_0 - R_0(\lambda) \qquad T_s = T_0 - T_0 T_H(\lambda) \qquad (4.3)$$

Френелове рефлексије и трансмисије на свим граничним површинама интерферирају међусобно као кохерентни таласи, и третиране су трансфер матрице методом. Светлост која је дифузно расејана (и у рефлексији и у трансмисији, окарактерисана коефицијентима  $R_s$  и  $T_s$ , респективно)

на хрпавој горњој површини љуспице није узета у обзир у трансфер матрице прорачуну, јер ове компоненте због своје стохастичке природе слабо утичу на интерференционо појачање и слабљење светлости. На тај начин, израчунат је рефлексионни спектар појединачног вертикалног региона хитинске љуспице.

На слици 4.4 је приказан део оптичког модела љуспице који се састоји од 6 вертикалних региона. У табели 1 су приказане вредности параметара оптичког модела, при чему су средње вредности дебљине хитинских и ваздушних слојева добијене усредњавањем скупа од 1000 вредности: љуспица је моделована са 500 вертикалних региона, у оквиру сваког региона постоје два хитинска слоја и два ваздушна слоја. Дебљине слојева су стохастички вариране, у складу са нормалном дистрибуцијом, са унапред дефинисаном стандардном девијацијом од 15 nm, а централне вредности за дебљине хитинских и ваздушних слојева су процењене са електронских микрографа – за хитинске слојеве то је 100 nm а за ваздушне 1000 nm. Вредности за средње квадратно одступање хрпавости материјала (мисли се на горњу, нано-структурисану површину љуспице) су процењене са електронских микрографа, и подешене у моделу. Индекс преламања хитина је преузет из литературе [327] и та бројна вредност је потврђена урањањем љуспице у течност са истим таквим индексом преламања (метод усаглашавања индекса преламања, објашњен у Материјалима и Методама).

За сваки вертикални регион симулиране љуспице, на основу израчунатог рефлексионог спектра, израчуната је боја и  $x, y$  координате боје које су приказане као тачка на CIE (скраћеница од француског израза Commission internationale de l'éclairage) 1931 дијаграму. Овај дијаграм је дизајниран да се блиско поклапа са човековом перцепцијом боје и описује квантитавну и квалитативну повезаност између расподеле таласних дужина радијације у оптичком делу спектра и човекове физиолошке перцепције боје [219, 220] (детаљније информације се налазе у Материјалима и Методама). Овакав приступ, који подразумева употребу CIE дијаграма, изабран је јер CIE дијаграм приказује спектар на једноставан и визуелно схватљив начин. Тиме се читав комплексни спектар приказује једном тачком. CIE дијаграм је значајан и због тога што ће се у технолошким применама користити камере које користе координате са овог дијаграма. На тај начин добијена је матрица правоугаоника одговарајућих боја, где сваком региону - правоугаонику одговара по једна тачка на CIE 1931 дијаграму. Боја правоугаоника је боја коју представља одговарајућа тачка на дијаграму. Та матрица, као и резултујућа расподела на CIE 1931 дијаграму, представљају један од резултата симулације дела љуспице који је приказан на слици 4.76.



**Слика 4.6.** Оптички модел појединачног вертикалног региона луснице *Issoria lathonia* лептира.  $R_0$ ,  $T_0$  – Френелови коефицијенти рефлексije и трансмисије;  $R_s$ ,  $T_s$  – коефицијенти рефлексije и трансмисије светлости на хрпавој површини, израчунати корекцијом Френелових коефицијената у складу са скаларном теоријом површинског расејања.



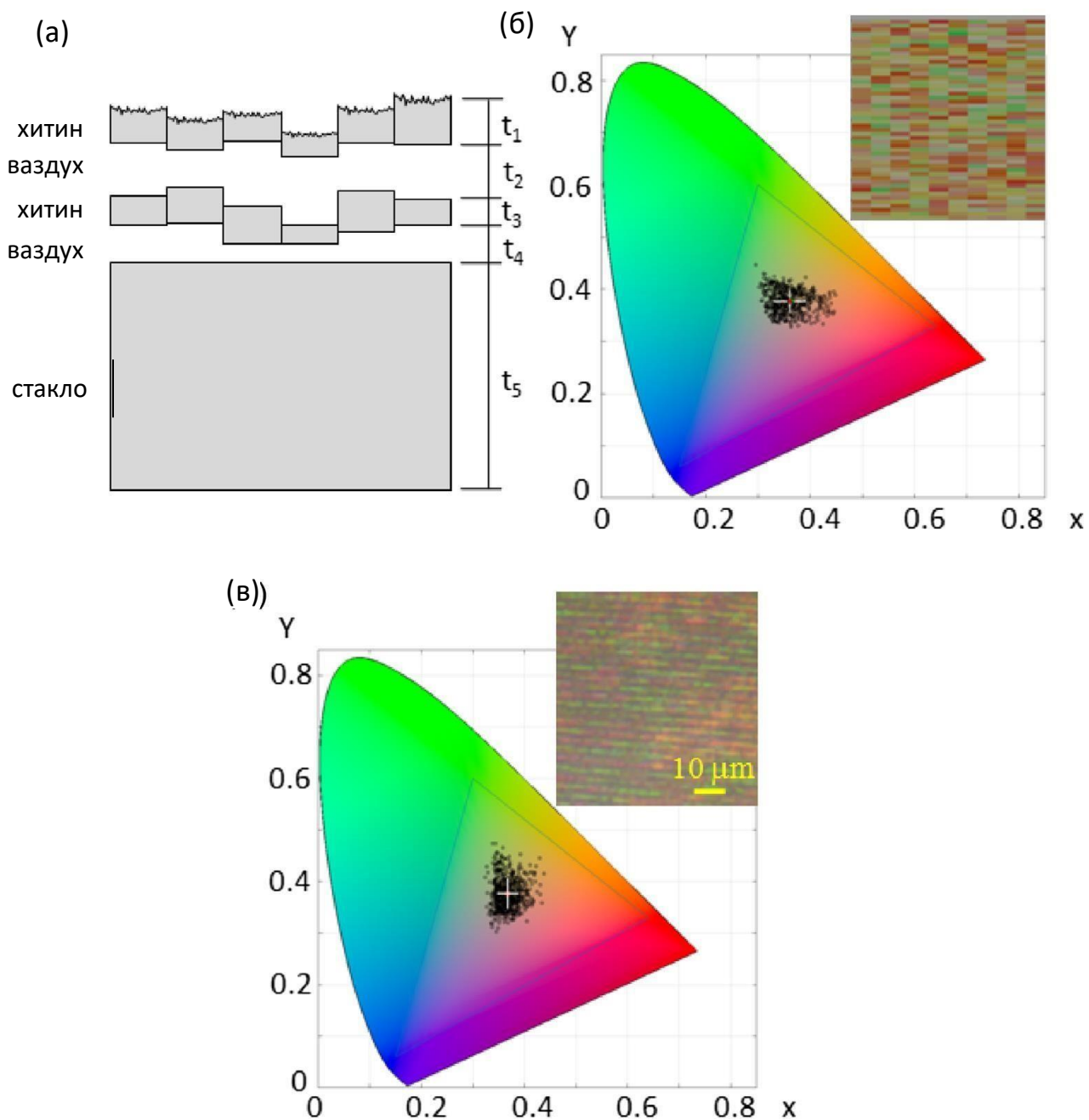
**Табела 1.** Параметри модела љуспице *Issoria lathonia* лептира.

Индекс преламања материјала (хитин)	1.57
Индекс преламања ваздуха	1
Средња вредност дебљине материјала (хитин)	108 нм
Средња вредност ваздушног слоја	969 нм
Средње квадратно одсупање храпавости материјала	59 нм
Природна варијабилност дебљине слојева	$\pm 15$ нм
Варијабилност упадног угла светлости	$\pm 3^0$

Због упоређивања експеримента и теоријског модела на СIE 1931 дијаграму је такође приказан и експериментални резултат – произвољна љуспица је камером фотографисана у рефлексији, на оптичком рефлексионом микроскопу, у правцу нормалном на површину љуспице. Анализирана је рефлексија са квадратног дела љуспице, слика 4.7в. На њему се види насумичан распоред региона различитог спектралног садржаја. РГБ вредност сваког пиксела са фотографије овог дела љуспице је приказана у СIE 1931 дијаграму. На слици 4.7в видимо скуп тачака које представљају РГБ вредности појединачних пиксела, као и њихову средњу вредност.

Није могуће добити потпуно поклапање СIE 1931 дијаграма симулације и експерименталног резултата тј. поклапање спектралног садржаја појединачних иридесцентних области на умецима слика 4.7б и 4.7в, али је остварено поклапање средње вредности координате боје за теоријски модел и фотографију љуспице у оптичкој рефлексији (средња вредност координате боје је важна јер представља „колективни ефекат“ – спектрални садржаји појединачних иридесцентних области се мешају ефектом локалног спектралног мешања и тако настаје резултујући рефлексионни спектар који се детектује и који представља средњу вредност појединачних спектра). Облик расподеле координата боје је различит за симулацију и експеримент али су стандардне девијације сличне.

Претпоставља се да је ово природна последица ћелијског шума [223], познате чињенице у биологији која резултира недетерминистичком везом генотипа и фенотипа (генотип је генетска конституција организма, у овом случају појединачне ћелије од које настаје љуспица лептира. Фенотип је скуп свих морфолошких и физиолошких својстава по којима се препознаје неки организам и по чему се он разликује од других организама исте врсте).



**Слика 4.7.** а) скица теоријског модела љуспице на стакленом супстрату, б) координате боје моделоване љуспице, приказане на CIE 1931 дијаграму, уметак: моделован образац боје љуспице, в) координате боје љуспице *Issoria lathonia* лептира, приказане на CIE 1931 дијаграму. Уметак: део љуспице, фотографија у оптичкој рефлексији, чије су координате боје приказане на CIE 1931 дијаграму. На CIE 1931 дијаграмима приказане су и средње вредности координата боја.

Ћелијски шум је појава која узрокује одређени степен насумичности параметара који одређују раст и развој ћелије, што узрокује јединственост сваке ћелије, без обзира на њену генетичку идентичност са осталим ћелијама из истог ткива. У ћелијама се одиграва мноштво биохемијских процеса, који су сви подложни термодинамичким флукуацијама. Иако су две ћелије генетички идентичне, и налазе се у истом ткиву, оне ће имати различите физичке

димензије и различите нивое експресије протеина [224, 225], што за последицу има постојање малих стохастичких разлика између генетички идентичних ћелија. Ове насумичне разлике између ћелија имају важне последице у биологији [221] и медицини [222], а у оквиру ове дисертације је показана и „оптичка“ последица у биофотоници (и њена технолошка примена, о чему ће бити речи касније, па означи овде редни број под-поглавља у коме говориш о примени): наиме, љуспица лептира је неживи, отврднути остатак ћелије, и због тога свака љуспица “замрзава“ ћелијски шум у стању у ком је био када је ћелија умрла. Самим тим, мале варијације у дебљинама физичких елемената љуспице (варијације у дебљини горње и доње хитинске плоче љуспице, варијације у дебљинама ламела које су саставни део сваког лонгитудиналног гребена, таласаст облик љуспице итд.), које узрокују варијације у оптичком одзиву, су последица ћелијског шума и као такве су потпуно насумичне. Свака љуспица је дакле, физички јединствена - све љуспице имају исти тип наноструктуре (две хитинске ламеле и слој ваздуха измеђи њих, сложену наноструктурисану горњу површину горње хитинске ламеле...), али вредности дебљине хитинских ламела, које су значајне за оптички одзив, варирају насумично код сваке љуспице. Из физичке јединствености сваке љуспице произилази јединственост њених структуром одређених оптичких особина (свака љуспица је у оптичком смислу иридесцентна, али је распоред иридесцентних области насумичан и различит за различите љуспице, ово је описано у делу 4.3), односно немогућност да се две физички идентичне љуспице генеришу природним путем. Ћелијски шум је универзална појава, и присутан је код свих ћелија. У том смислу, исти ниво јединствености се очекује и код свих осталих љуспица свих врста лептира [227], укључујући и оне код *I.lathonia* врсте.

Важан резултат симулације љуспице је и да дифракциона решетка са периодом мањим од таласне дужине светлости игра улогу оптичког дифузног рефлектора, јер „плави“ део спектра ( $\lambda \sim 400-500 \text{ nm}$ ) враћа у спољашњу средину расејавајући те таласне дужине у великом просторном углу. На овај начин, „плави“ део спектра је ефикасно елиминисан из иридесцентне рефлексије упадне светлости са крила и објашњено је одсуство „плаве“ компоненте из оптичке рефлексије (на сликама са оптичког рефлексионог микроскопа, слика 4.2а, уметак на слици 4.7в и слика 4.9а, уочава се одсуство „плавог“ дела спектра у иридесцентној рефлексији љуспице). Ово ће бити значајно код технолошке примене ових хитинских љуспица, о чему ће бити речи у под-поглављу 4.4. Поменуто расејање је донекле слично Рејлијевом расејању имајући у виду да дифракциона решетка се периодом мањим од таласне дужине светлости расејава „плави“ део спектра знатно интензивније од осталих оптичких таласних дужина. Међутим, за разлику од Рејлијевог расејања, које се дешава на честицама, овде имамо расејање на храпавој површини.

Због технолошке примене хитинских љуспица у заштити докумената, потребно је да оне испуњавају три услова који се тичу њихове нано-структуре и оптичких особина које њихова структура узрокује. Прво, свака љуспица треба да, у оптичком смислу, буде јединствена – њен оптички одзив треба да се разликује од оптичког одзива било које друге љуспице која постоји у природи. Ова особина онемогућава фалсификовање докумената коришћењем природног „дупликата“ аутентичне љуспице. Друго, потребно је да обрнути инжењеринг љуспице буде изузетно компликован, што спречава репликацију љуспице технологијом данашњице. Ово значи да нано-структура љуспице мора да буде довољно комплексна. Треће, потребно је да оптички одзив појединачне љуспице буде веома варијабилан, што онемогућава репликацију оптичког одзива једноставним колор или ласерским штампањем. У овом истраживању, за оптички одзив је изабрана иридесценција светлости са љуспице. Под варијабилношћу оптичког одзива се подразумева постојање довољно великог броја различитих иридесцентних области на хитинској љуспици – иридесцентне области са различитим спектралним садржајем, различитом угаоном и

поларизационом зависношћу спектралног садржаја итд. Јединственост и варијабилност оптичког одзива љуспица су анализирани у наредном делу истраживања.

### 4.3. Варијабилност и јединственост оптичког одзива крилних љуспица

Љуспице лептира имају довољан број степени слободе (дебљине хитинских слојева, таласаст облик љуспице, нано-структура на горњој површини љуспице, положаји лонгитудиналних гребена и њихова међусобна удаљеност и структурисаност...) који омогућава значајну варијабилност структуре а самим тим и варијабилност оптичког одзива појединачне љуспице. Варијабилност, веома важна са аспекта технолошке примене, се може дефинисати бројем степени слободе оптичког одзива љуспице на дефинисаном увећању [215, 216]. Пожељно је да број степени слободе буде што већи [226].

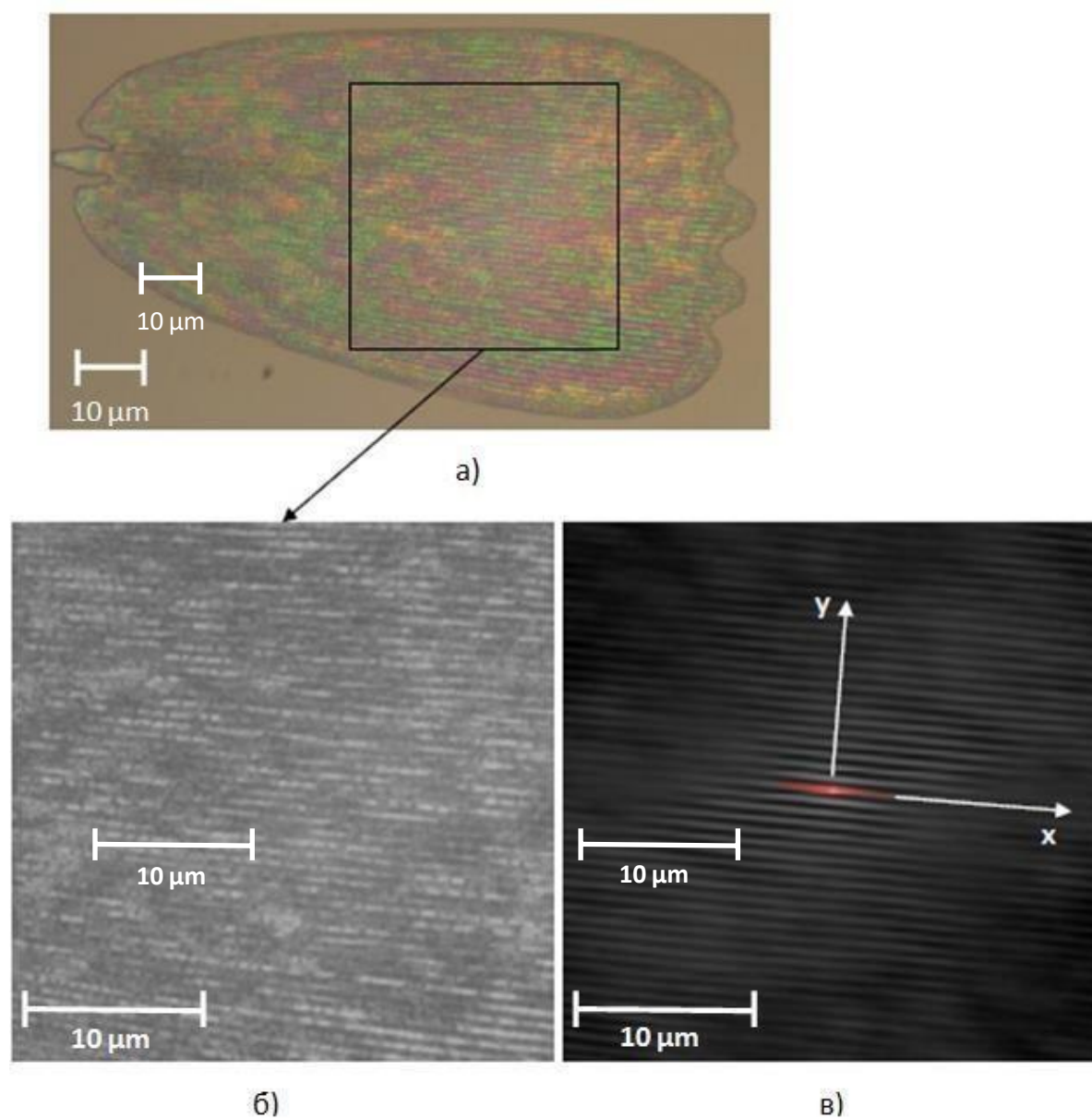
Природне варијације у нано-структури љуспице узрокују варијације у њеном оптичким одзиву. На увећаној фотографији љуспице са рефлексионог оптичког микроскопа уочава се одређени број малих светлих области различитог спектралног садржаја и високог интензитета рефлексије. Њихова позиција, оптички рефлексиони спектар и интензитет рефлектоване светлости су непредвидиви и они дефинишу степене слободе. Њихов број  $N$  је искоришћен за мерење варијабилности. Овај број се може проценити дељењем површине љуспице (горња површина љуспице ( $S$ ), која је у природном положају на телу инсекта окренута ка спољашњој средини) која се може израчунати са микрографије и просечне димензије појединачне иридесцентне области  $\Delta x$  (иридесцентне области различитог спектралног садржаја су уочљиве на микрографијама 4.1б, 4.2а и 4.9а, снимљеним у оптичкој рефлексији).

У наредном делу истраживања показана је оптичка јединственост љуспице, односно колико је тешко пронаћи у природи две љуспице са идентичним оптичким одзивом.

За параметар који се користи за одређивање јединствености љуспице, изабрана је расподела интензитета иридесцентне рефлектоване светлости у блиском пољу. Различите области љуспице рефлектују различит интензитет и спектрални садржај светлости. Фотографија лептирове љуспице (слика 4.9а) је искоришћена за анализу статистичких особина коришћењем РГБ компоненти фотографије. Анализа је извршена не узимајући у обзир облик љуспице. Из тог разлога, за анализу је употребљен означени правоугаони део са фотографије љуспице (слика 4.9а). Израчуната је 2Д аутокорељациона функција интензитета рефлектоване светлости по једном каналу боје и резултат је приказан на слици 3.8в. Пошто је степен корелације спектралних садржаја различитих области љуспице веома низак, очекује се да резултати статистичке анализе за сва три канала боје (црвени, зелени и плави канал) буду исти, па је зато анализа извршена узимајући у обзир само један од канала боје (слика 4.9б).

Аутокорељациона функција осцилује у правцу у осе и опада знатно спорије у правцу  $x$  осе. Претпостављено је да су интензитети рефлексије за две различите области љуспице статистички независни ако аутокорељација интензитета има вредност мању од 0,2. Област у којој аутокорељациона функција има ове вредности је означена црвеном бојом на слици 4.9в. Њена дужина у правцу  $x$  осе је  $\sim 30 \mu\text{m}$  а у правцу у осе  $\sim 1.5 \mu\text{m}$ .

Узимајући у обзир да су просечне димензије љуспице  $50 \times 100 \mu\text{m}$ , може се проценити да постоји приближно  $[50/1.5] \times [100/30] = 99$  региона са статистички независним спектралним садржајем на површини љуспице. Интензитет светлости по једном каналу боје може се приказати на барем 10 различитих нивоа - то је доступно на било којој јефтиној камери или камери са мобилног телефона. Дакле, може се проценити да постоји  $10^{99}$  љуспица са различитом расподелом интензитета светлости по сваком каналу боје. Са практичне тачке гледишта, пронаћи две љуспице са идентичним оптичким одзивом (са идентичном спектралном и амплитудском расподелом рефлектоване иридесцентне светлости у блиском пољу) је дакле потпуно немогуће.



**Слика 4.9.** а) фотографија љуспице *Issoria lathonia* лептира, снимљена на оптичком рефлексионом микроскопу. Део означен црним квадратом је изолован и приказана је његова зелена компонента боје, б) је употребљена за статистичку анализу; в) 2Д ауто-корелациона

функција расподеле интензитета светлости са слике б, црвена област означава регион у коме је вредност ауто-корелације већа од 0.2.

#### 4.4. Оптичка заштита са крилним љуспицама инсеката

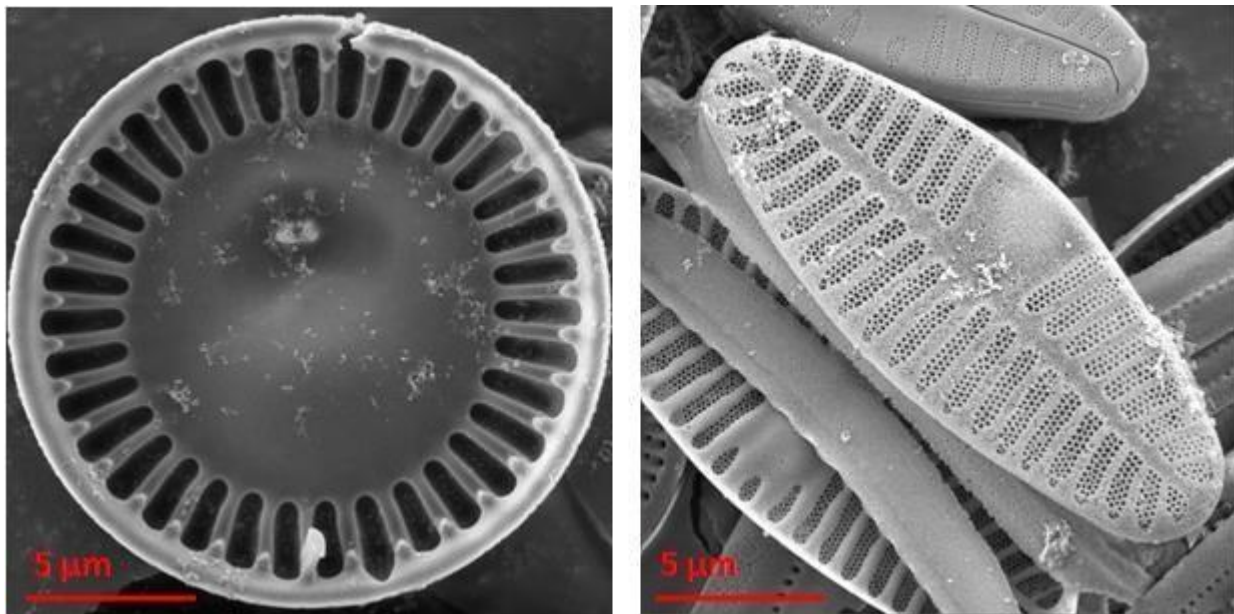
У 18.-ом веку, Бенџамин Франклин је репродуковао комплексне природне структуре са циљем заштите докумената. Његова идеја је била да распоред улегнућа и испупчења са листова биљака утисне на новчанице да би се спречило њихово фалсификовање [235, 236]. Са напретком технологије, Франклинов метод застарева и бива замењен различитим штампарским техникама као што су: дубока штампа, водени жиг, холограми итд. У данашње време, ову функцију обављају оптички варијабилни уређаји – који имају способност да мењају свој изглед са променом угла под којим се посматрају или осветљавају [237]. То могу бити различите врсте дифракционих решетки или холографских оптичких нано-структура. Они се користе због њихове инхерентне комплексне нано-структуре, сложеног оптичког одзива и могућности масовне производње, као и немогућности њиховог реплицирања фотокопирањем и сканирајућим техникама. Међутим, овакав приступ има озбиљан недостатак: велики број документа је заштићен идентичним оптичким варијабилним елементом. Дакле, ако се фалсификује заштитни оптички елемент, онда се може фалсификовати и заштићени документ и то у великим количинама. Решење за тај проблем је у индивидуализацији заштите, тако да сваки произведени заштитни елемент буде јединствен и тежак за фалсификовање. Оптички варијабилни елементи који се у данашње време користе као заштитни елементи нису погодни за индивидуализацију због тога што би онда цена њихове производње била знатно већа. Из тог разлога, важно је направити безбедносни медијум који би омогућио јединствену индивидуалну заштиту за сваки документ.

Варијабилни оптички елемент треба да буде интегрисан у безбедносни систем који се базира на три нивоа контроле [207]: први ниво је отвореног типа што значи да се контрола обавља визуелним путем, други ниво је полу-затвореног типа и подразумева примену одговарајуће контролне машине док је трећи ниво затвореног типа и базира се на форензичкој контроли високо-специјализованом опремом.

Потребно је да оптички ефекти буду локализовани, варијабилни, јединствени (овај фактор је веома карактеристичан за биолошке системе који имају потенцијал да се користе као заштитни оптички елементи, и подразумева да је готово немогуће наћи два идентична биолошка објекта у природи) и да буду последица интерференције, дифракције и расејања (укључујући поларизациону и угаону зависност) светлости са комплексне 3Д нано-структуре. Заштитни оптички елементи треба да испуњавају следеће особине: веома сложена и јединствена микро и нано-структура, да буду трајни, тежак обрнути инжењеринг и да их је веома тешко имитирати. Овакви објекти су познати под називом физичке једносмерне функције (*Physical One-Way functions*, а алтернативно се користи и назив *Physically Unclonable Functions*) [237]. То су физички објекти које је једноставно направити, али су изузетно компликовани за обрнути инжењеринг и копирање. На пример, овакви објекти се могу произвести уношењем насумично распоређених, микрометарских пластичних сфера у транспарентан материјал и детектовањем светлости расејане на оваквој структури [239]. Овакав систем има јединствене оптичке особине и његов оптички одзив је веома завистан од правца осветљења. Међутим, предложени метод је

ограничен физичким захтевима за мезоскопско расејање светлости јер заштитни оптички елемент треба да буде димензија 10 mm X 10 mm, са дебљином од 2,5 mm, што га чини непогодним за савремене безбедносне примене. Такође, расејавајуће честица су веома велике, пречника 500 – 800  $\mu\text{m}$ , уз просечно међусобно растојање од 100  $\mu\text{m}$ , што омогућава да се овај гломазан систем анализира техникама као што је микротомографија. Други пример физичких једносмерних функција је насумично расејање светлости на структурама сличним белом папиру – он се састоји од насумично испреплетаних избелјених влакана целулозе, одговарајућих пречника и индекса преламања, на којима долази до расејања упадне светлости [240]. Ласерски сноп је расејаван на таквој структури и мерене су његове карактеристике. Међутим, ово захтева скенирање велике површине објекта ласерским снопом, што је спор процес, и такође услед свакодневне употребе може доћи до значајних промена на мрежи влакана које затим могу узроковати промене у оптичком одзиву структуре.

Имитирање природних структура у сврху заштите докумената предложено је од стране Hamm-Dubischar-a [242], Biermann-a и Rauhe-a [243], и Rauhe-a [244], који су представили идеју заштите докумената уз помоћ био-минерализованих љуштура радиоларија и диатома. Ово су морски једноћелијски организми са минералном љуштуром, слика 4.10. Заштитна функција се базира на комплексности њихове структуре. Главни проблем је што оптички ефекти нису довољно изражени, и што се комплексност оваквих структура може испитивати само на морфолошком нивоу уз помоћ електронске микроскопије. Додатни проблем су мале варијације у структури љуштуре код припадника исте врсте.



(a)

(б)

**Слика 4.10.** Електронски микрографи двају врста диатома, морских организама са минералном љуштуром.

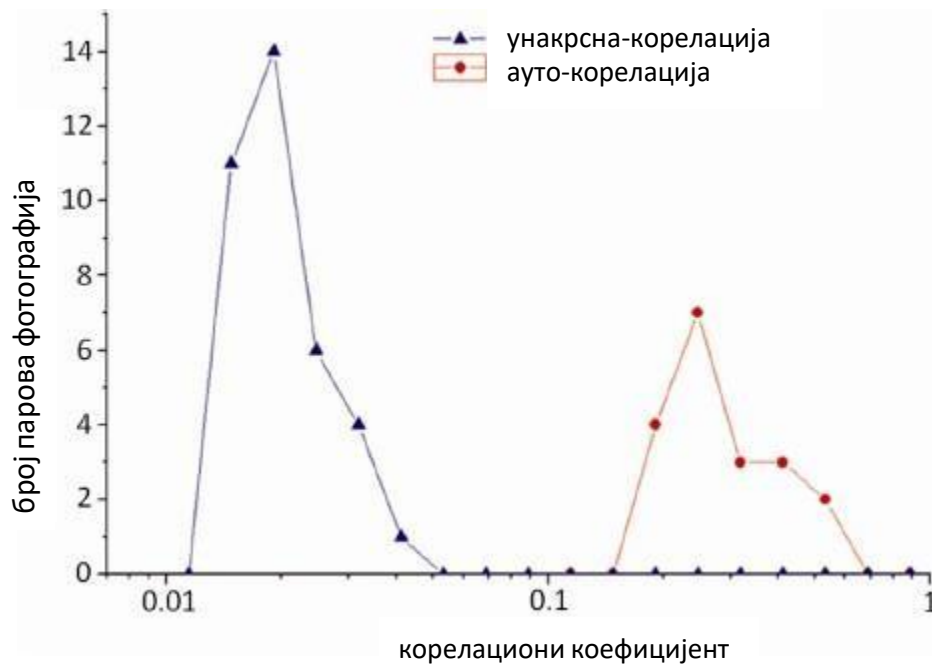
У овој дисертацији је предложено коришћење хитинских структура инсеката за заштиту докумената. Са аспекта примена у заштити докумената, најзначајнији резултат теоријског моделовања љуспица лептира описаног у делу 4.2 ове дисертације је да варијације у дебљини слојева од само  $\pm 15$  nm узокују експериментално детектибилну промену у рефлексивном оптичком одзиву. Дакле, да би се имитирао оптички одзив овакве нано-структуре, потребно је направити копију структуре која би имала сличност са оригиналом до на приближно 1,5 nm (ред величине мање у односу на поменутих 15 nm који доводе до оптичке промене која се може регистровати). Ово далеко превазилази могућности данашње технологије, а ћелијски шум онемогућава репликацију идентичне љуспице природним путем, па љуспица лептира представља физички једносмерну функцију.

Предложено је да се за технолошку примену употреби спектрална и амплитудска расподела иридесцентне рефлектоване светлости у блиском пољу која се читава оптичким микроскопом, а истражена је и могућност употребе и модификације флуоресцентних особина љуспица, о чему ће бити речи у наредном делу ове дисертације. Неколико практичних, експерименталних проблема је решено. Један од њих је немогућност постављања документа у идентичну позицију и оријентацију приликом сваког читавања. Ово захтева позиционо и ротационо инваријантан алгоритам за читавање рефлексивног оптичког одзива. Изабран је алгоритам који се базира на Фурије-Мелиновој трансформацији (ФМТ), која задовољава поменуте услове (алгоритам је објашњен у Материјалима и Методама) [246, 247].

Девет љуспица *I.latonia* лептира је постављено на стаклени супстрат и направљене су њихове фотографије на оптичком рефлексивном микроскопу, у неколико различитих позиција и оријентација љуспица (укупно 55 фотографија). Документоване слике су разложене на РГБ компоненте и зелена (Г) компонента је трансформисана ФМТ-ом. Корелације између одговарајућих ФМТ парова и статистичка расподела су приказани на слици 4.11. Корелациони коефицијент, који одговара љуспици постављеној на различитим позицијама, има вредности око 0.4 и његова вредност никада не пада испод 0.1. Најчешће вредности корелационог коефицијента за две различите љуспице су око 0.02 и никад нису биле веће од 0.06. Дакле, постављањем границе за валидност на вредност 0.08, загарантована је правилна дискриминација различитих љуспица.

Да би се кориговала дефокусираност фотографије, љуспице су фотографисане на 3-4 веома блиске фокалне позиције. Затим је употребљен алгоритам за уштавање слике по слојевима („*focus stacking*“ у оквиру PicoLay слободног софтвера да се издвоје добро фокусирани делови из сваке слике а затим су ти делови спојени у јединствену слику.





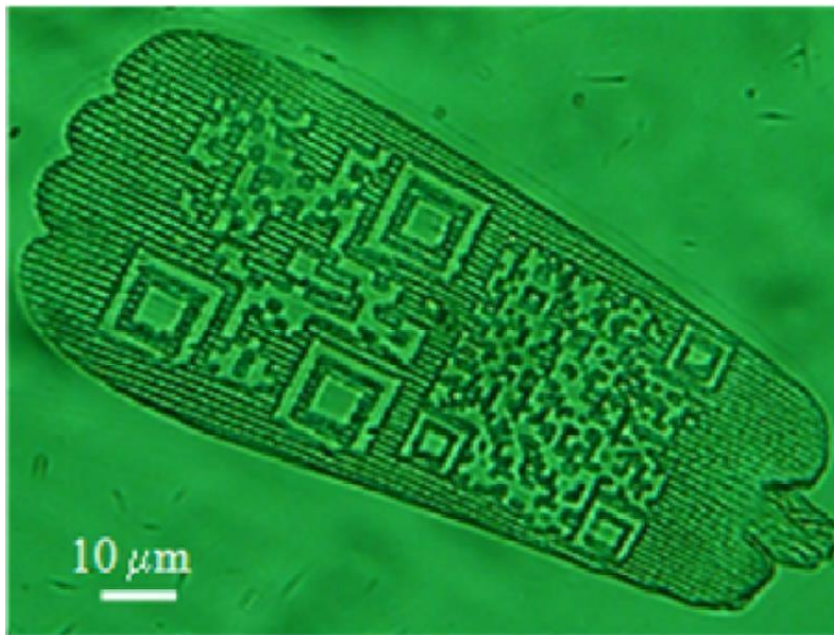
**Слика 4.11.** Унакрсна и ауто-корелација 55 парова фотографија љуспица *Issoria lathonia* лептира. На графику је приказан број парова фотографија и одговарајући коефицијент корелације. Максимални коефицијент унакрсне корелације је 0.02, док је ауто-корелациони коефицијент увек већи од 0.2

#### 4.5. Флуоресцентне особине крилних љуспица одабраних врста инсеката и ласерска обрада

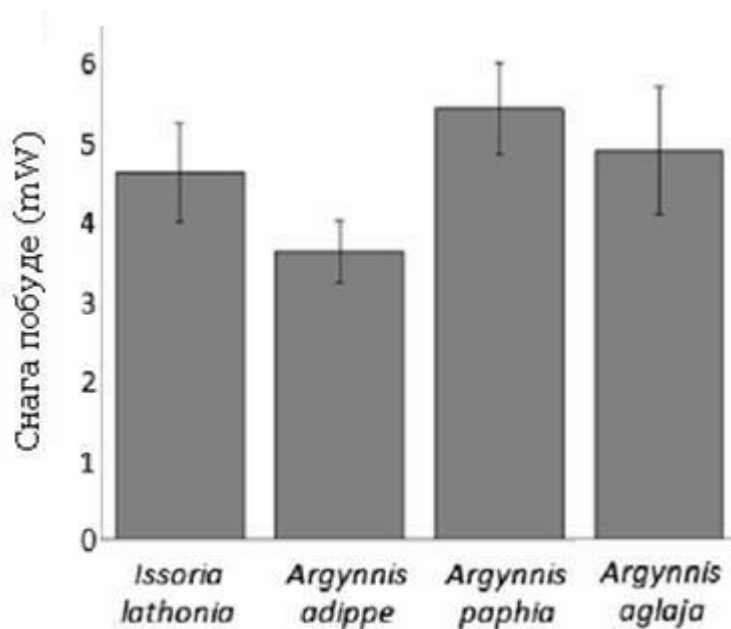
Да би се изградио квалитетан заштитно-оптички систем, потребно је заштити се од покушаја употребе привољне љуспице лептира. Да би се ово постигло, може се направити само-проверавајући документ уз помоћ дигиталног потписа издаваоца документа, у оквиру система јавног кључа. У овом делу дисертације је показано да се неопходна информација о аутентичности може записати директно на љуспицу, фемтосекундним ласером. Ласерска обрада љуспица фемтосекундним ласером омогућава контролисану модификацију физичких и оптичких особина љуспица и њихову потенцијалну примену као “write-only“ меморије. У ту сврху је модификован нелинеарни ласерски микроскоп, чији је детаљан опис дат у Материјалима и Методама, а искоришћено је и знање о нелинеарним оптичким особина хитина, главног градивног састојка љуспица. Ове особине су истражене у претходном делу ове дисертације. Сlike су добијене при снагама ласерске радијације мањим од 1 mW и са максималном попречном и осном резолуцијом од 0.7  $\mu\text{m}$  и 2.1  $\mu\text{m}$ , респективно. Због упоређивања оптичког и флуоресцентног сигнала, љуспице су фотографисане и у светлом пољу, Canon EOS 50D дигиталном камером.

Информација се може уписати физичким модификовањем љуспице (ласерско сечење или бушење) или поништавањем њене флуоресценције (фото-избељивање). Физичко модификовање мења иридесценцију љуспице, док фото-избељивање мења њен флуоресцентни профил при чему иридесценција љуспице и њене остале оптичке особине остају непромењене па се због тога овај процес може искористити да се на љуспицу запише додатна, прикривена информација у форми сиве слике („gray scale“ – слике са више нивоа дискретизације) (што ће касније бити показано). Позиције два галванометарска огледала у склопу нелинеарног ласерског микроскопа се компјутерски контролишу и ова огледала омогућавају померање ласерског снопа по узорку, у складу са задатом трајекторијом. Пре доласка на узорак, ласерски снап је проширен а затим фокусиран на узорак микроскопским објективом. Софтвер ласерског микроскопа је модификован тако да омогућава исцртавање произвољних облика коришћењем векторских слика. Таласна дужина и снага ласерске радијације, поларизација, време трајања импулса и брзина сканирања љуспице ласерским снопом су вариране да би се одредиле оптималне вредности ових параметара за сечење, бушење или фото-избељивање љуспица.

По потреби, ласерски се могу обрађивати и предња и задња страна љуспице, што значајно повећава криптографске могућности и информациони капацитет љуспице. Појединачне љуспице су узете са крила лептира и пребачене на микроскопско покровно стакло. Друго покровно стако је стављено преко љуспице (на горњу страну љуспице). Овако фиксирани љуспице се могу лакше манипулисати, што омогућава олакшану ласерску обраду обе стране љуспице. Приликом трансфера љуспица са крила лептира на покровно стакло долазило је до деформације љуспице. Ова деформација може бити природна или изазвана пребацивањем и позиционирањем љуспице. Проблем је решен кондензовањем водене паре у простору између супстрата и љуспице при чему долази до исправљања љуспице услед површинског напона. После испаравања воде, љуспица остаје поравната и причвршћена за супстрат.



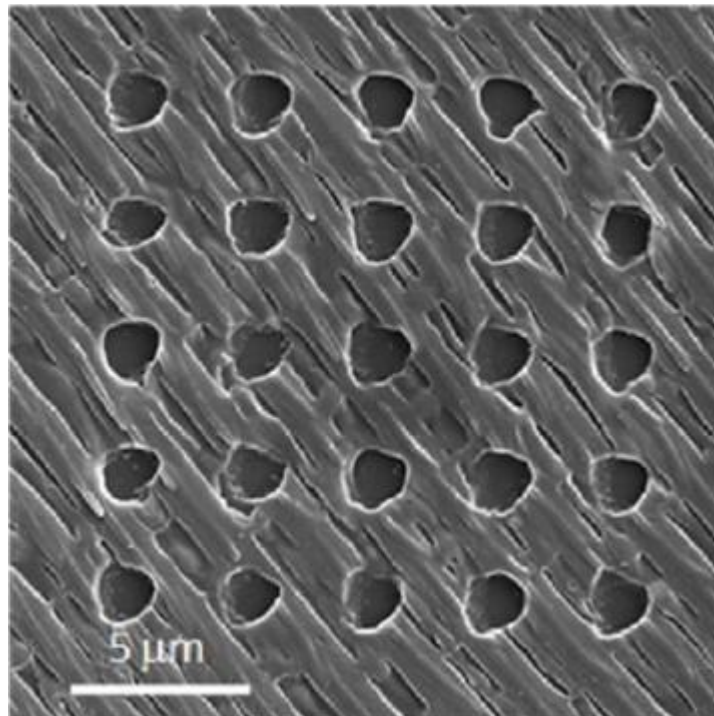
**Слика 4.12.** Фотографија љуспице *Issoria lathonia* лептира, на трансмисионом оптичком микроскопу. Љуспица је модификована - исечена фемтосекундним ласером. На љуспицу је утиснут „QR“ код.



**Слика 4.13.** Прагови оштећења ласерског сечења за 4 врсте лептира које су анализирани у овом истраживању.

Љуспице су првобитно осликане детекцијом флуоресценције која настаје услед двофотонске побуде хитина. Инструмент је затим пребачен у мод за векторско исцртавање. Повећана је снага фемтосекундног ласера тако да је могуће сећи љуспице (слика 4.12). Да би се утврдио праг оштећења (праг за сечење) исцртани су једноставни облици при различитим вредностима снаге ласера. Откривено је да прагови оштећења зависе од таласне дужине ласерске радијације, микроскопског објектива, и од врсте лептира (коришћени су *Issoria lathonia*, *Argynnis adippe*, *Argynnis paphia*, *Argynnis aglaja*), слика 4.13. Најнижи прагови оштећења су добијени на 730 nm, са 40X, 1.3NA микроскопским објективом. Сечење је могуће само у фемтосекундном режиму. У континуалном режиму ласера сечење није могуће ни на највећим снагама. Ово показује да су мултифотонски процеси одговорни за ласерско сечење.

Минимални пречник ласерски изазваног оштећења у овом истраживању је био 1.7  $\mu\text{m}$ . Најнижи прагови оштећења су 4,5 mW, када је коришћен 40X, 1.3NA микроскопски објектив и 8 mW када је коришћен 20X, 0.8NA микроскопски објектив, за  $\lambda = 730 \text{ nm}$ . У пракси је рађено на снагама изнад прага оштећења да би се обезбедила поуздана и поновљива ласерска обрада. Због тога је минимална ширина ласерског оштећења на узорку већа од латералне резолуције фемтосекундног система. У складу са овим чињеницама и узимајућу у обзир просечне димензије љуспице ( $\approx 50 \mu\text{m} \times 100 \mu\text{m} = 5000 \mu\text{m}^2$ ), процењен информациони капацитет љуспице је око 3000 битава, третирајући место оштећено ласером као бинарно 1, а неоштећено као бинарно 0. На слици 4.14 приказана је типична матрица отвора направљених ласером, која показује начин на који су анализирани информациони капацитет љуспице и оптималне вредности параметара ласерског снопа за максимизацију тог капацитета.

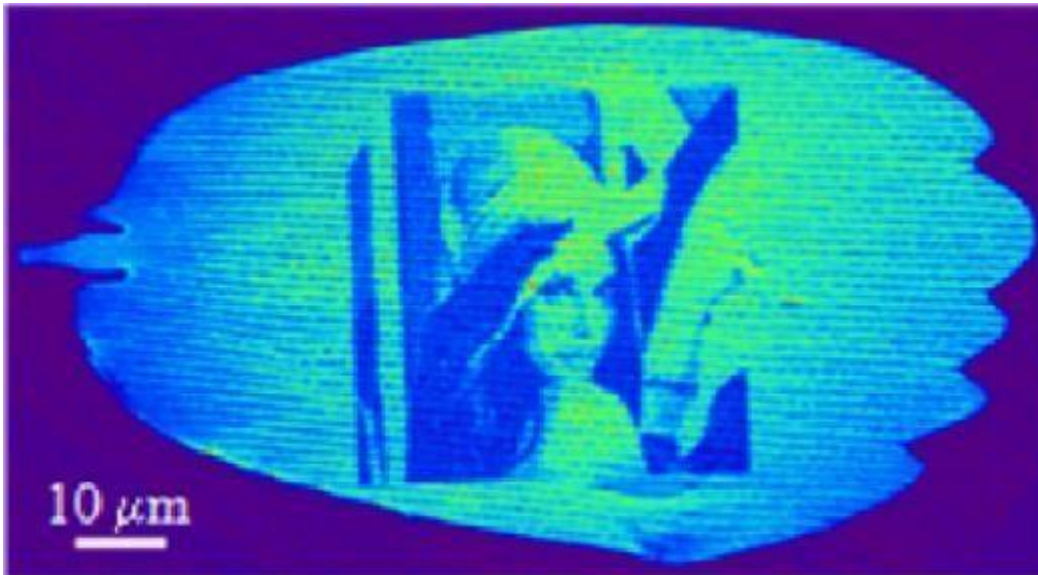


**Слика 4.14.** Матрица избушених отвора на љуспици *Issoria lathonia* лептира, електронски микрограф. Рупице су избушене титанијум-сафир ласером у фемтосекундном режиму, у оквиру нелинеарног ласерског микроскопа, са циљем одређивања минималног пречника ласерског оштећења на љуспици и, са тим у вези, одређивања информационог капацитета љуспице.

Сваки бит информације уписан на љуспицу лептира ласерским бушењем смањује број области на љуспици са статистички независним спектралним садржајем. На пример, ако се претпостави да је једна половина горње површине љуспице ласерски обрађена (што смањује нетакнуту површину љуспице са  $50 \times 100 = 5000 \mu\text{m}^2$  на приближно  $35 \times 70 = 2450 \mu\text{m}^2$ ; љуспица нема правилан геометријски облик па се зато употребљиве површине морају процењивати), онда остаје око 46 области љуспице са независним спектралним садржајем. Стога, процена броја различитих љуспица по сваком РГБ каналу, у овом случају, је  $10^{46}$ , при чему је свака љуспица заштићена са 1500 битова додатне информације.

Информациони капацитет љуспице није ни приближно потпуно искоришћен процесом бушења или сечења љуспице. Дво-фотонска апсорпција хитина (који је доминантан градивни састојак љуспица), описана у другом поглављу ове дисертације, може се искористити да се на љуспицу запише додатна, прикривена информација у форми сиве слике. Ово се може постићи ултра брзим ласером у склопу нелинеарног ласерског микроскопа. Таласна дужина ласера је изабрана тако да фото-избељивање настаје као последица једно-фотонског процеса апсорпције (када се користи континуална ласерска радијација) или дво-фотонског процеса (када се користи фемто-секундна ласерска радијација). Таласна дужина, снага ласерске радијације и брзина сканирања љуспице ласерским снопом одређују степен фото-избељивања. Таквим приступом на

љуспицу је утиснута фотографија, селективним ласерским избелјивањем одређених региона љуспице, слика 4.15. Информација се може регистровати УВ радијацијом ниског интензитета, као прикривени ниво заштите. У оптичкој рефлексији, информација се не може регистровати. Алтернативно, информација се може уписати УВ радијацијом ниског интензитета коришћењем УВ пројекционог система који се састоји од УВ лампе и одговарајућег објектива. Маска, која садржи транспарентне и нетранспарентне делове, који чине слику – информацију, поставља се у систем тако да се жељена слика пројектује директно на љуспицу. Фото-избелјивање се контролише интензитетом УВ радијације и временом озрачивања узорка.



(a)



(б)

**Слика 4.15.** Фото-избелјивање; а) селективно избелјена љуспица са мотивом Лене, б) селективно избелјена љуспица са мотивом отиска прста. Слике су добијене на нелинеарном

*ласерском микроскопу, на основу двофотонски побуђене флуоресценције хитина. Сlike Лене и отиска прста се не могу регистровати у оптичкој рефлексији.*

Описана заштита докумената је ограничена на машинско читавање. Ово може бити проширено на форензички ниво, читавањем слике са електронског микроскопа при чему насумична карактеристика могу, нпр, да буду растојања између суседних трансферзалних гребенова на горњој површини љуспице. Ако је потребна визуелна контрола, може се уместо једне, употребити велики број љуспица, које прекривају велику површину на супстрату, видљиву голим оком. На овај скуп љуспица, могу се ласерски угравирати различити облици – нпр. отисак прста власника или ирис ока власника документа, при чему одређени број љуспица због ласерске обраде стиче промењене оптичке особине. Једна од ласерски немодификованих љуспица се онда може изабрати за машинско и форензичко испитивање [206].

## **4.6. Разматрање оптичко-заштитне функције крилних љуспица инсеката**

Када се говори о заштити документа, поставља се важно питање: колико је тешко фалсификовати љуспицу лептира? То љуспице подразумева: имитирање саме структуре љуспице, која би онда у интеракцији са упадном светлошћу давала идентичан оптички одзив, или имитирање оптичког одзива љуспице неком другом, једноставнијом структуром. Први приступ се базира на обрнутом инжењерингу и на производњи идентичне структуре – љуспице, док се други приступ базира на имитирању оптичког ефекта.

Обрнути инжењеринг је процес који се састоји из две целине: прва подразумева анализу 3Д структуре целе љуспице, и анализу особина материјала од кога се љуспица састоји (индекс преламања и апсорпција). Други део обухвата синтезу копије љуспице која треба да има оптичке особине идентичне оригиналу, дакле постојање литографске технике којом би се копирала структура и особине материјала. Чак и уз употребу најбољих технологија данашњице (микротомографија, електронска или рентгенска холографија) овај приступ је немогућ због резолуције данашњих 3Д аналитичких и литографских техника (реда величине 10 nm), времена потребног за овако нешто и цене [228].

Имитирање оптичког одзива, с друге стране, захтева пажљиву анализу рефлексије у целом оптичком делу спектра и пуном просторном углу, уз поседовање метода да се веродостојно репродукује оптички таласни фронт. Овде се појављује фундаментално питање: да ли различите структуре могу да генеришу идентичне таласне фронтове? Овим питањем се бави теорија расејања, и постоји мноштво радова који се баве директним и инверзним проблемима ове врсте. Не постоји општи одговор на ово питање, јер он зависи од природе расејавача (транспарентан или нетранспарентан расејавач), граничних услова (проводник, диелектрик, појачавајућа средина), таласне дужине и просторног угла пробне радијације [229]. Постоје мање или више егзотичне ситуације у којима јединственост није загарантована, као што су појачавачка средина и оптички плаштови [230, 288]. Али, када се ради о предмету овог истраживања, одговор је – не постоје два различита расејавача који производе исто расејано оптичко поље (блиско и далеко)

[231].

Љуспице лептира су најбоље заштићене њиховом јединственошћу из које произилази неопходност фалсификовања сваког документа испочетка. Нано-структура сваке љуспице су јединствена (о овоме је било речи у деловима 4.2 и 4.3 ове дисертације ) и у интеракцији са светлошћу производи низ оптичких ефеката: општи облик рефлексивног сектора, иридесценција, апсорпција, поларизација, флуоресценција, Моире, дефекти, дифракција у блиском и далеком пољу, локални спектар итд. Додатно, љуспице појединих врста лептира имају различите оптичке особине на горњој и доњој површини што се може искористити за читавање оптичког одзива са обе стране љуспице у савршеном поравнању („see-through register“ – једна од техника која се примењује у области заштите, нпр. новчаница). Симултана употреба свих или неких од поменутих ефеката значајно повећава могућности употребе љуспица лептира као заштитног варијабилног оптичког елемента.

Важно питање је да ли љуспице лептира могу да буду копиране неком холографском методом. До сада су површински и запремински холограми копирани контактним [232], неконтактним [233], и сканирајућим методама [234]. Међутим, ове методе нису погодне за копирање слојевите нано-структуре љуспица лептира због синусоидне природе холографски генерисаних дифракционих решетака. Такође, дифракционе решетке са периодом мањим од таласне дужине светлости не могу да буду копиране због еванесцентних таласа који настају приликом дифракције. Ове сићушне структуре које се налазе на спољашњој површини сваке љуспице су суштински важне за оптички одзив целе љуспице, зато што узрокују униформно расејавање радијације из „плавог“ дела спектра, у целом просторном углу, као што је показано у оптичком моделу љуспице.

Нису све врсте *Lepidoptera* подједнако погодне за примену у заштити докумената. Као што је показано, овакве структуре морају да имају сложену нано-структуру, са великом варијабилношћу и морају бити веома тешке за анализу и за обрнути инжењеринг. У овом истраживању су анализирани поједине врсте које припадају породици *Nymphalidae* (то је породица која припада реду *Lepidoptera*; овај ред инсеката обухвата лептире и мољце). То је најбројнија породица лептирова, која броји више од 6000 врста. Многе врсте из ове породице лептира имају иридесцентне љуспице на крилима.

Материјал од кога су изграђене љуспице је хитин. У питању је изузетно дуготрајан материјал. У природњачким музејима се могу видети примерци иридесцентних лептирова старих по неколико векова. Старост примерка лептира *I. Lathonia* коришћеног у овом истраживању је око 30 година и сребрна боја на његовим крилима се ни мало не разликује у односу на живе примерке. Фосили инсеката задржавају своју иридесценцију после петрификације и њихова иридесценција се не мења ни после неколико милиона година [256]. Ово се дакле може поредити са недавно описаном 5Д меморијом [257], за коју се тврди да има неограничено време живота.

Љуспице лептира могу незнатно да промене своје димензије услед промене температуре [258], влажности и присуства различитих гасова [259]. Услед овога долази до промене у њиховом оптичком одзиву, али ова промена је сувише мала да би утицала на примену љуспица лептира у заштити докумената, при нормалним атмосферским условима. Систематске промене у дугим временским интервалима нису очекиване услед хидрофобности, нерастворљивости и биолошке инертности хитина – доминантног састојка љуспица [260]. Важећи период већине докумената је краћи од 10 година, што је период у коме се очекује да се љуспице не мењају. Узимајући у обзир физичку и хемијску стабилност хитина и чињеницу да оптички одзив

неколико година старих узорака показује изузетну сличност са оптичким одзивом свежих узорака, за очекивати је да су оптички одзиви љуспица веома стабилни и да могу имати дугорочне криптографске примене.

Осим љуспица лептира *Issoria lathonia*, у оквиру проучавања оптичких особина природних фотонских структура, експериментално и теоријски је анализиран хитински оптички систем који се налази на дорзалној страни крила мољца *Diachrysia chrysitis* [97]. Показано је да овај оптички систем представља природан фино-подешен оптички филтер који се састоји од два слоја љуспица (покровне и базне) и крилне мембране. Његов рефлексциони спектар показује велику сличност са рефлекснионим спектром злата. Љуспице поседују површинску нано-дифракциону решетку која „плави“ део упадне светлости интензивно расејева у унутрашњост крилне мембране. Тамо се време боравка ових фотона продужава ефектом локалног таласовода и тиме се значајно повећава апсорпција на овим таласним дужинама. На овај начин, „плави“ део упадне светлости бива ефикасно елиминисан из рефлексције што у комбинацији са интерференцијом преостале упадне радијације инсекту омогућава златну боју његових крила.



## 5. Радијативне термалне особине хитинских наноструктура биолошког порекла

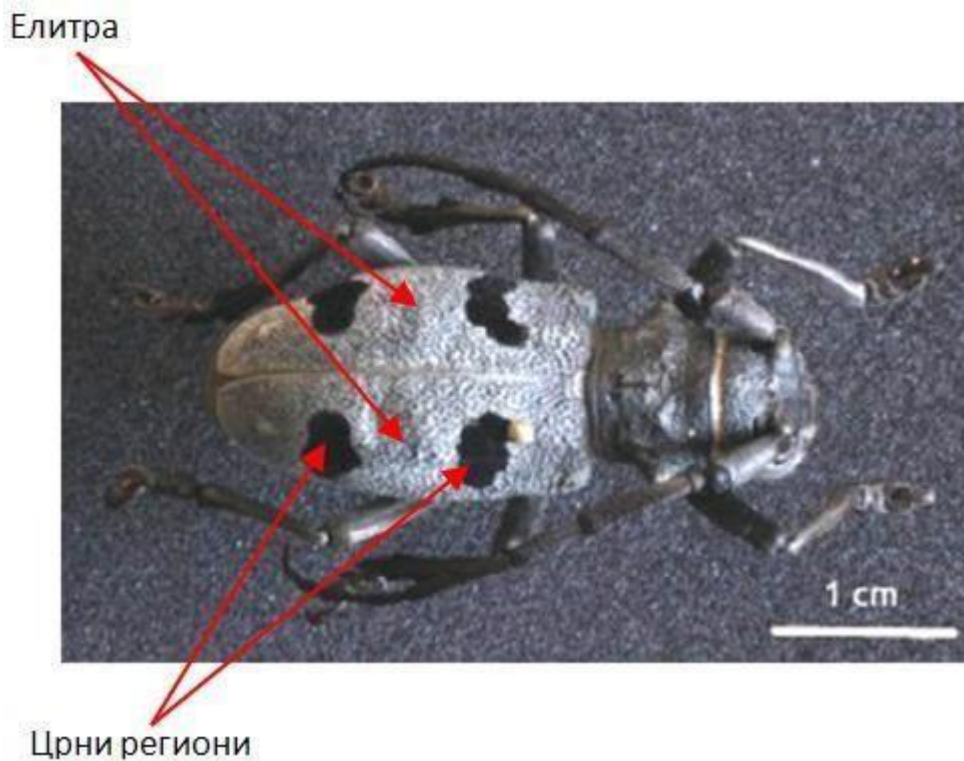
Природне хитинске микроструктуре могу, поред своје оптичке функције, имати и специфичне термалне особине. Њихова микро и наноструктура може узроковати симултану апсорпцију (или рефлексију) радијације из појединих делова оптичког спектра и ефикасну радијативну размену топлоте са околином. Код многих оваквих структура постоји адекватан баланс између апсорбоване радијативне енергије у оптичком делу спектра и ослобођене енергије у инфра-црвеном (ИЦ) спектралном опсегу [261-264, 290], којим инсект ефикасно дисипира топлотну енергију. Сложене фотонске структуре су код многих живих организама присутне и као део система за детекцију ИЦ радијације.

Интеракција природних хитинских микроструктура са ИЦ радијацијом је веома мало истраживана. Досадашња истраживања су углавном имала за циљ развијање квалитетног детектора ИЦ радијације и заснивала су се на промени микро и нано-структуре хитинске љуспице изазване променом температуре услед озрачивања ИЦ радијацијом. Хитинске микроструктуре се допирају различитим материјалима да би се повећала осетљивост, спектрална селективност и брзина одзива детектора. Већина данашњих приступа се заснива на употреби спектрално селективних ИЦ филтера или ИЦ апсорбера, што могу да буду, на пример, периодичне плазмонске [265-267] или периодичне фотонске структуре [268]. Додатна предност у односу на остале технике је што не постоји потреба за хлађењем инфра-црвеног детектора. У последње време су предложени различити дизајни и оперциони принципи за тзв. „нехлађену“ детекцију ИЦ радијације, као што су термалне биморфне структуре [269], микро-фотонски резонатори [270], термо-плазмонски уређаји [271] итд.

Хитинске љуспице лептира имају веома малу термалну масу што их чини одличним материјалом за примену у високо-осетљивој детекцији инфра-црвене радијације. Потенцијална резолуција је на нанометарском нивоу, због нанометарских димензија карактеристичних елемената хитинске структуре. На пример, микро и нано-структурисане хитинске љуспице лептира су допиране једнослојним карбонским нано-цевима [258]. Детекција ИЦ радијације се заснива на хомогеној термалној експанзији хитинске љуспице услед озрачивања, што доводи до повећања карактеристичних растојања унутар ове структуре (растојање између лонгитудиналних и трансферзалних гребенова, растојање између нано-гребенова на површинској нано-дифракционој решетки, растојање између горње и доње ламеле љуспице). Ова промена узрокује промену у оптичком одзиву структуре и ово се користи за детекцију инфра-црвене радијације. У другом истраживању, љуспице лептира су модификоване нано-структурама од злата [272]. Овај приступ се заснива на разлици у коефицијентима термалне експанзије за хитин и злато, услед чега долази до делимичне промене облика хитинске структуре приликом озрачивања ИЦ радијацијом. Ова промена се уочава у оптичком одзиву структуре.

У овом делу дисертације, истражен је утицај микро и наноструктуре на термалне особине биолошких система. Ово је посебно проучено на примеру елитре *Morimus asper funereus* (Mulsant, 1863) (Insecta: Coleoptera: Cerambycidae) инсекта (слика 5.1), чија је спољашња површина (она површина која је окренута ка спољашњој средини) прекривена хитинским микро-сочивима испод којих се налазе објекти који обликом и структуром подсећају на црна

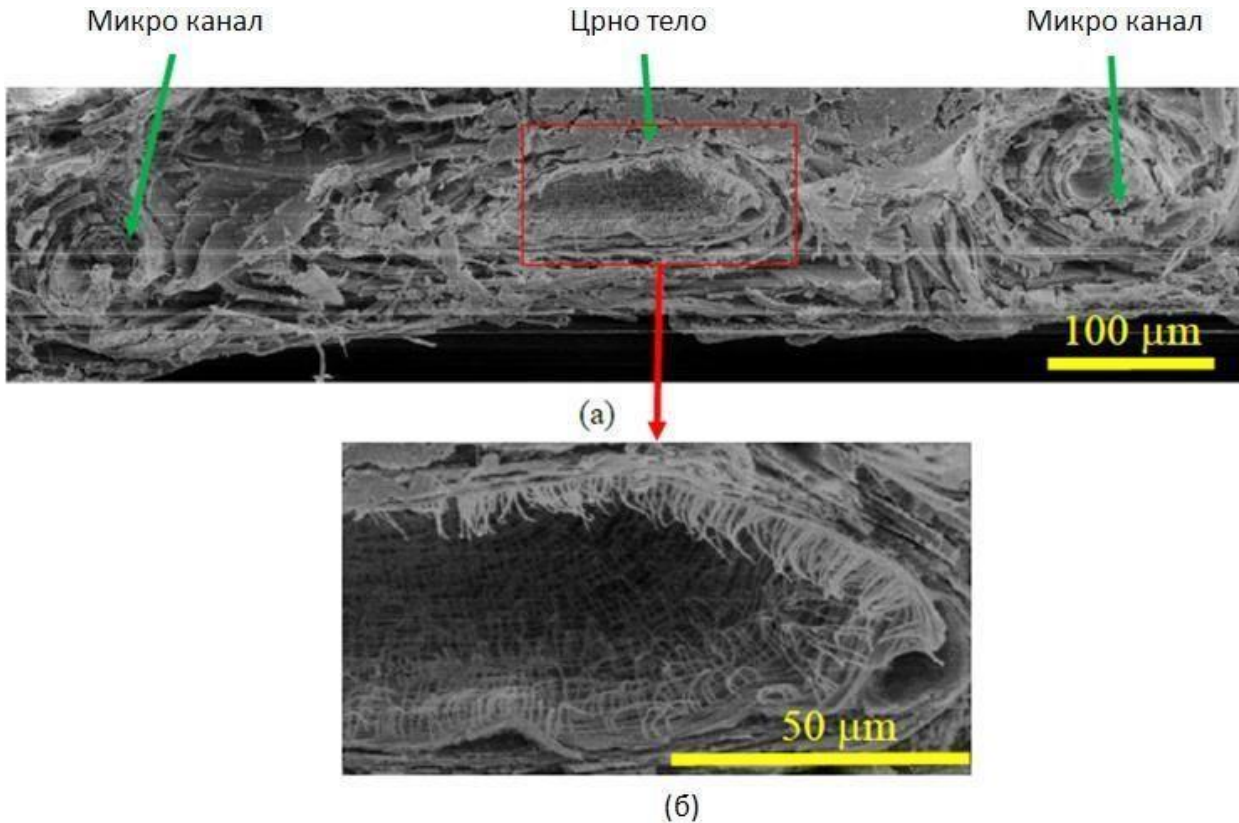
тела. Елитра је модификован предњи пар крила појединих редова инсеката (највећим делом тврдокрилаца), који представља својеврстан заштитни оклоп [273, 274]. Елитра испод себе скрива задњи пар крила, која инсектима служе за летење, али код овог инсекта су закржљала и немају никакву функцију. На њеној унутрашњој површини (она која је окренута ка телу инсекта) налази се ансамбл хипер-униформно распоређених микронских изралина конусног облика. Он можда има функцију стохастичке фотонске структуре која је оптимизирана за ИЦ део спектра, са потпуном фотонском забрањеном зоном. Поменуте морфолошке карактеристике синергијски повећавају ефикасност апсорпције и емисије ИЦ радијације. Оптичком и електронском микроскопијом су истражене морфолошке карактеристике спољашњег и унутрашњег дела елитре, а термалном камером радијативне особине у термалном ИЦ делу спектра (7.5 – 13  $\mu\text{m}$ ). Затим су креирани 3Д модел и теоријски термални модел структуре.



**Слика 5.1.** *Morimus asper funereus*, на сивој елитри уочавају се четири црна региона.

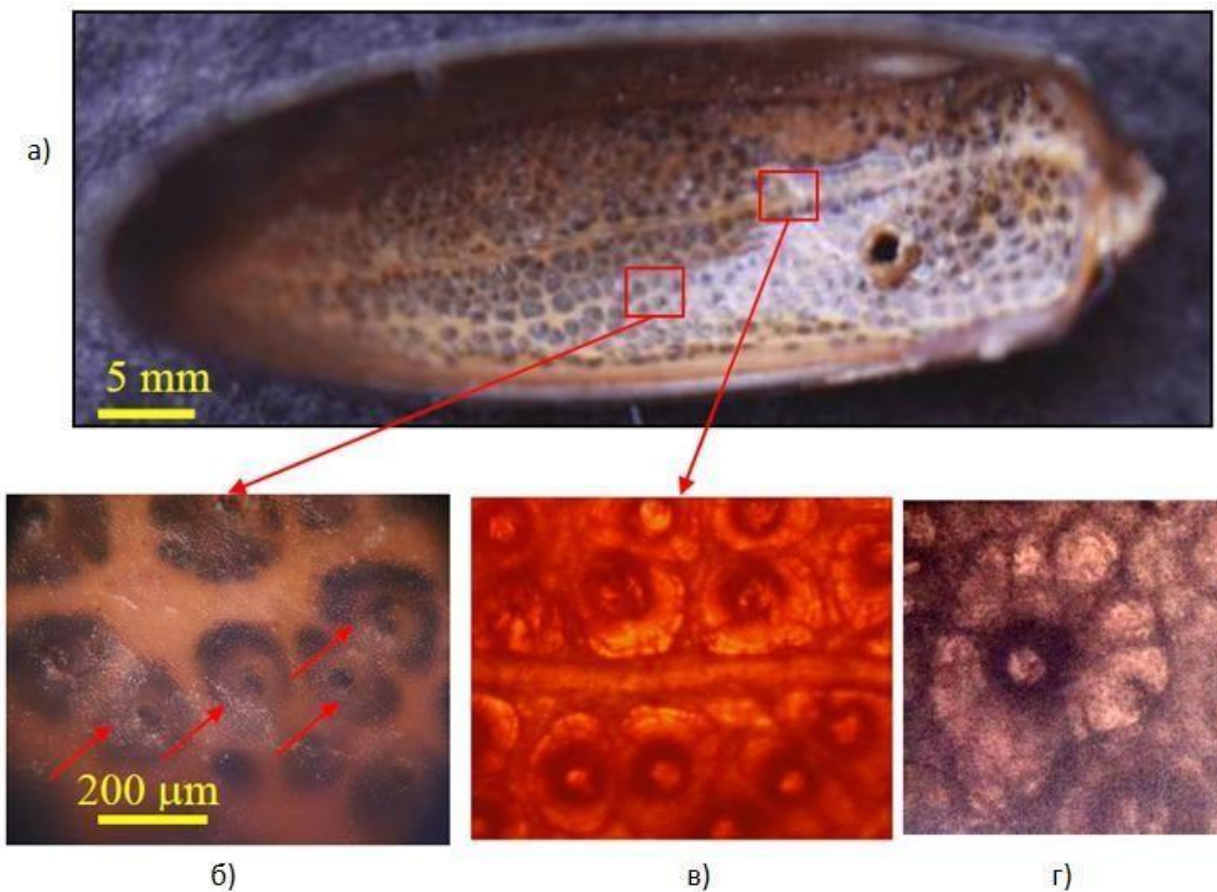
У првом делу истраживања је показано да инсект поседује хијерархијску структуру почев од макроскопског, па до микронског и нанометарског нивоа. Компјутеризована микротомографија показује да елитра има облик елипсоида, чија дебљина варира у опсегу 200-350  $\mu\text{m}$ . На слици 5.2 приказан је електронски микрограф попречног пресека дела елитре. Уочава се да је елитра слојевито структурисана, и слојеви хитина обухватају микро-канале кроз које протиче хемолимфа (телесна течност која циркулише кроз тело бескичмењака). На слици се уочавају два микро-канала а између њих се налази објекат елипсоидног облика са кружном апертуром у центру. Објекат изгледа као стандардан модел црног тела [275]. У елитри се, као што ће се видети на наредним фотографијама, налази мноштво оваквих објеката.

Унутрашња површина (површина окренута ка телу инсекта) елитре је храпава (слика 5.3а), са овалним црним зонама (величине 0.2 – 0.4 mm, слика 5.3б), окруженим светло-жутим зидовима. У оптичкој трансмисији уочава се да су зидови заправо комплексна мрежа повезаних канала кроз које протиче хемолимфа, слика 5.3в. Објекти који својим обликом и структуром подсећају на црна тела су тамно црвени (слика 5.3в). Црвена боја потиче од меланина, који има велику апсорптивност у „плавом“ и „зеленом“ делу спектра и значајну трансмитивност у „црвеном“ делу оптичког спектра.

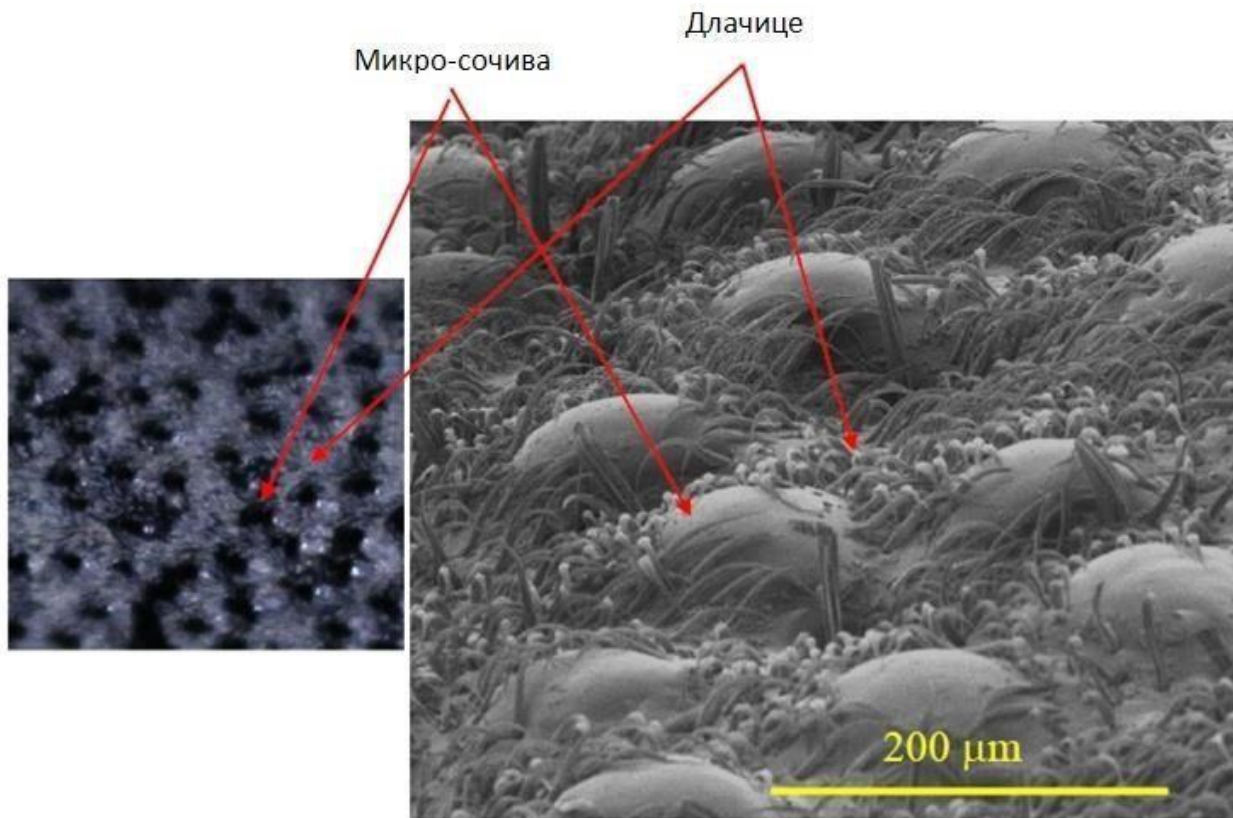


**Слика 5.2.** СЕМ снимци: а) попречни пресек елитре *M. asper funereus* инсекта, уочава се објекат који изгледа као црно тело, са микро каналима; б) увећана фотографија црног тела открива микро-сензиле (длачице микронских димензија) на унутрашњој површини црног тела.

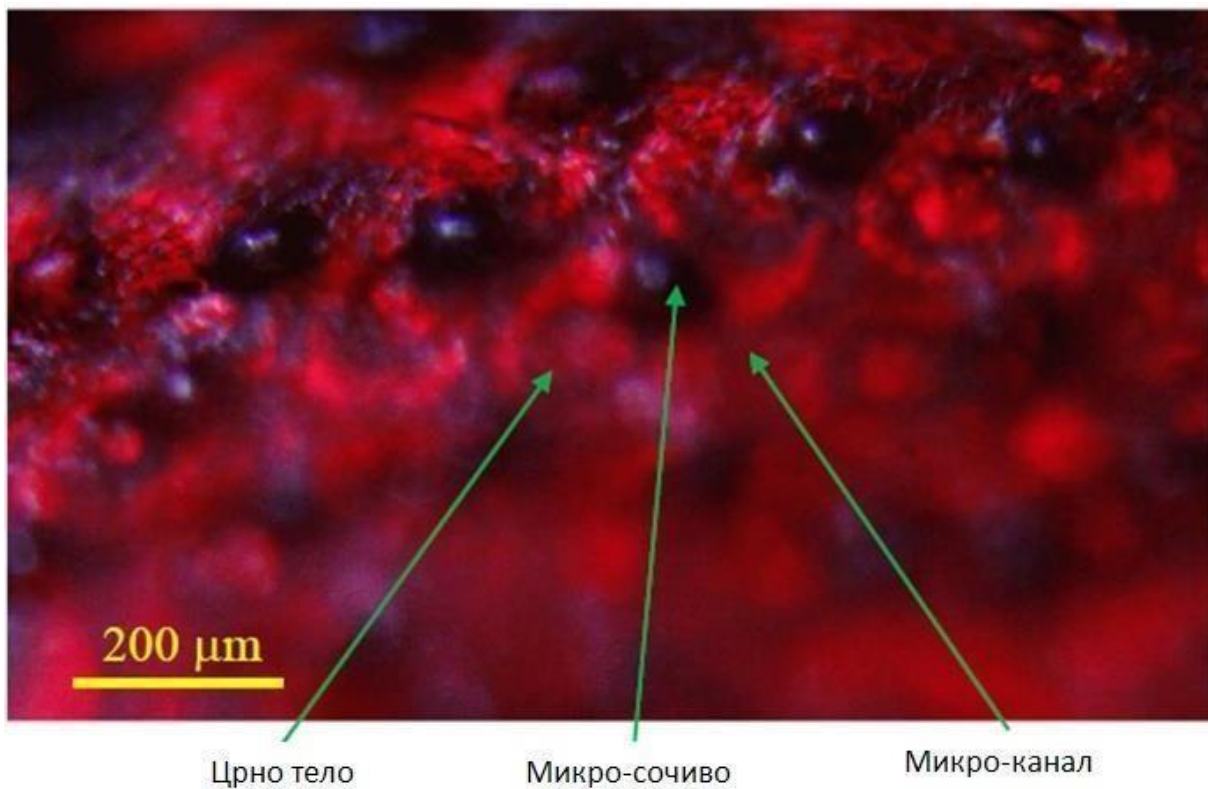
Спољашња површина (површина окренута ка спољашњој средини; на ову површину долази електро-магнетна радијација из спољашње средине) структуре поседује низ црних избочина, које имају облик микросочива, и окружене су длачицама (слика 5.4). Микросочива и црна тела имају прецизну међусобну оријентацију (слика 5.5), што се уочава симултаним детектовањем оптичке трансмисије и рефлексије структуре. Црно тело се налази у центру сваке овалне зоне, а микросочиво обухвата њену ивицу, и директно је фокусирано на канал испуњен хемолимфом.



**Слика 5.3.** а) оптичка фотографија унутрашње површине елитре *M. asper funereus* инсекта, у природном стању; б) увећани региони са фотографије а), уочавају се структуре сличне црном телу (сферног облика, са црном апертуром у центру, означене црвеним стрелицама); в) фотографија у оптичкој трансмисији открива систем канала који се гранају из централног канала и окружују црна тела; г) елитра избељена у водоник-пероксиду открива мрежу канала мањих димензија који повезују црно тело са централним каналом.



Слика 5.4. Спољашња површина елитре *M. asper funereus* инсекта, са микро-сочивима и длачицама. Оптичка фотографија је на левој страни а електронски микрограф на десној.

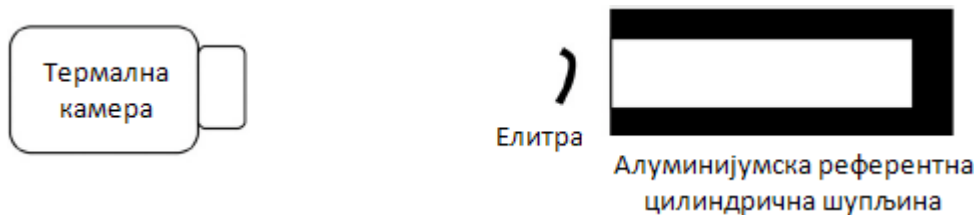


**Слика 5.5.** Фотографија елитре *M. asper funereus* инсекта на оптичком микроскопу, снимљена симултано у рефлексији и трансмисији. Микро-сочива су тамни региони, а испод њих се уочавају црна тела и канали.

## 5.1. Радијативне особине наноструктуре инсекта *Morimus asper funereus*

Радијативне особине структуре су истражене термографијом. Елитра инсекта је постављена испред референтне шупљине (са апсорптивношћу  $> 99\%$ ) [293] и осликана термалном камером која има детекциони опсег 7.5 - 13  $\mu\text{m}$  (опис камере је дат у Материјалима и Методама), слика 5.6. Због малих димензија инсекта, камера је позиционирана што је могуће ближе (на растојању 10-20 cm), а повремено је коришћено и додатно сочиво за додатно увећање. У оваквим условима постаје изражен „Narcissus“ ефекат (радијација коју емитује сама камера) [328, 329]. Због тога је анализирана биофотонска структура постављена изван термалног снопа који излази из објектива камере. Остатак камере је био прекривен алуминијумском фолијом.

Као референца за мерење термалне емисивности коришћена је алуминијумска шупљина на коју је нанесен апсорбујући материјал. Апсорптивност шупљине је теоријски израчуната и добијена је вредност од 0.996 [292].

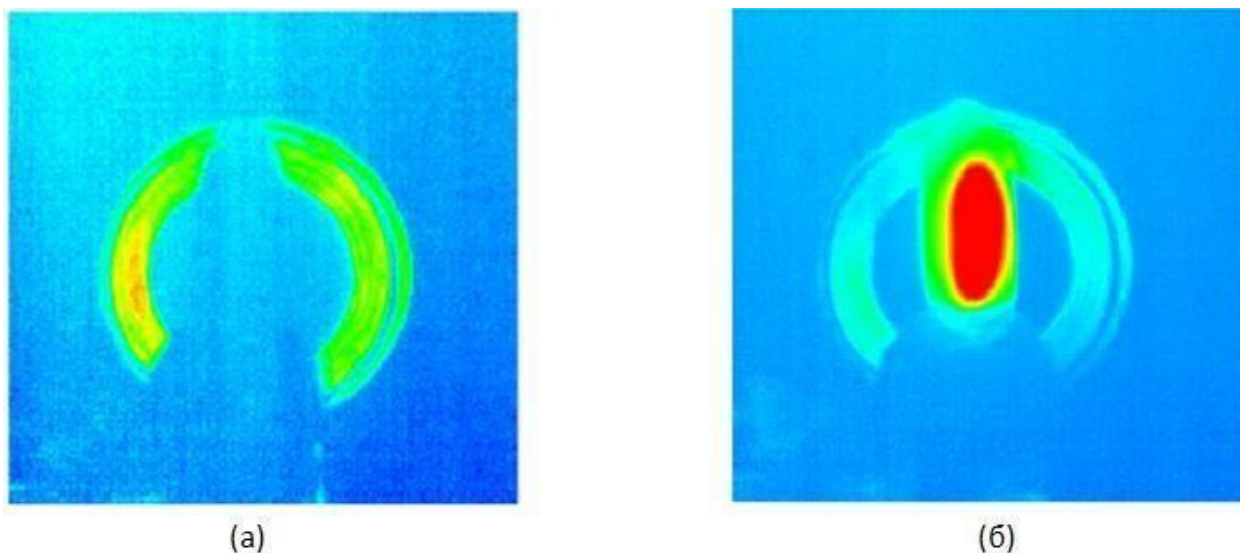


**Слика 5.6.** Шема експерименталне поставке за истраживање радијативних термалних особина елитре *Morimus asper funereus* инсекта

У стању термалне равнотеже, на собној температури, структура је неуочљива и постаје видљива само када се загрева ласерском радијацијом (слика 5.7). Ово важи за целу површину унутрашње и спољашње стране структуре. Дакле, може се закључити да је велика дирекциона емисивност ( $> 99\%$ ) константна на целој површини структуре, у једнакој мери и за црне и за сиве делове, и да структура има карактеристике Ламбертовог извора. Овакав извор емитује радијацију у складу са косинусним законом [275-278]:

$$I(\theta) = I_0 \cos \theta \quad (5.1)$$

где је  $I_0$  интензитет радијације коју емитује Ламбертов извор у правцу нормале на извор, а  $I$  је интензитет који извор емитује у правцу који са нормалом на извор формира угао  $\theta$ . Дакле, интензитет емитоване радијације је максималан у правцу нормале на Ламбертов извор, а затим, у осталим правцима, опада по косинусном закону.



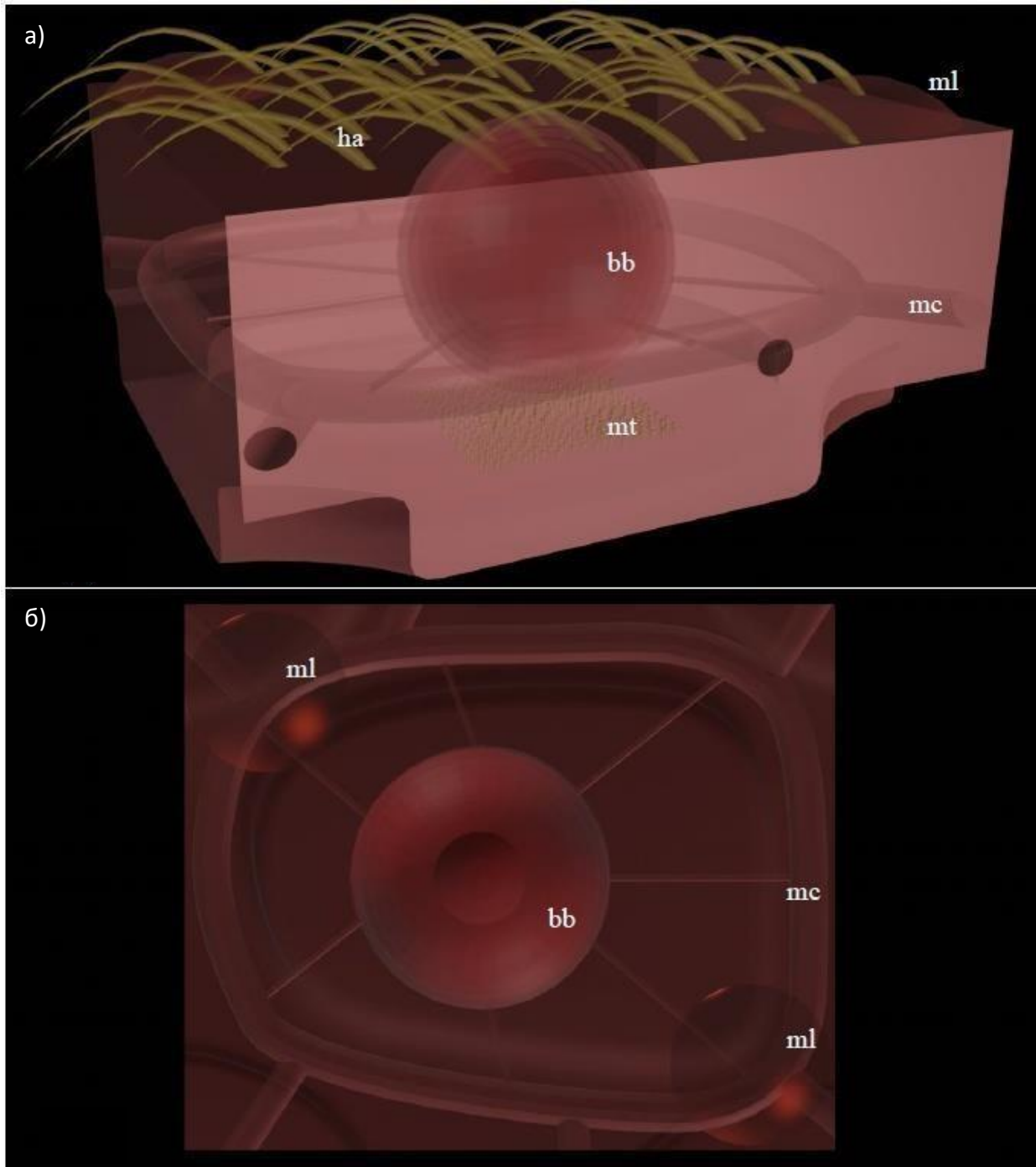
**Слика 5.7.** ИЦ фотографије елитре *M. asper funereus* инсекта, постављене испред црног тела. а) на собној температури, у стању термалне равнотеже, елитра је неочљива; б) загрејана ласерском радијацијом, елитра постаје видљива.

## 5.2. Термални модел наноструктуре инсекта *Morimus asper funereus*

У складу са описаном анатомијом структуре биолошког црног тела *M. Funereus*-а, формиран је модел. Елементарна јединица модела је овална зона, која се састоји од слојевитог црног тела са зидовима са микроканалима, слика 5.8. Она се налази се између два слоја, један (спољашњи слој – окренут ка спољашњој средини) је прекривен микросочивима а други (унутрашњи слој – окренут ка телу инсекта) микротрихијама. Модел је приказан коришћењем слободног, графичког 3Д софтвера (Blender, free under GPL). На слици 5.8 су приказана два погледа на елементарне ћелије (5.8.(а) бочно са спољашње стране, 5.8.(б) ортогонално са унутрашње стране), тако да су јасно видљиве просторне релације између микросочива, зидова са микроканалима и црног тела. „Ray tracing“ метод (објашњен у Материјалима и Методама) је употребљен као прва апроксимација пропагације електро-магнетне радијације, да би се стекао интуитивни увид у начин на који се електро-магнетна радијација простире кроз ову структуру. Овај метод је показао да микросочива фокусирају ИЦ радијацију директно на микроканал испуњен хемолимфом, слика 5.9. Ово важи за велики опсег упадних углова ( $-20^{\circ}$  до  $+20^{\circ}$ ) надлазеће ИЦ радијације, која се ефикасно апсорбује хитином (кофицијент апсорпције хитина је  $1000\text{ cm}^{-1}$  у опсегу  $8\text{-}14\text{ }\mu\text{m}$  и  $580\text{ cm}^{-1}$  у опсегу  $3\text{-}5\text{ }\mu\text{m}$ ) и водом и конвертује у топлоту.

Затим је методом коначних елемената урађено детаљно моделовање пропагације ИЦ радијације кроз структуру. У далеком атмосферском ИЦ прозору ( $8\text{-}14\text{ }\mu\text{m}$ ) радијација је, због великог коефицијента апсорпције хитина, ефикасно апсорбована у површинским слојевима структуре, слика 5.11. Ситуација је сложенија у блиском атмосферском ИЦ прозору ( $3\text{ - }5\text{ }\mu\text{m}$ ), где је апсорпција за ред величине мања [278]. Радијација из тог опсега се микросочивима фокусира на микроканале (који окружују црно тело), док је део термалне радијације који не пада на микросочива ефикасно рефлектован вишеслојним хитинским омотачем црног тела, слика

5.11. Микроканалы се брзо загреју надлазећом радијацијом и постоји конвективни трансфер термалне енергије у централну шупљину црног тела мрежом микроканала, налик на оне који су уочљиви на слици 5.3г. Сићушне длачице у унутрашњости ове шупљине (слика 5.2б) су вероватно сензиле (рецептори који детектују промену температуре), које сигнализирају инсекту да потражи хладније окружење, што је бихевиорална карактеристика инсекта.

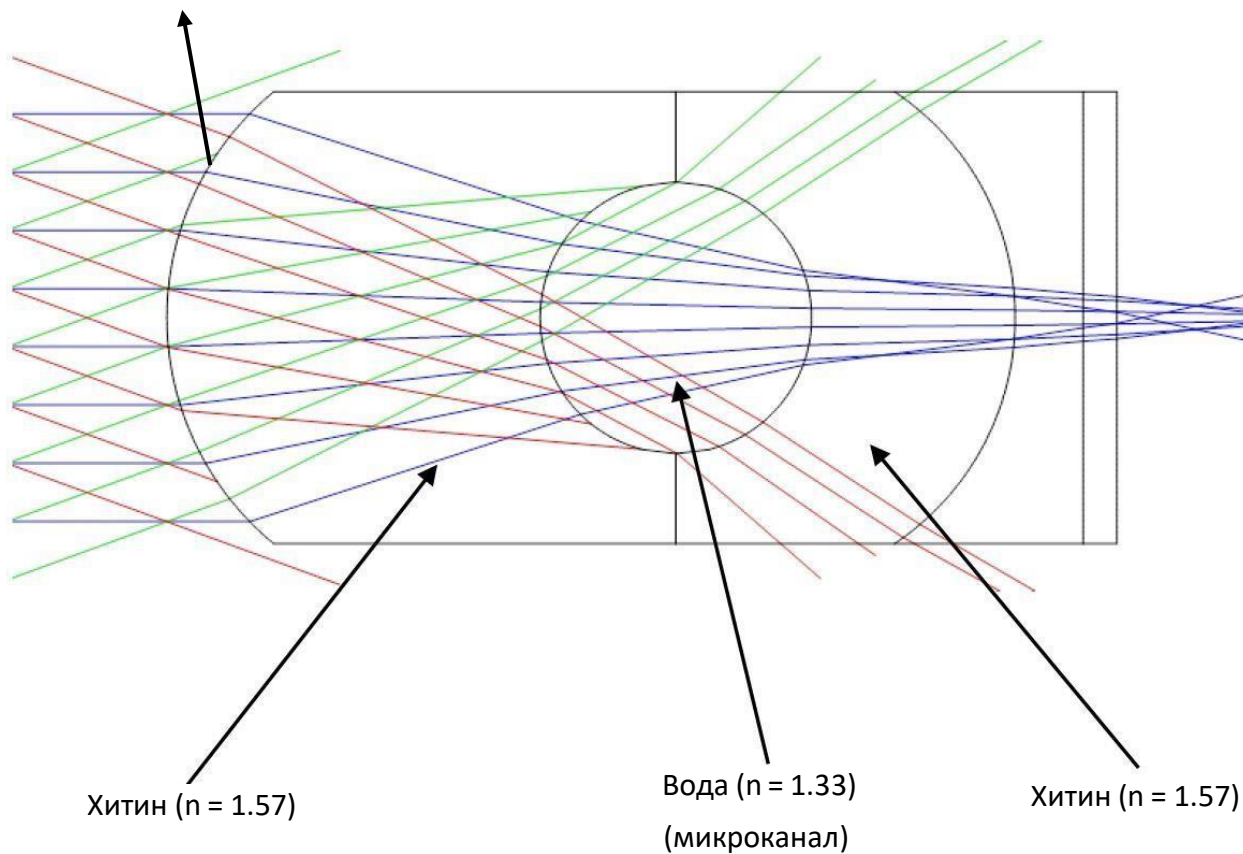


**Слика 5.8.** Полу-транспарентан 3Д модел елитре *M. asper funereus* инсекта у коме су приказане унутрашње структуре (*mt* – микротрихија, *mc* – микроканал, *ml* – микросочиво, *bb* – црно тело, *ha* - длачице); а) профил елитре на коме се уочава типичан положај микро-сочива на

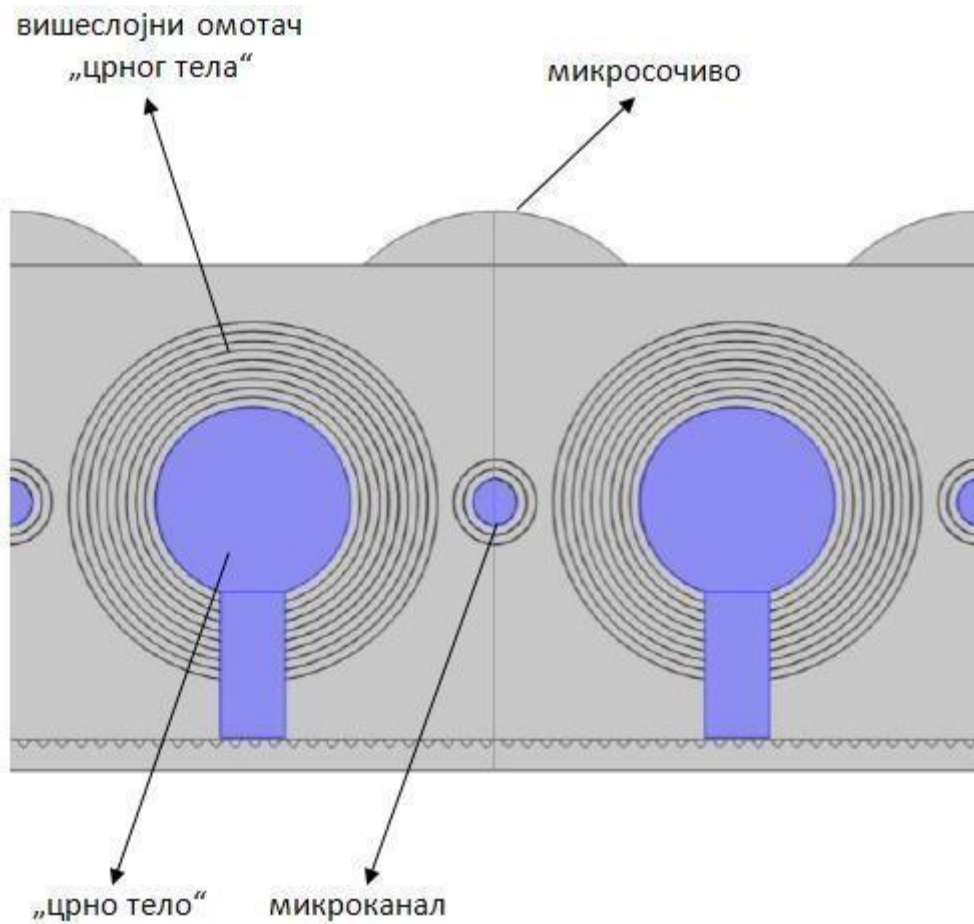


њеној спољашњој површини; б) вертикална перспектива, у којој је приказан просторни распоред микросочива и микроканала. Микроканал у потпуности окружује црно тело и мањим каналима је повезан са њим.

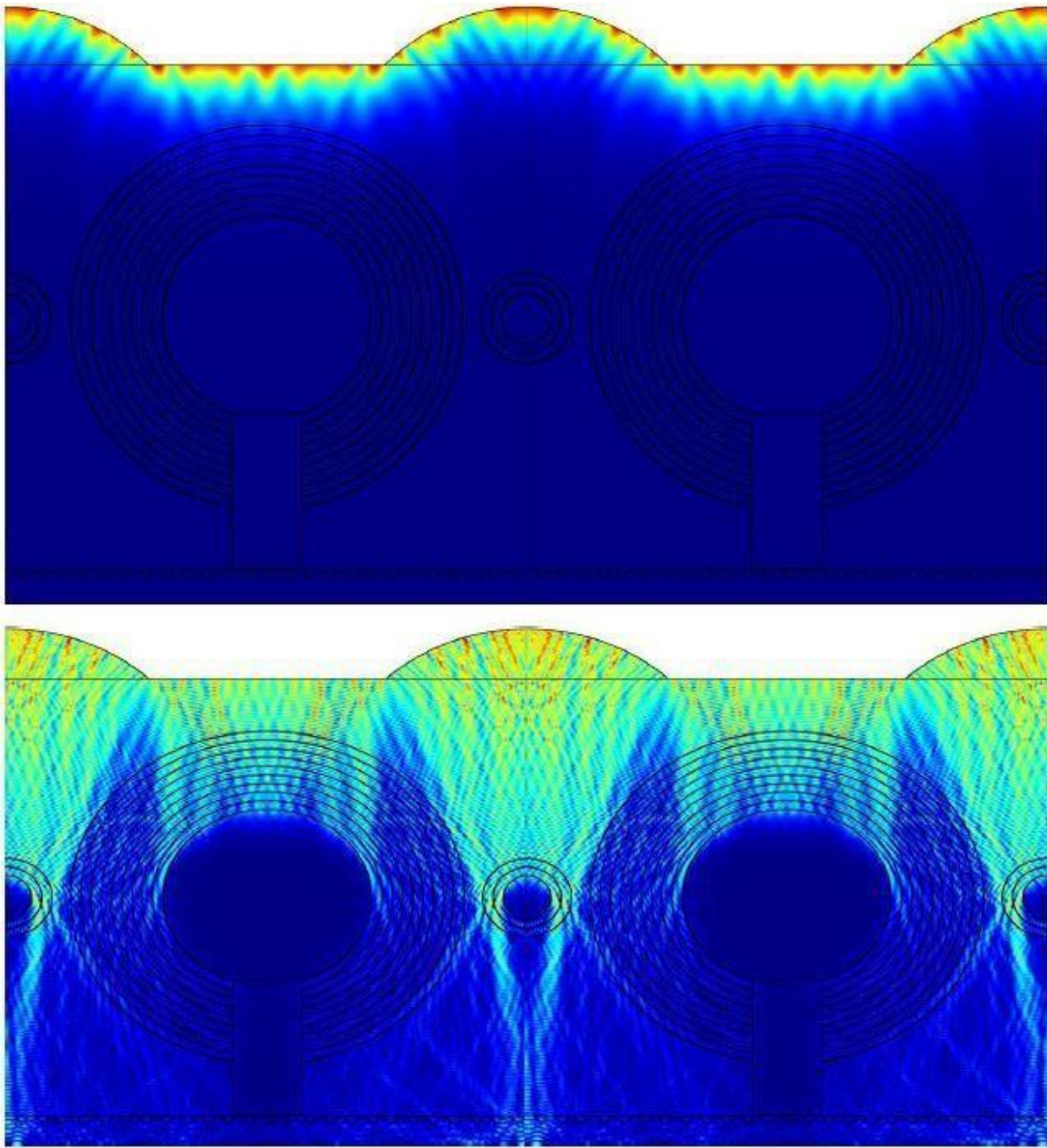
Спољашња површина микросочива



**Слика 5.9.** Ray tracing метод демонстрира правце простирања радијације у интервалу 3 – 5  $\mu\text{m}$  кроз микросочиво и микроканал. Плави зраци долазе под правим углом, а црвени и зелени зраци долазе на елитру под угловима  $+20^\circ$  и  $-20^\circ$ .



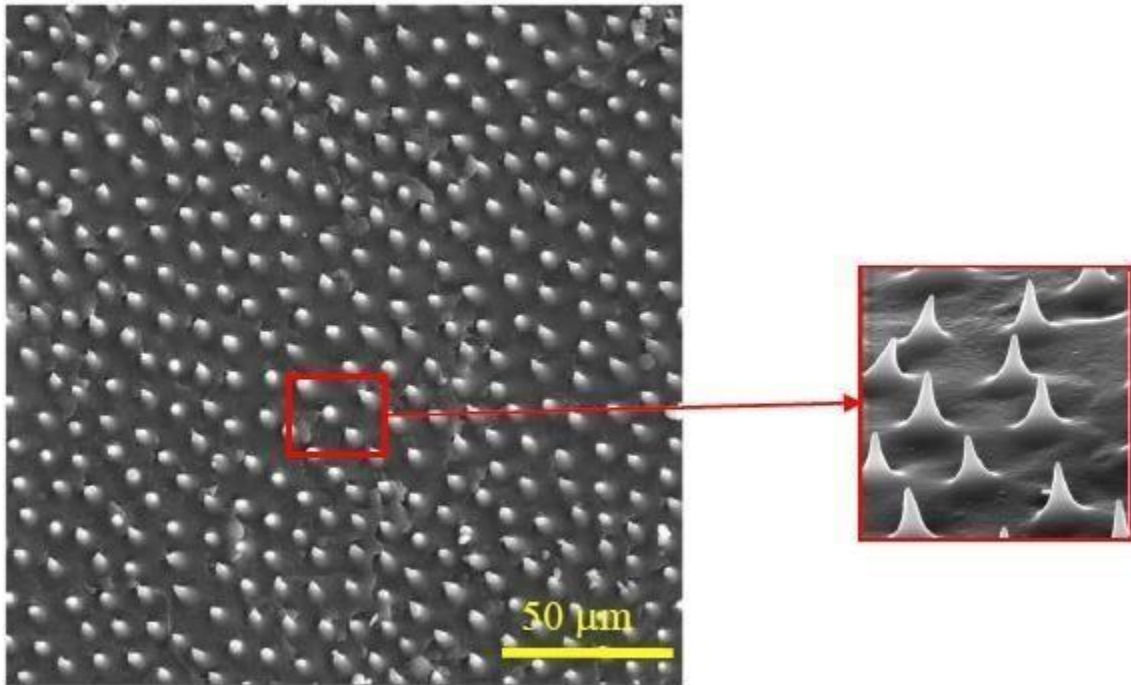
**Слика 5.10.** Модел елитре *M. asper fumereus* инсекта, који је употребљен за анализу пропације ИЦ радијације методом коначних елемената (у сивој боји је приказан хитин а у љубичастој боји је приказана хемолимфа).



**Слика 5.11.** Пропагација термалне ИЦ радијације унутар елитре *M. asper funereus* инсекта, израчуната методом коначних елемената. Анализирана су два спектрална опсега који одговарају далеком и блиском термалном атмосферском прозору:  $\lambda = 8-14 \mu\text{m}$  (приказан је резултат за  $\lambda = 10 \mu\text{m}$ , горња слика), и за  $\lambda = 3-5 \mu\text{m}$  (приказан је резултат за  $\lambda = 4 \mu\text{m}$ , доња слика).

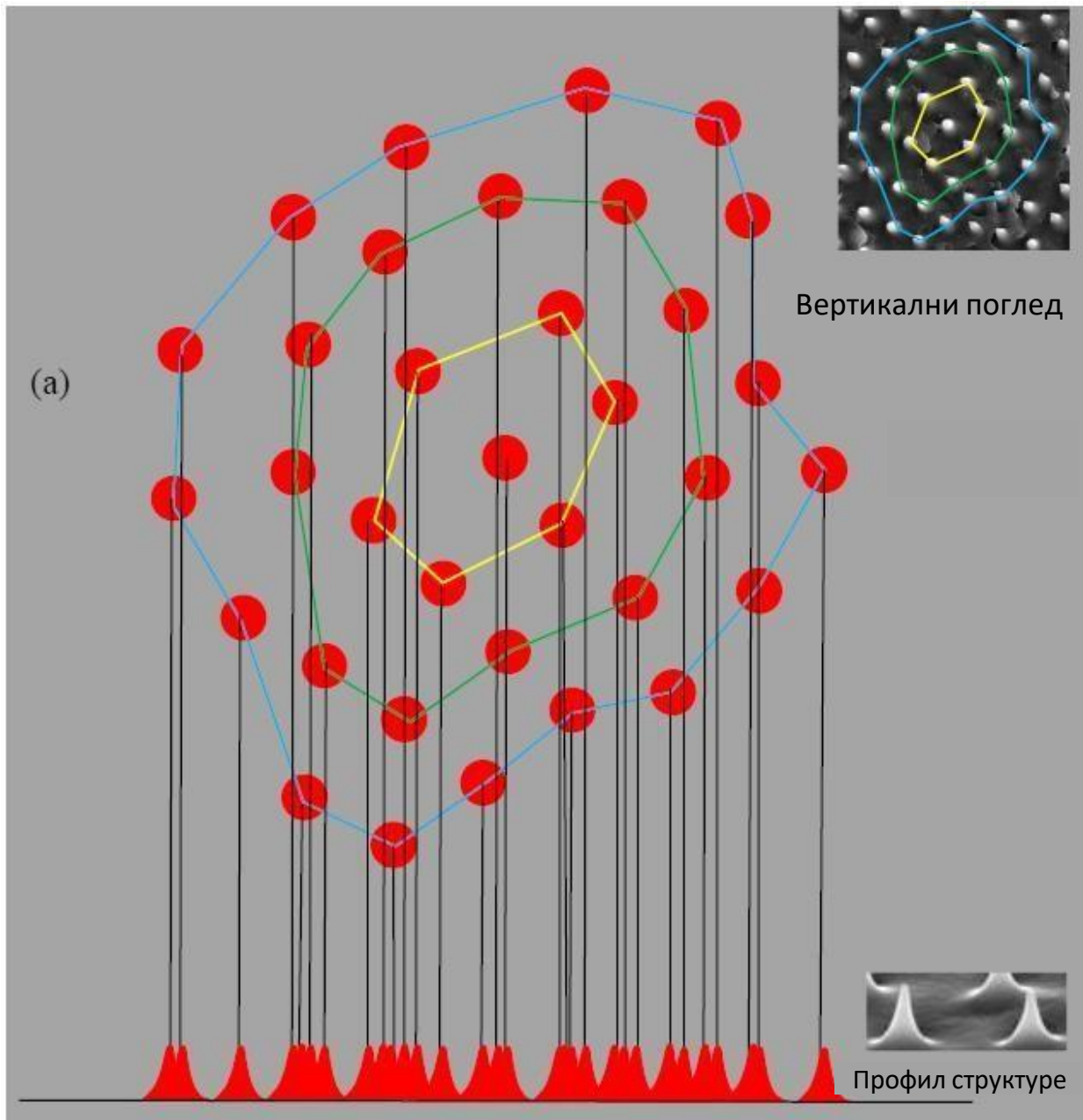
### 5.3. Хипер-униформност хитинских микроструктура

Још једна занимљива карактеристика је постојање површинских структура на унутрашњем делу елитре. Најбоље се уочавају на електронском микрографу унутрашње површине (која је окренута ка телу инсекта) елитре, а то су израстине конусног облика (тзв. микротрихије), висине  $\sim 4 \mu\text{m}$  и полупречника основе  $\sim 4.5 \mu\text{m}$ , слика 5.12. Њихов распоред је уређен али не и потпуно регуларан (просечно међусобно растојање је  $10 \mu\text{m}$ ). Код многих врста инсеката, оне причвршћују задња крила за елитру. Међутим, код *M. asper funereus* инсекта ово није случај, јер он има веома закржљала крила.



**Слика 5.12.** Електронски микрограф унутрашње површине елитре *M. asper funereus* инсекта и ансамбл микронских израстина, тзв. микротрихија. На левој слици је приказан изглед ансамбла из правца нормале на површину елитре, а на десном микрографу је приказана бочна перспектива, на којој се уочава да израстине имају облик конуса.

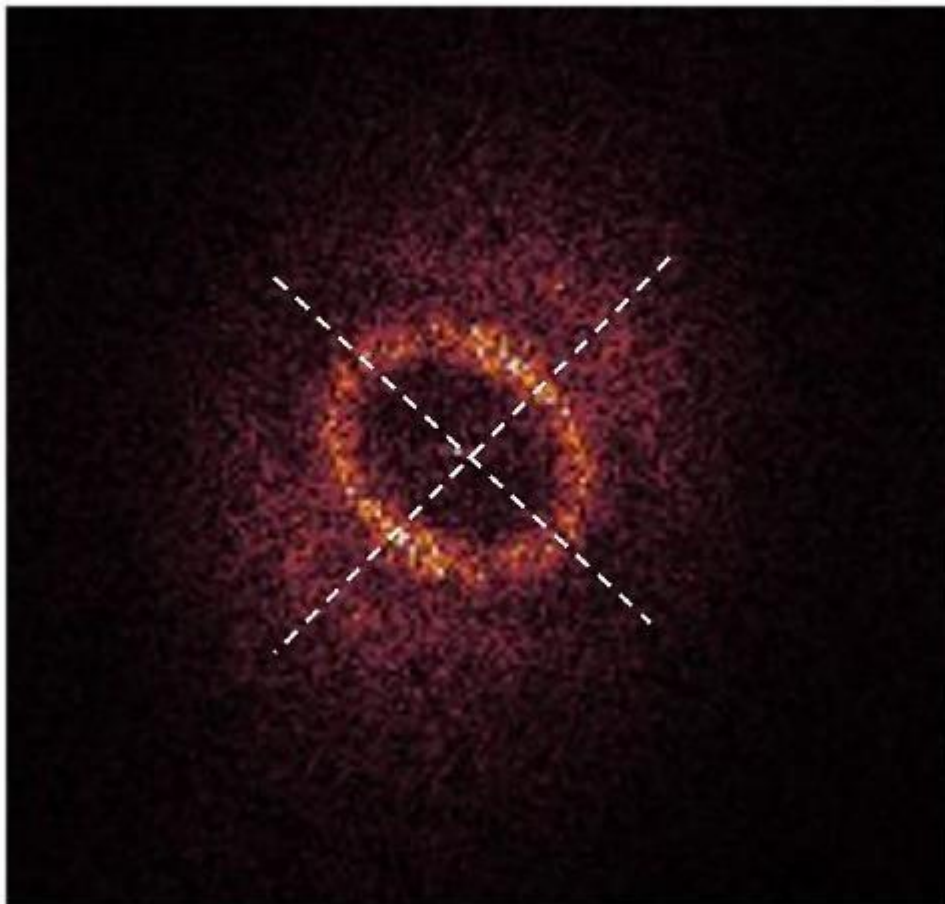
Ансамбл микротрихија је моделован као скуп конусних израстина на равној површини. Пречник основе свих конуса је  $4.4 \mu\text{m}$ , а висина је  $3.8 \mu\text{m}$ . Посматрано у правцу нормале на површину, распоред конуса је приказан на слици 5.13. На истој слици је приказан и бочни поглед на структуру где се види „преклапање“ конуса. Из тог разлога, радијација која долази под малим углом, блиско површини на којој се налазе конуси, има велику вероватноћу да наиђе на неки од конуса и буде апсорбована. Ово су елементарна разматрања на основу геометријске оптике. У наставку моделовања је примењен таласно-оптички приступ.



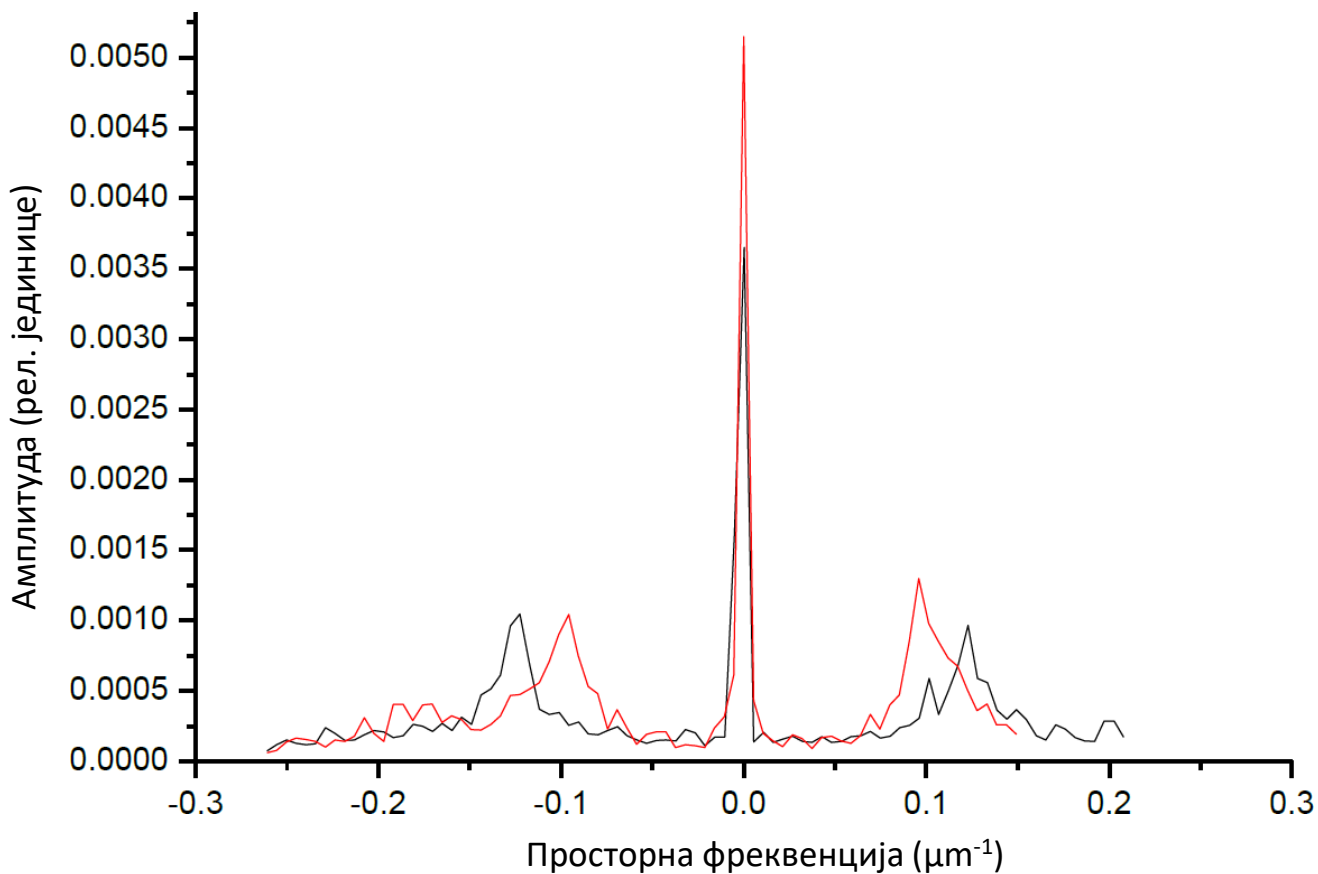
**Слика 5.13.** *Расподела конусних микроструктура у вертикалној перспективи, креирана по узору на електронски микрограф са слике 5.12. У горњем десном углу приказан је део електронског микрографа на основу кога је урађена скица расподеле. На дну слике је приказана профилна перспектива.*

Детаљним увидом у просторни распоред конуса уочава се да он није регуларан а ни потпуно насумичан. Фуријеов трансформ ансамбла конуса има облик прстена, слика 5.14. Његова просторна фреквенција је  $0.1 / \mu\text{m}$ , што одговара просечном растојању од  $10 \mu\text{m}$  између конуса, слика 5.15. На просторним фреквенцијама блиским централном Фуријеовом максимуму, амплитуда трансформа је веома мала. Ово је карактеристика хипер-униформне расподеле тачака, за коју је показано да се понаша као структура са потпуном фотонском забрањеном

зоном [280]. Блага елиптичност Фуријеовог трансформа је могућа последица елипсоидног облика површине на којој се налазе конуси.



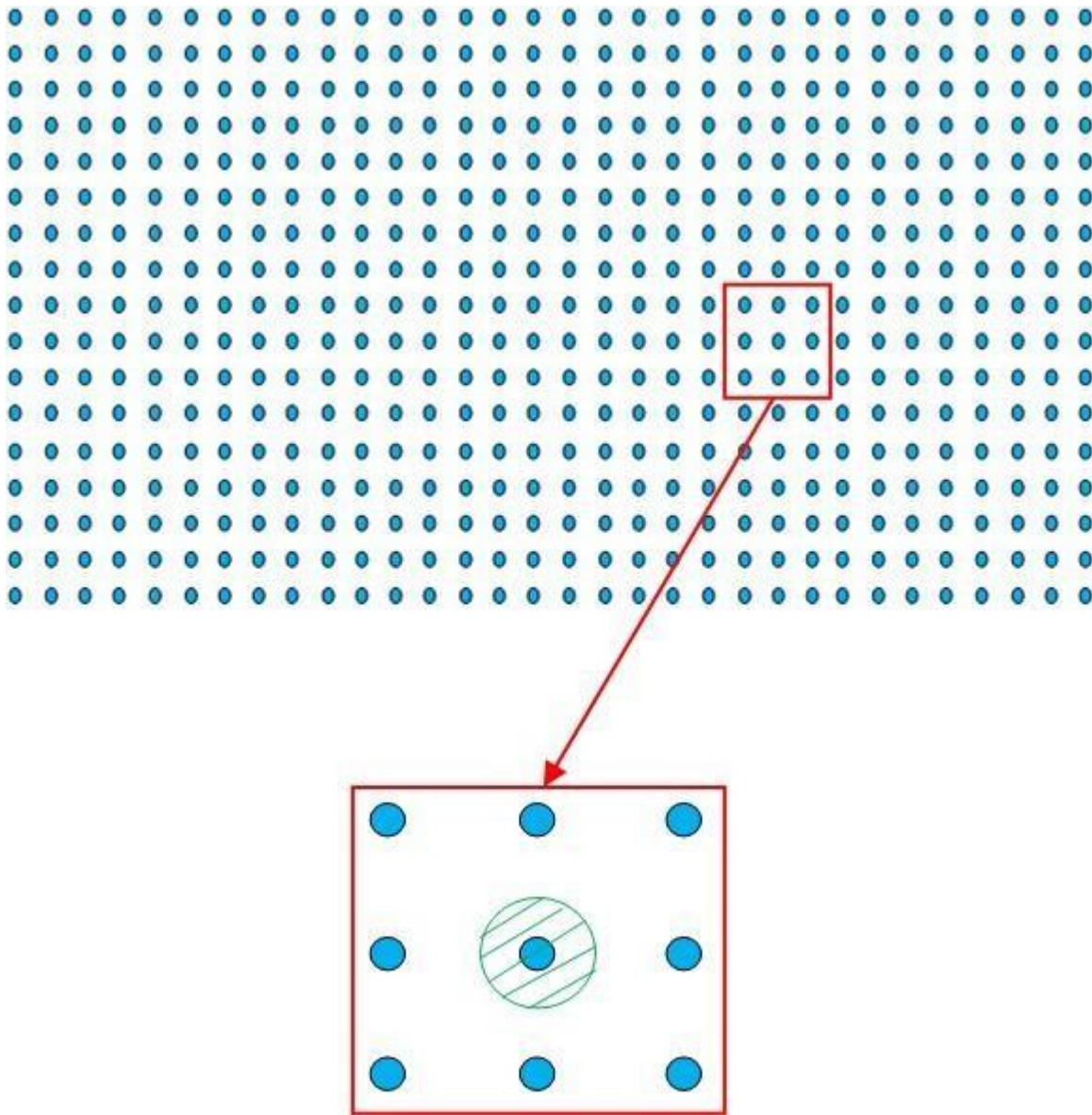
**Слика 5.14.** Фуријеов трансформ слике 5.12 на којој је приказана расподела конусних микроелемената. Трансформ има облик прстена са благом елиптичношћу.



**Слика 5.15.** Сканирање Фуријеовог трансформа са слике 5.14 у два ортогонална правца (приказана испрекиданим линијама на слици 5.14) открива максимум на просторној фреквенцији од  $\sim 0.1/\mu\text{m}$  који одговара просечном растојању од  $10 \mu\text{m}$  између конусних микроелемената.

Хипер-униформни систем честица има мале флукуације густине на великим растојањима [281]. Концепт хипер-униформности је креиран због класификације ансамбла тачака у складу са њиховим локалним густинама флукуација [279]. Ансамбл тачака је хипер-униформан ако се варијанса броја тачака  $\sigma^2(R) \equiv \langle N_R^2 \rangle - \langle N_R \rangle^2$  у сферној области полупречника  $R$  повећава спорије него запремина узорка полупречника  $R$ , за велике вредности  $R$  (што значи да се варијанса броја честица повећава спорије од  $R^d$ , где је  $d$  број димензија простора). Хипер-униформна расподела конусних микро-објеката анализирана у овом истраживању је дводимензионална. Хиперуниформност је карактеристика свих кристала и квазикристала, као и посебне подкласе неуређених структура.

Хипер-униформни 2Д систем се понаша као стохастички фотонски кристал са потпуном фотонском забрањеном зоном – материјал код кога постоји одступање од савршено уређене структуре али су одступања веома мала па се материјал понаша као фотонски кристал (на пример, у случају 2Д кристала ово значи да чворови кристала не формирају савршену 2Д решетку већ за сваки чвор постоји мала област одступања у његовој позицији, и у оквиру те области он може да има било коју позицију, слика 5.16) [282-285]. Ово се може закључити на основу облика Фуријеовог трансформа (слика 5.14).



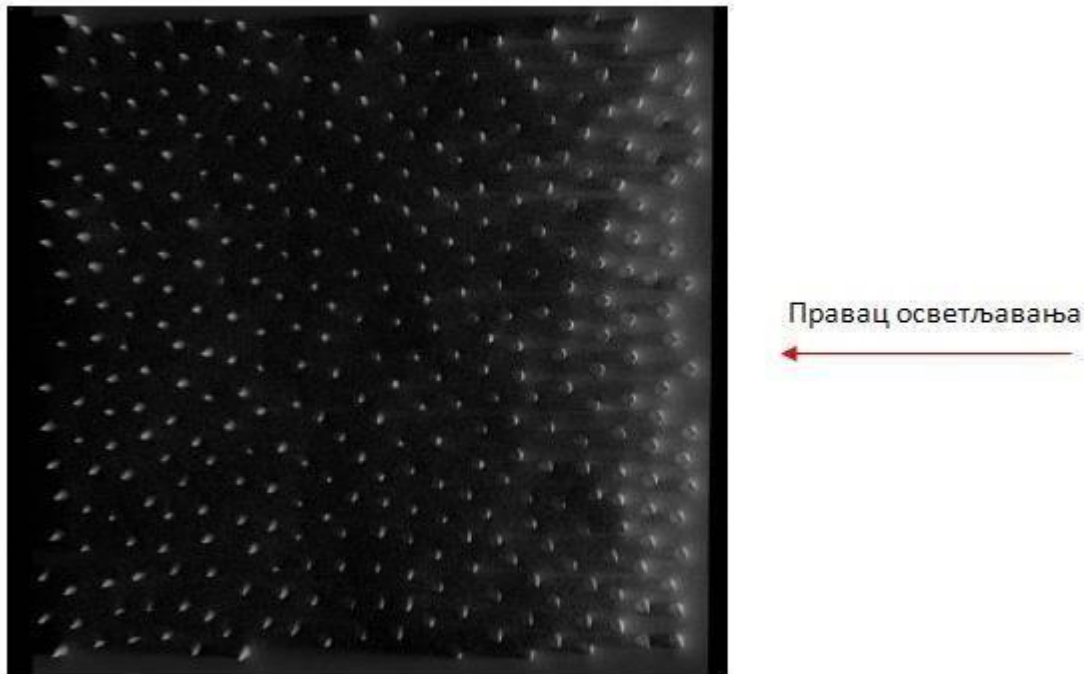
**Слика 5.16.** Шематски приказ распореда чворова идеалног 2Д кристала. Уколико се идеалан распоред наруши на адекватан начин, добија се хипер-униформни 2Д кристал. На доњем исечку је зеленим кругом приказана област одступања позиције централног чвора – његов центар може да буде у било којој тачки овог круга. Када се исти принцип примени на позиције свих чворова, уколико је област одступања позиције довољно мала, добија се хипер-униформни 2Д кристал.

Примењено на случај *M. Funereus*-а, за мале упадне углове радијације, када је правац простирања електро-магнетне радијације скоро паралелан равни конусних микроелемената, систем се понаша као Брегов рефлектор, блокирајући пропацију радијације на таласним дужинама:

$$\lambda = 2d/N \quad (5.2)$$



где је  $d$  период дифракционе решетке, тј. растојање између суседних конусних микроелемената, а  $N$  је цео број, уколико светлост пада на решетку под углом од  $90^\circ$ . За  $d = 10 \mu\text{m}$  и  $N = 2$ , Брегова таласна дужина ове структуре је  $10 \mu\text{m}$ , и налази се у далеком атмосферском прозору ( $\lambda = 8\text{-}14 \mu\text{m}$ ). Додатно, за  $N = 4$ , Брегова таласна дужина одговара другом атмосферском прозору, у опсегу ( $\lambda = 3\text{-}5 \mu\text{m}$ ).



**Слика 5.17.** Вертикални поглед на ансамбл конусних микроструктура. На слици је приказан и правац осветљавања, радијација се креће под малим углом у односу на хоризонталну раван у којој се налазе основе конусних микроструктура. Уочава се да конусне микроструктуре спречавају пропацију ИЦ радијације.

## 5.4. Завршна разматрања термалних особина анализираних хитинских микроструктура

На елитри *M. asper funereus* инсекта су уочене и друге оптички занимљиве структуре које нису детаљно проучаване у оквиру ове дисертације, али би могле да утичу на радијативне особине.

Ширина свих хитинских ламела у елитри *M. asper funereus* инсекта је 4-5  $\mu\text{m}$  са одговарајућом Бреговом таласном дужином 8-10  $\mu\text{m}$ . Сваки слој садржи адекватно оријентисана микровлакна, која у систем уносе двојно преламање, и њихова оријентација је различита у различитим слојевима. Граничне површине између свих слојева су храпаве и расејавају радијацију, па слојеви потенцијално имају функцију планарних таласовода који додатно апсорбују радијацију. Ансамбл конуса може да буде трансмисиона решетка за радијацију која пада под угловима блиским нормали на површину а дифракциони редови могу бити уведени у хитинске ламеле – планарне таласоводе.

У додатним мерењима, једна страна елитре је загревана ласерским снопом и, у стању термалне равнотеже, друга страна има температуру која је нижа чак за око 20<sup>0</sup>. Тешко је разграничити допринос радијативног ослобађања топлоте у односу на остале термалне процесе (конвекција и кондукција). Међутим, ова хитинска структура би могла да буде одличан модел за дизајн термално-изолационих материјала

Већ дуго времена научници покушавају да креирају високо-апсорптивне структуре и направљени су многи микро и нано структурисани материјали [286], али само емисивност низа вертикално распоређених наноцеви („VANTA black“) је блиска емисивности црног тела [287]. Упоредо са текућим истраживањима силицијумских фотонских структура за уређаје који раде у блиском ИЦ спектралном региону, у овом истраживању је показано да природне, мање комплексне, хитинске структуре могу да постигну сличне резултате захваљујући ансамблу конусних површинских микро-елемената. Адекватна хипер-униформна структура се ефикасно такмичи са високо-напредним материјалима са нано-цевима. За разлику од вештачког VANTA материјала, који је фрагилан и чији је производни процес компликован, природно решење је флексибилно и једноставно.

Дакле, у овом делу дисертације је показано да комбинација хитинских микросочива, „црних тела“ и хипер-униформно распоређених конусних микроструктура омогућава одличну контролу термалне радијације. Потенцијалне примене су бројне и могу се чак и приширити са блиско инфра-црвене на терахерцну технологију.

Истраживање оптичких и термалних особина хитинских структура биолошког порекла обухватило је и анализу микро и нано – структурисаног спољашњег омотача тврдокрилца *Rosalia alpina* (Coleoptera: Cerambycidae) [289]. Показано је да овај хитински систем функционише као ефикасан пригушивач (*optical beam dump*) упадне радијације из оптичког дела спектра, апсорбујући скоро сву упадну радијацију. У ИЦ региону, хитинска микроструктура омогућава ефикасно ослобађање вишка термалне енергије радијативним путем.

## 6. Закључак

У оквиру ове докторске дисертације експериментално су истражене поједине нелинеарне оптичке особине хемијски пречишћеног хитина применом двофотонски побуђене флуоресценције и генерисањем другог хармоника. Измерен је интензитет дво-фотонски побуђене флуоресценције хитина у функцији таласне дужине (у опсегу 830 – 930 nm) и средње снаге побудног фемто-секундног ласерског зрачења (у опсегу 3,4 – 13,6 mW. Мале вредности снаге су изабране да би се минимизирало фото-оштећење узорка. Резултати показују да интензитет дво-фотонски побуђене флуоресценције хитина опада са порастом таласне дужине побудне ласерске радијације у поменутом опсегу и да дво-фотонски побуђена флуоресценција има максималан интензитет када је побудна таласна дужина око 830 nm. Измерено је време флуоресценције хитина и добијена вредност од 5,2 ns. Такође је измерен и флуоресцентни спектар хитина за једно-фотонску побуду и он показује максимум на 440 nm и спектралну ширину од ~ 120 nm. Истражени су и ефекти фото-избељивања који настају услед продуженог озрачивања хитина ласерским зрачењем. Доказано је постојање другог хармоника за хемијски чист хитин.

Ови резултати су употребљени за анализу оптичких и флуоресцентних особина појединих хитинских микро и наноструктура биолошког порекла, и за истраживање контролисане модификације ових особина ласерском радијацијом. Одређени су оптимални параметри ласерске радијације и нелинеарног ласерског микроскопа (таласна дужина побудне ласерске радијације, репетиција, снага ласерског зрачења, поларизација, временско трајање фемто-секундних побудних ласерских импулса, време задржавања ласерског снопа на узорку...) за осликавање хитинских нано-структура коришћењем дво-фотонски побуђене флуоресценције хитина, и за контролисану модификацију (сечење и фото-избељивање ласерским зрачењем) ових нано-структура и њихових оптичких особина. Сlike су добијене при снагама ласерске радијације мањим од 1 mW у опсегу 720-850 nm где хитин показује интензивну дво-фотонски побуђену флуоресценцију и са максималном попречном и осном резолуцијом од 0.7  $\mu\text{m}$  и 2.1  $\mu\text{m}$ , респективно. Најнижи прагови оштећења су 4,5 mW, када је коришћен 40 X 1.3 НА микроскопски објектив и 8 mW када је коришћен 20 X 0.8 НА микроскопски објектив, на побудној таласној дужини ласерског зрачења  $\lambda = 730$  nm. Није неочекивано то што су најнижи прагови оштећења на овој таласној дужини ако се имају у виду резултати из првог дела ове дисертације где је показано да је у доступном опсегу побудне ласерске радијације (700 - 1000 nm) дво-фотонски побуђена флуоресценција хитина има највећи интензитет за краће таласне дужине из овог дела спектра (слика 2.1). Минимални пречник ласерски изазваног оштећења у овом истраживању је био 1.7  $\mu\text{m}$ . Фото-избељивање хитинске нано-структуре је остварено при минималним доступним снагама побуде (1-2 mW) у опсегу 720-850 nm где хитин показује интензивну дво-фотонски побуђену флуоресценцију.

Формиран је теоријски модел љуспице који објашњава њене оптичке особине, првенствено иридесценцију. У наставку истраживања, ови резултати су искоришћени за истраживање могућности употребе хитинских љуспица као заштитног варијабилног оптичког елемента. За потребе овог дела истраживања испитане су и друге важне особине као што су варијабилност и јединственост наноструктуре љуспица и њиховог оптичког одзива. Поред тога, због технолошке примене, показано је да се неопходна информација о аутентичности може записати директно на љуспицу, фемтосекундним ласером, у форми физичке модификације

љуспице. С тим у вези, узимајући у обзир просечне димензије љуспице ( $\approx 50 \mu\text{m} \times 100 \mu\text{m} = 5000 \mu\text{m}^2$ ) процењен је информациони капацитет љуспице на  $\approx 3000$  битова, третирајући место оштећено ласером као бинарно 1, а неоштећено као бинарно 0.

Истражене су и термалне радијативне особине природне хитинске микроструктуре. Показано је да ова хитинска микроструктура омогућава одличну контролу термалне радијације.

У будућности би се наставило са теоријским и експерименталним истраживањем механизма интеракције између упадне радијације и природних хитинских наноструктура. Могућности њихове контролисане модификације ће бити проширене са директног ласерског исписивања на холографску и електронску литографију. Од вештачких материјала ће се првити копије природних хитинских наноструктура. Испитиваће се утицај модификације ових структура на њихове опто-механичке особине, и могућност коришћења ових елемената као оптичких меморија, и термалних детектора. Развијаће се софтвер који је потребан да би се истраживања спровела на нелинеарном ласерском микроскопу. Истраживаће се и друге могућности за примену софистицираних оптичких структура.

# Литература

- [1] Chai Yeh, “Applied Photonics”, Elsevier, (2012).
- [2] Richard S. Quimby, “Photonics and Lasers: An Introduction”, John Wiley & Sons, (2006).
- [3] Goda, K., “Biophotonics and beyond”, *APL Photonics*, 4(5), 050401 (2019).
- [4] SPIE, “Gabriel Popescu plenary talk: Bridging Molecular and Cellular Biology with Optics”, *SPIE Newsroom*, (2015).
- [5] Newton, I. (1730), “Opticks”, 4th Ed., reprinted by Dover Publications, (1952).
- [6] Lord Rayleigh, “On the remarkable phenomenon of crystalline reflexion described by Prof. Stokes.”, *Phil. Mag.*, 26, 256–265, (1888).
- [7] A.A. Michelson (1911) LXI. “On metallic colouring in birds and insects”, *The London, Edinburgh, and Dublin Philosophical Magazine and Journal of Science*, 21:124, 554-567.
- [8] Lord Rayleigh, “On the optical character of some brilliant animal colours”, *Phil. Mag.*, 37, 98–111, (1918).
- [9] Lord Rayleigh O.M. F.R.S. (1919) VII. “On the optical character of some brilliant animal colours”, *The London, Edinburgh, and Dublin Philosophical Magazine and Journal of Science*, 37:217, 98-111.
- [10] Onslow, H. “The Iridescent Colours of Insects”, *Nature* 106, 215–218, (1920).
- [11] Lord Rayleigh, “Studies of iridescent colour, and the structure producing it. IV—Iridescent beetles”, *Proc. Roy. Soc.*, A103, 233–239, (1923).
- [12] Mayer, A. G., “On the colour and colour-patterns of moths and butterflies”, *Bull. Mus. Comp. Zool.*, 30, 169–254, (1897).
- [13] Michelson, A. A., “On metallic colouring in birds and insects”, *Phil. Mag.*, 21, 554–566, (1911).
- [14] Onslow, H., “On a periodic structure in many insect scales and the cause of their iridescent colours”, *Phil. Trans. R. Soc. Lond.*, B211, 1–74, (1921).
- [15] Merritt, E., “A spectrophotometric study of certain cases of structural color”, *Rev. Sci. Instrum.*, 11, 93–98, (1925).
- [16] S. Kinoshita, S. Yoshioka, Y. Fujii and N. Okamoto, “Photophysics of Structural Color in the Morpho Butterflies”, *Forma*, 17, 103–121, (2002).
- [17] Wilts, B. D., Saranathan, V., “A Literal Elytral Rainbow: Tunable Structural Colors Using Single Diamond Biophotonic Crystals in *Pachyrrhynchus congestus* Weevils”, *Small*, 1802328, (2018).
- [18] Shan, D., Gerhard, E., Zhang, C., Tierney, J. W., Xie, D., Liu, Z., & Yang, J., “Polymeric biomaterials for biophotonic applications”, *Bioactive Materials*, 3(4), 434–445, (2018).

- [19] M.J. Baker, C.S. Hughes, Hollywood K a., “Biophotonics: Vibrational Spectroscopic Diagnostics”, Morgan & Claypool Publishers, (2016).
- [20] S.T. Yang, L. Cao, P.G. Luo, et al., “Carbon dots for optical imaging in vivo”, *J. Am. Chem. Soc.* 131 (32), 11308–11309, (2009).
- [21] A.S. Stender, K. Marchuk, C. Liu, et al., “Single cell optical imaging and spectroscopy”, *Chem. Rev.* 113 (4), 2469–2527, (2013).
- [22] H. Zhu, S.O. Isikman, O. Mudanyali, et al., “Optical imaging techniques for point-of-care diagnostics”, *Lab a Chip*, 13 (1), 51–67, (2013).
- [23] Kolle M, Lee S., “Progress and opportunities in soft photonics and biologically inspired optics”, *Adv. Mater.* 30, 1702669, (2018).
- [24] Hecht, E., “Optics”, 2nd edn., Reading, MA: Addison-Wesley, (1974).
- [25] Plattner Luca, “Optical properties of the scales of *Morpho rhetenor* butterflies: theoretical and experimental investigation of the back-scattering of light in the visible spectrum”, *J. R. Soc. Interface*, 1: 49-59, (2004).
- [26] Peter Vukusic, J. Roy Sambles, “Shedding light on butterfly wings,” Proc. SPIE 4438, Physics, Theory, and Applications of Periodic Structures in Optics, (26 December 2001).
- [27] Srinivasarao, Mohan, “Nano-optics in the biological world: beetles, butterflies, birds, and moths”, *Chemical reviews*, 99(7), 1935-1962, (1999).
- [28] Han, Z., Mu, Z., Li, B., Niu, S., Zhang, J., Ren, L., “A High-Transmission, Multiple Antireflective Surface Inspired from Bilayer 3D Ultrafine Hierarchical Structures in Butterfly Wing Scales”, *Small* 12(6), 713–720, (2015).
- [29] J. P. Vigneron, M. Rassart, Z. Vértesy, K. Kertész, M. Sarrazin, L. P. Biró, D. Ertz, and V. Lousse, “Optical structure and function of the white filamentary hair covering the edelweiss bracts”, *Phys. Rev. E Stat. Nonlin. Soft Matter Phys.*, 71(1), 011906, (2005).
- [30] Hahn, David W., “Light scattering theory”, University of Florida, (2009).
- [31] Auber, L., “Formation of ‘Polyhedral’ Cell Cavities in Cloudy Media of Bird Feathers”, *Proceedings of the Royal Society of Edinburgh. Section B. Biology*, 74, 27-41, (1974).
- [32] Huxley John, “The coloration of *Papilio zalmoxis* and *P. antimachus*, and the discovery of Tyndall blue in butterflies”, *Proc. R. Soc. Lond. B.*, 193, 441–453, (1976).
- [33] Pradip Kumar Dutta, Joydeep Dutta, V.S.Tripathi, “Chitin and chitosan: Chemistry, properties and applications”, *Journal of Scientific & Industrial Research*, 63, 20-31, (2004).
- [34] Ernestine Alabaraoye, Mathew Achilonu, Robert Hester, “Biopolimer (Chitin) from Various Marine Seashell Wastes: Isolation and Characterization”, *Journal of Polimers and Environment*, 26(6), 2207-2218, (2017).

- [35] Zhang, F., Shen, Q., Shi, X., Li, S., Wang, W., Luo, Z., ... Shang, W., "Infrared Detection Based on Localized Modification of Morpho Butterfly Wings", *Advanced Materials*, 27(6), 1077–1082, (2014).
- [36] Li, Q., Zeng, Q., Shi, L., Zhang, X., & Zhang, K.-Q., "Bio-inspired sensors based on photonic structures of Morpho butterfly wings: a review", *Journal of Materials Chemistry C*, 4(9), 1752–1763, (2016).
- [37] Zhou, L., He, J., Li, W., He, P., Ye, Q., Fu, B., ... Shang, W., "Butterfly wing hears the sound: acoustic detection using biophotonic nanostructure", *Nano Letters*, (2019).
- [38] Wang, X.-S., Li, Y., & Shi, Y.-F., "Effects of sandwich microstructures on mechanical behaviors of dragonfly wing vein", *Composites Science and Technology*, 68(1), 186–192, (2008).
- [39] Slavica Grdanovska, "Characterization of radiation damage to a novel photonic crystal sensor", PhD Thesis, (2015).
- [40] Dutta P.K., Ravikumar M.N.V., Dutta J., "Chitin and chitosan for versatile applications", *JMS Polym Rev*, C42, 307, (2002).
- [41] Kast C.E., Frick W., Losert U., Schnurch A.B., "Thioglycolic acid conjugate: A new scaffold material for tissue engineering?", *Int.J.Pharmaceutics*, 256, 283, (2003).
- [42] Majeti N.V., Ravi Kumar, "A review of chitin and chitosan applications", *Reactive & Functional Polymers*, 46, 1-27, (2000).
- [43] H. Ghiradella, D. Aneshansley, T. Eisner, R. E. Silberglied and H. E. Hinton, "Ultraviolet Reflection of a Male Butterfly: Interference Color Caused by Thin-Layer Elaboration of Wing Scales", *Science*, 178, 1214–1217, (1972).
- [44] A. R. Parker, "The diversity and implications of animal structural colours", *J. Exp. Biol.*, 201, 2343–2347, (1998).
- [45] T. Hariyama, M. Hironaka, H. Horiguchi, D.G. Stavenga, in: S. Kinoshita, S. Yoshioka (Eds.), "Structural Colors in Biological Systems: Principles and Applications", *Osaka University Press*, Osaka, Japan, pp. 153–176, (2005).
- [46] J.P.Vigneron, M.Rassart, C.Vandenbem, V.Lousse, O.Deparis, L.P.Biro', D. Dedouaire, A. Cornet, P. Defrance, "Spectral filtering of visible light by the cuticle of metall woodboring beetles and microfabrication of a matching bioinspired material", *Phys. Rev. E*, 73, 041905, (2006).
- [47] J. Noyes, P. Vukusic, and I. Hooper, "Experimental method for reliably establishing the refractive index of buprestid beetle exocuticle", *Opt. Express*, 15, 4351-4358, (2007).
- [48] S. Yoshioka, S. Kinoshita, "Direct determination of the refractive index of natural multilayer systems", *Phys. Rev. E*, 83, 051917, (2011).
- [49] M. Nixon, A. Orr, and P. Vukusic, "Subtle design changes control the difference in colour reflection from the dorsal and ventral wing-membrane surfaces of the damselfly *Matronoides cyaneipennis*", *Opt. Express*, 21, 1479-1488, (2013).

- [50] A. E. Seago, P. Brady, J. P. Vigneron, and T. D. Schultz, “Gold bugs and beyond: a review of iridescence and structural colour mechanisms in beetles (Coleoptera)”, *J. R. Soc. Interface*, 6(Suppl 2), S165–S184, (2009).
- [51] Doekele G. Stavenga, Bodo D. Wilts, Hein L. Leertouwer, Takahiko Hariyama, “Polarized iridescence of the multilayered elytra of the Japanese jewel beetle, *Chrysochroa fulgidissima*”, *Phil. Trans. R. Soc. B*, 366, 709–723, (2011).
- [52] Deparis, O., Vandenbem, C., Rassart, M., Welch, V. L., Vigneron, J. P., “Color-selecting reflectors inspired from biological periodic multilayer structures”, *Opt. Express*, 14, 3547–3555, (2006).
- [53] Hariyama, T., Hironaka, M., Takaku, Y., Horiguchi, H., Stavenga, D. G., “The leaf beetle, the jewel beetle, and the damselfly; insects with a multilayered show case. In *Structural color in biological systems—principles and applications* (eds S. Kinoshita & S. Yoshioka)”, pp. 153–176. Osaka, Japan: *Osaka University Press*, (2005).
- [54] Kinoshita, S., Yoshioka, S., Miyazaki, J., “Physics of structural colors”, *Rep. Prog. Phys.*, 71, 076 401, (2008).
- [55] Vukusic P., Sambles J.R., Lawrence C.R., Wootton R.J., “Quantified interference and diffraction in single Morpho butterfly scales”, *Proc. R. Soc. Lond. B*, 266, (1999).
- [56] Serge Bethier, “Iridescences – The Physical Colors of Insects”, Springer, (2007).
- [57] Vukusic P., Wootton R.J. and Sambles J.R., “Remarkable iridescence in the hindwings of the damselfly *Neurobasis chinensis chinensis* (Linnaeus) (Zygoptera: Calopterygidae)”, *Proc. R. Soc. Lond. B*, 271, (2004).
- [58] A. Levy-Lior, E. Shimoni, O. Schwartz, E. Gavish-Regev, D. Oron, G. Oxford, S. Weiner, and L. Addadi, “Guanine-based Biogenic Photonic-Crystal Arrays in Fish and Spiders”, *Adv. Funct. Mater.*, 20, 320, (2010).
- [59] E. J. Denton, M. F. Land, “Mechanism of reflexion in silvery layers of fish and cephalopods”, 178, *Proc. R. Soc. Lond. B* (1971).
- [60] Jordan, T., Partridge, J. & Roberts, N., “Non-polarizing broadband multilayer reflectors in fish”, *Nature Photon*, 6, 759–763, (2012).
- [61] Hart, S. D. et al., “External reflection from omnidirectional dielectric mirror fibers”, *Science*, 296, 510–513, (2002).
- [62] Yang, S. H., Cooper, M. L., Bandaru, P. R., Mookherjea, S., “Giant birefringence in multi-slotted silicon nanophotonic waveguides”, *Opt. Express*, 16, 8306–8316, (2008).
- [63] Gessmann, T., Schubert, E. F., Graff, J. W., Streubel, K. & Karnutsch, C., “Omnidirectional reflective contacts for light-emitting diodes”, *IEEE Electron Dev. Lett.*, 24, 683–685, (2003).
- [64] Weber, M. F., “Giant birefringent optics in multilayer polymer mirrors”, *Science*, 287, 2451–2456, (2000).
- [65] Denton, E. J., Review Lecture: “On the organization of reflecting surfaces in some marine animals”, *Phil. Trans. R. Soc. B*, 258, 285–313, (1970).



- [66] Denton, E. J., Land, M. F., “Mechanism of reflexion in silvery layers of fish and cephalopods”, *Proc. R. Soc. B*, 178, 43–61, (1971).
- [67] McKenzie, D. R., Yin, Y., McFall, W. D., “Silvery fish skin as an example of a chaotic reflector”, *Proc. R. Soc. A*, 451, 579–584, (1995).
- [68] Zhang, D., Li, Z., Hu, W., Cheng, B., “Broadband optical reflector—an application of light localization in one dimension”, *Appl. Phys. Lett.*, 67, 2431–2432, (1995).
- [69] Tomasz M. Trzeciak, Peter Vukusic, “Photonic crystal fiber in the polychaete worm *Pherusa* sp.”, *Phys. Rev. E*, 80, 061908, (2009).
- [70] H. Kikuta, H. Toyota, W. Yu, “Optical elements with subwavelength structured surfaces”, *Optical Review*, 10, 2, 63–73, (2003).
- [71] Cao, Wei; Zhou, Xuhao; McCallum, Naneki C.; Hu, Ziyang; Ni, Qing Zhe; Kapoor, Utkarsh; Heil, Christian M.; Cay, Kristine S.; Zand, Tara; Mantanona, Alex J.; Jayaraman, Arthi, “Unraveling the Structure and Function of Melanin through Synthesis”, *Journal of the American Chemical Society*, 143 (7): 2622–2637, (2021).
- [72] Meredith, P., Riesz, J., “Radiative Relaxation Quantum Yields for Synthetic Eumelanin”, *Photochemistry and Photobiology*, 79(2), 211–216, (2007).
- [73] Mason, C. W., “Structural colors in feathers I”, *J. Phys. Chem.*, 27, 201–251, (1923a).
- [74] Mason, C. W., “Structural colors in feathers II”, *J. Phys. Chem.*, 27, 401–447, (1923b).
- [75] Greenwalz, C. H., Brandt, W., Friel, D. D., “Iridescent colors of humming-bird feathers”, *J. Opt Soc. Am.*, 50, 1005–1013, (1960).
- [76] Jean Pol Vigneron, Jean-Francois Colomer, Marie Rassart, Abigail L. Ingram, and Virginie Lousse, “Structural origin of the colored reflections from the black-billed magpie feathers”, *Phys. Rev. E*, 73, 021914, (2006).
- [77] Auber, L., “The structure producing “non-iridescent” blue colour in bird feathers”, *Proc. Zool. Soc. London*, 129, 455–486, (1957).
- [78] Dyck, J., “Structure and spectral reflectance of green and blue feathers of the rose-faced lovebird (*Agapornis roseicollis*)”, *Biol. Skr.*, 18(2), 1–67, (1971).
- [79] Prum, R. O., Torres, R. H., Williamson, S., Dyck, J., “Coherent light scattering by blue feather barbs”, *Nature*, 396, 28–89, (1998).
- [80] Prum, R. O., Torres, R., Williamson, S., Dyck, J., “Two-dimensional Fourier analysis of the spongy medullary keratin of structurally coloured feather barbs”, *Proc. R. Soc. London*, 266, 13–22, (1999).
- [81] Parker, A., McPhedran, R., McKenzie, D. *et al.*, “Aphrodite's iridescence”, *Nature*, 409, 36–37, (2001).

- [82] Jian Zi, Xindi Yu, Yizhou Li, Xinhua Hu, Chun Xu, Xingjun Wang, Xiaohan Liu, Rongtang Fu, “Coloration strategies in peacock feathers”, *Proceedings of the National Academy of Sciences*, 100 (22), 12576-12578, (2003).
- [83] Yizhou Li, Zhihua Lu, Haiwei Yin, Xindi Yu, Xiaohan Liu, and Jian Zi, “Structural origin of the brown color of barbules in male peacock tail feathers”, *Phys. Rev. E*, 72, 010902 (R), (2005).
- [84] Tomasz M. Trzeciak, Peter Vukusic, “Photonic crystal fiber in the polychaete worm *Pherusa* sp.”, *Phys. Rev. E*, 80, 061908, (2009).
- [85] Christopher Pedler, “The fine structure of the tapetum cellulosum”, *Experimental Eye Research*, 2, 189-195, (1963).
- [86] Lord Rayleigh Sec. R.S. XXVI., “On the remarkable phenomenon of crystalline reflexion described by Prof. Stokes”, *The London, Edinburgh, and Dublin Philosophical Magazine and Journal of Science*, 26:160, 256-265, (1888).
- [87] Yablonovitch, Eli, ”Inhibited Spontaneous Emission in Solid-State Physics and Electronics”, *Physical Review Letters*, 58(20): 2059–2062, (1987).
- [88] John, Sajeev, “Strong localization of photons in certain disordered dielectric superlattices”, *Physical Review Letters*, 58 (23): 2486–9, (1987).
- [89] P. Vukusic, J. R. Sambles, “Photonic structures in biology”, *Nature*, 424(6950), 852–855 (2003).
- [90] K. Kertész, Z. Bálint, Z. Vértésy, G. I. Márk, V. Lousse, J. P. Vigneron, M. Rassart, and L. P. Biró, “Gleaming and dull surface textures from photonic-crystal-type nanostructures in the butterfly *Cyanophrys remus*”, *Phys. Rev. E Stat. Nonlin. Soft Matter Phys.*, 74(2), 021922, (2006).
- [91] L. Biró, K. Kertész, Z. Vértésy, G. Mark, Z. Bálint, V. Lousse, J. Vigneron, “Living photonic crystals: Butterfly scales — Nanostructure and optical properties”, *Mater. Sci. Eng. C*, 27, 941–946, (2007).
- [92] J. W. Galusha, L. R. Richey, J. S. Gardner, J. N. Cha, and M. H. Bartl, “Discovery of a diamond-based photonic crystal structure in beetle scales”, *Phys. Rev. E Stat. Nonlin. Soft Matter Phys.*, 77(5), 050904, (2008).
- [93] J. D. Joannopoulos, S. G. Johnson, J. N. Winn, R. D. Meade, “Photonic Crystals: Molding the Flow of Light”, 2nd Ed., Princeton University Press, Princeton, NJ , (2008).
- [94] S. Kinoshita, “Structural Colors in the Realm of Nature”, World Scientific Publishing Company, Singapore, (2008).
- [95] Dejan Pantelić, Svetlana Savić-Šević, Dejan V. Stojanović, Srećko Ćurčić, Aleksandar J. Krmpot, Mihailo Rabasović, Danica Pavlović, Vladimir Lazović, Vojislav Milošević, “Scattering-enhanced absorption and interference produce a golden wing color of the burnished brass moth, *Diachrysia chrysitis*”, *Phys. Rev. E*, 95, 032405, (2017).

- [96] Rayleigh Sec RSL. XXVI. On the remarkable phenomenon of crystalline reflection described by Prof. Stokes, *Phil Mag.*, 26(160): 256-265, (1988).
- [97] M. Maldovan, E. L. Thomas, “Diamond-structured photonic crystals”, *Nature Materials*, 3, 593-600, (2004).
- [98] B. D. Wilts, K. Michielsen, H. De Raedt, D. G. Stavenga, “Iridescence and spectral filtering of the gyroid-type photonic crystals in *Parides sesostris* wing scales”, *Interface Focus.*, 2, 681-687, (2011).
- [99] Guldin, S., Huttner, S., Kolle, M., Welland, M. E., Muller- Buschbaum, P., Friend, R. H., Steiner, U., Tetreault, N., “Dye-sensitized solar cell based on a three-dimensional photonic crystal”, *Nano Letters*, 10, 2303–2309, (2010).
- [100] Almeida, V., Barrios, C., Panepucci, R. et al., “All-optical control of light on a silicon chip”, *Nature*, 431, 1081- 1084, (2004).
- [101] G. A. Ozin, S. M. Yang, “The Race for the Photonic Chip: Colloidal Crystal Assembly in Silicon Wafers”, *Adv. Funct. Mater.*, 11, 95-104, (2001).
- [102] A. Chutinan, S. John, O. Toader, “Diffractionless Flow of Light in All-Optical Microchips”, *Phys. Rev. Lett.*, 90, 123901, (2003).
- [103] F. Capolino, “Applications of Metamaterials”, CRC Press , Boca Raton, FL, (2009).
- [104] Jayawardana Kbskb, Gamalath Wkail, “Band Gaps of Diamond Structured Photonic Crystals”, *Open Acc J Photoen*, 2(1): 00018, (2018).
- [105] D. Levine, and P. Steinhardt, “Quasicrystals: A New Class of Ordered Structures”, *Phys. Rev. Lett.*, 53(26), 2477–2480, (1984).
- [106] Poladian, L., Wickham, S., Lee, K., Large, M. C., “Iridescence from photonic crystals and its suppression in butterfly scales”, *J. R. Soc. Interface*, 6(Suppl. 2), S233–S242, (2009).
- [107] Wilts, B. D., Michielsen, K., De Raedt, H., Stavenga, D. G., “Hemispherical Brillouin zone imaging of a diamond-type biological photonic crystal”, *Journal of The Royal Society Interface*, 9(72), 1609–1614, (2011).
- [108] Parker, A., Townley, H., “Biomimetics of photonic nanostructures”, *Nature Nanotech*, 2, 347–353, (2007).
- [109] Victoria Welch, Virginie Lousse, Olivier Deparis, Andrew Parker, and Jean Pol Vigneron, “Orange reflection from the three-dimensional photonic crystal in the scales of the weevil *Pachyrrhynchus congestus pavonius* (Curculionidae)”, *Phys. Rev. E*, 75, 041919, (2007).
- [110] Krisztián Kertész, Zsolt Bálint, Zofia Vértesy, Géza I. Márk, Virginie Lousse, Jean Pol Vigneron, Marie Rassart, and László P. Biró, “Gleaming and dull surface textures from photonic-crystal-type nanostructures in the butterfly *Cyanophrys remus*”, *Phys. Rev. E*, 74, 021922, (2006).

- [111] K.Michielsen, H. De Raedt, D.G.Stavenga, “Reflectivity of the gyroid biophotonic crystals in the ventral wing scales of the Green Hairstreak butterfly, *Callophrys ruby*”, *J. R. Soc. Interface*, 7, (2009).
- [112] Vinodkumar Saranathan, Chinedum O. Osuji, Simon G. J. Mochrie, Heeso Noh, Suresh Narayanan, Alec Sandy, Eric R. Dufresne, and Richard O. Prum, “Structure, function, and self-assembly of single network gyroid ( $I4_132$ ) photonic crystals in butterfly wing scales”, *Proceedings of the National Academy of Sciences*, 107 (26), 11676-11681, (2010).
- [113] K Michielsen, D.G Stavenga, “Gyroid cuticular structures in butterfly wing scales: biological photonic crystals”, *J. R. Soc. Interface*, 5, (2007).
- [114] Jeremy W. Galusha, Lauren R. Richey, John S. Gardner, Jennifer N. Cha, Michael H. Bartl, “Discovery of a diamond-based photonic crystal structure in beetle scales”, *Phys. Rev. E*, 77, 050904(R), (2008).
- [115] Bodo D. Wilts and Vinodkumar Saranathan, “A Literal Elytral Rainbow: Tunable Structural Colors Using Single Diamond Biophotonic Crystals in *Pachyrrhynchus congestus* Weevils ”, *Small*, 1802328, (2018).
- [116] Bodo D. Wilts, Kristel Michielsen, Jeroen Kuipers, Hans De Raedt and Doekele G. Stavenga, “*Brilliant camouflage*: photonic crystals in the diamond weevil, *Entimus imperialis*”, *Proc. R. Soc. B*, 279, (2012).
- [117] Jeremy W. Galusha, Matthew R. Jorgensen, and Michael H. Bartl, “Diamond-Structured Titania Photonic-Bandgap Crystals from Biological Templates”, *Adv. Mater.*, 22, 107–110, (2010).
- [118] Zhiwu Han, Shichao Niu, Chunhui Shang, Zhenning Liu and Luquan Ren, “Light trapping structures in wing scales of butterfly Trogonoptera brookiana”, *Nanoscale*, 4, 2879, (2012).
- [119] Schultz, T., Bernard, G., “Pointillistic mixing of interference colours in cryptic tiger beetles”, *Nature*, 337, 72–73, (1989).
- [120] Williamson, S. J., Cummins, H. Z., “Light and Color in Nature and Art”, Wiley, New York, (1983).
- [121] Welch, V., Lousse, V., Deparis, O., Parker, A. & Vigneron, J., “Orange reflection from a three-dimensional photonic crystal in the scales of the weevil *Pachyrrhynchus congestus pavonius* (Curculionidae)”, *Phys. Rev. E*, 75, 41919-1–41919-9, (2007).
- [122] Yang, S.-H., “Spintronics on chiral objects”, *Applied Physics Letters*, 116(12), 120502, (2020).
- [123] Finlayson, E. D., McDonald, L. T., Vukusic, P., “Optically ambidextrous circularly polarized reflection from the chiral cuticle of the scarab beetle *Chrysina resplendens*”, *Journal of The Royal Society Interface*, 14(131), 20170129, (2017).
- [124] Jewell, S. A., Vukusic, P., Roberts, N. W., “Circularly polarized colour reflection from helicoidal structures in the beetle *Plusiotis boucardi*”, *New Journal of Physics*, 9(4), 99–99, (2007).

- [125] De Silva, L., Hodgkinson, I., Murray, P., Wu, Q. H., Arnold, M., Leader, J., McNaughton, A., “Natural and Nanoengineered Chiral Reflectors: Structural Color of Manuka Beetles and Titania Coatings”, *Electromagnetics*, 25(5), 391–408, (2005).
- [126] Cécilia Boyon, Vanessa Soldan, and Michel Mitov, “Bioinspired, Cholesteric Liquid-Crystal Reflectors with Time-Controlled Coexisting Chiral and Achiral Structures”, *ACS Appl. Mater. Interfaces*, 13, 25, 30118–30126, (2021).
- [127] Lakshman De Silva, Ian Hodgkinson, Petra Murray, Qi Hong Wu, Matthew Arnold, John Leader, Andrew McNaughton, “Natural and Nanoengineered Chiral Reflectors: Structural Color of Manuka Beetles and Titania Coatings”, *Electromagnetics*, 25:5, 391-408, (2005).
- [128] Suet Ying Ching, Guixin Li, Hoi Lam Tam, David T. P. Goh, Joseph K. L. Goh, Kok Wai Cheah, “Chirality in Rhomborhina Gigantea beetle”, *Opt. Mater. Express*, 4, 2340-2345, (2014).
- [129] Hans Arwin, Roger Magnusson, Jan Landin, Kenneth Järrendahl, “Chirality-induced polarization effects in the cuticle of scarab beetles: 100 years after Michelson”, *Philosophical Magazine*, 92:12, 1583-1599, (2012).
- [130] G. E. Schröder-Turk, S. Wickham, H. Averdunk, F. Brink, J. D. Fitz Gerald, L. Poladian, M. C. J. Large, S. T. Hyde, “The chiral structure of porous chitin within the wing-scales of *Callophrys rubi*”, *J. Struct. Biol.*, 174, 290–295, (2011).
- [131] M. Saba, M. Thie, M. D. Turner, S. T. Hyde, M. Gu, K. Grosse-Brauckmann, D. N. Neshev, K. Mecke, G. E. Schröder-Turk, “Circular dichroism in biological photonic crystals and cubic chiral nets,” *Phys. Rev. Lett.*, 106, 103902, (2011).
- [132] S A Jewell, P Vukusic and N W Roberts, “Circularly polarized colour reflection from helicoidal structures in the beetle *Plusiotis boucardi*”, *New J. Phys.*, 9, 99, (2007).
- [133] Finlayson ED, McDonald LT, Vukusic P., “Optically ambidextrous circularly polarized reflection from the chiral cuticle of the scarab beetle *Chrysina resplendens*”, *J. R. Soc. Interface*, 14: 20170129, (2017).
- [134] Agez, G., Bayon, C., Mitov, M., “Multiwavelength micromirrors in the cuticle of scarab beetle *Chrysina gloriosa*”, *Acta Biomaterialia*, 48, 357–367, (2017).
- [135] Brink, D. J., van der Berg, N. G., Prinsloo, L. C., “The role of interface effects on the reflection of circularly polarised light from the thin-film structure of scarabus beetles”, *Surface and Interface Analysis*, 40(3-4), 769–771, (2008).
- [136] Mendoza-Galván, A., del Río, L.F., Järrendahl, K. *et al.*, “Graded pitch profile for the helicoidal broadband reflector and left-handed circularly polarizing cuticle of the scarab beetle *Chrysina chrysargyrea*”, *Sci Rep* 8, 6456, (2018).
- [137] Brink, D. J., van der Berg, N., Prinsloo, L., “Multi-color reflection from chiral thin-film stacks”, *Nanophotonic Materials VIII*, (2011).
- [138] Arwin, H., Magnusson, R., Järrendahl, K., Schoeche, S., “Effective structural chirality of beetle cuticle determined from transmission Mueller matrices using the Tellegen constitutive relations”, *Journal of Vacuum Science & Technology B*, 38(1), 014004, (2020).

- [139] Winter, B., Butz, B., Dieker, C., Schröder-Turk, G. E., Mecke, K., Spiecker, E., “Coexistence of both gyroid chiralities in individual butterfly wing scales of *Callophrys rubi*”, *Proceedings of the National Academy of Sciences*, 112(42), 12911–12916, (2015).
- [140] Hernández-Jiménez, M., Azofeifa, D. E., Libby, E., Barboza-Aguilar, C., Solís, Á., Arce-Marenco, L., ... Vargas, W. E., “Qualitative correlation between structural chirality through the cuticle of *Chrysina aurigans* scarabs and left-handed circular polarization of the reflected light”, *Optical Materials Express*, 4(12), 2632, (2014).
- [141] Coyle S, Prakash G V, Baumberg J J, Abdalsalem M, Bartlett P N, “Spherical micromirrors from template self-assembly: Polarization rotation on the micron scale”, *Appl. Phys. Lett.*, 83, 767–9, (2003).
- [142] P. Vukusic, B. Hallam, J. Noyes, “Brilliant whiteness in ultrathin beetle scales”, *Science*, 315(5810), 348, (2007).
- [143] Burresti, M., Cortese, L., Pattelli, L., Kolle, M., Vukusic, P., Wiersma, D. S., Steiner, U., Vignolini, S., “Bright-White Beetle Scales Optimise Multiple Scattering of Light.”, *Scientific Reports*, 4(1), (2014).
- [144] Schanda, János D., “Colorimetry” In Casimer DeCusatis (ed.), *Handbook of Applied Photometry*, OSA/AIP. pp. 327–412 (1997).
- [145] Stephen Westland, “CIE Whiteness”, *Encyclopedia of Color Science and Technology*, 27851-8, 5-1, (2015).
- [146] Michal Vik et al., “WHITENESS FORMULA BASED ON CIECAM02 AND THEIR TEXTILE APPLICATION”, Proceedings of the 29<sup>th</sup> CIE SESSION, Washington D.C., USA, (2019).
- [147] XYZ-CIE Tristimulus Values, Hunter Lab, Applications Note, Vol. 8, No. 1 (2008).
- [148] Ernst Ganz, “Whiteness: photometric specification and colorimetric evaluation”, *Appl. Opt.*, 15, 2039-2058, (1976).
- [149] Yoshioka, S., Kinoshita, S., “Structural or pigmentary? Origin of the distinctive white stripe on the blue wing of a *Morpho* butterfly”, *Proceedings of the Royal Society B: Biological Sciences*, 273(1583), 129–134, (2006).
- [150] Pedro David Garcia, Riccardo Sapienza, Cefe Lopez, “Photonic Glasses: A Step Beyond White Paint”, *Advanced Materials*, 22(1), 12–19, (2010).
- [151] Kuo, H. P., Chuang, M. Y., Lin, C. C., “Design correlations for the optical performance of the particle-diffusing bottom diffusers in the LCD backlight unit”, *Powder Technology*, 192(1), 116–121, (2009).
- [152] Harrison AW, Walton MR, “Radiative cooling of TiO<sub>2</sub> white paint”, *Sol Energy*, 20: 185–188, (1978).
- [153] Stavenga, D. G., Stowe, S., Siebke, K., Zeil, J., Arikawa, K., “Butterfly wing colours: scale beads make white pierid wings brighter”, *Proceedings of the Royal Society B: Biological Sciences*,

271(1548), 1577–1584, (2004).

[154] Yu, K., Fan, T., Lou, S., Zhang, D., “Biomimetic optical materials: Integration of nature’s design for manipulation of light”, *Progress in Materials Science*, 58(6), 825–873, (2013).

[155] Burrese, M., Cortese, L., Pattelli, L. *et al.*, “Bright-White Beetle Scales Optimise Multiple Scattering of Light”, *Sci Rep*, 4, 6075, (2015).

[156] Vukusic P., Sambles J.R., Lawrence C.R., “Structurally assisted blackness in butterfly scales”, *Proc. R. Soc. Lond. B.*, 271, (2004).

[157] Y. A. Akimov, W. S. Koh, S. Y. Sian, S. Ren, “Nanoparticle-enhanced thin film solar cells: Metallic or dielectric nanoparticles?”, *Appl. Phys. Lett.*, 96, 073111, (2010).

[158] E.Yablonovitch, G.D.Cody, “Intensity enhancement in textured optical sheets for solar cells”, *IEEE Trans. Electron Devices*, 29, 300, (1982).

[159] Nijhout, H. F., “The development and evolution of butterfly wing patterns”, Washington, DC: Smithsonian Institute Press, (1991).

[160] Silberglied, R. E., “Visual communication and sexual selection among butterflies”, In *The biology of butterflies, Symposium of the Royal Society of London, no. 11* (ed. R. I. Vane-Wright & P. E. Ackery), pp. 207–223. London: Academic, (1984).

[161] Brown, R. J. C., Brewer, P. J., Milton, M. J. T., “The physical and chemical properties of electroless nickel-phosphorus alloys and low reflectance nickel-phosphorus black surfaces”, *J. Mater. Chem.*, 12, 2749–2754, (2002).

[162] Arnold, K. E., Owens, I. P., Marshall, N. J., “Fluorescent signaling in parrots”, *Science*, 295, 92, (2002).

[163] Evans, J., Cuthill, I., Bennett, A., “The effect of flicker from fluorescent lights on mate choice in captive birds”, *Anim. Behav.*, 72, 393-400, (2006).

[164] Kevin J. McGraw, Matthew B. Toomey, Paul M. Nolan, Nathan I. Morehouse, Melanie Massaro, Pierre Jouventin, “A description of unique fluorescent yellow pigments in penguin feathers”, *Pigment Cell Res.*, 20, 301–304, (2007).

[165] Schumaier, G., P. C. Harrison, J. McGinnis, “Effect of colored fluorescent light on growth, cannibalism, and subsequent egg production of single comb white leghorn pullets”, *Poult. Sci.*, 47:1599–1602, (1968).

[166] Kevin J. McGraw, Melanie Massaro, Trevor J. Rivers, Thomas Mattern, “Annual, sexual, size- and condition-related variation in the colour and fluorescent pigment content of yellow crest-feathers in Snares Penguins (*Eudyptes robustus*)”, *Emu - Austral Ornithology*, 109:2, 93-99, (2009).

[167] Pete Vukusic, Ian Hooper, “Directionally controlled Fluorescence Emission in Butterflies”, *Science*, 310, 5751, (2005).

- [168] Lim, L. M. L., Land, M. F., Li, D., “Sex-specific UV and fluorescence signals in jumping spiders”, *Science*, 315, 481, (2007).
- [169] Sean J. Mulligan, Brian A. MacVicar, “Two-Photon Fluorescence Microscopy: Basic Principles, Advantages and Risks”, *Modern Research and Educational Topics in Microscopy*, 881-889, (2007).
- [170] Peter TC So, “Two-photon Fluorescence Light Microscopy”, *Encyclopedia of Life Sciences*, (2001).
- [171] Peter T. C. So, Chen Y. Dong, Barry R. Masters, Keith M. Berland, “Two-Photon Excitation Fluorescence Microscopy”, *Annual Review of Biomedical Engineering*, 2:1, 399-429, (2000).
- [172] P. Theer, M.T. Hasan, W. Denk, “Two-photon imaging to a depth of 1000  $\mu\text{m}$  in living brains by use of a Ti:Al<sub>2</sub>O<sub>3</sub> regenerative amplifier”, *Opt. Lett.*, 28, 1022–1024, (2003).
- [173] M. Oheim, E. Beaurepaire, E. Chaigneau, J. Mertz, S. Charpak, “Two-photon microscopy in brain tissue: parameters influencing the imaging depth”, *J. Neurosci. Methods*, 111, 29–37, (2001).
- [174] E. Beaurepaire, M. Oheim, J. Mertz, “Ultra-deep two-photon fluorescence excitation in turbid media”, *Opt. Commun.*, 188, 25–29, (2001).
- [175] E. Beaurepaire, J. Mertz, “Epifluorescence collection in two-photon microscopy”, *Appl. Opt.*, 41, 5376–5382, (2002).
- [176] A. Hopt, E. Neher, “Highly nonlinear photodamage in two-photon fluorescence microscopy”, *Biophys. J.*, 80, 2029–2036, (2001).
- [177] W. Denk, K. Svoboda, “Photon upmanship: why multiphoton imaging is more than a gimmick”, *Neuron*, 18, 351–357, (1997).
- [178] W. Denk, J. H. Strickler, W. W. Webb, “Two-photon laser scanning fluorescence microscopy”, *Science*, 248, 73–76, (1990).
- [179] C. Xu, W. Zipfel, J.B. Shear, R.M. Williams, W.W. Webb, “Multiphoton fluorescence excitation. New spectral windows for biological nonlinear microscopy”, *Proc. Natl. Acad. Sci. U.S.A.*, 93, 10763–10768, (1996).
- [180] R. Lansford, G. Bearman, S.E. Fraser, “Resolution of multiple green fluorescent protein color variants and dyes using two-photon microscopy and imaging spectroscopy”, *J. Biomed. Opt.*, 6, 311–318, (2001).
- [181] Masters BR, So PTC, Gratton E, “Multiphoton excitation fluorescence microscopy and spectroscopy of in vivo human skin”, *Biophysical Journal*, 72, 2405–2412, (1997).
- [182] Bewersdorf J, Rainer P, Hell SW, “Multifocal multiphoton microscopy”, *Optics Letters*, 23, 665–667, (1998).
- [183] Denk W, Delaney KR, Gelperin A et al., “Anatomical and functional imaging of neurons using 2-photon laser scanning microscopy”, *Journal of Neuroscience Methods*, 54, 151–162, (1994).



- [184] Mohler WA, Simske JS, Williams-Masson EM, Hardin JD, White JG, “Dynamics and ultrastructure of developmental cell fusions in the *Caenorhabditis elegans* hypodermis”, *Current Biology*, 8, 1087–1090, (1998).
- [185] Errington, R.J., Ameer-beg, S.M., Vojnovic, B., Patterson, L.H., Zloh, M., Smith, P.J., “Advanced microscopy solutions for monitoring the kinetics and dynamics of drug-DNA targeting in living cells”, *Adv. Drug Deliv. Rev.*, 57, 153–167, (2005).
- [186] Mouras, R., Rischitor, G., Downes, A., Salter, D., Elfick, A., “Non-linear optical microscopy for drug delivery monitoring and cancer tissue imaging”, *J. Raman Spectrosc.*, 41, 848-852, (2010).
- [187] Lin, S.J., Jee, S.H., Dong, C.Y., “Multiphoton microscopy: a new paradigm in dermatological imaging”, *Eur. J. Dermatol.*, 17, 361–366, (2007).
- [188] Tsung-Hua, T., Shiou-Hwa, J., Chen-Yuan, D., Sung-Jan, L., “Multiphoton microscopy in dermatological imaging”, *J. Dermatol. Sci.*, 56, 1–8, (2009).
- [189] Bagatolli, L.A., Sanchez, S.A., Hazlett, T., Gratton, E., “Giant vesicles, Laurdan, and two photon fluorescence microscopy: evidence of lipid lateral separation in bilayers”, *Methods Enzymol.*, 360, 481–500, (2003).
- [190] Krishnan, R. V., Saitoh, H., Terada, H., Centonze, V. E., Herman, B., “Development of a multiphoton fluorescence lifetime imaging microscopy system using a streak camera”, *Review of Scientific Instruments*, 74(5), 2714–2721, (2003).
- [191] J. B. Guild, C. Xu, and W. W. Webb, “Measurement of group delay dispersion of high numerical aperture objective lenses using two-photon excited fluorescence”, *Appl. Opt.*, 36, 397–401, (1997).
- [192] Cryan, J. R., “Molecular phylogeny of Cicadomorpha (Insecta: Hemiptera: Cicadoidea, Cercopoidea and Membracoidea): adding evidence to the controversy”, *Systematic Entomology*, 30(4), 563–574, (2004).
- [193] Siddique, R., Gomard, G., Hölscher, H., “The role of random nanostructures for the omnidirectional anti-reflection properties of the glasswing butterfly”, *Nat Commun*, 6, 6909, (2015).
- [194] Valerie R. Binetti, Jessica D. Schiffman, Oren D. Leaffer, Jonathan E. Spanier, Caroline L. Schauer, “The natural transparency and piezoelectric response of the Greta oto butterfly wing”, *Integrative Biology*, 1(4), 324–329, (2009).
- [195] Perez Goodwyn, P., Maezono, Y., Hosoda, N. et al., “Waterproof and translucent wings at the same time: problems and solutions in butterflies”, *Naturwissenschaften*, 96, 781–787, (2009).
- [196] Goodwyn, P. P., De Souza, E., Fujisaki, K., Gorb, S., “Moulding technique demonstrates the contribution of surface geometry to the super-hydrophobic properties of the surface of a water strider”, *Acta Biomaterialia*, 4(3), 766–770, (2008).
- [197] Bird, J. C. et al., “Reducing the contact time of a bouncing drop”, *Nature*, 503 (7476): 385-388, (2013).
- [198] Schmitz, H., Bleckmann, H., “The photomechanic infrared receptor for the detection of forest fires in the beetle *Melanophila acuminata* (Coleoptera: Buprestidae)”, *J Comp Physiol A*, 182, 647–657, (1998).

- [199] Evans, W. G., “Perception of Infrared Radiation from Forest Fires by *Melanophila Acuminata de Geer* (Buprestidae, Coleoptera)”, *Ecology*, 47(6), 1061–1065, (1966).
- [200] G. F. Robert, P. H. Adler, “Insect Biodiversity”, Science and Society, Chichester, UK: Willey-Blackwell, (2009).
- [201] Xiaofeng Zhou, Shalom W. Applebaum, Moshe Coll, “Overwintering and Spring Migration in the Bollworm *Helicoverpa armigera* (Lepidoptera: Noctuidae) in Israel”, *Environmental Entomology*, 29, 6, 1289–1294, (2000).
- [202] Nijhout, H.F., “The developmental physiology of color patterns in Lepidoptera”, In Berridge, M.J., Treherne, J.E., Wigglesworth, V.V.B. (ed), *Advances in Insect Physiology*, Volume 18. Academic Press, Florida, 141-248, (1985).
- [203] Prum, R.O., Quinn, T., Torres, R.H., “Anatomically diverse butterfly scales all produce structural colours by coherent scattering”, *The Journal of Experimental Biology*, 209: 748-765, (2006).
- [204] Doucet Stephanie M, Meadows Melissa G, “Iridescence: a functional perspective”, *J. R. Soc. interface.*, 6: 115–S132, (2009).
- [205] Tan, Y., Gu, J., Xu, W., Chen, Z., Liu, D., Liu, Q., Zhang, “Reduction of CuO Butterfly Wing Scales Generates Cu SERS Substrates for DNA Base Detection”, *ACS Applied Materials & Interfaces*, 5(20), 9878–9882, (2013).
- [206] Zhang, M., Meng, J., Wang, D., Tang, Q., Chen, T., Rong, S., ... Wu, Y., “Biomimetic synthesis of hierarchical 3D Ag butterfly wing scale arrays/graphene composites as ultrasensitive SERS substrates for efficient trace chemical detection”, *Journal of Materials Chemistry C*, 6(8), 1933–1943, (2018).
- [207] Tan, Y., Gu, J., Xu, L., Zang, X., Liu, D., Zhang, W., ... Zhang, D., “High-Density Hotspots Engineered by Naturally Piled-Up Subwavelength Structures in Three-Dimensional Copper Butterfly Wing Scales for Surface-Enhanced Raman Scattering Detection”, *Advanced Functional Materials*, 22(8), 1578–1585, (2012).
- [208] Zhang, W., Zhang, D., Fan, T., Gu, J., Ding, J., Wang, H., ... Ogawa, H., “Novel Photoanode Structure Templated from Butterfly Wing Scales”, *Chemistry of Materials*, 21(1), 33–40, (2009).
- [209] Fang, J., Song, G., Liu, Q., Zhang, W., Gu, J., Su, Y., ... Zhang, D., “Enhanced photocatalytic hydrogen production on three-dimensional gold butterfly wing scales/CdS nanoparticles”, *Applied Surface Science*, 427, 807–812, (2018).
- [210] Parker, A., Townley, H. “Biomimetics of photonic nanostructures”, *Nature Nanotech*, 2, 347–353, (2007)
- [211] Bhushan, B., “Biomimetics: lessons from nature-an overview”, *Philosophical Transactions of the Royal Society A: Mathematical, Physical and Engineering Sciences*, 367(1893), 1445–1486, (2009).

- [212] Franziska Schenk, Doekele G. Stavenga, “The Lesser Purple Emperor butterfly, *Apatura ilia*: from mimesis to biomimetics”, *Faraday Discussions*, 223, 145-160, (2020).
- [213] P. Vukusic, R. Kelly, I. Hooper, “A biological sub-micron thickness optical broadband reflector characterized using both light and microwaves”, *J. Roy. Soc. Interface*, 6, S193 – S201, (2009).
- [214] “Malin Space Science Systems – Mars Science Laboratory (MSL), Mars Hand Lens Imager (MHLI)”, Instrument Description.
- [215] Johnson, Dave, “How to Do Everything: Digital Camera (5th ed.)”, McGraw-Hill Osborne Media, p. 336, (2008).
- [216] Sidney F. Ray, “Applied Photographic Optics (3rd ed.)”, Oxford: Focal Press, p. 231-232, (2002).
- [217] D. Domine, F.-J. Haug, C. Battaglia, C. Ballif, “Modeling of light scattering from micro- and nanotextured surfaces”, *J. Appl. Phys.*, 107, 044504, (2010).
- [218] Y. A. Akimov, W. S. Koh, S. Y. Sian, S. Ren, “Nanoparticle-enhanced thin film solar cells: Metallic or dielectric nanoparticles?”, *Appl. Phys. Lett.*, 96, 073111, (2010).
- [219] J. e. Schanda, “Colorimetry: Understanding the CIE System”, Hoboken, NJ: John Wiley & Sons, (2007).
- [220] Smith, Thomas, Guild, John, “The C.I.E. colorimetric standards and their use”, *Transactions of the Optical Society*, 33 (3): 73–134, (1931–32).
- [221] I. G. Johnston et al., “Mitochondrial variability as a source of extrinsic cellular noise”, *PLoS Comput. Biol.*, 8, e1002416:1, (2012).
- [222] Kaern, M.; Elston, T.R.; Blake, W.J., Collins, J.J., “Stochasticity in gene expression: from theories to phenotypes”, *Nat. Rev. Genet.*, 6 (6): 451–464, (2005).
- [223] Lewin, Benjamin, “Genes”, 6<sup>th</sup> edition, Oxford University Press, (1997).
- [224] Maheshri N, O’Shea, “Living with noisy genes: how cells function reliably with inherent variability in gene expression”, *Annu. Rev. Biophys. Biomol. Struct*, 36: 413–434, (2007).
- [225] Johnston, I.G., “The chaos within: exploring noise in cellular biology”, *Significance*, 19 (4): 17–21, (2012).
- [226] G. T. di Francia, “Degrees of freedom of an image”, *JOSA*, 59, 799 - 804, (1969).
- [227] A. Dinwiddie, R. Null, M. Pizzano, L. Chuong, A. Leigh Krup, H. Ee Tan, N. H. Patel, “Dynamics of F-actin prefigure the structure of butterfly wing scales”, *Dev. Biol.*, 392, 404 (2014).
- [228] K. Watanabe, T. Hoshino, K. Kanda, Y. Haruyama, T. Kaito, S. Matsui, “Optical measurement and fabrication from a *Morpho*-butterfly-scale quasistructure by focused ion beam chemical vapor deposition”, *J. Vac. Sci. Technol. B*, 23, 570, (2005).
- [229] D. Colton, R. Kress, “Inverse Acoustic and Electromagnetic Scattering Theory”, 2nd ed. New York, NY: Springer, (1998).

- [230] F. Monticone, A. Alu, “Do clocked objects really scatter less?”, *Phys. Rev. X*, 3(041005), 1, (2013).
- [231] G. Bao, P. Li, J. Lin, F. Triki, “Inverse scattering problems with multi-frequencies”, *Inverse Probl*, 31, 093001, (2015).
- [232] S. Toxqui-López, A. Olivares-Pérez, I. Fuentes-Tapia, A. Quintero-Romo, “Duplication of holograms by using fingernail polish”, *Opt. Mater.*, 29, 1604 (2007).
- [233] Benjamin D. Chrysler, Raymond K. Kostuk, “Volume hologram replication system for spectrum-splitting photovoltaic applications”, *Appl. Opt.*, 57, 8887-8893, (2018).
- [234] Makoto Okui, Koki Wakunami, Ryutaro Oi, Yasuyuki Ichihashi, Boaz Jessie Jackin, Kenji Yamamoto, “Copying of holograms by spot scanning approach”, *Appl. Opt.*, 57, 4117-4122, (2018).
- [235] E.P. Newman, “Franklin Making Money More Plentiful”, *Proceedings of the American Philosophical Society*, 115, 341, (1971).
- [236] Farley Grubb, “Benjamin Franklin and the birth of the paper money economy”, Essay based on Mar. 30, 2006 lecture , published by Federal Reserve Bank of Philadelphia.
- [237] R. L. Van Renesse, “Optical document security”, 3rd ed., Norwood, MA: Artech House, (2004).
- [238] W. Zhang, J. Gu, Q. Liu, H. Su, T. Fan, D. Zhang, “Butterfly effects: novel functional materials inspired from the wing scales”, *Phys. Chem. Chem. Phys.*, 16, 19767, (2014).
- [239] C. Boehm, M. Hofer , “ Physically unclonable functions in theory and practice ”, Springer, (2013).
- [240] R. Pappu, B. Recht, J. Taylor, N. Gershenfeld, “Physical one-way functions”, *Science*, 297, 2026–2030, (2002).
- [241] J. D. R. Buchanan et al, “Forgery: “Fingerprinting” documents and packaging”, *Nature*, 436 (7050): 475, (2005).
- [242] Hamm-Dubischar, C. Patent No. WO 2007031077 (A1), “Inorganic marking particles for characterizing products for proof of authenticity method for production and use thereof”, (2007).
- [243] Biermann, N., Rauhe, H., “Method for Producing Security Markings”, WO2004070667 A2, (2004).
- [244] Rauhe, H., “Verfahren zur Herstellung von information stragenden mikropartikulären Gemischen”, Patent DE10238506 A1, (2004).
- [245] J. Wood, “Invariant pattern recognition”, *Pattern Recognition.*, 29, 1, 1-17, (1996).
- [246] A. Grace, M. Spann, “A comparison between Fourier-Mellin descriptors and moment based features for invariant object recognition using neural networks”, *Pattern Recognition Lett.*, 12, 635-643, (1991).
- [247] Y. Li, “Reforming the theory of invariant moments for pattern recognition”, *Pattern Recognition*, 25, 723-730, (1992).

- [248] Y. Sheng, H. H. Arsenault, “Experiments on pattern recognition using invariant Fourier-Mellin descriptors”, *J. Optical Soc. America A (Optics and Image Sci.)*, 3, 771-776, (1986).
- [249] R. Wu, H. Stark, “Three dimensional object recognition from multiple views”, *J. Optical Soc. America A (Optics and Image Sci.)*, 3, 1543-1557, (1986).
- [250] T. M. Caelli, Zhi-Qiang Liu, “On the minimum number of templates required for shift, rotation and size invariant pattern recognition”, *Pattern Recognition*, 21, 205-216, (1988).
- [251] Wood, J., “Invariant pattern recognition: A review.”, *Pattern Recognition*, 29(1), 1–17, (1996).
- [252] J. L. de Bougrenet de la Tocnaye, F. Ghorbei, “A rotation, scaling and translation invariant pattern classification system”, *Pattern Recognition Lett.*, 8, 55-58, (1988).
- [253] S. Kagcyu, N. Ohnishi, N. Sugie, “Augmented multilayer perceptron for rotation-and scale-invariant hand-written numeral recognition”, *Proceedings of 1991 IEEE International Joint Conference on Neural Networks*, 1, pp. 54-59. IEEE (1991).
- [254] Y. Sheng, J. Duvernoy, “Circular Fourier radial Mellin transform descriptors for pattern recognition”, *J. Optical Soc. America A (Optics and Image Sci.)*, 3, 885-888, (1986).
- [255] Y. Sheng, C. Lejeune, “Invariant pattern recognition using Fourier-Mellin transforms and neural networks”, *J. Optics*, 22, 223-228, (1991).
- [256] M. E. McNamara et al, “Fossilized Biophotonic Nanostructures Reveal the Original Colors of 47-Million-Year Old Moths”, *PLoS Biol.*, 9, e1001200:1, (2011).
- [257] J. Zhang, M. Gecevicius, M. Beresna, P. G. Kazansky, “Seemingly Unlimited Lifetime Data Storage in Nanostructured Glass”, *Phys. Rev. Lett.*, 112, 033901, (2014).
- [258] Pris, A., Utturkar, Y., Surman, C. et al., “Towards high-speed imaging of infrared photons with bio-inspired nanoarchitectures”, *Nature Photon* 6, 195–200, (2012).
- [259] Potyrailo, R., Ghiradella, H., Vertiatchikh, A. et al., “*Morpho* butterfly wing scales demonstrate highly selective vapour response”, *Nature Photon*, 1, 123–128, (2007).
- [260] Hsuan-Ming Hu, Jolanta A. Watson, Bronwen W. Cribb, Gregory S. Watson, “Fouling of nanostructured insect cuticle: adhesion of natural and artificial contaminants”, *Biofouling*, 27:10, 1125-1137, (2011).
- [261] Shi, N.N., Tsai, C.C., Camino, F., Bernard, G.D., Yu, N., Wehner, R., “Keeping cool: Enhanced optical reflection and radiative heat dissipation in Saharan silver ants”, *Science*, 349(6245), 298-301, (2015).
- [262] Gillott, C., “Food Uptake and Utilization”, *Entomology*, 487–513, (2005).
- [263] Gullan, P. J., Cranston, P.S., “The insects: an outline of entomology”, John Wiley & Sons, (2004).
- [264] Capinera, J.L., “Encyclopedia of entomology”, Springer Science & Business Media, New York, (2008).

- [265] Hui, Y., Gomez-Diaz, J. S., Qian, Z., Alu, A., Rinaldi, M., “Plasmonic piezoelectric nanomechanical resonator for spectrally selective infrared sensing”, *Nature communications*,7(1), 1-9, (2016).
- [266] Dao, T. D., Ishii, S., Yokoyama, T., Sawada, T., Sugavaneshwar, R. P., Chen, K., Wada, Y., Nabatame T., Nagao, T., “Hole array perfect absorbers for spectrally selective midwavelength infrared pyroelectric detectors”, *Acs Photonics*, 3(7), 1271-1278, (2016).
- [267] Ogawa, S., Okada, K., Fukushima, N., Kimata, M., “Wavelength selective uncooled infrared sensor by plasmonics”, *Applied Physics Letters*, 100(2), 021111, (2012).
- [268] Fleming, J. G., Lin, S. Y., El-Kady, I., Biswas, R., Ho, K. M., “All-metallic three-dimensional photonic crystals with a large infrared bandgap”, *Nature*, 417(6884), 52-55, (2002).
- [269] LeMieux, M. C., McConney, M. E., Lin, Y. H., Singamaneni, S., Jiang, H., Bunning, T. J., Tsukruk, V. V., “Polymeric nanolayers as actuators for ultrasensitive thermal bimorphs”, *Nano letters*, 6(4), 730-734, (2006).
- [270] Watts, M. R., Shaw, M. J., Nielson, G. N., “Microphotonic thermal imaging”, *Nature Photonics*, 1(11), 632-634, (2007).
- [271] Yi, F., Zhu, H., Reed, J. C., Cubukcu, E., “Plasmonically enhanced thermomechanical detection of infrared radiation”, *Nano letters*, 13(4), 1638-1643, (2013).
- [272] Zhang, F., Shen, Q., Shi, X., Li, S., Wang, W., Luo, Z., ... Shang, W., “Infrared detection based on localized modification of Morpho butterfly wings”, *Advanced materials*, 27(6), 1077-1082, (2015).
- [273] Michelle Gleeson, “Miniature Lives: Identifying Insects in Your Home and Garden”, CSIRO Publishing, page 313, (2016).
- [274] Augustus Radcliffe Grote, “Canadian Entomologist”, *Entomological Society of Canada*, 41, (1909).
- [275] Chandrasekhar, S., “Radiative Transfer”, Oxford University Press, (1950).
- [276] RCA Electro-Optics Handbook, page 18 .
- [277] Warren J. Smith, “Modern Optical Engineering”, *McGraw-Hill*, p. 228, 256, (2000).
- [278] Pedrotti & Pedrotti, “Introduction to Optics”, Prentice Hall, (1993).
- [279] Shi, N.N., “Biological and Bioinspired Photonic Materials for Passive Radiative Cooling and Waveguiding”, Doctoral dissertation, Columbia University, (2018).
- [280] Florescu, M., Torquato, S., Steinhardt, P.J., “Designer disordered materials with large, complete photonic band gaps”, *Proceedings of the National Academy of Sciences*, 106(49), 20658-20663, (2009).
- [281] Torquato S, Stillinger FH, “Local density fluctuations, hyperuniformity, and order metrics”, *Phys. Rev. E*, 68:041113/1–25, (2003).
- [282] Takeda, S., Viktorovitch, P., Obara, M., “Anderson localization of light in two-dimensional random photonic crystals”, *1st International Symposium on Access Spaces (ISAS)*, (2011).

- [283] Bingi, J., Nair, R. V., Vijayan, C., “Time dependent Bloch mode transmittance in self-assembled random photonic crystal for photonic time delay switching”, *Optical Materials*, 64, 95–99, (2017).
- [284] Asatryan, A. A., Robinson, P. A., Botten, L. C., McPhedran, R. C., Nicorovici, N. A., Martijn de Sterke, C., “Effects of disorder on wave propagation in two-dimensional photonic crystals”, *Physical Review E*, 60(5), 6118–6127, (1999).
- [285] Chiasera Alessandro, Scotognella Francesco, Criante Luigino, Varas Stefano, Valle Giuseppe Della, Ramponi Roberta, Ferrari Maurizio, “Disorder in Photonic Structures Induced by Random Layer Thickness”, *Science of Advanced Materials*, 7, 1207-1212(6), (2015).
- [286] Mizuno, K., Ishii, J., Kishida, H., Hayamizu, Y., Yasuda, S., Futaba, D.N., Yumura, M., Hata, K., “A black body absorber from vertically aligned single-walled carbon nanotubes”, *Proceedings of the National Academy of Sciences*, 106(15), 6044-6047, (2009).
- [287] De Nicola, F., Hines, P., De Crescenzi, M., Motta, N., “Thin randomly aligned hierarchical carbon nanotube arrays as ultrablack metamaterials”, *Physical Review B*, 96(4), 045409, (2017).
- [288] Leonhardt, U., Tyc, T., “Broadband invisibility by non-Euclidean cloaking”, *Science*, 323(5910), 110-112, (2009).
- [289] Pavlović, D., Vasiljević, D., Salatić, B., Lazović, V., Dikić, G., Tomić, L., Čurčić, S., Milovanović, P., Todorović, D., Pantelić, D. V., “Photonic structures improve radiative heat exchange of *Rosalia alpina* (Coleoptera: Cerambycidae)”, *Journal of Thermal Biology*, 76, 126–138, (2018).
- [290] Heinrich, B., “The hot-blooded insects: strategies and mechanisms of thermoregulation”, Springer Science & Business Media, New York, (2013).
- [291] Vollmer, M., Möllmann, K.P., “Infrared thermal imaging: fundamentals, research and applications”, John Wiley & Sons, (2010).
- [292] Prokhorov, A., “Effective emissivities of isothermal blackbody cavities calculated by the Monte Carlo method using the three-component bidirectional reflectance distribution function model”, *Applied Optics*, 51(13), 2322 – 2332, (2012).
- [293] Griffiths, P., de Hasseth, J. A., “Fourier Transform Infrared Spectrometry”, (2nd ed.), Wiley-Blackwell, (2007).
- [294] Manor, Joshua; Feldblum, Esther S., Arkin, Isaiah T., “Environment Polarity in Proteins Mapped Noninvasively by FTIR Spectroscopy”, *The Journal of Physical Chemistry Letters*, 3 (7): 939–944, (2012).
- [295] Brielle, Esther S., Arkin, Isaiah T., “Site-Specific Hydrogen Exchange in a Membrane Environment Analyzed by Infrared Spectroscopy”, *The Journal of Physical Chemistry Letters*, 9 (14): 4059–4065, (2018).
- [296] Rawat, P. S., Srivastava, R. C., Dixit, G., Asokan, K., “Structural, functional and magnetic ordering modifications in graphene oxide and graphite by 100 MeV gold ion irradiation”, *Vacuum*, 109700, (2020).
- [297] Deepty, M., Ch Srinivas, E. Ranjith Kumar, N. Krisha Mohan, C. L. Prajapat, TV Chandrasekhar Rao, Sher Singh Meena, Amit Kumar Verma, D. L. Sastry, “XRD, EDX, FTIR and ESR spectroscopic

studies of co-precipitated Mn-substituted Zn-ferrite nanoparticles”, *Ceramics International* ,45, 6, 8037-8044, (2019).

[298] Dole, M.N., Patel, P.A., Sawant, S.D., Shedpure, P.S., “Advance Applications of Fourier Transform Infrared Spectroscopy”, *Int. J. Pharm. Sci. Rev. Res.*, 7, 159–166, (2011).

[299] Haas, J., Mizaiko, B., “Advances in Mid-Infrared Spectroscopy for Chemical Analysis”, *Annu. Rev. Anal. Chem*, 9, 45–68, (2016).

[300] Li, G., Jing, W., Wen, Z., “Identification of Unknown Mixtures of Materials from Biopharmaceutical Manufacturing Processes by Microscopic-FTIR and Library Searching”, *Am. Pharm. Rev.*, 14, 60, (2011).

[301] Stefanowics, Z., Stefanowics, J., Mulas, K., “Determination of Tropicamide And Its Major Impurity in Raw Material By the HPLC-DAD Analysis and Identification of This Impurity Using the Offline HPLC-FT-IR Coupling”, *J. Pharm. Biomed. Anal.*, 49, 214–220, (2009).

[302] Basiuk, V.A., “Quantum chemical calculations of infrared spectra for the identification of unknown compounds by GC/FTIR/MS in exobiological simulation experiments”, *Adv. Space Res.*, 27, 255–260, (2001).

[303] Kumar Pandey, A., Rapolu, R., Raju, Ch.K., Sasalamari, G., Kumar, G.S., Awasthi, A., Navalgund, S.G., Surendranath, K.V., “The novel acid degradation products of losartan: Isolation and characterization using Q-TOF, 2D-NMR and FTIR”, *J. Pharm. Biomed. Anal.*, 120, 65–71 ,(2016).

[304] Roychoudhury, P., Harvey, L.M., McNeil, B., “The potential of mid infrared spectroscopy (MIRS) for real time bioprocess monitoring”, *Anal. Chim. Acta.*, 571, 159–166, (2006).

[305] Scholz, T., Lopes, V.V., Calado, C.R.C., “High-throughput analysis of the plasmid bioproduction process in *Escherichia coli* by FTIR spectroscopy”, *Biotechnol. Bioeng.*, 109, 2279–2285, (2012).

[306] Villar, A., Gorritxategi, E., Aranzabe, E., Fernandez, S., Otaduy, D., Fernandez, L.A., “Low-cost visible–near infrared sensor for on-line monitoring of fat and fatty acids content during the manufacturing process of the milk”, *Food Chem.*, 135, 2756–2760, (2012).

[307] Bi, X., Yang, X., Bostrom, M.P.G., Pleshko Camacho, N., “Fourier transform infrared imaging spectroscopy investigations in the pathogenesis and repair of cartilage”, *Biochim. Biophys. Acta*, 1758, 934–941, (2006).

[308] Nabers, A., Ollesch, J., Schartner, J., Kotting, C., Genius, J., Haußmann, U., Klafki, H., Wiltfang, J., Gerwert, K., “An infrared sensor analysing label-free the secondary structure of the Abeta peptide in presence of complex fluids”, *J. Biophotonics*, 9, 224–234, (2016).

[309] Barrios, V.A.E., Mendez, J.R.R., Aguilar, N.V.P., Espinosa, G.A., Rodríguez, J.L.D., “FTIR—An Essential Characterization Technique for Polymeric Materials”, *Materials Science, Engineering and Technology*, Theophanides, T., Ed.; IntechOpen: London, UK, (2012).

[310] Al-Ali, A.A.S., Kassab-Bashi, T.Y., “Fourier Transform Infra Red (FTIR) Spectroscopy of New Copolymers of Acrylic Resin Denture Base Materials”, *IJERSTE*, 4, 172–180, (2015).



- [311] Sardon, H., Engler, A.C., Chan, J.M.W., Coady, D.J., O'Brien, J.M., Mecerreyes, D., Yang, Y.Y., Hedrick, J.L., "Homogeneous isocyanate- and catalyst-free synthesis of polyurethanes in aqueous media", *Green Chem.*, 15, 1121–1126, (2013).
- [312] Schartner, J., Hoeck, N., Guldenhaupt, J., Mavarani, L., Nabers, A., Gerwert, K., Kotting, C., "Chemical Functionalization of Germanium with Dextran Brushes for Immobilization of Proteins Revealed by Attenuated Total Reflection Fourier Transform Infrared Difference Spectroscopy", *Anal. Chem.*, 87, 7467–7475, (2015).
- [313] Navarra, G., Cannas, M., D'Amico, M., Giacomazza, D., Militello, V., Vaccaro, L., Leone, M., "Thermal oxidative process in extra-virgin olive oils studied by FTIR, rheology and time-resolved luminescence", *Food Chem.*, 126, 1226–1231, (2011).
- [314] Poiana, M.-A., Alexa, E., Melania-Florina Munteanu, M.-F., Gligor, R., Moigradean, D., Mateescu, C., "Use of ATR-FTIR spectroscopy to detect the changes in extra virgin olive oil by adulteration with soybean oil and high temperature heat treatment", *Open Chem.*, 13, 689–698, (2015).
- [315] Malek, M.A., Nakazawa, T., Kang, H.-W., Tsuji, K., Ro, C.-U., "Multi-Modal Compositional Analysis of Layered Paint Chips of Automobiles by the Combined Application of ATR-FTIR Imaging, Raman Microspectrometry, and SEM/EDX", *Molecules*, 24, 1381–1397, (2019).
- [316] González-Gaitano, G., Isasi, J. R., "Analysis of the Rotational Structure of CO<sub>2</sub> by FTIR Spectroscopy", *The Chemical Educator*, 6(6), 362–364, (2001).
- [317] Woodbridge, E. L., Fletcher, T. R., Leone, S. R., "Photofragmentation of acetone at 193 nm: rotational- and vibrational-state distributions of the carbon monoxide fragment by time-resolved FTIR emission spectroscopy", *The Journal of Physical Chemistry*, 92(19), 5387–5393, (1988).
- [318] Ulenikov, O. N., Onopenko, G. A., Gromova, O. V., Bekhtereva, E. S., Horneman, V.-M., "Re-analysis of the (100), (001), and (020) rotational structure of SO<sub>2</sub> on the basis of high resolution FTIR spectra", *Journal of Quantitative Spectroscopy and Radiative Transfer*, 130, 220–232, (2013).
- [319] Daryl L. Logan., "A first course in the finite element method", Cengage Learning, (2011).
- [320] Born, M.; Wolf, E., "Principles of optics: electromagnetic theory of propagation, interference and diffraction of light", Oxford, Pergamon Press, (1964).
- [321] Speakman J.R., Ward S., "Infrared Thermography: principles and applications", *Zoology* 101, 224 – 232, (1998).
- [322] Tait Elder, John Strong, "The infrared transmission of atmospheric windows", *Journal of the Franklin Institute* 255 (3), 189-208, (1953).
- [323] Ronald G. Driggers, "Encyclopedia of optical engineering", Volume 3. CRC Press. p. 2303, (2003).
- [324] Demchenko, Alexander P., "Photobleaching of organic fluorophores: quantitative characterization, mechanisms, protection", *Methods and Applications in Fluorescence* 8(2), 022001, (2020).
- [325] Ghauharali, R. I., Brakenhoff, G. J., "Fluorescence photobleaching-based image standardization for fluorescence microscopy", *Journal of Microscopy*, 198, 88-100, (2001).

- [326] Shawkey Matthew D, Morehouse Nathan I, Vukusic Peter, “A protean palette: colour materials and mixing in birds and butterflies”, *J. R. Soc. Interface*, 6, S221–S231, (2009).
- [327] Barzic, A.I., Albu, R.M., “Optical properties and biointerface interactions of chitin”, *Polym. Bull.*, 78, 6535–6548, (2021).
- [328] Liang, Zhang, “Narcissus effect in staring infrared optical system”, *Infrared and Laser Engineering* (2006): S2.
- [329] Anthony S. Lau, “The Narcissus Effect In Infrared Optical Scanning Systems”, *Proc. SPIE* 0107, Stray Light Problems in Optical Systems, (1977).
- [330] D. C. Culver, T. Pipan, “The Biology of Caves and Other Subterranean Habitats”, Oxford University Press, Oxford, (2009).
- [331] K. Christiansen, “Morphological adaptations”, in *Encyclopedia of Caves*, W. B. White and D. C. Culver, Eds., 2nd ed., pp. 517–528, Elsevier, Amsterdam, (2012).
- [332] A. I. Camacho, “The Natural History of Biospeleology”, *Monografias del Museo nacional de ciencias naturales, Consejo superior de investigaciones científicas*, Madrid, (1992).
- [333] P. J. Gullan, P. S. Cranston, “The Insects: An Outline of Entomology”, John Wiley & Sons, New York, (2009).
- [334] M. Moseley, “Observations on the cave-associated beetles (Coleoptera) of Nova Scotia, Canada”, *Int. J. Speleol.*, 38, 163–172, (2009).
- [335] Cody, D. D., *AAPM/RSNA Physics Tutorial for Residents: Topics in CT. RadioGraphics*, 22(5), 1255–1268 (2002).
- [336] B. Nie et al., “Multimodal microscopy with sub-30 fs Yb fiber laser oscillator”, *Biomed. Opt. Express*, 3, 1750–1756, (2012).
- [337] E. J. Gualda et al., “In vivo imaging of anatomical features of the nematode *Caenorhabditis elegans* using non-linear (TPEF-SHG-THG) microscopy”, *Proc. SPIE*, 6630, 663003, (2007).
- [338] R. Carriles et al., “Imaging techniques for harmonic and multiphoton absorption fluorescence microscopy,” *Rev. Sci. Instrum.*, 80, 081101, (2009).
- [339] C. K. Chou et al., “Polarization ellipticity compensation in polarization second-harmonic generation microscopy without specimen rotation”, *J. Biomed. Opt.*, 13, 014005, (2008).
- [340] J.-A. Conchello, J. W. Lichtman, “Optical sectioning microscopy”, *Nat. Methods*, 2, 920–931, (2005).

## Прилог А

### Нелинеарна ласерска микроскопија хитинских структура инсеката

Нелинеарне оптичке особине хитина, које су истражене у првом делу овог истраживања, искоришћене су и за демонстрацију примена нелинеарне ласерске микроскопије хитина у ентомологији.

Анализирани су делови тела два пећинска инсекта: *Plusiocampa christiani* (Condé & Vareth, 1996, који припада подкласи *Apterygota* - инсекти без крила) и *Pheggomisetes ninae* (S. Ćurčić, Schönmann, Brajković, B. Ćurčić & Tomić, 2004, који припада подкласи *Pterygota* - инсекти са крилима). Ови инсекти су изабрани зато што не садрже пигменте, па је њихов доминантан градивни састојак хитин. Ова особина, настала услед адаптације на подземни стил живота [330], чини их веома погодним за ово истраживање – приликом озрачивања узорака ласерском радијацијом очекује се двофотонски побуђена флуоресценција и други хармоник од хитина, а не од комбинације одзива хитина и пигмената присутних код других (копнених) инсекта. Детектована је само природна ауто-флуоресценција инсеката. Кутикула, спољашњи тврд омотач, им је веома танак, са хомогено распоређеним хитином [331] што омогућава осликавање дубинских структура инсеката и ласерску хирургију.

*Plusiocampa christiani*, слика 3.5а, је изабран због карактеристичне беле боје која је последица потпуног одсуства пигмента [332]. Изузев одређене количине протеина, кутикула овог инсекта је окарактерисана као високо-хитинизована структура [333]. Ово је потврђено упоређивањем дво-фотонски побуђеног флуоресцентног спектра кутикуле и хемијски прочишћеног хитина (слика 3.6). На слици 3.6 се уочава велики степен сличности између кривих у опсегу 830-860 nm. На већим таласним дужинама флуоресценција инсекта је већа, услед присуства флуоресцентних пигмената у кутикули (највероватније протеини) који интензивније флуоресцирају у поменутом спектралном опсегу.

*Pheggomisetes ninae*, слика 3.5б, је слабо пигментисан инсект и његова флуоресценција највећим делом потиче од хитина, уз слабо изражено присуство флуоресценције која потиче од других компонената кутикуле [334].



(a)



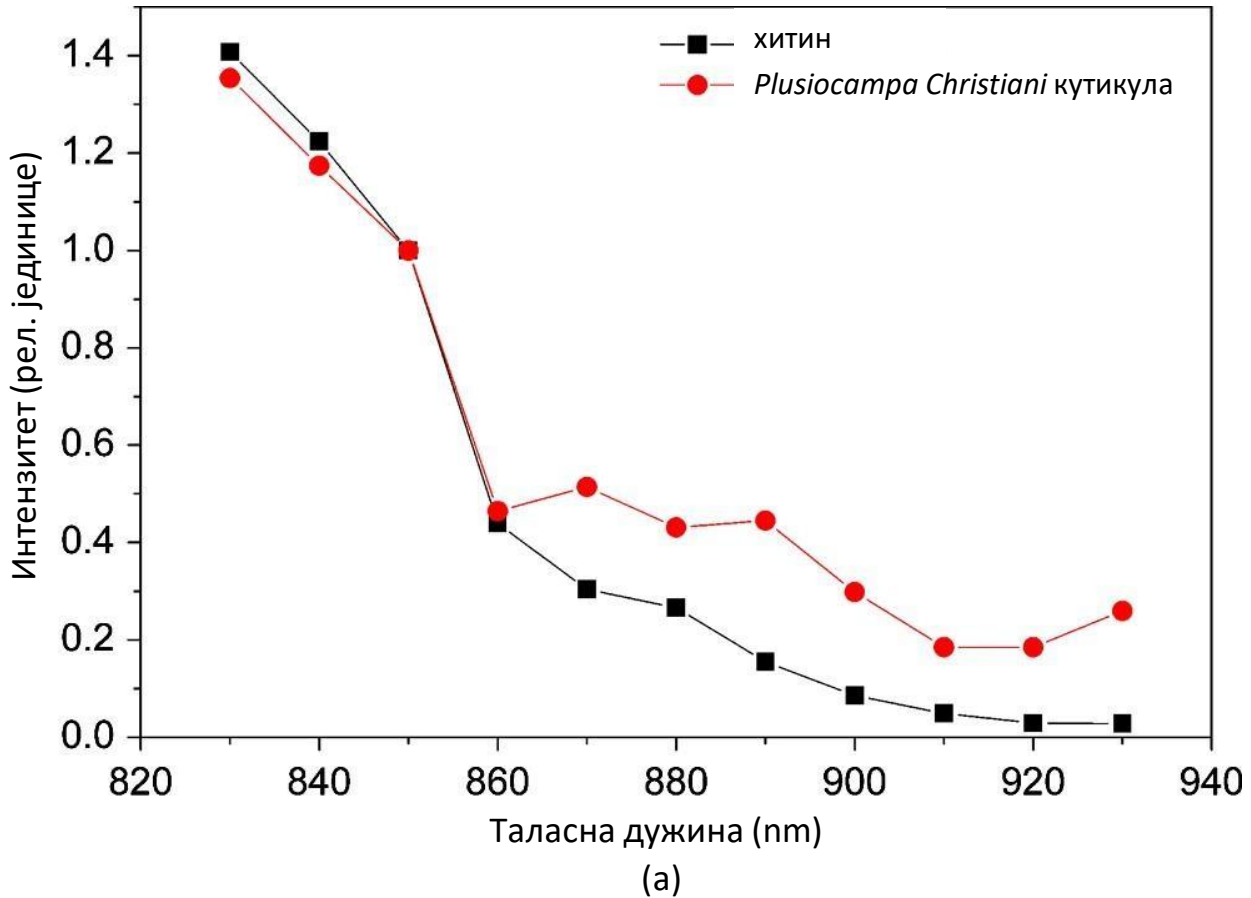
(б)

**Слика 3.5.** а) *Plusiocampa christiani* ; б) *Pheggomisetes ninae*. Фотографисао Драган Антвић, Биолошки факултет у Београду.

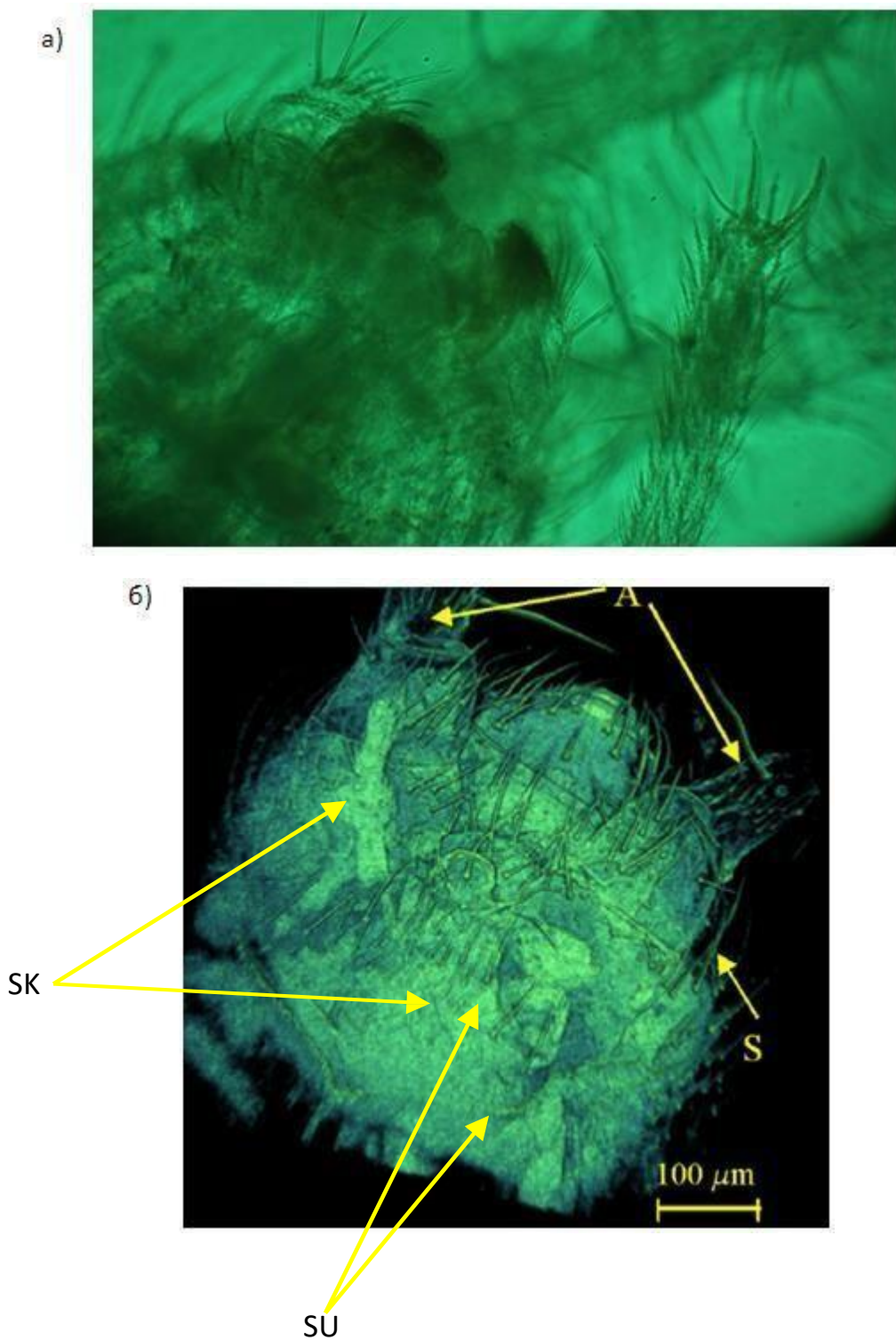
Значај флуоресцентне нелинеарне ласерске микроскопије у изучавању морфологије инсеката демонстриран је на сликама 3.7, 3.8, 3.9 и 3.10. На свим сликама се уочава знатно квалитетније и детаљније осликавање узорака коришћењем двофотонски побуђене флуоресценције хитина на нелинеарном ласерском микроскопу, у поређењу са оптичком микроскопијом. Све слике су добијене на релативно малим снагама ласерске радијације (10 – 12 mW). Интензитет сигнала је варирао у зависности од дела тела инсекта. Ширина видног поља (654  $\mu\text{m}$ ) омогућава да глава *Plusiocampa christiani* инсекта буде у целости осликана (слика 3.7б). Дубина продирања ласерске радијације ( $\sim 200 \mu\text{m}$ ) омогућава осликавање делова усне регије, који су смештени вентрално. Латерална резолуција нелинеарног ласерског микроскопа (630 nm X 915 nm, за објектив 40X, 0.65 NA) је довољна да на слици буду јасно уочљиви поједини детаљи дорзалног дела главе: антене, склерити (скелетне плоче којима је обавијен сваки телесни регион инсеката), сuture (бразде које се налазе између склерита), као и сете (ситне длачице којима је прекривено тело инсекта, многе сете имају функцију сензора). Ово је демонстрирано и на примерима задњег дела абдомена инсекта *Plusiocampa christiani* (слика 3.9) и апикалног дела главе *Pheggomisetes ninae* инсекта, у вентралној перспективи, приказаног на слици 3.10, на којој су веома видљиви делови усне регије (делови доње вилице (лат. *mandibula*), чељусти (лат. *maxillae*), усна (лат. *labium*)), укључујући детаљну површинску структуру и сете.

Мушке гениталије инсекта *Pheggomisetes ninae* инсекта су приказане на слици 3.8. Карактеристике мушког копулаторног органа су веома значајне у одређивању врсте организма па је зато мушки копулаторни орган (лат. *aedeagus*) веома често приказан и осликан у таксономским студијама. На слици 3.11, из бочног кадра едеагуса *Pheggomisetes ninae* инсекта се виде фини детаљи површинског рељефа, комплексна структура налик на зубе је видљива, а препознатљиви су и унутрашња врећица и веома окоштани делови едеагуса (ово је приказано на лонгитудиналним и попречним пресецима приказаним на сликама 3.11 а-г). Сви делови мушког репродуктивног органа су веома видљиви (средњи режањ, обе параметре са сетама, базална булба, копулаторни део, и унутрашња врећица). За све 4 фотографије (бр. 3.7, 3.8, 3.9 и 3.10) коришћена је побудна таласна дужина од 930 nm. Ова таласна дужина је изабрана да би се избегла флуоресценција резидуалног ткива заосталог после дисекције инсекта. Хитин релативно

слабо апсорбује радијацију на 930 nm, што је омогућило продирање ласерског зрачења дубље у тело инсекта и осликавање делова тела који се налазе испод кутикуле. Дубина продирања побудне ласерске радијације је процењена на 200  $\mu\text{m}$ . Све поменуте структуре су осликане са знатно више детаља у односу на светлосну или конфокалну микроскопију.



Слика 3.6. Спектар двофотонски побуђене флуоресценције хемијски чистог хитина и *Plusiocampa Christiani* кутикуле

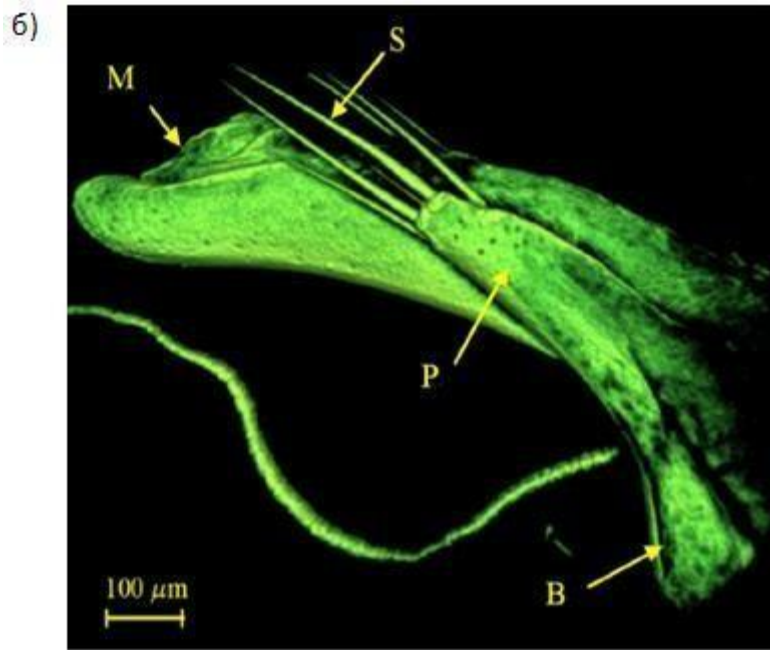


**Слика 3.7.** Нелинеарна ласерска микроскопија омогућава квалитетније осликавање хитинског узорка у поређењу са оптичком микроскопијом; а) фотографија са оптичког микроскопа, у светлом пољу, б) слика добијена двофотонски побуђеном флуоресценцијом хитина, на нелинеарном ласерском микроскопу. Слика је добијена коришћењем алгоритма пројекције максималног интензитета (опис алгоритма је дат у Материјалима и Методама) из скупа од 80 2Д фотографија, вертикално растојање између узастопних 2Д слика је 2 μm. Ове 2Д слике су

хоризонтални пресеци објекта и скуп ових слика се може приказати као транспарентан осликани објекат где се за разлику од реалног нетранспарентног објекта, може видети и његова унутрашња структура, што представља 3Д модел објекта. Ширина видног поља је 654  $\mu\text{m}$ . Обе слике су направљене 40X / 0.65 микроскопским објективом. А – антене, SK – склерити, SU – сuture, S – сете. На сликама је приказана дорзална страна главе *Plusiocampa christiani* инсекта.

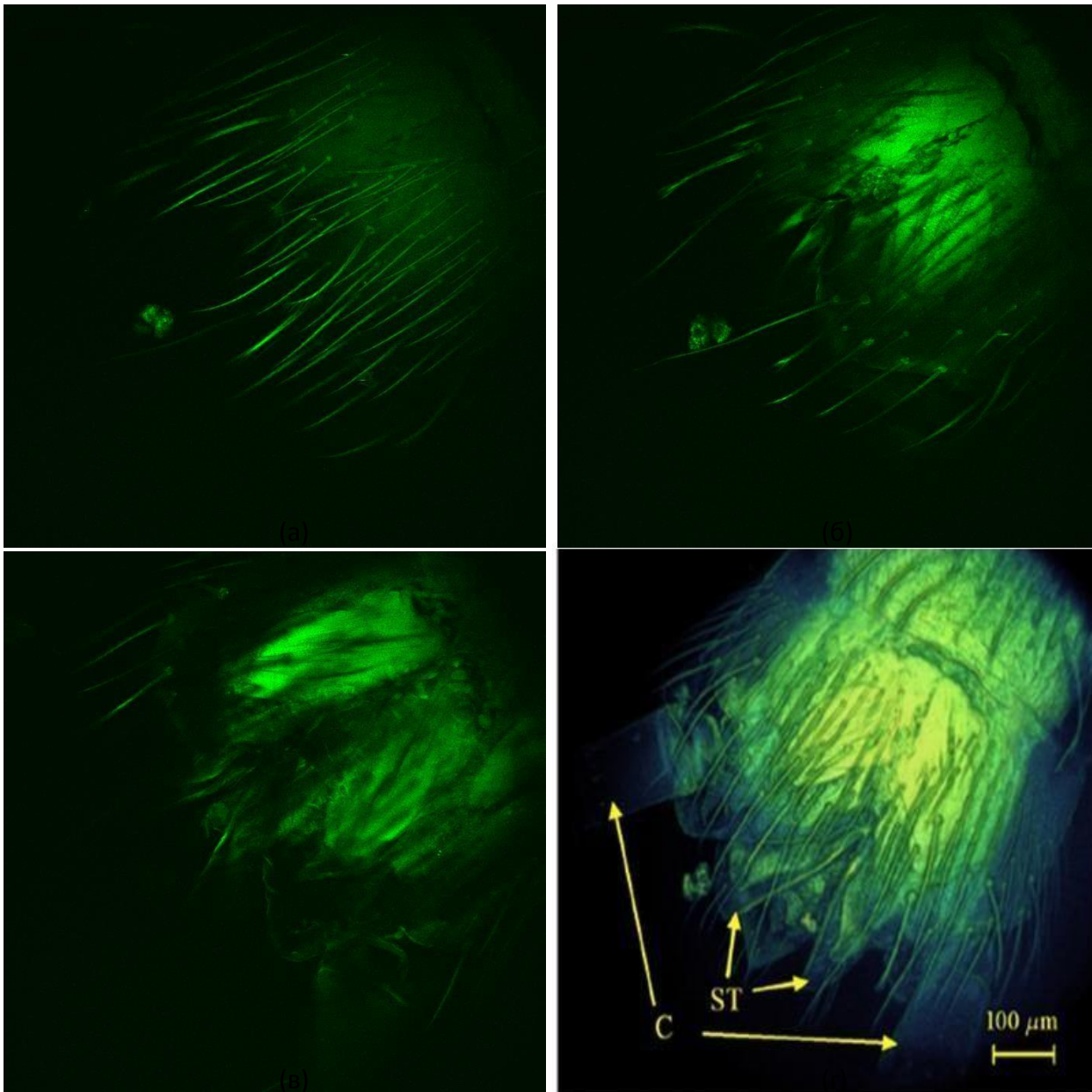
a)



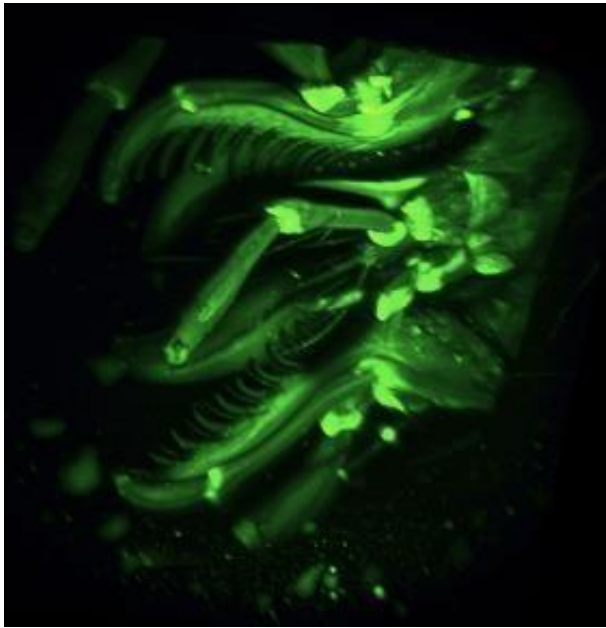


**Слика 3.8.** На овој слици су, као и на претходној (слика 3.7) представљене могућности нелинеарне ласерске микроскопије за квалитетније осликавање хитинског узорка. Нелинеарна микроскопија омогућава да се објекат ослика са много више детаља у поређењу са стандардном оптичком микроскопијом; а) фотографија са оптичког микроскопа, б) слика добијена двофотонски побуђеном флуоресценцијом хитина, на нелинеарном ласерском микроскопу. Слика је формирана на основу 120 2Д-слика уз помоћ VolView 3.4 софтвера, (вертикално) растојање између узастопних 2Д слика је 2  $\mu\text{m}$ . За обе слике је коришћен 40X / 0.65 микроскопски објектив. *Phegomysetes pinae* инсект, мушке гениталије у бочној перспективи; М – средњи режањ, Р – парамере, S – сете, В – базална булба.





**Слика 3.9.** Употреба алгоритма пројекције максималног интензитета у побољшању квалитета слике. Слика *д*) добијена је применом поменутог алгоритма на 80 хоризонталних пресека (на сликама *а*), *б*) и *в*) су приказана 3 пресека), вертикално растојање између узастопних пресека је 2  $\mu\text{m}$ . Слике су направљене 40X / 0.65 микроскопским објективом. На појединачним хоризонталним пресецима уочава се мање детаља у односу на коначну слику (*д*). Слике су добијене двофотонски побуђеном флуоресценцијом хитина, на нелинеарном ласерском микроскопу. На сликама је приказана дорзална страна задњег дела абдомена *Plusiocampa christiani* инсекта.



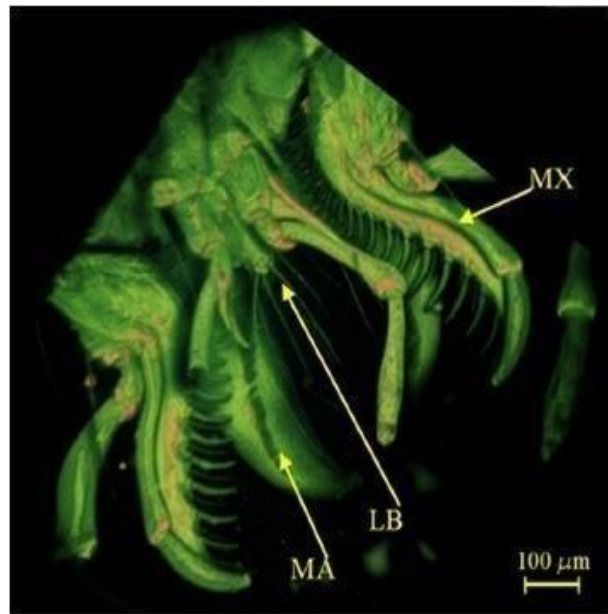
(a)



(б)



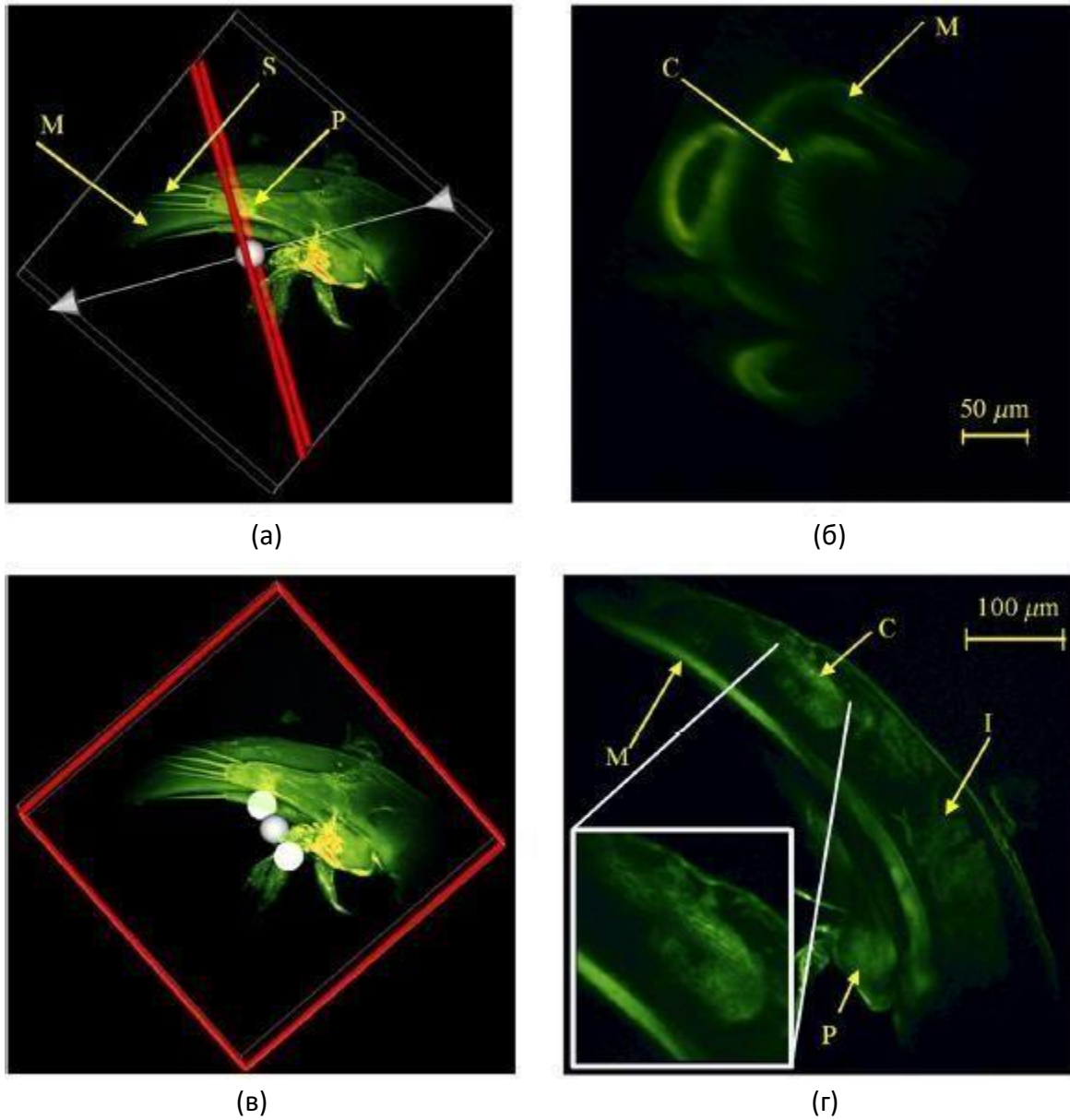
(в)



(г)

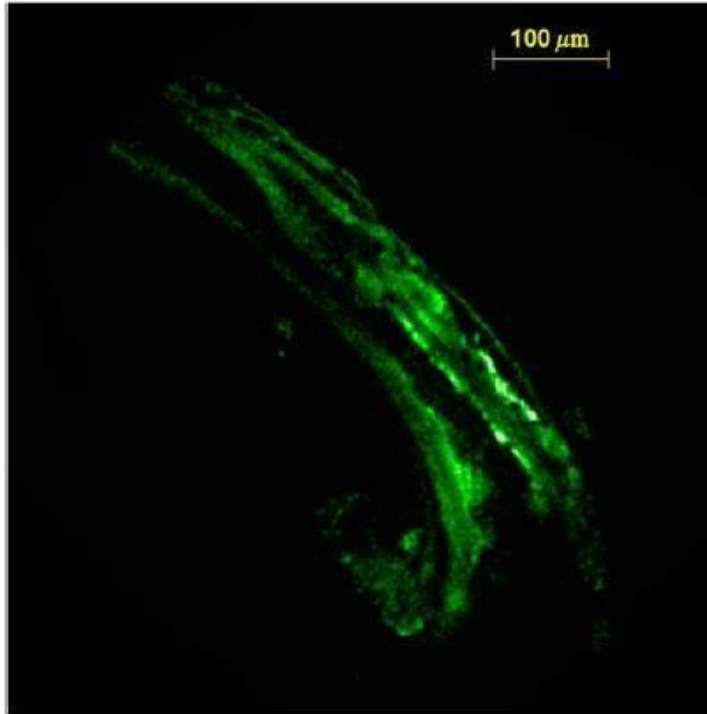
**Слика 3.10.** Приказ 3Д модела узорка, добијеног нелинеарном ласерском микроскопијом, под различитим угловима. Модел је формиран на основу 230 2Д-слика (добијених двофотонски побуђеном флуоресценцијом хитина) уз помоћ VolView 3.4 софтвера, (вертикално) растојање између узастопних 2Д слика је 2  $\mu\text{m}$ . Коришћен је 25X / 0.5 микроскопски објектив. Приказан је 3Д модел *Rheggomisetes pinae* инсекта, део његове главе са деловима усне регије, у вентралној перспективи. На слици г) су обележени карактеристични делови: MA – мандибула (доња вилица, лат. *mandibula*), MX – чељусту (лат. *maxillae*), LB – усна (лат. *labium*).

Одабиром адекватне побудне таласне дужине (840 – 930 nm или 1040 nm), могу се осликавати различити делови кутикуле, са различитим дубинама продирања ласерске радијације. На слици 3.12 је приказана унутрашња врећица репродуктивног органа *Pheggomisetes ninae* инсекта, осликана при побудној таласној дужини од 1040 nm и широкопојасној детекцији. Поређењем слика 3.11 г) и 3.12, уочавамо да су различите структуре осликане са различитим квалитетом на две различите побудне таласне дужине.



**Слика 3.11.** Могућност приказа 3Д модела узорка, добијеног нелинеарном ласерском микроскопијом, по различитим пресецима, на примеру пећинског инсекта *Pheggomisetes ninae*. Сlike су направљене 25X, NA 0.8, вода / глицерин имерзионим микроскопским објективом; а) мушке гениталије са приказаном равни попречног пресека (црвена линија), М – средњи режањ, Р – парамере, S – сете; б) одговарајући попречни пресек на коме се уочава средњи режањ М и копулаторни део С; в) мушке гениталије са означеном лонгитудиналном равни (црвени квадрат); г) одговарајући лонгитудинални пресек мушких гениталија, М- средњи режањ, Р –

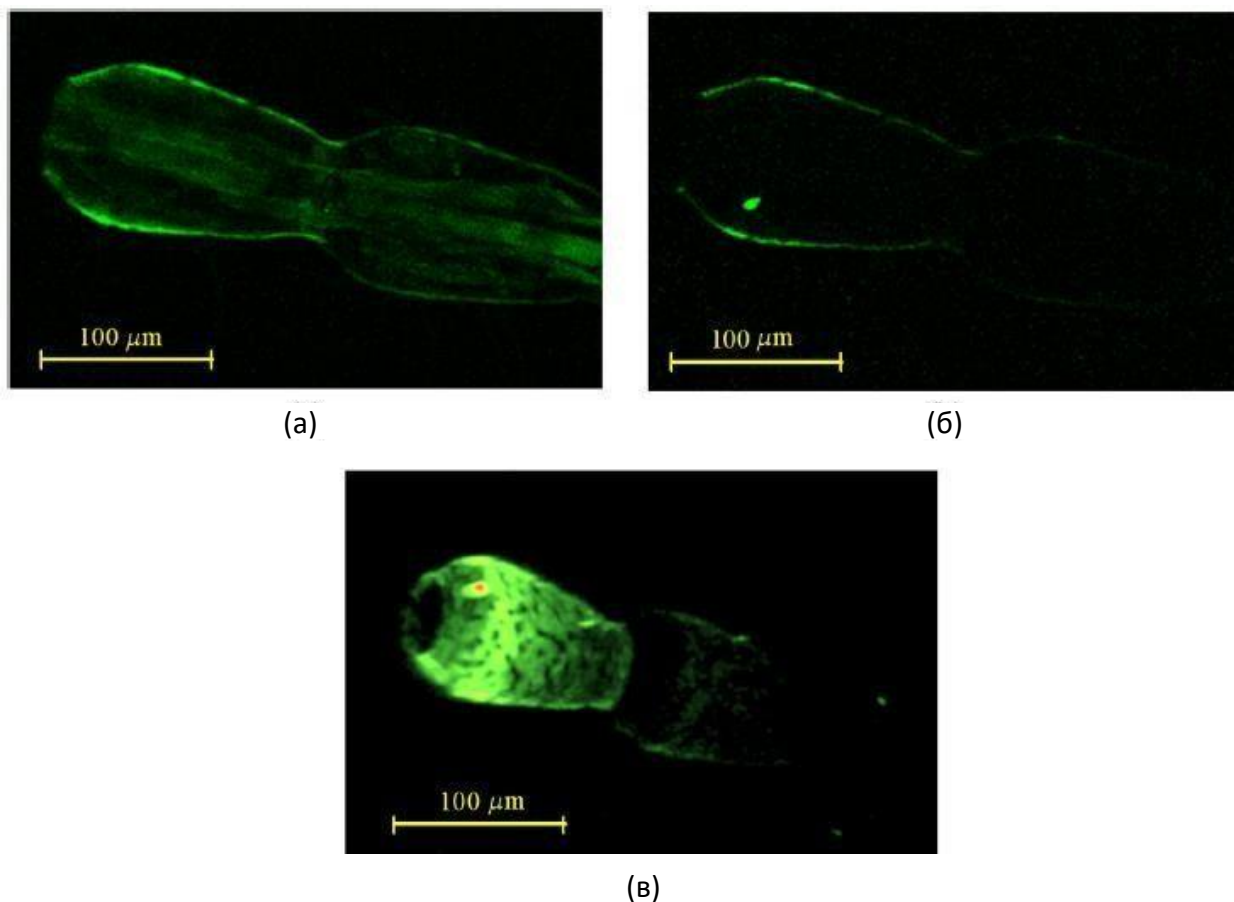
парамере, *I* – унутрашња врећица, *C* – копулаторни део. Уметак (бели квадрат): увећани копулаторни део са видљивом фином структуром, налик на површину зуба.



**Слика 3.12.** Промена таласне дужине омогућава да се виде различите структуре. Слика је добијена при побудној таласној дужини од 1040 nm и широко-појасној детекцији. У поређењу са сликом 3.11 г, која је снимљена на таласној дужини од 930 nm уочавају се различите структуре. На слици је приказана унутрашња врећица *Pheggomisetes ninae* едеагуса.

Постојање другог хармоника код природних хитинских структура као и његова употреба за осликавање су само успутно споменуте у референцама [336] и [337], без јаке експерименталне потврде. У овом истраживању, други хармоник је коришћен за осликавање хитина у кутикули инсекта. На пример, део антене инсекта *P. christiani* је осликан коришћењем другог хармоника и двофотонски побуђене флуоресценције (слика 3.13). Побудна таласна дужина је у оба случаја 840 nm. За детекцију двофотонски побуђене флуоресценције коришћен је широко-појасни филтер (400-700 nm, слика 3.13а), а за детекцију другог хармоника уско-појасни (420 nm, слика 3.13б) филтер. Са слике се може приметити да широко-појасна детекција омогућава осликавање финих детаља антене док уско-појасна детекција даје квалитетније осликавање ивица саме структуре. На основу слика добијених детекцијом другог хармоника формиран је 3Д модел антене инсекта (слика 3.13в). Сигнал другог хармоника је много слабији од флуоресценције на слици 3.13а, јер су и други хармоник и флуоресценција детектовани у рефлексији. Због тога није било потребе за коришћењем додатног филтера за елиминисање другог хармоника када је детектована флуоресценција.

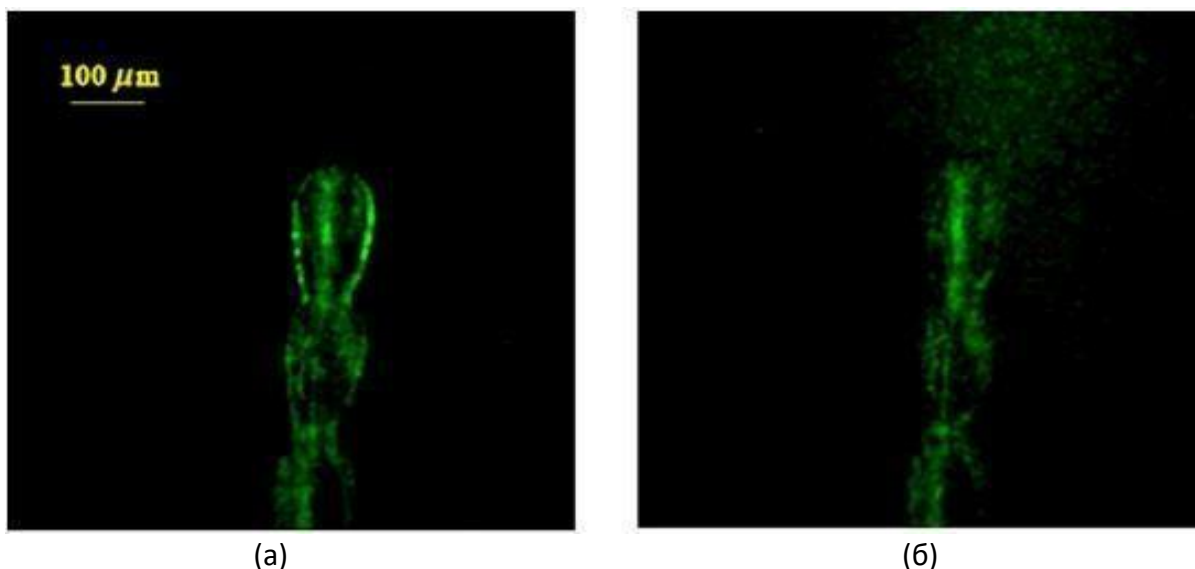
Због проучавања поларизационих ефеката, потврђено је да детекциони систем микроскопа није осетљив на поларизацију сигнала. Поларизациона елиптичност стечена у побудној грани микроскопа је занемарљива.



**Слика 3.13.** Разлике у осликавању хитинског узорка методама двофотонски побуђене флуоресценције и генерисања другог хармоника; а) побудна таласна дужина 840 nm и широко-појасна детекција у опсегу 400-700 nm; б) побудна таласна дужина 840 nm и уско-појасна детекција на 420 nm; в) запремиски приказ (“volume rendering”, објашњен у Материјалима и Методама) скупа слика добијених при побуди на 840 nm и детекцији на 420 nm. На сликама је приказан врх антене *Plusiocampa christiani* инсекта.

Познато је да зависност детектованог сигнала од поларизације побудне ласерске светлости може да указује на присуство другог хармоника у детектованом сигналу [339]. Међутим, у овом истраживању је откривено да су поларизациони ефекти уочљиви у оба случаја - када се као сигнал детектује други хармоник (840 nm побудна таласна дужина и детекција на 420 nm уско-појасним филтером) али и када је сигнал дво – фотонски побуђена флуоресценција (840 nm побудна таласна дужина и широко-појасна детекција у опсегу 400-700 nm). Због додатног истраживања овог феномена, у потпуности је елиминисан други хармоник коришћењем побуде на 850 nm и уско-појасне детекције на  $450 \pm 5$  nm. Чак и тада, јасно је уочљива зависност флуоресценције узорка од поларизације побудног ласерског зрачења (слика 3.14 на којој се види део антене *P. christiani* инсекта усликан са две ортогонално поларизоване побуде). Уочено је да се интензитет сигнала као и однос сигнал-шум могу значајно изменити ротацијом равни поларизације побудне ласерске радијације. Ова појава није честа, нити је у потпуности објашњена. Молекули хитина нису симетрични и имају одређену оријентацију (ови молекули имају облик влакна и груписани су у снопове), што може бити узрок различитих

интензитета сигнала и односа сигнал-шум. У складу са референцама [338] и [340], ово може се искористити за разликовање карактеристика узорка или процеса.



**Слика 3.14.** Зависност двофотонски побуђене флуоресценције узорка од поларизације побудног ласерског зрачења; а) хоризонтална поларизација; б) вертикална поларизација побудне ласерске радијације. На сликама је приказан врх антене *Plusiocampa christiani* инсекта.

У овом истраживању, за осликавање хитинских структура био је довољан мали део доступне снаге побудног ласера. Ако се повећа снага ласерске радијације (изнад 20 – 30 mW на површини узорка) долази до ласерског оштећења (термални ефекти отпаравања, топљење, промена хемијске структуре - карбонизација) појединих делова кутикуле и откривања унутрашњих делова тела инсекта. Овај вид ласерске хирургије ткива треба радити веома пажљиво, у смислу постепеног повећања интензитета снаге ласерске радијације, да би се локализовало ласерски индуковано оштећење. Ово ће бити предмет будућих истраживања.

У току истраживања, уочено је неколико експерименталних проблема којима је потребно веома пажљиво приступити када се снимају хитинске структуре инсеката. Узорци треба да буду фиксирани за микроскопско постолје материјалом који не флуоресцира. Откривено је да је глицерин погоднији од Канада балзама, који показује висок ниво ауто - флуоресценције. Инсекти попут *P. christiani* су пре снимања потопљени у уље, да би се ткиво конзервирало. Није детектована значајна ауто-флуоресценција уља нити промена флуоресцентних особина узорка после третмана (потапања у уље).

У овом истраживању су коришћени само мртви инсекти, али може се без проблема радити и са живим узорцима. То је експериментално потврђено. Уколико се адекватно контролише снага побудне ласерске радијације откривено је да она није опасна, чак и за веома осетљива ткива као што су инсектове очи - посматране су и осликане *in vivo* оматидије (основне јединице композитног ока инсеката) неколико инсеката без штетних ефеката ласерског зрачења. Ово је такође предмет будућих истраживања.

Током експеримената, истраживане су и друге врсте инсеката: *Apatura ilia*(Denis & Schiffermüller, 1775), *A. iris*(Linnaeus, 1758), *Pieris rapae*(Linnaeus, 1758)... Потврђено је да сви испитивани инсекти флуоресцирају приликом озрачивања ласерском радијацијом. Интензитет

сигнала је варирао, у зависности од дела тела инсекта и од врсте инсекта. Резултати потврђују погодност и ефикасност нелинеарне ласерске микроскопије хитина за примене у ентомологији, узимајући у обзир дубину продирања ласерске радијације, контролисано фото-избелјивање узорка и одсуство потребе за бојењем узорка флуоресцентним бојама (нпр. *calcofluor white*, родамин Б, родамин бГ, флуоресцеин...).

## Биографија

Владимир Лазовић је рођен 12.05.1986.-е године у Београду. После завршене средње школе, Девете београдске гимназије, уписује Физички факултет у Београду, 2005.-е године, смер Примењена физика и информатика. Дипломирао је 2012.-е године са просечном оценом 8,77. Исте године уписује докторске студије на Физичком факултету Универзитета у Београду, смер Квантна оптика и ласери, и постаје истраживач приправник у Центру за фотонику Института за физику у Београду, где ради и данас. Био је ангажован на пројекту Министарства просвете, науке и технолошког развоја под називом: „Генерисање и карактеризација нанофотонских функционалних структура у биомедицини и информатици“. 2015.-е године изабран је у звање истраживач сарадник. Бави се оптичком, електронском и нелинеарном микроскопијом. Истражује интеракцију светлости и материје, са акцентом на природне микронске и нанометарске фотонске структуре, и практичне примене ових структура. До сада је објавио 16 радова у међународним часописима (M21, M22 и M23), 1 патент признат на међународном нивоу, и две патентне пријаве.



Прилог 1.

## Изјава о ауторству

Име и презиме аутора Владимир Лазовић

Број индекса 8015 / 2019

### Изјављујем

да је докторска дисертација под насловом

Оптичке и флуоресцентне особине хитина и хитинских микроструктура биолошког порекла

---

---

- резултат сопственог истраживачког рада;
- да дисертација у целини ни у деловима није била предложена за стицање друге дипломе према студијским програмима других високошколских установа;
- да су резултати коректно наведени и
- да нисам кршио/ла ауторска права и користио/ла интелектуалну својину других лица.

**Потпис аутора**

У Београду, 25. 4. 2022.

---

Прилог 2.

## Изјава о истоветности штампане и електронске верзије докторског рада

Име и презиме аутора Владимир Лазовић

Број индекса 8015 / 2019

Студијски програм Фотоника и ласери

Наслов рада Оптичке и флуоресцентне особине хитина и хитинских микроструктура биолошког порекла

Ментор Дејан Пантелић

Изјављујем да је штампана верзија мог докторског рада истоветна електронској верзији коју сам предао/ла ради похрањена у **Дигиталном репозиторијуму Универзитета у Београду**.

Дозвољавам да се објаве моји лични подаци везани за добијање академског назива доктора наука, као што су име и презиме, година и место рођења и датум одбране рада.

Ови лични подаци могу се објавити на мрежним страницама дигиталне библиотеке, у електронском каталогу и у публикацијама Универзитета у Београду.

**Потпис аутора**

У Београду, 25. 4. 2022.

---

## Изјава о коришћењу

Овлашћујем Универзитетску библиотеку „Светозар Марковић“ да у Дигитални репозиторијум Универзитета у Београду унесе моју докторску дисертацију под насловом:

Оптичке и флуоресцентне особине хитина и хитинских микроструктура биолошког порекла

---

која је моје ауторско дело.

Дисертацију са свим прилозима предао/ла сам у електронском формату погодном за трајно архивирање.

Моју докторску дисертацију похрањену у Дигиталном репозиторијуму Универзитета у Београду и доступну у отвореном приступу могу да користе сви који поштују одредбе садржане у одабраном типу лиценце Креативне заједнице (Creative Commons) за коју сам се одлучио/ла.

1. Ауторство (CC BY)
2. Ауторство – некомерцијално (CC BY-NC)
3. Ауторство – некомерцијално – без прерада (CC BY-NC-ND)
4. Ауторство – некомерцијално – делити под истим условима (CC BY-NC-SA)
5. Ауторство – без прерада (CC BY-ND)
6. Ауторство – делити под истим условима (CC BY-SA)

(Молимо да заокружите само једну од шест понуђених лиценци.

Кратак опис лиценци је саставни део ове изјаве).

**Потпис аутора**

У Београду, 25. 4. 2022.

---

1. **Ауторство.** Дозвољаваате умножавање, дистрибуцију и јавно саопштавање дела, и прераде, ако се наведе име аутора на начин одређен од стране аутора или даваоца лиценце, чак и у комерцијалне сврхе. Ово је најслободнија од свих лиценци.

2. **Ауторство – некомерцијално.** Дозвољаваате умножавање, дистрибуцију и јавно саопштавање дела, и прераде, ако се наведе име аутора на начин одређен од стране аутора или даваоца лиценце. Ова лиценца не дозвољава комерцијалну употребу дела.

**3. Ауторство – некомерцијално – без прерада.** Дозвољаваће умножавање, дистрибуцију и јавно саопштавање дела, без промена, преобликовања или употребе дела у свом делу, ако се наведе име аутора на начин одређен од стране аутора или даваоца лиценце. Ова лиценца не дозвољава комерцијалну употребу дела. У односу на све остале лиценце, овом лиценцом се ограничава највећи обим права коришћења дела.

**4. Ауторство – некомерцијално – делити под истим условима.** Дозвољаваће умножавање, дистрибуцију и јавно саопштавање дела, и прераде, ако се наведе име аутора на начин одређен од стране аутора или даваоца лиценце и ако се прерада дистрибуира под истом или сличном лиценцом. Ова лиценца не дозвољава комерцијалну употребу дела и прерада.

**5. Ауторство – без прерада.** Дозвољаваће умножавање, дистрибуцију и јавно саопштавање дела, без промена, преобликовања или употребе дела у свом делу, ако се наведе име аутора на начин одређен од стране аутора или даваоца лиценце. Ова лиценца дозвољава комерцијалну употребу дела.

**6. Ауторство – делити под истим условима.** Дозвољаваће умножавање, дистрибуцију и јавно саопштавање дела, и прераде, ако се наведе име аутора на начин одређен од стране аутора или даваоца лиценце и ако се прерада дистрибуира под истом или сличном лиценцом. Ова лиценца дозвољава комерцијалну употребу дела и прерада. Слична је софтверским лиценцама, односно лиценцама отвореног кода.